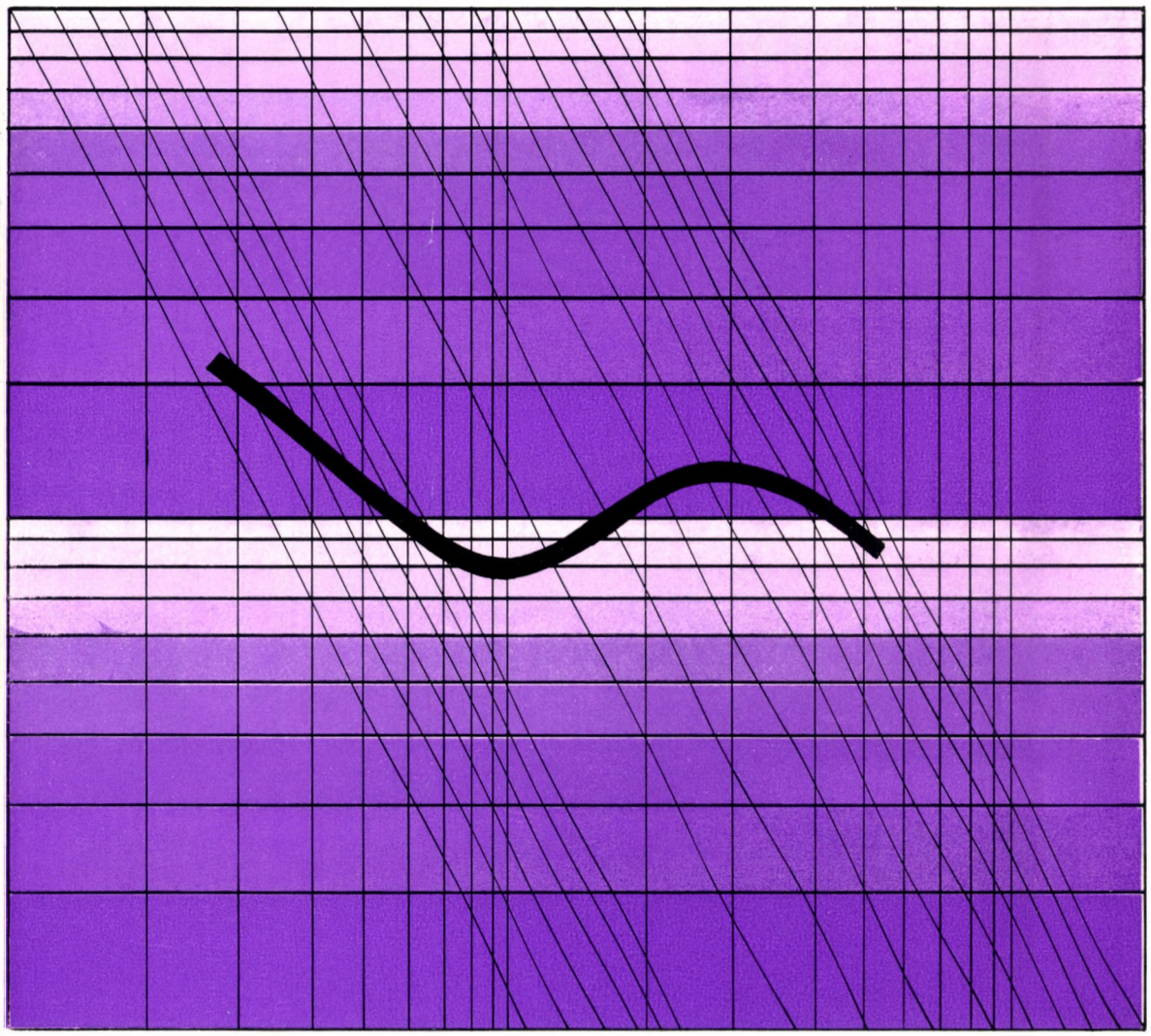
Editor-in-Chief

A. ÁDÁM

Geoelectric and Geothermal Studies

KAPG GEOPHYSICAL MONOGRAPH



AKADÉMIAI KIADÓ BUDAPEST

GEOELECTRIC AND
GEOTHERMAL STUDIES
(EAST-CENTRAL EUROPE,
SOVIET ASIA)

KAPG GEOPHYSICAL MONOGRAPH

Editor-in-Chief: A. ÁDÁM

Physical studies of the Earth, and especially of its upper mantle unavoidably meet problems either implicitly or explicitly in which the distribution of thermal energy has a dominant role. Therefore, the knowledge of the amount of heat flowing through the Earth's surface is of fundamental importance in geophysics. The very strong dependence of electrical conductivity on temperature makes the electromagnetic induction studies a very important tool for the investigation of geothermal activity in the depth.

This monograph contains the main results in geothermics and magnetotellurics in the socialist (so-called KAPG) countries during the last ten years. The monograph brings together in a series of articles a comprehensive presentation of both theoretical and practical aspects of these geophysical disciplines and their interpretation.

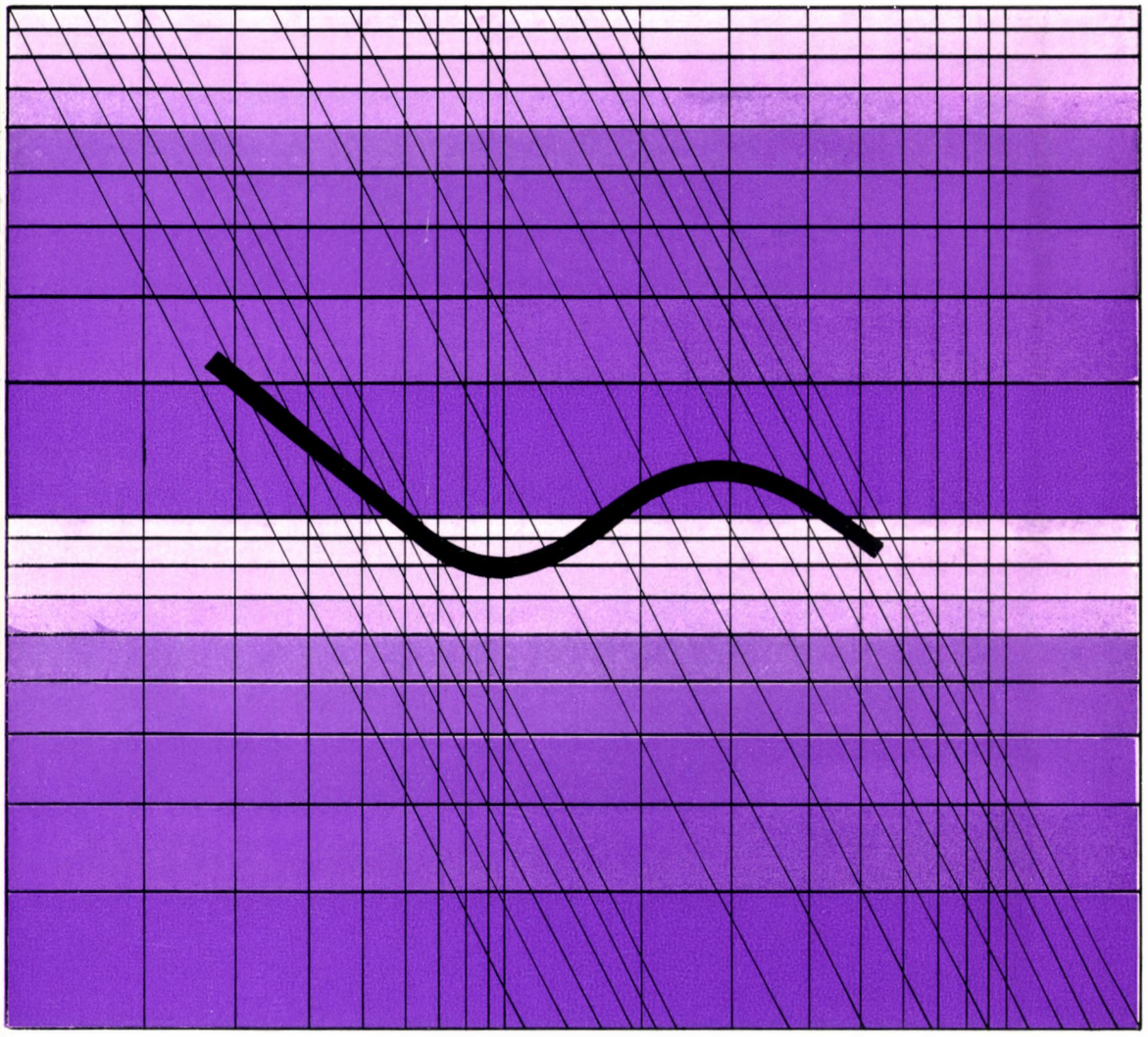
AKADÉMIAI KIADÓ
PUBLISHING HOUSE
OF THE HUNGARIAN ACADEMY OF SCIENCES
BUDAPEST

Editor-in-Chief

A. ÁDÁM

Geoelectric and Geothermal Studies

KAPG GEOPHYSICAL MONOGRAPH



AKADÉMIAI KIADÓ BUDAPEST

GEOELECTRIC AND
GEOTHERMAL STUDIES
(EAST-CENTRAL EUROPE,
SOVIET ASIA)

KAPG GEOPHYSICAL MONOGRAPH

Editor-in-Chief: A. ÁDÁM

Physical studies of the Earth, and especially of its upper mantle unavoidably meet problems either implicitly or explicitly in which the distribution of thermal energy has a dominant role. Therefore, the knowledge of the amount of heat flowing through the Earth's surface is of fundamental importance in geophysics. The very strong dependence of electrical conductivity on temperature makes the electromagnetic induction studies a very important tool for the investigation of geothermal activity in the depth.

This monograph contains the main results in geothermics and magnetotellurics in the socialist (so-called KAPG) countries during the last ten years. The monograph brings together in a series of articles a comprehensive presentation of both theoretical and practical aspects of these geophysical disciplines and their interpretation.

AKADÉMIAI KIADÓ
PUBLISHING HOUSE
OF THE HUNGARIAN ACADEMY OF SCIENCES
BUDAPEST

GEOELECTRIC AND GEOTHERMAL STUDIES

KAPG GEOPHYSICAL MONOGRAPH

Editorial board:

M. N. BERDICHEVSKY (Moscow), V. ČERMÁK (Prague),
G. FANSELAU (Potsdam), E. A. LUBIMOVA (Moscow),
CH. OELSNER (Freiberg), G. PORSTENDORFER (Freiberg),
L. STEGENA (Budapest), J. VERŐ (Sopron), M. P. VOLAROVICH
(Moscow)

GEOELECTRIC AND GEOTHERMAL STUDIES

(EAST-CENTRAL EUROPE, SOVIET ASIA)

KAPG GEOPHYSICAL MONOGRAPH

Editor-in-chief:

A. ÁDÁM

Geodetical and Geophysical Research Institute,
Hungarian Academy of Sciences, Sopron

AKADÉMIAI KIADÓ, BUDAPEST 1976

Assistant Editors:

CZ. J. MILETITS and Á. WALLNER

ISBN 963 05 0887 7

© Akadémiai Kiadó, Budapest 1976

Printed in Hungary

CONTRIBUTORS

A. Ádám	Geodetical and Geophysical Research Institute, Hungarian Academy of Sciences, Sopron, Hungary
I. M. Alperovich	Sakhalin Geological Office, Yuzhno-Sakhalinks, USSR
V. K. Amirov	Institute of Geophysics, Ukrainian Academy of Sciences, Kiev, USSR
G. N. Anishchenko	Spetsgeofizika Trust, Povarovo Moskovskoj Oblasti, USSR
T. Ashirov	Institute of Physics of the Earth and the Atmosphere, Turkmen Academy of Sciences, Ashkhabad, USSR
A. A. Avagimov	Institute of Physics of the Earth and the Atmosphere, Turkmen Academy of Sciences, Ashkhabad, USSR
L. Ballani	Central Institute of Physics of the Earth, Academy of Sciences of the GDR, Potsdam, GDR
V. T. Balobaev	Institute of Permafrost, Siberian Branch, USSR Academy of Sciences, Yakutsk, USSR
M. N. Berdichevsky	Moscow State University, Moscow, USSR
A. I. Bilinsky	Institute of Mathematics, Ukrainian Academy of Sciences, Lvov, USSR
A. P. Bondarenko	Institute of Mathematics, Ukrainian Academy of Sciences, Lvov, USSR
V. V. Borets	Far Eastern Scientific Center, USSR Academy of Sciences, SAKHKNII, Yuzhno-Sakhalinsk, Novo-Aleksandrovsk, USSR
G. I. Buachidze	Gruzian Polytechnical University Tbilisi, USSR
V. M. Bubnov	Krasnoyarsk Geological Office, Krasnoyarsk, USSR
V. P. Bubnov	VNIIGEOFIZIKA, Moscow, USSR
G. Buntebarth	Polytechnical University Clausthal, Institute of Geophysics, Clausthal-Zellerfeld, FRG
V. Čermák	Geophysical Institute, Czechoslovak Academy of Sciences, Prague, Czechoslovakia
G. A. Chernyavsky	VNIIGEOFIZIKA, Moscow, USSR
N. D. Chicherina	Leningrad State University, Leningrad, USSR
O. M. Chinareva	VNIIGEOFIZIKA, Moscow, USSR
N. A. Deniskin	Institute of Physics of the Earth, USSR Academy of Sciences, Moscow, USSR
V. N. Devyatkin	Institute of Permafrost, Siberian Branch, USSR Academy of Sciences, Yakutsk, USSR
M. A. Dobrovolskaya	Leningrad State University, Leningrad, USSR
V. I. Dmitriev	Moscow State University, Moscow, USSR
V. G. Dubrovsky	Institute of Physics of the Earth and the Atmosphere, Turkmen Academy of Sciences, Ashkhabad, USSR
G. Fanselau	Central Institute of Physics of the Earth, Academy of Sciences of the GDR, Potsdam, GDR
I. S. Feldman	Institute of Physics of the Earth, USSR Academy of Sciences, Moscow, USSR
G. A. Fonarev	IZMIR, USSR Academy of Sciences, Krasnaya Pakhra, Moskovskoj Oblasti, USSR
W. Göthe	Mining Academy, Department of Earth Sciences Freiberg, GDR

A. Grafe	Central Institute of Solar-terrestrial Physics, Academy of Sciences of the GDR, Berlin, GDR
E. Hurtig	Central Institute of Physics of the Earth, Academy of Sciences of the GDR, Potsdam, GDR
E. P. Kharin	Soviet Geophysical Committee, Moscow, USSR
P. Kisházi	Mining Research Institute, Division of Petrography, Sopron, Hungary
Yu. K. Konnov	Spetsgeofizika Trust, Povarovo, Moskovskoj Oblasti, USSR
A. A. Kovtun	Leningrad State University, Leningrad, USSR
A. G. Krasnobaeva	Institute of Geophysics, Ural Research Centre, USSR Academy of Sciences, Sverdlovsk, USSR
M. Krešl	Geophysical Institute, Czechoslovak Academy of Sciences, Prague, Czechoslovakia
S. N. Kulik	Institute of Geophysics, Ukrainian Academy of Sciences, Kiev, USSR
R. I. Kutas	Institute of Geophysics, Ukrainian Academy of Sciences, Kiev, USSR
I. M. Kutasov	Institute of Permafrost, Siberian Branch, USSR Academy of Sciences, Yakutsk, USSR
K. Lengning	Central Institute of Physics of the Earth, Academy of Sciences of the GDR, Potsdam, GDR
N. V. Lipskaya	Institute of Physics of the Earth, USSR Academy of Sciences, Moscow, USSR
I. M. Logvinov	Institute of Geophysics, Ukrainian Academy of Sciences, Kiev, USSR
E. A. Lubimova	Institute of Physics of the Earth, USSR Academy of Sciences, Moscow, USSR
A. M. Lyapishev	Far Eastern Scientific Center, USSR Academy of Sciences, SAKHKNII, Yuzhno-Sakhalinsk, USSR
S. V. Lysak	Institute of the Earth's Crust, Siberian Branch, USSR Academy of Sciences, Irkutsk, USSR
V. M. Lyuboshits	Institute of Physics of the Earth, USSR Academy of Sciences, Moscow, USSR
J. Majorowicz	Geological Institute, Department of Geophysics, Warsaw, Poland
B. E. Marderfeld	Far Eastern Scientific Center, USSR Academy of Sciences, SAKHKNII, Yuzhno-Sakhalinsk, USSR
P. I. Melnikov	Institute of Permafrost, Siberian Branch, USSR Academy of Sciences, Yakutsk, USSR
V. I. Mikhalevsky	VOSTSIBNIIGGIMS, Irkutsk, USSR
Cz. J. Miletits	Geodetical and Geophysical Research Institute, Hungarian Academy of Sciences, Sopron, Hungary
Yu. F. Moroz	East-Siberian Geophysical Trust, Irkutsk, USSR
K. Nepesov	Institute of Physics of the Earth and the Atmosphere, Turkmen Academy of Sciences, Ashkhabad, USSR
N. N. Nikiforova	Institute of Physics of the Earth, USSR Academy of Sciences, Moscow, USSR
V. N. Nikitina	Institute of Physics of the Earth, USSR Academy of Sciences, Moscow, USSR
Ch. Oelsner	Mining Academy, Department of Earth Sciences Freiberg, GDR
E. I. Parkhomenko	Institute of Physics of the Earth, USSR Academy of Sciences, Moscow, USSR
J. Pěčová	Geophysical Institute, Czechoslovak Academy of Sciences, Prague, Czechoslovakia
I. Petkov	University of Sofiя, Faculty of Physics, Sofia, Bulgaria
V. Petr	Geophysical Institute, Czechoslovak Academy of Sciences, Prague, Czechoslovakia
S. Plewa	Oil Institute, Department of Geophysics, Cracow, Poland
G. Porstendorfer	Mining Academy, Department of Earth Sciences Freiberg, GDR

V. I. Pospeev	VOSTSIBNIIGGIMS, Irkutsk, USSR
O. Praus	Geophysical Institute, Czechoslovak Academy of Sciences, Prague, Czechoslovakia
E. Ritter	Central Institute of Physics of the Earth, Academy of Sciences of the GDR, Potsdam, GDR
A. V. Rodionov	Far Eastern Scientific Center, USSR Academy of Sciences, SAKHKNII, Yuzhno-Sakhalinsk, USSR
I. I. Rokityansky	Institute of Geophysics, Ukrainian Academy of Sciences, Kiev, USSR
T. L. Rudneva	Moscow State University, Moscow, USSR
A. S. Safonov	VNIIGEOFIZIKA, Moscow, USSR
P. Schlosser	VEB Geophysik, Leipzig, GDR
U. Seipold	Central Institute of Physics of the Earth, Academy of Sciences of the GDR, Potsdam, GDR
V. A. Shaporev	Krasnoyarsk Geological Office, Krasnoyarsk, USSR
G. I. Shtekh	Yakutsk Geological Office, Yakutsk, USSR
V. N. Shuman	Institute of Geophysics, Ukrainian Academy of Sciences, Kiev, USSR
Ya. B. Smirnov	Institute of Geology, USSR Academy of Sciences, Moscow, USSR
L. S. Sokolova	Institute of Geology and Geophysics, Siberian Branch, USSR Academy of Sciences, Novosibirsk, USSR
L. Stegena	Eötvös Loránd University, Institute of Cartography, Budapest, Hungary
B. K. Sysoev	Geological Office, Tyumen, USSR
E. Takács	Polytechnical University for Heavy Industry, Institute of Geophysics, Miskolc-Egyetemváros, Hungary
R. Tanzer	Polytechnical University Dresden, Computing Center, Dresden, GDR
G. A. Tomara	Institute of Physics of the Earth, USSR Academy of Sciences, Moscow, USSR
R. Treumann	Central Institute of Solar-terrestrial Physics, Academy of Sciences of the GDR, Berlin, GDR
I. L. Trofimov	IZMIR, USSR Academy of Sciences, Krasnaya Pakhra, Moskovskoj Oblasti, USSR
L. L. Vanyan	Institute of Oceanography, USSR Academy of Sciences, Moscow, USSR
D. A. Varlamov	Spetsgeofizika Trust, Povarovo, Moskovskoj Oblasti, USSR
T. Velinov	University of Sofia, Faculty of Physics, Sofia, Bulgaria
J. Verő	Geodetical and Geophysical Research Institute, Hungarian Academy of Sciences, Sopron, Hungary
V. S. Vishnev	Institute of Geophysics, Ural Research Center, USSR Academy of Sciences, Sverdlovsk, USSR
N. P. Vladimirov	Institute of Physics of the Earth, USSR Academy of Sciences, Moscow, USSR
M. P. Volarovich	Institute of Physics of the Earth, USSR Academy of Sciences, Moscow, USSR
M. Węsierska	Oil Institute, Department of Geophysics, Cracow, Poland
I. A. Yakovlev	VNIIGEOFIZIKA, Moscow, USSR

CONTENTS

Preface 13

Chapter 1

COLLECTING AND PROCESSING OF GEOTHERMAL DATA

(Edited by Ch. Oelsner)

Ch. Oelsner: Introduction to Chapter 1 17
E. A. Lubimova, G. A. Tomara: Methods of marine geothermal investigations 19
Ch. Oelsner: Possibilities and limitations of infrared surface geothermics 25
M. Krešl: The measurement of thermal conductivity of rocks by means of an automatic apparatus 38
U. Seipold: The measurement of the pressure-dependence of the thermal diffusivity in rocks 44
S. Plewa: Correlation between thermal conductivity and other physical parameters of rocks 48
V. Čermák: Processing of heat flow data — thermal conductivity and temperature gradient 53
V. Čermák: Paleoclimatic effect on the underground temperature and some problems of correcting heat flow 59
Ch. Oelsner: Numerical solution of the direct problem of geothermics 67
E. A. Lubimova, V. M. Lyuboshits, V. N. Nikitina: Effect of contrasts in the physical properties on the heat flow and electromagnetic profiles 72

Chapter 2

COLLECTING OF GEOELECTRIC DATA; THEORY, DATA PROCESSING, LIMITATIONS

(Edited by G. Fanselau and G. Porstendorfer)

G. Fanselau, G. Porstendorfer: Introduction to Chapter 2 103
I. I. Rokityansky, S N. Kulik, V. N. Shuman: Theoretical fundaments of magnetic variation profiling (MVP) 105
R. Treumann: On the geomagnetic induction problem 124
I. I. Rokityansky: The technique of magnetic variation profiling data analysis 141
G. Porstendorfer: Electromagnetic field components and magnetotelluric sounding curves above horizontally inhomogeneous or anisotropic model media (Catalogue of models) 152
M. N. Berdichevsky, V. I. Dmitriev: Basic principles of interpretation of magnetotelluric sounding curves 165
V. Petr: Impedance of the electromagnetic field in a horizontally layered anisotropic half-space 222
O. Praus: Numerical solutions of the MT field in inhomogeneous structures 231
M. A. Dobrovolskaya, A. A. Kovtun: Behaviour of magnetotelluric field on the surface of horizontal inhomogeneous strata (model experiments) 245
A. Ádám, J. Verő: Magnetotelluric data processing methods 256
E. Takács: The role of the vertical pulsations of the magnetic field in magnetotelluric measurements 264

A. Grafe: Distribution of current density and homogeneity of the substorm field 274
A. Ádám, Cz. J. Miletits, J. Verő: Inhomogeneity of the pulsation field and its effect on the MT values 296
G. Fanselau, L. Ballani: Complex interpretation by means of physical fields; homology relations 303

Chapter 3

ELECTRICAL PROPERTIES OF ROCKS AT HIGH TEMPERATURES AND PRESSURES

(By M. P. Volarovich and E. I. Parkhomenko)

Electrical resistivity of rocks forming the sedimentary cover of the earth's crust depending on different factors 321
The effect of various factors on electrical resistivity of moisture-containing crystalline rocks 323
Brief summary of the theory of electrical conductivity of different materials 328
Electrical resistivity of minerals at high pressures and temperatures 332
Electrical resistivity of crystalline rocks of the „granite" and the „basalt" layers of the earth's crust in a wide temperature range 338
Electrical resistivity of rocks of ultrabasic composition at high temperatures and pressures 350
Serpentinization effect 351
Electrical resistivity of xenoliths, of ultrabasic rocks and of eclogites 355
Electrical resistivity of the "mantle" and the "crustal" eclogites 357
The effect of pressure on the electrical resistivity of different rocks at high temperatures 358
Electrical resistivity distribution in the earth's crust and upper mantle from laboratory data on rocks 362

Chapter 4

GEOTHERMAL DATA AND THEIR COMPLEX INTERPRETATION ON TEST AREAS

(Edited by V. Čermák)

V. Čermák: Introduction to Chapter 4 373
V. Čermák, E. A. Lubimova: Heat flow map of Central and Eastern Europe (1 : 10,000,000) 376
L. Stegena: Geothermal temperature map of Central and Eastern Europe 381
E. Hurtig, P. Schlosser: Geothermal studies in the GDR and relations to the geological structure 384
E. Hurtig, P. Schlosser: Vertical changes of the heat flow in boreholes in the North-German sedimentary basin 395
J. Majorowicz, S. Plewa, M. Węsierska: The terrestrial thermal field in Poland 402
V. Čermák: Heat flow investigation in Czechoslovakia 414
L. Stegena: The variation of temperature with depth in the Pannonian Basin 425
T. Velinov, I. Petkov: Some results of the geothermal investigations in Bulgaria 439
R. I. Kutas, E. A. Lubimova, Ya. B. Smirnov: Heat flow map of the European part of the USSR and its geological and geophysical interpretation 443
G. I. Buachidze: Interpretation of heat flow data in Georgia 450
S. V. Lysak: Heat flow geology and geophysics in the Baikal Rift zone and adjacent regions 455
L. S. Sokolova: Temperatures, heat flow and heat generation in South and West Siberia and Kamchatka 463
P. I. Melnikov, V. T. Balobaev, I. M. Kutasov, V. N. Devyatkin: Heat flow investigation in permafrost regions 473

Chapter 5

DEEP ELECTROMAGNETIC INVESTIGATIONS AND THEIR GEOTHERMIC INTERPRETATION ON TEST AREAS

(Edited by A. Ádám and M. N. Berdichevsky)

A. Ádám: Introduction to Chapter 5 483

I. German-Polish Sedimentary Basin 485

G. Porstendorfer, W. Göthe, K. Lengning, Ch. Oelsner, R. Tanzer, E. Ritter: Nature and possible causes of the anomalous behaviour of electric conductivity in the north of the GDR, Poland and the FRG 487
G. Fanselau: Splitting of magnetic fields into external and internal parts (S_q anomaly in the GDR) 501
Ch. Oelsner: Vertical temperature distribution in the North-German–Polish sedimentary basin and its relation to the North-German–Polish conductivity anomaly 509

II. Czechoslavakia 515

J. Pěčová, V. Petr, O. Praus: Depth distribution of the electric conductivity in Czechoslovakia from electromagnetic studies 517
V. Čermák, J. Pěčová, O. Praus: Heat flow, crustal temperatures and geoelectric cross-section in Czechoslovakia 538

III. Pannonian Basin 543

P. Kisházi: Hungary's geology: an outline 545
A. Ádám: Results of deep electromagnetic investigations 547
G. Buntebarth: Temperature calculations on the Hungarian seismic profile-section NP-2 561
A. Ádám: Connection between geoelectric and geothermal parameters in the earth 567
L. Stegena: Geothermics, magnetotellurics and tectonophysics of the Pannonian Basin 572

IV. East Carpathians 587

A. P. Bondarenko, A. I. Bilinsky: Anomaly of the geomagnetic bays in the East Carpathians 589
A. P. Bondarenko, R. I. Kutas: Geomagnetic sounding with S_q and geothermics in the East Carpathians 600
I. I. Rokityansky, V. K. Amirov, S. N. Kulik, I. M. Logvinov, V. N. Shuman: The electric conductivity anomaly in the Carpathians 604

V. USSR (with exception of the Carpathians) 613

N. P. Vladimirov: Deep magnetotelluric surveys in the Baltic-Scandinavian Shield and the Kokchetav Block 615
N. V. Lipskaya, N. A. Deniskin, N. N. Nikiforova: Deep magnetotelluric surveys on the Belorussian crystalline massif 617
A. A. Kovtun, N. D. Chicherina: Deep magnetotelluric surveys in the northwestern part of the Russian Platform 620

G. N. Anishchenko: Deep magnetotelluric surveys in the central part of the Russian Platform 628
I. I. Rokityansky, S. N. Kulik, I. M. Logvinov, V. N. Shuman: Deep magnetovariation studies in Ukraine 634
A. G. Krasnobaeva, V. S. Vishnev, T. L. Rudneva: Deep electromagnetic studies in the Ural 640
D. A. Varlamov, Yu. K. Konnov, I. S. Feldman: Deep magnetotelluric surveys in the Eastern Pre-Caucasus 646
A. A. Avagimov, T. Ashirov, V. G. Dubrovsky, K. Nepesov: Deep magnetotelluric surveys in Turkmenia and Azerbaijan 652
A. S. Safonov, V. M. Bubnov, B. K. Sysoev, G. A. Chernyavsky, O. M. Chinareva, V. A. Shaporev: Deep magnetotelluric surveys on the Tungus syneclise and on the West Siberian Plate 666
V. I. Pospeev, V. I. Mikhalevsky: Deep magnetotelluric surveys of the south of the Siberian Platform and in the Baikal Rift zone 673
I. A. Yakovlev, V. P. Bubnov: Deep magnetotelluric surveys in Yakutia 682
I. I. Rokityansky, E. P. Kharin, G. I. Shtekh: Deep magnetovariation studies in Yakutia 693
L. L. Vanyan, V. V. Borets, A. M. Lyapishev, B. E. Mærderfeld, A. V. Rodionov: Deep electromagnetic studies in the Far East 697
M. N. Berdichevsky, G. A. Chernyavsky, I. M. Alperovich: Deep magnetotelluric surveys in Sakhalin 702
Yu. F. Moroz, V. I. Pospeev: Deep magnetotelluric surveys in Kamchatka 708
I. L. Trofimov, G. A. Fonarev: Deep magnetotelluric surveys in the Arctic Ocean 712
M. N. Berdichevsky: Concluding remarks on the investigations in the USSR 716

Chapter 6

ON THE NATURE OF CONDUCTIVE LAYERS IN THE EARTH'S CRUST AND UPPER MANTLE

(By I. S. Feldman) 721

Subject index 731
Index of geographical names 745

PREFACE

There are many reasons to believe that global tectonic processes and the development of the earth's crust are the products of deep processes in the upper mantle to a depth of few hundred kilometers. It is clear nowadays that the uppermost layer of about 500–700 km is not radially symmetric, it contains important lateral inhomogeneities, connected with large scale motions.

As in practically all physical studies of the Earth, in the upper mantle investigations as well, theories are frequently encountered dealing with forces, either implicitly or explicitly, in which thermal energy has a dominant role. Therefore the knowledge of the amount of heat flowing through the earth's surface is of fundamental importance in geophysics. The strong dependence of electrical conductivity on temperature makes the electromagnetic induction studies an important tool for the investigation of geothermal activity in the depth.

The successful international activity during the International Geophysical Year and the program of the Upper Mantle Project encouraged the idea of joint organization and close cooperation among the various geophysical institutions of socialist countries in their long term scientific programs. As a concrete form of this cooperation the Committee of Academies of Sciences of Socialist Countries for Planetary Geophysical Investigation (so called KAPG program) was established in 1966. The activity of KAPG has gradually covered all geophysical branches, as well as hydrology, meteorology etc. *A major task of KAPG is to organize regional participation of international (UGGI) projects.*

The first meeting of the KAPG working group 1.4 "Geothermics" in Budapest, Hungary in 1967 and of group 1.2 "Magnetotellurics" also in Budapest in 1968 clearly demonstrated the necessity of joint effort. At the meeting in Leningrad, USSR, in 1970 an idea of preparing this monograph was first proposed; its content having been discussed and the final version then approved in Sopron, Hungary, in 1974.

The monograph contains the main results in geothermics and magnetotellurics in KAPG countries during the period 1960–1973. The monograph brings together in a series of articles a comprehensive presentation of both theoretical and practical aspects of these geophysical disciplines and their interpretation.

Modern geothermal research needs data from various geological and/or tectonical provinces and from territories of different surface conditions. To make electrical measurements of the crust and mantle, the probing currents must penetrate into considerable depth. This means that the field

measurements must be made at distances of up to a few hundred kilometers. For this purpose a close international cooperation is absolutely necessary.

The results of heat flow investigation, as well as deep magnetotelluric sounding have revealed a vast amount of scientific material which stimulated a quantitatively higher step in our geophysical knowledge. As a result of the work performed, the efficiency and limitations of applied methods became known, and the problem of the nature of anomalous regions has been raised together with their role in geophysical processes. The way of collecting and processing the data is the first necessary step for any interpretation. The accuracy and reliability of the primary material is inavoidable. Limitations and reliability of research methods, the real value of the results, factors influencing them must be known in order to avoid misinterpretations. That is why a survey of data collection and processing methods both in geothermics (Chapter 1) and induction sounding (Chapter 2) has been included, without claiming completeness, however. The study of depth distribution of conductivity anomalies is closely connected with high pressure and high temperature laboratory experiments. Chapter 3 gives a review of the most important results on the behaviour of the electrical conductivity of rocks at high temperatures and pressures. Complex interpretation of geothermal data from various locations in relation to other geophysical and geological results is discussed in Chapter 4.

The main task of this monograph is to analyze the connections between the results of geothermic and magnetotelluric investigations. Geoelectric data help to interpret deep temperature profiles based on estimated thermal conductivity and heat generation of the rocks and on extrapolation of measured temperature gradients and heat flow values on the surface. This extrapolation requires a lot of assumptions; electrical conductivity in the upper mantle, however, sets limits to such extrapolation, as conductivity anomalies are possible only in a limited temperature range. Results of combined electromagnetic and geothermic studies are given in Chapter 5 according to specific tectonic units. Chapter 6 presents some ideas concerning the physical causes of the enhanced conductivity.

The articles were written by experts in the respective fields and reflect their personal views of the significance and interpretation of the results obtained in different regions. No attempt has been done to standardize the approach of individual authors or to solve the contradictions among them; on the contrary, these contradictions may help the advance of our study of the problems of the earth's crust and upper mantle. Some disproportions and deficiencies are due to the fact that the corresponding scientists were not in the situation to account on their investigations.

A. Ádám

CHAPTER 1

COLLECTING AND PROCESSING OF GEOTHERMAL DATA

Edited by

CH. OELSNER

INTRODUCTION TO CHAPTER 1

CH. OELSNER

Chapter 1 of the present monograph contains nine papers dealing with geothermal measuring methods, measurement of thermal properties of rocks, processing and correction of primary geothermal data and theoretical considerations on inhomogeneous geothermal fields.

It is clear that all these questions cannot be dealt with comprehensively in a single chapter. Therefore, authors have mainly reported on typical results from their respective countries. This demonstrates a characteristic feature of the cooperation within the KAPG: to get a broad range of investigations first by concentration then by multilateral utilization of the single results.

Lubimova and Tomara report on the Soviet technology of marine geothermal investigations, developed in the Institute of Physics of the Earth. The utilized probe with telemetric shipboard data transmission is described. Heat flow data of the lake Issyk-Kul are presented together with helium concentrations of demersal water samples.

In the last years a variant of the infra-red surface geothermics has been developed in the GDR as an effective prospection method. Oelsner's paper reports on the fundamentals of this method and on some results. This method has been used earlier on airplanes and satellites; advantages and disadvantages of the surface variant are discussed.

In course of the infrared measurements large amounts of data per unit time are obtained. Thus data processing on computer is needed. A complex computer program is described, which makes a jump correction of the data calculating the temporal temperature variations.

Krešl reports on an automatic apparatus for the measurement of thermal conductivity of rock samples developed in the Geophysical Institute of the Czechoslovakian Academy of Sciences. The increasing number of boreholes to be measured geothermally requires ever more measurements of thermal conductivity; these have been made predominantly on rock samples. The described apparatus allows a large sampling rate and works a long time without failure.

The investigations reported by Seipold were carried out in the Laboratory for High Pressure and High Temperature of the Central Institute for Physics of the Earth of the Academy of Sciences of GDR. The description of the apparatus working up to 3 kb and first results are given.

Since *in situ* measurements of thermal conductivity as well as the conversion of values measured in laboratory to *in situ* conditions are problematic, many of the authors take pains to determine thermal conductivity indirectly from more easily measurable petrophysical parameters using statistical

correlations. Plewa's paper deals with investigations on the relationship between thermal conductivity and diffusivity, and the depth, density and porosity of the layer, respectively. The measurements were carried out on Cambrian sandstone samples.

Čermák describes two computer programs for the processing of heat flow data. The first calculates a mean value (rms) from a set of measured thermal conductivity values, whereby different contact resistances are taken into consideration. The second program calculates the temperature gradient *vs* depth function. The topographic correction, as well as the corrections for the deviation of the hole from the vertical and for the effect of past climatic changes can be calculated by means of subroutines.

In the last years several authors have found negative temperature gradients at some localities in the uppermost crust. Because this is an evidence of paleoclimatic changes, heat flow data must be corrected for this effect. Čermák summarizes in his second paper some questions on the effect of past climate by means of diagrams showing the disturbance of the geothermal gradient.

In order to interpret the geothermal data measured in the field, one has to solve the inverse problem of geothermics. The first step is the solution of the direct problem, i. e. determination of the influence of inhomogeneities in the geothermal field. Analytical solutions are known only for simple-shaped bodies, so far.

In the paper of Lubimova, Luboshits and Nikitina, a two-dimensional analysis of the boundary problems of geothermics and geoelectrics is presented for a horizontally layered half-space with vertical or inclined interfaces. For the analytical solution one-side Fourier-integral-transforms are used. The numerical examples show the influence of rectangular inhomogeneities on the heat flow values.

Oelsner's paper is also concerned with the numerical solution of the direct problem of geothermics. After a review of relaxation methods a five-point approximation formula using the successive overrelaxation method is deduced for the solution of the Poisson equation.

METHODS OF MARINE GEOTHERMAL INVESTIGATIONS

E. A. LUBIMOVA, G. A. TOMARA

INTRODUCTION

The principles of recording geothermal parameters at the bottom of oceans and seas are based on the assumption about the constancy of temperature in demersal water layer beyond its level of seasonal variations. Theoretically this level, corresponding to the depth of the solar radiation penetration, is 300 m. Usually most investigators perform heat flow measurements just below this mark, avoiding, as a rule, shelf areas, where errors are maximal also because of tidal friction. Recent observations in Alpine lakes showed it, however, that there really exist most quiet periods of the year from July to January. Then heat flow measurements are possible even at depths from 50 m with accuracy of 10–15% (Hänel, 1970).

Usually the geothermal gradient amounts to some hundredth parts of centigrade per 1 m and heat conductivity is about $2 \cdot 10^{-3}$ calcm^{-2}sec^{-1}. Heat flow is determined as a product of these two values, the total error of measurements equals about $\pm 10\%$.

Heat flow variations exceeding the instrument error depend on different local and regional factors, such as topography, contrasts in heat conductivity, effect of sedimentation processes etc. The field experience of marine geophysics gives evidence for the preferential measurements of the geothermal gradient in the bottom sediments if near bottom temperature is below $+4$ °C. The coefficient of thermal expansion of water changes very sharply near $+4$°C and it disturbs the thermal equilibrium of near bottom water layer.

Geothermal gradient is recorded by thermoprobes, constructed for the first time by Bullard (1954), then modified by von Herzen et al. (1962), Lister (1970). Now we will dwell on the most characteristic variants of thermoprobes of the Alpine type, Hänel probe and thermogradient penetrative plotter, developed in the USSR.

In most cases samples of bottom sediments are taken for the determination of their thermal conductivity coefficient λ by means of a piston corer just at the place of geothermal gradient measurement and the value of thermal conductivity coefficient is defined in a laboratory by needle probes or by per cent water content in bottom sediments. In some systems it has been tried to measure thermal conductivity by recording the results in a separate recorder channel. Thermal conductivity measurements have an error of 3–5%.

In the Soviet Union the thermogradient penetrative plotter "TPP" has been employed for measuring heat flow in the Arctic Ocean, in the Black and Caspian seas, Sea of Okhotsk, and in deep lakes (Issyk-Kul and Baikal). The combined measurements made in Issyk-Kul revealed a correlation of the heat flow with radiogenic helium emanation.

"ALPINE" SYSTEM OF THERMOPROBES

One of the standard thermoprobe design is the "Alpine" system. The instrument consists of a sampling tube with temperature probes and hermetic container fastened over it with a photo recorder. The sampling tube has internal diameter of 35 mm and length about 3 m. Cores for further measurements of thermal conductivity are taken into plastic tubes adjoining the thermoprobe's internal walls. Three thermistor probes are fixed along the thermoprobe, the fourth is fixed on the recorder container over the thermoprobe.

A galvanometer with mirror is used as recorder, four temperature sensors are connected to a Wheatstone bridge so that the galvanometer records the difference of resistances between probe 2 and probes 1, 3, 4. Besides a calibration of the bridge sensitivity is recorded during each cycle of the switch. The temperature difference Δt between the probes and the absolute temperature of demersal water can be determined from the probe calibration curves and from thermoprobe sensitivity. A bridge of hydrostatic pressure transducer is secured to the outer container wall. The depth of thermoprobe immersion is also fixed by this galvanometer. The pressure transducer is calibrated by the scale of the echo sounding.

The galvanometer circuit in the bridge for recording geothermal gradient is activated before placing the recorder into the container. Other circuits, namely: a bridge for hydrostatic pressure record, illuminators for galvanometers, a motor moving a photofilm, and a rotary switch are activated and disconnected while the container is closed. For this purpose it is necessary to connect for several seconds 6 V stabilized between the instrument case and one of the leads of disconnecting relay.

The photofilm of the records of the measurement is processed on board.

Decoding of a point record for obtaining geothermal gradient values or absolute temperature is made by means of calibration curves. This leads to a low accuracy of results.

HÄNEL PROBE

During the last years a remarkable progress has been reached in constructing marine thermoprobes in Europe by Hänel (Haenel, 1972).

An experimental unit has been used for measuring heat flow through the Ionian sea bottom (Fig. 1). This is a modification of Langseth's probe, described by Gerard et al. (1962) and it also consists of a sampling tube with needle probes extending vertically from its side, and a hermetic container with self-contained electronic recorder. The container is provided with outher stabilizers for strictly vertical entering the thermoprobe into marine sediments. Mounted over the container is the release of trigger weight, suspended on additional rope of length a some meters more than the total probe length. It serves for actuating the recorder before entering the probe into the bottom sediments.

An electronic registrator placed into hermetic container fulfils several functions and records all information obtained on magnetic tape. A rotary switch serves for connecting different probes to the common amplifier

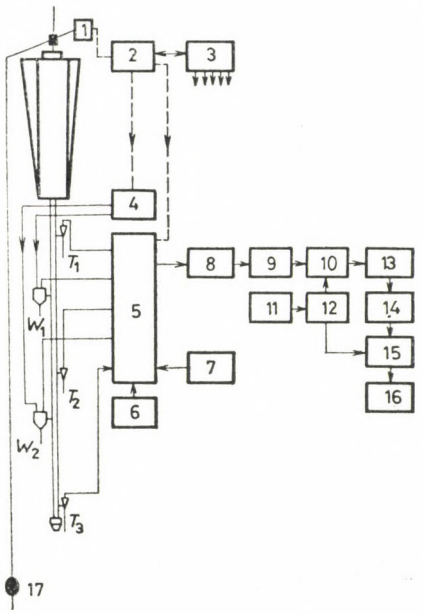


Fig. 1. Hänel probe block-diagram
1 – arching contact for start; 2 – counter with switching device; 3 – power unit; 4 – constant voltage source; 5 – rotary selector switch; 6 – clinometer; 7 – calibration marker; 8 – selector of bridge ranges; 9 – amplifier; 10 – analog-digital converter; 11 – quartz generator; 12 – pulse divider; 13 – counter; 14 – dynamicizer; 15 – coder and modulation; 16 – tape recorder; 17 – trigger weight

input (Fig. 1, No. 5). Immediately after switching on the recorder, the temperature is measured during 5 min by means of three thermistor probes T_1, T_2, T_3, fastened along the thermoprobe. An automatic selector makes a choice of one of 12 subranges, corresponding to temperature limits from -3 °C to $+70$ °C. The data measured are delivered onto the magnetic tape each 5 sec through amplifier and modulator. Following the 5 min temperature measurements, the needle probes W_1 and W_2 are connected by the rotary switch for measuring thermal conductivity *in situ* during 5 min. The needle probes are rather thin tubes, containing inside a heating wire almost along their full length, and a thermistor is the centre. The heater feeds from a stabilized voltage source (Fig. 1, No. 3). The thermistor's resistance variations with time are read out from the same Wheatstone bridge that is used for temperature measuring, and are transmitted to the amplifier (Fig. 1, No. 9). The thermal conductivity of the sediments is determined by Bullard's formula (Bullard, 1954). Thermal conductivity coefficient is determined with an accuracy of $\pm$ 5%.

The sensitivity of the recorder together with the thermistor probes is ± 0.01 °C. Geothermal gradient is calculated from the temperature data with an accuracy of ± 0.001 °C/m.

SYSTEMS OF THERMOGRADIENT PENETRATIVE PLOTTER

In the USSR the first ideas of development of the thermoprobes "TPP" date back to 1964. An experimental system has been used for the determination of a heat anomaly in the Baikal Lake (Lubimova et al., 1966). Since then the instruments have continuously been improved as to have higher sensitivity and reliability. A program of geothermal investigations from drift ice in Central Arctic stimulated the design of a higher instrument which is presently a basic model for the whole series of modifications.

The "TPP-3" unit is made as a needle probe, 2.5 m in length and 16–20 mm in diameter, with a hermetic container of 82 mm diameter and 800 mm length, fastened over. The high sensitivity of the recorder amplifier allows to use as thermosensitive elements thermocouples with 10 copper-constantan junctions. Distance between the elements is 2 m.

Figure 2 shows the functional diagram of thermoprobe "TPP-3MT". The thermocouple EMF is compensated by potentiometer 2. EMF value is determined by a servo-system, including amplifier 3 and integrating reversing motor 4. The potentiometer's sliding contact is set up in such a position that the difference between thermo–EMF and compensating EMF approaches zero. EMF increment of the potentiometer is proportional to the angle of rotation of its sliding contact (Lubimova et al., 1973).

The length of arc ΔS recorded by block 6 making a record on drum 5 is proportional to the EMF increment of the thermocouple and is determined as:

$$\Delta S = C(T_l - T_u)$$

where T_l, T_u are temperatures of the lower and upper junctions of the thermocouple and C is a factor of proportionality depending on potentiometer design and being 42 mm/0.1 °C for thermoprobe "TPP-3 MT".

Sensitivity of the instrument is $\pm$ 0.001 °C in the whole scale range of 1 °C. Time of autonomous operation is 2.5 hours, power consumption 0.3 W, weight 20 kg, maximum permissible depth of immersion 10,000 m.

The work with an autonomous instrument is difficult because of the lack of operative information. A telemetric communication channel not only improves the efficiency of each heat flow station, it allows a remote control of the instrument as well. At an experimental thermoprobe a cable-rope of 22 Ω/km resistivity in polyethylene insulation was used for this

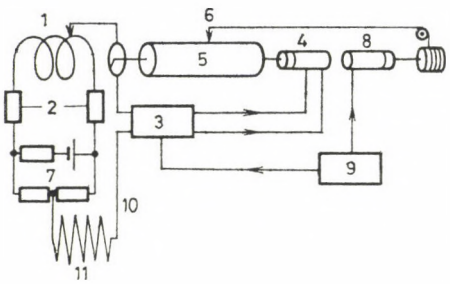


Fig. 2. Thermoprobe "TPP-3 MT" functional diagram
1 – spiral rheochord; 2 – bridge constant resistances; 3 – amplifier; 4 – integrating motor with reductor; 5 – recording drum; 6 – recording unit; 7 – battery of the potentiometer; 8 – time motor; 9 – power unit; 10 – upper thermocouple junctions; 11 – lower thermocouple junctions

communication channel. Information was transmitted with carrier frequency of 40 kHz, and received on ship-board by a simple broadcasting receiver.

During operation with the instrument it is convenient to listen to sound-tone changes through the receiver's loud-speaker. The operator can easily feel the moment when the thermoprobe is entering sediment, by a change in sound tonality, and may avoid the probe lifting in case of a strong drift of the vessel. One disadvantage of telemetric thermoprobes is the sensitivity of cable-rope to mechanical damages.

COMBINED GEOTHERMAL AND EMANATION MEASUREMENTS

During recent years a complex approach to geothermal measurements is considered as promising for studying heat flow and concentrations of radiogenic helium. This approach is based on the fact that the heat flow depends upon the decay of uranium and thorium distributed in the earth's crust. During this decay radiogenic gases like helium are originated. The total mass of uranium dispersed in the earth's crust is of the order of 10^{14} tons (Vinogradov, 1964). Being a very mobile element, helium migrates along permeable zones of fractured disturbances. Thus, helium-surveying can be used for an efficient mapping of deep fractures (Bulashevich and Bashorin, 1970). Not every fracture is associated with a helium anomaly,

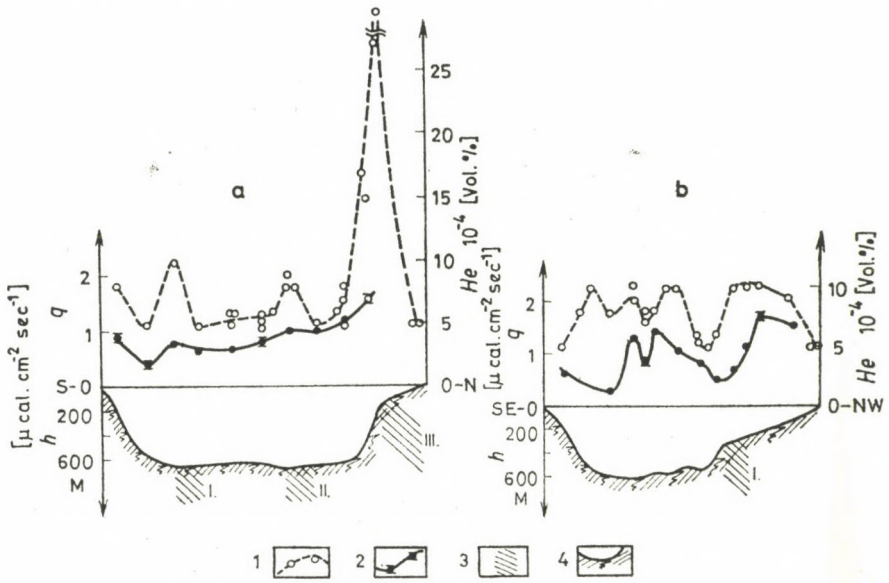


Fig. 3. Coinciding profiles of heat flow and radiogenic helium concentrations dissolved in demersal water
1 – The concentration in demersal layer in vol%; 2 – heat flow, (q); 3 – approximate position of fractures according to geological data; 4 – schematic topography of the Issyk-Kul mountain lake bottom in places of measurements

but each helium anomaly shows unambiguously the permeable fractured disturbances. Joining geothermal measurements with helium-surveying evidently decreases the ambiguity in the determination of deep fractures within the earth's crust.

First common measurements of helium content dissolved in a demersal water layer, and of heat flow were carried out on the Issyk-Kul lake bottom (with a depth of 600–700 m) (Bulashevich et al., 1973). Geothermal gradient was measured in sequence from vessel board and demersal water samples were taken preserving the gaseous phase. Helium concentration in the gas was determined in laboratory on a mass-spectrometer with an error of $\pm 10\%$. The coefficient of thermal conductivity of the bottom sediment samples was measured by a needle probe.

The results for two meridional profiles are shown in Figure 3. The structural pattern of Issyk-Kul lake's bottom is known rather poorly, the location of deep fractures, however, can be confirmed by the coinciding maximum values of heat flow and of helium concentration in demersal water.

So, marine geothermal measurements by "TPP" were for the first time joined with measuring radiogenic helium. The correlation obtained is of great interest for both theoretical and applied aspects of geothermics, such as investigations of the relationship between heat losses and heat generation as well as, to clarify regional locations of deep fractures.

REFERENCES

Bulasevich, Yu. P., Bashorin, V. V., 1970. Helium content of subsurface waters along deep seismic profiles eastwards from the Urals (in Russian). *Dokl. Akad. Nauk SSSR*, **193**, 573—575.

Bulasevich, Yu. P., Lubimova, E. A., Kartashov, N. P., Tomara, G. A., Bashorin, V. N., Aleksandrov, A. L., 1973. The distribution of helium and heat flow at the bottom of Lake Issyk-Kul (in Russian). *Dokl. Akad. Nauk SSSR*, **212**, 597–599.

Bullard, E. C., 1954. The flow of heat through the floor of Atlantic Ocean. *Proc. R. Soc. London, A*, **222**, 408–429.

Gerard, R., Langseth, M., Ewing, M., 1962. Thermal gradient measurements in the water and bottom sediment of the western Atlantic. *J. Geophys. Res.* **67**, 785–803.

Hänel, R., 1970. Eine neue Methode zur Bestimmung der terrestrischen Wärmestromdichte in Binnenseen. *Z. Geophys.* **36**, 725–742.

Haenel, R., 1972. Heat flow measurements in the Ionian Sea with a new heat flow probe. "*Meteor*" *Forsch. Erg., C*, No. 11, 105–108.

Von Herzen, R. P., Maxwell, A., Snodgrass, I., 1962. Measurement and control in science and industry, 3. Reinhold, London.

Lister, C. R. B., 1970. Measurement of in situ sediment conductivity by means of a Bullard-type probe. *Geophys. J. R. Astr. Soc.* **19**, No. 5.

Lubimova, E. A., Alexandrov, A. L., Duchkov, A. D., 1973. *A method of heat flow study through the ocean bottom.* Nauka, Moscow.

Lubimova, E. A., Sheliagin, V. A., Shushpanov, A. P., 1966. Instrument for measuring heat flow in the depth (in Russian). *Problemy glubinogo potoka*, Nauka, Moscow.

Vinogradov, A. P., 1964. Gas household of the Earth (in Russian). *Khimiya Zemnoi kory* **2**, Nauka, Moscow.

POSSIBILITIES AND LIMITATIONS OF INFRARED SURFACE GEOTHERMICS

CH. OELSNER

INTRODUCTION

Since the discovery of infrared radiation by William Herschel in 1800 infrared research has enormously developed much as all branches of natural sciences.

This development has made fast progress, particularly for military purposes, since the First World War. Ships and airplanes were already then located using the radiant heat emitted by glowing funnels or exhaust units. Using the evaporagraph developed by Czerny in 1929 differences in radiation temperature of 0.1 °C could already be proved. In Germany, since about 1940, the IR technique was further developed by various firms and institutions with the purely military aim of "thermic location". In 1941, in this connection the first airborne measurements of radiation temperature were made near Travemünde. Figure 1 shows a

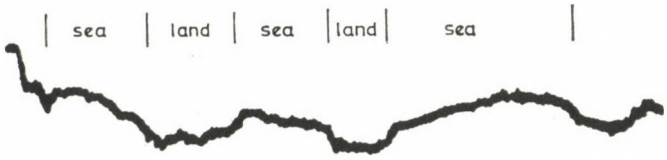


Fig. 1. Section from an aerial IR radiometer record of the year 1941

section of one of these records. The temperature difference between land and sea surfaces can be distinctly made out. After the Second World War more than a decade elapsed before infrared techniques could be used for peaceful purposes. Parallel to the development of satellite and space engineering, however, it has spread since then like an avalanche. At present numerous applications are known, especially from agriculture and forestry, geology and economic geology, hydrology, oceanography as well as environment control.

PHYSICAL FUNDAMENTALS

The theory of propagation of radiation energy can be considered either from the viewpoint of the classical theory of electromagnetic waves or from that of quantum mechanics. Quantum mechanics results in most cases in equations very similar to the classical results. In general, heat radiation can be regarded as a phenomenon that can be described by the classical theory of electromagnetic waves. Temperature radiators can be subdivided

into blackbodies and bodies with non-black surfaces. The blackbody is a perfect emitter.

Its emission is independent of direction and wavelength. According to Kirchhoff's law the emissivity $\varepsilon(\lambda, T)$ of a substance is equal to its absorptivity $a(\lambda, T)$

$$\varepsilon(\lambda, T) = a(\lambda, T) \tag{1}$$

In case of a blackbody $\varepsilon(\lambda, T) = a(\lambda, T) = 1$. The spectral distribution of the emissive power of a blackbody is described by Planck's radiation law. The total emissive power of a blackbody is obtained by integrating Planck's law over all wavelengths and directions of emission.

This so-called Stefan-Boltzmann law states that

$$E_s = \sigma T^4 \tag{2}$$

with $\sigma = 5.667 \cdot 10^{-8}$ $\mathrm{Wm^{-2}\,K^{-4}}$ (Boltzmann constant). Applying Kirchhoff's law for opaque bodies (i. e. for bodies in which no radiation is transmitted), one obtains

$$a(\lambda, T) + r(\lambda, T) = 1 \tag{3a}$$

and thus

$$\varepsilon(\lambda, T) + r(\lambda, T) = 1 \tag{3b}$$

where

$$r(\lambda, T) = \text{reflecting power.}$$

Non-opaque substances are transmissive for radiation, i.e. they possess a transmissivity $d(\lambda, T)$.

Correspondingly, in this case Eqs. (3a, b) change to

$$a(\lambda, T) + r(\lambda, T) + d(\lambda, T) = 1 \tag{4a}$$

or

$$\varepsilon(\lambda, T) + r(\lambda, T) + d(\lambda, T) = 1 \tag{4b}$$

The radiation of a non-black body at temperature T and for the wavelength λ will result from the multiplication of the blackbody radiation, at the same temperature and wavelength, by the emissivity $\varepsilon(\lambda, T)$ of the non-black body

$$E(\lambda, T) = \varepsilon(\lambda, T)\, E_s(\lambda, T) \tag{5}$$

Emissivity plays an important role in determining the true surface temperature. During the flight of the TIROS satellites over the Egyptian and Libyan deserts the oases at first appeared as hot points. Having taken into account the larger emissivity of the oases, as compared with the adjacent desert, the expected lower surface temperatures were obtained (Buettner and Kern, 1963).

Emissivities given in the literature for minerals and rocks as well as for natural ground surfaces vary between 0.71 and 0.99. Our investigations on

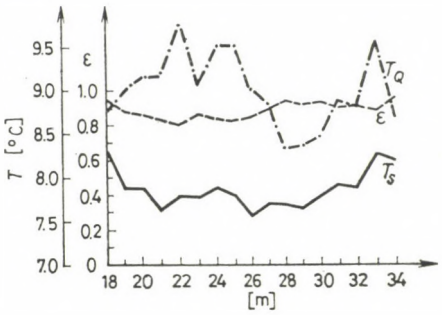


Fig. 2. Determination of emission coefficients along a profile: T_Q – true surface temperature, °C; T_S – radiation temperature; ε – emissivity

rock-forming minerals, e. g., yielded the following results at a temperature of 17 °C: quartz — 0.816, orthoclase — 0.813, muscovite — 0.822.

Emissivities of natural ground surfaces are best determined from true surface temperatures and the corresponding radiation temperatures. Figure 2 shows an example of such a determination of emissivities under natural conditions. The radiation temperature runs approximately parallel to the true surface temperature. Correspondingly, the emissivity, whose average value on the profile is 0.88, shows only very small variations (± 0.06).

INFLUENCE OF METEOROLOGICAL CONDITIONS

In measurements of radiation surface temperatures the radiation balance of the points measured has a direct influence on the result. This radiation balance S is composed of the following components:

$$S = I + H + G - \sigma T^4 - R \tag{6}$$

where

I is direct solar radiation,
H is diffuse sky radiation,
G is atmospheric downward radiation,
σT^4 is emission of the ground,
R is short-wave reflected radiation.

The spectral intensity distribution of S varies very much:

a) Solar and sky radiation belong to the short-wave range ranging from 0.3 μm to 2.2 μm.

b) The radiation emitted by the earth's surface and the atmospheric downward radiation are long-waved (6.8—100 μm).

The frequency of the intermediate range from 2.2 to 6.8 μm is present in both classes in less than 5%. Of all components of the radiation balance the only information of interest for earth sciences can be obtained by the radiation of the ground. Therefore, infrared surface-temperature measurements for geological purposes can only be carried out, if all other components

are zero or possibly small or constant. As the latter cannot be achieved, night measurements are recommended to realize the requirements mentioned. The short-wave components then disappear and the radiation balance takes the form:

$$S = G - \sigma T^4 \tag{7}$$

It still remains to realize the condition $G = \text{const}$. This is in general possible in radiant weather or with unchanging clouding (stratus). Particularly favourable conditions were found to exist shortly before sunrise.

While for geological purposes night measurements are necessary, for agricultural purposes, e.g., the near IR and the visible range are of interest. That means that for such tasks daytime measurements are necessary.

To all kinds of tasks, however, applies that infrared-surface-temperature measurement is a marked "fine-weather method". During precipitation no measurements are possible yielding valuable information. The considerable measuring advance characteristic of all remote sensing methods outweighs this drawback.

AIRBORNE IR METHODS

Due to the continuously increasing sensitivity of the measuring devices up-to-date measurements from satellites may have a resolving power only reached by airborne measurements until recently. Nevertheless, measurements made from airplanes and from satellites supplement each other as before. Because of the low flying altitude the ground resolution of airplane measurements is always greater than that of satellites. The advantages of aero-measurements are obvious:

a) fast measurement of vast areas,
b) information from inaccessible regions,
c) determination of large-scale regional structures of processes,
d) possibility of determining lateral changes of certain features by repeated flying over the given areas.

Satellites are especially for the latter task suited. The applications of IR measurements are increasing more and more. The main fields of application are:

1. geology and economic geology,
2. agriculture and forestry,
3. hydrology, oceanography and fishery,
4. control of environment.

Information for the earth sciences were obtained especially by the spacecrafts Apollo 9, Soyuz 7, Soyuz 8, Soyuz 9, the ERTS-satellite and the Skylab missions.

Lyon and Patterson (1969) were the first to report on the use of an IR spectrometer for geological mapping. It was found that the IR emission spectra of the rocks are distinguishable within the range from 9 μm to

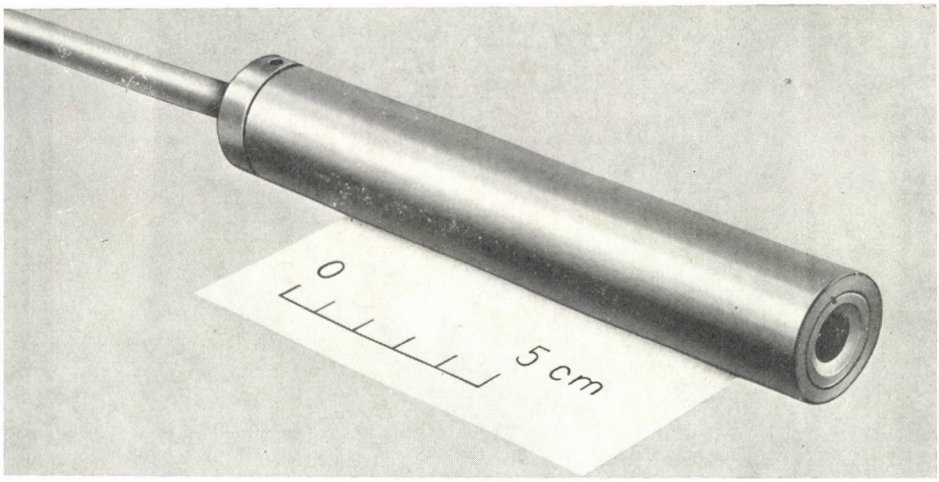


Fig. 3. Vacuum thermocouple after Kortum (Manufacturer: Zentralinstitut für Optik und Spektroskopie der Akademie der Wissenschaften der DDR. Abt. Strahlungsempfänger, GDR-69 Jena)

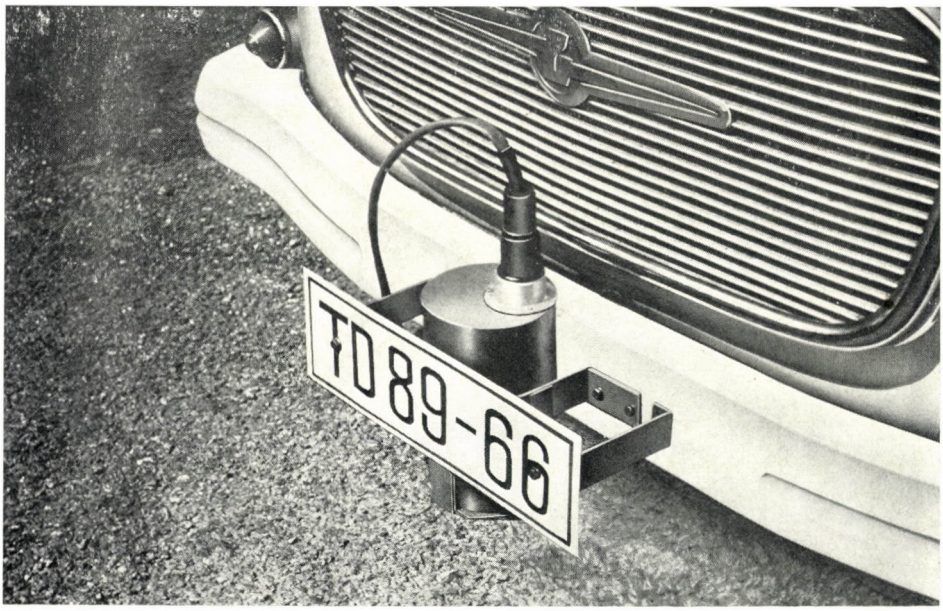


Fig. 4. Sensor attached to a car

12 μm. By using optical circular filters spectra with a very high resolving power were obtained in realtime simulation.

The spectra recorded on magnetic tapes are compared with known spectra by means of a computer. Using special programs the corresponding rocks or rock types can be determined from the measured spectra.

IR measurements from aircraft or satellites yield a great variety of important information. Although the resolving power reached is enormous (ERTS: less than 100 m at a flying altitude of 920 km; Skylab: less than 50 m at a flying altitude of 435 km) it is still insufficient for many problems of the earth sciences (Steiner, 1971).

In addition, it is very difficult to obtain geological information from IR pictures in mean latitudes because of the plant cover. Thus, the limits are drawn for the application of aero-methods for geological purposes.

CAR-BORNE VARIANT OF IR RADIOMETRY

At the Department of Earth Sciences of the Bergakademie Freiberg (GDR) a car-borne variant of IR radiometry has recently been developed into a geothermal method of exploration (Oelsner, 1969, 1970). The most essential part of the apparatus used is a vacuum thermocouple after Kortum with a KRS–5 entry window (Fig. 3). By this window transmissivity is restricted to the range from 0.6 to 40 μm. The pass-band width can be limited by optical filters.

Such a thermocouple is equipped with a compensating resistance allowing the building of a compensating circuit, by which the indicated thermoelectric voltage becomes independent of the cold end of the thermopile. The accuracy of the compensation depends on the constancy of the voltage fed into the circuit. In the necessary temperature range the compensating resistance has a linear temperature coefficient. After the correct choice of the feeding voltage of a Wheatstone bridge to be built, a temperature compensation is obtained over a long period smaller than 0.1 °C. Recording is made after amplification by means of a recording potentiometer or on a magnetic tape. Radiation differences of $6 \cdot 10^{-8}$ W or differences in temperature of 10^{-3} °C can be proved with the unit. For regional measurements the sensor is arranged in front of the radiator of the measuring vehicle at a height of about 50 cm above the road surface (Fig. 4).

As the thermocouple has an angular aperture of 90° the visual field of the thermocouple is a circle whose radius equals the height of the entry window over the radiating surface. The time constants of the thermocouples used are about 100 msec. Assuming an expansion time of 200 msec at the height of 50 cm a travelling speed of 18 km/h is possible in order that the radiation temperatures should be reproduced in their full height and undistorted.

The effect of the travel speed on the records is shown in Figure 5.

Despite increased speed the general nature of the records is maintained. With increasing speed high-frequency anomalies, i.e. small-scale anomalies of small amplitudes will disappear. In case of small amplitudes these will strongly decrease. Low-frequency anomalies with their amplitudes are largely preserved. There does not occur, however, any rounding effect propor-

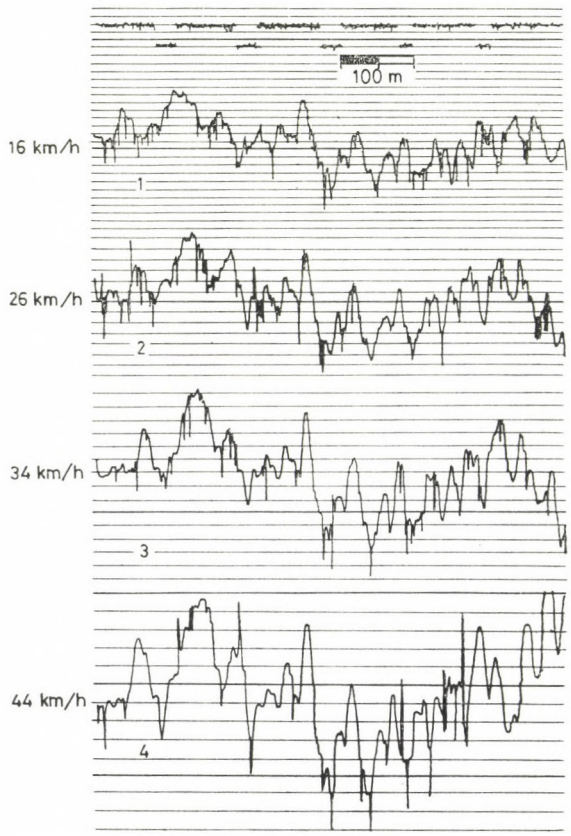


Fig. 5. Effect of travelling speed on a test profile

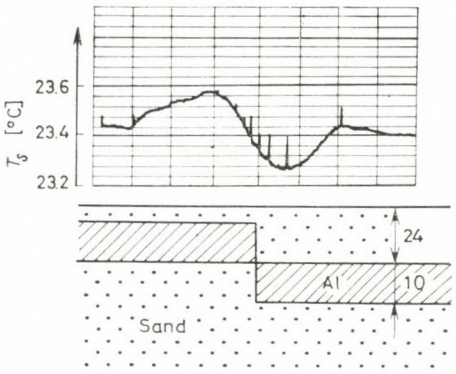
tional to speed. In the performance of measurements, what has been said above in connection with equation (7) should be kept in mind. Cooling in the night results in temperature differences that must be taken into account by a suitable measuring method. In measuring long profiles from a motor can, the records are frequently superimposed by short-period temperature disturbances having small amplitudes. They are easily removed by digital low-pass filtering.

Marked anomalies of the surface temperatures were obtained within the range of tectonic disturbances.

The numerical results about temperature anomalies of tectonic disturbances published by Geertsma (1971) have been confirmed by calculations and model measurements made by us. Figure 6 shows an original measuring curve obtained over a model of a vertical fault. As model layer aluminium was used. The fault model was in sand. Maximum and minimum are distinctly pronounced. The "outcrop" of the fault is exactly between the maximum and minimum.

The anomaly shape explained was also obtained in field measurements. As an example, results will be discussed obtained within the zone of

Fig. 6. Model measurement over a fault



the so-called "Central-German Main Line", a pronounced faulting system, by which the Central-German main block is separated in the north-east from the North-German basin of sedimentation.

Figure 7 is a section of a record obtained on a high-way in the direction of Berlin. The results of a to-and-fro measurement were averaged. They are represented in the lower part of Figure 8. The upper part of this figure shows the horizontal gravity gradients determined earlier by Bein (1961) from torsion-balance measurements. Using the torsion-balance results and the available bore-hole data, Bein (op. cit.) calculated a geological profile, too, represented in Figure 9.

Starting out from the gradient picture a division was made into high block, intermediate zone and deep block. An interpretation of the surface temperatures yielded the same result (Oelsner, 1969). On a parallel profile at a distance of about 3 km corresponding results were obtained.

The method is well suited for prospecting for hypothermal waters because of the relatively great temperature differences existing there. An example for this is given in Figure 10 representing IR radiation temperatures obtained at two different points of time and the temperatures in shallow boreholes at a depth of 3 m.

The profile measured crossed a thermal-water-bearing vein. All three curves measured qualitatively show the same behaviour. The steep slope towards north-east is caused by the vein dipping south-west.

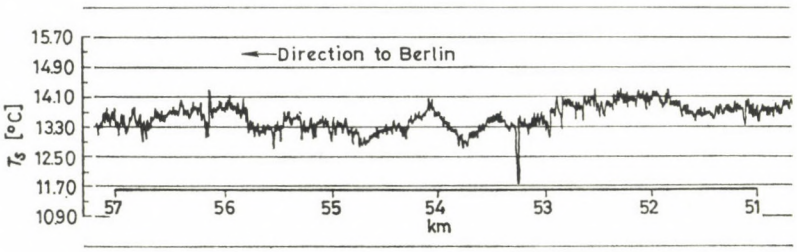


Fig. 7. Section from a continuous record of surface temperatures

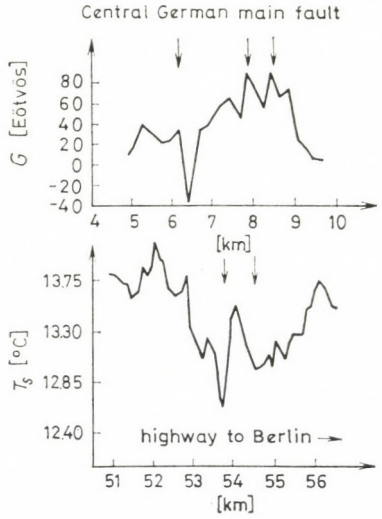


Fig. 8. Unfiltered surface temperatures (below), Gradients from torsion-balance measurements (above)

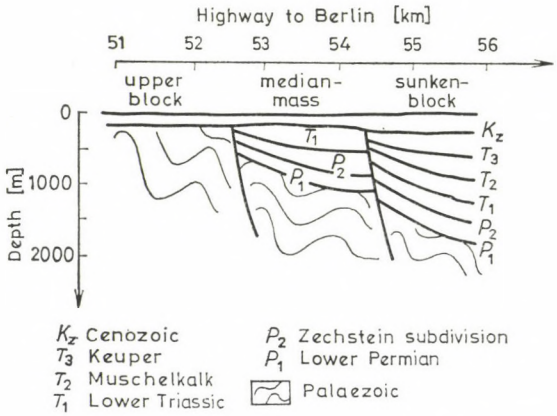


Fig. 9. Geological profile calculated from torsion-balance results after Bein (1961)

The main maxima are in each case in agreement. The level shift of the radiation temperatures is conditioned by seasonal changes. This measuring technique is excellently suited for exploring sulphide-ore bodies, as the formation of the oxidation zone is connected with exothermic reactions. The heat amount produced depends on the oxidation rate. It was found that the heat amounts produced in the Freiberg and Marienberg ore districts (Saxon Ore Mountains) are sufficient to cause pronounced increases of the surface temperature. In Figure 11 the results are arranged that were obtained on three profiles running approximately parallel with each other.

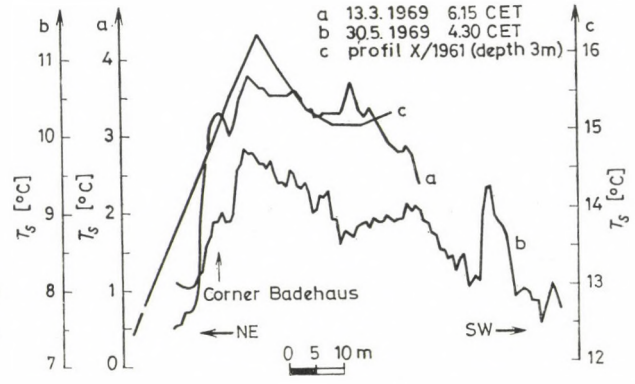


Fig. 10. Radiation temperatures and temperatures obtained in shallow boreholes over a thermal-water-bearing vein

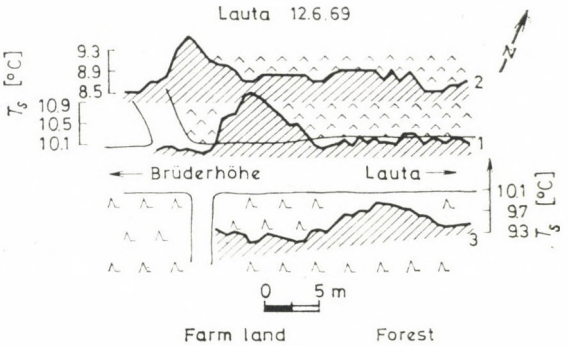


Fig. 11. Radiation temperatures over a sulphide-ore vein

This is a result obtained from the ancient Marienberg ore district. Surface conditions were different. Profile 1 was on a country-lane at the edge of a forest. Profile 2 was measured parallel to it on farm land. Profile 3 was somewhat inclined relative to the first ones and was located in the forest. All three profiles crossed an old row of dumps running approximately from north-west towards south-east. The line connecting the maxima is exactly in the direction of an old row of dumps indicating that ore was mined here about 100 years ago. From the asymmetry of the anomaly it can be concluded that the vein has a northward dip. The method proved extremely effective with other applications, too.

Although the measuring advance of aero-surveys is not reached, it surpasses by far that of all conventional geophysical methods. In contrast to aerial measurements it is easy to recognize effects of different surface features, i.e. jumps in the emissivity. That means that the external exactitude is higher here than with aerial photographs. The practical limitations are the unfavourable weather conditions, especially moisture and rain.

PROCESSING OF SURFACE-GEOTHERMAL DATA

Surface-temperature data are continuously recorded on a magnetic tape, path markings of 10 m, 50 m or 100 m being simultaneously recorded, which control the A/D-converter in reproduction (Oelsner and Donner, 1974) The data for further processing are generally available in the form of punched tapes.

Data processing consists of the following steps:

1. Differences between the emissivities of the surfaces surveyed act as jumps in recording. In some cases the zero point had to be shifted to allow the use of the full sensitivity range of the recording device.

2. Determination of the temporal temperature variation in the investigated area. For this purpose the measurements of surface temperature are carried out in the form of loops, the route being located in such a way as to

obtain a sufficient number of cross points. As a matter of fact, the temperature variation also depends on the microclimate of each measuring point but it is mainly determined by meteorological factors such as cloud cover, air moisture, which in good approximation can be assumed to be constant in any measuring loop.

3. For each measured value the temporal temperature variation has to be taken into consideration.

4. Further processing of the corrected primary data with a special program system: filtering out the spurious signals and finding special anomalies (matched filter) as well as graphical representation of the results.

COMPUTER PROGRAM FOR PROCESSING SURFACE-GEOTHERMAL DATA

The program is included by which the above mentioned steps 1–3 are achieved.

Programming language is a variant of ALGOL 60, created for the used computer Robotron 300 (corresponds approximately to IBM 1492) on the basis of ALGOL 60. Compared with SUBSET ALGOL 60 this variant contains additional standard functions and standard procedures corresponding to those of the programming language ALGAMS (Schirmer, 1970).

In what follows the program is briefly explained. From line 4 to line 9 the used code procedures, i.e. computer-internal subprograms are specified. Procedure FEMAX searches for the maximum of the absolute values of the field. The subsequent procedures concern magnetic-type work.

The first read comment (Line 11) comprises the number of all values (N), the number of repetition points (L) and the sum of all repetition measurements (SU). The magnitudes and fields required for the following calculations are defined in lines 12–15. The magnitude G is always smaller than 1 and indicates, which fraction of the amplitude differences of two consecutive values indicates a jump. The primary data are defined as field X. Field M designates the number of the single repetitions.

Lines 19 to 24 comprise the jump correction. For the recognition of a jump 4 consecutive points are used. A jump occurs between the second and the third point, if the absolute value of the amplitude difference of these points is G^{-1} times greater than the absolute value of the amplitude differences between points 1 and 2 as well as between 3 and 4. The "not jump-conditioned" portion of the anomaly is lost with this algorithm.

Because of the low capacity of the computer used (32K) the jump-corrected data are transferred on a magnetic tape. By switching on selector 1 the jump-corrected measured values can be given out on punched tapes (Line 28).

For variation correction (Lines 30 to 50) first the fields P and TW are read-in. P gives the numerical order, TW the measuring times of the repetition measurements. By means of field M amounts and measuring times can be transformed into the two-dimensional fields W[I, J] and T[I, J], where index J is to designate the number of the repetition (Line 34).

The variation curve is now composed of the differences of the amounts of the repetitions at the single points of repetition (Line 35, Field DW).

The starting point in this is repetition point I (Line 39), by which the skeleton of the variation curve is obtained. Into this field DWK [I, J] the other repetitions are inserted in linear sections (Lines 40 to 47).

In order to calculate the variation corrections for any measured value, first the two-dimensional field DWK has to be changed into the vector DWKV (Line 57). The corresponding procedure is to be performed with the field of the measuring times of the j-repetitions at the i-repetition points. In this, the times have to be arranged in ascending order (Lines 66–73). For checking purposes in line 77 the following data of the points of support of the correction curve are given:

Number of point, time and amount.

In order not to overcomplicate the measuring technique the determination of measuring time for each scanned value was dispensed with. In the calculation of the correcting value for each value the numerical order is referred to (Lines 79–82).

The error thus occurring in the calculation of the temperature-variation correction for the measured values given in each case disappears with constant travelling speed along the intervals between the points of repetition. To prevent the memory from becoming overloaded the correcting values are given out on an additional store (Line 87) and again read element by element (Line 89) with the corresponding elements of the jump-corrected primary values (Line 90) in order to effect the variation correction (Line 91). The variation corrected values are given out on punched tapes (Line 92) and printed by the high-speed printer (Line 93).

The punched-tape output allows a further processing according to step 4 mentioned above.

The program has up to now been successfully used for processing more than 25.000 values.

```
01 'BEGIN' 'COMMENT' SPRUNG- UND GANGKORREKTUR EINER MESSWERTFOLGE MIT
02 ZEITLICH VERAENDERLICHEM NULLPUNKT OELSNER 1972;
03 'INTEGER' I, J, K, L, N, R, SU, MA, B;
04 'REAL' 'PROCEDURE' FEMAX (V, I); 'INTEGER' 'ARRAY' V; 'INTEGER' I; 'CODE';
05 'PROCEDURE' FIRST (I); 'VALUE' I; 'INTEGER' I; 'CODE';
06 'PROCEDURE' LAST (I); 'VALUE' I; 'INTEGER' I; 'CODE';
07 'PROCEDURE' ADVANCE (I, K); 'VALUE' I, K; 'INTEGER' I, K; 'CODE'
08 'PROCEDURE' MTWRITE (I, J, A); 'VALUE' I, J; 'INTEGER' I, J; 'ARRAY' A; 'CODE'
10 'PROCEDURE' MTREAD (I, J, A); 'VALUE' I, J; 'INTEGER' I, J; 'ARRAY' A; 'CODE'
11 READ (N, L, SU);
12 'BEGIN' 'REAL' G, A; 'ARRAY' XI, GKXI [1 : 1], X [1 : N], P, PK, TW, TK, DWKV,
13 DWKVK [1 : SU]; 'INTEGER' 'ARRAY' M [1 : L]; READ (G, X, M);
14 MA: = ENTIER (FEMAX (M, I));
15 'BEGIN' 'ARRAY' W, DW, DWK, T [1 : L, 1 : MA]; 'REAL' X1, X2, X3, X4, DIF;
16 A: = 0; X1: = X [1]; X2: = X [2]; X3: = X [3];
17   'FOR' I: = 3 'STEP' 1 'UNTIL' N–1 'DO'
18
19   'BEGIN' 'COMMENT' SPRUNGKORREKTUR;
20   X4: = X [I + 1]–A; DIF: = G*ABS (X2–X3);
21   'IF' ABS (X1–X2) 'LESS' DIF 'AND' DIF 'GREATER' ABS (X3–X4)
22   'THEN' A: = X3–X2 + A;
23   X1: = X2; X2: = X3; X3: = X4–A; X [I]: = X2–A
24   'END';
25
26                'IF' SEL (1) 'THEN' OUTPUT (2, '('E')', X);
27
28   FIRST (1); 'FOR' I: = 1 'STEP' 1 'UNTIL' N 'DO'
29   'BEGIN' X I [1]: = X [I]; MTWRITE (1, I, XI) 'END'; LAST (1);
30   'BEGIN' 'COMMENT' GANGKORREKTUR;
31   READ (P, TW); B: = 0; 'FOR' I: = 1 'STEP' 1 'UNTIL' L 'DO'
```

```
'BEGIN' 'FOR' J: = 1 'STEP' 1 'UNTIL' M [I] -DO'
'BEGIN' K: = B + J: = P [K];
W [I, J]: = X [R]; T [I, J]: = TW [K];
DW [I, J]: = W [I, 1] − W [I, J]
    'END'; B: = M [I] + B
'END';

'FOR' J: = 1 'STEP' 1 'UNTIL' M [1] 'DO' DWK [1, J]: = DW [1, J];
DWK [2, 1]: = ((T [2, 1] − T [1, 1])/(T [1, 2] − T [1, 1])) * DWK [1, 2];
'FOR' J: = 2 'STEP' 1 'UNTIL' M [2] 'DO' DWK [2, J]: = DWK [2, 1] + DW [2, J];

'FOR' I: = 1 'STEP' 1 'UNTIL' (L − 2) 'DO'
'BEGIN' 'FOR' J: = 2 'STEP' 1 'UNTIL' M [I + 2] 'DO'
    'BEGIN' DWK [I + 2, 1]: = ((DWK [1, 2] − DWK [+1, 1])/
      (T [I, 2] − T [I + 1, 1])) * (T [I + 2, 1] − T [I + 1, 1]) + DWK [I + 1, 1];
      DWK [I + 2, J]: = DWK [I + 2, 1] + DW [I + 2, J]
    'END'
  'END'
'END'

'BEGIN' 'COMMENT' BERUECKSICHTIGUNG GANGKORREKTUR;
  'INTEGER' B, S, H, A; H: = 0; B: = 0;
    'FOR' I: = 1 'STEP' 1 'UNTIL' L 'DO'
    'BEGIN' 'FOR' J: = 1 'STEP' 1 'UNTIL' M [I] 'DO'
      'BEGIN' K: = B + J;
        DWKV [K]: = DWK [I, J]
            'END';
            B: = M [I] + B
        'END';
      TK [1]: = TW [1]; PK [1]: = P [1]; DWKVK [1]: = DWKV [1];

    PRINT ('('DATEN FUER KORREKTURKURVE')'); PRINT ('(' ')');
    PRINT ('('    PUNKT        ZEIT              BETRAG')');

     'FOR' K: = 2 'STEP' 1 'UNTIL' SU 'DO'
      'BEGIN' S: = 2; 'FOR' J: = 2 'STEP' 1 'UNTIL' SU 'DO'
        'BEGIN' 'IF' TW [K] 'GREATER' TW [J] 'THEN'
          'BEGIN' H: = 1;
              S: = H + S
        'END' 'ELSE' 'BEGIN' H: = 0; S: = S 'END'
        'END';

          TK [S]: = TW [K]; PK [S]: = P [K]; DWKVK [S]: = DWKV [K]
      'END';
      'FOR' K: = 1 'STEP' 1 'UNTIL' SU 'DO'
        PRINT (PK[K], TK [K], DWKVK [K]);
        'FOR' K: = 1 'STEP' 1 'UNTIL' SU − 1 'DO'
        'BEGIN' A: = PK [K]; B: = PK [K + 1];
        'FOR' J: = 1 'STEP' 1 'UNTIL' B − A 'DO' 'BEGIN' I: = A + J − 1;
        X [I]: = (J − 1) * (DWKVK [K + 1] − DWKVK [K])/(B = A);
X [I]: = DWKVK [K] + X [I]
              'END'
          'END';
    PRINT ('('KORRIGIERTE MESSWERTFOLGE')'); PRINT ('('    ')');
    FIRST (2); X [N]: = DWKVK [SU]; 'FOR' I: = 1 'STEP' 1 'UNTIL' N 'DO'
    'BEGIN' GKXI [1]: = X [I]; MTWRITE (2, I, GKXI) 'END'; LAST (2);
    ADVANCE (2, 0); ADVANCE (1, 0); 'FOR' I: = 1 'STEP' 1 'UNTIL' N 'DO'

    'BEGIN' MTREAD (1, I, XI); X [I]: = XI [1]; MTREAD (2, I, GKXI);
            X [I]: = X [I] + GKXI [1];
            OUTPUT (2, '('E')', X [I])
        'END'; PRINT (X)
      'END'
    'END'
  'END'
'END';
```

REFERENCES

BEIN, E., 1961. Ergebnisse von Drehwaagemessungen an der Mitteldeutschen Hauptlinie (Abbruch von Wittenberg). *Z. angew. Geol.* **7,** 396–403.

BUETTNER, K. J. K., KERN, C. D., 1963. Infrared emissivities of the Sahara from TIROS data. *Science* **142,** 673–674.

GEERTSMA, J., 1971. Finite element analysis of low temperature anomalies. *Geophys. Prosp.* **19,** 662–681.

LYON, R. P. R., PATTERSON, J., 1969. Airborne geological mapping using infrared emission spectra. Proc. 6. Symp. Rem. Sens. Envir., *Ann. Arbor. Mich.* 527–552.
OELSNER, CH., 1969. Geothermische Oberflächenprospektion mittels IR-Strahlungstemperaturen (in manuscript). Habilitationsschrift, Bergakademie Freiberg.
OELSNER, CH., 1970. Verfahren und Anordnung zur geothermischen Prospektion, insbesondere an der Erdoberfläche. DDR-Patentschrift 75584.
OELSNER, CH., DONNER, F., 1974. Zur Registrierung und automatischen Verarbeitung oberflächengeothermischer Meßdaten. *Geod. Geophys. Veröff. d. NKGG d. DDR.* Reihe III. (in print).
SCHIRMER, H., 1970. Programmiervorschrift für den R 300— ALGOL — Compiler. Rechenzentrum, Techn. Univ. Dresden.
STEINER, D., 1971. Towards earth resources satellites: the American ERTS and SKYLAB programs. *Photogrammetria*, **27**, 211–251.

THE MEASUREMENT OF THERMAL CONDUCTIVITY OF ROCKS BY MEANS OF AN AUTOMATIC APPARATUS

M. KREŠL

INTRODUCTION

The calculation of the terrestrial heat flow in a certain point of the earth's surface is based on the knowledge of the thermal field gradient and of the thermal conductivity of the rock in the point. Temperature measurements are carried out by means of logging thermometers in boreholes, without any substantial troubles up to the depth of 1500 m. A number of methods for measuring thermal conductivity has been elaborated, both in laboratory and *in situ*. (Bia and Combarnous, 1970, Čermák and Krešl, 1968, Hartge and Taylor, 1970, Lippmann, 1967, Pollack, 1965, Tye, 1969 and other works.) The routine measurement of a great amount of core samples requires a measuring method, which enables automation of the process. In choosing the method for the automatic device one must take into account the requirements for reliability and accuracy of the results as well as the shape of the rock sample. The automatic device is expected to carry out long-term measurements of a considerable number of samples and, therefore, the easy shaping of the core samples is one of the foremost items to be considered in choosing the method of measurement. Economically the most suitable shape seems to be a cylinder with parallel bases. The measuring method, working with cylindrical specimens, and offering a relatively easy way to express explicitly the majority of interfering influences is the divided-bar method. (Čermák and Krešl, 1968). The heat flow passes through the sample and the standard arranged in series and forms a temperature gradient across them. The ratio of the temperature gradient across the sample to that across the standard is directly proportional to the thermal resistance of the sample. The practical realization of the divided-bar method is subject to systematic errors (for their analysis see e.g. Čermák and Krešl, 1968).

THE THERMAL CONDUCTIVITY APPARATUS

In the Geophysical Institute, Czech. Acad. Sci., an apparatus was developed, designed for automatic measurements of the thermal conductivity of rocks, working on the principle of the divided-bar. Rock samples are of cylindrical shape, of diameter 21.5 mm, their thickness is from 3 to 10 mm.

The mechanical part is shown schematically in Figure 1. The substantial part consists of two steel bars, supported by two heat exchangers, connected to water circuits of two thermostats. The upper steel bar is firmly joined with the conductivity standard. Between the steel and the standard is sandwiched a thin copper disc holding a Cu-Ko thermocouple. The lower steel bar holds a similar copper disc with thermocouple as well as the other

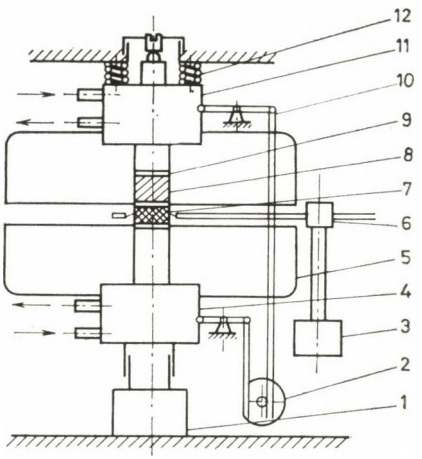


Fig. 1. Mechanical arrangement of the instrument
1 – electromotor and gear-box for fastening the samples between the clamps; 2 – circular potentiometer for measuring the thickness; 3 – electromotor and gear-box for revolving the container; 4 – lower heat exchanger; 5 – aluminium housing; 6 – container with samples; 7 – sample; 8 – standard; 9 – plate with thermocouples; 10 – leverage for turning the potentiometer; 11 – upper heat exchanger; 12 – springs for developing the pressure

side of the standard. The sample can be sandwiched between the clamps by a certain pressure. The bottom part of the divided-bar is movably mounted on leading rods and actuated over a gear box and screw by means of an electromotor. The thrusting power is balanced by springs, the shortening of which serves as a signal for shutting down the electric motor after the pressure set is reached by the control unit. The pressure can be set over a range of 300–1500 Nc m^{-2}. The measuring clamps are insulated by cotton wool and protected by an aluminium cover, 180 mm in diameter. During the measurement of thermal conductivity the thickness of the sample is measured as well. The information about the thickness is derived from the resistance of a precise circular potentiometer turned by a system of levers.

Before beginning a series of measurements the rock sample must be deposited in a round container the capacity of which is 20 samples. An electric motor turns the container and in regular intervals puts the samples to be measured between the clamps. The time interval can be preselected by a push-button control in six steps within the range from 10 min to 1 h.

The thermal conductivity standard is made of natural quartz crystal, the axis of the cylinder parallel with the optical axis of the crystal, length $H_n = 15$ mm, thermal conductivity $\lambda_n = 6.573 - 0.016\,T[\mathrm{Wm^{-1}K^{-1}}, °C]$.

The measuring range of the device encompasses all types of rocks: $\lambda_{s\,\min} = 0.4[\mathrm{Wm^{-1}K^{-1}}]$, $\lambda_{s\,\max} = 8[\mathrm{Wm^{-1}K^{-1}}]$ (Ratcliffe, 1959).

The Cu–Ko thermocouples measure the temperature difference across the standard ΔT_n and the sample ΔT_s. The thermocouple voltage is of the order of several tens of microvolts and therefore it is amplified by a D. C. amplifier of an amplification coefficient of 86 dB. The amplified signal is fed to the input of the divider unit. The output of the divider unit is proportional to the ratio $\Delta T_s/\Delta T_n$. This analogue voltage is fed to the digital voltmeter connected to a type printer.

The function of the whole instrument is controlled by a *control unit* (Fig. 2). This unit receives clock impulses. Each impulse gives a command to measure and print out the thickness of the sample and its thermal conductivity and to change the sample.

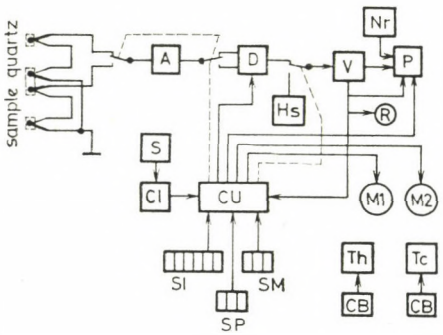


Fig. 2. Simplified circuit diagram of the electronic and control unit
A – amplifier; *D* – dividing unit with memory; *V* – digital voltmeter; *P* – printer; *Nr* – ordinal numbers of the sample; *Hs* – thickness of the sample; *R* – out-of-range indicator; *S* – stop watch; *Cl* – clock impulses; *CU* – control unit; *M1*, *M2* – electromotors; *Th*, *Tc* – thermostats; *CB* – control box for thermostat; *SI* – push-buttons for setting the time interval; *SM* – push-buttons for operating the motors; *SP* – push-buttons for operating the electronics

The temperature difference over the divided-bar is 25 °C, it is possible to choose this value between temperatures from 15 °C to 85 °C. The value of 25 °C is related to the requirement that heat losses over the divided-bar should be as low as possible and to the sensitivity of the amplifier with regard to the signal-to-noise ratio.

The functioning of the apparatus can be explained by means of the equation

$$\varrho_s H_s = \lambda^{-1}{}_n H_n(\Delta T_s/\Delta T_n) - R_k$$

The quantity $\varrho_s = \lambda_s{}^{-1}$ represents the specific thermal resistance of the sample, R_k is the total contact resistance, H_s the thickness of the sample. The magnitude of $\varrho_s H_s + R_k$ is the final result of a single measurement and it is proportional to the printed out number. Measurements of several samples of the same rock but of different thickness allow to eliminate the contact resistance R_k from the result. This may be done mathematically

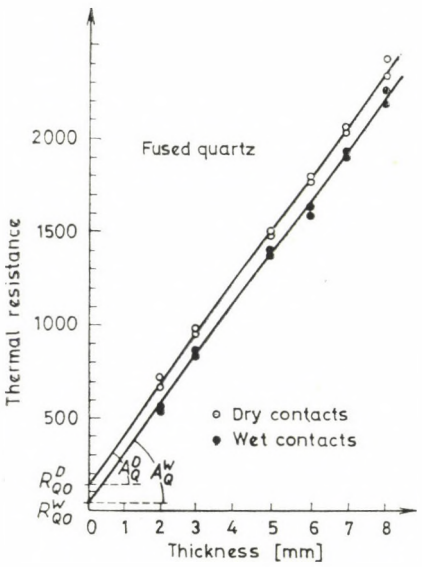


Fig. 3. Measured and adjusted values of thermal resistances of fused quartz (in relative numbers)

on a computer, using the least-squares method. When we measure inhomogeneous rocks, it frequently occurs that two samples of the same rock are not of the same composition. Therefore a program was elaborated, that allows to eliminate the influence of not representative samples. (See pp. 53–56.)

The device is calibrated by measuring samples of fused and crystalline quartz (Fig. 3). As an example let us follow the measuring of fused quartz ($\lambda_Q = 1.323 + 1.920 \cdot 10^{-3}T$[$Wm^{-1}K^{-1}$, °C]) (Ratcliffe, 1959). Each

TABLE 1

Calibration by means of fused quartz

Thickness [mm^{-2}]	Fused quartz, surface, dry						
	measurement		adjusted values	error			
	1.	2.		absolute		%	
200	669	716	685.07	−16.07	30.93	2.35	4.51
299	971	944	955.34	15.66	−11.34	1.64	1.19
499	1487	1486	1501.34	−14.34	−15.34	0.96	1.02
600	1768	1767	1777.07	− 9.07	−10.07	0.50	0.57
698	2033	2037	2044.61	−11.61	− 7.61	0.57	0.37
800	2312	2397	2323.07	−11.07	73.93	0.48	3.18
892	2600	2531	2574.23	25.77	−43.23	1.00	1.68

$$R_{Qo}^{(d)} = 139.07 \pm 16.42$$

$$A_Q^{(d)} = 2.73 \pm 0.03$$

Thickness [mm^{-2}]	Fused quartz, surface, wet						
	measurement		adjusted values	error			
	1.	2.		absolute		%	
200	547	544	561.89	14.89	−17.89	2.65	3.18
299	832	854	827.10	4.90	26.90	0.58	3.25
499	1369	1393	1363.21	5.79	29.79	0.42	2.19
600	1625	1576	1633.89	− 8.89	−57.89	0.54	3.54
698	1885	1911	1896.53	−11.53	14.47	0.61	0.76
800	2237	2164	2169.89	67.11	− 5.89	3.01	0.27
892	2402	2387	2416.45	−14.45	−29.45	0.60	1.22

$$R_{Qo}^{(w)} = 25.89 \pm 13.41$$

$$A_Q^{(w)} = 2.68 \pm 0.03$$

sample was measured four times: twice with dry contacts (subscript "d") and twice with wet contacts covered with a glycerine film (subscript "w"). In Table 1 are given the printed out relative numbers. These numbers are given by the constant of the analogue-digital converter and are used in all the following formulae.

The equation of the straight line of thermal resistances obtained by the least-squares method is

$$R_Q = R_{Q_0} + A_Q H$$

where R_{Q_0} is the contact resistance of quartz, A_Q is the slope of the line and H is the thickness of the sample. Adjusted results of an unknown rock lead to a similar equation

$$R_S = R_{S_0} + A_S H$$

The coefficient of thermal conductivity of that rock $\lambda_S = (R_S/H)^{-1}$ can be calculated from the formula

$$\lambda_S = \lambda_Q(A_Q/A_S)$$

whatever the coefficient of proportionality of the relative numbers may be.

The samples of fused quartz used for calibration have both their surfaces polished. For mass measurements of rocks it is impossible to polish the surface, not to speak about coarse grained materials, the surface of which is rough. This is the reason why both the contact resistance and the deviation of results are not so low in general as it is shown in Table 1. In this table the lowest obtainable values are compiled, their nature being originated in the construction of the electronics of the device. The influence of surface quality, the rate of occurrence of different sorts of surfaces and correlation between surface roughness and contact resistance is described in Čermák and Krešl (1968).

Measurements of samples thicker than about 12 mm have shown that thermal resistance, when plotted versus thickness, deviates from the straight line, the sign of the deviation being positive when the heat flow through the divided-bar has its direction from below upwards and vice versa. The deviation is caused by lateral heat losses from the sample, which is the only uninsulated part of the thermal circuit. Isotherms of the field in

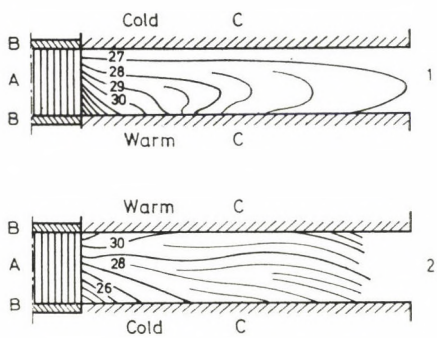


Fig. 4. Thermal field in the air gap between aluminium housings. The heat flow direction from below upwards (1) and from above downwards (2)
A – sample; B – thermocouple

the environment of the 12 mm thick sample are shown in Figure 4. With the thickness greater than 12 mm the isotherms in the tight surroundings of the sample are no more equidistant, causing the distorsion of results. The case when the range of linearity is exceeded is marked in the printout by an auxiliary symbol.

The automatic device is capable to work 24 hours a day. The attendance needs not to do anything but change the containers and fill them anew after the whole contents of the container have been measured. To make the operation proof against failures the device is equipped with a series of auxiliary and checking circuits.

ACKNOWLEDGMENTS

The author wishes to thank Dipl. Ing. Z. Podroužková, Geophys. Inst. Czech. Acad. Sci. for the construction of the mechanical part of the device and Dipl. Ing. I. Veselý for the design and realization of the basic electronic circuits and for preparing rock samples and carrying out the calibration.

REFERENCES

Bia, P., Combarnous, M., 1970. Measurement of thermal conductivity of rocks. *J. Phys., E, Sci. Instr.* **3,** 536.

Čermák, V., Krešl, M., 1968. Thermal conductivity of rocks and its measurement on the divided-bar apparatus. *Trav. Inst. Géophys. Acad. Sci. Tchécosl.* No. 274, Academia, Praha, 287.

Davydov, Yu. S., Chsachev, V. A., 1972. A method to determine thermal conductivity (in Russian). *Izmeritelnaya Tekhnika* 55.

Hartge, L. C., Taylor, R. E., 1970. Evaluation of direct heating methods for measuring thermal conductivities. *High Temp.-High Press.* **2,** 641.

Ho, C. Y., Taylor, R. E., 1969. Thermal conductivity. Proc. 8. Conf., Plenum Press, New York.

Krešl, M., Veselý, I., 1972. Instrument for the automatic measurement of the coefficient of heat conductivity of rocks. *Trav. Inst. Géophys. Acad. Sci. Tchécosl.* No. 361, Academia, Praha 317.

Lippmann, S., 1967. Ein Verfahren zur Bestimmung der Temperaturleitfähigkeit. *Exp. Techn. Phys.* **15,** 121.

Michejew, M. A., 1962. Grundlagen der Wärmeübertragung. VEB. Berlin.

Pollack, H. N., 1965. Steady state heat conduction in layered mediums. *J. Geophys. Res.* **70,** 645.

Ratcliffe, E. H., 1959. Thermal conductivities of fused and crystalline quartz. *Brit. J. appl. Phys.* **10,** 22.

Shorin, S. N., 1964. Thermal Conductivity (in Russian). Izd. Vysshaya Shkola, Moscow.

Tye, R. P., 1969. Thermal Conductivity. Acad. Press., London–New York.

Wagner, P., 1969. Measuring the thermal conductivity of a rod in the high temperature. *Brit. J. appl. Phys., D,* **2,** 293.

THE MEASUREMENT OF THE PRESSURE-DEPENDENCE OF THERMAL DIFFUSIVITY IN ROCKS

U. SEIPOLD

Determination of the thermal conductivity of rocks is a prerequisite for the calculation of heat flow. Apart from this, the value of thermal conductivity is necessary for all theoretical model calculations on the thermal history of the earth. In this context, the pressure- and temperature-dependence of this quantity are of particular interest.

The variation of thermal conductivity with temperature has been examined in a number of papers, the usual result being a proportional correlation, within the accuracy of measurements, of $1/T$. Measurements of this type are not free of problems, for it is to be feared that as the samples are heated cracks occur which simulate effects not corresponding to the behaviour in the earth's interior. It is therefore desirable that studies carried out at higher temperatures should be conducted, if possible, under a simultaneously increased pressure. The first observations on the pressure-dependence of λ were made by Bridgman on a few samples as early as 1924, but it had not been possible at this time to extend the method to higher pressures. Since then, no significant development has been made in this field apart from a few studies carried out under uni-axial pressure, and it is not known exactly whether these are representative for the conditions of hydrostatic pressure.

In these circumstances we tried to find a measuring method which would give results with sufficiently high accuracy even for very high pressures. A method of this kind has to take into account the following conditions:

1. the sample must be small and if possible its shape has to fit the pressure chamber used;
2. the only connection with the sample during measurement can be via electrical leads, and even the number of these should be minimized;
3. thermal insulation of the sample is not possible;
4. the measuring time should be as short as possible (a few minutes);
5. preparation must be possible even for hard rocks.

Taking all of these conditions into consideration, the stationary measuring method is immediately ruled out. In comparison with this, a modified Ångström method seemed to us as appropriate. The method makes use of a cylindrical sample surrounded by a tubular heater made of rheotan sheet (Fig. 1). A periodically fluctuating heating current of frequency ω flows through the heater, producing temperature waves in the sample flowing from the surface to the axis of the cylinder. By means of two thermocouples, the temperature at the surface and at the axis is measured as a

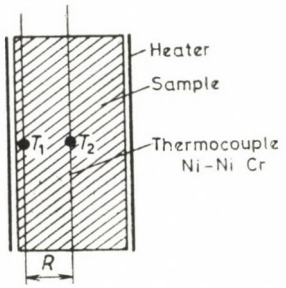


Fig. 1. Principle of measurement

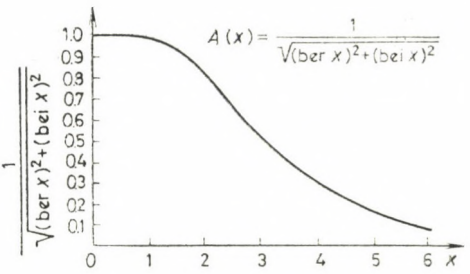


Fig. 2. Graph of $A(x)$

function of time. For evaluation, the amplitudes of temperatures T_1 and T_2 are determined from the recordings (see Fig. 1) and their ratio

$$A = \frac{T_2}{T_1}$$

is formed.

According to the theory of thermal conductivity, the following equation applies for the amplitude ratio:

$$A = [(\mathrm{ber}\ x)^2 + (\mathrm{bei}\ x)^2]^{-1/2}$$

where the auxiliary quantity $x = \left(\frac{\omega}{k}\right)^{1/2} R$ contains the thermal diffusivity k, "ber x" and "bei x" are special Bessel-functions, R = distance between the thermocouples. Evaluation is made by means of a graph, i.e., from the curve $A = A(x)$, x is determined for the measured value of A, and k is then calculated from the result. It can be seen from the curve $A(x)$ that in order to attain a high degree of accuracy one should, if possible, work in the central part of the curve, around $A = 0.5$ (Fig. 2). As a compromise between the requirement for a small sample size and for a high accuracy of measurement in determining distance R between the thermocouples, we chose a sample diameter of 10 millimeters. As for the frequency, in most rocks 0.1 Hz proves to be appropriate for coming into the favourable curve region.

In deriving the relations for the evaluation, a sample of infinite axial length is assumed. This condition is practically fulfilled if the length is four or five times the diameter. The length of the sample selected was, accordingly, 42 millimeters.

One problem to be faced was how to insert the thermocouples accurately into the sample without setting up contact resistances. This was solved by cutting slits in opposite sides of the sample cylinder by means of a thin abrasive disk (0.2 millimeters) held in a suitable device, and then cementing the thermocouples into the slits. The thermocouples, in the extended form required, were made by spot welding.

In the practical design, the sample is held by a suitable teflon mounting in a piston cylinder chamber. The measuring system is fitted on the base

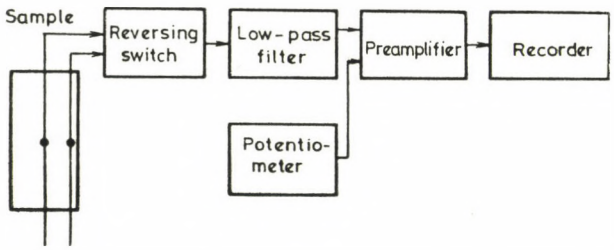


Fig. 3. Recorder system for thermoelectric power

screw which seals the bottom end of the pressure cylinder. The instrument leads to the thermocouples and the conductor for the heating current pass through holes bored in the screw. The opening at the top is closed by the pressure piston which is pressed into the chamber by a hydraulic press so as to generate pressure. The piston is sealed by a Bridgman mushroom-type seal.

For generating temperature waves, heat current fluctuations of some 120 A amplitudes are needed. These high currents are supplied by a high-current transformer. To produce the long-period fluctuations, the primary voltage of this transformer is varied by means of a magnetic amplifier. The magnetic amplifier has four control windings, the first of which is used for setting the operating point. The drive current for the second winding is supplied (after suitable amplification) by a low-frequency generator. Thus the resistivity of the transductor together with the primary voltage of the high-current transformer fluctuates with the generator frequency.

When heating up the sample it must be taken into account that the heating current is proportional to $\sin\omega t$, while the temperature wave generated is proportional to $\sin^2\omega t$. It is a known fact that decomposing the function $\sin^2\omega t$ it will contain, apart from $\sin 2\omega t$, also a term which is stable in time. This constant term leads to a steady heating of the sample, with the periodic temperature fluctuation superimposed.

Figure 3 shows the device for recording the thermoelectric voltage. A recording potentiometer with a response time of 0.2 seconds and maximum sensitivity of 1 mV for full scale deflection is used. A compensation voltage is fed in to suppress the constant thermo e.m.f. By this means, temperature waves with amplitudes of a few degrees can accurately be measured. The thermoelectric voltage at the two measuring points is recorded in succession. It is, however, possible to record them simultaneously, since the recorder

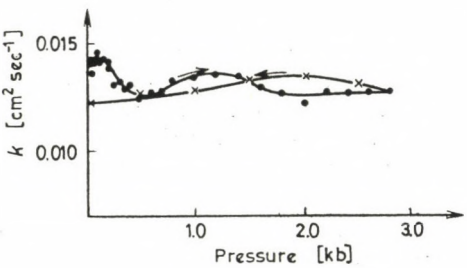


Fig. 4. Thermal diffusivity of anhydrite in function of pressure

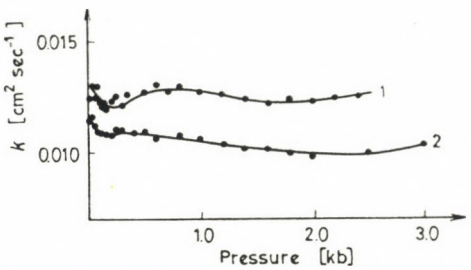


Fig. 5. Anisotropy of anhydrite
1 – axis of the sample perpendicular to the sedimentation area; 2 – axis of the sample in the sedimentation area

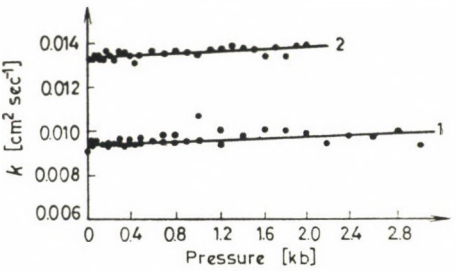


Fig. 6. Thermal diffusivity of sandstone in function of pressure
1 – sandstone, sample 1; 2 – sandstone, sample 60

has two separate channels. This is important for the determination of k by the phase shift between the waves at the two measuring points.

The first measurements were made on samples of sandstone and anhydrite. As a rule, against all expectations no marked pressure-dependence of thermal diffusivity has been found. Figure 4 shows the difference for increasing and decreasing pressure usually observed in high-pressure experiments and due to the irreversible changes produced in the sample. To ascertain possible anisotropy of thermal diffusivity, in case of anhydrite some of the cylindrical samples were cut out with the axis of the cylinder perpendicular to the plane of stratification, while in an other series the axis was in the plane of stratification. The measurements revealed no significant qualitative differences (Fig. 5). Figure 6 shows the thermal diffusivities measured in two different sandstones. On the whole, according to these preliminary investigations, the changes induced by pressure are below 10 % of the initial value. The measurements reported were made at pressures up to 3 kb.

CORRELATION BETWEEN THERMAL CONDUCTIVITY AND OTHER PHYSICAL PARAMETERS OF ROCKS

S. PLEWA

Rocks can be described by a set of various physical quantities, such as porosity, electrical, radiometrical and thermal parameters, which depend on the conditions of rock formation, their mineralogical and petrophysical characteristics and conditions of occurrence. Of these quantities, the thermal parameters of the rocks are amongst the most important. The thermal conductivity λ and thermal diffusivity k of rocks depend on temperature and pressure, as well as on mineral composition, bulk density, porosity and saturation. The relationships between these properties have not yet been fully recognized and understood, hence the interest in this problem.

In the present study for the determination of the thermal properties of rocks the stationary method (Chmura, 1968) was used, the rock samples being disks 42 and 50 mm in diameter and 12 to 14 mm thick. The majority of measurements were carried out in the Department of Geology and Hydrogeology of the Silesian Technical University, and some at the Institute of Geophysics of the Czechoslovak Academy of Sciences in Prague. Thermal conductivity, in W/mK was determined by the said method according to the formula

$$\lambda = \frac{Q \cdot \delta}{A \cdot \Delta T - 0.11 \cdot 10^3 \cdot Q} \left[\frac{\mathrm{W}}{\mathrm{mK}}\right]$$

Here, Q is thermal power in watts, δ is sample thickness in meters, A the area of its flat surface in square meters, and ΔT the temperature difference between the two flat surfaces in K.

In an earlier study (Plewa, 1966), the thermal conductivity and diffusivity of a few rocks were determined by employing a short-duration linear source of heat (Lubimova et al., 1964). These measurements were performed on rock samples 90 mm in diameter.

All of the measurements mentioned were carried out on fully water-saturated samples at an ambient temperature of 20 °C. Apart from thermal properties, the mineral composition, density, granular and chemical porosities were determined for all samples, whereas for some the electric conductivity, formation factor, velocity of propagation of longitudinal elastic waves, etc. were also determined.

The rock samples were taken from different stratigraphic series and different geological areas of Poland.

The sedimentary rocks examined have a thermal conductivity ranging between 0.884 to 1.642 W/mK for chalk and 5.536 W/mK for quartzite sandstone (conglomerate). Of the terrigenous rocks examined, shales have

TABLE 1

Mineral composition of sandstones

Mineral	Volume percentage		
	C-609	C-662	C-668
Quartz	85.0	68.5	87.0
Chalcedony	–	4.5	2.4
Feldspars	0.7	0.6	0.2
Micas	0.3	0.1	–
Accessory minerals	0.7	0.4	0.1
Opaque minerals	0.3	–	0.2
Femic minerals	–	1.1	–
Anhydrite	10.3	–	–
Kaolinite	2.7	4.8	–
Illite	–	18.2	4.1
Carbonates	–	1.8	0.6
Dolomite	–	–	5.4

the lowest thermal conductivity (1.221 W/mK). A detailed analysis was made on 32 samples of completely water-saturated Cambrian sandstones of the Podlasie Depression, and for sake of comparison, the thermal parameters of these rocks were also measured in air-dried state. These are fine- and very fine-grained quartzite sandstones cemented rather well by argillaceous matter with a predominance of kaolinite and illite. The mineral composition of three characteristic rock samples are given in Table 1. Their thermal conductivity at a temperature of 20 °C varies as: 2.98 W/mK for the sample C-662, 3.37 W/mK for the sample C-668, and 4.24 W/mK for the sample C-609. The values for the other samples are intermediate between those just stated.

An attempt was made for the same Cambrian sandstone samples to establish relationships between thermal conductivity λ, electric conductivity σ, formation factor F and longitudinal wave velocity V. The results obtained are given in Figures 1, 2 and 3. Since dispersion of the data is quite large, it was unfeasible to determine any functional relationships between these quantities by the correlation technique with any certainty.

Also investigated was the dependence of λ on depth of occurrence h and on rock density ϱ. The following formulae were found:

$$\lambda = -637.27 \frac{1}{h} + 4.88, \text{ with } r = 0.61$$

where h is in meters (only h's greater than 200 m were included in this investigation), and

$$\lambda = -20\,460 \frac{1}{\varrho} + 11.14 \text{ with } r = 0.57$$

where ϱ is in kg/m^3.

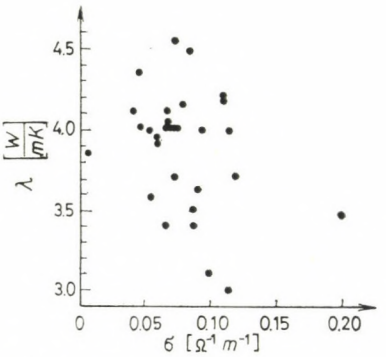


Fig. 1. Thermal conductivity λ *vs.* electric conductivity σ for Cambrian sandstone samples, Poland

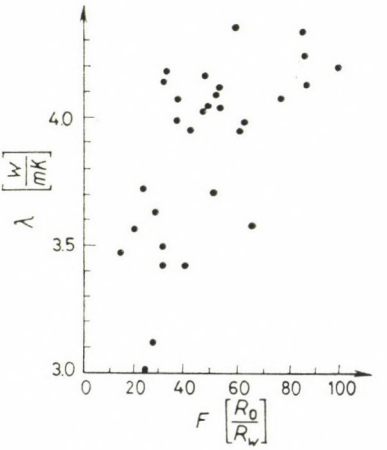


Fig. 2. Thermal conductivity λ *vs.* formation factor $F = R_0/R_w$ for Cambrian sandstone samples, Poland

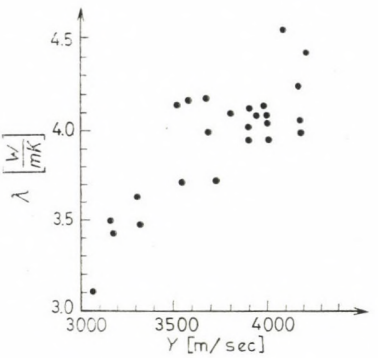


Fig. 3. Thermal conductivity λ *vs.* elastic wave velocity V for Cambrian sandstone samples, Poland

The dependence between thermal conductivity of sandstones and their SiO_2 content was obtained with an even smaller correlation coefficient ($r = 0.43$). It can be concluded that the admixture of other minerals affects the value of λ very strongly here.

For shales the dependence of λ on the depth of occurrence h has the form

$$\lambda = 0.00272\ h + 1.174, \text{ with } r = 0.72$$

where h is in meters (h $\geq$ 200 m), while for porosity φ we obtained

$$\lambda = 1.2\ \varphi^{-0.2}, \qquad \text{with } r = 0.61$$

Figure 4 presents the dependence of λ on porosity (in terms of water content) for Jurassic carbonates, expressed by the formula

$$\lambda = -\ 9.82\ \varphi + 4.12$$

obtained with a correlation coefficient of $r = 0.97$.

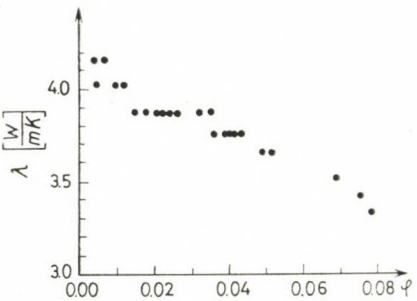


Fig. 4. Thermal conductivity λ *vs.* porosity φ for Jurassic limestone samples, Poland

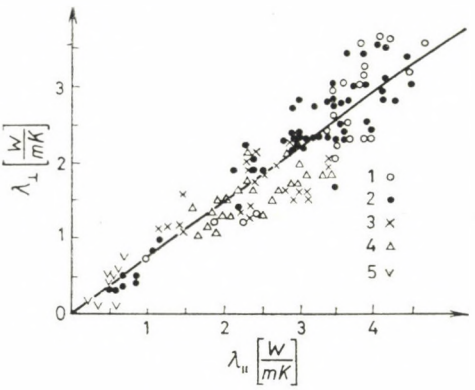


Fig. 5. Relationship between thermal conductivity measured parallel with ($\lambda_\parallel$) and perpendicularly to ($\lambda_\perp$) the stratification of rock samples (Chmura, 1968)
1 – grit; 2 – sandstones; 3 – siltstones; 4 – argillites; 5 – coals

The thermal conductivity of the Carboniferous hard coals and rocks of Upper Silesia was the topic of a research made by Chmura (1968). Figure 5 shows the dependence between the thermal conductivities measured parallel ($\lambda_\parallel$) and perpendicularly ($\lambda_\perp$) to the rock and coal strata. It turns out that stratification of rocks does not affect very much the results of measurements.

On the basis of the analyses performed it was ascertained that coarse-grained rocks have a higher thermal conductivity than fine and medium grained rocks in which there are many minute mineral particles of lower thermal conductivities.

Correlation dependences between the thermal diffusivity k and other rock parameters have also been determined. For sandstones the best correlation ($r = 0.67$) was that between k (in m^2/s) and porosity, viz.,

$$k = -5.98\,\varphi + 1.796$$

Here also, the porosity is equivalent to water content, for the examined samples were fully saturated with water.

Changes in the thermal diffusivity of sandstones for different depths of occurrence have been found to follow the relationship

$$k = -263.17\,\frac{1}{h} + 2.09, \quad \text{with } r = 0.55$$

where h is in meters ($h \geq 200$ m).

The results outlined here permit some conclusions to be made as regards the necessity of further researches on the relationship between the thermal conductivity and diffusivity of rocks and their mineralogico-petro-

graphical and granular compositions, porosity, temperature and pressure. It is believed that the saturation of rocks, especially as regards the kind of saturating medium and its content, substantially affects the thermal properties, for it is well known that the thermal conductivity of connate water reaches values of 0.35 to 0.50 W/mK and their thermal diffusivity ranges from $8.5 \cdot 10^{-2}$ to $11.5 \cdot 10^{-2}$ cm^2sec^{-1}.

Subsequent researches will deal with, alongside the thermal properties of rocks and their relationships with other physical properties, the thermal properties of connate waters and petroleum.

REFERENCES

CHMURA, K., 1968. Thermal properties of rocks and coals of the Upper Carboniferous Formations (in Polish). *Zeszyt Nauk. Politechn. Slaskiej* No. 190, Gliwice.

LUBIMOVA, E. A., STARIKOVA, G. N., SHUSHPANOV, A. P., 1964. Thermal investigations of rock formations (in Russian). *Geoterm. Issled.*, Nauka, Moscow.

PLEWA, S., 1966. Geothermal parameters of the various geological regions of Poland (in Polish). *Geofiz. i Geol. Naft.*, Kraków.

PROCESSING OF HEAT FLOW DATA — THERMAL CONDUCTIVITY AND TEMPERATURE GRADIENT

V. ČERMÁK

INTRODUCTION

The recent rapid growth of interest in heat flow and in prospecting for sources of geothermal energy has initiated a continuous effort to collect as much data on terrestrial heat flow as possible. To determine the terrestrial heat flow in an area, the vertical temperature gradient and the thermal conductivity of rocks in that area must be measured. Besides the common temperature logging for technical purposes, special precise discrete temperature measurements in holes are quite frequent in many countries at present. The general evidence on the distribution of the temperature gradient in individual geological sections and/or the geothermal profiles can be utilized for instance in oil prospecting or in hydrogeological research.

The determination of the coefficient of thermal conductivity of drilled rocks by *in situ* methods has not been successfully solved yet. So it is necessary to collect characteristic rock samples from a core or from the area of temperature measurement in a mine and to measure the thermal conductivity in laboratory. The necessity to handle a considerable (and ever increasing) number of rock samples conditions the search for either quick methods to determine thermal conductivity or to automate somehow the present ones.

The computer technique allows easy processing of a great amount of laboratory data as well as to build up a data bank of the temperature measurements performed in holes. When these data are interpreted for heat flow calculation, all the necessary corrections can be easily applied, such as small variations of the size of the laboratory specimens and temperature changes during the conductivity measurements; or the effect of topography, geological history, past climatic pattern, hole inclination etc. in temperature measurements.

In what follows two simple computer programs will be discussed: (1) processing of data of an automated divided-bar apparatus and thermal conductivity calculator, (2) analysis of temperature measurement in a hole smoothing the temperature gradient as a function of depth.

THERMAL CONDUCTIVITY CALCULATOR

Perhaps one of the greatest problems in the determination of heat flow is to obtain a good mean value of the thermal conductivity of rocks from a particular area. The usual practice is to collect what appears to be a representative number of specimens from a bore core or from a mine, where temperature measurement was performed. However, quite often in an apparently uniform piece of rock, belonging to the same petrological type,

the measured thermal conductivity of two small laboratory specimens cut just a few centimeters apart can differ by 20 per cent (and even more).

If the temperature in the hole had been measured before the rock samples were collected, the gradient analysis could help considerably to select the representative sections of a constant gradient to be sampled. By plotting the temperature gradient *versus* depth, all changes in the temperature field become more apparent; the rock samples must be taken regularly within these preselected intervals. When no temperature logging had been done before sampling, some help can be expected from a detailed petrological description of the core, which enables to select the typical rock types and their relative abundance. However, care should be taken when relatively thin layers alternate or when contacts between different layers are not certain.

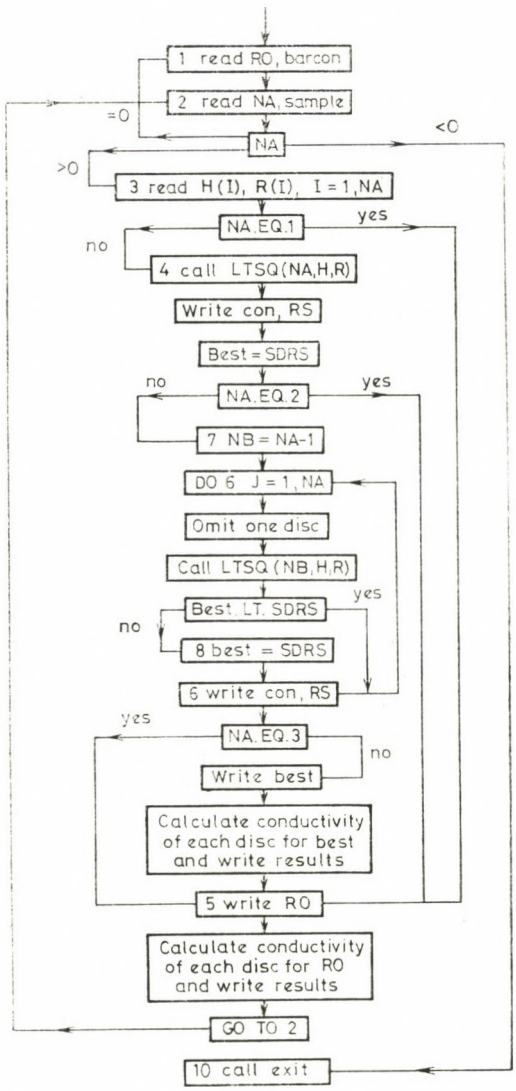
It was frequently found that sometimes significant changes in the temperature gradient occur even in a relatively uniform lithological section, and also that in some cases distinct changes in rock types were not accompanied by corresponding changes in the gradient. If these discrepancies are within 10—15 per cent of the observed heat flow value and they are more or less regularly distributed along the examined depth interval with no tendency to increase or decrease with depth, they might be neglected. If the number of samples were insufficient, some extra samples should be measured and the result should be checked by additional calculations of heat flow value in the most dubious sections. However, if the differences between heat flow calculated from different sections along the borehole are significant or if there is a systematic tendency of variation with depth, an explanation must be sought for. Among the possible reasons could be mentioned the insufficient thermal equilibrium of the hole (especially in oil wells and prospection holes), the incompensated effect of topography or past climatic changes, but most probably heat production within a particular section. Underground water movement (the most common reason for heat flow disturbances) can be interpreted in terms of heat generation for this purpose.

For the above mentioned reasons, simple sampling in regular depth intervals (e.g. a piece of rock every 20, 50 or 100 meters of borehole core) regardless of the lithology is not to be recommended, except in uniform geological areas. It is impossible to predict the minimum number of samples to be examined for a particular hole, the geological structure might be a very important factor. For a detailed heat flow investigation one sample every few meters of depth totalling some 150–200 rock samples for a 500–700 meter deep hole would be advisable. In most cases, however, a total of 20–40 samples for each kilometer of the borehole seems to be sufficient.

A more ambiguous problem arises in deep holes in sedimentary basins, usually drilled by rotary system, where there is only a limited number of samples to be chosen from. Quite often these sediments are very difficult to handle when laboratory specimens are prepared for conductivity measurements. If the scatter of local heat flow values calculated for individual sections along the hole profile is too large or if there is any doubt about the validity of conductivity measurements the heat flow determined for that hole should be considered as "not reliable".

The most widely used method for thermal conductivity determination is the relative measurement of the unknown conductivity of the sample in

Fig. 1. Block diagram of the CONDUCTIVITY CALCULATOR program



steady state conditions. Some form of a divided-bar apparatus is nowadays utilized in practically all heat-flow laboratories. In order to handle the increasing number of rock samples a fully automated version of the divided-bar apparatus was constructed in the Geophysical Institute of the Czechoslovak Academy of Sciences. The apparatus can be used for 24 hours a day and it measures 60–80 discs prepared from rock samples during that time. The output data, i.e. thickness and total thermal resistance of each disc together with its serial number are printed on a paper tape. To take into account the effect of the thermal contact resistance between the bars

and the rock disc a series of minimum 3 discs (but better 4–5 discs) of each rock sample must be measured. Since the introduction of this apparatus in 1970 several thousands of discs have been measured. (See pp. 38–43.)

However, even if the measuring process is fully automated, considerable time is needed to calculate the coefficient of thermal conductivity for each set of discs, which can be reduced by using computer technique.

Figure 1 shows flow-chart of a FORTRAN program to calculate thermal conductivity for a set of I = 1, . . ., NA measured pairs of values H(I) and R(I); where H is thickness and R the total thermal resistance of each disc, respectively. SAMPLE is the alpha-numerical code (name) for that particular sample. BARCØN is the relative conductivity of the bars found by the calibration, RØ is the expected value of the contact thermal resistance based on previous experiments. For similar rock material and surface finish the value of contact resistance does not change too much.

As usually, the thermal conductivity of each set of discs (CØN) is calculated from the slope of the least squares line in the "total thermal resistance — thickness" graph; the intercept of this line at zero thickness gives the contact resistance, RS. The input data consisting of H, R are analyzed by the least squares method and conductivity together with contact resistance for a particular set (together with standard deviations) are calculated. To be able to exclude a single disc of a "different" measured conductivity (either real value caused by local inhomogeneity or an apparent value caused by erroneous measurement, different surface finish etc.), the least squares analysis is applied to a set of NB=NA-1 discs, when consequently one disc is omitted. The contact resistance with the smallest standard deviation (BEST) is then found and the conductivity calculated for each disc considered as a single measurement; the same procedure is repeated for the preselected contact resistance of RØ.

TEMPERATURE GRADIENT CALCULATOR

Many original temperature records used for the first heat flow calculations in Czechoslovakia were based on temperature loggings performed by different logging centres of the Geological Survey of Czechoslovakia. These measurements used to be done by logging resistance thermometers, temperature being measured continuously. From these records the temperature was read at predetermined intervals (usually every 20 meters), with an accuracy of ± 0.1 °C (best) to ± 0.5 °C. Since 1968 a light portable termistor thermometer has been used, with sensitivity much better than ± 0.01 °C and absolute accuracy of ± 0.02 °C. The temperature is measured discretely, usually at 10 meters intervals.

To calculate heat flow we must know the temperature gradient. The computer program (Fig. 2) makes possible to find the mean temperature gradient for the whole interval measured together with an extrapolated surface temperature; to calculate gradient-versus-depth curve and the characteristic temperature gradients for all lithological sections in the hole. In the flow-chart of Figure 2, T is the temperature read at depth ZT, NTD is the total number of temperature data from the hole NAME. The gradient

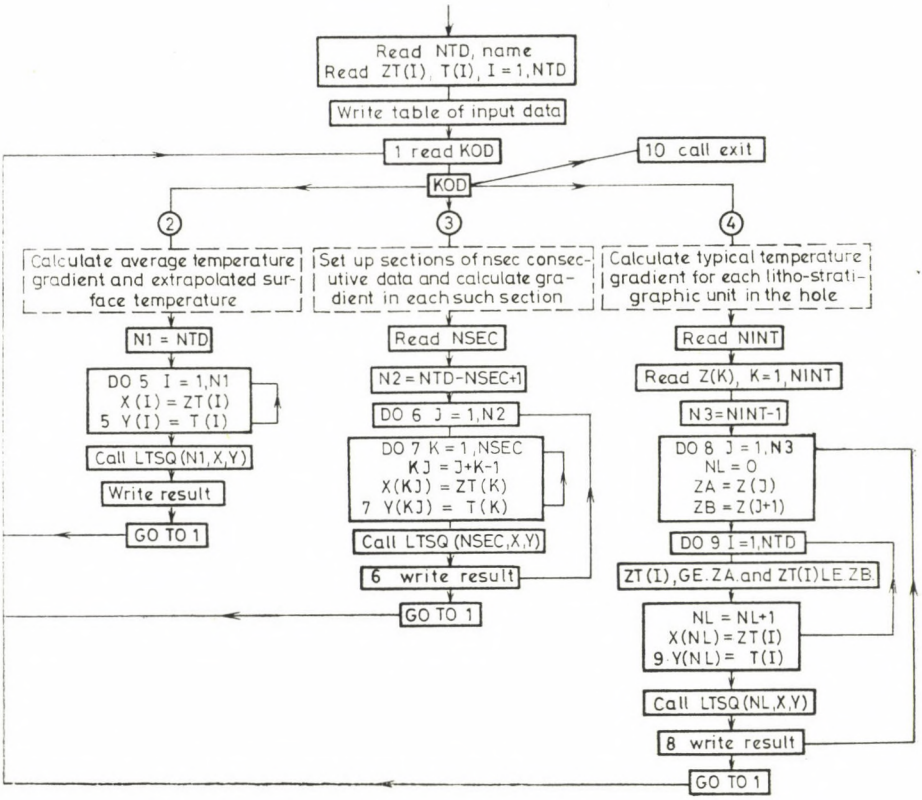


Fig. 2. Block diagram of the GRADIENT CALCULATOR program

is calculated by least squares analysis for all ZT, T data in a particular interval. To obtain the gradient-versus-depth curve the gradient is calculated for each possible section of NSEC consecutive data, e.g. from first to NSEC-th data, from second to the (NSEC + 1)-st, etc. By the use of different NSEC (corresponding to the different length of a section) a more or less smooth gradient curve is obtained. This curve is then combined with the measured thermal conductivity values of rock samples to find local heat flow. When the temperature measurement is performed in a hilly or mountainous region, the measured data must be corrected for topographical effects, similarly, if the hole inclines from the vertical or there is evidence to past climatic changes, the corresponding corrections must be carried out. The corrections can be found by calling a subroutine and the gradient of corrected temperatures is used then for heat flow calculation.

ACKNOWLEDGEMENTS

The original idea and encouragement received from Dr. A. M. Jessop at Earth Physics Branch, EM & R Dept., Ottawa, is greatly acknowledged. The author wishes to thank Dipl. Ing. M. Krešl and Dipl. Ing. I. Veselý, Geophysical Institute, CSAV, Prague, for their help in preparing rock samples for automatic measurement on divided-bar apparatus and to many workers of the Computing Centre, Institute of Applied Geophysics, Brno, for their help with the run of the programs. This work was supported by the Central Geological Institute, Prague, under project C-52-347-013 (ÚÚG-5109) "Study of the deep geological structure in the Neogene Foredeep and Flysch Zone of the Carpathians".

PALEOCLIMATIC EFFECT ON THE UNDERGROUND TEMPERATURE AND SOME PROBLEMS OF CORRECTING HEAT FLOW

V. ČERMÁK

INTRODUCTION

The value of terrestrial heat flow characterizes the outflow of thermal energy from the earth's interior. As such parameter it is primarily connected with deep processes occurring in the earth's crust and upper mantle. However, for the practical determinations of heat flow, temperatures are measured in holes or in mines up to a maximum of few kilometers depths. The temperature field near the surface may be considerably affected by surface topography and/or by surface history. Besides geological factors, such as uplift, erosion, sedimentation, etc., climatic changes must also be studied. The significant changes of surface temperature are slowly propagated downwards (Fig. 1) and the present underground temperature bears some kind of recollection of the past climate, which should be removed, i.e. correction of the measured heat flow is necessary.

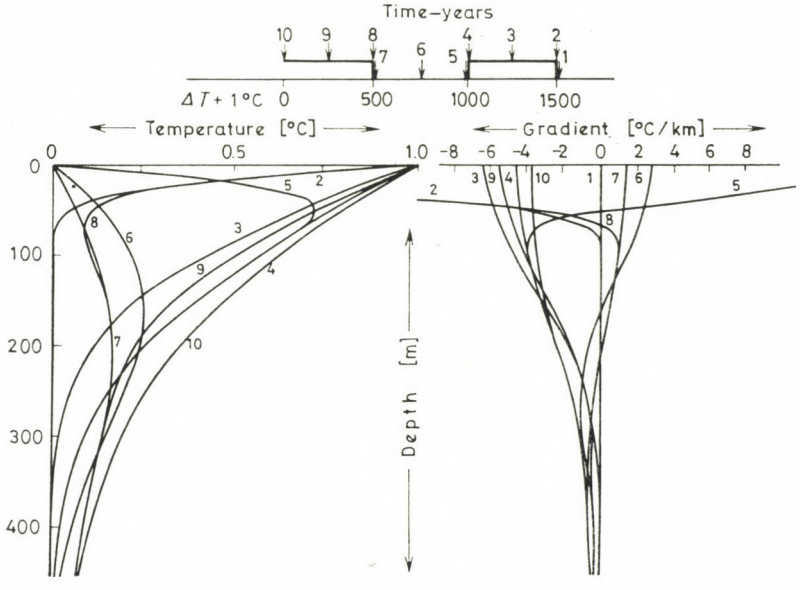


Fig. 1. Simple climatic model (surface temperature change + 1 °C) and corresponding disturbance in temperature and gradient distribution with depth at different times

The effect of the past climatic changes upon the temperature gradient was recognized by early heat-flow workers (Lane, 1923, Hotchkiss and Ingersoll, 1934). A general mathematical formulation is thoroughly discussed in Carslaw and Jaeger (1959), the theory of climatic corrections was put forth very completely by Birch (1948). Since then it was frequently applied by different authors, e.g. Jessop (1971), Čermák and Jessop (1971), Sass et al. (1971), etc. in terms of step functions; by Ciaranfi et al. (1973) in terms of finite Fourier series or by Gold and Lachenbruch (1973) in terms of a power series.

In a semi-infinite medium of constant thermal diffusivity k the disturbance of the present temperature $\Delta T(z)$ at depth z caused by a temperature difference T_i (which is supposed to have existed between present and past surface temperatures) at the interval (t_i, t_{i+1}) measured backwards from the present is

$$\Delta T(z) = T_i \{erf[z/(4kt_i)^{1/2}] - erf[z/(4kt_{i+1})^{1/2}]\}$$

Differentiating with respect to depth we obtain the corresponding disturbance of gradient, $\Delta G(z)$:

$$\Delta G(z) = T_i\{(\pi kt_i)^{-1/2}\exp(-z^2/4kt_i) - (\pi kt_{i+1})^{-1/2}\exp(-z^2/4kt_{i+1})\}$$

By combining a whole series of such terms, $i = 1, 2, \ldots, n$, the underground response can be calculated to any multiple step function of surface temperature. With the use of computers the time intervals may be made sufficiently small (n large) that any climatic history may be formally evaluated and any desired degree of accuracy may be obtained.

The crucial problem, however, is the determination of the value of t_i and T_i. The lack of information about the climatic history of different regions and the uncertainty about the real surface temperature during the individual time intervals, as well as, the uncertainty of what should really be considered a reference "today's" temperature, makes this calculation difficult.

GENERAL REMARKS

1. Untill recently it was believed that only temperature measurements in regions which were subjected to Pleistocene glaciation should be corrected. However, the decrease of surface temperature during ice-ages was obviously a world-wide phenomenon (Opik, 1967) and there is no reason to limit the application of climatic correction geographically. As the ice cover represented some insulation sheet under which temperature was kept close to the melting point, the bare land on the southern rim of the glacier may have been exposed (if snow failed to fall) to more severe conditions during the winters and thus mean annual surface temperature may have been lower here than below the ice.

2. The precipitation character and the snow fall regime are very critical parameters, as well as the vegetation cover, microclimate, prevailing wind system, topography etc. There could be a significant difference between

mean annual temperature (as measured in meteorology, estimated by paleobotanical evidence or determined e.g. by oxygen isotopic method) and the real surface (ground) temperature. The difference was estimated to be of about 5 °C in Kapuskasing area, Canada (Čermák, 1971) at present, but might be otherwise during the past or in other places.

3. There is considerable evidence that the world climate has undergone significant changes even during the recent few hundred years accompanied by temperature variations of a few degrees (Lamb, 1965, Čermák, 1971). Similar short-term climatic oscillations are likely to have existed in the past, too. A remarkable increase in annual temperature since about 1850 A. D. may reach 3 °C or even more (Mitchel, 1967). Many temperature profiles show negative gradient in the uppermost part (Jessop, 1968, Hyndman and Everett, 1968, Lubimova et al., 1966). The term "present" surface temperature is thus ambiguous and to find a real representative surface temperature over a long time interval could be doubtful.

4. The recent climatic history is relatively better known and recent excess surface temperatures have exerted more prominent effect on the temperature gradient than "older" changes (Birch, 1948) which are less supported by observational material. Anyhow, some attention should be paid to all Quaternary climatic pattern and even the present effect of Tertiary and Mesozoic warm non-glacial time may not be negligible (see Fig. 3).

5. The magnitude of the climatic correction depends on the thermal diffusivity of the rocks. The diffusivity $k = \lambda/c\varrho$ is very rarely measured itself, however, the specific heat c is relatively uniform for practically all rocks, being at interval 0.18—0.23 calg^{-1} (Kessler, 1927), and the density ϱ and the coefficient of thermal conductivity λ are measured. For crystalline rocks the diffusivity is of 0.010—0.015 cm^{2}sec^{-1}, for loose unconsolidated sediments it is lower, being at the interval 0.005—0.010 cm^{2}sec^{-1}. In a medium of smaller diffusivity the corresponding underground disturbances of temperature or gradient are more pronounced and shallower than in thermally more conductive rocks (Horai, 1969, Ciaranfi et al., 1973).

6. The representative ice-base temperature below the glacier is believed to be close to the melting point (Gow et al., 1968, Čermák, 1971), i.e. —1 to —2 °C depending on the thickness of the ice cover (Williams, 1967). The possible range of existing ice-base temperatures is broader, from 0 to —10 °C (or less). The lowest recorded ice-base temperature is —13 °C (Hansen and Langway, 1966). The ice-base temperature —4 °C proposed by Crain (1968) as representative value is probably too low. For a detailed calculation the pre-glacial environmental conditions, the possible occurrence of permafrost, the speed of glacier advance, the velocity of ice movement (the heat released by friction (Robin, 1955)) are to be accounted. Even when the glacier was very cold when it began to grow, its ice-base temperature was increasing slowly in time (if the snow accumulated quickly) due to the geothermal heat supply from beneath (Wexler, 1960).

7. The interglacials are usually believed to have been generally warm (Birch, 1948, Opik, 1967). As the total duration of interglacials exceeded the total Pleistocene glacial time, the value of excess surface temperature used in climatic corrections may be important, compensating considerable part of glacial effect on heat flow.

8. It is interesting to mention that by far the only precise deep temperature measurement performed in Flin Flon hole, Canada (Sass et al., 1971) failed to prove the existence of any large climatic recollections at depth.

MODELS OF PAST CLIMATE

Several models of the past climate (Fig. 2) based on various informations given in literature and representing different time intervals were selected. In Figure 3 the corresponding disturbances of the temperature gradient are plotted against depth. In all cases a uniform thermal diffusivity of 0.010 cm^2sec^{-1} was used.

a) M 0–50 model corresponds to an abrupt change in surface tempera-

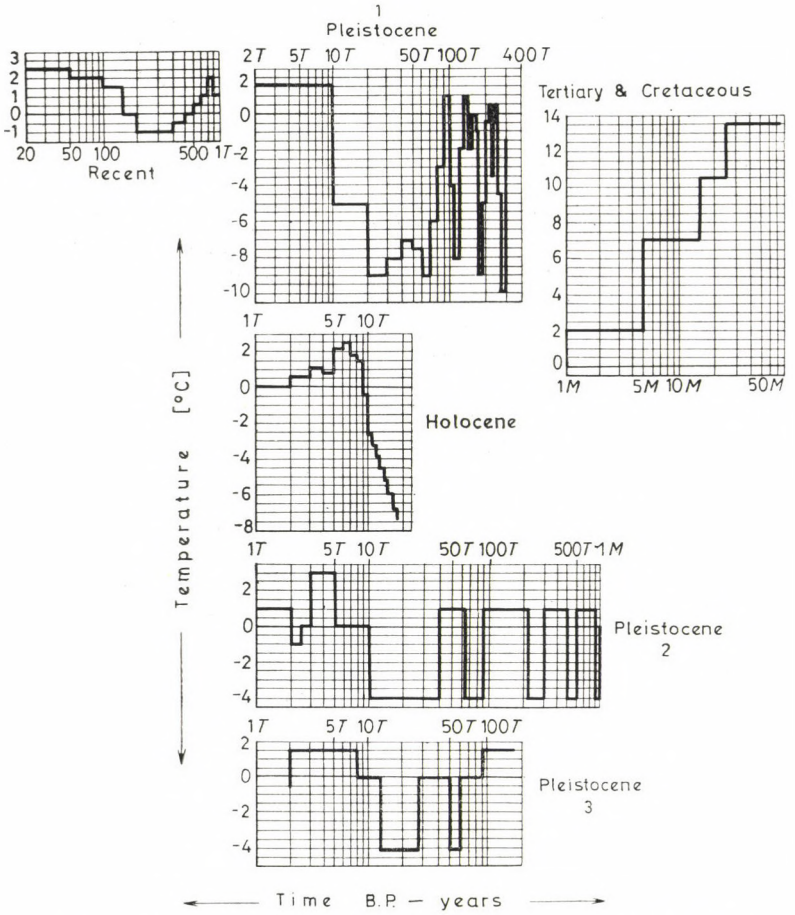


Fig. 2. Models of past climate for various time intervals (Note: T = thousand, M = million)

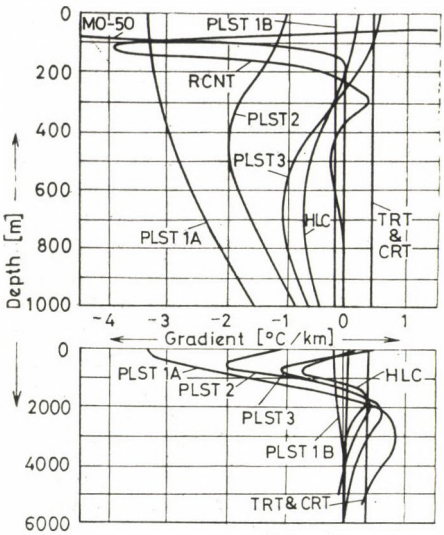


Fig. 3. Disturbance on the temperature gradient due to the past climatic changes (see Fig. 2). Coefficient of thermal diffusivity $k = 0.010$ cm^2 sec^{-1}. Upper part – detailed 0—1000 meters profile, lower part 0—6000 meters profile

ture +2.5 °C 50 years ago with no variations before. This model illustrates the possible effect of the increase of world mean temperature (Mitchell, 1967) and is to be combined with other models.

b) RCNT (recent) model covers the time span 50–1000 years B.P.; the model is based on the existence of two distinct climatic extremes, Little Climatic Optimum (700–1100 years B. P.) and Little Ice Age (200–500 years B.P.). The excess temperatures correspond to the results obtained by Čermák (1971) in two holes in the Canadian shield, the time sequence (a–b) was slightly modified to give more smooth temperature change in time.

c) HCL (Holocene) model (Fairbridge, 1967) covers the time span 1000–17,000 years B. P. and is aimed to show the effect of the increase of surface temperature following the Wisconsin (Würm) glaciation.

There are several models proposed for Pleistocene glaciation generally used when correcting measured heat flow.

d) PLST 1 (Pleistocene 1) model shows the fluctuations of mean annual land temperature in the time interval 1000–300,000 years B. P. proposed by Emiliani (1955). The time variations of open sea water temperature in the Pleistocene were estimated by vertical variation of the oxygen $^{18}O/^{16}O$ ratio in the pelagic foraminifera in oceanic sediments. This curve was then corrected to the variations of mean annual land surface temperature assuming that both land and open sea water temperatures varied proportionally (Horai, 1969).

Wisconsin (Würm) glaciation and the following warming is the main source of temperature distortion at depth compared with Illinoian (Riss) or Nebrascan (Günz) glaciations; to demonstrate the quickly decreasing amount of the recollection on the more remote climatic effect, two curves are shown in Figure 3, labelled PLST 1A and PLST 1B, which correspond to 1000–160,000 years B.P., resp. 160,000–300,000 years B.P. intervals.

e) PLST 2 (Pleistocene 2) model was used by Čermák and Jessop (1971) in northern Ontario, Canada. The model is based on Prest's (1957) Pleistocene chronology, the detailed local geological study by Bennett et al. (1967) and the Holocene history by Brysson and Wendland (1967) and is generally similar to Birch's (1948) 1B model. The total duration of Pleistocene in this model covers the time span 1000–1,000,000 years B.P. The key figures are: ice-base temperature −2 °C during ice ages (i.e. −4 °C relative to "present" surface temperature), interglacials +1 °C warmer than present, very warm Atlantic interval (4000–6000 years B.P.) and slightly colder sub-Atlantic interval (2000–3000 years B.P.).

f) PLST 3 (Pleistocene 3) model was proposed by Swanberg et al. (1974) for Scandinavia for the time interval 1000–165,000 years B.P. The firn line data by Liestöl (1960), polen diagram of Hammen et al. (1971) and mean annual ground temperatures (Norsk Meteorologisk Arbok, 1970) were utilized. This model is partly similar to Birch's (1948) 2B model.

g) TRT & CRT (Tertiary and Cretaceous) model shows the possible effect of the considerably warm climate in Pre-Pleistocene time (Opik, 1967). Temperature curve was set up according to results by Woldsteadt, Lowenstam, Epstein for isotopic temperatures of shallow seas in Europe and by Emiliani for equatorial Pacific and surface waters in polar latitudes.

DISCUSSION

Models shown in Figure 2 were chosen for different locations and are based on various evidence, so they cannot be of universal validity and are not recommended to be used to correct heat flow data without considering local conditions.

The effect of recent climatic changes (past millenium) is detectable only to the depth of a few hundred meters and is rapidly decreasing with depth. While the distortion of the heat flow may be of 20% at 100–200 m depth in shield areas where heat flow is low (~ 1 μcalcm^{-2}sec^{-1}), the effect is practically negligible below 300–400 meters ($< 1\%$).

Gradient disturbance due to the Wisconsin glaciation may reach −3 to −4 °C/km, but is partly reduced by warmer conditions of Climatic Optimum (Atlantic time) in interval 4000–6000 years B.P., so that the maximum correction would be of 1 to 2 °C/km at depth interval 300–800 meters. PLST 1 model yielding greatest disturbance −3 °C/km may be considered as extreme case due to low Wisconsin temperature, −7 to −9 °C relative to the present. Below 1000–1500 meters the disturbance changes sign, the climatic disturbance being positive below this depth, amounting to +0.5 to +1.0 °C/km.

When mean continental heat flow is considered of 1.5 μcalcm^{-2}sec^{-1} with a conductivity of 6 mcalcm^{-1}sec^{-1} °C, the uncertainty in heat to flow measurement is less than max. 10% (more probably 5–8%) below 300 meters. For temperature measurements in deep holes penetrating 2 km or more, the correction will be still smaller, partly cancelled by opposite contributions of colder and warmer periods, when the mean temperature gradient must be corrected in a whole hole.

The theoretical effect of the warm Tertiary and Cretaceous climate amounts to +0.4 °C/km, i.e. less than about 2% of heat flow value and is almost independent of depth within 0–6 km. This disturbance is small, for practical determination it is completely faded out by the greater effect of Pleistocene climate.

When studying the vertical changes in the temperature gradient in deep holes, the comparison of gradients calculated for regular short, e.g. 100 meters, depth intervals may reveal theoretical differences of up to 4 °C/km max. However, the deviations of a gradient-depth curve from its undisturbed value as a result of climatic changes will be discernible only under unusually favourable conditions. Negligible heat production, uniform thermal diffusivity, no effect of topography, underground water flows, erosion, uplift, etc. are only some of the many requirements which must be fulfilled. A direct experimental demonstration of the existence of the climatic record in the present underground temperature is so extremely intricate.

REFERENCES

BENNETT, G., BROWN, D. D., GEORGE, P. T., LEAHY, E. J., 1967. Operation Kapuskasing. Miscellaneous Papers 10, Ontario Department of Mines, Toronto, 98 pp.

BIRCH, F., 1948. The effect of Pleistocene climatic variations upon geothermal gradient. *Amer. J. Sci.* **246**, 729–760.

BRYSSON, R. A., WENDLAND, W. M., 1967. Tentative climatic patterns for some late glacial and postglacial episodes in Central North America. In: W. J. Mayer-Oaks (Ed.), Life, Land and Water. Univ. of Manitoba Press, Winnipeg, Man., 271–298.

CARSLAW, H. S., JAEGER, J. C., 1959. Conduction of Heat in Solids. Clarendon Press, Oxford, 386 pp.

ČERMÁK, V., 1971. Underground temperature and inferred climatic temperature of the past millenium. *Palaeogeography, Palaeoclimatol., Palaeoecol.* **10**, 1–19.

ČERMÁK, V., JESSOP, A. M., 1971. Heat flow, heat generation and crustal temperature in the Kapuskasing area of the Canadian shield. *Tectonophysics* **11**, 287–303.

CIARANFI, N., LODDO, M., MONGELLI, F., 1973. Paleoclimatic effect on the geothermal gradient in never ice-covered Mediterranean regions. *R. ital. Geofis.* **22**, 1–7.

CRAIN, I. K., 1968. The glacial effect and the significance of continental terrestrial heat flow measurements. *Earth Planet. Sci. Letts.* **4**, 69–72.

EMILIANI, C., 1955. Pleistocene temperatures. *J. Geol.* **63**, 538.

FAIRBRIDGE, R. W., 1967. Ice-age theory. In: R. W. Fairbridge (Ed.), Encyclopedia of Atmospheric Sciences and Astrogeology. Reinhold Publ. Corp., N. Y., 462–474.

GOLD, L. W., LACHENBRUCH, A. H., 1973. Thermal conductions in permafrost — A review of North American literature. In: Permafrost, Second International Conference, Yakutsk, July 13–28, 1973. National Academy of Sciences, Washington, D.C., 3–23.

GOW, A. J., UEDA, H. T., GARFIELD, D. E., 1968. Antarctic ice sheet: preliminary results of first core hole to bedrock. *Science* **161**, 1011–1013.

HAMMEN, T. van der, WIJMSTRA, T. A., ZAGWIJN, W. H., 1971. The floral record of the late Cenozoic of Europe. In: T. T. Kurekian (Ed.), Late Cenozoic Glacial Ages. Yale University Press, New Haven.

HANSEN, B. L., LANGWAY, Jr. C. C., 1966. Deep core drilling in ice and core analysis at Camp Century, Greenland, 1961–1966. *Antarctic J. U. S.* **1 (5)**, 207–208.

HORAI, K., 1969. Effect of past climatic changes on the thermal field of the Earth. *Earth Planet. Sci. Letts.* **6**, 39–42.

HOTCHKISS, W. D., INGERSOLL, L. R., 1934. Postglacial time calculations from recent geothermal measurements in the Calumet Copper Mines. *J. Geol.* **42**, 113–122.

HYNDMAN, R. D., EVERETT, J. E., 1968. Heat flow measurements in a low radioactivity area of Western Australian Pre-Cambrian shield. *Geophys. J.* **14**, 479–486.

JESSOP, A. M., 1968. Three measurements of heat flow in Eastern Canada. *Can. J. Earth Sci.* **5**, 61–68.

JESSOP, A. M., 1971. The distribution of glacial perturbation of heat flow in Canada. *Can. J. Earth Sci.* **8**, 162–169.

KESSLER, D. W., 1927. Building stones. In: E. W. Washburn (Ed.), International Critical Tables, 2. McGraw-Hill, N. Y., 47–56.

LAMB, H. H., 1965. The early mediaeval warm epoch and its sequel. *Palaeogeography, Palaeoclimatol., Palaeoecol.* **1**, 13–37.

LANE, E. C., 1923. Geotherms of the Lake Superior Copper County. *Bull. Geol. Soc. Amer.* **34**, 703–720.

LIESTÖL, O., 1960. Glaciers of the present day. In: O. Holtedahl (Ed.), Geology of Norway. *Norg. Geol. Unders.* **208**, 482–490.

LUBIMOVA, E. A., FIRSOV, F. V., LUSOVA, L. N., 1966. Some results of the determination of the heat flow from the earth's interior and the temperature of the crust. In: F. N. Makarenko (Ed.), Geothermal Investigation and the Utilization of the Earth's Heat (in Russian). Nauka, Moscow, 51–58.

MITCHELL, J. M. Jr., 1967. Climatic variation (Instrumental data). In: R. W. Fairbridge (Ed.), Encyclopedia of Atmospheric Sciences and Astrogeology. Reinhold Publ. Corp., N. Y., 211–213.

Norsk Meteorologisk Arbok, 1970. Prep. Det Norske Meteorologisk Institutt. H. Aschehoug & Co., A/S, Oslo, 1971.

OPIK, E. J., 1967. Climatic Changes. In: S. K. Runcorn (Ed.), Inter. Dictionary of Geophysics. Pergamon, Oxford, 179–193.

PREST, V. K., 1957. Pleistocene geology and surficial deposits. In: C. H. Stockwell (Ed.), Geology and Economic Minerals of Canada. Economic Geology Series No. 1, Geol. Survey Canada, Ottawa, 443–495.

ROBIN, G. de Q., 1955. Ice movement and temperature distribution in glaciers and ice sheets. *J. Glaciol.* **2**, 523–532.

SASS, J. H., LACHENBRUCH, A. H., JESSOP, A. M., 1971. Uniform heat flow in a deep hole in the Canadian shield and its paleoclimatic implications. *J. Geophys. Res.* **76**, 8586–8596.

SWANBERG, C. A., CHESSMAN, M. D., SIMMONS, G., SHMITHSON, S. B., GRØNLIE, G., HEIER, K. S., 1974. Heat flow — heat generation studies in Norway. Publ. No. 83 in the Norwegian Geotraverse Project. *Tectonophysics* **23**, 31–48.

WEXLER, H., 1960. Geothermal heat and glacial growth. *J. Glaciol.* **3**, 420–425.

WILLIAMS, P. J., 1967. The nature of freezing soil and its field behaviour. In: Properties and Behaviours of Freezing Soils. *Norweg. Geotechnical Inst., Publ.*, **72**, 91–119.

NUMERICAL SOLUTION OF THE DIRECT PROBLEM OF GEOTHERMICS

CH. OELSNER

INTRODUCTION

In comparison with other geophysical potential methods there are up to now only a few works available in the literature treating the direct problem of geothermics. *The direct problem of geothermics consists in the determination of a geothermal field disturbed by an anomalous body*, i.e. the solution of a certain boundary value problem. As a matter of fact, such investigations have not yet been needed, as geothermics was scarcely used as a prospecting method and also the number of heat flow measurements hardly required quantitative interpretations. On the other hand, the analytic solution of the equation of heat conduction is rather difficult, even with such a simple disturbing body as a cylinder is. In case of disturbing bodies of complicated shapes the analytical solution is impossible.

POSSIBILITIES FOR NUMERICAL TREATMENT

In most cases of interest the question is one of stationary fields. The equation of heat conduction for an isotropic inhomogeneous medium is for the two-dimensional case in Cartesian coordinates

$$\frac{\partial}{\partial x}\left(\lambda \frac{\partial T}{\partial x}\right) + \frac{\partial}{\partial y}\left(\lambda \frac{\partial T}{\partial y}\right) = -A(x, y) \tag{1}$$

where

T — temperature,
x, y — coordinates,
$\lambda(x, y)$ — thermal conductivity,
$A(x, y)$ — heat source density (radioactive heat generation).

If for some definite range $x_1 < x < x_2$ and $y_1 < y < y_2$ the boundary values and boundary conditions as well as the fields $\lambda(x, y)$ and $A(x, y)$ are given a numerical solution of differential equation (1) is possible in this range. There are two possible ways:

1. *Method of finite elements*: The above mentioned range, for which the boundary problem can be solved, is divided into a finite number of so-called finite elements. The geometry of these elements can largely be chosen at will. The problem is solved, if the temperature distribution is found that makes the total energy E minimum. This means the solution of the variational problem

$$\delta E(T) = 0 \tag{2}$$

Equation (2) results in a system of k linear equations (k — number of nodes), the numerical solution of which yields the temperatures at the n nodal points. This method was applied by Geertsma (1971) to calculate the near-surface temperature anomalies of salt plugs and fault-zones.

2. *Method of finite differences*: here, too, the above mentioned range is divided into a finite number of small areas by covering the region with a homogeneous or inhomogeneous rectangular grid. By this, an approximation of Eq. (1) is possible in that sense that derivatives in a point are approximated by quotients of differences over a small interval, i.e. $\partial u/\partial x$ is replaced by $(\Delta u/\Delta x)$, Δx being small. The solutions of finite-difference methods are as accurate as the initial values allow.

The methods of finite differences can be divided into *explicit methods* and *implicit methods*. In the explicit methods, by a corresponding formula, the magnitude sought for in an unknown net point is directly expressed by known net points. In the implicit methods k unknown net points are expressed by k known values.

The implicit methods are divided into *systematically iterative* and *alternating iterative* methods. In case of systematically iterative methods the $(n + 1)$-st approximation is used for computing the $(n + 2)$-nd one. An iterative process is convergent, if the difference between the exact solution and the successive approximations tends towards zero with increasing number of iterations.

Alternating iterative methods change the field problem into an alternating line problem. Iteration changes between lines and columns. If a calculation by columns represents the $(n + 1)$-st approximation, the following calculation by lines is the $(n + 2)$-nd approximation. As proved by Rachford and Peaceman (1955) these methods have a very good convergence for rectangular areas.

A survey of the methods is given in Table 1.

TABLE 1

Implicit methods of differences

Systematically iterative methods	Iterative alternating methods
Method of Jacobi (Simultaneous displacements)	Alternating-direction-implicit method (ADI)
Method of Gauss–Seidel (Successive displacements)	Implicit method of Crank–Nicolson (CNI)
Successive overrelaxation (SOR)	Iterative-alternating-direction-implicit method (i ADI) (Crank–Nicolson)

NUMERICAL SOLUTION OF THE TWO-DIMENSIONAL POISSON EQUATION BY THE METHOD OF SUCCESSIVE OVERRELAXATION

Poisson's equation (1) is to be solved for the range

$$XL < x < XR; \qquad YB < y < YT$$

i.e. in the rectangle

$$(XL,\ YT),\ (XR,\ YT),\ (XR,\ YB),\ (XL,\ YB)$$

The range is covered with a homogeneous rectangular net. Let us denote the horizontal grid distance by h, the vertical one by v. It is then possible to designate each grid point by the coordinates (x_i, y_i). It has been found that assigning the material parameters λ (thermal conductivity) and A (radioactive heat generation) to the points (x_i, y_i) is not very favourable. Therefore, following Sclater (1969), the mean values of λ and A over an elementary area of the net were assigned to the left upper vertex of the rectangle, i.e. $\lambda(i, j)$ represents the average thermal conductivity of the rectangle of vertices (i, j); $(i + 1, j)$; $(i + 1, j - 1)$; $(i, j - 1)$.

To the point (x_i, y_j), [whose designation is simplified to (i, j)], the average of the thermal conductivities or radioactive heat productions, resp., of the grid areas surrounding it should be assigned:

$$\lambda = \frac{1}{4}\big(\lambda(i-1,\ j+1) + \lambda(i, j+1) + \lambda(i, j) + \lambda(i-1, j)\big)$$

$$A = \frac{1}{4}\big(A(i-1, j+1) + A(i, j+1) + A(i, j) + A(i-1, j)\big) \tag{3}$$

If in Eq. (1) derivatives are replaced by the corresponding finite differences the so-called five-point approximation of Poisson's equation is obtained

$$\begin{aligned} T(i,j) = \frac{1}{4\lambda}\Bigg\{ & \frac{v^2}{v^2+h^2}\big[T(i+1,j)\big(\lambda(i,j) + \lambda(i-1,j)\big) + \\ & + T(i-1,j)\big(\lambda(i-1,j) + \lambda(i-1,j+1)\big)\big] + \\ & + \frac{h^2}{v^2+h^2}\big[T(i,j+1)\big(\lambda(i,j+1) + \lambda(i-1,j+1)\big) + \\ & + T(i,j-1)\big(\lambda(i-1,j) + \lambda(i,j)\big)\big] + 2A\,\frac{h^2v^2}{h^2+v^2}\Bigg\} \end{aligned} \tag{4}$$

The convergence of the successive overrelaxation method is accelerated as compared to the Gauss-Seidel iteration by an accelerating factor.

If we designate by $u_{(i,j)}^{(n)}$ the field magnitude at the point (i, j) after the n-th iteration we can write for the successive overrelaxation

$$u_{(i,j)}^{(n+1)} = u_{(i,j)}^{(n)} + \alpha \cdot R(i,j) \tag{5}$$

where $R(i,j)$ — current rest at point (i,j).

The relaxation factor α is a positive constant between 0.25 and 0.5. Rachford and Peaceman (1955) give the following formula for α:

$$\alpha \approx \frac{2 - \frac{\pi}{N}}{4} \tag{6}$$

where

N — number of grid points on one line. The necessary number of iterations η in order to reduce all errors by the factor 10^{-w} is

$$\eta = 2.3\, w \frac{N}{\pi} \tag{7}$$

The calculation model for solving Poisson's equation by the method of successive overrelaxation is obtained by substituting (4) in (5):

$$\begin{aligned} T_{(i,j)}^{(n+1)} = T_{(i,j)}^{(n)} + \alpha \Bigg\{ \frac{1}{4\pi} \Bigg(& \frac{v^2}{v^2 + h^2} \left[T_{(i+1,j)}^{(n)} \big(\lambda(i,j) + \lambda(i-1,j)\big) + \right. \\ & \left. + T_{(i-1,j)}^{(n+1)} \big(\lambda(i-1,j) + \lambda(i-1,j+1)\big) \right] + \\ & + \frac{h^2}{v^2 + h^2} \left[T_{(i,j+1)}^{(n)} \big(\lambda(i,j+1) + \lambda(i-1,j+1)\big) + \right. \\ & \left. + T_{(i,j-1)}^{(n+1)} \big(\lambda(i-1,j) + \lambda(i,j)\big) \right] + 2A \frac{h^2 v^2}{h^2 + v^2} \Bigg) - T_{(i,j)}^{(n)} \Bigg\} \end{aligned} \tag{8}$$

When treating equation (8) by a computer also the boundary conditions have to be considered. In order to ensure that no horizontal heat flow component should occur on the vertical boundaries we impose the condition $\partial T/\partial x = 0$. The conditions for the upper or the lower boundary, resp., have to be chosen in accordance with the problem (e.g. T = constant or $\lambda\ (\partial T/\partial y)$ = constant, resp.).

In programming Eq. (8) of course also different net distances v and h may be chosen. At the boundaries it is only necessary to pay attention to the correct application of the formula.

An example is explained in this book, pp. 509–513.

REFERENCES

GEERTSMA, J., 1971. Finite element analysis of shallow temperature anomalies. *Geophys. Prosp.* **19**, 662–681.

RACHFORD, PEACEMAN, 1955. The numerical solution of parabolic and elliptic equations. *J. Soc. Ind. a. Appl. Math.* **3**, 11, 28–41.

SCLATER, J. G., 1969. A machine method for computing the effect of a two-layered conductivity structure. MPL Technical Memorandum 198, Lajolla.

EFFECT OF CONTRASTS IN THE PHYSICAL PROPERTIES ON THE HEAT FLOW AND ELECTROMAGNETIC PROFILES

E. A LUBIMOVA, V. M. LYUBOSHITS, V. N. NIKITINA

INTRODUCTION

Recently the investigations of horizontal inhomogeneities in the earth's crust and upper mantle have become actual, in particular those of geothermic and geoelectric nature. In a mathematical formulation the problems associated with horizontal inhomogeneities are to be set as *two-dimensional boundary problems.*

Problems of this kind arise, for instance, in studying zones of transition from continental to oceanic crust, due to the principal difference in their structure. In this case it is necessary to define some field features, caused by the contact between two different horizontally layered media.

A similar problem arises for areas of linearly fractured tectonics as well as in rifts and ridges, Here the main fracture parameters have another scale, but the physical and mathematical formulation of the problem is principally the same, because we also speak about a contact between two zones with diverse horizontallylayered structures.

Investigations of areas with inclined or vertical contact are of particular importance. Naturally, the vertical contact problem can only be considered as a first approximation in the theory.

Thus, boundary problems over the vertical contact of horizontally-layered structures represent an extremely important class of two-dimensional boundary problems in mathematical geophysics and geology.

1. A DESCRIPTION OF THE MODELS DISCUSSED

A two-dimensional inhomogeneous medium with an arbitrary stepwise profile is typical for a whole series of problems in applied geology.

The Poisson equation holds e.g., for *thermal conduction processes* on the surface of two structures, separated by a vertical contact:

$$\Delta u = f \tag{1}$$

for propagation of *electromagnetic* fields the Helmholtz equation holds:

$$\Delta u + k^2 u = f \tag{1a}$$

for propagation of *elastic* oscillations a system of equations

$$\begin{cases} \Delta u_1 + k_1^2 u = f_1 & \text{(1b)} \\ \Delta u_2 + k_2^2 u = f_2 & \text{(1c)} \end{cases}$$

etc.

Let us consider the theory of applications of one-sided Fourier transformations for constructing solutions of various two-dimensional boundary problems:

(1) Equation of thermal conductivity in the form of Poisson and Laplace equations; (1a) Helmholtz equation for electromagnetic field propagation; and equations of elastic waves propagation (1b—1c).

The eight models considered in this paper are given in Figure 1 from a) to h).

The principal analytical basis of this method were developed for the case of a vertical contact between two horizontally-layered media, with different conductivity properties λ and heat generation G in the layers, or electrical conductivity σ and dielectrical permeability ε (see Fig. 1, a), (Lubimova and Nikitina, 1972).

The first model a) will conditionally be called as "ocean-continent" or "fracture zone". Evidently this case only schematically reflects the real situation existing in an intermediate zone between oceanic and continental earth's crust. In fact this intermediate zone is known as some inclined plane along which the epicentres of deep focused earthquakes are

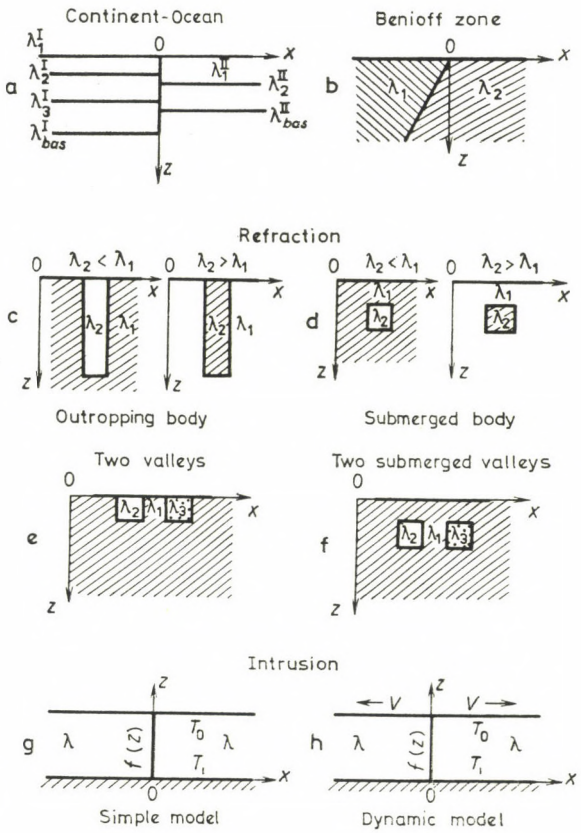


Fig. 1. Models of different media, resulting from a common two-dimensional problem with intersection of boundaries $x = x_i$ and $z = z_k$: a – continent-ocean; b – Benioff zone; c, d, e, f – refraction; g, h – intrusion

concentrated, and it is called Benioff zone. Accordingly, the model of inclined contact will be conditionally called as "Benioff zone" (Fig. 1,b). The inclined contact problem for electromagnetic fields has been considered in 1973 by Praus et al., (1973) by the finite difference approach.

We propose a geothermal variant, supplemented with several numerical examples accounting for the contrasts in physical properties (Fig. 1, c, d, e, f). These are different embeddings of conductivities λ_2, λ_3, ... λ_k differing from conductivity λ_1 of the surrounding medium.

These four models will be conditionally called as "refraction" models. The model in Fig. 1, c is the "refraction of outcropping bodies", that in Fig. 1, d the "refraction of submerged bodies". The model of two spaced bodies (Fig. 1, e) may be referred to as two "valleys"; but for two submerged bodies (Fig. 1, f) as a model of two "submerged valleys".

Finally, a so-called "intrusion model" having great importance for interpreting the heat flow in the area of mid-oceanic ridges can also be considered in detail (Fig. 1, g, h). Two cases, namely the intrusion model along a vertical contact without the medium's moving and the dynamic intrusion model, taking into account the mantle's material convection V to both sides from the contact axis, are discussed (Lubimova and Nikitina, 1974).

2. ANALYTICAL SOLUTION OF THE PROBLEM

It is known that a solution of the boundary problem for the case of piecewise-stepped medium section has not yet been obtained. There are procedures of its reduction to integral equations (Dmitriev and Zakharov, 1970). The method of one-sided Fourier transformations offered in this paper allows to investigate and solve a boundary problem of this class in an apparent analytical form with a general formulation of the generation and radiation conditions.

The physical formulation of two-dimensional boundary problems by means of Eqs (1) and (1a) may comprise different modes of excitation and radiation at infinity as $x, z \to \infty$. The conditions, however, that define the field behaviour at the interfaces — i.e. boundary conditions — are, as a rule, similar. Piecewise-constant values of the physical parameters are given as the initial data. Let a continental structure consist of n layers: s_i, G_i^{I}, λ_i^{I} where s_i is thickness of an i-th layer in the left side of the contact, G_i^{I} heat generation, λ_i^{I} the thermal conductivity coefficient for the i-th layer; $(i = 1, 2, \ldots, n)$, and an oceanic structure of m-layers: d_j, G_j^{II}, λ_j^{II}, $(j = 1, 2, \ldots, m)$. We introduce (as Fig. 2 shows) a new generalized numeration of horizontal boundaries z_k and thicknesses $l_k = z_k - z_{k-1}$; $(k = 1, 2, \ldots, N)$, where $N = n + m$. We also make a "false" prolongation of the boundary $z = z_k$ really existing only in one of the structures, into the adjacent structure (see broken lines).

The method of solution will be illustrated on the particular example of a heat contact between continent (I) and ocean (II). The problem consists of defining a temperature field $T = u(x, z)$ from equation (1) in the area $z \geq 0$.

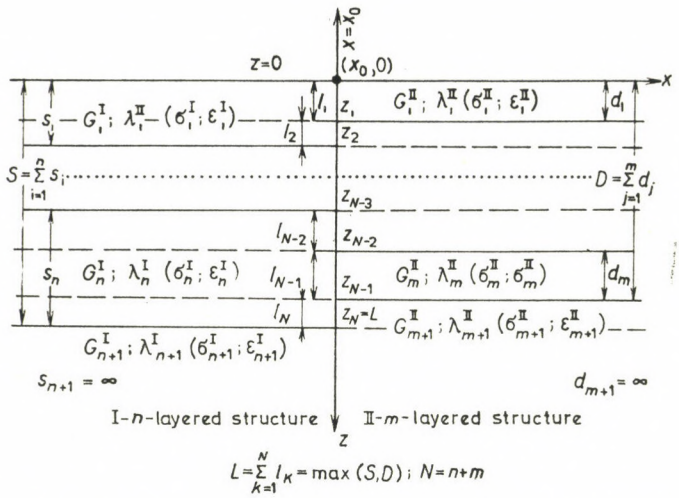


Fig. 2. A piece-wise layered medium in a zone of thermal contact between continent (I) and ocean (II):

$G(x, z) = G_k^{\mathrm{I,II}}$ – heat generation;

$\lambda(x, z) = \lambda_k^{\mathrm{I,II}}$ – thermal conductivity coefficient

Electrical parameters given in brackets:

$\sigma(x, z) = \sigma_k^{\mathrm{I,II}}$ electrical conductivity;

$\varepsilon(x, z) = \varepsilon_k^{\mathrm{I,II}}$ – dielectrical permeability.

Upper and lower indices denote changes of the physical properties in two directions x and z. Upper indices I and II correspond to change of parameters along x (at the left and right-hand sides of the contact), lower index $k = 1, 2, \ldots, N$ corresponds to change of the parameters with depth z

We represent a solution of the two-dimensional boundary problem as a sum:

$$u = \begin{cases} u_0^{\mathrm{I}}(x, z) + v^{\mathrm{I}}(x, z), & x \leq x_0 \\ u_0^{\mathrm{II}}(x, z) + v^{\mathrm{II}}(x, z), & x \geq x_0 \end{cases} \tag{2}$$

Here the functions u_0^{I} and u_0^{II} are the known solutions (due to the heat sources $f(x, z)$) for the corresponding one-dimensional boundary problems for two dissimilar one-dimensional layered structures, namely Ist and IInd, whose properties are only changed in the Z-direction (Tikhonov, 1937).

The additive function $v(x, z)$ means a pure anomalous field, associated with the vertical contact $x = x_0$ in a composite medium. For v we have to solve an auxiliary boundary problem. In case of one-dimensional heat-generation $f = f^{\mathrm{I,II}}(z)$ the contact function v satisfies the Laplace equation

$$\Delta v = 0 \tag{3}$$

and the additional conditions:

a) conjugation conditions at $x = x_0$

$$\begin{cases} v^{\mathrm{I}}|_{x=x_0-0} - v^{\mathrm{II}}|_{x=x_0+0} = \varphi(z) \\ \lambda^{\mathrm{I}} \dfrac{\partial v^{\mathrm{I}}}{\partial x}\Big|_{x=x_0-0} - \lambda^{\mathrm{II}} \dfrac{\partial v^{\mathrm{II}}}{\partial x}\Big|_{x=x_0+0} = 0 \end{cases} \tag{4}$$

where $\varphi(z) = u_0 \Big|_{x_0-0}^{x_0+0} = u_0^{\mathrm{II}}(z) - u_0^{\mathrm{I}}(z)$ is a known function of jump; (in the geothermal case)

b) boundary condition for additive temperature on the surface $z = 0$

$$v^{\mathrm{I}}|_{z=+0} = 0 \quad (x \leq x_0) \qquad \text{and} \qquad v^{\mathrm{II}}|_{z=+0} = 0 \quad (x \geq x_0) \tag{5a, b}$$

c) uniform boundary conditions on the horizontal boundaries $z = z_k$

$$v^{\mathrm{I}} \Big|_{z_k+0}^{z_k-0} = 0\,; \qquad \lambda^{\mathrm{I}} \frac{\partial v^{\mathrm{I}}}{\partial z}\Big|_{z_k+0}^{z_k-0} = 0 \tag{6a}$$

$$v^{\mathrm{II}} \Big|_{z_k+0}^{z_k-0} = 0\,; \qquad \lambda^{\mathrm{II}} \frac{\partial v^{\mathrm{II}}}{\partial z}\Big|_{z_k+0}^{z_k-0} = 0 \tag{6b}$$

d, e) radiation conditions at infinity, on z:

$$\frac{\partial v^{\mathrm{I,II}}}{\partial z}\Big|_{z\to\infty} = 0 \tag{7a, b}$$

and on x:

$$\frac{\partial v^{\mathrm{I}}}{\partial x}\Big|_{x\to-\infty} = 0 \quad \text{and} \quad \frac{\partial v^{\mathrm{II}}}{\partial x}\Big|_{x\to+\infty} = 0 \tag{8a, b}$$

A similar problem arises for electromagnetic field. Let us consider, e.g. a plane wave $e^{-i(\omega t - k_0 z)}$ incident from the air $z \leq 0$ to earth $z \geq 0$ ($\sigma|_{z\leq 0} \ll \sigma|_{z\geq 0}$). Parameters of the electromagnetic problem are shown in Figure 2 in brackets. In case of magnetic polarization $\mathbf{H} = (0, H_y, 0)$ and $\mathbf{E} = (E_x, 0, E_z)$ the problem is reduced to determining the magnetic component $H_y = u(x, z)$ from equation (1a) for $z \geq 0$. After representing the solution $u(x, z)$ as a sum, indicated in (2):

$$u = u_0^{\mathrm{I,II}}(z) + v(x, z)$$

we come again to a boundary problem for v.

The contact function v satisfies the wave equation

$$\Delta v + k^2 v = 0 \tag{9}$$

where

$$k^2 = i\omega\mu_0\sigma^*; \quad \sigma^*(x, z) = \sigma - i\omega\varepsilon; \quad \operatorname{Im} k > 0$$

and supplementary conditions for the additive part of the magnetic component H_y:

a)

$$\begin{cases} v^{\mathrm{I}}|_{x=x_0-0} - v^{\mathrm{II}}|_{x=x_0+0} = \varphi(z) \\ \dfrac{1}{\sigma^{*\mathrm{I}}} \dfrac{\partial v^{\mathrm{I}}}{\partial x}\Big|_{x_0-0} - \dfrac{1}{\sigma^{*\mathrm{II}}} \dfrac{\partial v^{\mathrm{II}}}{\partial x}\Big|_{x_0+0} = 0 \end{cases} \tag{10}$$

where

$$\varphi(z) = u_0 \Big|_{x_0-0}^{x_0+0} = u_0^{\mathrm{II}}(z) - u_0^{\mathrm{I}}(z)$$

is the jump function (electromagnetic case)

b)

$$v^{\mathrm{I}}|_{z=+0} = 0 \quad (x \leq x_0) \qquad \text{and} \qquad v^{\mathrm{II}}|_{z=+0} = 0 \quad (x \geq x_0) \tag{11a,b}$$

c)

$$\begin{cases} v^{\mathrm{I}} \Big|_{z_k+0}^{z_k-0} = 0\,; \quad \dfrac{1}{\sigma^{*\mathrm{I}}} \dfrac{\partial v^{\mathrm{I}}}{\partial z}\Big|_{z_k+0}^{z_k-0} = 0 \end{cases} \tag{12a}$$

$$\begin{cases} v^{\mathrm{II}} \Big|_{z_k+0}^{z_k-0} = 0\,; \quad \dfrac{1}{\sigma^{*\mathrm{II}}} \dfrac{\partial v^{\mathrm{II}}}{\partial z}\Big|_{z_k+0}^{z_k-0} = 0 \end{cases} \tag{12b}$$

d)

$$v^{\mathrm{I,II}}|_{z\to\infty} = 0 \tag{13a, b}$$

e)

$$v^{\mathrm{I}}|_{x\to-\infty} = 0 \qquad \text{and} \qquad v^{\mathrm{II}}|_{x\to+\infty} = 0 \tag{14a, b}$$

In the parallel problems (3–8) and (9–14) for v the solution is always unique, because the difference between two solutions of problems (3–8) or (9–14) satisfies the principal equation (3) or (9) with uniform and zero additional conditions everywhere and hence it identically equals zero.

It should be noted that in two-dimensional problems with equation (1) and (1a) the source function f is generally also two-dimensional: $f = f(x, z)$. Therefore a formulation of the problem for v will contain, generally speaking, two jump functions φ and ϑ:

$$\begin{cases} v \Big|_{x_0+0}^{x_0-0} = u_0^{\mathrm{II}}(x_0, z) - u_0^{\mathrm{I}}(x_0, z) = \varphi(z) \\ \dfrac{1}{\sigma^*} \dfrac{\partial v}{\partial x}\Big|_{x_0+0}^{x_0-0} = \dfrac{1}{\sigma^{*\mathrm{II}}} \dfrac{\partial u_0^{\mathrm{II}}}{\partial x}\Big|_{x=x_0} - \dfrac{1}{\sigma^{*\mathrm{I}}} \dfrac{\partial u_0^{\mathrm{I}}}{\partial x}\Big|_{x=x_0} = \vartheta(z) \end{cases} \tag{10a}$$

As can be seen, functions $\varphi(z)$ and $\vartheta(z)$ are single sources of the field in the problem for v.

Further constructions for problem (9–14) will be performed with a wave-equation, for Laplace's equation in an extreme case of the wave

equation as $k^2 \to 0$. Boundary conditions in problem (3–8) and (9–14) are also the same when substituting λ^{I} and λ^{II} instead of $1/\sigma^{*\mathrm{I}}$ and $1/\sigma^{*\mathrm{II}}$. Conditions at infinity after substracting the constant added, determined from the surface condition at $z = 0$, are also the same.

We solve problem (9–14) by separating the variables x and z:

$$v = X(x)\, Z(z)$$

$$\begin{cases} Z'' + \mu^2 Z = 0 \\ X'' - \beta^2 X = 0 \end{cases} \qquad (\beta^2 = \mu^2 - k^2)$$

or

$$\begin{cases} X'' + \lambda^2 X = 0 \\ Z'' - \alpha^2 Z = 0 \end{cases} \qquad (\alpha^2 = \lambda^2 - k^2)$$

in the classical form of Fourier integrals on μ or on λ (here λ is without indices). Let us apply integral Fourier transformations in a complex form to the functions defined on a semi-infinite axis (Titchmarsh, 1948).

One-sided Fourier transformations offer a convenient mathematical aid for solutions in adjacent angular areas $z \gtrless z_0$; $x \gtrless x_0$. In addition, the transformation is equally possible on z or on x.

When transformed with respect to z, the original function is considered separately for $x \leq x_0$ and for $x \geq x_0$ and is denoted by $v^{\mathrm{I}}(x, z)$ and $v^{\mathrm{II}}(x, z)$, respectively. Accordingly, we obtain z-images V^{I} and V^{II}.

Let us first consider the "junction" problem. Assume that $\sigma^*|_{x \leq x_0} \equiv \sigma_{\mathrm{I}}$ and $\sigma^*|_{x \geq x_0} \equiv \sigma_{\mathrm{II}}$ and that $v(x, z)$ is continuous and has a continuous derivative with respect to z for $z \geq z_0$, where z_0 is a fixed constant (equal to zero, or some arbitrary positive value). We introduce

$$V^{(+)}(\mu, x\,; z_0) = \int_{z_0}^{\infty} v e^{-i\mu z}\, dz \qquad (\mathrm{Im}\,\mu < 0) \qquad (15)$$

and inversely

$$\frac{1}{2\pi} \int_{-\infty - i\delta}^{+\infty - i\delta} V^{(+)} e^{i\mu z}\, d\mu = \begin{cases} 0; & z \leq z_0 \\ v(x, z)\,; & z \geq z_0 \end{cases} \quad (\mathrm{Im}\, k > \delta > 0) \qquad (16)$$

Differentiating (15) with respect to x under the integral symbol and using Eq. (9) we obtain:

$$\left.\frac{\partial^2 V(\mu, x\,; z_0)}{\partial x^2}\right|_{z \geq z_0} = -\int_{z_0}^{\infty} \frac{\partial^2 v}{\partial z^2} e^{-i\mu z}\, dz - k^2 \int_{z_0}^{\infty} v e^{-i\mu z}\, dz =$$

$$= \left[\frac{\partial v}{\partial z} e^{-i\mu z}\right]_{z_0}^{\infty} - i\mu \left[v e^{-i\mu z}\right]_{z_0}^{\infty} + (\mu^2 - k^2) \int_{z_0}^{\infty} v e^{-i\mu z}\, dz =$$

$$= e^{-i\mu z_0}\big(\psi(x) + i\mu\chi(x)\big) + (\mu^2 - k^2)\, V(\mu, x\,; z_0)$$

here:

$$\psi(x) = \left.\frac{\partial v}{\partial z}\right|_{z=z_0+0}; \quad \chi(x) = v\big|_{z=z_0+0} \tag{17}$$

Introducing the notation

$$F = F^{(+)}(\mu, x; z_0) = e^{-i\mu z_0}\big(\psi(x) + i\mu\chi(x)\big) \tag{18}$$

we arrive to the ordinary differential equation

$$\frac{\partial^2 V}{\partial x^2} - \beta^2 V = F(\mu, x; z_0); \beta^2 = \begin{cases} \beta_{\mathrm{I}}^2 = \mu^2 - k_{\mathrm{I}}^2; & (x \leq x_0) \\ \beta_{\mathrm{II}}^2 = \mu^2 - k_{\mathrm{II}}^2; & (x \geq x_0) \end{cases} \tag{19}$$

which serves as an operative equation for defining the Fourier z-images $V(\mu, x; z_0)$. Here k_{I} and k_{II} are constants for all $z \geq z_0$. The conjugation conditions at $x \to x_0$ follow from (10a) and (15):

$$\begin{cases} V^{\mathrm{I}}|_{x_0-0} - V^{\mathrm{II}}|_{x_0+0} = \int\limits_{z_0}^{\infty} \varphi(z)\, e^{-i\mu z}\, dz = \Phi^{(+)}(\mu; z_0) \\ \dfrac{1}{\sigma_{\mathrm{I}}}\left.\dfrac{\partial V^{\mathrm{I}}}{\partial x}\right|_{x_0-0} - \dfrac{1}{\sigma_{\mathrm{II}}}\left.\dfrac{\partial V^{\mathrm{II}}}{\partial x}\right|_{x_0+0} = \int\limits_{z_0}^{\infty} \vartheta(z)\, e^{-i\mu z} dz = \Theta^{(+)}(\mu; z_0) \end{cases}$$

At the infinity as $x \to \pm\infty$ the solutions $V^{\mathrm{I,II}}$, according to Eq. (14), approach zero.

The solution of the operative Eq. (19) is a sum of the general solution V_0 of a uniform equation with $F = 0$ and with non-uniform boundary conditions, and of a partial solution $\bar{V}$ of a non-uniform equation with $F \neq 0$, and with uniform boundary conditions.

For instance, the V_0-solution (in case of $\vartheta(z) \equiv 0$) has the form:

$$V_0^{\mathrm{I,II}} \begin{cases} D^{\mathrm{I}}(\mu)\Phi^{(+)}(\mu; z_0)\, e^{\beta_{\mathrm{I}} x}; (x \leq x_0), & D^{\mathrm{I}} = \dfrac{\sigma_{\mathrm{I}}\beta_{\mathrm{II}}\, e^{-\beta_{\mathrm{I}} x_0}}{\sigma_{\mathrm{I}}\beta_{\mathrm{II}} + \sigma_{\mathrm{II}}\beta_{\mathrm{I}}} \\ D^{\mathrm{II}}(\mu)\Phi^{(+)}(\mu; z_0)\, e^{\beta_{\mathrm{II}} x}; (x \geq x_0), & D^{\mathrm{II}} = -\dfrac{\sigma_{\mathrm{II}}\beta_{\mathrm{I}}\, e^{+\beta_{\mathrm{II}} x_0}}{\sigma_{\mathrm{I}}\beta_{\mathrm{II}} + \sigma_{\mathrm{II}}\beta_{\mathrm{I}}} \end{cases} \tag{20}$$

$$\mathrm{Re}\, \beta_{\mathrm{I,II}} \geq 0$$

Here $\Phi^{(+)}(\mu; z_0)$ is the one-sided Fourier transformation (15) of function $\varphi(z)$ for $z_0 \leq z < \infty$.

Formulas (20) and (16) define a solution v_0 existing both for $z \geq z_0$ and $z \leq z_0$.

$$v_0(x, z) = v_0^+(x, z) + v_0^-(x, z)$$

Here:

$$v_0^+ = \begin{cases} 0; & z \leq z_0 \\ v_0(x, z); & z \geq z_0 \end{cases} \qquad v_0^- = \begin{cases} v_0(x, z); & z \leq z_0 \\ 0; & z \geq z_0 \end{cases}$$

Function $v_0(x, z)$ is piecewise-analytical in x, i.e. it satisfies equation (9) and conditions (10) with the given jump function

$$\varphi^+(z) = \begin{cases} 0; & z \leq z_0 \\ \varphi(z) & z \geq z_0 \end{cases}$$

in a one-dimensional inhomogeneous medium with a wave-number depending only on x and not on z:

$$k \equiv \begin{cases} k_{\mathrm{I}}, & x \leq x_0 \\ k_{\mathrm{II}}, & x \geq x_0 \end{cases}$$

On the line $z = z_0$ the function $v_0(x, z)$ is continuous and has a continuous derivative with respect to z.

Solution $\bar{V}$ can be found, e.g. by means of operation calculus or by the constant variation method. Let us impose on it the uniform boundary conjugation conditions at $x \to x_0$:

$$\begin{cases} \bar{V}^{\mathrm{I}}|_{x_0-0} - \bar{V}^{\mathrm{II}}|_{x_0+0} = 0 \\ \dfrac{1}{\sigma_{\mathrm{I}}} \dfrac{\partial \bar{V}^{\mathrm{I}}}{\partial x}\Big|_{x_0-0} - \dfrac{1}{\sigma_{\mathrm{II}}} \dfrac{\partial \bar{V}^{\mathrm{II}}}{\partial x}\Big|_{x_0+0} = 0 \end{cases} \tag{21}$$

and zero radiation conditions at $x \to \pm\infty$. As a result we obtain:

$$\bar{V}^{\mathrm{I,II}} = \begin{cases} -\dfrac{e^{-i\mu z_0}}{2\beta_{\mathrm{I}}} \displaystyle\int_{-\infty}^{x_0} f^{\mathrm{I}}(\mu, \xi)\, e^{-\beta_{\mathrm{I}}|x-\xi|}\, d\xi + Ae^{\beta_{\mathrm{I}}x}; & (x \leq x_0) \\ -\dfrac{e^{-i\mu z_0}}{2\beta_{\mathrm{II}}} \displaystyle\int_{x_0}^{\infty} f^{\mathrm{II}}(\mu, \xi)\, e^{-\beta_{\mathrm{II}}|x-\xi|}\, d\xi + Be^{-\beta_{\mathrm{II}}x}; & (x \geq x_0) \end{cases} \tag{22}$$

where

$$A = e^{-i\mu z_0}[(D^{\mathrm{I}} + D^{\mathrm{II}})R - 2D^{\mathrm{I}}S]$$

$$B = e^{-i\mu z_0}[2D^{\mathrm{II}}R - (D^{\mathrm{I}} + D^{\mathrm{II}})S]$$

$$R(\mu) = \frac{1}{2\beta_{\mathrm{I}}} \int_{-\infty}^{x_0} f^{\mathrm{I}}(\mu, \xi)\, e^{\beta_{\mathrm{I}}\xi}\, d\xi; \qquad S(\mu) = \frac{1}{2\beta_{\mathrm{II}}} \int_{x_0}^{\infty} f^{\mathrm{II}}(\mu, \xi)\, e^{-\beta_{\mathrm{II}}\xi} d\xi$$

Here function $f^{\mathrm{I}}(\mu, \xi) = \psi^{\mathrm{I}}(\xi) + i\mu\chi^{\mathrm{I}}(\xi)$ and $f^{\mathrm{II}}(\mu, \xi) = \psi^{\mathrm{II}}(\xi) + i\mu\chi^{\mathrm{II}}(\xi)$ are given separately,[1] each on a semi-infinite axis, at $-\infty < x \leq x_0$

[1] If functions $\chi(x)$ and $\psi(x)$ serve as marginal values in problem (17) at $z \geq z_0$ for Eq. (9) with $k = \begin{cases} k_{\mathrm{I}}; & x \leq x_0 \\ k_{\mathrm{II}}; & x \geq x_0 \end{cases}$ they have to be mutually related. In a particular case when

and $x_0 \leq x < +\infty$, respectively. The second terms in Eq. (22) of form $A\,e^{\beta_I x}$ and $B\,e^{-\beta_{II} x}$ are additional terms. Coefficients $A(\mu)$ and $B(\mu)$ are constants of integration of Eq. (19). They are determined unambiguously from conditions (21).

Formulas (22) and (16) give the solution $\bar{v}(x, z)$ satisfying (9) under the uniform conditions (10) in the one-dimensional inhomogeneous medium $k = k(x)$. Function $\bar{v}(x, z)$ exists for both $z \geq z_0$ and $z \leq z_0$. It solves the "junction" boundary problem with the given jumps:

$$\psi(x) = \frac{\partial \bar{v}}{\partial z}\Big|_{z_0-0}^{z_0+0} \tag{17a}$$

and

$$\chi(x) = \bar{v}\Big|_{z_0-0}^{z_0+0}$$

$z \gtrless z_0$ (for the entire plane).

The given jumps $\chi(x)$ of the extreme values of $\bar{v}\Big|_{z_0-0}^{z_0+0}$ and $\psi(x)$ of the values $\dfrac{\partial \bar{v}}{\partial z}\Big|_{z_0-0}^{z_0+0}$ influence only the first, main terms of solution v during transition across the line $z = z_0$. The secone additional terms of the solution v have no jumps at $z = z_0$, neither their normal derivatives, i.e. they remain continuous. However, on the line of conjugation of different media at $x = x_0$ these additional terms are that solve the conjugation problem (21). They compensate for the jumps between values of the first terms and their derivatives with respect to x at $x = x_0 \pm 0$ and provide for the fulfilment of conditions (21) for the adjacent angular areas with different complex parameters σ_I and σ_{II}.

In case of the special[2] additional determination of solution $\bar{v}(x, z)$ in the external semiplane ($z \leq z_0$) as being identically zero, the partial solution (22), (16) takes an internal marginal value $\bar{v}\big|_{z_0+0}$ and $\dfrac{\partial \bar{v}}{\partial z}\Big|_{z_0+0}$ equal $\chi(x)$ and $\psi(x)$.

$k_I = k_{II} \equiv k$, such a relation has the integral character and is known in the apparent form:

$$\Psi(\lambda) = -\sqrt{\lambda^2 - k^2}\, X(\lambda)$$

where Ψ and X are Fourier x – images. In the general case when $k_I \neq k_{II}$, no such relation is known. Therefore two arbitrary independent functions $\psi(x)$ and $\chi(x)$ being given in the right-hand-side of Eq. (19) are not the marginal values in boundary problem (17) but are jumps:

$$\frac{\partial \bar{v}}{\partial z}\Big|_{z_0-0}^{z_0+0} \quad \text{and} \quad \bar{v}\Big|_{z_0-0}^{z_0+0} \quad \text{at} \quad -\infty < x < +\infty$$

on the line $z = z_0$ (17a).

[2] Because function (22) is holomorphic within the strip $-\operatorname{Im} k < \operatorname{Im} \mu < \operatorname{Im} k$ and vanishes with $\mu \to \infty$ as $1/\mu$, it may be represented as $(22) = (22)^- + (22)^+$, where $(22)^-$ is holomorphic for $-\operatorname{Im} k < \operatorname{Im} \mu$, and $(22)^+$ is holomorphic for $\operatorname{Im} \mu < \operatorname{Im} k$. In case of the above special determinations the functions ψ and χ must be mutually related so that $(22)^-$ should vanish, while function $(22)^+$ and (16) should be transformed into zero for all $z \leq z_0$ and should coincide with $\bar{v}(x, z)$ for $z \geq z_0$.

In order to solve the "junction" problem over the semiplane at $z \leq z_0$ it is necessary to use Fourier transformation "on the other side".

$$V^{(-)}(\mu, x; z_0) = \int_{-\infty}^{z_0} v\, e^{-i\mu z}\, dz; \quad \mathrm{Im}\, \mu > 0$$

(instead of Eq. (15)) and to take the right-hand side of $F = F^{(-)}$ in Eq. (19) with the opposite sign: $F^{(-)} = -e^{-i\mu z_0}(\psi + i\mu\chi)$ where

$$\psi(x) = \left.\frac{\partial v}{\partial z}\right|_{z_0-0} \quad \text{and} \quad \chi(x) = v|_{z_0-0}$$

Further on, both variable x and z are mathematically equivalent. For example, for adjacent areas $x \geq x_0$; $z \leq z_0$; $\sigma^* \equiv \sigma_1$ and $x \geq x_0$; $z \geq z_0$; $\sigma^* \equiv \sigma_2$ we introduce

$$W^{(+)}(\lambda, z; x_0) = \int_{x_0}^{\infty} v\, e^{-i\lambda x}\, dx; \quad \mathrm{Im}\, \lambda < 0 \tag{23a}$$

and inversely

$$\frac{1}{2\pi} \int_{-\infty-i\delta}^{+\infty-i\delta} W^{(+)}\, e^{i\lambda x}\, d\lambda = \begin{cases} 0; & x \leq x_0 \\ v(x, z); & x \geq x_0 \end{cases} \quad (\mathrm{Im}\, k > \mathrm{Im}\, \delta > 0) \tag{23b}$$

and obtain, quite similarly, the operative equation for the Fourier x-images $W(\lambda, z; x_0)$:

$$W''_{zz} - \alpha^2 W = P(\lambda, z; x_0); \quad (\alpha^2 = \lambda^2 - k^2) \tag{24}$$

where

$$P = P^{(+)} = e^{-i\lambda x_0}\big(h(z) + i\lambda g(z)\big)$$

$$h(z) = \left.\frac{\partial v}{\partial x}\right|_{x_0+0} \quad \text{and} \quad g(z) = v|_{x_0+0}$$

having solutions of two types $W_0(\lambda, z; x_0)$ and $\overline{W}(\lambda, z; x_0)$.

For the conjugation of adjacent angular areas in the semiplane $x \leq x_0$ we introduce

$$W^{(-)}(\lambda, z; x_0) = \int_{-\infty}^{x_0} v\, e^{-i\lambda x}\, dx; \quad (\mathrm{Im}\, \lambda > 0) \tag{25a}$$

and in contrary

$$\frac{1}{2\pi} \int_{-\infty+i\delta}^{+\infty+i\delta} W^{(-)}\, e^{i\lambda x}\, d\lambda = \begin{cases} v(x, z); & x \leq x_0 \\ 0; & x \geq x_0 \end{cases} \quad (\mathrm{Im}\, k > \delta > 0) \tag{25b}$$

and take the right-hand side of Eq. (24) with opposite sign.

In this way the solution of "junction" two-dimensional boundary problem for the semiplane $z \gtrless z_0$ (or $x \gtrless x_0$), with conjugating of two adjacent angular areas has been established.

Let us now turn to the initial problem (9–14). We will show that the solution of type of Eq. (20) and the boundary conditions (11–13) in combination with given method of constructing solutions of type (22) permit a unique determination of the successive approximations to the desired precise solution with simultaneous realization of all conditions for the problem being set. A desired solution of problem (9–14) may be described as a sum:

$$v(x, z) = v_0(x, z) + v_{add}(x, z) \tag{26}$$

Here the primary function v_0 is an arbitrary wave function satisfying (9) (with a piecewise-composite wave number $k(x, z) = k_k^{\mathrm{I,\,II}}$ on a real contact) and conditions (10), (14) independently of (11–13). Suppose, e.g., that function v_0 in each individual layer $z_{k-1} \leq z \leq z_k$ $(k = 1, 2, \ldots, N+1)$ is equal to

$$v_{0,k}^{\mathrm{I,\,II}}(x, z) = \begin{cases} \dfrac{1}{2\pi} \displaystyle\int_{-\infty - i\delta}^{+\infty - i\delta} D_k^{\mathrm{I}} \Phi_k(\mu)\, e^{\beta_k^{\mathrm{I}}(x - x_0)}\, e^{i\mu z}\, d\mu; & (x \leq x_0) \\ & \mathrm{Re}\ \beta_k^{\mathrm{I,\,II}} \geq 0 \\ \dfrac{1}{2\pi} \displaystyle\int_{-\infty - i\delta}^{+\infty - i\delta} D_k^{\mathrm{II}} \Phi_k(\mu)\, e^{-\beta_k^{\mathrm{II}}(x - x_0)}\, e^{i\mu z}\, d\mu; & (x \geq x_0) \end{cases} \tag{27}$$

$$D_k^{\mathrm{I}} = \frac{k_k^{\mathrm{I}} \beta_k^{\mathrm{II}}}{k_k^{\mathrm{I}} \beta_k^{\mathrm{II}} + k_k^{\mathrm{II}} \beta_k^{\mathrm{I}}}; \quad D_k^{\mathrm{II}} = -\frac{k_k^{\mathrm{II}} \beta_k^{\mathrm{I}}}{k_k^{\mathrm{I}} \beta_k^{\mathrm{II}} + k_k^{\mathrm{II}} \beta_k^{\mathrm{I}}}; \quad \Phi_k = \int_{z_{k-1}}^{z_k} \varphi(z)\, e^{-i\mu z}\, dz$$

Function (27) is piecewise analytical both in x and z. It satisfies Eq. (9) with the conjugation conditions (10) and radiation conditions (14). However, unlike the solution (20) and (16) it is discontinuous along lines $z = z_k$; $-\infty < x < +\infty$ because coefficients $D_k^{\mathrm{I,\,II}}$ are changed sharply into $D_{k+1}^{\mathrm{I,\,II}}$ after substituting for the number of the layer "$k+1$" instead of k. It should be noted that any other primary function v_0 differs from (27) by an additive term satisfying (9) and (14) with uniform conditions (10).

An addition to v_0 also a secondary function v_{add} has to be used to satisfy (11–13) without violating (10).

Investigation shows that $v_{\mathrm{add}}(x, z)$ is expressed as a series:

$$v_{\mathrm{add}}(x, z) = \sum_{i=1}^{\infty} v_{\mathrm{add}}^{(i)}(x, z) \tag{28}$$

To construct v_{add} we use Fourier transformation (23a — 23b) and (25a–25b) on both sides $-\infty < x \leq x_0$ and $x_0 \leq x < +\infty$. Let us find a composite partial solution:

$$\bar{v}(x, z) = \begin{cases} \bar{v}^{\mathrm{I}}(x, z); & x \leq x_0 \\ \bar{v}^{\mathrm{II}}(x, z); & x \geq x_0 \end{cases} \tag{29}$$

of type (22), defined by giving jumps of the marginal values

$$\bar{v}^{\mathrm{I,II}}\Big|_{x=x_0-0}^{x=x_0+0} = g^{\mathrm{I,II}}(z) \quad \text{and} \quad \frac{\partial \bar{v}^{\mathrm{I,II}}}{\partial x}\Big|_{x_0-0}^{x_0+0} = h^{\mathrm{I,II}}(z)$$

with uniform boundary conditions (11–13) on z. The solutions at $x \leq x_0$ and at $x \geq x_0$ are constructed separately. In the layer $z_{k-1} \leq z \leq z_k (k = 1, 2, \ldots, N+1)$ we have from Eq.(24)

$$\frac{d^2 \bar{W}_k}{dz^2} - \alpha_k^2 \bar{W}_k = P_k(\lambda, z; x_0); \quad \alpha_k = \begin{cases} \alpha_k^{\mathrm{I}} = \sqrt{\lambda^2 - k_k^{\mathrm{I}2}}; & (x \leq x_0) \quad (30\mathrm{a}) \\ \alpha_k^{\mathrm{II}} = \sqrt{\lambda^2 - k_k^{\mathrm{II}2}}; & (x \geq x_0) \quad (30\mathrm{b}) \end{cases}$$

For the left-hand-side structure $x \leq x_0$:

$$P_k^{(-)} = -\,\mathrm{e}^{-i\lambda x_0}[h_k^{\mathrm{I}}(z) + i\lambda g_k^{\mathrm{I}}(z)] \tag{30c}$$

For the right-hand-side structure $x \geq x_0$:

$$P_k^{(+)} = +\,\mathrm{e}^{-i\lambda x_0}[h_k^{\mathrm{II}}(z) + i\lambda g_k^{\mathrm{II}}(z)] \tag{30d}$$

Solving separately the two operative equations (30a) and (30b) with the uniform conditions (11–13) and using Eq. (24a, b) we obtain, respectively, two solutions $\bar{v}^{\mathrm{I}}$ and $\bar{v}^{\mathrm{II}}$ for the two different one-dimensional structures I and II with wave numbers $k^{\mathrm{I}}(z)$ and $k^{\mathrm{II}}(z)$, independent of x, and with jumps $g^{\mathrm{I}}, h^{\mathrm{I}}$ and $g^{\mathrm{II}}, h^{\mathrm{II}}$ on the line $x = x_0$:

$$g_k^{\mathrm{I}}(z) = \bar{v}_k^{\mathrm{I}}\Big|_{x_0-0}^{x_0+0}; \quad h_k^{\mathrm{I}}(z) = \frac{\partial \bar{v}_k^{\mathrm{I}}}{\partial x}\Big|_{x_0-0}^{x_0+0} \tag{I}$$

and

$$g_k^{\mathrm{II}}(z) = \bar{v}_k^{\mathrm{II}}\Big|_{x_0-0}^{x_0+0}; \quad h_k^{\mathrm{II}}(z) = \frac{\partial \bar{v}_k^{\mathrm{II}}}{\partial x}\Big|_{x_0-0}^{x_0+0} \tag{II}$$

For the one-dimensional solutions $\bar{v}^{\mathrm{I}}$ and $\bar{v}^{\mathrm{II}}$ described above the corresponding Fourier x-images $\bar{W}_k^{\mathrm{I,II}}(\lambda, z; x_0)$ are

$$\bar{W}_k^{(-),(+)} = -\frac{\mathrm{e}^{-i\lambda x_0}}{2\alpha_k^{\mathrm{I,II}}} \int_{z_{k-1}}^{z_k} p_k^{\mathrm{I,II}}(\lambda, \zeta)\, \mathrm{e}^{-\alpha_k^{\mathrm{I,II}}|z-\zeta|}\, d\zeta + A_k^{\mathrm{I,II}}\, \mathrm{e}^{\alpha_k^{\mathrm{I,II}} z} + B_k^{\mathrm{I,II}}\, \mathrm{e}^{-\alpha_k^{\mathrm{I,II}} z}$$

$$\mathrm{Re}\, \alpha_k^{\mathrm{I,II}} \geq 0 \tag{31a, b}$$

where

$$p_k^{\mathrm{I,II}}(\lambda, z) = \mp\,[h_k^{\mathrm{I,II}}(z) + i\lambda g_k^{\mathrm{I,II}}(z)]\,.$$

Here A_k^{I}, B_k^{I} are integration constants for Eq. (30a) and A_k^{II}, B_k^{II} for Eq. (30b). They are defined by conditions (11a–13a) and (11b–13b), correspondingly. The two systems of linear equations for A_k, B_k can be

solved algebraically. The values $A_k^{\mathrm{I,II}}$ and $B_k^{\mathrm{I,II}}$ appear as linear combinations of definite integrals

$$r_k^{\mathrm{I,II}}(\lambda) = \int_{z_{k-1}}^{z_k} p_k^{\mathrm{I,II}}(\lambda, \zeta)\, \mathrm{e}^{-\alpha_k^{\mathrm{I,II}}\zeta}\, d\zeta \quad \text{and} \quad s_k^{\mathrm{I,II}}(\lambda) = \int_{z_{k-1}}^{z_k} p_k^{\mathrm{I,II}}(\lambda, \zeta)\, \mathrm{e}^{\alpha_k^{\mathrm{I,II}}\zeta}\, d\zeta$$

similarly to the formulas for A and B, given above in solution (22).

From Eq. (31) we build a composite function $\bar{v}(x, z)$ (Eq. (29)), using the inversion formulas (24a, b):

$$\bar{v}(x, z) = \begin{cases} \bar{v}^{\mathrm{I}}\ ; & x \leq x_0 \\ \bar{v}^{\mathrm{II}}; & x \geq x_0 \end{cases} = [v] + w\,.$$

Here the symbol $[v]$ corresponds to the first main term in solution (31), (24) and w to the additional one.

Thus, the partial solution (29) satisfying (11–13) can be represented by means of jumps g^{I}, h^{I} and g^{II}, h^{II} in the form (31a) and (24a); (31b) and (24b).

Now, let the functions $\mathrm{g}^{*\mathrm{I,II}}(z)$ and $\mathrm{h}^{*\mathrm{I,II}}(z)$ denote instead of the jumps (I) and (II) for $\bar{v}^{\mathrm{I}}$ and $\bar{v}^{\mathrm{II}}$ the left-hand-side and right-hand-side marginal values of the composite function (29) and its normal derivative at $x = x_0 \pm 0$:

$$g_k^{*\mathrm{I}}(z) = \bar{v}_k^{\mathrm{I}}(x, z)|_{x \to x_0 - 0}\,; \quad h_k^{*\mathrm{I}}(z) = \left.\frac{\partial \bar{v}_k^{\mathrm{I}}}{\partial x}\right|_{x \to x_0 - 0}$$

and

$$g_k^{*\mathrm{II}}(z) = \bar{v}_k^{\mathrm{II}}(x, z)|_{x \to x_0 + 0}\,; \quad h_k^{*\mathrm{II}}(z) = \left.\frac{\partial \bar{v}_k^{\mathrm{II}}}{\partial x}\right|_{x \to x_0 + 0}$$

and let these functions satisfy the conditions:

$$\begin{cases} g_k^{*\mathrm{I}}(z) - g_k^{*\mathrm{II}}(z) = \varphi(z) \\ \dfrac{1}{\sigma_{\mathrm{I}}^*} h_k^{*\mathrm{I}}(z) - \dfrac{1}{\sigma_{\mathrm{II}}^*} h_k^{*\mathrm{II}}(z) = \vartheta(z) \end{cases} \tag{10a}$$

Then, obviously, they yield the desired exact solution of the problem (9–14).

As a matter of fact, in our two-dimensional boundary problem (9–14) these marginal functions g^*, h^* necessary for the exact solution are unknown.

We show that the conjugation conditions (10) at a real contact $x = x_0$, including the given jump function $\varphi(z)$, allow to determine the unknown functions $\mathrm{g}^{*\mathrm{I,II}}$ and $h^{*\mathrm{I,II}}$, thus providing by Eq. (29) an exact solution using successive approximation method. It turns out that the exact solution has the general appearance of (26), (28).

Let us substitute left-hand-side and right-hand-side boundary values of the primary function $v_0 =$ (27) and its derivative with respect to x at $x = x_0 \pm 0$ into the right-hand-side of (30c) and (30d) of operative equations

(30a, b) as zeroth approximation. These values are known at each interval $z_{k-1} \leq z \leq z_k$:

$$g_{0_k}^{\mathrm{I,II}}(z) = v_{0_k}^{\mathrm{I,II}}(x, z)|_{x \to x_0 \mp 0}; \quad h_{0_k}^{\mathrm{I,II}}(z) = \left.\frac{\partial v_{0_k}^{\mathrm{I,II}}}{\partial x}\right|_{x \to x_0 \mp 0}$$

Consequently, using Eqs (24), (31)we find the first approximation $v^{(1)} = \bar{v}_0$ to the solution of problem (9–14) in an evident analytical form:

$$v^{(1)}(x, z) = [v_0] + w \tag{29a}$$

It can be shown, that $[v_0]$ and the initial primary function v_0 defined by Eq. (27), are identical up to a known additive term which satisfies the uniform conditions (10). Hence, the first approximation, $v^{(1)}$, transforms identically into

$$v^{(1)}(x, z) = v_0(x, z) + w_0(x, z) \tag{29b}$$

where

$$v_0 = v_{0_k}^{\mathrm{I,II}} = -\frac{1}{2\pi} \int_{-\infty}^{+\infty} \frac{1}{2\alpha_k^{\mathrm{I,II}}} \left(\int_{-\infty}^{+\infty} p_k^{\mathrm{I,II}}(\lambda, \zeta)\, \mathrm{e}^{-\alpha_k^{\mathrm{I,II}}|z-\zeta|}\, d\zeta \right) \mathrm{e}^{i\lambda(x-x_0)}\, d\lambda \tag{32a, b}$$

(expressions (32a, b) and (27) are two different forms of the presentation of one and the same function $v_0(x, z)$)

and

$$w_0 = w_{0_k}^{\mathrm{I,II}} = \frac{1}{2\pi} \int_{-\infty}^{+\infty} \left[a_k^{\mathrm{I,II}}(\lambda)\, \mathrm{e}^{\alpha_k^{\mathrm{I,II}} z} + b_k^{\mathrm{I,II}}(\lambda)\, \mathrm{e}^{-\alpha_k^{\mathrm{I,II}} z} \right] \mathrm{e}^{i\lambda x}\, d\lambda \tag{33a, b}$$

$$a_k^{\mathrm{I,II}} = A_k^{\mathrm{I,II}} - S_k^{\mathrm{I,II}}; \quad b_k^{\mathrm{I,II}} = B_k^{\mathrm{I,II}} - R_k^{\mathrm{I,II}}$$

$$S_k^{\mathrm{I,II}}(\lambda) = \frac{\mathrm{e}^{-i\lambda x_0}}{2\alpha_k^{\mathrm{I,II}}} \int_{z_k}^{\infty} p_k^{\mathrm{I,II}}(\lambda, \zeta)\, \mathrm{e}^{-\alpha_k^{\mathrm{I,II}} \zeta}\, d\zeta$$

$$R_k^{\mathrm{I,II}}(\lambda) = \frac{\mathrm{e}^{-i\lambda x_0}}{2\alpha_k^{\mathrm{I,II}}} \int_{-\infty}^{z_{k-1}} p_k^{\mathrm{I,II}}(\lambda, \zeta)\, \mathrm{e}^{+\alpha_k^{\mathrm{I,II}} \zeta}\, d\zeta$$

$$p_k^{\mathrm{I,II}} \equiv p_{0_k}^{\mathrm{I,II}} = \mp \left[h_{0_k}^{\mathrm{I,II}}(\zeta) + i\lambda g_{0_k}^{\mathrm{I,II}}(\zeta) \right]$$

The additional terms w, w_0 from (29a, b) together with $[v_0]$, v_0 provides for the uniform conjugation conditions (11–13). However, w, w_0 are composite functions, and generally speaking, do not satisfy the uniform conditions (10).

Conditions (10) for the sum $v^{(1)} = v_0 + w_0$ are perturbed in the general

case. Therefore expression (29b) = (27) + (33) differs from the exact solution by a corrective term

$$v - v^{(1)} = \delta v$$

For δv the same problem (9–14) arises as for v, without any field sources except for the jumps at the contact $x = x_0$;

$$\delta v\Big|_{x_0+0}^{x_0-0} = \varphi_1(z)\,; \quad \frac{1}{\sigma^*}\,\frac{\partial(\delta v)}{\partial x}\Big|_{x_0+0}^{x_0-0} = \vartheta_1(z)$$

Hereby

$$\varphi_1(z) = -\,w_0\Big|_{x_0+0}^{x_0-0}; \qquad \vartheta_1(z) = -\,\frac{1}{\sigma^*}\,\frac{\partial w_0}{\partial x}\Big|_{x_0+0}^{x_0-0} \tag{10.1}$$

For δv we find the first approximation again,

$$(\delta v)^{(1)} = (\delta v)_0 + w_1$$

in a form of (29b), similar to (32) + (33) $\equiv$ (27) + (33).

Compose a sum: $v^{(2)} = v^{(1)} + (\delta v)^{(1)}$ i.e. a second approximation for $v(x, z)$. Let us consider the difference:

$$v - v^{(2)} = \delta^2 v$$

The second corrective term $\delta^2 v$ satisfies again the problem (9–14) with new jump functions:

$$\varphi_2(z) = -\,w_1\Big|_{x_0+0}^{x_0-0}; \qquad \vartheta_2(z) = -\,\frac{1}{\sigma^*}\,\frac{\partial w_1}{\partial x}\Big|_{x_0+0}^{x_0-0} \tag{10.2}$$

from which we find again

$$(\delta^2 v)^{(1)} = (\delta^2 v)_0 + w_2$$

Proceeding further, finally we shall have

$$v^{(n+1)} = v^{(1)} + (\delta v)^{(1)} + \ldots + (\delta^n v)^{(1)} = v_0 + \sum_{i=1}^{n} v_{\text{add}}^{(i)} + w_n$$

where $v_{\text{add}}^{(i)} = w_{i-1} + (d^i v)_0$. Thus, in the limit the solution $v = \lim\limits_{n\to\infty} v^{(n)}(x, z)$ really leads to the form of (26), (28).

The convergence of successive approximations is assured because of a well known constraint of the Fourier coefficients on μ ($D_k(\mu)$ in Eq. (27)) as well as on λ ($A_k(\lambda)$ and $B_k(\lambda)$ in Eq. (31)). The products $D_k A_k$ and $D_k B_k$ are in absolute value always definitely less than 1. As a result, during the successive solution of problem (9–14) each new term decreases as compared to the previous one, as a diminishing geometrical progression. The convergence rate in every particular case requires special investigation.

As geothermal and magnetotelluric problems are concerned we have shown that the continuity of the initial jump functions $\varphi(z)$ and $\vartheta(z)$ at $z =$

$= z_k$ $(k = 1, 2, \ldots, N)$ is the necessary and sufficient condition for the nonsingularity of an exact solution (26) possessing finite first derivatives for all x, z (Lubimova and Nikitina, 1974). This condition is equivalent to the natural physical requirement of the continuity of the field at angular points of conjugation of areas with diverse parameters. Our formulation of the problem (9–14) provides the condition of continuity φ and ϑ in all cases, and it holds at all stages of the successive solution.

The relative simplicity and general character of the proposed method of solution have evident advantages. The analytical form of solution (26) is convenient both for a direct analysis and for computer calculations.

Successive addition of the corrective terms of a similar form $(\delta^i v)^{(1)}$, $(i = 1, 2, \ldots)$ to the first result $v^{(1)}$ leads to the same computing algorithm, where all integrands in (27), (33) are quickly attenuated *vs.* μ and λ (not worse than $e^{-|\mu| \cdot |x|}/\mu$ and $e^{-|\lambda| \cdot |z|}/\lambda$) as $\mu, \lambda \to \infty$.

This method of solution can be generalized for arbitrary composite piecewise-layered media with vertical as well as inclined contact. The range of various geophysical applications where one-sided Fourier transformations can be successfully applied is wide and diverse. Some examples are given in what follows:

1) It includes the case of a composite piecewise stepped medium with two (and more) vertical contacts.

2) It makes possible to prescribe a general boundary condition of the 3rd kind on a surface

$$\left[\frac{\partial u}{\partial z}\bigg|_{z=0+0} - \psi_0(x)\right] - \gamma_{\mathrm{I,II}}[u\,|_{z=0+0} - \chi_0(x)] \equiv 0 \tag{34}$$

where ψ_0, χ_0 are arbitrary functions, having Fourier x-images:

$$\int_{x_0}^{\infty} \begin{Bmatrix} \psi_0 \\ \chi_0 \end{Bmatrix} e^{-i\lambda x}\, dx = \begin{Bmatrix} \Psi_0^{(+)}(\lambda; x_0) \\ X_0^{(+)}(\lambda; x_0) \end{Bmatrix} \quad \text{and} \quad \int_{-\infty}^{x_0} \begin{Bmatrix} \psi_0 \\ \chi_0 \end{Bmatrix} e^{-i\lambda x}\, dx = \begin{Bmatrix} \Psi_0^{(-)}(\lambda; x_0) \\ X_0^{(-)}(\lambda; x_0) \end{Bmatrix}$$

Further, e.g. if $\chi_0(x)$ is the temperature of the external medium in a Newtonian heat exchange and $\psi_0(x) \equiv 0$; then the vertical heat flow over a contact zone of oceanic and continental crust at the earth's surface equals:

$$q(x) = -\lambda_1^{\mathrm{I,II}}\, \gamma_{\mathrm{I,II}} \left[-\chi_0(x) + u_0^{\mathrm{I,II}}(z)\,|_{z=0} + \frac{1}{2\pi} \int_{-\infty}^{+\infty} D_1^{\mathrm{I,II}} \Phi_1^{*}\, e^{i|\mu|x}\, d\mu + \right.$$

$$\left. + \frac{1}{2\pi} \int_{-\infty}^{+\infty} (a_1^{*\mathrm{I,II}} + b_1^{*\mathrm{I,II}})\, e^{i\lambda x}\, d\lambda \right] \tag{35}$$

where

$$\varphi^* = g^{*\mathrm{I}} - g^{*\mathrm{II}}$$

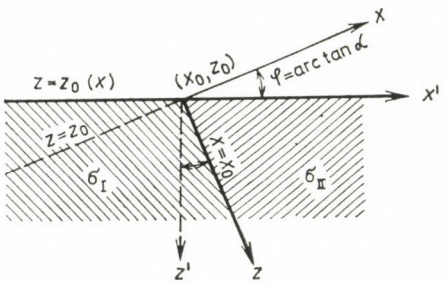


Fig. 3. A pattern of conversion from the x', z' coordinate system to the x, z system in case of inclined contact along $x = x_0$ with angle φ

3) In the theory of *dipole electromagnetic investigations* (so called frequency sounding) the solution for a composite medium (Fig. 2) is also constructed by the method described in this paper. Successive approximations are presented in a closed form of Fourier integrals.

4) The method also applies to *two-dimensional boundary problems of elasticity theory.* Elastic oscillations of circular frequency ω satisfy the system of wave equations (1b) and (1c). Boundary conditions at each of the boundary lines $z = z_k$; $x = x_0$ are described by four linear relationships between u_1 and u_2 and $\frac{\partial u_1}{\partial x}$, $\frac{\partial u_1}{\partial z}$ and $\frac{\partial u_2}{\partial x}$, $\frac{\partial u_2}{\partial z}$ with piecewise-constant coefficients. The problem is finally reduced to an algebraic one due to the linearity of these relations.

5) The method can be generalized for two-dimensional boundary problems of an *inclined contact between horizontally-layered media.* As a matter of fact, let the lower limit z_0 in the formula of semi-infinite Fourier transformations (15) depend on x : $z_0(x) = z_0 + a(x - x_0)$, where a is in accordance with the slope of the inclination between the axes x and x' (Fig. 3). Then, in Eq. (19) the right-hand-side F evidently depends on parameter a. Formula (18) for F is valid in the particular case of vertical contact $a \to 0$; $z_0(x) \to z_0$. In the general case of an inclined contact $a \neq 0$ and other function F is obtained. Expressions (20), (22) for V_0, $\overline{V}$ are changing accordingly, but of course the principle of constructing the solution remains the same.

6) Integrating with respect to frequency extends the range of application of a given mathematical solution to general *non-stationary* processes of arbitrary appearance.

7) It has been shown how the method of one-sided Fourier transformation can be used to investigate and solve diverse two-dimensional boundary problems by *separating the variables.* Besides the discussed example in Cartesian coordinates (x, y, z) this method is applicable in other coordinate systems as well for boundary problems whose exact solution have not yet been found. A few such geophysical applications are, e.g.: the well logging problem in media with plane horizontal boundaries as well as cylindrical, vertical boundaries expressed in cylindrical coordinates (ϱ, φ, z); geophysical fields in the transition zone from a continent to an ocean taking into account the earth's sphericity in spherical coordinates (r, ϑ, φ) etc.

3. NUMERICAL SOLUTION BY THE FINITE DIFFERENCE APPROACH

Some examples of the numerical solution of Problem (1) for "refraction" models (Fig. 1, c–f) by the finite-difference mesh method are given below.

In the mesh method we substitute the derivatives by finite differences in internal points of a spatial mesh (Tikhonov and Samarsky, 1972). Difference boundary conditions are formulated in external points. With boundary conditions of the 1-st kind the order of the algebraic system approximating the given differential problem is equal to the number of internal mesh points.

Since in geophysics the domain where an unknown function has to be determined is infinite, a difference problem in a finite domain can be formulated only with approximate boundary conditions: namely by assuming that the additional, anomalous field at the outer boundaries equals zero. Naturally, such formulation of the problem is the more accurate the larger the dimensions of the area where calculations are performed in comparison with the sizes of embeddings. On the other hand, the size of the embedding should be several times more than the mesh spacing.

These two conditions, in case of a regular mesh, are hardly met simultaneously, for the computer memory has to store over 10,000 unknown values even with two dimensions (x_1, x_2) and a "mean accuracy" (one hundred points in one direction), (Wazow and Forsythe, 1963).

Nevertheless, a regular mesh is better than an irregular one, because the latter requires a more complicated program and more time, and results have a lower accuracy.

Let us consider the equilibrium temperature distribution for an infinite layer of thermal conductivity λ_1 containing rectangular bodies of different thermal conductivities $\lambda_2, \lambda_3, \ldots, \lambda_k$. Let the temperatures at the upper and lower boundaries be equal to 0 and T_1, respectively. Such a distribution satisfies the Laplace equation with piecewise constant coefficients

$$\operatorname{div} (\lambda_i \operatorname{grad} T) \tag{36}$$

where

$$i = 1, 2, \ldots, k$$

The temperature and the normal heat flow at the boundary lines are continuous:

$$[T] = 0 \quad \text{and} \quad \left[\lambda \frac{\partial T}{\partial n}\right] = 0$$

Let us construct a different analogue of the Dirichlet's problem inside the rectangle: $0 \leq x_\alpha \leq hN_\alpha$; $(\alpha = 1, 2)$,

where $$N_1 = 64; \; N_2 = 62$$

A square mesh with spacing h is formed by the intersections of two $(\alpha = 1, 2)$ families of parallel lines $x_\alpha = i_\alpha h$; $i_\alpha = 0, 1, \ldots, N_\alpha$. The origin of

coordinates is located in the left upper corner. The boundary conditions for the distant sides of the domain of calculation, i.e. for $x_1 = 0$ and $x_1 = hN_1$ are as for a "normal" field without embeddings, that is:

$$T = \frac{T_1 x_2}{hN_2} \tag{37}$$

Due to the uniformity of the difference pattern the heat balance equations for heat flows along the coordinate axes give in each internal point the relationship (Tikhonov and Samarsky, 1972):

$$T_0 = \frac{\sum_{\alpha=1}^{2} \mu_{\pm\alpha} T_{\pm\alpha}}{\sum_{\alpha=1}^{2} \mu_{\pm\alpha}} \tag{38}$$

Here $T_0 = T(x_1, x_2)$; $T_{\pm\alpha} = T(x_\alpha \pm h, x_\beta)$; $\alpha \neq \beta$; $\alpha, \beta = 1, 2$

$$\mu_{\pm\alpha} = \left(\int_0^1 \frac{dS}{\lambda(x_\alpha \pm Sh, x_\beta)} \right)^{-1} \tag{39}$$

If the medium is piecewise heterogenous and the thermal conductivity coefficient λ has jumps along lines going through the mesh points, then:

$$\mu_{\pm\alpha} = \lambda(x_\alpha \pm 0, x_\beta); \quad \alpha \neq \beta; \ \alpha, \beta = 1, 2 \tag{40}$$

All $\mu_{\pm\alpha}$ are equal to each other for points out of the boundary lines and (38) goes over to the known difference approximation of the Laplace operator

$$T_0 = \frac{1}{4} \sum_{\alpha=1}^{2} T_{\pm\alpha}. \tag{41}$$

The nondisturbed "normal" distribution (37) was used as zeroth approximation for the solution of system (38) by the "Young-Frankel successive relaxation" method (Wazow and Forsythe, 1963):

$$\delta_j = T_0^{(j+1)} - T_0^{(j)} = \frac{\omega}{\sum_{\alpha=1}^{2} \mu_{\pm\alpha}} \left(\sum_{\alpha=1}^{2} \mu_{-\alpha} T_{-\alpha}^{(j+1)} + \sum_{\alpha=1}^{2} \mu_{+\alpha} T_{+\alpha}^{(j)} \right) - \omega T_0^{(j)} \tag{42}$$

Young's parameter is obtained from the approximate formula in Wazow and Forsythe (1963):

$$\omega = \frac{2}{1 + \sin \frac{\pi}{N_1}} \tag{43}$$

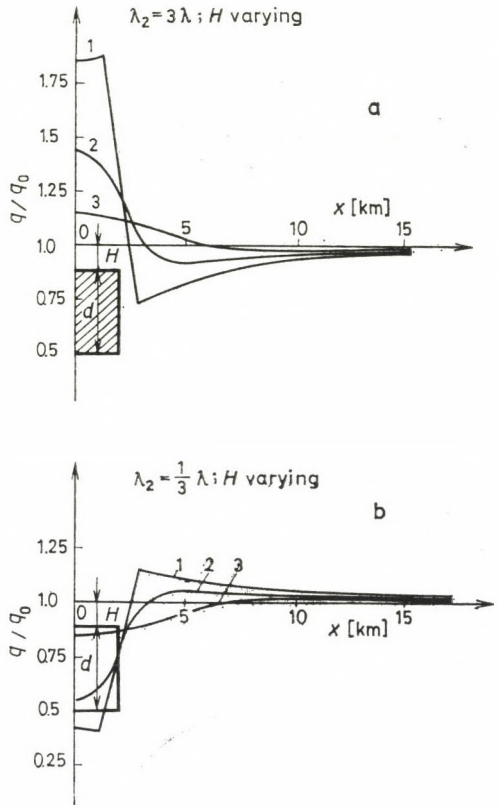


Fig. 4. Effect of depth of submersion of a square body on heat flow values
a – conducting body: $\lambda_2 = 3\lambda_1$;
b – insulating body: $\lambda_2 = 1/3\,\lambda_1$.
Notations: $q = q_0 + q_{add}$ – total heat flow; q/q_0 – relative heat flow; q_0 – normal heat flow without any embedding; square side $d = 4$ km $= 4h$; mesh spacing $h = 1$ km. Distance H from the upper edge of body to the surface is:
1 – $H = 0$; 2 – $H = h$ km;
3 – $H = 4h$ km

The maximum permissible number of points which allowed to store the subsequent approximations in one block of the digital computer's memory ($N_1 = 64$, $N_2 = 62$) has been employed in the calculations. It is possible to accept $T_1 = N_2$ in $T_0^{(0)}$ without limiting the generality. That means the "unit" vertical gradient for the non-dimensional "normal" field without embedding.

The process of iterations (42) has been interrupted when the difference between two subsequent approximations δ became less than 10^{-6}. The time of computation is 12 min for 120 iterations. In case of a symmetrical position of the anomalous embeddings it is possible to consider only the right-hand-side of the calculated rectangle and reduce the time to its half. It should be kept in mind that

$$\mu_{-1} = \mu_{+1}$$

$$T(x_1 - h, x_2) = T(x_1 + h, x_2) \tag{44}$$

at the axis of symmetry.

The heat flow on the surface is

$$q(x_1) = -\lambda \frac{\partial T}{\partial x_2}(x_1, 0) = \lambda \frac{T(x_1, h) - T(x_1, 0)}{h} - \lambda T''_{x_2^2}(x_1, 0) \frac{h}{2} + 0(h^2)$$

Taking into account Eqs (36) and (37) we obtain with an accuracy of h^2

$$q(x_1) = \lambda \frac{T(x_1, h)}{h}$$

The error of calculations itself is a value of the order of h^2 (Tikhonov and Samarsky, 1972).

Deep heat flow distortion, caused by contrasts in the coefficient of thermal conductivity was investigated for a square — $d_1 \times d_2 = 4h \times 4h$, $h = 1$ km (Fig. 4); for a vertical rectangle — $d_1 \times d_2 = 4h \times 16\ h$ (Fig. 5); for a horizontal rectangle — $d_1 \times d_2 = 16h \times 4h$ (Fig. 6); and also for two symmetrically located squares, spaced at a distance equal to their side (Fig. 7) and at a distance three times as much (Fig. 8). The thermal conductivity jump

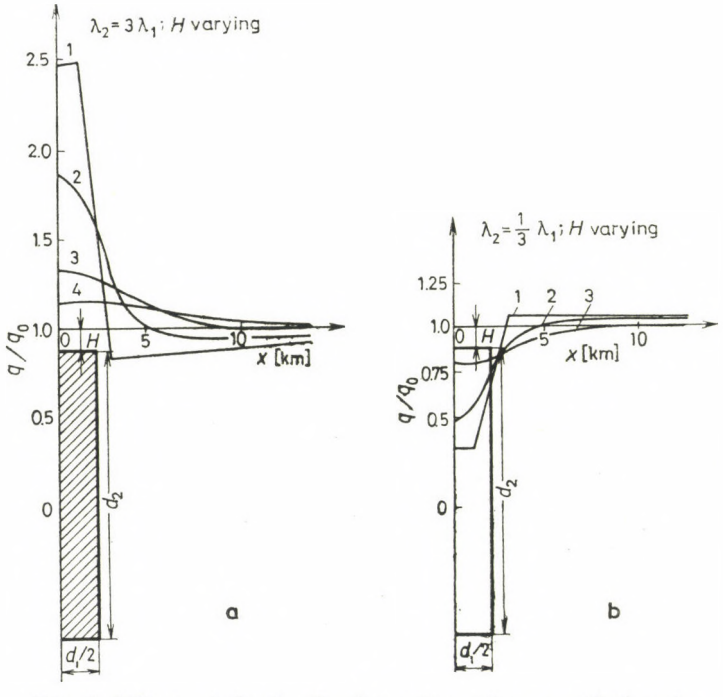


Fig. 5. Effect of depth of submersion of a vertical rectangle on surface heat flow: a – conducting body: $\lambda_2 = 3\lambda_1$; b – insulating body: $\lambda_2 = 1/3\ \lambda_1$. Notations as in Fig. 4, and 4 – $H = 8$ km. Rectangle sides: $d_1 = 4$ km; $d_2 = 16$ km

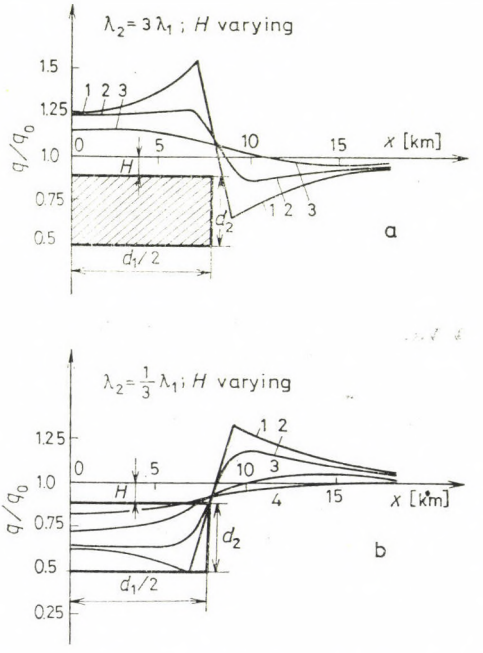


Fig. 6. Effect of depth of submersion of a horizontal rectangle on surface heat flow Notations as in Figs 4 and 5. Rectangle sides: $d_1 = 16$ km, $d_2 = 4$ km

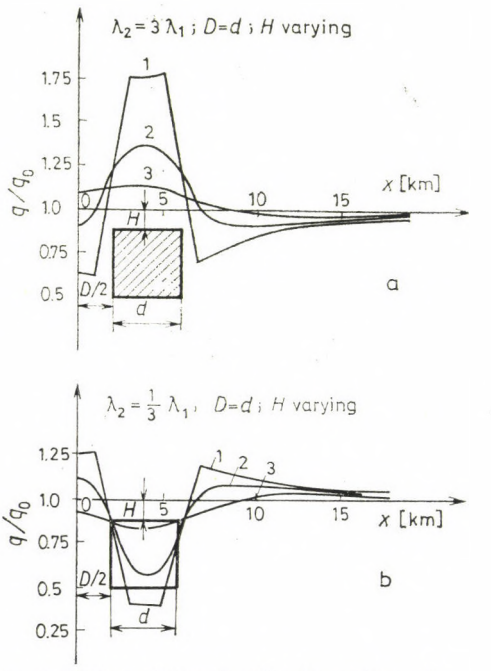


Fig. 7. Effect of depth of submersion of two square bodies of equal thermal conductivities ($\lambda_2 = \lambda_3$) on surface heat flow. Distance D between squares equals their side d. Notations as in Fig. 4

was 3 or 1/3 in all cases. An increase in the thermal conductivity jump from 3 up to 30 was also studied on a square embedding model. The maximum relative heat flow q, in case of square-side $d = 4h$, has proved to grow by less than 20% if the depth of submerging intrusion was $H = h$ and more.

Heat flow anomalies have the appearance of sign-changing curves. The central extremum is splitting up into two ones shifted to contact lines, if the embedding represents an outcropped sheet.

According to Figure 4 it can be affirmed that a square embedding of side d immersed at the depth $H = d$ causes a heat flow distortion $q(x_1)$ being not more than 15% of the "normal" heat flow q_0. The cases A) $\lambda_2 > \lambda_1$ and B) $\lambda_2 < \lambda_1$ differ in the positive resp. negative sign of the distortion, i.e. of the anomalous heat flow: $q - q_0 = q_{\text{add}}$. The "half-width" of the anomaly, that is its width at the 0.5 level from the maximum of the anomalous heat flow q_{add}, is equal to $1.5d$ if the thermal conductivity jump is not more than 3 (and not less than 1/3).

A conducting horizontal embedding ($\lambda_2 = 3\ \lambda_1$) under similar conditions $H = d_1$ is marked only by a larger "half-width" $\sim 4d_2$ (Fig. 6, a); while a vertical one causes the same heat flow anomaly with two-fold immersion depth, the "half-width" being of the order of $\sim 3d_1$ (Fig. 5, a).

An insulating body ($\lambda_2 = 1/3\,\lambda_1$) gives a 20% decrease in the heat flow observed at depth $H = 2d_1$ for a horizontal embedding ("half-width" $\sim 4d_2$, Fig. 6, b) and at depth $H = d_1$ for vertical embedding ("half-width" $\sim 1.5\,d_1$, Fig. 5, b).

Two square bodies at the surface $H = 0$ and at a small depth $H = d/4$ are resolved even at a distance $D = d$ between them, but the anomalies blend into one at depth $H = d$ (Figs 7 and 8).

Let us now consider a geoelectrical example. Figure 9 shows the curves calculated for a dipole axial electro-profiling over a high-resistivity ($\lambda_2 = 0$) square "valley" of side $d = 3$ km, outcropping at the surface $H = 0$, or immersed at the depth $H = 2/3\,d = 2$ km (the distance $r = 8$ km; $AB/MN = 3$; $MN = h = 1$ km). Calculations were carried out on a cubic mesh, measuring $31\,h \times 15\,h \times 14\,h$.

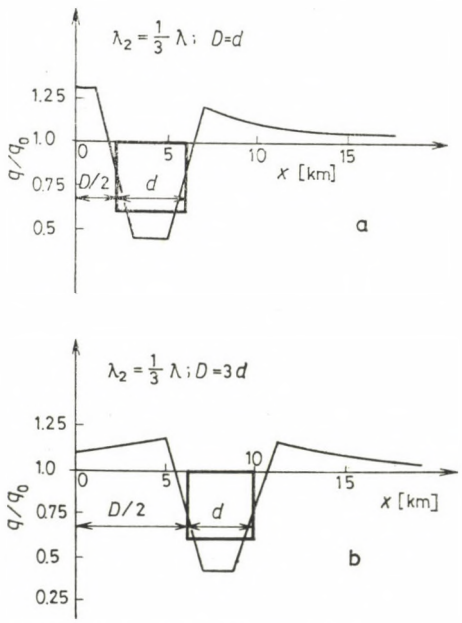


Fig. 8. Effect of D-distance between two squared "valleys" ($H = 0$) of equal thermal conductivities ($\lambda_2 = \lambda_3 = 1/3\,\lambda_1$) on surface heat flow a – $D = d$; b – $D = 3d$

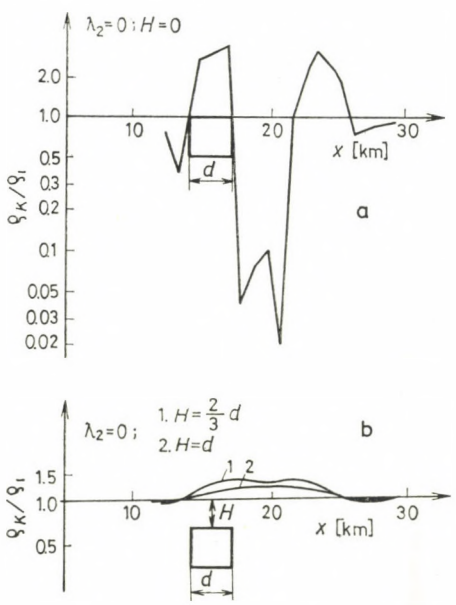


Fig. 9. Example of electrical profiling. Effect of depth of submersion of a square embedding of high resistivity ($\lambda_2 = 0$) with side $d = 3$ km on the dipole axial electrical profiling curves. Parameters: distance $r = 8$ km; dipoles $AB = 3$ km; $MN = 1$ km. Mesh spacing $h = 1$ km. Notations: ϱ_K – apparent resistance; $\varrho_1 = 1/\lambda_1$ – surrounding medium's resistance. Distance H from the upper body edge to the surface is different: a – body at the surface ("valley") $H = 0$; b – submerged body: $1 - H = 2$ km, $2 - H = 3$ km $= d$

For practical applications it should be noted that the heat flow sensibility is assumed as within 10—15%. With such sensibility the depth H_{max} of heat flow investigations over single square embeddings of threefold thermal conductivity with size d is roughly equal to this value: $H_{max} \cong d$. This is also true for horizontal conducting "lenses" of the same altitude d_1; and for vertical insulating "sheets" of similar width d_2. The depth H_{max} is roughly twofold for vertical conducting sheets and for horizontal insulating lenses.

As a result, the mesh-method of heat flow calculations can be used in both continental and marine geothermal investigations (with an accuracy within 1%, according to our calculations). More complicated structures can also be considered for the purpose of further interpreting the heat flow anomalies. Transition to the three-dimensional case is also possible.

4. A VERTICAL INTRUSION MODEL

An important geophysical case of problem (1—8) is the vertical "intrusion" model (Fig. 1, h) used for interpreting heat flow in the area of ocean ridges. The same model is applied for faulted zones with hydrothermal sources in the variant of a "simple ($\mathbf{v} = 0$) intrusion" (Fig. 1, g).

In this case the temperature distribution along the vertical contact, i.e. the $f(z)$ function, is assumed to be given. The physical meaning of function $f(z)$ is the following: Hot water (or mantle material) having temperature near T_1 (the melting point temperature) is located along the vertical boundary. It rises vertically from the basement (upper mantle), starting from the plate bottom (lithosphere bottom) $z = 0$ up to a level h, where $h < l$ (l is the thickness of the plate). Reaching the surface $z = l$ the intrusion material cools down, and $f(z = l)$ approaches T_0.

The dynamic ($\mathbf{v} \neq 0$) problem of hot material intrusion at the contact between two horizontally-layered media (see the model of Fig. 1, h) is reduced to problem (9) with simplified, practically ideal boundary conditions (11–13).

The temperature is expressed as a sum of a normal one-dimensional field and an anomalous two-dimensional field. Let us consider the equation of heat conductivity with a convective term:

$$\lambda \left(\frac{\partial^2 T}{\partial x^2} + \frac{\partial^2 T}{\partial z^2} \right) = \varrho \, C \, \mathbf{v} \frac{\partial T}{\partial x} \tag{45}$$

in equilibrium state with $\mathbf{v}|_{x<0} = -\mathbf{v}|_{x>0}$, using the representation $T = T_0(z) + \vartheta(x, z)$. The solution for the additional field is constructed on the basis of the canonical form of wave equation (9) with the purely imaginary wave number $i\varkappa$; $\varkappa = \varrho C \vartheta / 2\lambda$; $\varkappa$ being real. We introduce $\vartheta = \mathrm{e}^{-\varkappa x} w(x, z)$ and then

$$\Delta w - \varkappa^2 w = 0 \tag{46}$$

$$\text{with} \quad w|_{z=0+0} = 0 \quad \text{and} \quad w|_{z=l-0} = 0$$

at horizontal boundaries; and so far. The process of successive approximations in the above analytical solution is considerably simplified, ending just at the first term: $w = w^{(1)}(x, z)$ (Lubimova and Nikitina, 1974, 1975).

This partial case of the general problem (1–1a) yields a nonsingular solution to the intrusion model and makes it possible to calculate the surface heat flow distribution $q(x)|_{z=l}$ close to the axis $x = 0$ of the hydrothermal anomaly, as well as close to the spreading centre in the ocean ridge model.

The previous singular solution was valid only on the flanks of the ridges, i.e. at rather large distances from the intrusion centre. The new intrusion model eliminates the heat flow singularity associated with the discontinuous idealization of the temperature distribution in a previous plate tectonic heat flow model.

As a result of the new solution two important parameters l and m of the ocean ridge problem are obtained. One is the thickness l of the oceanic lithosphere. The other one, m is associated with the level h of hot material along the vertical axis of intrusion (relative height of the intrusion melt is represented as $h/l = 1 - 1/m$).

The parameter $m = l/(l - h)$ is determined from observations as $m = (q_{obs}(x = 0))/q_0$, where q_0 is the normal asymptotical value of heat flow on the flanks and $q_{obs}(x = 0)$ is the mean observed heat flow in the centre of anomaly. A formula for defining "half-width" $\delta(m)$ of the observed heat flow anomaly is given by the coefficient of the first term $(m/\pi)/\sin(\pi/m)$ of a series expression of heat flow. The thickness of lithosphere l in a given region can be defined by a mode of decreasing the heat flow function $q_{obs}(x)$ along the flanks.

General interpretation is based on a special set of theoretical calculating curves. Heat flow values at the earth's surface and elevations associated with the thermal extension were calculated numerically for the following parameters: oceanic lithosphere thickness $l = 50 \div 100$ km; velocity of the solid $1\ \mathbf{v} = \div 9$ cm/year in different sides from the axis; thermal conductivity coefficient $\lambda = 0.004 - 0.007$ calcm^{-1} °C^{-1} sec^{-1} (for the lithosphere material). Special diagrams convenient for interpretation, were constructed on the basis of these calculations. They could be used to analyse and correlate experimental curves of heat flow and of topography on ridges.

An example of combined interpretation of heat flow and elevation (topography) data is given in Figure 10, a and b (Lubimova and Nikitina, 1975).

Using the new solution we succeeded to calculate, for the first time the heat losses through all global ocean ridges (with a total length of 5×10^4 km) by the direct integration method for the additional heat flow $q_{add}(x)$. Heat losses from all ridges amounted to $7\% \div 17\%$ of Q for the averages: $m = 2.7$; velocity from 1.5 to 3 cm/year and $l = 75$ km. Here $Q = (7.7 \cdot 10^{12} \pm 10\%)$ calsec^{-1} is the total heat loss of the whole earth. After combined interpretation, however, the lithosphere thickness more likely equals $l_{eff} = 100$ km. With increasing l the heat losses in the investigated range of $\varkappa l \gg \pi$ are rising (according to calculations) as l^2. Then, with $l = 100$ km, $\mathbf{v}_{av} = 3$ cm/year and all other parameters unchanged, we estimate the heat losses from all ridges as 30% of the total terrestrial Q.

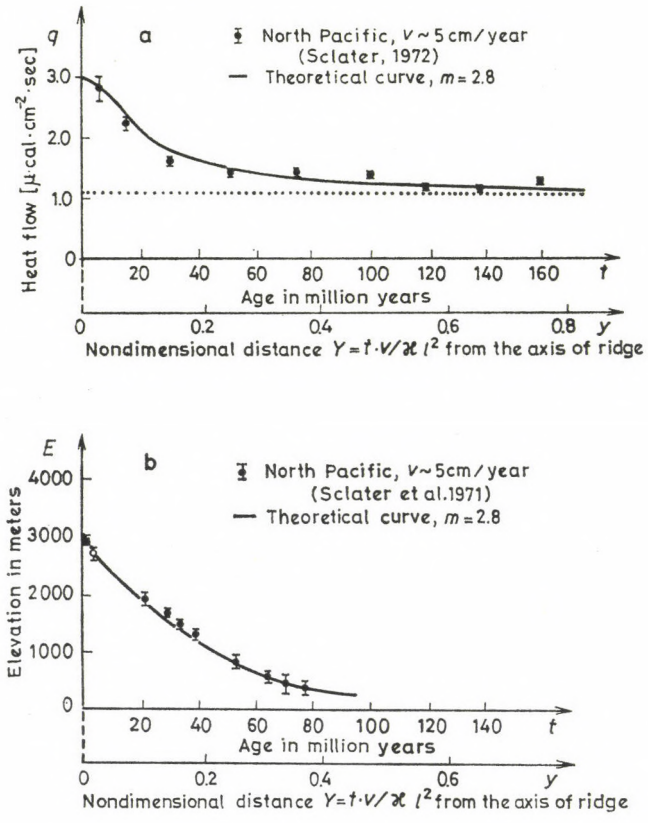


Fig. 10. Plot of the mean observed heat flow (*a*) and mean observed elevation (*b*) *vs.* age t of the ocean floor, or non-dimensional distance $y = \dfrac{x}{\varkappa l^2} = \dfrac{2\lambda t}{\varrho C\, l^2}$ from the ocean ridge axis. Solid lines are theoretical curves with parameters: $m = \dfrac{l}{l-h} = \dfrac{q_{obs}(x=0)}{q_0} = 2.8$; $l = 100$ km; $T_1 - T_0 = 1600$ °C; $l - h = 36$ km. (Φ = experimental values of Sclater et al., 1971, Sclater, 1972)

In conclusion, the obtained solution offers a way to a more realistic approach to understand the physical process of intrusion and also to set and solve the inverse geophysical problem in accordance with modern techniques of measurement and the data accumulated up to now. The corresponding inverse problem (45–46) consists in finding the depth-temperature function $f_{obs}(z)$ based on the surface experimental data about heat flow distribution $q_{obs}(x)$.

In our opinion the future work should be: 1. interpretation of such anomalies as hot springs and geothermal areas near fault zones, especially for the Central and Eastern part of Europe (for instance in Hungary, or Bul-

garia); 2. interpretation of thermal anomalies in rift valleys, like the Rhien graben in Europe or the Baikal Rift valley in Siberia. The reported method will also apply to these special regions taking zero velocity of the solid ($\mathbf{v} = 0$) in these cases. It would be also desirable to measure the magnetic anomaly pattern for rocks from the rift valleys in order to define the age t of the structure and connect it with the parameter $\mathbf{v}$ (if $\mathbf{v} \neq 0$) through the relation $x = \mathbf{v} \cdot t$, or more exactly as $x = \int_0^t \mathbf{v}\, dt$. It will give a new thermal criterion for recognizing a riftogenesis process.

REFERENCES

Dmitriev, V. I., Zakharov, E. V., 1970. A method for the solution of a problem of the electrodynamics of inhomogeneous media (in Russian). *Zh. vych. Matem. i Matem. Fiz.* **10,** No. 6.

Lubimova, E. A., Nikitina, V. N., 1972. Solution of two-dimensional boundary problems of thermal and electromagnetic field over a vertical contact of horizontally layered media (in Russian). *Ann. Univ. Sci. Budapestiensis, Sec. Geol.* **16,** 121.

Lubimova, E. A., Nikitina, V. N., 1974. Analysis of singularity of heat flow over middle oceanic ridges (in Russian). *Dokl. Akad. Nauk SSSR* **216,** No. 3.

Lubimova, E. A., Nikitina, V. N., 1975. On heat flow singularities over mid-ocean ridges. *J. Geophys. Res.* **80,** 232–243.

Praus, O., Červ, V., Verner, A., 1973. Magnetotelluric resistivities in models with dipping interfaces. *Studia Geophys. Geod. ČAV* **17,** 346.

Sclater, J. G., Anderson, R. N., Bell, L. M., 1971. Elevation of ridges and evolution of the Central Eastern Pacific. *J. Geophys. Res.* **76,** No. 32.

Sclater, J. G., 1972. Heat flow and elevation of the marginal basins of the Western Pacific. *J. Geophys. Res.* **77,** No. 29.

Tikhonov, A. N., 1937. On the effect of radioactive decay on the temperature of the earth's crust (in Russian). *Izv. Akad. Nauk SSSR, Ser. Geogr. i Geofiz.* No. 3.

Tikhonov, A. N., Samarsky, A. A., 1972. Equations of mathematical physics (in Russian). Nauka, Moscow.

Titchmarsh, E., 1948. Introduction to the theory of Fourier integrals (in Russian). OGIZ, M. L.

Wazow, V., Forsythe, J., 1963. Methods of finite differences for the solution of partial differential equations (in Russian). Innostrannaya Literatura, Moscow.

CHAPTER 2

COLLECTING OF GEOELECTRIC DATA; THEORY, DATA PROCESSING, LIMITATIONS

Edited by

G. FANSELAU and G. PORSTENDORFER

INTRODUCTION TO CHAPTER 2

G. FANSELAU, G. PORSTENDORFER

This chapter deals with the most important problems of interpretation and data processing of the geoelectrodynamic methods. Here it is necessary to consider the most essential facts of the external inducing magnetic field, as e.g. the homogeneity of the fields and their physical origin, the knowledge of these facts is necessary for successful measuring and interpretation. Of equal importance are the problems of splitting the fields into an inducing and an induced part, the treatment of models for horizontally inhomogeneous or anisotropic geological structures, and problems of complex interpretation, i.e. how to use geoelectrodynamic methods together with seismics, gravimetry, geothermics etc.

The principal ideas of the treatment of geomagnetic observational data according to the principles of theoretical physics are comprehended in the paper of Rokityansky, Kulik and Shuman. Here are given concisely all the theoretical results needed for the evaluation of observational data.

The interpretation of geomagnetic deep soundings and magnetotelluric methods is connected with models of geological structures. It is very important to know the field distortions generated by horizontally inhomogeneous or anisotropic media.

There are different methods for the determination of the different field-components. The classical analytical solution by the integral-equation method is described by Treuman from the theoretical point of view. He gives interesting aspects for the development of this method for three-dimensional cases. Berdichevsky and Dmitriev give results of analytical solutions by graphical representations for a great number of geological structure conditions. They summarize the great experiences gained in the USSR in this field and give ideas for the evaluation of measurements in complicated geological situations.

The paper of Petr gives the analytical solution for the horizontally layered anisotropic half-space based on a comprehensive work having been done by him during many years.

The necessity of more and more complicated models brings computer techniques to the foreground. Praus gives examples for the numerical solution by the finite-difference-method based on comprehensive computer calculations.

Model experiments in electrolytical troughs by high-frequency fields have been done since long in Leningrad by Dobrovolskaya and Kovtun. Their paper represents some of their results, especially interesting are those for three-dimensional structures.

The paper of Porstendorfer summarizes the numerous international works

on this field in a catalogue, compiled as a guide to the international literature available up to now on this subject.

The papers of Ádám and Verő and that of Rokityansky deal with the technics of evaluation of observational data in geomagnetic deep sounding and magnetotellurics. The proposed methods of evaluation are based on recent investigations of the authors.

In the paper of Takács the role of the vertical pulsations of the geomagnetic field is discussed with respect to indications of the changes of the structure of the highly resistant basement.

The papers of Grafe and of Ádám, Cz. Miletits and Verő deal with the physical characteristics of the inducing external geomagnetic field. Grafe discusses substorms (or bay disturbances) which are the most important types of geomagnetic variations used in the electromagnetic methods of geophysics. For this reason, substorms are also extensively treated as regards their origin in the magnetosphere. An exact knowledge of the current systems of the magnetosphere, with special respect to homogeneity and variability with space and time, is the presupposition for a proper interpretation.

An important contribution denoted to the above mentioned problem is the paper of Ádám, Cz. Miletits and Verő. It deals with the inhomogeneities of the geomagnetic variations used most frequently for magnetotellurics. The necessity of an exact physical knowledge of the structure of the geomagnetic field of pulsations is pointed out.

All geoelectromagnetic methods are, of course, in strong connection with each other, for their physical basis is the same. Complex interpretation of geoelectromagnetic methods seems to be necessary and has advanced, internationally, more and more. Fanselau and Ballani deal with this problem theoretically not only for geoelectromagnetic methods but they also touch upon complex interpretation together with magnetostatics, gravimetry, geothermics and not at last seismics. Homological relations, which are a good help for such considerations, are discussed. Suitable interpretation methods are proposed.

THEORETICAL FUNDAMENTS OF MAGNETIC VARIATION PROFILING (MVP)

I. I. ROKITYANSKY, S. N. KULIK, V. N. SHUMAN

LIST OF SYMBOLS

a – sphere resp. cylinder radius, major semi-axis of the ellipse
b – minor semi-axis of the ellipse
D, D_s, D_c – functions describing the frequency dependence of the anomalous magnetic field for a sphere and a cylinder
E_0 – normal electric field component of the magnetotelluric field
$G = \sigma_i Q$ – longitudinal conductivity of the cross section Q of the anomalous body
H_x – x-component of **H**
H_z – vertical component of **H** directed downward into the earth
H_0 – normal magnetic field component of the magnetotelluric field
H_a – anomalous part of **H**
h – depth, thickness of layer;
normalized anomalous field of the rotational type (formula (7)):

$$h_z = \frac{H_z}{H_{x0}}, \quad h_x = \frac{H_x}{H_{x0}} - 1$$

k_i – $(i\omega\mu\sigma)^{1/2}$ — wave number in the conducting medium
L – linear dimension of the conducting body
m_k – complex momenta of the cross section of the anomalous body (formula (18))
$s = \int_0^h \sigma(z)\,dz$ – longitudinal conductivity of the layer
T – variation period
V – function describing the frequency dependence of the anomalous field of a cylinder
$\beta_E; \beta_H$ – damping coefficient (functions of depth, period and size parameters)
$\gamma_1; \gamma_2$ – coefficients (formula (14))
ζ_0 – normal impedance, $\bar{\zeta}_0$ – impedance defined by (6b)
λ – wavelength
$\xi = X + iZ$, $\xi_i = X_i + iZ_i$ – points outside and inside of Q (16)
ϱ – electrical resistivity
σ – electrical conductivity, σ^* – effective conductivity of the body (12)
χ – prolongation function of spheroid
ω – angular frequency $= 2\pi/T$

r, Θ, φ – spherical coordinates
r, φ, z – cylindrical coordinates
x, y, z – Cartesian coordinates (x points to the North, y to the East, z downwards)

The interpretational basis of the MVP method is the solution of the problem of electromagnetic induction by an ionospheric-magnetospheric source of complex configuration in a heterogeneous earth. For a review of the theoretical state of arts the reader is referred to the contribution of Treumann on pp. 124–140 of the present volume. On the one hand such a problem is rather complex mathematically, on the other, due to the extreme variability of the variation field source, only a rough approximation of its parameters is possible (cf. Grafe's contribution on pp. 274–295 of the present volume). The difficulties can be significantly reduced by dividing the complex problem into two somewhat simpler problems:

1. Construction of a certain effective horizontally stratified earth with normal magnetotelluric field E_0, H_0 corresponding to the configuration and dimensions of the source.

2. Formation of an anomalous field above the local inhomogeneity due to the acting of E_0 and H_0. The smaller the dimensions of the electrical conductivity anomaly as compared to the dimensions of the source the better are the results provided by such a division.

Our further consideration will be based on this division.

GEOMAGNETIC VARIATIONS USED BY MVP AND THEIR NORMAL IMPEDANCE

Variations of periods from several minutes (a number of investigations have been carried out on oscillations, having periods from 15–200 sec) up to one day, most of all bay variations (T = 15–150 min) are commonly used in the MVP method. However, in order to determine the normal im-

TABLE 1

Parameters of the eight-layer section, corresponding to the MVS–MTS data on the normal continental structures

Layer number	ϱ [Ωm]	h [km]
1	1	$10^{-3} \cdot S$
2	1000	100
3	50	50
4	200	250
5	10	200
6	2	300
7	0.5	300
8	0.1	

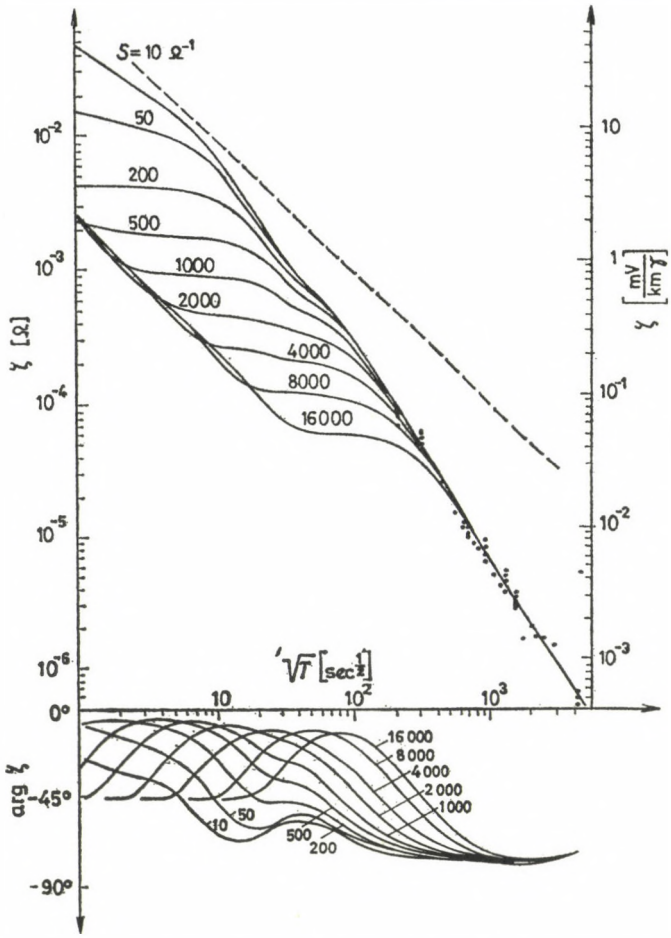


Fig. 1. Modulus and argument frequency curves of the impedance for a normal continental geoelectrical section, defined by Table 1. Points are MVS data. Curve index S is longitudinal conductivity of the upper layer. Dashed line is homogeneous semispace impedance $\varrho = 1000\ \Omega$m

pedance ζ_0, i.e. the given source impedance on the concentric stratified earth we will use long period variations which are feebly affected by anomalous fields.

Geomagnetic variation fields are mostly described by the following geometrical models: spherical and trigonometric harmonics, bandlimited current fields with uniform resp. Gaussian distributions of the current density. The solutions of the electromagnetic induction problem in a horizontally stratified earth for all the above-mentioned sources have been given in the literature (Lahiri and Price, 1939; Price, 1962, 1967; Srivastava, 1966; Berdichevsky et al., 1969a, 1969b and others).

For *continental structures* the normal impedance may be determined according to the global magnetic variation sounding (MVS) data, i.e. from a spherical analysis of the geomagnetic variation in the period interval 0.5 day – 0.5 year (Rokityansky, 1972). At shorter periods a strong influence of the *near-surface layer* will be observed, which has a rather variable conductance. It is therefore impossible to introduce a universal impedance for those periods, since it will substantially depend on the geoelectric structure of the region. The determination of ζ_0 for each separate region is possible by direct magnetotelluric measurements, but in general this is not too perspective. It is well known that MTS measurements are subjected to large distortions due to inhomogeneities of different size. In order to derive reliable data a large number of observations should be carried out outside of the anomaly of the electrical conductivity. That is why it is considered more perspective to use MVS data to determine ζ_0. Having found from these data the depth-dependent part $\sigma(z)$ and putting the mean value of longitudinal conductivity S of the upper layer in the working region, it is easy to calculate the normal impedance. A detailed description of the materials and the method used can be found in Rokityansky (1972), the available results are compiled in Table 1.

Figure 1 presents curves of the modulus and argument of the impedance calculated from the data of Table 1 for different values S of the upper layer.

FORMATION OF THE ANOMALOUS FIELD ABOVE LOCAL INHOMOGENEITIES

If the conductivity of the anomalous body cannot be taken as infinite and that of the surrounding medium is not zero, no analytical solution has been obtained for the vector problem of scattering of plane electromagnetic waves except those for a *sphere* and a *circular cylinder*.

The solution to the problem of diffraction of a plane wave on a sphere and a cylinder can be presented in the form of infinite series. The anomalous fields have a measurable amplitude if the radius of the body and the distance to the observation point are much less than the wavelength of the field in the surrounding medium. In this case we can restrict ourselves to the first two terms of the series, when describing the anomalous field. In the field of a vertically incident linearly polarized plane wave (E_0 lies in the plane $\varphi = 0$) the solution for a *sphere* (the axis $\Theta = 0$ is directed downward) is given according to Kaufman (1961) as

$$\begin{Bmatrix} H_{ra} \\ H_{\Theta a} \\ H_{\varphi a} \end{Bmatrix} = \sigma_e E_{0h} \frac{a^3}{r^2} \frac{\sigma_i - \sigma_e}{\sigma_i + 2\sigma_e} \begin{Bmatrix} 0 \\ \sin \varphi \\ \cos \Theta \cos \varphi \end{Bmatrix} -$$

$$- H_{0h} \frac{D_s(k_i a)}{2} \frac{a^3}{r^3} \begin{Bmatrix} -2 \sin \Theta \sin \varphi \\ \cos \Theta \sin \varphi \\ \cos \varphi \end{Bmatrix} \qquad (1)$$

Similarly, the solution for the *horizontal cylinder* with E_0 directed along the z-axis of the cylindrical coordinate system r, φ, z (Svetov et al., 1966) reads

$$\begin{Bmatrix} H_{ra} \\ H_{\varphi a} \\ H_{za} \end{Bmatrix} = -\frac{1}{2} E_{0h}\,\sigma_i\, V\left(k_i a \frac{\sigma_i}{\sigma_e}\right) \frac{a^2}{r} \begin{Bmatrix} 0 \\ 1 \\ 0 \end{Bmatrix} - H_{0h} D_c(k_i a) \frac{a^2}{r^2} \begin{Bmatrix} \sin\varphi \\ \cos\varphi \\ 0 \end{Bmatrix} \tag{2}$$

where

$$D_c = \frac{-I_2(k_i a)}{I_1(k_i a)} \xrightarrow[|k_i a| \ll 1]{} \frac{1}{16} i\omega\mu\sigma_i a^2 \tag{3}$$

$$D_s \xrightarrow[|k_i a| \ll 1]{} \frac{1}{6} i\omega\mu\sigma_i a^2$$

is a function continuously decreasing with period, and

$$V = \frac{\dfrac{I_1(k_i a)}{I_0(k_i a)} \dfrac{2}{k_i a} - \dfrac{\sigma_e}{\sigma_i}}{1 - \dfrac{\pi i k_i a}{2} \dfrac{I_1(k_i a)}{I_0(k_i a)} \left[1 + \dfrac{2i}{\pi} (\ln k_e a - 0.1159)\right]} \xrightarrow[|k_i a| \ll 1]{} 1 - \frac{\sigma_e}{\sigma_i} \tag{4}$$

The normal field components E_{0h}, H_{0h} at the level of the axis of the anomalous body, i.e. at depth h, are related to the fields on the surface E_0, H_0 by the following relations

$$E_{0h} = \beta_E(T, h, \sigma_e)\, E_0; \qquad H_{0h} = \beta_H(T, h, \sigma_e)\, H_0 \tag{5}$$

where β_E, β_H are functions of depth, period and normal cross section parameters. For a homogeneous surrounding medium one has $\beta_E = \beta_H = \exp(-k_e h/2)$. β is an increasing function of period, and $\lim_{T \to \infty} \beta = 1$. The dependence of the function V on $|k_i a|^{-1}$ for different ratios of the conductivities of the cylinder and the medium is presented in Figure 2. The first terms in Eqs (1) and (2) containing E_{0h}, correspond to an electrical or conductive type anomaly, respectively, the second terms, containing H_{0h}, to a magnetic or eddy type anomaly. *Electrical anomalies* arise because of the redistribution of the currents between the body and the surrounding medium. They are proportional to the normal electrical field, and consequently depend on the geoelectric structure below the working region. Defining normalized anomalous fields through $h_\varphi = H_{\varphi a}/H_0$, generally used in MVP, the expression for the conductive anomaly (2) produced by the cylinder may be written according to Eq. (5) in the following form

$$h_\varphi = -\frac{1}{2} \frac{\sigma_i a^2}{r} \zeta_0(T)\, V\left(k_i a, \frac{\sigma_i}{\sigma_e}\right) \cdot \beta(T, h, \sigma_e) \tag{6}$$

The product of the functions ζ_0, V, β gives approximate frequency characteristics of the anomalous field of a conductive anomaly. It is only approximate because the earth-air boundary and the interaction of the

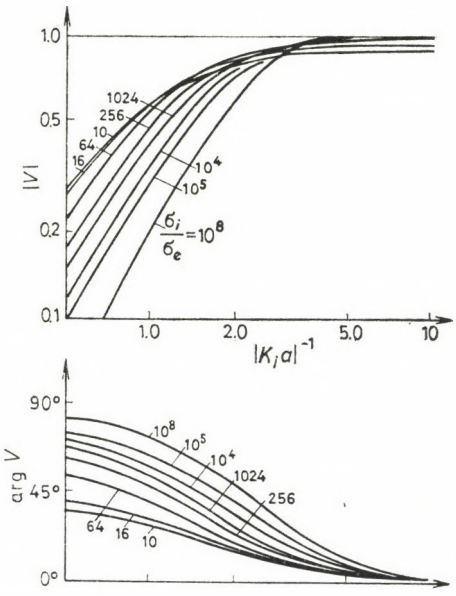


Fig. 2. V (σ_i/σ_e, $k_i\,a$) function for a circular cylinder. Curve index is σ_i/σ_e

anomalous currents in the body and in the conductive layers of the normal section have not been taken into account. The role of these factors under typical geoelectrical conditions is, however, small. As ζ_0 continuously decreases with period, and V and β are strictly increasing and bounded functions, the amplitude characteristics of the conductive type anomalous field have a maximum and downward branches. If $\zeta_0(T)$ and $\beta(T)$ are known, it is possible to define $V(T)$ according to the observed frequency characteristics of the anomalous field $h(T)$. Comparing it with the theoretical curves $V(1/k_i a)$ (Fig. 2), $\sigma_i a^2$ may be determined according to their horizontal shift. This is the essence of the interpretation method developed in the present paper.

Anomalies of the magnetic type are due to eddy currents occurring inside the anomalous body.

They do not depend on the conductivity of the surrounding medium and are proportional to the normal magnetic field component. Making use of Eqs (1), (2) and (5) and neglecting the details of the spatial distribution of the component, the eddy type normalized anomalous field may be presented as

$$h = -\beta_H D(k_i a) \begin{cases} \dfrac{a^3}{2r^3} & \text{for a sphere} \\ \dfrac{a^2}{r^2} & \text{for a cylinder} \end{cases} \tag{7}$$

The frequency characteristic is defined through the product $\beta_H D$. If the observed anomalous field is an eddy it is possible to determine $\sigma_i a^2$ from

the horizontal displacement of the right downward branch $h(T)$ relative to the theoretical function $D(1/k_i a)$ as it is usually done in the inductive methods of electrical prospecting (Svetov et al., 1966)

Eddy and conductive type anomalies are differently affected by the properties of the anomalous body, by the normal geoelectric cross section of the surrounding medium, and by the parameters of the source field.

Let us compare conductive and eddy type anomalies for a circular cylinder within a homogeneous medium at the point over the cylinder axis on the basis of Eqs (6) and (7). We write Eq. (6) in the form

$$h_x = -\frac{1}{2} V \beta_E \frac{a}{r} \zeta_0 \sigma_i a \sqrt{\frac{\sigma_e}{\sigma_i}} \sqrt{\frac{\sigma_i}{\sigma_e}} \tag{6a}$$

The dimensionless quantity

$$\bar{\zeta}_0 = \zeta_0 \sigma_i a \sqrt{\frac{\sigma_e}{\sigma_i}} \tag{6b}$$

plotted in double logarithmic scale versus $|k_i a|^{-1}$ is a straight line of $-45°$ slope (Fig. 3) passing through point (1,1) for a homogeneous medium $\beta_E = \beta_H = \exp(-1/\sqrt{2} \cdot k_e r) = \exp(-k_i a(r/a)\sqrt{\sigma_e/\sigma_i}$. Figure 3 presents the amplitude characteristics h_E and h_M for $\sigma_i/\sigma_e = 64,\ 1024,\ 10^5$, $a/r = 1/2$ according to Eqs (6a) and (7). At very short periods according to Eqs (2)–(4) the eddy type anomaly must exceed the conductive one. However, as shown in Figure 3, this only occurs on the distant part of the left downward branch of the frequency characteristics where the field is strongly attenuated in the containing medium. In the central part of the frequency characteristics, where there are good measurable amplitudes of the anomalous field,

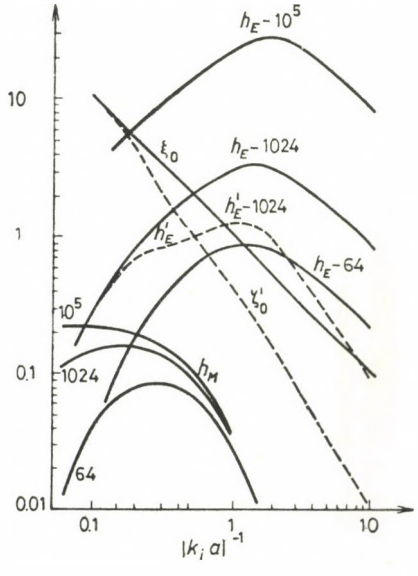


Fig. 3. Frequency characteristics of a conductive h_E and eddy h_M type anomalous field with $\sigma_i/\sigma_e = 64$, 1024 and 10^5 (curve index) for a circular cylinder in homogeneous semispace (normal impedance $\bar{\zeta}_0$). Dashed line is h_E with $\sigma_i/\sigma_e = 1024$, $a = 20$ km in a semispace, characterized by normal impedance $\bar{\zeta}_0$

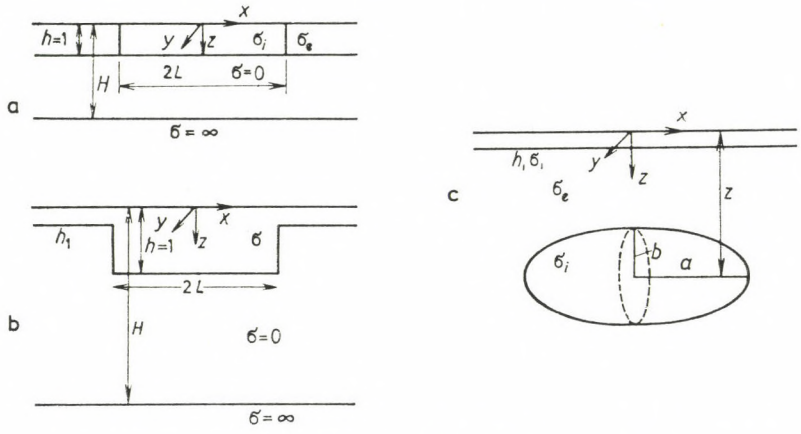


Fig. 4. Insertion (a), graben (b) and elliptical cylinder (c) models

and on the right downward branch, in MVP the conductive anomaly essentially prevails over the eddy type one for all real ratios σ_i/σ_e. In Figure 3 the dashed line $\bar{\zeta}_0'$ presents the normalized impedance for the normal continental section given by Table 1 with $\varrho_1 = \varrho_2 = 1/\sigma_e = 1024\ 1/\sigma_i$, and $a = 20$ km. The dashed curve h_E' presents the electrical type anomaly corresponding to $\bar{\zeta}_0'$, which for $|k_i a|^{-1} \geq 0.2$ is less than in case of a homogeneous medium. However, predominance of the electrical type anomaly is preserved sufficiently good. Varying σ_e, σ_i and the a-values, which are possible in MVP anomalies together with the normal section values $\sigma(h)$ we conclude that for a circular cylinder the conductive type anomaly predominates and the eddy type anomaly can be neglected. An analysis of the relation between electrical and magnetic type anomalies for cylindrical models with nonisometric cross sections (Rokityansky, 1972) shows that the contribution of the magnetic type anomaly depends on the shape of the section of the body. Predominance of eddy anomaly is possible only in cases where the conducting bodies have a large vertical extension. The vertical component Z_0 of the normal field also contributes to the formation of the anomalous field.

It is necessary to evaluate the normal field value Z_0/H_0 in order to compare these anomalies with those due to the horizontal components. Summing up the available scanty information on the ratio Z_0/H_0 in middle latitudes it can be said that for $T < 2000$ sec Z_0/H_0 does in average not exceed 0.1, and for $T < 9000$ sec — it does not exceed 0.2; although for some variations this ratio may increase up to unity and above. Nevertheless, the calculated values allow to neglect the contribution of Z_0 to the anomalous field formation in a local region and to consider the horizontal components as the principal factors forming an anomaly. On the basis of these estimations we will use the model of a vertically incident plane wave in what follows.

The set of solved magnetotelluric problems could be essentially expanded by the use of numerical methods, in the first place by the integral equation

method (Dmitriev, 1969), the net method (Madden and Swift, 1969), and the relaxation method (Price, 1949).

Let us coonsider the anomalous fields arising from rectangular nearsurface inhomogeneities of insertion and graben type (Dmitriev et al., 1974), and also fields from buried elliptical cylinders (Kaufman et al., 1971a).

An insertion is a rectangular inhomogeneity in the upper layer of constant thickness (Fig. 4). The problem has also been soved by Treumann (1970), and for thin layers by Weidelt (1971) (see also pp. 128–132 of the present volume). Analysis of the modulus and argument of the frequency characteristics of $h_z = H_z/H_{x0}$ in points $x = 2$; 2.5; 3; 4 and $h_x = (H_x/H_{x0} - 1)$ in points $x = 0$; 2; 2.25; 2.5 (in the upper layer thickness units) corresponding to the model with $L = 2.5$ shows that the central and long period parts of the amplitude characteristics are similar, the phases coincide for both components of the anomalous magnetic field in all points, where these components have high values. This fact is of great importance since it indicates the stability of the parameter determination of two-dimensional anomalous bodies from these parts of the frequency characteristics with respect to translations of the observation point, including the "special" point above the contact. The method is almost independent of the position of the observation point.

The calculation of insertions with $\sigma_i/\sigma_e = 5$; 10; 16 and ratios $2L/h < 10$ gives the same results. For thin insertions $2L/h > 10$ the identity of the central part of the frequency characteristic in various observation points

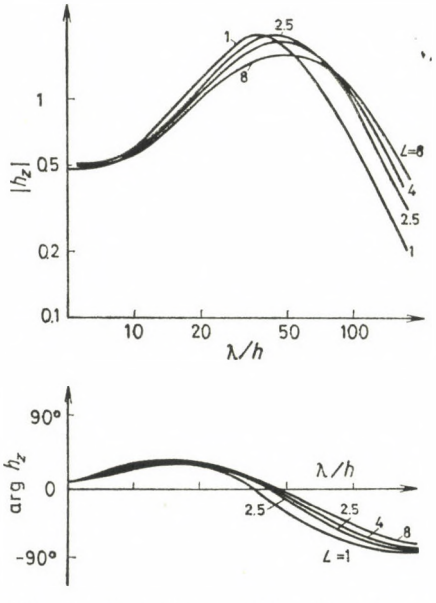


Fig. 5. Insertion width dependent frequency characteristics h_z in point $x = L$ (curve index) $\sigma_i/\sigma_e = 16$; $H = 21$

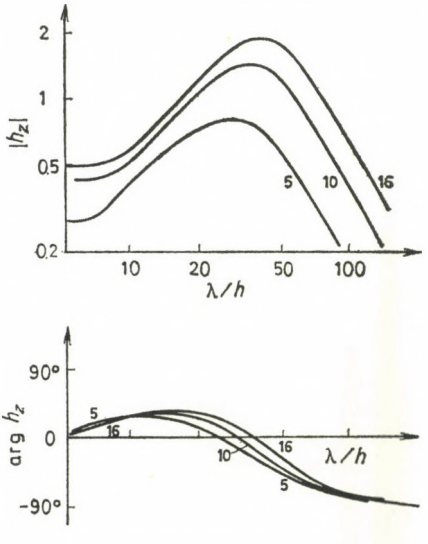


Fig. 6. The σ_i/σ_e (curve index) dependent frequency characteristics h_z in point $x = L$ for an insertion with $L = 1$; $H = 21$

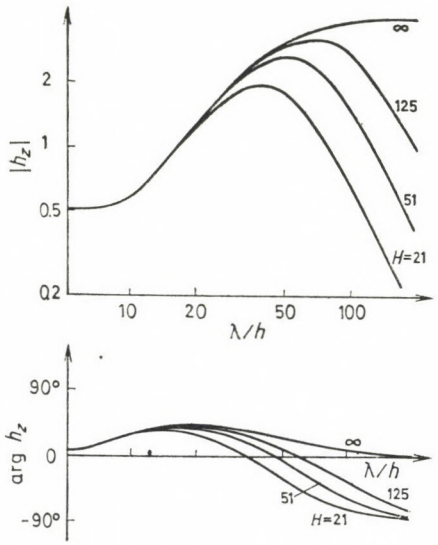


Fig. 7. H dependent frequency characteristics h_z in point $x = L$. H is depth to the ideally conducting layer for the insertion $\sigma_i/\sigma_e = 16$, $L = 1$

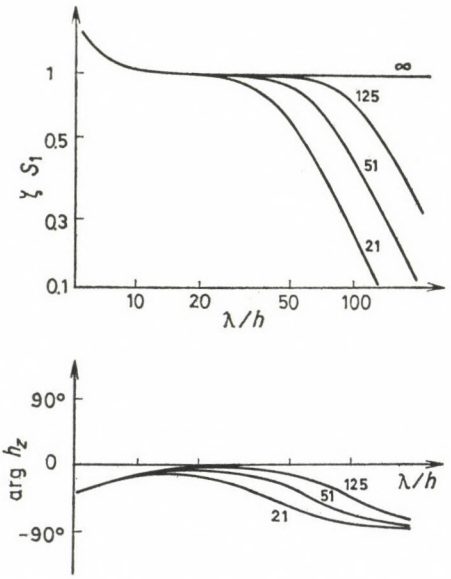


Fig. 8. Frequency characteristic of normal impedance multiplied by $S_1 = \sigma_e h_1$

is distorted by the influence of the horizontal skin-effect. Frequency characteristics which display the dependence of h_z on L are presented in Figure 5. The left parts of the curves coincide because at high frequencies the anomalous field depends only on the ratio σ_i/σ_e. Above the contact we find that, decreasing the frequency, difference between the curves is the larger the wider the insertion is. The dependence of h_z on σ_i/σ_e is presented in Figure 6. For long periods h_z is proportional to $(\sigma_i - \sigma_e)$ as it is observed for continuous currents. When the frequency is increased, the curves with $\lambda/h = 8$ approach the horizontal asymptote. Note that this asymptote is observed only just above the contact, in all other points h_z tends to zero with $\lambda/h \to 0$ due to attenuation.

The influence of depth H of the ideally conducting basement on the frequency characteristics h_z is presented in Figure 7 where it is seen that the maximum positions of the reversals of the amplitude and phase curves do not characterize a single-valued longitudinal conductivity of an anomalous field $2hL\sigma_i$, but depend on H, i.e. on the deep geoelectrical structure.

Figure 8 presents the impedance ζ_0 of a normal three-layered section $1/\varrho = \sigma_e$, 0, ∞; $h = 1$, H, ∞ (see Fig. 4) with H values corresponding to the curves in Figure 7. The similarity of the long period branches of h_z and ζ_0 in Figures 7 and 8 hints to the existence of a linear relationship between them, which indicates an electrical type anomaly. Introducing a function V in analogy to the formula for a cylinder which denotes the frequency depend-

ence h_a/E_0 and is normalized in such a way that $V \underset{T\to\infty}{\to} 1$, we can write Eq. (6) as:

$$h_z = VS_0\zeta_0 h_{z\infty} \tag{8}$$

where $S_0 = \sigma_e h$ is the longitudinal conductivity of the upper layer outside the insertion, and the constant $h_{z\infty}$ is defined as $h_{z\infty} = \lim_{\substack{T\to\infty \\ H\to\infty}} h_z$. From Eq. (8) we obtain a new estimation for the frequency characteristics of the anomalous field from the values calculated for a strongly idealized three-layered normal section (Fig. 5), and get values better corresponding to the real Earth, e.g. for the section given by Table 1 and the impedance in Figure 1.

The reliability of Eq. (8) is confirmed if the values $V = h_z/s_0\zeta_0 h_{z\infty}$ termined from the data of Figs 7 and 8 does not depend on H. Generalizing these data it can be assumed that coupling of the anomalous current in the insertion with currents in the conducting layer changes the anomalous field by less than 5% when $2L/H < 0.1$; and less than 10% when $2L/H < 0.2$. The high conducting layers of the earth are at a depth not less than 400 km, that is for 80 km wide anomalies the frequency characteristics can be synthetized with an error less than 10% by the product of V and the section's normal impedance, i.e. by means of Eq. (8). Note that the frequency characteristics of the graben and the insertion models practically coincide in all profile points, and just above the contact the difference does not exceed 10%. The difference is only remarkable at high frequencies when the upper layer of the normal section is no longer thin in comparison with wavelength. Thus, for the central and long-period parts of the characteristics, the insertion and the graben models are identical, and one may expect that the results received for the insertions would also apply to grabens.

Elliptical cylinder. This section is based on the results of Kaufman et al. (1971a, 1971b).

The comparison of the anomalous fields due to similar cylinders placed at depths $z = 2; 3; 5$ in a homogeneous semispace shows that to the first approximation the frequency characteristics are similar. At righ frequencies, however, h_a decreases faster if the cylinder is placed deeper. This seems to be conditioned by the absorption of the field in the surrounding medium.

Using the normal section impedance for the semispace the functions V with $a/b = 3$ are constructed (Figs 9–11) according to the frequency characteristics of the anomalous fields of all elliptical cylinders, presented by Kaufman et al. (1971a). In the construction of function V, the relation

$$V = \frac{h_x}{S_0\zeta_0 h_{x\infty}} \tag{8b}$$

has been used where $S_0 = \sigma_e b$. For such a choice of S_0 the dimensionless impedance $S_0\zeta_0$ is fixed on the graph $(\lambda_e/b, S_0\zeta_0)$ what allows to define the normalized constant $h_{x\infty}$. Coincidence and closeness of the V curves constructed for cylinders under and without sediments at long and medium periods show that the weakening of the anomalous field at periods satisfying

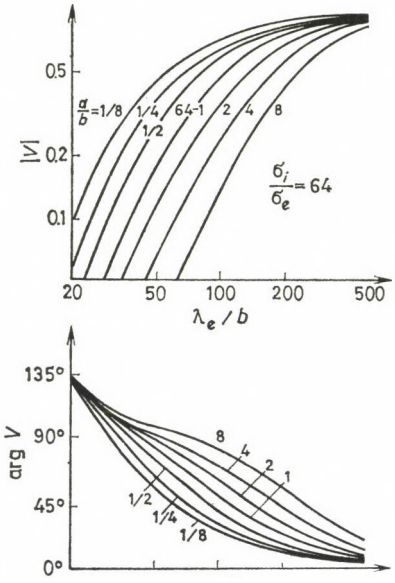


Fig. 9. *V* function for the elliptical cylinder. Curve index a/b with $\sigma_i/\sigma_e = 64$

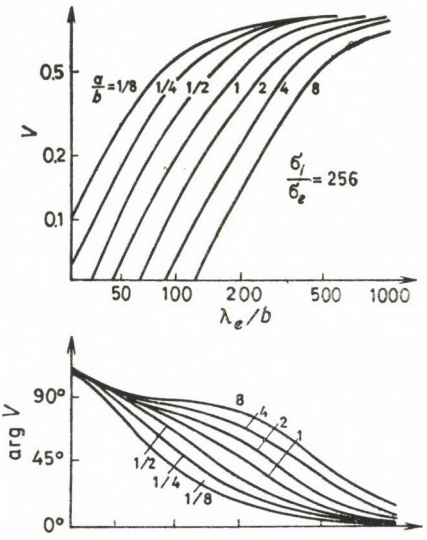


Fig. 10. *V* function for the elliptical cylinder. Curve index a/b with $\sigma_i/\sigma_e = 256$

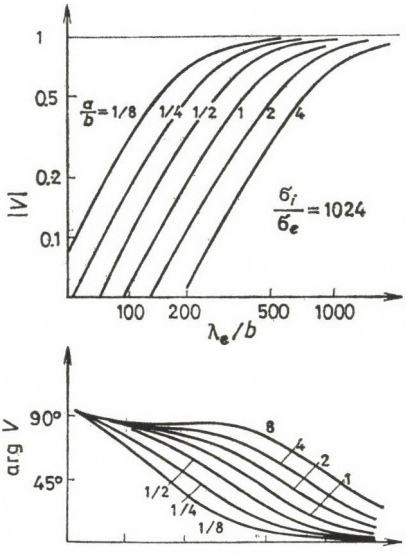


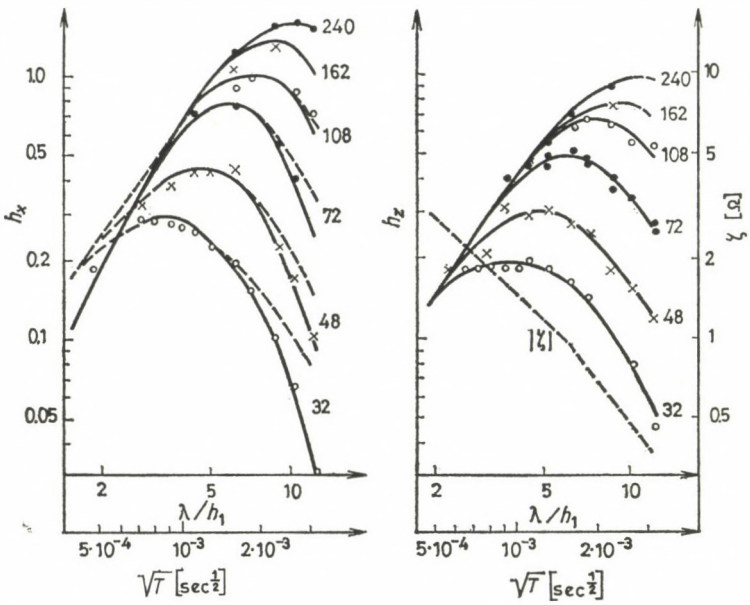
Fig. 11. *V* function for the elliptical cylinder. Curve index a/b with $\sigma_i/\sigma_e = 1024$

the condition $\lambda_1 > 10\,h$ is due first of all to the electrical field's decreasing proportionally to ζ_0.

An important conclusion which can be drawn is that the transition from h_a to V according to (8) and vice versa may also be done when there exists a conducting layer above the anomalous field. The parameters of the surface conducting layer are usually known, and its effect on the MVP anomalous field may be taken into account by subtracting the impedance curve from the anomalous field's frequency characteristics, calculated for a multi-layered model with an upper layer of longitudinal conductivity S.

Up-to-date V-graphs (Figs 9–11) together with the formula for a circular cylinder may be considered as the theoretical fundament of MVP deep-anomaly interpretation in the two-dimensional approximation.

The frequency characteristics of surface anomalies (insertions), and of a deep anomaly, i.e. elliptical cylinder have approximately the same shape, particularly in their central and long period parts. From this it can be concluded that deep and surface anomalies cannot be distinguished accord-



a b

Fig. 12. Anomalous field frequency characteristics above a horizontal brass plate with cross-section $1.5 \cdot 10^{-4} \times 0.02$ m^2 and length L_y cm, denoted in circles. Points, crosses and circles are experimental data for plates of different length. Solid lines are smoothed experimental data. a$-h_x^* = \dfrac{|H_x| - |H_{x0}|}{H_{x0}}$. Dashed line is $|h_x|$ received by integral transformation. b$-h_z = \dfrac{|H_z|}{H_{x0}}$. Dashed line is impedance on a two-layer section: $\varrho_1 = 0.24\,\Omega$m, $h = 0.405$ m, $\varrho_2 = 0$. At plotting λ/h on the abscissa axis h is equal to 0.405 m

ing to their frequency characteristics. This cannot be done even by taking into account the phase of the anomalous field, depending on the position of the frequency considered on the characteristics, defined first of all by the longitudinal conductivity G of the anomalous body and not by its depth.

A two-dimensional analysis is always idealized, as a matter of fact three-dimensional considerations are needed even to show its limitations. However, existing solutions for a constant current (e.g. for an elongated spheroid) do not help to explain the frequency dependency of a conductive type anomalous field. Appropriate model experiments (Rokityansky and Kulik, 1972) installed in Lvov (Bondarenko et al., 1971) have been carried out.

The anomalous body was a horizontal brass plate of thickness $L_z = 1.5 \cdot 10^{-4}$ m, and width $L_x = 0.02$ having a length varying from 0.32 up 2.4 m and a specific resistivity of $\varrho_i = 6.8 \cdot 10^{-8} \Omega$m. Sodium chloride solution of $\varrho_0 = 0.24\ \Omega$m served as surrounding medium. On the bottom of the tank at depth $H = 0.405$ m a solid brass plane has been placed to imitate the conducting base. Figure 12 presents the values for

$$h_x^* = \frac{|H_x^{\max} - H_{x0}|}{|H_{x0}|} \quad \text{and} \quad h_z = \frac{|H_z^{\max}|}{|H_{x0}|}$$

obtained at different frequencies for plates of different lengths. Supposing that $h_x^* = \operatorname{Re} h_x$, h_x (Fig. 12) and the phase characteristics were calculated by Hilbert integral transformation. Excluding frequency dependence which is inherent in impedance the values $V' = \dfrac{|h_z| + |h_x|}{2|\zeta_0|}$ and $\arg V' = \arg h_z - \arg \zeta_0$ (Fig. 13) were calculated. Figure 13 also shows the dependence of V' on L_y. At sufficiently low periods ($\lambda_e/L_y < 2.5$) the anomalous field does not depend on the length of the body, whereas at long periods ($\lambda_e/L_y > 8$) it approaches horizontal asymptotes and becomes independent of period. Apparently the dependence on length is the same as that for a continuous current in case of a spherical conductor (Svetov et al., 1966).

For an elongated spheroid in a constant current field we have (Pris and Svetov, 1964):

$$H_{\varphi a} = E_0 \sigma_e a \frac{1 - \dfrac{\sigma_e}{\sigma_i}}{\chi + 2\dfrac{\sigma_e}{\sigma_i}} R(r) \xrightarrow[\substack{\frac{a}{b} \to 0 \\ \chi \to 0}]{} \frac{1}{2} E_0 \sigma_i a \left(1 - \frac{\sigma_e}{\sigma_i}\right) \frac{a}{r} \tag{9}$$

where a is the minor semiaxis of the spheroid, b the major semiaxis, and χ is function of the elongation b/a,

$$\chi = 2\frac{a^2}{b^2} \frac{\dfrac{b}{c} \operatorname{arsh} \dfrac{c}{a} - 1}{\dfrac{b}{c}\dfrac{a^2}{b^2} \operatorname{arsh} \dfrac{c}{a} - 1} \tag{10}$$

where $c = \sqrt{b^2 - a^2}$.

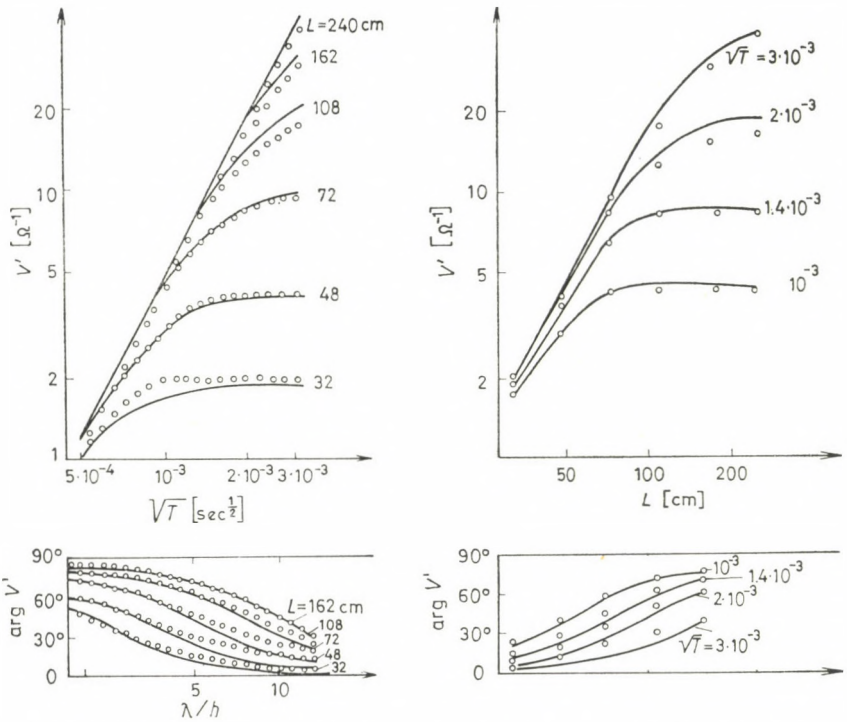


Fig. 13. The $V' = (h_x + h_z)/2\zeta_0$ function in dependance of period and length of the body. Points and circles are results of model measurements. Solid lines are calculated results according to the empirical formula (14)

The first term of the series describing the anomalous field of the cylinder for E polarization $H_{\varphi a} = 1/2 \cdot E_0 \sigma_i V(a/r) \ldots$ differs from the limiting formula (9) only by a factor which transforms into $(1 - \sigma_e/\sigma_i)$ for constant current. The function V shows how anomalously currents flowing across the section $Q = \pi a^2$ change with increasing frequency. Formally this current change may be attributed to the change of the effective conductivity $\pi a^2 \sigma_i$ by V times, i.e. $\sigma_i(1 - \sigma_e/\sigma_i) \to V\sigma_i$ with decreasing period. Using such a substitution, evident for a cylinder, we apply an inverse transformation in Eq. (9) for bodies of finite length

$$H_{\varphi a} = E_0 \sigma_e a \frac{1}{\chi + 2\dfrac{V_e}{V\sigma_i}} R(r) = \frac{1}{2} E_0 \frac{1}{\dfrac{\chi}{2\sigma_e} + \dfrac{1}{V\sigma_i}} aR(r) \tag{11}$$

The fraction

$$\sigma^* \equiv \frac{1}{\dfrac{\chi}{2\sigma_e} + \dfrac{1}{V\sigma_i}} \tag{12}$$

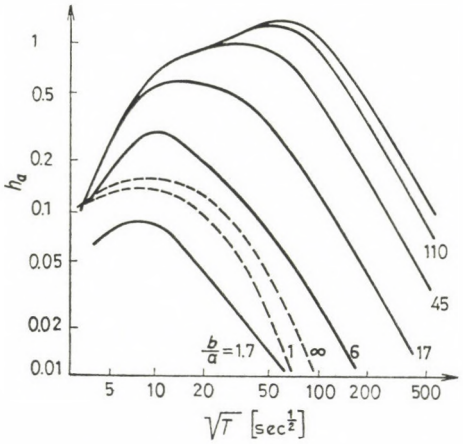


Fig. 14. Frequency characteristics of an eddy (dashed line) and conductive type anomalous field with $\sigma_i/\sigma_e = 1024$ on a spheroid of elongation b/a (curve index) placed in the second layer of the section, defined by Table 1. $\sigma_e = 10^{-3}\ \Omega^{-1}\mathrm{m}^{-1}$, $a = 20$ km, $r = 2a$

is the *effective conductance of the body*. On the basis of Eqs (9)–(12) the results obtained can be summarized in analogy to Eq. (6) as

$$h_a = \sigma_i a \zeta_0 \beta V^* \frac{R(r)}{2} \xrightarrow[L_y \gg r]{r > 2a} \sigma_i a \zeta_0 \beta V^* \frac{a}{2r} \tag{13}$$

where $V^* = \sigma^*/\sigma_i$. Taking the functions $\chi(b/a)$ and $V(T)$ at high $|k_i a|$ values (Svetov et al., 1966) one finds

$$\frac{h_a}{\zeta_0} = V' = \frac{1}{(c_1 + ic_2)\dfrac{1}{T^{\gamma_1}} + c_3 \dfrac{\sigma_i}{\sigma_e}\left(\dfrac{L_x}{L_y}\right)^{\gamma_2}} \tag{14}$$

The definition of the coefficients from the experimental data (Fig. 13) gave $\gamma_1 = 1 \pm 0.1$; $\gamma_2 = 2 \pm 0.2$; $C_1 = 3.3 \cdot 10^{-8}$ sec; $C_2 = 20 \cdot 10^{-8}$ sec; $C_3 = 1.5 \cdot 10^{-8}$ sec.

Figure 14 presents the frequency characteristics of the anomalous field of electric and magnetic type over a *spheroid* with different elongations, the initial field E_0 being parallel to the major semiaxis b. The electrical anomaly has been calculated according to Eq. (13). The eddy anomaly slightly depends on elongation (it is represented for a sphere and a cylinder through the dashed lines in Figure 14). At long periods the conductive anomaly decreases with decreasing elongation while the maximum of frequency characteristics gets displaced into the short period range. With $b/a \leq 3$ for a body of the parameters considered the conductive anomaly becomes smaller than an eddy anomaly in its characteristic central part.

All the results described above correspond to the central profile of the body. When the observations approach the ends of the body, the anomalous field decreases for long periods, and the maximum of the frequency characteristics shifts into the short period range.

INTERPRETATION OF MAGNETIC VARIATION ANOMALIES

The question about the uniqueness of the inverse MVP problem (cf. Treumann's contribution to the present volume) has still not been solved mathematically. In practice the inverse MVP problem is not unique in wide limits. This is confirmed by the similarity of the profile curves and frequency characteristics of the graben and the buried elliptical cylinder fields.

Moments. Suppose that two-dimensional anomalous bodies and currents j_{ya} are limited in the x, z plane to some region Q. Outside of Q an analytical function $H(\xi)$ may be introduced, and for an elementary of anomalous current line one can write

$$H(\xi) = H_{za}(\xi) + iH_{xa}(\xi) = \frac{j_a}{2\pi(\xi - \xi_i)} \tag{16}$$

where $\xi = x + iz$; $\xi_i = x_i + iz_i$ are the points outside and inside of Q. Considering the expansion $(\xi - \xi_i)^{-1}$ in the vicinity of a point removed to infinity and summing up all anomalous currents we obtain

$$H(\xi) = 2 \sum_{k=0}^{\infty} \frac{m_k}{\xi^{k+1}} \tag{17}$$

where

$$m_k = \frac{1}{4\pi} \iint_Q j_a \, \xi_i^k \, dQ \tag{18}$$

are complex momenta of the anomalous currents in section Q. Following Strakhov (1959) one obtains a formula connecting complex momenta with the anomalous field $H(x)$ on the earth surface $z = 0$:

$$m_k = -\frac{1}{2\pi i} \int_{-\infty}^{\infty} \left[x^k H(x) - 2 \sum_{l=0}^{k-1} m_l x^{k-l-1} \right] dx \tag{19}$$

Note that the calculation problem for the momenta belongs to the class of ill-posed geophysical problems. In the last years general rules for the solution of ill-posed problems have been applied to the problem of momentum termination (Ivanov and Chudinova, 1966).

Values $G = \sigma_i Q$ of the longitudinal conductivity of an anomalous body of section Q below the observation profile.

A first method arises from the zero momentum M_0 and defines the total G of all anomalous bodies crossed by the profile. According to (2) the total anomalous current of a cylindrical conductor may be represented by the expression $V\sigma_i Q E_{0y}$, from which by (5)

$$m_0 = \frac{1}{4\pi} V\beta\zeta_0 \sigma_i Q \tag{20}$$

Thus it is necessary to know m_0 at one period, ζ_0 and values V at the same period to estimate G. V is defined from the frequency characteristic, however, for a rough estimate one may use the inequality $|V| \leq 1$. The second way of estimating G is based on the frequency characteristics of the anomalous field.

It has already been pointed out that an electrical anomaly is proportional to the normal impedance which contributes information on the deep section to the anomalous field frequency characteristics. In order to take into account the normal section effect we calculate the value $V(T) = h_a(T)/\zeta_0(T)$. Comparing this with the theoretical dependence $V(1/k_i a)$, G is determined from the horizontal shift of the coordinate axis. In this case for a reliable determination of G it is sufficient to know the order of magnitude of σ_i/σ_e; moreover, the ratio of the maximum dimension of the section of the body to its minimum has not to exceed 10. If the latter condition were not met, G would become too low.

In conclusion we summarize the possibilities of MVP.

1. The observation of the anomalous behaviour of geomagnetic variations in a local region allows with absolute certainty to conclude about the existence of a conductivity anomaly.
2. According to the position of the extrema of the horizontal components of the anomalous field, resp. according to the change of the sign of the vertical component it is possible to determine the epicentre line of the anomalous body and its stretch.
3. From the shape of the anomalous field curves the maximum depth of the top of the conducting body may be determined.
4. Analyzing the central- and long-period parts of the frequency characteristics of the anomalous field it is possible to estimate the minimum and maximum values of the longitudinal conductivity $G = \sigma_i Q$ of the cross-section of the anomalous body.

Since the practical solution of the inverse MVP problem is multi-valued, supplementary data must be included that would reduce the number of acceptable solutions and specify the depth of the anomalous body. Such data may be divided into two classes: 1. Electrical prospecting data, first of all MTS data where electrical conductivity becomes a measurable parameter. 2. Geophysical, geological and physical data, suggesting definite relations of some other parameters with electrical conductivity. The study of these relations for deep objects has only begun, and the available data are mostly hypothetical and subjective.

REFERENCES

BERDICHEVSKY, M. N., VANYAN, L. L., FAINBERG, E. B., 1969a. Frequential sounding of the Earth by results of the spherical analysis of electromagnetic variations (in Russian). *Geomagn. i Aeron.* **9**, No. 2.

BERDICHEVSKY, M. N., VANYAN, L. L., FAINBERG, E. B., 1969b. About theoretical grounds of electromagnetic variation application to study electroconductivity of the Earth (in Russian). *Geomagn. i Aeron.* **9**, No. 3.

BONDARENKO, A. P., KOBZOVA, V. M., MOROZ, I. P., KLOS, V. I., 1971. On the laboratory modelling of electromagnetic induction problems in the earth (in Russian). *Geofiz. Sb. Akad. Nauk Ukrainian SSR* **43**.

DMITRIEV, V. I., 1969. Electromagnetic field in inhomogeneous media (in Russian). *Tr. Vych. tsentra Moskovskogo Univ.*

DMITRIEV, V. I., ZAKHAROV, E. V., KULIK, S. N., ROKITYANSKY, I. I., 1974. Geomagnetic variation anomalous fields on a rectangular inhomogeneity in the earth's upper layer and their application to the MVP method (in Russian). *Izv. Akad. Nauk SSSR, Ser. Fiz. Zemli.* No. 6.

IVANOV, V. K., CHUDINOVA, A. A., 1966. On a method of defining the harmonic moment of disturbing masses (in Russian). *Izv. Akad. Nauk SSSR, Ser. Fiz. Zemli*, No. 3.

KAUFMAN, A. A., 1961. Three ways of field disturbance in low frequency electrical prospecting of ore deposits (in Russian). *Geol. i Geofiz. Sib. O. Akad. Nauk SSSR*, No. 5.

KAUFMAN, A. A., TABAROVSKY, L. A., TERENTEV, S. A., 1971a. Electromagnetic field of an elliptical cylinder in a horizontally stratified medium (in Russian). Novosibirsk.

KAUFMAN, A., A., TABAROVSKY, L. A., TERENTEV, S. A., 1971b. Plane wave electromagnetic field in a medium containing an elliptical cylinder (E–polarization) (in Russian). Novosibirsk.

LAHIRI, B. N., PRICE, A. T., 1939. Electromagnetic induction in nonuniform conductors and the determination of the conductivity of the earth from terrestrial magnetic variations. *Phil. Trans. R. Soc. London A.*, **237**, 509.

MADDEN, T. R., SWIFT, C. M. Jr., 1969. Magnetotelluric studies of the electrical conductivity structure of the crust and upper mantle. The Earth's Crust and Upper Mantle, Geophys. Monograph, 13. Washington.

PRICE, A. T., 1949. The induction of electric currents in nonuniform thin sheets and shells. *Quart. J. Mech. appl. Mathem.* **2**, No. 3.

PRICE, A. T., 1962. The theory of magneto-telluric methods when source field is considered. *J. Geophys. Res.* **67**, 1907.

PRICE, A. T., 1967. Electromagnetic induction. The Earth Physics of Geomagnetic Phenomena, I. Acad. Press, New York.

PRIS, G. V., SVETOV, B. S., 1964. On the field disturbance's role in the low frequency inductive method of electrical prospecting (in Russian). *Tr. TS. N. I. G. R. I.* **59**.

ROKITYANSKY, I. I., 1972. Geophysical Methods of Magnetic Variation Sounding and Profiling (in Russian). Naukova Dumka, Kiev.

ROKITYANSKY, I. I., KULIK, S. N., 1972. Effect of body length on the MVP anomalous field (in Russian). *Geofiz. Sb. Akad. Nauk Ukrainian SSR*, No. 47.

SRIVASTAVA, S. P., 1966. Theory of the magnetotelluric method for a spherical conductor. *Geophys. J. R. Astr. Soc.* **2**, No. 4.

STRAKHOV, V. N., 1959. On the theory of the two-dimensional problem in magnetic prospecting (in Russian). *Izv. Akad. Nauk SSSR, Ser. Fiz. Zemli*, No. 2.

SVETOV, B. S. et al., 1966. Electromagnetic Prospecting Methods in Ore Geophysics (in Russian). Nedra, Moscow.

TREUMANN, R., 1970. The problem on electromagnetic induction in a plate with two-dimensional distribution of conductivity (in Russian). *Geomagn. i Aeron.* **10**, No. 3, 4.

WEIDELT, P., 1971. The electromagnetic induction in two thin half-sheets. *Z. Geophys.* **37**, 649.

ON THE GEOMAGNETIC INDUCTION PROBLEM

R. TREUMANN

1. INTRODUCTION

In the recent years the theory of geomagnetic induction has undergone a rapid development. Mark stones on this path were the progress in treating problems including the dependence of electrical conductivity $\sigma(\mathbf{x})$ on more than one space coordinate (Jones, 1971; Jones and Price, 1970, 1971; Mann, 1964; Treumann, 1970a, 1970d; Weidelt, 1966; Weaver, 1963, 1971; Weaver and Thomson, 1972) and in the solution of the inverse problem of geomagnetic induction (Backus and Gilbert, 1967; Bailey, 1970; Johnson and Smylie, 1971; Siebert, 1964; Weidelt, 1973). Some recent investigations (Schäfer and Treumann, 1975) are extended to a randomly distributed conductivity structure of the earth. Here we review some of these ideas to give the reader a crude impression of what has been achieved in the theory of electromagnetic induction in inhomogeneous media. Before proceeding further, let us first derive some general formulae governing geomagnetic induction theory.

Assume an arbitrary conductivity distribution $\sigma(\mathbf{x})$ and an earth that is for simplicity imagined as flat and bounded at $z = 0$. The transformation to a spherical earth is straightforward (Lahiri and Price, 1939).

The basic equation of geomagnetic induction theory is

$$\frac{\partial}{\partial \mathbf{x}} \times \frac{\partial}{\partial \mathbf{x}} \times \mathbf{E}(\mathbf{x}, t) = -\mu_0 \sigma(\mathbf{x}) \frac{\partial \mathbf{E}(\mathbf{x}, t)}{\partial t} \tag{1.1}$$

where $\mathbf{E}$ is the electric field. In (Lahiri and Price, 1939) a representation of $\mathbf{E}(\mathbf{x}, t)$ for arbitrary external field through particular solutions of (1.1) has been given for the case when $\sigma(\mathbf{x}) \equiv \sigma(z)$. For arbitrary $\sigma(\mathbf{x})$ we will state the problem in an alternative way. Fourier-transforming $\mathbf{E}(\mathbf{x}, t)$ and $\sigma(\mathbf{x})$ in x, y and t, but Laplace-transforming in z according to

$$\begin{Bmatrix} \mathbf{E}(\mathbf{k}, s, \omega) \\ \sigma(\mathbf{k}, s) \end{Bmatrix} = \int_{-\infty}^{\infty} \int \int_{0}^{\infty} \begin{Bmatrix} \mathbf{E}(\mathbf{x}, t) \\ \sigma(\mathbf{x}) \end{Bmatrix} \mathrm{e}^{i\mathbf{k}\cdot\mathbf{x} - sz - i\omega t} \, dx \, dy \, dz \, dt \tag{1.2}$$

where $\mathbf{k} = k_x \mathbf{e}_x + k_y \mathbf{e}_y$ is a two-dimensional wave-vector, we find from Eq. (1.1) an integral equation for the transformed electric field. Letting $\sigma = 0$ for $z < 0$, the field outside the earth, where the space charge vanishes, is given by

$$\mathbf{E}(x, y; z < 0; \omega) = \frac{1}{(2\pi)^2} \int_{-\infty}^{\infty} d\mathbf{k} \left[\mathbf{E}_+(\mathbf{k}) \, \mathrm{e}^{|\mathbf{k}| z} + \mathbf{E}_-(\mathbf{k}) \, \mathrm{e}^{-|\mathbf{k}| z} \right] \mathrm{e}^{-i\mathbf{k}\cdot\mathbf{x}} \tag{1.3}$$

Here $\mathbf{E}_-(k)$ is assumed to be known from the source field. If, for simplicity, space charges are only allowed to be present at the surface of the earth (a condition that is rather weak in the absence of too steep conductivity gradients), the equation for $\mathbf{E}(\mathbf{k}, s, \omega)$ becomes

$$(\mathbf{k} - i\,s\,\mathbf{e}_z)\,\mathbf{k}\cdot\mathbf{E} - (k_y^2 - i\,s^2)\,\mathbf{E}_x - (k_x^2 - i\,s^2)\,\mathbf{E}_y -$$

$$- \mathbf{k}(s\,E_z - E_{z+} - E_{z-}) + i\,\mathbf{e}_z\mathbf{k}\cdot(\mathbf{E}_+ + \mathbf{E}_-) - i(s + |\mathbf{k}|)\,(\mathbf{E}_{x+} + \mathbf{E}_{y+}) -$$

$$- i(s - |\mathbf{k}|)\,(\mathbf{E}_{x-} + \mathbf{E}_{y-}) = \tag{1.4}$$

$$= -\frac{\mu_0\omega}{(2\pi)^4}\int_{-\infty}^{\infty}\int_{\gamma-i\infty}^{\gamma+i\infty}\frac{\sigma(\mathbf{k}', s')\,\mathbf{E}(\mathbf{k}-\mathbf{k}', s'')}{s - s' - s''}\,ds'\,ds''\,dk', \qquad (s > s' + s'')$$

(It should be noted that a similar expression can easily be derived without the restriction imposed on the space charge.)

This inhomogeneous equation has to be solved for $\mathbf{E}(\mathbf{k}, s)$, and the solution inserted into

$$\mathbf{E}_+ + \mathbf{E}_- = \frac{1}{2\pi i}\int_{\gamma-i\infty}^{\gamma+i\infty}\mathbf{E}(\mathbf{k}, s)\,ds \tag{1.5}$$

to give a further integral equation from which $\mathbf{E}_+(\mathbf{k})$ in principle can be determined. Transforming back from the $(\mathbf{k}, s)$ space to the $\mathbf{x}$-space one finds the solution of the problem for arbitrary $\sigma(\mathbf{x})$. In this generalized way, however, the problem has still not been solved, and is obviously poorly treatable. E.g., already in the simplest two-dimensional E-polarization case, Eq. (1.4) reads [$\sigma = \sigma(y, z)$; $\mathbf{E} = E\,\mathbf{e}_y$].

$$E(k, s)\,(s^2 + i\,k^2) = \left[\left(s + |k|\,E_+(k)\right) + \left(s - |k|\,E_-(k)\right)\right] +$$

$$+ \frac{\mu_0\omega}{(2\pi i)^3}\int_{-\infty}^{\infty}\int_{\gamma-i\infty}^{\gamma+i\infty}\frac{\sigma(k', s)\,E(k-k', s'')}{s - s' - s''}\,ds'\,ds''\,dk';\ (s > s' + s'') \tag{1.6}$$

and $E_-(k)$ must be calculated from

$$E_-(k) = \frac{1}{2\pi i}\int_{\gamma-i\infty}^{\gamma+i\infty}E\big(k, s; E_-(k)\big)\,ds - E_+(k) \tag{1.7}$$

Equation (1.6) suggests an iteration procedure carried out until some arbitrary step. But the exact solution of the system (1.6)–(1.7) seems to be hopeless. Until now only the simplest conductivity structures have been solved. Some of them will be discussed in what follows.

2. THIN SHEETS

The simplest model of inhomogeneous conductivity structures is the arrangement of ideally conducting thin plates or regions of space. Since the electric field at the surface of all regions must vanish, the appropriate induction problem can be easily solved by conformal mapping and Schwartz's formula (Rikitake, 1966; Schmucker et al., 1967).

The next step is to assume $\sigma(\mathbf{x}) \neq \infty$ within the plate and to let the thickness of the plate infinitesimally thin. In such a case for arbitrary one-dimensional dependence of $\sigma(x)$ on x within the plate a simple boundary condition for the vector potential $\mathbf{A} = A_y \mathbf{e}_y$ can be derived, which allows to solve the problem exactly (Weidelt, 1966, 1971). Denoting the conductivity integrated over the plate thickness by $\tau(x)$, this condition is

$$A_y(x, 0) = \frac{\left.\dfrac{\partial A_y(x, z)}{\partial z}\right]_{z=-0}^{z=+0}}{\mu_0 \, i \, \omega \, \tau(x)} \tag{2.1}$$

A_y satisfies the two-dimensional Laplace equation $\Delta_2 A_y = 0$, $\Delta_2 = \partial^2/\partial x^2 + \partial^2/\partial z^2$ everywhere in space but in $z = \pm 0$ where it satisfies (2.1). (We note that differentiation of (2.1) with respect to x leads to the boundary condition of Price (1949)). Representing $A_y(x, z)$ according to (1.3) as

$$A_y(x, z) = \int_{-\infty}^{\infty} \begin{cases} [c_e(s)\, \mathrm{e}^{-|s|z} + c_i(s)\, \mathrm{e}^{|s|z}] \\ [c_e(s) + c_i(s)]\, \mathrm{e}^{-|s|z} \end{cases} \mathrm{e}^{isx}\, ds\,, \quad \begin{matrix} z \leqq 0 \\ z \geqq 0 \end{matrix} \tag{2.2}$$

and taking into account Eq. (2.1) we obtain an integral equation for $c_i(s)$ in dependence on the conductivity distribution and on $c_e(s)$ that is assumed to be known (Weidelt, 1971):

$$\begin{aligned} c_i(s) &= -\, c_e(s) + i \int_{-\infty}^{\infty} \alpha(s - t)\, |t|\, c_i(t)\, dt \\ \alpha(s) &= \frac{1}{\mu_0 \pi \omega} \int_{-\infty}^{\infty} \frac{e^{-isx}}{\tau(x)}\, dx \end{aligned} \tag{2.3}$$

For general conductivity structures $\tau(x)$ this integral equation is difficult to solve. The solution can, however, be easily found by standard techniques of the theory of singular integral equations (Muskhelishvili, 1962; Clemmov, 1951), if one restricts oneself to the model of two thin half-sheets (Weidelt, 1971). In that case Eq. (2.3) can be transformed into

$$-\int_{-\infty}^{\infty} c_e(s)\, \mathrm{e}^{isx}\, ds = \int_{-\infty}^{\infty} m_j(s)\, c_i(s)\, \mathrm{e}^{isx}\, ds\,; \quad j = \begin{cases} 1 & \text{for } x < 0 \\ 2 & \text{for } x > 0 \end{cases} \tag{2.4}$$

with $m_j = 1 - i\alpha_j |s|$; $\alpha_j = 2/\omega\mu_0\tau_j$ is now a constant parameter. The solution of (2.4) was given by Weidelt (1971). It can be written in the form

$$c_i(s) = -\frac{m_1 + m_2}{2m_1 m_2} c_e(s) + \frac{\alpha_2 - \alpha_1}{2\pi} F(s) P \int_{-\infty}^{\infty} F(-t)\, c_e(t) \frac{|t|\, dt}{t - s} \qquad (2.5)$$

where P indicates the principal value of the integral, and introducing $\Phi_j(s) = \arctan(\alpha_j s)$,

$$F(s) = \sqrt{\cos\Phi_1 \cos\Phi_2}\, \exp\left(\frac{1}{\pi}\int_{\Phi_1}^{\Phi_2} \lg|\tan\Phi|\, d\Phi\right) \begin{cases} e^{i|\Phi_2|}, & s < 0 \\ e^{i|\Phi_1|}, & s > 0 \end{cases} \qquad (2.6)$$

For a uniform external inducing field $B_0 = B_0\, \mathbf{e}_x$, $|s|\, c_e(s) = B_0\delta(s)$, one finds for $z \leqq 0$:

$$\frac{A_y(x,z)}{B_0} = -\frac{E_y(x,z)}{i\omega B_0} = -\frac{i}{2}(\alpha_1 + \alpha_2) + \frac{\alpha_1 - \alpha_2}{2\pi} P \int_{-\infty}^{\infty} F(s)\, e^{isx + |s|z}\, ds/s$$

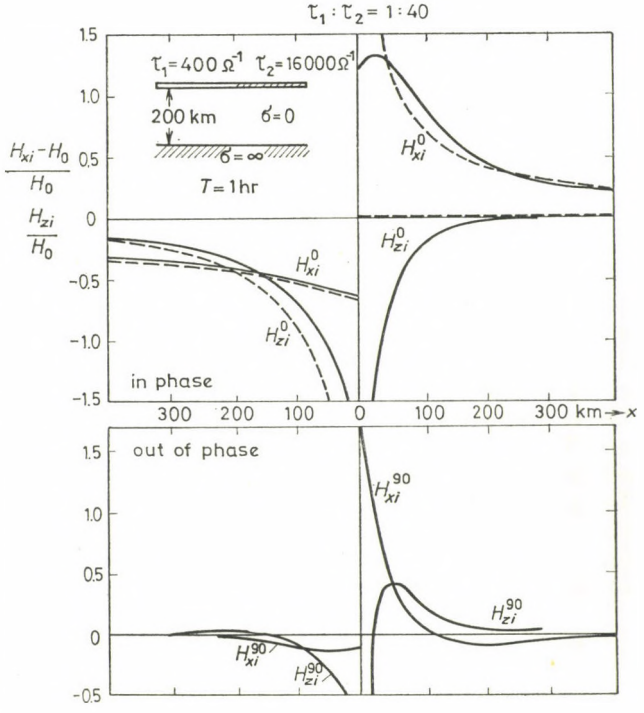


Fig. 1. The magnetic field at the surface ($z = -0$) of the two thin half-sheet model, indicated in the left upper corner. The fields are split into in- and out-of-phase parts, respectively. For comparison the field corresponding to the case of an insulating half sheet at $x < 0$ and a perfect conductor at $x > 0$ is given by the broken line. The interesting result is the divergence of H_{zi} and the discontinuity of H_{xi} at $x = 0$, as the change in the sign of H_{xi} (after Weidelt, 1971)

$$\frac{B_{xi}(x,z)}{B_0} = 1 + \frac{\alpha_2 - \alpha_1}{2\pi} \int_{-\infty}^{\infty} F(s)\, e^{isx+|s|z} \operatorname{sgn} s\, ds \tag{2.7}$$

$$\frac{B_{zi}(x,z)}{B_0} = \frac{\alpha_2 - \alpha_1}{2\pi i} \int_{-\infty}^{\infty} F(s)\, e^{isx+|s|z}\, ds$$

This field can be split into in- and out-of-phase parts. The former has a discontinuity of B_{xi} at $x = 0$, whereas B_{zi} diverges at this point; the latter is finite in both components. The field is found to be non-symmetrical with respect to the $x = 0$ plane.

It is interesting to note that the introduction of an infinitely conducting conductosphere underlying the plate in great depth symmetrizes the fields (Fig. 1). Application of this model to the Northern German anomaly has been given in papers of Weidelt (1966, 1971).

A similar model with conductivities decreasing to the edges has been recently calculated (Ashour, 1971). The solution of models with more complicated conductivity distributions is still problematic (Hewson-Browne, 1972). It is, however, clear that Eq. (2.3) forms the general basis for such calculations. On the other hand such structures can be treated by a more refined partition of the sheet into parts of different conductivities to arrive at a step-function approximation of $\tau(x)$. Such a model can be calculated by an approach similar to that for two half-plates outlined in this section. In this case the number j is enlarged up to the number of plates: $j = 1, 2, \ldots, n$ and we are faced with the Hilbert-problem for a system of n singular integral equations (Muskhelishvili, 1962).

3. PLATES WITH LATERAL NONUNIFORMITIES

The inclusion of a finite thickness d of the plates into the treatment considerably enlarges the mathematical difficulties. In this case the derivation of a simple boundary condition is impossible but the full set of boundary conditions at the surfaces of the plate must be used. For two different half-plates (or quarters of space) different formulations have been given by several authors (Jones, 1971; Jones and Price, 1970, 1971; Mann, 1964; Treumann, 1970a, 1970d; Weidelt, 1966; Weaver, 1963, 1971; Weaver and Thomson, 1972)[1] using approximate or numerical methods or introducing *ad hoc* assumptions about the induction process (see Fig. 2). Following Treumann (1970a) it is convenient to introduce the *Green function* Γ of the system through the representation of the electric field component for the two-dimensional E-polarization case (the B-polarization case is excluded from this review since it does not produce a B_z-component and there-

[1] For further references see the article of Rokityansky et al. on p. 123 of the present volume. A comprehensive review of model calculations was recently given by Hobbs (1975).

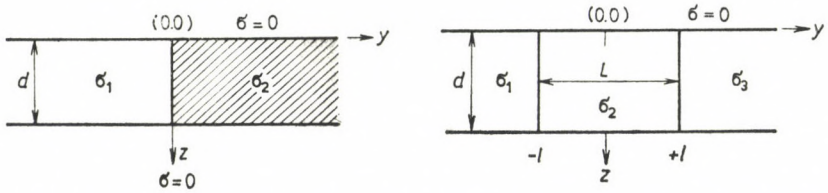


Fig. 2. Two models of plane parallel plates of thickness d with laterally inhomogeneous, but otherwise constant conductivities
a – two half sheets $\sigma_1 \neq \sigma_2$; b – a fault model $\sigma_1 \neq \sigma_2 \neq \sigma_3$. Such models have been treated in (Treumann, 1970a)

fore is of minor interest in magnetovariational sounding of two-dimensional structures):

$$E(y, z) = \int_{S_0} \frac{\partial E}{\partial z_0} \Gamma(y, z/y_0, z_0)\, dS_0 \tag{3.1}$$

Here S_0 is the surface of the conducting earth, and the conductivity $\sigma(y, z)$ is assumed to depend only on z and y. The difficulty lies on the one hand in the determination of Γ from the constitutive equations

$$\Delta_2 \Gamma(y, z/y_0, z_0) + k^2 \Gamma(y, z/y_0, z_0) = -\delta(y - y_0)\, \delta(z - z_0) \tag{3.2}$$

$$\frac{\partial \Gamma}{\partial z_0} = 0, \quad \lim_{y, z \to y_0, z_0} \Gamma = -(2\pi)^{-1} \lg \sqrt{(y - y_0)^2 + (z - z_0)^2} \tag{3.3}$$

$$\Gamma(y, z/y_0, z_0) = \Gamma(y_0, z_0/y, z); \; k^2 = -i\omega\mu_0\, \sigma(y, z) \tag{3.4}$$

for a given conductivity $\sigma(y, z)$, and on the other in the subsequent solution of the boundary conditions. For two half-plates (or quarters of space) the first part of this problem has been solved in the papers of Weidelt (1966), Treumann (1970a). As has been shown there, Γ can be found by an eigenfunction expansion, respectively by a superposition of the fields of a distribution of point sources. Using Eq. (3.1) and a representation of the field outside of the plate according to Eq. (1.3) for both regions $z \leq 0$ and $z \geq d$, the second part of the problem can be reduced to a set of singular integral equations containing kernels of the Cauchy-type (Treumann, 1970a). The solution of this system is, however, still impossible, since the kernels cannot be represented in closed form. For the case of two quarters of space a regularized Fredholm-representation of the remaining singular integral equation has been found. Instead of the solution of the exact integral equations an approximative procedure can be derived, if one represents the fields at the surface of the earth as superposition of the outer inducing and inner induced part (Weaver, 1964). This procedure is essentially an

iteration method for the magnetic field, according to the formulas (Treumann, 1970a):

$$B_z^{(m+1)}(y,z) = -\int_{-\infty}^{\infty} B_y^{(m)}(y_0,0)\left.\frac{\partial \Gamma}{\partial y}\right|_0 dy_0 - \int_{-\infty}^{\infty} B_y^{(m)}(y_0,d)\left.\frac{\partial \Gamma}{\partial y}\right|_d dy_0 \qquad (3.5)$$

$$B_y^{(m+1)}(y,z) = \int_{-\infty}^{\infty} B_y^{(m+1)}(y_0,0)\left.\frac{\partial \Gamma}{\partial z}\right|_0 dy_0 + \int_{-\infty}^{\infty} B_y^{(m+1)}(y_0,d)\left.\frac{\partial \Gamma}{\partial z}\right|_d dy_0 \qquad (3.6)$$

where

$$B_y^{(m)}(y,0) = 2B_{ye}(y,0) + \frac{1}{\pi} P \int_{-\infty}^{\infty} \frac{B_z^{(m)}(y_0,0)}{y_0 - y} dy_0 \qquad (3.7)$$

$$B_y^{(m)}(y,d) = 2B_{ye}(y,d) - \frac{1}{\pi} P \int_{-\infty}^{\infty} \frac{B_z^{(m)}(y_0,d)}{y_0 - y} dy_0$$

$$B_y^{(0)}(y,0) = 2B_{ye}(y,0),\ B_y^{(0)}(y,d) = 2B_{ye}(y,d),\ B_z^{(0)}\begin{pmatrix} y, & 0 \\ & d \end{pmatrix} = 0 \qquad (3.8)$$

are the surface fields, the suffix e denotes the external part, and (m) is the order of iteration. If e.g., no field sources lie below $z = d$, we have $B_{ye}(y,d) = 0$. In the zero-order approximation and for homogeneous external fields this procedure reduces to Weaver's (1963) assumption of a constant surface field. Zero and first-order fields (Fig. 3) have been calculated in the works of Treumann (1970a, 1970d) for the special case of a homogeneous inducing field, and using a different approximation procedure based on a paper of Mann (1964), by Weaver and Thomson (1972) for an inducing line current. It is, however, obvious from (3.5) - (3.8) that the above approximation technique is valid for arbitrary inducing fields and, as has been shown in (Treumann, 1970a), to an arbitrary order m (Fig. 4). It can, moreover, be generalized to an arbitrary number of parts of the plate and, if the determination of the Green function Γ is possible, also to arbitrary conductivity structures as, for instance, inclined interfaces between the different parts of the plate. An application of the calculation, using a simple interpretation formula

$$\frac{a_1}{a_2} = \left(\frac{\sigma_2}{\sigma_1}\right)^{1/2} \qquad (3.9)$$

was derived in Treumann (1970a, 1970d) where a_i $(i = 1, 2)$ are the zero values of B_z to the left and to the right of the conductivity jump; for the Northern German anomaly (Treumann, 1970b, 1970d) it gives a value $\sigma_2 : \sigma_1 = 1 : 4.6$. Here the higher conductivity belongs to the northern

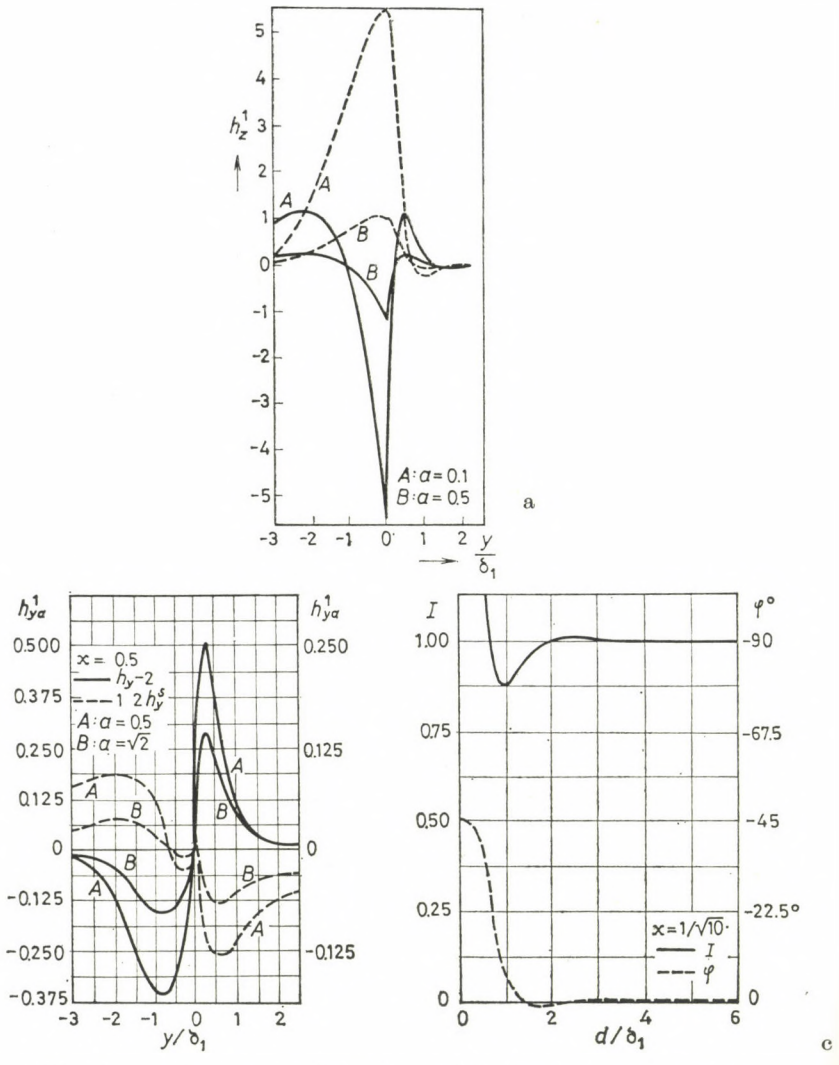


Fig. 3. a – the vertical field $h_z^1 = H_{zi}/H_0$ for homogeneous inducing fields, separated to in-phase (solid line) and out-of-phase parts (broken line) at the surface $z = -0$ of the model of Fig. 2a for a conductivity ratio $\sigma_1 : \sigma_2 = 1 : 10$ and for different plate thickness $a = d/\delta_1$ (δ_1 is the penetration depth in the half sheet); b – the horizontal field for the same model as in Fig. 3, a (Treumann, 1970a); c – phase φ and induction function I of the same model (Treumann, 1970a)

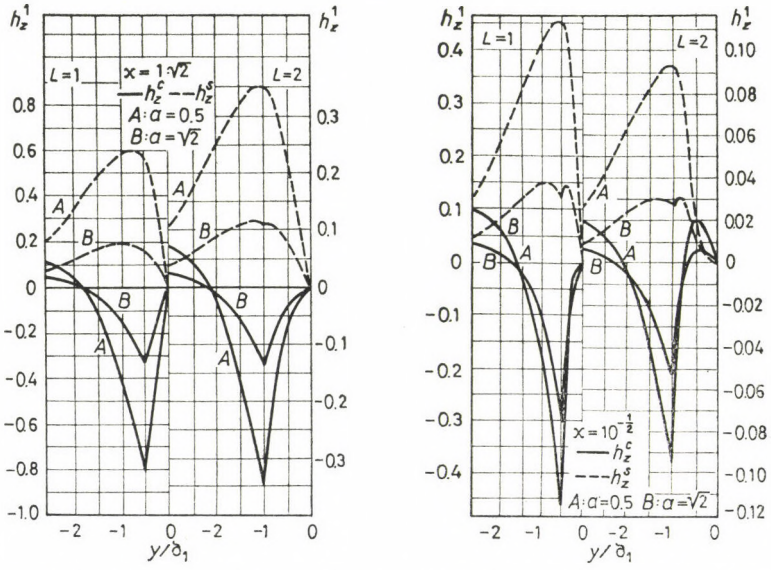


Fig. 4. The vertical field h_z^1 at $z = -0$ for two models of the kind of Fig. 2, b for different a, $\sigma_1 \equiv \sigma_3 \neq \sigma_2$, and $\varkappa^2 = \sigma_1 : \sigma_2$: *(a)* $\varkappa = (2)^{-1/2}$; *(b)* $\varkappa = (10)^{-1/2}$ (Treumann, 1970a)

part of the plate. A thorough discussion of the practical possibilities and restrictions of such model calculations of the conductivity structure of an inhomogeneous earth and the praxis of their application can be found in the contribution of Rokityansky et al. in the present volume. These authors derive simple interpretation formulae for the measurements of the anomalous geomagnetic variation field at the earth's surface. Furthermore, they express the impossibility to distinguish from model calculations between surface and deep conductivity anomalies, a fact the explanation of which lies in the multi-valuedness of the deterministic induction problem. (This point will be somewhat clarified in sections 5 and 6 of the present paper.)

4. THREE-DIMENSIONAL TREATMENT

For arbitrary three-dimensional conductivity distributions Maxwell's equations, neglecting displacement currents, can be written as (Treumann, 1970c):

$$\Delta \mathbf{B} + k^2 \mathbf{B} = \mu_0 \mathbf{E} \times \frac{\partial \sigma(\mathbf{x})}{\partial \mathbf{x}}, \qquad \frac{\partial}{\partial \mathbf{x}} \cdot \mathbf{B} = 0 \tag{4.1}$$

$$\Delta \mathbf{E} + k^2 \mathbf{E} = -\frac{\partial}{\partial \mathbf{x}} \left[\mathbf{E} \cdot \frac{\partial}{\partial \mathbf{x}} \ln \sigma(\mathbf{x}) \right]$$

$$\frac{\partial}{\partial \mathbf{x}} \cdot \mathbf{E} = -\mathbf{E} \cdot \frac{\partial}{\partial \mathbf{x}} \ln \sigma(\mathbf{x}) \tag{4.2}$$

This representation suggests that one can split the three-dimensional induction problem into two independent ones by setting $\mathbf{E}_{\parallel} = 0$, resp. $\mathbf{E}_{\perp} = 0$. The suffix $\parallel$, resp. $\perp$ is chosen with respect to the gradient of the conductivity distribution. The first case is governed by the equations (4.2) with right-hand sides equal to zero, the second case can be calculated from (4.1) with vanishing right-hand side:

$$\Delta(\mathbf{E}_{\perp}, \mathbf{B}) + k^2(\mathbf{E}_{\perp}, \mathbf{B}) = 0\,; \frac{\partial}{\partial \mathbf{x}} \cdot (\mathbf{E}_{\perp}, \mathbf{B}) = 0; (\mathbf{E}_{\parallel}, \mathbf{E}_{\perp}) = 0 \quad (4.3)\text{–}(4.4)$$

The solutions of these equations can be represented by an appropriate *Green's tensor* $\{\mathbf{G}\}(\mathbf{x}/\mathbf{x}_0)$, defined by

$$\Delta\{\mathbf{G}\}(\mathbf{x}/\mathbf{x}_0) + k^2\{\mathbf{G}\}(\mathbf{x}/\mathbf{x}_0) = -4\pi\{\mathbf{I}\}\,\delta(\mathbf{x} - \mathbf{x}_0),\ \{\mathbf{G}\}(\mathbf{x}/\mathbf{x}_0) = \{\mathbf{G}\}(\mathbf{x}_0/\mathbf{x})$$

$$G_{ik} = G_{ki}\,; \cdot \frac{\partial}{\partial \mathbf{x}} \cdot \{\mathbf{G}\} = -\frac{\partial}{\partial \mathbf{x}_0} \cdot \{\mathbf{G}\} = 0 \tag{4.5}$$

The above two cases are distinguished by the conditions

$$\{\mathbf{G}\}(\mathbf{x}^s/\mathbf{x}_0) = \{\mathbf{G}\}(\mathbf{x}/\mathbf{x}_0^s) \tag{4.6}$$

and

$$\mathbf{n} \times \left[\frac{\partial}{\partial \mathbf{x}} \times \{\mathbf{G}\}(\mathbf{x}^s/\mathbf{x}_0)\right] = \mathbf{n} \times \left[\frac{\partial}{\partial \mathbf{x}_0} \times \{\mathbf{G}\} \quad (\mathbf{x}/\mathbf{x}_0^s)\right] = 0 \tag{4.7}$$

respectively, where $\mathbf{n}$ is the outer normal to the surface of the conducting region, and s denotes surface values of the coordinates.

The solution of (4.4), e.g., is represented as

$$\mathbf{B}(\mathbf{x}) = -\frac{1}{4\pi} \oint_{S_0} \left[\frac{\partial}{\partial \mathbf{x}} \times \{\mathbf{G}\}(\mathbf{x}/\mathbf{x}_0^s)\right] \cdot \left(\mathbf{n} \times \mathbf{B}(\mathbf{x}_0^s)\right) dS_0 \tag{4.8}$$

Assuming $\{\mathbf{G}\}$ as known and making use of a separation method of the induction field at the earth's surface (Weaver, 1964) for three-dimensional structures, an iteration procedure similar to that of the previous section follows (Treumann, 1970c)

$$B_z^{(m)}(x) = \frac{1}{4\pi} \oint [(G'_{xx} - G'_{yx})\, B_y^{s(m-1)} - (G'_{xy} - G'_{yy})\, B_x^{s(m-1)}]\, dS_0^s \tag{4.9}$$

$$B_x^{(m)}(x) = \frac{1}{4\pi} \oint [(G'_{yx} - G'_{zx})\, B_y^{s(m)} - (G'_{yy} - G'_{zy})\, B_x^{s(m)}]\, dS_0 \tag{4.10}$$

($B_y^{(m)}(x)$ is obtained from (4.10) by cyclic variation of the indices, and $B_x \rightarrow B_y$) where

$$B_x^{s(m)} = 2B_x^{es} - M_1 B_z^{(m)}; \qquad B_y^{s(m)} = 2B_y^{es} - M_2 B_z^{(m)} \tag{4.11}$$

$$B_x^{s(0)} = 2B_x^{es}; \qquad B_y^{s(0)} = 2B_y^{es},\ B_z^{s(0)} = 0 \tag{4.12}$$

$G'_{ik} = \varepsilon_{ijm}(\partial G_{mk}/\partial x_{0j})$, and M_1, M_2 are two-dimensional Hilbert-operators defined in the papers of Weaver (1964), Treumann (1970c). Similar expressions can be derived for the iterative solution of (4.3).

Thus, knowing $\{\mathbf{G}\}$, the solution of the three-dimensional induction problem can be iteratively constructed up to an arbitrary order by direct integrations along the surface of the conducting earth. This has, however, not yet been done for any case, for the limitations of the procedure and of the separation (4.3), (4.4) have not been discussed yet.[2] A somewhat deviating method has been proposed in the paper of Hutson et al. (1972).

5. THE INVERSION PROBLEM OF GEOMAGNETIC INDUCTION

So far we have only discussed the direct method of calculating a distribution of the field at the earth's surface from a given conductivity distribution. The more lucrative problem, however, is the straightforward calculation of the conductivity distribution from the induction equations by use of the measured-field components. This problem is known as the inversion problem of magnetotellurics or geomagnetic induction. To our knowledge its formulation is only available for magnetotellurics; since, however, its extension to more complicated conductivity distributions seems possible, it will be briefly discussed in this section. For further references the reader is referred to Backus and Gilbert (1967), Bailey (1970), Johnson and Smylie (1971), Weidelt (1973). The representation given here is that of Weidelt (1973) who makes use of a general method (Gelfand and Levitan, 1951) for the inversion of the Sturm-Liouville problem. Magnetotellurics is governed by the equation:

$$\frac{d^2E(z,\omega)}{dz^2} = i\omega\mu_0\sigma(z)\,E(z,\omega) \tag{5.1}$$

and the response function $c(\omega) = -E(0,\omega)/[dE(0,\omega)/dz]$, the square of which determines the apparent resistivity $\varrho_a(\omega) = \omega\mu_0\,|c(\omega)|^2$. The properties of $c(\omega)$ have been extensively discussed in the paper of Weidelt

[2] Very recently a procedure subject to numerical integration and based on the calculations of a Green tensor for three-dimensional structures has been proposed by Raiche (1974) and applied to some models of three-dimensional form by Weidelt (1975).

(1973). A quantity of practical importance is the phase $\psi(\omega)$ of $c(\omega) = |c(\omega)| \exp(-i\psi)$:

$$\psi(T) \cong (\pi/4)\,[1 + d \lg \varrho_a(T)/d \lg T] \tag{5.2}$$

(T = period). Making use of the following substitution scheme:

$$\omega \to k = (i\omega\mu_0\sigma(0))^{1/2};\; z \to x = \int_0^z \left(\frac{\sigma(t)}{\sigma(0)}\right)^{1/2} dt \tag{5.3}$$

$$E(z, \omega) \to f(x, k) = \left(\frac{\sigma(z)}{\sigma(0)}\right)^{1/4} \left(\frac{E(z, \omega)}{E(0, \omega)}\right) \tag{5.4}$$

$$\sigma(z) \to u(x) = \left(\frac{\sigma(z)}{\sigma(0)}\right)^{1/4} \tag{5.5}$$

Equation (5.1) can be transformed into a Sturm-Liouville equation with equivalent potential $V(x) = [d^2 u(x)/dx^2]/u(x)$. Its general solution is

$$f_{\pm}(x, k) = \mathrm{e}^{\pm kx} + \int_{-x}^{x} A(x, t)\, \mathrm{e}^{\pm kt}\, dt \tag{5.6}$$

and leads to the following determination of $u(x)$ through A:

$$u(x) = \lim_{k \to 0} f_{\pm}(x, k) = 1 + \int_{-x}^{x} A(x, t)\, dt \tag{5.7}$$

Hence, the knowledge of A enables one to determine σ and z from

$$\sigma(z) = \sigma(0)\, u^4(x);\quad z = \int_0^x u^{-2}(x)\, dx \tag{5.8}$$

Defining two quantities $b(k) = [1 - k\, c(k)]/2$ and

$$B(x) = \frac{1}{2\pi i} \int_{\varepsilon - i\infty}^{\varepsilon + i\infty} b(k)\, \mathrm{e}^{kx}\, dk \tag{5.9}$$

a unique integral equation for A follows:

$$A(x, y) = B(x + y) + \int_{-x}^{x} A(x, t)\, [B(y + t) + B(y - t]\, dt\,;\; |y| < x \tag{5.10}$$

Since $b(k)$ depends on the response function $c(k)$, the solution of the integral equation (5.12) depends only on measured quantities and, therefore, rep-

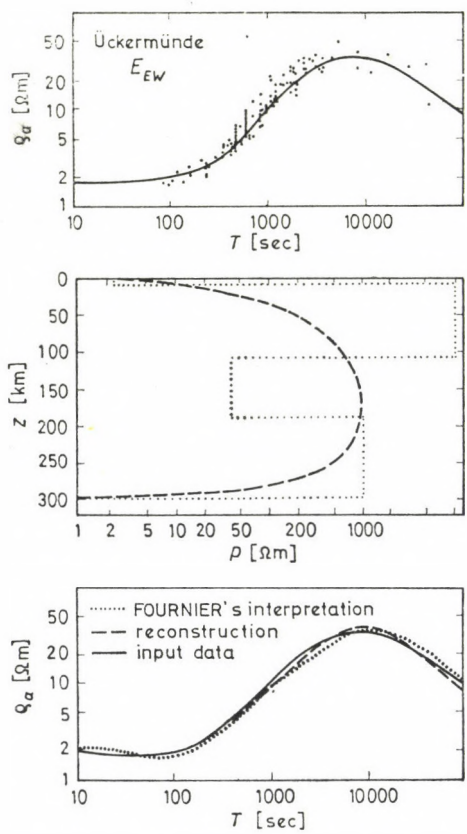


Fig. 5. Application of the inverse procedure to measurements of the apparent resistivity ρ_a at Ückermünde (upper-most part). The calculation leads to a smooth vertical conductivity profile (middle part) with a resistivity maximum of 1 kΩm near 150 km depth (broken line).
The conductosphere begins around 300 km. For comparison a layered model used by Fournier to interpret the data is shown (dotted line). The lower part of the figure shows the reconstruction of both ρ_a-curves compared with the measurements (after Weidelt, 1973)

resents the solution of the inverse problem. Transforming B according to

$$B(x) = \frac{1}{2\pi i} \int_{1/2-i\infty}^{1/2+i\infty} M(s)\, x^{-s}\, ds;\quad M(s) = [\Gamma(1-s)^{-1}] \int_{0}^{\infty \exp(i\pi/4)} f(k)\, k^{-s}\, dk \tag{5.11}$$

where $\Gamma(1-s)$ is the gamma function, Weidelt (1973) brought $B(x)$ into a practically more convenient form. Applications of the inverse procedure to measurements are given in (Weidelt, 1973) (Fig. 5). It is interesting to note that the method smoothes out possibly existing discontinuities of the conductivity, and implies an underlying perfect conductor that is situated in great depth. Moreover, the method is very sensible to uncertainties of the applied data. For a discussion see e.g. Parker (1971).

6. STATISTICAL APPROACH

The real conductivity distribution within the earth is extremely complicated. Hence all model calculations which use simple conductivity structures or calculations of the conductivity based on simple one- or two-dimensional assumptions must fail at least in a more refined description of the conducting properties of the earth. Instead one can assume the conductivity to be statistically distributed, thereby maintaining only a *mean over-all or global dependence* of conductivity on depth z: $\sigma_0(z)$. The real conductivity at every point is then given as the superposition of the global conductivity $\langle\sigma(z)\rangle$ and the deviation $\sigma_1(x)$. Here $\langle\sigma\rangle \equiv \sigma_0$, $\langle\sigma_1\rangle = 0$, where the brackets indicate average taken over the statistical ensemble. Assuming that this average can be replaced by a space average over the characteristic length of the variation of σ_1, σ_0 is a slowly varying function of space. Introducing these quantities into Ampère's law and averaging we find (Schäfer and Treumann, 1975):

$$(\partial/\partial\mathbf{x})\times\mathbf{B}_0 = \mu_0\sigma_0\mathbf{E}_0 + \mu_0\langle\sigma_1\mathbf{E}_1\rangle \tag{6.1}$$

$$(\partial/\partial\mathbf{x})\times\mathbf{B}_1 = \mu_0\sigma_0\mathbf{E}_1 + \mu_0\sigma_1\mathbf{E}_0 + \mu_0\sigma_1\mathbf{E}_1 - \mu_0\langle\sigma_1\mathbf{E}_1\rangle \tag{6.2}$$

where the indices 0, 1 denote global and local field components, respectively. The latter are assumed to be generated due to the presence of $\sigma_1(\mathbf{x})$ by induction of the *global* primary geomagnetic variation field. The remaining equations of the whole set of Maxwell's equations are invariant under the above statistical transformation and are the same for both global and statistical quantities.

Equation (6.1) expresses the fact that for a randomly distributed conductivity structure it is in general *not possible to use a simple global model* of the kind of magnetotellurics. The distribution makes an appreciable contribution to the current that changes the global structure of the fields $\mathbf{B}_0$ and $\mathbf{E}_0$. This contribution can be only neglected if either $|\sigma_1/\sigma_0| \ll 1$ or the spectrum of σ_1, $\mathbf{E}_1$ is homogeneous. Under the former condition the last two terms on the right-hand side of Eq. (6.2) can be neglected, and the problem of determination of the random fields reduces to a linear inhomogeneous one. Its solution depends on the global conductivity $\sigma_0(z)$ and the global field E_0. (This solution can, on the other hand, be inserted on the right-hand side of Eq. (6.1) where it adds a "quasilinear" correction to the global equation.)

An alternate problem is the determination of the mean square deviation $\langle|\sigma_1|^2\rangle$ of the conductivity from its global value σ_0. This problem can be solved under the simplifying linearizing assumption discussed above. For this purpose it is convenient to introduce the spatial field correlation tensor $\{\mathbf{K}_{ij}\} = \langle\mathbf{B}_1\,\mathbf{B}_1\rangle$, which is a measurable quantity. It can be used to derive an integral equation for $\langle|\sigma_1|^2\rangle$. In its most simple formulation for an infinite medium without boundaries this equation reads (Schäfer and Treumann, 1975):

$$\{\mathbf{K}_{ij}\}\,(\xi,\tau,\mathbf{x}) = \frac{1}{(2\pi)^4\,TL^3}\int d\omega d\mathbf{k}\;\mathrm{e}^{-i\mathbf{k}\cdot\xi - i\omega\tau}$$

$$\mathbf{B}_0(\omega,\mathbf{x})\,\mathbf{B}_0(-\omega,\mathbf{x})\left[\,\delta(\mathbf{k}) + \frac{\mu_0^2\omega^2|\sigma_1(\mathbf{k})|^2}{k^4 + (\omega\mu_0\sigma_0)^2}\right] \tag{6.3}$$

where T and L, respectively are the temporal and the spatial lengths over which the average has been taken. Its solution is

$$\frac{|\sigma_1(\mathbf{k})|^2}{\sigma_0^2} = \delta(\mathbf{k}) + TL^3(1 + k^2/\omega^2\mu_0^2\sigma_0^2)\,\mathbf{B}_0^{-1}(\omega,\mathbf{x}) \cdot$$

$$\cdot\,\{\mathbf{K}_{ij}\}\,(\mathbf{k},\,\omega;\,\mathbf{x}) \cdot \mathbf{B}_0^{-1}(-\omega,\,\mathbf{x}) \tag{6.4}$$

the "power-spectrum" of the conductivity fluctuation, from which after transforming back to the ξ-space $\langle\sigma_0^2(\omega,\,\xi;\,\mathbf{x})\rangle_\xi/\sigma_0^2(\mathbf{x})$, the mean squared fluctuating amplitude, can be calculated.

For structures involving a bounded earth the full representation (1.4) for the fields must be used. Calculations in this direction are underway. However, (6.4) does already reflect the interesting fact that the deviation can be only determined if the *whole frequency spectrum* of the variation is known. This situation is equivalent to that of the magnetotelluric inversion problem (§ 5) where the dependence of $c(\omega)$ on frequency is required to be known. Concerning the limitations of the method we note that Eq.(6.4) is sensible to the global conductivity model σ_0 used in the calculation and to errors of the measurements.

7. CONCLUSIONS

The review of the theory of geomagnetic induction in an inhomogeneous conducting earth given in this paper has shown that the theory of calculating field distributions from known conductivity distributions is well-established for the most simple conductivity structures as e.g. thin plates, where only simple singular integral equations have to be solved, or thick plates, where the solution can be reduced to a system of singular integral equations with bounded but non-closed kernels.[3] In the latter case, however, several approximate methods have been developed.

A method of a wider range of validity and its generalization to three-dimensional conductivity structures has been discussed. Whereas rigorous calculation of complicated models seems improbable, the approximation methods are applicable to arbitrary conductivity distributions if the Green functions or tensors can be constructed. This is, however, a further difficult problem.

Today the direct inversion of the induction problem finds growing interest. In this review the inversion problem has been discussed for two limiting cases: the magnetotelluric inversion problem and the statistical inversion problem. The first gives excellent results, if the model assumption is valid, thereby smoothing out discontinuities in the vertical conductivity distribution. Its generalization to more than one dimension has not yet been given, but seems possible.

[3] Numerical calculations related to these and some other models as e. g. spheres or cylinders have been reported by Rokityansky et al. on pp. 108–121.

The statistical theory brings a new view into induction theory. It clearly shows where the limitations of the usual theory lie and opens new vistas of refining magnetotelluric calculations by incorporating the concept of mean square deviation from the proposed global conductivity structure in the earth. As a matter of fact, so far this approach has been neither exactly formulated nor has it been ever applied successfully to measured data. It is still hoped, however, that it will not only give the theory of the geomagnetic induction problem a new impetus into an unexpected direction, but will also supply useful additional information about conductivity to magnetotellurics or the magnetotelluric inversion method, if transformed into a practicable fashion.

ACKNOWLEDGEMENT

The author thanks Prof. G. Fanselau for his guidance through the initial stages of his work on geomagnetic induction theory during the years 1965 to 1968. Further thanks are due to Dr. P. Weidelt for valuable discussions and informations especially about the inversion problem.

REFERENCES

Ashour, A. A., 1971. Electromagnetic induction in thin finite sheets having conductivity decreasing to zero at the edge, with geomagnetic applications. *Geophys. J. R. Astr. Soc.* **22,** 417.

Backus, G., Gilbert, F., 1967. Numerical applications of a formalism for geophysical inverse problems. *Geophys. J. R. Astr. Soc.* **13,** 247.

Bailey, R. C., 1970. Inversion of the geomagnetic induction problem. *Proc. R. Soc., London A,* **315,** 185.

Clemmov, P. C., 1951. A method for the exact solution of a class of two-dimensional diffraction problems. *Proc. R. Soc., London A,* **205,** 286.

Gelfand, I. M., Levitan, B. M., 1951. About the definition of an inverse time-equation over its spectral functions (in Russian). *Izv. Akad. Nauk SSSR, Ser. matem.* **15,** 309.

Hewson-Browne, R. C., 1972. The magnetic field of a current sheet confined to the surface of a sphere. *Geophys. J. R. Astr. Soc.* **28,** 91.

Hobbs, B. A., 1975. Analytic solutions to global and local problems of electromagnetic induction in the earth. *Phys. Earth Planet. Interiors* **10,** 250.

Hutson, V. C. L., Kendall, P. C., Malin, R. S. C., 1972. Computation of the solution of geomagnetic induction problems: a method with applications. *Geophys. J. R. Astr. Soc.* **28,** 489.

Johnson, I. M., Smylie, D. E., 1971. An inverse theory for the calculation of the electrical conductivity of the lower mantle. *Geophys. J. R. Astr. Soc.* **22,** 41.

Jones, F. W., 1971. Electromagnetic induction in a non-horizontally stratified two-layered conductor. *Geophys. J. R. Astr. Soc.* **22,** 17.

Jones, F. W., Price, A. T., 1970. The perturbations of alternating geomagnetic fields by conductivity anomalies. *Geophys. J. R. Astr. Soc.* **20,** 317.

Jones, F. W., Price, A. T., 1971. The geomagnetic effects of two-dimensional conductivity inhomogeneities at different depths. *Geophys. J. R. Astr. Soc.* **22,** 333.

Lahiri, B. N., Price, A. T., 1939. Electromagnetic induction in nonuniform conductors, and the determination of the conductivity of the Earth from terrestrial magnetic variations. *Phil. Trans. R. Soc., London A,* **237,** 509.

Mann, J. E., 1970. A perturbation technique for solving boundary value problems arising in the electrodynamics of conducting bodies. *Appl. Sci. Res.* **22,** 113.

Mann, J. E., Jr., 1964. Magnetotelluric theory of the sinusoidal interface. *J. Geophys. Res.* **69,** 3517.

MUSKHELISHVILI, N. I., 1962. Singular Integral Equations (in Russian). Fizmatgiz, Moscow.

PARKER, L. R., 1971. The inverse problem of electrical conductivity in the mantle. *Geophys. J. R. Astr. Soc.* **22**, 121.

PRICE, A. T., 1949. The induction of electric currents in nonuniform thin sheets and shells. *Quart. J. Mech. Appl. Mathem.* **2**, 283.

RAICHE, A. P., 1974. An integral equation approach to three-dimensional modelling. *Geophys. J. R. Astr. Soc.* **36**, 363.

RIKITAKE, T., 1966. Electromagnetism and the Earth's Interior Develop. Solid Earth Geophys. 2, Amsterdam.

SCHÄFER, K., TREUMANN R., 1975. Statistical approach to the geomagnetic induction problem for the infinite medium. *Gerlands Beitr. Geoph.* **34**, 117.

SCHMUCKER, U., FORBUSH, S. E., HARTMANN, O., GIESECKE, A. A., CASAVERDE, M., CASTILLO, J., SALGUEIRO, R., DEL POZO, S., 1967. Electrical conductivity anomaly under the Andes. *Carnegie Inst. Washington Yearbook* **65**, 11.

SIEBERT, M., 1964. Ein Verfahren zur unmittelbaren Bestimmung der vertikalen Leitfähigkeitsverteilung im Rahmen der erdmagnetischen Tiefensondierung. *Nachr. Akad. Wiss. Göttingen, mathem.-phys. Kl.* No. 2, 20.

TREUMANN, R., 1970a. The problem on electromagnetic induction in a plate with two-dimensional distribution of conductivity I. General theory (in Russian). *Geomagn. i Aeron.* **10**, 478.

TREUMANN, R., 1970b. The problem on electromagnetic induction in a plate with two-dimensional distribution of conductivity II. An approximated method and solutions (in Russian). *Geomagn. i Aeron.* **10**, 588.

TREUMANN, R., 1970c. The three-dimensional analysis of the problem of electromagnetic induction of magnetovariational and magnetotelluric sounding (in Russian). *Geomagn. i Aeron.* **10**, 1062.

TREUMANN, R., 1970d. Electromagnetic induction in inhomogeneous media (E-polarization). *Acta Geod. Geophys. Mont. Hung.* **5**, 61.

WEAVER, J. T., 1963. The electromagnetic field within a discontinuous conductor with reference to geomagnetic micropulsations near a coastline. *Can. J. Phys.* **41**, 484.

WEAVER, J. T., 1964. On the separation of local geomagnetic field into external and internal parts. *Z. Geophys.* **30**, 29.

WEAVER, J. T., 1971. The general theory of electromagnetic induction in a conducting half space. *Geophys. J. R. Astr. Soc.* **22**, 83.

WEAVER, J. T., THOMSON, D. J., 1972. Induction in a nonuniform conducting half-space by an external line current. *Geophys. J. R. Astr. Soc.* **28**, 163.

WEIDELT, P., 1966. Modellrechnungen zur Deutung der nord-deutschen Leitfähigkeitsanomalie als oberflächennahe Leitfähigkeitsänderung. Diplomarbeit, Göttingen.

WEIDELT, P., 1971. The electromagnetic induction in two thin half-sheets. *Z. Geophys.* **37**, 649.

WEIDELT, P., 1973. The inverse problem of geomagnetic induction. *Z. Geophys.* **39**, 257.

WEIDELT, P., 1975. Electromagnetic induction in three-dimensional structures. *Z. Geophys.* **41**, 85.

THE TECHNIQUE OF MAGNETIC VARIATION PROFILING DATA ANALYSIS

I. I. ROKITYANSKY

LIST OF SYMBOLS

A, B – coefficients of the linear relationship (17)
$\mathbf{C}_u$, $\mathbf{C}_v$ – induction vectors determined from Eq. (20)
$\mathbf{C}_w$ – Wiese-arrow (Eq. (22))
H_x, H_y, H_z – projections of the vector $\mathbf{H}$ in the directions of the axis x, y, z (z directed downwards)
$\mathbf{H} = \mathbf{H}_0 + \mathbf{H}_a$ – complete vector of the magnetic field variation; $\mathbf{H}_0$ the normal, $\mathbf{H}_a$ the anomalous part
h_{ik} – coefficients of the linear relationship in Eqs (8)
M_1, M_2 – integral operators (see Eq. (6))
T – period of variations, T_0 – period, where the frequency characteristics of the anomalous part has its maximum
t – time
$U(x, z) = H_{za}(x, z) + H_{xa}x, z)$ – analytical function (Eq. (2))
U_i, U_e – inner and outer parts of function U
σ – electric conductivity
θ – rotation angle of the coordinate system x, y, z around the axis OZ

The relations that form the basis of magnetic variation data processing are presented in this section.

Consider the stratified earth the electrical conductivity of which depends on depth and only differs in some bounded domain from the horizontal-stratified distribution. Assume that the anomalous domain is very elongated; that in some central part its electrical conductivity practically does not depend on one of the horizontal coordinates (y). If the dimensions of the anomaly are small in comparison with the earth's curvature we will use rectangular coordinates: z directed downwards, y being the homogeneity axis: $\mathrm{grad}_y\, \sigma = 0$, and x the direction where MVP is carried out. As it is known the anomalous magnetic field on the earth's surface only arises at E-polarization (H_x, H_z, E_y) and not at H-polarization (H_y, E_x, E_z). Using this terminology we assume the inhomogeneities of the source field are not essential in the anomaly region or at least in its central part (according to y). The Maxwell equations of the magnetic field at E-polarization have the form

$$\frac{\partial H_z}{\partial x} - \frac{\partial H_x}{\partial z} = j_y$$

$$\frac{\partial H_x}{\partial x} + \frac{\partial H_z}{\partial z} = 0 \qquad (1)$$

Introduce the notations $j = j_0 + j_a$, $H_z = H_{z0} + H_{za}$, $H_x = H_{x0} + H_{xa}$, (index a means anomalous part). In absence of the electrical conductivity anomaly relations (1) are satisfied for the normal field values, i.e. they are satisfied for their anomalous parts, too. For a local anomaly there exists some closed circuit C in the xz plane outside of which the anomalous currents are zero. Then outside of C relations (1) are equivalent to the *Cauchy–Rieman conditions*, i.e. we can introduce an analytical function

$$U(x, z) = H_{za}(x, z) + iH_{xa}(x, z) \tag{2}$$

for which the well-established techniques of the theory of analytical functions can be applied. Writing down Cauchy's formula for the circuit covering the upper (or lower) half-space where the inner U_i (or outer U_e) part of the field tends to zero at infinity, and setting

$$U = U_e + U_i \tag{3a}$$

we obtain

$$U_e(x_0) - U_i(x_0) = -\frac{i}{\pi} \int_{-\infty}^{\infty} \frac{U(x)}{x - x_0} dx = iKU \tag{3b}$$

where the integral operator K is defined as

$$KH(x) = -\frac{1}{\pi} \int_{-\infty}^{\infty} \frac{H(x)}{x - x_0} dx \tag{4}$$

Starting out from the system (3) we get the known formulae of field division (Kertz, 1954; Siebert, 1962), from which it follows (Kertz, 1954):

$$\begin{aligned} H_{xa}(x_0) &= -KH_{za}(x) \\ H_{za}(x_0) &= KH_{xa}(x) \end{aligned} \tag{5}$$

These *Hilbert transform relations* are of great practical significance as they allow to find the second component if one of the field components is known on the earth's surface and thus to check up the correctness of separation of the anomalous part. Generalization of formula (5) to three-dimensional anomalies results in the relations (Weaver, 1964; Rokityansky, 1972):

$$\begin{aligned} H_{xa} &= -M_1 H_{za} \\ H_{ya} &= -M_2 H_{za} \\ H_{za} &= 1/2\,[M_1 H_{xa} + M_2 H_{ya}] \end{aligned} \tag{6}$$

where the integral operators M_1 and M_2 are defined as

$$M_1 H_{ka}(x_0 y_0 0) = \frac{1}{2\pi} \iint_{-\infty}^{\infty} \frac{(x - x_0)\, H_{ka}(x, y, 0)}{[(x-x_0)^2 + (y-y_0)]^{3/2}}\, dx\, dy \; ; \; (k = x, y)$$

$$M_2 H_{ma}(x_0 y_0 0) = \frac{1}{2\pi} \iint_{-\infty}^{\infty} \frac{(y - y_0)\, H_{ma}\ (x, y, 0)}{[(x-x_0)^2 + (y-y_0)]^{3/2}}\, dx\, dy \; ; \; (m = y, z)$$

Expression (6) shows that the vertical component of the three-dimensional anomalous field carry the same information as the both horizontal ones.

The above relations have been obtained under the only restriction that *displacement current* should be neglectible. From this it follows that for variable anomalous fields of inner origin the relations (5–6) will hold for any time moment and for any frequency until the displacement currents are unessential, i.e. practically always for the MVP. Problems related to the harmonic analysis of the variations are not considered in this section, as these are intensively studied in connection with the MTS method.

Consider two-dimensional anomalies. The considerations can easily be extended for three-dimensional anomalies using relation (6) instead of (5); i.e. the conclusions will also relate to three-dimensional anomalies. Carrying out Fourier transform on relation (5) and passing to the *normalized complex amplitudes* $h_x = H_{xa}/H_{x0}$, $h_z = H_{zo}/H_{x0}$ of the anomalous field we get

$$\begin{aligned} h_x &= -K h_z \\ h_z &= K h_x \end{aligned} \tag{5a}$$

The complex amplitude $h_r = h_{ru} + i h_{rv}$, $r = x, z$ is an analytical function and consequently its real and imaginary parts are related by relations of type (5):

$$h_{ru}(T_0) = -\frac{1}{\pi} \int_{-\infty}^{\infty} \frac{h_{rv}(T)}{\lg T - \lg T_0}\, d(\lg T) = K h_{rv} \tag{7}$$

$$h_{rv} = -K h_{ru} \qquad r = x, z$$

Relations (5) and (7) show that if the real or imaginary part of one of the anomalous field components is given in the whole space-time domain (x, T), then the anomalous field is completely defined and the rest of its components can be computed by integral transforms (5), (7).

Figure 1 presents surfaces describing the normalized components of the anomalous field over a graben, calculated in the book of Dmitriev et al. (1973). Relations (5) and (7) show that only one surface, given on an infinite plane $(x, \lg T)$, is independent, the rest three are expressed by it.

For three-dimensional inhomogeneities, described by relations (6) the

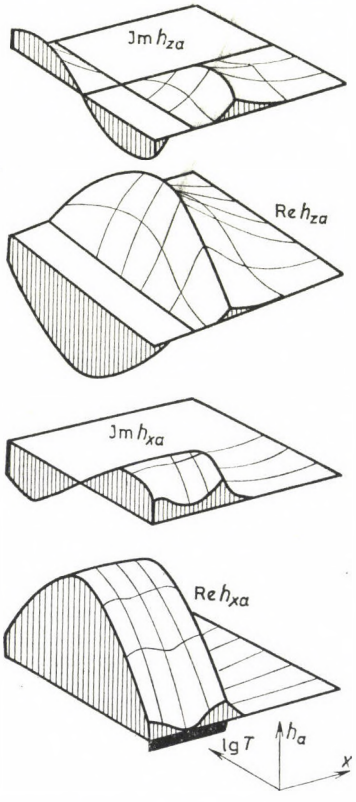


Fig. 1. Real and imaginary parts of the anomalous field over a graben in dependence of period T and the observation point position x on the profile

anomalous fields may be represented by four surfaces in the four-dimensional domain (x, y, lg T, h_a), only one of them being independent and the rest expressed by it according to integral equations (6–7) (with extending relation (7) by the formulae for h_y). Consequently, the measurement of only one or two anomalous field components is no limitation at least theoretically, which does not mean, however, that one would advise to measure only one component. In practice observations are bounded by frequency and space points where every component of the anomalous field is defined with considerable error. Under such conditions it is desirable to observe the various components to increase the accuracy of the information obtained provided the accuracy of the various components is comparable. If any component (in some cases the anomalous field phase) is measured with a considerable lower accuracy than the rest, it is not worth while to waste effort on its measurement (under measurement one understands field registration and processing). In practice the normalized anomalous field is generally received in the form of profile and frequency one-dimensional curves that are orthogonal sections of the corresponding surfaces in Figure 1. The form of the profile curves characterizes first of all the geometrical parameters of the anomalous body, the frequency curve position characterizes the longitudinal conductivity of the elongated anomalous body. The

main task of survey processing is to obtain profile and frequency curves of the normalized anomalous field.

Interpretation, i.e. the determination of parameters is carried out in the MVP method as a simultaneous observation processing on a profile or area, or by processing the observations at each point independently.

Let us now consider both processing methods.

The geomagnetic variation field can be decomposed into three main parts: initial part H_{0e} outer origin; secondary normal part H_{0i} due to currents induced in the horizontal stratified earth and secondary anomalous part H_a. Assuming the anomaly dimensions to be considerably smaller than the source ones, one may take $H_0 = H_{0e} + H_{0i}$ to be the anomaly-forming field. Due to the linearity of the equations of electrodynamics the anomalous currents and fields linearly depend on the normal field intensity that in general is expressed by the three-dimensional tensor relation (Schmucker, 1970)

$$\mathbf{H}_a(x, y) = \{\mathbf{h}_{ik}(x, y)\}\mathbf{H}_0(x, y) \tag{8}$$

or, writing out in components

$$\begin{aligned} H_a &= h_{11}H_0 + h_{12}D_0 + h_{13}Z_0 \\ D_a &= h_{21}H_0 + h_{22}D_0 + h_{23}Z_0 \\ Z_a &= h_{31}H_0 + h_{32}D_0 + h_{33}Z_0 \end{aligned} \tag{8a}$$

where H, D, Z are complex amplitudes of the field's spectral components, h_{ik} are complex coefficients depending on x, y, T. It can be shown that for bodies whose vertical size does not largely exceed the horizontal one, the first two columns present mostly conductive type anomaly, the third one the eddy type anomaly. This type of anomaly can be neglected in middle latitudes because of the small value of Z_0 particularly in case of elongated, narrow, anomalous bodies. Omitting the third column in Eq. (8) we will write

$$\begin{aligned} H_a &= h_{11}H_0 + h_{12}D_0 + \delta H \\ D_a &= h_{21}H_0 + h_{22}D_0 + \delta D \\ Z_a &= h_{31}H_0 + h_{32}D_0 + \delta Z \end{aligned} \tag{8b}$$

where δH, δD, δZ are uncorrelated (Schmucker, 1970) parts of the corresponding components that include all errors arising from the application of Eq. (8b), i.e. the errors due to inaccurate splitting the field into normal and anomalous parts, those due to neglecting the third column of (8a), those due to the influence of source parameters on the anomalous field (for the conductive type anomalous field the factors h_{ik} are proportional to the impedance whose variation may contribute to δH, δD, δZ), errors of the harmonic analysis etc.

Consider now the specific question of MVP as how to split the observation field into normal and anomalous parts. The basis for this division is the assumption that the spatial spectrum of the source contains only

low frequencies, and hence the high frequency part of the spatial spectrum may approximately be identified with the anomalous field. The reality of this assumption can be checked up by the well-known techniques of division of the field variation into outer and inner parts (e.g. Kertz, 1954; Rikitake, 1966) for the anomalous field must be of inner origin. Particularly, for a field of inner origin the integral relations (5) and (6) hold, that can also be used to check the correct selection of the anomalous part. Simultaneous observation data on a long profile or a large area are necessary for the above-mentioned controls. If the simultaneous observations cover a small area and integration is impossible, selection of the anomalous field is done by utilizing the basis station, whose field is taken as normal. Such a method could give good results for a local anomaly surrounded by a horizontal-stratified structure. Then the variation field observed at a distance large enough not to be influenced by the anomaly, but small enough not to be influenced by the source field change, may be taken normal for the whole anomalous region and the anomalous part can be easily computed. Alas, local anomalies are not surrounded by horizontal-stratified structures, as a rule, and the determination of the normal field can be only solved in a rough approximation. If a basis point lies in an anomalous region but the field on it is taken as normal the tensor $\{h_{ik}(x, y, B)\}$ obtained from solving Eq. (8) will be distorted and the interpretation will be erroneous. So, if in course of a subsequent survey the basis point turns out to be anomalous the results should be recalculated to another basis. Using the observation data one has to calculate the transition matrix from the field in the second basis (B_2) to the field in the first basis (B_1):

$$\mathbf{H}(B_1) = \mathbf{H}(B_2) + \mathbf{H}_a(B_1B_2) = \mathbf{H}(B_2) + \{h(B_1B_2)\}\mathbf{H}(B_2) \tag{9}$$

where $\mathbf{H}_a(B_1, B_2)$ is the anomalous field in B_1 under the assumption that normal field is observed in B_2. For each field point A_i at basis B_k we have

$$\mathbf{H}(A_i) = \mathbf{H}(B_k) + \{h(A_i, B_k)\} \cdot \mathbf{H}(B_k) \tag{10}$$

where the matrices $\big(h(A_i, B_k)\big)$ are determined from the solution of system (8). Substituting (9) into (10):

$$\begin{aligned}\mathbf{H}(A_i) = \mathbf{H}(B_2) + \{h(B_1, B_2)\} \cdot \mathbf{H}(B_2) + \{h(A_i, B_1)\} \cdot \mathbf{H}(B_2) + \\ + \{h(A_i, B_1)\} \cdot h(B_1, B_2)\} \cdot \mathbf{H}(B_2)\end{aligned} \tag{11}$$

Comparing Eq. (11) with the relation $\mathbf{H}(A_i) = \mathbf{H}(B_2) + \{h(A_i, B_2)\} \cdot \mathbf{H}(B_2)$ we obtain the expression for recalculation

$$\big(h(A_i, B_2)\big) = \big(h(B_1, B_2)\big) + \big(h(A_i, B_1)\big) + \big(h(A_i, B_1)\big) \cdot \big(h(B_1, B_2)\big) \tag{12}$$

The operations in Eqs (9–12) are carried out according to the rules of the complex matrix production and addition. Relation (12) is of great importance in case of a small number of simultaneous observation points (e.g. a work scheme at short periods: one basis point and 1–2 field ones).

Consider the sequence of the main steps in the profile processing method:

1. Choice of simultaneous recordings and their spectral analysis.
2. Determination of the H_0, D_0, Z_0 normal field of each realization by smoothing or according to the recording of the basis station selected after a preliminary point processing.
3. Separation of the anomalous field.
4. Solution of system (8b) for the determination of the parameters h_{ik}. For the solution of (8b) all methods can be applied which have been developed for analogous tensor impedance equations in MTS practice (Berdichevsky, 1968; Schmucker, 1970).
5. Checking the mutual relationships between the $[h_{ik}]$ tensor components. h_{ik} should satisfy certain conditions which we will deduce from integral transformation (6). Suppose that in Eq. (8b) the normal field has once H_0-component only, and the next time it contains only a D_0-component. Applying relation (6) to each of these cases we obtain:

$$\begin{aligned} h_{11} &= -M_1 h_{31} & h_{12} &= -M_1 h_{32} \\ h_{21} &= -M_2 h_{31} & h_{22} &= -M_2 h_{32} \\ h_{31} &= \frac{1}{2}(M_1 h_{11} + M_2 h_{21}) & h_{32} &= \frac{1}{2}(M_1 h_{12} + M_2 h_{22}) \end{aligned} \tag{13}$$

where M_1, M_2 are integral operators defined by Eq. (6). If on the whole region x, y where the anomalous field is not zero the calculation of h_{ik} is carried out exactly, then as follows from Eq. (13) only the two components h_{31} and h_{32} out of the six are independent. In each observation point one can plot the polar diagrams (Berdichevsky, 1968) from the h_{ik} tensor components or the induction vector **C** and the perturbation vectors **p**, **q** (Schmucker, 1970) defined by the relations

$$\begin{aligned} \mathbf{p} &= h_{11}\mathbf{i} + h_{21}\mathbf{j} \\ \mathbf{q} &= h_{12}\mathbf{i} + h_{22}\mathbf{j} \qquad \mathbf{i} \text{ is directed northward} \\ \mathbf{C} &= h_{31}\mathbf{i} + h_{32}\mathbf{j} \qquad \mathbf{j} \text{ is directed eastward.} \end{aligned} \tag{14}$$

These latter are generally plotted by solid line if computed from the real parts, and by dashed line if computed from imaginary parts of the h_{ik} coefficients. The **p** and **q** vectors have a simple physical meaning: rotating them anti clock-wise by an angle of 90° they will give the force and direction of the anomalous currents imposed on the perturbed normal current of westward **p** or northward **q** directions. If the medium is two-dimensional and the properties are constant along the y axis, relation (8b) takes the form

$$\begin{pmatrix} H_{xa} \\ H_{ya} \\ Z_a \end{pmatrix} = \begin{pmatrix} h_x & 0 \\ 0 & 0 \\ h_z & 0 \end{pmatrix} \cdot \begin{pmatrix} H_{x0} \\ H_{y0} \end{pmatrix} \tag{15}$$

Passing to the coordinate system rotated by angle θ° with respect to x, y expression (15) assumes the form

$$\begin{pmatrix} H_a \\ D_a \\ Z_a \end{pmatrix} = \begin{pmatrix} h_x \cos^2\theta & h_x \sin\theta\cos\theta \\ h_x \sin\theta\cos\theta & h_x \sin^2\theta \\ h_z \cos\theta & h_z \sin\theta \end{pmatrix} \begin{pmatrix} H_0 \\ D_0 \end{pmatrix} \tag{16}$$

The parameters h_x and h_z given at the x profile are mutually related by the Hilbert transformation (5). We introduce a definition: The anomalous field behaviour at some observation point (x, y) will be called quasi-two-dimensional if the h_{ik} tensor components correspond to (15) and (16) within the error limit of their determination. The prefix 'quasi' is justified because such anomalous field structure is also characteristic to a wide class of three-dimensional bodies, e.g. to axially symmetric bodies, compact bodies of a regular shape etc. Induction and perturbation vectors are the visual indices of the anomalous field structure. The principal feature of quasi-two-dimensionality is parallelism or antiparallelism between real and imaginary vectors of each type, as it is seen from Eq. (15).

Processing of point observations. All processing methods of point observations are based on the linear relation

$$Z = AH + BD \tag{17}$$

Here H, D, Z are the observed field components, consisting of normal and anomalous parts. Because of

$$H = H_0 + H_a = H_0 \left(1 + h_{11} + \frac{D_0}{H_0} h_{12} \right)$$

$$D = D_0 + D_a = D_0 \left(1 + h_{22} + \frac{H_0}{D_0} h_{21} \right)$$

and if

$$Z = Z_0 + Z_a \simeq Z_a$$

then according to (8)

$$A = \frac{h_{31}}{1 + h_{11} + \dfrac{D_0}{H_0} h_{12}}$$

$$B = \frac{h_{32}}{1 + h_{22} + \dfrac{H_0}{D_0} h_{21}} \tag{18}$$

We are interested in such A and B parameters that characterize the electrical conductivity anomaly and do not depend on the normal field polarization. The last member in the dominators of expression (18) is generally small and can be neglected. This neglection is also necessary since at point observations the change of polarization of the normal field

cannot be taken into account. Consequently even in the ideal case, when the primary field consists of vertically incident plane waves ($z_0 = 0$), the parameters of the medium A and B are defined approximately. The determination of A and B is only accurate in case of a quasi-two-dimensional field when the axis of quasi-homogeneity coincides with the direction of one of the measured components. The relative error due to the neglection of the third term in the dominators in Eq. (18) can be evaluated in case of a quasi-two-dimensional anomaly oriented at angle θ with the measured H component according to the formula

$$\delta \begin{Bmatrix} A \\ B \end{Bmatrix} = \frac{\begin{Bmatrix} D_0/H_0 \\ H_0/D_0 \end{Bmatrix} h_x \sin\theta\cos\theta}{1 + h_x \begin{Bmatrix} \cos^2\theta \\ \sin^2\theta \end{Bmatrix} + \begin{Bmatrix} D_0/H_0 \\ H_0/D_0 \end{Bmatrix} h_x \sin\theta\cos\theta} \tag{19}$$

which is easily deduced from Eqs (16, 18). The maximum error arises for $\theta = 45°$; if $D_0/H_0 = 1$ the error will be $0.5\, h_x/(1 + h_x)$. Above the epicentre of the anomaly h_x may attain unity and more that will cause an error of several tens per cent in the determination of the A and B parameters. At $h_x \leq 0.25$ the error does not exceed 10% and it can be neglected. For observations aside from the anomaly h_x is generally very small (e.g. land observations of some coastal effect). In this case processing of the observation at one point gives the best results. Another source of error in point processing is the influence of Z_0, that might lead to data scatter or to a systematical error in the A and B determined. Evaluation and analysis (e.g. Wiese, 1965) has shown that at middle latitudes for variation periods of from a few minutes up to several tens of minutes the Z_0/H_0 ratio does not exceed 0.1.

For higher latitudes Z_0/H_0 increases to 0.3–0.8 at 500–200 km distance from the electrojet epicentre, then decreases to zero and inside the auroral zone attains a negative maximum. Under these conditions the parameters A and B (17) will characterize not only the electrical conductivity distribution in the earth but the source parameters as well. The induction vector will tend to be oriented towards the source in the direction perpendicular to the electrojet strike.

We proceed now to a review of the methods of determination of parameters A and B by (17) and the ways of their graphic fitting. For the interpretation it is necessary to know the frequency to which the determined A and B correspond, all field components in (17) should be some harmonics characterized by complex amplitude. All methods used in the MTS can be applied to the determination of the complex A and B by Eq. (17), particularly the methods of least squares and the polarization vector methods, among others (Berdichevsky, 1968; Schmucker, 1970). These methods are generally realized by an electronic digital computer. From the complex A and B values found we plot the pair of vectors:

$$\begin{aligned} \mathbf{C}_u &= \mathrm{Re}\, A\mathbf{i} + \mathrm{Re}\, B\mathbf{j} \\ \mathbf{C}_v &= \mathrm{Im}\, A\mathbf{i} + \mathrm{Im}\, B\mathbf{j} \end{aligned} \tag{20}$$

that are close to the vectors defined by the third row of Eq. (14). Comparing $\mathbf{C}_u$ and $\mathbf{C}_v$ a number of conclusions can be drawn:

1. If the angle between $\mathbf{C}_u$ and $\mathbf{C}_v$ is near-perpendicular the anomalous field is the point has a three-dimensional character.

2. If $|\mathbf{C}_u| \gg |\mathbf{C}_v|$ the period T, for which the observations are carried out, is close to T_0 where the frequency characteristic of the anomalous field attains its maximum. From T_0 one can evaluate the longitudinal conductivity of the anomalous body (see pp. 105–123).

3. If $\mathbf{C}_u$ and $\mathbf{C}_v$ have approximately the same direction then $T < T_0$, the larger is $\mathbf{C}_v/\mathbf{C}_u$ the larger T_0/T.

4. If $\mathbf{C}_u$ and $\mathbf{C}_v$ have opposite directions then $T > T_0$, the larger is $\mathbf{C}_v/\mathbf{C}_u$ the smaller T_0/T.

Another way of graphic representation is made by means of *magnetic polar diagrams* (Berdichevsky, 1968). This requires rather cumbersome calculations and constructions and the received picture is less clear than that given by the $\mathbf{C}_u$ and $\mathbf{C}_v$ vector pair. The information content in both methods is the same. A number of simplified methods exist for the determination of A and B in which all values in Eq. (17) are considered as real.

The method of Wiese (1965) is concerned with two-dimensional anomalies and starts out from the relation

$$Z(t_0) = aH(t_0) + bD(t_0) \tag{21}$$

where t_0 is the time moment when the Z variation reaches its extremum. The *Wiese vector* is determined by the expression

$$\mathbf{C}_W = a\mathbf{i} + b\mathbf{j} \tag{22}$$

it is perpendicular to the anomalous currents and directed away from the axis of the body of increased conductivity. Berdichevsky and Smirnov (1971) showed for quasi-two-dimensional fields that

$$|C_W| = \frac{|C|}{\cos \arg C} \tag{23}$$

where $\mathbf{C} = A\mathbf{i} + B\mathbf{j}$

They also pointed out that for a three-dimensional inhomogeneous medium the Wiese vector loses its stability. Since it is known that for most middle-latitude observatories the Wiese vector can be successfully received it can be concluded that quasi-two-dimensional anomalies are rather wide spread. If the Wiese vectors are received along some x profile of a two-dimensional anomaly they can be used for quantitative interpretation, because

$$C_W = \left|\frac{h_z}{1 + h_x}\right| \cdot \frac{1}{\cos \arg \dfrac{h_z}{1 + h_x}} \tag{24}$$

where $\cos \arg \left(h_z/(1 + h_x)\right)$ may be taken as one, specially near the maximum of the frequency characteristics of the anomalous field. For a quantitative

interpretation of observations in separate points it is desirable to have theoretical curves of the value $h_z/(1 + h_x)$ (Fanselau and Treumann, 1966).

When processing the Wiese vector one may measure the extremum values instead of the three components at the moment t_0 according to (21) but the phase displacements between the components should be small, not exceeding $\pm 45°$. Then the measured amplitude deviation from $H(t_0)$ and $D(t_0)$ do not exceed 15%, and after statistical averaging there will be a fair coincidence between the a and b values and the result received strictly according to Wiese.

The Parkinson vector (Parkinson, 1959; Rikitake, 1966) is directed opposite to the Wiese vector (for a well-conducting body) it is perpendicular to its strike and its length is proportional to the sine of the angle of the inclination of the plane where variations lie, i.e.

$$\mathbf{C}_p = -\frac{\mathbf{C}_W}{(1 + \mathbf{C}_W)^{1/2}} \tag{25}$$

REFERENCES

Berdichevsky, M. N., 1968. Electrical Prospecting by Magnetotelluric Profiling Methods (in Russian). Nedra, Moscow.

Berdichevsky, M. N., Smirnov, V. S., 1971. On the observation processing methods at magnetic variation profiling (in Russian). *Geomagn. i Aeron.* **11**, No. 2.

Dmitriev, V. I., Zakharov, E. V., Kokotushkin, G. A., 1973. Master Curves for Magnetotelluric Sounding in Inhomogeneous Media (in Russian). 2, Moscow State University.

Fanselau, G., Treumann, R. 1966. Zur geomagnetischen Tiefensondierung. *Pure Appl. Geophys.* **65**, 54.

Kertz, W., 1954. Modelle für erdmagnetisch-induzierte elektrische Ströme im Untergrund. *Nachr. Akad. Wiss. Göttingen Math. Phys. Abt.* IIa, 101.

Parkinson, W. D., 1959. Direction of rapid geomagnetic fluctuations. *Geophys. J. R. Astr. Soc.* **2**, 1.

Rikitake, T., 1966. Electromagnetism and the Earth's Interior. Elsevier, Amsterdam.

Rokityansky, I. I., 1972. Geophysical Methods of Magnetic Variation Sounding and Profiling. Naukova dumka, Kiev.

Schmucker, U., 1970. Anomalies of geomagnetic variations in the southwestern United States. *Bull. Scr. Inst. Oceanogr.* **13**, Univ. of Calif.

Siebert, M., 1962. Die Zerlegung eines zweidimensionalen Magnetfeldes in äußeren und inneren Anteil mit Hilfe der Cauchyschen Integralformel. *Z. Geophys.* **28**, No. 5.

Weaver, I. T., 1964. On the separation of local geomagnetic fields into external and internal parts. *Z. Geophys.* **30**, No. 1.

Wiese, H., 1965. Geomagnetische Tiefentellurik. Akad. Verlag, Berlin.

ELECTROMAGNETIC FIELD COMPONENTS AND MAGNETOTELLURIC SOUNDING CURVES ABOVE HORIZONTALLY INHOMOGENEOUS OR ANISOTROPIC MODEL MEDIA (CATALOGUE OF MODELS)

G. PORSTENDORFER

The following are variants of solution of the Helmholtz equation derived from Maxwell's equations, for the determination of electromagnetic field components for horizontally inhomogeneous media:

1. Analytical solution
2. Solution by finite-difference methods on computers (numerical solution)
3. Solution by modelling on RC-networks
4. Solution by high-frequency modelling in electrolytic troughs.

Exact analytical solutions are known only for relatively simple models. The analytical solution by the method of integral equations allows the electronic computer to treat complicated models and creates the transition to numerical methods of solution. Division of the subsurface into finite elements for complicated models allows both a numerical solution by the finite-difference method on computers and modelling on RC-networks. Finally, there is the possibility of modelling with high-frequency fields for relatively complicated models.

In order to give a survey of model calculations available at present in the international field a catalogue (Table 1 and Fig. 1) has been compiled, which, of course does not claim completeness but is to facilitate the study of the corresponding special literature.

Table 2 and Figure 2 give some additional models, treated by the authors of this monograph.

TABLE 1
Catalogue of models shown in Figure 1

Model	Parameter	Polarization	Way of compution	Author
1	$\varrho_3 = 0$ $\varrho_3 = \infty$	H	Analytic	D'Erceville and Kunetz (1962)
1a	$\varrho_1 = \varrho_1^0 \cdot (a^2 + x^2)$		Analytic	Ashour (1973) (also for model 38)
	$\varrho_3 = 0$ $\varrho_3 = \infty$	H	Analytic	Obukhov (1969d)
	$\varrho_3 = \infty$	H	Analytic	Koshchlakov (1970)
	$\varrho_3 = \infty$	E	Analytic	Treumann (1970)
	$h = \infty$	H and E	Analytic	Thomson and Weaver (1971)
2	$\varrho_3 = \infty$ $\varrho_3 = 0$	H	Analytic	Rankin (1962)
	$\varrho_3 = \infty$	E	Analytic	Treumann (1970)
3		H	Analytic	Berdichevsky and Dmitriev (1969) Dmitriev and Kokotushkin (1971)
	$\varrho_2 = \infty$	H	Analytic	Kunetz and De Gery (1952)
	$\varrho_2 = \infty$	H	Analytic	Naake (1964)
	$\varrho_2 = 0$	E	Analytic	Schmucker (1970)
4		H	Analytic	Kokotushkin and Dmitriev (1963, 1971)
		H and E	Electrolytic trough	Bryunelli et al. (1963), Dobrovolskaya and Kovtun (1970)
5		H and E	Electrolytic trough	Bryunelli et al. (1963)
5a	$\varrho_2 = \infty$	H	Analytic	Dmitriev and Kokotushkin (1971)
5b	$\varrho_2 = \infty$	H	Analytic	Dmitriev and Kokotushkin (1971)

(TABLE 1 CONT.)

Model	Parameter	Polarization	Way of computation	Author
		E, *H*	Analytic	Schmucker and Jankowski (1972)
5c	$\varrho_2 = \infty$, $\varrho_3 = 0$	*E*	Analytic	Dmitriev and Kokotushkin (1971)
5d	$\varrho_2 = \infty$, $\varrho_3 = 0$	*E*	Analytic	Dmitriev and Kokotushkin (1971)
6	$\varrho_2 = \infty$	*H*	Analytic	Kunetz and De Gery (1952), Mann (1964), Obukhov (1969c)
		H and *E*		
6a		*E*, *H*	Analytic	Kaufmann and Tabarovsky (1970)
7		*H*	Analytic	Dmitriev (1965)
8		*H*	Analytic	Obukhov (1965)
9	$0 < \alpha < 2\pi$ $\varrho_2 = \infty$ $\varrho_1 = 0$	*H* and *E*	Analytic	Kovtun (1964)
		H	Numerical	Červ and Praus (1972)
		H and *E*	Electrolytic trough	Bryunelli et al. (1963)
	$\alpha = 3°$, $\varrho_2 = \infty$	*H* and *E*	Analytic	Berdichevsky (1961, 1968)
	$\alpha < 9°$		Analytic	Kostecki (1969)
10		*H* and *E*	Analytic	Berdichevsky (1969)
		H and *E*	Electrolytic trough	Bryunelli et al. (1963)
11		*H* and *E*	Analytic	Berdichevsky (1969)
12		*H* and *E*	Electrolytic trough	Dobrovolskaya and Kovtun (1970)
13		*H* and *E*	Electrolytic trough	Dobrovolskaya and Kovtun (1970)
14		*H* and *E*	Electrolytic trough	Dobrovolskaya and Kovtun (1970)

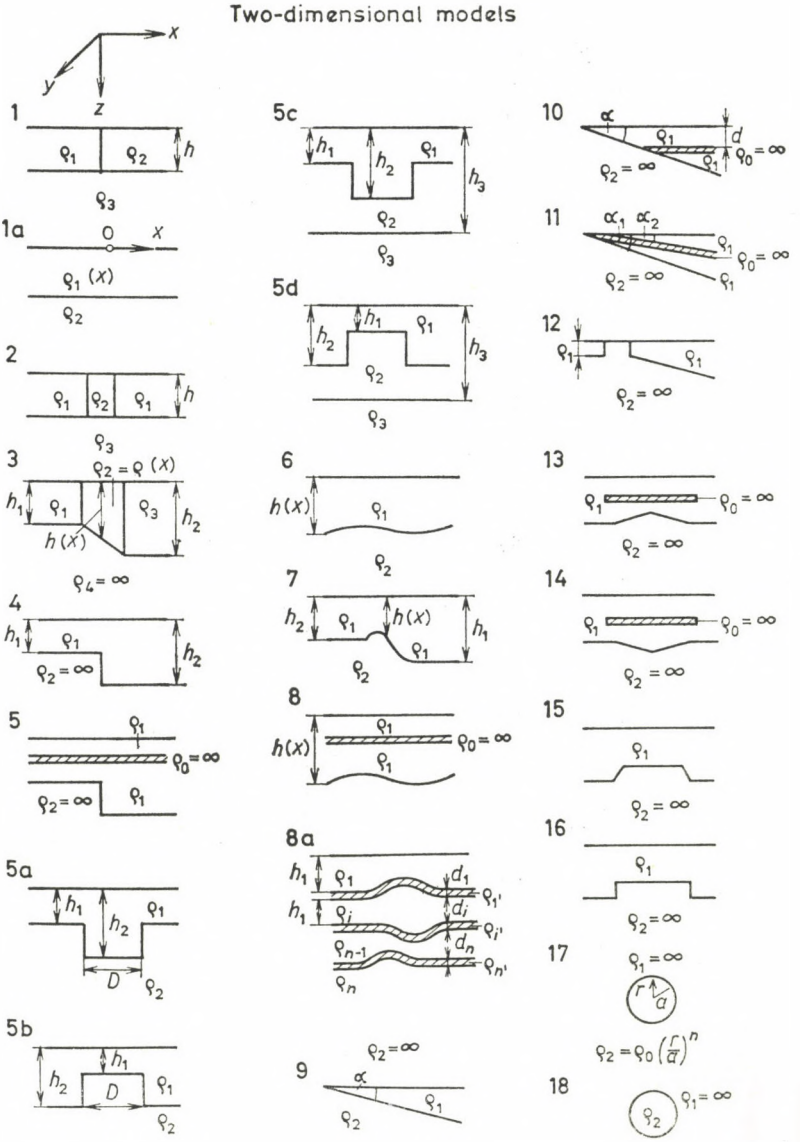
(TABLE 1 CONT.)

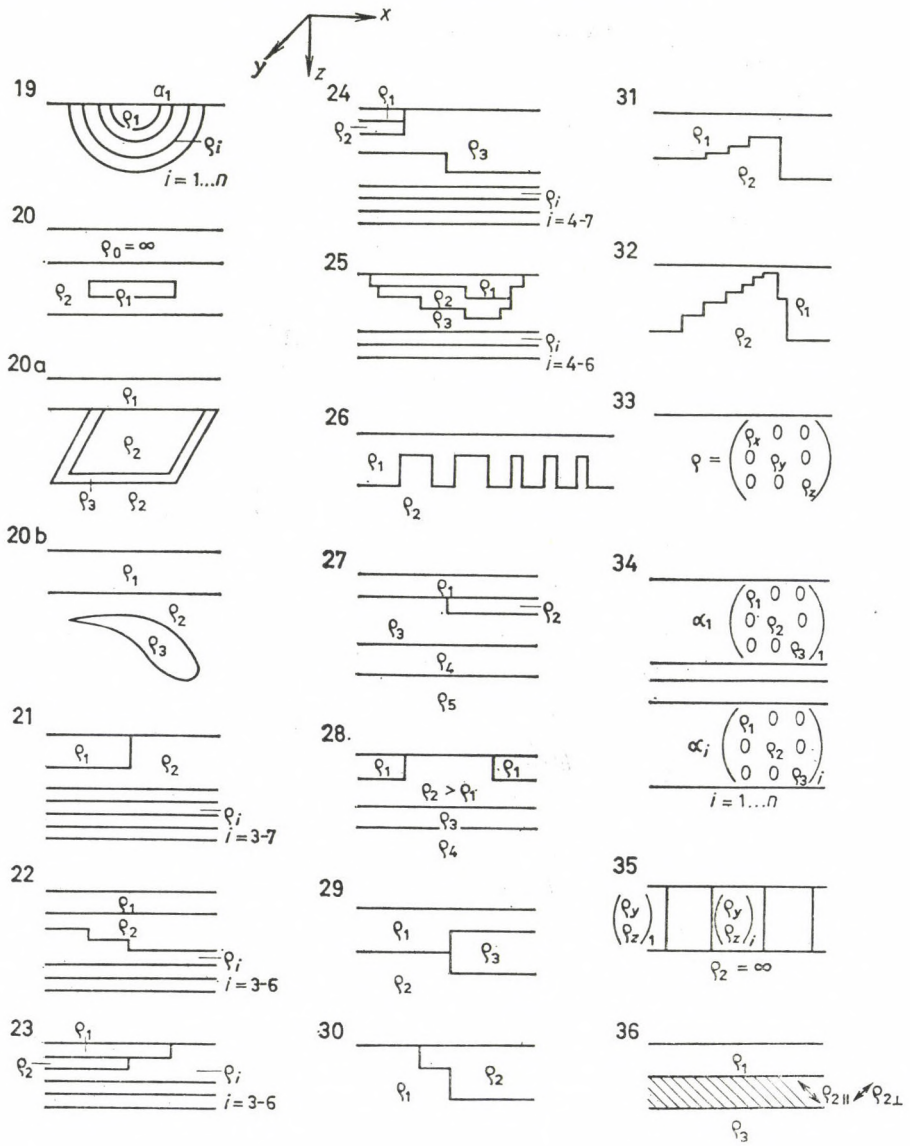
Model	Parameter	Polarization	Way of computation	Author
15		H and E	Electrolytic trough	Dobrovolskaya and Kovtun (1970)
16		H and E	Electrolytic trough	Bryunelli et al. (1969)
17		E	Analytic	v. Consbruch (1963)
18		E and H	Analytic	Hvoždara (1972)
		E and H	Analytic	Meyer (1963)
19		H	Analytic	Obukhov (1969b)
				Hobbs (1972)
20		E	Numerical	Latka (1966)
			Analytic	Jones and Price (1970)
		E	Electrolytic trough	Dosso (1966)
20a		H	Numerical	Silvester and Haslam (1972)
20b		H and E	Numerical	Silvester and Haslam (1972)
21		H and E	Numerical	Wright (1969)
22		H and E	Numerical	Wright (1969)
23		H and E	Numerical	Wright (1969)
24		H and E	Numerical	Wright (1969)
25		H and E	Numerical	Wright (1969)
				Schmucker and Jankowski (1972)
26		H and E	Numerical	Vozoff and Swift (1968)
27		E	Numerical	Geoscience Inc. (1969)
28	$\varrho_4 = 0$	H	RC-network	Taheri (1968)
	$\varrho_4 = \infty$	H		
29		E	Numerical	Vozoff and Swift (1968)
				Cox and Filloux (1973)

(TABLE 1 CONT.)

Model	Parameter	Polarization	Way of computation	Author
30		*E*	Numerical	Vozoff and Swift (1968)
31		*E*	Numerical	Vozoff and Swift (1968)
32		*E*	Numerical	Vozoff and Swift (1968)
33		*E* and *H*	Analytic	Petr (1967)
34		*E* and *H*	Analytic	Petr (1967) Ádám et al. (1972)
		E and *H*	Analytic	Puchkov (1965)
		E and *H*	Analytic	Douglas et al. (1967)
35		*H*	Analytic	Obukhov (1969a)
36		*H*	Analytic	Negi and Saraf (1972)
		H and *E*	Numerical	Geoscience Inc. (1969)
37	Three-dimensional		Analytic	Obukhov (1969c)
38	Three-dimensional		Analytic	Schmucker (1970), Berdichevsky et al. (1972), Negi et al. (1973), Wait (1973)
39	Three-dimensional		Electrolytic trough	Dobrovolskaya and Kovtun (1970)
40	Three-dimensional	*E* and *H*	Numerical	Jones (1973)
41	Three-dimensional	*E* and *H*	Analytic	Kaufman et al. (1971 a, b)

Two-dimensional models




x
y
z
19
α_1
ϱ_1
ϱ_i
$i = 1...n$
20
$\varrho_0 = \infty$
ϱ_2
ϱ_1
20a
ϱ_1
ϱ_2
ϱ_3
ϱ_2
20b
ϱ_1
ϱ_2
ϱ_3
21
ϱ_1
ϱ_2
ϱ_i
$i = 3-7$
22
ϱ_1
ϱ_2
ϱ_i
$i = 3-6$
23
ϱ_1
ϱ_2
ϱ_i
$i = 3-6$
24
ϱ_1
ϱ_2
ϱ_3
ϱ_i
$i = 4-7$
25
ϱ_2
ϱ_1
ϱ_3
ϱ_i
$i = 4-6$
26
ϱ_1
ϱ_2
27
ϱ_1
ϱ_2
ϱ_3
ϱ_4
ϱ_5
28
ϱ_1
ϱ_1
$\varrho_2 > \varrho_1$
ϱ_3
ϱ_4
29
ϱ_1
ϱ_3
ϱ_2
30
ϱ_1
ϱ_2
31
ϱ_1
ϱ_2
32
ϱ_1
ϱ_2
33
$\varrho = \begin{pmatrix} \varrho_x & 0 & 0 \\ 0 & \varrho_y & 0 \\ 0 & 0 & \varrho_z \end{pmatrix}$
34
$\alpha_1 \begin{pmatrix} \varrho_1 & 0 & 0 \\ 0 & \varrho_2 & 0 \\ 0 & 0 & \varrho_3 \end{pmatrix}_1$
$\alpha_i \begin{pmatrix} \varrho_1 & 0 & 0 \\ 0 & \varrho_2 & 0 \\ 0 & 0 & \varrho_3 \end{pmatrix}_i$
$i = 1...n$
35
$\begin{pmatrix} \varrho_y \\ \varrho_z \end{pmatrix}_1$
$\begin{pmatrix} \varrho_y \\ \varrho_z \end{pmatrix}_i$
$\varrho_2 = \infty$
36
ϱ_1
$\varrho_{2\parallel}$ $\varrho_{2\perp}$
ϱ_3

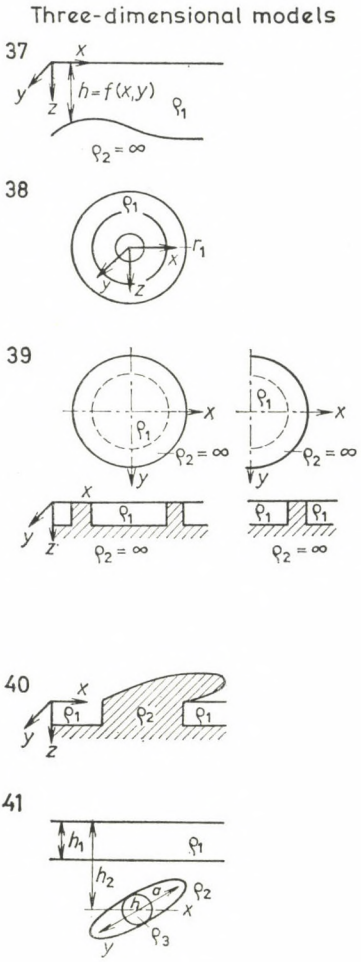


Fig. 1. Catalogue of the models for two- and three-dimensional, inhomogeneous and anisotropic subsurfaces, which were treated in the international literature, supplemented according to Porstendorfer (1975)

TABLE 2

Catalogue of models treated in this monograph (see also Fig. 2)

Model No.	Parameter	Polarization	Way of computation	Author
2	Thin sheets Plates with lateral non-uniformities		Analytic	Treumann
2a		*E* and *H*	Analytic	Berdichevsky and Dmitriev

(TABLE 2 CONT.)

Model No.	Parameter	Polarization	Way of computation	Author
3a		E and H	Analytic	Berdichevsky and Dmitriev
3b		E and H	Analytic	Berdichevsky and Dmitriev
5c		E and H	Analytic	Berdichevsky and Dmitriev
5d		E and H	Analytic	Berdichevsky and Dmitriev
5e		E and H	Analytic	Berdichevsky and Dmitriev
5f		E and H	Analytic	Berdichevsky and Dmitriev
7a		E and H	Analytic	Berdichevsky and Dmitriev
9		E and H	Numerical	Praus
9a		E and H	Numerical	Praus
9b	$\varrho_1 = \varrho_2$	E and H	Numerical	Praus
15		E and H	Electrolytic trough	Dobrovolskaya and Kovtun
16		E and H	Electrolytic trough	Dobrovolskaya and Kovtun
20a		E and H	Analytic	Berdichevsky and Dmitriev
25a		E and H	Analytic	Berdichevsky and Dmitriev
34		E and H	Analytic	Petr
37	Three-dimensional		Analytic	Treumann
39	Three-dimensional		Electrolytic trough	Dobrovolskaya and Kovtun
39a	Three-dimensional		Electrolytic trough	Dobrovolskaya and Kovtun
39b	Three-dimensional		Electrolytic trough	Dobrovolskaya and Kovtun

(TABLE 2 CONT.)

Model No.	Parameter	Polarization	Way of computation	Author
39c	Three-dimensional		Electrolytic trough	Dobrovolskaya and Kovtun
40a	Three-dimensional		Analytic	Berdichevsky and Dmitriev
41	Three-dimensional		Analytic	Berdichevsky and Dmitriev

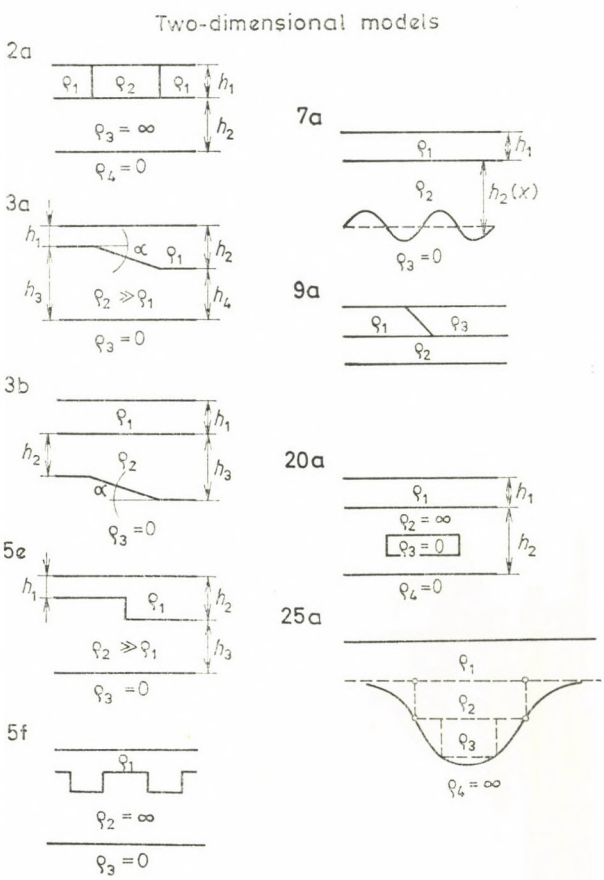


Fig. 2. Catalogue of horizontally inhomogeneous and anisotropic models which were treated in this monograph

REFERENCES

ÁDÁM, A., VARGA, G., VERŐ, J., 1972. Computation of anisotropic models for the magnetotelluric sounding curves of the Carpathian Basin. *Acta Geod. Geophys. Mont. Hung.* **7**, 125–136.

ASHOUR, A. A., 1973. Exact solutions for certain axi-symmetric problems of induction in thin non-uniform sheets. Abstr. IAGA Congr. Kyoto.

BERDICHEVSKY, M. N., 1961. Magnetotelluric field in a horizontally inhomogeneous medium (in Russian). *Prikl. Geofiz.* **31**, 136–164.

BERDICHEVSKY, M. N., 1968. Electrical prospecting with the method of magnetotelluric profiling (in Russian). Nedra, Moscow.

BERDICHEVSKY, M. N., 1969. Magnetotelluric field at the surface of a dipping layer, containing a non-conducting layer (in Russian). Magnitotellurichеskie Metody Izucheniya Stroeniya Zemnoi Kory i Verkhnei Mantii. 4, 113–119.

BERDICHEVSKY, M. N., DMITRIEV, V. I., 1969. Magnetotelluric field over a dipping high-resistance base (in Russian). Magnitotellurichеskie Metody Izucheniya Stroeniya Zemnoi Kory i Verkhnei Mantii. 4, 71–78.

BERDICHEVSKY, M. N., DMITRIEV, V. I., MERSHCHIKOVA, N. A., ROTANOVA, J. M., 1972. Magnetotelluric sounding curves for a spherical layered earth (in Russian). Gos. Univ. Moscow.

BRYUNELLI, B. E., DOBROVOLSKAYA, M. A., KOVTUN, A. A., KUZNETSOV, N. S., 1963. Magnetotelluric profiling over models with horizontal-inhomogeneous structure (in Russian). Novye Metody Elektricheskoi Razvedki na Neft i Gaz, Gostoptekhisdat, Moscow, 114–119.

BRYUNELLI, B. E., DOBROVOLSKAYA, M. A., KOVTUN, A. A., KUZNETSOV, N. S., 1969. Some results of MTP and MTS over models of inhomogeneous structures (in Russian). Magnitotellurichеskie Metody Izucheniya Stroeniya Zemnoi Kory i Verkhnei Mantii. 4, 125–129.

ČERV, V., PRAUS, O., 1972. MT-field of H-polarization in models with dipping interfaces. *Studia Geophys. Geod. ČSAV*, **16**, 285–291.

CONSBRUCH, C. v., 1963. Elektromagnetische Induktion im Zylinder räumlich variabler Leitfähigkeit. Dissertation, Ludwig Maximilian Univ. München.

COX, C. S., FILLOUX, J. H. F., 1973. Two-dimensional mathematical models of the California electromagnetic coastal anomaly. Abstr. IAGA Congr. Kyoto.

DMITRIEV, V. I., 1965. Method of computation of the magnetotelluric field over an inhomogeneous subsoil with variation of the surface of the final layer (in Russian). *Prikl. Geofiz.* **41**, 73–85.

DMITRIEV, V. I., KOKOTUSHKIN, G. A., 1971. Magnetotelluric sounding curves for inhomogeneous media (in Russian). Gos. Univ. Moscow.

DOBROVOLSKAYA, M. A., KOVTUN, A. A., 1970. Modellierung natürlicher elektromagnetischer Felder in horizontal-inhomogenen Medien. Akad. Nauk SSSR, Geophys. Comm. Leningrad.

DOSSO, H. W., 1966. Analogue model measurements for electromagnetic variations near vertical faults and dikes. *Can. J. Earth Sci.* **3**, 287–325.

DOUGLAS, P. D., O'BRIEN, P., MORRISON, H. F., 1967. Electromagnetic fields in an n-layer anisotropic half-space. *Geophysics* **32**, 668–677.

D'ERCEVILLE, I., KUNETZ, G., 1962. The effect of a fault on the earth's electromagnetic field. *Geophysics* **27**, 651–655.

HOBBS, B. A., 1972. Research Note: A comment on certain papers involving electromagnetic induction in uniformly-conducting hemispheric shells. *Geophys. J. R. Astr. Soc.* **29**, 109–115.

HVOŽDARA, M., 1972. Electromagnetic induction in a half-space with a cylindrical inhomogeneity. *Studia Geophys. Geod. ČAV*, **16**, 240–261.

JONES, F. W., 1972. The electromagnetic perturbation fields of conductivity anomalies within the Earth. *Geophys. J. R. Astr. Soc.* **30**. 211–218.

JONES, F. W., 1974. The effect of an island and bay structure on alternating geomagnetic fields at three periods. *Geophys. J. R. Astr. Soc.* **36**, 627–639.

JONES, F. W., PRICE, A. T., 1970. The geomagnetic effects of two-dimensional conductivity inhomogeneities at different depths. *Geophys. J. R. Astr. Soc.* **22**, 333–345.

JANKOWSKI, J., 1972. Techniques and results of magnetotelluric and geomagnetic deep soundings. Publ. of the Inst. Geophys. Polish Acad. Sci. No. 54.

KAUFMANN, A. A., TABOROVSKY, L. A., 1970. Basic Theory of Magnetotelluric Sounding Over Layers with Dipping Structures (in Russian). Novosibirsk.

KAUFMANN, A. A., TABOROVSKY, L. A., TERENTEV, S. A., 1971a. Electromagnetic Field of an Elliptical Cylinder in a Horizontal-layered Medium (in Russian). Novosibirsk.

KAUFMANN, A. A., KRIVOPUTSKY, V. S., TABOROVSKY, L. A., 1971b. Electromagnetic Field of a Conducting Spheroid in a Horizontal-layered Medium (in Russian). Novosibirsk.

KOKOTUSHKIN, G. A., DMITRIEV, V. I., 1963. Magnetotelluric field over a layer with a step-like structure (in Russian). *Prikl. Geofiz.* **52,** 104–110.

KOSHCHLAKOV, G. V., 1970. Effect of a vertical contact on magnetotelluric soundings (in Russian). *Geol. i Geofiz.* **11,** No. 31. 119–122.

KOSTECKI, A., 1969. Magnetotelluric field over a dipping bed conducting subsurface (in Russian). *Acta Geophys. Polon.* **17,** 67–73.

KOVTUN, A. A., 1964. Character of the electromagnetic field over an ideal conducting wedge in the range of low frequency (in Russian). *Voprosy Geofiziki, Gos. Univ. Leningrad,* 17–26.

KUNETZ, G., DE GERY, C., 1952. Exemples d'application de la representation conforme à l'interpretation du champ tellurique. EAEG-meeting Paper, Hannover.

LATKA, R., 1966. Modellrechnungen zur Induktion im elektrisch leitfähigen Untergrund. *Z. Geophys.* **32,** 12–17.

MANN, J. E., 1964. Magnetotelluric theory of the sinusoidal interface. *J. Geophys. Res.* **69,** 3517.

MEYER, L., 1963. Elektromagnetische Induktion in einem leitenden homogenen Zylinder durch äußere magnetische und elektrische Wechselfelder. *Mitt. Max Planck Inst. f. Aeron.* **13,** 67.

NAAKE, L., 1964. Die Programmierung geophysikalischer Auswerteprobleme und gravimetrischen und tellurischen Beispielen. Diplomarbeit, Inst. Angew. Geophys., Bergakademie Freiberg.

NEGI, J. G., GUPTA, C. P., RAVAL, U., 1973. Electromagnetic response of a permeable inhomogeneous conducting sphere. *Geoexploration* **11,** 1–20.

NEGI, J. G., SARAF, P. D., 1972. Impedance of a plane electromagnetic wave at the surface of a layered conducting earth with dipping anisotropy. *Geophys. Prosp.* **20,** 785–799.

OBUKHOV, G. G., 1965. Magnetotelluric field over shielded structures (H-polarization) (in Russian). *Prikl. Geofiz.* **44,** 112–126.

OBUKHOV, G. G., 1969a. Magnetotelluric field in horizontally inhomogeneous anisotropic media (in Russian). Magnitotellurichеskie Metody Izucheniya Stroeniya Zemnoi Kory i Verkhnei Mantii, 4, 106–112.

OBUKHOV, G. G., 1969b. Magnetotelluric field of inhomogeneous conducting layers with cylindrical surface (in Russian). Magnitotellurichеskie Metody Izucheniya Stroeniya Zemnoi Kory i Verkhnei Mantii, 4, 101–105.

OBUKHOV, G. G., 1969c. Approximation methods of investigation of the magnetotelluric field over horizontal-inhomogeneous media (in Russian). Magnitotellurichеskie Metody Izucheniya Stroeniya Zemnoi Kory i Verkhnei Mantii, 4, 79–88.

OBUKHOV, G. G., 1969d. The magnetotelluric field over horizontally inhomogeneous media with an ideal conducting base (in Russian). Magnitotellurichеskie Metody Izucheniya Stroeniya Zemnoi Kory i Verkhnei Mantii, 4, 95–100.

PETR, V., 1967. Impedanz des magnetotellurischen Feldes im geschichteten anisotropen Halbraum. *Studia geophys. geod. ČSAV,* **11,** 291–303.

PORSTENDORFER, G., 1975. Principles of magnetotelluric prospecting. (Geoexploration Monographs Series 1, No. 5, Geopublication Associates.)

PUCHKOV, G. G., 1965. Magnetotelluric field in anisotropic layers (in Russian). *Geol. Geofiz.* **7,** 68–81.

RANKIN, D., 1962. The magnetotelluric effect on a dike. *Geophysics* **27,** 666–676.

SCHMUCKER, U., 1970. Anomalies of geomagnetic variations in the south-western United States. *B. of Scripps Institution of Oceanography of Univ. Calif.,* **13.**

SCHMUCKER, U., JANKOWSKI, J., 1972. Geomagnetic induction studies and the electrical state of the upper mantle. *Tectonophysics* **13,** 233–256.

SILVESTER, P., HASLAM, C. R. S., 1972. Magnetotelluric modelling by the finite element method. *Geophys. Prosp.* **20,** 872–891.

TAHERI, F., 1968. Interpretation de mesures du champ tellurique au moyen de réseaux analogiques à resistances et capacites. Thèse a la faculté des sciences de Paris.
THOMSON, D. I., WEAVER, I. T., 1971. A solution of the "Coastline-effect". XV. IUGG Meeting Moscow.
TREUMANN, R., 1970. Electromagnetic induction in inhomogeneous media (E-polarization). *Acta Geod. Geophys. Mont. Hung.* **5**, 61–67.
VOZOFF, K., SWIFT, C. M., 1968. Magnetotelluric measurements in the north German basin. *Geophys. Prosp.* **16**, 454–473.
WAIT, I. R., 1959. The calculation of the field in a homogeneous conductor with a wavy interface. *Proc. IRE*, **47**, 1155.
WAIT, I. R., 1973. Electromagnetic induction in conductive shells. *Can. J. Phys.* **51**, 209–218.
WRIGHT, I. A., 1969. The magnetotelluric and geomagnetic response of two-dimensional structures. *Gamma*, **7**.
Geoscience Incorporated, 1969. Magnetotellurics in Petroleum Exploration.

BASIC PRINCIPLES OF INTERPRETATION OF MAGNETOTELLURIC SOUNDING CURVES

M. N. BERDICHEVSKY, V. I. DMITRIEV

INTRODUCTION

The method of magnetotelluric sounding (MTS), initiated by Tikhonov, is successfully applied in the USSR and in a number of other countries. MTS curves are usually interpreted by means of horizontally homogeneous models. This interpretation will be called *formal interpretation.* It is self-evident that formal interpretation produces good results when horizontal inhomogeneities do not essentially distort the electromagnetic field. However, such favourable conditions are rare. The geophysicist is more often confronted with strong geoelectric inhomogeneities distorting the electromagnetic field. This paper, therefore, deals with interpretation of results of deep magnetotelluric sounding in horizontally inhomogeneous media.

Let us consider the horizontally inhomogeneous model of the Earth with a three-dimensional distribution of resistivity $\varrho(x, y, z)$. In a point $M(x_M, y_M, 0)$ located on the earth's surface the MTS curve ϱ_a is obtained. This curve will be thought of as being undistorted, if it differs only slightly from the normal curve, i.e. the curve calculated for the normal model. As a normal model the horizontally homogeneous model with one-dimensional distribution of the resistivity $\varrho_M(z) = \varrho(x_M, y_M, z)$ will be considered, where $\varrho_M(z)$ agrees with the resistivity distribution of the horizontally inhomogeneous model in point M. If a curve ϱ_a substantially diverges from the normal one, it will be regarded as distorted. The normal and distorted resistivity curves are designated as ϱ_N and ϱ_T.

The deviation of ϱ_T from ϱ_N characterizes the degree of influence of horizontal geoelectrical inhomogeneities on the MTS results. This is the measure of distortion for MTS curves. An indication of distortion of the MTS curves is their dependence on the directions in which the components of the electromagnetic field are measured. If the MTS curves are not distorted, then with the turn of the measuring lines they remain practically unchanged.

The geophysicists are well aware of the difficulties of interpretation of distorted MTS curves. Since MTS curves depend on the orientation of the measuring lines, their formal interpretation gives different geoelectrical sections for the same point. The problem is to construct a reliable geoelectric section on the basis of numerous contradicting results through selection or averaging. Such constructions are only possible, if we have criteria that allow distinguishing distorted results from undistorted ones. These criteria have been worked out on the basis of a theoretical analysis of distortions of the electromagnetic field in horizontally inhomogeneous media. Until recently our knowledge of the character of field distortions was very poor and the MTS practice abounded in examples of uncon-

vincing, voluntaristic interpretations discrediting the possibilities of the method.

The aim of this paper is to show the ways to practical solution of the inverse MTS problem in horizontally inhomogeneous media. This problem was discussed by many authors (in the Soviet-Union Tikhonov, Dmitriev, Berdichevsky, Kaufman, Kovtun, Kokotushkin, Zakharov, Taborovsky, Obukhov, in France Kunetz, in Japan Rikitake, in the U.K. Price, in Canada Jones, Rankin, in the USA Swift, in Czechoslovakia Praus, in the GDR Porstendorfer, in Hungary Ádám). Our work is based mainly on the results obtained at the Moscow State University.

1. CLASSIFICATION OF DISTORTIONS OF MTS CURVES

The observations of short-period and baylike disturbances, yielding most of the materials for the MTS, show that in the temperate latitudes the external field slightly changes at distances of 100–200 km along the meridian and of 300–500 km along the latitude (see pp. 296–302). This determines the size of the region within which the application of models with a plane wave as an external field seems justified (Berdichevsky et al., 1971; Madden and Swift, 1969). In the present state of the art such models are of basic importance, since they give us a rather good idea of the properties of the field in horizontally inhomogeneous media. Numerous experimental data confirm the practical validity of application of such models that disregard the transversal magnetic mode of the external field, connected with the vertical currents in the atmosphere (Tikhonov and Berdichevsky, 1966).

Let us consider the horizontally homogeneous model excited by a plane wave (Tikhonov and Shakhsuvarov, 1956; Cagniard, 1953). The eddy field appearing in this model will be taken as the primary one. The structure of this field is simple: the current flows along the strata, no charges are brought about, MTS curves do not depend on the direction of the measuring lines, they reflect vertical changes of electrical conductivity.

Quite another picture is observed when the plane wave excites a horizontally inhomogeneous model. In this case excessive charges and currents appear forming the anomalous (secondary) field. Since no charges occur in the normal model, the charges appearing in case of inhomogeneity are excessive. To determine the excessive currents, one has to find the difference between the currents in the horizontally inhomogeneous model and the normal model.

Due to the excessive charges and currents, the MTS curves become distorted. They reflect not only vertical, but also horizontal changes of electrical conductivity.

The practice of interpretation of MTS curves calls for a classification of their distortions (Berdichevsky et al., 1973b). The elaboration of such a classification encounters many difficulties, for the anomalous electromagnetic field is a complicated physical phenomenon in which excessive currents and charges interact. To overcome these difficulties a number of simplifications must be introduced to distinguish the effect of excessive charges and of currents. The main simplification is a conditional division

of the anomalous electromagnetic field into two parts: one excited by excessive charges and called "galvanic", and the second excited by excessive currents and called "inductional" (Kaufman, 1961; Svetov and Petrovsky, 1966). Accordingly, one can speak about galvanic and induction effects of the inhomogeneities. Following this classification, the distortions of the MTS curves can be reduced to the following two types:

a) distortions of galvanic type, or galvanic effects;

b) distortions of the induction type, or induction effects.

Besides, *surface and deep effects should be distinguished*, associated with the influence of surface and deep inhomogeneities.

Concurrent with the above division of distortions by genetic characteristics, it is useful to introduce a classification incorporating the *character of influence of distortions on the results of interpretation of the MTS curves*, i.e. to distinguish distortions from the interpretation point of view. Within this classification three types of effects are considered:

a) effects smoothing out the changes of the deep geoelectric section;

b) effects causing the appearance of false layers in the section;

c) effects producing false structures in the relief of deep geoelectric boundaries.

The smoothing effects are characteristic of most of the geophysical methods, while the effects creating false layers and false structures are specific to deep MTS and are the most dangerous. These very effects are the object of our study.

While analyzing the distortions, we shall need the notion of galvanic and induction connections between layers. Layers are galvanically connected, if the current flows from one layer to another. The induction connection between layers is expressed in a mutual induction of currents flowing in these layers.

Our terminology is very convenient for practical purposes, though it is not without certain contradictions.

*

We shall begin the analysis of the distortions of the MTS curves with the easiest situation observed in regions of *linear elongated structures*, where the relation between the galvanic and the induction parts of the anomalous field depends substantially on the direction of the primary current.

For an analysis of this dependence we introduce the notion of *oriented MTS curves*. It is known that on the surface of the inhomogeneous medium the impedance is a tensor of components $\mathbf{Z_{xx}}$, $\mathbf{Z_{xy}}$, $\mathbf{Z_{yx}}$, $\mathbf{Z_{yy}}$ (Berdichevsky, 1968). The MTS curves are computed from the basic components Z_{xy}, Z_{yx}; correspondingly, we obtain ϱ_{xy} and ϱ_{yx}. The ϱ_{xy}-curve is assumed to be oriented along the x-axis, while ϱ_{yx} along the y-axis; thus, the orientation of a MTS curve is determined by the first index of the component of the impedance tensor.

MTS curves oriented across and along characteristic tectonic lines are called transversal and longitudinal curves, respectively, and are designated

as $\varrho^{\perp}$ and $\varrho^{\parallel}$. In case of linear elongated structures the axes of the structures are such tectonic lines. Here transversal and longitudinal MTS curves correspond to the flow of the current across and along the structures. In theoretical descriptions of elongated structures by two-dimensional inhomogeneous models the transversal and longitudinal MTS curves correspond to the H and E-polarized field.

Let the current flow across the structure *(H-polarization)*. The structure becomes charged. Excessive currents form long solenoids whose axes are parallel to the structure. Their effect is insignificant. The anomalous field is associated mainly with charges, i.e. its nature is galvanic. Consequently, for the transversal MTS curves distortions of galvanic type are characteristic (galvanic effects). The most important are two effects: the S-effect and the screening effect.

The S-effect is observed in media containing an intermediate high-resistance layer. This surface effect is manifested in the fact that due to the break of galvanic connection between the upper and the lower parts of the section the transversal impedance in the low-frequency band retains dependence on the total longitudinal conductivity S of the upper part of the section (in the normal model such dependence disappears with the decrease of frequency). Formal interpretation of the MTS curves, distorted by the S-effect, results in the appearance of false structures in the relief of deep geoelectric boundaries.

The S-effect is accompanied by the screening effect. This deep effect is connected with the screening action of the high-resistance intermediate layer. It is expressed in the fact that due to the break of the galvanic connection the transversal impedance has small reaction to the change of the lower part of the section. Formal interpretation of the MTS curves, distorted by the screening effect, levels the relief of deep geoelectric boundaries.

In the case, when the current flows along the structure *(E-polarization)*, the structure becomes much less charged, than when the current flows transversally, and its galvanic effect is small (when the length of the structure is infinite, excessive charges are completely absent). Excessive currents are linear and parallel to the structure. Their effect is considerable: the anomalous field is mainly of inductional character. Therefore, for the longitudinal MTS curves distortions of the induction type are characteristic (induction effects). These effects can be either surface or deep.

The peculiarity of surface induction effects lies in the fact that a decrease of frequency increases the contribution of excessive currents flowing far from the observation site. There is, therefore, an interval of low frequencies, within which the impedance has an increased sensitivity to the changes of electrical conductivity of the upper layers in distant zones. Formal interpretation of MTS curves distorted by the *surface induction effects* (i.e. by the influence of neighbouring structures) misrepresents the upper part of the geoelectrical section, it can even indicate the appearance of false conducting layers.

*

We proceed now to a more difficult situation observed in regions of *nonlinear structures*. In this case all the above effects are present, in a weaker form, though. New effects become more important. They are connected with the fact that the current flows around resistive structures *(flow-around effect)* and is concentrated in highly-conducting structures *(concentration effect)*. These surface effects belong, evidently, to the galvanic ones. Formal interpretation of the MTS curves distorted by flow-around and concentration effects misrepresents the upper part of the section and produces a false relief of deep geoelectric boundaries.

All these forms of distortions and means of their detection will be discussed in detail in the relevant parts of our work.

2.A. THEORETICAL PROBLEMS OF MAGNETOTELLURIC SOUNDING

The theory of magnetotelluric sounding of horizontally inhomogeneous media has a number of peculiarities.

The specificity of MTS is, first of all that we study multilayered media with local embeddings and infinitely extensive arbitrary interfaces. This is a new branch of the electrodynamics of inhomogeneous media, which has intensively been developing during the last few years due to problems of geoelectrics and geomagnetism.

Deep geoelectrical surveys measure the low-frequency fields (down from the tenth of a Hz). This is another specific aspect of the MTS problems.

It is more convenient to describe the low-frequency fields in a limited region of space by means of a quasi-stationary approximation, i.e. by disregarding the displacement currents. Neglecting displacement currents in the conducting layers of the earth is obviously justified, since here the dominant role is played by the conduction currents. The situation is much more complicated with the air and the non-conducting layers of the earth. Here neglecting the displacement currents is justified by the fact that the region important for the secondary electromagnetic field is smaller than the wave length. Many difficulties arise, however, in this case in connection with the determination of the primary field and with conditions on infinity. The mathematical formulation of the problem easily overcomes these difficulties, if we initially assume that the air and the non-conducting layers of the earth have a finite resistivity ϱ_0 and in the final calculation formulae we change to the limit $\varrho_0 \to \infty$. It should be noted that in this formulation the condition of radiation on infinity is substituted by the more convenient condition of absorption of the anomalous field.

One-dimensional and two-dimensional problems are most frequently studied. In these problems the specific resistance of the earth changes only along one or two coordinates; for example, along z oriented downwards or y and z, while the external field is a plane wave normally incident to the earth's surface. We can confine ourselves to the two-dimensional problem, because the one-dimensional problem is its particular case.

*

In the *two-dimensional* problem the field is constant along the x-axis. Such an axis is called the axis of homogeneity ($\partial/\partial x \equiv 0$). The total electromagnetic field splits into two independent modes:

1. H-polarized field (the magnetic field is directed along the homogeneity axis). Here $\mathbf{H} = \{H_x, 0, 0\}$, $\mathbf{E} = \{0, E_y, E_z\}$.

2. E-polarized field (the electric field is directed along the homogeneity axis). Here $\mathbf{H} = \{0, H_y, H_z\}$, $\mathbf{E} = \{E_x, 0, 0\}$.

The H- and E-polarized field components are expressed by the derivatives of the functions H_x and E_x, respectively:

$$E_y = \varrho \frac{\partial H_x}{\partial z}, \quad E_z = -\varrho \frac{\partial Hx}{\partial y}, \quad H_y = \frac{1}{i\omega\mu} \frac{\partial E_x}{\partial z}, \quad H_z = -\frac{1}{i\omega\mu} \frac{\partial E_x}{\partial y}$$

where ϱ is the specific resistance of the medium, μ the magnetic permeability, ω is circular frequency.

For the x-components of the field we obtain the following scalar problems.

I. *In case of H-polarization* the H_x function satisfies the equation

$$\operatorname{div}(\varrho \operatorname{grad} H_x) - k^2 \varrho H_x = 0 \tag{1}$$

where $k = \sqrt{-i\omega\mu/\varrho}$ is the wave number. The H_x function and $\varrho(\partial H_x/\partial n)$ are continuous at the boundaries of the layers ($\mathbf{n}$ is the normal to these boundaries). The condition for infinity is the decrease of the function $H_x - H_x^0$, where H_x^0 is the external field.

The formulation of this problem has an interesting feature, connected with the infinitely high resistivity of the air. In fact, if $\varrho_0 \to \infty$ and $\varrho(\partial H_x/\partial z)$ is everywhere continuous, then on the earth's surface (from the air side) the condition $\partial H_x/\partial z \to 0$ should be satisfied. This condition allows to analyze two independent problems relating, respectively, to the air and to the earth.

For the air we have

$$\Delta H_x - k_0^2 H_x = 0$$

with $-\infty < y < \infty$, $-\infty < z < 0$.

Here the boundary condition is $\partial H_x/\partial z = 0$, with $z = 0$ while in the infinity we have the condition $H_x - H_x^0 \to 0$ with $z \to -\infty$, where $H_x^0 = H_0 e^{-k_0 z}$.

The solution to this problem is the function

$$H_x(z) = H_0(e^{-k_0 z} + e^{k_0 z})$$

Therefore, with $z = 0$

$$H_x = 2 H_0 = \text{const}$$

i.e. at the earth's surface the magnetic field is two-times the external field.

This result considerably simplifies the formulation of the problem for

the earth. This problem is reduced to the solution of Eq. (1) in the lower half-space ($z > 0$) with the boundary condition

$$H_x(z = 0) = 2\,H_0 = \text{const}$$

and the condition for infinity $H_x \to 0$ with $z \to \infty$. Knowing $H_x(y, z)$, it is easy to calculate E_y for $z = 0$, and to find the impedance.

II. *In case of E-polarization* the E_x function satisfies the equation

$$\operatorname{div}\left(\frac{1}{\mu}\operatorname{grad} E_x\right) - \frac{k^2}{\mu} E_x = 0$$

The magnetic permeability of most rocks is practically that of the vacuum, μ_0. Therefore, in MTS problems we assume $\mu = \mu_0$. With this assumption E_x satisfies the Helmholtz equation

$$\Delta E_x - k^2 E_x = 0$$

and the conditions of the continuity of E_x and $\partial E_x/\partial n$ at the boundaries of layers. The condition for infinity is the decrease of the function $E_x - E_x^0$, where E_x^0 is the external field. These problems are more complex, than in case of the H-polarization, because the E_x function has to be determined for the entire space.

In the one-dimensional problem both analyzed modes produce the same result.

The solution of three-dimensional problems is much more complex, because the vector equations which arise cannot be reduced to systems of two scalar equations but in a few favourable cases related to the symmetry of the medium. These problems have only been insufficiently studied.

2.B. METHODS FOR SOLUTION OF MTS PROBLEMS

The theory of deep magnetotelluric sounding is based on the analysis of three fundamental models:

I. Horizontally stratified medium;
II. Stratified medium with surface inhomogeneities;
III. Stratified medium with deep inhomogeneities.

The first fundamental model provides theoretical groundwork for formal interpretation of the MTS curves and allows to study the general problems of the method.

The second fundamental model can be used to study the distortions of MTS curves caused by surface inhomogeneities.

The third fundamental model gives an idea of the influence of deep inhomogeneities.

The methods of solution of the problems in connection with the I fundamental model are simple and they are extensively covered in geophysical literature. In case of the fundamental models II and III rather difficult problems arise, since they are associated with partial differential equations

with variable coefficients and a complicated geometry of boundaries. These problems call for the employment of large electronic computers and special numerical methods.

Among *numerical methods* the basic ones are:

- finite difference methods;
- method of integral equations;
- method of eigenfunction expansion of partial domains and projection methods.

The gist of the method of *finite differences* is the following. The continuously changing variables are evaluated at a finite (discrete) set of points, called the grid, i.e. the continuous change of the field is approximately described by the grid function. Substituting the derivatives by difference quotients, the differential equation reduces to a system of linear algebraic equations relating to field values at the grid points. Boundary conditions are also reduced to difference conditions and are included in the system of algebraic equations. This system is usually solved by some iterative method (Samarsky, 1971; Swift, 1967).

An other effective way of solution of the problems considered is *the method of integral equations* (Dmitriev, 1968a; Taborovsky, 1972). Here the boundary value problem for the equations with partial derivatives is reduced to a system of integral equations. The simplest reduction produces equations for excessive currents. Such equations are deduced for the whole domain of inhomogeneity. At present there are methods for the reduction to integral equations formulated at the boundary of the inhomogeneity, which greatly facilitates their numerical solution (Dmitriev and Zakharov, 1970). These methods were those mainly applied by us to the solution of MTS problems in inhomogeneous media.

The *method of eigenfunction expansion* of the partial domains is less general than finite difference methods or the method of integral equations. However, in problems with a simple geometry of boundaries and an H-polarized field, the method can prove successful. The basic idea is that we divide the entire space into partial domains and in each of them represent the solution as a series by means of separation of the variables. Matching the solutions at the boundaries of domains, we obtain an infinite system of algebraic equations for the coefficients of these series. The system obtained is solved by standard methods yielding approximative values of the coefficients of any prescribed accuracy. The projection methods are generalizations of this method, when the field is divided not by the eigenfunctions of the problem, but by a certain most convenient complete system of functions.

The possibility of mass calculations and high accuracy make numerical methods the basic tool of MTS theory. The Moscow State University and the Institute of Geology and Geophysics of the Siberian Branch of the Acad. of Sc. of the USSR have published several albums of MTS curves for various two-dimensional models describing the typical geological situations (Dmitriev and Kokotushkin, 1971; Dmitriev et al., 1973; Kaufman et al., 1971). Three-dimensional problems are solved with difficulty, even with large computers. The set of calculated three-dimensional models is very limited.

Together with the numerical methods, *approximative (asymptotic) methods* are also used. These methods give the low-frequency branches of the MTS curves; their advantage lies in the possibility of determining the analytical connections between the characteristic features of the MTS curves and the parameters of the model. Such solutions provide for a better understanding of the mechanism of distortions of the MTS curves, the degree of their manifestation and their basic regularities. Moreover, they open the way for the practical study of three-dimensional problems.

The following approximative methods are applied in the theory of magnetotelluric sounding:

– methods using approximate boundary conditions on thin layers, i.e. layers whose thickness is much less than the wavelength (Dmitriev, 1969b; Tikhonov and Dmitriev, 1969),

– method of disturbances (Obukhov, 1969; Kaufman and Taborovsky, 1970),

– quasi-statistic methods in which the solution of the problems for direct current is partially used (Berdichevsky, 1964).

Many problems of the MTS theory were solved by means of these methods, particularly at the first stage of researches.

The third source of information about the MTS distortions is the *analogue modelling*. In this case a grid integrator, an electrolytical bath and conducting paper are used. With the help of the grid integrator two-dimensional problems of different complexity are solved (Berdichevsky and Ershov, 1972). The electrolytical bath and conducting paper allow three-dimensional problems with a complicated geometry of boundaries to be solved (Bryunelli et al., 1969; Bryunelli et al., 1963).

Below basic results from an analysis of fundamental models will be discussed. In all these models the external field is the plane wave normally incident onto the earth's surface.

3. MAGNETOTELLURIC SOUNDING OF HORIZONTALLY STRATIFIED MEDIUM (FUNDAMENTAL MODEL I)

In this model resistivity changes only with depth (along the z-axis). The $\varrho(z)$ function describes the stratified structure of the medium. If within a certain layer the function $\varrho(z)$ is variable, this layer will be called a gradient layer.

The external field is the plane wave propagating along z. The solution of the problem falls into two independent parts; one describes the behaviour of the E_x and H_y components, the other the E_y and H_x components. The impedance Z is introduced as the depth function determined from the ratio of mutually perpendicular components of the electrical and magnetic fields. The Z-function satisfies the *Riccati equation:*

$$\frac{dZ}{dz} - \frac{1}{\varrho(z)} \cdot Z^2 = i\omega\mu_0$$

In order to formulate the marginal condition, it is assumed that the base of the model ($z \geq h$) is formed by the infinite homogeneous layer of the resistivity ϱ_n. On the surface of such a layer:

$$Z(z = h) = \sqrt{\omega\mu_0 \varrho_n}\, e^{-i\frac{\pi}{4}}$$

For the step function $\varrho(z)$ the Riccati equation is resolved in hyperbolic functions:

$$Z(z = 0) =$$

$$= -\frac{i\omega\mu_0}{k_1} \coth\left\{k_1 h_1 + \operatorname{arcoth}\frac{k_1}{k_2}\coth\left[\left(k_2 h_2 + \ldots + \operatorname{arcoth}\frac{k_{n-1}}{k_n}\right)\ldots\right]\right\}$$

where $k_i = \sqrt{-i\omega\mu_0/\varrho_i}$; ϱ_i and h_i are specific resistances and thicknesses of the layers, respectively.

If the model contains gradient layers, the Riccati equation within them is solved numerically. For some simple functions, for example $\varrho(z) = \varrho_0 \exp(-pz)$ it is possible to obtain an analytical solution of the Riccati equation.

When interpreting the results of magnetotelluric sounding, the concept of *apparent resistivity* is applied. This is defined by the formula:

$$\varrho_a(\omega) = \frac{|Z(z = 0)|^2}{\omega\mu_0}.$$

We shall discuss a simplified model of a deep geoelectrical section comprised of three homogeneous layers. The upper layer of thickness h_1 and resistivity ϱ_1 overlies an insulating layer of thickness $h_2 \gg h_1$ underlaying by an absolutely conducting base. In this model

$$\varrho_a(\omega) = \varrho_1 |\tanh(k_1 h_1 + \operatorname{arth} k_1 h_2)|^2$$

Curve ϱ_a is shown in Figure 1. The curve consists of three characteristic elements:

– minimum, connected with the interference of waves in the upper layer;

– ascending branch, caused by the influence of the intermediate insulating layer;

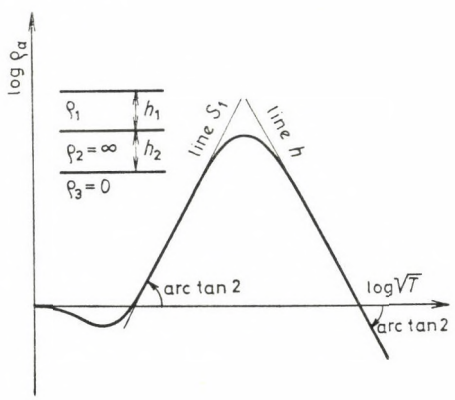


Fig. 1. The MTS curve for a three-layer horizontally homogeneous model $h_2/h_1 = 20$; $\varrho_2/\varrho_1 = \infty$; $\varrho_3/\varrho_1 = 0$

– descending branch, reflecting the influence of the absolutely conducting base.

For *the ascending branch* of the ϱ_a curve the impedance *is well defined by the asymptotic formula*

$$Z(\omega) \simeq \frac{1}{S_1}$$

where $S_1 = h_1/\varrho_1$ is the total conductivity of the upper layer. This frequency interval is called the S_1-interval. In the S_1-interval the ϱ_a curve asymptotically approaches the straight line, called the S_1-line.

For the descending branch the asymptotic formula

$$Z(\omega) \simeq -i\omega\mu_0 h$$

holds, where $h = h_1 + h_2$ is depth of the conducting base. This frequency interval is called the h-interval. In the h interval the ϱ_a curve asymptotically approaches the straight line, called the h-line.

Such a model characterized by simple asymptotics, is initial in the construction of fundamental models II and III, describing the influence of surface and deep inhomogeneities. These horizontally inhomogeneous models neglect a monotonous increase of the electrical conductivity in the upper mantle, but they are suited for analysis and provide a sufficiently complete insight into the distorting effect of the inhomogeneities.

The horizontally stratified models serve as the basis for formal interpretation of MTS curves. Interpretation methods are numerous, the most simple are those based on the use of asymptotic branches and extreme points on the MTS curves. The graphical methods of interpretation are widely applied (visual comparison of measured and theoretical curves and the selection of adequate models).

During the last years interpretation by computers has been developed, which provides an automated selection of adequate models. The selection is made by minimizing the mean square deviation of the theoretical curves from the measured one using a given number of layers (Dmitriev, 1970; Goltsman et al., 1969). The standard program of computer interpretation allows for selecting a model with gradient layers (Dmitriev and Rudneva, 1971).

4. MAGNETOTELLURIC SOUNDING OF STRATIFIED MEDIA WITH SURFACE INHOMOGENEITIES (FUNDAMENTAL MODEL II)

Fundamental model II makes it possible to study the distorting influence of surface inhomogeneities (inhomogeneities of the sedimentary cover). We shall analyze the influence of two-dimensional and three-dimensional inhomogeneities separately.

THE DISTORTING INFLUENCE OF TWO-DIMENSIONAL SURFACE INHOMOGENEITIES

A. Let us begin with a simple model, shown in Figure 2, a. The upper layer of permanent thickness h_1 has a rectangular embedding of the width $2L$. The resistivity of the layer, ϱ_1, changes with y within the inclusion while it is constant outside of it: $\varrho_1 = \varrho_1^i(y)$ if $|y| < L$ and $\varrho_1 = \varrho_1^e$ if $|y| > L$. The intermediate layer of permanent thickness h_2 has an infinitely large resistivity $\varrho_2 = \infty$. At depth $h = h_1 + h_2$ in the base of the model lies an absolute conductor: $\varrho_3 = 0$.

With $h_1 \ll h_2$, $L \ll h_2$ the low frequency asymptotics of the field are easily found. Such an approximative solution is given in the works of Tikhonov and Dmitriev (1969), Dmitriev (1969a). By means of boundary conditions, true for thin layers, the equations of the field are reduced to ordinary differential and one-dimensional integral equations. The following asymptotic formulae were derived for the transversal and longitudinal

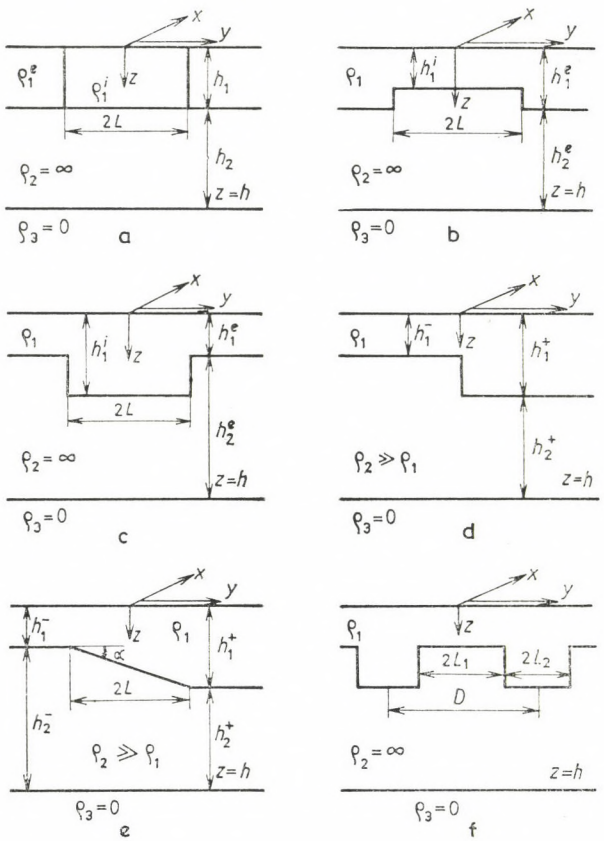


Fig. 2. Types of fundamental model II (two-dimensional structures) a – model of embedding; b–model of horst; c–model of graben; d – model of vertical escarpment; e–model of tilted escarpment; f – model of periodically recurring horsts

impedances, determined respectively with H and E polarization of the field

$$Z^{\perp} = -Z_{yx} = -\frac{E_y}{H_x} = \begin{cases} \dfrac{1}{S_1} & S_1\text{-interval} \\ -i\omega\mu_0 h \dfrac{S_1^e}{S_1} & h\text{-interval} \end{cases}$$

$$Z^{\parallel} = Z_{xy} = \frac{E_x}{H_y} = \begin{cases} \dfrac{1}{\tilde{S}_1(\omega)} & S_1\text{-interval} \\ -i\omega\mu_0 h & h\text{-interval} \end{cases} \tag{2}$$

where $S_1 = h_1/\varrho_1$ is the total conductivity of the upper layer at the observation site: $S_1 = S_1^i(y)$ if $|y| < L$ (inside the embedding) and $S_1 = S_1^e$ if $|y| > L$ (outside the embedding); $\tilde{S}_1(\omega)$ is the function of frequency, expressing the integral influence of longitudinal excessive currents induced in the upper layer. The $\tilde{S}_1(\omega)$ value is connected with the distribution of S_1 and has the meaning of the average total conductivity of the upper layer. The width of the zone of averaging depends on the frequency of the field. With decreasing frequency the zone of averaging expands, for the influence of excessive currents flowing far from the observation site increases. Thus, the function $\tilde{S}_1(\omega)$ reflects in a smoothed form the changes of S_1. To obtain the low frequency asymptotics of that function, the condition $h_2 \gg h_1$ is replaced by $h_2 \to \infty$ and the interval S_1 is assumed to infinitely continue towards low frequencies. Then with $\omega \to 0$ the electrical field within the upper layer becomes homogeneous, which facilitates the calculation of excessive currents, causing the anomalous magnetic field. As a result of such calculations, made on the basis of the Biot–Savart law, we obtain:

$$\tilde{S}_1(\omega) \to \tilde{S} \quad \text{with} \quad \omega \to 0$$

where

$$\tilde{S} = S_1^e \left\{ 1 + \frac{1}{2\pi h_1} \int_0^{h_1} \int_{-L}^{+L} \frac{(\varrho_1^e - \varrho_1^i)\, Z'\, dy'\, dz'}{\varrho_1^i [(y - y')^2 + (z')^2]} \right\}. \tag{3}$$

Let us compare the low frequency asymptotics of the transversal and longitudinal impedances (2) with the low frequency asymptotics of the normal impedance:

$$Z_N = \begin{cases} \dfrac{1}{S_1} & S_1\text{-interval} \\ -i\omega\mu_0 h & h\text{-interval} \end{cases} \tag{4}$$

The transversal and longitudinal impedances differ from the normal impedance by the K factors:

$$Z^{\perp} = Z_N \begin{cases} K_S^{(2,\perp)} & S_1\text{-interval} \\ K_h^{(2,\perp)} & h\text{-interval} \end{cases}$$

$$Z^{\parallel} = Z_N \begin{cases} K_S^{(2,\parallel)} & S_1\text{-interval} \\ K_h^{(2,\parallel)} & h\text{-interval} \end{cases}$$

The K factors will be called *distortion coefficients*. The lower index of the distortion coefficient determines the frequency interval, the upper indices the dimensions of the model and the orientation of the MTS curves. The distortions are absent, if $K = 1$. They are the stronger the more K differs from unity. The character of distortions considerably depends on the frequency interval and on the orientation of the MTS curves:

$$K_S^{(2,\perp)} = 1 \qquad K_S^{(2,\parallel)} = \frac{S_1}{\tilde{S}_1(\omega)}$$

$$K_h^{(2,\perp)} = \frac{S_1^e}{S_1} \qquad K_h^{(2,\parallel)} = 1 \tag{5}$$

As seen, the transversal impedance in the S_1-interval and the longitudinal impedance in the h-interval coincide with the normal impedance. The ascending branches of the transversal MTS curves, caused by the intermediate insulating layer, and the descending branches of the longitudinal MTS curves, caused by the conducting base, are free of distortions. Combining the ascending branches of transversal curves with the descending branches of longitudinal curves, we obtain the normal MTS curves, whose interpretation yields the true values of S_1 and h.

The distortions of the transversal impedance occur in the h interval. Here within the embedding the transversal impedance differs from the normal one by the factor S_1^e/S_1^i, i.e. it is in inverse proportion to the total conductivity of the upper layer in the observation site. The appearance of such a local dependence, connected with the influence of charges and absent in the normal model, is called the S-effect. This galvanic effect displaces the descending branches of the transversal MTS curves, caused by the conducting base.

Let us find the equation for the descending branches of the transversal MTS curves. In the h-interval:

$$\varrho^{\perp} = \frac{|Z^{\perp}|^2}{\omega\mu_0} = [K_h^{(2,\perp)}]^2 \frac{|Z_N|^2}{\omega\mu_0} = [K_h^{(2,\perp)}]^2 \varrho_N$$

therefore

$$\lg \varrho^{\perp} - \lg \varrho_N = 2 \lg K_h^{(2,\perp)} = 2 \lg \frac{S_1^e}{S_1^i}$$

It is evident that the descending branches of the transversal curves are

displaced with respect to the descending branches of normal curves by the value $2 \lg (S_1^e/S_1^i)$, i.e. downward, if $S_1^i > S_1^e$ and upward, if $S_1^i < S_1^e$. Formal interpretation of transversal curves gives apparent depth to the surface of the conducting base equal to $h_a = hK_h^{(2,\perp)}$ i.e. differing from the true depth by the factor S_1^e/S_1^i. Therefore, formal interpretation of such curves produces a false relief of the surface of the conducting base: to the S_1^i-minima there correspond the apparent depressions of this surface, while S_1^i-maxima will cause apparent uplifts.

The distortions of the longitudinal impedance appear in the S_1 interval. Here the longitudinal impedance differs from the normal by the factor $S_1/\tilde{S}_1(\omega)$, i.e. it is in inverse proportion to the average total conductivity of the upper layer. This integral dependence, connected with the influence of excessive currents, produces a number of induction effects distorting the ascending branches of the longitudinal MTS curves. Depending on the observation site and on the S_1 distribution, the ascending branches of the longitudinal MTS curves are displaced or deformed, or they flatten out or become steeper. The distortions reflect in a smoothed form the horizontal changes of the total conductivity of the upper layer. Thus, due to induction effects, sounding develops not only in the vertical, but also in the horizontal direction. With decreasing frequency, the ascending branches approach the $\tilde{S}$-lines, determined according to (3). In transition to the h-interval the induction effects disappear, because the density of excessive currents flowing in the upper layer becomes negligibly small (the current concentrates at the surface of the conducting base). Formal interpretation of the longitudinal curves smoothes out the S_1 changes and misrepresents the distribution of the resistivity ϱ_2 of the intermediate layer.

To illustrate induction effects, a model will be considered, where the upper layer contains a rectangular embedding of constant resistivity $\varrho_1^i = \text{const}$. The rigourous solution of the problem is given in the work of Zakharov (1973). The problem is solved by the method of integral equations. The asymptotic value of the function $\tilde{S}_1(\omega)$, according to (3), is defined by the formula

$$\tilde{S} = S_1^e \left\{ 1 + \frac{1}{2\pi} \left(\frac{\varrho_1^e}{\varrho_1^i} - 1 \right) \left[\frac{\alpha}{2} \ln \left(1 + \frac{1}{\alpha^2} \right) + \right. \right.$$

$$\left. \left. + \frac{\beta}{2} \ln \left(1 + \frac{1}{\beta^2} \right) + \arctan \alpha + \arctan \beta \right] \right\}$$

where

$$\alpha = \frac{L - y}{h_1} \qquad \beta = \frac{L + y}{h_1}$$

The results of calculations are collected in an album (Dmitriev et al., 1971). In Figures 3 and 4 two pages of this album are reproduced; they relate to the cases $\varrho_1^i/\varrho_1^e = 16$ and $\varrho_1^i/\varrho_1^e = 1/16$. The longitudinal MTS curves over the embedding and outside of it differ more or less considerably

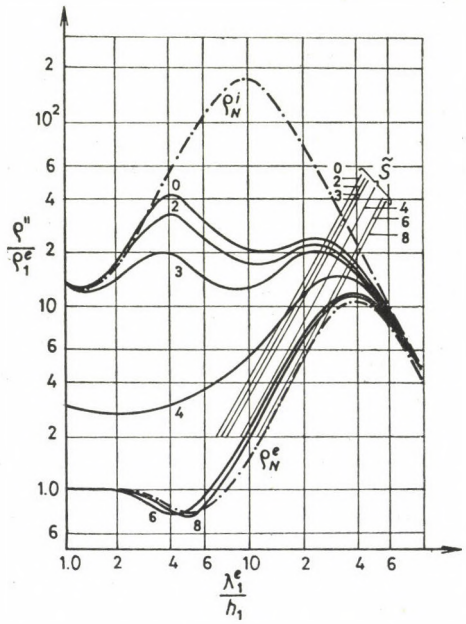


Fig. 3. Longitudinal MTS curves in the model of embedding of higher resistivity $\varrho_1^i/\varrho_1^e = 16$
$\varrho_2/\varrho_1^e = \infty$; $\varrho_3/\varrho_1^e = 0$; $h_2/h_1 = 20$; $L/h_1 = 4$; curves $\varrho^{\parallel}$ and $\tilde{S}$-lines are digitized by $|y|/h_1$

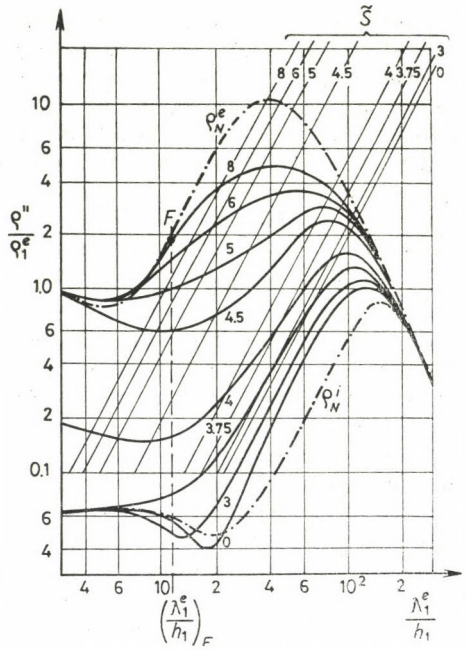


Fig. 4. Longitudinal MTS curves in the model of embedding of lower resistivity $\varrho_1^i/\varrho_1^e = 1/16$
$\varrho_2/\varrho_1^e = \infty$; $\varrho_3/\varrho_1^e = 0$; $h_2/h_1 = 20$; $L/h_1 = 4$: curves $\varrho^{\parallel}$ and $\tilde{S}$-lines are digitized by $|y|/h_1$

from the normal curves ϱ_N^i and ϱ_N^e calculated for the horizontally homogeneous models with the upper layer of resistivities ϱ_1^i resp. ϱ_1^e.

The longitudinal curves over the embedding of higher resistivity are the most deformed (Fig. 3). Let us take the longitudinal curve over the middle of the embedding ($y/h_1 = 0$). It is composed of two maxima and a minimum and looks like a five-layer curve. The intermediate insulating layer appears on this curve twice; initially in the form of the first ascending branch, close to the S_1^i-line, and then in the form of the second ascending branch, approaching the $\tilde{S}$-line. The ascending branches are divided by a deep minimum caused by the lateral influence of the zones of lower resistivity surrounding the inclusion. It can be observed that with decreasing frequency there is an increase in the distorting influence of excessive currents flowing far from the observation site, and that the longitudinal curve diverges from the normal one, thus reflecting the reduction of resistivity of the upper layer outside the embedding. In the low frequency band of the h-interval the influence of excessive currents terminates and the longitudinal curve coincides with the normal one.

The longitudinal curves for sites, displaced from the boundary of the embedding ($|y|/h_1 = 2;3$), have the same shape. The shorter the distance

to the inclusion boundary, the gentler the first ascending branch of the longitudinal curve becomes and the earlier it diverges from the normal curve.

Formal interpretation of these curves distorts the geoelectrical section by introducing a false conducting layer. This effect, connected with the appearance of additional minima of the apparent resistivity, will be called the effect of the false conducting layer.

Outside the embedding of higher resistivity this effect is not observed. Longitudinal curves, obtained with $|y|/h_1 = 6;8$, look like three-layer ones. At high frequencies they coincide with the normal curves. With a decrease of frequency the lateral influence of the embedding becomes apparent. It distorts the interference minima of the longitudinal curves and displaces upwards their ascending branches caused by the intermediate insulating layer. Farther from the embedding the displacement decreases. The position of the ascending branches is well controlled by the $\tilde{S}$-lines. In the h-interval the longitudinal curves coincide with the normal ones.

Thus, in the analyzed model formal interpretation of longitudinal MTS curves gives the true depth h, but smoothes out the S_1 changes at the boundaries of the embedding and creates a false conducting layer under the embedding.

Figure 4 shows longitudinal curves for the model of an embedding of lower resistivity. We will begin with the curve over the middle of the embedding ($y/h_1 = 0$). The lateral influence of zones of higher resistivity surrounding the inclusion distorts the interference minimum of this curve and increases the tilt angle of its ascending branch. The nearer the observation site approaches the boundary of the embedding ($|y|/h_1 = 3;\ 3.75$), the greater the lateral influence becomes and the more the ascending branches of longitudinal curves are displaced upwards. Their position is well controlled

TABLE 1

Distortions of MTS curves caused by a two-dimensional surface inhomogeneity

Frequency interval / Polarization of the field	Interval S_1 (ascending branch caused by the intermediate insulating layer)	Interval h (descending branch caused by the conductive base)
H-polarization (transversal MTS curve)	The curve is not distorted. *FI** gives the true distribution of S_1	The curve is distorted due to the S-effect. *FI* gives false relief of the conductive base
E-polarization (longitudinal MTS curve)	The curve is distorted by induction effects. *FI* smoothes out the S_1 changes and misrepresents the ϱ_2 distribution	The curve is not distorted. *FI* gives the true depth to the conducting base

* *FI* is formal interpretation.

by the $\tilde{S}$-lines. The curves for the outside of the embedding ($|y|/h_1 = 4.5$; 5; 6; 8) have gently ascending branches, which cross the $\tilde{S}$-line. A decrease of the tilt angle of the ascending branches is caused by the lateral influence of the embedding. An extensive minimum is observed near the embedding, it is superimposed on the interference minimum and rapidly disappears when moving off from the embedding. In the h-interval all curves coincide with the normal ones. Their formal interpretation gives the true depth h, but smoothes out the S_1 changes and forms a zone of decreased ϱ_2 values, surrounding the embedding.

A table can be compiled, generalizing the results of the analysis.

B. Let us now analyse other models, illustrating the S-effect and the induction effects caused by changes in the thickness of the upper layer.

As characteristic models we shall take the models shown in Figs 2, b and 2, c. The upper layer of constant resistivity ϱ_1 contains an inhomogeneity in the form of a horst or a graben of width $2L$. The thickness of the upper layer is equal to h_1^i if $|y| < L$, and h_1^e if $|y| > L$. The intermediate layer of thickness h_2 has an infinitely high resistivity $\varrho_2 = \infty$. The base of the models is the absolute conductor at a constant depth h.

The rigourous solution of this problem is given by Dmitriev (1968b), Kokotushkin (1969). The problem is solved by the projection method

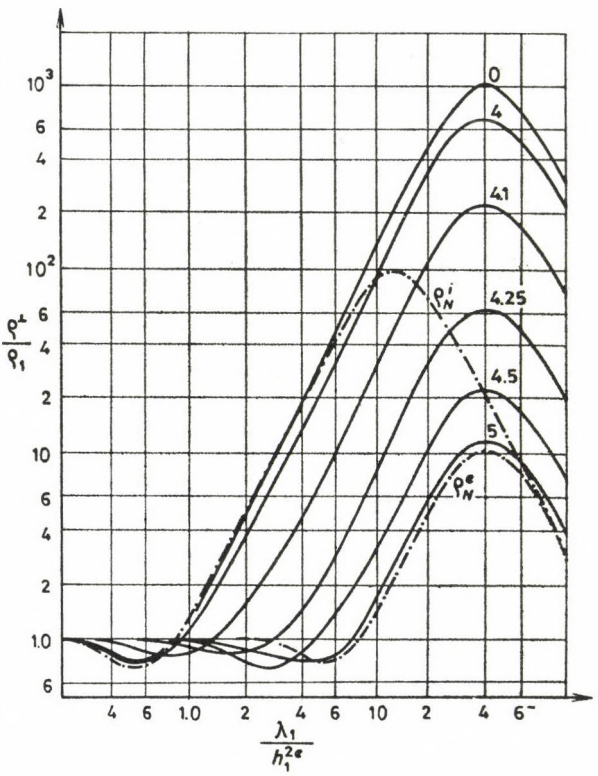


Fig. 5. Transversal MTS curves in the model of horst $\varrho_2/\varrho_1 = \infty$; $\varrho_3/\varrho_1 = 0$; $h_1^i/h_1^e = 0.1$ $h_2^e/h_1^e = 20$; $L/h_1^e = 4$; curves $\varrho^\perp$ are digitized by $|y|/h_1^e$

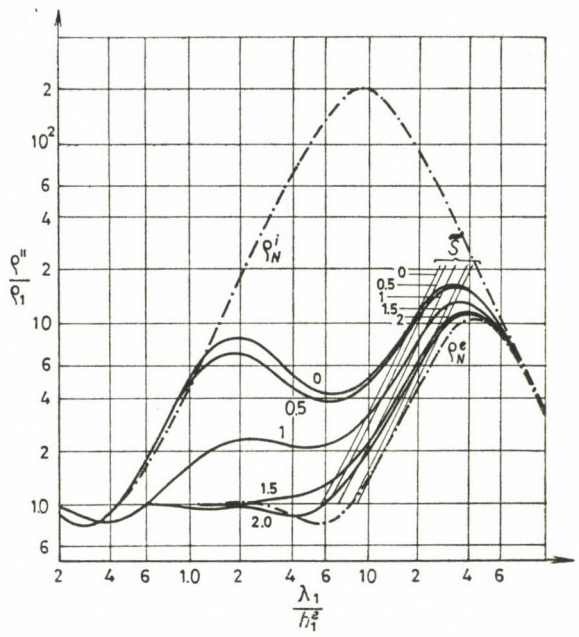


Fig. 6. Longitudinal MTS curves in the model of horst $\varrho_2/\varrho_1=\infty$; $\varrho_3/\varrho_1=0$; $h_1^i/h_1^e=0.05$; $h_2^e/h_1^e=20$; $L/h_1^e=1$; curves ϱ'' and $\widetilde{S}$-lines are digitized by $|y|/h_1^e$

(H-polarization) and by the integral equation method (E-polarization). In the models of the type being considered the asymptotic value of the function $\widetilde{S}_1(\omega)$, reflecting the integral influence of the longitudinal excessive currents, is expressed by the formula obtained similarly to (3) on the basis of the Biot–Savart law:

$$\widetilde{S} = S_1^e\left\{1 - \frac{1}{2\pi}\left[\frac{\alpha}{2}\ln\frac{\alpha^2+1}{\alpha^2+\gamma^2} + \frac{\beta}{2}\ln\frac{\beta^2+1}{\beta^2+\gamma^2} + \right.\right.$$

$$\left.\left. + \operatorname{arc\,tan}\alpha + \operatorname{arc\,tan}\beta - \gamma\left(\operatorname{arc\,tan}\frac{\alpha}{\gamma} + \operatorname{arc\,tan}\frac{\beta}{\gamma}\right)\right]\right\}$$

where

$$\alpha = \frac{L-y}{h_1^e} \qquad \beta = \frac{L+y}{h_1^e} \qquad \gamma = \frac{h_1^i}{h_1^e}$$

The results of calculations are collected in albums (Dmitriev and Kokotushkin, 1971; Dmitriev et al., 1973). Figures 5–8 reproduce the pages from these albums, relating to the horst and the graben models. The normal curves ϱ_N^i and ϱ_N^e are also shown; they are calculated for horizontally homogeneous models letting the thickness of the upper layer be h_1^i and h_1^e, respectively.

Let us analyze the transversal and longitudinal curves over the horst and in its vicinity.

The *transversal curves* are shown in Figure 5. By their forms they are almost like normal. Their ascending branches, caused by the intermediate

insulating layer, have a normal tilt angle and monotonously shift to the right from the S_1^i line over the middle of the horst, ($y/h_1^e = 0$) to the line S_1^e away from the horst, ($|y|/h_1^e > 5$). In the h-interval the S-effect is quite evident. The descending branches of the transversal curves caused by the conducting base are displaced upwards with respect to the descending branches of normal curves. Over the middle of the horst the displacement is maximal. Its value is equal to 2 lg S_1^e/S_1^i. Getting farther from the middle of the horst the displacement monotonously decreases. The maxima of all curves lie on a vertical line. Formal interpretation of these curves smoothes out the sides of the horst and forms a false depression in the surface relief of the conducting base whose relative amplitude $\Delta h/h$ is equal to the relative amplitude $\Delta h_1/h_1^i$ of the horst.

The *longitudinal MTS curves* are seen in Figure 6. Here the same phenomena are observed as in the model of the rectangular embedding of a higher resistivity. The curves obtained over the horst have a five-layer form. The intermediate insulating layer produces two ascending branches. The first branch coincides with the normal curve, the second approaches the $\tilde{S}$-line. The ascending branches are divided by a deep minimum caused by the lateral influence of the zones surrounding the horst. The curves for outside of the horst look like three layer curves. Due to the lateral influence of the horst, their ascending branches are shifted upwards. The position of the ascending branches is well controlled by the $\tilde{S}$-lines. In the h-interval all the curves coincide with the normal ones. Their formal interpretation produces the true h depth, but it indicates a false conducting layer under the horst and smoothes out the edges of the horst.

Now let us analyse the MTS curves for the model of a graben.

The *transversal curves* are shown in Figure 7. The curve over the middle

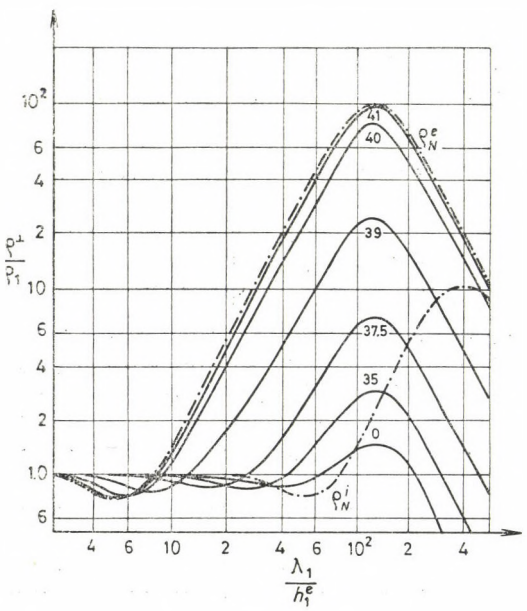


Fig. 7. Transversal MTS curves in the model of graben $\varrho_2/\varrho_1 = \infty$.; $\varrho_3/\varrho_1 = 0$; $h_1^i/h_1^e = 10$; $h_2^e/h_1^e = 200$; $L/h_1^e = 40$; curves $\varrho^\perp$ are digitized by $|y|/h_1^e$

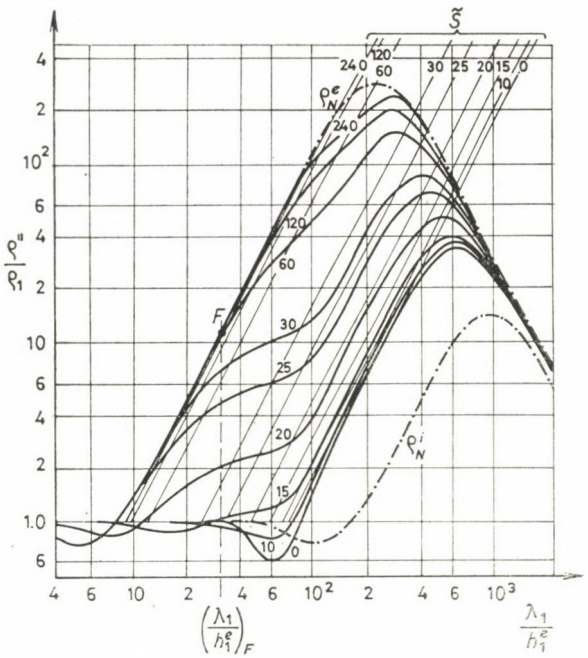


Fig. 8. Longitudinal MTS curves in the model of graben $\varrho_2/\varrho_1 = \infty$; $\varrho_3/\varrho_1 = 0$; $h_1^i/h_1^e = 20$; $h_2^e/h_1^e = 600$; $\tilde{L}/h_1^e = 20$; curves $\varrho^{\perp}$ and $\tilde{S}$-lines are digitized by $|y|/h_1^e$

of the graben ($y/h_1^e = 0$) has a distorted minimum and a gently ascending branch, which crosses the S_1^i-line. As the edge of the graben is approached, the ascending branches of the curves are shifted to the left and their tilt angle increases. Beyond the edge of the graben ($|y|/h_1^e \geq 41$) the ascending branch coincides with the S_1^e-line. The S-effect displaces the descending branches of the $\varrho^{\perp}$ curves downwards. The displacement monotonously increases towards the middle of the graben, where it reaches a value close to 2 lg (S_1^e/S_1^i) (in the model of the graben the S-effect manifests itself somewhat weaker than in the horst model, because the horst disturbs the electrical field more than the graben). The maxima of all curves lie on the same vertical line. Formal interpretation of these curves smoothes out the sides of the graben, creates a zone of lower ϱ_2 values under the graben and forms a false uplift in the surface relief of the conducting base, whose relative amplitude $\Delta h/h$ is close to the relative amplitude $\Delta h_1/h_1^i$ of the graben.

The *longitudinal curves* are shown in Figure 8. They greatly resemble the curves for the model of rectangular embedding of lower resistivity. The curve over the middle of the graben ($y/h_1^e = 0$) has a distorted interference minimum and a steep ascending branch. As the edge of the graben is approached, the ascending branches of the curves are displaced upwards ($|y|/h_1^e = 10$; 15). Their position is well controlled by the $\tilde{S}$-lines. At a distance from the graben the curves take a four-layer or even five-layer form ($|y|/h_1^e = 25$; 30). The ascending branches break into two parts divided by a highly conspicuous inflection, caused by the lateral influence

of the graben. The left parts of the ascending branches coincide with the S_1^e-line, while the right parts cross the $\tilde{S}$-line and locate near it. The longer the distance from the edge of the graben, the later the longitudinal curves begin to diverge from the S_1^e-line. At long distances ($|y|/h_1^e = 120; 240$) the inflection disappears and the influence of the graben is reduced to the deformation of the maxima of the curves $\varrho^{\parallel}$. In the h-interval all curves coincide with the normal ones. Formal interpretation of these curves gives the true depth h, but smoothes out the edges of the graben and produces false conducting layers, which branch off on both sides from the graben.

From the viewpoint of the geophysicist dealing with deep geoelectrics, the most dangerous effects are the S-effect and the effect of the false conducting layer. We shall analyse these surface effects in some detail.

The degree to which the S-effect distorts the descending branches of the transversal MTS curves depends on the form of the inhomogeneity of the upper layer and on the thickness and resistivity of the intermediate resistive layer.

Returning to the above models of the horst and graben ($\varrho_2 = \infty$) we see that over the horst the S-effect is stronger, than over the graben. The expansion of the graben enhances the S-effect. The S-effect is fully shown up if the transversal MTS curve has a well expressed ascending branch. This occurs if the intermediate resistive layer is sufficiently thick ($h_2 \gg h_1$). If h_2 is close to h_1, the ascending branch of the transversal MTS curve has no chance to develop and the S-effect is reduced. In the work of Berdichevsky and Ershov (1974) the S-effect over horsts of different h_2 is discussed. The problem is solved by analogue modelling on the grid integrator (Berdichevsky and Ershov, 1972). The distortion coefficient $K_h^{(2,\perp)}$ over the middle of the horst is determined by the approximative formula

$$K_h^{(2,\perp)} \approx \left(\frac{S_1^e}{S_1}\right)^{\nu}$$

where

$$\nu = \begin{cases} 1 & \text{if} \quad \dfrac{h_2^e}{h_1^e} > 10 \\ 1 - \lg \sqrt[3]{10 \dfrac{h_1^e}{h_1^i}} & \text{if} \quad 1 < \dfrac{h_2^e}{h_1^e} < 10 \end{cases}$$

In this case, formal interpretation of the transversal MTS curves would produce an apparent depth to the conductive base equal to $h_a = (S_1^e/S_1^i)^{\nu} h$. If $h_2^e/h_1^e > 10$ the relative amplitude of the false depression in the surface relief of the conducting base is equal to the relative amplitude of the horst; if $h_2^e/h_1^e = 1$ and $h_1^i/h_1^e = 0.2$, it is reduced almost by half.

C. In transition to the models with an intermediate layer of high but finite resitivity the mechanism of the S-effect becomes more complicated. Here the current flows through the intermediate layer (galvanic connection appears between the upper layer and the conducting base). Figure 2, d

shows the model of a stepwise change of thickness of the upper layer: $h_1 = h_1^+$ if $y > 0$ and $h_1 = h_1^-$ if $y < 0$. The intermediate layer has finite resistivity ϱ_2. The base of the model is the absolute conductor at a constant depth h. The problem is solved by the method of integral equations (Denisova et al., 1973). Figure 9 reproduces a page from the album (Dmitriev et al., 1973) of transversal MTS curves over the lifted and subsided edges of an escarpment. The normal curves ϱ_N^+ and ϱ_N^- are also shown, calculated for the horizontally homogeneous model with the respective thicknesses of the upper layer h_1^+ and h_1^-. Over the lifted edge of the escarpment the S-effect displaces the descending branches of the transversal curves upwards, and over the subsided edge it displaces them downwards. The maximum displacement is observed near the vertical edge of the escarpment ($y/h_1^+ = \pm 0.5$; ± 2.5). The magnitude of the displacement is much less than in case of an insulating intermediate layer. The descending branches of the curves approach the normal ones with distance from the vertical edge of the escarpment. At distances exceeding 25 h_1^+ the S-effect practically wears off. As seen, the finite resistivity of the intermediate layer considerably weakens the S-effect due to the flowing through of current. The distortions attenuate and locate near the vertical edge of the escarpment. Formal interpretation of these curves produces a false relief of the conducting base: on the side of the lifted edge a depression appears, on the side of the subsided edge there is an uplift. The relative amplitudes $\Delta h/h$ of the false structures are much less than the relative amplitude $\Delta h_1/h_1^+$ of the escarpment.

In the work of Dmitriev and Khrychikova (1975) the model of a tilted escarpment is discussed, illustrating the influence of the S-effect during the slow change in the thickness of the upper layer (Fig. 2,e). Here $2L$ is the width of the escarpment, h_1^- and h_1^+ are depths to the lifted and the subsided edges of the escarpment, respectively, α is the angle of its tilt.

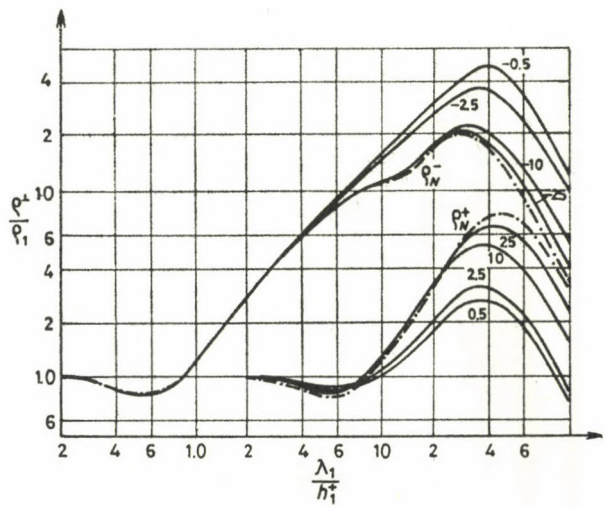


Fig. 9. Transversal MTS curves in the model of vertical escarpment $\varrho_3/\varrho_1 = 20$; $\varrho_2/\varrho_1 = 0$; $h_1^-/h_1^+ = 0.1$; $h_2^+/h_1^+ = 20$; curves $\varrho^\perp$ are digitized by y/h_1^+

The intermediate layer has a finite resistivity $\varrho_2 \gg \varrho_1$. At the depth $h \gg h_1$ lies the absolute conductor. The problem is solved by means of approximative boundary conditions true for thin layers. An important parameter of the problem is the value

$$\tau = \frac{1}{\sqrt{S_1 T_2}}$$

where $S_1 = h_1/\varrho_1$ is the total conductivity of the upper layer; $T_2 = \varrho_2 h_2$ is the total resistance of the intermediate layer. This value expresses the degree of galvanic connection between the upper layer and the conducting base and is called the galvanic constant. The thinner the intermediate layer and the lower its resistivity, the larger the galvanic constant (i.e. the better the galvanic connection between the upper layer and the conducting base) and the weaker the S-effect. In the work of Dmitriev and Khrychikova (1975) expressions are presented for the coefficient $K_h^{(2,\perp)}$ which characterizes the S-effect. If $\tau L \ll 1$ we have

$$K_h^{(2,\perp)} = \begin{cases} 1 + \left(\sqrt{\frac{h_1^+}{h_1^-}} - 1\right) e^{(y+L)\tau -} & \text{if} \quad y \leq -L \\ \frac{\sqrt{h_1^+ h_1^-}}{h_1(y)} & \text{if} \quad -L < y < L \\ 1 + \left(\sqrt{\frac{h_1^-}{h_1^+}} - 1\right) e^{-(y-L)\tau +} & \text{if} \quad y \geq L \end{cases}$$

where τ^- and τ^+ are the galvanic constants in the left- and the right-hand sides of the model, respectively.

The S-effect becomes practically noticeable if the distortion coefficient $K_h^{(2,\perp)}$ differs more than 10% from unity. Such values of $K_h^{(2,\perp)}$ are observed if $h_1^+/h_1^- > 1.2$, i.e. if the changes in the thickness of the upper layer exceed 10% of its mean value. Increasing the distance from the edge of the escarpment the influence of the S-effect diminishes, according to the exponential law $\exp(L - |y|)\tau$. It is evident that the larger the galvanic constant τ, which determines the rate of the current flowing through the resistive intermediate layer, the narrower the region of the S-effect. This region is easily found from the condition $|K_h^{(2,\perp)} - 1| > 0.1$, which is true if $h_1^+/h_1^- > 1.2$. Thus we have:

$$-L^- < y < L^+$$

where

$$L^- = L + \frac{1}{\tau^-} \ln 10 \left(\sqrt{\frac{h_1^+}{h_1^-}} - 1\right)$$

$$L^+ = L + \frac{1}{\tau^+} \ln 10 \left(1 - \sqrt{\frac{h_1^-}{h_1^+}}\right)$$

The less the tilt of the escarpment, the weaker is the S-effect. If

$$\tan \alpha \leq 0.2\, \tau^{-} h_1^{-}$$

the coefficient $K_h^{(2,\perp)}$ differs from 1 by not more than 10% at any L and h_1^{+}, i.e. the S-effect is practically unnoticeable.

In practice the S-effect can be detected by correlating the apparent depth values h_a with total conductivity S_1. If h_a and S_1 are in inverse dependence, the geophysicist is justified to assume that this is due to the S-effect. The degree of inverse correlation characterizes the extent of the S-effect. Another evidence of the S-effect is the fact that the abscissa of the maxima of MTS curves do not depend on the h_a values. And, finally, there are simple almost two-dimensional situations, when it is sufficient to compare the transversal MTS curves with the longitudinal ones to discover the S-effect.

A method can be suggested, which allows of reduction, if only partial, of the S-effect. It is the method of averaging h_a values for different structures. In the work of Berdichevsky and Ershov (1974), a model is studied composed of periodically recurring horsts with twofold and threefold changes in the thickness of the upper layer (Fig. 2, f). In this case $2L_1$ is the width of the horst, $2L_2$ the distance between the horsts, and $D = 2(L_1 + L_2)$ is the period of recurrence of structures. The base of the model is the absolute conductor at the constant depth h. The problem was solved on a grid integrator. The h_a values vary with amplitude exceeding 100%. Over the horsts $h_a > h$, and between them $h_a < h$. Averaging was made along the profile of length D. The average value

$$\tilde{h}_a = \frac{1}{D} \int h_a(y)\, dy$$

at different L_1/L_2 ratios differs from h by not more than 20%. As seen, averaging considerably increases the accuracy of determination of h.

*

We proceed now to the *effect of the false conducting layer*. This effect is connected with the occurrence of additional minima and inflections on the ascending branches of the longitudinal MTS curves and is observed near the zones characterized by high S_1 values, (e.g., near depressions or in the domes of the uplifts). The magnitude of the effect depends on the distance to these zones, on their total conductivity and on the geometry.

Let us now direct our attention to the models of embedding, horst and graben (Fig. 2, a and c) from Dmitriev's albums (Dmitriev and Kokotushkin, 1971; Dmitriev et al., 1973).

The effect of the false conducting layer manifests itself most conspicuously during the sounding over an embedding of higher resistivity or over a horst. Here the longitudinal curves might have well developed additional minima which, being formally interpreted, create a thick "conducting" layer wedging out to the edges of the structure. When the structure expands the minima are shifted towards lower frequencies and lose their emphasis: the "conducting" layer sinks and coincides with the conducting base of

the model. An increase of total conductivity S_i^1 (i.e. a decrease of resistivity of the embedding or the reduction of the amplitude of the horst) smoothes out the minima. The condition necessary for the development of additional minima is established by means of the following rough estimation:

$$\frac{LS_1^i}{h_1^e S_1^e} \leq 0.4 \quad \text{if} \quad \frac{h_2^e}{h_1^e} \geq 20 \tag{6}$$

The false conducting layer also appears when sounding near the embedding of lower resistivity, or near the graben. But in this case the effect is not so pronounced.

The additional minima appear only in the immediate vicinity of the embedding and disappear if the distances from the edge of the embedding exceed h_1.

In zones surrounding the graben the ascending branches of the longitudinal curves can have well-expressed inflections, which farther from the edge of the graben shift towards lower frequencies and disappear at distances exceeding $5h_1^i$ (no additional minima occur near the graben even at twentyfold changes in the thickness of the upper layer).

Formal interpretation of such curves produces zones of lower ϱ_2 values around the embedding and forms "conducting" layers, which branch off from the graben and, sinking, merge with the conducting base of the model. The larger S_1^i (i.e. the less the resistivity of the embedding or the larger the amplitude of the graben), the deeper the zones of lower ϱ_2 values penetrate and the thicker the "conducting" layers will be. This misleading pattern depends also on the width of the structure: the larger is L, the more prominent are the minima and inflections of the longitudinal curves. However, the influence of L is not so great as that of S_1^i since the dominant role in distorting the MTS curves is played by the excessive currents, flowing at the nearest edge of the structure. It is essential that the separation of the longitudinal curves from the normal ones, marking the beginning of influence of excessive currents, occurs at frequencies closely connected with the distance l of the observation site from the nearest edge of the structure. This connection is expressed by the following approximative formulae:

$$\begin{aligned} \left(\frac{\lambda_1^e}{h_1}\right)_F &\approx 4.5 \sqrt[3]{\left(\frac{l}{h_1}\right)^3} \quad \text{(embedding with lower resistivity)} \\ \left(\frac{\lambda_1}{h_1^e}\right)_F &\approx 4.5 \sqrt{\frac{l}{h_1^e}} \quad \text{(graben),} \end{aligned} \tag{7}$$

where $(\lambda_1/h_1)_F$ is the abscissa of the separation point F (Figs 4 and 8). Incidentally, this means that the depth to the false conducting layer obtained near the graben depends not so much on the amplitude of the graben, but rather on the distance to its edge.

Detection of false conducting layers and their elimination from the section is one of the basic problems in magnetotelluric sounding. The

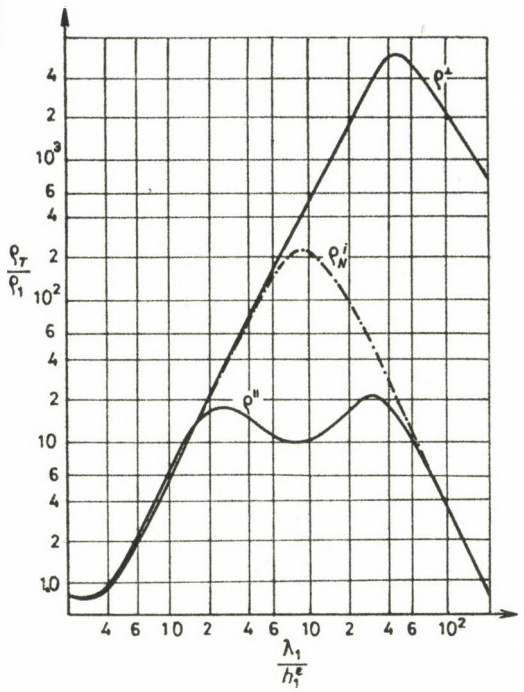


Fig. 10. Transversal and longitudinal MTS curves over the middle of the horst
$\varrho_2/\varrho_1 = \infty$; $\varrho_3/\varrho_1 = 0$;
$h_1^i/h_1^e = 0.05$; $h_2^e/h_1^e = 20$; $L/h_1^e = 2$

situation is complicated by the fact that in practice we deal with structures of finite size and the induction effects can be accompanied by galvanic ones distorting the pattern characteristic of two-dimensional models.

In the simplest (almost two-dimensional) situations it is sufficient to compare the longitudinal curves with the transversal ones in order to detect the false conducting layer. Such an example is shown in Figure 10. The longitudinal curve over the middle of the horst contains a minimum which is absent in the transversal curve. Evidently, this minimum is connected with the lateral influence of zones surrounding the horst. Combining the ascending branch of the transversal curve with the descending branch of the longitudinal curve, we obtain the normal curve ϱ_N^i representing a three-layer section.

As seen, joint interpretation of the transversal and the longitudinal MTS curves makes possible to eliminate the induction effect (the effect of the false conducting layer) distorting the ascending branch of the longitudinal curve, and also the galvanic effect (the S-effect) distorting the descending branch of the transversal curve.

In more complex situations such a method might seem not too convincing. In need to additional facts, illuminating the nature of minima and inflections of the longitudinal MTS curves, the geophysicist should direct his attention first of all to mathematical and physical two-dimensional models, approximating the structure of the sedimentary cover of the studied region. Extensive information on models of an embedding, a horst

and a graben is collected in Dmitriev's albums (Dmitriev and Kokotushkin, 1971; Dmitriev et al., 1973).

Besides, the estimation (6), given in the present paper, can also be of help. Important results can be obtained by the analysis of changes of coordinates of the characteristic points of the longitudinal MTS curves (for example, the separation points), when moving away from the structure.

The following factors discredit the existence of an intermediate conducting layer obtained by formal interpretation of longitudinal MTS curves: the presence of minima or inflections on the longitudinal curves and their absence on the transversal ones; good correlation with the model curves illustrating the effect of the false conducting layer; a regular increase of the abscissae of the separation points when moving away from the edge of the structure, in accordance with Eq. (7). On the other hand, the presence of minima or inflections on both the longitudinal and transversal curves; the absence of noticeable distortions on model curves corresponding to the section studied; a change of the abscissae of separation points not correlating with the regularity (7) — all these facts evidence in favour of an intermediate conducting layer. A serious argument, confirming the reality of the conducting layer, is the occurrence of minima or inflections on the longitudinal MTS curves both for the near-edge parts of the depression and for its most subsided central part.

*

Geophysical journals announce the discovery of intermediate conducting layers in the earth's crust and upper mantle in many regions of our planet. These anomalies are quite unexpected so the geophysicists are forced to look for satisfying proofs to verify the results obtained. Let us analyse two more methods, which help to reveal the nature of minima and inflections of longitudinal MTS curves.

The first method is based on a simplified quantitative evaluation of the induction effect. This can be achieved by means of $\tilde{S}$-lines. In order to determine the $\tilde{S}$-values, the sedimentary cover is approximated by a two-dimensional model, composed of an upper horizontally homogeneous layer of resistivity ϱ_1 and of a set of rectangles of resistivity ϱ_m ($m = 2, 3, \ldots$). Figure 11, a gives an example of such an approximation. The $\tilde{S}$-values are obtained with the formula:

$$\begin{aligned}\tilde{S}(y) = S_1 - \frac{1}{2\pi}\sum_{m=2}\frac{1}{\varrho_m}\Bigg\{&\frac{y-y_2^{(m)}}{2}\ln\frac{(y-y_2^{(m)})^2+(z_2^{(m)})^2}{(y-y_2^{(m)})^2+(z_1^{(m)})^2}+\\&+\frac{y-y_1^{(m)}}{2}\ln\frac{(y-y_1^{(m)})^2+(z_1^{(m)})^2}{(y-y_1^{(m)})^2+(z_2^{(m)})^2}+\\&+z_2^{(m)}\left(\arctan\frac{y-y_2^{(m)}}{z_2^{(m)}}-\arctan\frac{y-y_1^{(m)}}{z_2^{(m)}}\right)+\\&+z_1^{(m)}\left(\arctan\frac{y-y_1^{(m)}}{z_1^{(m)}}-\arctan\frac{y-y_2^{(m)}}{z_1^{(m)}}\right)\Bigg\}\end{aligned} \tag{8a}$$

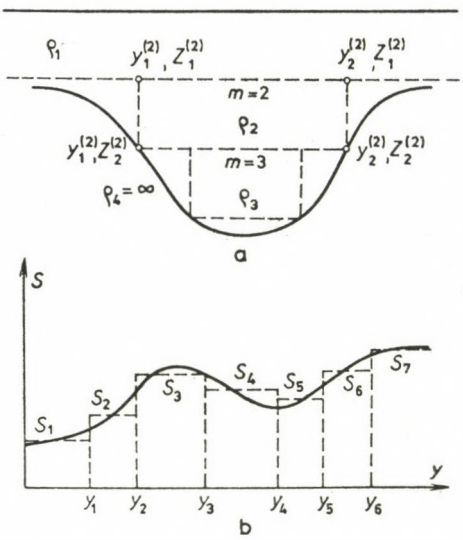


Fig. 11. Models for quantitative evaluation of the induction effect
a – approximation of the sedimentary cover by the sum of rectangles; b – approximation of the change of the total conductivity of the sedimentary cover by a step-function

where S_1 is the total conductivity of the upper horizontally homogeneous layer; $y_1^{(m)}$, $y_2^{(m)}$, $z_1^{(m)}$, $z_2^{(m)}$ are the coordinates of the vertices of the m-th rectangle. The $\widetilde{S}$-lines are drawn through the point having coordinates $\varrho_T = 1$, $\sqrt{T} = \widetilde{S}/356$ at an angle 63°25' to the axis of the abscissae. The domains of possible development of the induction effect lie to the left of the $\widetilde{S}$-line. If the minima or inflections of the longitudinal MTS curves are to the right of the $\widetilde{S}$-line, the alternative "conducting layer or induction effect" is resolved in favour of the conducting layer.

A similar estimation can be made by means of an approximate calculation of the function $\widetilde{S}_1(\omega)$. The $S_1(\omega)$ values are found with the empirical formula:

$$\widetilde{S}_1(\omega, y) = \frac{2}{\lambda} \int_{-\infty}^{+\infty} \frac{S(y')\,dy'}{1 + \frac{4\pi^2}{\lambda^2}(y - y')^2}$$

where λ is the length of the electromagnetic wave in the sedimentary cover (determined by the average longitudinal resistivity of the sedimentary cover in the vicinity of the observation site). By approximating the changes of the total conductivity $S(y)$ of the sedimentary cover by the step-function $S(y) = S_m$ for $y_{m-1} < y < y_m$, where $m = 1, 2, \ldots n$, while $y_0 = -\infty$ $y_n = \infty$, we have

$$\widetilde{S}_1(\omega, y) = \frac{1}{\pi}\left\{S_1\left[\arctan\frac{2\pi}{\lambda}(y_1 - y) + \frac{\pi}{2}\right] +\right.$$

$$+ S_n\left[\frac{\pi}{2} - \arctan\frac{2\pi}{\lambda}(y_{n-1} - y)\right] + \tag{8b.}$$

$$+ \sum_{m=2}^{n-1} S_m\left[\arctan\frac{2\pi}{\lambda}(y_m - y) - \arctan\frac{2\pi}{\lambda}(y_{m-1} - y)\right]\Bigg\}$$

An example of such an approximation is shown in Figure 11, b. The formulae overestimate the values of $\tilde{S}_1(\omega)$. Using these values the apparent resistivity $\tilde{\varrho} = 1/\omega\mu_0\tilde{S}_1^2(\omega)$ is calculated and the $\tilde{\varrho}$ curves are constructed. If the minima or inflections of the measured curves $\varrho^{\parallel}$ lie to the right of the calculated theoretical curves $\tilde{\varrho}$, the alternative "conducting layer or induction effect" is solved in favour of the conducting layer.

The second method is based on the analysis of magnetovariation data. A characteristic evidence of the induction effect, observed near the depressions, is growth of the vertical component H_Z of the magnetic field, appearing due to the asymmetry of the excessive currents permeating the sedimentary cover. At the same time the intermediate conducting layer lying in the crust or in the upper mantle diminishes the H_Z component (due to a decrease of the density of excessive currents in the sedimentary cover). Figure 12 presents the curves $|H_z/H_y|$ for the vicinity of the graben. Here the longitudinal MTS curves are also shown for comparison. The inflections of the MTS curves caused by the lateral influence of the graben correspond to the ascending branches of the curve $|H_z/H_y|$. The descending branches of the MTS curves caused by the conducting base of the model correlate with the descending branches of the curves $|H_z/H_y|$. Thus, if inflections (or minima) of the MTS curves develop in the frequency

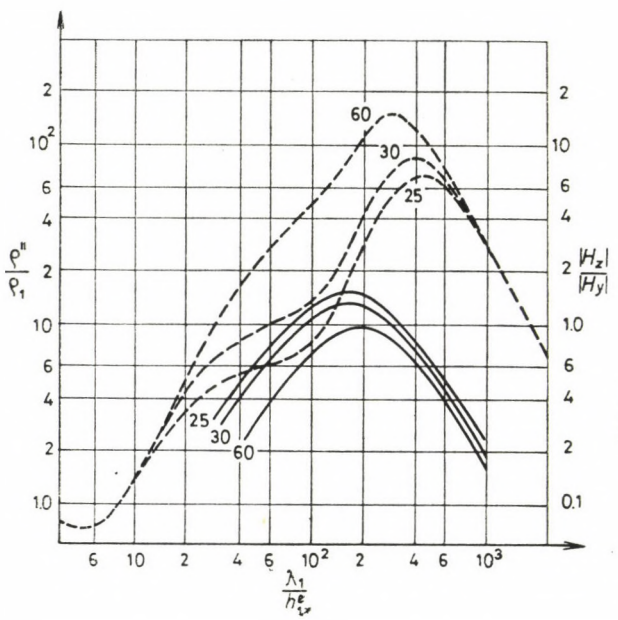


Fig. 12. Comparison of longitudinal MTS curves with the magnetovariation curves in the model of graben $\varrho_2/\varrho_1 = \infty$; $\varrho_3/\varrho_1 = 0$; $h_1^i/h_1^e = 20$; $h_2^e/h_1^e = 600$; $L/h_1^e = 20$; the curves are digitized by $|y|/h_1^e$; dashed lines are for $\varrho^{\parallel}$, solid lines for $|H_z|/|H_y|$

interval relating to the ascending branches of the magnetovariation curves, the alternative "induction effect or a conducting layer" should be settled in favour of the induction effect. And, on the other hand, the association of inflections (or minima) of the MTS curves with the descending branches of the magnetovariation curves evidences the existence of the conducting layer.

Simultaneous application of all the above methods provides a sufficiently complete set of criteria to distinguish false conducting layers from those existing in reality.

The accomplished analysis suggests the following conclusions. The transversal MTS curves are distorted by the S-effect, which deforms the relief of the deep geoelectric boundaries. This effect is easily detected, but difficult to eliminate. Therefore, the transversal curves, more often than not, are unsuitable for the study of deep electrical conductivity. The longitudinal MTS curves are distorted by the induction effect that creates false conducting layers. This effect can be almost always eliminated. The major advantage of longitudinal curves is that their low frequency branches are free of distortions. Therefore, the longitudinal MTS curves open the way for studying deep electrical conductivity.

DISTORTIONS DUE TO THREE-DIMENSIONAL SURFACE INHOMOGENEITIES

The distorting effect of three-dimensional surface inhomogeneities is much less studied. This is due to the extremely difficult mathematics hindering the rigorous solution of three-dimensional problems. Even today we have but a few approximative results, as the one to be analyzed in what follows.

The model is shown in Figure 13. The upper layer of thickness h_1 and of constant resistivity $\varrho_1 = \varrho_1^e$ contains a local embedding limited by some cylindrical surface with a generatrix parallel to the z-axis. Inside the embedding $\varrho_1 = \varrho_1^i(x, y)$. The intermediate layer of thickness h_2 has an infinitely high resistivity $\varrho_2 = \infty$. At the base of the model at depth h an absolute conductor ($\varrho_3 = 0$) is located. The model is a three-dimensional generalization of that analyzed at the beginning of the preceding section (Fig. 2, a).

The solution of the problem involves three stages.

A. At the first stage, the model without the embedding is considered. The solution of this horizontally homogeneous problem is well known. At $z = 0$ the electrical field $\mathbf{E}_0$ and the magnetic field $\mathbf{H}_0$ are related by

$$\mathbf{H}_0 = Y_0[\mathbf{1}_z \times \mathbf{E}_0] \tag{8}$$

where the admittance Y_0 is equal to

$$Y_0 = -\frac{k_1}{i\omega\mu_0} \operatorname{cth}(k_1 h_1 + \operatorname{arth} k_1 h_2) \tag{9}$$

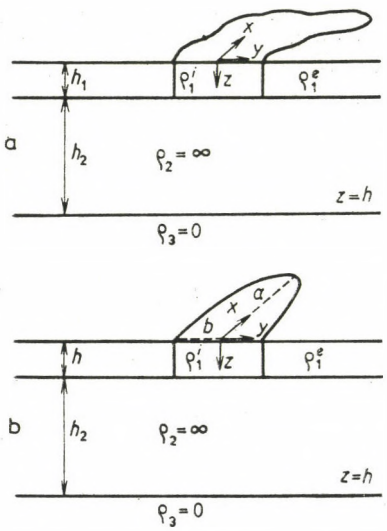


Fig. 13. Three-dimensional structures of fundamental model II
a – model of cylindrical embedding with arbitrary cross-section; b – model of cylindrical embedding with elliptical cross-section

while k_1 is the wave-number of the upper layer, $\mathbf{1}_z$ is the unit vector directed along the z-axis.

The second stage consists in the solution of a horizontally inhomogeneous stationary problem for the distribution of the constant electrical field in the upper layer containing the embedding. The primary electrical field $\mathbf{E}^0$ is homogeneous. The solution of this problem has the form:

$$\mathbf{E} = E_x^{(0)}\,\mathbf{F}^{(x)} + E_y^{(0)}\,\mathbf{F}^{(y)} \tag{10}$$

where $E_x^{(0)}$, $E_y^{(0)}$ are the components of the primary electrical field of the stationary problem, while $\mathbf{F}^{(x)}$, $\mathbf{F}^{(y)}$ are vector functions which can be found by solving the two-dimensional Laplace equation.

At this third stage the asymptotic solution of the total problem is constructed, based on the solution of the first two problems. Let us assume that the length of the electromagnetic wave in the upper layer and within the embedding is much greater than the thickness of the layer and the size of the embedding. Then we are justified to neglect the skin-effect and assume that the primary electrical field $\mathbf{E}_0$ is homogeneous within the upper layer and that it excites the embedding according to the laws of a direct current. Under these conditions the electrical field $\mathbf{E}$ of the total problem is calculated with Eq. (10) derived for the stationary horizontally inhomogeneous problem, i.e.

$$\mathbf{E} = E_{0x}\mathbf{F}^{(x)} + E_{0y}\mathbf{F}^{(y)} \tag{11}$$

Let us now define the magnetic field $\mathbf{H}$ for the total problem. It consists of the primary field $\mathbf{H}_0$ and of the anomalous field $\mathbf{H}_a$, i.e. the field of excessive currents, flowing in the upper layer:

$$\mathbf{H} = \mathbf{H}_0 + \mathbf{H}_a$$

The $\mathbf{H}_0$ field has only horizontal components which are computed according to Eq. (8). The horizontal components of the field $\mathbf{H}_a$ can be calculated by integrating the excessive currents on the basis of the Biot–Savart law. In order to obtain simple formulae, we shall restrict ourselves to a rough method of calculating $\mathbf{H}_a$ making use of the conditions of discontinuity of the magnetic field at the current layer:

$$\mathbf{H}_a \times \mathbf{1}_z = \frac{1}{2}(S_1\mathbf{E} - S_1^e\mathbf{E}_0) \tag{12}$$

Combining Eqs (9) and (12) we obtain the horizontal components of the total magnetic field:

$$\mathbf{H}_{hor} = \mathbf{1}_z \times \left[\frac{\mathbf{E}S_1}{2} + \mathbf{E}_0\left(Y_0 - \frac{S_1^e}{2}\right)\right] \tag{13}$$

In order to determine the impedance tensor $\{\hat{\mathbf{Z}}\}$ the expression $\mathbf{E} = \{\hat{\mathbf{Z}}\}\mathbf{H}_{hor}$ and the formulae (11) and (13) are applied. For $\mathbf{E}_0$ (E_{0x}, 0) and $\mathbf{E}_0$ (0, E_{0y}) the expression is reduced to the system of algebraic equations for the four elements of the impedance tensor:

$$\mathbf{F}^{(x)} = \{\hat{\mathbf{Z}}\}\left\{\mathbf{1}_z \times \left[\frac{\mathbf{F}^{(x)}S_1}{2} + \mathbf{1}_x\left(Y_0 - \frac{S_1^e}{2}\right)\right]\right\}$$

$$\mathbf{F}^{(y)} = \{\hat{\mathbf{Z}}\}\left\{\mathbf{1}_z \times \left[\frac{\mathbf{F}^{(y)}S_1}{2} + \mathbf{1}_y\left(Y_0 - \frac{S_1^e}{2}\right)\right]\right\}$$

B. The model gives the low frequency asymptotics of $\{\hat{\mathbf{Z}}\}$, so it illustrates very well the effects of flowing around and of concentration. It should be noted that the simplified calculation of the magnetic field exaggerates the anomalies of the magnetic field and reduces the distortions of the MTS curves.

Let us assume the embedding of the form of an elliptical cylinder of constant resistivity ϱ_1^i (Fig. 13, b). The solution of the stationary problem for this model is given in the works of Zaborovsky (1963), Berdichevsky et al. (1974). Suppose that a, b are the semi-axes of the embedding oriented along the x- and y-axes. In points of the y-axis

$$\mathbf{F}^{(x)} = \begin{cases} S_1^e \dfrac{a+b}{aS_1^e + bS_1^i}\,\mathbf{1}_x & \text{if } |y| < b \\ \dfrac{(a^2S_1^e - b^2S_1^i)\sqrt{a^2 - b^2 + y^2} + ab(S_1^i - S_1^e)\,|y|}{(a-b)(aS_1^e + bS_1^i)\sqrt{a^2 - b^2 + y^2}}\,\mathbf{1}_x & \text{if } |y| > b \end{cases}$$

$$\mathbf{F}^{(y)} = \begin{cases} S_1^e \dfrac{a+b}{bS_1^e + aS_1^i}\,\mathbf{1}_y & \text{if } |y| < b \\ \dfrac{(b^2S_1^e - a^2S_1^i)\sqrt{a^2 - b^2 + y^2} + ab(S_1^i - S_1^e)\,|y|}{(b-a)(bS_1^e + aS_1^i)\sqrt{a^2 - b^2 + y^2}}\,\mathbf{1}_y & \text{if } |y| > b \end{cases}$$

Therefore

$$\{\hat{\mathbf{Z}}\} = \begin{vmatrix} 0 & Z_{xy} \\ Z_{yx} & 0 \end{vmatrix}$$

$$Z_{xy} = \frac{F^{(x)}}{Y_0 + \frac{1}{2}(F^{(x)} S_1 - S_1^e)}$$

$$Z_{yx} = -\frac{F^{(y)}}{Y_0 + \frac{1}{2}(F^{(y)} S_1 - S_1^e)}$$

Substituting in these formulae the low frequency asymptotics of the admittance

$$Y_0 = S_1^e + \frac{i}{\omega \mu_0 h}$$

we obtain

$$Z_{xy} = \begin{cases} \dfrac{2F^{(x)}}{S_1^e + F^{(x)} S_1} = \dfrac{2F^{(x)} S_1}{S_1^e + F^{(x)} S_1} Z_N & \text{interval } S_1 \\ -i\omega\mu_0 h\, F^{(x)} = F^{(x)} Z_N & \text{interval } h \end{cases}$$

$$Z_{yx} = \begin{cases} -\dfrac{2F^{(y)}}{S_1^e + F^{(y)} S_1} = -\dfrac{2F^{(y)} S_1}{S_1^e + F^{(y)} S_1} Z_N & \text{interval } S_1 \\ i\omega\mu_0 h\, F^{(y)} = -F^{(y)} Z_N & \text{interval } h \end{cases}$$

where Z_N is the normal impedance.

The impedances Z_{xy} and Z_{yx} differ from the normal impedance Z_N by the coefficients:

$$K_S^{(3,xy)} = \begin{cases} \dfrac{2F^{(x)} S_1^i}{S_1^e + F^{(x)} S_1^i} & \\ \dfrac{2F^{(x)}}{1 + F^{(x)}} & \end{cases} \qquad K_S^{(3,yx)} = \begin{cases} \dfrac{2F^{(y)} S_1^i}{S_1^e + F^{(y)} S_1^i} & \text{if } |y| < b \\ \dfrac{2F^{(y)}}{1 + F^{(y)}} & \text{if } |y| > b \end{cases} \tag{14}$$

$$K_h^{(3,xy)} = F^{(x)} \qquad K_h^{(3,yx)} = F^{(y)} \qquad \text{if } 0 < |y| < \infty$$

These coefficients characterize the distorting influence of the three-dimensional surface inhomogeneity. The distortions can be reduced to the induction effect and to the S-effect, known from the two-dimensional model, and to the effect of flowing around or concentration connected with the bend of the field in the three-dimensional model. To separate these effects the three-dimensional model is compared with the two-dimensional one, which is obtained by means of infinitely elongating one of the axes of the inclusion, e.g. the axis $2a$. In such a two-dimensional

model one can observe the induction effect expressed by the coefficient $K_S^{(2,\parallel)}$, and also the S-effect expressed by the coefficient $K_h^{(2,\perp)}$. These coefficients are obtained with Formulae (5), which include the function $\tilde{S}_1(\omega)$ reflecting the integral influence of the excessive currents. In the range of low frequencies $\tilde{S}_1(\omega) \approx \tilde{S}$. The $\tilde{S}$ values are calculated according to Eq. (3) at $L = b$. In the analyzed three-dimensional model the magnetic field was determined by the approximation method, valid under the conditions $a \gg h_1$ and $b \gg h_1$. Therefore, in a two-dimensional model, when calculating $\tilde{S}$, an analogous approximation with $b \gg h_1$ will be applied. Then

$$\tilde{S} \approx \begin{cases} \dfrac{S_1^e + S_1^i}{2} & \text{inside the embedding} \\ S_1^e & \text{outside the embedding} \end{cases}$$

Consequently, according to Eq. (5)

$$K_S^{(2,\parallel)} \approx \begin{cases} \dfrac{2S_1^i}{S_1^i + S_1^e} & \text{if } |y| < b \\ 1 & \text{if } |y| > b \end{cases} \quad \text{interval } S_1$$

$$K_h^{(2,\perp)} \approx \begin{cases} \dfrac{S_1^e}{S_1^i} & \text{if } |y| < b \\ 1 & \text{if } |y| > b \end{cases} \quad \text{interval } h$$

Using this model approximation the induction effect and the S-effect are observed only over the embedding, though a strict calculation would have detected these effects outside the embedding as well.

Let us compare the distortions, observed in the three-dimensional and two-dimensional models. It is obvious that the deviation of $K_{S,h}^{(3)}$ from $K_{S,h}^{(2)}$ characterizes the extent of the flow-around and concentration effects.

Over the embedding $K_{S,h}^{(2)} \neq 1$. Here the flow-around and concentration effects are accompanied by the induction effect and the S-effect. In this case

$$\left.\begin{matrix} 1 > K_S^{(3)} > K_S^{(2)} \\ 1 < K_h^{(3)} < K_h^{(2)} \end{matrix}\right\} \text{for } S_1^i < S_1^e ; \qquad \left.\begin{matrix} 1 < K_S^{(3)} < K_S^{(2)} \\ 1 > K_h^{(3)} > K_h^{(2)} \end{matrix}\right\} \text{ for } S_1^i > S_1^e$$

i.e. the flow-around and concentration effects reduce the influence of the induction effect and of the S-effect. For instance, over the two-dimensional embedding of higher resistivity the S-effect causes an increase of impedance, while due to the current flowing around the three-dimensional embedding an impedance decrease occurs. Obviously, the flow-around effect, at least partially, compensates for the S-effect.

Outside the embedding $K_{S,h}^{(2)} = 1$. Here the flow-around and concentration effects begin to play a leading role. The character of distortions sub-

stantially depends on the orientation of the MTS curves. It is characteristic to the flow-around and concentration effects that

$$K_{s,h}^{(3,xy)} > 1\ ;\ K_{s,h}^{(3yx)} < 1 \qquad \text{flow-around effect } (S_1^e > S_1^i)$$

$$K_{s,h}^{(3,xy)} < 1\ ;\ K_{s,h}^{(3,xy)} > 1 \qquad \text{concentration effect } (S_1^e < S_1^i)$$

As it is seen, outside of the embedding an increase of the impedance Z_{xy} is accompanied by a decrease of the impedance Z_{yx}. This phenomenon has a simple physical interpretation. As an example an embedding of higher resistivity will be considered. When the current flows around this, the E_x (tangent) component increases, while the E_y (normal) component is reduced, causing an increase of the Z_{xy} impedance and a decrease of Z_{yx}.

The distorting effect of a three-dimensional surface inhomogeneity is observed at any orientation of the MTS curves and covers the intervals S_1 and h. In Figures 14 and 15 the curves ϱ_{xy} and ϱ_{yx} are presented over the three-dimensional embedding and outside of it. Normal curves ϱ_N^i and ϱ_N^e calculated for horizontally homogeneous models with the respective resistivities of the upper layer, ϱ_1^i and ϱ_1^e are also shown. The curves ϱ_{xy} and ϱ_{yx} essentially differ from the normal ones.

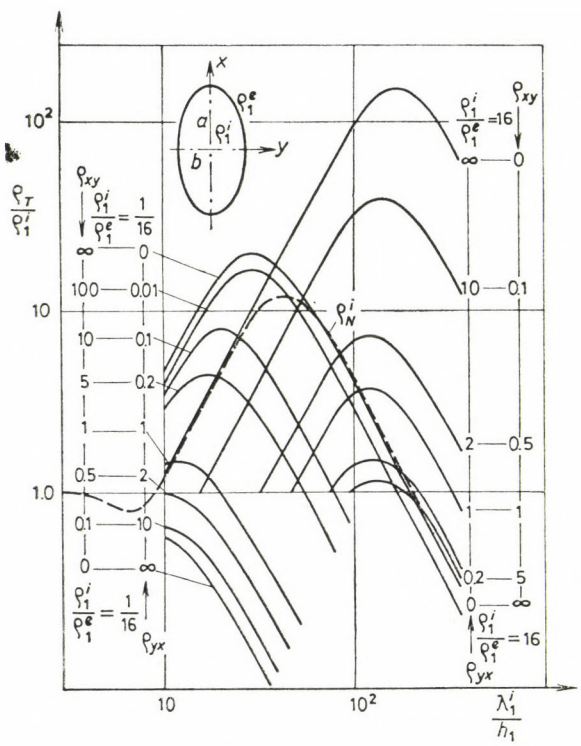


Fig. 14. MTS curves over the elliptical embedding $\varrho_2/\varrho_1^e = \infty$; $\varrho_3/\varrho_1^e = 0$; $h_2/h_1 = 20$; the curves are digitized by a/b and ϱ_1^i/ϱ_1^e in the case being considered ϱ_{xy} $(a/b) = \varrho_{yx}$ (b/a)

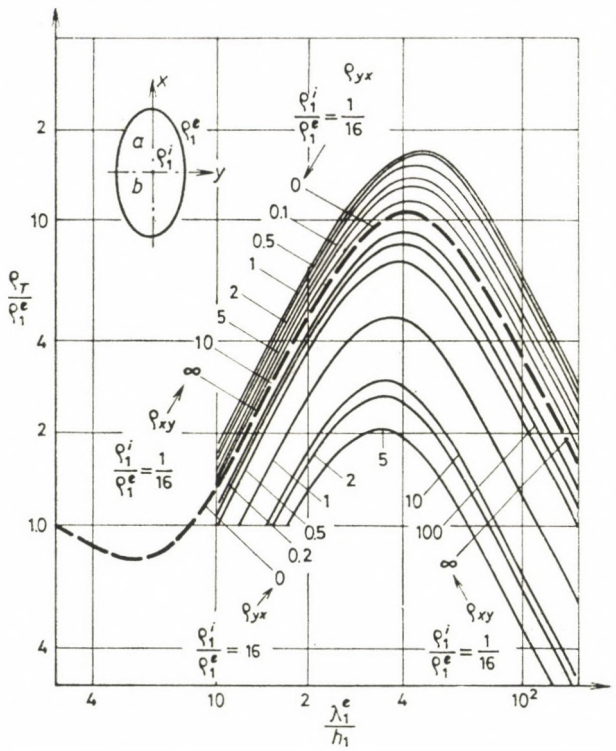


Fig. 15. MTS curves for the outside of the elliptical embedding $x/b = 0$; $|y|/b = 1.5$; $\varrho_2/\varrho_1^e = \infty$; $\varrho_3/\varrho_1^e = 0$; $h_2/h_1 = 20$; the curves are digitized by a/b and ϱ_1^i/ϱ_1^e; in case being considered ϱ_{xy} $(\varrho_1^i/\varrho_1^e) = \varrho_{yx}$ $(\varrho_1^e/\varrho_1^i)$

Over the embedding the electrical and magnetic fields are homogeneous. In this area the curves ϱ_{xy} and ϱ_{yx} do not depend on the observation site. They are distorted by the induction effect, by the S-effect and by the effects of flowing around or concentration. The curves ϱ_{xy} and ϱ_{yx} cross the normal curve, being displaced to the right in case of an embedding of higher resistivity and to the left in case of an embedding of lower resistivity. Most displaced are the curves plotted at $a/b = 0$ or $a/b = \infty$, i.e. at infinite elongation of the axis $2b$ or axis $2a$ of the embedding, when the three-dimensional model degenerates into a two-dimensional one. These extreme curves are distorted by the induction effect and the S-effect. The two-dimensional model is evidently a majorant of the distortion of the MTS curves observed in the three-dimensional model. This is due to the fact that the flow-around and concentration effects diminish the influence of the induction effect and of the S-effect.

Let us determine the conditions under which the three-dimensional and two-dimensional models produce practically the same result. With the impedance Z_{xy} oriented along the axis $2a$ of the embedding, the analysis of the dependence of the distortion coefficients $K^{(3)}_{S,h}$ on the ratio of the semi-axes of the embedding proceeds as follows (Figs 16, 17). The curves $K^{(3)}_{S,h}$ at $a/b \to 0$ and $a/b \to \infty$ merge with the horizontal asymptotes, corresponding to two-dimensional models excited by the H- and E-polarized

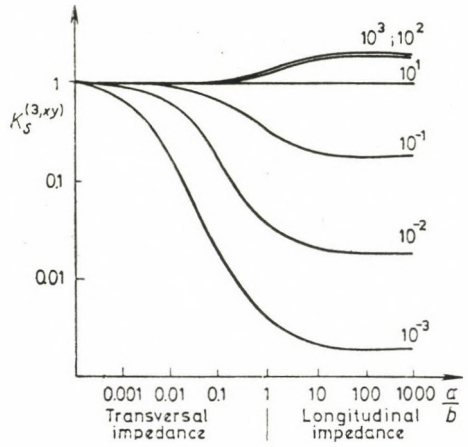


Fig. 16. Dependence of the distortion coefficient $K_S^{(3)}$ on the geometry of the embedding; the observation site is over the embedding
$\varrho_2/\varrho_1^e = \infty$; $\varrho_3/\varrho_1^e = 0$; $h_2/h_1 = 20$; the curves are digitized by S_1^i/S_1^e; in the case being considered $K_S^{(3,yx)}$ $(a/b) = K^{(3,xy)}$ (b/a)

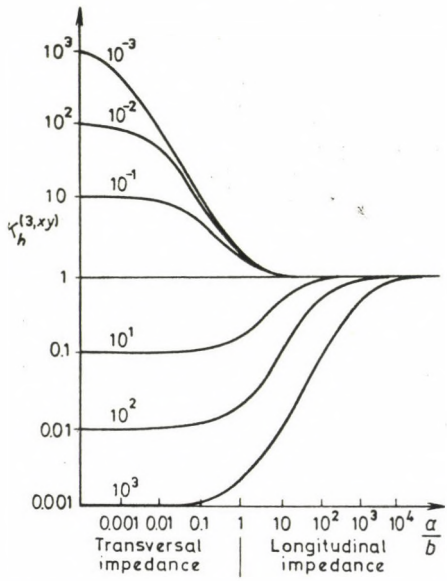


Fig. 17. Dependence of the distortion coefficient $K_h^{(3)}$ on the geometry of the embedding; the observation site is over the embedding
$\varrho_2/\varrho_1^e = \infty$; $\varrho_3/\varrho_1^e = 0$; $h_2/h_1 = 20$; the curves are digitized by S_1^i/S_1^e; in the case being considered $K_h^{(3,xy)}$ $(a/b) = K_h^{(3,yx)}$ (b/a)

field. Let us find the zones in which the $K_{S,h}^{(3)}$ coefficients differ by not more than 10% from their asymptotic values $K_{S,h}^{(2)}$. The boundaries of zones, within which an elliptical embedding can be approximated by a two-dimensional model, are shown in the following table.

TABLE 2

Conditions of applicability of a two-dimensional model

Polarization of the field in a two-dimensional model \ Frequency interval	Interval S_1	Interval h
H-polarization $S_1^i/S_1^e \leq 0.1$	$a/b \leq 0.25$ S_1^i/S_1^e	$a/b \leq 0.1$ S_1^i/S_1^e
$S_1^i/S_1^e \geq 1$	$a/b \leq 0.2$	$a/b \leq 0.1$
E-polarization $S_1^i/S_1^e \leq 1$	$a/b \geq 10$	$a/b \geq 10$
$S_1^i/S_1^e \geq 10$	$a/b \geq 10$	$a/b \geq 10$ S_1^i/S_1^e

As Table 2 shows the two-dimensional models can be applied, if the embedding is much elongated. It should be noted, however, that in models of three-dimensional uplifts and depressions a lesser elongation of the structures is necessary, since the distortions of the field in these models are weaker than in case of an embedding. Besides, it should be kept in mind that the results obtained are only true in the region of low frequencies.

Let us analyse the curves ϱ_{xy} and ϱ_{yx} outside of the embedding (Fig. 15). The observation site lies on the y-axis. These model curves *are only distorted by flow-around or concentration effect*. They almost repeat the normal curve, but, depending on their orientation and on the resistivity of the embeddings, they are shifted upwards or downwards. If the embedding is of higher resistivity, the curves ϱ_{xy} are displaced upwards, the curves ϱ_{yx} downwards (flow-around effect). In case of an embedding of lower resistivity the ϱ_{xy} curves are displaced downwards, the curves ϱ_{yx} upwards (concentration effect). The displacement of the curves significantly depends on a/b. At $a/b = 0$ or $a/b = \infty$ the curves ϱ_{xy} and ϱ_{yx} coincide with the normal curve.

The physical explanation of these results is as follows. Let us consider an embedding of higher resistivity and assume that its $2b$ axis on whose continuation lies the observation site, has a finite length. At $a/b = 0$ the embedding is absent and the curves ϱ_{xy} and ϱ_{yx} are not distorted. If $a/b > 0$ the flow-around effect comes to the foreground (the current flows around the impediment). The impedance Z_{xy} increases and displaces the curves ϱ_{xy} upwards, while impedance Z_{yx} decreases and displaces the curves ϱ_{yx} downwards. With increasing a/b, i.e. when the embedding elongates, the

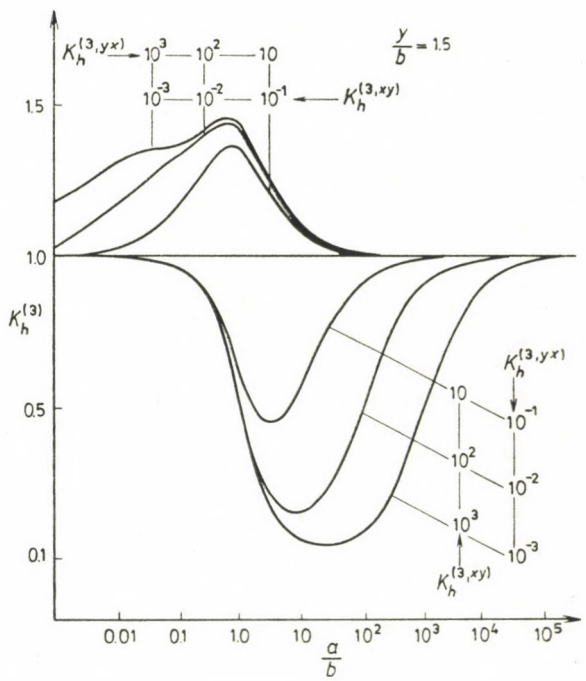


Fig. 18. Dependence of the distortion coefficient $K_h^{(3)}$ on the geometry of the embedding; the observation site is outside the embedding
$x/b = 0$; $|y|/b = 1.5$; $\varrho_2/\varrho_1^e = \infty$; $\varrho_3/\varrho_1^e = 0$; $h_2/h_1 = 20$; the curves are digitized by S_1^i/S_1^e; in the case being considered
$K_h^{(3,xy)}$ $(S_1^i/S_1^e) = K_h^{(3,yx)}$ (S_1^e/S_1^i)

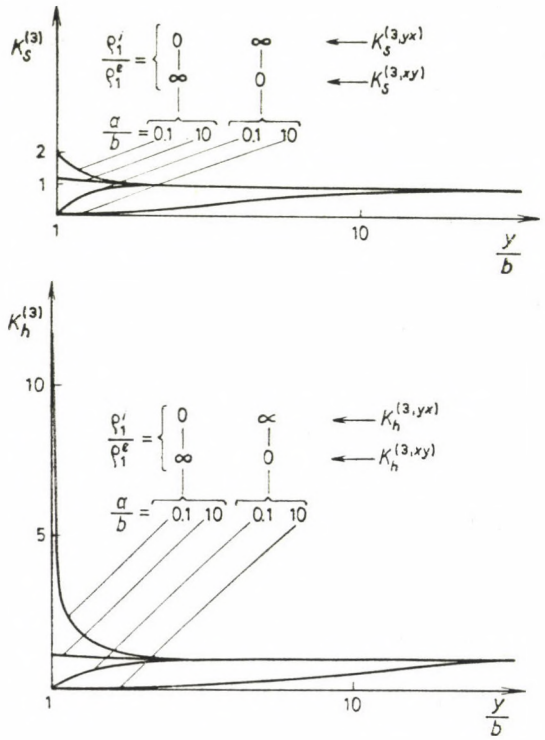


Fig. 19. Dependence of the distortion coefficients on the position of the observation site on the y-axis $\varrho_2/\varrho_1^e = \infty$; $\varrho_3/\varrho_1^e = 0$; $h_2/h_1 = 20$; the curves are digitized by a/b and ϱ_1^i/ϱ_1^e

flow-around effect becomes stronger, reaches its maximum and then it decreases. The flow of the current around a resistive embedding can be compared with the behaviour of a pedestrian meeting an obstacle. He skirts a short obstacle and crosses a long one over. The geometry of the embedding, causing the maximum flow-around effect, depends on its resistivity and on the position of the observation site. At $a/b = \infty$, i.e. when the $2a$ axis is infinitely elongated, the three-dimensional model degenerates into a two-dimensional: the flow-around effect disappears and the ϱ_{xy} and ϱ_{yx} curves coincide with the normal curve.

Figure 18 shows the dependence of the distortion coefficients $K_h^{(3)}$ on the ratios of the semi-axes of the inclusion. The curves $K_h^{(3,\,xy)}$ at $S_1^i/S_1^e < 1$ and $K_h^{(3,yx)}$ at $S_1^i/S_1^e > 1$ have a maximum whose abscissa is $a/b = 1$, while its ordinate does not exceed $1 + b^2/y^2$. The curves $K_h^{(3,xy)}$ at $S_1^i/S_1^e > 1$ and $K_h^{(3,yx)}$ at $S_1^i/S_1^e < 1$ have a deep minimum, whose position considerably depends on S_1^i/S_1^e. When $a/b \to \infty$ the value $K_h^{(3)}$ approaches 1 (the three-dimensional model degenerates into a two-dimensional). The conditions of applicability of a two-dimensional model are the same, as in Table 2.

Figure 19 shows how the distortion coefficients $K_{S,h}^{(3)}$ change, if we get farther away from the insulating or absolutely conducting embeddings, elongated along the x or y-axes. The observation sites lie on the y-axis. The distortions are practically unnoticeable, if the embedding is elongated

along the x-axis ($a/b = 10$) and the primary current flows along the embedding if $\varrho_1^i/\varrho_1^e = \infty$, or across it if $\varrho_1^i/\varrho_1^e = 0$. Otherwise, considerable distortions are observed, which disappear at distances compatible with the major axis of the embedding.

C. We have considered the low frequency asymptotics of MTS curves. It would be important to know, how do the MTS curves look like in the high frequency band. The qualitative pattern can be obtained by conjoining the interference minima and the ascending branches of the normal curves with the analyzed asymptotic curves ϱ_{xy} and ϱ_{yx}. If the ascending branches of the normal curves lie to the right of the ascending branches of the normal curves, additional inflections and minima will possibly appear, making the MTS curves look like five-layer ones (effect of the false conducting layer).

The above analysis shows that a formal interpretation of the curves ϱ_{xy} and ϱ_{yx}, over an embedding of higher resistivity might produce false conducting layers and false depressions of the conducting base. The contradictions of formal interpretation are most evident outside the embedding. If the geoelectrical section computed from the ϱ_{yx} curves contains a false conducting layer and a false uplift of the conducting base, the section constructed of the curves ϱ_{xy} does not contain the false conducting layer, while the false depression corresponds to the false uplift of the conducting base.

Formal interpretation of the curves ϱ_{xy} and ϱ_{yx} over an embedding of lower resistivity brings about a false uplift of the conducting base. Outside the embedding the discrepancies of the results of formal interpretation become obvious. If the curves ϱ_{xy} produce a false conducting layer and a false uplift of the conducting base, from the curves ϱ_{yx} we obtain a false depression of the conducting base.

Thus, the flow-around and concentration effects can give birth to false conducting layers and false structures in the relief of the conducting base. We will now consider methods for the practical analysis of these effects.

In order to detect the flow-around and concentration effects, it is the best to construct a chart of isolines $\varrho_{yx}/\varrho_{xy}$. As an example, we can take an elliptical embedding of lower resistivity, elongated along the y-axis, and construct the chart for $\varrho_{yx}/\varrho_{xy}$, according to the values of ϱ_{xy} and ϱ_{yx}, corresponding to the S_1-interval. This chart, demonstrating the concentration effect, is given in Figure 20. The embedding is surrounded by anomalous zones in which the ratio $\varrho_{yx}/\varrho_{xy}$ considerably differs from unity. The y-axis, along which the curves ϱ_{yx} are oriented, is adjoined by the zones, where $\varrho_{yx}/\varrho_{xy} > 1$, and the x-axis, along which the curves ϱ_{xy} are oriented, is adjoined by the zones in which $\varrho_{yx}/\varrho_{xy} < 1$. Such a distribution of anomalous zones is a characteristic feature of the concentration effect. The deviation of $\varrho_{yx}/\varrho_{xy}$ from unity determines the extent of the concentration effect. An analogous pattern represents the chart for $\varrho_{yx}/\varrho_{xy}$ in case of an embedding of higher resistivity, but the zones with $\varrho_{yx}/\varrho_{xy} > 1$ and $\varrho_{yx}/\varrho_{xy} < 1$ exchange places. This chart allows us to recognize the flow-around effect.

If the flow-around and concentration effects are profound, and the ratios $\varrho_{yx}/\varrho_{xy}$ in the zones surrounding the structure considerably differ from

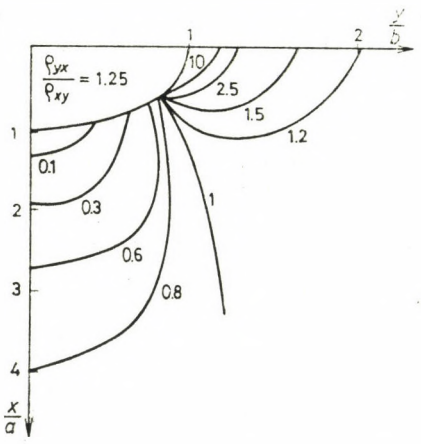


Fig. 20. Chart of isolines $\varrho_{yx}/\varrho_{xy}$ $S_1^i/S_1^e = 50$; $b/a = 2$; $\varrho_2/\varrho_1^e = \infty$; $\varrho_3/\varrho_1^e = 0$; the isolines are digitized by $\varrho_{yx}/\varrho_{xy}$

unity, the geophysicist should, obviously, doubt the reliability of the formal interpretation of the MTS curves. There are two different approaches to the problem. The first refers to the flow-around and concentration effects, the second to the additional influence of the induction effect and the S-effect.

Over uplifts and depressions the flow-around and concentration effects weaken the influence of the induction effect and of the S-effect. In this case, the MTS distortions can be estimated by means of a two-dimensional model, obtained by infinitely elongating the structure. The methods of analysis of two-dimensional models, excited by H- and E-polarized fields, were covered in details in the previous section of the paper. Two-dimensional models at H-polarization give a maximum distortion of the descending branches of the MTS curves (S-effect), and at E-polarization they give a maximum distortion of the ascending branches of the MTS curves (induction effect). Such estimations are particularly important when sounding over uplifts, where the MTS curves, independently of their orientation, can have additional inflections and minima, indicating false conducting layers. If the analysis of a two-dimensional case testifies in favour of the existence of a real intermediate conducting layer, the geophysicist can doubtlessly extend this result to the three-dimensional situation under study. The extent of S-effect, forming false structures in the relief of the conducting base, is evaluated in the same manner. If this effect is weak in the two-dimensional case, it is even more negligible in the three-dimensional one.

When sounding outside the uplifts and depressions (on slopes, in marginal zones) the flow-around and concentration effects can increase the influence of the induction effect and of the S-effect. Here the two-dimensional model does not majorize the distortions of the MTS curves. In this situation comes into importance the comparative analysis of the longitudinal and transversal MTS curves, oriented along and across the contour lines of the high-resistance horizon (a crystalline basement). The analysis consists of a qualitative comparison of the MTS curves and of the study of their

inner discrepancies. The model of an elliptical embedding can serve as a theoretical basis for such an analysis. As an example, the MTS curves for the vicinity of the depression will be considered. If the longitudinal curves have distinct inflections or minima and the transversal curves do not show these features, it can be supposed that the longitudinal curves are distorted by the induction and concentration effects. However, if the inflections and minima are observed on MTS curves of any orientation, this can be regarded as an argument for an intermediate conducting layer. This analysis does not always allow us to make definite conclusions. Additional facts can be obtained through the study of changes of the formal interpretation results or of the abscissae of the separation point when getting farther from the structure. Rough quantitative evaluations can also prove useful: they are performed with the help of the lines $\tilde{S}^*$ or curves $\tilde{\varrho}^*$. Let us assume the observation site lies on the y-axis. The values of $\tilde{S}^*$ and $\tilde{\varrho}^*$ are obtained with the formulae:

$$\tilde{S}^* = \frac{\tilde{S}}{K_S^{(3,xy)}} \qquad \tilde{\varrho}^* = \frac{[K_S^{(3,xy)}]^2}{\omega\mu_0 \tilde{S}_1^2(\omega)}$$

where $\tilde{S}$ or $\tilde{S}_1(\omega)$ characterize the induction effect: $K_S^{(3,xy)}$ determines the concentration effect. The values $\tilde{S}$, $\tilde{S}_1(\omega)$ correspond to the two-dimensional model, obtained by infinitely elongating the studied structure, they are calculated by Formulae (8a) or (8b). The values $K_S^{(3,xy)}$ correspond to the

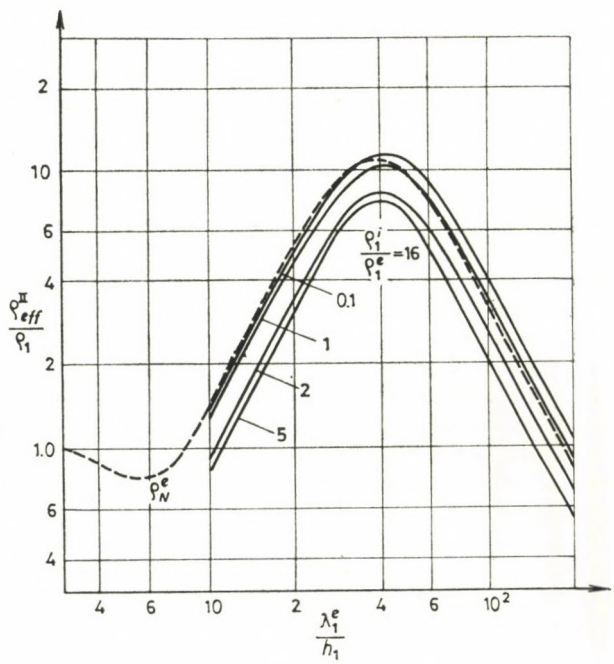


Fig. 21. Effective MTS curves outside the elliptical embedding $x/b = 0$; $|y|/b = 1.5$; $\varrho_1^i/\varrho_1^e = 16$; $\varrho_2/\varrho_1^e = \infty$; $\varrho_3/\varrho_1^e = 0$; $h_2/h_1 = 20$; the curves are digitized by a/b; in the case being considered $\varrho^{II}_{eff}(\varrho_1^i/\varrho_1^e) = \varrho^{II}_{eff}(\varrho_1^e\ \varrho_1^i)$

model of the elliptical embedding, approximating the structure under study; they are calculated by Formula (14). If the minima and inflection of the longitudinal MTS curves lie to the right of the lines $\tilde{S}^*$ or curves $\tilde{\varrho}^*$, the alternative "a conducting layer or the effect of concentration + induction" is solved in favour of the conducting layer.

The flow-around and concentration effects, observed in the vicinity of the isometric structures, can be largely attenuated by means of effective (average) MTS curves. There are two ways to determine the effective impedance (9):

$$Z^{\mathrm{I}}_{eff} = \sqrt{Z_{xx} Z_{yy} - Z_{xy} Z_{yx}}\,; \quad Z^{\mathrm{II}}_{eff} = \frac{Z_{xy} - Z_{yx}}{2}$$

In the model of an elliptical embedding the best results are produced by the impedance Z^{II}_{eff}. Figure 21 shows the curves $\varrho^{\mathrm{II}}_{eff}$, calculated by the impedance Z^{II}_{eff}. When $a/b = 1$ the descending branch of the $\varrho^{\mathrm{II}}_{eff}$ curve coincides with the normal curve. Deviations of the curves $\varrho^{\mathrm{II}}_{eff}$ from the normal one do not exceed 60% in the whole interval of the change of a/b. Good results are also given by the impedance Z^{I}_{eff} (deviation of the curves $\varrho^{\mathrm{I}}_{eff}$ from the normal curve does not exceed 100%). At the same time, the deviation of the curves ϱ_{xy} and ϱ_{yx} from the normal one, as seen in Figure 15, reaches 650%. Thus, the transition to effective impedances considerably reduces the distortions of the MTS curves, caused by the flow-around and concentration effects. During sounding regions with isometric structures, interpretation of effective MTS curves eliminates many difficulties, among them the false conducting layer observed in the vicinity of the isometric depression.

5. MAGNETOTELLURIC SOUNDING OF LAYERED MEDIA IN THE PRESENCE OF DEEP INHOMOGENEITIES (FUNDAMENTAL MODEL III)

This problem is in its stage of development. By now a number of representative results has been obtained, relating to two-dimensional cases. The models under study fall into two groups:

a) models with an uneven surface of the conducting base;

b) models, containing a conducting embedding in a resistive layer.

A. We will begin with the models of the first group, in which the upper layer of constant thickness h_1 and a constant resistivity ϱ_1 lies on the resistive intermediate layer of a constant resistivity $\varrho_2 \gg \varrho_1$. The thickness h_2 of this layer slowly changes along y, and $h_2 \gg h_1$. An absolute conductor lies at the base of the model. We restrict ourselves to the low frequency asymptotics of the impedance, since it is just here that the influence of deep inhomogeneities manifests itself. Such an approximative solution is given in the works of Dmitriev and Mershchikova (1974), Mershchikova (1973). By means of boundary conditions, valid for thin layers, the field equations are reduced to ordinary differential and integro-differential equations.

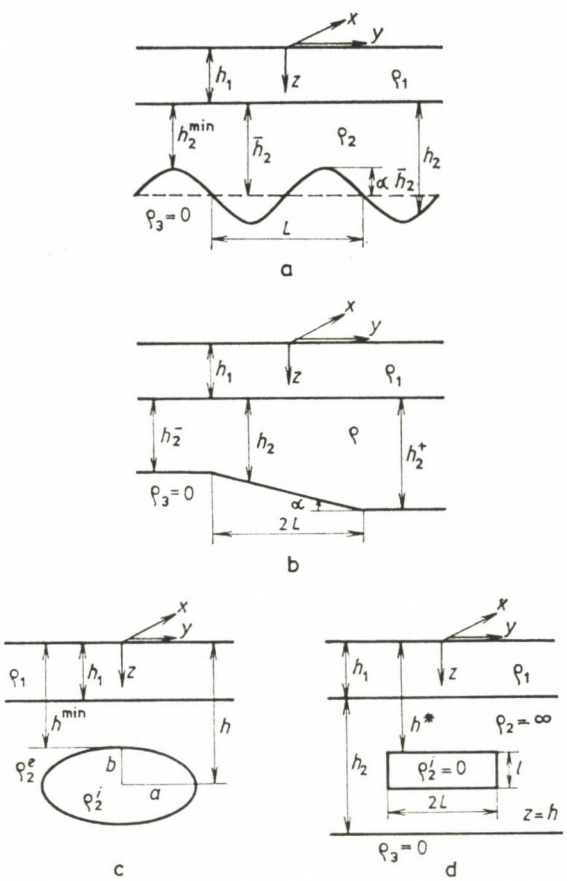


Fig. 22. Types of fundamental model III (two-dimensional structures) a – model of sinusoidal relief; b – model of deep tilted escarpment; c – model of elliptical cylinder; d – model of intercalation of finite width

For sake of illustration we will analyze the model with a sinusoidal surface relief of the conducting base (Fig. 22, a). In this model $h_2 = \bar{h}_2(1 - \alpha \sin(2\pi y/L))$, where $\bar{h}_2$ is the mean thickness of the intermediate layer, $\alpha\bar{h}_2$ and L are the amplitude and period of the oscillations of h_2. Let $\alpha \leq 1/4$ and $L \gg \alpha\bar{h}_2$. These conditions considerably facilitate the solution of the differential and integro-differential equations. The transversal and longitudinal impedances are determined with the asymptotic formulae:

$$Z^{\perp} = -Z_{yx} = \frac{1}{S_1 - \dfrac{1}{i\omega\mu_0 h_a^{\perp}}}\,; \quad Z^{\parallel} = Z_{xy} = \frac{1}{S_1 - \dfrac{1}{i\omega\mu_0 h_a^{\parallel}}}$$

where

$$h_a^{\perp} = h_1 + h_2\left(1 - p_{\alpha}^{\perp} \sin\frac{2\pi y}{L}\right)$$

$$h_a^{\parallel} = h_1 + h_2 \left(1 - p_\alpha^{\parallel} \sin \frac{2\pi y}{L} \right)$$

$S_1 = h_1/\varrho_1$ is the total conductivity of the upper layer; $p^{\perp}$ and $p^{\parallel}$ are auxiliary functions, whose plots are presented in Figure 23. Function $p^{\parallel}$ depends on $h_2^{\min}/L$, where $h_2^{\min} = \bar{h}_2(1 - \alpha)$ is the minimum thickness of the intermediate layer, function $p^{\perp}$ depends on $1/L\tau^{\min}$, where $\tau^{\min}$ is the galvanic constant, determined by $h_2^{\min}$;

$$\tau^{\min} = \frac{1}{\sqrt{S_1 T_2^{\min}}}; \qquad T_2^{\min} = \varrho_2 h_2^{\min}$$

Thus,

$$Z^{\perp} = \begin{cases} \dfrac{1}{S_1} = Z_N & \text{interval } S_1 \\ -i\omega\mu_0 \left[h_1 + \bar{h}_2 \left(1 - p^{\perp} \alpha \sin \dfrac{2\pi y}{L} \right) \right] = K_h^{(2)}(p^{\perp}) Z_N & \text{interval } h \end{cases}$$

$$Z^{\parallel} = \begin{cases} \dfrac{1}{S_1} = Z_N & \text{interval } S_1 \\ -i\omega\mu_0 \left[h_1 + \bar{h}_2 \left(1 - p^{\parallel} \alpha \sin \dfrac{2\pi y}{L} \right) \right] = K_h^{(2)}(p^{\parallel}) Z_N & \text{interval } h \end{cases}$$

where Z_N is the normal impedance.

The transversal and longitudinal impedances in the S_1 interval coincide with the normal impedance Z_N; in the h-interval they differ from Z_N by the coefficients:

$$K_h^{(2)}(p) = \frac{h_1 + \bar{h}_2 \left(1 - p\, \alpha \sin \dfrac{2\pi y}{L} \right)}{h_1 + \bar{h}_2 \left(1 - \alpha \sin \dfrac{2\pi y}{L} \right)}$$

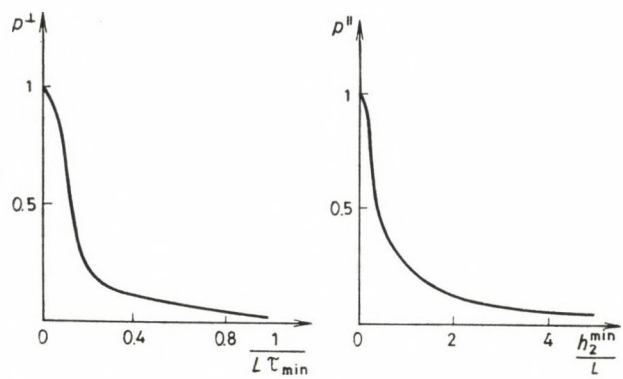


Fig. 23. Auxiliary functions $p^{\perp}$ and $p^{\parallel}$ in the model of sinusoidal relief

which displaces the descending branches of the MTS curves. Formal interpretation of such curves gives apparent depths to the conducting base:

$$h_a = K_h^{(2)}(p)\, h = h_1 + \bar{h}_2 \left(1 - p\,\alpha \sin \frac{2\pi y}{L}\right)$$

where $h = h_1 + h_2(y)$. The h_a values change according to the same sinusoidal law, but with amplitudes $p\alpha\bar{h}_2$. Therefore, the ratio of apparent amplitudes to the true ones is equal to p. Figure 23 shows that $p < 1$. Consequently, the h_a profile underestimates the amplitudes of the structures, i.e. it smoothes out the relief of the conducting base.

The physical nature of the distortions of transversal and longitudinal curves is different.

Transversal curves are distorted by the screening effect being one of the galvanic effects. The reduced sensitivity of these curves to changes of h is attributed to the violation of galvanic connections between the conducting base and the upper layer. It is significant that factor $p^{\perp}$, equal to the ratio of apparent amplitudes of structures to the true ones, is in direct correlation with the galvanic constant $\tau^{\min}$. The less $\tau^{\min}$, i.e. the weaker the galvanic connection between the conducting base and the upper layer, the less $p^{\perp}$, i.e. the stronger the screening. When $L\tau^{\min} \geq 12$ the screening effect shows itself only slightly ($p^{\perp} \geq 0.9$). When $L\tau^{\min} \leq 2$ practically complete screening occurs ($p^{\perp} \leq 0.1$).

Distortions of longitudinal curves are of an induction nature. The factor $p^{\parallel}$ depends only on the minimum thickness of the intermediate layer and on the horizontal size of the structures, i.e. on geometrical factors determining the degree of the induction connection between the conducting base and the upper layer. The larger $h_2^{\min}$ and the smaller L, the greater the smoothing out of the relief of the conducting base. The reduced sensitivity of longitudinal curves to changes of h can be explained by the natural weakening and averaging of the anomalous field when getting farther away from the inhomogeneity. At $h_2^{\min}/L \leq 0.2$ the relief of the conducting base is almost undistorted ($p^{\parallel} \geq 0.9$), while at $h_2^{\min}/L \geq 2.5$ it is almost levelled ($p^{\parallel} \leq 0.1$).

Let us compare the functions $p^{\perp}$ and $p^{\parallel}$, which are the measures of the screening and of the induction effects. The arguments $1/L\tau^{\min}$ and $h_2^{\min}/L$ of these functions differ by a factor depending on the ratio of total conductivities S_1 and $S_2^{\min}$:

$$\frac{1}{L\tau^{\min}} = \frac{h_2^{\min}}{L} \sqrt{\frac{S_1}{S_2^{\min}}}$$

where

$$S_2^{\min} = \frac{h_2^{\min}}{\varrho_2}$$

Under the usual geological circumstances $S_1 \gg S_2^{\min}$. Therefore, $1/L\tau^{\min} \gg h_2^{\min}/L$. In this case, as seen in Fig. 23, $p^{\parallel} \gg p^{\perp}$ i.e. the longitudinal MTS curves reflect the relief of the conducting base much better, than the transversal ones. If at $h_2^{\min}/L = 0.5$ the longitudinal curves give only a

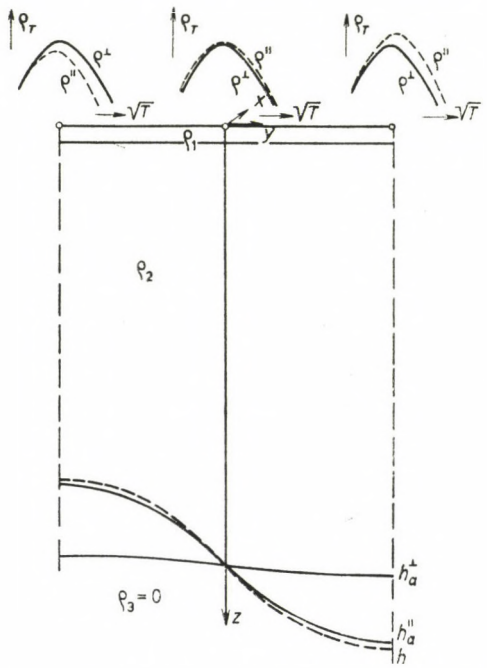


Fig. 24. Profiles of depths in the model of sinusoidal relief $h_2/h_1 = 25$; $\alpha = 0.2$; $S_1/S_2^{\min} = 100$; $L/h_1 = 400$; $L\tau^{\min} = 2$; h is the true depth to the conducting foundation, $h_a^{\perp}$ and $h_a^{\parallel}$ is apparent depths obtained from curves $\varrho^{\perp}$ and $\varrho^{\parallel}$

double reduction of the amplitudes of the structures ($p^{\parallel} = 0.5$) and allow to construct a well-pronounced qualitative pattern, then at the same time the transversal curves almost completely smooth out the structures ($p^{\perp} \ll \ll 0.1$).

A vivid representation of the influence of these deep effects is given by the profiles shown in Figure 24. The $h_a^{\perp}$ profile, obtained by the transversal curves $\varrho^{\perp}$, is very much levelled so that it almost does not mark the relief of the conducting base. At the same time the $h_a^{\parallel}$ profile, obtained by the longitudinal curves $\varrho^{\parallel}$, is near to the true relief. Here the screening effect levels the relief of the conducting base to a much greater extent, than the induction effect. The "inversion" of the descending branches of the transversal and longitudinal MTS curves is characteristic of this typical situation: for the uplift $\varrho^{\parallel} < \varrho^{\perp}$ while for the depression $\varrho^{\parallel} > \varrho^{\perp}$.

Let us analyse another model of the same group, which allows the determination of the size of the region, within which the screening effect shows up. The section corresponding to the model is shown in Fig. 22, b. The surface of the conducting base has an irregularity in the form of a tilted escarpment. In this model h_2^- and h_2^+ are the thicknesses of the intermediate layer over the lifted and lowered sides of the escarpment, $2L$ is the width of the escarpment, α is the angle of its tilt. In the work of Dmitriev and Mershchikova (1974) a case of H-polarization is studied and expressions are obtained for the distortion coefficient $K_h^{(2,\perp)}$. For

$$\frac{\tau L \sqrt{h_2^- h_2^+}}{h_2^+ - h_2^-} \ll 1 ; \qquad \frac{h_2^+}{h_2^-} \leq 5$$

we have

$$K_h^{(2,\perp)} \approx \begin{cases} 1 + \left(\sqrt{\frac{h_2^+}{h_2^-}} - 1\right) e^{(y+L)\tau^-} & \text{if} \quad y < -L \\ \sqrt{\frac{h_2^- h_2^+}{h_2(y)}} & \text{if} \quad -L < y < L \\ 1 + \left(\sqrt{\frac{h_2^-}{h_2^+}} - 1\right) e^{-(y-L)\tau^+} & \text{if} \quad y > L \end{cases}$$

Going away from the edges of the escarpment the screening effect decreases: the distortion coefficient $K_h^{(2,\perp)}$ approaches unity according to the exponential law $\exp(L - |y|)\,\tau$. The region of the action of this effect becomes the narrower, the greater is the galvanic constant τ. Starting out from the existing accuracy of measurements, assume that the screening effect noticeably distorts the results of sounding, if $|K_h^{(2,\perp)} - 1| > 0.1$. Such values of $K_h^{(2,\perp)}$ can be observed, if the changes of h_2 exceed 10% of its average value ($h_2^+ > 1.2\,h_2^-$). The region of prevalence of the screening effect is determined by the condition

$$-L^- < y < L^+$$

where

$$L^- = L + \frac{1}{\tau^-} \ln 10 \left(\sqrt{\frac{h_2^+}{h_2^-}} - 1\right)$$

$$L^+ = L + \frac{1}{\tau^+} \ln 10 \left(1 - \sqrt{\frac{h_2^-}{h_2^+}}\right)$$

As it is seen, the screening effect is localized in the band from L^- to L^+. Outside this band the transversal MTS curves give a depth to the conducting base which is close to the true one.

It is useful to know the tilt of the escarpment, at which the screening effect is practically absent. If

$$\tan \alpha < 0.2\,\tau^- h_2^-$$

then at any L and h_2^+ the $K_h^{(2,\perp)}$ coefficients differ from unity by not more than 10%. (See pp. 236–244.)

B. We will now consider models of the second group, which illustrate the influence of local conducting embeddings. These problems have been elaborated at the Siberian Branch of the Academy of Sciences of the USSR. In the work of Kaufman et al. (1972) a number of two-dimensional models with embeddings of the form of an elliptical cylinder are discussed. The problem is solved by the method of integral equations. The section of one of these models is shown in Fig. 22, c. The upper layer of constant thickness h_1 and constant resistivity ϱ_1 overlies the resistive base of resistivity ϱ_2^e containing an elliptical cylinder of resistivity ϱ_2^i. Here a and b are the horizontal and vertical semiaxes of the cylinder: h is the depth to its centre.

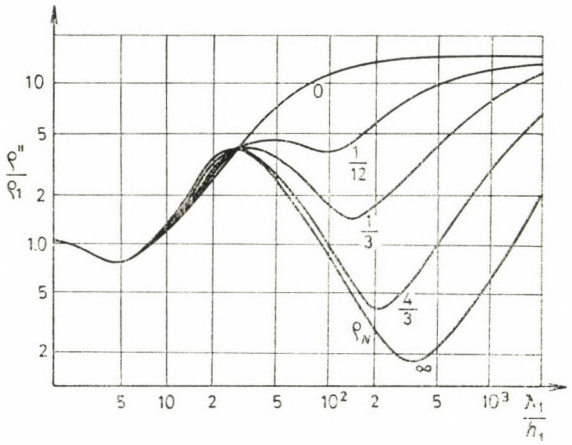


Fig. 25. Longitudinal MTS curves in the model of elliptical cylinder $\varrho_2^e/\varrho_1 = 16$; $\varrho_2^i/\varrho_1 = 1/16$; $h/h_1 = 12$; $b/h_1 = 4$; the curves are digitized by a/h

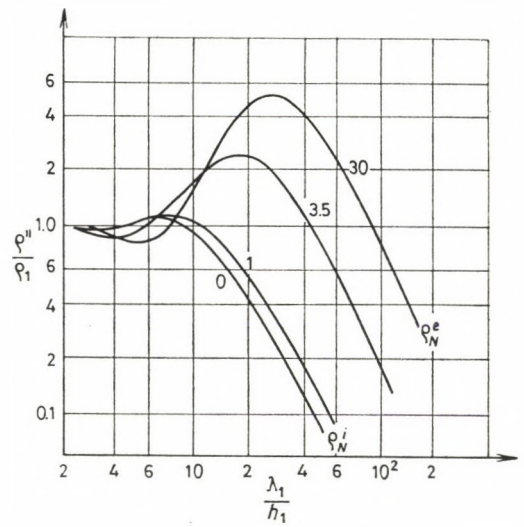


Fig. 26. Longitudinal MTS curves in the model of intercalation of finite width $h_2/h_1 = 10$; $L/h_1 = 1$; $l/h_1 = 0.3$; $h^*/h_1 = 1.3$; the curves are digitized by $|y|/L$

The calculations were made for the E-polarized field. The results are collected in the album (Kaufman et al., 1971). Figure 25 reproduces one of the pages of that album showing the longitudinal MTS curves over the centre of the cylinder. The curves $\varrho^{\|}$ in the low frequency band considerably differ from the normal curve ϱ_N. They have flatter descending branches and not so deep minima. The conducting cylinder manifests itself the better, the longer is its horizontal axis. If $a > h$ the minimum depth $h^{\min}$ to the surface of the cylinder is determined with an error not exceeding 10%. If $a > 2h$ the curve $\varrho^{\|}$ practically coincides with the normal one. If $a < 2h$, the formal interpretation of the longitudinal curves reduces the vertical axis of the cylinder and overestimates its specific resistance.

Figure 22, d shows the section of a less representative model. In this three-layer model the insulating intermediate layer contains an absolutely conducting intercalation of width $2L$ and thickness l at the depth h^*. At the base of the model lies an absolute conductor. The problem was solved by means of a grid integrator. The longitudinal MTS curves are shown in Figure 26 where the normal curves for an observation site over the intercalation and for one being farther away are also given. Over the centre of the intercalation ($y/L = 0$) the curve $\varrho^{\parallel}$ coincides with the normal curve ϱ_N^i and determines the depth to the intercalation. Approximately the same depth is given by the curve $\varrho^{\parallel}$ for the edge of the intercalation ($|y|/L = 1$). This good accuracy of the determination of h^* is due to the fact that the length of the intercalation is greater than the depth of its subsidence, while its conductivity is infinitely high. Going away from the edge of the intercalation, its influence rather quickly disappears. For $|y|/L > 5$ the curves $\varrho^{\parallel}$ approach the normal curve ϱ_N^e and give depths to the conducting base close to the true one.

*

Two important conclusions can be drawn from the above analysis of fundamental model III. First, in the study of the relief of the conducting layers of the earth's crust and upper mantle the longitudinal MTS curves have definite advantages over the transversal ones (see the models of the first group). Second, by means of the longitudinal curves the horizontally elongated conducting embeddings can be detected and localized (see the models of the second group).

6. INFLUENCE OF THE SPATIAL INHOMOGENEITY OF THE EXTERNAL FIELD

If the size of the surface- or deep inhomogeneities is of the order of a thousand or more kilometres and exceeds the limits of the region, where the plane-wave approximation of the external field is valid, there might be a discrepancy between fundamental models II and III and the experimental data.

An example of such a discrepancy is the edge effect, observed in long elongated depressions filled with well-conducting sediments. This galvanic effect is due to the influence of the edges of the depression, it shows up in the reduction of the transversal impedance, i.e. in a deformation of the transversal MTS curves. The ascending branches of the curves $\varrho^{\perp}$ are displaced downwards, they flatten out and acquire additional inflections and minima (Fig. 27). The descending branches of the curves $\varrho^{\perp}$ shift downwards and become steeper. In case of a strong edge effect, false descending branches might appear. Within the scope of models excited by a plane wave the edge effect is unaccountable. Let us take e.g. the model of elliptical embedding (Fig. 13, b) and assume that $a \gg b$ and $\varrho_1^i \ll \varrho_1^e$ (the embedding of lower resistivity is elongated along the x axis). According to Equation (14) if $|y| < b$ i.e. over the embedding, $K_S^{(3,xy)} > K_S^{(3,yx)} \approx 1$

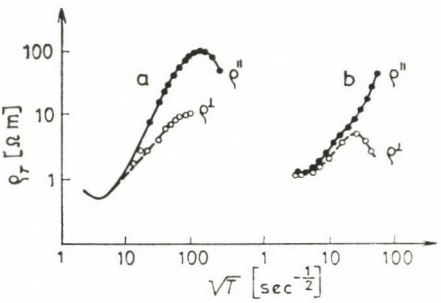


Fig. 27. Practical MTS-curves distorted by the edge effect a – Pre-Kopet-Dag downwarp; b – North-German depression; the descending branch of the curves $\varrho^\perp$ is caused by the edge effect

and $K_h^{(3,yx)} < K_h^{(3,xy)} < 1$, thus $\varrho_{xy} > \varrho_{yx} \approx \varrho_N$ in the S-interval and $\varrho_{yx} < \varrho_{xy} < \varrho_N$ in the h-interval, which is clearly seen in Figure 14. Therefore, in this model only the descending branches of the transversal MTS curves are distorted, while for the edge effect distortions of the ascending branches are also characteristic. Consequently, it can be supposed that the edge effect is connected with the spatial inhomogeneity of the external field. The mechanism of the edge effect has not been studied theoretically. It can only be stated that the depression serves as a channel for the current, and the low frequency electrical field polarizes along its axis, causing the reduction of the transversal impedance in the S- and h-intervals. Towards the edges of the depression this effect becomes stronger. Formal interpretation of transversal MTS curves distorted by the edge effect results in the appearance of false conducting layers and a false relief of deep geoelectrical boundaries. Hints to the edge effect are the stable quasi-linear polarization of the low frequency electrical field along the axis of the depression and the lowering of the transversal MTS curves ($\varrho^\perp < \varrho^\parallel$). The edge effect is also suggested by the growth of the $\varrho^\parallel/\varrho^\perp$ ratio towards the edges of the depression. A vivid example of the edge effect is given in the work of Berdichevsky (1973b).

CONCLUSION

The method of magnetotelluric sounding can provide valuable informations on the electrical conductivity of the earth's interior, its application is, however, hindered by the inhomogeneities of the sedimentary cover distorting the electromagnetic field. We have to realize that the interpretation of distorted MTS curves results in misrepresentation of the geoelectrical section corresponding to the earth's crust and upper mantle, thus creating false layers and a false relief. Magnetotelluric sounding is impossible without an analysis of the appropriateness of geoelectrical models. The considered theoretical models make it possible to understand the mechanism of the most typical distortions and to find their qualitative and quantitative characteristics. These characteristics are logical in nature, for they indicate the presence or absence of the different kinds of distortions (S-effect, edge effect, screening effect, flow-around and concentra-

tion effects, induction effects). For example, the presence of minima on the longitudinal MTS curves and their absence on transversal is characteristic to the induction effect forming the false conducting layer, while an inverse correlation between the total conductivity of the sedimentary cover and the apparent depth to the true conducting layer characterizes the *S*-effect, forming the false relief of deep geoelectrical boundaries. Thus, the interpretation of MTS curves is reduced to the distinguishing of distortions by their logical characteristics and to the extraction of undistorted results. Also very often one has to take recourse to the statistical method of analysis as well. For instance, the occurrence of minima on the majority of MTS curves for several adjacent regions of different tectonic build-up is indicative of the conducting layer, and by an averaging of depths the *S*-effect can considerably be reduced. Thus, in order to construct reliable geoelectric sections we must have numerous soundings covering a sufficiently large territory.

How to begin the interpretation of the results of MTS?

First of all, the optimum orientation of the MTS curves is selected. Up-to-date processing methods of magnetotelluric observations, based on the concept that the impedance is a tensor, provide the freedom of this selection. In regions with linear elongated structures of the sedimentary cover the MTS curves are oriented along and across the axes of structure. Under more complicated conditions the MTS curves should be oriented along and across the contour lines of the crystalline basement, or along and across the characteristic tectonic directions.

In the second step a preliminary formal interpretation of transversal and longitudinal MTS curves is made and all resulting discrepancies are disclosed.

The third step is the most difficult, the geophysicist has to pick out the distortions of longitudinal and transversal MTS curves by means of:

- comparative analysis of longitudinal and transversal curves;
- study of the correlation between deep and surface parameters;
- study of the dependence of deep parameters and coordinates of characteristic points of the MTS curves on the distance to the surface inhomogeneities;
- analysis of magnetovariation data;
- simplified quantitative evaluations;
- comparison with known theoretical and physical models;
- physical modelling of complex situations;
- application of previous experiences of interpretation in regions of similar geological conditions.

By such an analysis a conclusion can be drawn about the degree of the *S*-effect, edge effect, screening effect, induction effects, and flow-around and concentration effects.

The fourth step is analysis of the effective MTS curves: it should be determined to what extent the application of these curves allows to reduce the influence of the flow-around and concentration effects.

The last step involves the comparison of all separate data and selection of the reliable results from unreliable ones. This stage is terminated by the construction of a qualitative and, in favourable conditions, also of a

quantitative model of the geoelectrical section of the earth's crust and upper mantle.

The success of interpretation largely depends on the geometry of the structures of the sedimentary cover. The simplest situation is found in regions with linear elongated structures which can easily be described by two-dimensional models. The criterion of applicability of the two-dimensional approach is the absence of the *S*-effect distorting the longitudinal MTS curves. Under these conditions the analysis of the longitudinal and transversal MTS curves makes it possible to separate induction and galvanic effects.

Longitudinal curves are distorted by induction effects. These distortions are usually insignificant, especially in the zones of the deep basement. Over the uplifts additional minima or inflections arise, caused by the induction effect of depressions. The spurious character of these minima of inflections is determined by quantitative evaluations and theoretical models, as well as by the study of the dependence of coordinates of characteristic points of the MTS curves on the distance to the depression or by a comparison of longitudinal curves with transversal. Getting rid of the false conducting layers, interpretation of longitudinal curves provides an appropriate representation of the geoelectrical section of the earth's interior.

Galvanic effects are typical on the transversal curves (*S*-effect, edge effect, screening effect). These effects deform the transversal curves to such an extent that they become inapplicable for interpretation.

Thus, longitudinal MTS curves are basic. They yield not only qualitative, but also the quantitative pattern of a deep geoelectric section. Studies in such favourable regions should become tasks of primary importance in magnetotelluric sounding. The next most complex is the typical situation of the regions with isometric structures. Here galvanic and induction effects are closely interrelated and can hardly be separated. Under these conditions longitudinal and transversal MTS curves play an auxiliary role, for they only help to distinguish the summary action of galvanic and induction effects and to evaluate the extent of their influence (according to the ratios of longitudinal and transversal apparent resistivites, by the contradictions of formal interpretation, by the dependence of coordinates of characteristic points on the distances to structures, by means of quantitative evaluations and two-dimensional models majorizing the studied effects). Effective MTS curves become basic; they permit to exclude the flow-around and concentration effects, at least in zones, surrounding the structures. This kind of interpretation evidently implies a loss of information, especially in case of a strong manifestation of the *S*-effect, when the geophysicist is forced to abandon the detailed quantitative constructions and he has to restrict himself to a qualitative pattern and to depths determined as average values for the whole region. The best results can be anticipated in regions with a high resistance sedimentary cover and a gently sloping relief of the crystalline basement, where the *S*-effect is weak.

The most difficult regions are those characterized by a complex combination of regional and local structures, by conjugation of faults of different strikes, by ruptures of mountain framing, etc. In such cases a joint analysis of longitudinal, transversal and effective curves is necessary,

based on the above-considered system of logical characteristics and on physical modelling of the most complicated situations. Here the distortions of the MTS curves are not always detected with sufficient certitude and sometimes the results of sounding have to be regarded as hypothetical. To adopt these hypotheses we have to check whether they are geologically plausible, simple, without inner contradictions and in good accordance with most of the MTS curves, obtained in that region.

Special attention should be paid to the problem of combining magnetotelluric and magnetovariation methods. Obviously, these methods should supplement each other quite well. In fact, by means of magnetotelluric sounding we study the stratified structure of the earth's interior, while the magnetovariation sounding and profiling make it possible to study stratification breaks. The first results of such joint researches testify that in this direction geoelectrics could make a good progress.

During the last years in the USSR over 1000 soundings have been carried out. Their interpretation is based on the principles described in this paper. The most interesting result of these researches is the discovery of intermediate conducting layers in the Earth's crust and upper mantle in a number of regions (Berdichevsky et al., 1972; Berdichevsky et al., 1973a). Thus, according to MTS data, the earth's crust at the Vilyuisk syneclise has a well conducting layer at a depth of 20–30 km traced within the Aldan shield. The appearence of this layer can be attributed to dehydration and to the birth of a conducting deep hydrosphere favouring processes of granite formation. Supposedly, an other conducting layer exists in the upper mantle of the South-Caspian depression at a depth of about 60 km. The emergence of this layer is apparently associated with partial melting of the asthenosphere, i.e. with magma formation. There are all grounds to believe that such conducting layers are formed in the process of tectonic activization of the region. (See Chapter 5.)

Magnetotelluric sounding, despite all difficulties and limitations, provides essentially new information about the dynamics of the tectonosphere, since electrical conductivity best responds to changes of temperature, of physico-chemical conditions and of the phase state of the earth's interior.

REFERENCES

Berdichevsky, M. N., 1961. Magnetotelluric field in a horizontally inhomogeneous medium (in Russian). *Prikl. Geofiz.* **31.**

Berdichevsky, M. N., 1968. Electrical prospecting with the method of magnetotelluric profiling (in Russian). Nedra, Moscow.

Berdichevsky, M. N., Bondarenko, A. T., Vanyan, L. L., Parkhomenko, E. I., Fadeev, V. E., Feldman, I. S., 1973a. Electrical conductivity of the upper mantle and the conducting layers in the crust and upper mantle (in Russian). *Stroenie Zemnoi kory i verkhnei mantii morei i okheanov.* Nauka, Moscow.

Berdichevsky, M. N., Bubnov, V. P., Nechaeva, G. P., Druker, E. Z., 1974. Magnetotelluric sounding of horizontally inhomogeneous media (flow-around and concentration effect) (in Russian). *Prikl. Geofiz.* **76.**

Berdichevsky, M. N., Dmitriev, V. I., Vanyan, L. L., 1971. On the possibility of disregarding vertical currents in the theory of magnetotelluric sounding (in Russian). *Izv. Akad. Nauk SSSR, Ser. Fiz. Zemli,* No. 5.

BERDICHEVSKY, M. N., DMITRIEV, V. I., YAKOVLEV, I. A., 1973b. Magnetotelluric sounding of horizontally inhomogeneous media (in Russian). *Izv. Akad. Nauk SSSR, Ser. Fiz. Zemli*, No. 1.

BERDICHEVSKY, M. N., ERSHOV, V. M., 1972. Application of the grid integrator in problems of magnetotelluric sounding (in Russian). *Prikl. Geofiz.* **69.**

BERDICHEVSKY, M. N., ERSHOV, V. M., 1974. Magnetotelluric sounding of horizontally inhomogeneous media (*S*-effect) (in Russian). *Prikl. Geofiz.* **75.**

BERDICHEVSKY, M. N., VANYAN, L. L., FELDMAN, I. S., PORSTENDORFER, G., 1972. Conducting layers in the Earth's crust and upper mantle. *Gerlands Beitr. Geophys.* **81.**

BRYUNELLI, B. E., DOBROVOLSKAYA, M. A., KOVTUN, A. A., 1963. Modelling of inhomogeneous media (in Russian). *Elektromagnitnye zondirovaniya*, Leningrad University.

BRYUNELLI, B. E., DOBROVOLSKAYA, M. A., KOVTUN, A. A., 1969. Certain results of MTP and MTS on models of inhomogeneous structures (in Russian). Magnitotellurichеskie Metody Izucheniya Zemnoi Kory i Verkhnei Mantii, 4. Nauka, Moscow.

CAGNIARD, L., 1953. Basic theory of the magnetotelluric method of geophysical prospecting. *Geophysics* **18**, No. 3.

DENISOVA, I. M., ZAKHAROV, E. V., KOKOTUSHKIN, G. A., 1973. Magnetotelluric field in piecemeal-stratified medium (in Russian). *Vych. metody i programmirovanie* **20.** Moscow University.

DMITRIEV, V. I., 1968a. Electromagnetic fields in inhomogeneous media (in Russian). *Tr. Vych. tsentra Moskovskogo Univ.*

DMITRIEV, V. I., 1968b. The problem of calculating the magnetotelluric field in a layer with arbitrary bend of the lower surface in case of H-polarization (in Russian). *Prikl. Geofiz.* **51.**

DMITRIEV, V. I., 1969a. Magnetotelluric field in flat inhomogeneous layers (in Russian). *Vych. metody i programmirovanie*, **13,** Moscow University.

DMITRIEV, V. I., 1969b. On approximative boundary conditions on the thin inhomogeneous layer in the problems of electrical prospecting (in Russian). *Izv. Akad. Nauk SSSR, Ser. Fiz. Zemli*, No. 12.

DMITRIEV, V. I., 1970. Direct and reverse problems of magnetotelluric sounding of a stratified medium (in Russian). *Izv. Akad. Nauk SSSR, Ser. Fiz. Zemli*, No. 1.

DMITRIEV, V. I., KHRYCHIKOVA, T. S., 1975. On the influence of the variations of thickness of the surface layer on deep magnetotelluric sounding (in Russian). *Vych. metody i programmirovanie*, **24,** Moscow University.

DMITRIEV, V. I., KOKOTUSHKIN, G. A., 1971. Album of curves of magnetotelluric sounding in inhomogeneous media (in Russian). 1, Moscow University.

DMITRIEV, V. I., MERSHCHIKOVA, N. A., 1974. On the resolving power of deep magnetotelluric sounding (in Russian). *Izv. Akad. Nauk SSSR, Ser. Fiz. Zemli*, No. 8.

DMITRIEV, V. I., RUDNEVA, T. L., 1971. Algorithm of the solution of the inverse problem of magnetotelluric sounding (in Russian). *Tr. Vych. tsentra Moskovskogo Univ.*

DMITRIEV, V. I., ZAKHAROV, E. V., 1970. Method for the solution of electrodynamical problems in inhomogeneous media (in Russian). *Zh. Vych. Matem. i Matem. Fiz.* **10,** No. 6.

DMITRIEV, V. I., ZAKHAROV, E. V., KOKOTUSHKIN, G. A., 1973. Master curves for magnetotelluric sounding in inhomogeneous media (in Russian). 2, Moscow University.

GOLTSMAN, F. M., KOVTUN, A. A., POROKHOVA, L. N., 1969. Problems of machine interpretation of the MTS curves (in Russian). *Izv. Akad. Nauk SSSR, Ser. Fiz. Zemli*, No. 4.

KAUFMAN, A. A., 1961. Three methods of excitation of the field in the low-frequency electrical prospecting of ore deposits (in Russian). *Geol. i Geofiz.* No. 5.

KAUFMAN, A. A., TABOROVSKY, L. A., 1970. Electromagnetic field for gently sloping structures (in Russian). *Elektromagnitnye polya v geofizicheskikh metodakh issledovaniya*. Nauka, Moscow.

KAUFMAN, A. A., TABOROVSKY, L. A., TERENTEV, S. A., 1971. Electromagnetic field of the elliptical cylinder in a horizontally stratified medium (in Russian). *SO AN SSSR*. Novosibirsk.

KAUFMAN, A., A., TABOROVSKY, L. A., TERENTEV, S. A., 1972. To the theory of the inductive electrical mining prospecting in horizontally inhomogeneous media (in Russian). *Geol. i Geofiz.* No. 10.

KOKOTUSHKIN, G. A., 1969. On the calculation of the magnetotelluric field of E-polarization for the layer with alternating thickness (in Russian). *Vych. metody i programmirovanie*, **13**, Moscow University.

MADDEN, T. R., SWIFT, C. M., 1969. Magnetotelluric investigation of conductivity of Earth's crust and upper mantle. The Earth's crust and Upper Mantle. American Geophysical Union, Washington.

MERSHCHIKOVA, N. A., 1973. Magnetotelluric sounding with periodically changing depth to the upper mantle (in Russian). Magnitotellurichеskie polya v neognorodnykh sredakh. *Tr. Vych. tsentra Moskovskogo Univ.*

OBUKHOV, G. G., 1969. Approximative methods for the study of the magnetotelluric field in horizontally inhomogeneous media (in Russian). Magnitotellurichеskie Metody Izucheniya Zemnoi Kory i Verkhnei Mantii, 4. Nauka, Moscow.

SAMARSKY, A. A., 1971. Introduction to the theory of difference schemes (in Russian). Nauka, Moscow.

SVETOV, B. S., PETROVSKY, A. D., 1966. Electromagnetic methods of prospecting in mining geophysics (in Russian). Nedra, Moscow.

SWIFT, G. M., 1967. A magnetotelluric investigation of an electrical conductivity anomaly in the southwestern United States. Ph. D. Thesis M. I. T.

TABOROVSKY, L. A., 1972. Construction of integral equations and Green operators by the method of auxiliary sources (in Russian). *Geol. i Geofiz.* No. 9.

TIKHONOV, A. N., BERDICHEVSKY, M. N., 1966. The practice of application of magnetotelluric methods in the study of the geological structure of sedimentary basins (in Russian). *Izv. Akad. Nauk SSSR, Ser. Fiz. Zemli*, No. 2.

TIKHONOV, A. N., DMITRIEV, V. I., 1969. Influence of surface inhomogeneities on deep magnetotelluric sounding (in Russian). *Vych. Metody i programmirovanie*, **13**, Moscow University.

TIKHONOV, A. N., SHAKHSUVAROV, D. N., 1956. On the possibility of using the impedance of the natural electromagnetic field of the Earth for the study of its upper layers (in Russian). *Izv. Akad. Nauk SSSR, Ser. Geofiz.*, No. 4.

ZABOROVSKY, A. I., 1963. Electrical prospecting (in Russian). Gostoptekhizdat, Moscow.

ZAKHAROV, E. V., 1973. On the behaviour of the amplitude of MTS curves over a three-layered structure with inhomogeneous surface layer (in Russian). Magnitotellurichеskie polya v neodnarodnykh sredakh, *Tr. Vych. tsentra Moskovskogo Univ.*

IMPEDANCE OF THE ELECTROMAGNETIC FIELD IN A HORIZONTALLY LAYERED ANISOTROPIC HALF-SPACE

V. PETR

INTRODUCTION

An increasing number of magnetotelluric deep soundings has led to the conclusion that the crust and the upper mantle cannot be considered as a simple medium where each particular layer is characterized by a scalar conductivity. A generalization of the concept of conductivity was needed. A natural assumption was that the horizontal electrical conductivity is a tensor in any individual layer of a horizontally stratified cross-section (Rokityansky, 1961; Srivastava, 1963; Ádám, 1964; Praus, 1966). In calculating the impedance of a horizontally layered anisotropic medium we assume a plane electromagnetic wave incident perpendicularly at each individual horizontal interface. This problem will be solved in certain steps (Petr, 1966, 1967), which we are going to describe in what follows.

1. ELECTROMAGNETIC FIELD IN AN ANISOTROPIC LAYER

Let us assume a half-space containing a sequence of $(n-1)$ horizontal layers. The n-th layer in the bottom is a homogeneous infinite half-space (Fig. 1). The electromagnetic characteristics of the cross section are apparent from Figure 1. Let us calculate the electromagnetic field in any horizontal layer. Its conductivity is assumed to be a tensor

$$\{\boldsymbol{\sigma}^l\} = \begin{pmatrix} \sigma^l_{11}, & \sigma^l_{12} \\ \sigma^l_{21}, & \sigma^l_{22} \end{pmatrix} \tag{1}$$

The electromagnetic wave is defined by vectors

$$\mathbf{E} = \mathbf{E}_0 \, e^{i\omega t} \tag{2}$$

$$\mathbf{H} = \mathbf{H}_0 \, e^{i\omega t} \tag{3}$$

where $\mathbf{E}$ and $\mathbf{H}$ are vectors of the electric and magnetic fields, ω is angular frequency and t is time. Magnetic permeability $\mu = \mu_0 = 4\pi \cdot 10^{-7}$ [H/m] is assumed to be constant in the whole cross section.

Introduce a rectangular co-ordinate system x, y, z with the origin in the point of observation and with the positive z-axis directed into the half-

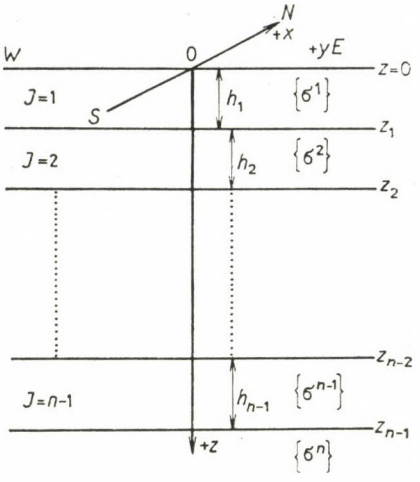


Fig. 1. Cross section of a horizontally stratified medium

space. The axes x and y coincide with NS and EW directions. Maxwell's equations for the fields in each layer are written in the following form

$$\operatorname{curl} \mathbf{H} = \{\boldsymbol{\sigma}^l\}\,\mathbf{E} \tag{4}$$

$$\operatorname{curl} \mathbf{E} = -\,i\omega\mu\,\mathbf{H} \tag{5}$$

$$\operatorname{div} \mathbf{H} = 0 \tag{6}$$

Equation (6) will be satisfied by introducing a magnetic vector potential **A** according to relation

$$\mathbf{H} = \operatorname{curl} \mathbf{A} \tag{7}$$

The vector of the electric field is obtained from Eqs (7) and (5) as

$$\mathbf{E} = -\,i\omega\mu\,\mathbf{A} + \operatorname{grad} \Phi \tag{8}$$

where Φ is any function of coordinates. On inserting Eqs (7) and (8) into (4) we get

$$\operatorname{grad} \operatorname{div} \mathbf{A} - \Delta\mathbf{A} = -\,i\omega\mu\{\boldsymbol{\sigma}\}\,\mathbf{A} + \{\boldsymbol{\sigma}^l\} \operatorname{grad} \Phi \tag{9}$$

Assuming plane electromagnetic waves, i. e. $H_3 = E_3 = 0$ we arrive at formulae

$$\frac{\partial A_2}{\partial x} - \frac{\partial A_1}{\partial y} = 0 \tag{10}$$

$$i\omega\mu\, A_3 = \frac{\partial \Phi}{\partial z} \tag{11}$$

Equation (10) will be satisfied by defining components of the vector potential A_1 and A_2 in terms of a function $P(x, y, z)$ in the following form

$$A_1 = \frac{\partial P}{\partial x}, \quad A_2 = \frac{\partial P}{\partial y} \tag{12}$$

The components of the vector Eq. (8) read

$$\frac{\partial^3}{\partial x \partial z^2}(\Phi - i\omega\mu P) = i\omega\mu\sigma'_{11}\frac{\partial}{\partial x}(\Phi - i\omega\mu P) + i\omega\mu\sigma'_{12}\frac{\partial}{\partial y}(\Phi - i\omega\mu P) \quad (13)$$

$$\frac{\partial^3}{\partial y \partial z^2}(\Phi - i\omega\mu P) = i\omega\mu\sigma'_{21}\frac{\partial}{\partial x}(\Phi - i\omega\mu P) + i\omega\mu\sigma'_{22}\frac{\partial}{\partial y}(\Phi - i\omega\mu P) \quad (14)$$

$$\frac{\partial^3}{\partial x^2 \partial z}(\Phi - i\omega\mu P) + \frac{\partial^3}{\partial y^2 \partial z}(\Phi - i\omega\mu P) = 0 \quad (15)$$

where relations (11) and (12) have been taken into account. Introducing the notation

$$\Phi - i\omega\mu P = S(x, y)\, T(z)$$

we can rewrite Eqs (13—15) in the form

$$\frac{\partial S}{\partial x}\left(\frac{d^2T}{dz^2} - i\omega\mu\sigma'_{11}T\right) - i\omega\mu\sigma'_{12}T\frac{\partial S}{\partial y} = 0 \quad (17)$$

$$\frac{\partial S}{\partial y}\left(\frac{d^2T}{dz^2} - i\omega\mu\sigma'_{21}T\right) - i\omega\mu\sigma'_{22}T\frac{\partial S}{\partial x} = 0 \quad (18)$$

$$\frac{\partial^2 S}{\partial x^2} + \frac{\partial^2 S}{\partial y^2} = 0 \quad (19)$$

In order that the solution of the system of Eqs (17) and (18) should not be trivial its determinant must be zero. We get, therefore,

$$\left(\frac{1}{i\omega\mu T}\frac{d^2T}{dz^2}\right)^2 - (\sigma'_{11} + \sigma'_{22})\left(\frac{1}{i\omega\mu T}\frac{d^2T}{dz^2}\right) + (\sigma'_{11}\sigma'_{22} - \sigma'_{12}\sigma'_{21}) = 0 \quad (20)$$

and its solution in the form

$$C_1^{(l)}(z=)T\exp\left[\sqrt{\left(i\omega\mu\frac{1}{2}\{\sigma'_{11}+\sigma'_{22}+\sqrt{[(\sigma'_{11}+\sigma'_{22})^2-4(\sigma'_{11}\sigma'_{22}-\sigma'_{12}\sigma'_{21})]}\}\right)}z\right]+ \quad (21)$$

$$+ C_{12}^{(l)}\exp\left[-\sqrt{\left(i\omega\mu\frac{1}{2}\{\sigma'_{11}+\sigma'_{22}+\sqrt{[(\sigma'_{11}+\sigma'_{22})^2-4(\sigma'_{11}\sigma'_{22}-\sigma'_{12}\sigma'_{21})]}\}\right)}z\right]$$

$$T_2^{(l)}(z) = C'_{21}\exp\left[\sqrt{i\omega\mu\frac{1}{2}\{\sigma'_{11}+\sigma'_{22}-\sqrt{[(\sigma'_{11}+\sigma'_{22})^2-4(\sigma'_{11}\sigma'_{22}-\sigma'_{12}\sigma'_{21})]}\}}z\right]+ \quad (22)$$

$$+ C_{22}^{(l)}\exp\left[-\sqrt{\left(i\omega\mu\frac{1}{2}\{\sigma'_{11}+\sigma'_{22}-\sqrt{[(\sigma'_{11}+\sigma'_{22})^2-4(\sigma'_{11}\sigma'_{22}-\sigma'_{12}\sigma'_{21})]}\}\right)}z\right]$$

According to tensor calculus the expressions

$$\sigma_1^l = \frac{1}{2}\{\sigma_{11}^l + \sigma_{22}^l + [(\sigma_{11}^l + \sigma_{22}^l)^2 - 4(\sigma_{11}^l\sigma_{22}^l - \sigma_{12}^l\sigma_{21}^l)]^{1/2}\} \tag{23}$$

$$\sigma_2^l = \frac{1}{2}\{\sigma_{11}^l + \sigma_{22}^l - [(\sigma_{11}^l + \sigma_{22}^l)^2 - 4(\sigma_{11}^l\sigma_{22}^l - \sigma_{12}^l\sigma_{21}^l)]^{1/2}\} \tag{24}$$

are known to be the principal components of conductivity tensor of the medium under investigation. Relations (21) and (22) can be rewritten in terms of σ_1^l and σ_2^l as

$$T_1^{(l)}(z) = C_{11}^l e^{\sqrt{i\omega\mu\sigma_1^l}z} + C_{12}^{(l)} e^{-\sqrt{i\omega\mu\sigma_1^l}z} \tag{25}$$

$$T_2^{(l)}(z) = C_{21}^{(l)} e^{\sqrt{i\omega\mu\sigma_2^l}z} + C_{22}^{(l)} e^{-\sqrt{i\omega\mu\sigma_2^l}z} \tag{26}$$

Inserting Eqs (25) and (26) into (17) and (18) we get

$$\begin{aligned} i\omega\mu(\sigma_1^l - \sigma_{11}^l)\, T_1^{(l)} \frac{\partial S}{\partial x} - i\omega\mu\sigma_{12}^l T_1^{(l)} \frac{\partial S}{\partial y} = 0 \\ i\omega\mu\sigma_{22}^l\, T_1^{(l)} \frac{\partial S}{\partial x} - i\omega\mu(\sigma_1^l - \sigma_{21}^l)\, T_1^{(l)} \frac{\partial S}{\partial y} = 0 \end{aligned} \tag{27}$$

$$\begin{aligned} i\omega\mu(\sigma_2^l - \sigma_{11}^l)\, T_2^{(l)} \frac{\partial S}{\partial x} - i\omega\mu\sigma_{12}^l T_2^{(l)} \frac{\partial S}{\partial y} = 0 \\ i\omega\mu\sigma_{22}^l\, T_2^{(l)} \frac{\partial S}{\partial x} - i\omega\mu(\sigma_2^l - \sigma_{21}^l)\, T_2^{(l)} \frac{\partial S}{\partial y} = 0 \end{aligned} \tag{28}$$

By analysing the latter equations we can show (Petr, 1967) that for any $T_1^{(l)}$ and $T_2^{(l)}$ the corresponding functions $S_1^{(l)}$ and $S_2^{(l)}$ are defined by the relations

$$\frac{\partial S_1^{(l)}}{\partial x} = \frac{\sigma_{12}^l}{\sigma_1^l - \sigma_{11}^l} \frac{\partial S_1^{(l)}}{\partial y} \tag{29}$$

$$\frac{\partial S_2^{(l)}}{\partial x} = \frac{\sigma_{12}^l}{\sigma_2^l - \sigma_{11}^l} \frac{\partial S_2^{(l)}}{\partial y} \tag{30}$$

The components of the electromagnetic field are now determined according to (7) and (8) as

$$\begin{aligned} H_1^{(l)} &= \frac{1}{i\omega\mu}\left(\frac{\partial S_1^{(l)}}{\partial y}\frac{\partial T_1^{(l)}}{\partial z} + \frac{\partial S_2^{(l)}}{\partial y}\frac{\partial T_2^{(l)}}{\partial z}\right) \\ H_2^{(l)} &= -\frac{1}{i\omega\mu}\left(\frac{\partial S_1^{(l)}}{\partial x}\frac{\partial T_1^{(l)}}{\partial z} + \frac{\partial S_2^{(l)}}{\partial x}\frac{\partial T_2^{(l)}}{\partial z}\right) \end{aligned} \tag{31}$$

$$E_1^{(l)} = \frac{\partial S_1^{(l)}}{\partial x} T_1^{(l)} + \frac{\partial S_2^{(l)}}{\partial x} T_2^{(l)}; \quad E_2^{(l)} = \frac{\partial S_1^{(l)}}{\partial y} T_1^{(l)} + \frac{\partial S_2^{(l)}}{\partial y} T_2^{(l)}$$

which can be transformed by means of Eqs (25), (26) and (29), (30) to the following formulae

$$H_1^{(l)} = \left[\sqrt{\frac{\sigma_1^l}{i\omega\mu}} C_{11}^{(l)} \frac{\partial S_1^{(l)}}{\partial y} e^{\sqrt{i\omega\mu\sigma_1^l} z} - \sqrt{\frac{\sigma_1^l}{i\omega\mu}} C_{12}^{(l)} \frac{\partial S_1^{(l)}}{\partial y} e^{-\sqrt{i\omega\mu\sigma_1^l} z} + \right.$$

$$\left. + \sqrt{\frac{\sigma_2^l}{i\omega\mu}} C_{21}^{(l)} \frac{\partial S_2^{(l)}}{\partial y} e^{\sqrt{i\omega\mu\sigma_2^l} z} - \sqrt{\frac{\sigma_2^l}{i\omega\mu}} C_{22}^{(l)} \frac{\partial S_2^{(l)}}{\partial y} e^{-\sqrt{i\omega\mu\sigma_2^l} z} \right] e^{i\omega t} \tag{32}$$

$$H_2^{(l)} = \left[-\sqrt{\frac{\sigma_1^l}{i\omega\mu}} C_{11}^{(l)} \frac{\sigma_{12}^l}{\sigma_1^l - \sigma_{11}^l} \frac{\partial S_1^{(l)}}{\partial y} e^{\sqrt{i\omega\mu\sigma_1^l} z} + \sqrt{\frac{\sigma_1^l}{i\omega\mu}} C_{12}^{(l)} \frac{\sigma_{12}^l}{\sigma_1^l - \sigma_{11}^l} \frac{\partial S_1^{(l)}}{\partial y} e^{-\sqrt{i\omega\mu\sigma_1^l} z} - \right.$$

$$\left. - \sqrt{\frac{\sigma_2^l}{i\omega\mu}} C_{21}^{(l)} \frac{\sigma_{12}^l}{\sigma_2^l - \sigma_{11}^l} \frac{\partial S_2^{(l)}}{\partial y} e^{\sqrt{i\omega\mu\sigma_2^l} z} + \sqrt{\frac{\sigma_2^l}{i\omega\mu}} C_{22}^{(l)} \frac{\sigma_{12}^l}{\sigma_2^l - \sigma_{11}^l} \frac{\partial S_2^{(l)}}{\partial y} e^{-\sqrt{i\omega\mu\sigma_2^l} z} \right] e^{i\omega t} \tag{33}$$

$$E_1^{(l)} = \left[\frac{\sigma_{12}^l}{\sigma_1^l - \sigma_{11}^l} \frac{\partial S_1^{(l)}}{\partial y} \left(C_{11}^{(l)} e^{\sqrt{i\omega\mu\sigma_1^l} z} + C_{12}^{(l)} e^{-\sqrt{i\omega\mu\sigma_1^l} z} \right) + \right.$$

$$\left. + \frac{\sigma_{12}^l}{\sigma_2^l - \sigma_{11}^l} \frac{\partial S_2^{(l)}}{\partial y} \left(C_{21}^{(l)} e^{\sqrt{i\omega\mu\sigma_2^l} z} + C_{22}^{(l)} e^{-\sqrt{i\omega\mu\sigma_2^l} z} \right) \right] e^{i\omega t} \tag{34}$$

$$E_2^{(l)} = \left[\frac{\partial S_1^{(l)}}{\partial y} \left(C_{11}^{(l)} e^{\sqrt{i\omega\mu\sigma_1^l} z} + C_{12}^{(l)} e^{-\sqrt{i\omega\mu\sigma_1^l} z} \right) + \right.$$

$$\left. + \frac{\partial S_2^{(l)}}{\partial y} \left(C_{21}^{(l)} e^{\sqrt{i\omega\mu\sigma_2^l} z} + C_{22}^{(l)} e^{-\sqrt{i\omega\mu\sigma_2^l} z} \right) \right] e^{i\omega t} \tag{35}$$

Owing to the fact that the components $H_1^{(l)}$, $H_2^{(l)}$, $E_1^{(l)}$, $E_2^{(l)}$ are independent of the x and y coordinates, the expressions $\partial S_1^{(l)}/\partial y$, $\partial S_2^{(l)}/\partial y$ must be constant functions. In virtue of this Eq. (19) is satisfied automatically, as well. Let us introduce the notations

$$E_{11}^{(l)} = \frac{\partial S_1^{(l)}}{\partial y} C_{11}^{(l)}; \quad E_{12}^{(l)} = \frac{\partial S_1^{(l)}}{\partial y} C_{12}^{(l)}; \quad E_{21}^{(l)} = \frac{\partial S_2^{(l)}}{\partial y} C_{21}^{(l)}; \quad E_{22}^{(l)} = \frac{\partial S_2^{(l)}}{\partial y} C_{22}^{(l)} \tag{36}$$

$$k_{l,1} = \sqrt{i\omega\mu\sigma_1^l}; \quad k_{l,2} = \sqrt{i\omega\mu\sigma_2^l} \tag{37}$$

and recall the tensor definitions

$$\frac{\sigma_{12}^l}{\sigma_1^l - \sigma_{11}^l} = \cot \alpha_l; \quad \frac{\sigma_{12}^l}{\sigma_2^l - \sigma_{11}^l} = -\tan \alpha_l \tag{38}$$

where α_l is the azimuth of the principal conductivity σ_1^l then the field components in a horizontal anisotropic layer read

$$H_1^{(l)} = \left[\sqrt{\frac{\sigma_1^l}{i\omega\mu}}\,(E_{11}^{(l)}\,e^{k_{l,1}z} - E_{12}^{(l)}e^{-k_{l,1}z}) + \sqrt{\frac{\sigma_2^l}{i\omega\mu}}\,(E_{21}^{(l)}e^{k_{l,2}z} - E_{22}^{(l)}e^{-k_{l,2}z})\right] e^{i\omega t} \quad (39)$$

$$H_2^{(l)} = \left[-\sqrt{\frac{\sigma_1^l}{i\omega\mu}}\,(E_{11}^{(l)}\,e^{k_{l,1}z} - E_{12}^{(l)}\,e^{-k_{l,1}z})\cot\alpha_l + \right.$$

$$\left. + \sqrt{\frac{\sigma_2^l}{i\omega\mu}}\,(E_{21}^{(l)}\,e^{k_{l,2}z} - E_{22}^{(l)}\,e^{-k_{l,2}z})\tan\alpha_l\right] e^{i\omega t} \quad (40)$$

$$E_1^{(l)} = [(E_{11}^{(l)}\,e^{k_{l,1}z} + E_{12}^{(l)}\,e^{-k_{l,1}z})\cot\alpha_l - (E_{21}^{(l)}\,e^{k_{l,2}z} + E_{22}^{(l)}\,e^{-k_{l,2}z})\tan\alpha_l]\,e^{i\omega t} \quad (41)$$

$$E_2^{(l)} = (E_{11}^{(l)}\,e^{k_{l,1}z} + E_{12}^{(l)}\,e^{-k_{l,1}z} + E_{21}^{(l)}\,e^{k_{l,2}z} + E_{22}^{(l)}\,e^{-k_{l,2}z})\,e^{i\omega t} \quad (42)$$

2. CALCULATION OF THE IMPEDANCE TENSOR COMPONENTS

Relations (39)—(42) are used to calculate the impedance tensor components of the electromagnetic field in a horizontally layered anisotropic medium. First, we find the field in an anisotropic half-space in the basement of the model (Fig. 1). This section is labelled as n-th medium. We obtain the components of the electromagnetic field from Eqs (39)—(42) by respecting, at the same time, the condition for the field to vanish in the infinity. It holds

$$H_1^{(n)}(z) = \left[-\sqrt{\frac{\sigma_1^n}{i\omega\mu}}\,E_{12}^{(n)}\,e^{-k_{n,1}z} - \sqrt{\frac{\sigma_2^n}{i\omega\mu}}\,E_{22}^{(n)}\,e^{-k_{n,2}z}\right] e^{i\omega t} \quad (43)$$

$$H_2^{(n)}(z) = \left[\sqrt{\frac{\sigma_1^n}{i\omega\mu}}\cot\alpha_n\,E_{12}^{(n)}\,e^{-k_{n,1}z} - \sqrt{\frac{\sigma_2^n}{i\omega\mu}}\tan\alpha_n\,E_{22}^{(n)}\,e^{-k_{n,2}z}\right] e^{i\omega t} \quad (44)$$

$$E_1^{(n)}(z) = [\cot\alpha_n\,E_{12}^{(n)}\,e^{-k_{n,1}z} - \tan\alpha_n\,E_{22}^{(n)}\,e^{-k_{n,2}z}]\,e^{i\omega t} \quad (45)$$

$$E_2^{(n)}(z) = [E_{12}^{(n)}\,e^{-k_{n,1}z} + E_{22}^{(n)}\,e^{-k_{n,2}z}]\,e^{i\omega t} \quad (46)$$

Now we can proceed to the determination of the impedance tensor at the top of $(n-1)$-st layer, i. e. for $z = z_{n-2}$. With this tensor the electromagnetic field can be expressed in the form

$$\begin{pmatrix} E_1 \\ E_2 \end{pmatrix} = \begin{pmatrix} Z_{11}, Z_{12} \\ Z_{21}, Z_{22} \end{pmatrix} \begin{pmatrix} H_1 \\ H_2 \end{pmatrix}$$

By equating the field components at the boundary $z = z_{n-1}$ the formulae (39)—(46) yield the parameters $E_{12}^{(n)}$, $E_{22}^{(n)}$, $E_{21}^{(n-1)}$, $E_{22}^{(n-1)}$ in terms of constants $E_{11}^{(n-1)}$ and $E_{12}^{(n-1)}$. Inserting these results into Eqs (39)—(42)

we get the field components in terms of constants $E_{11}^{(n-1}$ and $E_{12}^{(n-1)}$ as

$$H_1^{(n-1)}(z_{n-2}) = H_1\,[E_{11}^{(n-1)},\ E_{12}^{(n-1)}];\quad H_2^{(n-1)}(z_{n-2}) = H_2\,[E_{11}^{(n-1)},\ E_{12}^{(n-1)}] \tag{47}$$

$$E_1^{(n-1)}(z_{n-2}) = E_1\,[E_{11}^{(n-1)},\ E_{11}^{(n-1)}];\quad E_2^{(n-1)}(z_{n-2}) = E_2[E_{11}^{(n-1)},\ E_{12}^{(n-1)}] \tag{48}$$

The constants $E_{11}^{(n-1)}$ and $E_{12}^{(n-1)}$ are in the next step expressed in terms of $H_1^{(n-1)}(z_{n-2})$ and $H_2^{(n-1)}(z_{n-2})$ from equations (47) and inserted into (48). The resulting formulae read

$$E_1^{(n-1)}(z_{n-2}) = Z_{11}^{(n-1)}(z_{n-2}H_1^{(n-1)}(z_{n-2}) + Z_{12}^{(n-1)}(z_{n-2}\,H_2^{(n-1)}(z_{n-2}) \tag{49}$$

$$E_2^{(n-1)}(z_{n-2}) = Z_{21}^{(n-1)}(z_{n-2})\,H_1^{(n-1)}(z_{n-2})\,Z_{22}^{(n-1)} + (z_{n-2})\,H_2^{(n-1)}(z_{n-2}) \tag{50}$$

where the following definitions were introduced

$$\begin{aligned}
Z_{11}^{(n-1)}(z_{n-2}) = {} & [1/N^{(n-1)}(z_{n-2})]\Big\langle \frac{1}{2}\,\varkappa_{n-1}\mu_{n-1}^{-3/2}\,[\varkappa_{n-1}\cosh\xi_1^{(n-1)}\sinh\xi_2^{(n-1)} - \\
& - \sinh\xi_1^{(n-1)}\cosh\xi_2^{(n-1)}]\sin 2\alpha_{n-1} + \\
& + Z_{11}^{(n)}(z_{n-1})\varkappa_{n-1}\mu_{n-1}^{-1}\Big\{\cos^2 2\,\alpha_{n-1} + \frac{1}{2}\,[2\cosh\xi_1^{(n-1)}\cosh\xi_2^{(n-1)} - \\
& - (\varkappa_{n-1} + \varkappa_{n-1}^{-1})\sinh\xi_1^{(n-1)}\sinh\xi_2^{(n-2)}]\sin^2 2\alpha_{n-1}\Big\} + \\
& + Z_{12}^{(n)}(z_{n-1})\,\varkappa_{n-1}\mu_{n-1}^{-1}\Big\{\frac{1}{4}\sin 4\,\alpha_{n-1} + \frac{1}{2}\,[-\cos 2\alpha_{n-1}\cosh\xi_1^{(n-1)}\cosh\xi_2^{(n-1)} + \\
& + (\varkappa_{n-1}\cos^2\alpha_{n-1} - \varkappa_{n-1}^{-1}\sin^2\alpha_{n-1})\sinh\xi_1^{(n-1)}\sinh\xi_2^{(n-2)}]\sin 2\alpha_{n-1}\Big\} + \\
& + Z_{21}^{(n)}(z_{n-1})\,\varkappa_{n-1}\mu_{n-1}^{-1}\Big\{\frac{1}{4}\sin 4\,\alpha_{n-1} + \frac{1}{2}\,[-\cos 2\alpha_{n-1}\cosh\xi_1^{(n-1)}\cosh\xi_2^{(n-1)} - \\
& - (\varkappa_{n-1}\sin^2\alpha_{n-1} - \varkappa_{n-1}^{-1}\cos^2\alpha_{n-1})\sinh\xi_1^{(n-1)}\sinh\xi_2^{(n-1)}]\sin 2\alpha_{n-1}\Big\} + \\
& + \frac{1}{2}\,[Z_{11}^{(n)^2}(z_{n-1}) + Z_{12}^{(n)}(z_{n-1})\,Z_{21}^{(n)}(z_{n-1})]\,\mu_{n-1}^{-1/2}\,[\cosh\xi_1^{(n-1)}\sinh\xi_2^{(n-1)} - \\
& - \varkappa_{n-1}\sinh\xi_1^{(n-1)}\cosh\xi_2^{(n-1)}]\sin 2\alpha_{n-1}\Big\rangle
\end{aligned} \tag{51}$$

$$\begin{aligned}
Z_{12}^{(n-1)}(z_{n-2}) = {} & [1/N^{(n-1)}(z_{n-2})]\Big\langle \varkappa_{n-1}\mu_{n-1}^{-3/2}\,[\varkappa_{n-1}\sin^2\alpha_{n-1}\cosh\xi_1^{(n-1)}\sinh\xi_2^{(n-1)} + \\
& + \cos^2\alpha_{n-1}\sinh\xi_1^{(n-1)}\cosh\xi_2^{(n-1)}] + \\
& + Z_{11}^{(n)}(z_{n-1})\,\varkappa_{n-1}\mu_{n-1}^{-1}\Big\{\frac{1}{2}\sin 4\alpha_{n-1} - [\cos 2\alpha_{n-1}\cosh\xi_1^{(n-1)}\cosh\xi_2^{(n-1)} + \\
& + \sinh\xi_1^{(n-1)}\sinh\xi_2^{(n-1)}]\sin 2\alpha_{n-1}\Big\} +
\end{aligned}$$

$$+ Z_{12}^{(n)}(z_{n-1})\,\varkappa_{n-1}\,\mu_{n-1}^{-1}\left\{\frac{1}{2}\sin^2 2\alpha_{n-1} + (\cos^4\alpha_{n-1} + \sin^4\alpha_{n-1})\cosh\xi_1^{(n-1)} \times\right.$$

$$\left.\times\cosh\xi_2^{(n-1)} + (\varkappa_{n-1} + \varkappa_{n-1}^{-1})\sin^2\alpha_{n-1}\cos^2\alpha_{n-1}\sinh\xi_1^{(n-1)}\sinh\xi_2^{(n-1)}\right\} +$$

$$+Z_{21}^{(n)}(z_{n-1})\,\varkappa_{n-1}\,\mu_{n-1}^{-1}\left\{\frac{1}{2}\sin^2 2\alpha_{n-1} - 2\sin^2\alpha_{n-1}\cos^2\alpha_{n-1}\cosh\xi_1^{(n-1)}\cosh\xi_2^{(n-1)} -\right.$$

$$\left. - (\varkappa_{n-1}\sin^4\alpha_{n-1} + \varkappa_{n-1}^{-1}\cos^4\alpha_{n-1})\sinh\xi_1^{(n-1)}\sinh\xi_2^{(n-1)}\right\} -$$

$$- [Z_{11}^{(n)2}(z_{n-1}) + Z_{12}^{(n)}(z_{n-1})\,Z_{21}^{(n)}(z_{n-1})]\,\mu_{n-1}^{-1/2}[\cos^2\alpha_{n-1}\cosh\xi_1^{(n-1)}\sinh\xi_2^{(n-1)} +$$

$$\left. + \varkappa_{n-1}\sin^2\alpha_{n-1}\sinh\xi_1^{(n-1)}\cosh\xi_2^{(n-1)}]\right\} \tag{52}$$

$$Z_{21}^{(n-1)}(z_{n-2}) = [1/N^{(n-1)}(z_{n-1})]\left\{-\varkappa_{n-1}\mu_{n-1}^{-3/2}[\varkappa_{n-1}\cos^2\alpha_{n-1}\cosh\xi_1^{(n-1)}\sinh\xi_2^{(n-1)} +\right.$$

$$+ \sin^2\alpha_{n-1}\sinh\xi_1^{(n-1)}\cosh\xi_2^{(n-1)}] +$$

$$+ Z_{11}^{(n)}(z_{n-1})\,\varkappa_{n-1}\,\mu_{n-1}^{-1}\left\{\frac{1}{2}\sin 4\alpha_{n-1} + [-\cos 2\alpha_{n-1}\cosh\xi_1^{(n-1)}\cosh\xi_2^{(n-1)} +\right.$$

$$\left. + (\varkappa_{n-1}\cos^2\alpha_{n-1} - \varkappa_{n-1}^{-1}\sin^2\alpha_{n-1})\sinh\xi_1^{(n-1)}\sinh\xi_2^{(n-1)}]\sin 2\alpha_{n-1}\right\} +$$

$$+Z_{12}^{(n)}(z_{n-1})\,\varkappa_{n-1}\mu_{n-1}^{-1}\left\{\frac{1}{2}\sin^2 2\alpha_{n-1} - [2\sin^2\alpha_{n-1}\cos^2\alpha_{n-1}\cosh\xi_2^{(n-1)}\cosh\xi_2^{(n-1)} +\right.$$

$$\left. + (\varkappa_{n-1}\cos^4\alpha_{n-1} + \varkappa_{n-1}^{-1}\sin^4\alpha_{n-1})\sinh\xi_1^{(n-1)}\sinh\xi_2^{(n-1)}]\right\} +$$

$$+Z_{21}^{(n)}(z_{n-1})\,\varkappa_{n-1}\mu_{n-1}^{-1}\left\{\frac{1}{2}\sin^2 2\alpha_{n-1} + (\cos^4\alpha_{n-1} + \sin^4\alpha_{n-1})\cosh\xi_1^{(n-1)}\cosh\xi_2^{(n-1)} +\right.$$

$$\left. + (\varkappa_{n-1} + \varkappa_{n-1}^{-1})\sin^2\alpha_{n-1}\cos^2\alpha_{n-1}\sinh\xi_1^{(n-1)}\sinh\xi_2^{(n-1)}\right\} +$$

$$+ [Z_{11}^{(n)2}(z_{n-1}) + Z_{12}^{(n)}(z_{n-1})\,Z_{21}^{(n)}(z_{n-1})]\,\mu_{n-1}^{-1/2}[\sin^2\alpha_{n-1}\cosh\xi_1^{(n-1)}\sinh\xi_2^{(n-1)} +$$

$$\left. + \varkappa_{n-1}\cos^2\alpha_{n-1}\sinh\xi_1^{(n-1)}\cosh\xi_2^{(n-1)}]\right\} \tag{53}$$

$$Z_{22}^{(n-1)}(z_{n-2}) = -Z_{11}^{(n-1)}(z_{n-2}) \tag{54}$$

and

$$N^{(n-1)}(z_{n-2}) = \varkappa_{n-1}\,\mu_{n-1}^{-1}\cosh\xi_1^{(n-1)}\cosh\xi_2^{(n-1)} -$$

$$- Z_{11}^{(n)}(z_{n-1})\mu_{n-1}^{-1/2}[\varkappa_{n-1}\sinh\xi_1^{(n-1)}\cosh\xi_2^{(n-1)} - \cosh\xi_1^{(n-1)}\sinh\xi_2^{(n-1)}]\sin 2\alpha_{n-1} +$$

$$+ Z_{12}^{(n)}(z_{n-1})\,\mu_{n-1}^{-1/2}[\varkappa_{n-1}\cos^2\alpha_{n-1}\sinh\xi_1^{(n-1)}\cosh\xi_2^{(n-1)} +$$

$$+ \sin^2\alpha_{n-1}\cosh\xi_1^{(n-1)}\sinh\xi_2^{(n-1)}] -$$

$$- Z_{21}^{(n)}(z_{n-1})\,\mu_{n-1}^{-1/2}\,[\varkappa_{n-1}\sin^2\alpha_{n-1}\sinh\xi_1^{(n-1)}\cosh\xi_2^{(n-1)} +$$

$$+ \cos^2\alpha_{n-1}\cosh\xi_1^{(n-1)}\sinh\xi_2^{(n-1)}] -$$

$$- [Z_{11}^{(n)2}(z_{n-1}) + Z_{12}^{(n)}(z_{n-1})\,Z_{21}^{(n)}(z_{n-1})]\sinh\xi_1^{(n-1)}\sinh\xi_2^{(n-1)} \tag{55}$$

$$\varkappa_l = (\sigma_1^l/\sigma_2^l)^{1/2}; \quad \mu_l = \sigma_1^l/\sigma_1^1; \quad \xi_1^{(l)} = k_{l,1}h_l; \quad \xi_2^{(l)} = k_{l,2}h_l \tag{56}$$

$$Z_{11}^{(n)}(z_{n-1}) = \frac{1}{2}\mu_n^{-1/2}(\varkappa_n - 1)\sin 2\alpha_n$$

$$Z_{12}^{(n)}(z_{n-1}) = \mu_n^{-1/2}(\cos^2\alpha_n + \varkappa_n\sin^2\alpha_n) \tag{57}$$

$$Z_{21}^{(n)}(z_{n-1}) = -\mu_n^{-1/2}(\sin^2\alpha_n + \varkappa_n\cos^2\alpha_n)$$

The impedance tensor components obtained from (51)—(54) can be formally considered as impedance tensor elements of a fictitious homogeneous half-space combining the n-th and $(n-1)$-st layers. In the next steps we may repeat the same reasoning and calculations for the boundaries at $z = z_{n-2}$, $z = z_{n-3}$, ... until the superficial boundary at $z = 0$ is reached.

In this way, formulae for impedance tensor components can be obtained for any number of horizontal anisotropic layers. In particular, the recurrent expressions make the calculations effective and easy on the computer.

REFERENCES

ÁDÁM, A., 1964. Über die Berechnung der magnetotellurischen (MT) Anisotropie. *Freiberger Forschungshefte*, C 168, 1–48.

PETR, V., 1966. Magnetotellurisches Feld in einem homogenen anisotropen Medium. *Stud. geophys. geod. ČSAV*, **10**, 446.

PETR, V., 1967. Impedanz des magnetotellurischen Feldes im geschichteten anisotropen Halbraum. *Studia geophys. geod. ČSAV*, **11**, 291.

PRAUS, O., 1966. The field of a plane electromagnetic wave at the surface of two-layer anisotropic earth. *Stud. geophys. geod. ČSAV*, **10**, 460.

ROKITYANSKY, I. I., 1961. Application of the magnetotelluric method over anisotropic and inhomogeneous massives (in Russian). *Izv. Akad. Nauk SSSR, Ser. Geofiz.*, 1607.

SRIVASTAVA, S. P., 1963. Application of the magnetotelluric method to anisotropic and inhomogeneous bodies. *J. Geophys. Res.* **68**, 5857.

NUMERICAL SOLUTIONS OF THE MT FIELD IN INHOMOGENEOUS STRUCTURES

O. PRAUS

INTRODUCTION

Magnetotelluric (MT) and geomagnetic deep soundings (GDS) have lately become effective methods for obtaining information on the depth-distribution of the electrical conductivity, which is one of the important indicators of the structural conditions in the earth's interior. Numerous results of actual soundings, however, were in many cases inconsistent by suggesting substantially different internal structures at adjacent localities on the basis of MT curves. It has become clear that horizontal inhomogeneity of the geoelectric conditions must cause serious distortions of the field distribution with subsequent effects on sounding curves.

To account properly for these effects theoretical investigations on the electromagnetic field distribution have been carried out for several horizontally non-homogeneous models, with the restriction to two-dimensional inhomogeneities. Principles of solving these problems analytically and some numerical results are given in the papers of Dmitriev (1969), and Berdichevsky (1968).

In this contribution we wish to summarize results obtained by a different approach. By solving the relevant partial differential equations in the finite difference approximation we obtained results for some models of importance for actual interpretation. The finite difference approach to solve MT fields in non-homogeneous models was first used in the work of Neves (1957), and further developed in the papers of Jones and Price (1970), Jones and Pascoe (1971). Our contribution is based on using a non-uniform mesh and on introducing corrections for dipping boundaries.

1. EQUATIONS, BOUNDARY CONDITIONS AND FINITE DIFFERENCE APPROXIMATION

For two-dimensional inhomogeneous media with the axis of homogeneity in the x-coordinate and with changes of the electrical parameters in the yz coordinate plane, two independently tractable modes of the field are known to be decoupled from the general system of Maxwell's equation (the MKS system of units and the time factor $\exp(i\omega t)$ are used throughout).

a) *H-polarization*, (the H_x component in the axis of homogeneity), with the *Helmholtz equation* of the form

$$\left(\frac{\partial^2}{\partial y^2} + \frac{\partial^2}{\partial z^2}\right) H_x - (i\omega\mu\sigma_k)\, H_x = 0 \qquad (1.1)$$

to be solved in each k-th subregion of the model with boundary conditions requiring (i) the continuity of the solution at all internal boundaries and (ii) the continuity of tangential components of the electrical field yielding $\sigma_k^{-1}(\partial H_x/\partial n) = \sigma_{k+1}^{-1}(\partial H_x/\partial n)$, where n is the normal to a relevant boundary. The corresponding components of the electrical fields are derived from solution H_x according to Maxwell's equation as

$$E_y = \sigma^{-1}\left(\frac{\partial H_x}{\partial z}\right); \quad E_z = \sigma^{-1}\left(\frac{\partial H_x}{\partial y}\right) \tag{1.2}$$

Notation σ is used for the electrical conductivity of the superficial layer.

With a finite difference approximation the boundary conditions at external boundaries must be defined explicitly, as well. At the earth's surface, ($z = 0$) the condition $H_x = H_0$ (conventionally $H_0 = 1$) is obtained independently of any distribution of the electrical conductivity inside the earth, provided the air is assumed to be a perfect insulator ($\sigma = 0$).

At vertical boundaries, limiting the horizontal extent of the model far enough from non-horizontal contacts, or from embedded inhomogeneities, the field values are given by formulae for a horizontally homogeneous, or layered medium. For an N-layered cross section with electrical conductivities $\sigma_1, \sigma_2 \ldots \sigma_N$ and boundaries at depths $d_1, d_2, \ldots d_{N-1}$ the decay of the magnetic field with depth ($+z$ coordinate) is given by

$$\begin{aligned}
&H_{x1}(z) = \cosh \mu_1 z + Z_{HN} \sinh \mu_1 z; && 0 \leq z \leq d_1 \\
&H_{x2}(z) = H_{x1}(d_1)\,[\cosh \mu_2(z - d_1) + Z_{H(N-1)} \sinh \mu_2(z - d_1)]; && d_1 \leq z \leq d_2 \\
&H_{x3}(z) = H_{x2}(d_2)\,[\cosh \mu_3(z - d_2) + Z_{H(N-2)} \sinh \mu_3(z - d_2)]; && d_2 \leq z \leq d_3 \\
&\vdots \\
&H_{xN}(z) = H_{x(N-1)}(d_{N-1}) \exp\,[\mu_N(d_{N-1} - z)]; && z \geq d_{N-1}
\end{aligned} \tag{1.3}$$

where $\mu_k = (i\omega\mu\sigma_k)^{1/2}$. In Eqs (1.3) Z_{HN}, $Z_{H(N-1)} \ldots$ are the impedances of the N-, $(N-1)$-layered cross section. Their recurrence is apparent. For example, the field in the second layer is calculated from the field $H_{x1}(d_1)$ at the top of the second layer (replacing the analogical value of $H_0 = 1$ at the earth's surface), shifting, at the same time, the origin of the depth coordinate by $(z - d_1)$. Impedance $Z_{H(N-1)}$ is then for $(N-1)$-layered medium with superficial layer (conductivity σ_1) left behind. The field in other layers is obtained analogously. The impedances Z_{HN} can be calculated by recurrence formulae for any number of layers as shown in the papers of Berdichevsky (1968), Praus and Petr (1969).

The depth extent of the model is limited by field values which are small enough compared with the required accuracy of the solution.

b) *E-polarization*, (the E_x component in the axis of homogeneity), with the *Helmholtz equation* of the same form as in (1.1)

$$\left(\frac{\partial^2}{\partial y^2} + \frac{\partial^2}{\partial z^2}\right) E_x - (i\omega\mu\sigma_k)\, E_x = 0 \tag{1.4}$$

to be solved in each subregion of the model with boundary conditions requiring the continuity of both the solution and its normal derivatives with respect to the relevant boundary. The latter condition is due to the continuity of magnetic components at the internal boundaries. They are obtained from the solution of E_x by

$$H_y = (-i\omega\mu)^{-1}\left(\frac{\partial E_x}{\partial z}\right); \quad H_z = (i\omega\mu)^{-1}\left(\frac{\partial E_x}{\partial y}\right) \tag{1.5}$$

The conditions at external boundaries are introduced analogously to the H-polarization case

$$\begin{aligned}
&E_{x1}(z) = E_0\,(\cosh\,\mu_1 z + Z_{EN}\sinh\,\mu_1 z); && 0 \leq z \leq d_1\\
&E_{x2}(z) = E_0 E_{x1}(d_1)\,[\cosh\,\mu_2(z-d_1) + Z_{E(N-1)}\sinh\,\mu_2(z-d_1)]; && d_1 \leq z \leq d_2 \qquad (1.6)\\
&\vdots\\
&E_{xN}(z) = E_0\,E_{x(N-1)}(d_{N-1})\exp\,[\mu_N(d_{N-1}-z)]; && z \geq d_{N-1}
\end{aligned}$$

However, the relation $Z_{EN} = Z_{HN}^{-1}$ holds between impedances, as can be shown by calculating the apparent resistivites for E- and H-polarizations in a horizontally homogeneous medium.

Certain normalizing factors must be introduced for the electric field distribution at the earth's surface. For sake of simplicity, consider a model with a vertical boundary between two blocks of different electrical conductivities σ_l and σ_p at its left and right sides, respectively. Assuming the total surface values of H_y to be the same at both external boundaries we obtain the condition $\sigma_l^{1/2} E_{0l} = \sigma_p^{1/2} E_{0p}$ by reasoning according to Jones and Price (1970). A layered medium at both sides of the boundary, however, needs generalization, because at different periods of the inducing field the apparent conductivities σ_{al} and σ_{ap} are obtained on the earth's surface in this case. The corresponding formulae are derived by calculating the surface impedance $Z(0) = |E_{x1}(0)/H_{y1}(0)|$ for an N-layered medium according to Eq. (1.4). The modified condition (1.6) reads for a certain period T (all permeabilities μ are assumed to be equal to $\mu_0 = 4\pi \cdot 10^{-7}\ H/m$):

$$(\sigma_l)^{1/2}\,|\,Z_{EN}(T)\,|_l\,E_{0l} = (\sigma_p)^{1/2}\,|\,Z_{EN}(T)\,|_p\,E_{0p} \tag{1.7}$$

The electric field over an air layer above the earth's surface must be considered in the E-polarization case. The air layer must be thick enough to attenuate the secondary field produced by the internal inhomogeneity. The distribution of the electric field at the left and right limits of the air layer are given for an N-layered model by

$$E_v(z) = E_0(1 + \mu_1 z\, Z_{EN}) \qquad h \leq z \leq 0 \tag{1.8}$$

with E_0 replaced by the relevant E_{0l} or E_{0p}, respecting the condition (1.7) as well. A simple linear function for the distribution of the electric field between the extremes at the top of an air layer can be used (Jones and Price, 1970).

In order to solve Eqs (1.1) and (1.4) numerically, we cover the region with a rectangular non-uniform mesh defined by two systems of orthogonal

straight lines and denote their intersections as mesh points. The mesh spacings $p_i = y_{i-1} - y_i$ and $k_j = z_{j-1} - z_j$ in the directions of corresponding coordinate axes need not be constant and, in fact, the spacings were intentionally assumed to be adjustable to the specific requirements of the subregion of the model in the vicinity of boundaries and near the surface of the model, where the normal derivative must be estimated for calculating the field components according to Eqs (1.2) or (1.5).

In deriving the finite difference approximation of basic equations use is made of the integration method for a five point pattern described in the work of Varga (1962). Referring to our previous paper (Praus et al. 1973a) the following equations have to be solved in each subregion of the model

$$\begin{aligned}&(k_j + k_{j+1})p_i^{-1}\, u^{(1)}_{(2)\,i+1,j} + (k_j + k_{j-1})p_{i-1}^{-1}\, u^{(1)}_{(2)\,i-1,j} + \\ &+ (p_i + p_{i-1})k_{i-1}^{-1}\, u^{(1)}_{(2)\,i,j-1} + (p_i + p_{i-1})k_i^{-1}\, u^{(1)}_{(2)\,i,j+1} - \\ &- (k_{j-1} + k_j)(p_{i-1} + p_i)[(p_i p_{i-1})^{-1} + (k_j k_{j-1})^{-1}]\, u^{(1)}_{(2)\,i,j} \pm \\ &\pm (k_{j-1} + k_j)\,(p_{i-1} + p_i)\,\frac{1}{2}\,\omega\mu\sigma_l\, u^{(2)}_{(1)\,i,j} = 0\end{aligned} \tag{1.9}$$

where the general function $u_{i,j}$ was introduced instead of H_x or E_x. This equation holds for internal mesh points. For those at the boundary, however, special equations were obtained by introducing the boundary conditions according to the method recommended in the paper of Allen (1954). At each vertical boundary, separating the regions with conductivity contrast $\mu_{l,l+1} = (\sigma_{l+1}/\sigma_l)$, the following equation was obtained ($u_{i,j-1} = U_{i,j-1}$, $u_{i,j} = U_{i,j}$, $u_{i,j+1} = U_{i,j+1}$, $p_i = p_{i-1}$, $P_{i-1} = P_i$ at the boundary):

$$\begin{aligned}&P_i^{-1}\, U^{(1)}_{(2)\,i+1,j} + \mu_{l,l+1}\, p_{i-1}^{-1}\, u^{(1)}_{(2)\,i-1,j} + [k_{j-1}(k_j + k_{j-1})]^{-1}(P_i + \mu_{l,l+1}\, p_{i-1})\, U^{(1)}_{(2)\,i,j-1} + \\ &+ [k_{j-1}(k_j + k_{j-1})]^{-1}(P_i + \mu_{l,l+1}\, p_{i-1})\, U^{(1)}_{(2)\,i,j+1} - \\ &- \{P_i^{-1} + P_i(k_j k_{j-1})^{-1} + \mu_{l,l+1}[p_{i-1}^{-1} + p_{i-1}(k_j k_{j-1})^{-1}]\}\, U^{(1)}_{(2)\,i,j} \pm \\ &\pm \frac{1}{2}\,(\omega\mu\sigma_{l+1})\,(p_{i-1} + p_i)\, U^{(2)}_{(1)\,i,j} = 0\end{aligned} \tag{1.10}$$

Analogously, for the horizontal boundary of two subregions with conductivity contrast $\mu_{k,k+1} = \sigma_{k+1}/\sigma_k$ one has

$$\begin{aligned}&K_j^{-1}\, U^{(1)}_{(2)\,i,j+1} + \mu_{k,k+1}\, k_{j-1}^{-1}\, u^{(1)}_{(2)\,i,j-1} + [p_{i-1}(p_i + p_{i-1})]^{-1}(K_j + \mu_{k,k+1}\, k_{j-1})\, U^{(1)}_{(2)\,i-1,j} + \\ &+ [p_i(p_i + p_{i-1})]_{-1}(K_j + \mu_{k,k+1}\, k_{j-1})\, U^{(1)}_{(2)\,i+1,j} -\end{aligned}$$

$$- \{K_j^{-1} + K_j(p_i p_{i-1})^{-1} + \mu_{k,k+1}[k_{j-1}^{-1} + k_{j-1}(p_i p_{i-1})^{-1}]\} U_{i,j}^{(\frac{1}{2})} \pm$$

$$\pm \frac{1}{2}(\omega\mu\sigma_{k+1})(k_{j-1} + K_j) U_{i,j}^{(\frac{2}{1})} = 0 \qquad (1.11)$$

In Eqs (1.9) – (1.11) the upper sign and index were used for the real part of the solution, the others for the imaginary part.

Equations (1.10) and (1.11) were used for solving the models with rectangular blocks, where the mesh can be adjusted so that each boundary may coincide with some particular mesh line. In the solution of the above problems for inclined contacts corrections must be introduced for a different relative position of the interface and the mesh region defined by five-point pattern. Approximations derived in the paper Červ and Praus (1972) have to be applied instead of Eqs (1.10) and (1.11) for mesh points affected by the sloping contact.

2. FINITE DIFFERENCE SOLUTION AND EVALUATION OF RESULTS

The finite difference approach to the above problems reduced their solution to finding the real and imaginary components, relevant to a particular mode at each internal mesh point from a system of linear algebraic equations. The resulting system was solved by the block overrelaxation iterative method with an accelerating parameter ω_c being in general between 0 and 2. Tests with some models showed the optimal value of ω_c to be between 1.4 and 1.5. However, this depends on the particular model geometry and on mesh uniformity. For many models we inserted $\omega_c = 1$ and the procedure was reduced to the Gauss-Seidel iterative process.

The relative accuracy of the solution was estimated by the ratio $|(u_n - u_{n-1})/u_n|$, where u_n is the solution after the n-th iteration.

For estimating the behaviour of apparent resistivities in the H-polarization case, the surface impedance must be calculated from the ratio $|E_y(0)/H_x(0)|$. Due to the constant value of $H_x = 1$ at the earth's surface, $(z = 0)$, for any period and any distribution of the electrical conductivity inside the earth, the behaviour of the surface impedance and, consequently, of apparent resistivities is fully coherent with that of the E_y component, obtained from Eq. (1.2). Therefore, the apparent resistivities at the earth's surface were estimated from the formula

$$\varrho_z^{(H)}(T) = k_H \sigma^{-2} T[(\Delta H_{xr}/\Delta z)^2 + (\Delta H_{xs}/\Delta z)^2] \qquad (2.1)$$

where the ratio of differences $(\Delta H_{xr}/\Delta z)$ etc. approximate the derivatives calculated by the interpolation formula from four superficial mesh points. The parameter k_H involving all the conversion factors may be neglected. For σ the electrical conductivity relevant to a specific superficial region must be inserted. In Eq. (2.1) H_{xr} and H_{xs} stand for the real and imaginary parts of the solution, T for field period in sec.

For estimating the surface impedances in the E-polarization case the formula (1.5) is used to obtain first the H_y component of the magnetic field. One gets approximately in terms of differences

$$|H_y| = (\omega\mu)^{-1} [(\Delta E_{xr}/\Delta z)^2 + (\Delta E_{xs}/\Delta z)^2]^{1/2}$$

The behaviour of both the electric and magnetic components is now involved in the ratio $|E_x(0)/H_y(0)|$ and, thus, in producing a specific distribution of apparent resistivities at the earth's surface. The apparent resistivities are obtained from the formula

$$\varrho_z^{(E)}(T) = k_E T^{-1} (E_{xr}^2 + E_{xs}^2) [(\Delta E_{xr}/\Delta z)^2 + (\Delta E_{xs}/\Delta z)^2]^{-1} \qquad (2.2)$$

with indices r and s again specifying the real and imaginary parts of the solution.

The horizontal inhomogeneity of the model and related distortion of the electric current distribution is known to be the source of an anomalous vertical component of the magnetic field H_z. It can be estimated according to (1.5) with derivatives replaced by finite differences

$$|H_z| = (\omega\mu)^{-1} [(\Delta E_{xr}/\Delta y)^2 + (\Delta E_{xs}/\Delta y)^2]^{1/2} \qquad (2.3)$$

with the same notation as in Eqs (2.1) and (2.2).

3. NUMERICAL RESULTS AND THEIR GEOPHYSICAL SIGNIFICANCE

Electromagnetic field distribution for a variety of horizontally inhomogeneous models in two dimensions was analysed. The results for block inhomogeneities were published in the paper of Praus et al. (1973a). In our opinion, the most significant conclusions have been obtained recently by analyzing models with dipping boundaries (Červ and Praus, 1972; Praus et al. 1973b) and we wish to summarize and supplement them here in brief.

The model of a two-dimensional inhomogeneous structure with a simple sloping contact of two media was investigated for both the H- and E-polarizations. Dipping angles between $90° \geq \alpha \geq 20°$ were assumed for two basic types of structure, differing by interchanged electrical conductivites on both sides of the contact. In this way we were in the position to study the effects of either submerging a less conductive material beneath the better conductor, or vice versa. The former model may obviously well account for the realistic geological situation in a marginal part of some sedimentary basins, where relatively conductive sediments were deposited on the slopes of a less conductive basement. This model will be referred to as "type I". The latter model, i. e. that with submerging conductive material beneath a less conductive one, seems to be rather hypothetical, nevertheless, it is of certain theoretical significance. It will be referred to as "type II" below.

The solution for the actual field can be obtained from the real and imaginary parts with the time factor exp ($i\omega t$) included. The field is given by

$$H^* = (H_{xr}^2 + H_{xs}^2) \cos\left[\arctan\left(\frac{H_{xs}}{H_{xr}}\right) + \left(\frac{2\pi t}{T}\right)\right]$$

For $t = 0$, however, one gets simply $H^* = H_{xr}$. An example of the spatial distribution at instant $t = 0$, i. e. for $H^* = H_{xr}$, is shown in Figure 1,a and b for both types I and II, respectively. The electrical conductivities of the regions under contact, dipping at 45°, were $\sigma_1 = 10^{-3}\ [\Omega\mathrm{m}]^{-1}$ and $\sigma_2 = 10^{-2}\ [\Omega\mathrm{m}]^{-1}$ for type I and interchanged values for type II.

The following important features are apparent from the spatial distr-

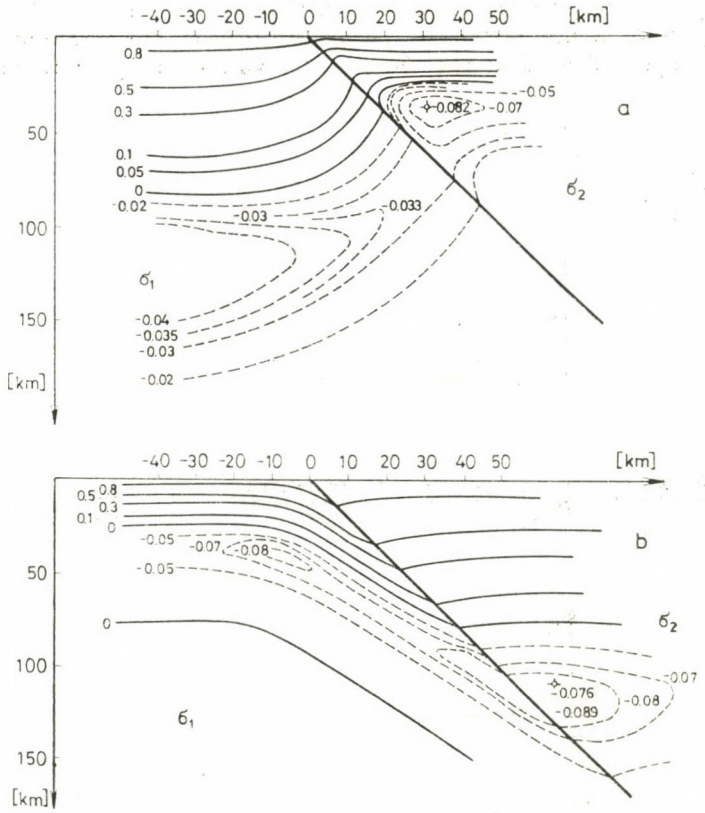


Fig. 1. a – isolines of the actual field $H^* = H_{xr}$ at an instant $t = 0$ for the model consisting of two blocks contacting along the boundary dipping at 45°. Electrical conductivities in $[\Omega\mathrm{m}]^{-1}$: $\varrho_1^{-1} = \sigma_1 = 10^{-3}$; $\varrho_2^{-1} = \sigma_2 = 10^{-2}$. Period $T = 10$ sec. (Type I); b – isolines at the $H^* = H_{xr}$ field for the model of the same geometry as in Fig. 1, a but for interchanged conductivites $\sigma_1 = 10^{-2}$, $\sigma_2 = 10^{-3}$. Period $T = 10$ sec. (Type II)

butions of the field isolines: (i) a different attenuation rate of the field as ruled by different conductivities of both blocks, (ii) refraction of isolines due to boundary conditions at the interface, (iii) the formation of vortices in more conductive parts of the models and their shaping by the dip of the boundary. In general, a similar distribution of E component was obtained for the E-polarization. However, no isoline refraction takes place at the interface owing to the continuity of the derivatives.

The current flow vortices in more conductive parts of the model, as suggested by isoline curls, seem to be identical with "the superfluous currents" mentioned in the discussion of the results obtained from analytical solutions of the MT field above the horst and graben structures (Berdichevsky and Dmitriev, 1972). They are a source of anomalous behaviour of the field components in the vicinity of non-horizontal boundaries.

The apparent resistivity functions, obtained from formula (2.1) are plotted in Figure 2, a and b for the period of 10 sec. The conversion factors were not respected so that the asymptotic values at opposite sides of the

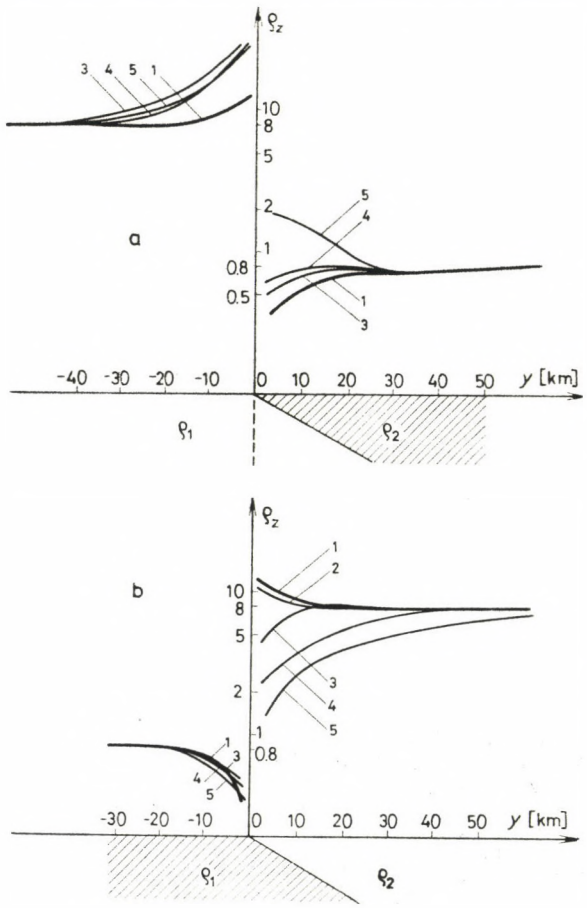


Fig. 2. H-polarization case, $T=10$ sec. Apparent resistivities along the profile across the inclined contact of two blocks for the following slope angles
1 – 90°; 2 – 75°; 3 – 60°; 4 – 45°; 5 – 30°. Electrical conductivies in $[\Omega m]^{-1}$ are the same as in Figure 1, a and b

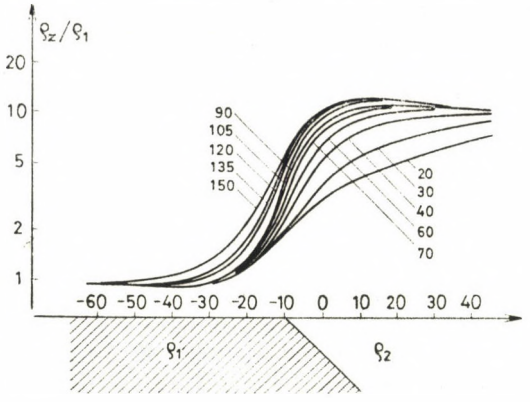


Fig. 3. *E*-polarization case, $T = 10$ sec. Apparent resistivities along the profile across the contact of two blocks for slope angles as labelled. Electrical conductivites are the same as in Figure 1, a and b

model do not correspond to true resistivities. However, the difference of one decimal order between their amplitudes is strictly in accordance with the given conductivity contrast.

On proceeding to the boundary from the homogeneous part of the type I model, we find a zone about 30 km wide, within which the apparent resistivities increase above ϱ_1 progressively when approaching the edge. At the boundary the discontinuous character of the apparent resistivity functions is due to the discontinuous behaviour of the E_y component of the electric field. After crossing the edge, the apparent resistivities fall below the value which would correspond to the true resistivity ϱ_2 of the other block and they reach this value within a recovery zone, about 30 km wide. The effect of steep slopes seems to be relatively small in the more conductive part of the model. Thus, the underthrusting of a less conductive material remains almost undetected behind the boundary, but only for angles below 45°. The observed effects for vertical contact are in accordance with the results obtained analytically (D'Erceville and Kunetz, 1962).

On analyzing the apparent resistivities in the type II model we find a reversed effect only for the structure with a vertical contact. For slopes under 75° substantially depressed values of apparent resistivity were detected above the sloping boundary. The amplitude of the depression, the rate of recovery and, thus, the horizontal extent of the recovery zone depend strongly on the sloping angle as seen in Figure 2, b. The behaviour of the apparent resistivities in this model fits well the geometrical distribution of conductive matter in the basement. For decreasing sloping angles and for a given penetration depth the more conductive material is underthrust to greater distances from the edge and, therefore, its presence in the basement is felt within an extended recovery zone.

The apparent resistivities in the *E*-polarization case are exhibited in Figure 3 for the model with the same parameters as in the *H*-polarization example and for the same period of 10 sec. Owing to the smooth character of the apparent resistivity functions, the results for both types I and II are compiled in one graph, the sloping angles being between 20° and 150°. The characteristic feature of these plots is the continuous behaviour of the corre-

sponding apparent resistivity functions on crossing the boundary in virtue of the fact that all the field components involved in evaluating the surface impedance are continuous.

The values of the apparent resistivites in Figure 3 were normalized with respect to undisturbed resistivity in the homogeneous region of the more conductive block. Consequently, they all display a smooth increase of the apparent resistivities between 1 and 10 in accordance with the assumed conductivity contrast of the structure. The rate of increase depends substantially on the slope angle. The effect is pronounced for angles between $90° \geq \alpha \geq 20°$, which corresponds to underthrusting a more conductive material along the slope. A much smaller effect, on the other hand, is exerted on the apparent resistivities by underthrusting a less conductive material. As in H-polarization an asymmetry of anomalous effects for models of both types seem to suggest an increased influence of better conductive inhomogeneities compared with less conductive ones.

The anomaly of the vertical component of the magnetic field measured by $|kH_z|$ is presented in Figure 4 for angles between $90° \geq \alpha \geq 20°$ For vertical contact the maximum of the anomaly is located in the close vicinity of the edge, but still in the more conductive part of the model. For decreasing slopes the maximum flattens and slightly shifts in the direction of the underthrust more conductive material. At the same time, the asymmetry of the anomaly increases progressively in virtue of a slower decay of the anomalous field above the slope.

Effects of the sloping contact in a layered medium were studied on models schematically shown in Figures 5 and 7. The investigation was aimed at analyzing expected distortions of two-layer MT sounding curves in the vicinity of contact.

Let us analyze first the model consisting of two superficial layers with conductivities $\sigma_1 = 10^{-3}\,[\Omega\mathrm{m}]^{-1}$ and $\sigma_3 = 10^{-2}\,[\Omega\mathrm{m}]^{-1}$ and of the thickness of 40 km. They are contacting along an interface dipping at 45°. In their basement a horizontally homogeneous layer with conductivity

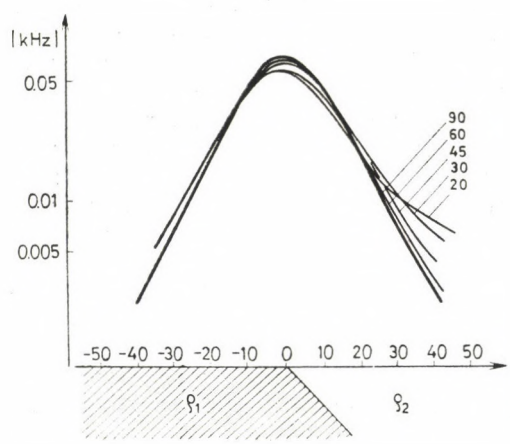


Fig. 4. E-polarization case, $T = 10$ sec. The vertical magnetic component anomaly across the contact of two blocks for slope angles as labelled. Electrical conductivities are the same as in Figure 1, a and b

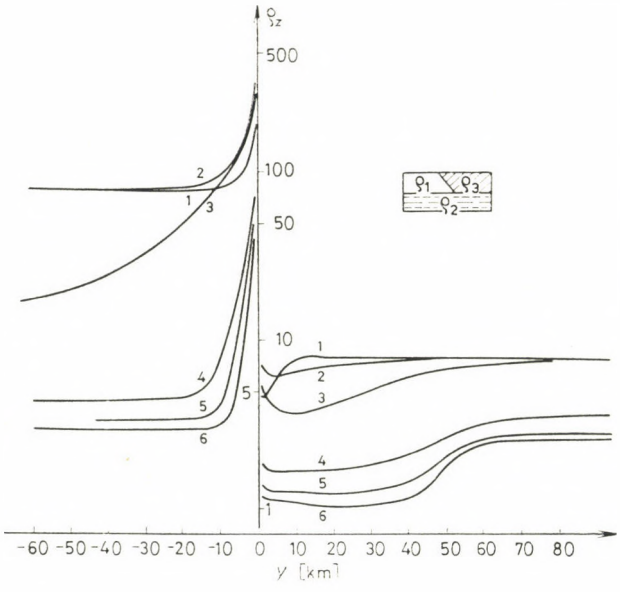


Fig. 5. *H*-polarization. At 45° sloping contact of two blocks above a horizontally homogeneous layer of increased conductivity. Electrical conductivities in $[\Omega m]^{-1}$ ($\varrho_i^{-1} = \sigma_i$): $\sigma_1 = 10^{-3}$, $\sigma_2 = 10^{-1}$, $\sigma_3 = 10^{-2}$. Apparent resistivity functions for following periods T [sec]: 1 – 1; 2 – 10; 3 – 100; 4 – 500; 5 – 1000; 6 – 1800

$\sigma_2 = 10^{-1}\,[\Omega m]^{-1}$ is assumed. This layer is, therefore, by one or two decimal orders of magnitude more conductive than the superficial layers.

The apparent resistivities at the earth's surface were estimated according to Eq. (2.1) for periods between 1 and 1800 sec. The conversion factors, constant for all periods, were omitted as only the relative position of the curves is important.

Starting the analysis of apparent resistivity functions in Figure 5 with a period of 1 sec, we found the resistivities to behave in a similar way as in the case of a simple inclined contact. This is natural since there is almost no effect of the lower layer on the field for this particular period. For increasing periods we observe a rapid decrease of apparent resistivities in the less conductive part of the model far from the contact with values approaching asymptotically the theoretical limits for a horizontally homogeneous two-layer model with a conductivity contrast of 1 : 100. The approach to the edge from the left is indicated by about 15 km wide zone of progressively increasing resistivities.

After crossing the edge of the contact we find a zone of depressed apparent resistivities with a minimum for periods of 1, 10 and 100 sec obviously shifting to greater distances from the edge. For even longer periods the minimum flattens and the depressed apparent resistivities slowly recover and reach asymptotically the values which correspond to the apparent resistivities in a horizontally homogeneous two-layer medium with a conductivity contrast of 1 : 10.

The above mentioned effects have an important bearing on MT sounding curves. They are obtained from apparent resistivity functions estimated for a series of different periods at a particular site. They are conveniently

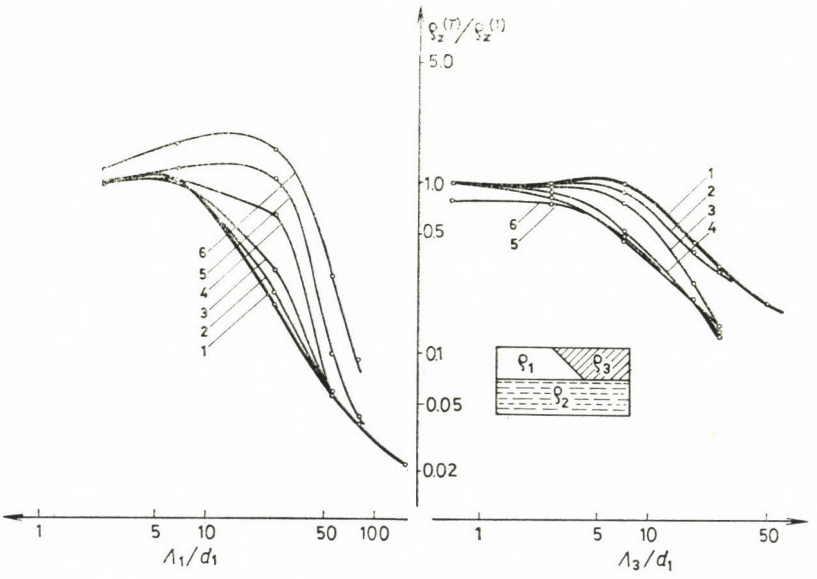


Fig. 6. *H*-polarization. MT sounding curves $\varrho_z(T)/\varrho_0 = f(\Lambda_{1,3}/d_1)$ on both sides of the sloping contact for the same parameters as in Figure 5. The curves are labelled according to the distance y [km] from the edge as follows: 1 — 80 km; 2 — 60 km; 3 — 40 km; 4 — 20 km; 5 — 10 km; 6 — 5 km

presented as the functions $\varrho_z(T)/\varrho_0 = f(\Lambda/d_1)$, where $\varrho_z(T)$ is the apparent resistivity in Ωm at a period of T [sec], ϱ_0 stands for the specific resistivity of the superficial layer of thickness d_1 [km], and Λ is the wave length [km] evaluated from the formula $\Lambda = (10\varrho T)^{1/2}$.

To express the results in this specific form we indentified the apparent resistivity at a period of 1 sec with ϱ_0, i. e. $\varrho_0 = \varrho_z(1)$. In the close vicinity of the edge, however, $\varrho_z(1)$ behaves anomalously so that the normalizing resistivity had to be extrapolated from the undisturbed value in the region far from the contact.

The results of this presentation are shown in Figure 6. Two families of sounding curves were obtained in different halves of the model with each curve being related to some specific distance from the edge, as labelled and explained in the caption. Both undisturbed curves, labelled as 1, were obtained at distances $y > 80$ km from the edge. They coincide within an accuracy better than 1% with the theoretical master curves for the two-layer model with conductivity contrast of 1 : 10, or 1 : 100 on the other side.

The apparent resistivity curves at the surface of the less conductive block are progressively distorted approaching the edge. The distortion involves vertical shifts of the curves and changes of their type as well. For example, the curves labelled 5 and 6 in Figure 6, are transformed to a type that might suggest a virtual presence of a less conductive material

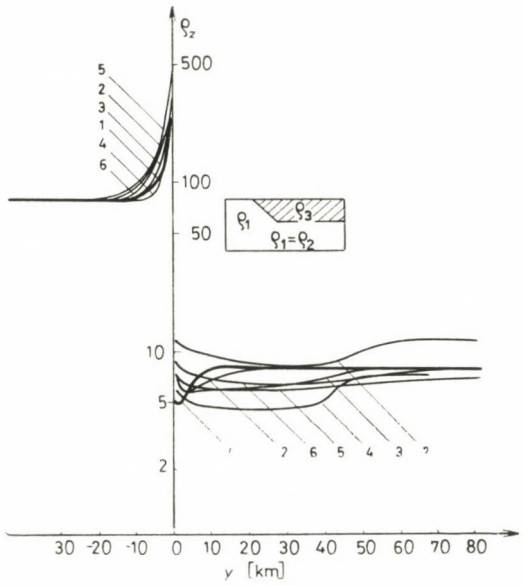


Fig. 7. *H*-polarization. At 45° sloping contact of two blocks above a horizontally homogeneous layer of decreased conductivity. Electrical conductivities in $[\Omega m]^{-1}$ are $\sigma_1 = \sigma_2 = 10^{-3}$, $\sigma_3 = 10^{2}$. Apparent resistivity functions are for periods T [sec] 1—1; 2 – 5; 3 – 10; 4 – 25; 5 – 50; 6 – 100; 7 – 250

above the more conductive layer in the basement. On the other hand, the sounding curves in the more conductive half do not change their type substantially, only a vertical nearly parallel shift towards lower resistivites by a factor of about 1/2 takes place. This would result in underestimating the thickness of the superficial layer.

On inserting $\sigma_1 = \sigma_2 = 10^{-3}$ $[\Omega m]^{-1}$ and $\sigma_3 = 10^{-2}$ $[\Omega m]^{-1}$ in the above model, we obtained also results of practical importance. They might approximate the electromagnetic conditions in marginal parts of a sedimentary basin with a less conductive basement. Following the same procedure, as in analyzing the distribution for the above model, we obtained the apparent resistivity functions for periods between 1 and 250 sec and they are exhibited in Figure 7. They suggest again a strong edge effect in the less conductive part of the model and depressed apparent resistivities on the surface of the basin within a zone which is larger than the projection of the sloping boundary upon the earth's surface. The sounding curves derived at different sites above the sloping boundary show no substantial deformation of their type. However, they are shifted towards lower resistivities compared with the curves in the homogeneous part of the model far from the contact. Extrapolating these results for models with higher conductivity contrast the S-interval (the longitudinal conductivity S) will develop clearly on the sounding curve. The above-mentioned effect will shift the curve so as to increase the S-value with consequent overestimating the thickness of the superficial layer.

4. CONCLUSION

The principles were outlined for solving numerically a finite difference approximation of the Helmholtz partial differential equation with appropriate boundary conditions. The results of analyzing the spatial distribution of electromagnetic fields for the H- and E-polarizations were discussed for some important models of two-dimensional inhomogeneous structures. In particular, the effects of dipping boundaries on sounding curves were investigated in detail.

In conclusion, it should be emphasized that the above results are approximative and they must be considered as qualitative to some extent. There may be involved some unknown effects of the mesh dimensions.

REFERENCES

ALLEN, D. N. G., 1954. Relaxation Methods. McGraw-Hill, N.Y. 198.

BERDICHEVSKY, M. N., 1968. Electric Prospecting by the Magnetotelluric Profiling method (in Russian). Nedra, Moscow.

BERDICHEVSKY, M. N., DMITRIEV, V. I., 1972. Magnetotelluric fields over horsts and grabens (in Russian). KAPG Symposium, Prague.

ČERV, V., PRAUS, O., 1972. MT field of H-polarization in models with dipping interfaces. *Studia Geophys. Geod. ČSAV*, **16**, 285.

DMITRIEV, V. I., 1969. Electromagnetic fields in inhomogeneous media (in Russian). *Tr. Vych. tsentra Moskovskogo Univ.*

D'ERCEVILLE, I., KUNETZ, G., 1962. The effect of a fault on the earth's natural electromagnetic field. *Geophysics* **27**, 651.

JONES, F. W., PASCOE, L. J., 1971. A general computer program to determine the perturbation of alternating electric currents in a two-dimensional model of a region of uniform conductivity with an imbedded inhomogeneity. *Geophys. J. R. Astr. Soc.* **24**, 3.

JONES, F. W., PRICE, A. T., 1970. The perturbations of alternating geomagnetic fields by conductivity anomalies. *Geophys. J. R. Astr. Soc.* **20**, 317.

NEVES, A. S., 1957. The Generalized Magnetotelluric Method. PhD. Thesis, Mass. Inst. Techn.

PRAUS, O., ČERV, V., NEDOMA, J., VERNER, A., 1973a. Distribution of the electromagnetic field in some horizontally non-homogeneous models of the earth (Case of H-polarization). *Trav. Inst. Géophys. Sci. Tchécosl.* No. 358, Academia, Praha.

PRAUS, O., ČERV, V., VERNER, A., 1973b. Magnetotelluric resistivities in models with dipping boundaries. *Studia Geophys. Geod. ČSAV*, **17**, 346.

PRAUS, O., PETR, V., 1969. Magnetotelluric calculations for the interaction of polarized fields with anisotropic layered media. *Can. J. Earth Sci.* **6**, 759.

VARGA, R. S., 1962. Matrix Iterative Analysis. Prentice-Hall, Inc., N.J., 161.

BEHAVIOUR OF MAGNETOTELLURIC FIELD ON THE SURFACE OF HORIZONTAL INHOMOGENEOUS STRATA (MODEL EXPERIMENTS)

M. A. DOBROVOLSKAYA, A. A. KOVTUN

During a number of years in the Department of the Physics of the Earth of Leningrad University a research of electromagnetic fields by means of models has been carried out in order to investigate the possibilities of magnetotelluric profile measurements and sounding of horizontal inhomogeneous strata.

The equipment for modelling allowed to solve a wide range of problems, connected with the behaviour of fields in a horizontal inhomogeneous conductive layer, having a high-resistance basis. The paper sums up results of investigations carried out for years. Description of the modelling equipment and method had been published earlier in separate papers (Bryunelli et al., 1969; Kovtun et al., 1970a; Dobrovolskaya et al., 1971). Here only the basic parameters will be given.

1. The conductive layer in the modelling set is the sodium chloride solution having the resistivity $\varrho_1 \simeq 0.05$ Ωm, poured out in a wooden vessel 4.2×4.2 m^2. The layer thickness h_1 varies from 3 to 30 cm according to the given aim. The resistivity of the lower semispace is more than 10^4 Ωm. Nonconducting structures were made of gypsum, paraffin, marble or by modification of the vessels' second bottom.

The source of electromagnetic field — a coil with six parallel rectangular cross-section (4×1.6 m^2) windings — is suspended above the vessel by means of a turning device. The GS-1001 generator feeds the coil.

Brass tubes, connected by conductors thrown over the aerial, were placed along vessel borders perpendicular to aerial winding to increase homogeneity of the field. Besides, on two other walls a metal net was hung and electrically connected to the solution. Thus the homogeneous field area was enlarged. In the area of 1.5×2 m^2 the field components are constant with the accuracy of 2%. Distribution of the field according to depth is close to the theoretical one.

The operating frequency range from 40 to 5000 kHz which corresponds to wave lengths in the conductive layer of 0.3—3.4 m. The measurement of electric (E) and magnetic (H) field components are taken by means of specially made electric and magnetic dipoles. The size of the dipoles is 3 and 1.5 cm, respectively. The dipoles are connected by a screened wire with symmetrical input of selective microvoltmeter IP-12-2V. All measurements were taken by two field polarizations: in case of two-dimensional heterogeneities by magnetic polarization, when the electric vector is perpendicular to homogeneity axis, and electric polarization, when the electric vector is directed along the homogeneity axis; in case of three-dimensional heterogeneities — I and II field polarizations (I — electric vector parallel with

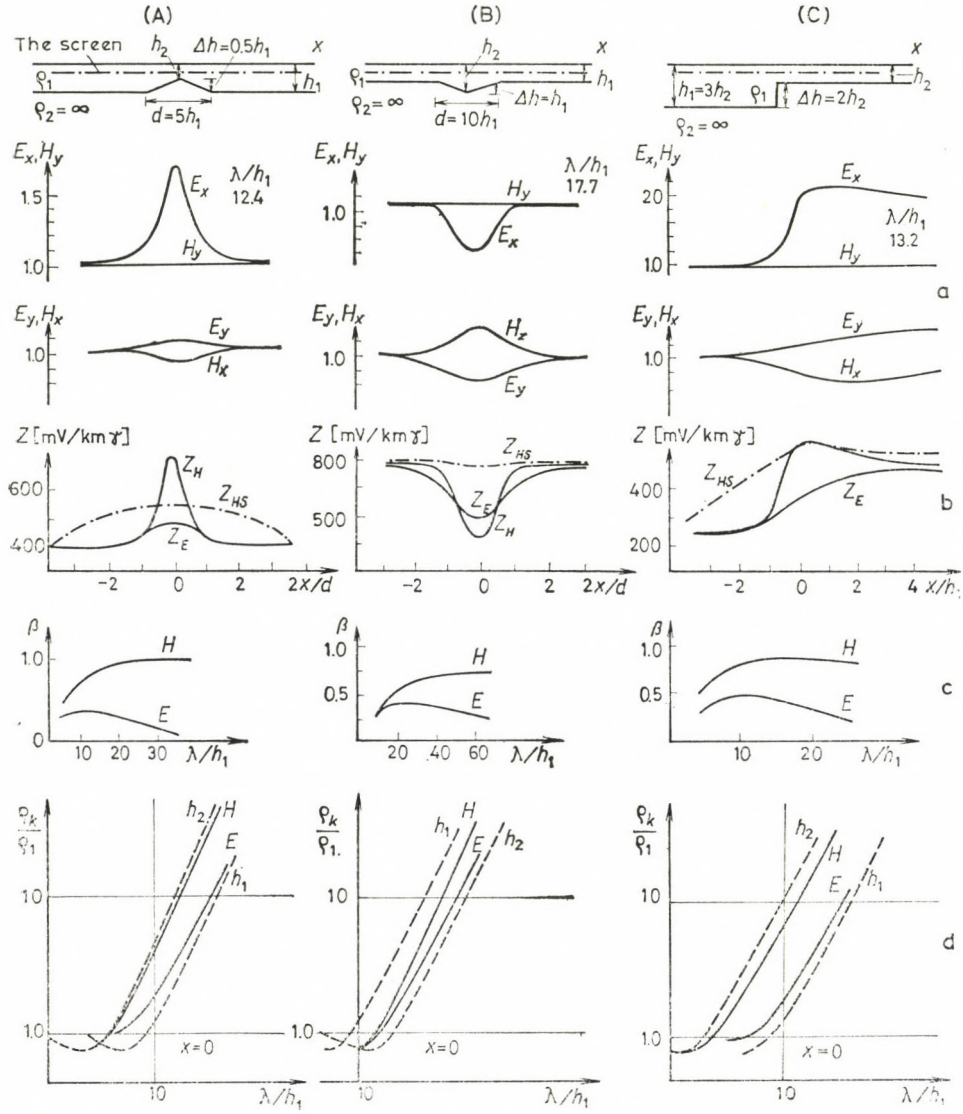


Fig. 1. Results of modelling two-dimensional high-resistivity structures for H- and E-polarization for: (A) – rampart; (B) – trough; (C) – rectangular step.

a – distortion of the relative amplitude of the field-components; b – distortion of the impedances: Z_E – impedance for E-polarization, Z_H – impedance for H-polarization, Z_{Hs} – impedance in case of a high resistant screen, c – dependence of the relative anomalous amplitude on the wave-length, d – sounding curves for the centres of the models. Dotted line represent curves for horizontal layers (thickness h_1 or h_2), λ – wavelength in the uppermost layer. For detailed explanation see text

the central measurement profile, II — electric vector perpendicular to the central measurement profile). For two-dimensional and axially symmetric three-dimensional structures the impedance tensor components, calculated by E- and H-field polarizations (or I and II polarizations), completely characterize the electric properties of the medium.

Investigations have been made for a sufficiently large class of two dimensional and three-dimensional structures (Dobrovolskaya et al., 1971, 1972; Kovtun et al., 1970a, b) and this has revealed some general regularities in the behaviour of the magnetotelluric field.

2. First of all let us dwell on the results of modelling two-dimensional structures, since in this case many properties of the field can be seen in a simpler and more distinct form.

Figure 1 shows results of modelling some two-dimensional structures: A — "rampart", B — "trough", C — "rectangular step".

Figure 1 shows for each model the behaviour of field components for H- and E-polarizations (a), the impedances $Z_H = E_x/H_y$ and $Z_E = E_y/H_x$ (b) and the dependence of relative anomaly amplitude on wave length (c).

The relative anomaly amplitude β was calculated according to the formula:

$$\beta = \frac{\Delta Z}{Z_{\text{extr}}} \Big/ \frac{\Delta h}{h_1}$$

where $\Delta Z = |Z_N - Z_{\text{extr}}|$, Z_N is the impedance over the homogeneous layer (in case of asymmetric structures Z_N is the impedance over a deeper part of the high resistance basis); Z_{extr} is the impedance over the centre of the structure (in case of a rectangular step Z_{extr} is the impedance measured over the raised part at a distance h_1 from the step). Figure 1, d shows the sounding curves at two polarizations $\varrho_H = 0.2 \cdot TZ_H^2$ and $\varrho_E = 0.2 \cdot TZ_E^2$ in points, shown in the diagrammatic representation of the models (Fig. 1).

Comparing the results of modelling two-dimensional structures one observes a series of regularities in the behaviour of field components, impedances and sounding curves.

In case of two-diemensional structures the behavioural character of field components, impedances and apparent resistivity essentially depends on primary field polarization.

In case of H-polarization the anomaly of the field's electric component and impedance, as a rule, reflects very well the location and size of heterogeneity. The magnetic component remains constant, the presence of heterogeneity does not affect it. In the region of profiling ($\lambda/h_1 > 8$) the relative value of heterogeneity $\Delta h/h_1$(Δh — is the amplitude of the structure, h_1 — the thickness of the containing homogeneous layer) can be well estimated on the basis of the relative value of the anomalous impedance amplitude. The error in determination of structure parameters does not exceed 15%, and in some cases 2–3% (see Fig. 1, b and c).

MTS curves practically coincide with the theoretical two-layer curves for the infinite inhomogeneous layer, of thickness equal with the local thickness in the point of sounding (theoretical curves are given by dotted line in Figure 1, d; the curve-code means thickness of the conductive layer). Thus

in case of an H-polarized primary field interpretation of results within the frames of the theory of horizontally inhomogeneous strata is quita possible.

The above said is only valid in case of convex structures. The situation is a bit worse, when one makes a magnetotelluric study of concave structures. The anomalous amplitude of the electric field component and impedance is always less than the hollow amplitude. The error grows with the increase of the ratio $\Delta h/d$, where Δh is the hollow amplitude, d the width. For $\Delta h/d \approx 0.1$ the error in determination of the hollow amplitude reaches 30%.

In case of E-polarization the presence of heterogeneity appears in the behaviour of both field and impedance components, but considerably weaker, than by H-polarization. Slow field component changes begin far from the structure, the relief of nonconducting structure is reproduced in a smoothed form (Fig. 1, a). The anomalous amplitudes in electric, as well as in magnetic components in most cases do not exceed 15–20% of structure amplitude.

The Z_E impedance change along a profile reflects structure parameters much less than in the case of H-polarization. The anomalous impedance amplitude depends significantly on wave-length. It reaches its maximum in the wave-length range of $5 < \lambda/h_{\max} < 10$, where $h_{\max}$ is the maximum depth of a conductive layer in the vicinity of the inhomogeneity. For wave-lengths, exceeding the width of the structure, the anomalous amplitude begins to decrease. The maximum value of the relative anomalous amplitude in case of "rampart" and "trough" type structures depends on the structure width. The wider the structure, the nearer the maximum value of the relative anomalous amplitude to $\Delta h/h_1$. In case of a "rectangular step" structure the maximum anomalous amplitude value is approximately in proportion to the value of $\Delta h/h_1$. For $\Delta h/h_1 = 0.8;\ 0.67;\ 0.50;\ 0.33$, investigated by means of models, the correlation

$$\frac{\Delta h}{h_1} \approx 2 \left(\frac{\Delta Z}{Z_{\text{extr}}} \right) \max$$

remains in force.

The sounding curves at points, situated over the structure, significantly differ from those for two-layers medium. This difference appears in the fact that the curves tend asymptotically to the values of ϱ_k over the "containing" homogeneous layer, beginning with wave-lengths comparable with the size of heterogeneities. In case of convex structures the rising branches in the region of great wave-lengths ($\lambda > d$, where d is the structure width) go at an angle, less than 63° and approach the curve over the more vigorous homogeneous layer as λ increases. In case of concave structures the tendency is the same, and the curves have slopes greater than 63°. Interpretation of these curves by means of the theory of horizontally homogeneous strata gives false information about the vertical geoelectric profile.

By means of two-dimensional structures the influence of a screening high-resistivity layer was studied ($\varrho_{\text{screen}} > 10^4 \Omega$m). The thin high-resistivity layer of 1.5×1.5 m^2 was placed over a structure at various distances from its surface. *In case of H-polarization* over the screen, the surplus current

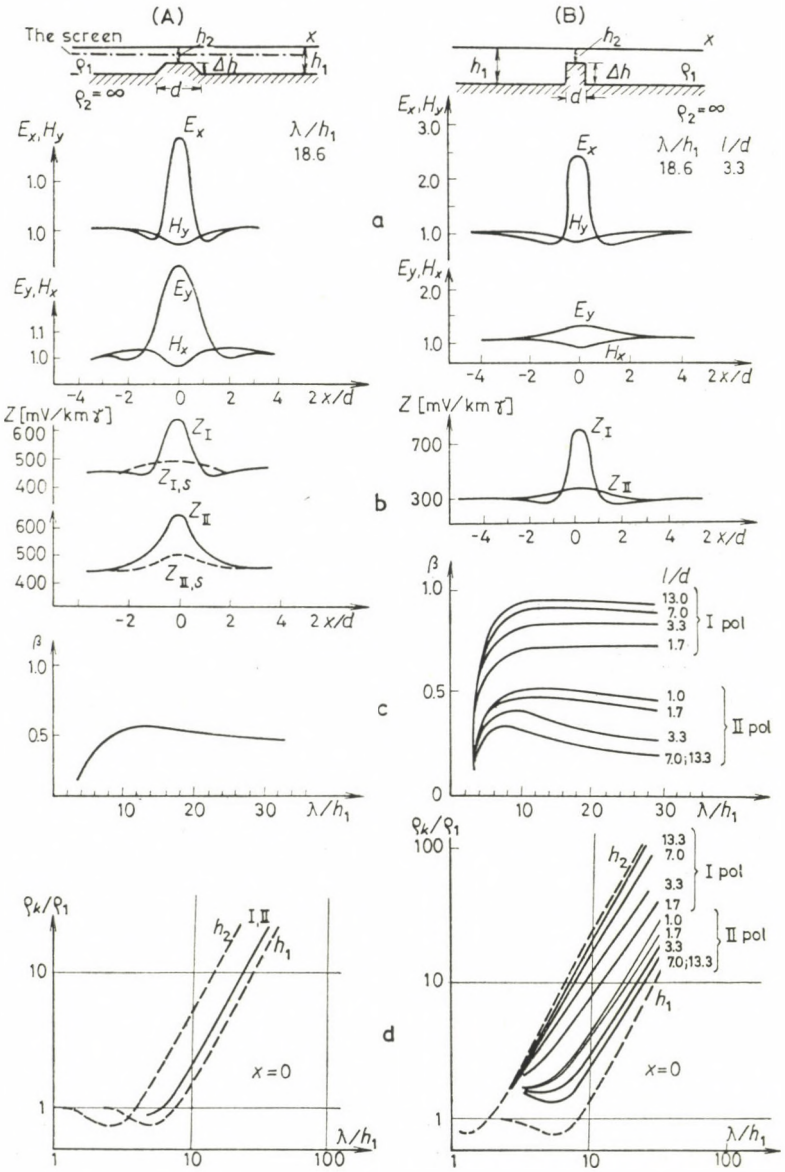


Fig. 2. Results of modelling high-resistivity three-dimensional structures for: (A) – axially symmetric projections; (B) – short rampart
I – polarization of H in the direction of the prolonged structure (y);
II – polarization of E in the direction of the prolonged structure (y); l = length of the structure in direction of strike. For meaning of Z, β, λ and the sounding curves see Figure 1 and the text

density appears all over it and leads to appearance of a positive anomaly in the values of electric component and impedance Z_{HS}, with the width equal to the extent of the screen. As an example a dotted line in Figure 1, b displays the behaviour of impedance Z_{HS} at H-polarization, in the case when the screen is situated as shown in the scheme. No dependence upon the submersion depth of the screen has been found. In case of concave structures (model B) the thin high-resistivity layer screened completely the structure.

In case of E-polarization the screen practically does not influence the behaviour of the field components and impedances, and therefore it is necessary to use E-polarization for approximate evaluation of two-dimensional structure parameters in the presence of the high-resistivity screen.

3. The two-dimensional approximation is of course an idealization of real structures, and in this connection the behaviour of a magnetotelluric layer in case of three-dimensional structures is of greatest interest. Because of computational difficulties calculations of theoretical fields in presence of a three-dimensional structure have been only made in case of sloping structures of a small amplitude (Kaufman and Tabarovsky, 1970), therefore solution of such problems by means of modelling is of considerable interest. Figure 2 presents results of investigation of an axially symmetric projection (A) and a short rampart (B). There are given the main field characteristics by two polarizations I and II, similar to H- and E-polarizations, respectively, in case of prolonged structures.

In case of three-dimensional axially symmetric structures sharp distinctions between the properties of polarizations I and II are absent. In both polarizations the electric and magnetic components of the field show the presence of heterogeneity. But the anomalous amplitude in the magnetic component is considerably smaller than in the electric one (Fig. 2, a).

The impedance values of the first (Z_{I}) and second (Z_{II}) field polarizations differ only over the structure edges, where polarization I marks the structure edges clear, while polarization II passes smoothly to normal impedance values (Fig. 2, b). The anomalous amplitude in the impedance values visibly depends on wave-length, it increases with λ/h and attains a practically constant value in the profiling area ($\lambda/h_1 > 8$). When wave-lengths are greater than the structure diameter, a tendency to anomaly amplitude reduction begins to show. The maximum value of the relative amplitude of impedance anomaly is two times smaller, than the relative value of heterogeneity (Fig. 2, c).

The sounding curves over the structure have a low-frequency asymptote of a slope somewhat smaller than 63°, but they are noticeably displaced to the side of wave-length with regard to the theoretical curve for a horizontal-homogeneous two-layer profile with conductive layer thickness equal to the local one in the sounding point. With growth of λ/h_1 the values of $\varrho_{\mathrm{I,II}}$ slowly approach the values of ϱ_k over the homogeneous layer of thickness h_1 (Fig. 2, d).

The presence of a thin high-resistivity screen, covering the structure, greatly alters the picture of the field. The anomalous amplitudes in the field components and impedance become noticeably smaller (Fig. 2, b), the screening coefficient grows with increasing wave lengths, the sounding

curves change significantly over the centre of the structure. The curves are considerably more slanting than the theoretical ones, their interpretation within the frames of the horizontally homogeneous strata theory leads to too small resistance values of the substructure (Kovtun et al., 1970a).

Investigations of prolonged three-dimensional structures (a rectangular rampart with parameters $l/d = 1$; 1.7; 3.3; 7; 13.3, proportion $d/h_1 = 1.2$; 2.4 and height of $\Delta h/h_1 = 0.44$; 0.77) have allowed to learn the regularities of the fields's behaviour in relation to the structure stretch. Results of the investigation are shown in Figure 2,b.

The electric component in the I-polarization case (the cross one) has a distinct anomaly over the structure. The anomalous value grows with the ratio l/d, approaching the value over the two-dimensional structure (Fig. 2, a). Anomaly in the magnetic components is not great and decreases with increasing structure stretch.

In case of polarization II a reverse tendency is observed in the behaviour of the electric component — the anomalous amplitude decreases with the increase of l/d. The anomaly in magnetic component is small and does not change significantly with l/d. Therefore, anomalous amplitudes in impedance values over the structure grow with increasing l/d for polarization I and decreases for polarization II.

As main quantitative characteristics of impedance behaviour over the structure, relative amplitude behaviour is analyzed, determined as

$$\beta = \frac{\Delta Z}{Z_{\max}} \Big/ \frac{\Delta h}{h_1}, \quad \text{where} \quad Z = Z_{\max} - Z_0$$

$Z_{\max}$ is the impedance value over the centre of the structure, Z_0 the same over the horizontally homogeneous layer beyond the structure.

Figure 2 shows the dependence of β on wave-length for different l/d ratios and constant values of structure width and height ($d/h_1 = 1.2$; $\Delta h/h_1 = 0.77$).

In case of cross polarization β attains its maximum for $6 \leq \lambda/h_1 \leq 10$. By a further increase of λ/h_1, the value of β gets stabilized, and the anomalous value for $\lambda/h_1 > 10$ only depends on structure length. If the structure width (d/h_1) and height ($\Delta h/h_1$) are constant, the value of β in case of cross polari-

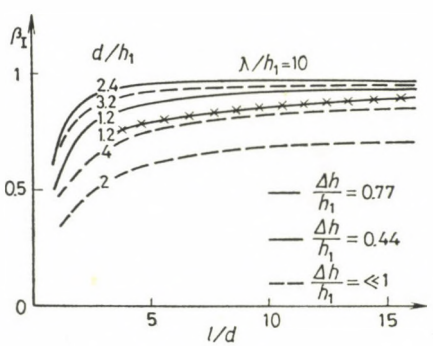


Fig. 3. Dependence of the anomaly amplitude β_I (see text) on the different model-parameters of Figure 2

zation increases, asymptotically approaches the value β_H of a two-dimensional structure (in case of H-polarization this value is equal to 1). For $l/d > 5$ the differences do not surpass 10%.

The growth of structure width implies an increase of anomalous amplitude for any λ/h_1, but if the ratio l/d is great enough ($l/d > 4$), this growth is insignificant in case of cross polarization. That means that by the growth of structure width the approach to "two-dimensionality" already occurs at smaller values of l/d. This is shown in Figure 3, where the dependence of β_1 on l/d for the same structure height ($\Delta h/h_1 = 0.77$) and different widths — $d/h_1 = 2.4$ and $d/h_1 = 1.2$ — is represented. For the structure with $d/h_1 = 2.4$ already for $l/d > 3$ the distinction from the unity (i.e. "two-dimensionality") becomes less than 10%.

The decrease of structure amplitude leads to reduction of relative anomalous amplitude, especially in case of cross polarization. The same Figure 3 presents the dependence of anomalous amplitude β on l/d for structures of equal width ($d/h_1 = 1.2$) and smaller amplitude ($\Delta h/h_1$) = 0.44. It is evident from Figure 3 that for smaller projection amplitudes the properties of two-dimensionality appears for greater l/d ratios.

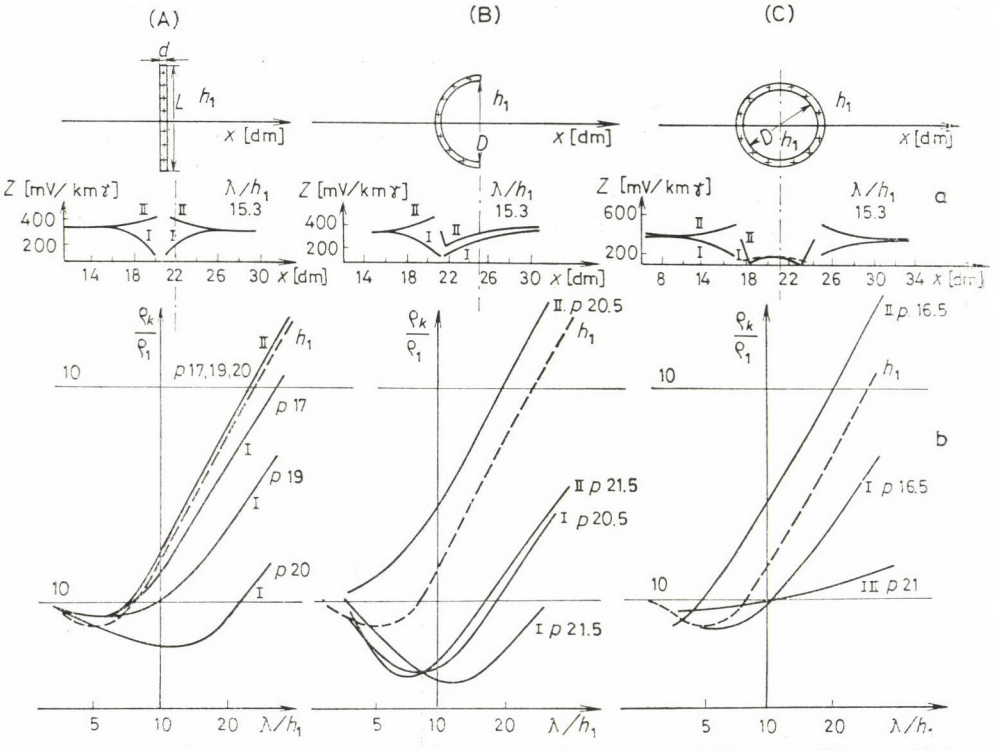
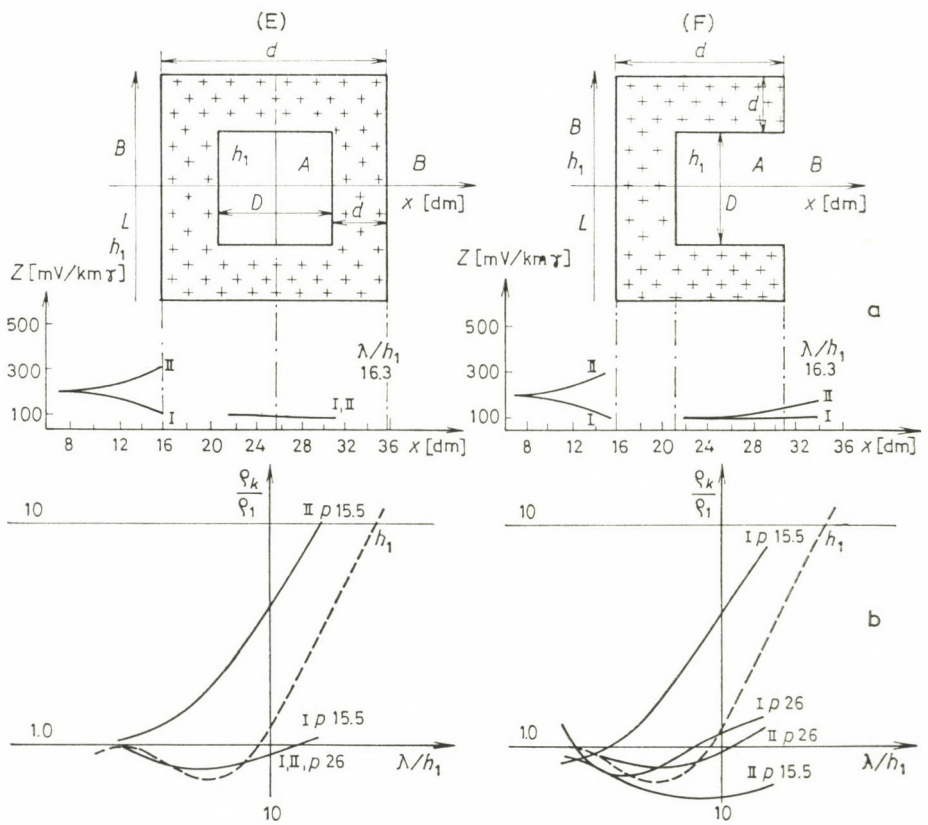


Fig. 4. Results of three-dimensional high-resistivity base-modelling for different high-resistant vertical screens (here the first row is as seen from above)

In the same figure the calculated curves for slanting structures ($\Delta h/h_1 \ll 1$; Kaufman and Tabarovsky, 1970) are compared with experimental ones for structures of great projection amplitude ($\Delta h/h_1 = 0.44$; 0.77). It can be seen in Figure 3 that theoretical curves act as bottom borders, to which the β_I values tend as $\Delta h/h_1$ decreases.

In case of slanting structures of small projection amplitude the "two-dimensionality" appears for greater values of l/d. So, if the projection width is $d/h_1 = 2$, then even for $l/d > 30$ the anomaly amplitude β_I would differ from the amplitude β_H of a two-dimensional structure by more than 20% and it is only for $d/h_1 > 8$ and $l/d > 5$ that the difference becomes less than 10%.

As a result of investigating prolonged three-dimensional heterogeneities we can draw a number of practical conclusions about the possibility of using magnetotelluric fields to determine structure parameters in a high-resistivity substructure.



(A) – vertical wall; (B) – half-ring; (C) – ring; (E) – square; (F) – opened square; I – polarization of H in y-direction; II – polarization of E in y-direction. For meaning of Z, λ and the sounding curves see Figures 1, 2 and text

The main information about structure amplitude is carried by the cross (I) polarization. The amplitude of a wide structure ($d/h_1 > 8$) can be determined if the structure is sufficiently elongated ($l/d > 5$).

In case of a structure of great amplitude ($\Delta h/h_1 > 0.5$) the limitations of width falls away and the estimation according to "two-dimensional" criteria with the indicated extent of exactness can be fulfilled if $l/d > 5$ also in case of narrow structures ($d/h_1 \geq 1$).

4. By means of a number of models there was studied a frequently met kind of heterogeneities — juts of high-resistivity substructure on the surface of well-conductive sediments. The high-resistivity juts had different forms: ring, semiring, square, a $\sqcap$ formed jut, a wall (Fig. 4). Measurements of horizontal field components have been carried out along the central profile, coincident with the symmetry axis X of the structure for two field polarizations: a cross one (I) where the component E in the primary wave is parallel to the X axis, and a longitudinal one (II) where the component E is perpendicular to X.

Analysis of the results allows to make some general conclusions concerning the behaviour of the magnetotelluric field in regions, which are completely screened by substructural high-resistivity juts in partly screened regions and near juts of wall-kind.

As one can see in Figure 4, in the completely screened regions, regardless of the barriers' form and thickness (a thick ring and a square with thick walls), a less intensive electromagnetic field is induced, than in a homogeneous infinitely-spread conductive layer of the same thickness, if the wave-length λ is greater than D, where D is the least cross size of the region.

The character of the dependence of Z/Z_N on λ and h_1 in the region of $\lambda/D > 1$ can be approximately evaluated according to the formula

$$|Z/Z_N| = c\sqrt{h}\,e^{-\alpha\frac{\lambda}{D}}$$

where h is thickness of the layer inside the region, $\alpha = 0.40$; $c = 0.45$

For $\lambda > D$ the impedance inside the screened region approaches the normal value. By $\lambda/D \leq 1/2$ the impedance differs from the normal one by less than 5%.

In regions partly screened by high-resistivity substructure juts, the quantitative description of field behaviour is very difficult owing to the great variety of screening conditions (form and dimensions of the region).

In particular, one fails to give an analytical expression for the dependence of Z/Z_N on λ/D, as it could be done for completely screened regions.

In case of partial screening decrease of impedance inside the region takes place not exponentially, as in completely screened regions, and beginning with wave-lengths $\lambda > 4D$ the impedance values become stabilized. This regularity can be distinctly traced at the sounding curves. The curves in screened regions are very close to the curves over the homogeneous semi-space for both field polarizations. If the region is semi-enclosed, a second rising branch appears at the sounding curves (Fig. 4, b).

Field investigations near the wall have shown that the greatest field alteration takes place by polarization I. The degree of alteration is determined

by the value λ/L. As it is shown in the figure, for one and the same λ/L and close values of λ/h_1 the behaviour of Z/Z_N appears to be the same regardless of the wall thickness d. For $\lambda/L > 2$ and $\lambda/h_1 > 8$ the picture of alterations becomes stabilized.

The following description of the impedance behaviour near the high-resistivity wall is correct to 5%:

$$|Z/Z_N| = 1 - e^{-\alpha X/L}$$

where

$$\alpha = \frac{4.0}{1 - e^{-1.25\lambda/L + 0.55}}$$

The wall bend decreases a little the region of impedance alterations.

For polarization II (a longitudinal one) impedances near the high-resistivity border are too great and become greater with increasing structure width. In case of a thin wall ($\lambda \gg d$) the impedance values are practically the same as in case of a horizontal homogeneous two-layer profile.

In summary it can be said that in future, with the advent of digital computers, the need of investigating two-dimensional structures by models will fall off, even though one must remember that the first results about two-dimensional structures were received by means of modelling (Bryunelli et al., 1963). For investigating three-dimensional heterogeneities the modelling is at the present state of the arts the simplest and almost unique method to solve concrete geophysical problems.

REFERENCES

Bryunelli, B. E., Dobrovolskaya, M. A., Kovtun, A. A., Kuznetsov, N. S. 1963. Magnetotelluric profiling over models with horizontal-inhomogeneous structure (in Russian). Novye Metody Elektricheskoi Razvedki na Neft i Gaz, Gostoptekhizdat, Moscow, 114–119.

Bryunelli, B. E., Dobrovolskaya, M. A., Kovtun, A. A., Kuznetsov, N. S., 1969. Some results of MTP and MTS over models of inhomogeneous structures (in Russian). Magnitotellurichеskie Metody Izucheniya Stroeniya Zemnoi Kory i Verkhnei Mantii, **4**, 125–129.

Dobrovolskaya, M. A., Kovtun, A. A., Nepesov, K., Gladky, T. D., 1970. Magnetotelluric modelling investigations on the case of high-resistance jut (in Russian). *Izv. Akad. Nauk SSSR, Ser. Fiz. Zemli*, No. 12, 85–88.

Dobrovolskaya, M. A., Gladky, T. D., Kovtun, A. A., 1971. The magnetotelluric modelling investigations in the case of "rectangular step" in none-conductive base (in Russian). Problems of geophysics 21, Uchenye Zapiski Gos. Univ. Leningrad, 166–173.

Dobrovolskaya, M. A., Gladky, T. D., Kovtun, A. A., 1972. The magnetotelluric modelling investigations in the case of "sloping jut" (in Russian). Problems of geophysics 22, Uchenye Zapiski Gos. Univ. Leningrad, 179–185.

Kaufman, A., A., Tabarovsky, L. A., 1970. The Basic Principles of the MTS Theory in Strata with Sloping Structures (in Russian). Nauka, Novosibirsk.

Kovtun, A. A., Dobrovolskaya, M. A., Gladky, T. D., Kuznetsov, N. S., 1970a. MTS and MTP on the model of three-dimensional structures (in Russian). *Izv. Akad. Nauk SSSR, Ser. Fiz. Zemli*, No. 9, 94–97.

Kovtun, A. A., Dobrovolskaya, M. A., Gladky, T. D., 1970b. MTP and MTS on the model of two-dimensional structures (in Russian). *Geofiz. Razvedka*, **42**, 64–68.

MAGNETOTELLURIC DATA PROCESSING METHODS

A. ÁDÁM, J. VERŐ

INTRODUCTION

It is advantageous to treat the two variants of the magnetotelluric method, i.e.

magnetotelluric profiling (MTP) and
magnetotelluric sounding (MTS)

separately from the point of view of data processing, too. There are several methods described in the literature. What follows is a description of the methods used by the Geodetical and Geophysical Research Institute of the Hungarian Academy of Sciences.

THE MTP-METHOD

The MTP-method can be used for the determination of the horizontal conductivity S of the sediments in sedimentary basins. This is proportional to the thickness of sediments, thus one has a possibility to trace the relief of the non-conductive ($\varrho_n = \infty$) basement.

The aim of data processing is to determine the value S and its anisotropy, as well as to construct S-ellipses.

According to Berdichevsky (1960) the asymptotic formula of the MTP-method is:

$$S = 796 \left(\frac{1}{|Z_n|} - \sqrt{\frac{T}{10\,\varrho_n}} \right) \tag{1}$$

Here $Z_n = E_x/H_y$ is the input impedance, T the period of variations. This formula can be used with an error less than 10 per cent in case of two- or several-layer magnetotelluric sounding curves of type H, e.g. ($\varrho_1 > \varrho_2 < \varrho_3$) in the period interval corresponding to the right-side increasing branch of the curve. This is the so-called S-interval lying in case of two-layer curves between the period limits

$$3.6\,T_{\min} \leq T \leq 1.6\,T_{\min} \frac{\varrho_2}{\varrho_1}\,; \quad (\varrho_2 = \varrho_n) \tag{2}$$

where

$$T_{\min} = 2.8 \frac{h_1^2}{\varrho_1} \tag{3}$$

In this case we have

$$0 > \varphi > -20^\circ \tag{4}$$

$$\varphi = \arg E_x - \arg H_y$$

for the phase conditions of the S-interval.

DETERMINATION OF THE S-ANISOTROPY

In practice one can start from the determination of the telluric (E) and geomagnetic (H) absolute ellipses deduced by Kunetz (1957) from the statistic rules of the movement of the corresponding variation-vectors. In case of the absolute ellipse of a station, the radius vectors are equal to the average value of the field in different directions.

The absolute ellipse can be determined among others by means of

a) the total variation method (e.g. for x, $V_x = \sum_{t_1}^{t_2} |\Delta x|$), (Kunetz, 1957), or by

b) the tangent of the variations: $x_1 = dx/dt$ (Verő, 1960).

The formulas for the determination of the directions and lengths of the axes of the ellipses can be found in the papers quoted.

For the determination of the total ellipse one has to measure the total variation of three components in the time interval $\Delta t = t_1 - t_2$. This value can be immediately measured in field with the so-called total-counter, described by Ádám and Bencze (1964).

The absolute ellipse is a tensor expressing a linear vector transformation. The matrix characterizing the linear vector function

$$\begin{pmatrix} a_{E,H} & b_{E,H} \\ c_{E,H} & d_{E,H} \end{pmatrix} \tag{5}$$

can be determined by the axes of the ellipse (A major, B minor axis) and by the angle α between major axis and (geomagnetic or geographic) North, both in case of the E electric and H magnetic field (Verő, 1960).

$$a_{E,H} = A_{E,H} \cos^2 \alpha_{E,H} + B_{E,H} \sin^2 \alpha_{E,H}$$

$$d_{E,H} = A_{E,H} \sin^2 \alpha_{E,H} + B_{E,H} \cos^2 \alpha_{E,H}$$

$$b_{E,H} = c_{E,H} = \frac{1}{2} (A_{E,H} - B_{E,H}) \sin 2\alpha_{E,H} \tag{6}$$

The connection between tensors $\{\mathbf{E}\}$ and $\{\mathbf{H}\}$ is according to Ádám (1964):

$$c\{\mathbf{S}\} = \{\mathbf{F}\}\ \{\mathbf{H}\}\{\mathbf{E}\}^{-1} \tag{7}$$

where $\{\mathbf{F}\}$ is a tensor which rotates the magnetic field by 90° in direction

of the electric field. According to the rules of tensor multiplication the matrix of the tensor $c\{(\mathbf{S})\}$ is

$$c\{\mathbf{S}\} = \begin{Vmatrix} \frac{1}{t_E}(a_{FH}d_E - b_{FH}c_E) & \frac{1}{t_E}(b_{FH}a_E - a_{FH}b_E) \\ \frac{1}{t_E}(c_{FH}d_E - d_{FH}c_E) & \frac{1}{t_E}(d_{FH}a_E - c_{FH}b_E) \end{Vmatrix} = \begin{pmatrix} a_s & b_s \\ c_s & d_s \end{pmatrix} \quad (8)$$

where

$$t_E = a_E d_E - b_E c_E \quad (9)$$

i.e. the determinant of tensor $\{\mathbf{E}\}$.

The parameters of the ellipse representing the anisotropy of the horizontal conductivity can be expressed by means of the matrix of $c\{\mathbf{S}\}$:

$$\frac{A}{B} = \frac{1}{2}(a_s + d_s \pm \sqrt{(a_s + d_s)^2 - 4t_s}) \; ; \; \alpha = \text{arc cot} \frac{-b_s}{a_s - A} \quad (10)$$

where t_s is the determinant of the matrix.

Since according to Eq.(4) the phase shift can be neglected in the S-interval, the S-ellipse can be also constructed from individual variations from point to point using the same normalization method as for the telluric relative ellipse (Ádám, 1964).

A PROGRAM FOR MTS DATA PROCESSING

If the signals of different frequencies are separated by using filtering techniques, a program for the determination of the MT impedance tensor has to carry out the following operations (in case of spectral analysis, there can be some difference):

1. Separation of signals with different periods by using mathematical filters.
2. Selection of informations that can be used for the determination of the tensor.
3. Computation of the elements of the impedance tensor.
4. Determination of quantities deduced from the impedance tensor (impedance and apparent resistivity in different directions, direction of the maximum and minimum values of these quantities etc.).

In what follows the short description of a program is given, which has intensively been used in the Geodetical and Geophysical Research Institute of the Hungarian Academy of Sciences.

1. The components of different periods (frequencies) are separated from the digital records of the H_x, H_y, E_x, E_y components by using mathematical filters. The convolution-type filters used compute the whole complex field vector in certain period bands and in certain time intervals with the help of in-phase and out-of-phase components. The shortest period to be filtered is the Nyquist-period; the longest period is set by the condition that for the determination of 8 impedance components at least 4×2 equations, i.e.

4 repetitions of a given period are required. That means that periods longer than 1/4 of the complete digital record cannot be used separately for the determination of the impedance tensor, but only supplemented with records of similar period.

The formulas of the filters truncated by Hanning-functions are:

$$F(t) = \frac{1}{\pi t}\left(\sin\frac{2\pi t}{p_1} - \sin\frac{2\pi t}{p_2}\right)\left(\cos\frac{2\pi t}{T} + 1\right)\frac{1}{2} \tag{11}$$

$$F(o) = \frac{2d}{p_1} - \frac{2d}{p_2}$$

$$G(t) = \frac{1}{\pi t}\left(\cos\frac{2\pi t}{p_1} - \cos\frac{2\pi t}{p_2}\right)\left(\cos\frac{2\pi t}{T} + 1\right)\frac{1}{2} \tag{12}$$

$$G(o) = 0$$

here F means the in-phase, G the out-of-phase component, t is time, p_1 and p_2 the limiting periods of the transmitted band, d the sampling rate, T the half length of the filter, all in sec.

2. Practical experiences have shown that it is by no means an obvious task to select the proper time-interval for the determination of the impedance tensor. Namely, it is supposed that even in case of correct recording there are cases when the basic formulas by Tikhonov-Cagniard do not apply. There occur intervals, for instance, when according to Price the source of the pulsations has not the proper dimensions for the simple case. Such parts and in addition all parts when recording is artificially disturbed must be excluded from the further processing.

There are two possible ways for this:

a) The whole record is divided into sections, and in each section the coherency of the pairs E_xH_y and E_yH_x is determined. If these coherencies are less than a limit — in optimum cases 0.95, in case of very noisy records as a minimum 0.8 — the section is excluded from further processing.

As this procedure is equivalent with the neglection of secondary impedances, it is possible that the coherency conditions do not hold due to the great value of the secondary impedances. In order to include such cases, a second coherency computation is made in all cases when less than a half of the sections fulfils the first condition. In the second computation the secondary impedances are also taken into account. The preliminary impedance-elements needed for this computation are deduced from the complete material. Coherencies are computed between measured electric vectors and electric vectors computed from the magnetic vectors with the help of the preliminary impedances. The condition is the same as in the first case.

It should be mentioned that the coherencies have not the same meaning in both cases. In the first case amplitudes do not play any role, as the examination is carried out inside of a section. In the second case, however, changes of the amplitude ratio (e.g. unnoticed change of the scale value) play a role, too. Therefore the coherencies in the second procedures can be smaller than in the first case.

b) An other possibility which has not been yet used in practice is to give all values of the group a weight which honours better the correspondence to the impedances determined from the complete data set. This principle leads to iterations (Steiner, 1965). With this principle, impedances can be determined in all cases, and even a posteriori coherencies can be determined to judge their reliability.

3. In the following step the impedance elements are determined from the filtered data. Swift's (1967) formulas are used:

$$Z_{xx} = \frac{|E_x|}{|H_x|} \cdot \frac{\mathrm{Coh}(E_x, H_x) - \mathrm{Coh}(E_x, H_y) \cdot \mathrm{Coh}(H_y, H_x)}{1 - |\mathrm{Coh}(H_x, H_y)|^2} \tag{13}$$

$$Z_{xy} = \frac{|E_x|}{|H_y|} \cdot \frac{\mathrm{Coh}(E_x, H_y) - \mathrm{Coh}(E_x, H_x) \cdot \mathrm{Coh}(H_x, H_y)}{1 - |\mathrm{Coh}(H_x, H_y)|^2} \tag{14}$$

$$Z_{yx} = \frac{|E_y|}{|H_x|} \cdot \frac{\mathrm{Coh}(E_y, H_x) - \mathrm{Coh}(E_y, H_y) \cdot \mathrm{Coh}(H_x, H_y)}{1 - |\mathrm{Coh}(H_x, H_y)|^2} \tag{15}$$

$$Z_{yy} = \frac{|E_y|}{|H_y|} \cdot \frac{\mathrm{Coh}(E_y, H_y) - \mathrm{Coh}(E_y, H_x) \cdot \mathrm{Coh}(H_x, H_y)}{1 - |\mathrm{Coh}(H_x, H_y)|^2} \tag{16}$$

Here:

$$|E_x| = \langle E_x E_x^* \rangle^{1/2}; \quad |H_x| = \langle H_x H_x^* \rangle^{1/2} \tag{17}$$

i.e. E_x is the mean amplitude of the component E_x in the period band investigated. The coherencies are found from the following formula:

$$\mathrm{Coh}(A, B) = \frac{\langle A B^* \rangle}{|A| \cdot |B|} = \frac{\langle A^r B^r + A^i B^i \rangle + i \langle A^i B^r - A^r B^i \rangle}{\sqrt{\langle A^{r2} + A^{i2} \rangle \langle B^{r2} + B^{i2} \rangle}} \tag{18}$$

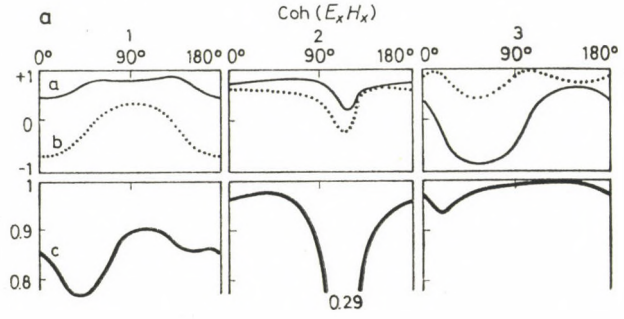
Asterisk denotes complex conjugate, **A** and **B** are arbitrary vectors.

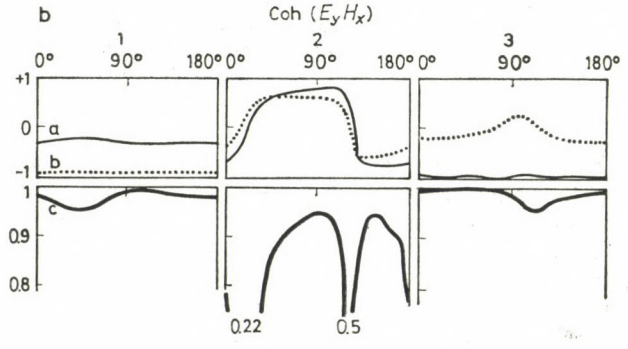
In order to find the final values of the impedance elements, a supplementary computation is made. The equation $\mathbf{H} = \{\mathbf{A}\}\mathbf{E}$ must hold in addition to the equation $\mathbf{E} = \{\mathbf{Z}\}\mathbf{H}$ for the given set of data (here $\{\mathbf{A}\}$ means the admittance tensor). For tensors $\{\mathbf{A}\}$ and $\{\mathbf{Z}\}$, $\{\mathbf{Z}\} \cdot \{\mathbf{A}\} = 1$ is true. As this is not true for the computed elements of the impedance and admittance tensors (the latter being determined with the same method, only by interchanging both types of data, magnetic and electric) an iterative method is used to find the tensors $\{\mathbf{Z}''\}$ and $\{\mathbf{A}'',\}$ being reciprocals of each other: in both steps of the iteration, tensors $\{\mathbf{A}\}$ and $\{\mathbf{Z}\}$ are substituted by $\{\mathbf{A}'\}$ and $\{\mathbf{Z}'\}$ for which:

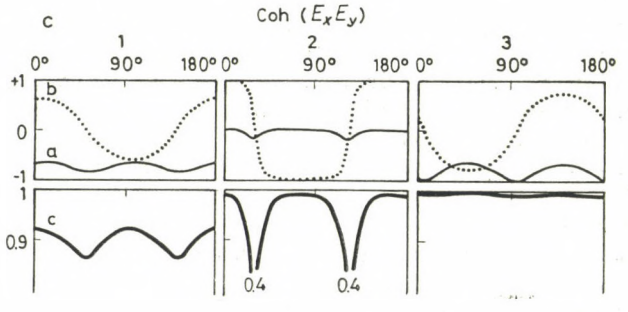
$$\begin{aligned} \{\mathbf{Z}'\} &= 0.5 \cdot (\{\mathbf{Z}\} + \{\mathbf{A}^{-1}\}) \\ \{\mathbf{A}'\} &= 0.5 \cdot (\{\mathbf{A}\} + \{\mathbf{Z}^{-1}\}) \end{aligned} \tag{19}$$

The iteration is stopped if the product of the two tensors approximates the unit tensor with a prescribed error.

We have found that it is possible to compute impedance tensors from records of the lengths 1000–3000 sec for about 8 to 10 periods in conditions


a
Coh ($E_x H_x$)
1
2
3
0°
90°
180°
+1
0
-1
a
b
1
0.9
0.8
c
0.29


b
Coh ($E_y H_x$)
1
2
3
0°
90°
180°
+1
0
-1
a
b
1
0.9
0.8
c
0.22
0.5


c
Coh ($E_x E_y$)
1
2
3
0°
90°
180°
+1
0
-1
b
a
1
0.9
c
0.4
0.4

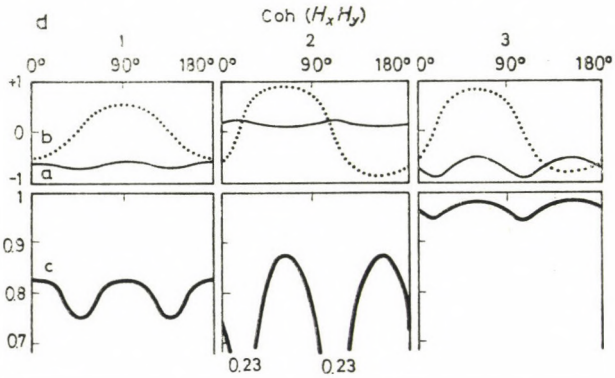


Fig. 1. Changes of Coh (E_x, H_x), Coh (E_y, H_x), Coh (E_x, E_y), Coh (H_x, H_y) with the direction at three stations. Dotted lines represent real components, full lines imaginary components

of the Carpathian Basin. At present the periods to be used are found subjectively from the original analogue record, as data are digitized manually.

The results have shown that the method is very efficient in eliminating incoherent noise. Namely all noises are taken by this procedure as incoherent (Verő, 1972), and they are eliminated as such. Serious problems arise, however, if the absolute value of the coherency of the magnetic components is more than 0.8; if it is more than 0.9, the impedance can be determined only in direction of the polarization of the magnetic field.

If the strong polarization of the electric field appears independently of a polarization of the magnetic field, i.e. it is due to geological causes, the computation of the impedance tensor is not strongly influenced (in spite of the mixture of both tensors during the iteration).

The computations are very illustrative, and easy to check; errors can be either quickly found (such as bad scalings, change of components, erroneous data etc.), or they are eliminated by the program itself.

As illustrative examples, the changes of the coherencies $E_x - H_x, H_x - H_y$, $E_x - E_y, E_x - H_y$ are shown for three stations in function of the direction on Figure 1.

4. The value of the impedances in different directions can be computed by Berdichevsky's formulas (1968, pp. 102–105), whereas the determination of the impedance ellipse is treated by Verő (1973).

5. The method of magnetotelluric data processing described here (and generally all computer methods) results in impedance tensors, or values of the primary and secondary impedances in different directions, respectively. A significant part of theoretical models (see pp. 165–221) yields resistivity curves in different directions. The transformation between them means no problem in a considerable part of cases: if geological structures can be taken as two-dimensional, the values of the secondary impedances equal zero in the direction of the maxima and minima of the primary impedances.

These directions correspond to the E- and H-polarizations, meaning that the component named in the polarization lies in the strike of the structure. The knowledge of the direction of the E-polarization has special importance in elimination of the S-effect (see p. 181).

In more complicated cases — and these are characteristic for areas with strong tectonic deformations — great values of the secondary impedances are characteristic, and the value of the secondary impedances is no more 0 at the extrema of the primary impedances (e.g. Carpathian Basin, the foredeep of the Ural Mts). In such cases resistances can be computed as tensor products from impedance tensors (see e.g. Ádám, 1964). The determination of the directions of the E- and H-polarizations can be made using statistics of important geologic directions (basin axis, fracture zones, dislocations). A certain help can be expected from regional MT-anisotropy, too (Ádám, 1969).

A delicate problem appears in consequence of the change of the direction of structural trends with depth, when e.g. formations of different age are lying discordantly above each other, or when due to orogenic movements fractures of different directions are present. In such cases impedance-diagrams rotate in function of period (penetration depth), and apparent layer indications may appear (see p. 554). The determination of the geological information is in such cases very difficult.

REFERENCES

ÁDÁM, A., 1964. Über die Berechnung der magnetotellurischen (MT) Anisotropie. *Freiberger Forschungshefte C.* **168,** 1–48.

ÁDÁM, A., 1969. Appearance of the electrical inhomogeneity and anisotropy in the results of the complex electrical exploration of the Carpathian Basin. *Acta Geod. Geophys. Mont. Hung.* **4,** 187–197.

ÁDÁM, A., BENCZE, P., 1964. Ein Gerät zur Summierung des absoluten Wertes der Felderänderungen (Totalvariationen) bei tellurischen und magnetotellurischen Messungen. *Bergakademie* **1,** 22–25.

BERDICHEVSKY, M. N., 1960. Principles of magnetotelluric profiling (in Russian). *Prikl. Geofiz.* **28,** 70—91.

BERDICHEVSKY, M. N., 1968. Electric Prospecting with the Method of Magnetotelluric Profiling (in Russian). Nedra, Moscow.

KUNETZ, G., 1957. Anwendung statistischer Eigenschaften der Erdströme in der praktischen Geophysik. *Freiberger Forschungshefte C.* **32,** 5–19.

STEINER, F., 1965. The analysis of Bouguer-anomaly maps (in Hungarian). Dissertation, Miskolc University for Heavy Industries.

SWIFT, C. M., 1967. A magnetotelluric investigation of an electrical conductivity anomaly in the Southwestern United States. Ph. D. Thesis, MIT.

VERŐ, J., 1960. Die Bestimmung der tellurischen Stationsellipsen. *Gerlands Beitr. Z. Geophys.* **69,** 257–268.

VERŐ, J., 1972. On the determination of the magnetotelluric impedance tensor. *Acta Geod. Geophys. Mont. Hung.* **7,** 333–351.

VERŐ, J., 1973. Determination of MT-impedance ellipses from the computed components of impedance tensors. *Acta Geod. Geophys. Mont. Hung.* **8,** 193–196.

THE ROLE OF THE VERTICAL PULSATIONS OF THE MAGNETIC FIELD IN MAGNETOTELLURIC MEASUREMENTS

E. TAKÁCS

INTRODUCTION

On the surface of the earth, two electric and magnetic horizontal components (E_x, E_y, H_x, H_y) and one vertical magnetic component (H_z) of the electromagnetic pulsations can be measured. The vertical electric component cannot be measured directly on the surface, as the specific resistivity of the air is practically infinite, and so the current density is very small perpendicularly to the surface.

At magnetotelluric measurements for the detection of structure hitherto only the horizontal components have been taken into consideration and only some hints are found for the component H_z. Outstanding early experiments were carried out in Hungary (Annau et al., 1954).

In the case of horizontally inhomogeneous structures some problems arise in the geological interpretation of the magnetotelluric data which is needed for the knowledge of both local values and regional variations of the greatest possible number of electromagnetic parameters. So our efforts were directed towards a possible use of the component H_z in the interpretation (Takács, 1964).

Following field experiments in 1962, experiments were carried out on behalf of the Seismic Research Department of the Hungarian Oil and Gas Trust in the years 1967—68 with the component H_z. The results of these experiments are summarized in this paper.

The vertical components of longer period variations — bays, S_q — have been treated several times and some characteristic anomalies have been found. These anomalies are in connection with horizontal resistivity inhomogeneities in the earth's crust in the form of relatively conductive zones. Similar anomalies are found along the shores of the oceans, where the rise of the seafloor causes increase of the current-density. The geological aspects of the subject are treated fundamentally by Wiese (1963), who investigated the relationship of the vertical and horizontal components of geomagnetic bays along regional profiles also in Hungary. It is, however, probable that in his interpretation he over-emphasizes the role of conducting blocks bordered by vertical discontinuities, because many of the anomalies can be interpreted in terms of the variations of sediment-thickness (Porstendorfer, E. and Porstendorfer, G. 1965; Ádám, 1968).

Berdichevsky (1968), in connection with the pulsation has already treated the so-called magnetic parameter similarly expressing the relationship of H_z to the horizontal component. It makes possible the determination of the strike and of the nature of horizontal inhomogeneities. Its practical use is, however, unknown to us.

PHYSICAL AND GEOLOGICAL CAUSES OF THE VERTICAL COMPONENT

The primary natural electromagnetic field can be taken as a plane wave parallel with the surface, accordingly no H_z component can be found above horizontally stratified media.

According to Maxwell's second law, the vertical magnetic induction of internal origin is related to the vertical component of the curl of the electrical field:

$$\frac{\partial E_y}{\partial x} - \frac{\partial E_x}{\partial y} = \frac{\partial B_z}{\partial t} \tag{1}$$

This can be written, assuming $\mu = 1$, thus substituting the induction by magnetic forces as:

$$\frac{\partial E_y}{\partial x} - \frac{\partial E_x}{\partial y} = \frac{\partial H_z}{\partial t} \tag{2}$$

The structures can be regarded as two-dimensional in most cases. For the following discussion only this case will be considered. The x-axis lies in the direction of the dip, the y-axis in that of the strike, so component E_x does not vary along the strike of the structure and:

$$\frac{\partial E_y}{\partial x} = \frac{\partial H_z}{\partial t} \tag{3}$$

For periodic functions of the form $H_z = H_z^0 \cdot \exp i\omega t$, the right-hand-side of Eq. (3) can be derived:

$$\frac{\partial E_y}{\partial x} = i\omega H_z^0 \mathrm{e}^{i\omega t} \tag{4}$$

also

$$H_z = \frac{1}{i\omega} \frac{\partial E_y}{\partial x} \tag{5}$$

According to this, the vertical magnetic component depends on the change of the electrical component in the strike-direction along the dip, thus reflecting the variation of the mean specific resistivity down to the penetration depth of the wave. The electric field-vector of an arbitrary polarized plane wave can always be resolved into two independent components in the directions of the strike and dip, respectively (E and H polarization). The vertical magnetic component will be produced from these only by that which is in the direction of the strike, if its amount considerably changes along the dip. In case of an electric field exclusively in the direction of the dip, no vertical magnetic component of internal origin can appear.

Contrary to the above-mentioned investigations the horizontal impedance (Z_h) — i.e. the ratio of the amplitudes of the electrical and the corresponding vertical magnetic components — was used as a parameter which depends on the direction of the electric field (α). This parameter indicates with

greater relative values a change in structural conditions at the periods of pulsations (i.e. at periods which are interesting for the exploration of geological structures) than the ratio of the amplitudes of the horizontal and vertical magnetic components, because the direction and magnitude of the electric field are much more influenced by horizontal structural inhomogeneities than the parameters of the magnetic field.

The components corresponding to the E and H polarizations of an electric variation vector, along the axis x' in an angle α to the direction of the dip are:

$$E_x^0 = E_{x'}^0 \cos\alpha \quad \text{and} \quad E_y^0 = E_{y'}^0 \sin\alpha \tag{6}$$

where E_x^0, $E_{x'}^0$ and E_y^0 are amplitudes of the projections of the field variations in the directions x, x' and y. These, after normalizing them by the amplitude of H_z give the components in the direction of the dip and strike of our parameter, from which:

$$\frac{|E^0|}{H_z^0}(\alpha) = Z_h(\alpha) = \frac{|\sqrt{(E_x^0)^2 + (E_y^0)^2}|}{H_z^0} \tag{7}$$

Observing that if $\alpha = 0$, then $Z_h(\alpha) = \infty$ — as $E_y = 0$ and so $H_z = 0$ — Eq. (7) corresponds to a pair of straight lines. The values of $Z_h(\alpha)$ drawn in the direction of the electric vector accordingly give a pair of straight lines on both sides of the origin which join the positive and negative values of the former parameter, the senses of which are determined by the sense of

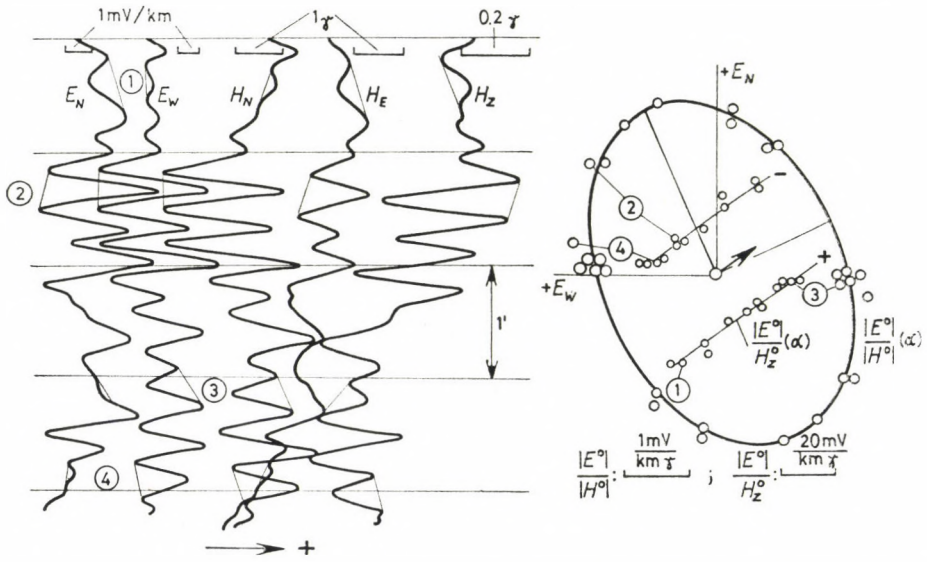


Fig. 1. Part of a record, and the corresponding polar diagrams of the vertical impedance from the station Oltárc-1

the variation H_z. These straight lines are perpendicular to the strike of geological structures in the depth range of the wave penetration.

Instead of this pair of straight lines a vector — $Z_{h\min}$ — is represented on the maps in a direction parallel with them so that the straight line of the positive values should lie to the right of it and the magnitude should be equal to their distances from the origo.

Figure 1 shows a part of the record in the vicinity of the borehole Oltárc-1 and the results of its processing. The pair of straight lines and the impedance ellipse are constructed together.

Geological informations can be obtained from the magnitude of the vector $Z_{h\min}$, from its direction and position with respect to the axis of the impedance ellipse.

DETERMINATION OF THE DIRECTION OF DIP

Above two-dimensional structures the direction of the greatest resistivity change, i.e. the direction of the dip can unambiguously be determined with the aid of component H_z.

In that case the corresponding variation vectors E and H are perpendicular for electrical vectors polarized in the direction of dip (x) and strike (y), respectively, and their values can be expressed by the input impedances:

$$E_x = Z_{xy} H_y \quad \text{and} \quad E_y = Z_{yx} H_x \tag{8}$$

From Eq. (8) the impedance corresponding to the electric vector at an angle α to the dip can be expressed as:

$$\frac{|E_0|}{|H_0|}(\alpha) = Z_v(\alpha) = \frac{Z_{xy} Z_{yx}}{\sqrt{Z_{xy}^2 \sin^2 \alpha + Z_{yx}^2 \cos^2 \alpha}} \tag{9}$$

Equation (9) is the equation of an ellipse with the main axes in the direction of the dip and strike, their magnitudes equalling the impedances Z_{xy} and Z_{yx}, respectively.

The last statement was verified by measurements. However, the major axis can lie, depending on the type of the inhomogeneity (buried anticline, outcropping monocline, conducting zones, etc.) both in dip and strike directions (Takács, 1969). The uncertainty of the orientation of the ellipse can be removed by the component H_z. The main importance of this fact is not only the possibility of unambiguous determination of the direction of dip which is essential for geological interpretation and for plotting further measurements, but — what is perhaps even more significant — that the information content of the main impedances can only be judged in case of elongated ellipses, if their position with respect to the structure is known.

It was shown that the vector representing $Z_{h\min}$ always lies in the direction of the greatest resistivity change, i.e. in a direction perpendicular to the axis of inhomogeneity. From the possible two values of the dip direction the right one — i.e. the direction of the rise of the structure or that of the increase of the current density — can be picked out with the aid of the

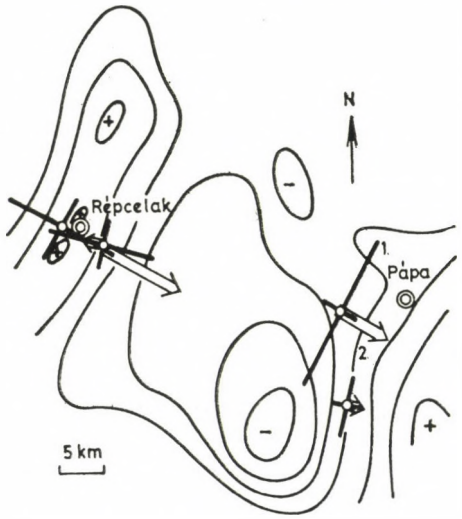


Fig. 2. Axes of impedance ellipses and vectors of the minimal horizontal impedance with Bouguer isogals in the area of the Mihályi crystalline ridge and the NW foreland of Bakony Mts

sense of $Z_h(\alpha)$, depending on its turn on H_z, and this direction. According to Eq. (5) the sense of H_z with respect to E_y depends on the character of the variations of E_y along the dip. If care is taken for the constant orientation of the electric measurement lines and for that of the magnetometers, as well as for the right polarity of the galvanometers, one obtains over opposite dipping slopes of a two-dimensional structure H_z variations corresponding to, and opposite to the electrical field variations projected into the strike. Above known structures, the measuring apparatus can be adjusted for the determination of the dip.

Figure 2 shows some results from the SE wing of the Mihályi ridge and from the NW foreland of Bakony Mts together with isogals of Bouguer-anomalies. In spite of the direction of the major axes of the impedance ellipses along the dip (Mihályi structure), then along the strike (Bakony foreland), the vector $Z_{h\,\min}$ reliably shows the correct dip of the basement.

INDICATION OF THE TYPE OF THE STRUCTURE AND OF A CHANGE OF THE MAIN HORIZON

It is clear from the above discussion that a common analysis of the impedance ellipses and the quantity $Z_h(\alpha)$ allows certain conclusions to be drawn on the geological model of the investigated area which bear a greater importance than the determination of the dip.

In the maximum zone of buried anticlines of the very resistant basement, the vector $Z_{h\,\min}$ lies parallel to the major axis of the impedance ellipse which is elongated in function of the depth.

An orientation parallel with the minor axis can be produced by:

1. outcrops of the very resistant basement or those of intermediate layers with great resistivity in the vicinity of the station;

2. zones of the basement with low resistivity;
3. deflecting effect of a buried anticline with great specific resistivity above the wings of the structure.

The actual cause can be determined with the aid of the relative ratio of the magnetotelluric parameters as well as by their areal variations. The possibility is treated in more details in the paper of Csókás and Takács (1969).

In what follows we shall try to outline the effects arising from the superposition of several two-dimensional structures or when the structure cannot be considered as two-dimensional. In that case no coordinate system can be found where the simple relations according to Eq. (8) between electrical and magnetic components should hold. In that case one has:

$$E_x = Z_{xx}H_x + Z_{xy}H_y \tag{10}$$

$$E_y = Z_{yx}H_x + Z_{yy}H_y \tag{11}$$

where Z_{xy} and Z_{yx} mean the main, Z_{xx} and Z_{yy} the complementary (secondary) impedances. The polar diagram of the impedance can be written as

$$\frac{|E^\circ|}{|H^\circ|}(\alpha) = Z_y(\alpha) = \tag{12}$$

$$= \frac{Z_{xx}Z_{yy} - Z_{xy}Z_{yx}}{\sqrt{(Z_{yy}^2 + Z_{yx}^2)\cos^2\alpha - (Z_{xy}Z_{yy} + Z_{xx}Z_{yx})\sin 2\alpha + (Z_{xx}^2 + Z_{xy}^2)\sin^2\alpha}}$$

Equation (12) is the equation of an ellipse with the main axes:

$$\frac{A^2}{B^2} = \frac{(Z_{xx}Z_{yy} - Z_{yx}Z_{xy})}{(Z_{xx}^2 + Z_{xy}^2) + (Z_{xy}Z_{yy} + Z_{xx}Z_{yx})\cot\left(\varphi + \begin{matrix}0^\circ\\90^\circ\end{matrix}\right)} \tag{13}$$

and the angle between the major axis and x-axis:

$$\varphi = \frac{1}{2}\arctan\frac{(Z_{yy}^2 + Z_{yx}^2) - (Z_{xx}^2 + Z_{xy}^2)}{2(Z_{xy}Z_{yy} + Z_{xx}Z_{yx})} \tag{14}$$

The vertical magnetic component is in a more complicated connection with the electric components:

$$H_z = Z_{zx}E_x + Z_{xy}E_y \tag{15}$$

From this the polar diagram of $Z_h(\alpha)$ can be written as:

$$\frac{|E^\circ|}{|H_z^\circ|}(\alpha) = Z_h(\alpha) = \frac{1}{\sqrt{Z_{zx}^2\cos^2\alpha + Z_{zx}Z_{zy}\sin 2\alpha + Z_{zy}^2\sin^2\alpha}} \tag{16}$$

representing an ellipse with the main axes:

$$\frac{a^2}{b^2} = \frac{1}{Z_{zy}^2 + Z_{zx}Z_{zy}\cot\left(\varphi + \begin{matrix}0^\circ\\90^\circ\end{matrix}\right)} \tag{17}$$

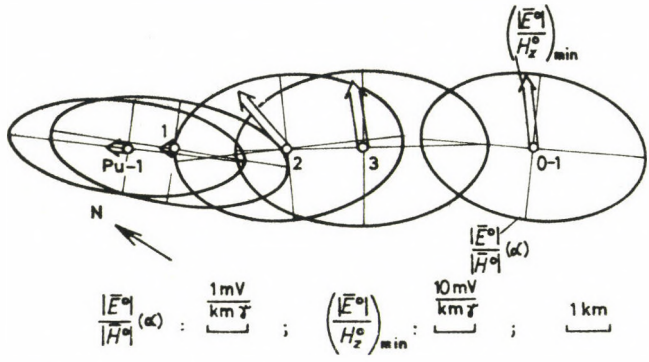


Fig. 3. Impedance ellipses and vectors of the minimum horizontal impedance in the area of the Hahót crystalline ridge

and having an angle φ with the x-axis:

$$\varphi + \begin{matrix} 0^\circ \\ 90^\circ \end{matrix} = \frac{1}{2} \arctan \frac{Z_{zx}^2 - Z_{zy}^2}{Z_{zx} Z_{zy}} \tag{18}$$

If the polar diagram of the quantity $Z_h(\alpha)$ turns into an ellipse with its main axis in a direction deviating from those of the impedance ellipse, the structure cannot be interpreted as a two-dimensional one. The practical importance of this fact is that a magnetotelluric measurement extended by component H_z indicates the resistant intermediate layers with a dip different from that of the basement, respectively changes of the main horizon.

An instructive example is the profile between the boreholes Pusztamagyaród-1 and Oltárc-1 in the area of the paleozoic crystalline ridge of Hahót (Fig. 3). The borehole Pusztamagyaród-1 lies in the strike of the crystalline train along the Lake Balaton and reached in a depth of 1992 m crystalline rocks, on the other hand Oltárc-1 stopped at a depth of 3001 m in Upper-Miocene sediments.

The turning of the vector $Z_{h\min}$ beginning at station 2 and a simultaneous increase in the length of the minor axis of the impedance ellipse in stations $2 - O_1$ of the profile hint at the effect of the crystalline ridge and in addition to it — if it lies within the penetration depth — at other horizontal inhomogeneities in the direction NE-SW. The turning of the vector $Z_{h\min}$ at station 2 can be explained by a superposition of the components H_z coming from the paleozoic surface and from a new horizon appearing here. This results in a maximum of H_z for a polarization between the major and minor axes of the impedance ellipse. Further on, along the profile the paleozoic surface deepens, accordingly the amplitude of H_z diminishes from this layer and the new layer obtains the role of the main horizon.

If the geological structure consists of several structural elements with similar or nearly perpendicular axes, the orientation of the main axis of the impedance ellipse remains identical with the structural axis. In case of

identical structural axes, the vector $Z_{h\min}$ lies in the direction of the dip, the ratio of the axes of the impedance ellipses and the lengh of the vector $Z_{h\min}$, however, differ from those in case of only two layers.

The measurement of the component H_z gives a means to decide about the cause of the elongation of the impedance ellipses. The distortion of the polar diagram of the input impedance to an ellipse can be due not only to horizontal inhomogeneities, but also to the anisotropy of the sediments. Anisotropy, however, does not cause any H_z component above a horizontal resistant basement, as the electric component suffers no spatial variation. The examination of the ratio between the elongation of the ellipse and the length of $Z_{h\min}$ gives surplus information in this respect, too.

INVESTIGATION OF THE SOURCE EFFECT

The magnetic vertical component can be also used for the examination of the so-called source effect. The changing dimensions and distance of the source of pulsations might influence the impedance values measured on the surface, i.e. they do not depend on the geological structure alone. It should be decided whether the assumption of the plane waves holds in nature, as it was assumed in the derivation of the basic equation of the magnetotelluric survey.

Investigations up to now have shown that these effects can appear above sedimental basins in case of sources with very restricted dimension, — say some 100 km-s. Above shallow basins, however, it must be taken into consideration, especially in the long period part of the frequency sounding curves (Takács, 1964).

The investigations published by Srivastava et al (1963), and by Ádám et al. (1965), based on correlation of records from stations at distances of several hundred km-s, aim to clarify the theoretical side of the question — i.e. to what degree is it allowed to substitute the electromagnetic field of the earth by a plane wave. In practice the interpreter needs some means to decide whether the impedance value derived from a single variation or from a group of variations is affected by source effects or not. This decision must be taken into account mainly in the exploration of the crust.

The basic idea of such a test could be the fact that in case of a vertically incident plane wave H_z, purely of internal origin, and the polar diagram of $Z_h(\alpha)$ can be averaged into a pair of straight lines or into an elongated ellipse. Diminishing dimensions of the source change the wave front to a curved surface and for this reason a H_z component of external origin will appear in the proximity of the source. The polar-diagrams of $Z_h(\alpha)$ change in time or are accidental. So deviations from the plane wave form appear as deviations from the average straight line of $Z_h(\alpha)$, a change of the sense, or sometimes as a change of the direction of the average straight line.

A further check is possible, if in addition to the straight lines $Z_h(\alpha)$ the straight lines $\frac{|H^0|}{|H_z|}(\alpha)$ are constructed, too. With the aid of both it can be unambiguously decided, whether an external part in H_z is present or not.

In this case the actual value lies farther off from both straight lines. Our measurements have shown no considerable source effect, as the polar diagrams of $Z_h(\alpha)$ can be constructed relatively easily and they suffer no time variations. It is, however, clear that the different intervals of the day are different from the point of view of the source effect. In some parts of the day the straight lines of $Z_h(\alpha)$ are very definite, in other cases significant deviations occur from the average at the same station. The sense of the component H_z differs, however, only very seldom from the mean corresponding to the actual polarization. Accordingly, rough source effects are not to be feared.

THE ROLE OF THE COMPONENT H_z IN THE DETERMINATION OF THE IMPEDANCE ELLIPSES

The knowledge of the component H_z helps to solve some problems of processing, too. In case of nearly linearly polarized variations it may occur that only one axis of the impedance ellipse can be determined. In some cases the admittance ellipse does not provide results either, as although the component H seldom remains linearly polarized for a longer time, it may occur that in a shorter record the direction of the component H does not change. In such cases the significantly greater dependence on polarization of $Z_h(\alpha)$ allows for a determination of the dip, if the structure is two-dimensional.

The angle between the electrical and magnetic components can be written as (Takács, 1964)

$$\tan(\varphi_H - \varphi_E) = \frac{\tan\varphi_H - \tan\varphi_E}{1 + \frac{Z_{yx}}{Z_{xy}}} \tag{19}$$

where φ_H and φ_E denote the angle of the magnetic and electric vectors, respectively, with the direction of dip, Z_{xy} and Z_{yx} are the components of the impedance in the direction of the dip and strike, which means the lengths of the main axes of the ellipse. As φ_H and φ_E can be calculated in the knowledge of the direction of the dip, the ratio of the axes can be determined, too.

*

Summarizing, it can be stated that in telluric and magnetotelluric measurements, especially in their first phase or in some special cases the measurement of the component H_z is absolutely justified. With its aid the following facts can be given:

— the direction of the dip of the basement with great specific resistivity;
— the type of the geological model needed for the interpretation;
— the outlines of changes in the geological structure or in the main horizon.

Its anomalous values hint at the effect of the source. In case of extremely polarized variations, it facilitates the construction of the impedance ellipse.

To complete these investigations theoretical calculations and model experiments are needed for different types of structures, taking frequency dependency also into consideraton.

REFERENCES

ANNAU, E., ERKEL, A., SZABADVÁRY, L., 1954. Connections between rapid variations of the geomagnetic field and telluric currents (in Hungarian). *Bányászati L.* **9,** 544–549.

ÁDÁM, A., 1968. Informations of electromagnetic measurements in Hungary (in Hungarian). *Geofizikai Közlemények* **17,** 23–38.

ÁDÁM, A., VERŐ, J., WALLNER, Á., 1965. Areal distribution of the pulsations of the terrestrial electromagnetic field (in Hungarian). *Geofizikai Közlemények* **14,** 25–66.

BERDICHEVSKY, M. N., 1968. Electrical Prospecting with the Method of Magnetotelluric Profiling (in Russian). Nedra, Moscow, 140–153.

CSÓKÁS, J., TAKÁCS, E., 1969. Report on investigations to improve the magnetotelluric method (Manuscript in Hungarian).

PORSTENDORFER, E., PORSTENDORFER, G., 1965. Modelle zur Deutung des anomalen Verhaltens geomagnetischer Variationen über großen zylindrischen Sedimentbecken. *Acta Techn. Hung.* **52,** 351–360.

SRIVASTAVA, S. P., DOUGLASS, J. L., WARD, S. H., 1963. The application of the magnetotelluric and telluric methods in Central Alberta. *Geophysics* **28,** 426–446.

TAKÁCS, E., 1964. Development of magnetotelluric apparatures and methods and their use in geophysical prospecting (in Hungarian). Dissertation.

TAKÁCS, E., 1969. The orientation of the magnetotelluric impedance ellipses. *Acta Geod. Geophys. Mont. Hung.* **4,** 415–423.

WIESE, H., 1963. Geomagnetische Tiefentellurik. Teil III. *Geofis. Pura e Appl.* **56,** 101–114.

DISTRIBUTION OF CURRENT DENSITY AND HOMOGENEITY OF THE SUBSTORM FIELD

A. GRAFE

INTRODUCTION

In geomagnetic deep sounding the period range of the so-called bay disturbances plays an important part. It is a well-known fact that it was the study of the local distribution of these bay disturbances which led to the discovery of locally-existing induction currents in the earth's crust, these being produced by the outer field of these bay disturbances and the lateral inhomogeneity of conductivity in the earth's crust. The methods for calculating the parameters of these induction currents generally assume an ideally homogeneous outer horizontal variation field. For medium latitudes, this is justified in most cases. It is, however, always essential that the structure of the outer variation field should be known. For this reason, local and time variations of the bay disturbance field or, to be more precise, of the "polar magnetic substorm" field will be discussed in this chapter. To begin with, we explain what is meant by the "magnetospheric substorm".

A magnetic substorm always occurs when the solar wind has reached a certain degree of activity and when certain conditions are present in the magnetosphere, these conditions still being to a large extent unknown at the present time. The interaction of the solar wind with the earth's magnetosphere leads to explosive processes within the magnetosphere which, when taken as a whole, can be called a "magnetospheric substorm". During these explosive processes, magnetic field energy is generally transformed into kinetic particle energy, i.e. there is an acceleration of the charged particles in the magnetosphere. This process of transformation is known as "magnetic field merging" or "annihilation of magnetic field lines". The explosive processes predominantly occur on the night side of the magnetosphere, i.e. in the magnetospheric tail. But explosive processes have been observed on the day side as well. These include in particular those processes which occur on the day side in high latitudes (between 70° and 80° geomagnetic latitude) in the so called "*Polar cusp*" and lead to midday polar aurora. Since these processes are also linked with the activity of the solar wind, it is not entirely clear whether the term "magnetospheric substorm" should be used for only the explosive processes on the night side of the earth or whether those occurring on the day side can also be covered by it. The magnetospheric substorm can occur either individually as a "single substorm" or as a series of several more or less strong substorms. The latter is called a magnetospheric storm, the sum of all magnetospheric substorms constitutes only a part of the magnetospheric storm, but this part essentially determines the main phase of the storm. During the initial phase of the storm the plasma pressure from the sun has the main effect, it produces

compression of the magnetosphere on the day side. Akasofu (1968) has expressed this with the following simple relation:

$$\text{Magnetospheric storm} = \text{Compression} + \Sigma\,\text{Magnetospheric substorm}$$

It has recently become apparent that the parameter stimulating the substorm is not the velocity of the solar plasma but the interplanetary magnetic field. The substorms show a close correlation with the southward component of the interplanetary magnetic field. The attendant phenomena of the magnetospheric substorm, which occur in the polar ionosphere, are covered by the term "polar substorm". This embraces a large number of individual phenomena. During a magnetospheric substorm there is an in crease of particle precipitation, particularly in the auroral zones areas. This results in areas in the ionosphere which have increased ionization, high conductivities and heavy electrical currents. Aurorae occur more frequently and an "auroral substorm" develops. The aurorae, which also exist at quieter times, first begin to become more intense at midnight and as the substorm progresses the intensification spreads out in all directions. The changes in the ionospheric parameters during a magnetospheric substorm are covered by the term "ionospheric substorm". The changes in the ionization in the lower ionosphere (100 km) are particularly great. As a result of increased cunductivities in the areas of the auroral zones during a substorm and where there is an electrical field, in particular on the night side of the earth, a highly concentrated westward current is formed. This current is termed an electrojet. However, on the afternoon side there also is an electrojet, and this one flows eastwards. These electrical currents cause much disturbance of the magnetic field on the earth's surface, these being called "polar magnetic substorm". This manifestation of the magnetospheric substorm was the first known. To describe the elementary magnetic disturbances in the auroral zone, Chapman introduced the term "polar magnetic substorm".

During a magnetospheric substorm, however, disturbances also occur in many other fields of observation. For example, through the rapid movement of active aurorae ultrasonic waves are produced which can be received on the earth's surface. This is an "infrasonic substorm". The term "micropulsation substorm" refers to the additionally occurring geomagnetic micropulsations during a magnetic substorm. The "VLF substorm" is connected with an increased emission of waves of very low frequency. It should also be mentioned that during a magnetospheric substorm an increased emission of X-rays develops. The electrons precipitating during a magnetospheric substorm emit X-rays, if they are accelerated by collisions with uncharged particles. This is known as an "X-ray substorm".

In what follows we will be dealing exclusively with the polar magnetic substorm, which as we know is closely connected with the magnetic variations known as bay disturbances. We will refer back to the known representations of the substorm field in the form of equivalent ionospheric current systems, in order to obtain an answer as to the homogeneity of this outer field of current.

1. THE MAGNETIC FIELD OF THE POLAR MAGNETIC SUBSTORM

A. OBSERVATION OF THE MAGNETIC FIELD OF THE POLAR MAGNETIC SUBSTORM

During a magnetospheric substorm, characteristic variations appear in the magnetic variometer recordings on the earth's surface. These have a different appearance for different latitudes. In low and medium latitudes we know these as "bay disturbances". It has long been known (Steiner, 1921) that the magnetic bays in medium latitudes show a clear *l*ocal-time dependence. Accordingly, particularly at night and in the morning positive bay disturbances occur in the horizontal component and in the afternoon and evening hours there are only negative bay disturbances. Statistics by Wiese (1951) on bay disturbances in medium latitudes show that these disturbances have their maximum frequency in the winter. The greatest diurnal variation of bay frequency is also in the winter. The disturbances of the magnetic field in the auroral zone during a magnetospheric substorm look more complicated. Figure 1 shows a typical "single polar magnetic substorm". This too exhibits a clear local-time dependence. Negative effects occur in the night and morning hours and positive ones in the afternoon and evening. Occasionally these variations in auroral latitudes are also called bay disturbances. From the point of view of definitions there is no uniform opinion as to whether "polar magnetic substorm" and "bay disturbance" mean one and the same process. It is very likely that the event which occurs in auroral latitudes as a polar magnetic substorm only takes the form of a bay disturbance in medium and low latitudes. Rostoker (1969), however, thinks differently. His view is that a bay disturbance represents a variation with a period of 1 to 6 hours, occurring as a deviation from a level which is largely undisturbed magnetically. By comparison, polar magnetic substorms are disturbances which are merely superimposed on a bay disturbance and which have a period of less than one hour. However, it is quite possible to see it the other way. In what follows we will use the expression "bay disturbance" for the effects of the magnetospheric substorm in medium and low latitudes, and for those in auroral latitudes we will use the term "polar magnetic substorm". The intensity of the bay disturbances is never more than a fraction of that of the polar magnetic substorm. As Figure 2 shows, for a certain medium latitude no bay disturbance occurs in connection with

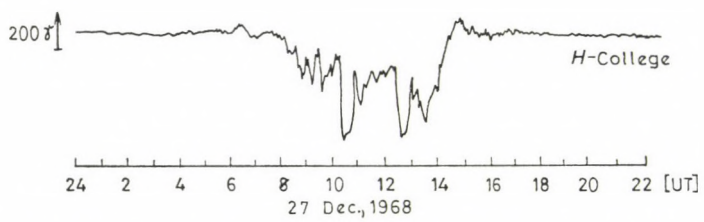


Fig. 1. Example of a substorm in the magnetic horizontal component by College (LT = UT – 10h)

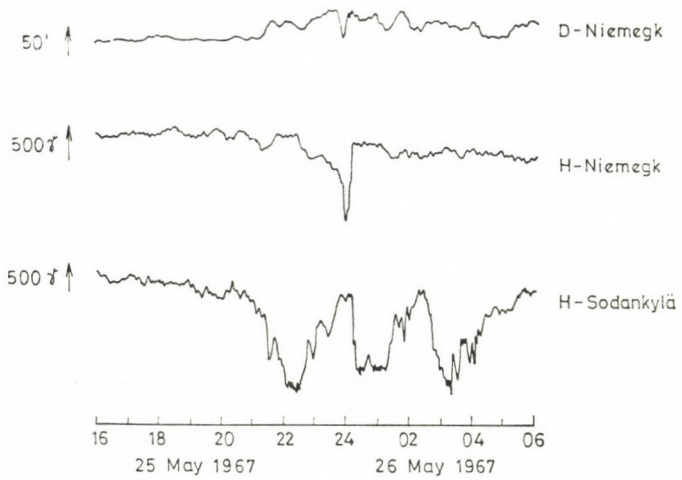


Fig. 2. Examples of substorms in middle and auroral zone latitudes

a polar magnetic substorm. In Sokadnkylä on 25/26 May 1967 three powerful substorms occured in succession. But only for the second substorm was there also in medium latitudes, in Niemegk, a powerful disturbance. No bay disturbances were observed for the other two substorms.

It is not possible to determine precisely the exact beginning of a substorm

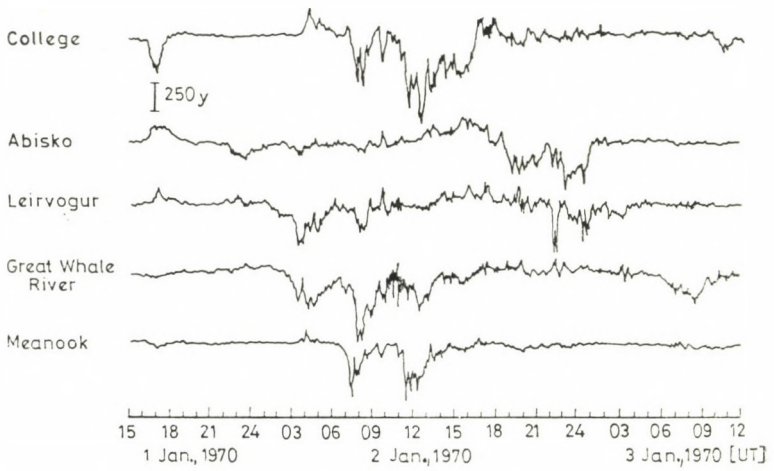


Fig. 3. Recording of the magnetic horizontal component at several observatories in the auroral zone. Differences between LT and UT are in Abisko + 1 h, in Leirvogur – 1 h, in Great Whale – 5 h, in Meanook – 8 h

on the basis of the recordings made at one station. Figure 3 shows recording of a substorm made at several observatories in the auroral zone. It can be seen that the substorm does not begin at the same time at all the different places. The substorm always begins first at that station which is nearest to the midnight meridian at the start of the magnetospheric substorm. The stations (starting with Abisko) clearly come into the substorm one by one due to the rotation of the earth. The substorm variations are not so clearly marked at observing stations in the polar cap. Sometimes the effects of the substorm seem to add hardly anything at all to the disturbances caused by other means in the polar cap. Figure 4 shows an example. At the top of this figure a case is shown where a tangible effect occurs in the polar cap at the same time as a substorm at auroral latitudes. For the substorm shown below there is no substorm effect in the polar cap.

The chronological development of a magnetospheric substorm is characterized by three phases, the "growth phase" (McPherron, 1970), the "expansive phase" and the "decay phase". These three phases are to be expected with the polar magnetic substorm correspondingly. However, the growth phase is seldom clearly defined in the magnetic ground data, and Akasofu and Snyder (1972) consider it impossible to determine the growth phase using these data. The expansive phase begins with the emergence of a strong field strenght gradient and ends as a rule when the extreme field strength value is reached. During this time there is a strong formation in the ionosphere of a westward electrojet in the night and morning hours. This has, on average,

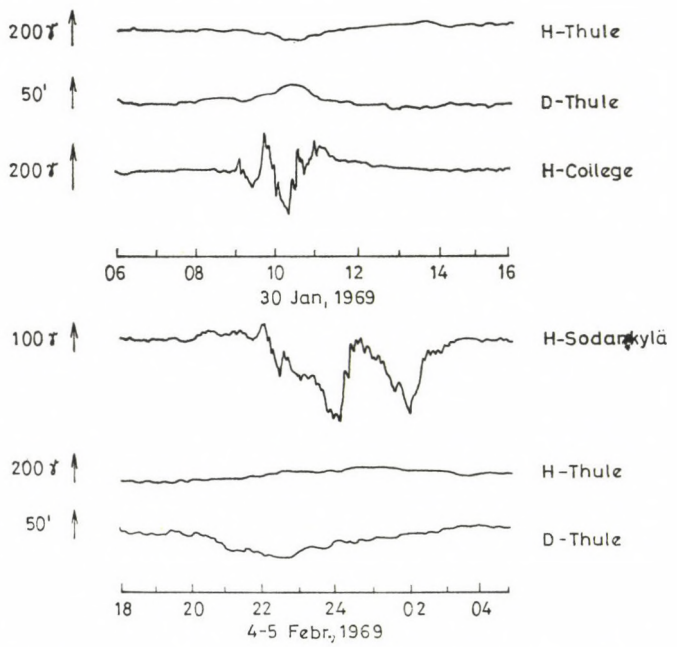


Fig. 4. Example of a substorm with and without effect in the polar cap

a latitudinal dimension of about 5°. The longitudinal dimension can exceed 90°. The total current strength of these electrojets can attain values $> 10^6$ A, whilst the current density can be subjected to considerable fluctuation from case to case. The decay phase, clearly recognizable for a polar magnetic substorm, begins after the extreme value has been reached and is characterized by a slow approximation of the field strength value to the level before the substorm began. The decay phase can, however, be interrupted by the reappearence of substorm disturbances.

The processes which take place in the ionosphere and magnetosphere during the individual phases of a substorm are at present only known roughly and will in the future be the subject of thorough studies.

B. ANALYSIS OF THE MAGNETIC FIELD OF THE POLAR MAGNETIC SUBSTORM

B. 1. Equivalent ionospheric current systems

In this chapter we are primarily interested in the local distribution of the magnetic substorm field, but also in the change produced in this local distribution in the course of the substorm. Analysis of the substorm field has in the past been carried out essentially in two different ways. The first is the derivation of so-called equivalent ionospheric current systems and the second consists of the representation of the electrojet variations in declination, horizontal intensity and vertical intensity along a geomagnetic meridian. The drawback of the horizontal equivalent current systems as compared with the meridian profile representation method is that these systems give no information on the vertical component. Besides, they are indeed nothing more, than "equivalent current systems" and they certainly have nothing to do with reality. It is much more reasonable to assume that the magnetic substorm disturbances observed at the earth's surface are produced by a three-dimensional ionospheric-magnetospheric current system. Three-dimensional substorm current systems have been made known in publications by several authors (see e.g. Birkeland, 1913; Kirkpatrick, 1952; Atkinson, 1967; Akasofu and Meng, 1969; Meng and Akasofu, 1969; Kamide and Fukushima, 1972; Crooker and McPherron, 1972).

Equivalent ionospheric current systems are represented in a horizontal plane without taking into account the sphericity of the earth. The basic idea is as follows: for certain times during the polar magnetic substorm, the horizontal disturbance vector at a particular station is calculated and this magnetic disturbance vector is then collated perpendicularly above the station in the ionosphere (at a height of about 120 km) with a current vector, the direction of which is found from the well-known right-hand rule. The choice of reference level for deriving the magnetic disturbance vector is particularly problematic and most certainly this is one of the reasons for the different equivalent current systems obtained. A distinction is drawn between statistically equivalent current systems and instantaneous equivalent current systems. Statistically equivalent current systems have the advantage that the determination of average values for a large number of polar magnetic

substorms (or bay disturbances) means that the drawback of having an insufficient number of observing stations in high latitudes is cancelled out. However, statistically equivalent current systems do not reflect the wide variety of equivalent current systems, which exist for the different substorms. On the other hand, instantaneous equivalent current systems are obtained by using an insufficient amount of observation data, so these current systems always have a somewhat arbitrary nature. Accordingly, it cannot be expected that they give a realistic picture of the situation in every detail. Finally, the distribution of horizontal magnetic disturbance vectors can be represented by a large number of possible current systems. It is very likely that the real current system of the polar magnetic substorm is a three-dimensional ionospheric-magnetospheric current system. The results of measurements using space probes make that clear. It cannot, however, be ascertained purely on the basis of data obtained on the ground whether the current system, which is the source of the polar magnetic substorm, is two- or three-dimensional (Fukushima, 1969).

A simple quantitative derivation of the electric current density i from the strength of the magnetic disturbance vector ΔX can be found in Chapman and Bartels (1940). According to this

$$i = \frac{10^{-9} f \Delta X}{2\pi} \, [\mathrm{Am}^{-1}]$$

The observed quantity ΔX [Weber cm^{-2}][1] consists of the horizontal

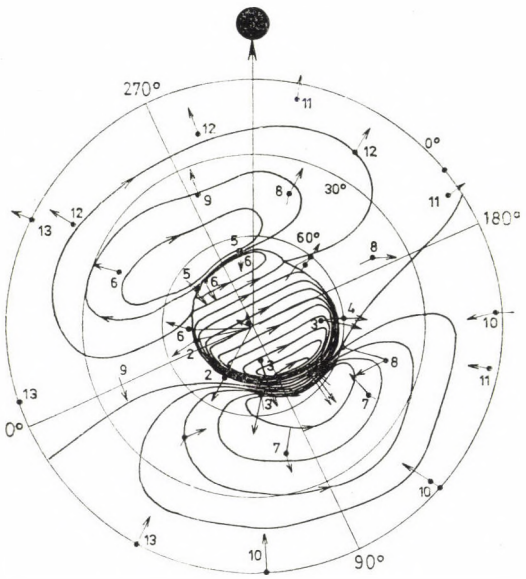


Fig. 5. Statistical equivalent current system of a polar magnetic substorm (Silsbee and Vestine, 1942)

[1] For all quantities expressed in γ it must be observed that $1\gamma = 10^{-9}$ [Weber m^{-2}]

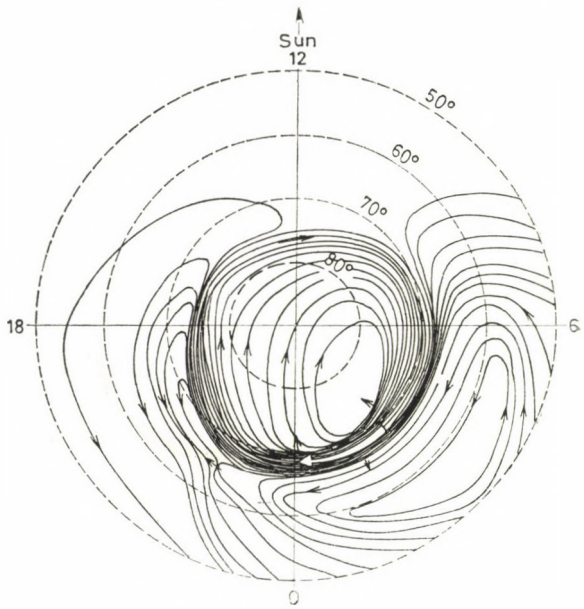


Fig. 6. Statistical equivalent current system of an intense polar magnetic substorm (Akasofu et al., 1965)

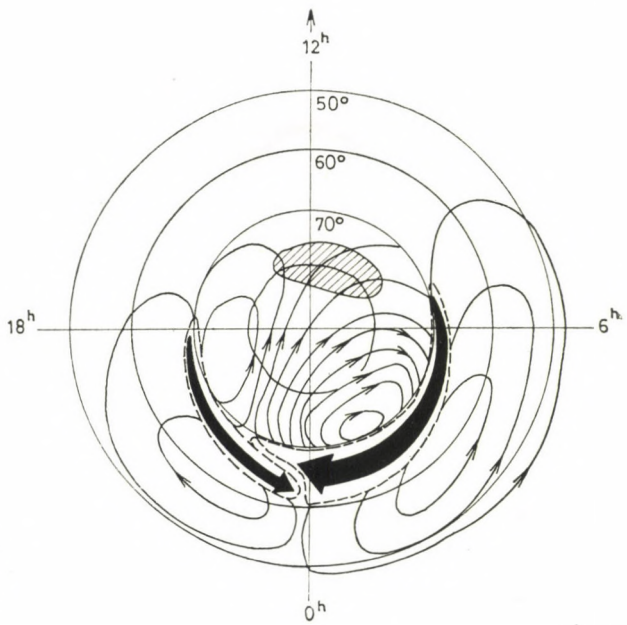


Fig. 7. Statistical equivalent current system of geomagnetic bay activity (Sugiura and Heppner, 1965)

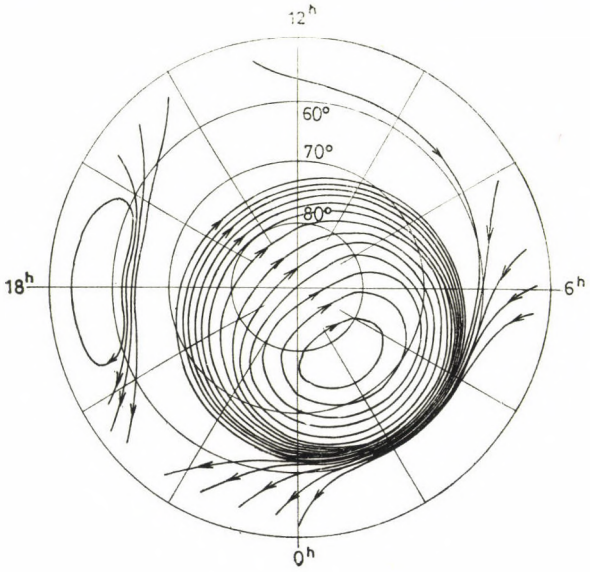


Fig. 8. Statistical equivalent current system for daily magnetic variation (Feldshtein and Zaitsev, 1965)

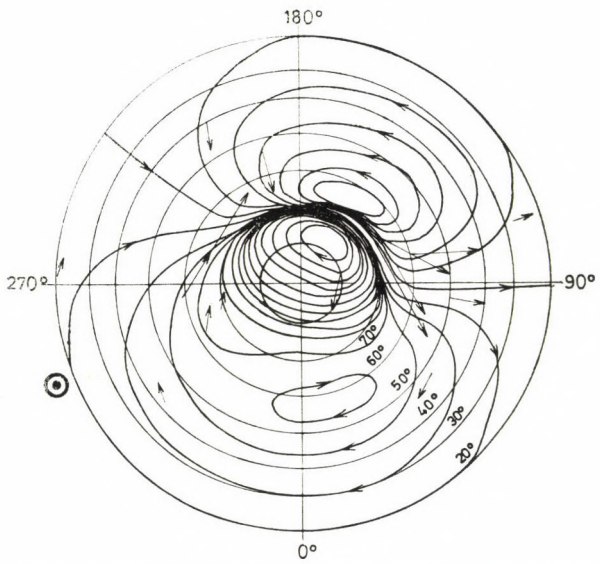


Fig. 9. Equivalent current system for an instant of the substorm on 30 April 1933 (Fukushima, 1953)

disturbance vector of the current system and that of the current system induced in the conductive interior of the earth. For this reason only a fraction $f \cdot \Delta X$ comes from the current in the ionosphere. In general the value 0.6 is taken for f. For the general derivation and representation of equivalent current systems we refer again to Chapman and Bartels (1940). The first statistically equivalent current systems of bay disturbances come from Hatakeyama (1937) and Silsbee and Vestine (1942). Figure 5 illustrates the bay disturbance current system according to Silsbee and Vestine.

In addition, statistical current systems of the polar magnetic substorm have been derived by Sugiura and Heppner (1965), Akasofu et al. (1965) and Rostoker (1967). Figure 6 shows the current system of Akasofu et al. (1965) and Figure 7 that of Sugiura and Heppner (1965). Similarly, statistical current systems of polar disturbances (DP) have been published with seasonal dependence by Feldshtein in particular and also by Mishin (Feldshtein, 1963; Feldshtein and Zaitsev, 1965; Feldshtein, 1966; Feldshtein and Zaitsev, 1968; Afonina and Feldshtein, 1968; Zaitsev, 1970; Mishin et al., 1970a; Mishin et al., 1970b; Mishin and Popov, 1971). Figure 8 shows a DP current system for winter, according to Feldshtein. An average DP current system during the growth phase and the expansive phase was set forth by Nagata et al. (1972).

For investigating the behaviour of a polar magnetic substorm in the course of time, instantaneous equivalent current systems were also derived by several authors. Here characteristic changes in these current systems became apparent in the individual phases of the substorm. The first instantaneous current systems of a polar magnetic substorm come from Vestine et al. (1947) and Fukushima (1953). A typical current system of this type can be seen in Figure 9. Other instantaneous current systems of polar magnetic substorms can be found in the following publications: Iijima and Nagata (1968), Grafe (1969), Best et al. (1969), Best and Grafe (1969), Troshichev and Feldshtein (1970), Pudovkin and Troshichev (1971), Grafe (1972a) and Troshichev and Feldshtein (1972).

For the basic question we are considering, i.e. as to the distribution of the substorm field, it is not essential to have recourse to equivalent current systems. Representations of the distribution of horizontal magnetic disturbance vectors or horizontal equivalent current vectors are quite sufficient. It cannot be denied that equivalent current systems are clearer, but because the observing stations are so few and far between they are always somewhat arbitrary. Vector representations of the type mentioned can be found in Knapp (1961), Fairfield (1963), Heppner (1967), Rao (1969), Ivliev et al. (1970), Loomer and van Beek (1971, 1972).

The main feature of all equivalent current systems is the existence of a current directed strongly westwards in the auroral zone, occurring mainly at midnight and in the early hours of the morning. This is at its most intense during the maximum of the polar magnetic substorm. This westward electrojet has reverse currents flowing (a) directly over the polar cap and (b) in low latitudes. Admittedly, an eastward electrojet is also a characteristic of most equivalent current systems, but opinions differ strongly as to whether this eastward electrojet also has reverse current in polar caps and low latitudes (Silsbee and Vestine, 1942), whether it only has reverse currents in low latitudes (Feldshtein and Zaitsev, 1965, 1968), or whether it is itself only a reverse current of the westward electrojet (Akasofu et al., 1965). Closely linked with this is the question as to whether the equivalent current system of the polar magnetic substorm is a unicellular current system (with prevailing westward electrojet) (Akasofu et al., 1965; Feldshtein and Zaitsev, 1965, 1968) or a bicellular current system (Silsbee and Vestine, 1942); Mishin et al., 1970a). Grafe (1969) is of the opinion that both forms of equivalent current system can occur alternately during a geomagnetic

storm. It is also most probable that the bicellular current system develops particularly at the beginning and during the recovery phase of a polar magnetic substorm and the unicellular current system with a prevailing westward electrojet mainly during the expansive phase. In the case of the unicellular current system, the westward electrojet flows along the auroral oval, i.e. along the area in which the arcs of the aurorae are found. Assuming a bicellular current system, the auroral oval does not correspond to the region of electrojet flux. There are obvious problems here.

B.2. Meridional profiles of the magnetic field of the polar magnetic substorm

The local variations of the substorm field are often presented in the form of meridional profiles of the disturbance components. In particular these are always profiles running obliquely to the polar electrojet. The first latitudinal profile of this type for the Z component comes from Birkeland (1913). Latitudinal profiles for all three components (D, H and Z) were published by Vestine and Chapman (1938). Figure 10 shows the representation of a profile for ΔZ and ΔH according to Walker (1964). The effects of the westward electrojet with its reverse currents in medium and very high latitudes can be seen here. The centre of the westward electrojet is at 68° geomagnetic latitude. The local gradient in the region of the electrojet is in this case approximately 1.1 γ/km. Further meridional profiles of the magnetic disturbance components can be found in Bonnevier et al., (1970), Kisabeth and Rostoker (1971), Rostoker (1972a), Rostoker (1972b), Kamide and Fukushima (1972). The most extensive studies of this type were carried out in Canada by Kisabeth and Rostoker (1971) using a meridional profile closely packed with observing stations. One of the main results of these studies is a double structure of the westward electrojet which develops during the expansive phase. At the northern limit of the electrojet an ad-

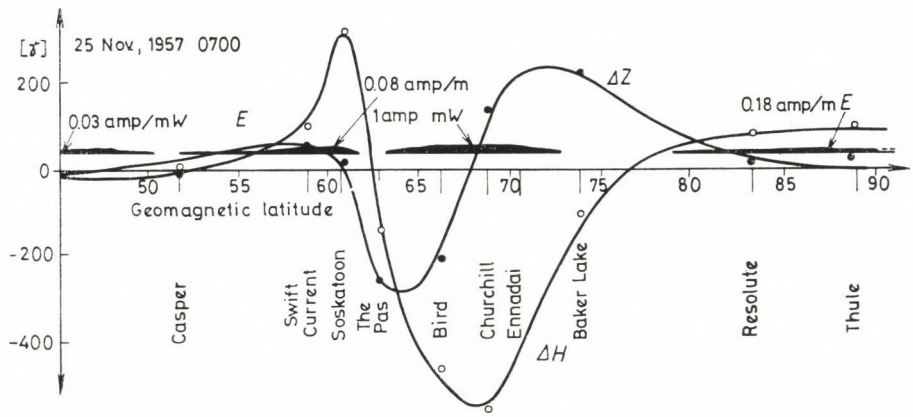


Fig. 10. The observed magnetic field of the auroral zone electrojets (Walker, 1964)

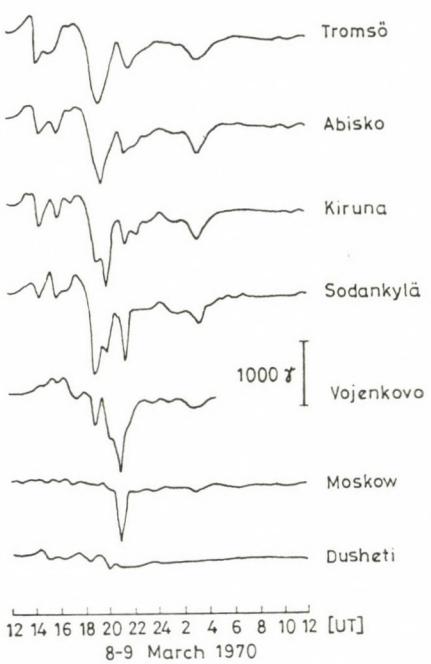


Fig. 11. Magnetic X component for different observatories along the geomagnetic meridian 105° on 8/9 March 1970

ditional current amplification and concentration comes into play. A meridional profile perpendicular to the eastward electrojet is described in Kamide and Fukushima (1972).

Akasofu and Meng (1969) use a different representation of the distribution of the magnetic components along a meridian. In this case the recordings of one component for a given time and for several observing stations lying on approximately the same geomagnetic meridian are simply shown one beneath the other. This type of representation is shown in Figure 11, in which the horizontal magnetic component of several observatories along the geomagnetic meridian 105° has been drawn. This figure gives a good picture of the variations in time and position of some substorms.

C. THE GLOBAL DISTRIBUTION OF THE MAGNETIC FIELD OF THE POLAR MAGNETIC SUBSTORM

It is possible to give a simple description of the global distribution of the substorm field on the basis of the analyses which have been undertaken of the substorm field in the form of equivalent current systems and meridional profiles. The equivalent current systems show that the substorm field has certain characteristics which are dependent on latitude and on time and place. For example, as the current systems in Figures 7 and 8 illustrate, up to 70° geomagnetic latitude no effects of the substorm field take place at midday. But first of all we want to deal with the local distri-

bution of the substorm field in auroral latitudes. During polar magnetic substorms in these latitudes the two polar electrojets occur which in the evening hours are directed eastwards and in the morning westwards. As the mean equivalent current systems in Figures 7 and 8 show, the maximum of the electrojets is located at approximately 67° geomagnetic latitude. Where the effect is strong, however, it is quite possible that a latitude of about 60° can be reached. Not in all equivalent current systems, but particularly in that of Sugiura and Heppner (1965), at the border between the eastward and the westward electrojet towards midnight, a zone appears where the two electrojets overlap. Heppner (1971) has chosen to call this phenomenon the "Harang discontinuity" since it was first found by Harang (1946) in his representations of the lines of equal disturbance components. Meridional currents flow southwards from this Harang discontinuity.

The polar electrojets are regarded as surface currents with an average total current strength of 10^6A. For the height of this conducting layer, 120 km is generally chosen, i.e. the lower E-layer. Here there are particularly favourable conditions of conductivity. The intensity distribution in this layer is assumed to be homogeneous. For this magnetic components H (horizontal and vertical to the direction of the current) and Z at a particular observation point according to Chapman (1951) in [Weber · m^{-2}] follow in the form

$$H = 2 \cdot 10^9 \, i \arctan \frac{2ch}{h^2 + l^2 - c^2}; \quad Z = 10^9 \, i \ln \frac{(l + c)^2 + h^2}{(l - c)^2 + h^2}$$

—where i is the current density in Am^{-1}, h the height of the layer, c half the width of the layer and l the distance of the observation point from the point on the earth's surface which is under the mid-point of the current

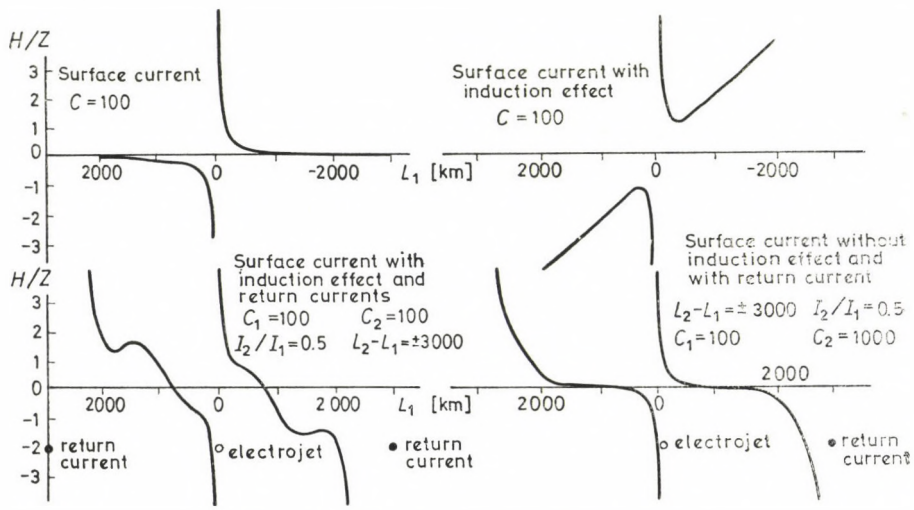


Fig. 12. *H/Z* sections of surface currents

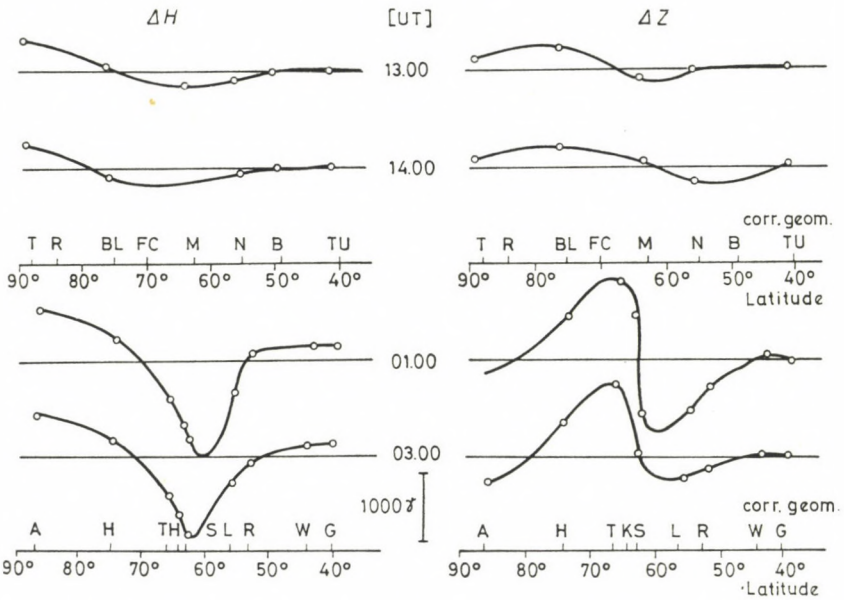


Fig. 13. Meridional sections of ΔH and ΔZ for 25/26 May 1967, perpendicular to the direction of the westward electrojet

layer. The width of the current layer is subjected to a certain amount of fluctuation but averages 5°. Of course, observation is not sufficient for these simple relations of a conducting layer. It is primarily the reverse currents of the electrojet which complicate the situation, but also the induction effect of the electrojet and its reverse currents produced in the earth's crust. This can, however, be taken into account in model calculations. Figure 12 shows examples of model graphs for the relation H/Z. Four different models were used here:

1. Simple current layer according to the relations given above.
2. Taking into account the induction effect of the ionospheric current layer. Here it was assumed that the earth is not conductive to a depth of 250 km and from then on has infinite conductivity (see Chapman, 1951). In that case the induction current flows at a depth of $h + 500$ km.
3. Surface current of the electrojet plus that of the reverse currents, excluding their induction effects ($L_2 - L_1$ here is the distance of the electrojet from the corresponding reverse current).
4. Surface current of the electrojet plus that of the reverse currents including their induction effects. To which model is the observation most similar? Figure 13 shows meridional sections for ΔH and ΔZ for substorms of the geomagnetic storm of 25/26 May 1967 for the corrected geomagnetic meridian $\Lambda_{corr} = 110°$ and $\Lambda_{corr} = 310°$ according to Grafe (1972b). In Figure 14 the $\Delta H/\Delta Z$ curves corresponding to Figure 13 are represented. If these are compared with the model curves in Figure 12, it is seen that the

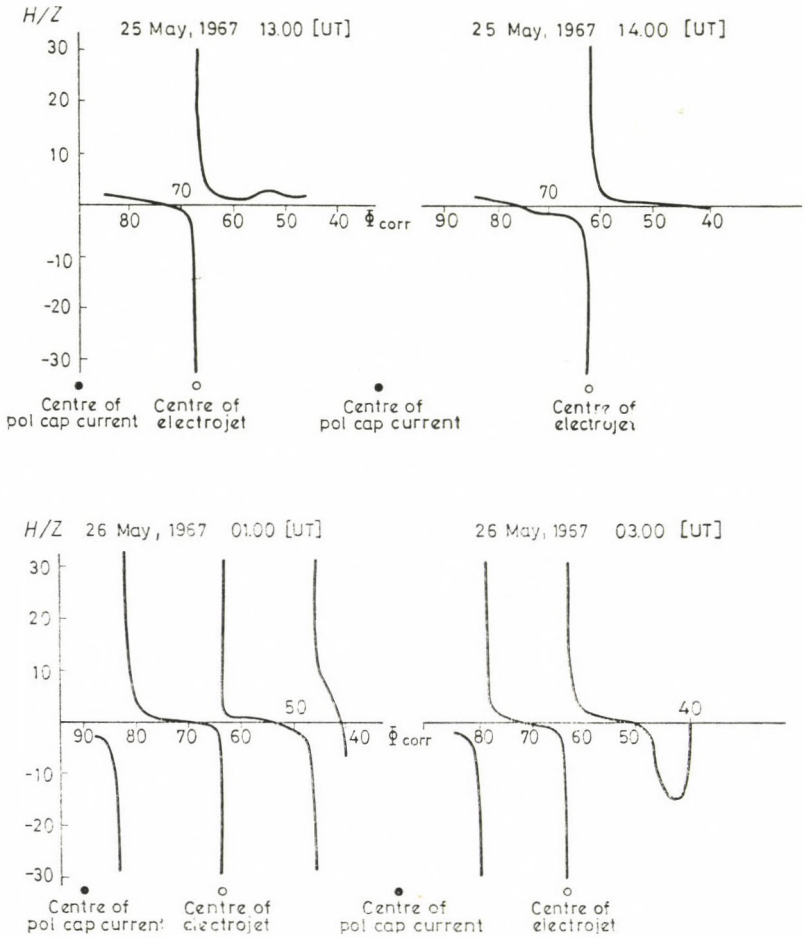


Fig. 14. $\Delta H/\Delta Z$ curves for the examples in Fig. 13

observation curves correspond very well to those curves for which the induction effect has been ignored. The observation curves of 25 May at 1300 UT and 1400 UT also lack reverse current effects and therefore correspond very well to the model curve of a simple electrojet surface current. These results indicate that in the region of the electrojet for this period there is an almost total absence of global induction effects.

The parameters of the electrojet can also be read very well from the meridional sections in Figure 13. The position of the centre of the current layer is marked by the point $Z = 0$ and the width of the current layer by the distance of the maximum from the minimum in the ΔZ section. These parameters are put together in Table 1, with the mean local field gradient in the horizontal component for a specific latitude range. There are certainly changes in the position of the electrojet as well as clear variations in the

width of the current layer. The fact that the width of the westward electrojet for the examples dated 25 May is much larger than that for the examples from 26 May can also be seen from Grafe's (1972a) equivalent current systems.

As Table 1 shows, even in medium latitudes (50°– 60°) there can be appreciable field gradients. We should not, however, forget that the sub-

TABLE 1

Date	UT	Centre of current layer	Width of current layer	Local field gradient in ΔH in latitude range	γ/km
25. 5. 1967	1300	65.8°	14.5°	49.0°–62.0°	0.14
	1400	61.5°	23.5°	49.0°–67.5°	0.11
26. 5. 1967	0100	64.0°	6.0°	54.5°–60.0°	2.25
	0300	63.5°	7.0°	50.5°–62.0°	1.00

storm on 26 May 1967 was a very strong one in which maximum disturbances of more than 1000 γ were caused by the electrojet. In the meridional profiles of substorms by Rostoker (1972a,b) very strong field gradients occur only to a southern limit of approximately 60° geomagnetic latitude ($\sim 2.5\gamma$/km for 62° latitude). Between 55° and 60° geomagnetic latitude a value of 0.2 γ/km is scarcely exceeded at all. This is how the situation looks in the region of the westward electrojet and its reverse currents in medium latitudes. The eastward electrojet can be examined in much the same way. According to the example given by Kamide and Fukushima (1972), for latitudes south of 59° geomagnetic latitude there is a homogeneous external field, and north

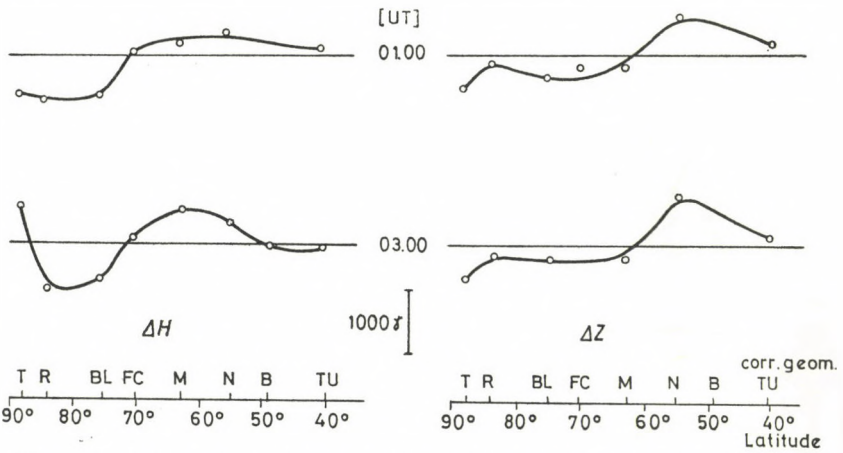


Fig. 15. Meridional sections of ΔH and ΔZ for 26 May 1967, perpendicular to the direction of the eastward electrojet

of 60° geomagnetic latitude there is a local gradient of 0.8 γ/km. Figure 15 shows, for two substorms during the storm of 26 May 1967, the meridional section across the eastward electrojet. Whilst for the instant of time 0100 UT the external magnetic field to the south of the electrojet is approximately homogeneous, in the 0300 UT section south of the electrojet there is a mean local gradient of about 0.4 γ/km in the latitude range from 49° to 63°.

The equivalent current systems also show that shortly before midnight meridional currents flow from North to South and in the early morning currents flow from South to North. Here it is no matter whether these currents flow in the ionosphere or along the magnetic lines of force as field aligned currents into the magnetosphere or from the magnetosphere into the ionosphere. Our task consists only of examining the local distribution of the magnetic field as produced by these meridional currents. These meridional currents manifest themselves by a strong declination or Y component. Figure 16 shows an example of the change in declination along three different geomagnetic latitude profiles for the substorm at 1840 UT on 3 February 1969. Table 2 lists, corresponding to the various profiles, the observatories from which data were used for deriving Figure 16. According to this figure there is a clear reduction in declination and an increasing homogenization of the field from North to South. The increasing homogenization is certainly connected with a broadening of the meridional current in low latitudes. At the sides of the current layer local field gradients occur, which for the northern profile are of the order of 0.16 γ/km, for the middle profile 0.06 γ/km and for the southern one 0.04 γ/km. With a maximum disturbance component in horizontal intensity amounting to about 750 γ, this substorm is not one of the strongest substorms. It is therefore to be expected that the field inhomogeneities for stronger substorms in the evening and morning sector are higher than the values given here.

Fairly strong field strength gradients also occur in the polar cap in the region of the day side of the auroral oval during a substorm. This is the current referred to by Mishin et al. (1970b) as the "inner electrojet". But strong currents can also flow directly over the polar cap. Examples of such strong polar cap currents can be found in Grafe (1969), Figure 4, a, and Grafe (1972a), Fig. 1, a. These strong polar cap currents occur especially during

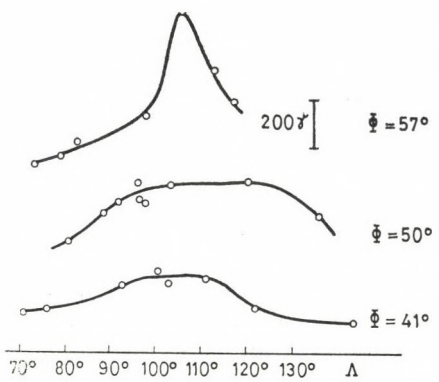


Fig. 16. Latitudinal sections of magnetic declination for three different geomagnetic latitudes on 3 February 1969, 1840 UT

TABLE 2

Station	Geomagnetic latitude	Geomagnetic longitude
Eskdalemuir	58.5°	82.9°
Lovö	58.1	105.8
Nurmijärvi	57.9	112.6
Valentia	56.1	73.1
Leningrad	56.0	117.0
Rude Skov	55.8	98.5
Hartland	54.6	79.0
Niemegk	52.2	96.6
Dourbes	51.7	88.7
Moscow	50.8	120.5
Chambon-la-Forêt	50.4	83.9
Belsk	50.4	104.1
Pruhonice	49.9	97.3
Fürstenfeldbruck	48.9	92.4
Sverdlovsk	48.5	140.7
Wien-Kobenzl	47.9	97.9
Odessa	43.8	111.1
Grocka	43.6	100.9
Toledo	43.6	75.7
L'Aquila	42.9	93.0
San Fernando	41.0	71.3
Panagurishte	40.9	103.4
Tbilisi	36.7	122.1
Tashkent	32.4	143.7

the initial phase of geomagnetic storms and probably during the growth phase of substorms as well. This has, however, not yet been proved beyond doubt. There is a possibility that these polar cap currents are not part of the substorm (DPI) current system.

Compared with the disturbances in high latitudes, those in equatorial latitudes are insignificant. At the same time it is not yet clear whether single substorms are accompanied by variations in the asymmetrical ring current in equatorial latitudes. Loomer and van Beek (1971) have found no connection between substorm disturbances and storm time variations (D_{St}). However, as the equivalent current systems make it clear, very low local field strength gradients are to be expected in equatorial latitudes.

For geomagnetic soundings the connection between primary Z- and H-component is important. In each case this connection depends on the structure of the polar electrojets, as well as on its return currents in low latitudes and on the local time. Therefore it is quite impossible to give generally valid values for the connection between Z- and H-component. It is clearly shown by Figure 14 how much the ratio H/Z can vary in each case.

D. CHRONOLOGICAL DEVELOPMENT OF THE MAGNETIC FIELD OF THE POLAR MAGNETIC SUBSTORM

Very little is known at present about the chronological development of the polar disturbance field and so we can give no more than a short description of the sequence of events. During a geomagnetic storm definite changes occur in the equivalent current systems (Grafe, 1969). Shortly after the *ssc* there is only a more or less intense eastward electrojet and a polar cap current which is sometimes very strong. A westward electrojet does not yet exist. During the initial phase a westward electrojet develops and a clearly bicellular current system eventually forms. Whilst the eastward electrojet shows only a significant increase in intensity, during the main phase of the storm very strong westward electrojets are formed. This is the case when intense substorms occur. The sketch in Figure 17 shows this chronological development of the DP field.

Similar situations occur if equivalent current systems are derived during the phases of single substorms. Current systems of this type for the growth phase and the expansive phase come from Nagata et al. (1972). During the growth phase the eastward electrojet is stronger than the westward one. The opposite applies to the expansive phase. Nevertheless, both current systems show a distinct bicellular form. In course of the decay phase conditions similar to those in the growth phase occur again. It is, however, still unclear whether the polar magnetic substorm also has a growth phase. Akasofu and Snyder (1972), anyway, consider it impossible to determine a growth phase from magnetic ground observations.

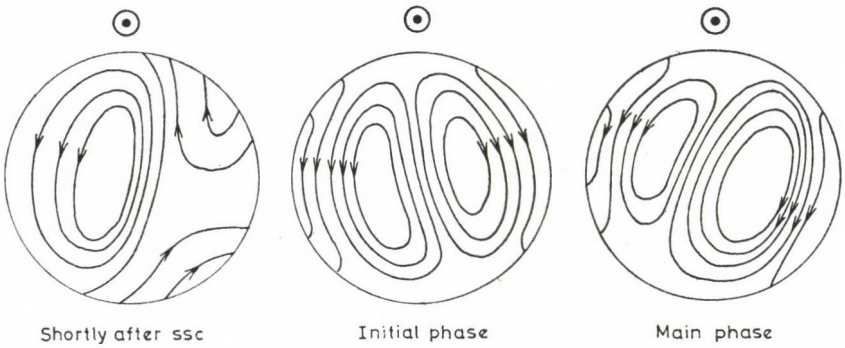


Fig. 17. Sketches of equivalent current systems during each phase of a storm

2. CONCLUDING REMARKS

The aim of the foregoing was to compile information about the glo ba distribution of the geomagnetic disturbance field during a magnetospheric substorm. At the same time, the values of occurring field strength gradients were given for specific latitudes and local times. Since knowledge of the

inhomogeneity of the outer substorm field is important for all investigations to do with geomagnetic deep sounding, the following points must be observed:

1. The strongest field inhomogeneities occur in the regions of the electrojets. In this case it is not possible to use the geomagnetic deep sounding methods which presuppose a homogeneous outer field. At the same time the region in question is primarily that of the westward electrojet which usually occurs at night and in the morning between 65° and 70° geomagnetic latitude, but which can by all means wander southwards. Regions which must also be taken into account, are those of the eastward electrojet (in the afternoon near 65° geomagnetic latitude), the "polar cusp" current (at midday between 70° and 80° geomagnetic latitude) and the meridional currents flowing in the evening and morning along geomagnetic meridians.

2. Strong field strength gradients can also occur occasionally in medium latitudes, outside the electrojet regions. There can therefore occur field inhomogeneities up to 2 γ/km in medium latitudes. The question is whether under these conditions calculations on geomagnetic deep soundings carried out in the normal way are admissible.

3. In low and equatiorial latitudes, the local field gradients during a substorm are really very small. It should be possible here to use the normal methods of geomagnetic deep sounding.

REFERENCES

Afonina, R. G., Feldshtein, Ya. I., 1968. Polar magnetic disturbances and the precipitation of energetic particles in the ionosphere (in Russian). *Kosmicheskie Issled.* **6**, 150–152.

Akasofu, S. I., 1968. Polar and Magnetospheric Substorms. D. Reidel Publishing Co., Dordrecht-Holland.

Akasofu, S. I., Chapman, S., Meng, C. I., 1965. The polar electrojet. *J. Atmosph. Terrestr. Phys.* **27**, 1275–1305.

Akasofu, S. I., Meng, C. I., 1969. A study of polar magnetic substorms. *J. Geophys. Res.* **74**, 293–313.

Akasofu, S. I., Snyder, A. L., 1972. Comments on the growth phase of magnetospheric substorms. *J. Geophys. Res.* **77**, 6275–6277.

Atkinson, G., 1967. The current system of geomagnetic bays. *J. Geophys. Res.* **72**, 6063–6067.

Best, A., Fanselau, G., Grafe, A., Lehmann, H. R., Wagner, C. U., 1969. The variations of the geomagnetic field in middle and high latitudes during the proton flare event of July 1966. *Ann. of IQSY* **3**, 413–425.

Best, A., Grafe, A., 1969. The variations of the geomagnetic field in northern latitudes and of the ring current field during the proton flare events from 27th August to 7th September, 1966. *Geod. Geophys. Veröff. R. II* H. **10**, 63–73.

Birkeland, K., 1913. The norwegian aurora polaris expedition 1902–1903. 1. Section 2, H. Aschhong, Christiania.

Bonnevier, B., Boström, R., Rostoker, G., 1970. A three-dimensional model current system for polar magnetic substorm. *J. Geophys. Res.* **75**, 107–132.

Chapman, S., 1951. *Archiv für Meteorologie, Geophysik und Bioklimatologie Ser. A.* **4**, 368–390.

Chapman, S., Bartels, J., 1940. Geomagnetism, Chapter VII, Oxford.

Crooker, N. V., McPherron, R. L., 1972. On the distinction between the auroral electrojet and partial ring current system. *J. Geophys. Res.* **77**, 6886–6889.

Fairfield, D. H., 1963. Ionosphere current patterns in high latitudes. *J. Geophys. Res.* **68**, 3589–3602.

Feldshtein, Ya. I., 1963. On morphology of auroral and magnetic disturbances in high latitudes (in Russian). *Geomagn. i Aeron.* **3**, 227.

FELDSHTEIN, YA. I., 1966. Peculiarities in the auroral distribution and magnetic disturbance distribution in high latitudes caused by the asymmetrical form of the magnetosphere. *Planet. Space Sci.* **14,** 121–130.

FELDSHTEIN, YA. I., ZAITSEV, A. N., 1965. Disturbed solar-daily variations in high latitudes during the IGY period (in Russian). *Geomagn. i Aeron.* **5,** 477–486.

FELDSHTEIN, YA. I., ZAITSEV, A. N., 1968. S_D-variation of the magnetic field in high latitudes with different intensity of magnetic disturbances. *Ann. Geophys.* **24,** 1–8.

FUKUSHIMA, N., 1953. Polar magnetic storm and geomagnetic bays. *J. Faculty of Science University of Tokyo, Section II,* **8,** 291–412.

FUKUSHIMA, N., 1969. Equivalence in ground geomagnetic effect of Chapman-Vestines and Birkeland-Alfvens electric current-system for polar magnetic storms. *Rep. Ionosph. a. Space Res. Japan* **23,** 219–227.

GRAFE, A., 1969. On the dynamics of the DP-current system. *Planet. Space Sci.* **17,** 1395–1408.

GRAFE, A., 1972a. About the connection between equatorial ring current and polar electrojet. *Planet. Space Sci.* **20,** 183–204.

GRAFE, A., 1972b. Die räumlich-zeitlichen Variationen des geomagnetischen Substormfeldes. Lecture, KAPG-Symposium, Working Groups 1.2 and 2.1, Prague.

HARANG, L., 1946. The mean field of disturbance of polar geomagnetic storms. *Terrestr. Magn.* **51,** 353–380.

HATAKEYAMA, H., 1937. Preliminary discussion on the bay-disturbance in the terrestrial magnetic field. *Geophys. Mag.* **11,** 1–11.

HEPPNER, J. P., 1967. High latitude magnetic disturbances. Aurora and Airglow (ed. by B. M. McCormac) Reinhold, New York, 75–92.

HEPPNER, J. P., 1971. The Harang-discontinuity in auroral belt ionospheric currents. Preprint GSFC X-645'72-1.

IIJIMA, T., NAGATA, T., 1968. Constitution of polar magnetic disturbance. *Rep. Ionosph. Space Res. Japan* **22,** 1–24.

IVLIEV, D. YA., PUDOVKIN, M. I., ZAITSEVA, S. A., 1970. Development of elementary magnetic disturbance (in Russian). *Geomagn. i Aeron.* 300–304.

KAMIDE, Y., FUKUSHIMA, N., 1972. Positive geomagnetic bays in evening high latitudes and their possible connection with partial ring current. *Rep. Ionosph. Space Res. Japan* **26,** 79–101.

KIRKPATRICK, C. B., 1952. On current systems proposed for S_D in the theory of magnetic storms. *J. Geophys. Res.* **57,** 511–526.

KISABETH, J. L., ROSTOKER, G., 1971. Development of the polar electrojets during magnetic substorms. *J. Geophys. Res.* **76,** 6815–6828.

KNAPP, D. G., 1961. Some features of magnetic storms in high latitudes. *J. Geophys. Res.* **66,** 2053–2085.

LOOMER, E. I., van BEEK, J. G., 1971. Magnetic substorm, December 5, 1968. *Publ. earth Physics Branch* **41,** 183–198.

LOOMER, E. I., van BEEK, J. G., 1972. Polar magnetic substorms 03-06, UT December 5, 1968. *Publ. earth Physics Branch* **42,** 157–165.

MCPHERRON, R. L., 1970. Growth phase of magnetic substorms. *J. Geophys. Res.* **75,** 5592–5599.

MENG, C. I., AKASOFU, S. I., 1969. A study of polar magnetic substorms 2. Three-dimensional current system. *J. Geophys. Res.* **74,** 4035–4053.

MISHIN, V. M., POPOV, G. V., 1971. Effects of earth's daily rotation on currents in the earth's magnetosphere (UT-effects) (in Russian). *Issled. geomagn. aeron. i fizike solntsa* **19,** 1–11.

MISHIN, V. M., POPOV, G. V., SAMSANOV, V. P., BASARZHAPOV, A. D., MISHINA, N. A., SAIFUDINOVA, T. I., 1970a. Corpuscular intrusions into ionosphere and a scheme of substorm development: capture-accumulation explosure. Report presented at the International Symposium on Solar-terrestrial Physics, Leningrad, May 1970.

MISHIN, V. M., SAMSANOV, V. P., SAIFUDINOVA, T. D., KURILOV, V. A., 1970b. Main zones of particle precipitation in the ionosphere (in Russian). *Issled. geomagn. aeron. i fizike solntsa* **11,** 3–23.

NAGATA, T., HIRASAWA, T., IIJIMA, T., FUKUNISHI, H., 1972. Auroral and magnetic substorms in the southern region (in Russian). *Issled. geomagn. aeron. i fizike solntsa* **23,** 7–35.

PUDOVKIN, M. I., TROSHICHEV, O. A., 1971. On the nature of various kinds of the high latitude geomagnetic variations. Paper presented at the XV. Assembly of IAGA, Moscow.

RAO, K. S. R., 1969. On the axial asymmetry of the geomagnetic disturbance field in the low latitudes. *J. Atmosph. Terrestr. Phys.* **31,** 803–816.

ROSTOKER, G., 1967. A determining factor in the form of the equivalent current system for geomagnetic bays. *Earth Planet. Sci. Letts.* **2,** 119–122.

ROSTOKER, G., 1969. Classification of polar magnetic disturbance. *J. Geophys. Res.* **74,** 5161–5168.

ROSTOKER, G., 1972a. Interpretation of magnetic field variations during substorms. Earth's Magnetospheric Processes, 379–390. D. Reidel Publ. Comp. Dordrecht-Holland.

ROSTOKER, G., 1972b. Polar magnetic substorms. *Rev. Geophys. Space Phys.* **10,** 167–211.

SILSBEE, H. C., VESTINE, E. H., 1942. Geomagnetic bays, their frequency and current systems. *Terrestr. Magn.* **47,** 195–208.

STARKOV, G. V., FELDSHTEIN, YA. I., 1970. Instantaneous distribution of auroras and polar magnetic disturbances (in Russian). *Polyarn. Siyan.* **19,** 32–41.

STEINER, L., 1921. On a special form of magnetic disturbance. *Terrestr. Magn.* **26,** 1–14.

SUGIURA, M., HEPPNER, J. P., 1965. The earth's magnetic field, an introduction to Space Science, ed. by W. N. Hess, p. 45. Gordon and Breach, New York.

TROSHICHEV, O. A., 1969. A zone of unstable radiation and its effects on the earth's surface (in Russian). Thesis, Sibizmir.

TROSHICHEV, O. A., FELDSHTEIN, YA. I., 1970. The ring current in the magnetosphere and the polar magnetic substorms (in Russian). *Geomagn. i Aeron.* **10,** 1114–1117.

TROSHICHEV, O. A., FELDSHTEIN, YA. I., 1972. The ring current in the magnetosphere and the polar magnetic substorms. *J. Atmosph. Terrestr. Phys.* **34,** 845–858.

VESTINE, E. H., CHAPMAN, S., 1938. The electric current-system of geomagnetic disturbance. *Terrestr. Magn.* **43,** 351.

VESTINE, E. H., LA PORTE, L., LANGE, I., SCOTT, W. E., 1947. The geomagnetic field-description and analysis. Carnegie Inst. Washington Publ. 580.

WALKER, J. K., 1964. Space-time association of the auroral and magnetic disturbance. *J. Atmosph. Terrestr. Phys.* **26,** 951–958.

WIESE, H., 1951. Die erdmagnetischen Bays und ihre Beziehungen zu den Strömungsverhältnissen der Ionosphäre. *Z. Meteor.* **5,** 341–347.

ZAITSEV, A. N., 1970. S_D-variation of the magnetic field in high latitudes with different intensity of magnetic disturbances (in Russian). *Polyarn. Siyan.* **19,** 51–60.

INHOMOGENEITY OF THE PULSATION FIELD AND ITS EFFECT ON THE MT VALUES

A. ÁDÁM, CZ. J. MILETITS, J. VERŐ

INTRODUCTION

According to Price (1962), the magnetotelluric method can be only applied efficiently, if the horizontal extent of the inducing field is known. To describe this quantitatively, Price introduced the parameter ν the reciprocal value of which is proportional to the wave length of the inducing field: $\Lambda = 2\pi/\nu$ [cm].

Impedance $Z(z)$ is the function of ν. If the source has infinite dimension, i.e. $\nu = 0$, Cagniard's case will arise.

The magnetic scalar potential of an inducing field outside the conductor can be expressed as a sum (or integral) of simple expressions of the form:

$$Ae^{-\nu z}P(x, y, \nu) = Ae^{-\nu z} \cos \nu x$$

The change of the field quantities along one of the coordinate axes can be expressed by the Fourier-transform:

$$A^*(x) = \frac{1}{2\pi} \int_{-\infty}^{\infty} A(\nu)\, e^{-i\nu x}\, d\nu$$

Srivastava (1967) calculated two- and three-layer theoretical curves for five different ν values.

Price proved that by means of the factor $\sqrt{\sigma/T}$ the calculations can be extended over other parameters of a layer, too (σ = conductivity, T = period).

For ν two limiting values were given: $1.57 \cdot 10^{-9}$ and $1.57 \cdot 10^{-7}$ [cm^{-1}].

Takács (1964) proved by transforming Price's model to the geoelectric conditions of the Pannonian Basin that it can be investigated with fields of almost local extent ($\lambda > 500$ km).

ON THE DETERMINATION OF ν

According to the foregoing the empirically determined amplitude functions $A^*(x)$ of the electrical (E) or geomagnetic (H) components can be used for the determination of ν. Such are known from the literature for some types of pulsations (e.g. for *Pi* 2; Jacobs and Sinno, 1960) along the magnetic meridian. The amplitude of the pulsations increases in the polar zone "impulse-likely", thus its spatial spectrum is — depending on

the "signal form" — almost continuous in a certain frequency range. The question is, which spectral line is determinant at magnetotelluric sounding?

The amplitude of the pulsations changes along the latitude circles, too, in dependence of the pulsation type. While e.g. *Pc*-pulsations are governed by the local time, a *Pi* 2 pulsation is mostly a world-wide occurring event that can be traced on the day-side of the Earth as the increase of the *Pc*-amplitudes. Since the changes of amplitudes along the meridian and the latitude circles are considerably different: $v_\varphi \neq v_\lambda$.

This is illustrated by the correlations for *Pc* and *Pi* 2 (*Pt*) pulsations shown in Figure 1. This is the result of a two-dimensional amplitude-analysis by Ádám et al. (1966). Observatories are connected with each

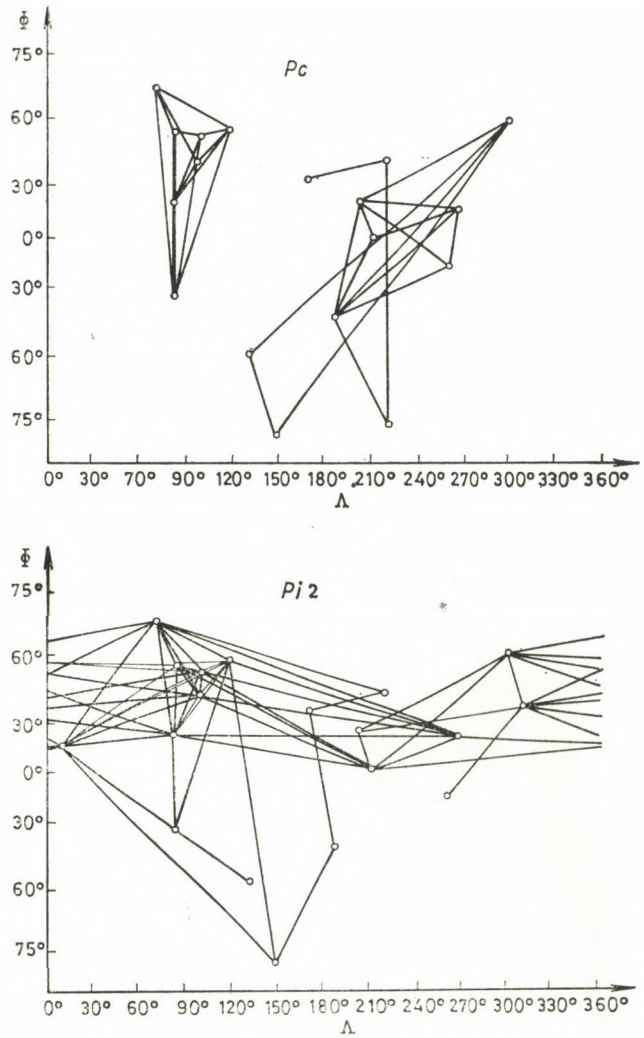


Fig. 1. Correlations between amplitudes of *Pc* 3—4 and *Pi* 2-type pulsation-events. Observatories are connected where the correlation between 2.5 min-maxima of pulsations was above 0.6 above – for the *Pc* 3—4 of June 9, 1958, 12h00–13h00; below – for the *Pi* 2 of June 9, 1958, 18h00–19h00

other, where the correlation between the maximum amplitudes of the pulsations (measured in 2.5 min time intervals) was greater than 0.6. On the basis of these correlations Ádám (1967) attempted to determine dimensions, too. Even for the considerably smaller extent of *Pc* pulsations along the geographical longitude circles a value of $v < 10^{-8}$ cm^{-1} resulted.

The complicated structure of the pulsation field, however, cannot be characterized by amplitude-correlations alone. In this connection we refer to the change of the period with latitude, to the propagation mechanism and the phase differences connected to it, to the different properties of meridional and zonal components, to the distortion of the induced field etc.

An attempt has been made to estimate the Priceian space dimension of the pulsation field.

After the above rough estimations we determine instead of the proposed world-wide analysis of the horizontal magnetic field, the change in time of the MT apparent resistivity (or impedance) or the change in time of the ratio of the horizontal and vertical magnetic components. This gives information about the effect of the source-field on sounding.

In what follows two complicated field-structures of pulsations will be shown together with the results of their analyses.

Two pulsation series were investigated, both having been considered as pulsations of typically small dimensions. They were chosen from the KAPG-measurements in Aug.–Sept. 1969. The first event occurred between 18h52 and 19h25 GMT on Sept. 4; it was a *Pc* 4 (*Pg* in the old nomenclature) of small dimension. The second was a pulsation series of type *Pc* 3, it occurred between 8h03 and 8h45 GMT on Sept. 3, 1969, and showed a strong latitude-dependence of the period already at a first glance.

ANALYSIS OF THE *Pc* 4 EVENT

This variation group occurred with a considerable amplitude. According to the available data the maximum value reached even 10–12 γ in the subauroral zone (at about 52°); in other areas it was between 1 and 5 γ. There was a rather sharp maximum on the basis of European data (Fig. 2), but a practically world-wide occurrence of the activity with similar period and distribution could have been observed, too. According to 13 data from the northern and 3 of the southern hemisphere the average period in both components was 120 sec; smaller values can be considered — at least partly — as results of artificial disturbances. The frequency distribution of the periods of all investigated stations does not even exclude a harmonic structure.

In this case variations were investigated after all, which occurred very similarly all over the Earth with the same period, but with a strongly increased amplitude in the subauroral zone. The v value is also not greater than 10^{-8}. The magnetotelluric sounding curve of Nagycenk together with the values calculated from this interval is shown on Figure 3. Points with periods about 100–400 sec correspond well with the basic curve and their scatter is not high, either.

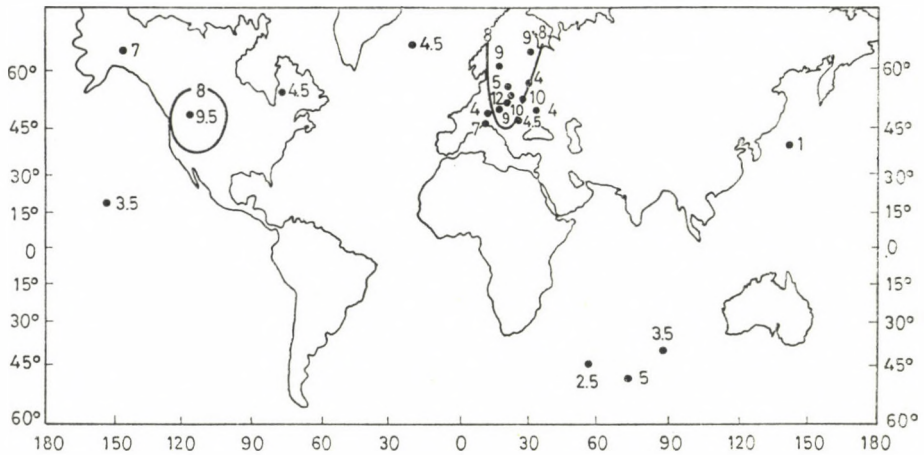


Fig. 2. **Maximum amplitudes of the *Pc* 4–5 event in γ-s from Sept. 4, 1969, 18h52– 19h25**

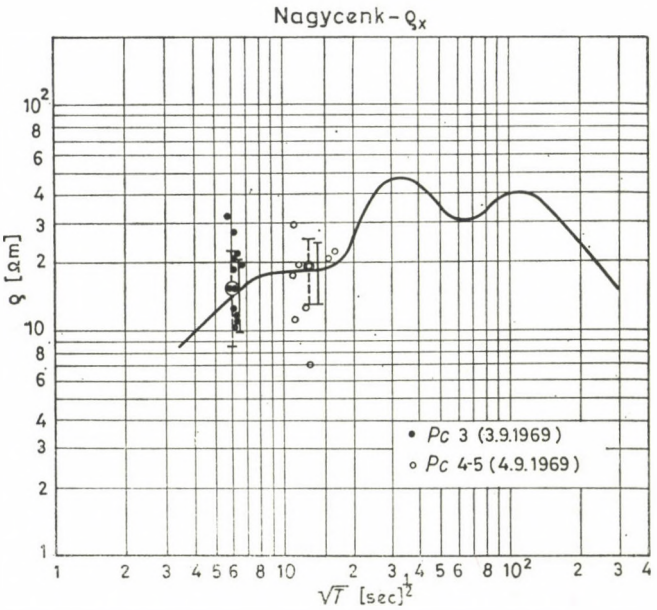


Fig. 3. MT-sounding curve (ϱ_x) of the Nagycenk Observatory, with standard deviations in some intervals (full line), and points from the *Pc* 3 and *Pc* 4–5 event of Figs 2 and 4, with the respective standard deviations (dotted line)

ANALYSIS OF A *Pc* 3 EVENT

In contrast to the former event, the *Pc* 3 variations recorded between 8h03 and 8h15 on Sept. 3, 1969 were variations with small amplitudes and their periods were very much latitude-dependent. Table 1 shows average periods for different latitudes on the basis of stations lying on the northern hemisphere:

The data used for the calculation can be seen in Figure 4. Data from the southern hemisphere do not fit into this pattern.

The frequency distribution of the periods does not exclude in this case a harmonic structure (this cannot be seen from the average periods). When taking into account the now greater number of stations, a period distribution similar to the figure published by Ádám et al. (1972) was received,

TABLE 1

Changes of the periods of geomagnetic pulsations at different latitudes in the Sept. 4 event

H_x	Increase per cent/degree	H_y	Increase per cent/degree
45° 13 sec		15 sec	
50° 15.5 sec	+ 4%	17 sec	+3%
55° 24 sec	+10%	18.5 sec	+2%
60° 14.5 sec	?	20 sec	+2%

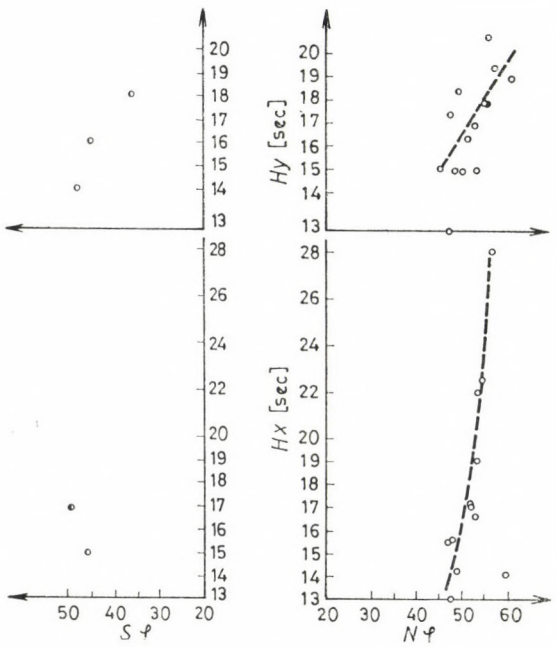


Fig. 4. Mean periods of the *Pc* 3-event of Sept. 3, 1969, 08h03–08h45 from mid-latitude stations

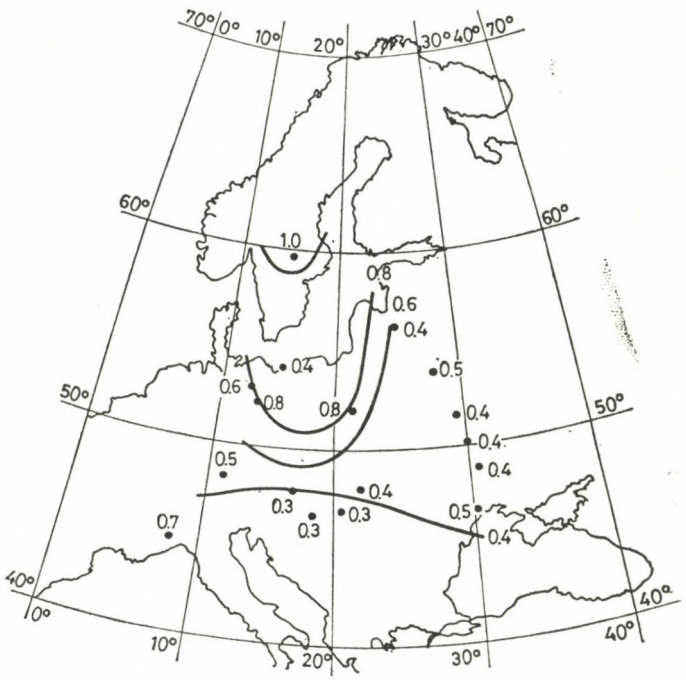


Fig. 5. Amplitudes of the *Pc* 3-event of Fig. 4 at European stations in γ-s

i.e. the idea of occurring more higher harmonics as approaching the pole can be maintained. The thickness of the resonating shelves is theoretically taken as 0.1 L, what would be a value of the order of 100 km at the surface at the latitude of 50°. Somewhat — but not considerably — higher value can be deduced from the H_x component of the *Pc* 3 event studied. According to that the ν value is about $5 \cdot 10^{-8}$ cm^{-1}.

Proper data for the amplitude distribution were available in this case only for Europe. They showed an amplitude decrease from 1 to 0.3–0.4 γ from NW to SE (Fig. 5), but the characteristic length belonging to that is considerably higher than the characteristic length of the period change.

The magnetotelluric apparent resistivity values calculated for this time interval in the Observatory near Nagycenk are shown on Figure 3, too. It is a satisfying result that no observable deviations from the basic curve are seen and the scatter of the points is not higher than for values calculated from other events.

REFERENCES

ÁDÁM, A., 1967. On Price's criticism of the magnetotelluric method (MT) (Determining the dimension of the field of pulsations) (in Hungarian). *Geofizikai Közlemények* **16**, No. 1–2, 3–16.

ÁDÁM, A., Cz. MILETITS, J., VERŐ, J., 1972. Das Mikropulsationsfeld in Osteuropa. *Acta Geod. Geophys. Mont. Hung.* **7**, 289–304.

ÁDÁM, A., VERŐ, J., 1971. First results concerning the KAPG electromagnetic records (in Russian). *Acta Geod. Geophys. Mont. Hung.* **6**, 223–234.

ÁDÁM, A., VERŐ, J., WALLNER, Á., 1966. Die räumliche Verteilung der Pulsationen des elektromagnetischen Feldes der Erde. *Acta Geod. Geophys. Mont. Hung.* **1**, 379–417.

JACOBS, J. A., SINNO, K., 1960. Occurrence frequency of geomagnetic pulsations, Pc. *J. Geophys. Res.* **65**, 107–133.

PRICE, A. T., 1962. The theory of magnetotelluric methods when the source field is considered. *J. Geophys. Res.* **67**, 1907–1918.

SRIVASTAVA, S. P., 1967. Magnetotelluric two- and three-layer master curves. *Publ. of the Dominion Observatory* **35**, No. 7.

TAKÁCS, E., 1964. Study of development of MT instruments and methodics and their application in geophysical exploration. (Manuscript in Hungarian.)

COMPLEX INTERPRETATION BY MEANS OF PHYSICAL FIELDS; HOMOLOGY RELATIONS

G. FANSELAU, L. BALLANI

For complex interpretation, the first category of methods uses all physical indications available at the earth's surface for the elucidation of a geological or geotectonic object. Only in very rare cases can the direct indications from greater depths, as e.g. deep borings and the like, also be used. If these data, which are of the greatest importance for inverse interpretation, are not initially taken into account, we must restrict ourselves to observations which can be made at the earth's surface. Of course the results obtained this way may belong to a wide range of natural sciences. Mathematical-physical methods are just as important as the statistical methods or systematic investigations.

One of the greatest difficulties of complex interpretation consists in fitting together the physical, chemical, petrographic and other indications obtained by applying the various methods, available, in order to obtain a composite picture of the geologic-tectonic body. In view of the variety of methods, the parameters are obtained with quite different accuracies and, above all, are not even fully identical, so that a coupling may lead to great uncertainties.

A different situation arises when only one category of inverse interpretation, e.g. the evaluation of physical fields, is used. In this case one can largely eliminate the above mentioned problems by making use of homologous phenomena. The physical factors are defined in a much clearer way; the methods can be fitted together so that uncertainties in the evaluation of the accuracies of the physical parameters should not be so important. The evaluation of observations of physical fields obtained at the earth's surface provides information on the geometry and physics of the formation to be investigated, or on the physical aspects only, if the boundaries of the body are defined as inhomogeneities in the distribution of the physical parameters.

A second category of complex interpretation has a much greater task than that outlined above. In this case it is attempted to utilize the physical parameters obtained not only in the description of the geologic-geotectonic formation itself, but also in the investigation of its genesis, its development, and generally in considerations concerning time variations of structure and geometry. These latter considerations shall not be further discussed here, because of the high degree of speculation involved; instead in what follows we address ourselves to the first category, i.e. to field interpretation.

In the present case, we are in essence dealing with electromagnetic phenomena. Therefore, first of all, complex interpretations of this type, together with the corresponding homology considerations, will be carried

out for the electromagnetic fields. To begin with, such problems arise in connection with electromagnetic inductive fields, i.e. in tellurics, magnetotellurics, and geomagnetic deep sounding. These methods are closely interlinked and permit a relatively simple complex interpretation to be carried out in a theoretical way. A further step forward in complex interpretation consists in the inclusion of magnetostatic fields, which may likewise provide valuable supplements to the above mentioned electromagnetic methods, provided that indications at the earth's surface are available. From electromagnetism, complex investigations also lead to the field of mechanics. Here three important applications of homology, and of the complex interpretation based on it, should be mentioned, namely gravimetry, geothermics, and seismology. Finally, the removal of the limitation to static, stationary, and quasi-stationary fields leads to the possibility of complex interpretation in case of dynamic fields as well, i.e. to the fields of electromagnetic induction methods and seismology.

Among the variety of methods available, we shall discuss in detail only one as an example, namely a serial test method (Fanselau 1969, 1973, 1974; Fanselau et al., 1972, Webers 1974), the structure of which clearly shows the features of complex interpretation and homology and thus has the above mentioned advantages of inverse interpretation.

In the following, we shall list the expressions of theoretical physics required in dealing with the various physical fields. Before these formulae are partially derived and discussed in detail, we shall begin with some generally valid remarks.

For all of the following investigations, we shall use a right-handed Cartesian coordinate system: x is positive on the upward semi-axis, y is positive to the right, z is positive to the rear. These coordinates are denoted by unprimed letters, if they define the position of the field point, which is identical with the measuring point. On the other hand, if we are dealing with volume or surface elements of the source region, these coordinates are written with primes. Further we have the general relations:

$$r^2 = x^2 + y^2 + z^2; \quad \varrho^2 = x^2 + y^2$$

and accordingly the same quantities written in primed coordinates for the source point. In addition,

$$R^2 = (x - x')^2 + (y - y')^2 + (z - z')^2 = \xi^2 + \eta^2 + \zeta^2$$

Correspondingly, for two dimensions, $P^2 = \xi^2 + \eta^2$. The volume element will be denoted by $d\tau$, where $d\tau = dx'dy'dz'$. A similar relation applies for the surface element $d\sigma$:

$$d\sigma_x = dy'dz'$$

and corresponding relations hold for the other surface elements.

In accordance with the character of this monograph, the following considerations will be mainly concerned with magnetic and electromagnetic fields (Fanselau and Lange, 1969; Fanselau, 1968, 1970, 1971; Fanselau and Treumann, 1966, 1968). Since, however, certain homology considerations will also be carried out, it will be useful to include other field types:

gravitational field, thermal field, and the stress and strain fields of seismology. For sake of a simple treatment, static fields such as the gravitational one will be considered first. For the gravitational potential W, the following relation generally applies as a solution of the Poisson differential equation:

$$W = \int \frac{\bar{k}}{R} \, d\tau \tag{1}$$

where

$$\bar{k} = f \cdot k$$

f = gravitational constant

k = density.

For the components of acceleration, we obtain from Eq. (1)

$$W_x = - \int \bar{k} \frac{x - x'}{R^3} \, d\tau \tag{2}$$

Correspondingly, for two dimensions we have:

$$w_x = - 2 \int \bar{k} \frac{x - x'}{P_z^2} \, d\sigma \tag{3}$$

Eq. (3) can be derived from Eq. (2) as follows: Suppose that in one direction the geological body, the density of which is assumed to be constant, extends in the shape of a cylinder of any cross section; then the integration over the source region can be carried out initially in this direction. Suppose further that the cylindrical body extends in the z-direction, then Eq. (2) can be written as:

$$W_x = - \int \bar{k}(x', y') \frac{x - x'}{R^3} \, d\sigma_z \, dz' = - \int \bar{k}(x', y') \frac{x - x'}{P_z^2} \left[\frac{z - z'}{R} \right]_{z_1'}^{z_2'} d\sigma_z \tag{3a}$$

Finally,

$$W_x = - \int \bar{k}(x', y') \frac{x - x'}{P_z^2} \left(\frac{1}{\sqrt{1 + \frac{P_z^2}{(z - z_2')^2}}} - \frac{1}{\sqrt{1 + \frac{P_z^2}{(z - z_1')^2}}} \right) d\sigma_z \tag{3b}$$

If, in Eq. (3b), the boundaries of the cylindrical body are very large compared to the other dimensions, the three-dimensional problem becomes a two-dimensional one. This is readily shown by expanding the roots in the denominator of Eq. (3b) into a Taylor series and passing to the limit for large values of z_1' and z_2'. This leads directly to Eq. (3).

Later on, in connection with homology considerations, we shall return to the formulae concerning the gravitational field, which have been stated here in brief.

Another static field is the magnetostatic one. This can be derived,

similarly to the gravitational field, from a scalar potential V:

$$V^{(s)} = \frac{1}{4\pi} \int (\mathbf{M}, \nabla') \frac{1}{R} d\tau \tag{4}$$

Here **M** denotes the vector of volume magnetization. As usual, the field strength of this static magnetic field is given as

$$H^{(s)} = - \nabla V^{(s)} \tag{5}$$

In this case, too, one easily passes to two-dimensional considerations as in the case of gravitational potential. The magnetostatic potential V^s can be treated in a way analogous to that used above for the field strength W_x. From Eq. (4) we obtain:

$$v^s = - \frac{1}{2\pi} \int \left(\mathbf{M}(x', y'), \nabla'\right) \ln P \, d\sigma \tag{4a}$$

where v^s in Eq. (4a) means the two-dimensional magnetic potential.

The magnetostatic potential $V^{(s)}$ can also be expressed by means of two other magnetostatic parameters: the magnetic volume density ϱ_m and the magnetic surface density o_m. Both quantities are of purely macroscopic, phenomenological character. They are related to the volume magnetization in the following way:

$$\varrho_m = - \operatorname{div} \mathbf{M} \quad \text{and} \quad o_m = - \mathbf{M}_v \tag{6}$$

With the use of ϱ_m and o_m, the magnetostatic field is written as follows:

$$V = \frac{1}{4\pi} \int \frac{\varrho_m}{R} \, d\tau + \frac{1}{4\pi} \int \frac{o_m}{R} d\sigma \tag{7}$$

In contrast to

$$\int \bar{k} \, d\tau \neq 0 \quad \text{we have} \quad \int \varrho_m \, d\tau = \int o_m \, d\sigma = 0 \tag{8}$$

After these introductory remarks on static fields, we shall now discuss the electromagnetic fields in somewhat greater details. By their very nature, all three of these methods are comprised in the Maxwell equations of electrodynamics. If we restrict ourselves to stationary fields, the following laws and material equations are required for the calculations (Fanselau and Treumann, 1966, 1968; Fanselau, 1970, 1971):

The law of induction

$$\dot{\mathbf{B}} = - \operatorname{curl} \mathbf{E} \tag{9}$$

the Biot–Savart law

$$\mathbf{H} = \frac{1}{4\pi} \int \left[\nabla \frac{1}{R}, \mathbf{I}\right] d\tau = \frac{\mathbf{I}}{4\pi} \mathbf{p}; \quad \mathbf{p} = \int \left[\nabla \frac{1}{R} d\mathbf{r}'\right] \tag{10}$$

he extended form of Ohm's law

$$E = IW + \dot{I}L \tag{11}$$

Moreover, the following material equations should be noted:

$$\mathbf{B} = \mu\mathbf{H}; \quad \mathbf{I} = \lambda\mathbf{E}; \quad I = \int \mathbf{I}_r \, d\sigma; \quad d = \frac{4\pi}{\sqrt{2\omega\mu\lambda}} \tag{12}$$

(penetration depth)

The three electromagnetic methods of geophysics differ in the selection of the elements used for interpretation. While the telluric method uses the quantities E and I, where I has to be determined by additional measurements, I is replaced by $\mathbf{H}^{(i)}$ in the field of magnetotellurics. Here $\mathbf{H}^{(i)}$ means that part of the geomagnetic field which is caused by the geological body, i.e. the part originating in the earth's interior. Finally, in the field of geomagnetic deep sounding, E is replaced by $\mathbf{H}^{(a)}$, where $\mathbf{H}^{(a)}$ represents the external part of the geomagnetic field, originating in the ionosphere or the magnetosphere.

Using the above-mentioned laws, we obtain the following picture for the individual methods.

TELLURICS

After elimination of periodic time dependence, one obtains from Eq. (11):

$$|E_z| \, e^{i\chi} = |I_z| \, e^{i\psi^T} \sqrt{W_z^2 + \omega^2 L_z^2} \, e^{i\varphi}, \quad \varphi = \arctan \frac{\omega L_z}{W_z} \tag{13}$$

and hence, separated according to absolute value and phase:

$$\frac{|E_z|}{|I_z|} = \sqrt{W_z^2 + \omega^2 L_z^2} \tag{14a}$$

$$\chi = \psi^T + \arctan \frac{\omega L_z}{W_z} \tag{14b}$$

For sake of simplicity, in the above equations it has been assumed that the voltage tapping for E is carried out in the z-direction. For this reason all quantities which are, properly speaking, of scalar character, should be given the index z in order that anisotropic situations should not be excluded a priori. Together with E, also I has the index z, and likewise the material parameters W and L.

In the phase relation (14b), χ can be set equal to zero as a reference point for phase counting. Since, as has already been pointed out, I_z cannot be directly measured, the relations (14a) and (14b) can be valued only theoretically and serve as analogues for the methods described below, i.e. for magnetotellurics and geomagnetic sounding.

MAGNETOTELLURICS

As has already been mentioned, the uncertainty introduced into the telluric method by I_z is avoided here by making use of the Biot–Savari law, Eq. (10). This law replaces the current flowing in the earth's interior by the magnetic field generated by it. Analogously to Eq. (13) one obtains

$$E_z = \frac{4\pi \mathbf{H}_x^{(i)}}{\mathbf{p}_x}(W_z + i\omega L_z) = \frac{4\pi \mathbf{H}_y^{(i)}}{\mathbf{p}_y}(W_z + i\omega L_z) \tag{15}$$

and passing to absolute value and phase produces

$$|E_z|\, e^{i\chi} = \frac{4\pi}{|\mathbf{p}_x|\, e^{i \arg \mathbf{p}_x}} |\mathbf{H}_x^{(i)}|\, e^{i\psi_x} \sqrt{W_z^2 + \omega^2 L_z^2}\, e^{i\varphi} \tag{15a}$$

$$|E_z|\, e^{i\chi} = \frac{4\pi}{|\mathbf{p}_y|\, e^{i \arg \mathbf{p}_y}} |\mathbf{H}_y^{(i)}|\, e^{i\psi_y} \sqrt{W_z^2 + \omega^2 L_z^2}\, e^{i\varphi} \tag{15b}$$

Finally, from Eqs (15a) and (15b) the absolute values and phases can be expressed as:

$$\frac{|E_z|}{|\mathbf{H}_x^{(i)}|} = \frac{4\pi}{|\mathbf{p}_x|} \sqrt{W_z^2 + \omega^2 L_z^2}; \quad \chi - \psi_x = \arctan \frac{\omega L_z}{W_z} - \arg \mathbf{p}_x \tag{16a}$$

$$\frac{|E_z|}{|\mathbf{H}_y^{(i)}|} = \frac{4\pi}{|\mathbf{p}_y|} \sqrt{W_z^2 + \omega^2 L_z^2}; \quad \chi - \psi_y = \arctan \frac{\omega L_z}{W_z} - \arg \mathbf{p}_y \tag{16b}$$

where again we may set $\chi = 0$ as an initial point for phase counting. For practical calculations the real and imaginary parts of Eqs (15a) and (15b) can be treated separately. For the real part we obtain:

$$|E_z| \cos \chi = \frac{4\pi}{\mathbf{p}_x} |\mathbf{H}_x^{(i)}| [W_z \cos \psi_x - \omega L_z \sin \psi_x] \tag{17a}$$

and for the imaginary part:

$$|E_z| \sin \chi = \frac{4\pi}{\mathbf{p}_x} |\mathbf{H}_x^{(i)}| [W_z \sin \psi_x + \omega L_z \cos \psi_x] \tag{17b}$$

Now, in Eqs (17a, b) we may again set $\chi = 0$. After dividing by $\mathbf{H}_x^{(i)}$ one ebtains

$$\frac{|E_z|}{|\mathbf{H}_x^{(i)}|} = \frac{4\pi}{\mathbf{p}_x}(W_z \cos \psi_x - \omega L_z \sin \psi_x) \tag{18a}$$

$$0 = \frac{4\pi}{\mathbf{p}_x}(W_z \sin \psi_x + \omega L_z \cos \psi_x) \tag{18b}$$

In all equations of magnetotellurics, in addition to the vertical component of the internal field, $\mathbf{H}_x^{(i)}$, the horizontal component $\mathbf{H}_y^{(i)}$ has also been

formally included. As a matter of fact, it is required in this case in much the same way as in geomagnetic deep sounding that from the first only the vertical component should apply to the internal field, whereas the horizontal components $\mathbf{H}_y$ and $\mathbf{H}_z$ apply to the external field only. Unless we intend to carry out any test calculations with $\mathbf{H}_y$, $\mathbf{H}_y^{(i)}$ should be set equal to zero everywhere in the preceding equations.

It should be pointed out that Eq. (18b) can also be written as follows:

$$\tan \psi_x = -\frac{\omega L_z}{W_z} \tag{18c}$$

The method of *geomagnetic deep sounding* goes one step further. Here not only I is connected with the internal magnetic field by the Biot–Savart law, but also E is related to the external, inducing magnetic field. Hence, the theoretical treatment of this method is based on the assumption that it is possible to distinguish between $\mathbf{H}^{(i)}$ and $\mathbf{H}^{(a)}$. So, first of all it must be investigated how such a separation — even though it is approximate — can be carried out, or at least how could it be made plausible that the absolute values of certain components are numerically dominant in the internal field. The methods which can be used for that purpose will not be discussed here in detail.

In view of these suppositions, the law of induction (9) has to be included in the calculation as the third physical law. If Eq. (9) is integrated over a surface which is influenced by an inducing component of $\mathbf{H}^{(a)}$, the following relation is obtained:

$$\int \mu(\mathbf{n}, \dot{\mathbf{H}}^{(a)}) d\sigma = -\int (\mathbf{n}, \operatorname{curl} \mathbf{E})\, d\sigma = -\oint \mathbf{E} d\mathbf{r} = -E \tag{19}$$

If $\dot{\mathbf{H}}^{(a)}$ does not vary within the surface considered, and if the surface itself is not subject to any time variations, Eq. (19) can be written as follows:

$$-\mu\omega q\, e^{i\frac{\pi}{2}} (\mathbf{n}, \mathbf{H}^{(a)}) = E = I(W + i\omega L) = \frac{4\pi \mathbf{H}_x^{(i)}}{\mathbf{p}_x} (W + i\omega L) \tag{20}$$

where q means $\int d\sigma$. On the right-hand-side of Eq. (20), both the extended form of Ohm's law and the Biot–Savart law have been used to eliminate E and I — see Eqs (10) and (11). Moreover, as already indicated above, a separation between the external inducing and the internal induced field has been carried out in the following way: $\mathbf{H}^{(a)}$ has only the two components $\mathbf{H}_y^{(a)}$ and $\mathbf{H}_z^{(a)}$, while $\mathbf{H}^{(i)}$ has the single component $\mathbf{H}_x^{(i)}$. As already mentioned, it should be examined to what extent this restriction applies in each case. In Eq. (20), the following expression occurs:

$$(\mathbf{n}, \mathbf{H}^{(a)}) = \alpha \mathbf{H}_x^{(a)}) + \beta \mathbf{H}_y^{(a)} + \gamma \mathbf{H}_z^{(a)} \tag{21}$$

where α, β, γ are the direction cosines of the unit vector of the surface normal. It should, however, be taken into consideration that, according to the assumptions about the separation of internal and external field, in

the present case $\mathbf{H}_x^{(a)}$ is identical to zero. Thus the inner product consists of only two terms, i.e.

$$(\mathbf{n}, \mathbf{H}^{(a)}) = \beta \mathbf{H}_y^{(a)} + \gamma \mathbf{H}_z^{(a)} \tag{22}$$

If, observing the given suppositions, the absolute values and phases of the complex quantities are introduced into Eq. (20), one obtains:

$$-\frac{\mu}{4\pi}\omega q \mathfrak{p}_x e^{i\left(\frac{\pi}{2}-\varphi\right)} \frac{1}{\sqrt{W^2+\omega^2 L^2}} (\beta |\mathbf{H}_y^{(a)}| e^{i\psi_y^a} + \gamma |\mathbf{H}_z^{(a)}| e^{i\psi_z^a}) = |\mathbf{H}_x^{(i)}| e^{i\psi} \tag{23}$$

Just as in Eq. (15), also here the absolute values and phases can be separated. We shall not explicitely state these formulae, but rather proceed to the separate treatment of the real and imaginary partial equations. For the real partial equation, we have

$$\begin{aligned} |\mathbf{H}_x^{(i)}| \cos\psi = A\{\omega L(\beta |\mathbf{H}_y^{(a)}| \cos\psi_y^a + \gamma |\mathbf{H}_z^{(a)}| \cos\psi_z^a) - \\ - W(\beta |\mathbf{H}_y^{(a)}| \sin\psi_y^a + \gamma |\mathbf{H}_z^{(a)}| \sin\psi_z^a)\} \end{aligned} \tag{24a}$$

or also

$$\mathbf{H}_x^{(i)}| \cos\psi = A \sqrt{W^2+\omega^2 L^2}\, \{\beta |\mathbf{H}_y^{(a)}| \sin(\varphi - \psi_y^a) + \gamma |\mathbf{H}_z^{(a)}| \sin(\varphi - \psi_z^a)\} \tag{24b}$$

Correspondingly, one obtains for the imaginary partial equation:

$$\begin{aligned} |\mathbf{H}_x^{(i)}| \sin\psi = A\{\omega L(\beta |\mathbf{H}_y^{(a)}| \sin\psi_y^a + \gamma |\mathbf{H}_z^{(a)}| \sin\psi_z^a) + \\ + W(\beta |\mathbf{H}_y^{(a)}| \cos\psi_y^a + \gamma |\mathbf{H}_z^{(a)}| \cos\psi_z^a)\} \end{aligned} \tag{25a}$$

or also

$$|\mathbf{H}_x^{(i)}| \sin\psi = A \sqrt{W^2+\omega^2 L^2}\, \{\beta |\mathbf{H}_y^{(a)}| \cos(\varphi - \psi_y^a) + \gamma |\mathbf{H}_z^{(a)}| \cos(\varphi - \psi_z^a)\} \tag{25b}$$

where

$$A = -\frac{\mu}{4\pi}\omega q \mathfrak{p}_x \frac{1}{W^2+\omega^2 L^2} \quad \text{and} \quad \varphi = \arctan\frac{\omega L}{W}$$

The further considerations will be restricted to Eqs (24a) and (24b). Here again we may set $\psi = 0$. Further it should be taken into account that β and γ are the direction cosines of the external field being effective in two dimensions.

$$\mathbf{H}_x^{(a)} = 0$$

Consequently

$$\cos\vartheta = \beta \quad \text{and} \quad \sin\vartheta = \gamma$$

From Eq. (24a):

$$\begin{aligned} |\mathbf{H}_x^{(i)}| = A\{\cos\vartheta |\mathbf{H}_y^{(a)}| (\omega L \cos\psi_y^a - W \sin\psi_y^a) + \\ + \sin\vartheta |\mathbf{H}_z^{(a)}| (\omega L \cos\psi_z^a - W \sin\psi_z^a)\} \end{aligned} \tag{26}$$

or, in a more concise form,

$$|\mathbf{H}_x^{(i)}| = a \cos \vartheta\, |\mathbf{H}_y^{(a)}| + b \sin \vartheta\, |\mathbf{H}_z^{(a)}| \tag{27}$$

where

$$a = A(\omega L \cos \psi_y^a - W \sin \psi_y^a); \quad b = A(\omega L \cos \psi_z^a - W \sin \psi_z^a) \tag{28}$$

The imaginary partial equation (25b) can be similarly discussed. As $\psi = 0$ in this case, consequently one obtains

$$\frac{\gamma}{\beta} = \tan \vartheta = -\frac{|\mathbf{H}_y^{(a)}|}{|\mathbf{H}_z^{(a)}|} \frac{\cos(\varphi - \psi_y^a)}{\cos(\varphi - \psi_z^a)} \tag{29}$$

The question arises whether the quantity q, which has occurred in the derivation of the formulae for geomagnetic deep sounding in Eq. (20), can be replaced by other data, since it is at once clear that no numerical value of q can be determined by geomagnetic deep sounding. Instead of substituting $\mathbf{H}^{(i)}$ for E in Eq. (20) by means of the Biot–Savart law as in geomegnatic deep sounding, it could be attempted to couple $\mathbf{H}^{(a)}$ with E directly, in the sense of a *modified magnetotellurics*. If the laws of geomagnetic deep sounding are coupled with those applying to this modified magnetotellurics, it would be possible to eliminate q and ϑ. This would require, however, that magnetotelluric measurements were carried out simultaneously with geomagnetic deep sounding. Here, of course, the magnetotelluric profile must be perpendicular to the profiles of the geomagnetic deep soundings. As pointed out above, one obtains then a new, known datum, i.e. quantity E. To eliminate ϑ analytically it is determined from the first relation in Eq. (20). Writing out Eq. (20) in terms of absolute value and phase, one obtains

$$-\mu\omega q\, e^{i\frac{\pi}{2}}(\beta\, |\mathbf{H}_y^{(a)}|\, e^{i\psi_y^a} + \gamma\, |\mathbf{H}_z^{(a)}|\, e^{i\psi_z^a}) = |E|\, e^{i\chi} \tag{30}$$

One may pass again to real and imaginary partial equations and set $\chi = 0$. The real part is given by

$$\mu\omega q\, (\cos \vartheta\, |\mathbf{H}_y^{(a)}|\, \sin \psi_y^a + \sin \vartheta\, |\mathbf{H}_z^{(a)}|\, \sin \psi_z^a) = |E| \tag{31a}$$

Similarly to the geomagnetic deep soundings in Eq. (27) it is possible to write Eq. (31a) as follows:

$$a_1 \cos \vartheta\, |\mathbf{H}_y^{(a)}| + b_1 \sin \vartheta\, |\mathbf{H}_z^{(a)}| = |E| \tag{31b}$$

The above considerations will now be followed by establishing some homologous relationships between the derived laws. From among the various possibilities, we will give homologous couplings between the gravimetric potential on the one hand and magnetostatic potential v^s as well as the magnetic field strengths $\mathbf{H}^{(i)}$ generated by currents on the other. In this context homology means that the analytical form of the mathematical law is the same for two physical fields, whereas the respective physical quantities are different. This relationship will be denoted by the sign of

homology $\approx$. It is possible to derive the following interesting relationships, which are, perhaps, not of merely formal character, but express also the physical law, especially in case of magnetic fields. As it may be observed from the foregoing, this law is different for magnetostatic fields and stationary magnetic fields. For static fields we obtain:

$$V^{(s)} \approx (\nabla W, \mathbf{e}); \quad \mathbf{H}^{(s)} = -\nabla V^{(s)} \tag{32}$$

and correspondingly for stationary magnetic fields, i.e. for magnetic fields generated by stationary electric currents:

$$\mathbf{H}^{(i)} \approx [\nabla W, \mathbf{e}] \quad \text{where} \quad \mathbf{e} = (1, 1, 1) \tag{33}$$

In the inverse interpretation of geophysical profiles, we seldom if ever have closed mathematical expressions. Instead we have to use approximate representations of these exact formulae. In this case it does not matter in principle what sort of series is used. Naturally, no infinite series can be used: the number of terms must be restricted for numerical-technical reasons. These finite series are then appropriately called polynomials. In what follows, we will list some expressions of this kind, restricting ourselves to two dimensions. These series can be directly derived from the mathematical expressions given above. The following is obtained:

$$w_a = -2\left(\ln \varrho \int \bar{k} d\sigma - \sum_{n=1}^{\infty} \frac{1}{n\varrho^n} (a_n \cos n\varphi + b_n \sin n\varphi)\right) \tag{34}$$

Here w_a is the two-dimensional gravitation potential for the mass-free external space. From Eq. (34) we obtain the following relations for the components of acceleration:

$$w_{xa} = -2 \sum_{n=0}^{\infty} \frac{1}{\varrho^{n+1}} \left(a_n \cos (n+1)\varphi + b_n \sin (n+1)\varphi\right) \tag{35a}$$

$$w_{ya} = -2 \sum_{n=0}^{\infty} \frac{1}{\varrho^{n+1}} \left(a_n \sin (n+1)\varphi - b_n \cos (n+1)\varphi\right) \tag{35b}$$

The corresponding expressions for the mass-free internal space read as follows:

$$w_i = -2\left(\int \bar{k} \ln \varrho d\sigma - \sum_{n=1}^{\infty} \frac{1}{n} \varrho^n (c_n \cos n\varphi + d_n \sin n\varphi)\right) \tag{36}$$

and correspondingly, for the components of acceleration,

$$w_{xi} = 2 \sum_{n=0}^{\infty} \varrho^n (c_{n+1} \cos n\varphi + d_{n+1} \sin n\varphi) \tag{37a}$$

$$w_{yi} = 2 \sum_{n=0}^{\infty} \varrho^n (c_{n+1} \sin n\varphi - d_{n+1} \cos n\varphi) \tag{37b}$$

Here the terms a_n, b_n, c_n and d_n are abbreviations for the source-point quantities (the so-called moments):

$$\left.\begin{matrix} a_n \\ b_n \end{matrix}\right\} = \int \bar{k}\, \varrho'^n \begin{matrix} \cos n\,\varphi' \\ \sin n\,\varphi' \end{matrix} d\sigma \tag{38a}$$

$$\left.\begin{matrix} c_n \\ d_n \end{matrix}\right\} = \int \bar{k} \frac{1}{\varrho'^n} \begin{matrix} \cos n\varphi' \\ \sin n\varphi' \end{matrix} d\sigma \tag{38b}$$

For sake of completeness, we shall state the series expressions for arbitrary gradients of w_a. For the gradient of the j-th order, one obtains (Webers, 1969, 1974):

$$w_{\underbrace{x \ldots x}_{j} a} = (-1)^j 2 \sum_{n=j}^{\infty} \prod_{l=0}^{j-2} (n-l-1) \frac{1}{\varrho^n} (a_{n-j} \cos n\,\varphi + b_{n-j} \sin n\,\varphi)\,; j > 1 \tag{39}$$

If we make use of the homology-relations to pass on the other fields considered here, we obtain identical series expansions, where only the source-point quantities have a different physical meaning. Therefore, in order to distinguish between the respective source-point terms, from now on we shall identify the terms applying to the gravitational field, a_n, b_n, c_n and d_n, by means of an upper index. In the form restricted to the external field, the *homology relations* read as follows:

Magnetostatics:

$$\mathbf{H}_x^S \approx w_{xx}\,; \quad \mathbf{H}_y^S \approx w_{xy} \tag{40}$$

Magnetotellurics:

$$\mathbf{H}_x^{MT} \approx w_y\,, \quad \mathbf{H}_y^{MT} \approx w_x \tag{41}$$

Geomagnetic deep sounding:

$$\mathbf{H}_x^{TS} \approx w_y\,, \quad \mathbf{H}_y^{TS} \approx w_x \tag{42}$$

According to the above stipulations, the notations a_n^S, b_n^S, a_n^{MT}, b_n^{MT}, a_n^{TS}, b_n^{TS} apply in Eqs (40), (41) and (42), respectively. In detail we have:

$$a_n^S = \frac{1}{2\pi} \int (\mathbf{M}_x - \mathbf{M}_y \tan\varphi')\, \varrho'^n \cos n\,\varphi'\, d\sigma \tag{43}$$

$$b_n^S = \frac{1}{2\pi} \int (\mathbf{M}_x + \mathbf{M}_y \cot\varphi')\, \varrho'^n \sin n\,\varphi'\, d\sigma$$

$$\left.\begin{matrix} a_n^{MT} \\ b_n^{MT} \end{matrix}\right\} = E_z \frac{1}{4\pi} \int \frac{1}{\sqrt{W^2 + \omega^2 L^2}} \varrho'^n \begin{matrix} \cos n\,\varphi' \\ \sin n\,\varphi' \end{matrix} d\sigma \tag{44}$$

$$\left.\begin{matrix} a_n^{TS} \\ b_n^{TS} \end{matrix}\right\} = -\int \frac{\mu}{4\pi} \omega q \frac{1}{W^2 + \omega^2 L^2} \{(\omega L \cos\psi_y^a - W \sin\psi_y^a) \cos\vartheta\, |\mathbf{H}_y^{(a)}| + (\omega L \cos\psi_z^a - W \sin\psi_z^a) \sin\vartheta\, |\mathbf{H}_z^{(a)}|\}\, \varrho'^n \begin{matrix} \cos n\varphi' \\ \sin n\varphi' \end{matrix} d\sigma \tag{45}$$

For tellurics and modified magnetotellurics, similar expansions cannot be given, at least not in the analytical form chosen in this case. In Eqs (40), (41) and (42) we used the sign of homology in order to express that the form of the mathematical law is the same on both sides, whereas the physical meaning is different. The sign of homology used in these equations can therefore be replaced by an equality sign if, in the series expansions for w, a_n^G and b_n^G are replaced by the respective source-point parameters for $\mathbf{H}^S$, $\mathbf{H}^{MT}$ and $\mathbf{H}^{TS}$.

In order to utilize the homology relations (40), (41) and (42) for interpretation purposes, it is convenient to use an interpretation method which would provide for an expansion into a series. The problem in using such series is that the point of origin where this expansion is referred to, can be selected arbitrarily. Naturally, the calculated numerical values of a finite number of the source-point parameters a_n, b_n, which will finally be used in the calculation of the geometrical and physical properties of the source region, depend on the selection of this origin. This numerical uncertainty is eliminated by a recently developed serial test method (Fanselau, 1974; Fanselau et al., 1970; Lange, 1967; Webers, 1969, 1974), which provides for varying the position of the point of origin used for the interpretation. For example, let us briefly characterize the numerical procedure in case of Eq. (35a) for w_{xa}.

For a given position of the origin of the coordinate system used, in Eq. (35a) a_n^G and b_n^G are the required unknowns, i.e. the source-point factors of the individual terms of the series or the moments. The numerical values of the test-point factors, which are characterized by ϱ and φ, are given in this equation. In addition, the measured numerical values of w_{xa} are known for a great number of measuring points when preparing a two-dimensional profile. Consequently, the source point factors or moments have to be calculated according to the method of least squares. Together with the moments the errors of these quantities as well as the $[vv]$ of the total curve fitting are also obtained. Of course these numerical values vary within the bounds of variability of the origin selected for the coordinate system.

In practice a complete grid of such origin positions will be used for interpretation. For all positions of the origin the truncated potential series is used up to some fixed order n_0. Now the errors of the moments as well as the $[vv]$ are utilized in a very simple way for determining the optimum position of the origin. Such a position will be reached when the sum of squared errors reaches a minimum. It yields the physically most significant numerical values of the first moments, so that the above mentioned numerical uncertainty is eliminated. It yields the best series convergence as well. Of course, for the purpose of interpretation, we can try further possibilities of varying the method. To begin with, the order n_0 of the series can be varied and the results obtained with different numbers of terms, i.e. with different convergence conditions, can be compared, especially as regards their variability with respect to the choice of the origin. A third possibility of variation lies in the selection of the coordinate system, i.e. in selecting the form of the approximating body.

It should be mentioned that the moments of the potential series have a

physical meaning in gravimetry: total mass, centre of gravity, principal moments of inertia, and principal axes of inertia. The same applies for higher order moments. All these quantities are definitely coupled with the profile; hence they are not ambiguous and do not represent any *a priori* restriction of the uncertainty encountered in the solution of the inverse problem. The question of ambiguity proper does not arise until the available moments are to be utilized in the final determination of the mass distribution and the geometric shape of the source region. In this case, too, the variability of the origin of the coordinate system is of importance. From the distribution of the errors of moments certain geometric quantities can be approximately determined, so that a rough approximation of the disturbing body can be obtained. As has already been pointed out, this postulates *a priori* selection of the coordinate system and so leads to a certain kind of approximation. Thus, in the simplest case, Cartesian coordinates are connected with the rectangular approximation of a source region of any shape.

Let us point out an other important aspect of the method which has been described in brief. According to Eq. (35a), the vertical component of the gravitational field $w_{x\alpha}$ has been used in the discussion of the method. Varying the position of the origin will produce the result that the law for the mass-free external space is not always applicable to the complete profile. Translating the origin certain parts of the profile will get into the region of the mass field and even into that of the mass-free internal field. If the law governing the external field is used in the curve fitting procedure, this will result in series which are less and less convergent and may even diverge. This shows up in the calculated numerical values of the moments, in the error values, and finally in the residues, when the series is used to carry out a reverse calculation, i.e. a synthesis of the profile, and the difference between observed and synthetized values is called a residue. Especially when higher moments are used, the positions of the circles of convergence can be approximately determined for the applicable law. These circles of convergence give valuable indications of the location of the disturbing region. Of course it is possible to make an *a priori* set-up for the source-point parameters as being produced by an inhomogeneous distribution of the physical quantity in question. The mathematical form of this inhomogeneity is best expressed by a power series or a polynomial, which of course must be matched to the given coordinate system. In view of the ambiguity, a non-constant distribution sometimes means a considerable restriction. It should be noted that the homologous equations given by (40), (41) and (42) for the two-dimensional case are contained as a special case in the general three-dimensional relations (32) and (33).

Let us add some remarks as to why the test method described is most suitable for complex interpretation. In their homologous structure, Equations (40), (41) and (42) show the same analytical, and hence also numerical, character. This means that the programs developed for numerical evaluation can be used immediately for a profile of any type. The point here is that the profiles can be evaluated with nearly the same relative accuracy, further that the number of measuring values used within such a profile is nearly the same, and finally that also the metrics of the coordinate systems employed coincide. In such cases a uniform evaluation of the

profiles yields exactly comparable parameters in the sense of complex interpretation. Naturally, the physical meaning of these parameters differs from one profile to another, but in all of these cases one has the possibility to determine the geometrical and physical parameters of the respective source regions. As has already been mentioned, the same numerical methodology of evaluation yields not only the same parameters, but also the same errors of the latter and, above all, the same variation of all these quantities within the grid of origins. Of course several quite different physical facts have to be previously harmonized, above all the selection of a suitable origin on the basis of the least squares error sum. It cannot be taken for granted that the "centres of gravity" of the different profiles will prove indentical; instead, certain differences will appear from the beginning which will have to be taken into account in the above mentioned comparisons. In principle the test method described yields a separate evaluation of the different profiles on a uniform mathematical basis. But it is just this fact which makes possible to carry out a detailed comparison of the source-point parameters of all of these profiles.

In the developments reported hitherto a potential series has always been used in the test method. The selection of such a series is necessary in order to give the source-point parameters a certain physical meaning. However, particularly in Cartesian coordinates the Taylor development of R^{-1} does not require the use of orthogonal function systems. Therefore, it is obvious that the obtained course of a profile can also be expanded into a series of orthogonal functions. In the three-dimensional case this leads to a series of Laplace's spherical harmonic functions, in the two-dimensional case to trigonometric functions. As with all systems of orthogonal functions, the numerical values of the source-point factors remain unchanged, when the series is extended to higher orders. However, there are some other difficulties, especially with the systems of orthogonal functions just mentioned above. On the one hand the source-point parameters in the form obtained cannot be directly evaluated with respect to the geometry and physics of the source region. On the other hand, there is no possibility for an analogous variation as has been done in case of the Cartesian development through the selection of the coordinate origin. If, for sake of simplicity, we consider again the two-dimensional case, we have the trigonometrical series mentioned above. In this case, too, there are certain possibilites of variation, which relate mainly to the extension of the interval from 0 to 2π and to its position in relation to the profile. Here, too, then, it is possible to consider certain optimization problems concerning the metrics of the domain of definition of the orthogonal functions as well as the position of the point of symmetry for this interval. But on no account can, at the end of interpretation, the transition from the constituents of the polar development to the source-point parameters of the terms of the Cartesian series be avoided. As regards the formulae themselves, this transition is elementary. The above mentioned benefit of using orthogonal functions in the expansion of the profile will, however, be lost. Naturally, the finally calculated source-point factors of the terms of the Cartesian series will depend again on the extension of the series. Of course the extensions of the two types of series have to be matched.

In this connection we should briefly point out the possibility of using natural orthogonal functions. Although such natural orthogonal functions have a statistical character, they can be very useful in many ways. Above all the derivation of natural orthogonal functions appears quite possible within the numerical procedure of the test method, and in this way we may also find additional indicative material for a complex interpretation.

Finally we will list some homologous relations between electromagnetic interpretation methods and the thermal and seismic processes. For sake of brevity, let it be permitted to restrict homologous relations between seismology and the electromagnetic methods to magnetotellurics. We will only state the corresponding field equations in their homologous form, as to the further handling of interpretation, we refer to Chauveau (1967). For sake of simplicity, suppose that the electric field strength has a component in the y-direction only, the corresponding H-component pointing only in the z-direction. Suppose that these two components are only variable in the vertical direction, i.e. in the x-direction. The transversal electromagnetic waves are governed by the two Maxwell equations; when the above mentioned simplifications are taken into consideration and a Fourier transformation is carried out, these Maxwell equations become:

$$\frac{\partial^2 H}{\partial x^2} = -\mu(\varepsilon\omega^2 + i\omega\lambda)H \tag{46}$$

$$E = \frac{1}{\varepsilon\omega i - \lambda}\frac{\partial H}{\partial x} \tag{47}$$

The corresponding homologous equations of seismology are, on the one hand, the fundamental equations for the propagation of vibrations in deformable bodies, and on the other hand Hooke's law. After Fourier transformation, these two equations likewise read as follows:

$$\frac{\partial^2 U}{\partial x^2} = -\frac{\omega^2}{v^2}U \tag{48}$$

$$P = kv^2\frac{\partial U}{\partial x} \tag{49}$$

Equations (48) and (49) describe the behaviour of longitudinal waves. The symbols used have the following meaning: U is the Fourier transform of the deformation, k is density, v the velocity of propagation, P the Fourier transform of stress. From the two sets of Equations (46), (47) and (48), (49), the corresponding physical quantities are readily identified. It should be noted in addition that the laws derived above for magnetostatics have not been directly obtained from the equations of oscillation of the electromagnetic field, but rather with the assumption of stationary processes. Of course these two approaches are practically identical, but have to be matched to the homologous character. Since it is homology to seismology

which is being discussed here, the homology has to be obtained directly from the equations of oscillation.

For thermal fields, homologous relations to both magnetotellurics (46) and seismology (48) can also be established. Carrying out a Laplace transformation, the physical law of the thermal field — i.e. the equation of heat conduction — reads as follows:

$$\frac{\partial^2 \Theta}{\partial x^2} = -\frac{\alpha k C}{\lambda} \Theta, \quad \alpha > 0 \tag{50}$$

where Θ means the Laplace transform of the temperature, C is specific heat, and λ is thermal conductivity.

REFERENCES

CHAUVEAU, J., 1967. Sur l'analogie des calculs d'un sismogramme et d'un sondage magnétotellurique théorique. *Ann. Geophys.* **23**, 4–60.

FANSELAU, G., 1968. Zur Problematik der geophysikalischen Forschung. *Leopoldina* **14**, 105–109.

FANSELAU, G., 1969. Testverfahren zur Deutung geophysikalischer Meßprofile. *Acta Geod. Geophys. Mont. Hung.* **4**, 397–413.

FANSELAU, G., 1970. Theoretical aspects of electromagnetic induction methods. *Acta Geod. Geophys. Mont. Hung.* **5**, 423–428.

FANSELAU, G., 1971. Remarks on Magnetotellurics. *Gerlands Beitr. z. Geophys.* **80**, 383–390.

FANSELAU, G., 1972. Über Invariantenbildung bei höheren Momenten. *Gerlands Beitr. z. Geophys.* **81**, 281–286.

FANSELAU, G., 1973. On the Problem of Ambiguity. *Gerlands Beitr. z. Geophys.* **82**, 164–165.

FANSELAU, G., 1974. Über die Ambiguität in einem Reihentestverfahren mit Variabilität des Koordinatenursprungspunktes. *Gerlands Beitr. z. Geophys.* **83**, 163–169.

FANSELAU, G., 1975a. Über ein Testverfahren zur Interpretation geophysikalischer Profile. *Geofys. Sb.* (in press).

FANSELAU, G., 1975b. Zum Problem der Ambiguität und Approximation bei inverser Interpretation. *Veröff. Zentralinst. Physik der Erde* (in press).

FANSELAU, G., BALLANI, L., 1975. Komplexinterpretation mit Hilfe der elektrodynamischen Verfahren in der Geophysik. *Z. angew. Geol.* **21**, 222–226.

FANSELAU, G., LANGE, G., 1969. Zur Profildeutung statischer Potentialfelder. *Z. Geophys. u. Geol.* **14**.

FANSELAU, G., RITTER, E., WEBERS, W., WOLTER, H., 1970. Verwendung von Reihen als numerisches Testverfahren. *Geod. u. Geophys. Veröff. NKGG, Ser.* **3**, No. 16.

FANSELAU, G., RITTER, E., WEBERS, W., 1972. Geomagnetische Tiefensondierungen in der Slowakei. Wiss. Techn. Informationen des ZGI. Sonderheft 5.

FANSELAU, G., TREUMANN, R., 1966. Zur geomagnetischen Tiefensondierung. *PAGEOPH.* **65**, 54–72.

FANSELAU, G., TREUMANN, R., 1968. Untersuchungen zur Interpretation der Ergebnisse geomagnetischer Tiefensondierungen. *Z. Geol.* **17**, 76–92.

LANGE, G., 1967. Ein Verfahren zur dreidimensionalen Interpretation gravimetrischer Anomalien. M. Sc. Thesis, Karl-Marx-Universität, Leipzig.

WEBERS, W., 1969. Reihenentwicklungen zur Interpretation von Potentialfeldern. M. Sc. Thesis, Humboldt-Universität, Berlin.

WEBERS, W., 1974. Mathematisch-physikalische Aspekte eines Reihentestverfahrens. Dissertation, Potsdam.

CHAPTER 3

ELECTRICAL PROPERTIES OF ROCKS AT HIGH TEMPERATURES AND PRESSURES

By

M. P. VOLAROVICH and E. I. PARKHOMENKO

ELECTRICAL RESISTIVITY OF ROCKS FORMING THE SEDIMENTARY COVER OF THE EARTH'S CRUST DEPENDING ON DIFFERENT FACTORS

According to geological and geophysical data sedimentary rocks form the upper part of the earth's crust to a depth of about 10 km. As to their abundance clays occupy one of the first places among these rocks, then follow sandstones, limestones, siltstones and dolomites.

Characteristic of the sedimentary rock complex is that it contains interstitial moisture the amount of which is determined by the porosity ratio k. The most probable values of porosity range between 20—50% for clays, 5—20% for sandstones and 1.5—15.0% for limestones. A wide range of porosity values for a type of rock implies, naturally, considerable variations in interstitial moisture content. Water-saturated sedimentary rocks should be considered as two-phase systems. The solid phase is often represented by minerals (calcite, quartz and others) the overwhelming majority of which possesses a high resistivity ($\varrho > 10^{10}$ Ωm), the fluid phase is an electrolyte of high conductivity ($1.5 \cdot 10^{-1} - 10$ Ωm).

Because of the great difference between the electrical resistivity of the fluid and the solid phases, the main factors which determine electrical parameters of sedimentary rocks are the amount of interstitial solution contained in the rocks, its concentration and the pattern of its distribution depending on the structural features of the rocks. Interstitial moisture is present in rocks in the form of tightly bound, loosely bound and free water. Depending on the ratio of these three types of water not only the electrical parameters but also the nature of their dependence on temperature and pressure vary in a wide range. Free interstitial solution prevails in argillaceous rocks, sandy-argillaceous rocks, loosely cemented sandstones and carbonate rocks (limestones and dolomites), i. e. in rocks for which a large porosity is common when the rocks are completely saturated. Available data for different water-saturated rocks show that when the porosity increases from 4 to 40%, the resistivity decreases approximately a hundredfold.

Since the resistivity of sedimentary rocks is determined in the main by their interstitial electrolyte content, the concentration of the latter also has a considerable effect on the resistivity of rocks. In natural bedding the degree of interstitial water salination in sedimentary rocks varies in a wide range reaching sometimes 200 g/l. More often the salt content varies within the limits of 1 to 10 g/l and depends on the topography, depth of occurrence, climatic conditions etc. By way of illustration electrical resistivity values for some sedimentary rocks are presented in Table 1 for two ranges of salt concentration obtained by VES (vertical electrical sounding) and by logging; results of laboratory measurements of air-dry samples are also given for comparison (Dortman et al., 1964).

It should be noted that clays and sands equally saturated by solutions of weak concentration have different electrical resistivities: the resistivity of sands is greater. An inverse regularity is observed for solutions of high concentration — in this case the resistivity of clays is greater than that of sands.

It is quite obvious that for a proper interpretation and the construction of the geoelectrical profile of the sedimentary thickness experimental data

TABLE 1

Resistivity of sedimentary rocks

Rocks	ϱ [Ωm] from samples with hygroscopic moisture	ϱ [Ωm], taken by VES and by logging	
		saturated by weakly brackish stratal waters (up to 3 g/l)	saturated by saline water (over 3 g/l)
1	2	3	4
Clays	10^3–10^5	10–10^2	1–10
Clayey shales	10^3–10^5	$5 \cdot 10$– $5 \cdot 10^2$	1– $5 \cdot 10$
Porous sandstones	10^5–10^6	$3 \cdot 10$– $2 \cdot 10^2$	1–10
Compact sandstones	10^5–10^6	10^2–10^3	5–10
Fissured limestones	10^4–10^6	10^2–10^3	$5 \cdot 10$–10^2
Compact crystalline limestones	10^4–10^6	10^3–10^5	10^2–10^3

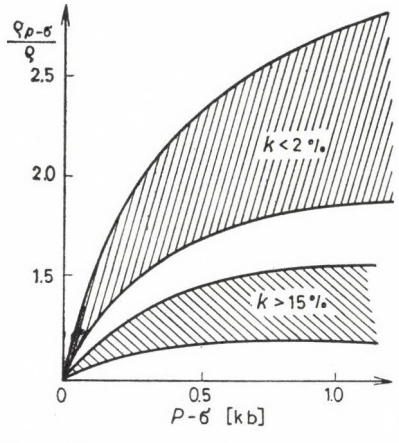


Fig. 1. Ranges of $\varrho_{p-\sigma}/\varrho$ for sedimentary rocks with different porosities k at high pressures; p – uniform pressure, σ – pore pressure

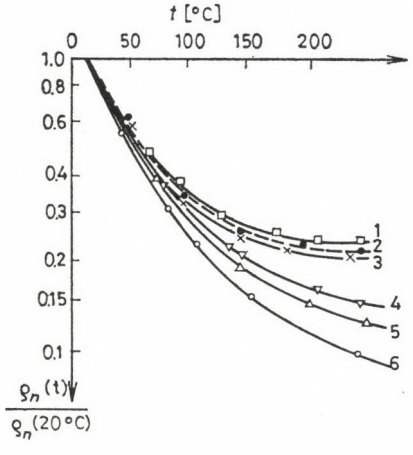


Fig. 2. Temperature induced relative changes of the specific electrical resistivity of sedimentary rocks saturated by 2N NaCl solution
1 – limestone; 2 – 2 N NaCl solution; 3 – high porosity argillite, k=28%; 4 – aleurolite, k=14.8%; 5 – low-porosity argillite, k = 3%; 6 – clay

are needed on the dependence of the electrical resistivity of rocks on temperature and pressure.

Experimental and theoretical works show that the resistivity of water-saturated rocks increases with an increase in hydrostatic pressure and decreases with an increase of pressure in the formation (Dobrynin, 1970; Avchyan, 1971). The extent of the increase of resistivity with increasing pressure is chiefly a function of porosity, rock-structure, type and cement content. This increase of resistivity lies within the limits of 10—20% for water-saturated sandstones and other rocks with porosity exceeding 8%, whereas for compact rocks with slit-like porosity ($k < 2\%$) the effect is much greater and amounts to 200—400% (Fig. 1). As we can see the greatest increase in ϱ occurs at the initial range of loading up to 400—500 kg/cm^2, associated mainly with the change of pore space geometry, i. e. with the increase of the length of current-conducting canals. The type of cementation is also of importance. Resistivity variation due to pressure is the most strongly stimulated by basal cementation. If the pore pressure of the rock-saturating electrolyte increases, the resistivity of the rock decreases due to an increase in the cross section of current-conducting canals.

An increase in temperature causes an inverse variation of ϱ as compared with that caused by the rise of hydrostatic pressure, i. e. resistivity decreases with increasing temperature. Besides, according to Avchyan's and Stefankevich's data, the relative variation in the resistivity of rocks containing a considerable amount of clay fraction is greater than that of the electrolyte; if there is no such fraction the relative variation is less (Fig. 2); this phenomenon appears to be associated with surface conductance.

THE EFFECT OF VARIOUS FACTORS ON ELECTRICAL RESISTIVITY OF MOISTURE-CONTAINING CRYSTALLINE ROCKS

The most wide-spread crystalline rocks in the earth's crust are granites, gabbro, diabases, andesites, diorites, as well as metamorphic rocks — gneisses, amphibolites, slates and crystalline limestones. The porosity of these rocks lies in the range of 0.01—3%. In spite of the fact that the porosity and hence the moisture content of these rocks is much less than those of sedimentary rocks, interstitial solutions have a considerable effect on their electrical resistivity. The degree of water-saturation is at that of a decisive importance.

Experimental data presented in Figure 3 for a number of rocks show that an increase in moisture content is accompanied by a drastic decrease in resistivity. This is most strongly pronounced in the initial region of moistening, the width of which depends on structural features of the rock (Parkhomenko and Bondarenko, 1972; Parkhomenko et al. 1972).

In a bilogarithmic coordinate system the relationship $\lg \varrho = f(\lg w)$ has a linear character (Fig. 4). In the range of small moisture contents (up to 0.1—0.2%) breaks in the straight line are usually observed for which a number of causes may be responsible. Physical-chemical features of the

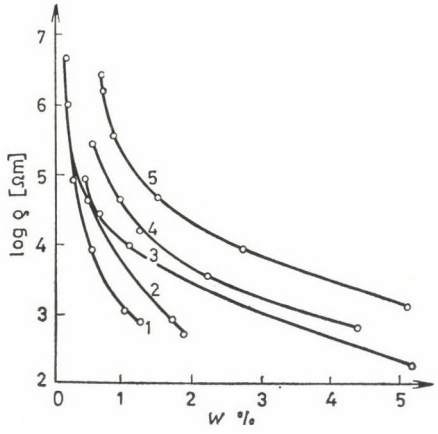


Fig. 3. Dependence of resistivity on the NaCl solution content for rocks 1 – albitophyre with solution concentration $c = 3$ g/l; 2 – basalt, $c = 3$ g/l; 3, 4, 5 – gneiss with $c = 0$, 10, 20 g/l NaCl, respectively

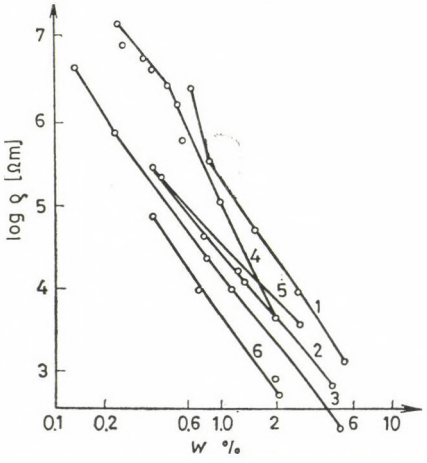


Fig. 4. Dependence of resistivity on NaCl solution content (in a logarithmic coordinate system). 1, 2, 3 – gneiss with solution concentration of 0, 10, 20 g/l; 4 – albitophyre (6 g/l of NaCl); 5 and 6 – basalt with 0.5 and 3 g/l of NaCl

rock matrix and variations in the ratio of the loosely bound water to tightly bound water appear to be the principal causes.

An experimentally obtained linear dependence between $\lg \varrho$ and $\lg w$ is described by

$$\lg \varrho = a \lg w + b$$

where the coefficients a and b depend on the concentration of the electrolyte saturating the rock and on structural features of the rock. For the three rocks investigated the coefficients a and b vary within the limits $b = 3.5-5.1$, $a = 3-4.6$. For the section of the straight line corresponding to moisture contents $w < 0.2\%$ the coefficients vary in a wider range, for in this case an essential role is played by physical-chemical properties of the solid phase.

In igneous and metamorphic rocks together with moisture content much importance has to be attributed to the degree of salinity of the interstitial solution which in the central and partly in the northern regions of the USSR may reach 3 g/l and is increasing with depth (Dortman et al., 1964). It is thus important to know the nature of resistivity dependence of crystalline rocks on salinity in a wide range of concentrations. Rock resistivity decreases with increasing NaCl-concentration, the most intensive variation occurs at a low salinity of the electrolyte (from 1.5 to 3.0 g/l NaCl). The extent of the decrease of resistivity with increasing electrolyte salinity is different for different rocks, and when the concentration increases from 0 to 20 g/l, it varies from a few times to two orders of magnitude (Fig. 5). To a considerable extent this is due to the diversity of the physical-chemical proper-

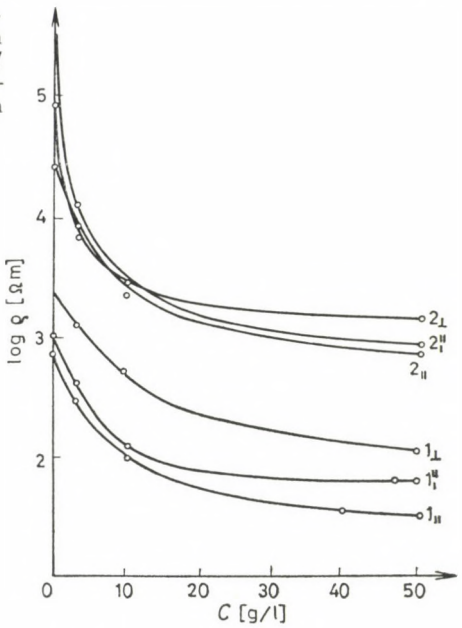


Fig. 5. Dependence of the electrical resistivity of NaCl electrolyte on concentration c (g/l) for rocks: $1_{\perp}$, $1_{\parallel}$, $1'_{\parallel}$ – quartzite 427 (the Urals, Lake Serobory); $2_{\perp}$, $2_{\parallel}$, $2'_{\parallel}$ – gneiss; $1_{\perp}$, $2_{\perp}$ – perpendicular to lamination $1_{\parallel}$, $1'_{\parallel}$, $2_{\parallel}$, $2'_{\parallel}$ – along lamination

ties of the rock matrices; a certain effect being also produced by their specific surface. The ratio of bound water to free water, and hence the contribution of surface conduction to total conductivity depends on the extent of the specific surface development. Surface conduction produces a considerable effect in the small concentration range as substantiated by the data obtained for albitophyre and other rocks. The porosity parameter of these rocks, $P_n = \varrho_{bn}/\varrho_e$ (ϱ_{bn} is the resistivity of an electrolyte-saturated rock, ϱ_e is electrolyte resistance), sharply increases with increasing electrolyte concentration up to 1.5 g/l NaCl and then remains practically constant (Parkhomenko and Bondarenko, 1972).

Metamorphic and igneous rocks in the earth's crust are subject to pressures and temperatures varying in a wide range as well as to different states of stress. For this reason the electrical properties of the rocks should be studied not only at high hydrostatic pressures but at uniaxial and quasi-hydrostatic pressures as well.

Under unidirectional compression some rocks (granites, migmatites, albitophyres, gneisses, basalts etc.), if not completely saturated with the electrolyte, show a decrease in resistivity. In this case the electrical resistivity-pressure coefficient $(1/\varrho)\cdot(\mathrm{d}\varrho/\mathrm{d}p)$ has its greatest value in the initial range of loading up to 400 kg/cm^2, and the decrease of resistivity related to the initial value amounts to 10—40% depending on water-saturation. The degree of interstitial electrolyte concentration does not cause any alterations in the character of the relationship $\varrho = f(p)$ for crystalline rocks and in a number of cases it does not bring about any quantitative changes either (Parkhomenko and Bondarenko, 1972; Parkhomenko et al. 1972). At the same time the water-saturation of the rocks is of fundar

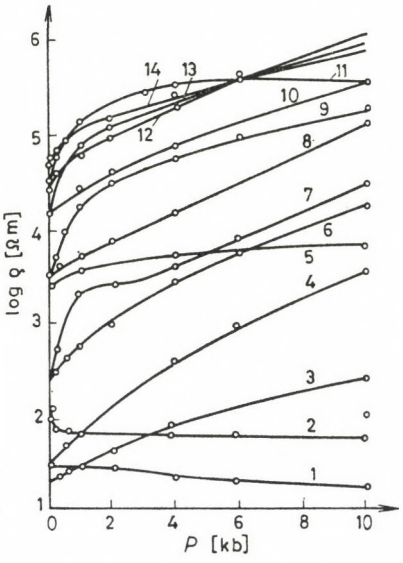


Fig. 6. Dependence of the electrical resistivity on pressure for rocks
1 – rhyolite tuff; 2, 8, 10 – gabbro; 3, 7 – limestones; 4, 5 – diabases; 6 – peridotite; 9 – sandstone; 11, 12 – dunites; 13 – granite; 14 – felsite

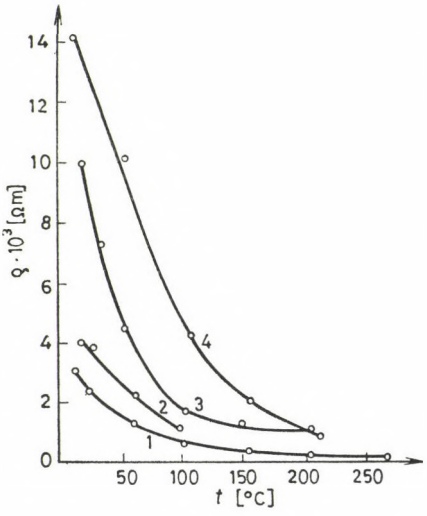


Fig. 7. Dependence of the electrical resistivity on temperature
1 – gabbro; 2, 3 – granites; 4 – syenite

importance. In case of completely saturated igneous rocks their resistivity increases with the hydrostatic pressure, the value of the pore pressure σ_i remaining constant. The greatest rate of variation of resistivity in this case was observed in the pressure range of 0.01—1.5 kb (Brace et al., 1965). In Figure 6 experimental curves are presented showing that the resistivity of a number of rocks increases by two orders of magnitude when the quasi-hydrostatic pressure rises from 1 to 10 kb. These investigations have shown that for rocks composed of high-resistance minerals the rate of increase of resistivity with hydrostatic pressure depends, first and foremost, on pore-space geometry rather than on the properties of the rock-forming minerals. Indicative of this is the great difference in the degree of resistivity variations versus pressure of petrographically identical rocks and yet a practically equal increase of ϱ with pressure of many rocks of different mineral composition (Brace et al., 1965).

Of the greatest interest are, naturally, the experimental data on resistivities of rocks obtained for thermodynamical conditions closely approaching those occurring in the deep interior of the Earth. As yet we are short of such data, and acquisition of them is one of the important tasks.

As can be seen from the graphs presented in Figure 7 temperature has quite a strong effect upon rock resistivity. The nature of the variation of electrical resistivity with increasing temperature is identical for all the four rocks. The greatest change in ϱ due to temperature variations takes

place within the interval 20—150 °C, then the curve flattens out. In a coordinate system $\lg \varrho = f(1/T)$ the experimental points fall into a single straight line. Hence, the temperature dependence for water-saturated samples is governed by an exponential law:

$$\varrho = \varrho_0 \exp\left(+\frac{E_0}{KT}\right)$$

where E_0 is activation energy, K is Boltzmann's constant and T is absolute temperature. The activation energy of the investigated rocks varies within the limits of 0.16—0.19 eV, for water it is $E_0 = 0.2$ eV (Parkhomenko et al., 1972). Close values of the activation energy for rocks and for water indicate that electric conductivity is realized by the rock-saturating electrolyte, while other factors have no substantial influence on the curves $\lg \varrho = f(1/T)$. The logarithm of the pre-exponential coefficient ϱ_0 for these rocks varies from 3.3 to 4.75 (Ω cm). Besides, there are available data on the electrical conductivity of two rocks — granite and syenite — in function of hydrostatic pressure at higher temperatures. At all the temperatures, i. e. 20, 50, 100 and 150 °C, an increase in their resistivity with increasing pressure is noted. However, these rocks differ in the way as their electrical resistivity varies with increasing pressure. A distinctly pronounced break in curves $R = f(p)$ is observed for granite (Fig. 8, a) when p values become close to 700 kg/cm^2. The increase of electrical resistivity in function of pressure of a syenite sample is characterized by an almost linear dependence $R = f(p)$ for the entire temperature range 20—154 °C (Fig. 8, b). The granite and syenite samples (of porosity $k = 0.48\%$ and $k = 2.22\%$, respectively) having been taken as examples, an inverse relationship was established between electrical resistivity coefficient $(1/\varrho) \cdot (d\varrho/dp)$ and porosity.

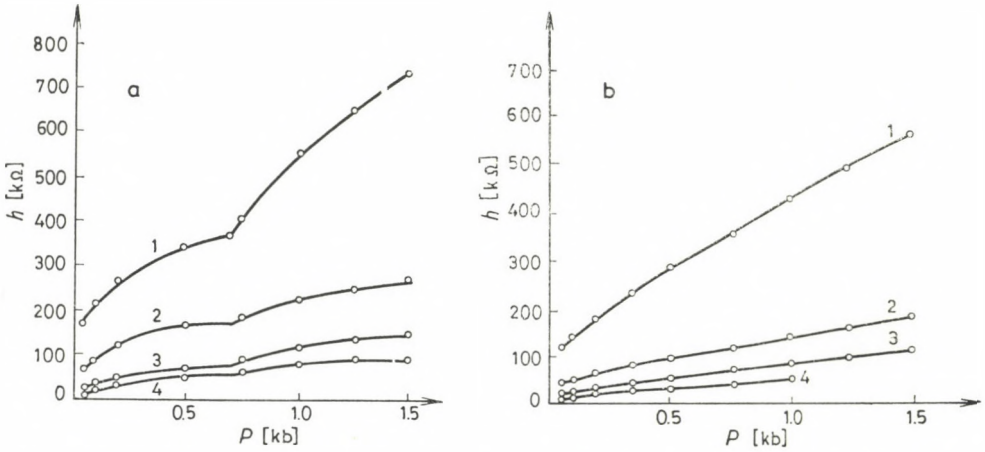


Fig. 8. Dependence of the electrical resistivity of granite samples (a) and syenite samples (b) on pressure at different temperatures
1 – 20 °C; 2 – 50 °C; 3 – 100 °C; 4 – 150 °C

This peculiarity should be associated with a greater amount of slit-like pores in granite as in syenite. A complication of the geometry of current-conducting canals is known to lead to an increase of the rate of variation of the resistivity of the rock with increasing pressure.

The increase in electrical resistivity with pressure (up to 1500 kg/cm^2) is considerable for both rocks and can to a certain extent offset the reducing effect of temperature on the electrical resistivity of rocks.

BRIEF SUMMARY OF THE THEORY OF ELECTRICAL CONDUCTIVITY OF DIFFERENT MATERIALS

According to their electrical conductivity solid materials are divided into three groups: conductors, semiconductors and dielectrics.

Minerals possessing metallic conductivity only occur in the form of native metals and are the least wide-spread group of minerals. The model of a metal is represented as an assembly of positive ions situated at crystal lattice points with a large number of free electrons between them. Similarly to the ions also these electrons are in a state of random motion. Under the influence of an electric field the electrons acquire an additional velocity along the field owing to which electric current is originated. When the temperature rises the oscillations of ions of the crystal lattice get intensified which creates obstacles in the path of the electrons' directed motion. This leads to a reduction of the mean free path and of the mobilities of electrons. And so with increasing temperature the specific resistance of metals increases.

Most of the ore minerals — oxides, sulphides, tellurides and selenides — belong to semiconductors. Electrical conductivity of metals and semiconductors is caused by one and the same current carrier, namely electrons. The basic difference between metals and semiconductors is associated with the energetic state of electrons.

The activation energy of electrons in a metal is equal to zero, while in semiconductors it varies from a few tenths of an eV to a few eV. A small number of valence electrons participating in the current transfer accounts for a considerably smaller value of electrical conductivity of semiconductors as compared with metals, whereas the mobilities of charge carriers in semiconductors can be both greater or less than in metals.

In semiconductors electrical conductivity may be brought about by electrons and by "holes" which are equivalent to positive carriers of current. Depending on the prevailing role of the said charge-carriers, p-type semiconductors with a hole conduction mechanism and n-type semiconductors with an electron conduction mechanism are distinguished. The electrical conductivity of semiconductors is highly sensitive to impurities which are additional sources of charge-carriers.

The electrical conductivity of semiconductors is varying with temperature increase due to variations in the concentration and mobilities of charge-carriers. The most typical cases of variations of the concentration of charge-carriers, on the one hand, and of electrical conductivity, on the other, for semiconductors with different percentage of impurities are presented in Figures 9 and 10. The slope of the straight line in the interval $a - b$ and

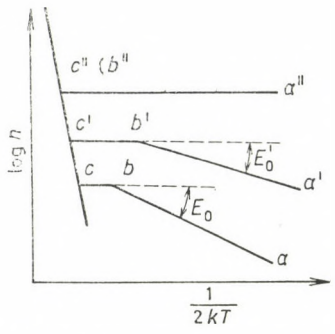


Fig. 9. Dependence of the concentration of charge-carriers n on temperature for different impurity contents $a < a' < a''$; a – b – impurity conduction; $c - c''$ – intrinsic conduction

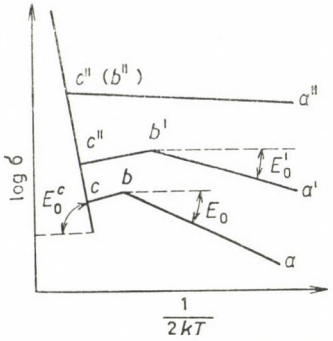


Fig. 10. Dependence of the electrical conductivity of semiconductors with different impurity content $a < a' < a''$ on temperature; $a - b$ – impurity conduction; $c - c''$ – intrinsic conduction

the temperature of the transition from impurity conduction to intrinsic conduction in Figure 10 depend on the amount of impurities. The greater their amount the higher the transition temperature and the less the slope of the straight line characterized by activation energy E_0. The mobilities of charge-carriers in semiconductors slightly depend on temperature and have a different character in atomic and ionic semiconductors. In atomic lattices the temperature dependence of mobility is determined by the formula

$$U = aT^{3/2} + bT^{-3/2}$$

where a and b are constants of proportionality.

If the electrical conductivity in semiconductors is realized in the region of impurity conduction by particles with activation energy E_0'' and in the region of intrinsic conduction by particles with activation energy E_0, the formula for electrical conductivity has the form

$$\sigma = \sigma_1 \exp\left(-\frac{E_0}{2KT}\right) + \sigma_2 \exp\left(-\frac{E_0''}{2KT}\right)$$

where K is Boltzmann's constant, T is absolute temperature.

Most minerals are ionic crystal dielectrics. In such dielectrics current conduction is realized first and foremost by ions of the smallest size if their charges are equal, or by ions of the smallest charges if their dimensions differ only slightly. In dielectrics, just as in semiconductors, two types of electrical conductivity are distinguished — impurity conduction and intrinsic conduction depending on by what kind of ions the current is generated. The mechanism of electrical conductivity in ionic crystals is associat-

ed with the availability of defects in them. Two kinds of defects occur: Frenkel defect (interpoint ion and vacancy) and Schottky defect (anionic and cationic vacancies). Responsible for the current flow in dielectrics is the motion of defects which becomes regular under the influence of the external electric field.

The electrical conductivity of a mineral or of a rock which is a dielectric having both impurity and intrinsic conductions is described by the formula

$$\sigma_1 = \sigma_0' \exp\left(-\frac{E_0'}{KT}\right) + \sigma_0'' \exp\left(-\frac{E_0''}{KT_2}\right)$$

In the region of low temperatures E_0' is small; it is considerably less than E_0'' is at high temperatures since in the former case it is equal to the energy required only for the migration of the already existing charge-carriers (impurity ions), while at high temperatures intrinsic defects occur during the increase of temperature, so that additional energy is needed for their formation.

EFFECT OF PRESSURE ON ELECTRICAL CONDUCTIVITY OF DIFFERENT MATERIALS

Electrical conductivity of most metals and semiconductors increases with increasing pressure which is mainly due to variation of electron mobilities. The inverse regularity is seldom observed, it is associated with an increase of the effective mass of charge-carriers.

The character of activation energy variations has a dominating effect on the character of pressure-dependence of electrical conductivity of semiconductors. It has been established that the width of the forbidden band and hence the value of the activation energy may both increase or decrease with decreasing interatomic distances. For this reason hydrostatic pressure calls forth in some semiconductors an increase in electrical conductivity while in others a decrease or even a minimum of it. A decrease of the distances between atoms under the effect of pressure reduces the amplitudes of their thermal vibrations. This results in a decrease of the thermal scattering of the charge-carriers, and an increase in the mobilities of the charge-carriers takes place.

Zharkov (1958, 1968) has obtained an equation describing the pressure dependence of electrical conductivity by means of integral compressibility which also takes into account the number of carriers and their mobilities. This equation can be used to evaluate the electrical conductivity of the lower part of the mantle.

Experimental data for semiconductors show that the regularity of variation of their resistivity with pressure is different for semiconductors of the n-type or of the p-type.

The effect of pressure on the electrical conductivity of materials of ionic conductivity was studied on samples of alkali metal halides (Jast and Men-

TABLE 2

Electrical resistivity of oxide minerals at high temperatures

Name	ϱ [Ω m] at t °C					
	300	600	800	900	1000	1100
Corundum monocrystal	—	—	—	$9.9 \cdot 10^7$	10^6–$5.0 \cdot 10^6$	10^5–$4 \cdot 10^5$
Corundum ceramics	$4.0 \cdot 10^{12}$	$3.0 \cdot 10^{11}$	$3.3 \cdot 10^6$	—	—	—
Magnesium oxide technically pure	—	10^7	—	$3 \cdot 10^3$	10^3	$6.2 \cdot 10^2$
Magnesium oxide spectroscopically pure	—	$5 \cdot 10^{10}$	$4.0 \cdot 10^9$	$9.0 \cdot 10^8$	$7.0 \cdot 10^6$	$6.0 \cdot 10^5$
Calcium oxide	—	—	$\sim 6.0 \cdot 10^5$	$5.0 \cdot 10^4$	—	—

nenon, 1950; Shapiro and Koltoff, 1948), the electrical conductivity of these ionic dielectrics was found to decrease with increasing pressure.

In conclusion it should be noted that the present state of development of the theory of semiconductor and dielectric electrical conductivity allows no theoretical calculation of the necessary accuracy of the value of electrical conductivity of minerals and rocks at high pressures and temperatures. For this reason experimental data in this field becomes of particular importance.

ELECTRICAL RESISTIVITY OF MINERALS AT HIGH PRESSURES AND TEMPERATURES

To predict the value and the dependence on pressure and temperature of the electrical conductivity of rocks of a known mineral composition one has to know the electrical parameters of the constituent minerals under similar thermodynamic conditions.

The chemical composition of crystals and the type of crystal structure are among the chief factors which determine physical properties of crystals. In order to demonstrate how these factors affect the dependence of the electrical conductivity of minerals on pressure and temperature, the available experimental data will be grouped according to certain types of chemical compounds and to certain structural classes. Prevailing in the earth's crust are oxygen compounds in the form of oxides and various salts, mainly silicates. It is for this reason that from the point of view of the electrical conductivity of the Earth's interior data on these compounds are of the utmost importance.

Oxides. The most widespread oxides in the earth's crust are SiO_2, Al_2O_3, MgO, CaO, FeO, Fe_2O_3. Of these only CaO almost never occurs in pure form. Data presented in Table 2 are intended to give an idea of the electrical resistivity of these oxides.

Corundum, periclase, calcium oxide and quartz are highly insulating due to the presence of ionic bonds in these oxides and to the small ionic radii of the cations having insignificant polarizability. As can be seen from the data in Table 3 a correlation is observed for corundum, periclase and calcium oxide between the value of electrical resistivity and the cation radius, polarizability and the crystal lattice energy.

The decrease of electrical resistivity with increasing cation radius is accounted for as follows. As a first approximation, it may be assumed that the relationship between ionization energy w and ionic radius r can be written as $w = q^2/r$, where q is the charge of the ion. Hence, an increase in radius leads to a decrease in ionization energy and this implies an increase in electrical conductivity (Vorobiev, 1960).

Hematite and magnetite belong to oxides of transition metals which do not possess many of the properties characteristic of silicium and germanium type semiconductors. Neither Hall effect nor photoconduction are observed for the former. Electrical conduction in oxides of transition metals is by an electron transition from an ion of a certain valency to an ion of some other valency. For example, a simultaneous presence in magnetite of Fe^{3+}

TABLE 3

Cation	$\varrho_{1000°}$ [Ωm]	Cation radius [$r \cdot 10^8$ cm]	Polarizability [$\alpha \cdot 10^{24}$ cm^3]	Lattice energy, eV for a pair of ions
Al^{3+}	10^7	0.57	0.067	157.0
Mg^{2+}	$8.0 \cdot 10^6$	0.78	0.114	41.3
Ca^{2+}	10^5	1.08	0.531	37.5

as well as of Fe^{2+} facilitates an easy exchange of electrons. When a part or all of the Fe^{2+} ions are replaced by ions of other bivalent metals, the electrical conductivity of ferrites decreases. A qualitative explanation of this phenomenon is that a great energy is required for an electron to leave an ion of some other bivalent metal.

At this point we should dwell on the electrical conductivity of spinels. As for the value of electrical conductivity they may be divided into three groups: aluminates possessing high resistivity, chromites of medium resis-

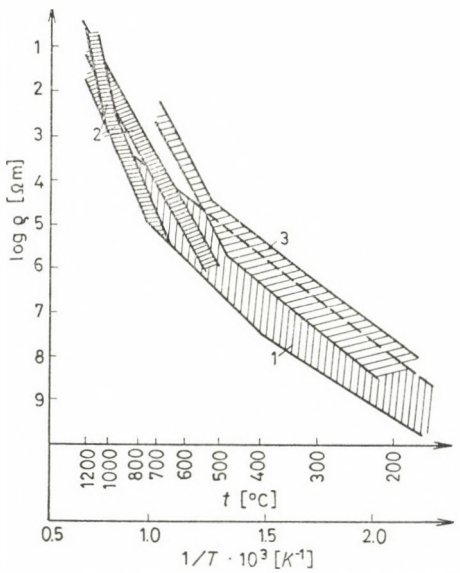


Fig. 11. Summarized diagram of the dependence on temperature and pressure of the resistivity of olivines and olivine-containing rocks
1 – impurity conduction range; 2 – intrinsic conduction ranges; 3 – resistivity limits at $p = 20$ kb (Parkhomenko and Bondarenko 1972; Bondarenko and Feldman 1973)

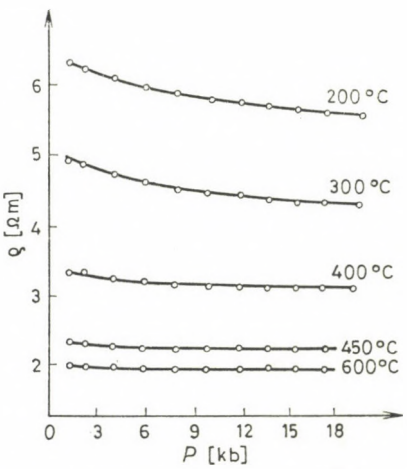


Fig. 12. Dependence of resistivity of olivine on pressure at high temperatures

tivity and ferrites of low resistivity (Cherepanov and Tresvyatsky, 1974). The value of resistivity depends on the type of cation as well as on the chemical nature of the Me_2O_4 compound.

The analysis of the available experimental data on oxide minerals allows the following conclusions. The basic factors determining the electrical properties of oxide minerals in a wide temperature range are: a) the type of metal serving as cation, b) structural features, c) the quantity and specific features of impurities, d) energetic parameters of the compounds (ionization energy of the cation and lattice energy), e) "pre-history" of the mineral, preliminary thermal treatment being implied among other things, f) composition of the gaseous medium enclosing the sample undergoing measurements under high temperatures.

Silicates. Some 1/3 of all the mineral species known to exist in nature belong to the class of silicates; in terms of weight they make up about 75% of the earth's crust. In view of the different nature of silicon-oxygen tetrahedron combinations the silicates are divided into five subclasses. Let us consider the available experimental data for each group separately.

Silicates with isolated tetrahedrons comprise two very important groups of minerals, those of olivine and of garnet. The olivine group includes forsterite, fayalite and olivine proper. Olivine is the principal constituent of the mantle and of meteorites, and as such it attracts the attention of many researchers.

Figure 11 presents data of the studies of olivines and olivine-containing rocks of hypogene origin in the temperature range 100—1200 °C at atmospheric pressure, and at pressures up to 20 kb and temperatures up to 700 °C. The fayalite content in olivines was 8—12%. For one group of olivenites and olivine-containing rocks the impurity conduction range extends to 500 °C and is characterized by $E_0 = 0.62$ eV and $\varrho_0 = 10^2\ \Omega$m, for the other group the respective range is up to 600 °C with $E_0 = 0.80$ eV and $\varrho_0 = 1.2 \cdot 10^1\ \Omega$m. The intrinsic conduction range depending on the range of temperatures of its manifestation is characterized by the parameters $E_0 = 1.8$ eV and $\varrho_0 = 2 \cdot 10^{-6}\ \Omega$m (800—1200 °C). It is to be noted that the value and rate of resistivity variation in olivines with increasing pressure (Fig. 12) depends on the fayalite content. As seen from Figure 13, with an increase in the latter the resistivity decreases while the degree of variation of E_0 under the effect of pressure increases.

The garnet group differs from the olivine group in its more complex chemical composition. The most interesting of this group of minerals are garnet-pyrope ($Mg_3Al_2Si_3O_{12}$) which does not contain ferric oxides and almandite ($Fe_3Al_2Si_3O_{12}$) containing 43% of FeO. In this case the same regularity is observed as for the minerals of the olivine group. Garnet-almandite reveals a higher and more intensively varying conductivity and activation energy than pyrope in the pressure and temperature range considered. Figure 14 and the data presented in Table 4 show the variations of resistivity and of the parameters E_0 and $\lg \varrho_0$ for pyrope and almandite in wide pressure and temperature ranges (Parkhomenko and Bondarenko, 1972).

Andradite which contains 31.5% of Fe_2O_3 and 33.0% of CaO should have the greatest electrical conductivity among the minerals of andradite series.

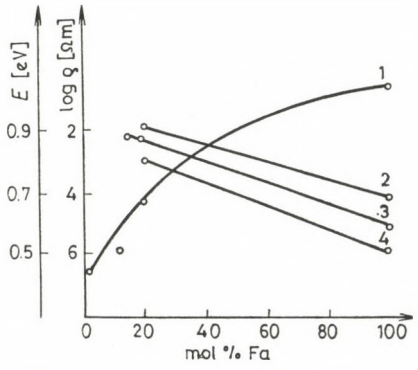


Fig. 13. Dependence of the electrical resistivity (1) and activation energy (2) – (4) of olivines on fayalite content at p equal to: 2–12 kb; 3 – 22 kb; 4 – 33 kb

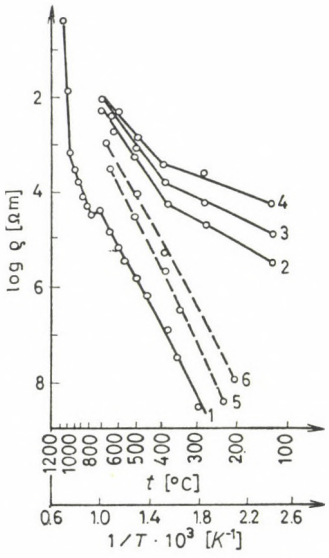


Fig. 14. Dependence of the electrical resistivity of almandite garnet and of garnet-pyrope (broken lines) on temperature at different pressures 1 – atmospheric; 2–0.97 kb; 3–5 kb; 4–20 kb; 5 – 0.5 kb; 6 – 20 kb

TABLE 4

Mineral	Pressure [kb]	Temperature range [°C]	E_ϱ [eV]	lg ϱ_0 [Ωm]
Garnet-pyrope	0.5	150– 700	1.06	3.7
	20	150– 700	0.96	3.8
Garnet-almandite	10^{-3}	150– 700	1.02	2.4
		700–1000	1.54	2.4
	0.97	150– 400	0.3	2.4
		400– 650	0.9	3.3
	5	150– 400	0.22	2.42
		400– 650	0.76	2.3
	20	150– 400	0.20	1.8
		400– 600	0.66	3.4

It may be supposed that its electrical conductivity will be substantially higher than that of almandite as it contains besides Fe_2O_3, a considerable amount of CaO instead of Al_2O_3, the latter possessing a higher resistance.

Silicates with continuous chains of silicium-oxygen tetrahedrons include two very important groups of minerals: *pyroxenes* and *amphiboles*. Figure 15 presents the temperature dependence of electrical conductivities of *pyroxenes*—chromediopside, diopside, jadeite, hedenbergite, aegirite, spodumene and enstatite. Though these minerals have identical structure they sharply differ both in the value of electrical conductivity and activation energy. This verifies the above mentioned dominating role of cations in general and of the simultaneous presence of Fe^{3+}-cations and Fe^{2+}-cations in particular in building up the value of electrical conductivity. Moreover, the combination of ferric cations and Na^+-cations in minerals is a stimulating factor for an increase of the rate of resistivity variation with pressure. The presence of calcium cations in the chemical formula of pyroxenes has in this respect a considerably less influence, as follows from a comparison of the electrical resistivities of jadeite and diopside, and of aegirite and hedenbergite (Fig. 16). As can be seen from the data presented in Figure 16, changes in the chemical composition of pyroxenes in the series enstatite, diopside, spodumene, jadeite and aegirite, i. e. an increase in the number of ferric ions together with a simultaneous substitution of monovalent cations Na^+ and Li^+ for bivalent cations Mg^{2+} and Ca^{2+}, leads to a wide range of electrical conductivity values for this group of minerals. A series of isotherms presented for these minerals at $t = 200$ °C and $t = 600$ °C

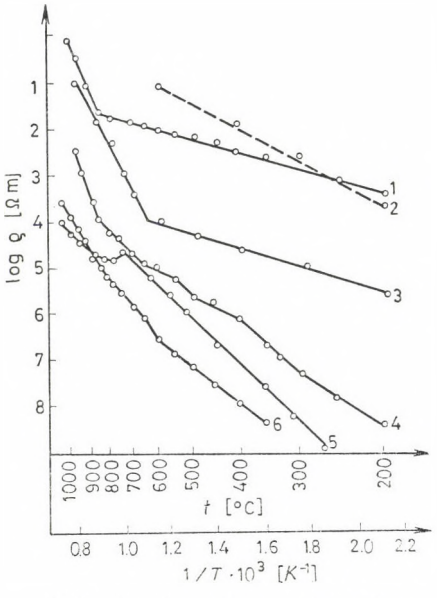


Fig. 15. Dependence of the electrical resistivity of pyroxenes on temperature
1 – aegirite; 2 – hedenbergite; 3 – jadeite; 4 – spodumene; 5 – diopside; 6 – enstatite

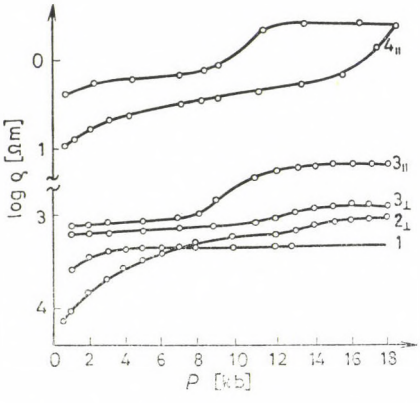


Fig. 16. Dependence of the electrical resistivity of pyroxenes on pressure at $t = 600$ °C
1 – chrome-diopside; 2 – enstatite; 3 – diopside; 4 – aegirite; parallel and perpendicular to axis C

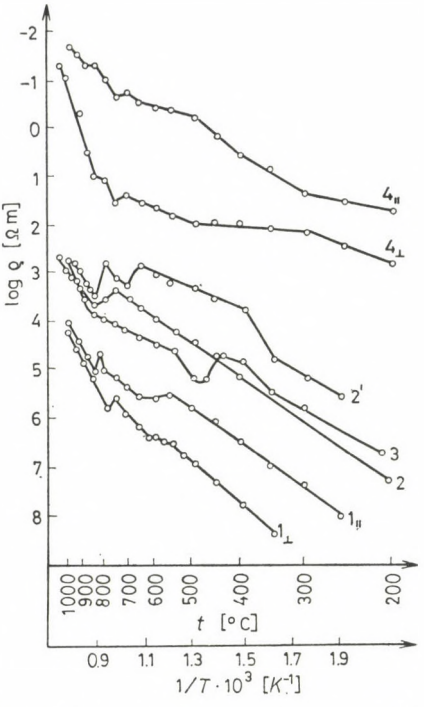


Fig. 17. Dependence of the electrical resistivity of amphiboles on temperature
1 – tremolite; 2 – hornblende; 3 – actinolite; 4 – riebeckite; parallel and perpendicular to axis *C*

shows that the scope of electrical conductivity values remains as wide with increasing pressure as it was at atmospheric pressure. Besides, minerals with a larger ferric cation content, namely aegirite and hedenbergite, show a considerably greater variation of ϱ with pressure than the other investigated pyroxenes. The activation energy of the investigated pyroxenes changes insignificantly with increasing pressure, the change observed for most of them being a decrease.

The amphibole group differs from pyroxenes by the presence of $(OH)^{-1}$ in the chemical formula, which causes certain specific features in the temperature course and in the character of variation of their electrical conductivity with pressure. Due to the presence of consitutional water in the composition of the minerals, first a break of the bond $(OH)^{-1}$ and then separation of H_2O, i. e. dehydration takes place when a certain temperature is reached. This process causes an anomalous variation of electrical conductivity on a certain temperature interval. This may manifest itself through a sharp decrease in resistivity in a narrow temperature range which after a further increase in temperature begins to increase or remains practically constant up to a certain temperature (Fig. 17).

The isotherms of electrical resistivity at dehydration temperatures show, as a rule, an increase in the rate of its variation which sometimes proceeds by jumps.

For this series of minerals, similarly as for pyroxenes, the effect of chemical composition rather than that of structure is of primary importance.

The minerals tremolite and actinolite (there is no ferrum in the chemical formula of the former and only a small quantity of it in the latter) are characterized by the highest resistivity and a slight decrease in resistivity with pressure. Amphibole ($\Sigma Fe_{1-x} O_x = 12\%$) shows a greater rate of decrease in ϱ with increasing pressure, while the greatest variation of ϱ is experienced in riebeckite which contains the maximum quantity of ferric oxides and a high percentage of Na_2O. Common for all these minerals is a certain shift of the start of the dehydration process towards the lower temperature range given by the linear dependence $\lg \varrho = f(1/T)$

Minerals with continuous three-dimensional frameworks of silicium tetrahedrons, namely albite, oligoclase, orthoclase and microcline which we have studied are noted for an almost complete absence of ferric oxides in their composition. Typical for this group of minerals as well as for quartz are the relatively high values of ϱ and a complicated dependence of resistivity on pressure, the form of which depends on the experimental temperature and on the crystallographic direction. For nepheline and microcline the minimum of electrical resistivity is apparent along one of the crystallographic directions and shifts towards lower pressures as temperature increases. For other crystallographic directions only an insignificant decrease of ϱ is observed in case of pressures up to 10 kb, with a further increase in pressure practically no change or only a slight increase will be obtained.

In conclusion it should be noted once again that the structural classes of minerals considered at one and the same temperature are characterized by a wide range of values of electrical resistivity caused mainly by the differences in chemical composition. The principal effect is due to the type of cation, that is its charge, ionic radius and polarizability. Ferric cations occupy a special position in this respect; when these are present a special mechanism of electrical conductivity is in action with low activation energy $E_0 = 0.1$ eV, which is characteristic of transition metals. A combination of ferric cations with natrium cations in the chemical formula of a mineral decreases the value of the mineral's resistivity and extends the rate of ϱ's decreasing with pressure.

ELECTRICAL RESISTIVITY OF CRYSTALLINE ROCKS OF THE "GRANITE" AND THE "BASALT" LAYERS OF THE EARTH'S CRUST IN A WIDE TEMPERATURE RANGE

According to geophysical and geological data the depth of occurrence of the "granite" layer does not exceed 25 km for the continental crust and the maximum temperature at the utmost depth of the folded zone is about 600 °C (Lubimova, 1968). The "granite" layer may be represented by granites, granodiorites, syenites as well as by different metamorphic rocks: gneisses, shales and others. Limestones may also occur in this layer. The elastic wave velocities obtained for a number of samples of these rocks at high pressures corrected for temperature correspond to formational velocities of elastic waves in the "granite" layer (Volarovich et al., 1974).

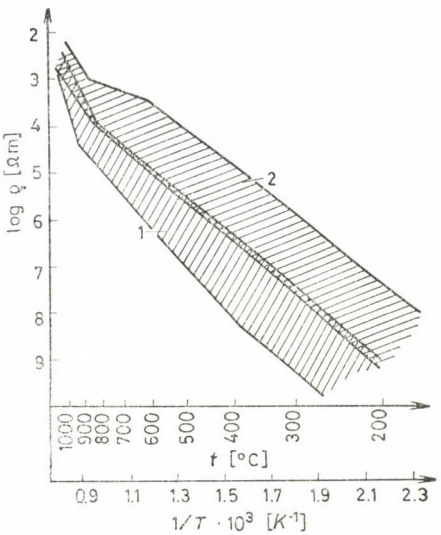


Fig. 18. Ranges of resistivity values at high temperatures for 1 – granites; 2 – granodiorites, quartz-diorites and diorites

Granites, granodiorites and diorites unaffected by processes of weathering by cataclasm, and by secondary processes show high electrical resistivity values in a wide temperature range. The most probable range of the resistivity values of these rocks in the temperature interval 200—1000 °C is shown in Figure 18. For rocks of the granite-diorite series a resistivity decrease is noted when the amount of minerals of dark colouring increases while the quartz content decreases. Change of mineral composition in this series is accompanied by a simultaneous increase in the total content of oxides Fe_2O_3, FeO and CaO which contributes to a decrease of resistivity.

The effusive analogues of these rocks, having a similar chemical composition, such as acidic glass (obsidian), porphyrites, andesites, have electrical resistivities by about one-two orders smaller than the respective values for granites and diorites, due to the presence of an amorphous phase and to their fine-grained structure. Both factors increase the number of charge-carriers with small values of activation energy, and that contributes to an increase in rock conductivity.

The process of cataclasm combined with secondary processes (albitization, pelitization etc.) causes the greatest reduction in electrical conductivity of acidic and intermediate rocks. In this case the resistivity in the range of impurity conduction may decrease by 2—3 orders of magnitude. This can be seen from the data presented in Table 5. The difference in the ϱ values in the range of intrinsic conduction for fresh rocks as well as for rocks altered by secondary processes is considerably smaller.

As is known, *andesites* are effusive analogues of diorites with respect to their chemical composition and are to a considerable extent similar to them in their mineral composition. However, andesites have a substantially smaller resistivity than that of the diorite group in the entire temperature range from 200 to 1000 °C. At 1000 °C ϱ for andesites is about a hundred times smaller than that for diorites. The activation energy in a range sen-

TABLE 5

Range of resistivities of acidic rocks and intermediate rocks

Rock	Resistivity [Ωm] at temperature t [°C]				
	200	300	400	500	1000
Fresh granites	$1.11 \cdot 10^9$–$1.0 \cdot 10^{10}$	$5.0 \cdot 10^7$–$1.0 \cdot 10^9$	$5.0 \cdot 10^6$–$1.43 \cdot 10^8$	$5.0 \cdot 10^5$–$1.66 \cdot 10^7$	$1.0 \cdot 10^3$–$6.66 \cdot 10^3$
Cataclastic granites	$5.0 \cdot 10^5$–$1.43 \cdot 10^8$	$1.11 \cdot 10^4$–$5.0 \cdot 10^6$	$1.66 \cdot 10^4$–$5.0 \cdot 10^5$	$2.0 \cdot 10^4$–$1.81 \cdot 10^5$	$2.5 \cdot 10^2$–$2.0 \cdot 10^3$
Fresh diorites	$1.66 \cdot 10^7$–$1.43 \cdot 10^9$	$1.0 \cdot 10^6$–$1.0 \cdot 10^8$	$1.0 \cdot 10^5$–$1.0 \cdot 10^7$	$1.0 \cdot 10^5$–$3.33 \cdot 10^6$	$1.78 \cdot 10^2$–$1.0 \cdot 10^3$
Cataclastic diorites	$2.0 \cdot 10^5$–$1.11 \cdot 10^6$	$2.0 \cdot 10^4$–$5.0 \cdot 10^4$	$3.03 \cdot 10^3$–$8.33 \cdot 10^4$	$6.66 \cdot 10^2$–$1.28 \cdot 10^4$	10^2

TABLE 6

Resistivity range and averaged resistivity values for different gneisses

Rock	Resistivity [Ωm] at t [°C]				
	200	300	400	500	600
Gneisses, mainly of quartzmicrocline-albite composition	$1.3 \cdot 10^8$–$1.3 \cdot 10^9$	$5.2 \cdot 10^7$–$1.6 \cdot 10^8$	$4.2 \cdot 10^6$–$1.0 \cdot 10^7$	$9.5 \cdot 10^5$–$9.8 \cdot 10^5$	$5.0 \cdot 10^4$–$4.0 \cdot 10^5$
Amphibole gneiss	$2.0 \cdot 10^6$	$1.6 \cdot 10^5$	$5.2 \cdot 10^4$	$4.5 \cdot 10^3$	$3.3 \cdot 10^3$
Orthogneiss of ultrabasic composition	$1.1 \cdot 10^5$	$1.0 \cdot 10^4$	$1.5 \cdot 10^3$	$4.0 \cdot 10^2$	$8.6 \cdot 10^2$
Cataclastic gneisses	$1.0 \cdot 10^5$–$4.5 \cdot 10^6$	$1.0 \cdot 10^4$–$1.0 \cdot 10^5$	$3.0 \cdot 10^4$–$3.5 \cdot 10^5$	$2.6 \cdot 10^3$–$1.0 \cdot 10^4$	$1.0 \cdot 10^2$–$9.0 \cdot 10^4$

TABLE 7

Electrical resistivity of shales of different mineral composition

Shale	Resistivity [Ωm] at t [°C]				
	200	300	400	500	600
Cyanite slates	—	$4.0 \cdot 10^7$–$2.0 \cdot 10^8$	10^7–$5.0 \cdot 10^7$	$3.0 \cdot 10^5$–$2.0 \cdot 10^6$	$6.0 \cdot 10^4$–$5.0 \cdot 10^5$
Quartz-micaceous slates	$3.0 \cdot 10^6$–$3.0 \cdot 10^8$	$4.0 \cdot 10^5$–$1.5 \cdot 10^7$	$9.0 \cdot 10^4$–$1.0 \cdot 10^7$	$2.0 \cdot 10^4$–$1.2 \cdot 10^5$	$6.0 \cdot 10^3$–$1.1 \cdot 10^4$
Chlorite slate	$2.0 \cdot 10^6$	$1.3 \cdot 10^5$	$2.0 \cdot 10^4$	$5.0 \cdot 10^3$	$1.1 \cdot 10^3$
Graphitized slate	$1.9 \cdot 10^6$	$1.9 \cdot 10^5$	$1.4 \cdot 10^4$	$4.0 \cdot 10^3$	$8.1 \cdot 10^2$
Shales with 5% content of ore minerals	$1.3 \cdot 10^2$–$5.6 \cdot 10^2$	$5.4 \cdot 10^1$–$3.6 \cdot 10^2$	$2.1 \cdot 10^1$–$2.5 \cdot 10^2$	$7.8 \cdot 10^1$–$1.4 \cdot 10^2$	$4.4 \cdot 10^1$–$2.7 \cdot 10^2$
Phyllite slates, along schistosity	$1.4 \cdot 10^2$–$9.8 \cdot 10^4$	$9.8 \cdot 10^2$–$5.5 \cdot 10^4$	$7.2 \cdot 10^1$–$4.1 \cdot 10^4$	$4.3 \cdot 10^1$–$8.3 \cdot 10^3$	$9.8 \cdot 10^1$–$2.1 \cdot 10^3$
across schistosity	$2.5 \cdot 10^6$–$1.2 \cdot 10^7$	$5.4 \cdot 10^5$–$7.6 \cdot 10^5$	$5.1 \cdot 10^4$–$6.6 \cdot 10^4$	$3.3 \cdot 10^3$–$7.1 \cdot 10^3$	$1.2 \cdot 10^2$–$5.0 \cdot 10^3$

sitive-to-structure lies within the limits 0.54—0.74 eV. Yet, at high temperatures the activation energy of the intrinsic charge-carriers for andesites is considerably lower than for diorites and does not exceed 1.4 eV, whereas the characteristic value for diorites is 2.0 eV. The principal cause for the differentiation of the investigated rocks as regards their electrical properties at high temperatures is a structural factor, namely the remains of an uncrystallized matrix and the fine-grained structure.

Metamorphosed rocks of the "granite" layer. The most representative rocks of this type are gneisses and shales. Both are notable for a considerable diversity of chemical composition which results in a wide range of their resistivity values. A great number of the investigated samples of *gneisses* of different chemical composition made it possible to obtain intervals of their electrical resistivities for a wide temperature range. These data are presented in Table 6.

Gneisses with a mineral composition akin to that of granites are found to have the highest resistivity. The presence in gneisses of minerals belonging to the amphibole group, namely hornblende or actinolite reduces the resistivity of the rock by one order of magnitude or more.

In case of the hydrothermal alteration of a plagioclase, expressed in substitution by sericite, pelite and zoisite, the resistivity of gneisses decreases and there occur sections on the graphs $\lg \varrho = f(1/T)$ with anomalously low activation energy values or an irregular character of the variation of ϱ with increasing temperature will be found. All these phenomena are caused by the exudation of crystallization or of constitutional water.

As compared with gneisses, *shales* have a still wider range of electrical resistivity values. Cyanite schists and slates composed of quartz and mica possess the highest resistivity. The greatest decrease in resistivity for the shale series is observed at the transition from ore-free varieties to those containing a great amount of magnetite, graphite, etc. As shown by Table 7, the intermediate position between these two varieties is occupied by shales containing magnesium — ferruginous chlorite.

In transition from the amphibolite facies which is characteristic mainly of the "granite" layer and is most developed within crystalline shields, to the granulite facies of metamorphism a substantial change in rock composition takes place. In the "basalt" layer the granulite facies of metamorphism is represented by quartz-feldspathose gneisses with garnet and pyroxene and without mica. Hornblende may be present only in a relatively low-temperature subfacies. The absence of hydroxyl-containing minerals of the mica and amphibole group results in a very low water-content in the rocks of the high-temperature granulite subfacies of metamorphism. However, the latest experimental data reveal that mineral associations with amphibole might exist and could be formed in a wide pressure and temperature range. For example, the lower limit of the amphibole stability in basic rocks in case of a regional metamorphism corresponds to temperatures 400—430 °C at water vapour pressure $p_{H_2O} = 1—7$ kb, the upper limit corresponds to 590—650 °C at $p_{H_2O} = 6.5$ kb.

The upper part of the "basalt" layer may be formed by rocks of the low-temperature granulite subfacies of metamorphism, that is by amphibolites, gabbro-amphibolites and diabases.

TABLE 8

The range of the electrical resistivity of amphibolites

Rock	Resistivity [Ωm] at t [°C]			
	200	300	400	500
Actinolite amphibolites and hornblende amphibolites	10^7–$2.0 \cdot 10^7$	10^6–$2.4 \cdot 10^6$	$3.0 \cdot 10^4$–$5.0 \cdot 10^4$	$1.0 \cdot 10^3$–$4.0 \cdot 10^3$
Silificated amphibolites	$3.0 \cdot 10^5$–$2.3 \cdot 10^7$	$9.0 \cdot 10^4$–$2.0 \cdot 10^6$	$1.0 \cdot 10^4$–$6.0 \cdot 10^5$	$4.0 \cdot 10^3$–$1.0 \cdot 10^5$
Amphibolites with evidence of deuteric alterations and with exposure of ore minerals along mineral boundaries	$1.0 \cdot 10^2$–10^5	$5.5 \cdot 10^1$–$3.2 \cdot 10^4$	$6.0 \cdot 10^1$–$4.0 \cdot 10^4$	$7.6 \cdot 10^1$–$2.2 \cdot 10^4$

Rock	Resistivity [Ωm] at t [°C]				
	600	700	800	900	1000
Actinolite amphibolites and hornblende amphibolites	$1.5 \cdot 10^2$–$3.0 \cdot 10^3$	$9.5 \cdot 10^2$–$2.0 \cdot 10^3$	$3.0 \cdot 10^1$–$2.5 \cdot 10^2$		
Silificated amphibolites	$2.0 \cdot 10^3$–$4.0 \cdot 10^4$	$7.0 \cdot 10^3$–$1.0 \cdot 10^4$	$9.0 \cdot 10^3$–$2.0 \cdot 10^4$	$3.0 \cdot 10^3$–$4.0 \cdot 10^3$	$2.0 \cdot 10^2$–$5.0 \cdot 10^2$
Amphibolites with evidence of deuteric alterations and with exposure of ore minerals along mineral boundaries	$3.0 \cdot 10^2$–$7.2 \cdot 10^3$	10^2–$1.0 \cdot 10^3$	$2.0 \cdot 10^1$–$2.2 \cdot 10^2$	$1.7 \cdot 10^1$–$1.8 \cdot 10^2$	$1.5 \cdot 10^1$–$1.3 \cdot 10^2$

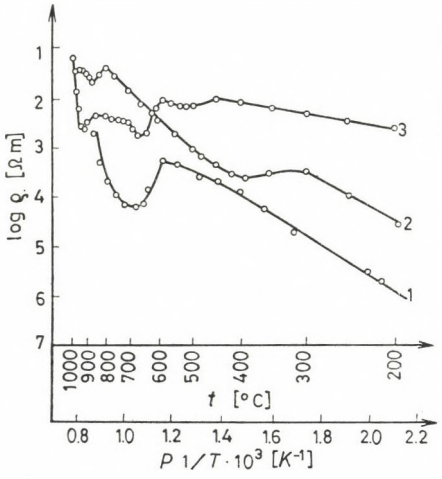


Fig. 19. Dependence of the resistivity on temperature for amphibolites of different composition
1 – granitizated amphibolite; 2 – amphibolite (plagioclase, green hornblende, ore minerals); 3 – biotite – amphibolite (actiphillite, biolite and sphene)

Amphibolites are usually composed of two minerals: amphibole and plagioclase. However, due to the great diversity in chemical composition of the amphiboles and, mainly, due to the wide range of the total content of oxides FeO, Fe_2O_3, and Na_2O, their electrical resistivity may vary in the range of several orders of magnitude at the same temperature and pressure. (See Table 8 and Figure 19.)

Rocks formed by tremolite and actinolite belong to high-resistance amphibolites. Hornblende amphibolites occupy an intermediate position. Amphibolites formed by magnesium-ferruginous minerals are characterized by low resistivity. It should be noted that amphibole rocks as well as amphibolites are characterized by sections of anomalous ϱ variations with temperature. For some of them in a narrow temperature range a steep decrease in resistivity is observed most probably associated with reactions taking place in ferruginous amphiboles in course of their dehydration. If the amount of ferric oxides contained in them is not great, then flat sections of electrical conductivity can usually be observed in a certain temperature range corresponding to the synthesis of water. It seems that the temperature associated with the ϱ anomaly may be used to determine the limiting temperature of the stability of hydroxyl containing minerals as well as to determine the range of temperatures at which the dehydration process proceeds at a given rate of temperature increase. The electrical resistivity values of granulites not affected by weathering and those of high-resistance amphibolites are overlapping.

The *gabbro-basalt* group is the most important among the basic intrusive and effusive rocks. Its abundance in the earth's crust is comparable to that of granites. Gabbro belongs to deep-seated completely crystallized rocks of an equigranular structure composed of basic plagioclase (50–60%) and of some coloured mineral (pyroxene or amphibole).

The resistivity of fresh gabbro and that of gabbros affected by cataclasm and metamorphism as well as by weathering are quite different. The latter are characterized by a substantially lower resistivity, as it can be seen

TABLE 9

The range of the electrical resistivity of gabbro

Rock	Resistivity [Ωm] at t [°C]			
	200	300	400	500
Gabbro-norites and hypersthenic gabbro containing excessive amount of iron	$5.0 \cdot 10^6$–$1.2 \cdot 10^7$	$1.0 \cdot 10^6$–$4.0 \cdot 10^6$	$2.5 \cdot 10^5$–$9.0 \cdot 10^5$	$2.0 \cdot 10^4$–$5.0 \cdot 10^4$
Amphibole gabbro, diopside gabbro, and myloncratic gabbro	10^8–$3.3 \cdot 10^8$	$1.5 \cdot 10^7$–$2.0 \cdot 10^7$	$1.5 \cdot 10^6$–$2.5 \cdot 10^6$	$2.5 \cdot 10^5$–$6.0 \cdot 10^5$
Cataclastic gabbro and albitized gabbro	$2.0 \cdot 10^5$–$9.0 \cdot 10^6$	$5.5 \cdot 10^4$–$2.5 \cdot 10^6$	$1.6 \cdot 10^3$–$2.0 \cdot 10^5$	$3.5 \cdot 10^2$–$1.0 \cdot 10^5$

Rock	Resistivity [Ωm] at t [°C]				
	600	700	800	900	1000
Gabbro-norites and hypersthenic gabbro containing excessive amount of iron	$3.0 \cdot 10^3$–$4.0 \cdot 10^3$	10^3–$3.0 \cdot 10^3$	$1.5 \cdot 10^2$–$5.0 \cdot 10^2$	10^2	$3.0 \cdot 10^1$
Amphibole gabbro, diopside gabbro, and myloncratic gabbro	$2.0 \cdot 10^4$–$3.0 \cdot 10^5$	$2.5 \cdot 10^4$–$1.5 \cdot 10^5$	$5.0 \cdot 10^4$–$8.0 \cdot 10^4$	10^4–$2.0 \cdot 10^4$	$1.5 \cdot 10^3$–$2.0 \cdot 10^3$
Cataclastic gabbro and albitized gabbro	$1.5 \cdot 10^2$–$3.1 \cdot 10^4$	$8.0 \cdot 10^2$–$1.1 \cdot 10^4$	$3.5 \cdot 10^2$–$2.5 \cdot 10^3$	10^2–$9.0 \cdot 10^2$	$6.0 \cdot 10^1$–$2.5 \cdot 10^2$

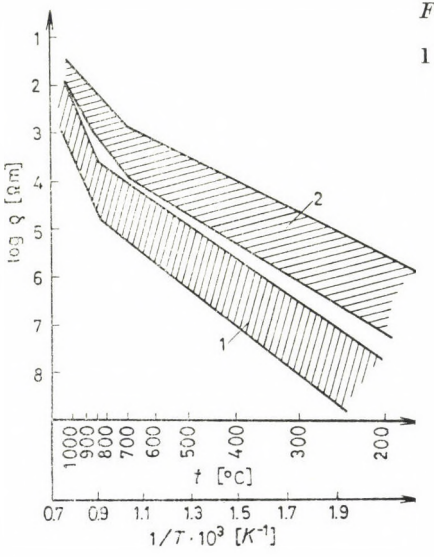


Fig. 20. Dependence of electrical resistivity on temperature
1 – unaltered gabbro of different composition;
2 – cataclastic gabbro

from Figure 20 showing the ranges of resistivity values for fresh gabbro and for gabbro with evidence of the development of deuteric processes in the temperature range 200—1000 °C. The resistivity value of unaltered varieties depending on the content of labradorite of pyroxene type may vary in the range of one and a half order of magnitude (Table 9).

The straight lines $\lg \varrho = f(1/T)$ for the gabbro-norites containing great amounts of labradorite and of rhombic hypersthene are in the upper part of range 1 shown in Figure 20. In the lower part are data for the gabbro containing mostly pyroxene in the form of enstatite and for amphibole gabbro with a minimum ferric oxide content. The value of ϱ for the altered gabbro at high temperatures also depends on the petrographic features. Of the lowest resitivity are gabbro which have undergone cataclasm and deuteric alteration of the albitization and pelitization types (kaolin-like cloudiness and change of feldspar species), as well as gabbros enriched in ferric oxides and having the form of magnetite located along the boundaries of rock-forming minerals. As the degree of the manifestation of deuteric alterations in plagioclase and in other minerals decreases, the resistivity of gabbro increases.

A comparison of gabbros with respect to their activation energy values shows that in the low-temperature range (below 600 °C) diopside gabbros have the minimum activation energy ($E_0 = 0.63—0.7$ eV); the activation energies of other gabbros lie within the limits 0.74—0.88 eV. In the intrinsic conduction range (600—1100 °C) the order of gabbros according to their activation energy values is as follows: amphibole gabbros (1.0—1.6 eV), hypersthene gabbros (1.6—1.9 eV) and diopside gabbros (1.7—2.5 eV). An irregular change of electrical resistivity in the range 600—800 °C associated with the dehydration process is observed for amphibole gabbros,

TABLE 10

The range of the resistivity of diabases at high temperatures

Diabase type	Resistivity [Ωm] at t [°C]				
	200	300	400	500	900
Diabases affected by saussuritization, chloritization, talcization processes: 3–7% of ore mineral content	$1.5 \cdot 10^4$–$5.0 \cdot 10^4$	$1.4 \cdot 10^3$–$1.0 \cdot 10^4$	$1.5 \cdot 10^3$–$2.5 \cdot 10^3$	$1.5 \cdot 10^1$–$3.0 \cdot 10^2$	1.0–5.5
Actinolitizated gabbro-diabases containing 3–7% of ore mineral	$2.2 \cdot 10^5$–$8.0 \cdot 10^5$	$1.8 \cdot 10^4$–10^5	$3.2 \cdot 10^2$–$1.2 \cdot 10^4$	$8.2 \cdot 10^2$–$3.1 \cdot 10^3$	8.5–$6.0 \cdot 10^1$
Actinolitizated gabbro-diabases	$5.0 \cdot 10^5$–$1.8 \cdot 10^6$	$4.0 \cdot 10^4$–$4.0 \cdot 10^5$	$1.9 \cdot 10^3$–$1.8 \cdot 10^4$	10^3–$3.0 \cdot 10^3$	10^1–$2.5 \cdot 10^1$
Leucocratic, silificated gabbro-diabases	10^6–10^7	$2.2 \cdot 10^5$–$9.0 \cdot 10^5$	$2.1 \cdot 10^4$–10^5	$4.0 \cdot 10^3$–$2.5 \cdot 10^4$	$9 \cdot 10^1$–$2.1 \cdot 10^2$

the temperature dependence of their electrical resistivity is determined chiefly by the amphibole.

Gabbro-diabases and diabases picked out from the surface or out of a well are as a rule affected by deuteric processes. Their differentiation according to ϱ is made possible by the different development of deuteric alterations, by the different content of ore minerals and the nature of their exposure. The exposure of ore minerals along the boundaries of rock-forming minerals, saussurization, albitization and other deuteric alterations cause the greatest reduction in the resistivity of these rocks (Table 10). Actinolitizated diabases not so deeply affected by metamorphism are characterized, as shown by the data presented, by a greater resistivity. Leucocratic and little-altered gabbro-diabases show resistivity by approximately 1.5—2 orders of magnitude greater than that of the most high-resistance ones. A low activation energy is typical for all diabases.

Effusive rocks. Basalts are the most important representatives of effusive rocks. They are widely distributed in nature on continents among the products of platform magmatism and geosynclinal magmatism, in oceans and in transitional zones from continents to oceans (Vilensky, 1967). Basalts include plagioclase (labradorite) and ferruginous magnesium minerals, chiefly augite; the occurrence of a considerable amount of ore mineral impurities is also possible.

The presence of a significant amount of amorphous phase in basalts complicates the dependence of their electrical resistivity on the mineral and chemical composition; not only the amount, also the chemical composition of this phase is of great importance. The electrical conductivity of glasses is known to greatly depend on the alkali oxides content in case of their low concentration, and on ferric oxides content. An introduction of bivalent oxides, of CaO and MgO e. g., produces a reverse effect, i. e. a decrease in electrical conductivity.

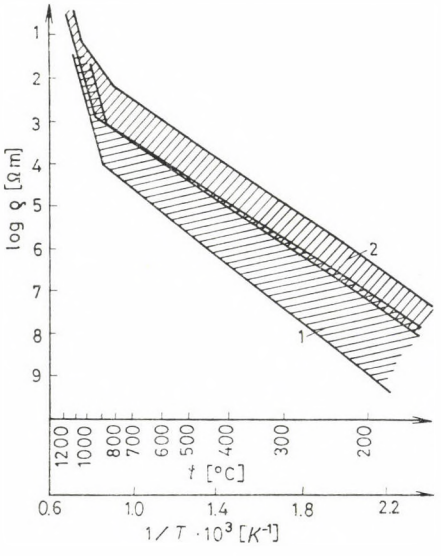


Fig. 21. Ranges of resistivity values for 1 — Caucasian basalt; 2 — dolerites

With respect to structure, basalts and dolerites should be distinguished. The latter, contrary to basalts, are polycrystalline rocks with grain size exceeding 0.5 mm. A study of the electrical resistivity of the Caucasian basalts and dolerites shows that ϱ values for dolerites are confined to a more narrow range, shifted upwards as compared with the basalt range (Fig. 21). The main factor causing the conductivity properties of dolerites to exceed those of basalts is the presence and the form of exposure of an ore mineral, mainly of titanomagnetite having a structure of a solid solution disintegration, i. e. a sponge-like character. Moreover, intercalations of

TABLE 11

Electrical resistivity of basalts of different chemical composition

Rock	Resistivity [Ωm] at t [°C]		
	200	300	400
Caucasian dolerites	$1.0 \cdot 10^6$–$1.7 \cdot 10^7$	$6.2 \cdot 10^5$–$1.8 \cdot 10^6$	$8.3 \cdot 10^4$–$1.2 \cdot 10^5$
Sikhote-Aline dolerites	$6.2 \cdot 10^6$	$2.0 \cdot 10^5$	$3.1 \cdot 10^4$
Sikhote-Aline alkali basalts	10^6–10^7	$1.4 \cdot 10^5$–$5.0 \cdot 10^5$	$3.1 \cdot 10^3$–$5.0 \cdot 10^4$
Sikhote-Aline basalts (high-aluminiferous series)	$2.0 \cdot 10^6$–$4.8 \cdot 10^6$	$1.2 \cdot 10^5$–$3.8 \cdot 10^5$	$1.7 \cdot 10^4$–$3.8 \cdot 10^4$
Basalts of the Baikal area	$4.3 \cdot 10^4$–$6.0 \cdot 10^7$	$7.2 \cdot 10^3$–$5.1 \cdot 10^6$	$1.4 \cdot 10^3$–$6.5 \cdot 10^5$
Basalts of the rift zone of the Indian Ocean	$3.3 \cdot 10^4$–$4.0 \cdot 10^6$	$5.0 \cdot 10^3$–$7.1 \cdot 10^5$	$1.8 \cdot 10^3$–$1.0 \cdot 10^5$

Rock	Resistivity [Ωm] at t [°C]		
	500	600	1000
Caucasian dolerites	$5.0 \cdot 10^3$–$1.8 \cdot 10^4$	$8.4 \cdot 10^3$–$1.4 \cdot 10^4$	$2.5 \cdot 10^1$–$2.2 \cdot 10^2$
Sikhote-Aline dolerites	$5.0 \cdot 10^3$	$3.1 \cdot 10^3$	$2.6 \cdot 10^1$
Sikhote-Aline alkali basalts	$2.2 \cdot 10^3$–$2.0 \cdot 10^4$	10^3–$9.8 \cdot 10^3$	$1.2 \cdot 10^1$–$5.0 \cdot 10^1$
Sikhote-Aline basalts (high-aluminiferous series)	$3.8 \cdot 10^3$–$1.5 \cdot 10^4$	$9.8 \cdot 10^2$–$5.0 \cdot 10^3$	2.5–$1.7 \cdot 10^2$
Basalts of the Baikal area	$5.0 \cdot 10^2$–$6.5 \cdot 10^4$	$2.2 \cdot 10^2$–$6.4 \cdot 10^3$	3.2–$1.9 \cdot 10^1$
Basalts of the rift zone of the Indian Ocean	$9.8 \cdot 10^3$–$2.5 \cdot 10^3$	$6.1 \cdot 10^2$–$6.2 \cdot 10^3$	$1.8 \cdot 10^1$–$1.6 \cdot 10^2$

titanomagnetite in pyroxene and the dust-like precipitation of it within volcanic glass are observed in a number of samples.

Among the Sikhote-Aline basalts (Table 11), alkali-olivine basalts are noted for the highest electrical conductivity. Other petrographic varieties of the basalts of this region generally overlap with the lower limit of the resistivity of the Caucasian basalts. The basalts of the rift zones of the Indian Ocean and of the Baikal area are marked for the low values of their electrical parameters.

The presence of 4—6% of ore minerals and their exposure along grain boundaries or in the form of fine dust-like phase, the presence of ferruginous pyroxene (hypersthene) as well as of the amorphous phase are factors which cause a considerable decrease in the resistivity of basalts. It is to be noted that at temperatures over 800 °C the resistivity is chiefly determined by the chemical composition of the rock-forming minerals while at lower temperatures it is determined by the amount and form of exposure of the ore minerals and of the amorphous phase. However, the possibility is not ruled out that there might be cases when the two last factors would have a decisive influence on the course of the $\lg \varrho = f(1/T)$ curve at high temperatures too. From a comparison of the electrical conductivities of basalts of different geological structure and mineral composition (Fig. 22) it follows that according to the data obtained for the investigated samples, basalts of the rift zones of the Baikal area and of the Indian Ocean have the lowest resistivity. The alkali-basalts have ϱ values close to these and the Caucasian basalts are of the highest resistivity.

ELECTRICAL RESISTIVITY OF ROCKS OF ULTRABASIC COMPOSITION AT HIGH TEMPERATURES AND PRESSURES

The rocks of the ultrabasic feldspar-free complex are divided according to the olivine content into olivenites (100% of olivine), dunites ($\sim$100%), pyroxene olivenites (70—85%), peridotites (30—70%), olivine-pyroxenites (10—30%) and pyroxenites (10%). These rocks are subjected to metamorphism of the serpentization type which is responsible for the wide range of their electrical resistivity values. The effect of this process is considered below. However, the data for rocks unaffected by this process are of utmost importance for the determination of the most probable range of resistivity for the upper part of the mantle.

Among rocks of the ultrabasic complex dunites have the highest resistivity at high temperatures, $t > 800$ °C. Similarly as olivenites and dunites, they consist of olivine but differ from the former in their chromite content (up to 3%), chromite dunites containing even a greater amount of it. As chrome ions do not participate in the recharge of Fe^{2+} and Fe^{3+}, the process of electron transition from one ion to another which increases rock conductivity is inhibited. According to the experimental data the resistivity of olivenites strongly depends on fayalite content and, as it has been pointed out above, decreases with an increase of the latter. Due to this fact a discrepancy of one order of magnitude and sometimes

even greater is observerd between the ϱ values for the same values of thermodynamical parameters.

For the olivenites-pyroxites series a certain increase in electrical resistivity, especially noticeable at high temperatures, is observed when pyroxene is represented by enstatite or by diopside, i. e. by minerals whose composition does not contain ferric cations even in the form of impurities (Table 12).

The values of E_0 and ϱ_0 for ultrabasic rocks in the ranges of both the impurity conduction and intrinsic conduction are presented in Table 13.

TABLE 13

Electrical parameters of ultrabasic rocks

Rock	Temperature range [°C]	E_0 [eV]	ϱ_0 [Ωm]	Expected mechanism of conduction
Olivenites	100– 500	0.62	10^2	Impurity-ionic and
	100– 750	1.0	1	semiconductor
	500–1200	1.8	$2 \cdot 10^{-6}$	intrinsic-ionic
	800–1200	2.55	$5 \cdot 10^{-7}$	
Pyroxenites	100– 600	0.6	$6.2 \cdot 10^1$	
	600– 900	1.0	$8.0 \cdot 10^{-2}$–$2.5 \cdot 10^{-5}$	
	900–1100	2.2–2.5	10^{-5}–$3.1 \cdot 10^{-7}$	
Peridotites	550–1200	2.3	$1.7 \cdot 10^{-6}$	

SERPENTINIZATION EFFECT

The ultrabasic feldspar-free complex of rocks is liable to undergo a metamorphic transformation of the serpentinization type. This process is most intensive in zones of crush. Serpentinization substantially affects the values of elastic wave velocity, density, strength and other properties. The difference between the seismic velocities in the unaltered rocks and in rocks altered by completely serpentinized olivenites is about 2000 msec^{-1}: the velocity decreases from 7.3 kmsec^{-1} to 5.3 kmsec^{-1}. The density decreases from 3.2 g/cm^3 to 2.4 g/cm^3 at the same time.

The change of the mechanical characteristics is accompanied by a certain change in the electrical parameters of the given rocks as well. The main feature of serpentinous rocks devoid of moisture is an unusually wide range of resistivity values (6—8 orders of magnitude) under the conditions of atmospheric pressure and room temperature. For water-saturated rocks the scatter in ϱ values is less and equals 3—4 orders of magnitude at most, while according to the data for one deposit the difference in the resistivity of such rocks in natural bedding is only 1—2 orders of magnitude (Vagshal, 1970, Parkhomenko et al. 1973). With increasing temperature the resis-

TABLE 12

Electrical resistivity of ultrabasic rocks and eclogites and their xenoliths

Rock	Resistivity [Ωm] at t [°C]			
	200	500	600	700
Olivenites	$3.3 \cdot 10^8$–$2.5 \cdot 10^9$	$4.1 \cdot 10^5$–$2.9 \cdot 10^7$	$1.4 \cdot 10^4$–$2.6 \cdot 10^4$	$2.0 \cdot 10^3$–$1.0 \cdot 10^5$
Olivine-pyroxenites (80–90% of pyroxene)	$2.5 \cdot 10^9$–10^{10}	$3.2 \cdot 10^6$–$7.1 \cdot 10^6$	$1.1 \cdot 10^6$	$2.0 \cdot 10^5$–$2.6 \cdot 10^5$
Dunite	$6.6 \cdot 10^8$	$1.7 \cdot 10^6$	$7.1 \cdot 10^5$	$4.1 \cdot 10^5$
Dunite, pipe "Obnazhennaya"	$3.1 \cdot 10^9$	$1.0 \cdot 10^6$	$2.4 \cdot 10^5$	$6.2 \cdot 10^4$
Spinel dunites, pipe "Obnazhennaya"	$1.2 \cdot 10^8$–$2.5 \cdot 10^8$	$3.2 \cdot 10^5$–$6.3 \cdot 10^5$	$1.1 \cdot 10^4$–$7.1 \cdot 10^4$	$1.0 \cdot 10^4$–$2.5 \cdot 10^4$
Pyrope-peridotite, pipe "Obnazhennaya"	$1.2 \cdot 10^9$–$3.4 \cdot 10^{10}$	$8.3 \cdot 10^5$–$2.5 \cdot 10^7$	$1.9 \cdot 10^5$–$3.5 \cdot 10^6$	$3.9 \cdot 10^4$–$1.8 \cdot 10^6$
Pyrope-eclogites from kimberlites	$5.0 \cdot 10^8$–$6.2 \cdot 10^9$	$2.6 \cdot 10^5$–$1.4 \cdot 10^6$	$6.2 \cdot 10^5$–$1.7 \cdot 10^7$	$7.0 \cdot 10^4$–$1.3 \cdot 10^5$
Crustal eclogites of Kazakhstan	$6.0 \cdot 10^5$–$1.1 \cdot 10^8$	$7.1 \cdot 10^3$–$1.0 \cdot 10^4$	$3.6 \cdot 10^3$–$2.4 \cdot 10^4$	$1.3 \cdot 10^3$–$8.3 \cdot 10^3$
Crustal eclogites of the Urals	$1.3 \cdot 10^7$–$6.6 \cdot 10^8$	$3.6 \cdot 10^4$–$6.2 \cdot 10^4$	$1.2 \cdot 10^4$–$2.0 \cdot 10^4$	$4.0 \cdot 10^3$–$5.1 \cdot 10^3$

Rock	Resistivity [Ωm] at t [°C]			
	800	900	1000	1100
Olivenites	$3.0 \cdot 10^2$–$2.0 \cdot 10^3$	10^2–$2.5 \cdot 10^2$	$1.6 \cdot 10^1$–$1.2 \cdot 10^2$	$3.3 \cdot 10^1$–$1.0 \cdot 10^1$
Olivine-pyroxenites (80–90% of pyroxene)	$3.2 \cdot 10^4$–$4.5 \cdot 10^4$	$1.0 \cdot 10^4$–$1.8 \cdot 10^4$	$1.4 \cdot 10^3$–$1.8 \cdot 10^3$	
Dunite	$6.0 \cdot 10^4$	$1.4 \cdot 10^4$	$1.1 \cdot 10^3$	$4.5 \cdot 10^2$
Dunite, pipe "Obnazhennaya"	$2.5 \cdot 10^4$	$1.1 \cdot 10^4$	$1.0 \cdot 10^3$	$3.9 \cdot 10^1$
Spinel dunites, pipe "Obnazhennaya"	$2.0 \cdot 10^3$–$4.0 \cdot 10^3$	$2.9 \cdot 10^2$–$3.1 \cdot 10^3$	$1.0 \cdot 10^2$–$1.6 \cdot 10^3$	$4.6 \cdot 10^1$–$3.3 \cdot 10^2$
Pyrope-peridotite, pipe "Obnazhennaya"	$8.3 \cdot 10^3$–$7.7 \cdot 10^5$	$1.1 \cdot 10^3$–$2.2 \cdot 10^5$	$2.5 \cdot 10^2$–$2.5 \cdot 10^4$	$1.0 \cdot 10^1$–$1.7 \cdot 10^4$
Pyrope-eclogites from kimberlites	$2.0 \cdot 10^4$–$6.7 \cdot 10^4$	10^3–$1.7 \cdot 10^4$	$5.0 \cdot 10^3$–$1.4 \cdot 10^4$	10^2–$2.0 \cdot 10^3$
Crustal eclogites of Kazakhstan	$3.7 \cdot 10^2$–$1.6 \cdot 10^3$	$3.4 \cdot 10^2$–$9.9 \cdot 10^2$	$5.0 \cdot 10^2$–$1.8 \cdot 10^3$	
Crustal eclogites of the Urals	$1.9 \cdot 10^3$–$6.6 \cdot 10^3$	$5.3 \cdot 10^2$–$8.3 \cdot 10^2$	$5.2 \cdot 10^1$–$1.5 \cdot 10^2$	

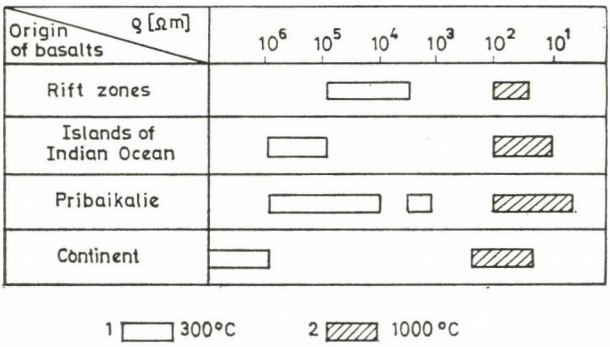


Fig. 22. Intervals of the values of electrical resistivities of basalts of different origin at: 1 – 300 °C; 2 – 1000 °C

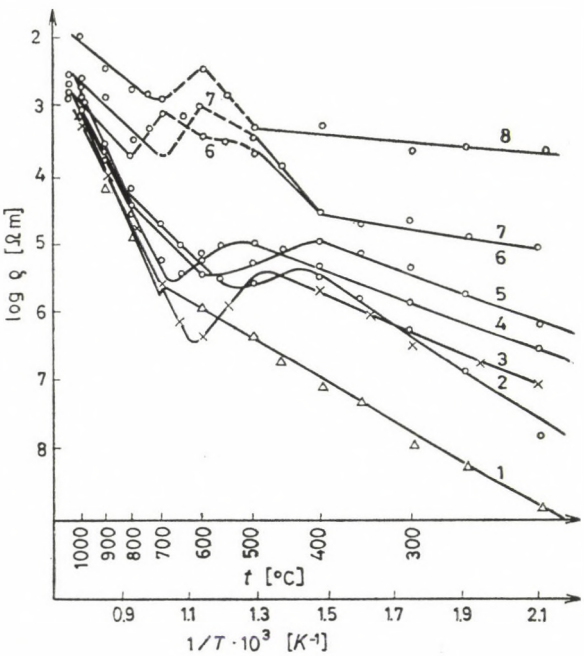


Fig. 23. Dependence on temperature of the electrical resistivity of serpentinous ultrabasic rocks 1 – 5 dunites; 6 – 8 periodites

tivity range for dry rocks gets reduced but still remains considerably wide up to 800—900 °C as can be seen from Figure 23.

A study of the dependence of the electrical resistivity of serpentinous rocks on the amount of serpentine (Fig. 24) reveals that the resistivity has a tendency to decrease with increasing serpentine amount, and that there is a wide range of ϱ for the same amount of serpentine. The rock resistivity depends on the nature of distribution of the ore mineral (magnetite, titanomagnetite or chromite with magnetite) exposed as a result of serpentinization and on the amount of the ore mineral for the same amount of serpentine.

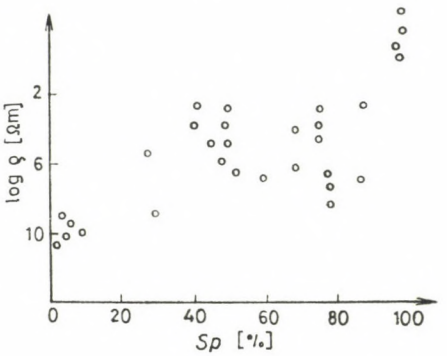


Fig. 24. Values of ultrabasic rock resistivities depending on serpentine content at $t = 200$ °C

The serpentinization process is not always accompanied by the exposure of the ore mineral. According to the existing notions serpentinization proceeds in two stages. The first stage (autometamorphism) results in the formation of the chrysolite variety and is not accompanied by magnetite exposure. During the second stage (allometamorphism) antigorite is formed and an intensive exposure of ore minerals takes place. According to whether the rock has undergone only one or both stages of metamorphism a principal difference in the electrical parameters is observed. A similar difference was observed by Moskaleva (1969) for the magnetic properties of rocks.

ELECTRICAL RESISTIVITY OF XENOLITHS, OF ULTRABASIC ROCKS AND OF ECLOGITES

Among the most interesting data for the study of the material composition of the mantle are those on the electric parameters of xenoliths. At present experimental data are available on xenoliths, eclogites and other ultrabasic rocks, namely dunites, peridotites, olivenites out of the pipe "Obnazhennaya" of the Avachi volcano on Kamchatka, basalts of the Baikal area and of the Seychelles Islands in the Indian Ocean (Parkhomenko and Bondarenko, 1972). The experimental data are presented in Figure 25 and in Tables 12 and 14. The highest resitivity is characteristic of the xenoliths of eclogites containing up to 50% of pyrope and chrome-diopside. The resistivity of these rocks exceeds the resistivity of xenoliths of other mineral composition by about one order of magnitude in the entire temperature range under study. The most akin to eclogites as for resistivity is olivine of predominantly forsterite composition, and pyrope peridotites composed of high-magnesium olivine, chrome-diopside, enstatite and pyrope garnet. Olivine kimberlites are also characterized by a high resistivity. The resistivity olivine of kimberlites out of the pipe "Obnazhennaya" is higher than that of samples from the tube "Udachnaya". The data presented below show that they also differ in their activation energy value and in the onset temperature of the intrinsic conduction mechanism.

TABLE 14

Electrical characteristics of kimberlite olivenites

Rock, deposit	Temperature range [°C]	ϱ [Ωm] at the point of break	E_0 [eV]	ϱ_0 [Ωm]
Kimberlite-olivenite 1411, pipe "Obnazhennaya"	100– 500	$1.0 \cdot 10^{11}$	0.6	$1.3 \cdot 10^{2}$
	500– 950	$2.5 \cdot 10^{6}$	1.2	$1.2 \cdot 10^{-1}$
	950–1200	$1.0 \cdot 10^{3}$	3.5	$1.0 \cdot 10^{-9}$
Kimberlite 1319, pipe "Udachnaya"	150– 400	$2.5 \cdot 10^{7}$	0.3	$2.0 \cdot 10^{1}$
	400– 470	$2.5 \cdot 10^{6}$	–	
	470– 700	10^{7}	1.0	$1.1 \cdot 10^{-1}$
	700–1200	$2.5 \cdot 10^{5}$	2.8	10^{-8}

The resistivity of almandine eclogites, olivine xenoliths from the basalts of the Baikal area, of the Avachi Volcano on Kamchatka and of the Seychelles Islands in the Indian Ocean is usually lower, especially in the high temperature range 800—1200 °C.

Thus the experimental evidence shows that the pyrope-containing xenoliths from kimberlites have resistivity by one-two orders of magnitude greater than the olivine xenoliths or pyroxene xenoliths from basalts. The spinel-containing xenoliths have a considerably smaller value of electrical resistivity than dunites containing no spinel.

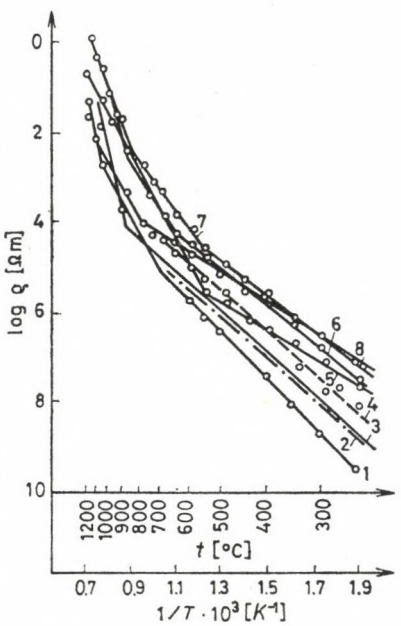


Fig. 25. Dependence on temperature of the electrical resistivity of xenoliths in kimberlites 1 – olivine-forsterite; 2 – pyrope-peridotite I; 3 – dunite; 4 – pyrope-peridotite II; 5 – spinel dunite in basaltoids; 6 – olivinite; 7 – olivinite of Lake Reunion, 8 – olivine nodule of the Baikal area (Parkhomenko and Bondarenko, 1972)

Since for the rock complex under consideration the values of E_0 and of ϱ_0 may serve as initial data for theoretical calculations of the distribution of electrical resistivity in function of depth in the mantle, we are giving below the values of the activation energy and of the resistance coefficient for the high temperature range.

ELECTRICAL RESISTIVITY OF THE "MANTLE" AND THE "CRUSTAL" ECLOGITES

Since on the boundary between the earth's crust and the upper mantle rocks of the eclogite facies may occur in addition to the basic and ultrabasic rocks, experimental data are also presented for "crustal" and "mantle" eclogites which differ in a number of mineralogical and petrological features. In particular, garnet-almandine ($Fe_3Al_2Si_3O_{12}$) is part of the mineralogical composition of the former and garnet-pyrope ($Mg_3Al_2Si_2O_{12}$) — of the latter. Experimental data also reveal that under high thermodynamical conditions they are characterized by different electrical properties.

The electrical resistivity of *crustal eclogites* at high temperatures and pressures was studied mainly on the rock samples obtained from the Kokchetav massif (Kazakhstan) and from the Urals. Within the massif in Kazakhstan deep-seated rocks of the foundation of a young Epi-Hercynian platform are laid bare (Efimov, 1968).

It has been established that the Kazakhstan eclogites distinctly differ from the *mantle eclogites* as regards their electrical resistivity. On the contrary, the crustal eclogites of the Southern Urals have intermediate values of ϱ and their upper and lower values overlap with the mantle eclogites on the one side and with the crustal eclogites, on the other side (Fig. 26).

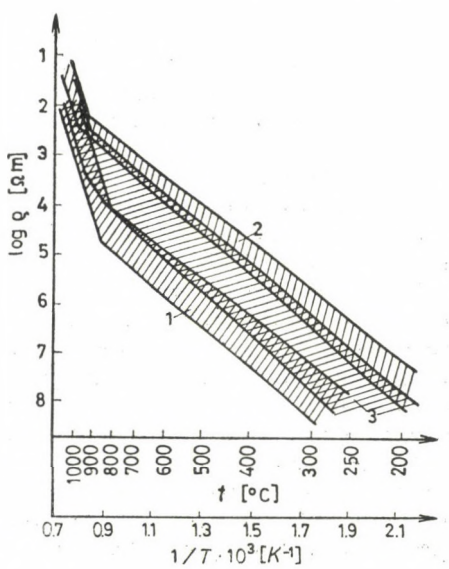


Fig. 26. Ranges of electrical resistivity values of eclogites in a wide temperature interval
1 – mantle eclogites; 2 – eclogites from the Urals; 3 – eclogites from Kazakhstan

This is mainly accounted for by their mineral composition and by the degree of metamorphism. The high-resistance mineral pyrope predominates in the composition of the mantle eclogites while the crustal eclogites of Kazakhstan possessing maximum conductivity are composed of garnets of predominantly almandite composition. Besides, the latter contain 30% of omphacite and 15% of hornblende. The most important contribution to electrical conductivity is made by omphacite due to its high content of ferric cations and of sodium cations as well as to the hydroxil group $(OH)^{-1}$. Hornblende may have a considerable effect causing a reduction of the ϱ values.

According to their electrical characteristics the *Ural eclogites* are in the main subdivided into three groups corresponding to the three stages of metamorphism: progressive metamorphism in the eclogite facies environment; "deep diaphthoresis" (glaucophane slate facies); diaphthoresis (green slate facies).

The rocks of the first group composed of garnet (90%) chiefly of the almandite composition have the lowest resistivity. The presence of amphibole in the second group somewhat reduces its resistivity. Besides, it causes anomalous ϱ variations over some sections with increasing temperature.

The resistivity value for the third group of eclogites frequently overlaps the ϱ values of the first two groups. Similarly to amphibole, the presence of chlorite, up to 40%, results in ϱ-anomalies at high temperatures associated with the separation of hydroxyl group $(OH)^{-1}$.

THE EFFECT OF PRESSURE ON THE ELECTRICAL RESISTIVITY OF DIFFERENT ROCKS AT HIGH TEMPERATURES

The available experimental data on the electrical resistivity of crystalline rocks devoid of water in the range of impurity conduction (100—650 °C) and for the pressure range $p = 1—20$ kb show that under these conditions the character of the dependence $\varrho = f(p)$ is determined by the physicochemical properties of the rock-forming minerals, by the porosity ratio and by the structural features of the rock. The overwhelming majority of rocks show a decrease in resistivity with pressure increasing up to 20 kb. The dependence $\varrho = f(p)$ is frequently of a *linear* character, mainly for pressures over 6 kb.

The rate of resistivity reduction accompanying an increase in pressure can be quite different for samples of the same petrographic type and for samples of different groups of rocks. In some cases certain varieties of rocks, such as alkaline rocks (juvite, ijolite) are characterized by a sharp drop in ϱ in the initial pressure range from 1 to 6—8 kb. At higher pressures $d\varrho/dp$ considerably decreases and its value may approach zero.

Graphs presented in Figure 27 for some widespread rocks illustrate the most typical pattern of their resistivity variations accompanying pressure increase in the temperature range 200—600 °C. Besides, values of ϱ at high pressures and temperatures are presented in Table 15 for rocks of different

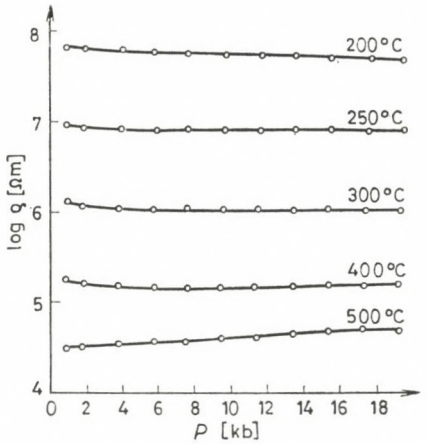


Fig. 27a. Dependence on pressure and temperature of the electrical resistivities of granites

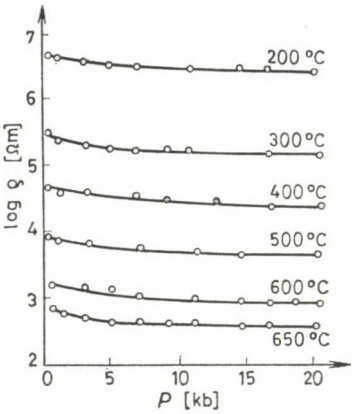


Fig. 27b. Dependence on pressure and temperature of the electrical resistivities of eclogites

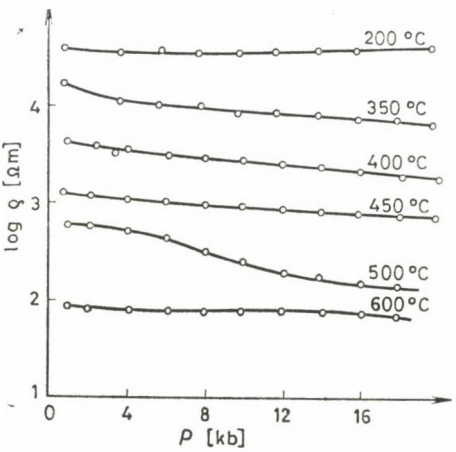


Fig. 27c. Dependence on pressure and temperature of the electrical resistivities of dunites

mineral composition, for fresh rocks as well as for those affected by deuteric alterations. It can be seen that for the granite-diorite series, which has not been altered by deuteric processes, the dependence $\varrho = f(p)$ has a different character for rocks of different mineral composition. For instance, granites with a high quartz content show a small (a few per cents) increase in resistivity rather than a decrease (Fig. 27a). This is due to the essentially different character of the law $\varrho = f(p)$ for quartz and minerals of the feldspar group as compared with the majority of silicates. Some of them exhibit either resistivity minima in certain crystallographic directions or only an increase in resistivity with increasing pressure, as already stated above.

TABLE 15

Resistivity of different rocks at high pressures and temperatures

Rock	t [°C]	ϱ [Ωm] at p [kb]		$\Delta\varrho/\varrho \cdot 100\%$
		1	20	
Granite	200	$1.8 \cdot 10^7$	$1.1 \cdot 10^7$	39.0
	300	$1.2 \cdot 10^7$	$7.2 \cdot 10^6$	40.0
	400	$7.7 \cdot 10^5$	$5.9 \cdot 10^5$	23.0
	500	$1.2 \cdot 10^5$	$9.8 \cdot 10^4$	14.0
	550	$4.3 \cdot 10^4$	$3.0 \cdot 10^4$	29.0
Diorite	200	$3.1 \cdot 10^7$	$8.3 \cdot 10^6$	26.8
	300	$3.5 \cdot 10^6$	$4.5 \cdot 10^5$	12.8
	400	$5.0 \cdot 10^5$	$1.8 \cdot 10^5$	36.0
	500	10^5	$2.7 \cdot 10^4$	27.0
Gabbro	200	$1.3 \cdot 10^8$	$7.7 \cdot 10^7$	59.2
	300	$9.8 \cdot 10^6$	$6.3 \cdot 10^6$	64.3
	400	$7.1 \cdot 10^5$	$5.0 \cdot 10^5$	70.4
	500	$8.3 \cdot 10^4$	$4.3 \cdot 10^4$	51.8
	600	$5.0 \cdot 10^3$	$3.4 \cdot 10^3$	68.0
Pyrope peridotite	200	$6.6 \cdot 10^9$	$4.7 \cdot 10^9$	71.2
	400	$1.5 \cdot 10^6$	$2.7 \cdot 10^5$	18.0
	570	$9.1 \cdot 10^4$	$3.6 \cdot 10^4$	39.5
	620	$2.5 \cdot 10^4$	$1.4 \cdot 10^4$	56.0
Spinel dunite	200	$2.5 \cdot 10^7$	$1.0 \cdot 10^7$	40.0
	400	$1.3 \cdot 10^5$	$4.7 \cdot 10^4$	36.1
	550	$5.9 \cdot 10^4$	$2.2 \cdot 10^4$	37.2
	680	$1.5 \cdot 10^3$	$5.5 \cdot 10^2$	36.6
Pyrope eclogite	200	$2.2 \cdot 10^9$	$7.7 \cdot 10^8$	35.0
	400	10^5	$3.9 \cdot 10^4$	39.0
	500	$8.3 \cdot 10^4$	$4.5 \cdot 10^4$	54.2
	600	$2.5 \cdot 10^4$	$5.0 \cdot 10^3$	20.0
	650	$2.0 \cdot 10^3$	$1.2 \cdot 10^3$	60.0
Olivenite	300	$5.5 \cdot 10^7$	$2.3 \cdot 10^7$	41.8
	400	$5.9 \cdot 10^6$	$2.4 \cdot 10^6$	40.6
	500	$1.8 \cdot 10^5$	$5.2 \cdot 10^4$	28.8
	600	$1.1 \cdot 10^4$	$4.2 \cdot 10^3$	38.1
	650	$3.5 \cdot 10^3$	$1.0 \cdot 10^3$	28.5

The characteristic feature of diorites and granodiorites is that their resistivity, unlike that of granites, always decreases with increasing pressure. This is explained by the fact that the main contribution to their electrical conductivity is made by colored minerals, namely by amphiboles, and the resistivity of the latter decreases under the effect of pressure. The rate of decrease of the resistance reduction depends in this case on the total content of ferric oxides and sodium oxides.

A smaller variation of resistivity with increasing pressure is characteristic of gabbro as compared with acidic and intermediate rocks. The decrease in ϱ varies from 40% to 60% depending on temperature and on the mineral composition as pressure increases from 1 to 20 kb.

If the rocks considered above, i. e. granites, diorites and gabbro have undergone deuteric alterations (cataclasm, pelitization, albitization etc.) they will show a much greater decrease in resistivity due to an increase of pressure. In the pressure range considered above their resistivity may decrease by one — one and a half order of magnitude. In basalts, similarly as in gabbro, only a reduction of resistivity is observed with increasing pressure and the rate of decrease diminishes as pressure increases.

As it has already been stated, xenoliths of ultrabasic composition, such as pyrope peridotite, spinel dunite and others possess a high resistivity that decreases under the effect of pressure at temperatures up to 650 °C. This decrease is, as a rule, rather small as shown by the data presented in Table 13. The resistivity of olivenites and mantle eclogites varies only in a small degree, too.

It is important to note that for all rocks a direct proportionality holds between the percentage of resistivity reduction ($\Delta\varrho/\varrho \cdot 100\%$) and the porosity. The existence of slit-like pores is at that of a particular importance. A study of gneisses has shown that in case of a strong anisotropy the rate of resistivity decrease with increasing pressure is greater across the lamination than along it and that this difference diminishes with increasing temperature.

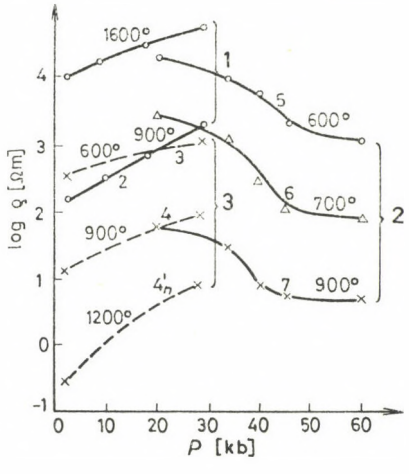


Fig. 28. Dependence on pressure of the electrical resistivity of 1— albite; 2— olivine; 3— basalt at high temperat ures

There is still an insufficient amount of data on rock studies at temperatures over 650—700 °C and at pressure higher than 20 kb to have a notion of the values of resistivity in the mantle substance and of the character of its variation with depth. The studies were in the main concerned with a few minerals and rock varieties (Bradley et al. 1964; Hamilton, 1965; Bondarenko and Feldman, 1973; Schober, 1971; Khitarov and Slutsky 1965, 1971; Watanabe, 1970, 1972). Figure 28 presents curves $\varrho = f(p, t)$ for pressures up to 60 kb for albite, basalt and olivenite according to the data of different authors. The largest increase in resistivity was observed for albite, a somewhat smaller one for basalt, while olivenite is characterized by a decrease in resistivity. For forsterite, on the contrary, an increase in resistivity and in the activation energy is observed.

The smooth variation of electrical resistivity at high thermodynamical parameters may be distrubed by a polymorphic transition. A sharp decrease in ϱ of two orders of magnitude is established for the transition of fayalite of the olivine structure into spinel at $p = 33$ kb and $t \approx 600$ °C (Akimoto and Fujisawa, 1965). The transition of cyanite into sillimanite at $t = 1130$ °C and $p = 19$ kb is, on the contrary, accompanied by an increase in resistivity of an order of magnitude (Slutsky, 1968). The polimorphic transition in sodalite also manifests itself in the resistivity variation.

ELECTRICAL RESISTIVITY DISTRIBUTION IN THE EARTH'S CRUST AND UPPER MANTLE FROM LABORATORY DATA ON ROCKS

To solve a number of geophysical problems connected with the study of the earth's crust and upper mantle, with the physics of earthquake foci as well as with the search for useful minerals further data are required on the structure and material content of the earth's interior. During the entire period of development of geophysics seismological, gravimetric and magnetometric field data were the principal sources of information. A lot of material has been accumulated on the electrical characteristics of deeply seated rocks thanks to the introduction of magnetotelluric sounding into the field observation practice. On the other hand, laboratory data on the electrical resistivity of the most widespread groups of rocks at high thermodynamical parameters are also available.

Geoelectric models of the earth's crust and upper mantle constructed for the known structural schemes of the crust and the mantle are presented below. Since the electrical resistivity of rocks is very sensitive to changes of temperature and in view of the fact that at the present state of development of the geothermal science temperature ranges of only 100—200 °C can be determined, we have constructed two models for the most probable limiting temperature distributions.

A shield. According to geological and seismic data, the upper strata of a shield earth crust, i. e. the so called "granite" layer, reaches a depth of 20 km. It may be represented by granites and shales. The longitudinal elastic wave velocity V_p and the density of these rock samples in the pressure

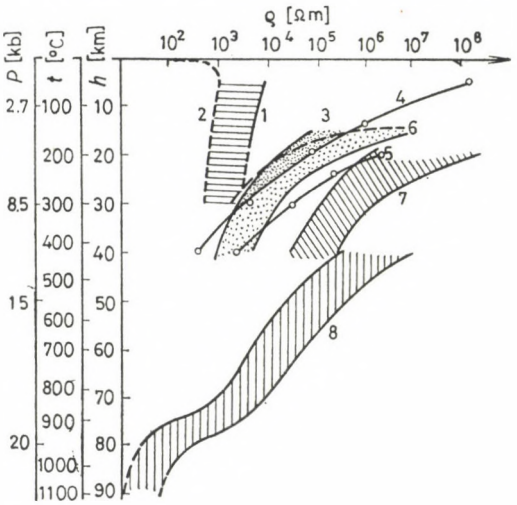


Fig. 29. Resistivity variation with depth for different shield-forming rocks
1, 2 – water-saturated granites and diabases; average data for: 3 – shales; 4 and 5 – diabases of different degree of metamorphism; ranges of values for: 6 – amphibolites; 7 – gabbro; 8 – ultrabasic rocks

range from 1 to 5 kb have values which correspond to the values obtained by geophysical methods. The temperature distribution shown in Figure 29 is taken from the paper of Lubimova (1968) where a calculation is given of the dependence of temperature on depth down to 100 km for the Pechenga region on the Kola Penninsula.

The shaded area in Figure 29 limited by curves 1 and 2 is constructed from the experimental data for water-saturated granites (1) and diabases (2). Curve 1 limits the experimental points obtained for granites saturated with a 3 g/l NaCl solution in the 0.1—1.5 kb pressure range and the 20—150 °C temperature range as well as points extrapolated for higher pressures and temperatures. Curve 2 is obtained by way of introduction of a correction for the corresponding pressure and temperature for diabases saturated also with a 3 g/l NaCl solution. Curves 3, 4 and 5 are drawn from the averaged experimental data for a quartz-chlorite schist (3) and for diabases (4,5) devoid of moisture, the pressure and temperature effects being taken into account. The resistivity values for dehydrated granites and diorites for corresponding values of p and t lie much to the right of curves 4 and 5 because their resistivities in the range 20—600 °C are by 2—3 orders of magnitude higher than those of diabases. It appears that a dehydrated state of rocks in the earth's interior at depths of 10—20 km is not possible since the resistivity of dry rocks is much higher than that recorded with the use of field methods. At a depth exceeding 20 km ϱ values for water-saturated rocks and for some rocks devoid of water appear to come closer.

The most probable representatives of the upper part of the "basalt" layer are the rocks of the amphibolite facies of metamorphism and of the deeper part of this layer the rocks of the granulite-basic facies. In this connection we have indicated the ranges of the most typical resistivity values for amphibolites (6) and gabbro (7) in case of the given variations of temperature and pressure with depth. Moreover, the data for moisture-

containing rocks are extrapolated to a depth of 30 km, which corresponds to temperatures of about 300 °C and pressures of 8.5 kb.

It should be noted that for amphibolites enriched by a large amount of ferruginous-sodium amphiboles, having a similar composition as riebeckites, an extension of the said range by one to one and a half orders of magnitude may be observed. When rocks of the gabbro type are present in the earth's crust at the Moho discontinuity the resistivity may vary according to Figure 29 (7) in the limits of $4 \cdot 10^4 - 4 \cdot 10^5$ Ωm if no account is taken on the rarely occurring gabbro of a greater resistivity of about $5 \cdot 10^6$ Ωm at $p = 10$ kb and $t = 400$ °C. The resistivity range for amphibolites appears to be smaller by about an order of magnitude. The effect of the interstitial solution on the resistivity values apparently extends to the rocks of the "basalt" layer, too. One may assume, however, that in connection with the closure of slit-like pores and with a compaction of rocks the role of the moisture diminishes and a certain rise in resistivity with depth becomes possible. Consequently, the most probable value of the maximum resistivity in the upper part of the crust at the Moho discontinuity is $5 \cdot 10^5 - 5 \cdot 10^6$ Ωm, the minimum being 10^3 Ωm. The electrical resistivity distribution in the upper part of the mantle is constructed from the data obtained for olivenites and peridotites under conditions of simultaneously applied pressure and temperature. A drop of resistivity of some two orders of magnitude at a depth of 70—80 km is possible for there is an intensive decrease in the resistivities of these rocks at temperatures 850—1100 °C. However, it should be taken into account that the experiments were performed in the open air and the observed rise of conductivity may be due to the transition of a part of iron from a bivalent state to a trivalent one. Under the conditions of a reducing medium this phenomenon is ruled out. Besides, in the intrinsic conduction range the increasing pressure leads to an increase rather than to a decrease in the resistivity of forsterite and of peridotite; the predominating effect of pressure at the depth from 70 km down may therefore result in a certain increase in resistivity rather than in a decrease. It should be noted that the right-hand curve (8) delineates the data for ultrabasic rocks containing a great amount of ferric oxides while the left-hand-side one delineates the data for the same rocks but of a predominantly magnesium composition.

While shields are characterized by a minimum heat flow, the Baikal depression, island arcs, regions of recent volcanism possess a high heat flow and high thermal gradients are typical for them. In terms of laboratory data it is thus most interesting to analyse the possible character of the resistivity-depth variations for regions of recent tectonic activity. These are usually characterized by the presence of a sedimentary stratum 10—12 km thick, of a "granite" layer occurring at depths of 10—25 km, and of a "basalt" layer reaching a depth of 45—50 km.

The determination of the resistivity distribution in the sedimentary stratum is based on the following data. As it is well known, there is an increase in the elastic wave velocity in the sedimentary stratum from 2.5 kmsec^{-1} in the near-surface part of the stratum to 4.5 kmsec^{-1} at its boundary with the "granite" layer. This is to a considerable degree associated with a substantial increase in rock density and hence with the reduction of water

content. On the other hand, the experimental data for sedimentary rocks of small porosity show that the effect of temperature at a depth of 5 km may be compensated by pressure. It is possible that a similar situation would be observed down to the depths of 10—12 km. The maximum resistivity value for sedimentary rocks evidently cannot exceed the resistivity of water-saturated igneous rocks for the same values of p and t. Using experimental data for sedimentary rocks and the correlation existing between the V_p and ϱ values for these rocks we can obtain the most probable values of ϱ which fall into the region shown in Figure 30.

The resistivity distribution in the "granite" layer is shown according to the laboratory data for water-saturated granites (1), as well as for rocks devoid of free water, namely granites (2), diorites (3) and diabases (4). Data on temperature dependence up to 1000 °C and on pressure dependence up to 15 kb for gabbro were used in constructing the geoelectric profile of the "basalt" layer. The resistivity of its upper part may correspond to the analogous data for amphibolites. Thus, according to the curves presented, the minimum resistivity for the "granite" layer at a depth of 20 km may amount to $4 \cdot 10^2$ Ωm, and the maximum resistivity may reach 10^4 Ωm. Assuming that the composition of the "basalt" layer corresponds to that of gabbro or amphiboles we obtain for the Moho discontinuity the values of $\varrho_{\min} = 10^3$ Ωm and $\varrho_{\max} = 10^4$ Ωm. The resistivity of the upper part of the mantle was determined approximately by extrapolating the experimental data, obtained for temperatures up to 1200 °C at atmospheric pressure, for xenoliths of dunite and eclogite composition.

It should be pointed out that there is a possibility for anomalous resistivity values in the deep fault zones. Deep faults frequently form belts which stretch for distances from a few hundred to a few thousand kilometers and are a few hundred kilometers wide (Borisov, 1967). The magma of basic, ultrabasic or alkaline composition frequently penetrates along such permanent faults (Galakhov, 1966). Regions of dislocated rocks, phenom-

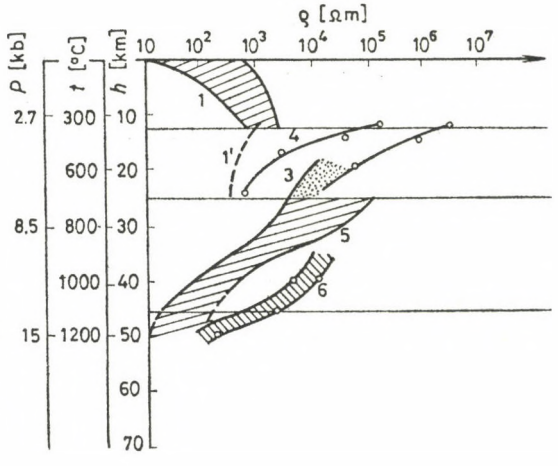


Fig. 30. Resistivity variations with depth for different rocks which form tectonically active structures
1 – water-saturated granites; 2 – "dry" granites; 3 – "dry" diorites; 4 – diabases; 5 – gabbro; 6 – mantle eclogites

ena of breakdown and an advanced degree of metamorphism, phenomena of cataclasm and of alkaline metasomatosis are frequently confined to such faults (Borisov, 1967). In fault zones the process of serpentinization becomes more active. As shown above all these processes greatly reduce rock resistivity. As a result of deuteric processes highly alkaline rocks, the serpentinous ultrabasic rock complex as well as acidic and intermediate rocks, have a resistivity reduced by two and sometimes even by three orders of magnitude as compared with fresh rocks. Simultaneously with the electrical parameters there is a change in elastic wave velocity and in density, and in case of the serpentinization of ultrabasic rocks a substantial increase in magnetic permeability.

Conducting layers in the earth's crust and upper mantle. It has been recently indicated that there are layers in the earth's crust and upper mantle which possess electrical conductivity by two or three orders of magnitude higher than in the overlying or underlying strata. Several assumptions have been made as to the origin of these layers in the earth's crust (Gornostaev et al., 1970; Parkhomenko, 1971; Parkhomenko and Bondarenko, 1972; Bondarenko, 1973; Berdichevsky et al., 1973).

According to an analysis of laboratory data on resistivity of different rocks at high temperatures and pressures the presence of conducting layers in the earth's crust may be explained as follows:

1. Presence of metamorphosed rocks of the types of gneisses, amphibolites and slates enriched by ferric and sodium oxides. Saturation by solutions of high concentration (5—10 g/l of NaCl and other salts) may cause a substantial reduction of resistivity. In the latter case these layers must occur under water-resisting strata of rocks restricting moisture diffusion.

2. Presence of masses of serpentinites or of masses of serpentinous rocks which have undergone the second state of metamorphism.

3. Process of rock dehydration, in course of which the rock is enriched by a highly conducting solution. Besides, if magnesium-ferruginous minerals are present in the rocks this process appears to be accompanied by chemical reactions resulting in a decrease of ϱ of the solid phase by 1—2 orders of magnitude.

4. Process of melting of rocks of granite composition in the transition zone from the "granite" layer to the "basalt" layer.

The first two assumptions require a geological substantiation of the possibility that strata of the said rocks several kilometers thick and stretching for hundreds of kilometers can really exist. On the other hand, dehydration and melting processes in rocks of the amphibolite facies of metamorphism, in granites and in gneisses are possible only at high temperatures (600 °C and more) and thus can take place only in regions with a high heat flow.

The responsibility of dehydration and melting processes for the conducting layers is corroborated by the anomalies observed by other geophysical methods. Zones of an increased electrical conductivity in certain regions are also characterized by lower values of seismic velocities, density and strength. The latter is expressed by the confinement of seismic activities exactly to the depths of 15—20 km (rift structures, alpine mountain systems and intraplatform activation zones).

As to the origin of the conducting layers in the upper part of the mantle

only one assumption can be made, namely that it is due to the manifestation of a complete or of a partial melting.

Khitarov and his collaborators have shown that the onset of the melting of rocks is accompanied by a jump in electrical resistivity of two or three orders of magnitude, the subsequent development of the process causing no further substantial variation of ϱ. A decrease in resistivity also takes place in case of a partial amorphization of rocks. All the effusive rocks have resistivity by one or two orders of magnitude lower than their intrusive analogues. As the content of the amorphous phase in basalts increases, their resistivity decreases in a wide temperature range. The effect of the amorphous phase enriched in iron and sodium cations, and located along the grain boundaries is especially strong (Mazurin, 1962).

In the earth's interior under certain thermodynamical conditions a situation can arise when melting occurs only along grain boundaries as a result of a known physical phenomenon: the melting point of the contact of two chemically different substances is by 10—30 °C lower than the melting point of each substance separately. Thus, contact melting will result in the coating of the solid phase by a highly conducting melt which will determine the electrical conductivity of the whole system.

A partial melting will naturally affect other physical parameters, too, especially the velocities and absorption of elastic waves, as it has many times been recorded in field studies.

Geoelectric boundaries at depths of 400—800 km can be associated with phase transitions, polymorphic transformations and chemical reactions. Thus the transition of fayalite from olivine structure to spinel structure is marked by an increase in the electrical conductivity by three orders of magnitude (Akimoto and Fujisawa, 1965).

REFERENCES

Akimoto, S., Fujisawa, H., 1965. Demonstration of the electrical conductivity jump produced by the olivine-spinell transition. *J. Geophys. Res.* **70,** No. 2.

Avchyan, G. M., 1971. Physical Properties of Sedimentary Rocks at High Pressures and Temperatures (in Russian). Nedra, Moscow.

Avchyan, G. M., Matveenko, A. A., Stefankevich, Z. B., 1968. Pressure and temperature effects on physical properties of water-saturated sedimentary rocks (in Russian). *Fiziko-mekhanicheskie svoistva gornykh porod verkhnei chasti zemnoi kory.* Nauka, Moscow.

Berdichevsky, M. N., Bondarenko, A. T., Vanyan, L. L., Parkhomenko, E. I., Fadeev, V. E., Feldman, I. S., 1973. Electrical conductivity of the upper mantle and the conducting layers in the crust and the upper mantle (in Russian). *Stroenie zemnoi kory i verkhnei mantii morei i okeanov.* Nauka, Moscow.

Bondarenko, A. T., 1973. On the nature of the anomalous electrical conductivity in the earth's crust of the Vilyuisk syneclise from experimental data obtained on samples (in Russian). *Dokl. Akad. Nauk SSSR,* **209,** No. 1.

Bondarenko, A. T., Feldman, I. S., 1973. The electrical conductivity parameters of olivenites at high temperatures and pressures (in Russian). *Izv. Akad. Nauk SSSR, Ser. Fiz. Zemli,* No. 5.

Borisov, A. A., 1967. Deep Structure of the USSR Territory from Geophysical Data (in Russian). Nedra, Moscow.

Brace, W. F., Orange, A. S., Madden, T. B., 1965. The effect of pressure on the electrical resistivity of water-saturated crystalline rocks. *J. Geophys. Res.* **70,** No. 22.

BRADLEY, R. S., JAMIL, A. K., MUNRO, D. C., 1962. Electrical Conductivity of Fayalite and Spinel. *Nature*, **193.**

BRADLEY, R. S., JAMIL, A. K., MUNRO, D. C., 1964. The electrical conductivity of olivine at high temperatures and pressures. *Geochim. Cosmochim. Acta* **28,** No. 11.

CHEREPANOV, A. M., TRESVYATSKY, S. T., 1974. High Refractory Materials and Oxide Products (in Russian). Metallurgia, Moscow.

DOBRYNIN, V. M., 1970. Deformation and Change of Physical Properties of Oil and Gas Reservoirs (in Russian). Nedra, Moscow.

DORTMAN, N. B., VASILEVA, V. I., VEINBERG, A. K. et al., 1964. Physical Properties of Rocks and Economic Minerals of the USSR (in Russian). Nedra, Moscow.

EFIMOV, I. A., 1968. Stratigraphy and facies of the metamorphism of the Pre-Cambrian rocks of the Kokchetav block (in Russian). *Izv. Akad. Nauk Kazakhskoi SSR, Ser. Geol.* No. 1.

GALAKHOV, A. V., 1966. On alkali-ultrabasic magmatism manifestation in the Khibinsk tundra (Kola Peninsula) (in Russian). *Dokl. Akad. Nauk SSSR*, **170,** No. 3.

GORNOSTAEV, V. P., MIKHALEVSKY, V. I., POSPEEV, V. I., 1970. Deep magnetotelluric sounding in the Southern part of the Siberian Platform and in the Baikal rift zone (in Russian). *Geol. Geofiz.* No. 4.

HAMILTON, R. M., 1965. Temperature variation at constant pressures of the electrical conductivity of periclase and olivine. *J. Geophys. Res.* **70,** No. 22.

JAST, W., MENNENON, C., 1950. The pressure dependence of ionic conductivity of silver halides. *Z. Phys. Chem.* **196.**

KHITAROV, N. I., SLUTSKY, A. B., 1965. Effect of pressure on the melting temperature of albite and of basalt (from electrical conductivity measurement data) (in Russian). *Geochimia*, No. 12.

KHITAROV, N. I., SLUTSKY, A. B., REVIN, N. I., 1971. Variation of the electrical conductivity of basalts during melting under high pressure conditions (in Russian). *Fizicheskie svoistva gornykh porod pri vysokikh termodinamicheskikh parametrakh.* Naukova Dumka, Kiev.

LUBIMOVA, E. A., 1968. Thermal Properties of the Earth and the Moon (in Russian). Nauka, Moscow.

MAZURIN, O. V., 1962. Electrical Properties of Glasses (in Russian). Goskhimizdat, Leningrad.

MOSKALEVA, S. V., 1969. Effect of deuteric alteration on the physical properties of ultrabasic rocks. Proceedings of the Second Urals Petrographic Conference (in Russian). *Magmaticheskie formatsii metallogenya Urala.* Sverdlovsk.

PARKHOMENKO, E. I., 1965. Electrical Properties of Rocks (in Russian). Nauka, Moscow.

PARKHOMENKO, E. I., 1971. On the nature of the layers of high electrical conductivity in the earth's crust and the upper part of the mantle from laboratory data (in Russian). *Fizicheskie svoistva gornykh porod pri vysokikh termodinamicheskikh parametrakh.* Naukova Dumka, Kiev.

PARKHOMENKO, E. I., BELIKOV, B. P., DVORZHAK, Z. 1973. Effect of serpentinization on elastic and electrical properties of rocks (in Russian). *Izv. Akad. Nauk SSSR, Ser. Fiz. Zemli*, No. 8.

PARKHOMENKO, E. I., BONDARENKO, A. T., 1972. Electrical Conductivity of Rocks at High Pressures and Temperatures (in Russian). Nauka, Moscow.

PARKHOMENKO, E. I., STEFANKEVICH, Z. B., VYSOKOVA, I. L., 1972. On the role of moisture for the electrical conductivity of crystalline rocks at high pressures and temperatures (in Russian). *Izv. Akad. Nauk SSSR, Ser. Fiz. Zemli*, No. 5.

SCHOBER, M., 1971. The electrical conductivity of some samples of natural olivine at high temperatures and pressures. *Z. Geophys.* **37,** No. 2.

SHAPIRO, I., KOLTOFF, I. M., 1948. Effect of pressure on the electrical conductivity of silver halides. *J. Chem. Phys.* **17.**

SLUTSKY, A. B., 1968. Electrical conductivity variation at kyanite-sillimanite transformation under the conditions of high pressures and temperatures (in Russian). *Dokl. Akad. Nauk SSSR*, **179,** No. 4.

VAGSHAL, D. S., 1970. On the electrical conductivity of serpentinites (in Russian). *Dokl. Akad. Nauk SSSR*, **190,** No. 3.

VILENSKY, A. M., 1967. Petrology of the Intrusive Traps of the Northern Part of the Siberian Platform (in Russian). Nauka, Moscow.

ΔOLAROVICH, M. P., BAYUK, E. I., LEVYKIN, A. I., TOMASHEVSKAYA, I. S., 1974. Physical-mechanical Properties of Rocks and Minerals at High Pressures and Temperatures (in Russian). Nauka, Moscow.

VOLAROVICH, M. P., PARKHOMENKO, E. I., KIREENKOVA, S. M., 1972. Electrical conductivity and elastic properties of eclogites at high pressures and temperatures (in Russian). *Izv. Akad. Nauk SSSR, Ser. Fiz. Zemli*, No. 4.

VOROBIEV, A. A., 1960. Physical Properties of Ionic Crystalline Dielectrics I. (in Russian). Gos. Univ. Tomsk.

WATANABE, H., 1970. Measurements of electrical conductivity of basalt at temperatures up to 1500° and pressures to about 20 kilobars. *Contrib. Geophys. Inst. Kyoto Univ.*, No. 10.

WATANABE, H., 1972. Measurements of electrical conductivity of granite under high pressures. *Contrib. Geophys. Inst. Kyoto Univ.*, No. 12.

ZHARKOV, V. N., 1958. On the electrical conductivity and temperature of the earth's mantle (in Russian). *Izv. Akad. Nauk SSSR, Ser. Geofiz.*, No. 4.

ZHARKOV, V. N., KALININ, V. A., 1968. Equations of State of Solids at High Pressures and Temperatures (in Russian). Nauka, Moscow.

CHAPTER 4

GEOTHERMAL DATA AND THEIR COMPLEX INTERPRETATION ON TEST AREAS

Edited by

V. ČERMÁK

INTRODUCTION TO CHAPTER 4

V. ČERMÁK

Terrestrial heat flow is the study of the outflow of heat from the earth's interior by conduction, but in broader sense it includes many other geothermal problems. From the energetical point of view this outflow of energy is the most impressive terrestrial phenomenon. Its present rate is estimated to be of about 2×10^{20} cal/year and it is by orders of magnitude greater than the energy of all other geophysical features, such as earthquakes, earth tides, volcanism, etc. Moreover, thermal energy plays a dominant role in many geophysical theories of the earth's origin, structure and development. Temperature and pressure are the most important parameters within the earth; extrapolation of the surface heat flow observations together with some assumptions on thermal conductivity and heat production distribution allow to evaluate crustal temperatures. Uneven temperature distribution within the crust and the upper mantle causes regional differences in thermal flux and represents the driving force in the geological evolution of the uppermost parts of the earth.

The chapter "Geothermal data and their complex interpretation on test areas" contains 13 papers dealing with heat flow measurements in Central and Eastern Europe and Soviet Asia. It covers most of the activity of the Working Group for Geothermics of the KAPG during the past 10–15 years in collecting and interpreting heat flow data. The individual articles reflect, however, personal views of the authors on the significance and interpretation of the results obtained in particular regions. The editor of the chapter has not tried in any way to bring these contributions under some uniform scheme. It is believed that the various methods of analyzing and interpreting the results applied by the different authors might help to overcome the complexity of the problem.

Two maps of the KAPG Working Group for Geotermics are included as a part of this Monograph. Geothermal Map of the Temperature at 1 km Depth (edited by L. Stegena) and Heat Flow Map (edited by V. Čermák and E. A. Lubimova). Both maps are to the scale 1 : 10,000,000 and they cover most of the territory of Central and Eastern Europe. The temperature at 1 km depth does not represent in geophysics an information as valuable as heat flow. However, the number of temperature measurements considerably exceeds the number of heat flow stations and deep temperatures have been measured in many areas from where no heat flow data exist. Moreover, the geothermal map gives immediate evidence of temperature distribution obtained by direct measurement and not influenced by involving corrections for topography, recent climatic cnhages, geological history

etc. It may be of great importance in applied geophysics, in hydrogeology and in temperature forecast in mining or drilling.

A brief description of the Heat Flow Map (see pp. 376—380) is also incorporated in this chapter. The map is based on all available heat flow data and contour lines were drawn with respect to the regional geology. The discussion of the map is limited to the statistics of mean heat flow values for individual tectonic provinces.

The number of temperature and/or heat flow measurements in mines, tunnels and especially in boreholes has increased during the last 10 years. Nevertheless, the distribution of the stations is still far from being uniform and there are large areas where data are missing (Fig. 1). The highest concentration of measurements is in Central Europe: in German Democratic Republic (87 values), Czechoslovakia (71 values), Poland (27 values) and in Hungary (7 values). In the USSR (540 values) most data are concentrated in a broad strip stretching from Western Ukraine across the Ukrainian shield in the north and Crimean Peninsula in the south to the Caucasus mountains; other regions where heat flow was measured are Kola Peninsula (Baltic shield) and the Ural mountains. Fairly good information about geo-

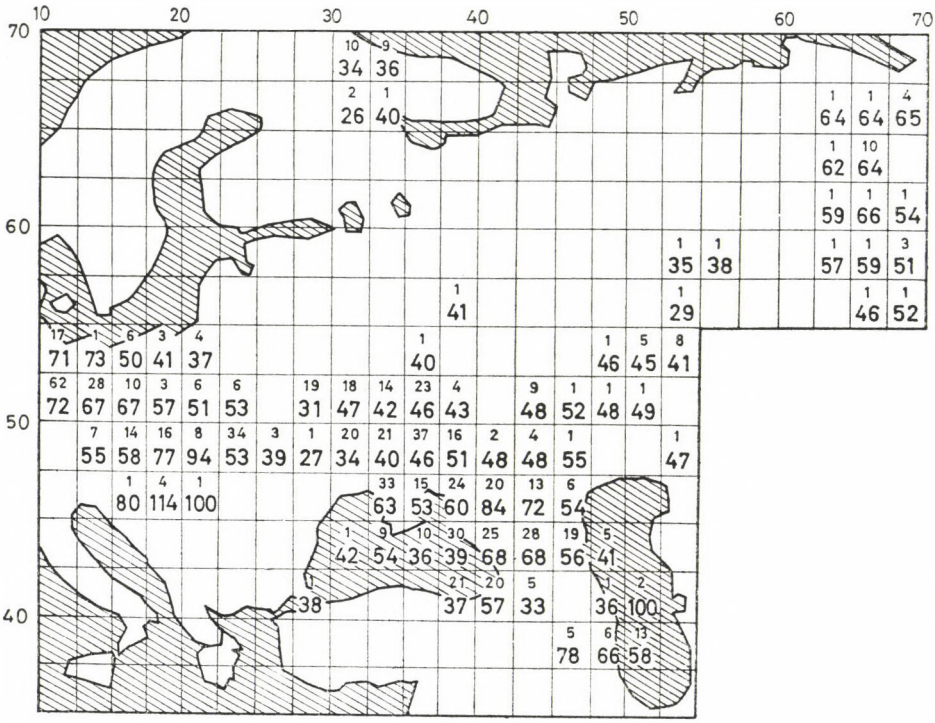


Fig. 1. Heat flow data in $2.5° \times 2.5°$ grid for Central and Eastern Europe. In each grid element, the upper value is the number of measurements and the lower value is the mean heat flow in mWm^{-2}

thermal activity was obtained by marine heat flow measurements in the Black and Caspian Seas (80 values).

The following papers are dealing with the interpretation of heat flow as well as deep temperature measurements in individual KAPG-countries. Usually one paper summarizes the results for each country: Hurtig and Schlosser for the German Democratic Republic; Čermák for Czechoslovakia; Majorowicz, Plewa and Wesierska for Poland; Stegena for Hungary and Petkov and Velinov for Bulgaria.

The interesting results on the vertical changes in heat flow in the North-German sedimentary basin are reported in a special paper by Hurtig and Schlosser.

More than 60% of all heat flow data have been obtained in the USSR, the statistical evaluation of the geothermal activity of individual tectonic units is dealt with by Kutas, Lubimova and Smirnov. More detailed information about the heat flow field in the area of the Caucasus mountains can be found in the paper of Buachidze. Originally the Monograph was proposed to deal with the results of geothermics and magnetotellurics in Central and Eastern Europe only; however, more results from several regions in non-European parts of the USSR were supplied by Soviet colleagues and it was felt that these data should be incorporated into the Monograph to keep the continuity for the whole Euroasian continent. The paper written by Lysak on the Baikal rift zone and by Sokolova on the Kamchatka Peninsula and the Okhotsk Sea represent good examples of complex interpretation of heat flow from a specific tectonic unit and their conclusions have more general application. Temperature measurements in permanently frozen ground are nowadays an important research tool in the Arctic, therefore the article by Melnikov, Balobaev, Kutasov and Devyatkin dealing with heat flow investigation in permafrost and discussing mainly data from Yakutia was included, as well.

HEAT FLOW MAP OF CENTRAL AND EASTERN EUROPE (1 : 10,000,000)

V. ČERMÁK, E. A. LUBIMOVA

During the Upper Mantle Project the significance of the study of the thermal state of the earth in the complex geophysical investigation of crustal structure, dynamic processes and their relation to deep-seated geological phenomena became fully awarded. This paper is a brief description of the preliminary map of heat flow in Central and Eastern Europe to the scale 1 : 10,000,000. The map is the result of a joint effort of many contributors from Bulgaria, Czechoslovakia, German Democratic Republic, Hungary, Poland, Roumania and the USSR organized in the Working Group for Geothermics in the KAPG program, and it represents the interpretation of data obtained during the period 1960–1973. When speaking about Central and Eastern Europe in what follows only territories of these respective countries are meant.

First data on geothermal activity were published in the above countries by Stenz (1954) for Poland, Boldizsár (1956) for Hungary, Schlosser and Schwarzlose (1959) for the GDR, Lubimova et al. (1961) for the USSR, and by Čermák (1967) for Czechoslovakia. Recalling that in 1965 Lee and Uyeda catalogued only 31 reliable heat flow values for Central and Eastern Europe, we find that during the last 10 years the number of heat flow measurements has increased dramatically. At present 812 measurements have been published or are in the final stage of completion.

For the evaluation of the regional distribution of heat flow all available data were used as check points and extrapolated on the basis of regional geology. As the geographical distribution (see Fig. 1 of the Introduction of this chapter) and the density of data are uneven and from large territories data are missing (e.g. northern part of the USSR) or only preliminary data exist (Bulgaria and Roumania) isolines of heat flow were drawn only in those areas from where fairly reliable information on heat flow activity is available. In addition to the regional geological pattern, the preliminary map of geoisotherms at 1 km depth (Stegena, 1972) was used to aid the construction of the map in South-Eastern Europe. On the territory of the GDR, where considerable number of unpublished data exist (Hurtig, personal communication) the isolines were corrected according to these data.

Generally the density of heat flow stations is of about 5–6 points in a $5^\circ \times 5^\circ$ square in stable tectonic areas of the Precambrian shields and old platforms, and 3—4 points in a $1^\circ \times 1^\circ$ square in tectonically active areas of the Alpine folding. The available material indicates that maximum point concentration would be desirable in zones that join diverse tectonic structures, to have sufficient observation density for finding provinces with similar heat flow.

The discussion of the map is limited to broad features of continental scale and only little attention is paid to the many interesting smaller areas. Details of individual measurements are also not treated, these are reported in the original publications or in the following papers in this chapter.

According to the proposal of the International Heat Flow Committee new heat flow units [mWm^{-2}] were used throughout the preparation of this map and heat flow isolines were drawn at 15 mWm^{-2} (=0.36 $\mu calcm^{-2}sec^{-1}$) intervals. This interval usually exceeds two to three times the uncertainty in individual heat flow determination due to instrumental error. As the regional heat flow variations of 0.2 $\mu calcm^{-2}sec^{-1}$ are generally assumed to be significant (Lee and Uyeda, 1965), the chosen interval of 15 mWm^{-2} has facilitated a good description of the heat flow pattern.

The arithmetic mean of 812 values is 57.1 ± 27.1 mWm^{-2} (= 1.36 $\mu calcm^{-2}sec^{-1}$) which is lower than the mean value proposed by Lee and Uyeda (1965), $1.5 \pm 10\%$ $\mu calcm^{-2}sec^{-1}$, usually taken as typical value for terrestrial heat flow. This is probably caused by the fact that the majority of data used for the construction of the heat flow map are from tectonically stabilized East-European platform, which is the region of a "lower than normal" geothermal activity.

Several heat flow anomalies evidently related to underground water movement have been found, e.g. in northern Bohemia, Pannonian Lowland, northern Crimea, Georgia, etc. Such data may not be representative of the conducted heat flow. Considerable high heat flow values were observed in the North-German Lowland, obviously connected with salt tectonics. Sharp contrast in the thermal conductivity of the salt and surrounding sedimentary rocks may cause local anomalous heat flow, such data therefore may not be typical for a particular large geographical unit. If these data are excluded, the mean heat flow decreases. However, several of the low heat flow values (< 25 mWm^{-2}) could be supposed not to be representative either. To make reasonable selection of all data is very difficult and requires detailed studies of the local geologies. There are only three data from hot spring area of Teplice in Czechoslovakia (Čermák, 1967), obviously disturbed by underground thermal water which were excluded. In addition, three very high sea bottom heat flow values over 200 mWm^{-2} (Nos 879, 909, 910 in Lubimova et al., 1973) are also uncommon and were excluded.

There may be a more or less pronounced influence of such geological phenomena on observed heat flow as sedimentation, erosion, uplift, etc., as well as the effect of past climatic changes. For further study attention should be paid to these perturbations and reasonable corrections should be evaluated. For the present state of investigation and map construction preference was given to "uncorrected" values rather than introduce something that might be a subjective standpoint. This, of course, has nothing to do with the application of technical corrections, such as local topography, conductivity contrast, borehole inclination, etc. used by individual authors.

Heat flow, especially in Cenozoic depressions, such as marginal foredeeps, intermountainous and neotectonic basins, as well as in outskirt and internal seas may have been considerably affected by non-equilibrium factors of intensive sedimentation or erosion. Heat flow value here may be underestimated by 10 to 50% in comparison with the equilibrium value. This is why

the heat flow map, based on measured (uncorrected) values has to be considered carefully in areas of young geological history.

The mean heat flow for 806 data is 56.1 ± 24.9 mWm^{-2}. From these data there are 729 stations on the continent, mean heat flow 57.1 ± 25.0 mWm^{-2}, and 77 stations in the Black and Caspian Seas, mean value 46.9 ± 21.6 mWm^{-2}. The statistics about mean heat flow values for individual

TABLE 1

Statistics of heat flow values for major geological features in Central and Eastern Europe

Geological feature	Number of values N	Mean		Standard deviation [mWm^{-2}]	Standard error [mWm^{-2}]
		μcal cm^{-2} sec^{-1}	mWm^{-2}		
1. Precambrian shields	83	0.86	36.0	6.9	0.8
Baltic shield	22	0.83	34.8	4.9	1.0
Ukrainian shield	61	0.87	36.4	7.5	1.0
2. Post-Precambrian non-orogenetic areas	325	1.33	55.7	17.1	0.9
old platforms (Russian platform)	182	1.09	45.6	8.7	0.6
epi-Paleozoic platforms					
Scythian plate	127	1.67	69.9	17.1	1.5
North-German Lowland	16	1.41	59.0	8.7	2.2
3. Post-Precambrian orogenetic areas	321	1.51	63.2	19.8	1.1
Paleozoic orogenetic areas	144	1.61	67.4	14.6	1.2
Central Europe	118	1.64	68.7	15.6	1.4
Ural mountains	26	1.47	61.5	6.3	1.3
Mesozoic-Cenozoic orogenetic areas	177	1.42	59.5	22.5	1.7
Frontal foredeeps	86	1.25	52.3	12.5	1.4
Intermountainous depressions	48	1.55	64.9	31.4	4.5
Faulted systems	43	1.63	68.2	21.6	3.3
4. Seas	77	1.12	46.9	21.6	2.5
Black sea	56	0.97	40.6	16.1	2.1
Caspian sea	21	1.54	64.5	24.7	5.4

tectonic provinces is summarized in Table 1 and in the histograms of Figure 1. From this formal statistics and from the map as well we can see that the heat flow pattern can be well correlated with major geological structure. It is easy to distinguish areas of approximately similar heat flow. Precambrian shields are characterized by relatively low heat flow of 36.0 ± 6.9 mWm^{-2} with almost no regional variations. Uniform heat flow field is also typical for old platforms: East-European or Russian platform 45.6 ± 8.7

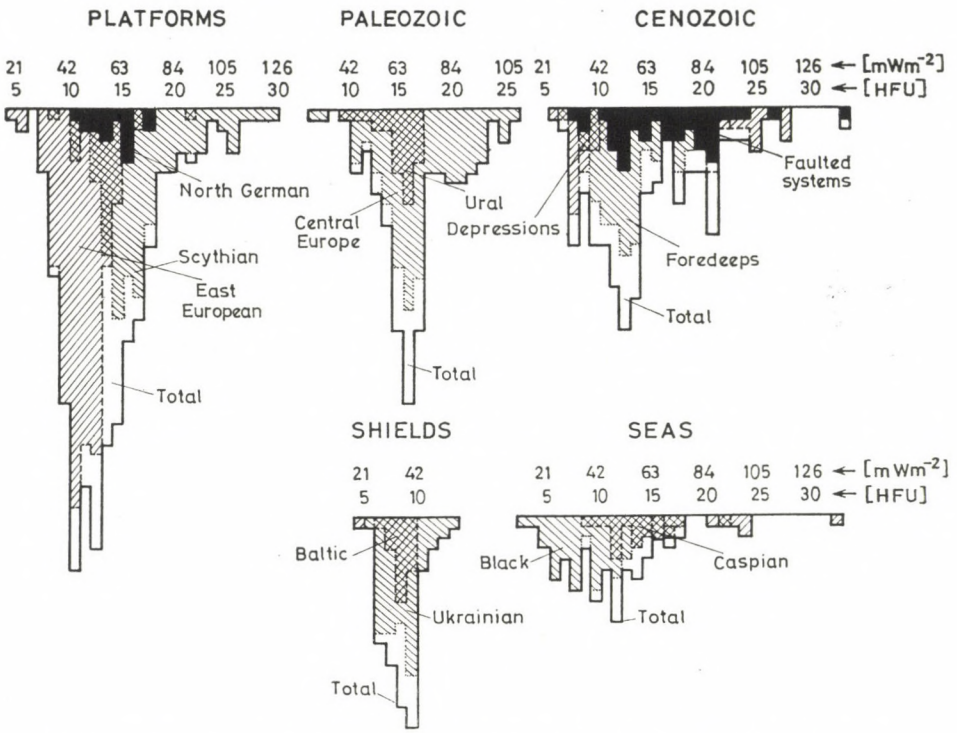


Fig. 1. Histograms of heat flow values from Central and Eastern Europe

mWm^{-2}, and North-German platform 59.0 ± 8.7 mWm^{-2}. Considerable scatter of observed heat flow and an increased geothermal activity is obvious for the Alpine folded structures, quite prominent is the high heat flow in intermountainous depressions filled by Neogene sediments, namely in the Pannonian Lowland 93.1 ± 19.4 mWm^{-2}, or in areas affected by Tertiary volcanism (Central Slovakia, Lesser Caucasus, etc.).

There is generally a good agreement between mean heat flow values in Table I and the results obtained by other authors correlating heat flow and geological features (Lee and Uyeda, 1965; Lubimova and Polyak, 1969, etc.). Only the mean heat flow for Mesozoic-Cenozoic orogenetic areas of Central and Eastern Europe is surprisingly lower than the value of 70–80 mWm^{-2} usually reported. This is caused by the considerable number of measurements performed in foredeeps where heat flow is low. High heat flow (> 70 mWm^{-2}) on the Scytian plate (Cis-Caucasus) on the other hand, increases the mean value for epi-Paleozoic platform. These high heat flows in the Predkavkaz Foredeep are problematic ones. The proximity of young orogenetic belt of the Caucasus in the south, with volcanically still active Elburs Mtn., may explain relatively higher geothermal activity of this region.

ACKNOWLEDGMENTS

The construction of the heat flow map of Central and Eastern Europe has been made possible only due to the joint effort of many contributors from many countries. The authors wish to express their thanks to all of the representatives of individual countries — participants in KAPG program: L. Stegena — Chief of Working Group for Geothermics (Hungary), I. Petkov (Bulgaria), Ch. Oelsner (German Democratic Republic), S. Plewa (Poland) and C. Demetrescu (Roumania), who had compiled data from their countries and prepared national reports.

Special thanks go to E. Hurtig, who had checked the contour map and corrected it for the territory of the GDR.

The final technical preparation of the map for printing was carried out in the Institute of Cartography, Eötvös Lóránd University in Budapest.

REFERENCES

Boldizsár, T., 1956. Terrestrial heat flow in Hungary. *Nature*, **178**, 35.

Čermák, V., 1967. Results of geothermic investigation of heat flow in Czechoslovakia in 1964–1966. *Studia Geophys. Geod. ČSAV*. **11**, 342–344.

Lee, W. H. K., Uyeda, S., 1965. Review of heat flow data. In: W. H. K. Lee (Ed.), Terrestrial Heat Flow, Geophys. Monograph, No. 8, AGU Washington D.C., 87–190.

Lubimova, E. A., Lusova, L. N., Firsov, F. V., Starikova, G. N., Shushpanov, A. P., 1961. Determination of surface heat flow in Mazesta (USSR). *Ann. Geofis.* **14**, 157–167.

Lubimova, E. A., Polyak, B. G., 1969. Heat flow map of Eurasia. In: P. J. Hart (Ed.), The Earth's Crust and Upper Mantle, Geophys. Monograph, No. 13, AGU Washington D.C., 82–88.

Lubimova, E. A., Polyak, B. G., Smirnov, Ya. B., Kutas, R. I., Firsov, F. V., Sergienko, S. I., Lusova, L. N., 1973. Heat flow on the USSR territory. Catalogue of data. Soviet Geophys. Committee, USSR Acad. Sci., Moscow.

Schlosser, K., Schwarzlose, J., 1959. Geophysikalische Wärmeflussmessungen (Grundlagen und Ergebnisse). *Freiberger Forschungshefte C*, **75**, 120.

Stegena, L., 1972. Geothermal map of Eastern Europe. *Geothermics* **1**, 140.

Stenz, E., 1954. Deep-well temperatures and geothermal gradient at Ciechocinek. *Acta Geophys. Polon.* **2**, 159–168.

GEOTHERMAL TEMPERATURE MAP OF CENTRAL AND EASTERN EUROPE

L. STEGENA

INTRODUCTION

A former experiment (Stegena, 1972) showed that there were enough data to attempt the construction of an international geotemperature map for the depth of 1 km, to the scale 1 : 10,000,000 for Central and Eastern Europe (the KAPG countries). Based on this, the Geothermal Working Group of the KAPG began the preparatory work of the map. The first decisions about scale, depth on which geotemperatures should be delineated, construction principle of isotherms was made at the Sofia meeting (1971) and later at the Freiberg meeting (1972). The first assortment was corrected at the Tbilisi meeting (1973), the final conciliation at the Sopron meeting (1974). The map was cartographed and printed at Budapest, Eötvös Loránd University, Institute of Cartography.

CONSTRUCTION PRINCIPLES USED

The scale was determined partly by the density of data and partly by the purpose of giving a general picture about geothermal conditions. The depth on which geotemperatures are delineated was given by the highest frequency of the temperature measurements.

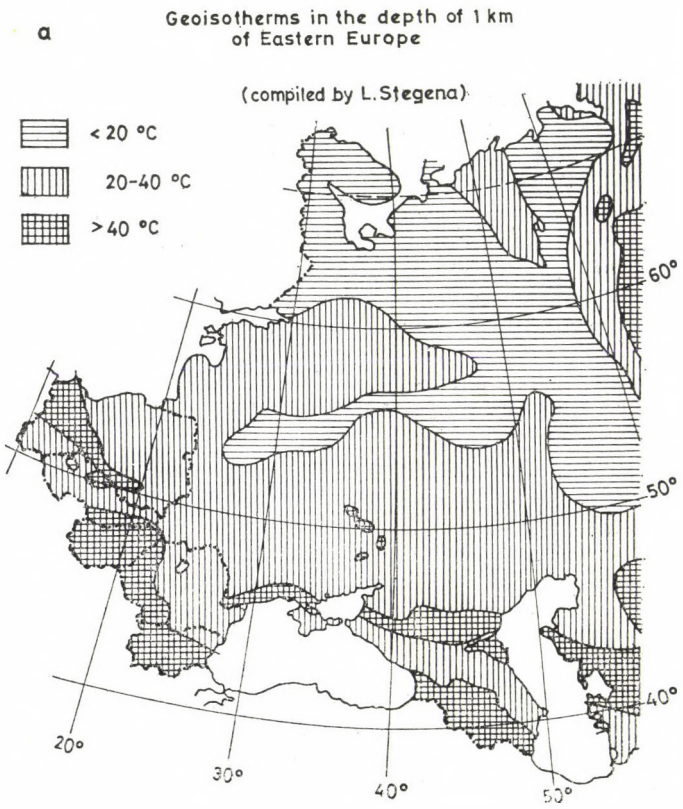
As basis of construction the national maps mostly in greater scale or national data banks were used. Informations about some of these maps are published in this volume.

Apart from technical (e.g. inequilibrium) and local corrections (neglecting e.g. anomalous faults or superthermal local zones), no general correction (topographic, climatic etc.) has been used.

For the construction of isotherms there were two possibilities: to use some mathematical method (approximation by higher polynomials or application of filter theory) or the form of geologic features (e.g. Carpathians, boundaries of interplatform subsidences, etc.) as an aid to construct isolines. This latter method has been accepted and used.

PRELIMINARY ANALYSIS OF THE MAP

A belt of geothermal high is developed which roughly coincides with the areas of the Alpine orogenic zone. This geothermal high essentially coincides with the seismic zone. Besides, it coincided with the rising areas of the recent crustal movements (Meshcherikov, 1971) (Fig. 1). In the Pannonian Basin, the seismicity is concentrated to that areas where the horizontal geothermal gradient is high ($>1.3\,^{\circ}C/10$ km).



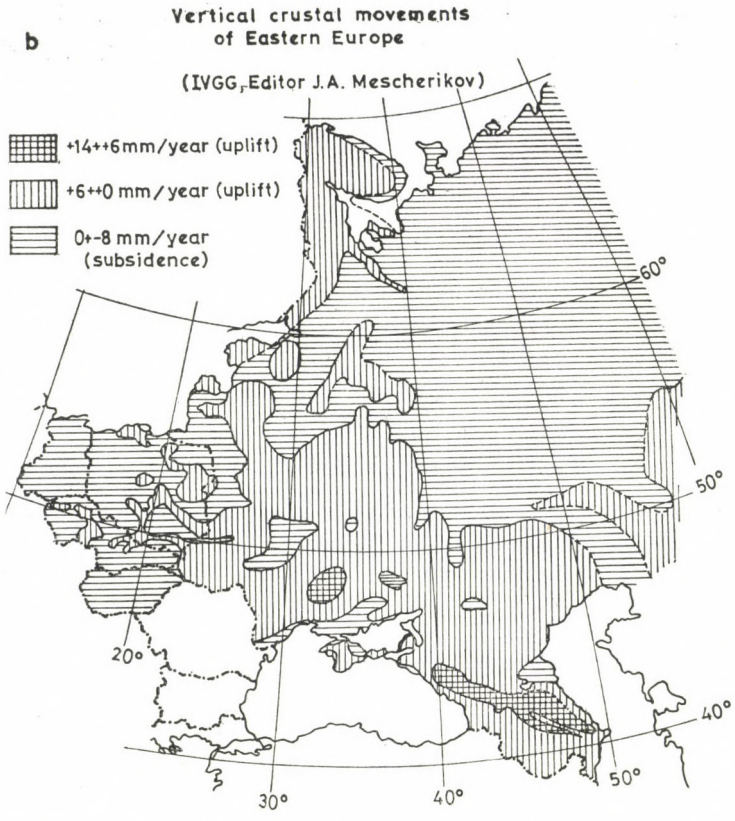


Fig. 1. Geoisotherms in the depth of 1 km and vertical crustal movements in Eastern Europe (generalized maps)

REFERENCES

MESHCHERIKOV, J. A., 1971. (Ed. in Chief) Map of recent vertical crustal movements of Eastern Europe. Glavn. Upr. Geod. i Kart. pri Sov. Min. SSSR. Moscow.

STEGENA, L., 1972. Geothermal map of Eastern Europe. *Geothermics* **4**, 140–141.

GEOTHERMAL STUDIES IN THE GDR AND RELATIONS TO THE GEOLOGICAL STRUCTURE

E. HURTIG, P. SCHLOSSER

INTRODUCTION

The paper presents a description of the status of geothermal studies in the GDR, in comparison with the heat flow map of Central and Eastern Europe.

THE DATA

TEMPERATURE MEASUREMENTS

During the last few years numerous rock temperature measurements have been carried out in the GDR. Most of them were performed in deep boreholes (Table 1). The measurements can be divided into three categories:

TABLE 1

Temperature measurements in the GDR

Type of measurement	Number of measurements*
Measurements using resistance thermometers	236
Measurements using maximum thermometers during test operations	55
Measurements using maximum thermometers. Thermal equilibrium reached	67
Measurements in mines	11

* Including 23 data obtained by repeated measurements in some boreholes

- When measuring with electric resistance thermometers, a continuous temperature-depth curve is obtained. The accuracy is $\pm$ 0.5°C.
- In course of test operations, measurements of the temperature within the ranges of the test horizons are carried out by means of maximum thermometers. The time after ceasing mud circulation is varying. Temperature data of this kind obtained at different depths in a borehole can be used for calculating the geothermal gradient and the heat flow.
- In a number of boreholes, measurements by means of maximum thermometers were carried out at different depths. The time after the ceasing of the circulation of the drilling fluid is extremely long, so that thermal equilibrium has been reached. The temperature data are suitable to calculate the terrestrial heat flow.

At present there are 346 geothermal stations (boreholes and mines) suitable

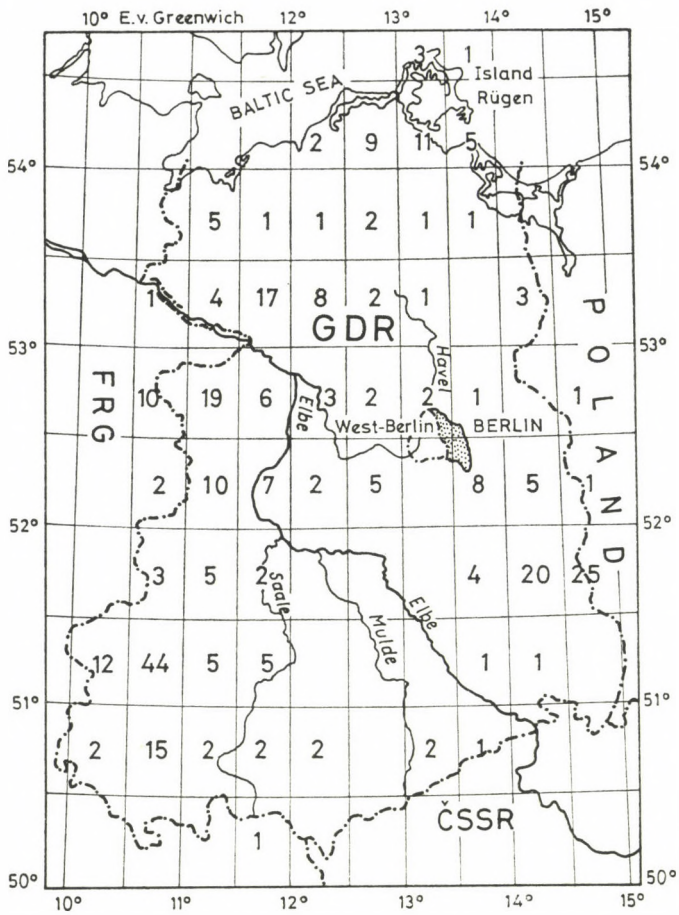


Fig. 1. Regional distribution of geothermal stations in the GDR

for evaluation of heat flow. Regional distribution of the stations is shown in Figure 1. For the central and southern regions of the GDR there are only few temperature data.

THERMAL CONDUCTIVITY DATA

Due to the considerable inhomogeneity of the rocks the determination of thermal conductivity is problematic. Three methods have been applied:

- Laboratory measurements of thermal conductivity on rock samples. The *in-situ* conditions (pressure, temperature, pore filling fluid, water saturation) are not fulfilled. Selection of samples depends on the available core material and is therefore not always representative of the stratigraphic situation.

Tables 2, 3 and 4 give a summary of the available laboratory data.

From Mesozoic and Cenozoic formations there are only few values by no means representative of the whole northern part of the GDR. Thermal conductivity values for the Zechstein formation, the Lower Permian, and Upper Carboniferous are better established. Especially from the northern part of the North-German sedimentary basin a sufficient number of data

TABLE 2

Thermal conductivity data from the northern part of the GDR and the Thüringian Basin. Cenozoic and Mesozoic formations

Formation	Rock type	Mean value		Number of values
		[Wm^{-1}/K^{-1}]	[mcal cm^{-1} sec^{-1} $°C^{-1}$]	
Tertiary	siltstone	0.84	2.0	1
Cretaceous	claystone	1.84	4.4	2
	siltstone	1.30	3.1	4
	sandstone	2.30	5.5	5
	marlstone	1.13	2.7	2
	limestone	2.89	6.9	2
	clay band	2.47	5.9	1
Jurassic	claystone	1.76	4.2	19
	siltstone	1.09	2.6	19
	sandstone	2.22	5.3	5
	marlstone	1.63	3.9	1
	limestone	3.10	7.4	1
	clay band	2.14	5.1	6
Upper Triassic (Keuper)	claystone	1.38	3.3	25
	siltstone	1.59	3.7	3
	sandstone	2.47	5.9	13
	clayey marlstone	2.30	5.5	1
	marlstone	1.84	4.4	4
Middle Triassic (Muschelkalk)	claystone	1.80	4.3	4
	clayey marlstone	1.63	3.9	4
	dolomite	2.68	6.4	1
Lower Triassic (Buntsandstein)	claystone	1.55	3.7	44
	siltstone	1.55	3.7	17
	sandstone	2.38	5.7	86
	clayey marlstone	1.84	4.4	4
	marlstone	1.50	3.6	1
	limestone	2.09	5.0	4
	dolomite	3.51	8.4	2
	anhydrite	3.80	9.1	1

are available for calculating representative average thermal conductivities for these formations.

- Determination of thermal conductivity in a borehole by means of a probe. Methodology and first results have been described by Oelsner et al., (1968).
- Determination of thermal conductivity from results of geophysical borehole measurements (acoustic, electric, and radioactive borehole measurements). The calculations are based on a linear model (see Hurtig and Schlosser pp. 395–397):

$$\lambda = \lambda_1 M_1 + \lambda_2 M_2 + \lambda_3 P$$

M_1; M_2: volume percentages of the mineral components, P: porosity.

TABLE 3

Thermal conductivity data from the northern part of the GDR and the Thüringian Basin. Palaeozoic formations

Formation	Rock type	Mean value		Number of data
		[Wm^{-1}/K^{-1}]	[mcal cm^{-1} sec^{-1} $°C^{-1}$]	
Zechstein	anhydrite	4.01	9.6	212
	dolomite	3.93	9.4	157
	limestone	2.26	5.4	30
	claystone	1.84	4.4	1
Lower Permian (Rotliegendes)	claystone	1.84	4.4	11
	siltstone	2.13	5.1	18
	sandstone	2.51	6.0	82
	conglomerate	2.01	4.8	26
	porphyry	1.97	4.7	26
	quartz porphyry	2.34	5.6	13
	porphyrite	1.84	4.4	2
	melaphyre	1.50	3.6	3
	tuff	1.80	4.3	2
	limestone	1.76	4.2	1
Permo-Carboniferous	claystone	1.96	4.7	12
	siltstone	2.63	6.3	28
	sandstone	3.42	8.2	88
Upper Carboniferous	claystone	2.51	6.0	12
	siltstone	3.01	7.2	5
	sandstone	3.80	9.1	13
Lower Carboniferous	marlstone	2.22	5.3	7
	limestone	2.42	5.8	6
Ordovician	claystone	1.71	4.1	15
	siltstone	2.55	6.1	12

Calculating thermal conductivity according to this relation leads to useful results for rock types composed of two mineral components (e.g. sandstone-claystone; limestone-claystone; salt rocks).

TABLE 4

Thermal conductivity data of rock samples obtained from the southern (Hercynian) part of the GDR

Rock type	Mean value		Number of data
	[Wm^{-1}/K^{-1}]	[mcal cm^{-1} sec^{-1} $°C^{-1}$]	
Clayey shales and phyllites	1.67	4.0	25
Sandstones and quartzites	3.90	7.4	19
Gneisses and micaceous schists	2.13	5.1	15
Basalts	1.84	4.4	4

THE GEOTHERMAL REGIME IN THE GDR

TEMPERATURE VS. DEPTH DISTRIBUTION

In Figure 2 are compiled all available temperature data from deep boreholes of the northern part of the GDR. Lower and upper curves are envelops of all data. The temperature *vs.* depth distribution gives some important characteristics:

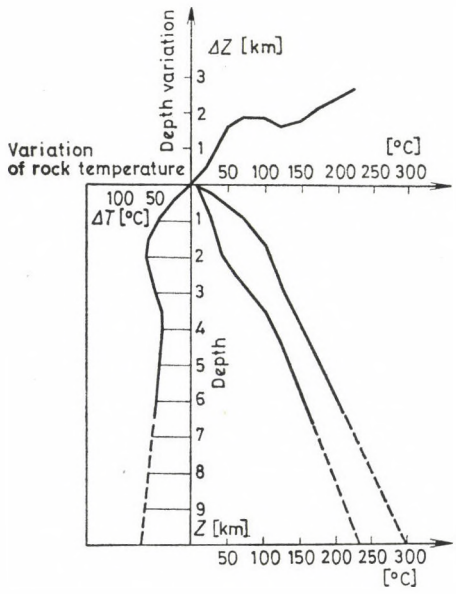


Fig. 2. Temperature *vs.* depth curves in the North-German sedimentary basin and scatter of the parameters

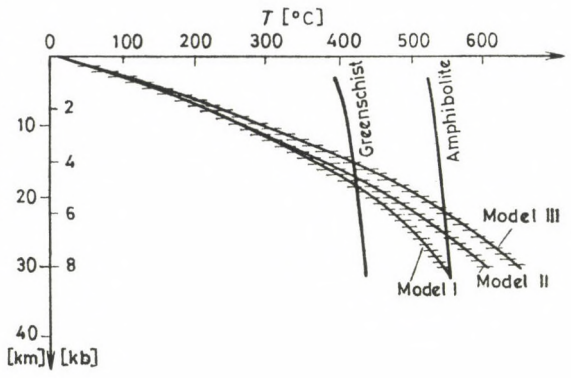


Fig. 3. Temperature curves for three heat generation models. Models I and II are representative for thick sedimentary layers covering the basement (North-German sedimentary basin), model III characterizes the mean crustal structure in the southern part of the GDR with outcropping crystalline rocks

- In the depth range from 1 to 3 km, the variation of the temperature data is higher. The lateral variations can reach almost 70 °C due by part to varying thicknesses and depths of the Zechstein formation. The salt formations of the Zechstein, which have a high thermal conductivity, lead to a strong distortion of the temperature field in the younger sedimentary layers (Mesozoic and Cenozoic formations).
- Within the salt formation and immediately below the Zechstein formation, the variation of temperature values decreases.
- With increasing depth the temperature values scatter again in a wide range. For temperatures between 200 and 250 °C, the depth variation can amount to 3 km. Accordingly at depths of 7 km lateral temperature variations of approximately 70 °C and more should be taken into account.

Based on near-surface temperature and heat flow data, and taking an average heat generation for typical crustal rock types, the depth distribution of the temperature and heat flow down to the Mohorovičič discontinuity can be calculated (see Fig. 3). Within the territory of the GDR, the heat flow entering the earth's crust from the upper mantle ranges between 16 and 33 mWm^{-2} (0.4 and 0.8 $\mu calcm^{-2}sec^{-2}$).

TEMPERATURE PATTERN AT A DEPTH OF 1000 M

Schlosser (1968) described the temperature pattern at 1000 m depth for the northern part of the GDR. According to the summarized depth distribution of temperature (Fig. 2), the latter shows only slight variations at a depth of 1000 m. The highest temperature values are obtained within a zone extending in W–E direction across the central part of the GDR.

THE HEAT FLOW PATTERN

From the available data the regional heat flow pattern can be derived (Fig. 4). In connection with the rough tectonic subdivision of the GDR (Fig. 5) the following geothermal structures are encountered:

a) Northern part of the GDR

Geological features: platform formations are covering a basement of yet uncertain age, thickness of the sedimentary layers being more than 7 km, deformations by salt tectonics are present.

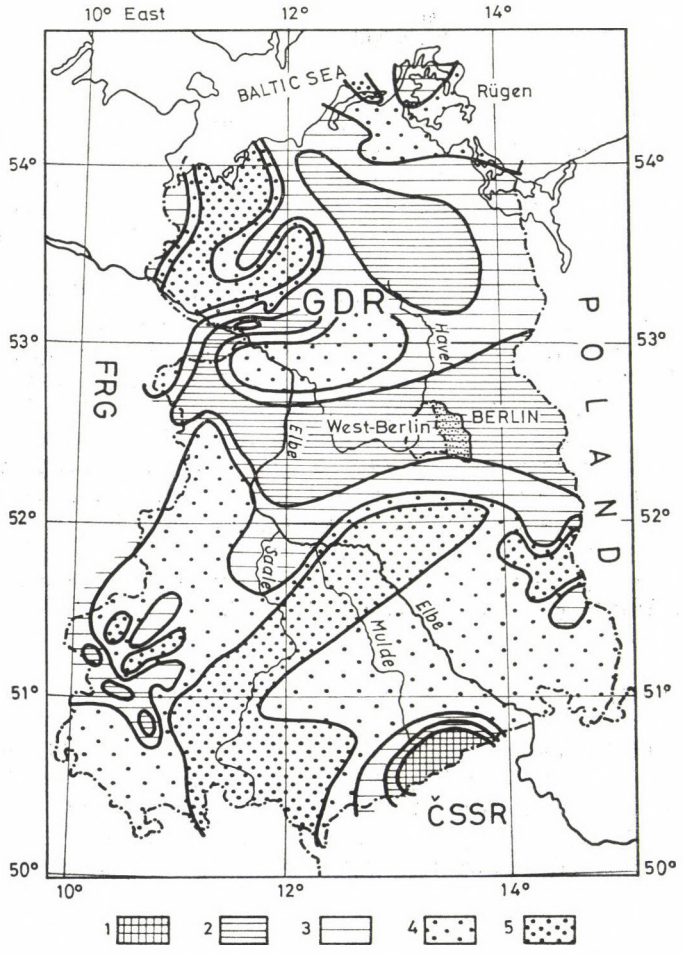


Fig. 4. Heat flow pattern of the GDR
1 – >84 mWm^{-2} (>2.0 μcalcm^{-2} sec^{-1}); 2 – 75–84 mWm^{-2} (1.8 – 2.0 μcalcm^{-2} sec^{-1}); 3 – 67–75 mWm^{-2} (1.6 – 1.8 μcalcm^{-2}sec^{-1}); 4 – 58–67 mWm^{-2} (1.4 – 1.6 μcalcm^{-2}sec^{-1}); 5 – < 58 mWm^{-2} (< 1.4 μcalcm^{-2} sec^{-1})

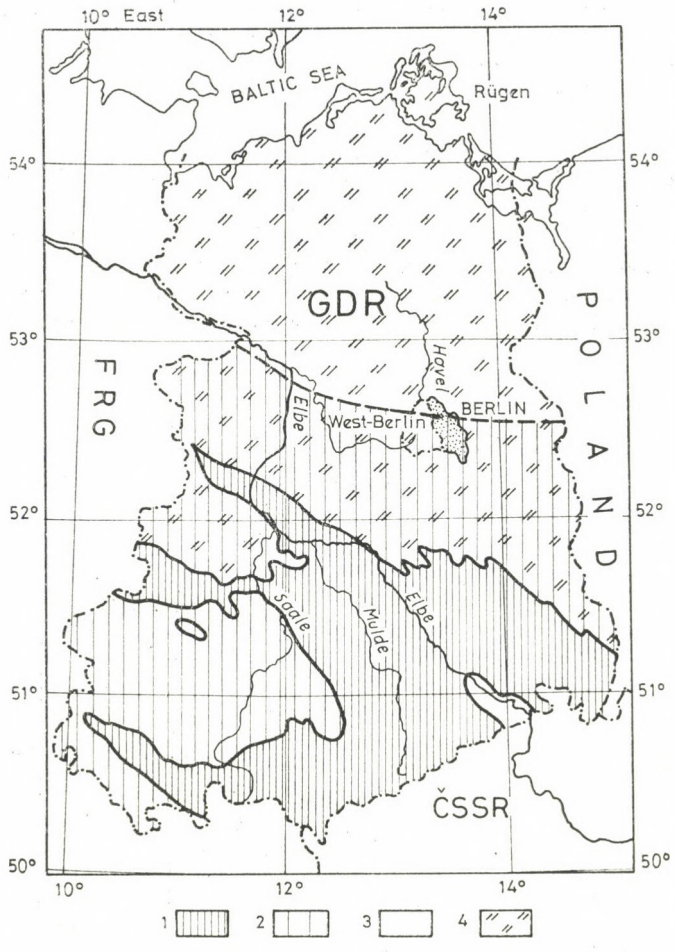


Fig. 5. Sketch of the tectonic map of the GDR
1 – Hercynian basement outcropping or being covered by sedimentary layers; 2 – Hercynian basement with a thick sedimentary cover; 3 – Basement of uncertain age covered by thick sedimentary layers; 4 – Areas with intensive salt tectonics

- *A zone of increased heat flow* crosses the northern part of the North-German sedimentary basin in NW-SE direction. The further continuation, especially in southeast direction, is yet uncertain.
- *A spur of a high heat flow* area along the Upper Rhine graben (the so-called "Altmark-Zone") protrudes into the western part of the GDR. Further continuation towards northeast cannot be observed.

b) Southern part of the GDR
Geological features: The basement consolidated by the Hercynian

orogeny is covered in part by thick Upper Palaeozoic and Mesozoic-Cenozoic sedimentary layers. In the south the Hercynian basement crops out over large areas.

- *A zone of high heat flow values* extending in E–W direction is most characteristic. It is situated in the area of transition from the Hercynian basement to the platform area in the north.
- *High heat flow values* occur in the region of the Erzgebirge Mts. along the Czechoslovakian border.
- There is a SW–NE trending *zone of low heat flow values*. It has not yet been established in all details, for in the central part of the GDR only a small number of temperature and heat flow data are available. This area of low heat flow seems to be in relationship with

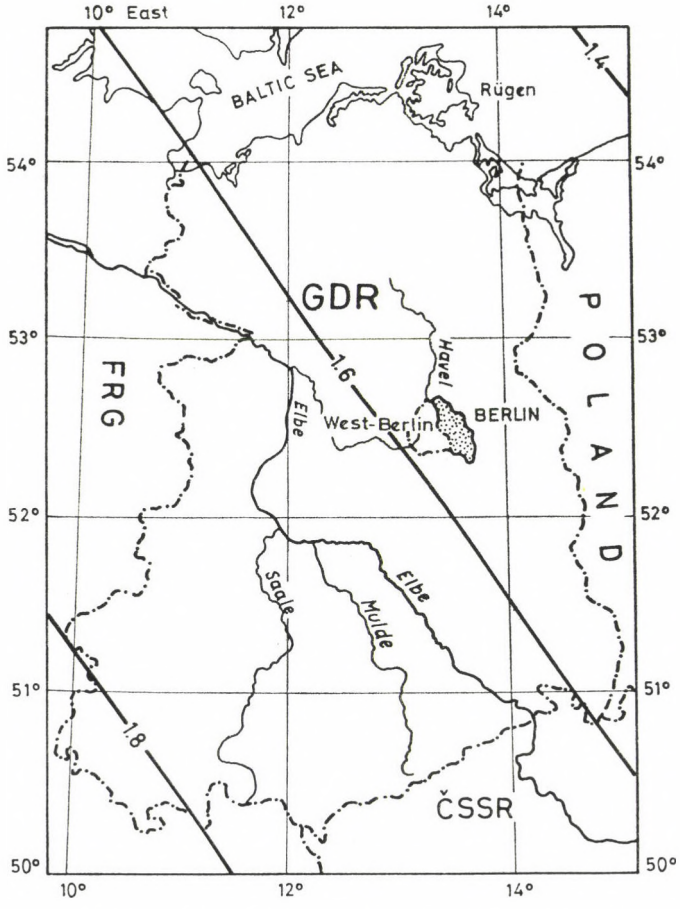


Fig. 6. Heat flow isolines of the lst order trend surface. Units in μcalcm^{-2} sec^{-1}

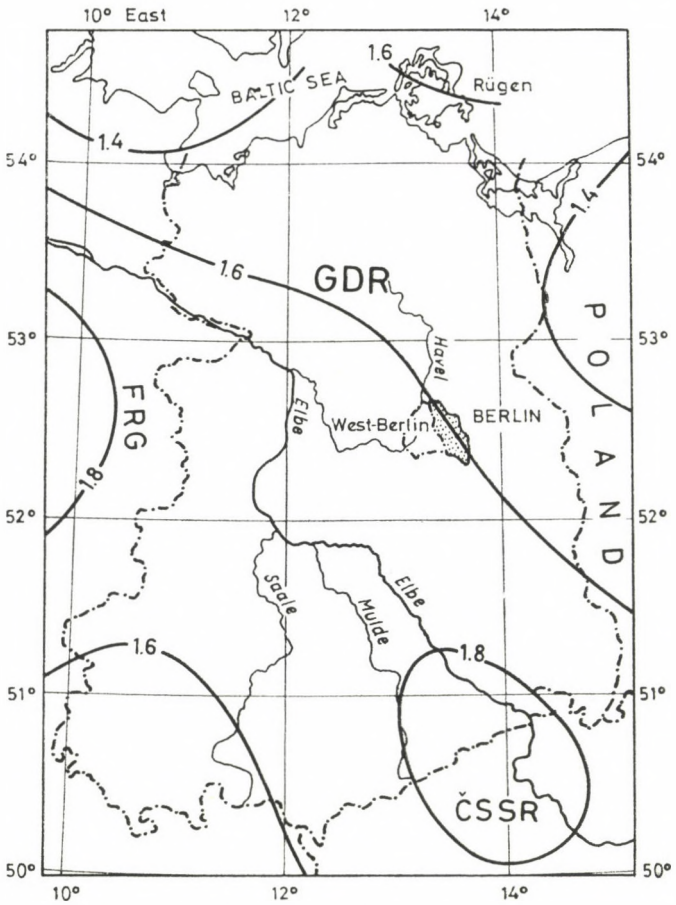


Fig. 7. Heat flow isolines of the 6th order trend surface.
Units in μcalcm^{-2} sec^{-1}

the East-Thüringian shale mountains and their northern continuation.

- In the Thüringian basin there is a *number of minor heat flow anomalies* related with the relief of the crystalline or metamorphic basement.
- For the southeast of the GDR (the area of outcropping granite of the Lusatian plate) at present it is not possible to make any definite statements on the heat flow pattern, because there have been only very few temperature measurements in this area.

Certain general features of the geothermal field can be represented by means of trend surface analysis. Trend surface maps give some kind of a "normal geothermal field". For the area of the GDR, trend surface analysis including heat flow values from the neighbouring countries were calculated from the 1st to the 6th order. Figures 6 and 7 show the results for the trend surface of the 1st and 6th order, respectively.

The 1st order trend surface map indicates a general decrease of the heat flow values towards northeast in the direction of the East European platform. On the 6th order trend surface map there appears a marked NW-SE trending geothermal high covering almost the whole southern part of the GDR.

Summarized, in the GDR there are 346 geothermal stations. Some models of temperature and heat flow distribution down to 30 km depth are calculated. They show that the heat flow entering the earth's crust from below should range between 16 and 33 mWm^{-2}.

The heat flow anomalies are correlated to the geological structure. Most important are high heat flow values within a W–E extending zone in the midst of the GDR. The trend surface of 1st order shows a general decrease of heat flow towards northeast in direction to the East European platform.

REFERENCES

HÄNEL, R., 1971. Heat flow measurements and a first heat flow map of Germany. *Z. Geophys.* **37**, 975–992.

HÄNEL, R., ZOTH, G., 1973. Heat flow measurements in Austria and heat flow maps of Central Europe. *Z. Geophys.* **39**, 425–439.

HURTIG, E., SCHLOSSER, P., 1973. Der Wärmefluß in Mitteleuropa. *Z. f. Geol. Wissensch.* **1**, 461–466.

OELSNER, CHR., LEISCHNER, H., PISCHEL, S., 1968. Eine kalibervariable Sonde für Wärmeleitfähigkeitsmessungen in situ. *Freiberger Forschungshefte C*, **232**, 47–65.

SCHLOSSER, P., 1968. Eine erste Einschätzung der geothermischen Parameter im obersten Bereich der Erdkruste des mittleren und nördlichen Teils des Territoriums der DDR und ihre Bindung an geologisch-geophysikalische Strukturelemente. *Freiberger Forschungshefte C*, **238**, 13–22.

SCHUSTER, K., 1968. Methodische und apparative Entwicklungen geothermischer Verfahren für Anwendungen im Bergbau und in der Tiefenerkundung. *Freiberger Forschungshefte C*, **232**, 5–45.

VERTICAL CHANGES OF THE HEAT FLOW IN BOREHOLES IN THE NORTH-GERMAN SEDIMENTARY BASIN

E. HURTIG, P. SCHLOSSER.

INTRODUCTION

A great number of rocktemperature and thermal conductivity measurements obtained in deep boreholes are available in the GDR. In general there are variations of the heat flow along the borehole axis. There are several factors which may cause these vertical changes, e.g. climatic effects of pleistocene glaciation, disturbances by water movements, and lateral changes of the thickness of salt formations. All these factors can strongly disturb the steady state geothermal field.

In order to get representative mean heat flow values of the steady state geothermal field it is necessary to evaluate the heat flow as function of depth continuously or for as many depth ranges as possible.

CONTINUOUS CALCULATION OF THERMAL CONDUCTIVITY IN BOREHOLES

In general it is not possible to have enough and well established thermal conductivity data from laboratory measurements, especially of the weak Mesozoic and Cenozoic sedimentary rocks.

Since attempts to develop special *in-situ* thermal conductivity probes have not been satisfactory, it was tried to calculate thermal conductivity from the results of other geophysical (electric, acoustic, and radiometric) borehole measurements. Actual rocks can be characterized as media composed of at least one mineral component and the pore volume usually filled with more or less mineralized water.

The thermal conductivity of porous mono- and polymineral rocks can be estimated on the basis of two simple model concepts: the linear and the disperse model, from among which the more probable should be chosen. The corresponding formulae are (see e.g. Brailsford and Major, 1964; Beck, 1965; Hurtig, 1965):

a) *linear model*: individual conductivities parallel:

$$\lambda = \lambda_1 p_1 + \lambda_2 p_2 + \ldots + \lambda_n p_n$$

individual conductivities in series:

$$\frac{1}{\lambda} = \frac{p_1}{\lambda_1} + \frac{p_2}{\lambda_2} + \ldots + \frac{p_n}{\lambda_n}$$

b) *disperse model*:

$$\lambda = \frac{p_1 + A\,\lambda_2 + B\,\lambda_3}{(p_1/\lambda_1) + A + B}$$

λ_i: thermal conductivity of the individual components
p_i: fraction of the individual components

$$A = 3p_2/(2\lambda_1 + \lambda_2)$$

$$B = 3p_2/(2\lambda_1 + \lambda_3)$$

The dependence of thermal conductivity on porosity for a two-component medium (quartz/water and quartz/air, respectively) for the different models is shown in Figure 1. Experimental results (see Fig. 2) indicate a quasi-linear relationship between thermal conductivity and pore volume (density, respectively). Beck (1965) refers to similar results.

The calculation of thermal conductivity from geophysical borehole measurements has to start with the following functional relationship

$$\lambda = f(M, P)$$

where

M: mineral composition of the rocks;
P: kind and volume fraction of the pore filling medium.

The following parameters must be known:

– Lithologic main type (e.g. sandstone/claystone, limestone/claystone, salt

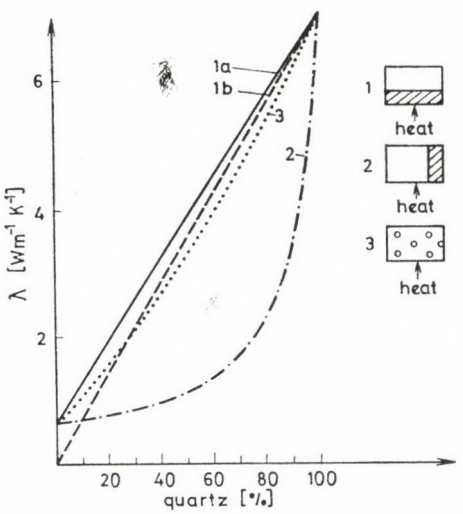


Fig. 1. Thermal conductivity *vs.* quartz content
1 – linear model (conductivities parallel): a – quartz-water mixture; b – quartz-air mixture; 2 – linear model (conductivities in series); 3 – disperse model

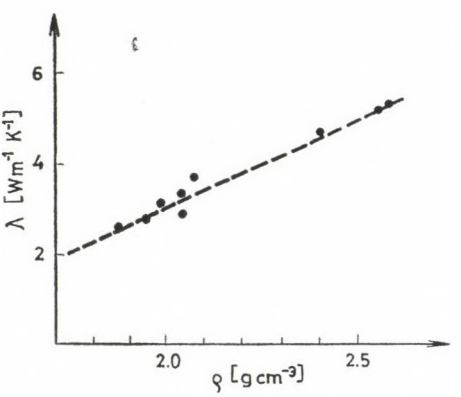


Fig. 2. Thermal conductivity *vs.* density. Sandstone samples, laboratory measurements

rocks, effusive rocks). The thermal conductivities of the individual mineral components are changing, so calculation for different types of sedimentary (and effusive) rocks must be carried out separately.
- Mineral composition within the lithologic main types, especially the quartz-clay content in sandstones and the clay content in limestones and marls.
- Porosity.
- Kind of the pore filling fluid and water saturation.

From routine interpretation of geophysical borehole measurements these parameters are yielded. Regarding the spacing of geophysical borehole-probes the calculation of thermal conductivity in formations with alternating thin beds of different rock types will be uncertain. The following limitations should also be kept in mind:
- Since the calculations are based on a linear model they may be affected with systematic errors.
- Thermal conductivity values of the mineral components are not well established.

Thermal conductivity of quartz crystals perpendicularly to the principal axis amounts to 6.7 $Wm^{-1}K^{-1}$ (16.5 $mcalcm^{-1}sec^{-1}\,°C^{-1}$), whereas in a direction parallel to the crystallographic axis it is about 13.4 $Wm^{-1}K^{-1}$ (32 $mcalcm^{-1}sec^{-1}\,°C^{-1}$). For nonporous closely packed polycrystalline quartz rocks (quarzite) with random orientation of the crystallographic axis and variable grain sizes, a thermal conductivity of 7.1 $Wm^{-1}K^{-1}$ (17 $mcalcm^{-1}sec^{-1}\,°C^{-1}$) can be derived from available experimental results.

The thermal conductivity of calcite parallel to the crystallographic principal axis amounts to 4.2 $Wm^{-1}K^{-1}$ (10 $mcalcm^{-1}sec^{-1}\,°C^{-1}$). For closely packed nonporous, polycrystalline limestone samples thermal conductivity values of about 3.3 $Wm^{-1}K^{-1}$ (8 $mcalcm^{-1}sec^{-1}\,°C^{-1}$) have been determined. These values have been used for calculating thermal conductivity.

Thermal conductivity of clay minerals are very uncertain. There are only few experimental results. For close packed anhydrous clay minerals (e.g. biotite) the values range between 2.0 and 2.5 $Wm^{-1}K^{-1}$ (5 and 6 $mcalcm^{-1}sec^{-1}\,°C^{-1}$). A mean value of 2.3 $Wm^{-1}K^{-1}$ (5.5 $mcalcm^{-1}\,sec^{-1}\,°C^{-1}$) appears reasonable.

Nevertheless the values of thermal conductivity for clay minerals might be affected with larger errors.

Using these mineral thermal conductivities the following relations are obtained for calculating the thermal conductivity of the individual thin sedimentary layers:

Sandstone-claystone layer: $\lambda_i = 17\,Q_i + 5.5\,C_i + 1.5\,P_i$

Limestone-claystone layer: $\lambda_i = 8\,Ca_i + 5.5\,C_i + 1.5\,P_i$

Q_i: quartz content within the i-th layer
C_i: clay content within the i-th layer
Ca_i: calcite content within the i-th layer
P_i: porosity of the i-th layer

VERTICAL CHANGES OF THE THERMAL FLOW IN BOREHOLES OF THE GERMAN SEDIMENTARY BASIN

Figure 3 shows the histogram of the heat flow values in the depth ranges 0–1500 m and deeper for the same boreholes.

In the upper part of the boreholes the heat flow is in general somewhat lower and increases with depth. But the detailed thermal situation and the factors affecting it may be quite complicated in a well.

Figures 4 and 5 give two examples. Borehole 1 (Fig. 4) is located in a fault zone. Accordingly, disturbances of the geothermal field by circulating water cannot be excluded. The behaviour of the temperature *vs.* depth curve indicates such effects, the values of the geothermal gradient for both the 50 m and 100 m intervals show considerable variations.

The depth range from 1200 to 1850 m is not suitable for calculation of thermal conductivity, for claystones, limestones, and sandstones with clayey-limey cement occur in a narrow alternating series of beds.

Down to approximately 1850 m there is a quite uniform sequence of sandstones, claystones, and siltstones (upper Carboniferous). It is followed underneath by a monotone alternation of claystones, clayey marlstones, limey marlstones, and limestones (lower Carboniferous). Thus in these two depth ranges favourable conditions are given for the calculation of thermal conductivity.

At approximately 1850 m depth, the calculated value of thermal conductivity ranges between 4.94 $Wm^{-1}K^{-1}$ (11.8 $mcalcm^{-1}\,sec^{-1}\,°C^{-1}$) for sandstone horizons and 3.14 $Wm^{-1}\,K^{-1}$ (7.5 $mcalcm^{-1}\,sec^{-1}\,°C^{-1}$) for claystone-siltstone sequences. From approximately 1850 m down to approximately 2200 m, the thermal conductivity varies around 3.14 $Wm^{-1}K^{-1}$ (7.5 $mcalcm^{-1}\,sec^{-1}\,°C^{-1}$) for limestone and limey marlstone beds. At the transition to claystone and clayey marlstone sequences thermal conductivity drops to 2.5–2.7 $Wm^{-1}\,K^{-1}$ (5.8 and 6.5 $mcalcm^{-1}\,sec^{-1}\,°C^{-1}$).

A direct comparison of the evaluated thermal conductivity values and data from laboratory measurements has not been possible.

On the other hand, numerous thermal conductivity data from the same region and the same formations are available (see Table 1).

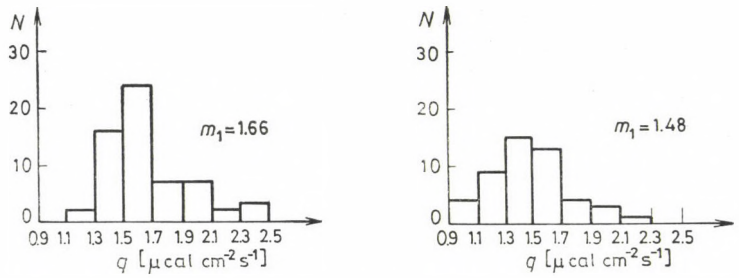


Fig. 3. Histogram of heat flow data in the North-German sedimentary basin
a – depth range 0 – 1500 m; b – deeper than 1500 m

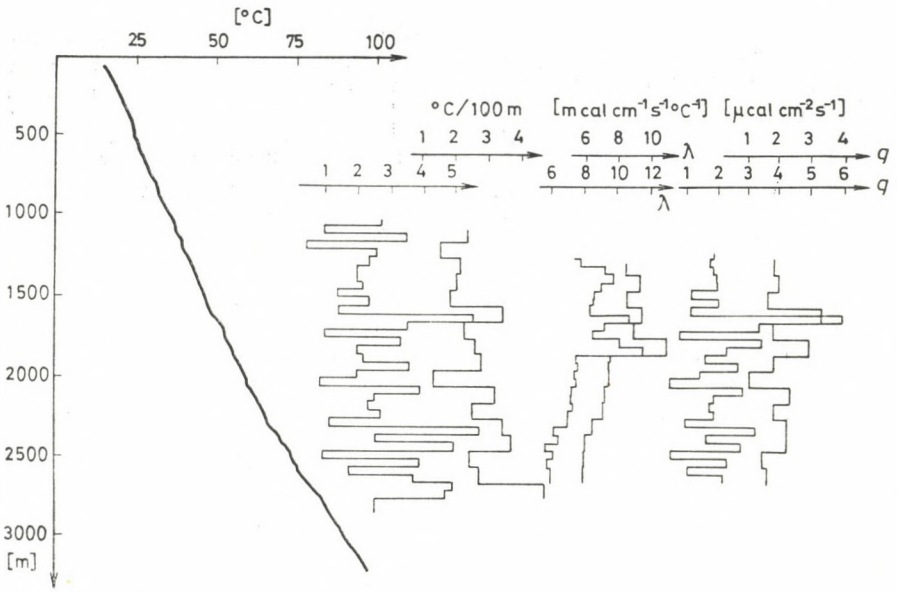


Fig. 4. Borehole 1: continuous calculation of thermal conductivity and heat flow

TABLE 1

Thermal conductivity data (laboratory measurements) for the Upper and Lower Carboniferous

Formation rock type	m	N	$\pm\sigma$
Upper Carboniferous			
Red sequence			
sandstone	3.44 (8.23)	88	0.06 (0.14)
siltstone	2.65 (6.34)	28	0.11 (0.27)
claystone	1.95 (4.67)	12	0.10 (0.23)
Grey sequence			
sandstone	3.82 (9.13)	13	0.22 (0.53)
siltstone	3.02 (7.22)	5	0.35 (0.83)
claystone	2.52 (6.03)	12	0.11 (0.26)
Lower Carboniferous			
marlstone	2.23 (5.34)	7	0.07 (0.17)
limestone	2.44 (5.84)	6	0.07 (0.17)

m: mean value $Wm^{-1}K^{-1}$ (mcal cm^{-1} sec^{-1} $°C^{-1}$)
N: number of values
σ: variance, $Wm^{-1}K^{-1}$ (mcal cm^{-1} sec^{-1} $°C^{-1}$)

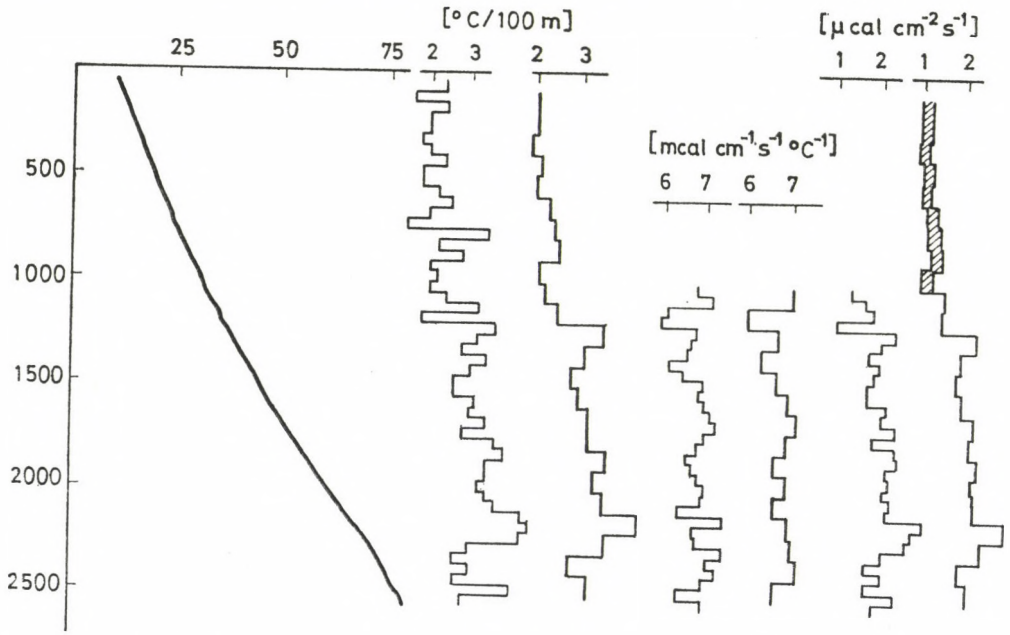


Fig. 5. Borehole 2: continouous calculation of thermal conductivity and heat flow

The sandstone samples can attain as high as 5.69 $Wm^{-1}K^{-1}$ (13.6 $mcalcm^{-1}\,sec^{-1}\,°C^{-1}$) values.

The mean laboratory values are slightly lower than the calculated ones. This should be expected, because the laboratory measurements cannot be carried out under *in-situ* conditions (pressure and water saturation). From this point of view, the laboratory values agree satisfactorily with the calculated thermal conductivity data. The heat flow has been calculated from the mean values of thermal conductivity for 50 m and 100 m intervals, respectively (see the right hand part of Fig. 4). Down to approximately 1350 m, only small variations of the heat flow are encountered ranging between more than 252 mWm^{-2} (6 $\mu calcm^{-2}\,sec^{-1}$) and 42 mWm^{-2} (1 $\mu calcm^{-2}\,sec^{-1}$).

These variations are associated with tectonic faults and fissure systems, where convective heat transport can take place.

In the second borehole (Fig. 5) water movements are not observed. Mesozoic formations (Cretaceous with chalk formations and Triassic) build up the depth range down to approximately 1000 m. Below there is a monotone alternation of marlstone, limestone, and limey claystone beds (Lower Carboniferous). The temperature *vs.* depth curve indicates an increase of thermal gradient (see 2nd and 3rd curve from below). The calculated thermal conductivity values for 50 m and 100 m intervals, respectively (see 4th and 5th curve), range between 2.5 and 3.9 $Wm^{-1}K^{-1}$ (6.0 and 7 $mcalcm^{-1}\,sec^{-1}\,°C^{-1}$)

and show only slight variations. The last two curves give the heat flow for 50 m and 100 m intervals.

The thermal conductivity values in the upper part of the borehole (Mesozoic formations) have not been calculated from geophysical borehole measurements, but they should range between 2.1 and 2.5 $Wm^{-1}K^{-1}$ (5 and 6 $mcalcm^{-1}sec^{-1}\,°C^{-1}$). In this borehole the heat flow increases with depth. Below ca. 1500 m the values are more or less uniform, some peaks may indicate that convective heat transport by moving water is taking place even in this borehole.

INTERPRETATION

Both examples show strong vertical changes of the heat flow but of quite different type, though the distance between the two boreholes only amounts to some kilometers. In the first case the variations are more or less random and are due to strong disturbances by water circulation.

In the second hole the heat flow systematically increases with depth, probably due to climatic changes during pleistocene glaciation (see e.g. Čermák, 1971; Crain, 1968). Both types of vertical changes of heat flow are very common in the boreholes in the North-German sedimentary basin. The decision, whether there are "normal" (that is undisturbed by water movements) or disturbed thermal conditions in a borehole or in a given depth range is only possible by means of calculating the heat flow continuously along the borehole.

The results show that the evaluation of thermal conductivity from geophysical borehole measurements yields a method to overcome the problems connected with the measurements on rock samples in the laboratory.

Further, corrections (especially climatic corrections) on heat flow values should only be applied if the vertical changes along the borehole axis have been studied. Because of very complex geological and tectonical structure of the North-German sedimentary basin even neighbouring boreholes might show quite different thermal conditions.

REFERENCES

Beck, A. E., 1965. Techniques of measuring heat flow on land. In: W. H. K. Lee: Terrestrial heat flow. Geophys. Monograph, No. 8, AGU, 24–57.

Brailsford, A. D., Major, K. G., 1964. The thermal conductivity of aggregates of several phases, including porous materials. *Brit. J. appl. Phys.* **15**, 313–319.

Čermák, V., 1971. Underground temperature and inferred climatic temperature of the past millenium. *Palaeogeography, Palaeoclimatol., Palaeoecol.* **10**, 1–19.

Crain, I. K., 1968. The glacial effect and the significance of continental terrestrial heat flow measurements. *Earth Planet. Sci. Letts.* **4**, 69–72.

Hurtig, E., 1965. Untersuchungen der Wärmeleitfähigkeits-Anisotropie von Sandsteinen, Grauwacken und Quarziten. *PAGEOPH*, **60**, (I), 85–100.

Hurtig, E., 1968. Ergebnisse von Wärmeleitfähigkeitsmessungen an Gesteinsproben aus der DDR im Rahmen komplexer petrophysikalischer Untersuchungen. *Freiberger Forschungshefte C*, **238**, 101–118.

THE TERRESTRIAL THERMAL FIELD IN POLAND

J. MAJOROWICZ, S. PLEWA, M. WĘSIERSKA

The first studies in the field of geothermics in Poland (Heurich, 1904; Michael and Qwitzow, 1910; Arctowski, 1924) had only been concerned with the determination of the geothermal degree and gradient in some boreholes. Later, results of measurements of these parameters were elaborated on a regional scale. The first map of the geothermal degree in Poland was prepared by Rozycki (1948) on the basis of twelve values measured in Poland and neighbouring countries. The next maps were constructed by Plewa (1966) on the basis of measurements in 10 to 26 boreholes, depending on the depth interval. The first maps of geotemperatures were given by Węsierska for depths of 500, 1000 and 1500 m. Recently, new maps of the geothermal degree were published by Majorowicz (1972), who had access to much more data than Plewa had, namely, 20–54 values of geothermal degree for the various depth intervals.

In the last two years the number of recorded thermal logs has increased considerably, creating a need for up-dating the geothermal maps. With this in view, all accessible thermograms have been scrutinized and 72 logs were picked out. These are logs recorded in wells after a standstill of at least 9 days, but usually several weeks, at depths greater than 1000 m. The locations of the boreholes are shown in Figure 1 on a map of the temperature of the neutral layer, which occurs in Poland at a depth of about 20 m.

Temperatures were measured with Soviet-made electric logging thermometers (usually of the ETMI-55 type) in boreholes in which the thermal conditions could be assumed to be close enough to the thermal equilibrium state.

Studies on the density of the surface heat flow were initiated in Poland in 1963. Up to 1966 the heat flow density was measured in six boreholes located in different regions (Plewa, 1966). Thermal conductivity measurements were carried out by the heat pulse technique employing a linear heat source.

The next stage of research on the terrestrial heat flow density in Poland was the work done by Węsierska (1973a) and Majorowicz (1972, 1973a, b). Laboratory measurements of thermal conductivity were carried out by the fixed heat-flow conditions technique (Węsierska, 1973b). These measurements were accomplished with an apparatus designed and built at the Silesian Technical University by Chmura (1970).



Fig. 1. Location of boreholes in which geothermal logging was performed against map of isotherms of the neutral level

GEOISOTHERM MAPS

Figures 2 and 3 show the regional terrestrial thermal field in Poland (geoisotherms) for depths of 1 km (Fig. 2) and 2 km (Fig. 3). These maps were procured with actual measurement data as the basis. Thermometric data were obtained from measurements at depths greater than or equal to 2 km. In a few cases temperatures for the depth of 2 km were obtained indirectly by extrapolating functions approximating the variations of temperature measured at depths smaller than 2 km, but always greater than 1.3 km.

The pattern of geoisotherms is similar at both depths. In general, the lowest values of temperature are observed in NE- and N-Poland, where temperatures at 1 km are lower than 30 °C and those at 2 km are lower

than 50 °C. Such low values in this region of Poland are characteristic of the entire Pre-Cambrian Platform of Eastern Europe, proceeding eastwards right up to the Ural Mts, as is seen from maps given, among others, by Stegena (1971).

The highest temperatures are observed in SW-Poland, especially in the northern fringe of the Cis-Sudetic Monocline. Here, temperatures reaching 45 °C at a depth of 1 km and 80 °C at 2 km are not unusual. Such high temperatures are characteristic also of the GDR territories adjacent to this region, as shown by the geoisotherm map for a depth of 1 km (Schlosser, 1970). The high temperature zone observed in SW-Poland is the eastern marginal zone of the high-temperature region characteristic of the entire so-called Paleo-Europe, and is in contrast with the low-temperature region in N- and NE-Poland, which is probably associated with the region of the Pre-Cambrian Platform.

In the Carpathian region there is observed a rise in temperature when going from the marginal Flysch zone southwards towards the Root zone.

This general outline of the pattern of terrestrial temperature variations indicates a correlation with the main geotectonic units dividing the area of Poland, hence, the Paleozoic and Pre-Cambrian Platform and the Alpine Folding Area. Imposed on this pattern are a number of local variations,

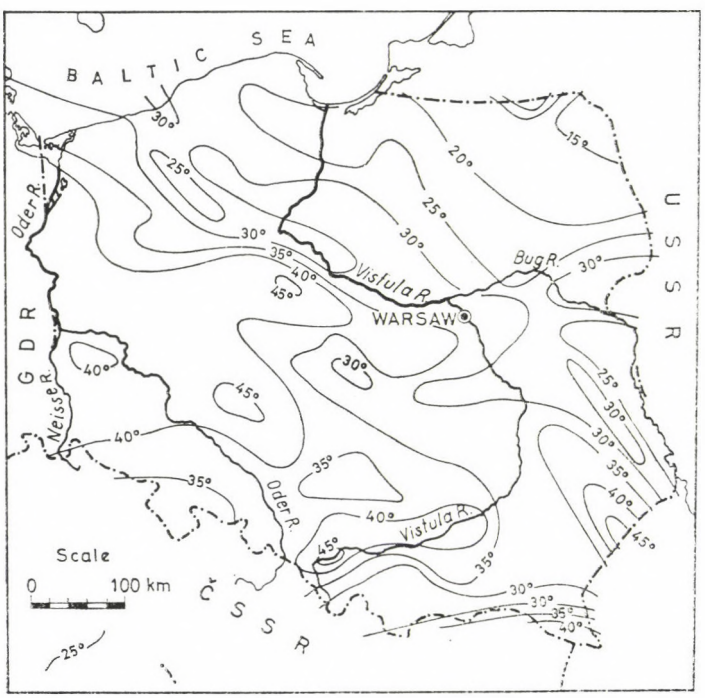


Fig. 2. Geoisotherms for a depth of 1 km in centigrades; 25° – isoline corresponding to 25 °C

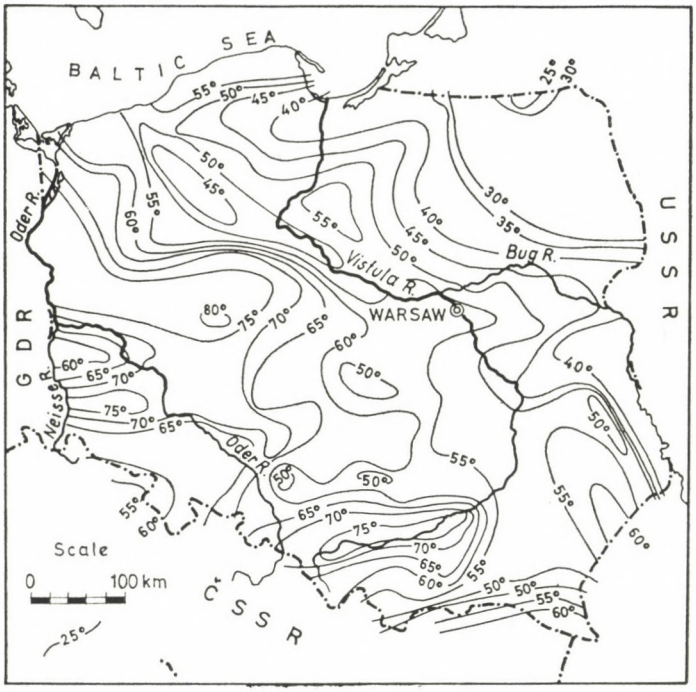


Fig. 3. Geoisotherms for a depth of 2 km in centigrades; 25° – isoline corresponding to 25 °C

the interpretation of which requires closer recognition of the distribution of thermal conductivities of the various rock formations and detailed knowledge of heat flow and heat generation alike.

GEOTHERMAL GRADIENT MAPS

The mean weighted geothermal gradients were calculated over the intervals 200–1000 m and 200–2000 m for the boreholes specified in Figure 1. The results of calculations corresponding to thermograms of very differentiated runs were made more accurate on the basis of a linear approximation procedure performed on Odra 1013 and 1204 computers. The gradient values obtained for the first of the examined intervals lie within the limits from 0.0045 to 0.0383 Km^{-1}, the minimum lying at the point Krz-1 and the maximum at GI-IG-1. In the other depth intervals the smallest value of gradient, equal to 0.0107 Km^{-1}, is also at the Krz-1 well, whereas the maximum 0.0353 Km^{-1} at the boreholes Sr-IG-1 and U-1.

The results of calculations show that for some boreholes not very distant from each other the values of gradient differ considerably. This is true of the Ba-IG-1 and Kt-IG-1 wells in NE-Poland, for which in the first

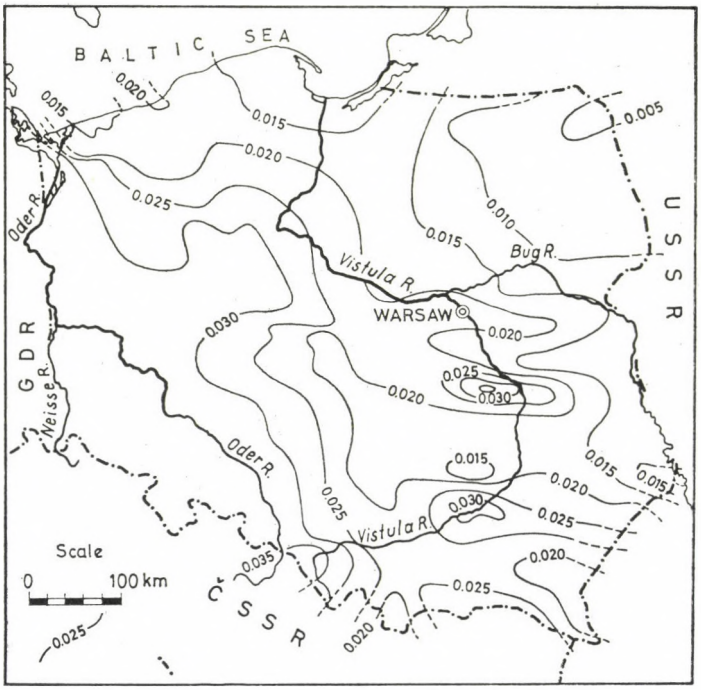


Fig. 4. Isolines of geothermal gradient for the depth interval of 200–1000 m; 0.020 – isoline corresponding to gradient values of 0.020 Km^{-1}

interval the gradients are 0.0125 and 0.0080 Km^{-1}, respectively. This is presumably due to a fault running latitudinally between these wells, causing a lowering of the crystalline basement in the Ba-IG-1 well by about 600 m relative to the Kt-IG-1 well. Another reason for this difference is the less stable thermal regime in the Kt-IG-1 borehole, which is indicated by the character of the thermograms. Similar circumstances occur in the Kk-7 and Kk-12 boreholes in the Lublin Synclinorium, where the respective gradients are 0.0186 and 0.0226 Km^{-1}. Especially interesting is another pair of boreholes, GI-IG-1 and R-IG-1, in NW-Poland. The values of the gradient for the first interval are 0.0322 and 0.0166 Km^{-1}, respectively. These two boreholes are in different tectonic provinces (Szczecin Synclinorium and Pomeranian Anticlinorium). The magnitude of the difference is also affected by the thick tertiary formations of low thermal conductivity in the GI-IG-1 well, which do not occur at all in the R-IG-1 well. The geothermal gradient for a 400 m layer of these formations is 0.0520 Km^{-1}.

For the construction of isogradients 72 measurements were used in the depth interval 200–1000 m and 56 in the depth interval 200–2000 m (Figs 4 and 5).

For the sake of clarity the isolines of geothermal gradient are plotted every 0.005 Km^{-1}, using graphical linear interpolation. Attempts to construct

the maps using a digital computer by means of fitting with higher-order polynomials showed it was not a very reliable method in cases involving a denser set of measurement points and large variations of values in such regions; therefore, it was not used here.

The character of the variations in both cases is similar to and is generally compatible with those of earlier maps (Plewa, 1966; Majorowicz, 1972). NE-Poland features low values of geothermal gradient, in central Poland and the Carpathian Mts with the Cis-Carpathian Depression the values are intermediate, whereas in the Cis-Sudetic Monocline and the Upper Silesian Coal Basin they are the highest.

A more detailed explanation of the gradient variations in Poland was attempted by comparing the geothermal map over the 200–2000 m interval which depicts variations presumably caused mainly by the heat flow distribution, with local lithological, stratigraphical, hydrogeological and other factors (Kraskowski, 1961). So it is possible to single out regions in which the isolines run very similarly to each other. These are the Mazury-Suwalki Swell, the Podlasie Depression, the north-western part of the Lublin Synclinorium, and the south-western part of the Swiety Krzyz Anticlinorium. For these regions the shapes of the isolines presumably are determined chiefly by the heat flow distribution. A comparison of the gradient

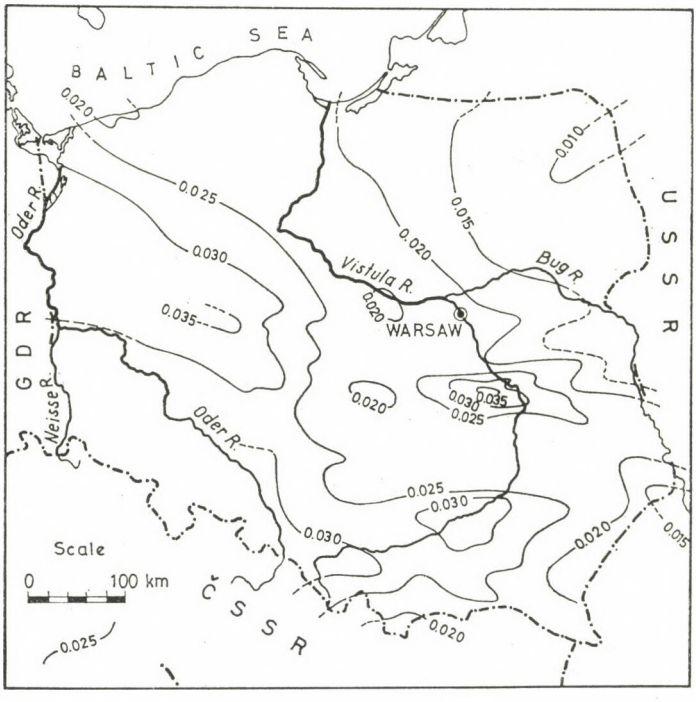


Fig. 5. Isolines of geothermal gradient for the depth interval of 200–2000 m; 0.020 – isoline corresponding to gradient value of 0.020 Km^{-1}

map for the depth 200–2000 m with the structural map of the consolidated basement (Pozaryski, 1970) shows that the Pre-Cambrian Platform region in Poland has, in general, low geothermal gradients. Within the Mazury-Suwalki Swell there is an increase of the gradient in the south-western direction, caused by a sinking of the crystalline basement. The rather uniform thermal field of the Platform is perturbed in the Podlasie Depression region, where the highest value of 0.0242 Km^{-1} is recorded in the DW-1 well. The higher geothermal gradient is probably due to the effect of deep tectonic fractures and scissions. The abnormally high values of gradient in the north-western part of the Lublin Synclinorium (0.0353 Km^{-1} at the U-1 well) correspond to the largest depth of occurrence of the crystalline basement in the Marginal Synclinorium. At the present state of our knowledge of the basement structure in the south-western part of the Swiety Krzyz Anticlinorium it is difficult to give an explanation of the extreme geothermal gradient (0.0345 Km^{-1} in the Z-1 well).

The Paleozoic Platform region in the Central Poland Anticlinorium features a geothermal gradient approximately equal to the mean value for Poland, i.e. about 0.020 Km^{-1}. No isolines of geothermal gradient are plotted in the Sudetic Block region because of the lack of experimental data.

Owing to the fact that the basement in the north-western and northern parts of Poland occurs at large depths (from 4 to 12 km), it would be worth while to construct a map of the geothermal gradient for a much larger interval. The small number of thermometric measurements hitherto performed under thermal equilibrium conditions at depths greater than 2000 m do not yet provide firm grounds for a more detailed explanation.

THE SURFACE HEAT FLOW

Poland is especially interesting from the point of view of geothermal research, for it lies at three large geotectonic regions: the Pre-Cambrian Shield of Eastern Europe, the Paleozoic Platform (Paleo-Europe) and the Alpine Folding Area. The correlation of heat flow Q with tectonic regions has been ascertained statistically on a globular scale (Smirnov, 1968; Lee and Uyeda, 1965) as well as for the region of the Pre-Cambrian Shields of the Paleozoic Platforms and provinces featuring Meso-Cenozoic Folding of Europe and Poland (Majorowicz, 1972, 1973a). The average values for these regions of Europe are as follows:

Q (Pre-Cambrian Platform) = 42.29 ± 8.79 mWm^{-2} (1.01 ± 0.21 HFU);
Q (Paleozoic orogenic regions) = 69.10 ± 13.82 mWm^{-2} (1.65 ± 0.33 HFU);
Q (Meso-Cenozoic orogenic regions) = 80.82 ± 19.68 mWm^{-2} (1.93 ± 0.47 HFU).

Data on heat flow corroborate these correlations within the area of Poland in a majority of cases.

The heat flow data obtained (Fig. 6) show that most of the low values of Q, near 42 mWm^{-2} (1.0 HFU), are observed in the north-eastern parts of Poland.

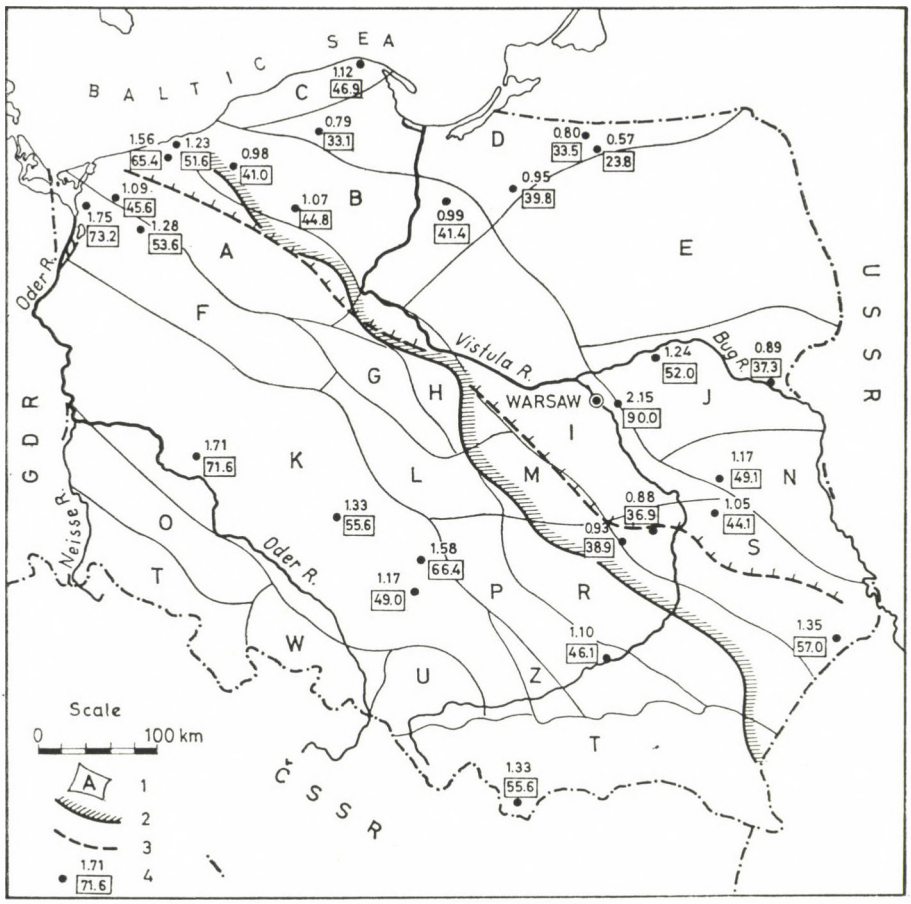


Fig. 6. Map of surface heat flow against tectonophysical elements of upper earth's crust in Poland

1 – first-order tectonic units of Poland: A – Pomeranian Anticlinorium; B – Pomeranian Synclinorium; C – Leba Swell; D – Peri-Baltic Syneclise; E – Mazury-Suwalki Swell; F – Szczecin Synclinorium; G – Mogilno Synclinorium; H – Kujawy Anticlinorium; I – Warsaw Synclinorium; J – Podlasie Depression; K – Cis-Sudetic and Silesian-Cracow Monocline; L – Lodz Synclinorium; M – Rawa-Gielnow Anticlinorium; N – Podlasie-Lublin Swell; S – Lublin Synclinorium; P – Nidzica Synclinorium; R – Swiety Krzyz Anticlinorium; O – North-Sudetic Ridge; T – Western Sudetes Mts; W – Eastern Sudetes Mts; V – Upper Silesian Coal Basin; Y – Carpathian Mts; Z – Miechow Elevation;

2 – NW boundary of zone of strong regional gradient of magnetic anomalies, after Pozaryski (1973);

3 – SW boundary of continuous region in which extreme seismic refractive velocities exceed 6100 msec^{-1} corresponding to the boundary of the region of consolidated basement, after Pozaryski (1973);

4 – values of terrestrial heat flow in HFU and in new units (mWm^{-2}), after Plewa (1966), Węsierska (1973a, b), Majorowicz (1972, 1973a, b, c)

In the Peri-Baltic Syneclise, which is a region known to be a part of the Eastern European Platform, the values are low, less than 42 mWm^{-2}, and range between 23.8 and 39.8 mWm^{-2} (0.57 and 0.79 HFU). Values of the same order of magnitude are observed in the Pomeranian Synclinorium, where the minimum and maximum values are 41.0 mWm^{-2} (0.98 HFU) and 44.8 mWm^{-2} (1.07 HFU), respectively. Values which should also be acknowledged as characteristic of the marginal region of the East European Platform's Pre-Cambrian zone should be those recorded in the Podlasie-Lublin Swell, $Q = 49.1$ mWm^{-2} (1.17 HFU) and the Lublin Synclinorium, $Q = 36.9$–57.0 mWm^{-2} (0.88–1.35 HFU). The value 57.0 mWm^{-2} is one which deviates from the average value for this region, which are close to 42 mWm^{-2}, but is similar to values measured in the border territory of the Ukraine in the region of the Paleozoic Lvov Depression (Kutas, 1972), where the values range from 54.44 to 71.19 mWm^{-2} (1.3 to 1.7 HFU). In the Podlasie Depression heat flow values oscillate between 37.3 and 52.0 mWm^{-2} (0.89 and 1.24 HFU), whereas at the boundary between the Warsaw Synclinorium and the Podlasie Depression a value of 90.0 mWm^{-2} (2.15 HFU) has been measured, which in the light of other data obtained for the eastern part of the Platform should be considered to be an anomaly. In the Brest Depression region, in the Byelorussian SSR territory adjacent to Poland, values of heat flow higher than the mean for the Platform have been recorded. These are values ranging between 51.51 and 58.63 mWm^{-2} (1.23 and 1.40 HFU), as follows from the data of Bogomolov (1972). Values of the order of 50.25–58.63 mWm^{-2} (1.2–1.4 HFU) are characteristic of the marginal zones of this type of platform depression and are also observed in some places of the Dnieper–Donets Aulocogene (found by Kutas, 1972).

A low heat flow has also been measured in the Leba Swell, where $Q = 46.9$ mWm^{-2} (1.12 HFU).

In general, the values of heat flow in south-western Poland are higher than in the south-eastern regions. In the Cis-Sudetic Monocline and Silesian-Cracow Monocline the heat flow assumes values from 49.0 to 71.6 mWm^{-2} (1.17 to 1.71 HFU). Such values should also be expected in the western part of the Sudetes Mts within Poland, as suggested by data obtained by Čermák (1968a) in the border region between Poland and Czechoslovakia (the Zacler-Svatonovice Basin), where the heat flow reaches 66.58 mWm^{-2} (1.59 HFU), and by data on the geothermal gradient in the Sudetes Mts. High heat flow is also to be expected in the region of the Upper Silesian Depression because of the high values of geothermal gradients observed there. This is also suggested by the heat flow values of 72.87 to 78.31 mWm^{-2} (1.74 to 1.87 HFU) recorded in the border region of the Upper Silesian Basin in Czechoslovakia by Čermák (1968b). High heat flows have also been measured in north-western Poland, corroborated by data from the border region of the GDR (Schlosser, 1970). In the northern part of the Szczecin Synclinorium we have values between 53.6 and 73.2 mWm^{-2} (1.28 and 1.75 HFU).

These rather high values of heat flow measured in north-western Poland are in many cases close to the mean values characteristic of Paleo-Europe (Majorowicz, 1973a, b).

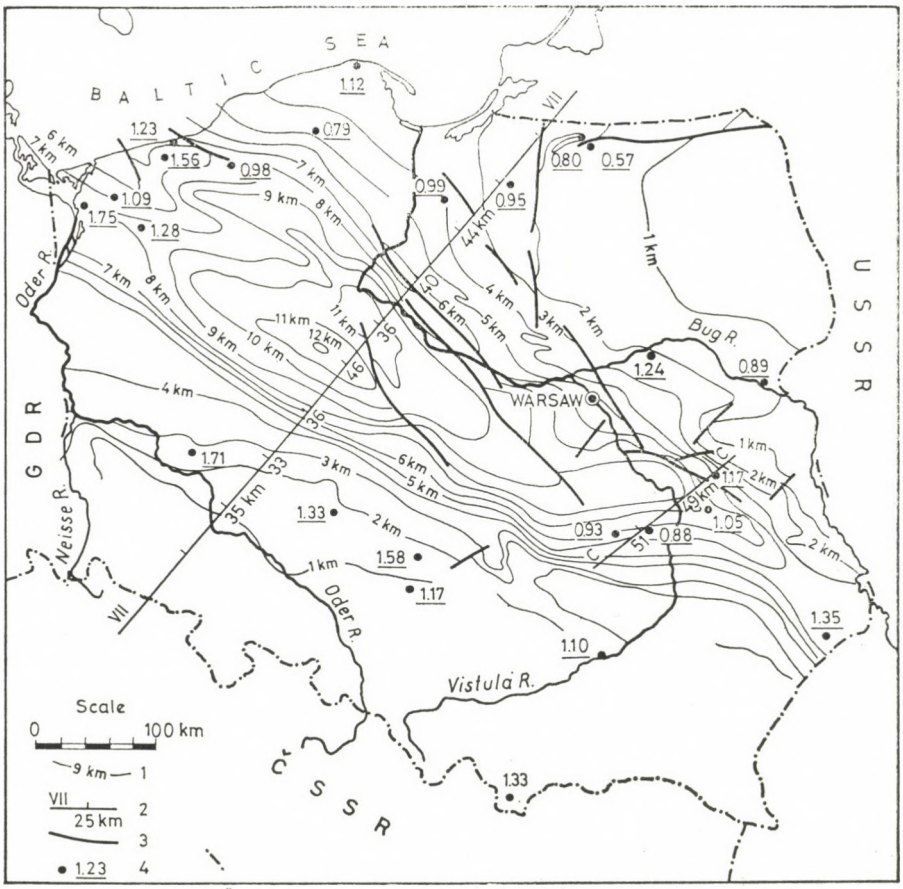


Fig. 7. Surface heat flow against seismic data on structure of the earth's crust 1 – isolines of depth of consolidated basement in kilometers relative to sea level, after Pozaryski (1970); 2 – profiles of deep seismic soundings with data on the Moho boundary, in kilometers, after Guterch et al. (1973); 3 – dislocation lines, after Pozaryski (1970); 4 – values of heat flow after Plewa (1966), Węsierska (1973a, b) and Majorowicz (1972, 1973a, b, c)

In the Alpine Folding areas of Poland only one value was measured in a well at Zakopane, where Q was found 55.6 mWm^{-2} (1.33 HFU) (Plewa, 1966). As follows from the data of Čermák (1972) and Kutas (1972), these values should probably increase as the inner regions of the Carpathian Geosyncline are approached.

The small number of data from the marginal zone of the Pre-Cambrian Platform in the area of Poland does not permit them to be linked up with other tectonic elements. It must be borne in mind, however, that in the provinces westwards of the "Tornquist line" adopted from the map of the magnetic component Z and considered as the western boundary of the

Pre-Cambrian Shield of Eastern Europe, we observe in north-western Poland — that is in the marginal zone of this Platform — both low values of heat flow (45.6 and 51.6 mWm^{-2} or 1.09 and 1.23 HFU) and high ones (65.4 mWm^{-2} or 1.59 HFU). At the same time, we can see that low heat flows are generally observed eastwards of the line constituting the boundary of the region in which extreme refraction velocities exceed 6100 $msec^{-1}$, that is, in the region where the basement is strongly consolidated (Fig. 7).

A plot of the heat flow data against depth of the consolidated basement in Poland or, in other words, against the thickness of sediments indicates that there is no correlation between Q and the bed-rock morphology. High heat flow values are observed both in regions where the thickness of the sedimentary horizon is small, e.g., the Cis-Sudetic Monocline, or large, such as in north-western Poland. High Q values can be observed in places where the crystalline basement rises up, as in north-eastern Poland, as well as in places where it is deeply embedded, as in north-western Poland and the Lublin Synclinorium.

Data on the depth of the Moho discontinuity acquired at the VII international profile and local profile C (Guterch et al., 1973) are not adequate for providing a complete picture of the crustal thickness in the area of Poland. None the less, a regular feature can be noticed, namely that the highest values of heat flow are observed in those places where the Moho depths are the smallest (30 km), whereas twice as small values are observed at sites where the Moho interface is known to occur at the greatest depths (40–45 km) (Majorowicz, 1973a, b).

CONCLUSIONS

Poland is a region very interesting from the points of view of geothermics and tectonics. The data available from measurements heretofore do not give grounds for farreaching conclusions, but there are reasons to suppose that the thermal fields in Poland correlate with the tectonically different provinces.

At the same time research is still being carried out on the problem of perturbations of the thermal field by the presence of bodies of varying conductivities and heat generation features. In the future there will be a research project involving the content of the radio-isotopes U238, Th232 and K40 in the crystalline bed-rock formations.

REFERENCES

Arctowski, H., 1924. Nowe pomiary gradientu geotermicznego w szybach naftowych Boryslawia. Krosna, Bitkowa, *Kosmos, ser. A.*

Bogomolov, G. B., 1972. Geothermic zones on the territory of the Byelorussian SSSR (in Russian). Nauka i Tekhnika, Minsk.

Čermák, V., 1968a. Heat flow in Zacler-Svatonovice Basin. *Acta Geophys. Polon.* **16**, 3.

Čermák, V., 1968b. Heat flow in the Upper Silesian Coal Basin. *PAGEOPH*, **69**, 119.

ČERMÁK, V., 1972. Heat flow and gravity in Czechoslovakia. *Studia Geophys. Geod. ČSAV*, **16**, 77.
CHMURA, K., 1970. Własnosci fizyko-termiczne skał niektórych polskich zagłebi górniczych. Wysawnictwo "Sląsk", Gliwice.
DEPOWSKI, S., SAPUŁA, J., 1969. Wyniki badań termicznych w południowo-wschodniej częsci Nizu Polskiego. *Kwart. Geol.* **13**, 198.
GUTERCH, A., MATERZAK, R., PAJCHEL, J., PERCHUC, E., 1973. Wstępne założenia tektonofizycznej struktury skorupy ziemskiej w strefie brzeznej platformy prekambryjskiej na obszarze Polski. Archiwum Instytutu Geologicznego, Warszawa.
HEURICH, F., 1904. Über die Temperaturen in dem Bohrloch Paruschowitz V. *Z. f. Bergwesen*, **52.**
KRASKOWSKI, S. A., 1961. On the heat flow in shields (in Russian). *Izv. Akad. Nauk SSSR, Ser. Geofiz.* No. 3, 387. Moscow.
KUTAS, R. J., 1972. Investigation of heat flow in the Ukraine. *Geothermics* **1**, 35.
LEE, W. H. K., UYEDA, S., 1965. Review of heat flow data. W. H. K. Lee ed., AGU, Geophys. Monograph, No. 8, Washington.
MAJOROWICZ, J., 1972. Związki elementów pola cieplnego z wiekiem konsolidacji podłoza. *Kwartalnik Geologiczny* **16**, 4.
MAJOROWICZ, J., 1973a. Heat flow in Poland and its relation to the geological structure. *Geothermics* **2**, 24.
MAJOROWICZ, J., 1973b. New heat flow data on the Polish Territory. *Acta Geophys. Polon.* **21**, 85.
MAJOROWICZ, J., 1973c. Heat flow data from Poland. *Nature Phys. Sci.* **243**, No. 105.
MICHAEL, H., QWITZOW, W., 1910. Die Temperaturmessungen im Tiefbohrloch Czuchów Oberschlesien. *Jb. Preuss. Geol. Landesamt*, **31**, Teil 2, Berlin.
PLEWA, S., 1963. Wyniki badań stopnia i gradientu termicznego. *Nafta* No. 9, 205.
PLEWA, S., 1966. Regionalny obraz parametrów geotermicznych obszaru Polski. *Prace Geofiz. i Geol.* **1**, Wydawn. Geofiz. i Geol. Naft., Kraków, 1.
PLEWA, S., 1967. Measurement results of the surface heat flow on the Polish Territory. Selected problems of upper mantle investigations in Poland. Polish Sci. Publishers, 103.
POZARYSKI, W., 1970. Powierzchnia skonsolidowanego podłoza. Geofiz. i Geol. Naft. Kraków, p. 87.
POZARYSKI, W., 1973. Main Pre-Alpine tectonic elements of Poland. *Publs. Inst. Geoph. Pol. Acad. Sci.* **60**, 11.
ROZYCKI, S. Z., 1948. Uwagi o rozmieszczeniu stopnia geotermicznego w Polsce i krajach sąsiednich. Spr. Tow. Nauk., Warszawa.
SCHLOSSER, P., 1970. Einbeziehung petrophysikalischer Bohrlochmessergebnisse in Bestimmungen des terrestrischen Wärmeflusses. *Geophys. Geol.* **15.**
SMIRNOV, J. B., 1968. Connection between the deep geothermal fields and the structure of the earth's crust (in Russian). *Geotektonika* **4**, 3.
STEGENA, L., 1971. Deep structure and geothermic conditions in Hungary (in Russian). *Ann. Univ. Sci. Budapestiensis, Sec. Geol.* **14**, 153.
WĘSIERSKA, M., 1973a. A study of terrestrial heat flux density in Poland. *Publs. Inst. Geoph. Pol. Acad. Sci.* **60**, 135.
WĘSIERSKA, M., 1973b. Termiczne własnosci skał. Materiały Sesji Naukowej PAN, 152, Kraków.

HEAT FLOW INVESTIGATION IN CZECHOSLOVAKIA

V. ČERMÁK

INTRODUCTION

The first heat flow measurement in Czechoslovakia dates back to 1964 when Boldizsár (1964) published a preliminary heat flow value for an old mine in Báňska Štiavnica. However, systematic heat flow investigation did not start until after 1962 when the Czechoslovak UMP Committee recommended that a geothermal research be undertaken. Particular efforts were exerted to begin regular heat flow measurements, to collect all available (and reasonably good) temperature logging-records from the local branches of the Geological Survey and to conceive a laboratory technique to measure thermal conductivity of rocks.

During the period 1964–66, 34 heat flow measurements were performed throughout all the country (Čermák, 1967a). The work resulted in the first clear recognition that the mean geothermal activity in the Bohemian Massif was less than in the Carpathian region. Anomalous heat flow (over 150 mWm^{-2}) was found in the thermal spring area of Teplice in North Bohemia (Čermák, 1967b), demonstrating the hydrothermally disturbed region and the effect of underground water movement on the geothermal field. An increased heat flow zone in the Cretaceous Basin in North-Eastern Bohemia was interpreted in terms of tectonic structure and a possible weakening of the earth's crust along the supposed old tectonic suture following the system of Saxonic faults (Čermák et al., 1968a). The effect of drilling and fluid circulation in a hole on the natural thermal field conditions was discussed (Čermák, 1968a; Čermák et al., 1968c) together with the interpretation of the heat flow in Permo-Carboniferous Coal Basins of Upper Silesia (Čermák, 1968a), Lower Silesia (Čermák, 1968b) and in Central Bohemia (Čermák, 1967c). The results of regional geothermal surveys in various specific geological regions completed the general picture on deep temperature distribution as well as heat flow activity: in the Carpathian Frontal Foredeep (Čermák, 1968c), Neogene depressions of the Carpathians (Čermák and Krčmář, 1968a; Čermák, 1968d) and in the Bohemian Massif (Čermák et al., 1968b; Čermák and Krčmář, 1968b, 1968c). The correlation between heat flow distribution and the tectonic structure and geological evolution was described by Čermák (1968e, 1968f).

Heat flow data from the period 1964–66 were completed with additional determinations during 1967–72 (Novák, 1971; Čermák, 1971, 1974). The systematic difference in geothermal structure of the Bohemian Massif and the Western Carpathians was confirmed; more refined evaluation revealed the correlation between heat flow and the geological age of different tectonic units (Čermák et al., 1973). Preliminary information concerning the relationship between geothermal activity and gravity field based on mutual

comparison of the heat flow data and the geoid shape (Čermák, 1972) facilitates the complex interpretation of the heat flow field to the deep crustal structure (Čermák et al., see pp. 538–542) and the temperature distribution within the earth's crust (Čermák, 1975).

TECHNIQUES OF MEASURING HEAT FLOW AND THERMAL CONDUCTIVITY RESULTS

The heat flow value is usually calculated by combining field measurements of a temperature-depth profile with laboratory determinations of the thermal conductivity. During the period 1964–66 a great amount of temperature measurements by means of logging electrical thermometers were utilized (the accuracy of such determinations is about ± 0.2–0.4 °C), maximum mercury thermometers were used to check the bottom temperature (the accuracy of ± 0.5 °C). At present a light portable thermistor thermometer is mostly used with absolute error less than 0.05 °C and relative accuracy up to ± 0.005–0.01 °C. The readings are taken at intervals of 5 or 10 meters, the gradient being calculated by the least squares method for particular lithological or stratigraphical sections.

Compared to the first heat flow measurements based on only a few conductivity data, about 40–60 rock samples per 1 kilometer of depth are collected at present to evaluate the conductivity distribution. The coefficient of thermal conductivity of the rocks was measured on Beck's (1957) type divided-bar apparatus constructed in the Geophysical Institute (Čermák and Krešl, 1968). Later a routine technique on a fully automated version of divided-bar has been developed (Krešl and Novák, 1970; Krešl and Veselý, 1973) using the computer facilities and programme analysis of output data (Čermák, see pp. 53–58).

A considerable number of rock specimens from various locations were measured and the dependence of conductivity on age, density and water saturation and/or porosity of some sedimentary rocks was studied (Čermák, 1967d). Measured conductivities of sandstones were 1.2–3.5 $Wm^{-1}K^{-1}$, clays and claystones 0.9–2.5 $Wm^{-1}K^{-1}$, siltstones 0.9–2.3 $Wm^{-1}K^{-1}$,

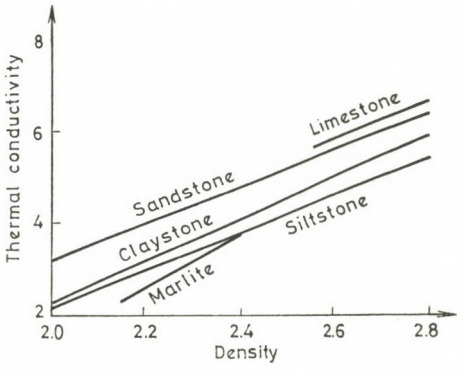


Fig. 1. Thermal conductivites of some sedimentary rocks and their dependence on density (Čermák, 1973); 1 mcalcm^{-1} sec^{-1} °C^{-1} = 0.4187 $Wm^{-1}K^{-1}$

marlites 0.8–1.7 $Wm^{-1}K^{-1}$ and limestones 2.5–3.0 $Wm^{-1}K^{-1}$. The relationship between conductivity λ and density ϱ was assumed in a linear form: $\lambda = a\varrho + b$, where a and b are constants (Fig. 1). The effect of the age of the rocks, manifesting itself in a greater consolidation was observed as a higher a value in the above linear formula. The increase of the coefficient of thermal conductivity with water content approximately satisfies the experimental formula $\lambda_w = \lambda_d e^{0.024p}$, where λ_w is "wet" conductivity, λ_d "dry" conductivity and p the water content in volume percentage.

HEAT FLOW AND GEOLOGICAL STRUCTURE

The territory of Czechoslovakia belongs from the geotectonic point of view to two substantially different provinces of the European geological structure.

The following brief description of tectonic structure of Czechoslovakia is mainly taken from Máška et al. (1960). The western part (taking up almost the whole "Czech" or "Bohemian" Massif) belongs to the Variscian province, this is a platform-type kratonic block, emerging from the relatively sunken surrounding units of Meso-Europe of the same age. The eastern part built by the Western Carpathians belongs to the young orogenetic Alpine-Carpathian belt of Neo-Europe.

The present shape of the deep geological structure has been attained after a long geological development initiated deep in the Precambrian times. The Czechoslovak territory forms therefore a composite tectonic pattern in the structure of which the products of practically all principal European tectonic cycles once played some part. The Bohemian Massif occupies an area completely consolidated by the Variscian tectogenesis, while the Western Carpathians continued in further geosynclinal development which in its last signs exists until now. Both these main structures are separated by the narrow Carpathian Frontal Foredeep. However, there is some mutual relation between the Bohemian Massif and the Carpathians. The Alpine tectonic movements occurred also in the Bohemian Massif by marked Saxonic tectonics, and on the other hand old structures of the Bohemian Massif continue into the Pre-Neoidic basement not only to the Carpathian Foredeep but also to the extern (flysch) Carpathian zone to the "peri-Pieninian lineament".

At the present time more than 70 individual heat flow observations from Czechoslovakia are available (Fig. 2). The statistically determined mean heat flow (excluding the anomalous values from the geothermal area of Teplice) is 69.9 ± 16.4 mWm^{-2} which is slightly higher than the world arithmetic mean according to Lee and Uyeda (1965), but is in good agreement with the average value of the heat flow in Central Europe.

The relation between heat flow and the age of basement rocks has been studied by several authors (Lee and Uyeda, 1965; Lubimova, 1967; Hamza and Verma, 1969). It was found that heat flow shows a general definite correlation with age; a relatively high heat flow characterizes a younger basement. These results enable us to correlate geothermal field with geology, notably with the ages of tectonic events which have participated in building the earth's crust. Čermák et al. (1973) attempted to compare the geothermal activity of individual tectonic units of Czechoslovakia, which resulted in good agreement with the above general conclusion and showed good characteristic connection of the heat flow and the geological age even

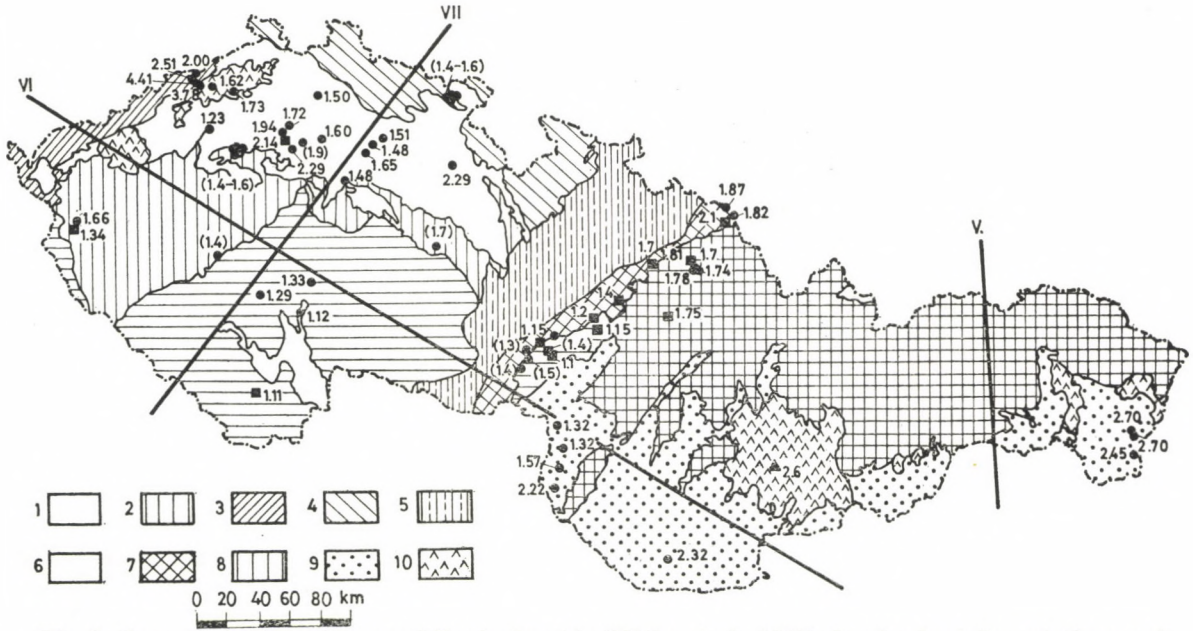


Fig. 2. Generalized tectonic map of Czechoslovakia (Máška et al., 1960) showing heat flow stations and international deep seismic sounding profiles (heat flow values are given in 10^{-6} calcm^{-2} sec^{-1}; 10^{-6} calcm^{-2} sec^{-1} = 41.87 mWm^{-2})

Explanations: 1 – Moldanubian region; 2 – Teplá-Barrandian region; 3 – Sachsen-Thüringen region; 4 – West-Sudetic region; 5 – Moravian-Silesian region; 6 – Bohemian Cretaceous Basin; 7 – Carpathian Frontal Foredeep; 8 – Carpathian Pre-Neogene folded units; 9 – Neogene depressions; 10 – Tertiary volcanites

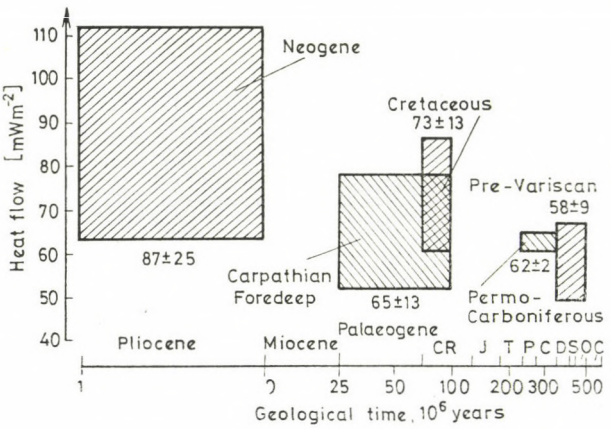


Fig. 3. Correlation between heat flow and geological age (Čermák et al., 1973)

for a relatively small territory as Czechoslovakia (over 125,000 km²). The average heat flow in the Bohemian Massif is 68.3 ± 12.9 mWm^{-2} (37 values), the average heat flow in the Carpathian Frontal Foredeep 64.5 ± ± 13.2 mWm^{-2} (20 values) and the average heat flow in the Western Carpathians 84.8 ± 23.8 mWm^{-2} (11 values).

Even if a more detailed division is applied to individual tectonic zones, the above pattern remains valid (Figure 3 shows only data obtained before 1970). The mean heat flow in old blocks forming the basement structure of the southern part of the Bohemian Massif is 57.4 mWm^{-2} (8 values). Higher heat flow (up to 80 mWm^{-2}) was found in the Sachsen-Thüringen region on the northern part of the Bohemian Massif, obviously connected with high radioactive content of granitic basement (Čermák, 1974). The Permo-Carboniferous sediments (with the exception of the Upper Silesian Coal Basin in the northern part of the Carpathian Foredeep) display a tectonic character of a sedimentary cover; they are discordantly deposited on the lower structure and little disturbed by later orogenetic processes. The heat flow from the Central Bohemian Coal Basin and the Czechoslovakian part of the Lower Silesian Coal Basin has a comparatively stable value with the mean of 62.4 mWm^{-2} (9 values). The Cretaceous and Tertiary platform sediments of Northern Bohemia are characterized by a mean heat flow of 72.9 mWm^{-2} (15 values). While the relatively low heat flow in the southern part of the Carpathian Frontal Foredeep does not differ appreciably from that in the adjacent part of the Bohemian Massif, the heat flow increases here from SW to NE from about 45 to 85 mWm^{-2}; the higher heat flow 75–80 mWm^{-2} in the Upper Silesian Coal Basin was apparently influenced by the creation of the Carpathian belt (Čermák, 1968a). So far there are only two preliminary values on the heat flow of the Pre-Neogene folded regions of the Western Carpathians (64.5 mWm^{-2}); the average heat flow determined in the Neogene depressions is 87.1 mWm^{-2} (8 values), which is lower than a single value obtained in the region of Tertiary volcanites, 109 mWm^{-2} (Boldizsár, 1964).

HEAT FLOW AND GRAVITY

Several authors (Lee and MacDonald, 1963; Wang, 1963; MacDonald, 1965) when analyzing the global distribution of heat flow, suggested that there was some similarity between geothermal activity and the geoid. In places where the geoid is elevated, the heat flow is low and vice versa. Contrary to these results based on global harmonic analysis which neglected the variations of surface heat flow on a scale of less than 2000 km, Scheffer (1964) showed an opposite tendency for Middle Europe. The formal statistical

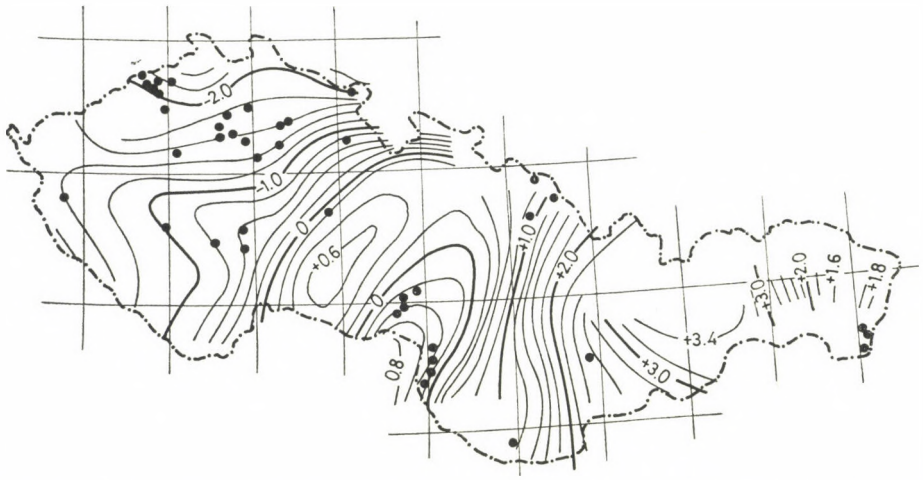


Fig. 4a. Preliminary map of the geoid showing heat flow stations (geoid heights given in meters)

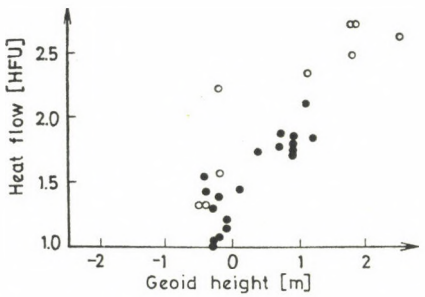


Fig. 4b. Correlation between heat flow value and geoid height in the Carpathians. Solid circles – Carpathian Foredeep; open circles – Neogene depressions

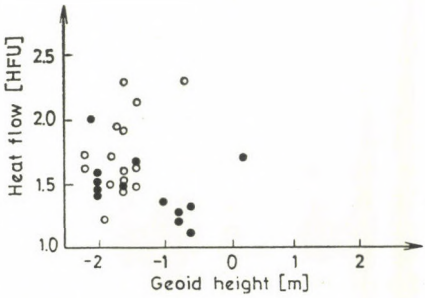


Fig. 4c. Correlation between heat flow value and geoid height in the Bohemian Massif. Solid circles – individual consolidated blocks of the Bohemian Massif; open circles – Bohemian Cretaceous Basin

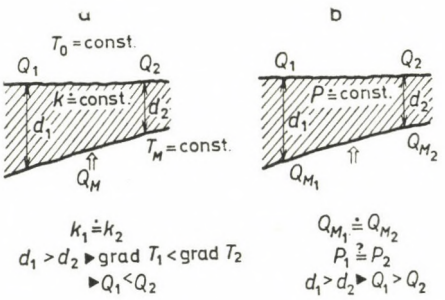


Fig. 5. Simplified models of the earth's crust a – Neogene depressions, where positive correlation between heat flow and geoid is valid; b – Bohemian Massif, where negative correlation may be theoretically expected

comparison of heat flow data with the shape of the geoid for Czechoslovakia (after Pick, 1955) (Fig. 4c) and/or combined gravity anomaly (Vyskočil, 1961) revealed a positive correlation (Čermák, 1972). This applies especially to the data from the Carpathian Foredeep and Neogene depressions (Fig. 4a) whereas the values for the Bohemian Massif (Fig. 4b) are scattered with no or even slightly negative correlation.

The local variation of the geoid reflects the mass distribution in the crust and the upper mantle, the elevations of the geoid correspond to the presence of material of greater density nearer the surface. Figure 5 reflects two very simple models for the explanation of positive (Fig. 5, a) and negative (Fig. 5, b) correlation between heat flows and local geoid undulations. Nevertheless, the recent direct correlation between the heat flow and the crustal thickness based on seismic data (see next paragraph) has not supported unambiguously this second idea.

HEAT FLOW, CRUSTAL THICKNESS AND CRUSTAL TEMPERATURES

Deep seismic sounding performed along three international profiles (Beránek and Dudek, 1972) together with the interpretation of the map of the deflection of the vertical (after removing the topographical masses, Burša, 1971) provided sufficient material for the map of Moho-depth on the territory of Czechoslovakia (Fig. 6) (Beránek and Praus, 1972). In Figure 6 the correlation between heat flow and crustal thickness is shown for individual tectonic regions.

On the whole, a negative character of such a correlation is apparent, i.e. higher heat flows are found over local Moho-elevations (see model in Fig. 5, a). This picture is quite distinct for the Vienna Basin and inner Neogene depressions of the Carpathians and surprisingly also for data from the fundamental blocks forming the lower structure of the Bohemian Massif (compared with the previous heat flow — gravity correlation). Data from the Carpathian Frontal Foredeep and the Cretaceous Basin are rather scattered.

The above DSS results were used for constructing crustal cross-sections for several selected sites for which temperature-depth profiles were calculated (Čermák, 1975). (For more information see Figs 1, 2 on pp. 541–542.)

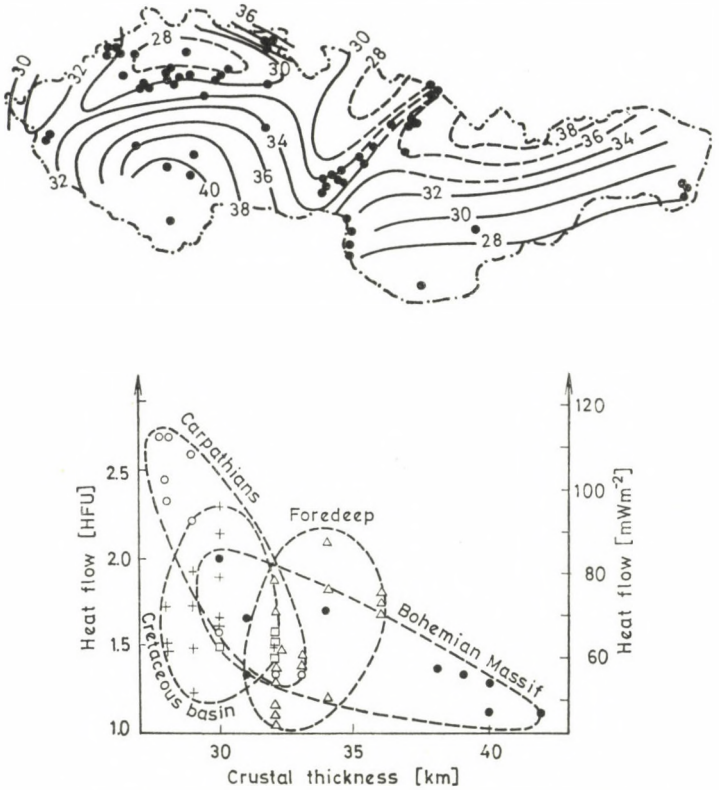


Fig. 6. Correlation between heat flow and crustal thickness
Solid dots – Bohemian Massif; crosses – Bohemian Cretaceous Basin; squares – Permo-Carboniferous basins; triangles – Carpathian foredeep; open circles – Carpathians (Neogene depressions and Tertiary volcanites) and a preliminary map of Moho depth showing heat flow stations (crustal thickness given in kilometers)

The Moho-temperature of about 500 °C beneath the Bohemian Massif is increasing to 800–1000 °C beneath the inner Neogene depressions of the Carpathians. The regional differences in the upper mantle heat flow between both these provinces may reach up to 40 mWm^{-1}. Because of high subsurface temperatures in the Pannonian Basin partial melting at the depth of about 30 km cannot be excluded.

HEAT FLOW AND HEAT PRODUCTION

Combined radioactivity and heat flow measurements in some plutons (Roy et al., 1968) have revealed linear relationship between the heat flow (Q) and surface heat production of radioactive sources (P): $Q = Q_0 + bP$. In this relation Q_0 and b are constants characteristic of large geographical provinces of uniform tectonic structure. Up to now only two such combined values are known in Czechoslovakia: Holubov (48°54′ N; 14°19′ E) $Q =$ $= 46.5$ mWm^{-2}, $P = 0.63$ μWm^{-3}; Vítkov (49°49′ N; 12°40′ E) $Q = 56.1$ mWm^{-2}, $P = 3.14$ μWm^{-3} (Čermák, 1974), which gave $Q_0 = 44$ mWm^{-2} and $b = 3.8$ km.

It may rightly be asked whether these two data may be considered representative of the particular part of the earth's crust (Bohemian Massif). No definite answer can be given before more combined measurements from other localities become available. Anyhow, according to the seismic investigation the depth range of various plutons and bodies of crystalline schists wedged into the basement of the Bohemian Massif varies from 3 to 8 km, so that the unexpected low value of b found may have its geophysical justification.

SUMMARY

The total number of 81 heat flow determinations and density of one measurement per approximately 1500 km^2 seem to be a comparatively great amount for geothermal mapping, however, it is still hardly sufficient for a really detailed study of a territory tectonically so heterogeneous as Czechoslovakia. The knowledge of the distribution of heat sources in the crust and the upper mantle is of primary importance for future research. The study of the transfer of heat energy beneath Neogene depressions of the Carpathians is another basic problem to be solved. If the conditions on the contact of the Carpathians with the Meso-Europian region are not steady state, the solution should be looked for in the presence of a transient heat sink under this zone. The existence of amazing regional difference in the Moho heat flow between the Bohemian Massif and the Carpathians is extremely important. Such a variation of energy inflow may be the driving force for geological evolution and as such the critical parameter for the geophysical understanding of deep processes. The contact zone represents the belt where there are considerable horizontal temperature gradients on the base of the crust. The uneven temperature distribution with depth might be the main reason for the accumulated tension here and certain slight tectonic "liveliness" of this belt.

The internal heat of the earth is the motivating force behind all geodynamic processes, the temperature depth curves together with the distribution of heat sources give us the most informative insight into these. The present number of heat flow stations should be gradually increased to cover regularly all parts of the territory. However, the recent more or less "cumulative" period of collecting heat flow data will have to change to an approach of incorporating heat flow data into complex geophysical and geological interpretation. (See map, attached.)

REFERENCES

BECK, A. E., 1957. A steady state method for the rapid measurement of the thermal conductivity of rocks. *J. Sci. Instr.* **34**, 186–191.

BERÁNEK, B., DUDEK, A., 1972. The results of deep seismic sounding in Czechoslovakia. *Z. Geophys.* **35**, 415–422.

BERÁNEK, B., PRAUS, O., 1972. Die bisherigen Ergebnisse der Untersuchungen des tiefen Aufbaus der Erdkruste auf dem Gebiet der ČSSR. 7. Plenary KAPG Meeting, Prague, March 14–21.

BOLDIZSÁR, T., 1964. Terrestrial heat flow in the Carpathians. *J. Geophys. Res.* **69**, 5269–5276.

BURŠA, M., 1971. Correlation between deflections of the vertical and the axes of zones of increased macroseismic mobility. UMP Project programme in Czechoslovakia, 1962–1970; Final report, 135–139. Academia, Prague.

ČERMÁK, V., 1967a. Results of geothermic investigation of heat flow in Czechoslovakia in 1964–1966. *Studia Geophys. Geod. ČSAV*, **11**, 342–344.

ČERMÁK, V., 1967b. Heat flow near Teplice in North Bohemia. *Geophys. J. R. Astr. Soc.* **13**, 547–549.

ČERMÁK, V., 1967c. Heat flow in the Kladno-Rakovnik Coal Basin. *Gerlands Beitr. z. Geophys.* **76**, 641–646.

ČERMÁK, V., 1967d. Coefficient of thermal conductivity of some sediments and its dependence on density and water saturation. *Chemie d. Erde* **26**, 271–278.

ČERMÁK, V., 1968a. Heat flow in the Upper Silesian Coal Basin. *PAGEOPH*, **69**, 119–130.

ČERMÁK, V., 1968b. Heat flow in the Žacléř-Svatoňovice Basin. *Acta Geophys. Polon.* **16**, 3–9.

ČERMÁK, V., 1968c. Terrestrial heat flow in the Alpine-Carpathian Foredeep in South Moravia. *J. Geophys. Res.* **73**, 820–821.

ČERMÁK, V., 1968d. Terrestrial heat flow in eastern Slovakia. *Trav. Inst. Géophys. Tchécosl. Acad. Sci.*, No. 275. Geofysikálni sbornik 1967, 305–319.

ČERMÁK, V., 1968e. The correlation of heat flow values with the tectonic structure in Czechoslovakia. *Nature*, **218**, 556–557.

ČERMÁK, V., 1968f. Terrestrial heat flow in Czechoslovakia and its relation to some geological features. 23. Geol. Congr., Prague. Collected papers 5, 75–85.

ČERMÁK, V., 1971. Vztah tepelného toku k hlubinné stavbě na území Československa. 3. ročník interdisciplinárního semináře. Výzkum hlubinné geologické stavby Československa, Loučná, March 8–11., 1971. Sborník referátů, 63–76.

ČERMÁK, V., 1972. Heat flow and gravity in Czechoslovakia. *Studia Geophys. Geod. ČSAV*, **16**, 77–87.

ČERMÁK, V., 1973. Thermal conductivity of rocks, its measurement and role in heat flow investigation. *Mineralia Slovaca* **5**, 507–513.

ČERMÁK, V., 1974. First results of heat flow-heat generation study in Czechoslovakia. In preparation.

ČERMÁK, V., 1975. Temperature-depth profiles in Czechoslovakia and some adjacent areas derived from heat-flow measurements, deep seismic sounding and other geophysical data. *Tectonophysics* **26**, 103–119.

ČERMÁK, V., JETEL, J., KRČMÁŘ, B., 1968a. Terrestrial heat flow in the Bohemian Massi d its relation to the deep structure. *Sb. geol. věd, řada UG*, **7**, 25–38.

ČERMÁ K, V., KÁRNÍK, M., KRČMÁŘ, B., 1968b. Měření teploty a tepelný tok v příbramských dolech. *Čas. min. geol.* **13**, 215–216.

ČERMÁK, V., KRČMÁŘ, B., 1968a. Der Erdwärmefluss in der südwestlichen Slowakei. *Acta Geod. Geophys. Mont. Hung.* **3**, 319–329.

ČERMÁK, V., KRČMÁŘ, B., 1968b. Měřeni tepelného toku ve dvou šachtách v západních a jižních Čechách. *Věstnik ÚÚG*, **43**, 415–422.

ČERMÁK, V., KRČMÁŘ, B., 1968c. Tepelný tok ve vrtu NV-1 (Nová Ves u Chýnova). *Věstník ÚÚG*, **42**, 445–448.

ČERMÁK, V., KREŠL, M., 1968. Thermal conductivity of rocks and its measurement on a divided-bar apparatus. *Trav. Inst. Géophys. Tchécosl. Acad. Sci.*, No. 274. Geophysikální sborník 1967. 287–304.

ČERMÁK, V., KREŠL, M., VESELÝ, I., 1968c. Experimental determination of the coef-

ficient of heat transfer during hole boring and the re-establishment of the temperature field equilibrium. *Earth Planet. Sci. Letts.* **5**, 153–158.

ČERMÁK, V., KREŠL, M., NOVÁK, V., VENHODOVÁ, D., 1973. Heat flow in Czechoslovakia: Relationship with geological age. Jhingran Commemorative Volume, Hindustan Publ. Corp., India, Part II. (1974).

HAMZA, V. M., VERMA, R. K., 1969. The relationship of heat flow with age of basement rocks. *Bull. Volcan.* **33**, 123–152.

KREŠL, M., NOVÁK, V., 1970. Terrestrial heat flow in the territory of Czechoslovakia and the measurement of thermal conductivity with fully-automatic apparatus. *Geothermics (Spec. Issue 2)* **2**, Part 2, 1261–1265.

KREŠL, M., VESELÝ, I., 1973. Instrument for the automatic measurement of the coefficient of heat conductivity of rocks. *Trav. Inst. Geophys. Tchécosl. Acad. Sci.*, No. 361, Geofysikální sborník 1971, 317–334.

LEE, W. H. K., MACDONALD, G. J. F., 1963. The global variation of terrestrial heat flow. *J. Geophys. Res.* **68**, 6481.

LEE, W. H. K., UYEDA, S., 1965. Review of heat flow data. W. H. K. Lee (Ed.): Terrestrial Heat Flow. AGU Geophys. Monograph, No. 8, Washington 1965, 87–190.

LUBIMOVA, E. A., 1967. Terrestrial heat flow for the USSR and its connection with other geophenomena. 14. Generaly Meeting IUGG, Abstracts 2a, B-3.

MACDONALD, G. J. F., 1965. Geophysical deductions from observations of heat flow. W. H. K. Lee (Ed.): Terrestrial Heat Flow. AGU Geophys. Monograph, No. 8, Washington 1965, 191–210.

MÁŠKA, M., MATĚJKA, A., ZOUBEK, V., 1960. Tectonic Development of Czechoslovakia (Collected papers and the tectonic map 1 : 1,000,000), Nakl. ČSAV, Praha, pp. 224.

NOVÁK, V., 1971. Zemský tepelný tok v hlubinných vrtech Žarošice-1 a 2 v oblasti Ždánického lesa. *Věstník ÚÚG*, **46**, 277–283.

PICK, M., 1955. Vorläufige Karte des Geoids auf dem Gebiet der Tschechoslowakischen Republik. *Trav. Inst. Géophys. Tchécosl. Acad. Sci.*, No. 15, Geofysikální sborník 1954, NČSAV, Praha.

ROY, R. F., BLACKWELL, D. D., BIRCH, F., 1968. Heat generation of plutonic rocks and continental heat flow provinces. *Earth Planet. Sci. Letts.* **5**, 1–12.

SCHEFFER, V., 1964. The European values of terrestrial heat flow. *Geofis. Meteor.* **13**, 99–103.

VYSKOČIL, V., 1961. Anomaly field of gravity in gravimetric prospecting. *Trav. Inst. Géophys. Tchécosl. Acad. Sci.*, No. 131, Geofysikální sborník 1960, NČSAV, Praha.

WANG, C., 1963. On the distribution of surface heat flow and the second order variations in the external gravitational field. *Res. Space Sci., Spec. Rept.* **134.**

THE VARIATION OF TEMPERATURE WITH DEPTH IN THE PANNONIAN BASIN

L. STEGENA

THERMAL CONDITIONS OF THE PANNONIAN BASIN

During the recent decades — mainly in the course of oil and thermal water explorations — geothermal temperatures have been measured in several thousand boreholes in Hungary. Owing to these observations we were able to construct the geothermal maps of Hungary for various depths (Fig. 1).

The most laborious part of the work was the collection and critical analysis of data. Geothermal measurements are affected by errors, which are sometimes unknown and very high. In the course of analysis of the reliability of data the area of the country has been divided into 75 parts (sheets of the 1 : 100,000 map) and for every sheet a temperature-depth diagram has been prepared. The thermal history of the bore-hole, study of the measuring method and of the geological conditions as well as the agreement of data with one another within an area and the comparison of depth-temperature curves of neighbouring territories gave us possibilities to eliminate erroneous data.

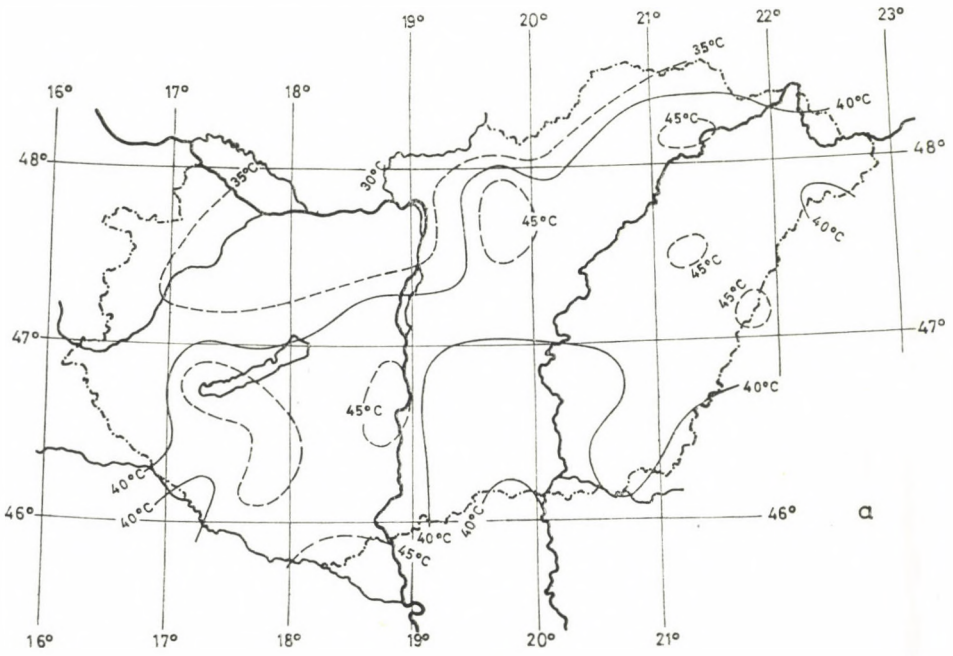


Fig. 1a

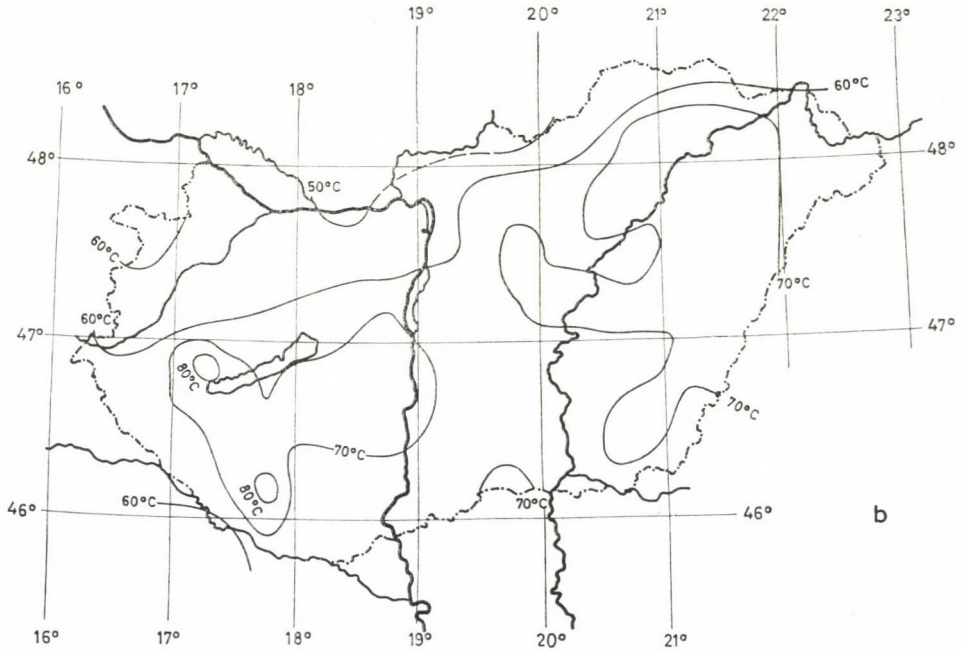

16°
17°
18°
19°
20°
21°
22°
23°
48°
47°
46°
50°C
60°C
70°C
80°C
b

Fig. 1b

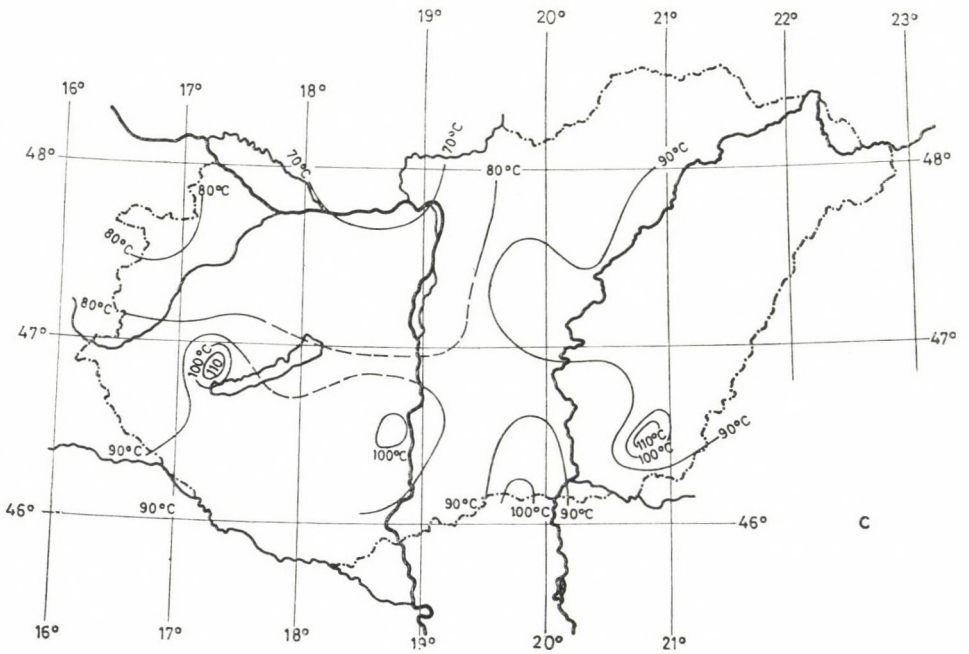

16°
17°
18°
19°
20°
21°
22°
23°
48°
47°
46°
70°C
80°C
90°C
100°C
110°C
c

Fig. 1c

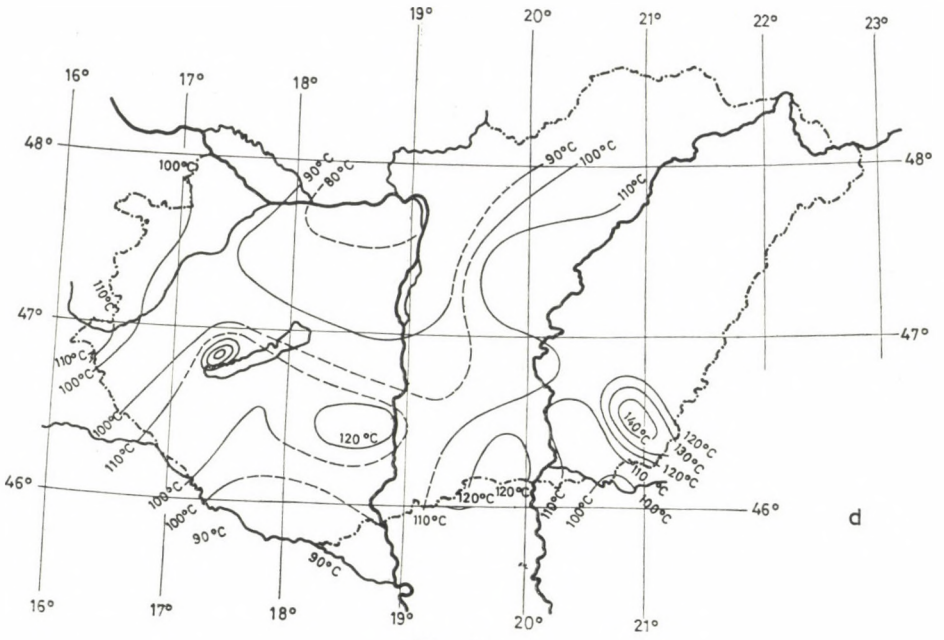

16°
17°
18°
19°
20°
21°
22°
23°
48°
47°
46°
15°
100°C
90°C
80°C
110°C
120°C
140°C
130°C
d

Fig. 1d

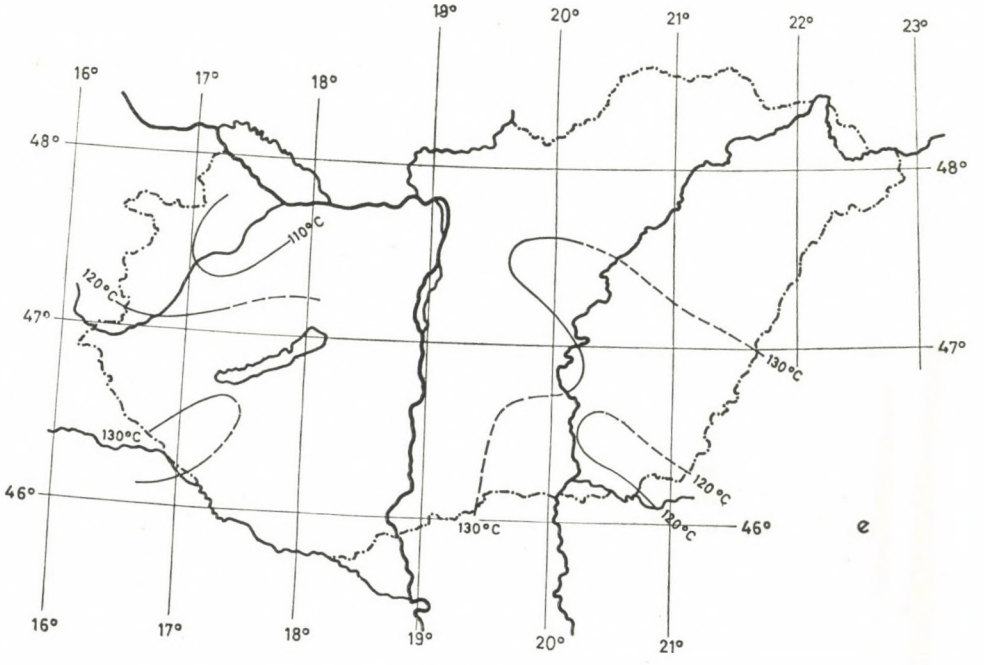

16°
17°
18°
19°
20°
21°
22°
23°
48°
47°
46°
110°C
120°C
130°C
e

Fig. 1e

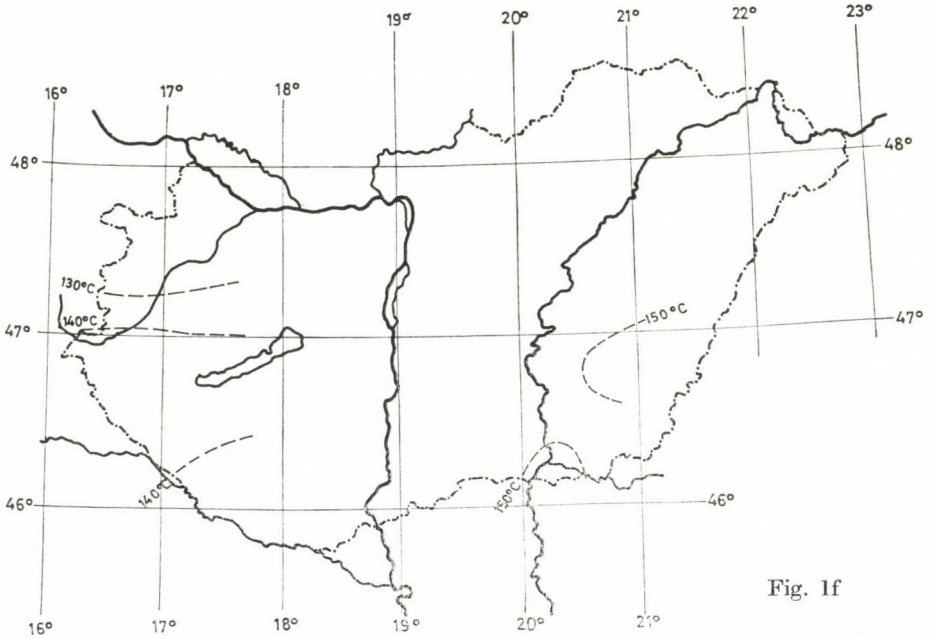


Fig. 1. Mean geothermic temperatures and geoisotherms on the area of Hungary at a depth of 0.5 km (a), 1.0 km (b), 1.5 km (c), 2.0 km (d), 2.5 km (e), 3.0 km (f)

The reduction to depth of observational data was made by a procedure of us called the method of master-curves: it was possible to construct a reliable temperature-depth function for the whole of the country, and for its larger area-units as well as for those sheets of the 100,000 scale map, where we had a sufficient amount of data. We observed that these temperature-depth functions are similar and any of them can be obtained with a good approximation — especially for neighbouring areas — by multiplying by a constant, i.e. we have:

$$T'(z) = nT(z)$$

where n is a number near unity (0.6–1.5) and the initial value of the temperature is the yearly average on the surface (10 °C, Fig. 2).

Using this method (Fig. 2, A and B as examples), individual geothermic data could be reduced without any special assumptions to the depth values 0.5, 1, 1.5, 2, 2.5 and 3 km chosen for the construction of isotherms; thus we obtained for each of the 75 sheets an average temperature value for the given depths. Construction of geoisotherms has been based on these temperature values.

The annexed maps are generalized versions of the prepared more detailed charts. The estimated error of the maps is of about 1 °C.

From the maps the following conclusions can be drawn: The Pannonian basin is one of the geothermally most strikingly warm areas of Europe

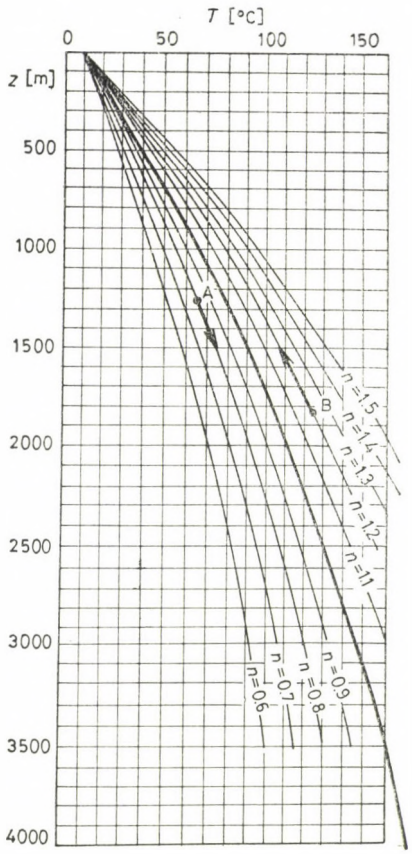


Fig. 2. Mean depth-function (T/z) of geothermic temperatures and master-curves used for the reduction to depth of the observed temperatures ($n = 0.6$–1.5)

(Stegena, 1972b), as it can also be seen on the geothermal map of Eastern-Europe contained in the present volume. The average geothermal temperature for Hungary at the depth of 1 km is 65 °C.

Average geothermal gradients are shown in Table 1.

TABLE 1

Average values of geothermal gradient in Hungary

Depth-interval [m]	°C/m	m/°C	Depth-interval [m]	°C/m	m/°C
0– 500	0.056	17.9	0– 500	0.056	17.9
500–1000	0.054	18.5	0–1000	0.055	18.2
1000–1500	0.050	20.0	0–1500	0.053	18.9
1500–2000	0.044	22.7	0–2000	0.051	19.6
2000–2500	0.038	26.3	0–2500	0.048	20.8
2500–3000	0.032	31.3	0–3000	0.046	21.8

The average value of geothermic gradient in the upper sedimentary layer of 1 km thickness is 0.055 °C/m [18 m/°C]. The areal distribution of geothermal temperature reflects in broad lines the relief of the mesozoic-paleozoic basement of the Miocene-Pliocene basin; at places, where the compact basement approaches the surface, the temperature becomes higher, although the correlation is not too strong.

Based on the data of Table 1 and on Figure 2

$$\frac{dT}{dz} \approx 5.0 \cdot 10^{-4} \text{ °C cm}^{-1} \quad \text{and} \quad \frac{d^2T}{dz^2} \approx -8 \cdot 10^{-10} \text{ °C cm}^{-2}$$

in average for the upper 2 km of sediments. By the one-dimensional Poisson-equation

$$\lambda \frac{d^2T}{dz^2} + \frac{d\lambda}{dz} \frac{dT}{dz} = -A$$

where for λ, as a mean value, $\lambda \approx 4.5 \cdot 10^{-3}$ cal cm^{-1} sec^{-1} °C^{-1} can be supposed, from laboratory measurements, for an average depth of 1 km. $d\lambda/dz$ is not known enough, but it is certainly positive (z is downwards positive). So

$$A \leq 22 \cdot 10^{-13} \text{ cal cm}^{-3} \text{ sec}^{-1} = 22 \text{ HGU}$$

Using for $d\lambda/dz \approx 0.5 \cdot 10^{-8}$ cal cm^{-2} sec^{-1} °C^{-1} (a determination from Buntebarth, 1975)

$$A \approx 11 \cdot 10^{-13} \text{ cal cm}^{-3} \text{ sec}^{-1} = 11 \text{ HGU}$$

This value, as regards the order of magnitude, agrees with the average value $A \approx 6$ HGU, computed from sporadic radiometric measurements.

WATER MIGRATION AND GEOTHERMAL CONDITIONS IN THE SEDIMENTS OF THE PANNONIAN BASIN

Figures 3 and 4 show specimen observational areas, where the therma waters migrating upwards along fault lines have strongly disturbed geothermal conditions.

The average depth-density function of the Pannonian Basin is well known (Stegena, 1970). Departing from this we can compute an average porosity-depth function, too (Figure 5), supposing that the density of recently settled Pannonian sea-sediments had been constant. Porosity is decreasing with depth by a rate shown on Figure 5. From this decrease we can calculate that from the Miocene-Pliocene sediments of the basin having a thickness of about 3 km, during a time interval of about 5 million years, some 15,000 km^3 water have moved away towards the surface owing to the compaction (and consolidation) of rocks.

This calculation is supported by the heavy-water-determinations, too (Fig. 5). The heavy-water content of strata-waters is increasing with depth owing to the fact that D_2O has a smaller mobility than H_2O. The viscosity

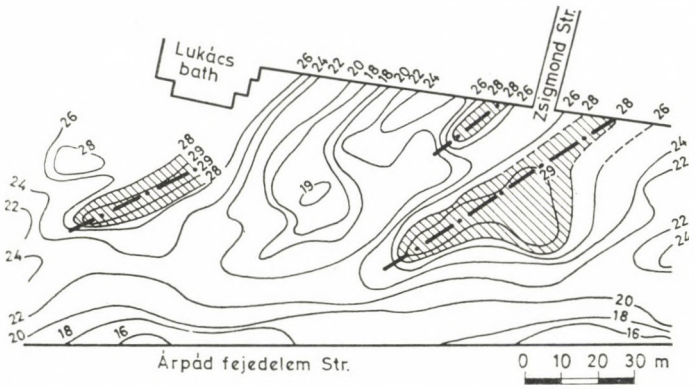


Fig. 3. Geothermic soil-temperature at a depth of 2 m in the surroundings of Lukács-bath in Budapest. Thermal waters flowing upwards along fault lines are producing geothermal anomalies of 10–20 °C

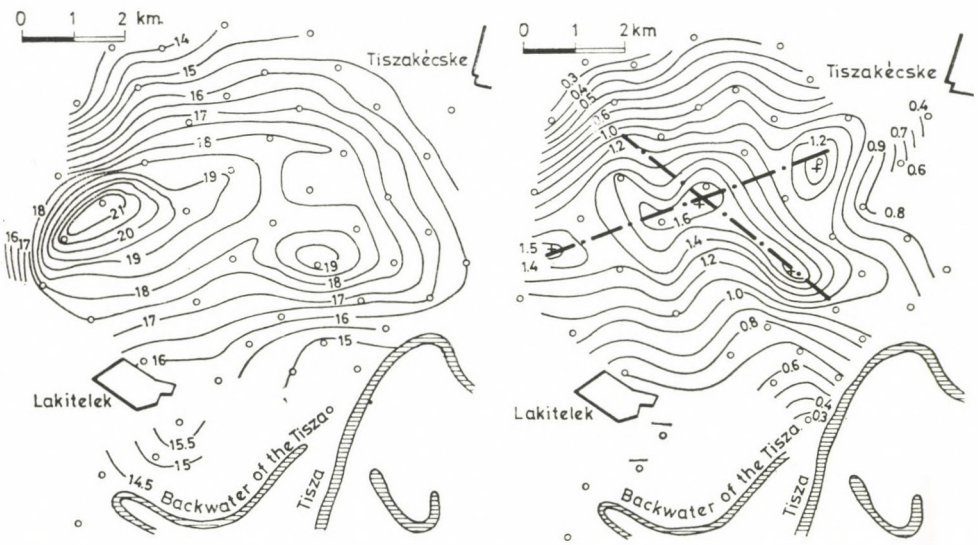


Fig. 4. On the left: Geothermic gradients (m/°C) near the river Tisza. On the right: Gradients freed from the alternation of clay- and sand-layers (heat flow isolines) (according to Alföldi and Gálfi, 1966). The right-hand graph indicates the crossing of faults, along which the thermal waters causing the geothermal anomaly are flowing upwards

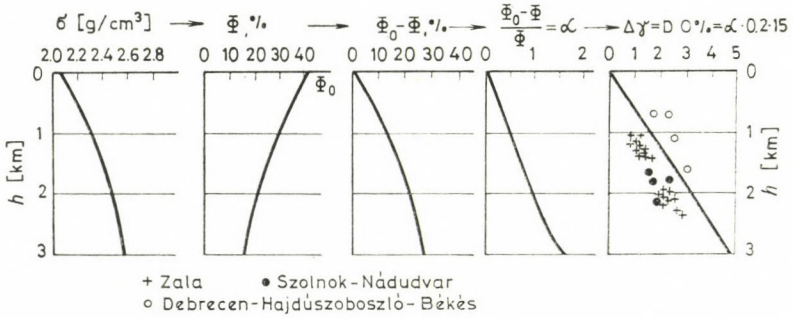


Fig. 5. Average depth-density function of the sediments of the Pannonian Basin, the depth-porosity function calculated on the basis of the former, and the function Φ_0–Φ being the measure of the water moved away; α indicates the ratio of the water moving away against the remaining amount. From α and from the viscosity ratio of D_2O/H_2O the enrichment in D_2O of the remaining water at various depth can be computed. Signs denote measured values

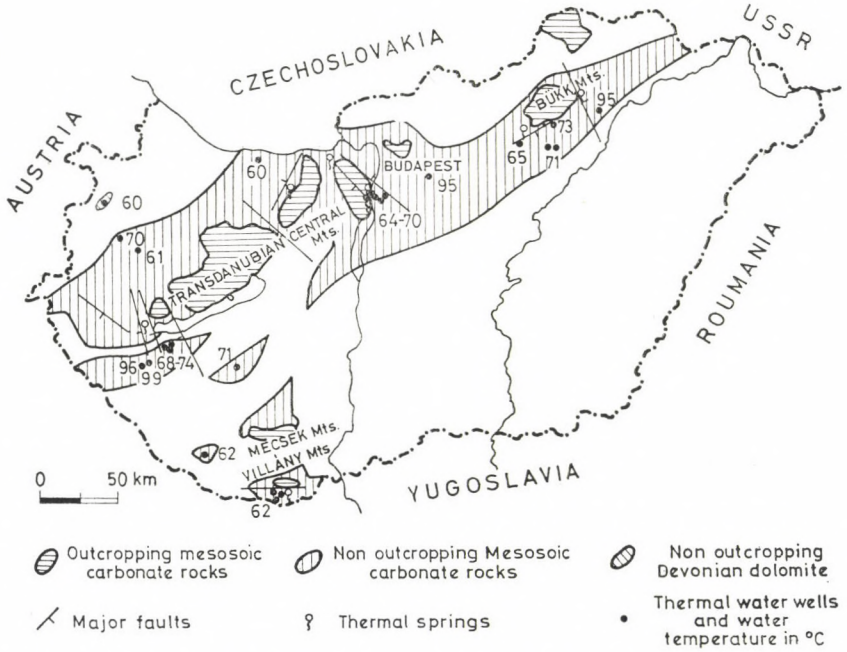


Fig. 6. Thermal water wells and springs issuing from the fractured basements in Hungary. After Korim (1972)

of D_2O is by 1.25 higher than of H_2O: from this and from the measured D_2O concentrations one can also determine the amount of water moved away owing to compaction. This determination shows a fair agreement with the amount computed by the basis of porosity-decrease.

On the geothermic anomaly-area shown in Figure 4 thermal waters are migrating upwards along the crossing of two fault lines. One has carried out relative heat-flow measurements on this area. Based on these and taking into account the extension of the anomaly-area we can give an estimate of the water-flow of the migration on this area. The amount obtained is $0.8 \cdot 10^{-3}$ km³/year (Stegena, 1972a). Comparing this with the total amount of water moved away by compaction we can state that a few upward streams comparable to the fault-system of Tiszakécske (Fig. 4) were necessary to carry towards the surface the compaction waters of the basin during its life of about a few million years. Such open faults carrying the hot strata-waters towards the surface are well known as existing also in our times at several places, especially at the borders of the basin (Héviz, Végardó, Fig. 6).

PETROLEUM GENESIS AND GEOTHERMAL CONDITIONS

More than 90% of mineral oil accumulations of the earth show a temperature of 110 °C or below it. The hottest oil-sources: Wasco Field, California (Parker, 1954), Pato-2, Venezuela (Hedberg, 1964), Stravropol (Tkhostov, 1963), have a temperature between 150 and 180 °C. Mineral oils are always containing porphyrin-complexes, disintegrating — according to laboratory tests — at 250–300 °C ("porphyrin-thermometer").

These temperatures enable us to construct prognostic depth-oil-maps based on geothermic considerations. The depth of 110 °C geoisotherm is marking the frontiers of the very promising zones for oil prospecting, while that of 170 °C can be supposed as indicating the depth border of a zone still hopeful for oil occurrence. The geoisotherm of 250 °C can be taken as the theoretically lowermost boundary of mineral oil occurrence (Fig. 7).

These considerations are in agreement with the important result of modern mineral oil genetics that oil-genesis is linked with a certain transformation (metamorphosis, diagenesis, carbonization degree) of the organic matter contained in the rocks. Diagenesis of organic matter is a function of thermodynamic conditions (p, T); since the depth dependence of pressure is rather constant, an approximative determination of the depth-interval producing oil genesis is possible by means of geothermic temperatures. This depth interval was called by Vassoevich (1973) as "the main phase of oil genesis", while Hunt (1973) gave it the name of "liquid window" (Fig. 8). Here the liquid hydrocarbons are produced: above this zone or below it hydrocarbonic gases develop, above it mainly methane, below it we can find — owing to the result of cracking processes — homologues of higher order, too.

The lower boundary of the liquid window is marked by the geothermal temperature of 75–80 °C, while its upper border is given by 150–170 °C

geothermal temperature (Hunt, 1973). Figure 7 shows the depth contours of the 170 °C isothermic surface, Figure 8 the 80 °C one.

The main physical processes of mineral oil genesis are as follows: The organic matter of sandy layers generally degenerates, becomes oxidized prior to going into depth. The organic matter of argilliferous rocks goes into depth and undergoes a diagenesis at the suitable values of p and T, thus producing mineral oil dispersed finely in the clayey layer. The dispersed oil moves away during the primary migration from the clayey mother rock to the neighbouring porous transporting layers (if such are existing) and then in course of a secondary migration it will be transported to the places of accumulation. A subsequent tectonic movement may lead to a re-accumulation of the oil bed (tertiary migration).

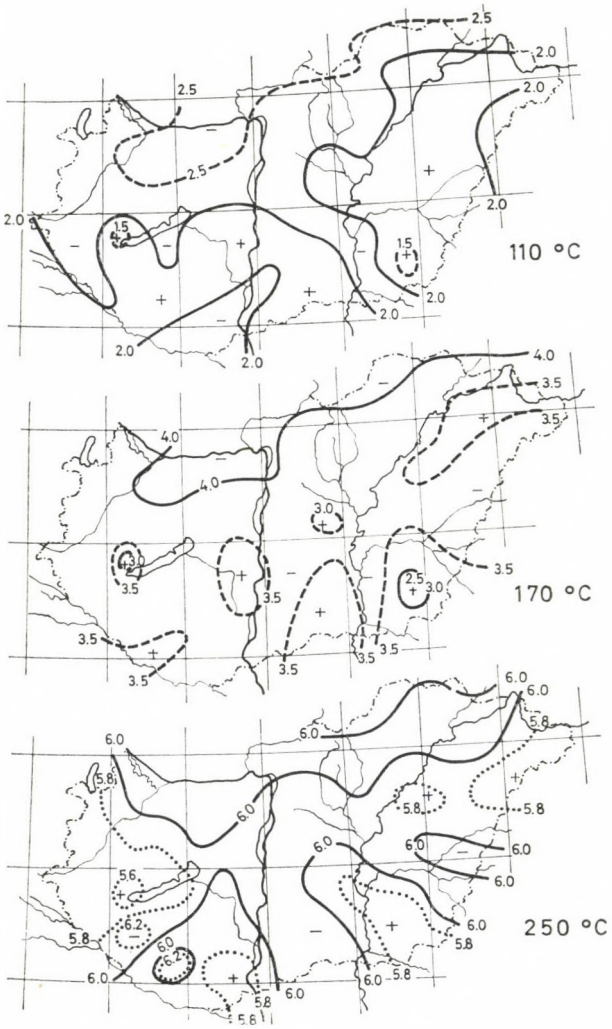


Fig. 7. Depth contours of isothermic surfaces of 110, 170 and 250 °C temperature in Hungary [in km]

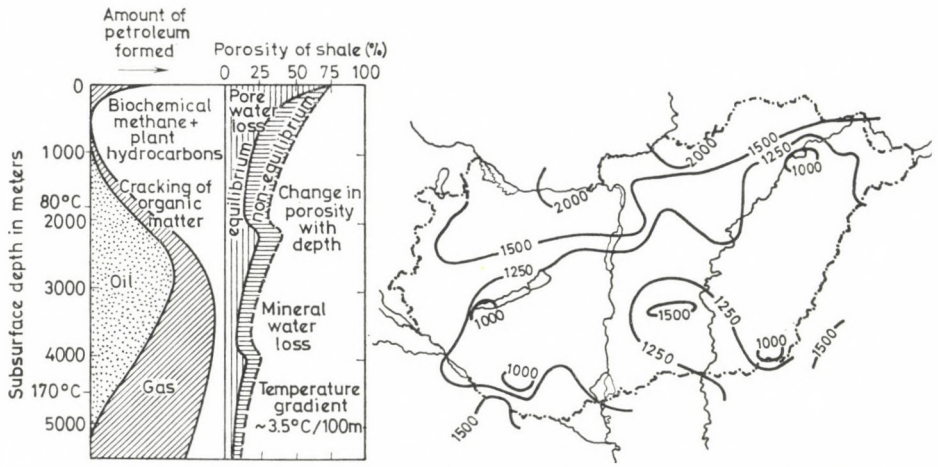


Fig. 8. Petroleum generation and depth zones of compaction according to Hunt (1973), and the 80 °C isothermal depth-contours in m for Hungary

A most discussed question of oil genesis is the process of primary migration. Considerations and experiment of Hill and Levorsen indicate that the dispersed oil can migrate out of the clayey rock only in case of a very high hydraulic gradient. Experiments of Kapolyushnikov, Dvali, Zhuze, Sokolova and Mironov (1962) showed that in case of a high pressure the gases can well dissolve the liquid hydrocarbons out of the clayey mother rock; nevertheless the general possibility of a primary migration based on gas-made dissolution presents some difficulties (Yurkevich, 1962). Recently, the origin of primary oil-migration is attributed to the clay mineral-diagenesis. The montmorillonite — being present in great amounts in the sediments on most places — transforms into illite owing to the effect of certain pressure and temperature. This transformation is accompanied by water-loss and volume-increase, since the density of the bounded water of montmorillonite is about 1.3 g/cm^3 (Nemetz, 1970). This increase of volume produces the hydraulic gradient expelling the dispersed oil from the clayey mother rock into the neighbouring porous transporting layers.

Figure 9 shows the depth of the Hungarian hydrocarbon accumulations and the depth zones of the montmorillonite-illite clay mineral diagenesis. This latter is determined by the geo-pressure and geotemperature (Burst, 1969; Jones, 1970); in case of an average rock density this is marked by the geothermal temperatures of 80–100 °C. Out of the 40 hydrocarbon accumulations investigated 33 fall within the geothermal depth zone of montmorillonite-illite diagenesis within a deviation of $\pm$200 m. For each of the hydrocarbon accumulations falling outside the zone it can be shown that it has moved away from its original site owing to a tertiary migration. Figure 9 supports the theory of primary migration based on clay mineral diagenesis.

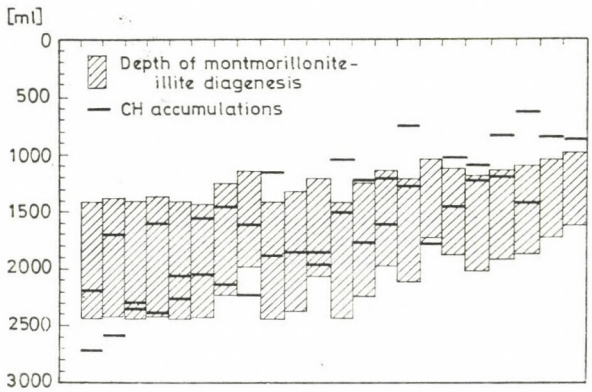


Fig. 9. Arrangement of oil-deposits and of the depth intervals of geo-temperatures of 80–100 °C which correspond to the montmorillonite-illite clay mineral diagenesis at the Hungarian hydrocarbon beds

EARTHQUAKES AND GEOTHERMAL CONDITIONS

The Pannonian Basin is a slightly seismic area with crustal shocks of small magnitude. One can suppose that shocks — at least partly — are brought about by horizontal temperature differences, which generate mechanical stresses in the crust.

Figure 10 shows the map of the horizontal geothermic gradient for 1 km depth, constructed on the basis of the geothermal map of Figure 1. The absolute value of the gradient for any point was given by the mean values of the temperature-differences of the neighbouring points lying to North, South, East and West. Figure 10 contains the gradient-isolines deduced from these values (Márton, 1974). Figure 10 also shows — after the investigations of Csomor (1974) — the seismic energy released during 100 years computed for the area of a sheet of the 1 : 100,000 map (350 km^2). Csomor (1974) has computed — using a method similar to those found in the literature — on the basis of macroseismic observations the magnitudes of earlier earthquakes without instrumental registration. Seismic energies shown in Figure 10 are based on these investigations.

Figure 10 shows that in the territory of Hungary earthquakes are released on areas with a high horizontal geothermic gradient. Taking into account the numerical values of the released seismic energies — not showed on the map — we obtain the following results:

The extension of the area having a horizontal geothermic gradient greater than 1.3 °C/10 km is 45,900 km^2. The seismic energy released on this area during 100 years amounts to $1.720 \cdot 10^{20}$ ergs, while the density of energy is $3.75 \cdot 10^{15}$ ergs/km^2. The area with a horizontal gradient smaller than 1.3 °C/10 km is 47,000 km^2 (50.5%); the seismic energy released during 100 years on this area is $0.098 \cdot 10^{20}$ ergs, the density of energy is $0.21 \cdot 10^{15}$ ergs/km^2.

A more accurate calculation of the correlation cannot be carried out owing to the inaccuracy of geothermal and seismic data. Moreover, the statistical character of the two average energy densities is highly influenced

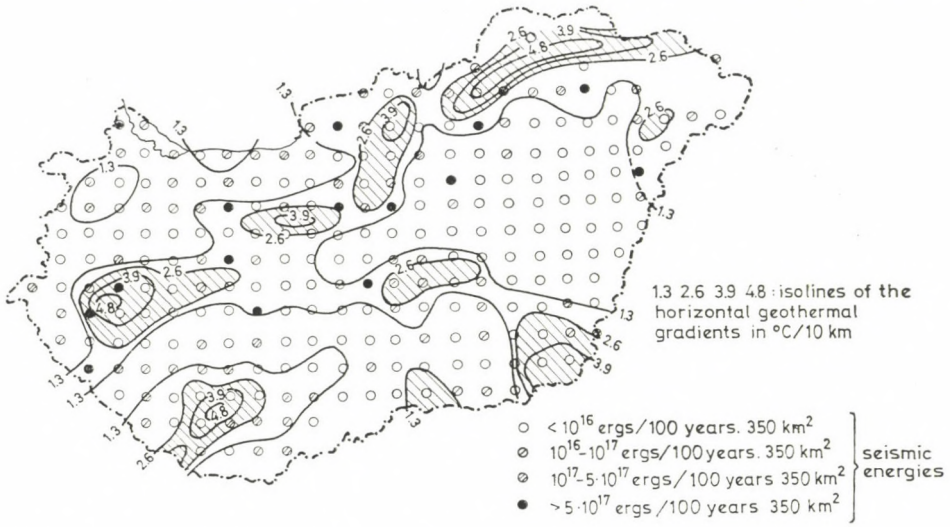


Fig. 10. Isolines of the horizontal geothermic gradient valid for 1 km depth and values of seismic energy released on the territory of Hungary during the past 100 years

by a few stronger shocks. Leaving aside the three strongest quakes (Kecskemét, Eger and Dunaharaszti) we get for the seismic energy density on the area with great horizontal geothermic gradient $0.39 \cdot 10^{15}$ ergs/km^2 and for territories with a small gradient $0.21 \cdot 10^{15}$ ergs/km^2. Thus the correlation is rather satisfying and it seems that the earthquakes of the Pannonian Basin are generated mostly by the horizontal temperature-differences in the crust.

SUMMARY

The Pannonian Basin is a young intermountain (interarc, retroarc) basin covered by miocene and mainly pliocene sediments of an average thickness of 3 km and having a thin sialic crust. Geothermal temperatures are remarkably high. At a depth of 1 km the average geothermal temperature is 65 °C, the mean geothermic gradient is 0.055 °C/m. High geothermal values are as a rule characteristic of interarc basins.

The vertical gradient of the geothermic depth gradient is $d^2T/dz^2 = -8 \cdot 10^{-10}$ °C/m^2 on the average. From this we can compute the value of the mean heat production of the sediments as $A \leq 22$ HGU (heat generation unit 10^{-13} cal/cm^3 sec) which is in agreement — as regards the order of magnitude — with the average value computed from radiometric measurements (≈ 6 HGU).

More than 90% of mineral oil deposits of the world has a geothermal temperature lower than 110 °C, while the hottest of them show a temperature of about 170 °C. These facts, as well as the so-called porphyrin-

thermometer afford us opportunity to prepare prognostic depth-oil maps based on geothermal temperatures.

The Pannonian Basin is a slightly seismic area with crustal shocks of small magnitude. The bulk of the seismic energy is released at places of high horizontal geothermic gradient, thus indicating that the mechanical stresses inducing these shocks are generated by horizontal temperature-differences. (See map, attached.)

REFERENCES

ALFÖLDI, L., GÁLFI, J., 1966. Hydrogeological and geophysical investigations of a geothermal anomaly in Hungary. *BIASH.*, **6,** 1.

BUNTEBARTH, G., 1975. Wärmeleitfähigkeitsberechnungen für die Oberkruste in Ungarn. *Ann. Univ. Sci. Budapestiensis Sec. Geol.* 99–102.

BURST, J. F., 1969. Diagenesis of Gulf Coast clayey sediments and its possible relation to petroleum migration. *B. AAPG.* **53,** 73–77.

CSOMOR, D., 1974. Cand. thesis. Library of MTA, Budapest.

HEDBERG, H. D., 1964. Geological aspects of origin of petroleum. *B. AAPG.* **48,** 1755–1803.

HUNT, J. M., 1973. An Examination of Petroleum Migration Processes. Geochemie (Vorträge zu geochemischen und chemisch-physikalischen Problemen. VII. Int. Konf. des Kohlenwasserstoffbergbaus); Budapest, *OGIL*, 219–229.

JONES, P. H., 1970. Geothermal resources of the Northern Gulf of Mexico Basin. UN Symp., Pisa.

KORIM, K., 1972. Geological aspects of thermal water occurrences in Hungary. *Geothermics* **3.**

MÁRTON, M., 1974. M. Sc. thesis. Library of ELTE, Budapest.

NEMETZ, E., 1970. Present state of the investigation of clay minerals in the oil geochemistry (in Hungarian). Application of geochemical methods in oil prospection. Szeged, 35–41.

PARKER, F. S., 1954. Origin, migration and trapping of oil in Southern California. Geology of Southern California: Bull. 170 m, 9, Oil and Gas, Div. of Mines, San Francisco, 11–19.

SOKOLOVA, M. N., MIRONOV, S. I., 1962. On the primary migration of hydrocarbons and other oil components under the action of compressed gases (in Russian). Geokhim, nefti i neftjanikh most. Izd. Akad. Nauk SSSR.

STEGENA, L., 1957. Praktische geothermische Untersuchungen in Ungarn. *Ann. Univ. Sci. Budapestiensis Sec. Geol.* **1.**

STEGENA, L., 1970. Compaction, heavy water content and water flow in the sediments of the Hungarian Basin (in Hungarian). *MTA X. Oszt. Közl.* **3,** 317–319.

STEGENA, L., 1972a. Petroleum accumulation and geological water flows in the sediments of the Hungarian Basin (in Hungarian). 2nd Symp. of Material and Energy Flows (II. Anyag- és Energiaáramlási ankét). Akad. Kiadó, Budapest, 199–209.

STEGENA, L., 1972b. Geothermal map of Eastern Europe. *Geothermics* **4,** 140–141.

STEGENA, L., 1973a. Hydrocarbon accumulation and geological water migration in the sediments of the Hungarian Basin. Studies on the material and energy flows of the Earth (Ed. E. Szádeczky-Kardoss). Budapest, 262–270.

STEGENA, L., 1973b. Clay minerals and migration of natural oil in the Pannonian Basin. Studies on the material and energy flows of the Earth (Ed. E. Szádeczky-Kardoss). Budapest, 258–261.

TKHOSTOV, B. A., 1963. Initial rock pressures in oil and gas deposits. Pergamon Press.

VASSOEVICH, N. V., 1973. Principal zone of oil formation. Geochem. Cosmochem. 6th Congr. Int. Paris.

YURKEVICH, I. A., 1962. The study of geochemical facies (in Russian). Geokhim. nefti i neftjanikh most. Izd. Akad. Nauk SSSR.

SOME RESULTS OF THE GEOTHERMAL INVESTIGATIONS IN BULGARIA

T. VELINOV, I. PETKOV

The geothermal investigations in Bulgaria are related to the search and exploration of ores, minerals and thermomineral waters.

The main information about the thermal field is obtained from temperature measurements in wells. On the basis of these measurements maps of the temperature and of the gradient on 500, 1000 and 2000 m levels (1500 m for North Bulgaria) have been drawn for the whole country. About 140 wells are used in the most complete maps (for 500 m). A smaller number of data is used for the other maps, consequently they are of a schematic character.

The measurements are carried out with standard electrical methods and in some cases with mercury maximum termometers. The admissible error varies from 0.5 to 2 °C according to the type of the thermometer used.

The time necessary for the ascertainment of the thermal regime varies from 2–3 days to several months. Those measurements which in one or another way prove to be of good quality are used for the constructions. In most cases the section of the isolines of temperatures is 2 °C, and for the gradient 0.5 °C/100 m. No systematic determination of thermal conductivity and of heat flow has been practically done.

The analysis of the maps shows that in many cases they are highly informative (especially for the ascertainment of regional geological problems). Studies of some local geological problems on the basis of geothermal results are carried out, too. The purpose of these researches is to establish a relation between the thermal characteristics of rocks and their geological and other properties such as lithology, oil-gas-saturation and porosity. The thermal characteristics of different parts of the oil-gas structures have been also studied.

An experiment was made to correlate the geothermal field with the gravity and magnetic field.

The basic regularities of the thermal field are as follows:

A regional decrease of temperature at all levels from West to East connected with the decrease of the thickness of the sedimentary complex has been observed in North Bulgaria. The North Bulgarian uplift and South Dobrudja, where the accumulations of Valanginian (Cr_1) are being fed with fresh waters, have temperatures several degrees lower than the temperature of North-West Bulgaria and Central-North Bulgaria. The decrease of temperature from West to East-North East is bound well with the gradual rise of Valanginian (Cr_1) in the same direction and the presence of circulating waters in it. North Bulgarian uplift is characteristic for its low values of temperature and gradient.

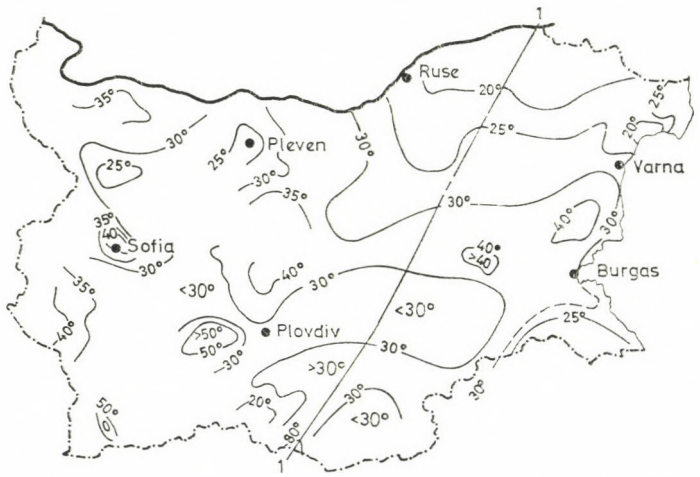


Fig. 1. Geotemperatures at the depth of 500 m, for Bulgaria, in centigrades. After Georgiev, Velinov and Boyadzhieva

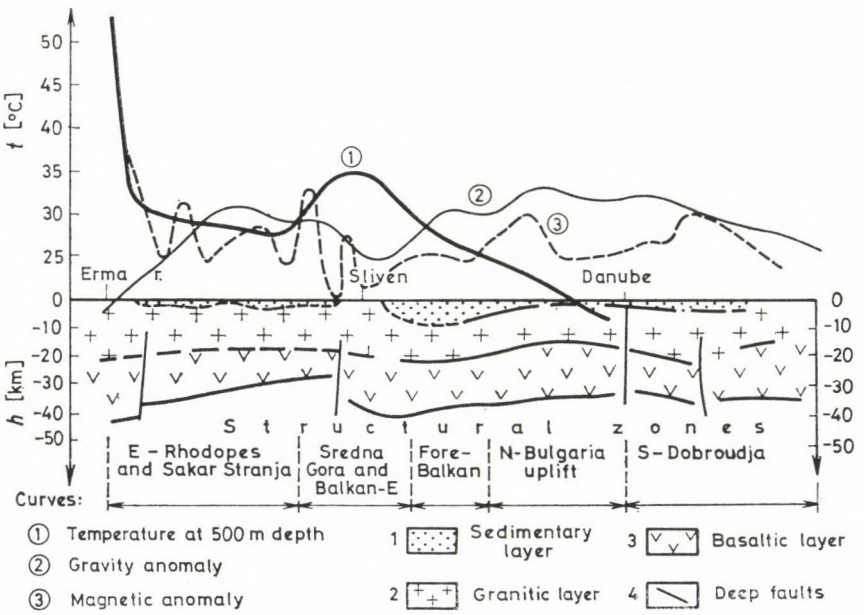


Fig. 2. Crustal section and geotemperatures in 500 m
1 – sediments; 2 – upper crust; 3 – lower crust; 4 – dislocation. Location at Fig. 1, 1—1

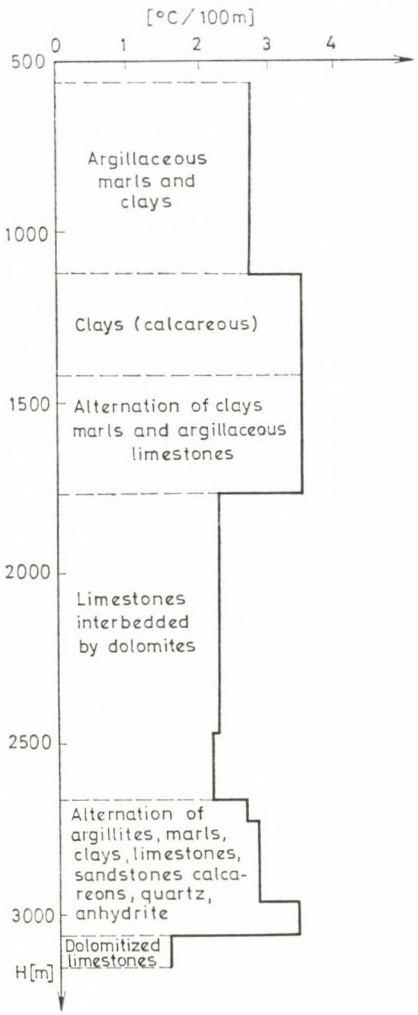


Fig. 3. General correlation between petrology and geothermal gradients in Bulgaria

For these reasons it can be assumed that the regional variation of temperature and gradient is determined by the lithological-stratigraphical characteristics of the rocks, and by the structural position of Valanginian for the discussed depths.

The Balkan Mountains' region has been studied the least of all. Generally the region up to 1000 m is of lower temperature expecting some local temperature anomalies around thermal springs.

Sredna Gora as a whole is an area of higher temperatures.

The geological and thermal picture of South Bulgaria is rather complicated due to the presence of a great number of faults mainly in the western part where the epicentres of the strongest earthquakes in the eastern part of the Balkan Peninsula are found.

A characteristic feature of the western part (Rila-Rodope Massif), which appears to be an active tectonic region, are the sharply expressed local temperature anomalies (Sofia Valley, Iakorouda, Velingrad, Blagoevgrad, Kyustendil, Sandansky-Melnik region, the Erma River) with temperature above 50 °C (for 1000 m depth) and gradient from 4–11 °C/100 m (for 500 m depth).

The Eastern part comprising the Eastern Rhodopes and Strandja Mountain is characteristic for its lower values and gradual modification of the temperature (up to 40 °C for 1000 m depth and gradient up to 3.0 °C/100 m for 500 m depth) (Fig. 1).

Owing to the limited quantity of temperature measurements, no definite conclusion for the presence of a relation between the heat field and the thickness of the earth's crust can be drawn. The increase of temperature in regions with a big thickness of the earth's crust (South-Western Bulgaria) is probably connected with the presence of deep-faults and tectonic activity of the region.

A certain correlation is noticed between the gravitational and thermal fields (Fig. 2). To the places along the profile that connects the Erma River, Sliven and the Danube, characteristic for their lower temperature, higher values of the gravitational field correspond and vice versa.

From the present data no other connection of the heat field with other physical parameters can be established.

The comparison of the heat field with the depth structure of Rila-West Rodope Massif allows the supposition that the radioactive decay, which takes place in the crust, particularly in the granite layer, has a certain importance as regards the development of the thermal field.

In most of the analyzed wells in North Bulgaria a clear link between the geothermal gradient and the lithology of rocks has been established (Fig. 3). It is ascertained that the highest gradient (above 3.5 °C/100 m) is characteristic of clays, argillites and sandstones and the lowest (below 2 °C/100 m) of limestones.

Some regularities between the thermal parameters and the reservoir characteristics of oil-gas layers have been noticed, but we have not enough data for a more thorough analysis.

The main conclusion from the work done up to now is that systematic geothermal investigations on the necessary technical level can be widely used for the solution of a number of geological problems in total, regional and local aspects.

REFERENCES

BONCHEV, E., 1971. Problems of the Bulgarian Geotectonics. St. Publ. H. Technica, Sofia.

VELTSCHEV, Z., PETKOV, I., DATSCHEV, H. 1971. Morphotectonical structures of Bulgaria and their reflections on the geophysical fields (in Russian). *Acta Geol. Hung.* **15.** Budapest.

VELTSCHEV, Z., PETKOV, I., DATSCHEV, H., 1973. Über die Tiefenstruktur der Erdkruste in der V. R. B. nach geophysikalischen Daten. *Proc. Bulg. Acad. Sci.* **26,** No. 11.

HEAT FLOW MAP OF THE EUROPEAN PART OF THE USSR AND ITS GEOLOGICAL AND GEOPHYSICAL INTERPRETATION

R. I. KUTAS, E. A. LUBIMOVA, YA. B. SMIRNOV

INTRODUCTION

During recent years the number of heat flow values on the land of the USSR and beneath the surrounding seas has notably increased. The investigations performed have covered the main tectonic provinces of the European part of the USSR. This area has a complicated geological history and includes provinces of different ages from ancient Archean blocks belonging to the Baltic and Ukrainian shields, to Cenozoic folding of the south orogeny belt.

Heat flow values beneath the marginal and internal marine basins were determined by temperature gradients in the bottom sediments by the Soviet heat flow probes. The results of heat flow determinations were summarized by Lubimova et al. (1973).

DATA PRESENTATION AND CONSTRUCTION OF THE HEAT FLOW MAP

The total number of heat flow values over the European part of the USSR exceeds 600 points. Their distribution is very uneven. On the map (Fig. 1, attached) heat flow values are given in μcal cm^{-2} sec^{-1}, and they are plotted and summarized in accordance to the legend into intervals. Heat flow isolines were drawn at the interval of 0.4 HFU (0.4 μcalcm^{-2} sec^{-1}) (i.e. 0.8, 1.2, 1.6 and 2.0 μcalcm^{-2} sec^{-1}), which exceeds two-to-three times the uncertainty of the measurement (Lee and Uyeda, 1965).

The following are the main features of the heat flow distribution within the investigated area: The most obvious result is the prevalence of relatively low and stable heat flow values ranging from 29–50 mWm^{-2} (0.7 to 1.2 HFU) observed over most area of the East European or Russian Platform (see Fig. 1, I). The lowest heat flows (25–42 mWm^{-2}, i.e. 0.6–1.0 HFU) correspond to the Baltic and Ukrainian shields (36 mWm^{-2} = 0.85 HFU). (See Fig. 1, II and III.)

Minimum heat flow values of 25 mWm^{-2} (0.6 HFU) were found at Revda, Lovosero massif and at Kovdor on the Baltic shield (Kola Peninsula) (Lubimova et al., 1973).

Considerable heat flow variations were noted in the Ukrainian shield on the basis of 50 determinations. Within the Ukrainian shield of the Hercynian Age (Fig. 1, III) a belt of low heat flow values can be distinguished not exceeding 33 mWm^{-2} (0.8 HFU) (Kutas and Gordienko, 1973).

Two slightly higher heat flow values (49 mWm^{-2} = 1.17 HFU) were

recorded in the Paleozoic Khibin (Koashva) alkaline massif in the centre of the Kola Peninsula. Presumably the heat flow value may reach even 50–54 mWm^{-2} (1.2–1.3 HFU). It is likely that this enhanced heat flow is associated with a young Paleozoic activity.

Stable heat flow values of 42–50 mWm^{-2} (1.0–1.2 HFU) were observed in anticlines and synclines and within the Pripyaty and Dnepr graben-like foredeeps in the western part of the Russian Platform (Bogomolov et al., 1972).

Higher values (54–59 mWm^{-2}, 1.3–1.4 HFU) in the Russian Platform correspond to zones of Zhigulevskaya and Dono-Medvedskaya faults (Makarenko and Polyak, 1972). On individual structures the heat flow may increase to 67 mWm^{-2} (1.6 HFU) and even to 75 mWm^{-2} (1.8 HFU). Several local anomalies with 67–75 mWm^{-2} heat flow (1.6–1.8 HFU) are separated with Dnepr and Pripyaty grabens in direction to the southern part of the Russian Platform.

Increased 50–71 mWm^{-2} (1.2–1.7 HFU) heat flow values were observed in angular depressions of the Russian platform: Timano-Pechorian (XIV) and Pre-Caspian depression (XIII). Similar geothermal provinces are common also for the North Sea depression (Haenel, 1971). A narrow belt of relatively higher heat flow 54–67 mWm^{-2} (1.3–1.6 HFU) is extended along the south-western margin foredeep of the Russian Platform.

The folded Donets structure occupying the southwestern part of the Dnepr–Donets region displays relatively higher heat flow (1.2–1.6 HFU) (Kutas and Gordienko, 1973).

The southern geosynclinal outline of the ancient platform has a very complicated heat flow pattern. Heat flow changes from 54 to 84 mWm^{-2} (1.3 to 2.0 HFU); higher values forming local anomalies of 75 to 84 mWm^{-2} (1.8 to 2.0 HFU) are concentrated in narrow strips (such as the anomalies of the Prikumskoye, Kanevsko-Berezanskoye and Tarkhankutskoye uplifted zones). A unique oval anomaly with relatively high heat flow of Stavropol uplift (VI) is very clear, heat flow increases here to 105–126 mWm^{-2} (to 2.5–3.0 HFU) (Sikharev et al., 1966, 1972).

In comparison to the mean heat flow of the Epihercynian Scythian plate, the angular West-Kuban (VII), Tersko-Caspian (VIII) foredeeps joining the southern rim of this plate have relatively low heat flow of 33–52 mWm^{-2} (0.8–1.2 HFU) (Lubimova, 1968).

A single area of increased heat flow of 67–71 mWm^{-2} (1.6–1.7 HFU) exists in the northern corner of the outer foredeep zone. This area extends along the margin of the East-European Platform, in the northeast direction it continues on the territory of Poland. Low heat flow values were observed in Rion, Kura river valley (X) and Araksin valley in the Lesser Caucasus area (XII) 33–46 mWm^{-2} (0.8–1.1 HFU). Similar heat flow pattern was found in the outer foredeep of the Carpathians (IV), where heat flow is usually low. On the contrary, heat flow is high in the intermountainous depressions (V), such as in the East-Slovakian (in Czechoslovakia, Čermák, 1968) and Pannonian (in Hungary) one.

In the Carpathians heat flow raises gradually from 50–54 mWm^{-2} (1.2–1.3 HFU) in the marginal part of the outer Carpathians (IV) to 67–84 mWm^{-2} (1.6–2.0 HFU) towards the south. The same gradual increase from internal foredeeps to central folded zones may be observed in the

Caucasus Mts. The heat flow field in the mountains of Crimea is of different nature. Heat flow of 50–54 mWm^{-2} (1.2–1.3 HFU) was obtained, only a single value of 71 mWm^{-2} (1.7 HFU) was recorded at the south of the Crimean foredeep. In the deep basin of the Black Sea heat flow data are similar to the results from Rion valley, i.e. 33–48 mWm^{-2} (0.8–1.1 HFU). Low values not exceeding 33–38 mWm^{-2} (0.8–0.9 HFU) dominate in the central part of the Black Sea where the earth's crust is of suboceanic type with thick sedimentary layers up to 10 km and more. A strip of higher heat flow 59–84 mWm^{-2} (1.4–2.0 HFU) extends from the shore of Crimea southwards to the deepwater sea.

Heat flow measurements in the Caspian sea were made at the South and Middle Caspian depressions having a suboceanic earth's crust. A higher heat flow anomaly of 71–100 mWm^{-2} (1.7–2.4 HFU) was distinguished in the Shatsk uplift area to the S of Apsheron Peninsula (Lubimova et al., 1974). This anomalous zone is surrounded by lower heat flow not exceeding 33–50 mWm^{-2} (0.8–1.2 HFU). An estimated correction for the sedimentary effect can be about 0.2 HFU. The heat flow within Iran basin is normal. Heat flow of about 134–209 mWm^{-2} (3.2–5.0 HFU) was found in three points in the Derbent depression, Middle Caspian basin. Most probably these data are connected with local hydrothermal conditions, though a link with a more intensive deep seismicity should not be excluded.

RELATIONSHIP BETWEEN GEOTHERMICS AND TECTONICS

The connection between the geothermal provinces described and tectonics is very uneven.

The central part, the East European (or Russian) Platform is the most stable geostructural unit of the whole European continent. This ancient platform is surrounded from east, west and south by younger tectonic elements (VI, VII, VIII) whose development had began in Paleozoic and have not yet been completed. This feature of the geological structure of the European part of the USSR is reflected in the heat flow distribution (Fig. 1). For many parts of the Russian Platform relatively normal and even low stable heat flow persists of 29–50 mWm^{-2} (0.7–1.2 HFU). Within the southern orogenic zones a sharp field differentiation is observed and heat flow varies from 33 to 126 mWm^{-2} (0.8 to 3.0 HFU).

Analyzing the heat-flow distribution in structures of different age and origin, we have come to the conclusion about the existence of some genetic relation between the amount of heat flow and the age of geosyncline folding and recent volcanism (Fig. 2). Highest heat flows over 84 mWm^{-2} (2.0 HFU) correspond to areas of Neogene volcanism of the Lesser Caucasus (XII) and the Cis-Carpathians (IV). Then follow structures of Alpine orogenism with 67–84 mWm^{-2} (1.6–2.0 HFU) and of Hercynian orogenism with 50–63 mWm^{-2} (1.2–1.5 HFU).

It should be noted that this relationship is not generally valid. Evidently not all folding or tectonic activity lead to heat flow increase. For instance, the mountainous part of Crimea, which has undergone an uplift in the

Alpine orogeny, has a rather low heat flow of about 54 mWm^{-2} (1.3 HFU), which is in accord with structures of Hercynian age.

No significant increase of heat flow has been observed in platform depressions (such as the Black Sea depression, Dnepr–Donets depression etc.) or in piedmont foredeeps. Generally the tectonic processes are connected with the outflow of heat energy from the earth's interior. This energy comes out mainly with products of the mantle differentiation and leads to a general increase of temperature and heat flow in the earth's crust. Such an increase in heat flow was observed in geosynclinal areas and volcanic zones. On the other hand tectonic activity disturbes the structure of the earth's crust and changes the conditions of heat transfer, i.e. temperature and heat flow distribution. As a result we get not only positive, but also negative anomalies of heat flow.

Some positive anomalies of increased heat flow coincide with zones of tectonic activation and dislocation on the ancient Russian Platform (I). They may be explained either by the energy inflow connected with tectonic activity, or by the influence of structural features of the dislocations.

A special feature of heat flow over the European part of the USSR is its low level in piedmont and in many intermountainous foredeeps like VII, VIII. This decrease in heat flow is caused by several factors: crustal movements, sedimentation, the insulating effect of a thick deposited layer with low thermal conductivity; reconstruction of the earth's crust and upper mantle due to foredeep formation, sedimentation in the marine basins etc. The most essential disturbance of the field is caused by the sedimentation process. For instance, in the Kura river depression (X in Fig. 1) the Cenozoic deposits reach in thickness 20 km. A sedimentary layer over 1000 m has been deposited during the quaternary period only. With this sedimentation rate the heat flow decrease in the upper part of the section is not less than 50%. Sedimentations in the Black and Caspian seas have a strong impact. So, in the Black Sea about 13 km layer had been deposited since Miocene. With such a sedimentation rate the minimum error may be of about 30%. The maximum undisturbed (corrected) heat flow value for the Black Sea may be equal to 2.0 HFU.

Zones of active faults are clearly delineated in the heat flow field. Within the Black Sea a belt of higher values extending southwards from the

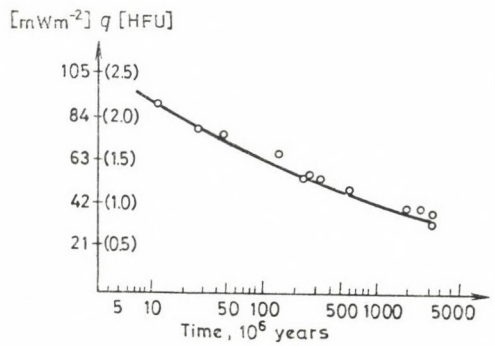


Fig. 2. Heat flow *versus* the age of latest folding events in the USSR

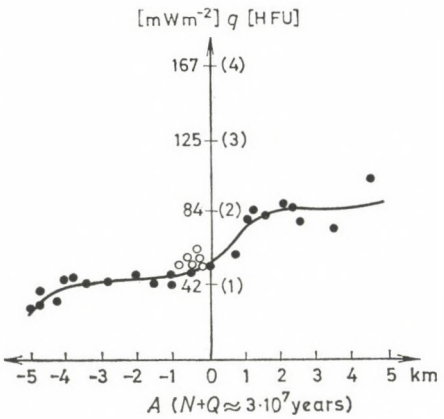


Fig. 3. Correlation between heat flow values q and the amplitude of Neogene-Quaternary vertical crustal movements for the Pre-Caucasus. Open circles show heat flow values from anticlines in foredeeps

Crimean shores, corresponds to the Yalta fault zone where increased seismic activity was observed (Goncharov et al., 1972). In the middle part of the Caspian Sea the high heat flow within the Derbent depression may be connected with a region of high deep seismic activity having foci at 100 km depth. The highest heat flow in the Greater Caucasus (XI) corresponds to the Cavminvodsky bench and the Stavropol oval uplift (VI), both crossed by deep lateral faults (Milanovsky, 1968).

The heat flow in young Alpine structures correlates with the amplitude and gradients of vertical tectonic movements. In Figure 3 the curve shows a relationship between heat flow and amplitude of vertical movements during the Neogene and Quaternary period in the Pre-Caucasus. As may be seen from this picture the higher heat flow corresponds to positive movements, while the lower ones to subsidences. It should be noted, however, that this is not an overall rule, in regions of the ancient platform it may fail.

Temperature strongly affects the physical properties of rocks (density, magnetization, electric conductivity, etc.). This fact serves as basis for the correlation between heat flow and other geophysical fields (such as gravity, geomagnetism), as well as, the position of physical boundaries in the crust and mantle. Some upheaved position (at 40–60 km depth) of the layer of high electrical conductivity was found in zones with high heat flow in the South Caspian depression (Berdichevsky et al., 1971) in the Pannonian Basin (V) (Ádám, 1970), and in the Cis-Carpathian foredeep (IV) (Bondarenko et al., 1969).

The low velocity layers in the earth's crust were found in the Cis-Carpathian foredeep (Tchekunov, 1972), where higher heat flows exist.

SUMMARY

Heat flow distribution is affected by tectonic evalution and geological history. The original heat field developed by radiogenic heat undergoes significant changes.

The nonuniformities of heat flow distribution are caused by many factors and may not always be explained uniquely.

The heat flow generated in the earth's crust of the Kola Peninsula (II) equals to 8–13 mWm^{-2} (0.2–0.3 HFU) and that of the mantle to 21–29 mWm^{-2} (0.5–0.7 HFU) (Arshavskaya et al., 1971). Calculations for two models of radioisotope distribution in the Ukrainian shield (III) fall approximately within these limits (Kutas and Gordienko, 1973). This calculation is based on numerous laboratory determinations of radioactive U, Th, K in surface rocks of Baltic (II) and Ukranian (III) shields. Heat generation from these rocks varies mainly from 4.2 mWm^3 (1 HGU $= 1 \cdot 10^{-13}$ $calcm^{-3}\,sec^{-1}$) to 42 mWm^3 (10 HGU), though some rocks release much more. Calculation of radiogenic heat flow was made for the two 4-layer models. In one of them the heat generation occurred over the entire so called granitic layer. From the basaltic layer the heat flow was taken equal to 5 mWm^{-2} (0.12 HFU). According to such a model a heat flow of about 25–29 mWm^{-2} (0.6–0.7 HFU) is generated in the earth's crust and of about 6–10 mWm^{-2} (0.15–0.25 HFU) from the upper mantle. Heat flow from the upper mantle varies markedly in its amount within geosyncline areas. So, according to calculations made for the Pre-Caucasus (VI, VII, VIII) it equals 17–21 mWm^{-2} (0.4–0.5 HFU) for the Russian Platform and exceeds 42 mWm^{-2} (1.0 HFU) within several locations of the Scythian plate, due to local tectonic and magmatic activities.

Generally, the heat field of the European USSR is determined by two major factors: the distribution of radioactive elements in the earth's crust and the deep energetic processes favouring heat generation from the earth's interior, connected with and perhaps transported by the products of partial melting and differentiation in the upper mantle. In some areas the steady state heat flow is superimposed by disturbances of different nature caused by heat transfer processes in the earth's crust and by surface conditions (topography, climatic changes, ground water circulation, thermal conductivity contrast etc.). As a rule, these factors are of local character and they add to the regional changes of heat flow.

REFERENCES

Ádám, A., 1970. Some results of the magnetotelluric survey in the Carpathian Basin and its complex interpretation. *J. Geomagn. Geoelectr.* **22**, 223–232.

Arshavskaya, N. I., Berzina, I. G., Lubimova, E. A., 1971. Geochemical and geothermal parameters for the Pechenga and Rico Latva regions, Baltic shield. *Geothermics* **1**, No. 1.

Berdichevsky, M. N., Burdovsky, V. G., Lubimova, E. A., Manafli, A. I., Nepesov, K. H., Feldman, I. S., 1971. Electric conductivity anomalies in the upper mantle and their geothermal interpretation (in Russian). *Izv. Akad. Nauk SSSR, Ser. Fiz. Zemli*, No. 7, Moscow.

Bogomolov, G. V., Tsibulya, L. A., Atroschenko, P. P., 1972. Geothermal Zonality of the Belorussian SSR (in Russian). Nauka i Tekhnika, Minsk.

BONDARENKO, A. P., BILINSKY, A. I., TIMOSHIN, B. V., SHEITCHENKO, E. A., SHILOVA, A. M., SHPORTYUK, Z. M., 1969. Magnetotelluric investigations in the Soviet Carpathians and adjacent regions of the Belorussian SSR. "Construction and Physics of the Deep Interior of the USSR's Western Region." Nauka i Tekhnika, Minsk.

ČERMÁK, V., 1968. Der Wärmefluss in der ČSSR und sein Zusammenhang mit Tiefenstrukturen. *Freiberger Forschungshefte, C*, **238**, 25–32.

HAENEL, R., 1971. Heat flow measurements and a first heat flow map of Germany. *Z. Geophys.* **37**, 975–992.

GONCHAROV, V. P., NEPROKHNOV, YU. P., NEPROKHNOVA, A. F., 1972. The bottom relief and deep structure of the Black Sea depression (in Russian). Nauka, Moscow.

DYAMALOVA, A. S., 1969. A deep heat flow on Dagestan territory (in Russian). Nauka, Moscow.

KUTAS, R. I., GORDIENKO, V. V., 1971. The heat flow of Ukraine (in Russian). Naukova dumka, Kiev.

KUTAS, R. I., GORDIENKO, V. V., ZAGORODNAYA, O. V., 1972. The heat flow of the Ukrainian shield and its slopes (in Russian). Geophys. Collection. Acad. Sci. USSR, 50, Naukova dumka, Kiev.

KUTAS, R. I., GORDIENKO, V. V., 1973. New data on the heat flow in the south western part of Ukraine (in Russian). Geophys. Collection. Acad. Sci. USSR, 56. Naukova dumka, Kiev.

LEE, W. H. K., UYEDA, S., 1965. Review of heat flow data. "Terrestrial heat flow", Washington, D.C.

LUBIMOVA, E. A., 1968. Thermal studies of the Earth and the Moon (in Russian). Nauka, Moscow.

LUBIMOVA, E. A., TOMARA, G. A., VLASENKO, V. I., SMIRNOVA, E. V., ZEKTSER, I. S., MESKHETELY, A. I., 1974. First measurements of heat flow through the Caspian sea bottom (in Russian). *Izv. Akad. Nauk, SSSR, Ser. Fiz. Zemli*, No. 4.

LUBIMOVA, E. A., SAVOSTIN, L. A., 1973. Heat flow in the central Black sea depression (in Russian). *Dokl. Akad. Nauk, SSSR*, **212**, No. 5.

LUBIMOVA, E. A., POLYAK, B. G., SMIRNOV, YE. B., KUTAS, R. I., FIRSOV, F. B., SEGIENKO, S. I., LYUSOVA, L. N., 1973. Catalogue of heat flow data over the USSR territory. Moscow.

MAKARENKO, F. A., POLYAK, B. G. (chief editors), 1972. Thermal Regime in the USSR interior (in Russian). Nauka, Moscow.

MILANOVSKY, E. E., 1968. Newest Caucasus Tectonics (in Russian). Nauka, Moscow.

SIKHAREV, G. M., VLASOVA, S. P., TARANUKHA, YU. K., 1966. On the question about heat flow values in some regions of the Big Caucasus and the Ante Caucasus (in Russian). *Izv. Akad. Nauk. Ser. Neft i Gaz*, No. 5.

SIKHAREV, G. M., TARANUKHA, YU. K., VLASOVA, S. P., 1969. A heat flow from the Azerbaidzhan interior (in Russian). *Sov. Geol.* No. 8.

SIKHAREV, G. M., VLASOVA, S. P., TARANUKHA, YU. K., KAMALOVA, S. V., 1972. A heat flow from the interior of the Caucasus and the south rim of the Russian Platform (in Russian). *Tr. Geol.* **46.**

TCHEKUNOV, A. V., 1972. The structure and tectonics of the earth's crust at the South of the USSR's European part (in Russian). Naukova dumka, Kiev.

VINOGRADOV, A. P., 1972. Mean chemical abundances of elements in the major igneous rocks of the earth's crust (in Russian). *Geokhimiya* No. 7.

INTERPRETATION OF HEAT FLOW DATA IN GEORGIA

G. I. BUACHIDZE

GEOLOGICAL OUTLINE

The geological structure of Georgia is represented by the whole complex of rocks from granitoids and Paleozoic crystalline schists to Quaternary deposits. Two main geostructural complexes could be distinguished — crystalline basement (Pre-Jurassic deposits) and Meso-Cenozoic sedimentary volcanogenic rocks. The recent structure of Georgia mainly resulted from Alpine orogenesis. The following main geotectonic units are distinguished (from North to South) (Geology of the USSR, 1964) (Fig. 1):

1. The folded system of the southern slope of the Great Caucasus
2. Georgian block
3. Adzharo-Trialety folded system
4. Artvin-Somkhity block.

According to geophysical data the basement outline can be described as follows: under the southern slope there is a great depression located in the central part at the depth of 6–8 km, deepening eastward and westward up to 12–15 km. On the Georgian block it emerges as Dziruli massive and subsides westward under Kolkheti lowland to the depth of 6–7 km and further on under the Black Sea to the depth of 10 km, and then wedges out under the eastern depression of the Black Sea. In the eastern part of the Georgian block the surface of the basement lies at the depth of 8–10 km. Under the Adzharo-Trialety folded system the basement also subsides to the depth of 6–11 km.

Meso-Cenozoic deposits are characterized by intense tectonic effect in folded systems (intensive folding, regional faults, etc.) and rather gentle bedding on the Georgian block.

HEAT FLOW MEASUREMENTS

60 heat flow measurements were carried out on the territory of Georgia, 23 of them on the Georgian block, 7 in Adzharo-Trialety and 3 on the Southern slope. No measurements have been made on the Artvin-Somkhity block. Marine heat flow measurements were made at 27 stations; most of them were confined to the continental slope (500–1200 m depth). Maximum depth of measurements has not exceeded 1740 m.

When analyzing the deep thermal gradient many factors were taken into account. These are: underground water movement, rock bedding, surface relief, surface reservoirs, vertical crustal movements and glacia-

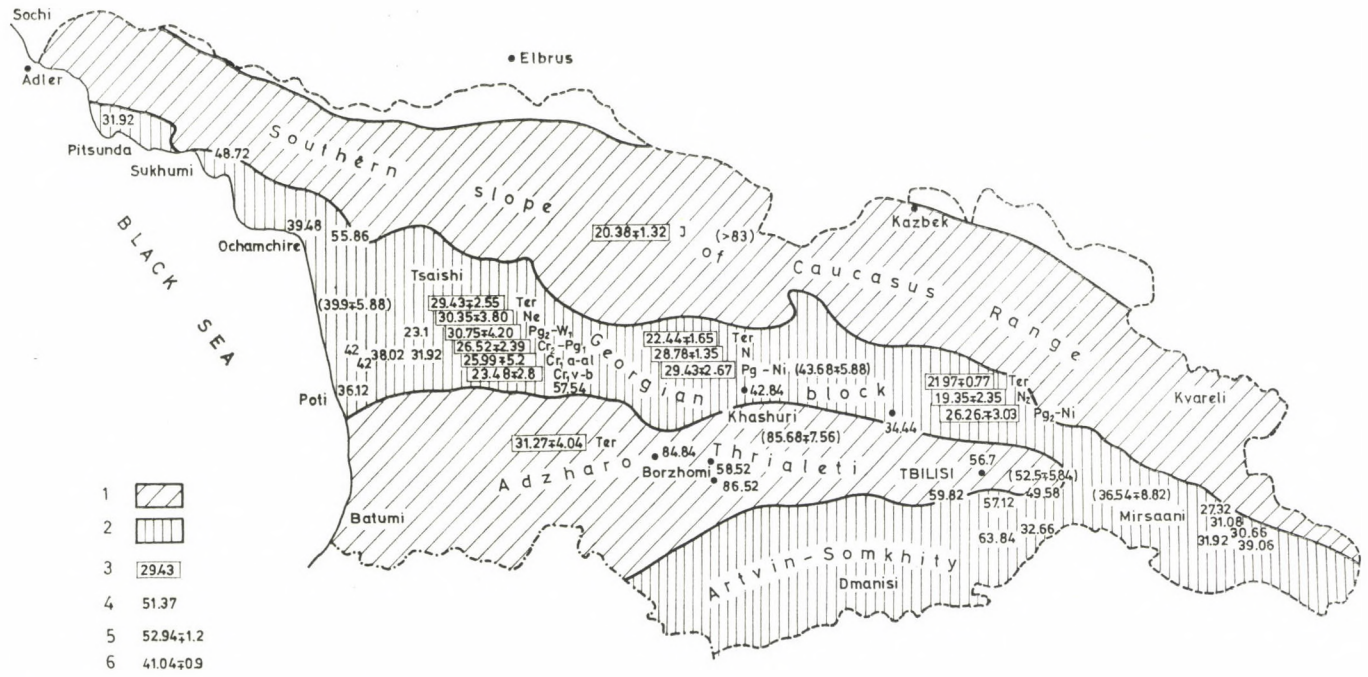


Fig. 1. Regional structure and heat flow measurements in Georgia
1 – Folded systems; 2 – Blocks; 3 – Temperature gradient of corresponding geological horizons in [10^{-3} Km^{-1}]; 4 – Heat flow in bore holes, [mWm^{-2}]; 5 – Mean heat flow for regions, [mWm^{-2}]; 6 – Mean heat flow for Georgia, [mWm^{-2}]

tion periods. It was concluded that in the areas of intensive circulation of underground water the main disturbance is caused by geological conditions. In marine areas correction of sedimentation was applied, too.

Temperature gradient was determined in the interval where the thermal properties of the rocks were estimated. Some heat flow values were averaged. The hypothesis of normal distribution was checked by statistical analysis, the evaluation of general dispersion was made by Pearson's criterium; the general mean value was checked by Student's criterium.

Heat flow density values are presented in new international units [mWm^{-2}]

It was found that heat flow is closely related to geotectonic structure (Fig. 1) (Buachidze et al., 1970). Thus, high values are peculiar for folded systems: $q_m = 73.08 \pm 7.56$ mWm^{-2} for Adzharo-Trialety; $q_m = 38.2 \pm \pm 4.46$ mWm^{-2} for the Georgian block. Somewhat smaller value on the Southern slope is evidently due to hydrogeological opening of the zone with intensive circulation of cold (due to low mean annual temperature), underground water (the fact which lowers geothermal gradient up to $20 \cdot 10^{-3}$ Km^{-1}) and only due to the high thermal conductivity of rocks (to $3.36 \cdot 10^{-3}$ $Wm^{-1}K^{-1}$), is it maintained higher than 63 mWm^{-2}. The Adzharo-Trialety folded system (a young Alpine structure) has a high heat flow. The highest value of heat flow is associated with the central part where crystalline basement comes near to the surface. In the East (Tbilisi region) the system terminates periclinally and passes into the Georgian block. Here heat flow values decrease and the mean value $q_m = 52.50 \pm 5.04$ mWm^{-2} takes an intermediate place between the mean values for the folded systems and the block. In the west the Adzharo-Trialety folded system passes into the Pontid. Heat flow measurements from the bottom of the sea in Batumi region and further westward showed high values which suggest a continuation of this system in the Black Sea. This hypothesis has been confirmed by the latest geological-geophysical data (Hydrogeology of the USSR, 1970).

The Georgian block (divided into two parts by the Dziruli massive) is best studied geothermally. The Eastern part of the Georgian block has the lowest heat flow values: $q_m = 36.12 \pm 8.82$ mWm^{-2}. Thick tertiary deposits are well developed here and downward movements of the crust continue at present. Heat flow increases westwards along the elevation of the basement, and in the immediate vicinity of the Dziruli massive (Khashuri region) it exceeds 42 mWm^{-2}. The western part of the Georgian block is characterized by the average heat flow value $q_m = 39.9 \pm 5.88$ mWm^{-2}. The relatively large number of measurements permits to distinguish anomalous areas influenced by hydrogeological and geostructural factors.

Discharge from intensive thermal horizons results in the formation of local anomalous areas with high heat flow values (Buachidze and Shaorshadze, 1967).

Determination of thermal energy of undergound water permits to calculate the convective heat flow.

The convective component of heat flow resulted in the following data: for the entire territory of Georgia it is $q_{conv} = 2.52$ mWm^{-2}, for Adzharo-

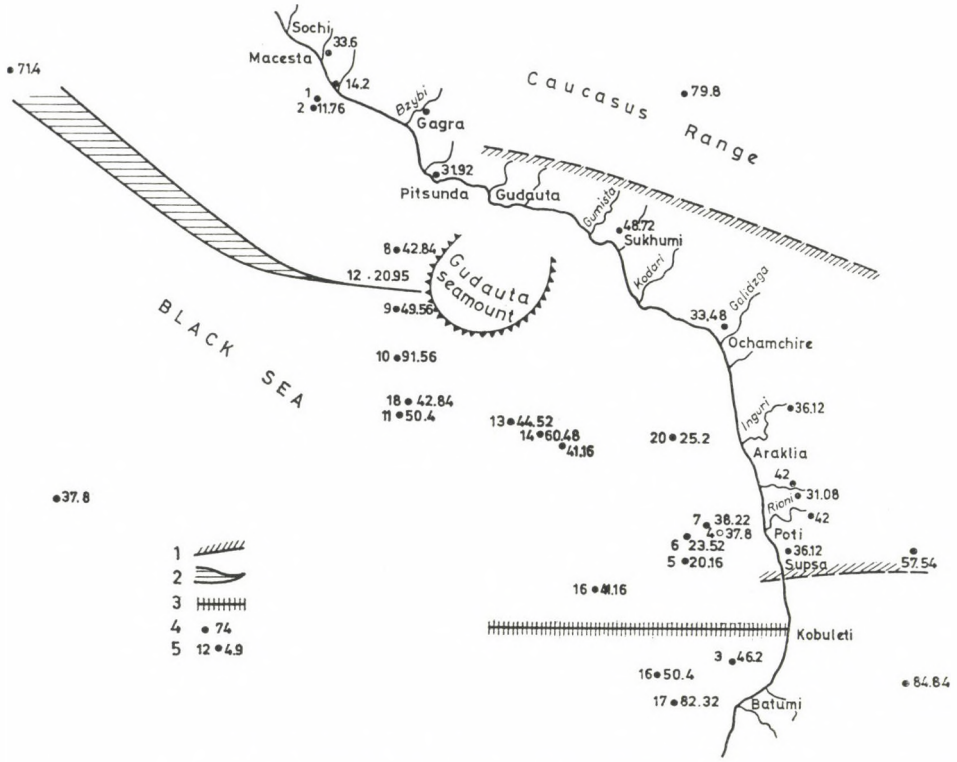


Fig. 2. Sea-bottom heat flow measurements
1 – Boundaries of folded systems; 2 – Magnetic anomalies; 3 – Deep fault; 4 – Heat flows on the land, [mWm^{-2}]; 5 – Heat flows on the sea, [mWm^{-2}]. Station number at left

Trialety $q_{conv} = 1.68$ mWm^{-2}, for the Georgian block $q_{conv} = 7.68$ mWm^{-2}, for the western part of the Georgian block $q_{conv} = 16.8$ mWm^{-2} and for some anomalous areas it increases and reaches $q_{conv} = 25.2$ mWm^{-2} (Tsaishi region).

The effect of the geostructural factor manifests itself in a smaller degree, but is of a regional nature. It is made evident by the increase of heat flow towards the folded systems which can be clearly observed at the boundary with the Adzharo-Trialety system.

Low heat flow observed at the bottom of the sea confirms the continuation of the Georgian block into the sea (Fig. 2). At the same time heat flow values increase towards the depression (Poti region). North-West of the Georgian coast there are very low heat flow values. The values of the order $q = 12.6$ mWm^{-2} are confirmed to a trough which stretches parallel to the coast and is filled with sedimentary deposits of 10 km thickness. The cooling effect of underground water discharged seawards should not be excluded. High heat flow values in the Gudautia region are particularly noticeable. Geophysical investigations have revealed structural-morpholog-

ical elevations with the mean value $q_m = 84$ mWm^{-2}. The maximum value $q = 205.8$ mWm^{-2} has been found in the southern part in the region of positive magnetic anomaly.

Scattering of sea measurements is much greater (10 fold) than that on land (2.3 fold). The 205.8 mWm^{-2} value has been rejected as not peculiar for the general totality (for the criterion τ) and the mean value $q_m = 46.2 \pm \pm 12.6$ mWm^{-2} has been obtained. On comparing it with the mean value for the land the zero hypothesis has been accepted (that is the difference between them is negligible).

SUMMARY

It can be concluded that the distribution of heat flow data in Georgia does not disagree with the most common (global) regularities. This is confirmed by the high heat flow values in folded systems and average values in the block; by the influence of hydrogeology in the formation of thermal anomalies; by the increase of heat flow towards the surface of the crystalline basement and the boundaries of folded systems; by the decrease of heat flow values in the areas with intensive Quaternary sedimentation; by highly dispersed values of heat flow from the Black Sea bottom and the equality of its mean value with those of the land.

REFERENCES

BUACHIDZE, G. I., SHAORSHADZE, M. P., 1967. The question of the determination of speed filtration in geothermal research (in Russian). *Trans. Sci. Res. Lab. Hydrogeol. and Engin. Geol. Problems*, Tbilisi, **3**, 175–177.

BUACHIDZE, I. M., BUACHIDZE, G. I., SHAORSHADZE, M. P., 1970. Thermal waters of Georgia. *Geothermics* **2**, 1092–1101.

1964. Geology of the USSR (in Russian). The Georgian SSR, Nedra, Moscow, 10, 655.

1970. Hydrogeology of the USSR (in Russian). The Georgian SSR, Nedra, Moscow, 10, 404.

HEAT FLOW GEOLOGY AND GEOPHYSICS IN THE BAIKAL RIFT ZONE AND ADJACENT REGIONS

S. V. LYSAK

It has been established for a number of large tectonic structures of the earth that terrestrial heat flow depends on the age of tectogenesis, on the thickness of the earth's crust, on the average velocities of recent vertical motions, on the existence of velocity and density inhomogeneities in the earth's crust, gravity and magnetic anomalies (Birch, 1947; Simmons, 1967; Van Bemmelen, 1967; Lubimova, 1968a; Lachenbruch, 1970; Čermák, 1972). A direct correlation between the mentioned parameters was shown to exist in tectonically active belts (Smirnov, 1967).

Detailed studies carried out in the Baikal Rift zone have shown that these correlations have a more complex nature. Perhaps, this was due to the heterochronity of the rift zone basement formed by Baikalian, Caledonian, and partially Hercynian structures which took place in the process of the Cenozoic activity in a unequal degree.

Not only the considerable difference of the heat flow in the Baikal Rift zone and in the adjacent regions but also its sharp and rather clear interior differentiation (Fig.1) in conformity with the details of a geological structure and the recent tectonic processes allowed to establish these facts.

Maximum heat flows were observed in rift depressions, in zones of active faults or in places of high density of fractures, in regions of "thinning" of the earth's crust, and contrasting relief, and in regions of earthquake epicentre concentration.

In the rift depressions the temperature gradients exceed 0.03–0.005 Km^{-1}, the thermal conductivity of the rocks is 0.8–1.7 $Wm^{-1}K^{-1}$ particularly in the bottom sediments of the Baikal Lake or in the disintegrated fractures of the rift zones, and the heat flow reaches 80–130 mWm^{-2} or more and it is 1.5–2 times more in the active fault zones (Lysak, 1968a; Lubimova, 1968b). The earth's crust is usually thinned here up to 30–35 km, absolute values of negative gravity anomalies are high (e.g., an average value of the gravity isostatic gradient is equal to 1.40 mgal km^{-1}), the average elevation gradient is also high (0.100–0.127 km km^{-1}) the earthquake magnitude reaches 6–7 1/2, and there is a layer of a high electrical conductivity at 12–15 km depths. In the rift zones there exist a number of thermal springs whose water temperature reaches 40–70 °C (Lysak, 1968b).

The temperature gradients hardly exceed 0.015–0.020 Km^{-1} in a rift mountain system, on the intertrench areas, and in the adjacent regions of the Siberian platform and Transbaikalia. The thermal conductivity increases sharply up to 2.5–3.5 and even to 4.0 $Wm^{-1}K^{-1}$ in carbonate-halogen sediments of the platform. Heat flows are very low — less than 50–40 mWm^{-1} (Lysak, 1968c). In this regions the thickness of the earth's

crust reaches 40–50 km, the elevation gradients and isostatic anomalies are low and correspondingly equal to 0.015 and 0.47 km km^{-1}. This territory is practically aseismic and the layer of higher electrical conductivity can be located at 70–100 km. Thermal springs are absolutely absent and ground waters are got warm up to 20 °C only at more than 1.5 km depth.

A quantitative relationship between the heat flow and various geological-geophysical parameters may be established and mathematically expressed in some cases by means of statistical analysis.

The comparison of heat flow (q) with the earth's crust thickness (H) by means of 85 points demonstrated the existence of a reliable correlation between the selected parameters, the correlation coefficient r being 0.67 (Fig. 2, a). The obtained formula of regression is

$$q = 0.228\,H^2 - 30.32\,H + 741.78 \qquad (1)$$

The heat flow increases when the thickness of the earth's crust decreases and vice versa, but there is no constant proportionality. For example,

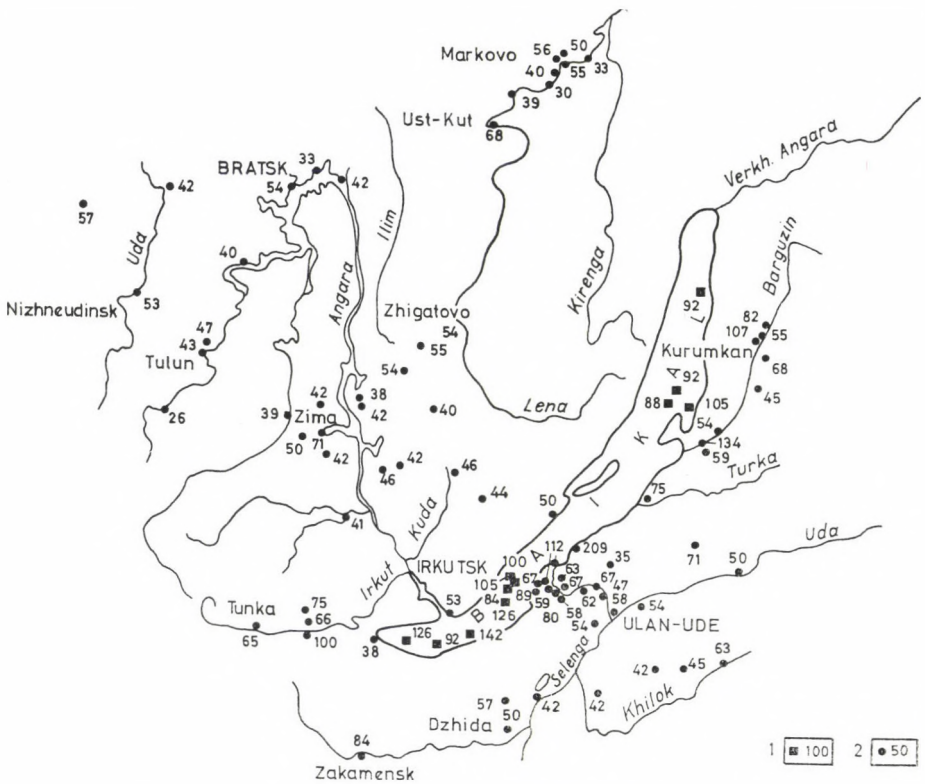


Fig. 1. Heat flow distribution
1 – through the Baikal bottom; 2 – on the surface in [mWm^{-2}]

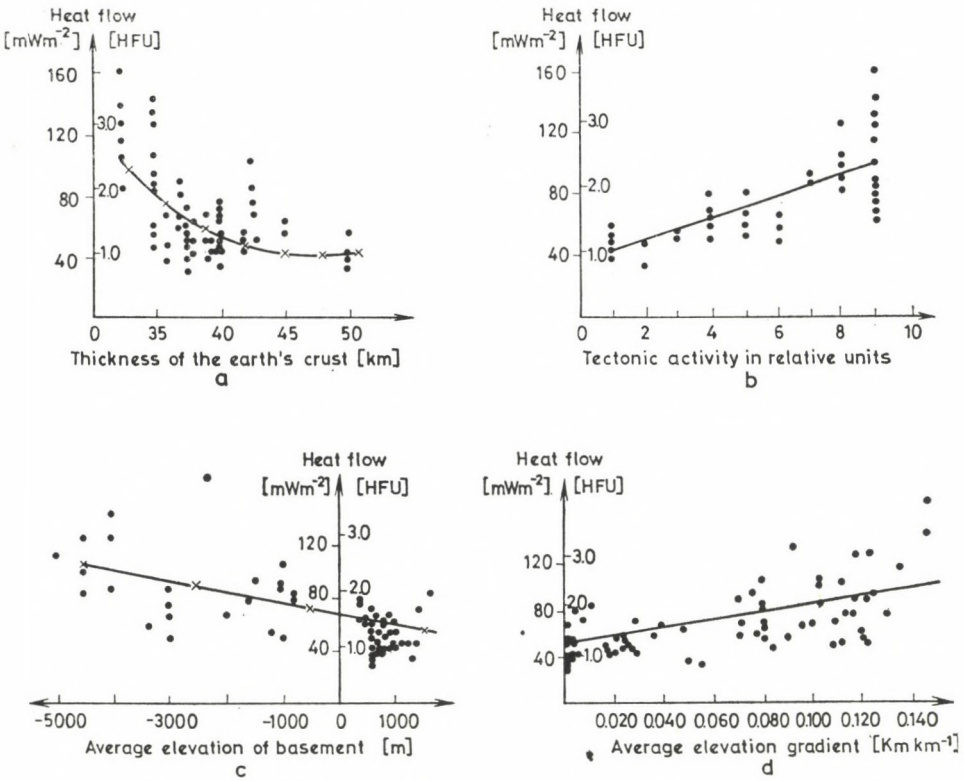


Fig. 2. Correlation of heat flow with tectonic activity
a – with the earth's crust thickness (Zorin, 1971); b – with tectonic activity (Solonenko, 1968). A relative line of the tectonic activity of the main geological structures: 1 – Transbaikalian type depressions; 2 – trench-fault rise; 3 – arched rise; 4 – relics of the Tertiary depressions; 5 – descending depressions of the Baikalian type; 6 – graben-shaped depressions; 7 – areas of the Baikal depression with a week interdepression differentiation of the basement; 8 – areas of the Baikal depression with a sharp interdepression differentiation of the basement; 9 – Cenozoic activity or seismic faults; c – with the recent structure (Zorin, 1971); d – with the average elevation gradient (Novosolova, 1973)

average heat flow reaches 125 mWm^{-2} when the thickness of the crust is less than 35 km, and it is equal to 40 mWm^{-2} when the thickness increases to 50 km. Thus, one may suppose that the thinning out of the earth's crust in the Baikal Rift zone promotes a more intensive terrestrial (mantle) heat flow in comparison with the adjacent regions.

Indeed, radiogenic heat flow generated in the earth's crust is about 30% of the observed value. The greatest part of terrestrial heat flow is produced by the crustal bottom and the upper mantle (Lysak, 1973). Some investigators (Arteev and Artyushkov, 1971; Zorin, 1971; Sherman, 1971) suppose that in the upper mantle of the Baikal Rift zone there exist rising streams of a convection flow which lead to a high heating, to the

spreading and thinning of the earth's crust and give rise to a tectonic activity of the region.

If one determines qualitatively, in terms of the predominant type of deformations, the gradient of recent tectonic motions and seismic activity, the relative line of recent tectonic activity in the main geological structures and compares it with heat flow (Fig. 2, b), a direct linear relation seams to exist between the selected parameters (50 points) with a correlation coefficient of $r = 0.73$. The equation of regression is:

$$q = 7.14x + 34.4 \pm 6 \tag{2}$$

where x is the relative unit of a tectonic activity line (see Fig. 2, b).

It follows that average heat flow values are close to 50 mWm^{-2} in the intermountain depressions of Transbaikalia and on the intertrench areas of the rift zone, and they exceed 120–150 mWm^{-2} in the proper Baikal depression and in zones of seismic faults.

The relation of heat flow with recent tectonic activity may be estimated using the other parameters, such as, for example, the recent structural

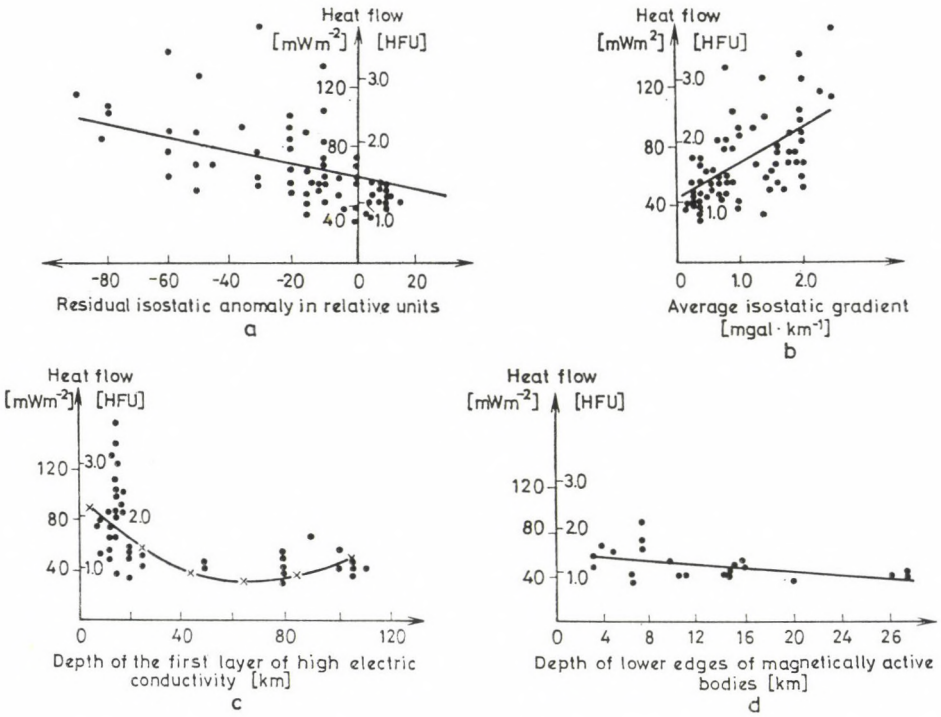


Fig. 3. The correlation of heat flow with some geophysical parameters a – with averaged isostatic anomalies; b – with average isostatic gradient (Zorin, 1971); c – with the depth of the first layer of high electric conductivity (Gornostaev, 1972); d – with the depth of the lower edges of magnetically active bodies (Novosolova, 1973)

forms being the final results of the deformation of the Cretaceous-Paleogene ancient flat surface (Fig. 2, c), or the average elevation gradient of a deformed surface reflecting the degree of contrast of neotectonic motions (Fig. 2, d).

There exists an inverse correlation (according to 81 points), with $r = -0.64$, between heat flow and the elevations of the deformed ancient flat surface (h), described by

$$q = 2.52 \cdot 10^{-6} h^2 - 9.41 \cdot 10^{-3} h + 69.3 \pm 7 \quad (3)$$

Maximal heat flows are characteristic for negative structural forms. Heat flow increases up to 80–130 mWm^{-2} and even more with the sinking of the basement from 0 to 2–5 km below sea-level. Conversely, the heat flow decreases to 50 mWm^{-2} and less if the elevation reaches 1–2 km.

A direct proportional increase of heat flow corresponds to an increase of the elevation gradient grad h, where $r = 0.69$ and

$$q = 394.8 \operatorname{grad} h + 45.4 \pm 4 \quad (4)$$

(Fig. 2, d).

The correlation between heat and gravity fields (Fig. 3, a, b) can be established by comparing heat flow with isostatic anomalies of the gravity (g_{is}) and with their gradients (grad g_{is}) showing density inhomogeneities in the earth's crust and upper mantle. It was found according to 81 points that

$$q_1 = 59.2 - 0.42 g_{is} \pm 5 \quad (5)$$

and

$$q_2 = 43.7 + 24.36 \operatorname{grad} g_{is} \pm 5 \quad (6)$$

the respective correlation coefficients being $r_1 = -0.59$ and $r_2 = 0.60$. The correlation in these cases indirectly reflects the same connection of heat flow with the recent tectonic activity.

The increase of heat flow is associated with the decrease of the depths of magnetically active bodies (h_m) and vice versa. As it is seen from the analysis of only 27 points (Fig. 3, d) an inverse linear relation exists between values ($r = -0.47$):

$$q = 60.9 - 0.82 h_m \pm 5 \quad (7)$$

This relation also shows that the depth-limit of magnetically active bodies is determined by the heat condition of the earth's crust. According to Novosolova's data (1973) the thickness of a magnetically active layer is on the average 13 km for the Baikal Rift zone, and 17 km and 26 km for Transbaikalia and the southern part of the Siberian platform, respectively.

There is a close relationship between heat flow and the depth of the first layer of high electric conductivity (h_ϱ) (according to 60 points) by which (Fig. 3, c) $r = 0.75$ and

$$q = 0.015 h_\varrho^2 - 2.1 h_\varrho + 101.6 \pm 8 \quad (8)$$

i.e. a conducting layer approaches the earth's surface up to 12–15 km in the regions of maximum heat flows.

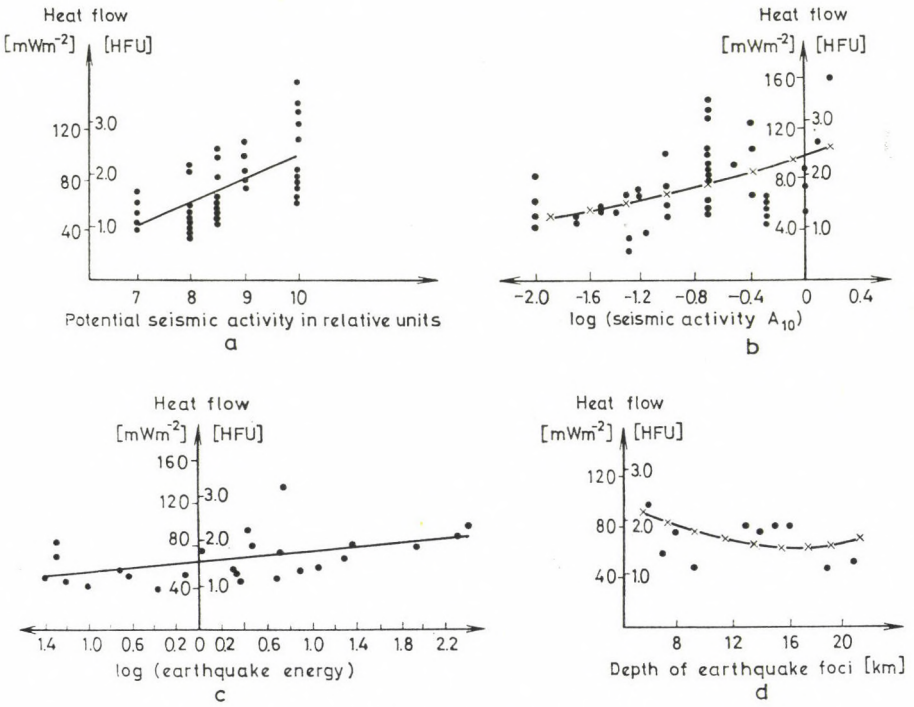


Fig. 4. Correlation of heat flow with seismic activity
a – with the potential seismic activity (Solonenko, 1968); b – with the seismic activity of A_{10} (Riznichenko et al., 1969); c — with the energy of earthquakes (Treskov, 1968); d – with the depth of earthquake foci (Treskov, 1968)

A definite correlation between heat flow intensity and seismic activity was observed in the Baikal Rift zone. Qualitatively this fact has been established earlier (Lysak and Sherman, 1970). A quantitative estimation has shown that heat flow, as a rule, is higher than 80–100 mWm^{-2} in regions of the concentration of the earthquake epicentres of magnitudes exceeding 6–7 1/2 (Fig. 4).

Comparing the degrees of potential seismic danger (n) with heat flow distribution (according to 55 points) a direct connection has been found between these parameters (Fig. 4, a), with $r = 0.62$ and

$$q = 18.9\, n - 88.2 \pm 6 \tag{9}$$

Heat flow also correlates with the average frequency of the recurrence of earthquakes belonging to the tenth energetic class (Riznitchenko et al., 1969) on a definite area (A_{10}) (Fig. 4, b), here $r = 0.67$ and

$$q = 4.62 \lg A_{10}^2 + 46.6 \lg A_{10} \pm 9 \tag{10}$$

During an earthquake a number of processes lead to heat production in the focal zone. About 85% or even 100% of the energy formed by a fault displacement of the crustal blocks are transformed into heat by sliding friction and material destruction (Bridgeman, 1955). Thus, one can estimate, using probability theory the heating of the earth's crust owing to earthquake energy if these take place rather often. The comparison of the energy E of more than 8000 earthquakes of magnitude $>4\,1/2$ which has taken place on the studied region from 1961 till 1968, with heat flow (Fig. 4, c) has shown that there exists a direct linear connection between the investigated parameters, with $r = 0.46$ and

$$q = 9.24\,E + 64.7 \pm 8 \qquad (11)$$

It is of interest that regions of high heat flows are well correlated with the areas of shallow earthquakes ($r = 0.90$). However, one cannot consider this dependence as finally established, because due to the small number of correlated pairs the probability of the relation is < 0.90 in this case while it was >0.95 in all previous cases.

CONCLUSIONS

The correlation of heat flow with various geological-geophysical parameters of the Baikal Rift zone and adjacent regions suggests that there exists a reliable correlation between the mentioned parameters $r_q > 0.35$–0.50.

First of all, the heat flow depends on tectonic activity (on the Cenozoic in this case). Inside the tectonic region (in the Baikal Rift zone) the local geological structure of the separate areas strongly affects heat flow, which can deviate from its average within the limits of $\pm 50\%$ and more. High heat flows are found in the rift depressions and fault zones. The heat flow depends on the variations of the thickness of the earth's crust, seismic activity, and other factors.

REFERENCES

Arteev, M. E., Artyushkov, E. V., 1971. Structure and isostasy of the Baikal Rift. Mechanism of Rifting. *J. Geophys. Res.* No. 4.

Birch, F., 1947. Crustal structure and surface heat flow near the Colorado Front Range. *Trans. Amer. Geophys. Union*, **28.**

Bridgeman, P., 1955. Investigation of Large Plastic Deformations and Fractures. Moscow.

Čermák, V., 1972. Heat flow and gravity in Czechoslovakia. *Studia Geophys. Geod. ČSAV*, **16.**.

Gornostayev, V. P., 1972. On the deep geoelectrical model of Pribaikalia (in Russian). *Geol. i Geofiz.* No. 9. Novosibirsk.

Lachenbruch, A. H., 1970. Crustal temperature and heat production: Implications of the linear heat flow relation. *J. Geophys. Res.* **75,** 17.

Lubimova, E. A., 1968a. Thermal Studies of the Earth and the Moon (in Russian). Nauka, Moscow.

Lubimova, E. A., 1968b. The thermal anomaly in the region of the Baikal Rift (in Russian). The Baikal Rift Zone. Nauka .Moscow.

LYSAK, S. V., 1968a. Some data about thermal waters and the geothermy of Pribaikalia (in Russian). The Baikal Rift Zone. Nauka, Moscow.

LYSAK, S. V., 1968b. Geothermal studies of Pribaikalia (in Russian). *Geol. i Geofiz.* No. 9. Novosibirsk.

LYSAK, S. V., 1968c. Geothermal Conditions and Thermal Waters of the Southern Part of East Siberia (in Russian). Nauka, Moscow.

LYSAK, S. V., 1972. Terrestrial heat flow of the west Transbaikalia (in Russian). Geofizika. Scientific Information of the Institute of the Earth's Crust, Irkutsk.

LYSAK, S. V., 1973. The geothermal field of the Baikal Rift zone and the adjacent regions. Results of the geological-geophysical research finished in 1972 (in Russian). Scientific Information of the Institute of the Earth's Crust, Irkutsk.

LYSAK, S. V., SHERMAN, S. I., 1970. On the influence of some tectonic processes on the formation of the therms of the Baikal Rift zone (in Russian). Materials of the 4th Meeting on Ground Waters of Siberia and the Far East. Irkutsk–Khabarovsk.

NOVOSOLOVA, M. K., 1973. Earth's crust structures of the northeastern part of the Baikal Rift zone from geophysical data. Results of the geological-geophysical research finished in 1972 (in Russian). Scientific Information of the Institute of the Earth's Crust, Irkutsk.

RIZNICHENKO, YU. V., PSHENNIKOV, K. V., ZORIN, YU. A., 1969. Seismic activity of the Pribaikalia in comparison with the relief and with gravity anomalies (in Russian). *Izv. Akad. Nauk SSSR. Ser. Fizika Zemli*, No. 10.

ROY, R. F., BRUNE, N., HENVEY, T. L., WASSERBURG, G. S., 1967. Heat flow in a zone of high creep rate along the San Andreas fault., California. *Trans. Amer. Geophys. Union* **48**, 1.

SHERMAN, S. I., 1971. Forming mechanism and the main stages of the development of the Baikal Rift zone (in Russian). *Izv. of the East Siberia.* Department of the Geographical Society of the USSR, **68**, Irkutsk.

SIMMONS, G., 1967. Interpretation of heat flow anomalies. I. Contrast in heat production. *Rev. Geophys. Space Phys.* **5**, 1.

SMIRNOV, YA. B., 1967. Investigation of the genetic relations of heat flow with the structure and development of the earth's crust (in Russian). *Dokl. Akad. Nauk SSSR*, **177**, 1.

SOLONENKO, V. P., 1968. Seismotectonics and the recent structure development of the Baikal Rift zone (in Russian). The Baikal Rift Zone. Nauka, Moscow.

TRESKOV, A. A., 1968. Seismicity and the structure of the earth's crust in the Baikal Rift zone (in Russian). The Baikal Rift Zone. Nauka, Moscow.

VAN BEMMELEN, R. W., 1967. On the interpretation of the apparent form of the geoid of the terrestrial heat flow. *Tectonophysics* **4**, 1.

ZORIN, YU. A., 1971. The Recent Structure and Isostasy of the Baikal Rift Zone and the Adjacent Territories. Nauka, Moscow.

TEMPERATURES, HEAT FLOW AND HEAT GENERATION IN SOUTH AND WEST SIBERIA AND KAMCHATKA

L. S. SOKOLOVA

Temperatures of the earth's crust were calculated for 11 areas over the Siberian territory and for the South-East part of Kamchatka Peninsula. The geothermal method, based on the solution of one-dimensional stationary heat conduction equation for the horizontal-layer model of the earth's crust, was used. The models were constructed from geological and geophysical data available for this territory and from the measured thermal conductivity coefficient of the rocks and the concentration of radioactive elements. Since the reliability of geophysical data is not satisfactory, definite informations about the mineral composition of the earth's crust are lacking and because for the construction of the models a number of simplifications have been made, it is not possible to estimate strictly the error and hence the reliability of the obtained temperatures.

The computed data are presented in Figure 1 as thermograms using mean heat flows at every area while Figures 2 and 3 exemplify a map of temperature distribution at 40 km depth, based on data of Figure 1 and

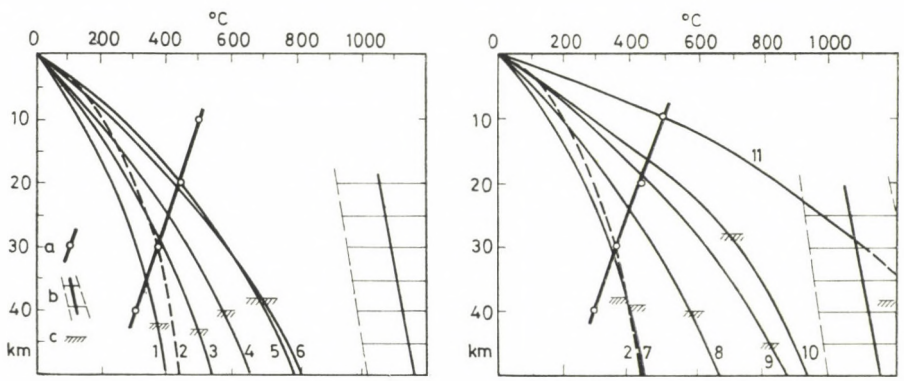


Fig. 1. Average temperature *vs.* depth for different regions of S Siberia and SE Kamchatka

(A) 1 – Kuznetsky Alatau ($q = 0.9$); 2 – West-Siberian Plate ($q = 1.0$); 3 – Mountain Shoria ($q = 1.5$); 4 – East Sayan ($q = 1.15$); 5 – Kuznetsk depression ($q = 1.35$); 6 – South-Minusinsk depression ($q = 1.35$); a – variation of titanomagnetite Curie temperature *vs.* depth of their origin; b – area of probable basalt melting, by Affen and Jessop; c – Moho-boundary line

(B) 7 – Southern part of Siberian Platform ($q = 1.0$); 8 – South-West Zabaikalie; Udinsk depression's ara ($q = 1.35$); 9 – South-West Zabaikalie, Dgidinsky region ($q = 1.8$); 10 – South-East Kamchatka (Paratunsk and Koryaksko-Avachinsk depression) ($q = 1.5$); 11 – South Baikal depression ($q = 2.7$). Heat flows in HFU

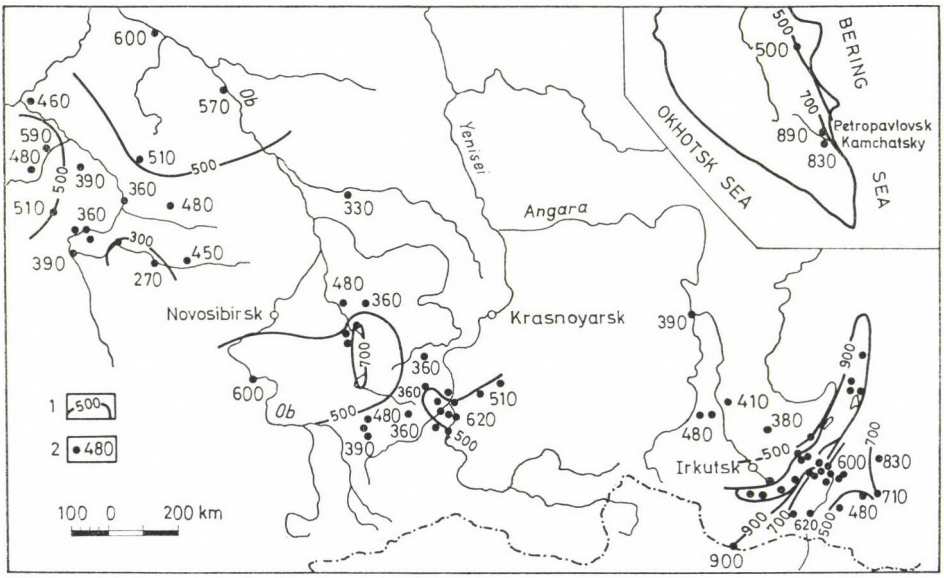


Fig. 2. Map of temperature distribution in the Earth Crust at 40 km depth in Siberia and in the South-West part of Kamchatka
1 – isotherms in °C; 2 – sites of heat flow measurements and temperature in °C at 40 km depth

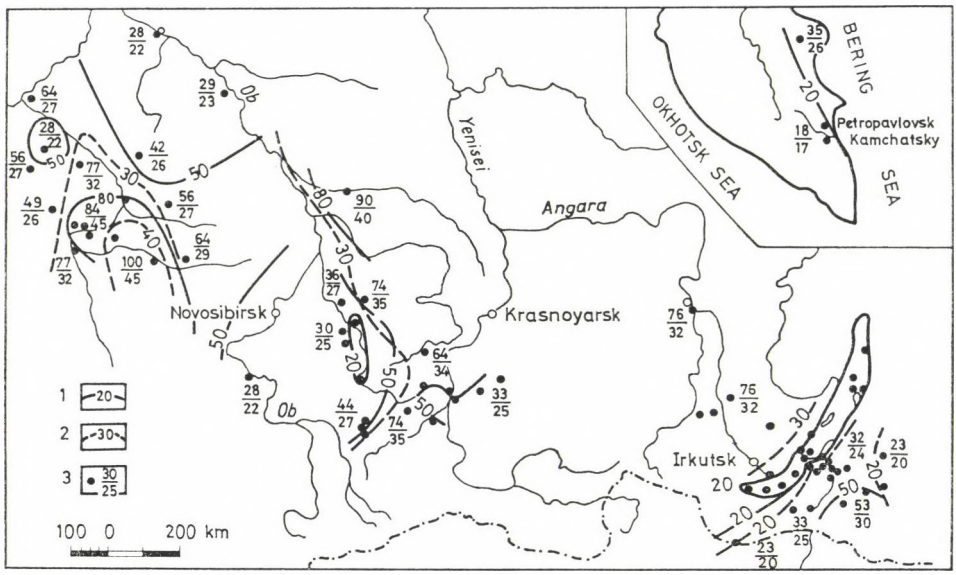


Fig. 3. A map of 500 °C isotherms and Curie isotherms
1 – isolines of similar depths, in km, 500 °C isotherms; 2 – depth of Curie isotherm of titanomagnetite; 3 – sites of heat flow determination, numerator depth of the 500 °C isotherm, denominator depth of the Curie isotherms

a map of the depth of the 500 °C isotherm and of the Curie isotherm for the investigated area. These thermograms characterize mean temperatures *vs.* depth for wide areas, where considerable local fluctuation of I are possible, due to heat flow variety. Figure 1 also shows an area of probable partial melting or complete fusion of basalts (Beloussov, 1966) as well as the Curie temperature of titanomagnetite depending on depth of their origination (Bagin et al., 1971). It is obvious that temperatures are too low even for a partial melting. A relation between the results of Figure 1 and the parameters of the accepted local crustal model has been studied. The temperature distribution is shown to depend, mainly, on heat flow and variations of thermal conductivity of rocks with depth. If q does not exceed 1.4–1.5 HFU, the variation of λ is unessential. So for q-s less than 1.5 HFU a correlation was obtained, enabling to estimate the local temperatures at the level of Moho boundary (at about 40 km depth) from the heat flow values. The error of the method is 50–100 °C.

For South and West Siberia (Moho-depth 38–39 km) equal temperatures of 400 °C were computed, despite considerable distinctions in their structure and tectonic evolution. For the Southern part (7) of the Siberian platform this value is evidently rational everywhere with deviations of no more than 50 °C. For the West Siberian Plate (2) the Moho-temperature can vary from 300 to 650 °C due to heat flow variations. Mean temperatures of the upper crustal layers are higher here (Fig. 1). This effect is caused by the thermogenic sedimentary cover and vanishes practically at 25–30 km depth.

Caledonides in Altai-Sayan area (1, 4) show a more intensive growth of temperature with depth. At the level of the Moho boundary (40–43 km) the temperature equals on the average 500 °C, changing from 350 (Kuznetsky Alatau (1)) to 550 °C (Eastern Sayan (4)): In South-Minusinsk (6) and Kuznetsk depression (5) the mean temperatures are higher through the whole earth's crust section. Here the Moho temperature is 600–700 °C with deviations from 440 to 960 °C.

A higher heat flow was found in South-West Zabaikalie (8, 9). While the earth's crust temperatures in the region of Udinsk depression (8) are close to that in Eastern Sayan (4), they are much higher over the Dgidinsky area (9). In Udinsk (8) the Moho boundary lies at 40 km and the mean temperature is 580 °C with variations from 470 to 800 °C. In the Dgidinsky area (9) the Moho depth is 45 km and the temperature 830 °C, with variations from 650 to 950 °C.

Especially high temperatures and variations were computed for the earth's crust within the South Baikal valley (11). A rapid increase in temperature with depth is caused here by a high subcrustal heat flow.

At the Moho boundary (38 km) the temperature corresponding to stationary heat flow is on the average 1200–1300 °C with possible deviations from 1000 to 1500 °C. Thus, the temperature at 40 km depth in the Baikal Rift zone is by 700–800° higher than in the southern part of the Siberian Platform and by 500–600° higher than in the Udinsk area. High temperatures of the crust and the upper mantle were computed in South-East Kamchatka (10) (Paratunsk and Koryaksko-Avachinsk depressions), inspite of a relatively low heat flow measured at the surface. At 40–50 km depths

the temperature reaches 800 °C. The crust's temperature is rather high even in the Kronotsky region, where $q = 0.9$ calcm^{-2} sec^{-1}. The reason is a high subcrustal heat flow which is similar to the Baikal Rift zone conditions. Temperatures, calculated for depths of 20–30 km and more, probably do not always correspond to the recent values, because of the slowness of heat

TABLE 1

Time necessary to approach steady state heat conditions at different depths

Depth in km	Time up to 10%	(mill. years) up to 20%	Notes
0	51	38	Thermal diffusivity
10	31	21	0.01 cm^2 sec^{-1}
20	13	10	
30	3	2.5	

processes. As an example, Table 1 gives estimates of the time of thermal equilibrium in an infinite homogeneous layer, with a constant heat flow q_0 at the boundary of this layer.

It follows from Table 1 that steady state conditions at the earth's surface are only attained after 40–50 million years (within 10–20%). The temperature-depth function computed from surface heat flow would correspond to the actual recent temperature distribution only if q were constant during all these periods.

Judging by geological data the constancy of heat flow can be assumed for South-Siberian plate and the Siberian Platform. In other regions some variations of the subcrustal heat flow are possible during the Cenozoic era, as Neogene-Quaternary and recent volcanism and intensive neotectonic vertical movements were observed there. At these areas the computde crustal temperatures should be considered as crustal temperatures some 20–40 million years ago that is during the Upper Paleogene-Lower Neogene. At the present time crustal rocks get warmer in Altai-Sayansk area and South-East Kamchatka, and cooler in the Baikal Rift zone. This should be kept in mind when interpreting the results of deep temperature calculation.

CORRELATION WITH THE GEOLOGICAL AND GEOPHYSICAL DATA

According to Figures 1–3 the highest temperatures are found at the Baikal Rift zone. Here basalts can melt already near the crust base (30–40 km).

In the Dgidinsky region the temperature of basalt melting (1100–1200 °C) is attained lower, at 70–80 km depth (Table 2). The melting favours the formation of basalt magma, that can rise to the surface. Within the Baikal Rift zone and the Dgidinsky region volcanism existed in the Neogene-

TABLE 2

Temperature in the earth's crust and upper mantle in South Siberia and South-East Kamchatka

Region	Mean heat flow [HFU]	Moho boundary line depth	Temperature at Moho in [°C]	Isotherm depth in km		
				Curie	500 °C	1200 °C
	Altai-Sayansk folded area					
1. Kuznetsky Alatau	0.9	42	370	35	75	330
2. East Sayan	1.15 / 0.8 – 1.45	40	580 / 300 – 750	25	30	135
3. Mountain Shoria	1.05 / 0.9 – 1.1		500 / 380 – 600	29	45	190
4. South-Minusinsk depression	1.35 / 1.1 – 1.6	38	600 / 500 – 870	20	25	100
5. Kuznetskaya depression	1.35	38	640	20	25	110
	West-Siberian Plate					
6. Central and South region	1.0 / 0.8 – 1.3	38	400 / 300 – 650	30	70	460
	Baikal area					
7. Southern part of Siberian Platform	1.0 / 0.9 – 1.1	39	400 / 380 – 500	30	75	470
8. South-Baikal depression	2.8 / 2.2 – 3.4	38	1270 / 1050–1500	10	10	30–40
9. Dgidinsky region	1.8 / 1.65 – 1.9	45	830 / 700 – 900	20	23	70–80
10. Udinsk depression region	1.95 / 1.1 – 1.8	40	580 / 500 – 800	25	32	135
	South-East Kamchatka					
11. Paratunsk and Koryaksko-Avachinsk depression	1.5	28–40	700–850	15	20	60–70
11a. Kronotsky peninsula	0.9	28–40	440–550	25	34	

Note: Curie-isoterm-depths were determined using the dependence of Curie temperature on depth, according to Bagin et al. (1971).

Quaternary, as this was discovered by geological investigations (Logachev, 1968). As this process only stopped in the Quaternary, the recent Moho-temperatures should be somewhat higher than calculated.

In all other regions of the Baikal and Altai-Sayansk areas the depth of possible basalt melting, according to our data, exceeds 100 km. In such conditions the penetration of magma to the surface is difficult, even though the present temperatures of deep earth crust and upper mantle layers can be higher than those calculated. No indications of magmatic activity younger than Mesozoic age has been discovered over this territory.

In the region of the Koryaksko-Avachinsk volcanic group in Kamchatka the basalt melting temperature is attained at 60–70 km depth. The roofing of the main magma chamber is located just at these depth (Polyak, 1966). Because of the inertia of the heat field it is possible that present mean temperatures in the Upper Mantle within this region are higher than the calculated ones.

The depth of the 1200 °C isotherm under the Siberian Platform and the West Siberian plate is roughly estimated as 400–500 km.

The temperatures in the upper layers of the earth can be estimated from the results of magnetotelluric, seismic and gravimagnetic investigations, using the temperature dependence of the corresponding physical properties of rocks.

Magnetovariation and magnetotelluric deep investigation carried out in Baikal region (Gornostaev et al., 1970; Popov and Zorin, 1972; Fotiady et al., 1965) lead to the discovery of two layers of increased electric conductivity in the earth's crust and upper mantle; the depth of their occurrence changes with the transition from one tectonic zone to other (Table 3)

TABLE 3

Depth of occurrence of the surfaces of electroconductive layers in the Baikal region from magnetotelluric investigations

Region	Upper boundary depth [km]		
	First layer, after Popov and Zorin (1971)	Second layer after Popov and Zorin (1971)	Isotherms 1000–1100 from geothermal data
Southern part of Siberian Platform, Rift zone	100–120	about 200	320–390
South-Baikal Depression	16– 20	68– 80	25– 30
Tushkinskaya Depression	15– 18	58	
South-West Zabaikalie Udinsk depressions area	38	110	100–120

and is minimal in the rift zone. If the temperature is the reason of higher electrical conductivity, then the data measured indicate a high recent temperature of the earth's crust and upper mantle in the rift zone. According to Zorin (1971) the roof of the second electro-conducting layer whose resistance is estimated as 100 Ω m can be roughly identified with the loca-

tion of the 1000–1100 °C isotherm. From Table 3 it follows that both methods (magnetotelluric sounding and geothermal) provide minimum depth of the above isotherm within the rift zone, but the difference between the respective depths is large. To some extent this discrepancy may be attributed to the low accuracy of the methods. For instance, the depth of the second electroconducting layer has been estimated quite differently by various investigators (Gornostaev et al., 1970, Popov and Zorin, 1972) (see Table 3). If the only reason for the above deviations is in accuracy, then the data obtained show a heat anomaly in the rift zone, having been existing since about 30–40 million years. But such a spread of results may be caused also by the cooling of an additional heat source acting during the Neogene. Thus, information about the heat field dynamics can be gained from a complex interpretation of geothermal and magnetic investigations, in case of an adequate accuracy of the methods.

A heat anomaly in the Rift area is also confirmed by seismological investigations. We have previously mentioned the large horizontal temperature gradient between the separate tectonic zones in the Baikal area. The horizontal temperature gradient inside the earth's crust contributes to the development of thermoelastic stresses, which may be a source of seismic activity (Lubimova, 1968; Magnitsky, 1965). Thermoelastic stresses, emerging between blocks of different temperature may be roughly estimated from the formula:

$$\sigma_T = 0.1\,\alpha\,E\,\Delta T$$

where α, E are the coefficient of thermal expansion and the Young module, respectively. With $\alpha \approx 3.0 \cdot 10^{-5}\ ^\circ\mathrm{C}^{-1}$, $E \approx 3.0 \cdot 10^{12}$ dyne cm^{-2}, $\sigma_T = 0.9 \cdot 10^7\,\Delta T$. Thus, strength of the rocks of the order of 10^8–10^9 dyne cm^{-2} is reached at $\Delta T = 100$–200 °C.

Such a horizontal temperature difference is observed in the Baikal area already at 5 km depth and more, and in the Altai-Sayan area at 10 km and more. According to seismological data the foci of earthquakes lie in the Baikal Rift zone mainly at a depth of 10–12 km (Baikal Rift, 1968), whereas the depth of earthquake foci in Altai-Sayan area equals 15 ± 7 km (Tsibulchik, 1966).

Horizontal temperature variations may also explain the areas of decreased velocities (LVL) found during seismic investigations. The seismic velocity V_r in the Baikal Rift zone at the Moho surface is 7.7–7.8 km sec^{-1}, while in adjacent, relatively stable regions it is 8.1–8.2 km sec^{-1} (Krylov et al., 1972).

The effect of temperature on the velocity of elastic waves in rocks is described by

$$\Delta V = P\,\Delta T$$

where ΔV is change of velocity due to a temperature difference ΔT, while $P = (\partial V/\partial T)\,P$. If let $p = -(4\text{–}5) \cdot 10^{-4}$ km/sec °C (Berch, 1972), then ΔV will be 0.3–0.4 km/sec^{-1} that is approximately the velocity difference observed.

A LVL appears not only in the rift zone, but also in a part of the Western Baikal rift valley. This fact may indicate an increase of the temperature in the deep crust and mantle layers.

A similar comparison for the Kamchatka site, where according to seismic data the LVL ($\bar{V} = 7.2$–7.8 kmsec^{-1}) is situated at 60–160 km depth, show the accordance of the two methods.

Magnetization of rocks is known to be decreasing with increasing temperatures. At temperatures higher than the Curie point the magnetic properties disappear. So, informations about the intensity of magnetic field anomalies and the depth of occurrence of the lower margins of magnetoactive bodies allow to conclude about the temperatures in the upper mantle.

There is no definite opinion as regards the value and variability of the Curie temperature (T_c) in the crust and the upper mantle. Bagin et al. (1971) claim that the Curie temperature of titanomagnetites is reduced with depth. In this case $T_c = 300$ °C at 40 km level. The same T_c value was used by Bulmasov (1968) for the interpretation of the magnetic field in the Baikal Rift zone.

Mean depths of Curie temperatures, computed from the thermograms in Figure 3 and from the dependence T_c on T (Bagin et al., 1971) as well as the mean depth of the 500 °C isotherms for the tectonic zones discussed are given in Table 4. For high heat flows, $q \geq 1.3$–1.4 HFU, they practically

TABLE 4

Depth of the lower margins of magnetic bodies in some regions of South Siberia

Region	Depth in km		
	500 °C Isotherm (from Table 2)	Curie Isotherm (from Table 2)	Lower margine of magnetic bodies
Southern part of Siberian Platform	75	30	25
Rift zone Zabaikalie	10	10	10
Dgidinsk region	23	20	15–17
Udinsk region	32	24	15–17
West Siberian Plate	70	30	30

coincide, and their values are low: 20–30 km in regions adjoining the rift zone, 10 km in the rift zone itself. For low heat flows the depths are sharply increased up to 70–75 km, and the 500° isotherm is situated considerably lower than the "Curie isotherm". The latter circumstance shows, in our opinion, a probable reduction of T_c with depth.

The depths of Curie isotherms are compared in Table 4 with the depths of the lower boundary of the magnetoactive part of the crust obtained by interpreting local magnetic anomalies.

The somewhat greater depths of the Curie isotherm compared to that of the magnetoactive boundary in Zabaikalie, as well as the results of the seismic studies discussed imply that Neogene temperatures were higher than the recent ones.

The Curie isotherm, as inferred from Table 4 is situated practically in all regions within the "basalt" layer at 20–35 km depths (Kamchatka —

15 km). It is lifted in the "superbasalt" layer under the rift zone. Thus, the thickness of magnetoactive layers, as to our calculations, does not exceed the thickness of the earth's crust. This conclusion is valid for the majority of regions even when using the 500 °C isotherm. This isotherm is burried up to 70–75 km only in 4 regions (Siberian platform, West-Siberian Plate, Kuznetsky Alatau and Mountain Shoria).

The described results about magnetoactive thickness differs from the conclusions of Borisov et al. (1972), based on analyses of magnetic field anomalies for the USSR territory. According to these conclusions "the Curie surface" is situated below the Moho boundary line practically throughout the continents, and lower than 100 km in the southern part of Siberia.

The heat anomaly established in the Baikal Rift zone area is also reflected by the gravitational field. A negative gravitational field anomaly is observed over more heated blocks of the earth's crust because a higher temperature causes softening of the rocks. The degree of this anomaly is approximately given by the formula:

$$\Delta\sigma = \alpha\sigma\Delta T$$

Accepting for ultrabasic rocks $\alpha \approx 3 \cdot 10^{-5}\ ^\circ\mathrm{C}^{-1}$ and $\sigma = 3.35\ \mathrm{gcm}^{-3}$, we obtain $\Delta\sigma = 11.05 \cdot 10^{-5}\ \Delta T$, where ΔT is temperature deviation from its average value. Calculated horizontal T variations in the rift zone are 500–600°C, i.e. $\Delta\sigma = 0.06$–$0.07\ \mathrm{gcm}^{-3}$. If the thickness of the heated body is several tens of kilometers, the thermal softening of matter is adequate to explain the gravitational minimum existing here.

CONCLUSION

Temperature *vs.* depth in the crust have been investigated for different tectonic areas. The lowest temperatures of about 400 °C at the Moho boundary are characteristic to platform regions. The highest ones, up to 1000 °C and more were computed for the south-east Kamchatka regions and the Baikal Rift zone. Thus, the Moho boundary is not isothermic, the temperature differences along it can reach 500–800°.

Temperature distributions obtained by our calculations do not contradict the results of the electromagnetic, gravimetric, seismic and geological investigations over the area considered.

REFERENCES

Bagin, V. I., Brodskaya, S. Yu., Petrova, G. N., Pechersky, D. M., 1971. The depth of volcanic foci on the Kurilo-Kamchatsk island according to a thermomagnetic investigation of volcanic rocks (in Russian). *Izv. Akad. Nauk SSSR. Ser. Fiz. Zemli*, No. 5.

Baikal Rift, 1968. Chief Editor: N. A. Florentsov.

Beloussov, V. V., 1966. Continental Earth Crust and Upper Mantle. Nauka, Moscow.

Berch, F., 1972. Density and composition of the upper mantle (first approximation by supposing the olivine composition) (in Russian). "The Earth's Crust and Upper Mantle." Ed. P. Hart. Mir, Moscow.

Borisov, A. A., Kruglyakova, G. I., Firsova, D. B., 1972. Temperature in the mantle summit in the light of geomagnetic data analysis (in Russian). *Dokl. Akad. Nauk. SSSR* **20**, No. 5.

Farberov, A. I., Levykin, A. I., 1971. Velocities of elastic waves in Kamchatka mountain rocks at pressures up to 30 kbar. (in Russian). "Volcanism and the Earth's depth." Nauka, Moscow.

Fotiady, E. E., Vanyan, L. L., Kharin, E. P., 1965. Deep Magnetovariation soundings at the south of Central Siberia and in Zabaikalie (in Russian). *Dokl. Akad. Nauk. SSSR* **164**, No. 3.

Gornostaev, V. P., Mikhalevsky, V. P., Pospeev, V. V., 1970. Deep magnetotelluric soundings at the South Siberian platform and in the Baikal Rift zone (in Russian). *Geol. i Geofiz.* No. 4.

Krylov, S. V., Mishenkin, B. P., Petrik, G. V., 1972. On the study of the Upper Mantle part summit by GSP in Baikal Rift Zone (in Russian). Coll. Seismicity of Siberia. Part I. Editors Gaisky, V. N., Tresnov, A. A. Novosibirsk.

Logachev, N. A., 1968. Sedimentary and volcanic formations of the Baikal Rift zone. Coll. "Baikal Rift". Nauka, Moscow.

Lubimova, E. A., 1968. Thermal Studies of the Earth and the Moon (in Russian). Nauka, Moscow.

Magnitsky, V. A., 1965. The Earth's Interior and Physics (in Russian). Nedra, Moscow.

Polyak, B. G., 1966. Geothermal Features of Areas of Recent Volcanism (in Russian). Nauka, Moscow.

Popov, A. M., Zorin, Yu. A., 1972. Deep magnetotelluric soundings in the region of Tunkinsk Rift depression (in Russian). Collect. Geofizika (Scientific Information) Acad. Sci. USSR, Irkutsk.

Tsibulchik, I. D., 1966. On the depths of earthquake foci in the Altai-Sayan area. *Geol. i Geofiz.* No. 5.

Zorin, Yu. A., 1971. Newest Structure and Isostasy of the Baikal Rift Zone and Adjoining Territories (in Russian). Nauka, Moscow.

HEAT FLOW INVESTIGATION IN PERMAFROST REGIONS

P. I. MELNIKOV, V. T. BALOBAEV, I. M. KUTASOV,
V. N. DEVYATKIN

In determining the permafrost temperature and thickness, advantage is taken mainly of results of geothermal observations in deep boreholes. Due to specific features of the frozen zone, representative data can be obtained only from multiple observations over an extended time. At present, numerous geothermal observational data of considerable interest relative to the deep drillholes in Yakutia are available.

Field observations have been carried out during 15 years using semiconductor resistance thermometers which allow to determine the temperature with an error of 0.03–0.05 °C. In the period of 15 years, 5–10 temperature measurements were made in each borehole. The analysis of thermometric observational data shows that during the drilling process the natural rock temperature field may be considerably disturbed along the length of the hole even at significant distances from the axis. The presence of permafrost considerably affects both the character and the duration of the re-establishment of thermal equilibrium. The latter may last more than 10 years (Balobayev, 1971).

Let us consider in greater detail the re-establishment of the natural temperature field after drilling on the example of the Bakhynai borehole (Fig. 1).

The hole was drilled from May 17, 1956 to April 8, 1958 to a depth of 2824 m by rotary drilling with clay mud as circulating fluid. Sands and poorly cemented sandstones interbedded with clays and aleurolites were penetrated from 19 to 1500 m below the surface. Observations show that a northern borehole returns to thermal equilibrium particularly slow. In the past 10 years the temperature in the Bakhinai hole dropped to a subfreezing point only from above to a depth of 300 m, permafrost thickness being about 680 m. The duration of freezing of the layer thawed by drilling strongly depends on natural rock temperature. As seen from Figure 2, a decrease in rock temperature by 1 °C may reduce the freezing time by a factor of 4–5. The re-establishment of thermal regime in the Bakhynai hole, as in the case of other holes, is accompanied by the formation of practically gradient-free sections along the length of the hole (Fig. 1). In consequence, if a borehole has no sufficient time to return to thermal equilibrium with its surroundings, an incorrect interpretation of gradient-free sections may be possible due to various geological and geographical factors. A prolonged process of the return of the borehole to thermal equilibrium presents serious problems in measuring the permafrost thickness. The rock freezes especially slowly at the base of permafrost (Balobayev, 1971; Melnikov, 1962).

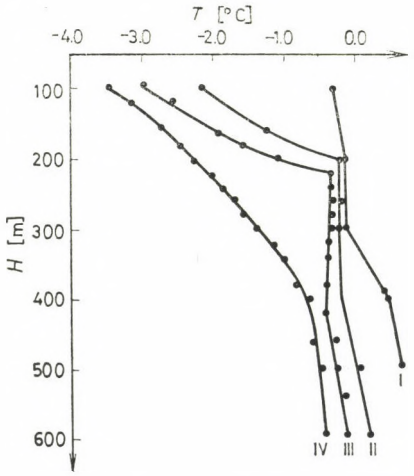


Fig. 1. Re-establishment of the temperature field along the Bakhynai hole. Temperature observations were conducted after completion of drilling, in 0.4, 1.5, 3.4 and 10.4 years, respectively

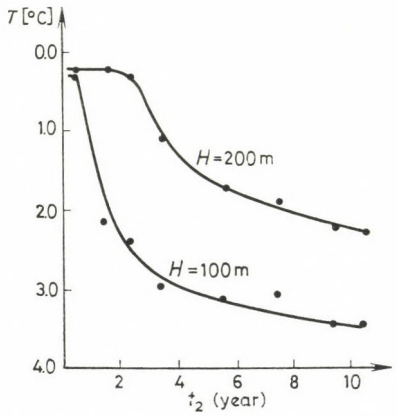


Fig. 2. Temperature re-establishment curve at 100 and 200 m depths in the Bakhynai hole

Naturally, because of economic and logistical reasons, it is difficult to conduct prolonged temperature observations simultaneously in many deep holes on the vast territory of the north-eastern USSR. In this connection, the position of the lower boundary of permafrost is often defined by extrapolating the temperature curve to the freezing point. In doing so, it must be ascertained that the temperatures in the upper layers, by which the extrapolation is made, are with a fair accuracy close to natural temperatures. Let us show that after completion of freezing the curve of the re-establishment of temperature equilibrium in the hole can be described analytically. It is well known that in fine-grained frozen ground water freezes in a certain temperature range. Because of this, the course of the re-establishment of ground temperature equilibrium after completion of drilling can be described by the following diagram (Fig. 3). In this case,

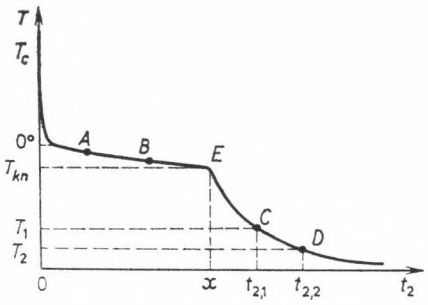


Fig. 3. Re-establishment of temperature equilibrium in a borehole

denote by T_{kn} the temperature at the completion of phase transitions of water to ice.

Suppose we have conducted a number of thermometric field observations, A, B, C, D (Fig. 3). Taking into account the extreme slowness of the freezing process, it can be assumed that at the completion of freezing x the temperature field in the hole and frozen ground is described by the following distribution:

$$f_1 = \begin{cases} T_{kn}; & 0 \leq r < r_0 \\ T_{kn} - (T_{kn} - T_n)\dfrac{\ln r/r_0}{\ln R_e}; & r_0 \leq r \leq r_0 R_e \\ T_n; & r > r_0 R_e \end{cases} \tag{1}$$

$$R_e = 1 + D_0\sqrt{F_0}; \qquad F_0 = \frac{x a_M}{r_0^2}$$

where R_e – is the effective radius of influence,
D_0 – const.,
T_n – the natural rock temperature,
a_M – the rock's thermal diffusivity,
r_0 – the hole radius,
r – the cylindrical coordinate.

As to the given form of the temperature distribution (1), the following equation was found earlier for the temperature along the hole axis (Kutasov, 1971)

$$\frac{T(0_\perp, \bar{t}_2) - T_n}{T_{kn} - T_n} = -\frac{Ei - \left(\dfrac{D}{n}\right) + \ln n - D_1}{\ln F_0 + 2\ln D_0}, \tag{2}$$

$$\bar{t}_2 = t_2 - x, \quad D = 1.1485, \quad D_1 = 0.7154, \quad 2\ln D_0 = 1.5248$$

where $Ei(-\sigma)$ is the exponential integral function.

Suppose we have two temperature measurements C and D (Fig. 3) at time $t_{2.1}$ and $t_{2.2}$. The time will be counted from the moment x:

$$\bar{t}_{2.1} = t_{2.1} - x \qquad \bar{t}_{2.2} = t_{2.2} - x$$

It is convenient to express the quantity x in fractions of $t_{2.1}$

$$x = m t_{2.1}; \qquad 0 < m < 1$$

Then

$$n = \frac{t_2 - x}{x}; \quad n_1 = \frac{1 - m}{m}; \quad n_2 = \frac{k - m}{m}; \quad k = \frac{t_{2.2}}{t_{2.1}}$$

In using values, $T_1 = T(0, t_{2.1})$ and $T_2 = T(0, t_{2.2})$ we obtain from the

formula (2) an equation for the determination of the parameter m

$$\gamma = \frac{T_{kn} - T_1}{T_{kn} - T_2} = \frac{\ln(1-m) + Ei\left(-\frac{Dm}{1-m}\right) + B}{\ln(k-m) + Ei\left(-\frac{Dm}{1-m}\right) + B} \tag{3}$$

where

$$B = \ln \frac{a_M t_{2.1}}{r_0^2} + 2 \ln D_0 - D_1$$

Equation (3) admits only a graphical solution.

The natural temperature of frozen ground at a given depth can be determined from the formula (2) in two ways. In the first case the parameters $T_1 = T(0, t_{2.1})$, n_1, and in the second the parameters $T_2 = T(0, t_{2.2})$, n_2 are used.

At the Permafrost Institute, Siberian Division, USSR Academy of Sciences, authors have performed experiments on modelling the "disturbance-re-establishment" process of the temperature field in the surroundings of the hole. A test site 4 m in diameter was selected in the underground laboratory (research cave) of the Institute at a depth of 15 m where the temperature is held constant (−3.8 °C). The main hole was 1 m deep and 4 cm in diameter. The thermal action of the drilling mud was imitated by an electric heater.

Observation holes were drilled at 7 to 192 cm from the main hole. Temperatures in the main and observation holes were measured at depths of 20, 50 and 80 cm. Experiments were carried out in frozen sand containing 20 % moisture by weight. We will consider in more detail experiment No. 2.

In this experiment, the heater of 58 kcal/h capacity operated during 91 hours. Results of these observations are shown in Table 1 (second column).

TABLE 1

Experimental (T_e) and calculated (T_p) values of transient temperature. Test No. 2

t_2 [hour]	T_e [°C]	$t_{kn} = -0.1$ °C T_p	$T_{kn} = -0.2$ °C T_p
51	−0.37	–	–
54	−1.35	−1.35	−1.35
57	−2.21	−2.21	−2.21
60	−2.52	−2.53	−2.48
63	−2.71	−2.71	−2.64
66	−2.82	−2.84	−2.78
72	−3.03	−3.02	−2.94
78	−3.09	−3.15	−3.06
96	−3.33	−3.38	−3.27
120	−3.49	−3.52	−3.41
144	−3.60	−3.60	−3.48

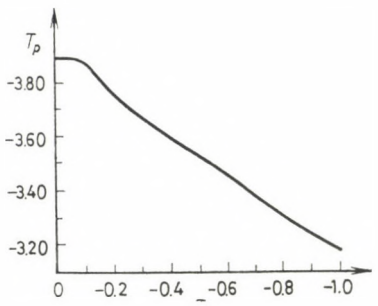


Fig. 4. Dependence of the predicted temperature in frozen sand on the temperature at the completion of freezing

For given sands, temperatures below -1 °C lie evidently beyond the temperature spectrum of phase transitions.

Therefore, $T_1 = -1.35$ °C; $T_2 = -2.21$ °C were taken as initial temperatures for calculations. The error in computing the parameter γ from test data depends on the determination accuracy of the value of T_{kn}. It was known that the given type of sand freezes practically at -0.2 °C. Authors have established the relationship between the predicted temperature of frozen ground and the prescribed accuracy of the parameter T_{kn} (Fig. 4). It is seen from the graph that, if $T_{kn} < -0.3$ °C, phase transitions do not take place, because in this case the temperature of frozen ground is > -3.8 °C.

In constructing the graph (Fig. 4), the parameter γ was determined in each case. Then the value of m was defined from the curve $\gamma = f(m)$. Values of the transient temperature for two different T_{kn}-s were found from the formula (2) (Table 1). Comparison between experimental and calculated data shows that the temperature $T_{kn} = -0.1$ °C fits well the test results. In applying formulas (2, 3) for the calculation of the natural temperature of frozen ground from data obtained during field observations, consideration should be given to the fact that these relationships take into account only radial heat exchange. Hence, it is not recommended to use the suggested method for depths close to the base of permafrost, since, in this case, the rate of re-establishment of thermal equilibrium after completion of drilling is, to a large extent, governed by freezing from above. Thus, knowing from calculations or field observations temperature values for two depths, one can determine the value of the temperature gradient in homogeneous frozen strata (A_M). The heat flow from the permafrost side to the phase interface between frozen and unfrozen zones is given by

$$q_M = A_M \lambda_M$$

where λ_M is thermal conductivity of the frozen ground. Correspondingly, the heat flow from the side of ground having positive temperature to the interface is given by $q_T = \lambda_T A_T$. The relation between q_T and q_M is expressed by Stephan's condition $q_M - q_T = ZWh'$, where W is the ice content per unit volume of ground; Z is the heat of fusion of ice; h is the vertical coordinate of the interface surface between frozen and thawed zones; h'

TABLE 2

Geothermal parameters of holes in Yakutia

	Location	Coordinates		Depth of investigation [m]	Time after drilling [year]	Permafrost thickness [m]	Geothermal gradient [°C/100 m]		Heat flow (q_T) [mWm^{-2}]
		N.L.	E. Lon.				A_M	A_T	
1.	Deputatsky (30 holes)	69°17	139°51	500	2–4	250–500	1.8 –3.2	2.6	80.0
2.	Ege-Khaya (47 holes)	67°32	134°54	540	1–4	200–400	1.6 –2.8	2.4	67.0
3.	Ulakhan-Egelyakh (20 holes)	66°48	134°36	400	1–4	200–330	1.3 –3.3	2.4	75.0
4.	Sarylakh (13 holes)	64°27	141°40	590	1–2	290–380	2.0 –3.2	2.5	84.0
5.	Bakhynai sett., hole No. 1-R	66°01	123°56	1500	10.4	650	1.0	2.13	50.0
6.	Sobo-Khaya, hole No. 2-R	64°17	126°27	800	10.0	80	2.5	3.30	59.0
7.	Promyshlenny sett., hole No. 5-R	64°15	126°15	975	12.2	140	1.98	3.43	54.0
8.	Kysyl-Syr sett., hole No. 3-R	63°57	123°25	1475	7.8	460	1.30	3.00	50.0
9.	Nedzheli sett., hole No. 2-R	63°34	124°43	1475	6.1	415	1.00	3.25	54.0
10.	Khatyryk sett., Namsk. hole No. 1-R	62°56	129°28	850	15.4	485	0.68	2.17	46.0
11.	Kenkeme, hole No. 2-C	62°00	128°30	500	2.0	390	0.90	2.10	35.0
12.	Yakutsk, hole No. 5	61°55	129°42	500	3.5	330	0.69	1.36	42.0
13.	Pokrovka sett., Amginsk. hole No. 1-R	60°43	131°34	500	14.3	225	1.72	1.86	50.0

is the rate of freezing (thawing). Steady-state heat flows in frozen and unfrozen zones will be equal and $h' = 0$. If $q_M > q_T$, we obtain $h' > 0$, i.e. an increase in the thickness of permafrost. Finally, with $q_M < q_T$ we have $h' < 0$, i.e., a decrease in the permafrost thickness with time. Thus, the relation between the heat flows in frozen and thawed zones at their phase interface may serve as an indicator of the thermal state of frozen ground. From this it follows that in permafrost regions it is necessary to identify the values of q_M and q_T.

However, important information on the rate of freezing or thawing can be obtained from the comparison of the temperature gradients in frozen and thawed zones, since thermal conductivity of dense sedimentary rocks (sand, sandstones, shales, limestones), when frozen increases only by 5–20%. Table 2 gives the geothermal parameters for boreholes in Yakutia. Thermal conductivity of samples of thawed ground (λ_T) was determined by the steady-state heat flow method. When calculating q_T, in some cases, values of λ_T for cores obtained from nearby boreholes were also used (with regard to lithology). In consequence of this, we estimate the accuracy of determining the value of q_T as 10–20%.

Actually, points 1–4 (Table 2) are heat flow stations because temperature measurements made in 13–47 boreholes were used for construction of the geotemperature field in these mountain regions. The geotemperature field was determined using spatial modelling on the USM-1 analog computer. Preliminary analysis of data obtained from temperature observations in deep boreholes reveals that these areas are characterized by a steady-state regime of permafrost layers ($q_T = q_M$). This allowed to simulate the geotemperature field on the basis of the Laplace equation. Variation in values of A_M reflects the influence of the mountain relief on the temperature field. Quantities of A_T for the above mentioned four locations were obtained from simulation and they represent values of the subsurface geothermal gradient. It is seen from Table 2 that $q_T \approx q_n$ and $h' \approx 0$ also hold for the Amga borehole. For all other holes $q_T \geqslant q_M$ and $h' < 0$.

Thus the areas where these holes are located are characterized by decreasing permafrost thickness. It is seen from computations that the rate of thawing accounts for 1–2 cm/year. The results of *in situ* observations (Table 2) show that, in principle, it is impossible to determine the terrestrial heat flow from temperature measurements within frozen strata. Because of the movement of the interface between unfrozen and frozen ground, the temperature field in the thawed zone may also be disturbed (1). As a result of an approximate solution of the ground thawing problem, the disturbed gradient in the unfrozen zone is given by

$$\frac{dT_T}{dy} = A_T\left[1 + \frac{h'}{a_T}(H - y)\right], \quad h < y < H$$

where y is the vertical coordinate, a_T the thermal diffusivity of the unfrozen ground, H the time-dependent thickness of the zone with disturbed temperature field in thawed ground.

The true values of the terrestrial heat flow can be obtained from measurements made below the depth H. Above this boundary, the heat flow

during the permafrost thawing may be lesser, while by freezing it may be greater.

Thus, the amount of heat flow H affects both the distribution of temperatures in permafrost and changes in its thickness with time.

The findings presented above must be taken into account when conducting geothermal observations in permafrost regions (cryolithozone).

REFERENCES

BALOBAYEV, V. T., 1971. Collected articles: Geocryological Investigations. Yakutsk.
KUTASOV, I. M., 1971. Exploration and Protection of Mineral Resources, No. 2.
MELNIKOV, P. I., 1962. Collected articles: Permafrost and Related Phenomena on the Territory of the Yakutian ASSR. Publ. Acad. Sci. USSR.

CHAPTER 5

DEEP ELECTROMAGNETIC INVESTIGATIONS AND THEIR GEOTHERMIC INTERPRETATION ON TEST AREAS

Edited by

A. ÁDÁM and M. N. BERDICHEVSKY

INTRODUCTION TO CHAPTER 5

A. ÁDÁM

In the fifties the number of geomagnetic soundings, in the sixties that of magnetotelluric and magnetovariation soundings increased significantly. The induction methods revealed more and more conductivity anomalies all around the world, so in the territory of the KAPG-countries, too. New possibilities opened to check and develop theories on the nature of the anomalies and on their role in physical processes of the earth. The importance of deep geoelectrical data has increased in global tectonics.

A great number of interesting tectonical units are included here, e.g. consolidated crystalline shields, platform areas and youngest orogenic zones.

The chapter is divided into five parts. The first four deal with the geoelectric structure of the German-Polish depression, the Czech Massive, the Pannonian Basin, the Carpathians, as well as their transition zones. Depth-temperature functions are used to reveal correlations between geothermal and geoelectric parameters in the earth's crust and upper mantle, and to support geodynamical hypotheses (e.g. for the Pannonian Basin).

The contact area of this region and the Russian Platform is the Carpathian Mts. Some data on its Sovietic part are contained in the fourth part (Bondarenko, Bilinsky, Kutas, Rokityansky).

The fifth part contains electromagnetic induction data from 16 areas of the Soviet Union and their interpretation.

About half of the papers refer to the Asian part of the Soviet Union. We deemed it necessary to show illustrative results on the geological structures of Soviet Asia. A general summary for this part is written by the coeditor of this chapter, M. N. Berdichevsky.

The tectonical units described in the first four parts can be characterized by a wide difference of geothermal (heat flow) values. The widest range is found in Czechoslovakia where tectonic units of the most differing age are present (e.g. the Czech Massive and the Carpathians). The eminent temperature of the Pannonian Basin is well-known. From the points of view of both geothermics and geoelectricity transition zones among them, mainly fracture zones of great extension are of interest (e.g. between the Inner and Outer Carpathians, the Rhine-graben, the fracture zone of Transdanubia (Hungary), connected with Pliocene volcanism). Conductivity anomalies are hopeful sources of geodynamical informations.

The papers presented in this chapter yield in addition to their informative value (geoelectric data), experiments for the interpretation of the measurements. Data are first of all to be freed from distortion effects of (superficial) tectonic structures; reliable data for the location of conductive zones can only be collected afterwards. This elimination has not yielded the expected

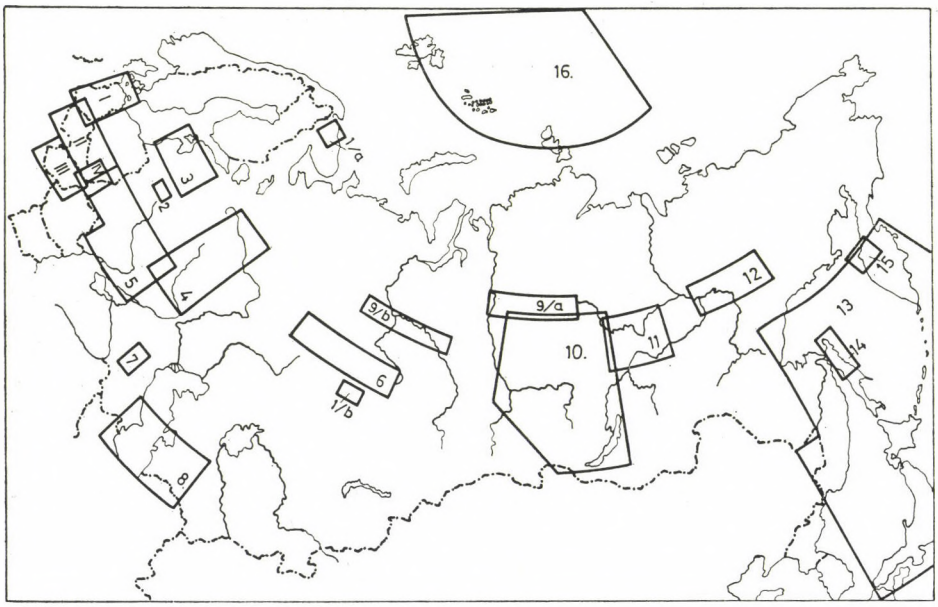


Fig. 1. Areas treated in Chapter 5

Roman numbers refer to papers of sections: I. – German-Polish sedimentary basin, II. – Czechoslovakia; III. – Pannonian Basin; IV. – East Carpathians.

Arabic numbers refer to papers of section V. (USSR): 1/a – Baltic-Scandinavian shield; 1/b – Kokchetav Block; 2 – Belorussian Massif; 3 – NW-part of the Russian Platform; 4 – Central part of the Russian Platform; 5 – Ukrainian shield; 6 – Ural; 7 – Eastern Pre-Caucasus; 8 – Turkmenia; 9/a – Tungus syneclise; 9/b – West Siberian Plate; 10 – Siberian Platform and Baikal Rift zone; 11, 12 – Yakutia; 13 – Far East; 14 – Sakhalin; 15 – Kamchatka; 16 – Arctic Ocean

result in all cases, as depth data prove. It is possible that a part of the distortions will not be resolvable in spite of the increased use of computers due to the ambiguity of the problems. Methodical investigations are of great importance on this field. Reliability of data is to be increased by measurement-nets. A statistical interpretation of these data would offer possibilities for regional studies, but at the same time it prevents to find local changes.

On all areas investigated, some fitting of geothermal and geoelectric data has been carried out. Comparisons of states (e.g. partial melting) in the different papers shows the dependence on the choice of rock models and depth-temperature functions. The differences and contradictions point to the fields where further data collection and laboratory experiments are needed.

I. GERMAN-POLISH SEDIMENTARY BASIN

NATURE AND POSSIBLE CAUSES OF THE ANOMALOUS BEHAVIOUR OF ELECTRIC CONDUCTIVITY IN THE NORTH OF THE GDR, POLAND AND THE FRG

G. PORSTENDORFER, W. GÖTHE, K. LENGNING, CH. OELSNER, R. TANZER, E. RITTER

INTRODUCTION

The picture obtained from geomagnetic induction arrows (Wiese-arrows) of a large-scale Central European conductivity anomaly extending from Poland over the north of the GDR into the FRG is analyzed in detail, particularly for the central part of the territory of the GDR.

From geomagnetic and magnetotelluric measurements areas could be delimited, where the longitudinal conductivity of the crustal zones participating in the conductivity anomaly reach or surpass 5000 Ω^{-1}.

A detailed analysis of electrical borehole measurements of the well-conducting sedimentary layers of the Neozoic and Mesozoic allowed to design a real horizontal-inhomogeneous model for the covering layers along a north-south section through the anomaly for subsequent computer calculation. In this, a comparison between measured and calculated magnetotelluric sounding curves showed that the typical trend of the sounding curves cannot be explained by longitudinal conductivity and horizontal inhomogeneity of the covering layers alone, but that deeper-lying factors must play a role, too.

From a geothermal crustal section along the same profile also calculated on a computer and by using results of Soviet sample investigations under extreme PT-conditions a plausible hypotheses could be stated for the distribution of conductivity in the deeper layers of the lithosphere, which agrees better with the actually measured shapes of the magnetotelluric sounding curves.

1. DESCRIPTION OF THE CONDUCTIVITY ANOMALIES

The existence of a larger anomaly of the electrical conductivity in Central Europe manifests itself mainly in the opposite behaviour of the Z-components of natural magnetic variations along meridional sections, of which Figure 1 shows an example.

Wiese (1955) performed pioneer work and introduced a suitable magnitude of evaluation. This Wiese arrow requires a two-dimensional distribution of conductivity and is defined for harmonic variations by

$$c = \frac{|H_z|}{|H_x| \cos(\varphi_{Hx} - \varphi_{Hz})}$$

$|H_z|$ = Amplitude of the Z-component

$|H_x|$ = Amplitude of the horizontal field component normal to the strike of the conductivity anomaly

φ_{Hz} = Phase of the Z-component

φ_{Hx} = Phase of the H_x-component.

In other words, c corresponds to the instantaneous amplitudes of H_x and H_z at the time of the maximum of H_z. c is vertical to the axis of the conductivity anomaly and points from the well-conducting to the bad-conducting medium.

In the centre of the anomaly c disappears and it shows a maximum at the margins within the range of the strongest horizontal inhomogeneity.

Measurements made in Central Europe resulted in a pattern of Wiese arrows represented in Figure 2.

Three axes of more considerable conductivity anomalies at once strike the eye:

1. An axis striking almost east-west in the north of Poland, the GDR and FRG (the so-called "North-German-Polish conductivity anomaly").

2. An axis approximating to the Carpathian Arch in Southeast Europe on the territory of Czechoslovakia, Poland and the Soviet Union (the so-called "Carpathian anomaly").

3. An axis trending from the southwest of the FRG in the direction of Göttingen (in the south: the so-called "Upper Rhine Graben anomaly", in the north: the so-called "Göttingen anomaly").

Anomaly 1 for the central part of Europe is that determining the regional picture of the Wiese arrows. It is especially anomaly 3 that results only in a deviation from the predominant azimuth of the Wiese arrows, a simple vectorial composition of the Wiese arrow based upon the Wiese arrows of two individual anomalies being impossible (Göthe et al., 1975).

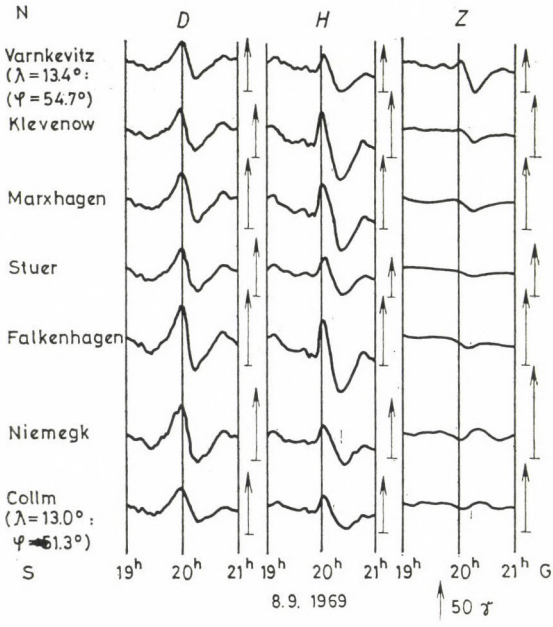


Fig. 1. Character of the geomagnetic variations along a north-south profile in the GDR

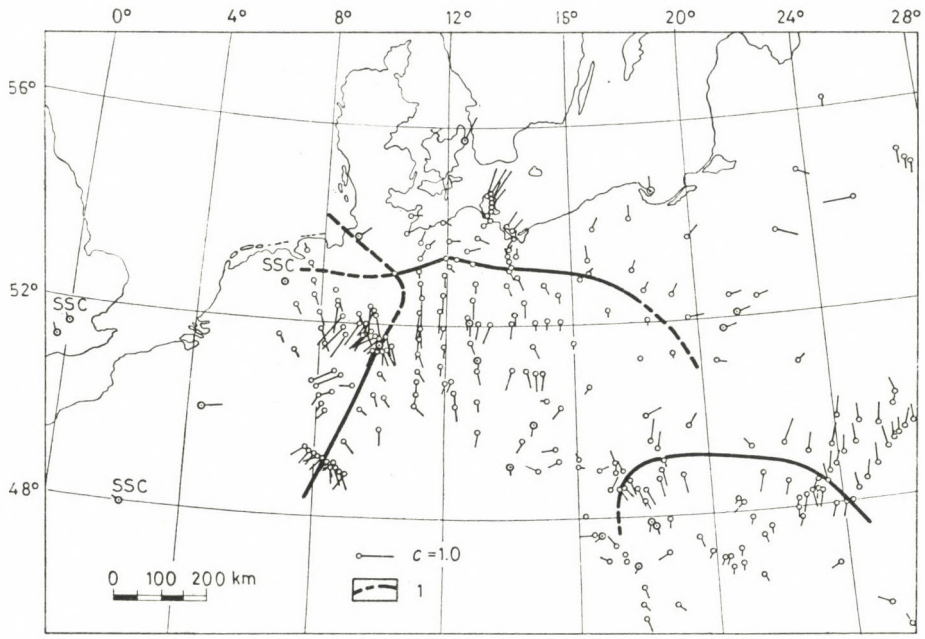


Fig. 2. Wiese-arrows in Central Europe for $T \approx 20$–60 min after Ritter (1970). 1 – axes of conductivity-anomalies

The maps of the Wiese arrows for different period-groups worked out for the territory of the GDR by Ritter (1970) based upon measurements of Wiese and of his own (see Fig. 3) show the following characteristics:

Conformable for all period groups:

In the north of the GDR (Isle of Rügen): Strong increase in the amount of c with predominant arrow direction north-north-east.

In the south of the GDR (starting from the region north of Berlin): Strong increase in the amount of c with subsequent gradual decrease towards the south with predominant southward arrow direction. (Relative minimum in the region south of Leipzig.)

Different for the individual period groups:

Concerning the central part of the anomaly in the north of the GDR amounts of c disappearing for short periods or relatively small with frequent phase inversions of H_z are characteristic, whereas for longer periods (18–40 min) a predominant eastward direction of the arrows becomes visible, which, for greater periods, again turns to a northeast direction.

The anomaly is not only visible in the period-interval of bay-disturbances but also in the S_q-variation (active period 14 hours). Fig. 6 (p. 504) shows

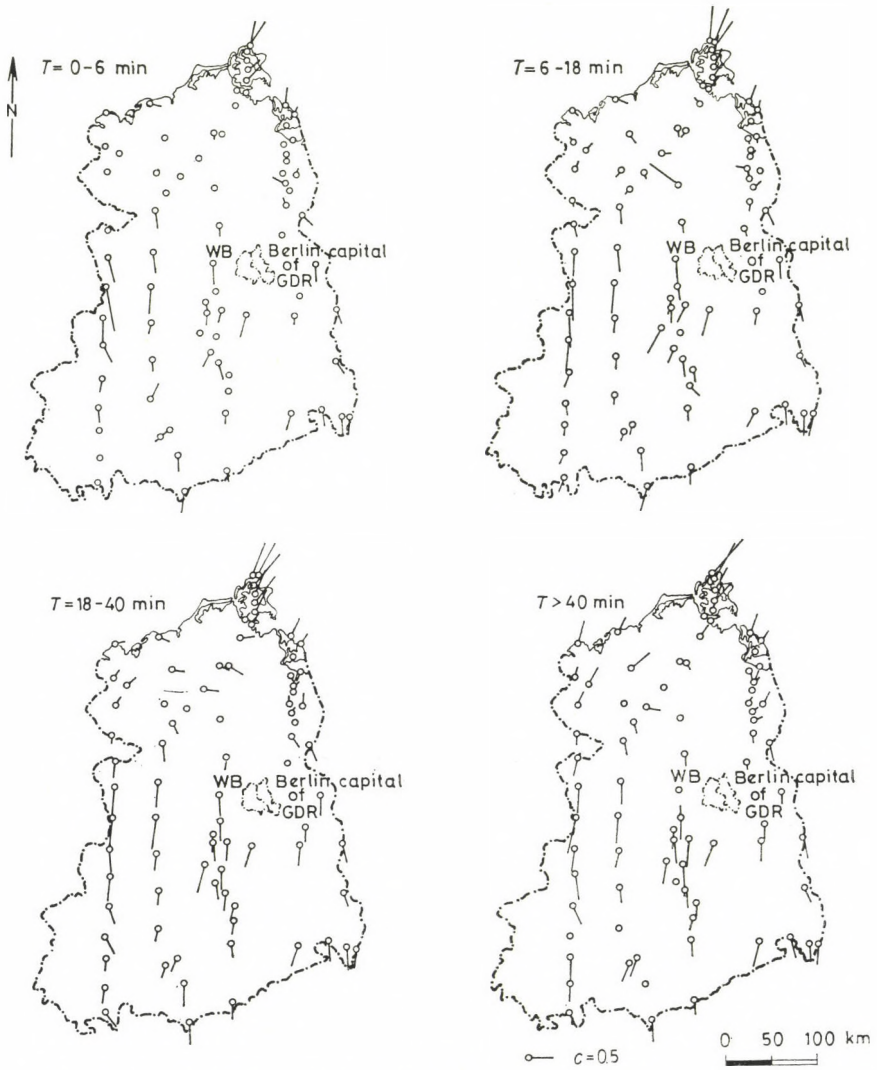


Fig. 3. Wiese-arrows for the territory of the GDR of different period-groups, after Ritter (1970) ($|c| = \pm 0.05$, azimuth $c \pm 7°$)

the results of a north-south-profile from the Baltic Sea to the Niemegk Observatory, given by Fanselau (1970).

Both the differences of the S_q-ranges in H_x and H_z show an anomalous behaviour, and especially the differences of H_z are very similar to the corresponding amplitudes of bay-disturbances.

From this behaviour it becomes evident that in the nature of the anomaly various lateral and vertical conductivity anomalies should have a share.

2. THE CAUSES OF THE ANOMALIES

A first possibility of explanation strikes the eye at once, i.e. the explanation offered by the well-conducting sedimentary layers of the large sedimentary basin extending from Poland over the north of GDR into the FRG (Fig. 4).

It can be seen that on the territory of Poland the axis of the conductivity anomaly closely approaches the dead level floor of the basin, while westwards an increasing divergence between the dead level floor of the basin and the anomaly axis is recorded.

There are in principle three ways to arrive at quantitative conceptions on the longitudinal conductivity S of the well-conducting layers participating in the anomaly:

1. Estimation of S from the ratio of the "anomalous" portion of the magnetic variations to the "normal" one based upon magnetotelluric calibration curves at observatories. This course was followed by Rokityansky (1972) who obtained a good *a priori* guess about the conductivity distribution

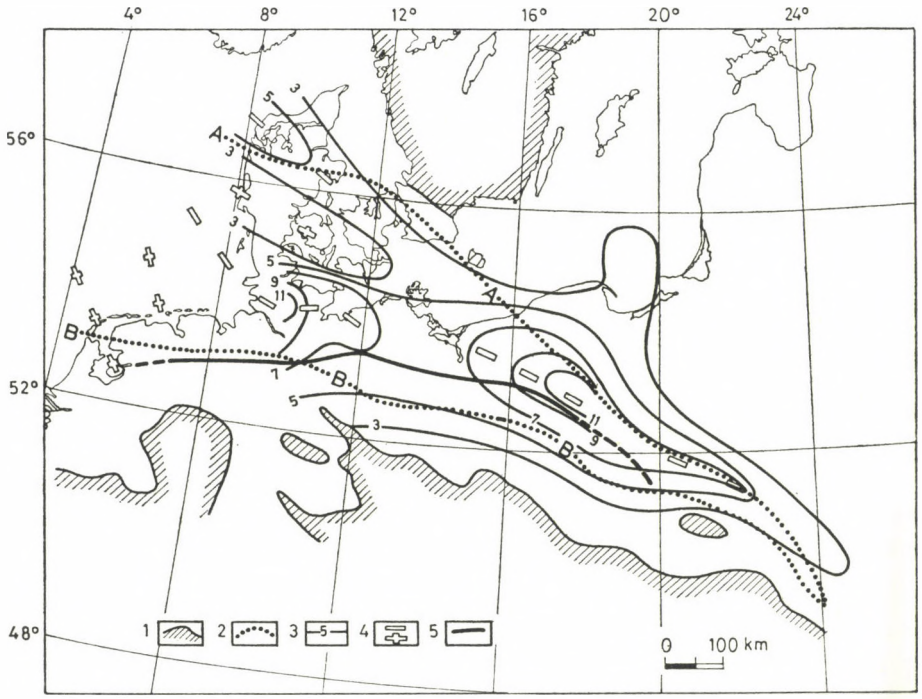


Fig. 4. Map of the probable base of the sedimentary layers in Central-Europe, constructed after International Tectonical Map (1964), German Research Group (1964) Sorgenfrei (1966), Skorupa (1970), Levin (1971)

1 – outcropping base at the surface of the earth; 2 – A – probable south-border of caledonical folded basement; 2 – B – probable north-border of varistical folded basement; 3 – lines of equal depth of the non-folded sedimentary basin; 4 – anticlinal and synclinal zones; 5 – axis of the conductivity anomaly

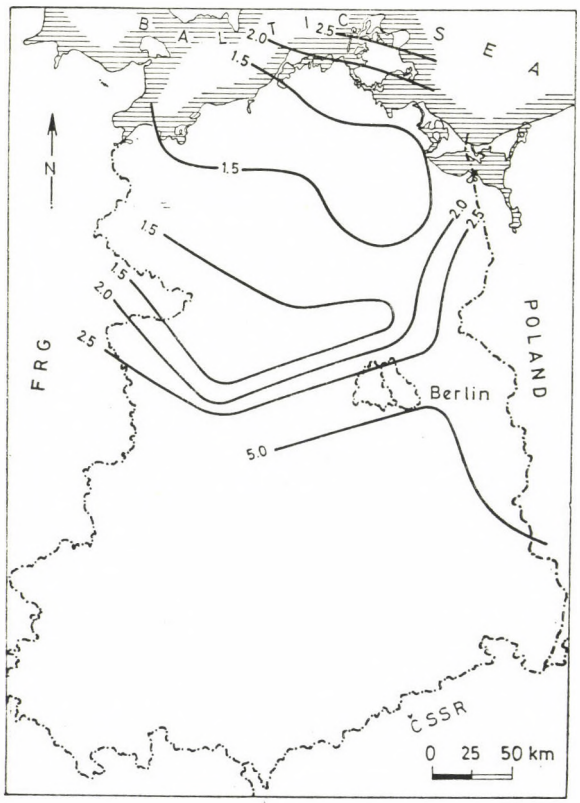


Fig. 5. Relative shape of the medium specific longitudinal resistivities of the Mesozoic and Neozoic layers, related to the minimal value of about 1 Ωm, after E. Porstendorfer

of the "North-German-Polish" conductivity anomaly (see Fig. 57 of Rokityansky, 1972).

2. Calculation of the specific longitudinal resistance of longitudinal conductivities of the conducting Neozoic and Mesozoic layers from borehole measurements. This was done by E. Porstendorfer (1968) who succeeded, within limits of accuracy of 10%, to estimate the contribution of the well-conducting layers above the Zechstein salt to the total anomaly and to determine the distribution of the mean specific longitudinal resistance in the uppermost layers (Fig. 5). The evaluation showed that the minimum resistances were in the order of magnitude of about 1 Ωm, i.e. that the area of the conductivity anomaly possesses an extraordinary low resistivity even in the uppermost overlying beds. On the sedimentary layers below the high-resistivity Zechstein the electric borehole measurements give a heterogeneous picture characterized by frequent occurrences of volcanic rocks in the Rotliegendes. It is concluded that there may be local well-conducting layers down to 5 Ωm, but generally resistances greater than 30 Ωm should be expected.
3. Areal surveys of magnetotelluric sounding curves and estimation of the total longitudinal conductivity from the asymptotic behaviour of the

sounding curves for long periods. This approach was initiated by Porstendorfer (1965) and later continued on a large scale by the VEB Geophysik, Leipzig (Thieme, Engelmann, Sachweh, Rauch, Terekhin, Nikitenko).

The magnetotelluric sounding curves confirm the apparent picture of the petrophysical parameters of the covering layers above the Zechstein salt as they were derived from borehole measurements. In the period range up to 100 sec there is a possibility to determine the longitudinal conductivity of the layers up to the Zechstein salt from the ascending curve branch.

In the period range $>$ 100 sec distinct differentiation occurs between the sounding curves taken in the predominant direction of current (E-polarization) and perpendicularly to it (H-polarization). The predominant direction of current is distinctly northwest-southeast within the anomaly and could be determined both from absolute telluric ellipses, magnetotelluric impedance diagrams and extremely long telluric measuring lines. The directions of current drawn in Figure 6 were obtained either from numerous individual measurements in the respective areas of measuring by averaging ($\pm 10°$) or from the telluric measurements on extremely long measuring lines carried out by Lengning (1968).

Curves of H-polarization drop in the GDR in the range of larger periods to low apparent resistivities, and curves of E-polarizations reveal a stepped

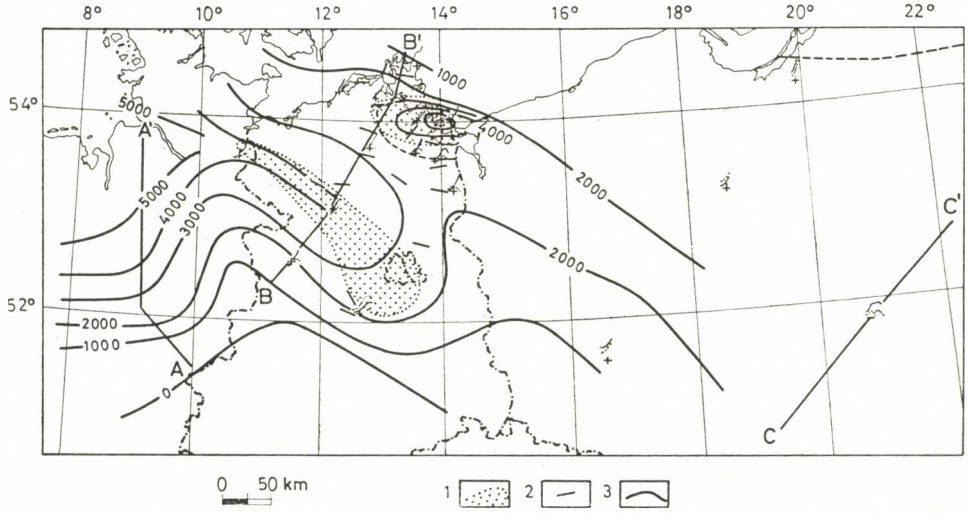


Fig. 6. Integral longitudinal conductivities of the North-German-Polish conductivity anomaly determined from geomagnetic and magneto-telluric deep soundings. Typical magnetotelluric sounding curves and electrical main directions are also shown 1 – districts with differences greater than 2000 Ω^{-1} between the magnetotelluric integral longitudinal conductivities and the longitudinal conductivities, determined from the evaluation of well-logs of layers above the Zechstein-salt; 2 – predominant directions of the electrical field, determined from 5—8 single values; 3 – line of equal integral longitudinal conductivity in Ω^{-1}. The sounding curves belong to E-polarization, resp. H-polarization (dotted line). The coordinate-cross is the intersection of the line $\varrho_s = 1\ \Omega$ m and $\sqrt{T} = 10\ \mathrm{sec}^{1/2}$. AA', BB', CC' – profiles of the computer-calculations, shown in Fig. 10

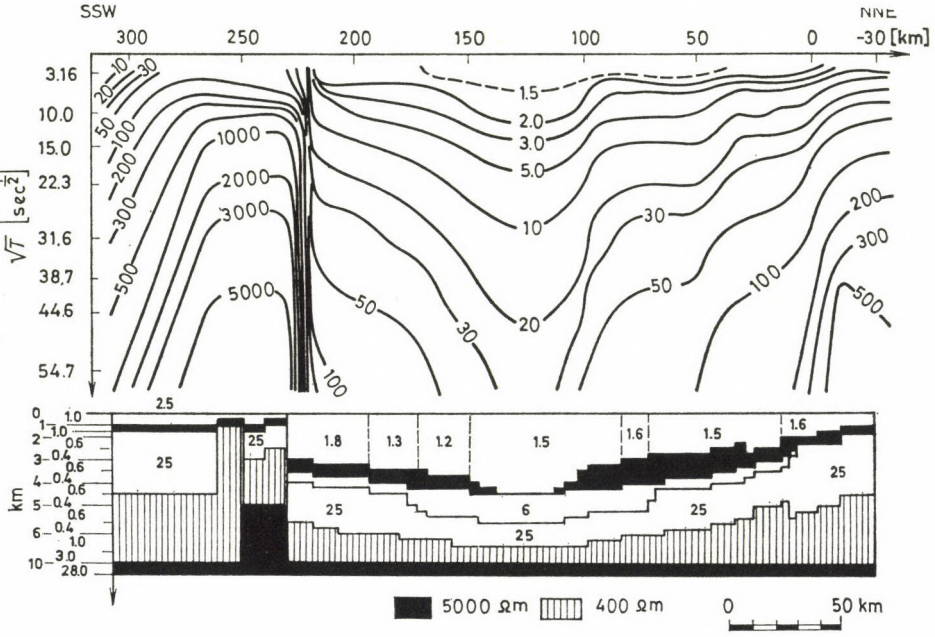


Fig. 7. Results of a computer model-calculation along the profile BB' of Figure 6 for H-polarization without respect of well conducting layers in the deeper lithosphere. The numbers give the apparent specific resistivity (upper part of the figure) resp. the fictitious true specific resistivity (lower part of the figure) in Ωm

structure with subsequent further rise. To get an impression of the shape of the sounding curves within the range of the anomaly, curves were selected from Poland, the GDR and the FRG as shown in Figure 6. From the asymptotic final branches of the E-polarization curves the total longitudinal conductivities can be determined. They well agree with the description given by Rokityansky (1972) of the total longitudinal conductivity and confirm the calculated maximum values of about 5000 Ω^{-1}.

Besides this, a second extremely well-conducting area results within the Isle of Usedom. For a vertical subdivision of the causes contributing to the anomaly, it is first necessary to subtract the longitudinal conductivities met in boreholes.

The areas with deviations greater than 2000 Ω^{-1} between the total longitudinal conductivities determined by magnetotelluric measurements or by geomagnetic deep sounding, and the conductivities obtained by electrical borehole measurements to the Zechstein are represented in Figure 6 in dotted lines. In this, also the longitudinal conductivities for the Mesozoic sedimentary range were taken into account that were found by Steveling (1973) along a profile Wingst-Göttingen in the FRG.

Thus, those areas are delimited where "deeper causes" of the conductivity anomaly are to be expected.

3. MODEL CALCULATIONS AND CONCLUSIONS

In a quantitative interpretation of the sounding curves for such an inhomogeneous medium it should be taken into account that the probe curves of the apparent resistivity as function of the period reflect the behaviour of resistance distribution both with depth and with horizontal distance.

Therefore, along profile BB' running across the GDR from southwest to northeast a geoelectrical profile was made considering the geologic findings in the sedimentary range from deep wells (Fig. 7). The model was divided into grid points by the finite-difference method (see pp. 231–236 in this book) and modelled for H-polarization on a computer by Tanzer using the Gausse Seidel iteration technique. Comparing this with the experimentally observe-resistivities shown in Figure 8, much too high resistance values were found and the observed characteristic drop in resistance at high periods — showd in the experimetal sounding curves of the upper part of Figure 8 (full-linn

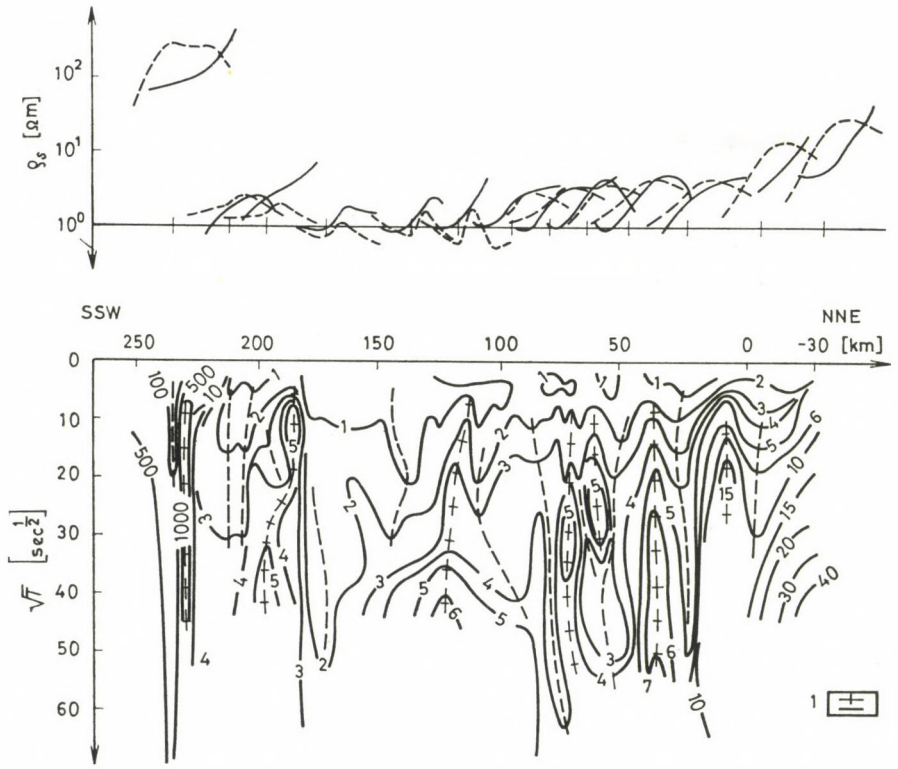


Fig. 8. Section of the apparent resistivity for H-polarization after experimental results along the profile BB'

1 – relative maxima- or minima-areas of the apparent resistivites. In the upper part of the figure calculated sounding curves are given (dotted lines) after the model of Figure 9 and the experimental sounding curves (full lines) at the same points. Crosses belong to $\varrho_s = 1\ \Omega$m and $\sqrt{T} = 10\ \text{sec}^{1/2}$

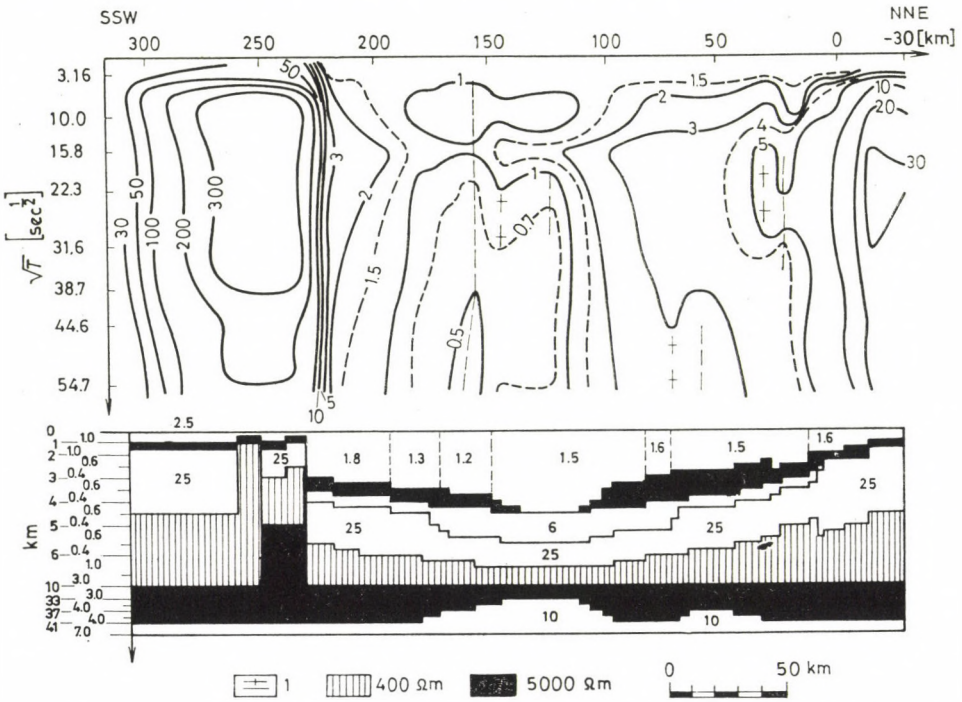


Fig. 9. Results of a computer model-calculation along the profile BB' of Figure 6 for H-polarization with respect to the well-conducting layers of the deeper lithosphere 1 – relative maxima- and minima-areas of the apparent specific resistivities. The numbers give the apparent specific resistivity (upper part of the figure) resp. the fictitious specific resistivity (lower part of the figure) in Ωm

curves) — did not take place. Therefore, this resistance drop cannot be caused by the horizontal inhomogeneity of the Neozoic and Mesozoic overburden, but should have been brought about by well-conducting ranges within deeper-seated lithospheric layers.

In order to test, whether the occurrence of such ranges fits to the results of other geophysical measurements (gravimetric, magnetic, seismic methods), a probable lithospheric structure was assumed by Oelsner (pp. 509–513 in this book).

On the basis of the temperatures met in bore-holes at a depth of 1000 m, thermal conductivity and heat production in the substantially probable layers down to the Moho, Oelsner, also using the finite-difference method, succeeded in calculating a geothermal crustal section for model BB'. Using the results of the experiments of Volarovich et al., (1970) on the electrical conductivity of rocks under high PT-conditions, a distribution of the electrical conductivity resulted, which was taken as a basis for the computer model of Figure 9. The section thus obtained and the sounding curves of the apparent resistivity with H-polarization shown in the dotted sounding curves of the upper part of Figure 8 are in the order of magnitude of the data obtained experimentally.

To compare the corresponding variants of interpretation of the causes of the Nort-Germae-Polish conductivity anomaly in the states bordering on the GDR, three model sections have been drawn for the profiles AA', BB' and CC' of Figure 10 wich were calculated independently by different authors.

The variant of interpretation worked out in the FRG by Steveling (1973) on the profile AA' based upon the frequency-sensitive behaviour of geomagnetic deep sounding also cannot do without assuming an increase of conductivity in the deeper layers of the crust. Contrary to the variant of interpretation on the GDR profile BB', however, the intermediate range of the central crust is reckoned with relatively low resistivities of about 10 Ωm.

Jankowski's variant of interpretation (Schmucker and Jankowski, 1972) on the profile CC' in Poland dispenses with a well-conducting intermediate layer, because the found longitudinal conductivities of 2000 Ω^{-1} can be explained in Poland by the action of the sediments alone.

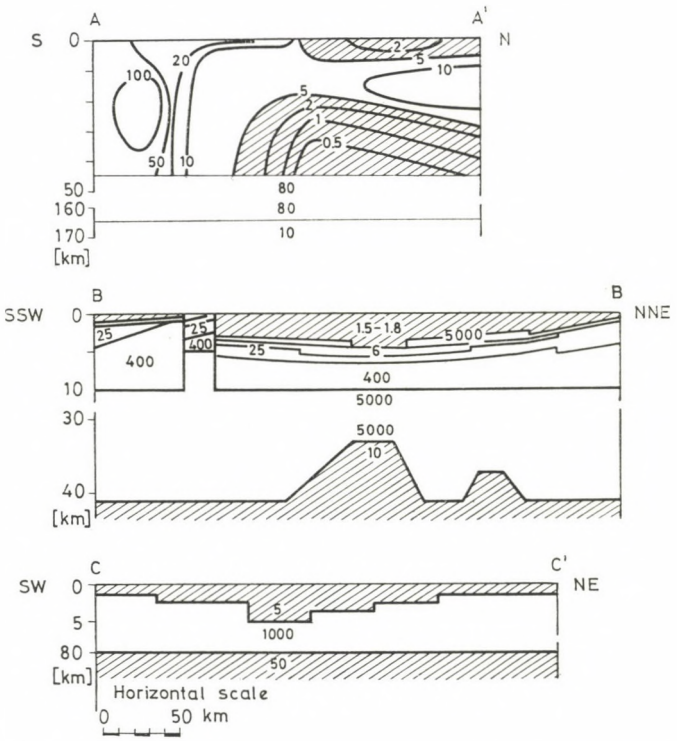


Fig. 10. Comparison of the conductivity-sections, belonging to computer model-calculations in the GDR, Poland (after Schmucker and Jankowski, 1972) and the FRG (after Steveling 1973). Dotted areas are layers of relative low specific resistivity. The numbers give the specific resistivities in Ωm. The geographical positions of the profiles are shown in Figure 6

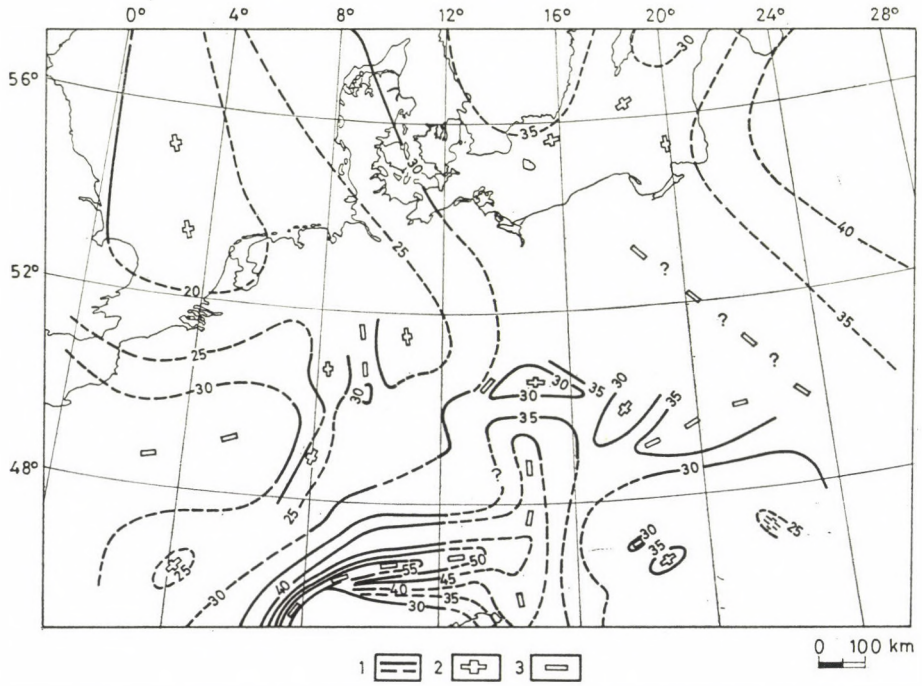


Fig. 11. Generalized shape of the Moho-discontinuity after Hurtig
1 – certain or uncertain (dotted line) trend of the depth-line, depth in km; 2 – relative anticline of the Moho; 3 – relative syncline of the Moho

Summarizing, it can be said that in spite of the probable occurrence of further well-conducting layers in the upper earth mantle — such as deters mined in the GDR by the evaluation of soundings made at the observatorie-Niemegk and Ückermünde and in the south of the GDR — in the central and western parts of the anomaly on the territory of the GDR and the FRG the conductivity anomaly can be only explained by the combined action of well-conducting layers within the sedimentary range and the deeper crust or the upper earth mantle, respectively.

As to the cause of the creation of the well-conducting area in the deeper lithosphere the relative shallow position of the Moho (Fig. 11) in combination with the zones of high heat flow, shown in Figure 12, may be of some importance.

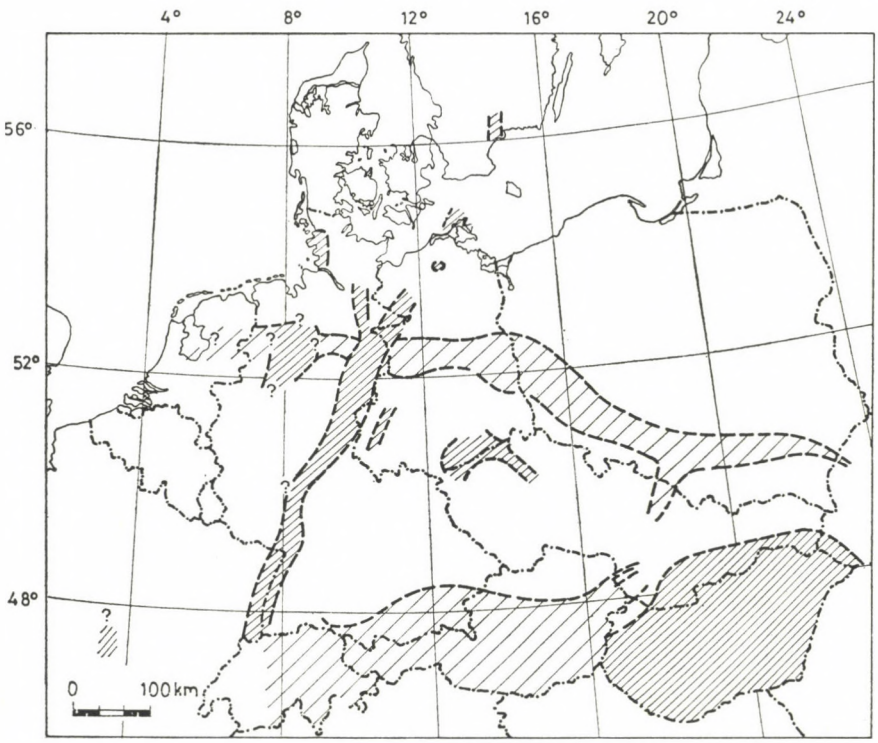


Fig. 12. Map of the zones of high heat-flow in Central-Europe after Hurtig and Schlosser (1973)
Narrow hatched: heat-flow values $> 2\mu$ calcm^{-2} sec^{-1}; wide hatched: heat-flow values $1.4 - 2\ \mu$ calcm^{-2} sec^{-1}

ACKNOWLEDGEMENTS

We want to thank the VEB Geophysik, Leipzig, (Director Dipl.-Min. Körner) for giving us access to the results of the magnetotelluric soundings and the Rechenzentrum of the Technische Universität Dresden (Director Prof. Dr. Stahl) for taking charge of the geoelectric computer modelling.

REFERENCES

ÁDÁM, A., VERŐ, J., WALLNER, Á., 1972. Regional Properties of Geomagnetic Induction Arrows in Europe. *Acta Geod. Geophys. Mont. Hung.* **7**, 251–287.

FANSELAU, G., 1970. The Use of Long-Period Variations for Geomagnetic Depth-Sounding. *Acta Geod. Geophys. Mont. Hung.* **5**, 79–86.

FOURNIER, H., 1968. Proposition d'une méthode pour déterminer la structure du premier millier de kilomètres de la terre d'après la résistivité apparante. *Acta Geophys. Polonica* **16**, 215–248.

GÖTHE, W., PORSTENDORFER, G., RÖSLER, R., 1975. Zum Problem der Zuordnung gemessener Wiesepfeile zu getrennten Leitfähigkeitsanomalien. (In preparation.)

HURTIG, E., SCHLOSSER, P., 1973. Der Wärmefluß in Mitteleuropa. *Z. Geol. Wiss. Berlin* **1**, 461–466.

LENGNING, K., 1968. Untersuchung der Beobachtungsergebnisse von Erdstromregistrieranlagen mit Potentialabgriffen von unterschiedlicher Länge am Adolf-Schmidt-Observatorium für Erdmagnetismus in Niemegk. *Geod. Geophys. Veröff.* II, Hft. 6.

LEVIN, L. E., 1971. Über das gefaltete Grundgebirge der Strukturvertiefungen der Nord- und Ostsee. *Z. angew. Geol.* **17**, 381–388.

NIKITENKO, K. J., TEREKHIN, E. J., FOMINA, V. J., 1971. Complex deep investigations by means of electric prospecting methods (in Russian). *Prikl. Geofiz.* **62**, 79–88.

PAWLISZYN, J., JANKOWSKI, J., 1973. The results of preliminary treatment of magnetotelluric investigations on the VII. International Profile. *Materialy i Prace Inst. Geofiz. Pol. Akad.* **60**, 111–119.

PORSTENDORFER, E., 1967. Längswiderstände für die Magnetotellurik. Inst. f. angew. Geophys. Bergakademie Freiberg.

PORSTENDORFER, E., 1968. Methodik der Auswertung elektrischer Bohrlochmessungen zur Berechnung mittlerer spezifischer Längswiderstände für die Magnetotellurik. *Freiberger Forschungshefte*, **C 233**, 43–49.

PORSTENDORFER, G., 1965. Methodische und apparative Entwicklung magnetotellurischer Verfahren mit Anwendung auf die Tiefenerkundung im Bereich der norddeutschen Leitfähigkeitsanomalie. *Veröff. Inst. f. Geodynamik Jena*, Hft. 3.

PORSTENDORFER, G., 1966. Die Verteilung tellurischer Ströme mit Perioden von 30 min in Mitteleuropa. *Bergakademie* **8**, 461–464.

RITTER, E., 1970. Frequenzabhängige geomagnetische Tiefensondierungen in der Anwendung auf verschiedene Leitfähigkeitsanomalien in Europa. Dissertation, Karl-Marx-Univ., Leipzig.

ROKITYANSKY, J. J., 1972. Geophysical Methods of Magnetovariation Sounding and Profiling (in Russian). Naukova dumka, Kiev.

SCHMUCKER, U., JANKOWSKI, J., 1972. Geomagnetic induction studies and electrical state of the upper mantle. *Tectonophysics* **13**, 233–256.

SKORUPA, J., 1970. Morphology of the consolidated basement in Poland in the light of seismic refraction surveys. *Materialy i Prace, Warszawa*, **34**, 85–96.

SORGENFREI, T., 1966. Strukturgeologischer Bau von Dänemark. *Geologie, Berlin*, **15**, 641–660.

STEVELING, E., 1973. Erdmagnetische Tiefensondierung mit Variationen und Pulsationen im Einflußbereich der Norddeutschen Leitfähigkeitsanomalie. Dissertation, Univ. Göttingen.

VOLAROVICH, M. P., PARKHOMENKO, E. J., BONDARENKO, A. T., 1970. The electric conductivity of rocks at high pressures and temperatures (in Russian). Symposium "Joint Investigations of the Geoelectric Parameters of the Earth's Crust and Upper Mantle", Leningrad.

VOZOFF, K., SWIFT, C. M., 1968. Magnetotelluric measurements in the North-German basin. *Geophys. Prosp.* **16**, 454–473.

WIESE, H., 1955. Tiefentellurik, Erforschung der Erdkruste durch geomagnetische Variationen. *Geologie, Berlin*, **4**, 520–525.

German Research Group for Exploration Seismology, 1964. Crustal Structure in Western Germany. *Z. Geophys.* **30**, 209–234.

International Tectonical Map of Europe 1 : 2,500,000, 1964, Moscow.

SPLITTING OF MAGNETIC FIELDS INTO EXTERNAL AND INTERNAL PARTS (S_q ANOMALY IN THE GDR)

G. FANSELAU

The splitting of a magnetic field into an internal and an external part is a special task within a very complex problem. This problem consists of the splitting of a physical field, produced by different sources, into the corresponding partial fields. The solution of this problem is very difficult and can be carried out by means of complicated mathematical methods only. In the general case, one gets only approximative result, if any. These problems will not be discussed here.

The time-dependence of physical fields is variable. Besides the static fields stationary and quasi-stationary fields, as well as dynamic ones, are of interest, especially in electromagnetism and mechanics. Here the discussion will be restricted to the static and stationary case, and only the electromagnetic field will be considered.

The splitting of the geomagnetic field into an internal and external part is very important for the research of the electromagnetic induction method. It can be shown that for special frequencies, i.e. for pulsations and substorms, the splitting of the geomagnetic field is automatically given: the vertical component characterizes the internal part, the two horizontal components the external inducing one. There are many publications on this problem (Rokityansky, 1972).

More difficult is the splitting of the geomagnetic field for local conductivity anomalies using longer periods, i.e. the solar quiet daily variation S_q and the lunar variation L. For the solution of this problem it is necessary to use other methods to be discussed in what follows.

It was pointed out in some earlier papers (Fanselau, 1968a; Fanselau, 1968b) that the S_q-range values can be used for the interpretation of profiles of geomagnetic depth-sounding. In Figure 1 the quiet diurnal variation

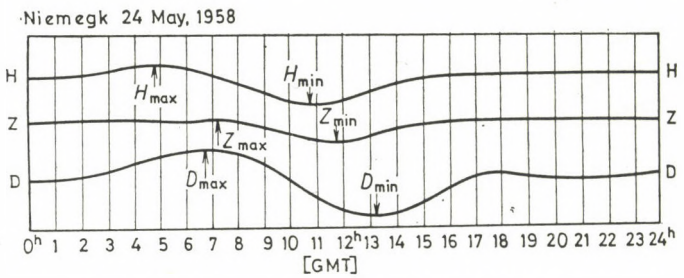


Fig. 1. Typical quiet variation in Niemegk

— S_q — is given for all three elements. It can be seen that this S_q-variation has a distinct maximum and a pronounced minimum for each geomagnetic element, as it is particularly marked in Figure 1. As usual, the range is formed from the difference between the maximum and the minimum of the curve.

The basic idea of the method is to compare the ranges at a movable station of a profile with those of a fixed station. The comparison is done by simple difference-formation. The range-differences between the movable station on the profile and the fixed station quite expectedly show the dependence on latitude for the corresponding element D, H or Z. The rest of the values show a clear connection with the geological structure of the subsoil, if the latitude-dependence, which is comparatively regular, is compensated by a trend. Hence, these difference values are in the main characterized by the electromagnetic induction field of the subsoil. The geomagnetic main field is eliminated by range formation. Comparing the ranges of the movable stations with a fixed station near to them the influence of solar activity, too, is to a large extent eliminated. Since regionally induced magnetic fields are also eliminated, actually only small regional or locally conditioned indications of the surveyed profile remain. More details (also on the mathematical interpretation of the results obtained) were given in the work of Fanselau (1968b). The method described there has since then been further developed, based on the knowledge gained in the discussion of the harmonic analysis of the S_q with regard to ionospheric facts (Fanselau, 1969). It was found that the amplitude of the first harmonic in the analysis of S_q strongly depends on the length of the basis interval. The interval lengths in question were 8, 10, 12 . . . up to 24 hours, all of them centred around the local noon. The amplitude of the first har-

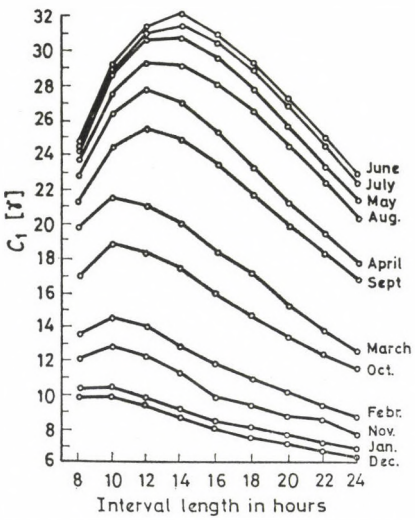


Fig. 2. c_1-values of typical quiet days (D) of different interval lengths

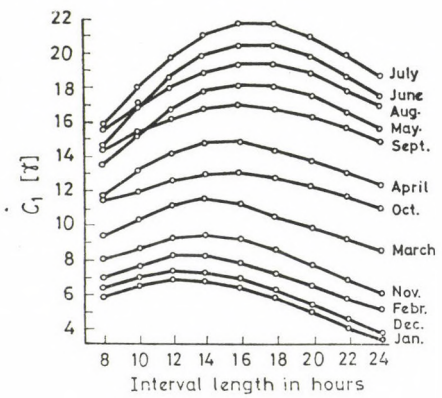


Fig. 3. c_1-values of typical quiet days (H) of different interval lengths

monic c_1 had its largest values for the declination in June when it was based on an interval of 14 hours centred around local noon. In all other intervals this amplitude decreases. Conditions are similar to the horizontal intensity, but here the optimal interval for June is about 18 hours. Quite reasonably, the optimal interval shows a clear seasonal dependence, i.e. there are shorter interval lengths in autumn and winter. Figures 2 and 3 illustrate the seasonal dependence of the optimal intervals for the c_1-amplitudes as well as for the c_1 values themselves. As expected, not only the optimal interval, but also the amplitude itself decreases. Thus, c_1 in the optimal interval is a suitable physical parameter which will certainly also react well to electromagnetically induced effects in the interior of the earth as far as these are reflected in the S_q.

Thus it was an obvious idea to use the knowledge gained in a different field of research for the purpose of geomagnetic deep sounding. In this, the method remains the same excepting one fact: for the formation of the difference with the fixed station one does not use the range-values taken directly from the curves but the c_1D and c_1H values derived from harmonic analysis. An improvement of the signal-to-noise-ratio could be expected for, of course, the harmonic analysis implies a certain smoothing. As mentioned, the harmonic analysis has always been extended to the optimal interval. To perform the analysis a harmonic analyzator of MADER–OTT was used, the accuracy of which is sufficient for the purpose in question.

It should be mentioned it is easy to prove mathematically (Fanselau, 1969) that those parts in the course of S_q which are outside the optimal interval have no significant influence on the harmonic coefficients of the optimal interval itself (at least up to the third order). Corresponding analyses for the vertical component Z have not been concluded so far. But the same optimal intervals as for the declination can be assumed for Z with sufficient accuracy (cf. Fig. 1).

Figures 4, 5 and 6 represent the results obtained at ten stations in the northern part of the GDR. The Niemegk observatory was used as fixed station. Results of measurement are given for D, H and Z. Whereas with D there are hardly any significant differences against Niemegk, H and Z show distinct local anomalies. In case of the horizontal intensity these anomalies follow a trend which is indicative of increasing range-difference with increasing geographic latitude. For vertical intensity, too, a dependence on latitude can be noticed, i.e., decreasing range-differences with increasing latitude. Apart from that a jump situated over the North German conductivity anomaly is clearly seen in the range-differences against Niemegk, and that almost completely in the very place which had earlier been found by the evaluation of the induction effects of bay-disturbances (Wiese, 1965). The horizontal intensity also shows, in the same place as Z, a clearly pronounced modulation, even though this is much less (about one third) than for Z. With Z, the range-differences are positive north of the jump mentioned; south of it they are negative. It should be noted that the level of the profile is dependent on the fixed station chosen, and that the level changes with it. A suitable trend or basis must, of course, be used for a theoretical evaluation of such profiles.

As indicated above, an improvement of the signal-to-noise ratio was ex-

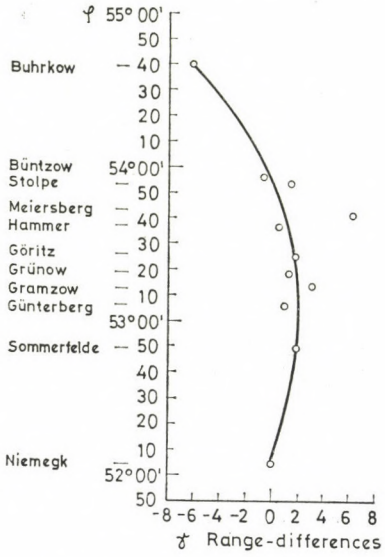


Fig. 4. Mean differences of the S_q-D-range between Niemegk and field stations

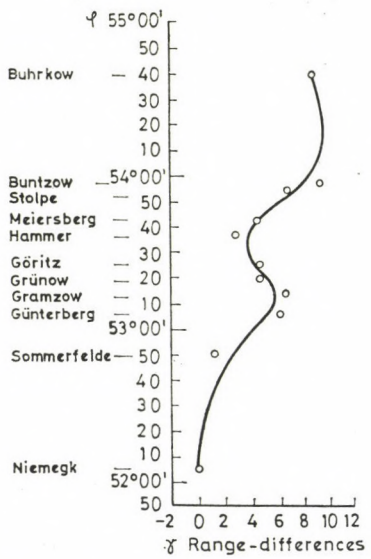


Fig. 5. Mean differences of the S_q-H-range between Niemegk and field stations

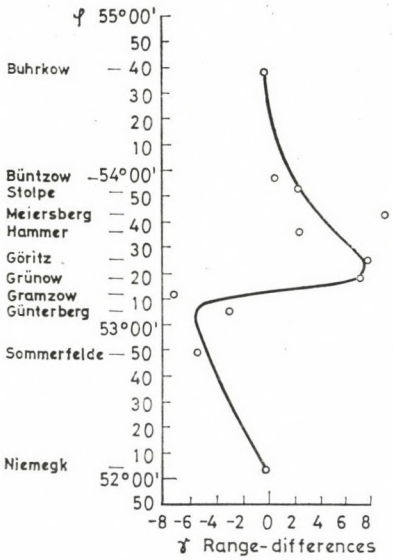


Fig. 6. Mean differences of the S_q-Z-range between Niemegk and field stations

pected of the transition from the direct range-differences (as obtained from the registration curves) to the c_1-differences of the harmonic analysis of the optimal interval. This improvement could actually be observed. In this, surprisingly enough, it emerged that the c_1-differences also have a distinct dependence on the A_k-numbers, i.e., on the numbers used to characterize the geomagnetic activity of one day. To demonstrate this effect four stations were chosen, two of them situated north and two south of the zone of increased conductivity in Northern Germany. For H as well as for Z a distinct dependence on activity could be seen for the stations situated in the zone of increased conductivity, while this effect could not be observed for stations situated at greater distance. Table 1 gives numerical values of

TABLE 1

c_1-differences (Δc_1) for 4 stations against Niemegk in dependence on the magnetic activity A_k

Station	S_qH $\Delta c_1/A_k$	S_qZ $\Delta c_1/A_k$
Göritz	0.7γ	0.0γ
Grünow	1.8	−1.0
Zone of increased conductivity		
Günterberg	1.1	−0.2
Sommerfelde	0.1	0

these effects for H and Z, in dependence on A_k for the c_1-differences of the four stations against Niemegk. These numbers clearly show that the zone of increased conductivity affects also the variations of lesser period occurring in geomagnetic activity.

It must be taken into account that the days concerned were quiet ones with only relatively small disturbances caused by the geomagnetic activity. As Table 2 shows, a significant improvement is achieved against the non-reduced values if the c_1-differences are reduced to $A_k = 0$ by means of the numerical values in Table 1. In Table 2 the numerical values are given of the different methods for the four stations mentioned above.

In the mean the error at each station reduces to about its half. If the four stations are compensated by a curve in accordance with a profile the error naturally becomes even less. As difference between the extreme values which can be observed when transgressing the conductivity anomaly we then obtain

$$\text{for } H\text{: } 7\gamma \pm 3\ \gamma, \quad \text{for } Z\text{: } 13\ \gamma \pm 2\gamma$$

It should be noted that the field magnitudes obtained here are to a large extent free from outer disturbances, i.e. they represent inner field contri-

TABLE 2

Reduction of the c_1-differences (Δc_1) between stations and Niemegk on the magnetic activity $A_k = 0$

Station	A_k	Δc_1	red on $A_k = 0$	c_1 red
S_qH				
Grünow	5	8.6γ	— 9.0	— 0.4γ
	8	16.6	—15.2	1.4
	3	4.4	— 5.4	— 1.0
	3	12.2	— 5.4	6.8
			mean	1.7$\pm$3.1
Günterberg	8	3.2	— 9.0	— 5.8
	6	— 0.4	— 6.8	— 7.2
	10	9.0	—11.2	— 2.2
	6	— 0.8	— 6.8	— 7.6
	4	2.4	— 4.5	— 2.1
	10	3.4	—11.2	— 7.8
			mean	— 5.4$\pm$2.9
S_qZ				
Grünow	5	3.4γ	4.7	8.1γ
	8	3.9	7.6	11.5
	3	8.9	2.9	11.8
	3	7.2	2.9	10.1
			mean	10.4$\pm$1.7
Günterberg	8	— 6.1	1.7	— 4.4
	6	— 6.8	1.2	— 5.6
	10	— 3.0	2.1	— 0.9
	6	— 1.1	1.2	0.1
	4	— 3.5	0.8	— 2.7
	10	— 4.9	2.1	— 2.8
			mean	— 2.7$\pm$2.1

butions of the S_q as caused by electromagnetic induction effects in the interior of the earth. For the time being, it should be emphasized, however, that obviously the longer periods of S_q (which are in the magnitude-range of 14 to 18 hours in summer) show much similar effects as those observed in shorter periods of the bay-disturbances.

The problem of splitting the geomagnetic field into an external and internal part requires a reliable trend both for local and regional profiles. This trend should eliminate all parts of the geomagnetic field disturbing the interpretation of the anomaly. Physical errors of the trend influence all numerical calculations and thus cause inexact indications of the sources.

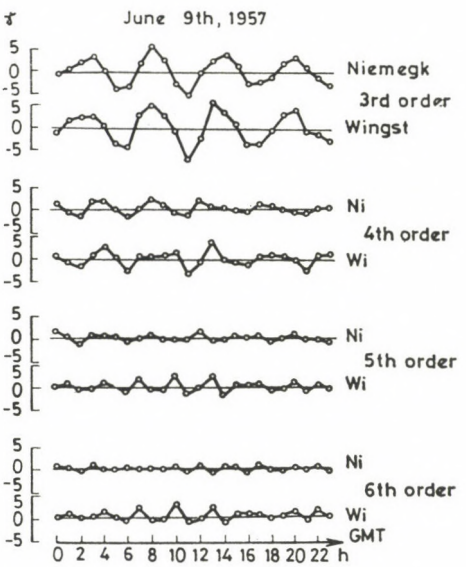


Fig. 7. Residua of the 3rd to 6th order for $S_q Z$ of Niemegk and Wingst

It is very interesting to see that the long-period variations, e.g. S_q· also show — by harmonic analysis — the behaviour of the shorter periods, Figure 7 shows for the Wingst and Niemegk observatories the harmonic residua from the third to the sixth order for the 9th June, 1957. The third and fourth residua show the same course for the two observatories, but the fifth and sixth ones show the well-known inversion of the vertical intensity between the two observatories. The amount of these periods is only a few hours, being the same as in the substorms. It should also be mentioned that this inversion cannot be observed during the whole day, it is concealed by statistical noise. Clear marked effects can be traced between noon and the early evening, indicating the change of the inducing field during the day. The cause of this phenomenon — perhaps inhomogeneities of the inducing field — shall not be discussed here.

ACKNOWLEDGEMENT

The registration curves have been made available by Dr. E. Ritter who performed the measurements at the stations of the profile with utmost care. The measurements were carried out with field-registration stations developed in the Niemegk observatory (Fanselau et al., 1968; Fanselau, 1965). I should like to express my particular gratitude to Mr. H. Wolter, for assistance in the evaluation of the curves and for taking care of the calculations, and to Dr. L. Ballani for useful discussions.

REFERENCES

FANSELAU, G., 1965. Eine neue Feldregistrierstation. *Z. angew. Geol.* **11**, 259–264.

FANSELAU, G., 1968a. Einige Bemerkungen zur kleinregionalen Veränderlichkeit von S_q. *Gerlands Beitr. z. Geophys.* **77**, 35–41.

FANSELAU, G., 1968b. The use of range-differences for the interpretation of conductivity anomalies. *Phys. Earth Planet. Interiors* **1**, 177–180.

FANSELAU, G., 1969. Zur harmonischen Analyse des S_q. *Gerlands Beitr. z. Geophys.* **78**, 27–40.

FANSELAU, G., RITTER, E., WOLTER, H., 1968. Über die Genauigkeit geomagnetischer Feldregistrierstationen. *Geophys. Prospecting* **16**, 94–106.

ROKITYANSKY, I. I., 1972. Geophysical Methods of Magnetovariation Sounding and Profiling (in Russian). Kiev.

WIESE, H., 1965. Geomagnetische Tiefentellurik. Abh. Geomagn. Inst. Dt. Akad. Wiss. Berlin, No. 36. Berlin.

VERTICAL TEMPERATURE DISTRIBUTION IN THE NORTH-GERMAN—POLISH SEDIMENTARY BASIN AND ITS RELATION TO THE NORTH-GERMAN—POLISH CONDUCTIVITY ANOMALY

CH. OELSNER

INTRODUCTION

For the treatment of geothermal problems, numerical approximation methods are being more and more used. This concerns particularly the calculation of temperature distribution within a given geological section with given boundary temperatures and boundary conditions. On this, the reader is referred to the works of Geertsma, (1971), Mundry, (1966), Sclater and Miller, (1969), Sievert, (1972). Possible methods are dealt with elsewhere in this volume (see pp. 67–68). Here, a description will be given of the results obtained on a 225 km long profile crossing the North-German-Polish sedimentary basin from south-southwest towards N–NE.

MODEL PARAMETERS AND RESULTS

Based upon various geophysical data a four-layer crust model was designed consisting of: a) Mesozoic and crystalline rock, b) granitic, c) basaltic and d) peridotitic material. The individual complexes are given with different markings in Figure 3.

The model was covered with a regular rectangular mesh. The horizontal distance between mesh points was 5 km, the vertical distance 1 km. As upper boundary the depth of 1 km was chosen, using for the temperatures of the upper boundaries the "1000-m-temperatures" obtained from borehole measurements. From these and the corresponding heat-flow values for each of the 1860 mesh points an initial temperature and also the lower boundary temperature were calculated. The assumed depth of the lower boundary was 40 km.

According to the mesh distances chosen rectangular areas of $5 \cdot 1$ km^2 size were formed, to each of which a definite value of thermal conductivity and radioactive heat generation corresponding to the predominant rock were assigned. Thermal conductivities assumed for the single layers and radioactive heat productions, respectively, are represented in Figures 1 and 2. They were compiled using values available in the literature, paying due attention to the geological situation.

The ratios of thickness chosen in Figures 1 and 2 correspond to each other and apply approximately to the central range of the profile. By the method of successive over-relaxation (SOR) (see pp. 69–71) the Poisson equation was solved subject to the boundary conditions valid for the problem. The result is shown in Figure 3.

The geological structure is characterized by two ranges with relative shallow position of the Moho. The "normal" range of depth of the Moho

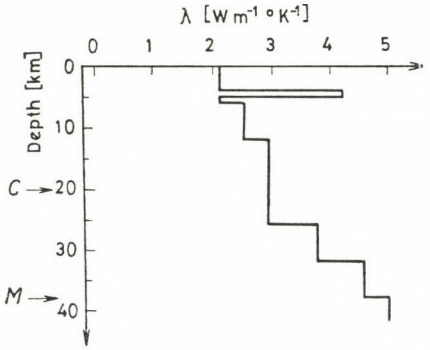


Fig. 1. Thermal conductivity *vs.* depth used in the numerical computations

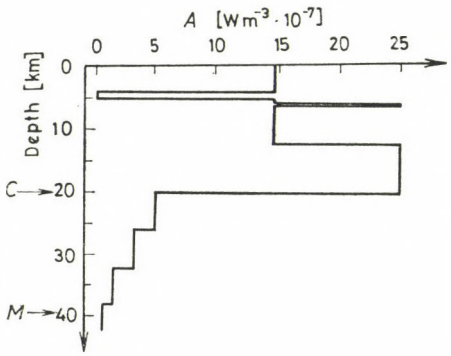


Fig. 2. Radioactive heat generation *vs.* depth, used in the numerical computation

in the central range of the profile and also the upper and lower boundaries (Conrad discontinuity) of a layer of granitic material reveal a relatively shallow position. The thickness of this layer increases distinctly towards S-SW.

Down to a depth of about 10 km the temperature does not show large variations. At 5 km depth the average temperature for the entire range of the profile is 156 ± 15 °C. The corresponding values for 15 km and 30 km are 376 ± 32 °C and 590 ± 50 °C, respectively. These data are averages from 46 values in each case of the depths quoted. The visually evident increase of temperature variations with depth is thus also confirmed by the mean

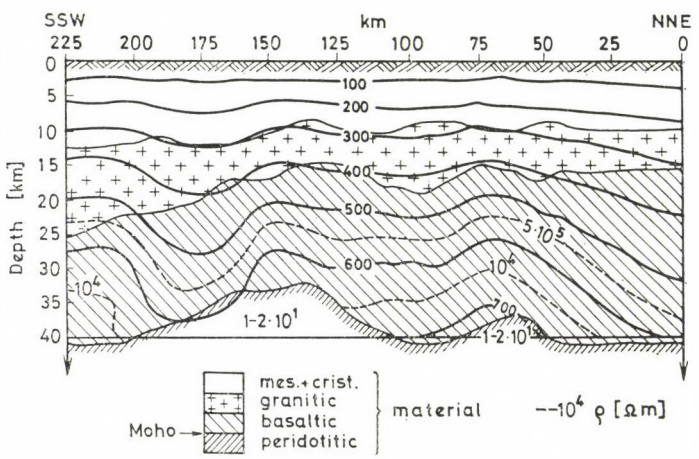


Fig. 3. Computed vertical distribution of temperature of a profile in the northern part of the GDR

square deviations. Not only the magnitudes of the calculated variations increase with depth — as it is reasonable because of the temperatures' rising with depth — but the relative value of the mean square deviations as well. The corresponding values are:

	Mean horizontal gradient (°C/km)	Mean root-square °C/km	deviation %
5 km	1.06	0.11	10.4
15 km	1.45	0.17	11.7
30 km	2.28	0.27	11.8

Besides the temperature rises within the range of shallow position of the Moho, which are of particular importance for the electric conductivities, the rather marked plunging of the isotherms towards N-NE should also be noted. This is a consequence of the fall off of heat flow values in the same direction (Hurtig and Schlosser, 1973). The temperatures of the Moho vary between 600 and 700 °C.

TEMPERATURE DEPENDENCE OF ELECTRIC CONDUCTIVITY

The temperature dependence of electric conductivity is given by

$$\sigma(T) = \sum_{i=1}^{4} \sigma_{i0} \exp\left(-\frac{E_i}{kT}\right). \tag{1}$$

Index i designates the possible conductivity mechanisms: Ion or electron defect and excess conduction. E_i designates the corresponding activation energies, k is the Boltzmann constant and T temperature in K. (See pp. 329–330).

The most important contributions to the temperature and pressure dependence of electric conductivity are due to Tikhonov and his school. Abundant material was presented by Parkhomenko and Bondarenko (1972). Experimental data reported by Volarovich et al., (1970) concerning the activation energy E and the so-called pre-exponential coefficient $\lg \sigma_0$ for peridotites, pyroxenites and olivinites were used for the estimation of the conductivity conditions in the deeper crustal zones of the north of the GDR. For the listed rocks and physical properties limit values are given in the paper of Volarovich et al. (1970) for some ranges of the temperature and the parameters. Activation energies E and pre-exponential coefficients $\lg \sigma_0$ are shown in Figure 4.

In order to obtain discrete values of the temperature dependence of electric conductivity, for the calculation according to formula (1) the central lines of these ranges marked by greater thickness were used. The temperature dependence of resistivity of peridotites, pyroxenites and olivinites determined from them is represented in Figure 5.

While in the temperature range considered the resistivity of pyroxenites

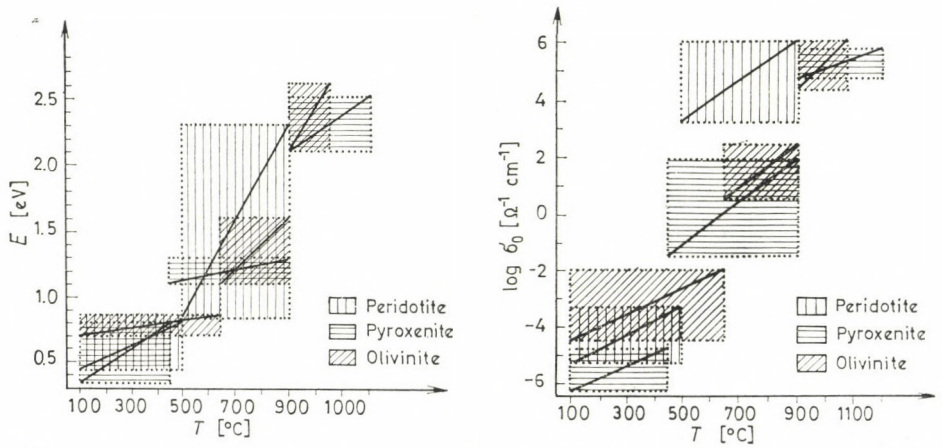


Fig. 4. Temperature dependence of the activation energies and the pre-exponential coefficient for olivinites, pyroxenites and peridotites, after Volarovich et al. (1970)

and olivinites more or less decreases with rising temperature, peridotite reveals a jump-like rise of conductivity as a result of a changed process of conducting. In the calculated temperature section above the Moho olivinitic-pyroxenitic material was assumed. Material below the Moho, however, was regarded as peridotitic. The temperatures obtained in the Moho range were between 600 °C and 700 °C. The resistivities for the temperature range 550–700 °C shown in Figure 5 were also entered into Figure 3. The conductivity differences amount to 4 decimal powers at the most. Based upon these results it was assumed that a part of the experimentally determined conductivity anomaly is caused by the relations explained above. The investigations of Porstendorfer et al. (see pp. 487–500) also confirm this assumption whereby the electromagnetic model calculations were also based on the conductivity model resulting from our investigations. It was taken into consideration that the used average values in Figure 4 still allow deviations of the calculated resistivities.

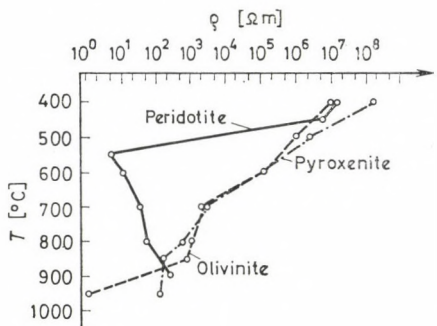


Fig. 5. Temperature dependence of the specific electric resistivity for olivinites, pyroxenites and peridotites

REFERENCES

GEERTSMA, J., 1971. Finite element analysis of shallow temperature analysis. *Geophys. Prospecting* **19,** 662–681.

HURTIG, E., SCHLOSSER, P., 1973. Der Wärmefluß in Mitteleuropa. *Z. geol. Wiss.* Berlin **1,** 461–466.

MUNDRY, E., 1966. Berechnung des gestörten geothermischen Feldes mit Hilfe eines Relaxationsverfahrens. *Z. Geophys.* **32,** 157–162.

PARKHOMENKO, E. I., BONDARENKO, A. T., 1972. Electric Conductivity of Rocks at High Pressures and Temperatures. Nauka, Moscow.

SCLATER, J. G., MILLER, S. P., 1969. A machine method for computing the effect of a two-layered conductive structure. MPL Technical Memorandum 198.

SIEVERT, P., 1972. Beiträge zur Berechnung geothermischer Anomalien über Störungsmodellen. M. Sc. Dissertation, Bergakademie Freiberg.

VOLAROVICH, M. P., PARKHOMENKO, E. I., BONDARENKO, A. T., 1970. Die elektrische Leitfähigkeit der Gesteine bei hohen Drücken und Temperaturen. Proc. Symp. "Gemeinschaftliche Untersuchungen der geoelektrischen Konstanten der Erdkruste und des oberen Mantels" 18–20. Nov. 1970., Leningrad.

II. CZECHOSLOVAKIA

DEPTH DISTRIBUTION OF THE ELECTRIC CONDUCTIVITY IN CZECHOSLOVAKIA FROM ELECTROMAGNETIC STUDIES

J. PĚČOVÁ, V. PETR, O. PRAUS

INTRODUCTION

Geophysical investigation of the earth's crust and upper mantle on the territory of Czechoslovakia covered mainly three profiles Nos V, VI and VII outlined in Central Europe by the Geophysical Commission of the Carpatho-Balkan Geological Association and designed originally as profiles of deep seismic sounding (DSS). They have become, however, principal research lines along which results of other geophysical methods have been accumulated by systematic measurements.

Temporal variations of the geomagnetic field, together with telluric currents have been studied systematically along the Czechoslovak part of profile VI and, recently (1973), new data and preliminary results have been obtained by synchronous measurements on a series of field stations located along profile V passing the Carpathians on the territories of Poland and Czechoslovakia. From all these measurements conclusions were drawn on the electrical conductivity and on its regional, or local pecularities for crustal and upper mantle depths.

In this paper we deal mainly with conclusions drawn from measurements at profile VI. Other results obtained by analysing recent data on profile V and by analysing records of permanent observatories at Průhonice and Budkov, which are located approximately on profile VII, will be mentioned occasionally within the general electrical characteristics of the territory

GEOLOGICAL AND STRUCTURAL CHARACTERISTICS OF THE PROFILE

Striking SE from the GDR-Czechoslovak border in the Krušné hory, profile VI passes the Teplá-Barrandien, Moldanubian and Moravian block. of the Bohemian Massif. They are formed by granitoid rocks either direct on the earth's surface, or covered by crystalline schists which penetrate locally down to about 10 km depth.

Further SE, approximately from the Boskovice furrow in the eastern part of the Moldanubicum, granitoid rocks submerge gradually under the platform series (from Paleozoic to Neogene Ages) of the Carpathian foredeep and under the cover of the outer flysch zone, (Vienna Basin). The maximum thickness of the total cover was estimated to be more than 6 km.

Passing the Malé Karpaty Mts. the profile continues into the Pannonian block with up to 5 km thick Neogene sediments of the Danube Lowland.

Interpretation of the DSS results along the profiles, as summarized in

the papers of Beránek (1971), Beránek et al. (1971), Beránek and Dudek (1972), revealed that the Bohemian Massif, except for its north-western part, submerges deeply into the mantle compared with the Pannonian block in the south-eastern part of the profile. The greatest thickness of the earth's crust has been found in the area of the Moldanubicum and in the Central Bohemian pluton. Here the Moho was located at a depth of 38 km, while in the Pannonian block its depth was estimated as about 28—30 km.

By analyzing seismic wave patterns, the Bohemian Massif was found to be divided by a number of deep-penetrating faults of first-order importance. They usually bound blocks with different crustal thickness. In the west, the Krušné hory fault zone bounds the block of increased thickness in the Bohemian Massif. Similar importance was attributed to the Central Bohemian fault zone at the north-western border of the Central Bohemian pluton, to the Přibyslav fault zone at the eastern border of the Central Moldanubian Massif and to the Lednice fault zone at the western margin of the Vienna Basin.

Key importance, however, was attributed to the Peripieninian lineament in the eastern margin of the Vienna Basin. It borders the block of increased crust thickness and forms a deep-penetrating boundary between the Bohemian Massif and the Carpathians.

Another important result of DSS is a possible existence of low velocity channels at crustal depths below the Danube Lowland and below the Bohemian Massif as well. They are located at depths between 10—20 km. According to some geological evidence from the Bohemian Massif, they may be explained as an effect of partial melting.

Other geophysical data were correlated with the DSS results. Magnetic survey, for example, revealed certain positive magnetic anomalies that may indicate zones with basic material nearer to the surface. The basic material may have intruded along principal deep-seated fault zones and a close correlation with seismically detected fault zones seems to be evident. This has actually been proved for the area of Krušné hory, Central Bohemia, Lednice, Přibyslav and other fault zones. The Peripieninian lineament, however, is marked by a magnetic anomaly only in its eastern part (East Slovakia).

Equally important for understanding the deep structure of the Bohemian Massif is profile VII which runs from the Polish Paleozoic platform across the Sudetes, the Czech Cretaceous Basin and the Central Bohemian pluton. It further penetrates into the Moldanubicum and, in the Bavarian side, across the Bavarian molasse into the Alps. The greatest thickness of the crust in the Bohemian Massif (about 42 km) was found in the SSW part of the profile.

For the study of the Carpathian region on the Czechoslovak territory an important geophysical research line is the international profile V. It runs from the Polish Paleozoic platform, passes into the Carpathian foredeep, penetrates the Outer and Central Carpathians and terminates in the Pannonian block.

The DSS studies revealed the greatest depths of the Moho discontinuity in the area of the outer Flysch (about 50 km). In this profile an important fault with a vertical jump of about 15 km was established at the boundary

between the Outer and Central Carpathians. This fault zone has been identified with the northern branch of the Peripieninian lineament already mentioned with the results of profile VI.

Information on the structure below the M-discontinuity is provided by seismological evidence obtained mainly from velocity-depth determinations by means of travel-time curves for deep earthquakes and from amplitude curves of seismic body waves. It will be referred to later.

ELECTROMAGNETIC DATA AND THEIR EVALUATION

The bulk of the electromagnetic data was obtained by recording simultaneously the temporal variations of the geomagnetic field and the earth current potentials at a series of field stations located within $\pm$ 20 km along the profile VI, some of them on profiles V and VII. The stations with relevant information are listed in Table 1.

The records were obtained for 3 geomagnetic elements (Z, H, D or dZ/dt, $X = dH/dt$, $Y = dD/dt$), and two components of the telluric field, (E_x = NS, E_y = EW). As a rule two recording sets were kept in operation for 2–3 months, preferably during an interval from the end of August to the end of October. The period range of pulsations from about 1 to 150 sec was covered by a rapid-run set with 30 mm/min chart speed. Medium and long period ranges from about 3—5 min to several hours were recorded by a normal-run set with a chart speed of 60 mm/h. The description of the above sets can be found in the work of Pěčová et al. (1969).

Also the data of permanent observatories at Průhonice and Budkov (both the Geophys. Inst. of the ČSAV, Prague) and Hurbanovo (Geophys. Inst. of the SAV, Bratislava) were taken into consideration to implement the data of profiles VI and VII.

Additional information of great value for the electromagnetic study was kindly supplied to us by Ritter (Adolf-Schmidt-Observatorum für Erdmagnetismus, Niemegk). These data represent induction vector characteristics for four bands of periods at several field stations over the Czechoslovak territory, as obtained from the geomagnetic field records carried out by the research groups of Wiese and Ritter (Wiese, 1965a, 1965b).

The whole volume of electromagnetic data was analyzed either visually, or by spectral analysis (Fourier transform, power spectrum). The results were used to obtain induction characteristics, (Wiese vector, or parameters of the preferred plane of Parkinson), information on the directional characteristics, apparent and principal impedances of the electromagnetic field at individual stations and the corresponding sounding curves. Results for groups of stations were published in the papers of Petr et al. (1964), Petr et al. (1967), Praus et al. (1966), Pěčová et al. (1969), Praus et al. (1970), Pěčová et al. (1972).

DIRECTIONAL CHARACTERISTICS OF ELECTRIC CONDUCTIVITY

The realistic structure of the superficial section of the earth's crust is far from being a homogeneous, or a simple horizontally stratified medium. Fault zones, dislocations and other structural features resulting from agents of the geological evolution have reworked the horizontal layering, or have brought into contact blocks, or layers with substantially different conductivities. As a result, the geolectric conditions vary horizontally. Such structures may be characterized as horizontally inhomogeneous where local, or regional distortions of the induced electromagnetic field are known to take place. These effects manifest themselves by a specific distribution of the field at the surface.

TABLE 1

Directional characteristics

Profile VI

Station	Geographic coordinates	Phenomenon (range of periods)	θ (σ max)	λ	θ_w	|C|	θ_p	θ_v
Šrobárová (Š)	47°49'; 18°16'	Pc 3	150	2.3	—	—	—	—
		Pi 2	150	1.8	—	—	—	—
		b	140	7?	149	0.15	—	—
Gabčikovo (G)	47°52'; 17°33'	Pc 3	140	1.3	—	—	—	—
		Pi 2	130	1.2	—	—	—	—
		Pc 5	80	1.5	—	—	—	—
		b	80	2.2	—	—	—	—
Štrkovec (Št)	48°12'; 17°50'	Pc 3 (20 sec)	—	—	51	0.31	—	—
		Pi 2 (100 sec)	—	—	60	0.42	—	—
		b	—	—	166	0.21	—	—
Nitra (Ni)	48°19'; 18°05'	v_1	—	—	59	0.66	—	—
		v_2	—	—	187	0.87	—	—
		v_3	—	—	150	0.22	—	—
		v_4	—	—	—	—	—	—
Nitrianská Blatnica (NB)	48°34'; 17°58'	Pc 3	45	4	—	—	345	
		Pi 2	50	4	—	—		
		b	50	8	143	0.31	160	14
		v_1	—	—	115	0.55	—	—
		v_2	—	—	135	0.42	—	—
		v_3	—	—	158	0.50	—	—
		v_4	—	—	180	0.25	—	—
Piešťany (Pi)	48°35'; 17°51'	v_1	—	—	99	0.51	—	—
		v_2	—	—	147	0.54	—	—
		v_3	—	—	160	0.44	—	—

Prievaly (Pr)	48°34'; 17°20'	Pc 3	130	1.6	—	—	140	—
		Pi 2	120	1.6	—	—	—	—
		Pc 5	90	?	—	—	—	—
		b	90	6.3	155	0.29	145	11
Jablonica (Ja)	48°36'; 17°25'	v_1	—	—	81	0.37	—	—
		v_2	—	—	116	0.42	—	—
		v_3	—	—	141	0.31	—	—
		v_4	—	—	158	0.56	—	—
Myjava (My)	48°45'; 17°34'	v_1	—	—	59	0.35	—	—
		v_2	—	—	107	0.39	—	—
		v_3	—	—	158	0.36	—	—
		v_4	—	—	131	0.27	—	—
Sekule (Se)	48°36'; 17°00'	v_1	—	—	—	—	—	—
		v_2	—	—	268	0.34	—	—
		v_3	—	—	33	0.38	—	—
Hodonin (Ho)	48°54'; 17°06'	Pc 3	350	2.2	—	—	—	—
		Pi 2	0	1.4	—	—	—	—
		Pi 2	340	3.6	—	—	—	—
		Pc 5	350	4.8	—	—	—	—
		Pc 5	330	3.5	—	—	—	—
		b	330	3.5	—	—	—	—
		b	350	2.9	11	0.24	0.0	11
Veseli (Ve)	48°57'; 17°24'	v_1	—	—	328	0.15	—	—
		v_2	—	—	356	0.29	—	—
		v_3	—	—	344	0.26	—	—
		v_4	—	—	1	0.54	—	—
Střilky (St)	49°08'; 17°13'	v_1	—	—	330	0.30	—	—
		v_2	—	—	333	0.25	—	—
		v_3	—	—	339	0.31	—	—
		v_4	—	—	346	0.33	—	—

Station	Geographic coordinates	Phenomenon (range of periods)	θ (σ max)	λ	θ_w	|C|	θ_p	θ_e
Nosislav (No)	49°00'; 16°40'	Pc 3 (20s)	290	2.6	—	—	—	—
		Pc 3 (30s)	310	2.3	—	—	—	—
		Pi 2 (68s)	320	2.1	—	—	—	—
		Pi 2 (105s)	350	2.1	—	—	—	—
		Pc 5 (450s)	30	3.7	—	—	—	—
		b (1870s)	30	1.8	—	—	—	—
		b (3000s)	10	1.8	67	0.20	60	9
Šemíkovice (Še)	49°03'; 16°08'	Pc 3 (21s)	70	2.6	—	—	—	—
		Pc 3 (32s)	70	2.2	—	—	—	—
		Pi 2 (74s)	70	2.3	—	—	—	—
		Pc 5 (270s)	90	2.9	—	—	—	—
		Pc 5 (480s)	80	2.1	—	—	—	—
		b (2700s)	80	3.0	94	0.13	110	9
Čiměř (Č)	49°12'; 16°00'	v_1	—	—	340	0.20	—	—
		v_2	—	—	339	0.18	—	—
		v_3	—	—	345	0.19	—	—
		v_4	—	—	243	0.24	—	—
Mrákotín (Mr)	49°13'; 15°22'	Pc 3	190	5	—	—	—	—
		Pi 2	170	6	—	—	—	—
		Pc 5	190	6	—	—	—	—
		b	190	2–6	250	0.20	230	10
Pelhřimov (Pe)	49°26'; 15°14'	v_1	303	—	303	0.26	—	—
		v_2	—	—	262	0.28	—	—
		v_3	—	—	262	0.29	—	—
		v_4	—	—	262	0.29	—	—
Hrádek (Hr)	49°43'; 15°07'	Pc 3	150	3.6	—	—	—	—
		Pc 3	120	4.7	—	—	—	—

		Pi 2	150	2.9	—	—	—	—
		Pc 5	190	4.2	—	—	—	—
		b	150	4.1	202	0.17	—	—
Krupá (Kr)	50°10'; 13°44'	Pc 3	240	—	—	—	—	—
		Pi 2	250	—	—	—	—	—
		Pi 2	220	—	—	—	—	—
		Pc 5	230	—	—	—	—	—
		b	220	—	—	—	—	—
		b	230	—	180	0.27	—	—
Boží Dar (BD)	50°25'; 12°55'	Pc 3	240	—	—	—	—	—
		Pi 2	240	—	—	—	—	—
		Pi 2	240	—	—	—	—	—
		Pc 5	240	—	—	—	—	—
		b	240	—	—	—	—	—
		b	230	168	168	0.28	160	12
		Profile VII						
Sukorady (Su)	50°26'; 15°02'	v_1	—	—	—	—	—	—
		v_2	—	—	180	0.34	—	—
		v_3	—	—	219	0.31	—	—
		v_4	—	—	226	0.29	—	—
Průhonice (Ph)	49°59'; 14°33'	b	—	—	202	0.35	—	—
Kamýk (Km)	49°38'; 14°15'	v_1	—	—	205	0.15	—	—
		v_2	—	—	223	0.25	—	—
		v_3	—	—	205	0.29	—	—
		v_4	—	—	187	0.25	—	—
Budkov (Bu)	49°05'; 14°01'	Pc 3	220	5	270	0.19	—	—
		Pi 2	220	5	270	0.10	—	—
		b	210	5	210	0.12	—	—
		b	—	—	210	0.16	—	—

Station	Geographic coordinates	Phenomenon (range of periods)	θ (σ max)	λ	θ_w	|C|	θ_p	θ_v
Domanín (Do)	48°58'; 14°44'	v_1	—	—	288	0.25	—	—
		v_2	—	—	285	0.22	—	—
		v_3	—	—	294	0.24	—	—
		v_4	—	—	225	0.31	—	—
Konst. Lázné (KL)	49°47'; 12°58'	v_1	—	—	160	0.27	—	—
		v_2	—	—	190	0.61	—	—
		v_3	—	—	186	0.35	—	—
		v_4	—	—	288	0.30	—	—
		Profile V						
Malý Lipník (ML)	49°21'; 20°48'	P_1 (4–17 m)	—	—	188	0.30	—	—
		P_2 (17–28 m)	—	—	188	0.31	—	—
		P_3 (28–43 m)	—	—	190	0.31	—	—
		P_4 (43–57 m)	—	—	180	0.29	—	—
		P_5 (>57 m)	—	—	176	0.28	—	—
Plavnica (Pl)	49°16'; 20°47'	Pc 3 (20s)	—	—	177	0.22	—	—
		Pi 2 (90s)	—	—	205	0.26	—	—
		P_1 (6–15 m)	—	—	188	0.44	—	—
		P_2 (16–29 m)	—	—	185	0.47	—	—
		P_3 (30–50 m)	—	—	183	0.46	—	—
		P_4 (>50 m)	—	—	181	0.43	—	—
Vyšný Slavkov(VS)	49°04'; 20°49'	P_1 (6–15 m)	—	—	182	0.52	—	—
		P_2 (15–25 m)	—	—	186	0.58	—	—
		P_3 (25–42 m)	—	—	188	0.56	—	—
		P_4 (42–57 m)	—	—	187	0.48	—	—
		P_5 (>—57 m)	—	—	189	0.40	—	—

Bardejov (Bd)	49°20'; 21°16'	v_2	—	—	282	0.14	—	—
		v_3	—	—	310	0.22	—	—
		v_4	—	—	180	0.24	—	—
Herlany (H)	48°48'; 21°29'	v_2	—	—	200	0.58	—	—
		v_3	—	—	192	0.42	—	—
		v_4	—	—	169	0.47	—	—
Čeladná (Če)	49°33'; 18°19'	v_2	—	—	0	0.48	—	—
		v_3	—	—	13	0.43	—	—
		v_4	—	—	35	0.35	—	—
Makov (Ma)	49°22'; 18°22'	v_2	—	—	348	0.49	—	—
		v_3	—	—	13	0.26	—	—
		v_4	—	—	32	0.58	—	—
Klačno-Reváň (KR)	48°57'; 18°37'	v_1	—	—	113	0.76	—	—
		v_2	—	—	130	0.62	—	—
		v_3	—	—	169	0.43	—	—
		v_4	—	—	180	0.30	—	—
Bojnice (Bo)	48°46'; 18°34'	v_1	—	—	133	0.82	—	—
		v_2	—	—	187	0.56	—	—
		v_3	—	—	173	0.42	—	—
Donovaly (Dn)	48°52'; 19°13'	v_1	—	—	127	0.50	—	—
		v_2	—	—	165	0.51	—	—
		v_3	—	—	174	0.47	—	—

Explanation: The data v_1–v_4 are by Wiese and Ritter for the following ranges of periods: $v_1 = <6$ min; $v_2 = 6$–18 min; $v_3 = 18$–40 min; $v_4 = >40$ min

The study and proper explanation of these supply us with valuable information the internal structure of the section. Relevant conclusions can be made by relating linearly the geomagnetic components. These characteristics express certain integral anomalous induction effect and the information is of regional character. Owing to the increased sensitivity of the electric field to local inhomogeneities it carries information on a rather local scale.

Geomagnetic and electromagnetic data were analysed by several methods (Rokityansky, 1961, Ádám, 1964, Berdichevsky, 1968). Results of these investigations are summarized in Table 1 for stations located at profiles VI, VII and V. The results were supplemented by Ritter's relevant values.

The estimates entered in Table 1 represent the azimuths of maximum electrical conductivity θ (σ_{max}) together with the inhomogeneity measure λ obtained by electromagnetic methods. Azimuths were rounded up to ten degrees. Maximum weight was allotted to results based on the analysis of the tensor relations between electromagnetic components. If available, estimates for different variation periods are pointed out (Pc3, Pi2, Pc5, b). Results of induction arrow parameters, (azimuths and moduli), are inserted under columns θ_W and $|C|$, also for different periods (notation v_1-v_4 with Ritter's results). For a few stations estimates are given also for the Parkinson angles θ_p and θ_v as azimuths of the preferred plane and its deviation from the horizontal plane, respectively.

The induction arrows for variations with periods between 20 and 40 min are displayed on the geological map of Czechoslovakia (Fig. 1) to illustrate their relation to specific geological features.

To interpret the directions of the induction arrows, it should be kept in mind that in the ideal case of a two-dimensional structure, (two-dimensional relief of the basement, long conductive body, etc.), the induction arrow is theoretically oriented in the direction of the rise of the non-conductive basement, or in the direction from a well conductive body with an anomalous concentration of the electric current.

The stations Š, Št, Hb, Ni in the Carpathian Basin are characterized by vectors oriented approximately in SSE to S directions. A similar tendency was found for the Hungarian territory (Ádám, 1969; Ádám and Verő, 1970). These directions, however, seem to prevail for longer periods only, ($T > 20$ min), because at some stations strong period-dependence of the induction effects was found. In particular, this was observed in stations Št and Ni, where the vectors for shorter periods (few min), showed NE to E orientation. We think this effect should be attributed to elevations of the crystalline basement, probably with Mesozoic cover, in the continuation of the Tribeč and the Považský Inovec core mountains. This suggestion is supported by the much larger induction moduli at Ni compared with Št. The attenuation of these effects is indicated by the rapid decrease of induction moduli to about 0.21 toward longer periods.

At station Š the azimuth of maximum conductivity in NW-SE direction was obtained for periods from about 20 sec to bays and, apparently no period-dependence was observed. The predominant direction fits well with the induction arrow for bays. The induction modulus of about 0.15, within spatially homogeneous distribution of vectors over the whole area suggests a rather low inhomogeneity at long periods.

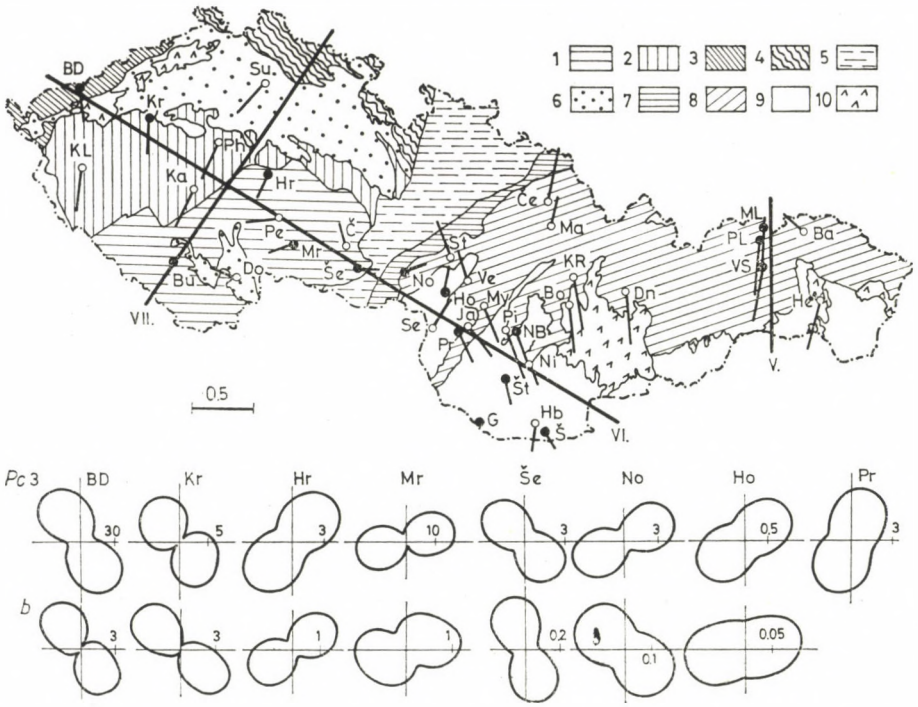


Fig. 1. Geological map of Czechoslovakia with DSS profiles Nos V, VI and VII. Induction vectors are displayed for the variation periods within 20 and 40 min range. Open circles specify observation sites of the GDR groups (Wiese and Ritter). Station symbols are according to Table 1. In the lower part the typical polar diagrams of the principal impedance tensor element are displayed for the majority of MTS stations. Polar plots for two different events (*Pc* 3, *b*) are shown.

The geological map was corrected according to Bouček and Kodym: Geologie II, Prague, 1963. Geological symbols: *Bohemian Massif:* 1 – Moldanubian block; 2 – Assynthian block; 3 – Saxo-Thüringian block; 4 – West Sudetan block; 5 – Moravian-Silesian zone; 6 – Cretaceous and Tertiary platform deposits; 7 – Alpine-Carpathian foredeep. *Carpathian region:* 8 – pre-Neogene folding of Carpathian unit; 9 – Neogene basin of Carpathian region; 10 – Tertiary eruptive rocks

At the station G the same electromagnetic method were used as at Š but two substantially different directions of maximum conductivity were found (see Table 1). Some important differences between the structural conditions in the basement seems to exist for stations Š and G. In general, the results are consistent with the geoelectric conditions reported from further southward in Hungary (Ádám and Verő, 1970).

Complex geoelectric conditions are suggested by the results of the station of NB located at the marginal part of the Carpathian Basin in close vicinity of the Považský Inovec mountains. Two sets of data were available here, because the GDR group carried out observations of the geomagnetic field simultaneously with our MT group. Induction characteristics derived from the two sets of data coincide reasonably well for the corresponding ranges of periods.

The induction vector directions fit to the general distribution over the Carpathian Basin, (SSE-S), the moduli, however, run at much higher level, ($|C| > 0.3$), compared with stations in the central parts of the basin. Considered in view of similar results from stations further to the NW, the induction characteristics are strongly affected by the anomalous zone of the Outer Carpathians connected with the Peripieninian lineament.

The electromagnetic characteristics at NB suggest directions of maximum conductivity which obviously follow the strike of the contact zone of relatively well conductive sedimentary rocks with a non-conductive core of the Považský Inovec.

The most remarkable effects of anomalous induction are observed in the Outer Carpathians. Inversion of induction vector, observed first by Wiese (1965a), was investigated at numerous stations over this geologically important area, where rocks of the Bohemian Massif submerge under the flysch zone of the Outer Carpathians and, under several km thick superficial layer, come into contact with the West Carpathians. The inversion zone is indicated between the stations Se-Pr, Se-Ho, Ho-Ja, Ve-My approximately on profile VI. It extends, however, toward NE beyond profile VI. Observations of the GDR group at four localities detected the inversion between Makov (Ma) — Klačno-Reváň (KR) and Wiese's results in Eastern Slovakia suggest the same effect between stations Bad and H. Our recent results, (1973), from profile V (stations ML, Pl, VS), have supplied us with information that locates a possible inversion zone beyond the Czechoslovak border on Polish territory.

A summary of the results obtained in Czechoslovakia, Poland, USSR (Ukraina) and Roumania has revealed a strong linear extension of the anomalous zone on a regional scale encompassing the whole Carpathian system in Central and South-Eastern Europe.

Attempts have been made to explain the observed features as an effect of intense electrical current confined to a high conductive cylindrical channel of long extent. Its depth and diameter were estimated as about 20 and 10 km, respectively (Wiese, 1965a, Rokityansky, 1972, Petr et al. in print). The ambiguity of this explanation leaves space for a variety of other models compatible with the observed induction effects.

The directional characteristics derived from MT data are available at stations Pr and Ho on both sides of the inversion zone. In rough features, they are consistent with those obtained from geomagnetic observations.

The geoelectric conditions in the western part of the Vienna basin can be characterized by MT results of the station at No. According to a DC electric survey (Prokeš and Šafránek, 1959) the depth to non-conductive basement is about 700 m and the basement is dipping SE-wards. Directional characteristics were derived by treating MT data according to Rokityansky, (1961), Berdichevsky, (1968). The results suggest azimuths increasing with the variation period from 290° over N to 30° E. The directions of maximum conductivity for pulsation periods (20 to 120 sec) seem to be connected with the SE-ward dipping of the non-conductive basement and, thus, with increasing thickness of a relatively well conducting cover.

The directional characteristics for longer periods (Pc5, bays) obtained from both the geomagnetic and MT data, coincide within 30° with each

other and indicate approximately NEE principial direction. Proceeding to the station Še further NW on profile VI, (already in the Bohemian Massif), we find a similar direction, almost no period dependence and a very low value of the induction modulus. The results at both these stations, (No and Še), and also at stations Či, Mr, Pe seem to indicate an influence of some deep-seated effect in the eastern margin of the Bohemian Massif.

Considering the structure at crustal depths of the Bohemian Massif in this area, as suggested by the results of DSS, important changes of electrical conductivity can be associated with the Přibyslav deep fault zone, where a local rise of the basalt zone of the earth's crust is anticipated on the basis of different geophysical methods.

The induction characteristics over the Bohemian Massif are rather sparsely distributed, as compared with the Carpathian region, for example. Nevertheless, they seem to express the main structural features sufficiently well. In our opinion they reveal mainly the induction effects from the deeper structure, because no sedimentary cover of important thickness is present at the majority of these stations. The only exception is the station at Do, where the induction characteristics may be contaminated by the influence of sedimentary matter of the Třebon and Budějovice Basins.

The spatial distribution of predominant directions is homogeneous over the main area of the massif displaying azimuths between 180°—200° E with no substantial period-dependence. Therefore, a relative electric homogeneity seems to prevail in the main bulk of the Massif.

An important deviation from this general pattern is suggested by the results from stations Pe, Mr, and Do in the eastern part of the Moldanubicum. The vectors here were found directed essentially toward W, probably as an effect of the Přibyslav fault zone.

The directions of maximum electric conductivity in the Bohemian Massif derived from MT data are available for the stations Mr, Bu, Kr, BD. In rough features the azimuths are compatible with the results of induction studies for the relevant bands of periods.

RESULTS OF MAGNETOTELLURICS

MT results from altogether 11 stations were available on profile VI. Similar data from the Budkov observatory, located beyond the area of profile VI, are also of interest, for they characterize the geoelectric conditions in the region with maximum crustal depths in the Bohemian Massif.

For the majority of stations the tensor relations were solved and tested by computational rotation for the presence of a two-dimensional structure with principal axes in those particular azimuths which make the diagonal elements Z_{xx} and Z_{yy} zeros, or at least minimum. Maximum and minimum elements in the corresponding azimuths were used to calculate the MT sounding curves in principal directions. This procedure was performed for several groups of events with different periods (Pc 3, Pi 2, Pc 5, b). For some stations only approximate curves $\varrho_{max}(\sqrt{T})$ were obtained by projecting the maxima of hodographs of both the electric and magnetic fields into the azimuth of maximum resistivity resp. maximum conduc-

tivity determined by approximative methods (Rokityansky, 1961; Ádám, 1964). In addition to these basic data, the whole set of apparent resistivity curves ϱ_{ax} and ϱ_{ay} in geographical NS and EW directions was also considered. In this way two sets of MT data were obtained and treated by a different approach.

First we approached the results by restricting the curves in principal directions to those which correspond to parallel polarization and give according to theory and extensive experience, the most reliable information on the internal geoelectric structure. To select these curves we considered the relations between the magnetic and electromagnetic directional characteristics (induction vectors, Parkinson's preferred plane, azimuths of maximum and minimum impedance) and related them to the local geological features.

The induction vectors were usually perpendicular to remarkable geological inhomogeneities such as deep-penetrating fault zones, contact zones of sedimentary basins with marginal mountain ranges, etc. These conditions, for example, were found in the vicinity of the Carpathians, which intersect the profile between stations Ho and Pr. The same perpendicular orientation to the inhomogeneity was observed on profile V (stations ML, Pl and VS), in vicinity of the Polish-Czechoslovak border (northern branch of the Peripieninian lineament).

Similar conditions seem to be valid for the Krušné hory fault zone striking SSW-NNE-ward andcrossing profile VI east of the station BD. The angles of the maximum dip of Parkinson's preferred plane coincide with a reasonable accuracy with the induction vector.

When considering the mutual orientation of the induction vectors and of the maximum conductivity azimuths along the profile, (for corresponding periods), we found them close to perpendicular in the vicinity of these remarkable inhomogeneities (stations NB, Pr, BD, Kr, Mr).

In areas without any remarkable geological feature, as a rule in the central parts of the sedimentary basins, the azimuths of the induction vector coincide within a few degrees with the maximum conductivity (stations Š, Ho, No and Še).

Accordingly, we considered the angle between an induction vector and a corresponding maximum conductivity azimuth as an indicator of the presence of a strong inhomogeneity.

In sense of the above reasoning we restricted the interpretation to those curves obtained from maximum impedances in regions without any remarkable geological feature (stations Š, G, Pr, Ho, No). On the other hand, in regions with a strongly deformed MT field by local inhomogeneities, we interpreted the MT curves corresponding to the azimuth of maximum conductivity being parallel to the strike of the inhomogeneity. In both cases the azimuths of the parallel curves were roughly perpendicular to the induction vectors.

The whole set of the MT results can be divided into three groups corresponding to different geological conditions over a particular region. The geological conditions influence the range of resistivities ϱ_a, the penetration depth and the curves develop certain characteristic types.

The first group consists of the curves in the Bohemian Massif with MT

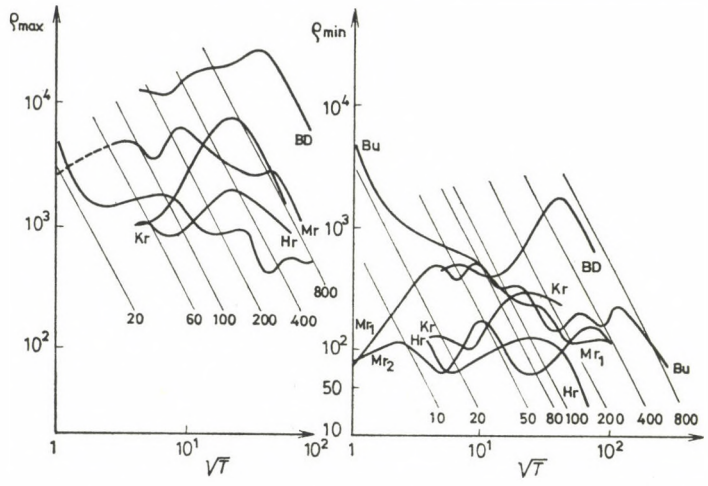


Fig. 2. Set of MTS curves in principal directions for stations in the Bohemian Massif. Curves from the station Bu are about 25° off the principal direction. Individual curves are labelled by station symbols
Special notation: Mr_1 – curve ϱ_{max}; Mr_2 – curve ϱ_{min}

stations BD, Kr, Hr, Mr and Bu in the south-western part of the Moldanubicum (Fig 2). The curves run at high values of apparent resistivities (ϱ_{max} about $5 \cdot 10^2 - 5 \cdot 10^4\ \Omega$ m, ϱ_{min} about $5 \cdot 10 - 5 \cdot 10^3\ \Omega$ m), with maximum resistivities at the marginal station of BD. MT curves from Bu, with their decreasing resistivities seem to be close to the type for the granitoid basement with high resistivity, characteristic of shield areas (Fournier, 1968). The curves at Kr, Hr and BD are similar to those from the Russian Platform (Tikhonov et al. 1964).

The analysis of the principal directions usually revealed their small scatter. The polar diagrams suggest a more general than a simple two-dimensional structure. The azimuths of Z_{max} are within a sector limited approximately by EW and NW-SE directions, in the whole Massif. This particular direction is almost perpendicular to the strike of the major fault zones of deep foundation in the Bohemian Massif, as evidenced by the results of DSS. For example, the Krušné hory fault zone striking NNE-wards, bounds a block of increased crustal thickness in the Bohemian Massif from the Saxo-Thuringian region. Of similar importance for the Bohemian Massif are the Central Bohemian Suture and the Přibyslav fault zone. These geological features seem to be so important that they determine the regional strike of the deep homogeneity axis. Owing to this fact we think that the ϱ_{min} curves characterize the parallel polarization.

The sounding curves from No, Ho and Pr belong to *the second group* (Fig. 3). The area covered by these stations is a typical geological unit. In the west, it is bounded by the margin of the Bohemian Massif, in the east by the Carpathians. The area forms a certain transition zone between

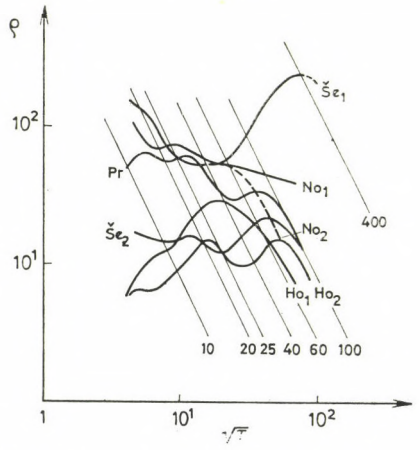


Fig. 3. Set of MTS curves selected for interpretation in the transition zone between the Bohemian Massif and the Carpathians. The curves in the principal directions are displayed together with some apparent curves close to the principal directions. Basic labelling is by station symbols with indices specifying the curve type: Pr – $\varrho_{ax} \doteq \varrho_{max}$, $Še_1$–ϱ_{max}, $Še_2$–ϱ_{min}, No_1 – ϱ_{max}, No_2 – ϱ_{min}, Ho_1 – ϱ_{max}, Ho_2 – $\varrho_{ay} \doteq \varrho_{max}$ at long periods

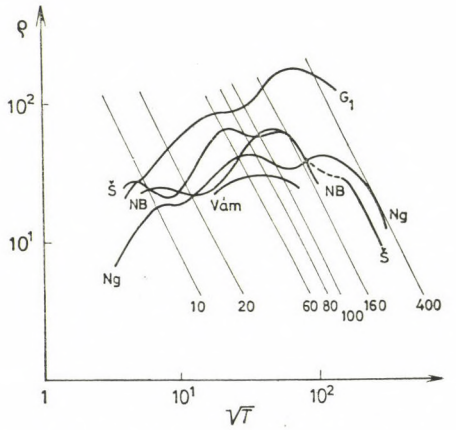


Fig. 4. MTS curves from the Danube Lowland. Labelling is by station symbols. Two Hungarian sites, Vám – Vámosmikola and Ng – Nagycenk, were included according to Fournier et al. (1971). Notation used: Š – ϱ_{max}; G_1–$\varrho_{ax} \doteq \varrho_{max}$, NB – ϱ_{eff}

both geological units, where relatively thick sedimentary and flysch formations cover the submerging crystalline rocks of the Bohemian Massif.

The station Ho was located approximately above the axis of the basin, two other stations No and Pr were located at the west and east margins of the basin with reduced thickness of sedimentary and flysch cover. The MT curves at Ho run at about 1—10 Ω m range and can be considered as characteristic of the structure type with a thick sedimentary cover, as defined by Fournier from the data at Ückermünde (Fournier, 1968).

The azimuths of maximum impedance at these stations flow approximately the general strike of the flysch zone. The polar diagrams suggest a well-developed two-dimensional structure at Pr, in the NW direction the conditions of two-dimensionality deteriorate.

MT curves from the station Še were also included into this region. The latter site was located already in the eastern margin of the Bohemian Massif. However, the directional characteristics of the field show a still strong influence of the transition zone, and also the range of apparent resistivities support this choice.

MT results from the Danube Lowland make up *the third group*. Stations Š and G were considered on our territory. The station NB was located at the very margin of the Danube Lowland near the outcrops of the Považský Inovec core mountains. Data from this region were supplemented by sound-

ings at Hungarian sites Vámosmikola and Nagycenk (Fig. 4) (Fournier et al. 1971).

Two principal directions are important in this region. The NE-SW strike of the West Carpathians is at the same time a natural axis of the geoelectric homogeneity. The strongest changes of the electrical parameters, caused by undulation of the crystalline basement, should be expected in the direction perpendicular to the Carpathians, according to the DSS results. An other important direction is approximately the EW Danube azimuth which seems to be connected with a deep-seated effect in the basement, because it appears dominant at longer periods. These principal directions are connected with the maximum impedance.

The second approach to MT data interpretation was based on an estimation of the typical depths of possible conductive zones statistically. From all estimated conductive zone depths at individual stations along the whole profile the summation curve was derived (Fig. 5). It was composed of partial summation curves which delimit certain depth ranges with acceptable deviations for individual zones of increased conductivity.

This approach to interpretation might be subject to criticism, for the depth estimates are certainly biased by local inhomogeneities and fictitious zones may appear. Nevertheless, we tried this interpretation for sake of comparison with the results obtained from selected curves.

The results of both approaches are summarized schematically in Figure 6. They suggest possible zones of increased conductivity along profile VI. From the statistical treatment a higher geoelectric differentiation of the cross section has been obtained. In general, the two sets of results coincide within reasonable limits.

The characteristic features of a suggested model can be summed up in the following points:

1. A continuous zone of increased electrical conductivity is suggested along the profile at a depth of about 20 km. This particular depth roughly coincides with the transition from granitic to basaltic layer of the earth's crust, as seen from Figure 6 (the structural scheme by Beránek (1971)). A

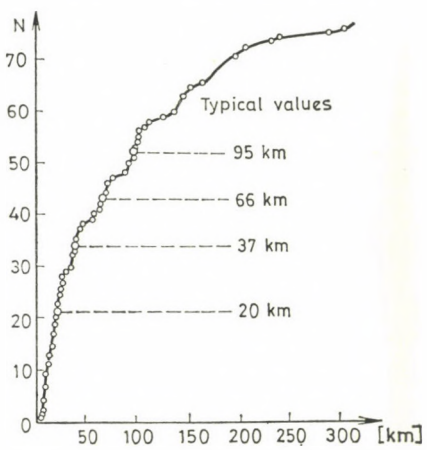


Fig. 5. Summation curve for the statistical treatment of the depth estimates

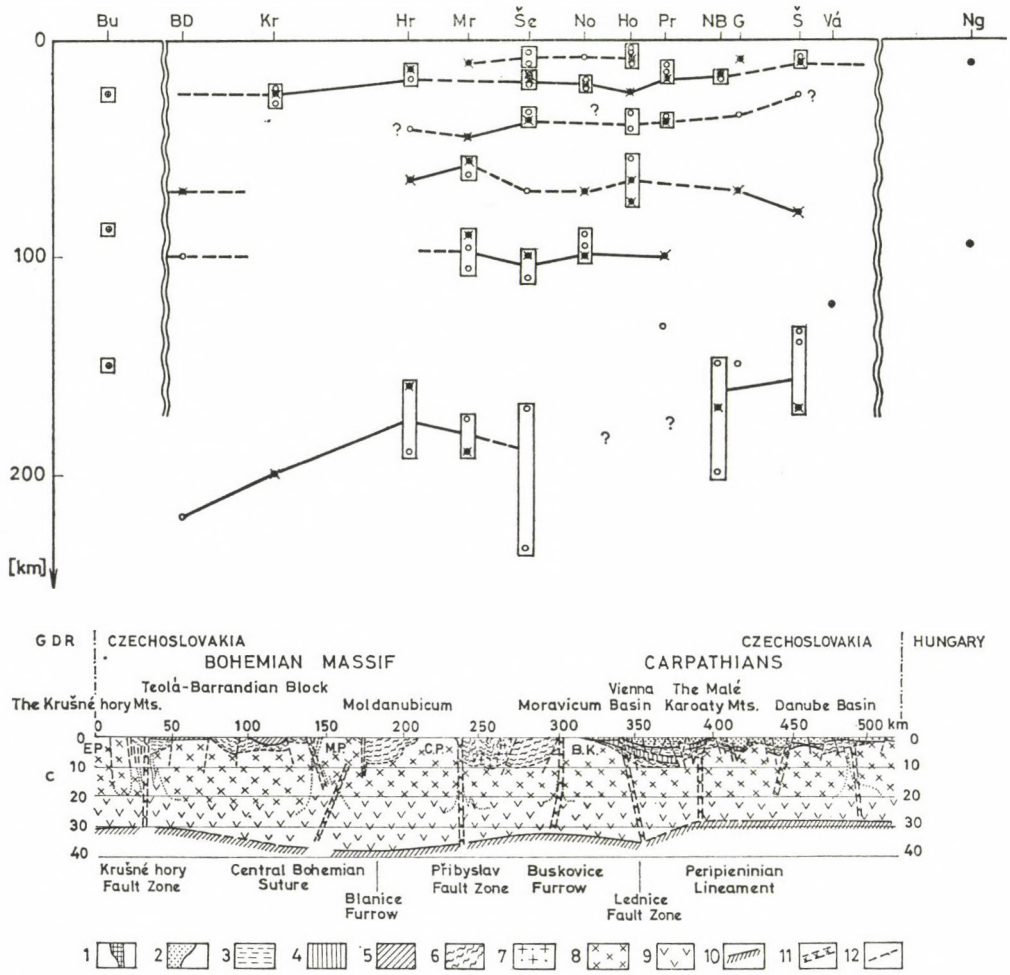


Fig. 6. Tentative geoelectric cross-section along profile VI at crustal and upper mantle depths as suggested by the interpretation of selected MTS curves and by the statistical treatment. Notations: full dots with crosses are results where estimates from selected curves and from the statistical treatment coincided; open circles are depths from apparent MTS curves attributed to a certain boundary on the basis of the statistical treatment. Estimates for Budkov (Bu) and Nagycenk (Ng) observatories are shown in separate blocks, because of their substantial distance from profile VI. A structural scheme of the earth's crust structure along profile VI, as suggested by geological interpretation of the DSS results (Beránek and Dudek, 1972) is shown in the lower part.

Explanation of geological symbols: 1 – neovulcanics; 2 – Neogene sediments; 3 – flysch belt; 4 – Mesozoic; 5 – Paleozoic; 6 – crystalline schists; 7 – durbachits; 8 – granite zone; 9 – basalt zone; 10 – M-discontinuity; 11 – deep faults; 12 – principal regional faults

similar zone was evidenced in other areas, for example, in the Vilyuisk syneclise and under the Aldan shield, where it was correlated with the granit-basalt boundary at the depth of the Conrad discontinuity (Berdichevsky et al., 1972).

Correlation with the low velocity channel at crustal depths, as suggested by DSS along profile VI between 10—20 km (Beránek, 1971) is possible. The DSS results from different regions give a LVL between 15—20 km, as pointed out in a generalized model of the velocity distribution in a continental type earth's crust and the upper mantle (Davidova et al., 1972).

2. A zone of increased conductivity at about 40 km depth was obtained from the statistical treatment. It might be correlated indirectly with the Moho discontinuity. However, it has not been established as yet that this discontinuity is marked by a substantial increase of electric conductivity and some investigators claim (Fournier, 1968) that it is not detectable by electromagnetic methods.

3. Two zones of increased conductivity are suggested between 60—70 km and at about 100 km depths. May be they are not two separate zones, as the resolving power of the MT method seems to be insufficient to discriminate between them. The latter zone at 100 km depth is detected more reliably. In particular, it was evidenced between stations Mr and Pr that is, below the transition zone between the Bohemian Massif and the Carpathians. It is usually correlated with the LVL in the upper mantle and we favour this interpretation.

4. A zone between 150—200 km was found at all stations from the Bohemian Massif and also in the Inner Carpathian region. The scatter of depths is serious. However, a certain dipping tendency towards the Bohemian Massif can be observed.

5. The sounding curves at the stations in the Bohemian Massif, further at G and Nagycenk, suggest with great scatter the deepest zone between 350—500 km. This boundary was not included in Figure 6. However, the suggested depths are compatible with seismological evidence (20° discontinuity) and with estimates obtained by analysing the long period variations of geomagnetic data on global scale.

The conductive zones between 60—70 km, 100, 200 and 400 km are also reported from other regions. Estimates scatter within rather broad limits. Close to our territory we refer to: Fürstenfeldbruck — 55 km, Göttingen — 70 km, Freiberg (Sachs) — 80 km, average from Hungary — 50 to 70 (90) km (Fournier, 1970).

Seismological evidence of the upper mantle structure in South-eastern Europe allow three discontinuities between 50 and 90 km and the LVL between 90—140 km (Vaněk, 1972). Other discontinuities are estimated at 13°, 15° and 20°, which correspond to depths 150, 200 and 400 km, respectively. The model for the western part of the USA by Archambeau et al. (1969) for different types of basement (basins and platforms) assumes a velocity decrease between 50—70 km and the zone terminates with a sudden increase of velocities between 150—200 km. The discontinuity at 400 km depth is also characterized by an abrupt increase of velocities.

CONCLUSION

The contribution summarizes the results of electromagnetic studies in the broader zone along the DSS profile No VI. The results of interpreting the MTS curves are summed up in a structural scheme in Figure 6. We consider this as a tentative model which should be further developed by providing additional evidence from other stations and by increasing the accuracy of the present estimates.

REFERENCES

ÁDÁM, A., 1964. Über die Berechnung der magnetotellurischen (MT) Anisotropie. *Freiberger Forschungshefte, C*, **168**, Leipzig.

ÁDÁM, A., 1969. Appearance of the electrical inhomogeneity and anisotropy in the results of the complex exploration of the Carpathian Basin. *Acta Geod. Geophys. Mont. Hung.* **4**, 187.

ÁDÁM, A., VERŐ, J., 1970. Das elektrische Modell des oberen Erdmantels im Karpatenbecken. *Acta Geod. Geophys. Mont. Hung.* **5**, 5.

ARCHAMBEAU, C. B., FLINN, E. A., LAMBERT, D. G., 1969. Fine structure of the upper mantle. *J. Geophys. Res.* **74**, 5825.

BERÁNEK, B., 1971. Deep seismic sounding in Czechoslovakia (in Czech). *Geologický průzkum*, **13**, 289.

BERÁNEK, B., DUDEK, A., SUK, M., WEISS, J., 1971. Geological interpretation of deep seismic sounding in Czechoslovakia (in Czech). *Geologický průzkum*, **13**, 353.

BERÁNEK, B., DUDEK, A., 1972. The results of deep seismic sounding in Czechoslovakia. *Z. Geophys.* **38**, 515.

BERDICHEVSKY, M. N., 1968. Electric Prospecting by the Method of Magnetotelluric Profiling (in Russian). Nedra, Moscow, 91.

BERDICHEVSKY, M. N., VANYAN, L. L., FELDMAN, I. S., PORSTENDORFER, G., 1972. Conducting layers in the earth's crust and upper mantle. *Gerlands Beitr. z. Geophys.* **81**, 187.

DAVIDOVA, N. I., KOSMINSKAYA, I. P., KAPUSTIAN, N. K., MIKHOTA, G. G., 1972. Models of the earth's crust and M-boundary. *Z. Geophys.* **38**, 369.

FOURNIER, H. G., 1968. Proposition d'une méthode pour déterminer la structure du premier millier kilométres de la terre d'après la résistivité apparente. *Acta Geophys. Pol.* **16**, 215.

FOURNIER, H. G., 1970. Contribution au développement de la méthode magnétotellurique notamment en vue de la détermination des structures profondes. Thèse, Faculté des Sciences de l'Université de Paris.

FOURNIER, H. G., ÁDÁM, A., DE MIGUEL, L., SANCLEMENT, E., 1971. Proposal for a first upper mantle magnetotelluric E-W profile across Europe. *Acta Geod. Geophys. Mont. Hung.* **6**, 459.

PĚČOVÁ, J., PETR, V., PRAUS, O., TOBYÁŠOVÁ, M., 1969. Magnetotelluric deep sounding at field stations Nitrianská Blatnica, Nadrlenisko (Prievaly) and Pánov (Hodonin), Czechoslovakia. *Trav. Inst. Geophys. Tchécosl. Acad. Sci.*, No. 311, Geofysikální sborník, 17, Prague.

PĚČOVÁ, J., PRAUS, O., PETR, V., TOBYÁŠOVÁ, M., 1972. Magnetotelluric inhomogeneity in the Eastern Part of the Bohemian Massif. *Trav. Inst. Geophys. Tchécosl. Acad. Sci.* Geofysikální sborník 20, Prague.

PETR, V., PĚČOVÁ, J., PRAUS, O., 1964. A study of the electric conductivity of the earth's mantle by magnetotelluric measurements at Šrobárová (Czechoslovakia). *Trav. Inst. Geophys. Tchécosl. Acad. Sci.*, No. 208, Geofysikální sborník, Prague. 1965.

PETR, V., PĚČOVÁ, J., PRAUS, O., TOBYÁŠOVÁ, M., HVOŽDARA, M., 1967. Anisotropy and horizontal inhomogeneity of the electrical conductivity derived from the analysis of the magnetotelluric field at Šrobárová (Czechoslovakia). *Trav. Inst. Geophys. Tchécosl. Acad. Sci.*, No. 283, Geofysikální sborník, Prague, 1968.

PETR, V., PĚČOVÁ, J., PRAUS, O., Charakteristiky pole geomagnetických poruch v oblasti styku Českého masivu s Karpatskou soustavou. Sborník "Hlubinná geologická stavba Československa", Smolenice 1973 (in print).

PRAUS, O., PĚČOVÁ, J., PETR, V., TOBYÁŠOVÁ, M., 1966. The depth distribution of electric conductivity and its anisotropy according to magnetotelluric measurements at the station Gabčikovo (Czechoslovakia). *Trav. Inst. Géophys. Tchécosl. Acad. Sci.*, No. 259, Geofysikální sborník, Prague. 1967.

PRAUS, O., PĚČOVÁ, J., PETR, V., DVOŘÁK, Z., TOBYÁŠOVÁ, M., 1970. Magnetotelluric inhomogeneity of the transition zone between the Bohemian Massif and the West Carpathians. *Trav. Inst. Géophys. Tchécosl. Acad. Sci.*, No. 336, Geofysikální sborník, 18, Prague.

PROKEŠ, I., ŠAFRÁNEK, V., 1958. Závěrečná zpráva o geologickém průzkumu prováděném v roce 1958. Brno 1959 (not published).

ROKITYANSKY, I. I., 1961. On the use of the MT method over anisotropic and inhomogeneous massives (in Russian). *Izv. Akad. Nauk SSSR*, No. 11, 1607.

ROKITYANSKY, I. I., 1972. Electric conductivity anomalies of the earth's crust in the Carpathians (in Russian). *Izv. Akad. Nauk SSSR, Ser. Fiz. Zemli*, No. 10, 97.

TIKHONOV, A. N., LIPSKAYA, N. V., YANOVSKY, B. M., 1964. Some results of the deep magnetotelluric investigations in the USSR. *J. Geomagn. Geoelectr.* **15**, 275.

VANĚK, J., 1972. Seismological evidence on discontinuities in the mantle. *Z. Geophys.* **38**, 355.

WIESE, H., 1965a. Geomagnetische Tiefentellurik. Abh., No. 36. Geomagn. Inst. Potsdam, Akademie Vlg. Berlin.

WIESE, H., 1965b. Geomagnetische Induktionspfeile in der ČSSR, hervorgerufen durch grossräumige elektrische Leitfähigkeitsstrukturen. *Studia Geophys. Geod. ČSAV*, **9**, 415.

HEAT FLOW, CRUSTAL TEMPERATURES AND GEOELECTRIC CROSS-SECTION IN CZECHOSLOVAKIA

V. ČERMÁK, J. PĚČOVÁ, O. PRAUS

The characteristic features of the geoelectric model of the earth's crust and of the upper mantle derived from magnetotelluric and geomagnetic investigations at profile VI of the deep seismic sounding (DSS) were presented in the previous paper. Zones of increased electrical conductivity were suggested at crustal depths between 15—25 km, further between 40—70 km and at about 100 km depth in the upper mantle. There are certain depth fluctuations at individual stations due to horizontal inhomogeneities, but, in general, the zone depths tend to increase from the Pannonian Basin to the Bohemian Massif.

Owing to the strong dependence of electric conductivity on temperature, the zones of increased conductivity are usually accounted for by specific geothermal conditions. Laboratory experiments on electric conductivity as a function of temperature have shown that it generally increases with increasing temperature (Parkhomenko, 1965). However, the conductivity range and the rate of increase are different for the various types of rocks. Averaged curves of electric conductivity as function of temperature for various types of rocks (granites, basalts, ultrabasics) were used to estimate its generalized distribution under continents down to 100 km depth (Bondarenko, 1968). This model seems to fit the distribution of the electric conductivity in shield areas with relatively low temperatures at the base of the earth's crust (about 300 °C).

The distribution of electric conductivity in geologically young areas, however, may be expected to differ substantially from the above model because much higher temperatures can be assumed at crustal depths according to geothermal measurements. The very important role of even a small amount of water must also be taken into account. Under such conditions melting processes with a subsequent increase of electric conductivity by 2 to 3 decimal orders are possible at crustal and upper mantle depths (Berdichevsky et al., 1972).

To relate the magnetotelluric results in the Czechoslovakian part of profile VI with the possible temperature distribution in the crust, more than 80 heat flow determinations were carried out. They were obtained by systematic measurements in bore holes and their interpretation can be found in this monograph (see pp. 414-424). On investigating the heat flow values by geological units in Czechoslovakia we found an average of 1.6 HFU (HFU — 10^{-6} calcm^{-2} sec^{-1}) in the Bohemian Massif, 1.4 HFU in the Carpathian Foredeep and a high value of 2.1 HFU in the Pannonian Basin. Therefore, substantially different temperatures can be expected in the Bohemian Massif and in the Carpathians.

The measured values of the terrestrial heat flow, heat production due to radioactive heat sources and thermal conductivity together with some assumptions on the structure of the earth's crust and vertical distribution of radioactivity and conductivity enable the calculation of crustal temperatures. Using the results of DSS together with gravity and magnetic data and determinations of the radioactive content in crustal rocks, we constructed reasonable geothermal models of the earth's crust for several locations on the Czechoslovakian territory (Čermák, 1975). The sites for calculated temperature-depth profiles were chosen in places (Fig. 1) where the crustal structure is relatively well known and where the crustal profile may represent a typical structural pattern for a particular large seismotectonic unit.

Thermal conductivity (Čermák, 1967) and heat production (Čermák and Matolín, 1974) for surface rocks was measured for several hundreds of specimens from various locations. These data, however, can be only used for the calculations in the uppermost layer. To extrapolate the temperature curve downwards, the vertical decrease of radioactivity and the temperature-dependence of thermal conductivity must be evaluated. For a given heat flow, temperatures at shallow depths are little influenced by heat generation, although at the base of the crust they are affected to an important degree by this factor. Changing the thermal conductivity in the model affects the temperatures at all depths, but because of the limited range of values shown by crustal rocks at temperatures 200—500 °C, changing this quantity has usually less influence on the temperature than changing the heat flow at the surface by the amounts permitted by observations.

To overcome these difficulties the equation of heat conduction was simplified by assuming steady state conditions and solving the one-dimensional problem only. A simple empirical temperature-dependence of the coefficient of thermal conductivity $\lambda_T = (AT + B)^{-1}$, where A, B are constants, was introduced, according to the data of Birch and Clark (1940). All temperature-depth curves were calculated for a model of uniform granite radioactivity, the value of which should represent the average value in the total granite section. To show the possible variations in temperature due to the heat production used, several curves for each model are given in Figure 1.

The most important result from temperature calculations are the existing regional temperature differences at the base of the crust between the Bohemian Massif and the Carpathians which may reach 500 °C or even more for the heat flow range 1.2—2.5 HFU. Equally important is the fact that between both tectonic systems regional variations in the upper mantle heat flow of up to 1.0 HFU may exist. Such a variation, especially when concentrated on a relatively short distance may lead to significant horizontal temperature gradients, to uneven distribution of crustal temperatures, and the energy flow from below the crustal base may be the driving force for geological evolution and/or the critical factor for the geophysical interpretation. This may be the case of the Cretaceous Table, the Vienna Basin and the rapid change in heat flow along DSS profile VII.

The calculated temperatures at the base of the crust at 35—40 km under

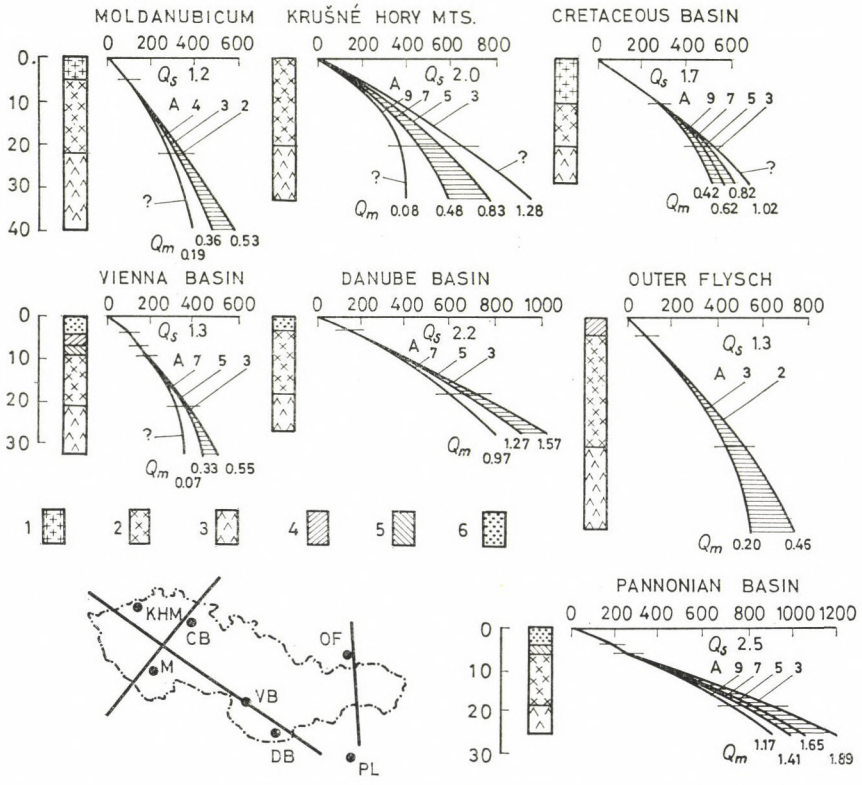


Fig. 1. Temperature *vs.* depth curves for selected sites in Czechoslovakia, Poland and Hungary. A – average heat production (10^{-13} cal cm^{-3} sec^{-1}), Q_s – surface heat flow, Q_m – Moho heat flow HFU Explanations: 1 – crystalline schists; 2 – granite; 3 – basalt; 4 – Carpathian flysch; 5 – Mesozoic; 6 – Neogene

the Bohemian Massif are within 500—550 °C, with local maxima of 600—650 °C in regions of enhanced surface heat flow. The Carpathian frontal foredeep is characterized by crustal base temperatures of 450—600 °C, however, the low calculated mantle heat flow in this zone still remains a puzzle (mainly in the Outer Flysch zone) and the existence of steady state conditions is dubious.

The hyperthermal region of the Pannonian Basin, which partly covers the southernmost part of Slovakia, has typical extreme subsurface temperatures. The mantle heat flow may be about 1.0 HFU in the Danube Basin and 1.4 HFU in the Pannonian Basin on the Hungarian territory. The corresponding temperatures at the Moho-discontinuity are in the interval 800—1100 °C.

In Figure 2, together with temperature curves, the temperatures of the beginning of melting processes are plotted for granite in the presence of water, for schists and dry granites (Berdichevsky et al., 1972; Villi and

Tattel, 1963; Menert, 1968). The depths where the two sets of curves cross each other are between 15—20 km for the Danube Basin. The crossing becomes less definite for the Moldanubian Block of the Bohemian Massif, but is still possible at depths of about 30 km. Accordingly, observed zones of increased electric conductivity at crustal depths and also their dipping towards the Bohemian Massif seem to be explainable by melting processes in associations close to granites.

A similar reasoning for ultrabasic rocks anticipated in the upper mantle is less definite, because the extrapolation of temperature curves beyond 30 km depths may be rather uncertain. The temperature curves for heat generation $P = 5—7 \cdot 10^{-13}$ cal cm^{-3} sec^{-1} if extended downwards to the upper mantle intersect the solidus for dry pyrolite (Clark and Ringwood, 1964) at about 35 km. By other authors (Berdichevsky et al., 1971) the temperature distribution curves in the upper mantle were plotted simultaneously with the melting curves for quartz, tholeite, pyrolite and basalts. They found a possible intersection range between 40—70 km. This result relates to another part of the Pannonian Basin. The difference of depths between the two estimates is probably due to the uncertainty of temperature and melting curves rather than an effect of local conditions.

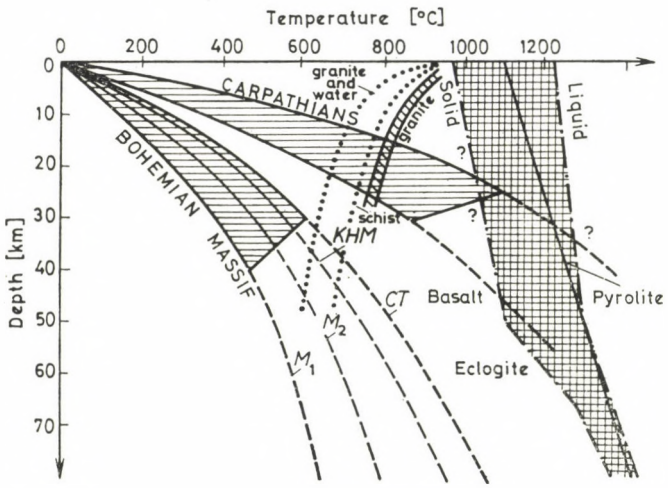


Fig. 2. Range of crustal temperatures below the Bohemian Massif and the Neogene depressions of the Carpathians. M_1 and M_2 are the minimum and maximum temperature curves for the Moldanubicum, CT – average temperature for the Cretaceous Table, KHM – average temperature for the Krušné Hory Mts. Cross-hatched are the melting relations for basalt and eclogite (Yoder and Tilley, 1962), pyrolite solidus curve is taken from Clark and Ringwood (1964). The curves showing melting temperatures for granite, crystalline schist and granite with water are taken from Villi and Tattel (1963), Menert (1968) and Berdichevsky et al. (1972)

REFERENCES

BERDICHEVSKY, M. N., DUBROVSKY, V. G., LUBIMOVA, E. A., MANAFLI, A. I., NEPESOV, K. N., FELDMAN, I. S., 1971. Anomalies of upper mantle electrical conductivity and their geothermal interpretation (in Russian). *Izv. Akad. Nauk SSSR, Ser. Fiz. Zemli*, No. 7, 56–67.

BERDICHEVSKY, M. N., VANYAN, L. L., FELDMAN, I. S., PORSTENDORFER, G., 1972. Conducting layers in the earth's crust and upper mantle. *Gerlands Beitr. z. Geophys.* **81**, 187–196.

BIRCH, F., CLARK, H., 1940. The thermal conductivity of rocks and its dependence on temperature and composition. *Amer. J. Sci.* **238**, 529–558.

BONDARENKO, A. T., 1968. Generalization of the results on electrical conductivity of eruptive rocks under high temperatures in relation to the structure of the earth's crust and of the upper mantle (in Russian). *Dokl. Akad. Nauk SSSR*, **178**, 1058–1060.

ČERMÁK, V., 1967. Coefficient of thermal conductivity of some sediments and its dependence on density and water content of rocks. *Chemie d. Erde* **29**, 271–278.

ČERMÁK, V., 1968. Terrestrial Heat Flow in Czechoslovakia and Its Relation to Some Geological Features. 23. Intern. Geol. Congress, Prague, 5, 75–85.

ČERMÁK, V., 1975. The thermal structure of the crust in Czechoslovakia *Veröff. Zentr. Inst. Phys. Erde* **31** (2) 347—355.

ČERMÁK, V., MATOLÍN, M., 1974. Radioactivity and heat production of rocks of the Bohemian Massif (in preparation).

CLARK, S. P., RINGWOOD, A. E., 1964. Density distribution and constitution of the mantle. *Rev. Geophys.* **2**, 35–88.

MENERT, K., 1968. New data on the problem of granites (in Russian). Moscow.

PARKHOMENKO, E. I., 1965. Electrical Properties of Rocks. Nauka, Moscow, 93.

VILLI, R., TATTEL, O., 1963. Melting in the earth's crust. Trudy Mezhdunarodnogo geologicheskogo Kongressa, 2, Moscow.

YODER, H. S., TILLEY, C., 1962. Origin of basalt magmas, and experimental study of natural and synthetic rock systems. *J. Petrol.* **3**, 342–532.

III. PANNONIAN BASIN

HUNGARY'S GEOLOGY: AN OUTLINE

P. KISHÁZI

Geologically, the whole area of Hungary belongs to the Pannonian Basin. It is a young basin-like subsidence between the eastern margin of the Alps, the arc of the Carpathians (to the E of the Bihar Mountains in Transylvania) and the Dinaric ranges, thus extending in almost all directions the borders of Hungary.

A mountain range, the Hungarian Central Mountains, diagonally crosses the area striking SW-NE, divided by the river Danube into two parts: the SW part is the Transdanubian Central Mts, the NE part the Northern Central Mts (Fig. 1). The Island Mountains of Baranya arise from their surroundings in the corner of the rivers Danube and Dráva. In the W part, the easternmost foothills of the central range of the Alps appear. All other parts of the country are lowlands or rolling lands. To the NW from the Central Mts one finds the Little Hungarian Plain, to the SE the Great Hungarian Plain. The latter is the most extended part of the Pannonian Basin.

Morphologically the whole country is largely a basin and all its mountains are not greater than medium height.

The geological construction of Hungary contains Precambrian, Paleozoic and Mesozoic rocks (basement), older Tertiary formations covering them (overlain), younger Tertiary and Quaternary rocks in the depressions (basin sediments).

The oldest rocks appear on the surface in the W border and partly in the NE corner in small areas, but they have a much greater role in the basement according to some boreholes. They are mainly strongly metamorphosed crystalline schists (gneisses, mica schists, amphibolites, quartzites, etc.), and supposedly they were sediments of an Algonkian — early Old-Paleozoic geosyncline. Less metamorphosed rocks (mainly phyllites and slates, seldom limestones, siliceous shales, quartz porphyries, etc.) are known from the basement and from outcrops, mainly in the area of the Central Mountains, as ingredients of the late Old-Paleozoic geosyncline. The rocks of the



Fig. 1. Geographical units of Hungary

New-Paleozoic are even less metamorphosed, or unmetamorphosed (slates, shales, limestones, siltstones, sandstones, conglomerates, sometimes Variscian granites). They are found on the surface in the SW and middle parts of the Transdanubian Central Mts, in the NE part of the Northern Central Mts and in the Island Mts of Baranya.

In the geological build-up of Hungary, sediments of the Mesozoic geosyncline have an important role. This group being able to reach several thousand m contains mainly limestones and dolomites, then shales, marls, sandstones and sporadically eruptive rocks (diabase, gabbro, phonolite, trachydolerite). It also contains some important utilizable deposits (coals, bauxites, manganese and iron ores). Originally the Mesozoic rocks could have covered the Precambrian — Paleozoic basement rather uniformly (although with some stratigraphic hiatuses), but in the Neogene this cover became structurally disintegrated, thrust up and partly denuded, therefore they lack from certain strips of the basement. In greatest spreading on the surface it is present in the Transdanubian Mts, but it is also known from the NE part of the Northern Central Mts and from the Island Mts of Baranya.

In the Cenozoic age the Alpine-Carpathian orogeny having started in the Cretaceous, ran through with crustal movements of changing intensity, accompanied by volcanic activity. The crustal movements caused transgressions and regressions of the Tertiary shallow seas repeatedly, depositing clayey, marly, limy, muddy, sandy or pebbly sediments including important brown coal beds, besides some oil and gas fields. The volcanic activity resulted in rhyolitic, dacitic and mainly andesitic lava flows and pyroclastics with copper and polimetallic ores and industrial clay beds.

The majority of superficial and buried Paleogene sediments can be found in the middle and NE part of the Transdanubian Mts, and in the greatest part of the Northern Central Mts. In the latter area, an important volcanic and subvolcanic activity had been present yet. The Little and Great Hungarian Plains could be continents largely in this age.

Volcanic activity was strongest in the Northern Central Mts at the beginning of the Neogene due to strong faulting movements of the crust. These crustal movements caused subsidences of different intensity in the whole area of the country, resulting in an archipelagos. The sinking reached its maximum in the younger Neogene, simultaneously the sea changed into fresh water and became an inland sea gradually. This inland sea filled up at the end of the Neogene, and since then continental erosion and sedimentation is going on. Some traces of basaltic volcanism from the end of the Neogene can also be found. The maximum thickness of the young sedimentary cover in the Little Hungarian Plain is about 3000 m, in the Great Hungarian Plain about 3500 m.

Tectonically there is a strong difference between the strongly folded-overthrust structure (nappe) of the basement of the W blocks connected with the Alps and the remaining part of Hungary being of faulted-folded character. The main dislocation zones are divided into two systems: the first is striking N-S (NNW-SSE), and E-W (ENE-SWS), the second NE-SW (longitudinal) and NW-SE (transversal). The former is Variscian or older, the latter Alpine.

RESULTS OF DEEP ELECTROMAGNETIC INVESTIGATIONS

A. ÁDÁM

NEAR SURFACE GEOELECTRIC INFORMATIONS

The resistivity of the Paleozoic-Mesozoic basement (ϱ_2) is considerably higher than that of the sediments (ϱ_1), ($\varrho_2/\varrho_1 > 100$). Thus the relief of the basement can be traced with the telluric method.* The accuracy of depth calculations using this method is improved by a resistivity-correction determined from DE soundings.

Plotting the areas of relative telluric ellipses against period (Fig. 1) one obtains the relative telluric frequency sounding curve (RTFS) (Ádám and Verő, 1964, 1967). In the period range of the telluric method (10–100 sec), the RTFS curves give information about the general character of the electric structure of the uppermost part of the earth's crust. Adopting a two-layer crust model, the values t_{25-100} — being proportional to the tangent of the RTFS curves between 25 and 100 sec — should reflect the ratio ϱ_2/ϱ_1 (Ádám, 1970a). ϱ_2 is in this case the mean resistivity of the basement rock that includes conductive intermediate layers, too. The map of the t_{25-100} values (Fig. 2) indicates greater regional anomalies of the earth's crust in the Pannonian Basin, e.g. the area within the isoline $t_{25-100} = -10$ in Transdanubia (it corresponds to $\varrho_2/\varrho_1 < 1$).

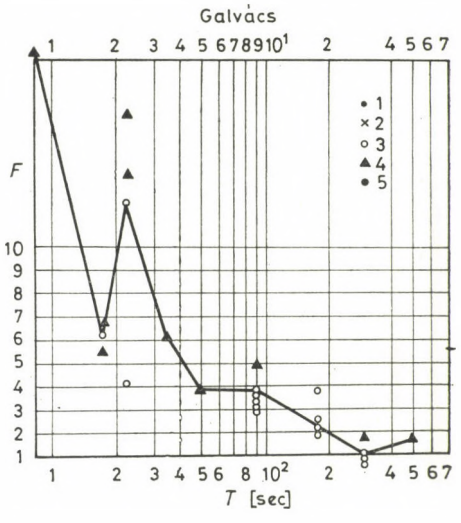


Fig. 1. Relative frequency-sounding curve (Galvács)
F = area of the relative ellipse (1–5 data in order of increasing reliability)

* Such measurements were carried out in the early sixties in Hungary.

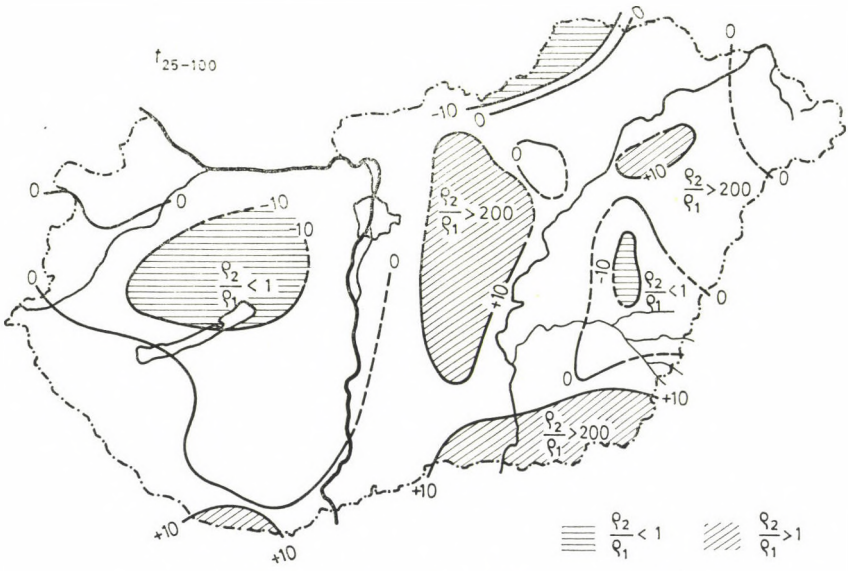


Fig. 2. Map of the relative frequency-soundings

CONDUCTIVITY ANOMALIES IN THE DEEP STRUCTURE OF THE PANNONIAN BASIN

In Hungary the most complete picture on the electric structure has been obtained from magnetotelluric sounding curves of the Observatory near Nagycenk (Ádám and Verő, 1967) (Fig. 3). The curves ϱ_x and ϱ_y have been determined from about 500 independent variations by means of the apparent amplitude method. The direction of ϱ_{max} changes at increasing period (T) from E-W towards N-S. Geological considerations show that the direction N-S (x) can be accepted as the regional strike of the sedimentary basin, therefore the ϱ_x curve is less influenced by the S effect (see p. 181). It can be approximated by the layer sequence of Table 1.

TABLE 1

Layer	Resistivity ϱ [Ωm]	Thickness h [km]
1	3.5	1.5
2	130	15
3	10	8
4	5000	75
5	10	60
6	1000	250
7	0.1	

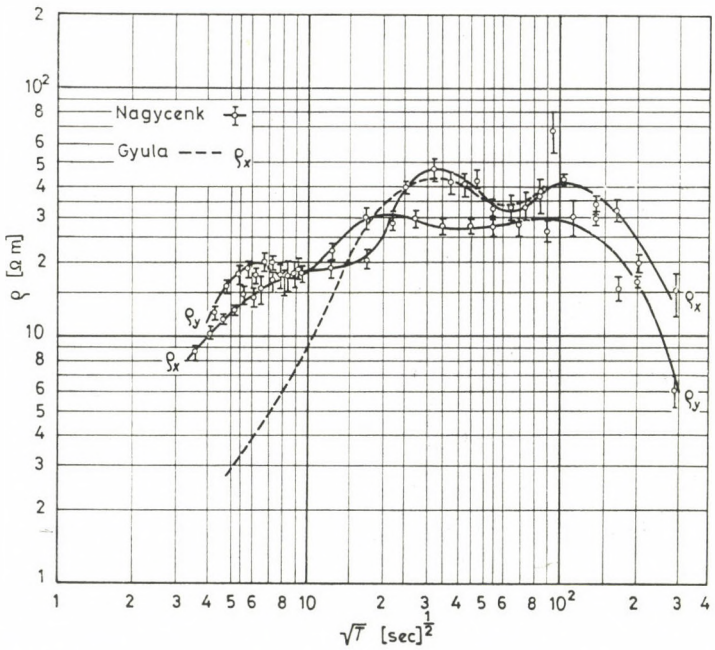


Fig. 3. MT-sounding curves measured in Nagycenk and Gyula

A similar layer sequence is indicated by the ϱ_y curve, but the depth values differ from those in Table 1 in consequence of the MT-anisotropy.

On Figure 3 the ϱ_x curve from Gyula is also shown; it shows a different electric structure in the earth's crust, but a concordant one in the upper mantle.

On the basis of the above sounding curves, following conductivity anomalies (CA) have been studied:

(a) CA in the earth's crust at a depth of 5–20 km;

(b) CA in the upper mantle above 100 km and below 100 km.

(a) THE ANOMALY IN THE EARTH'S CRUST

The distribution of the anomalies in the earth's crust can be outlined on the basis of the t_{25-100} map (Fig. 2). Figure 4 shows the MTS-points on a map where the depths of the conductivity anomalies in the earth's crust are also given. The CA-s correspond on both maps.

The most important CA lies within the RTFS isoline $t_{25-100} = -10$ in Transdanubia (Fig. 5). In this area the conductive layer is nearest to the surface (about 6 km). Its relief and horizontal conductivity (S) was studied in details by means of MTS along profiles in the direction NNW—SSE and ENE—WSW.

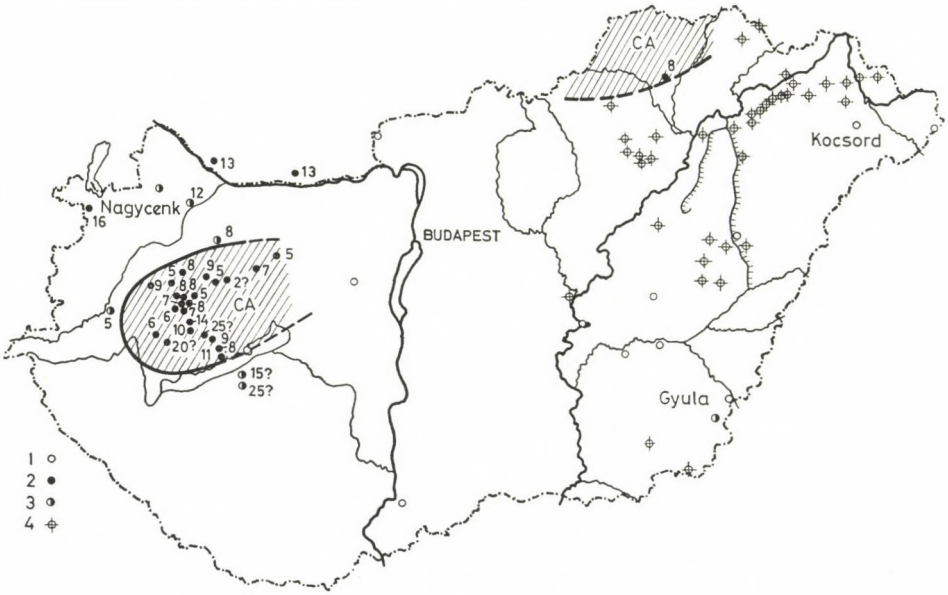


Fig. 4. MT sounding points in the Pannonian Basin
1 – no CA in the earth's crust; 2 – presence of CA in the earth's crust; 3 – CA indicated only in one direction by MT sounding; 4 – no CA in the earth's crust (measurements of Takács, 1964)

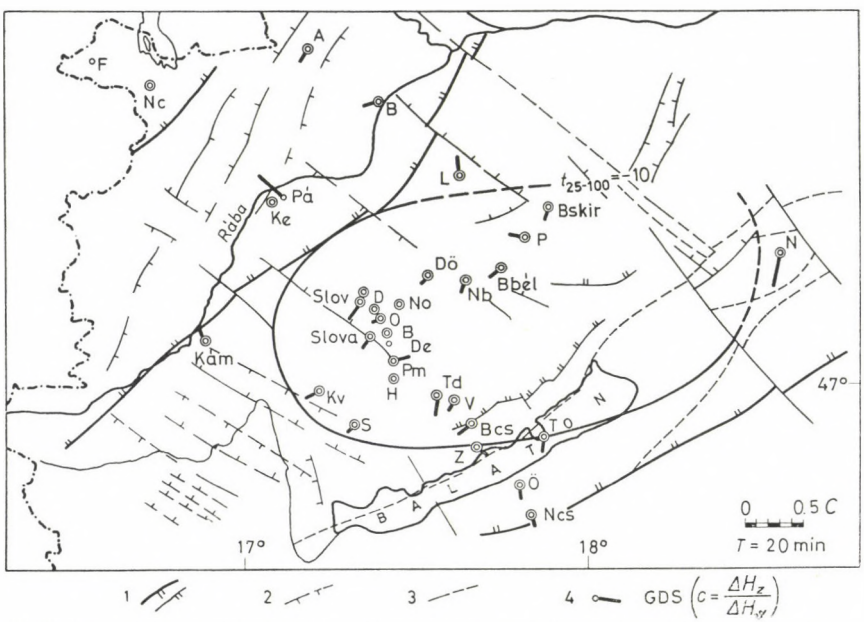


Fig. 5. Points of the profiles measured across the CA in the earth's crust in Transdanubia with results of different electromagnetic induction measurements
1 – upthrust; 2 – faults; 3 – fractures; 4 – Wiese-arrows

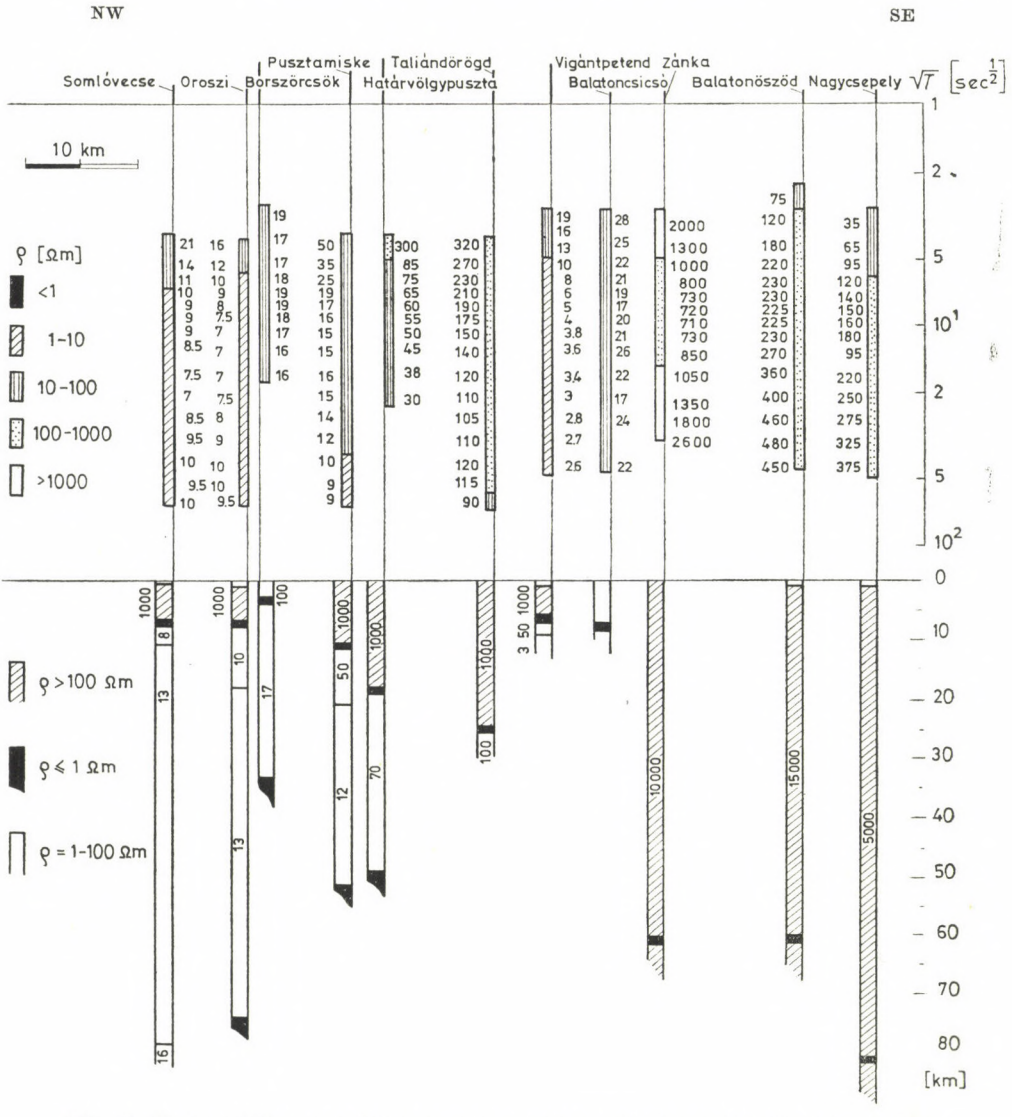


Fig. 6. Data of the sounding curves ϱ_x measured along the Transdanubian crust-profile and one-dimensional models approximating them

Since the measurement area (the Bakony Mts and the basins in its northern and southern foreground) has a complicated geological structure, the curves ϱ_x and ϱ_y reveal the most different distortions. Their direct interpretation (with one-dimensional theoretical models) would give false informations. For sake of demonstration, the theoretical models calculated on the basis of ϱ_x-curves, are shown here (Fig. 6). These approximate best the ϱ_{max}-curves.

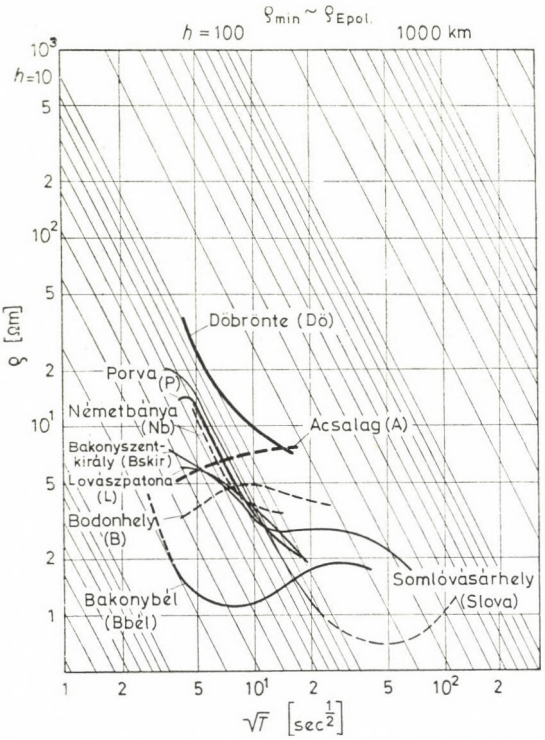


Fig. 7. MT-sounding curves from CA in Transdanubia and to the North of it (letters in brackets refer to Fig. 5)

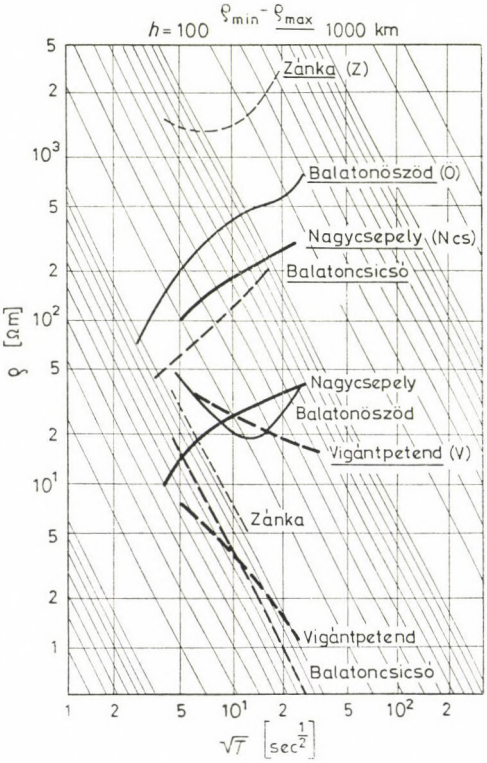


Fig. 8. The ϱ_{min} and ϱ_{max} MT sounding curves measured on both sides of the Balaton-line

One sees here an improbable leap in the depth of the CA at the northern shore of the Balaton (at Zánka) near the outcrop of the Permian, which can be attributed to the *S*-effect.

In order to eliminate this, the curves $\varrho_{min} = \varrho_E$ parallel to the regional strike of the area have been determined, too (Figs 7 and 8). Depth values, calculated from the latter can already be used for geophysical correlations. The southern part of the profile (horizons denoted in Figure 9 by ?-s) is distorted by the effect of the conductive zone outside of its area. Therefore the CA has been indicated at increasing depth with decreasing *S*-value southwards from Zánka (i.e. from the northern shore of the Lake Balaton). In Figure 7 the MTS curves of the northern transition zone of CA are shown, too. (See Acsalag, Bodonhely.)

The CA corresponds to one of the deeper stages of the Paleozoicum (Silurian?) in the territory to the north from the great tectonic "Balaton-line". The first idea was that the CA can consist of graphites or graphitic schists as deduced from the great anisotropy. Its relief shows a deepening similar to that of the Moho (at the bottom of Fig. 9).

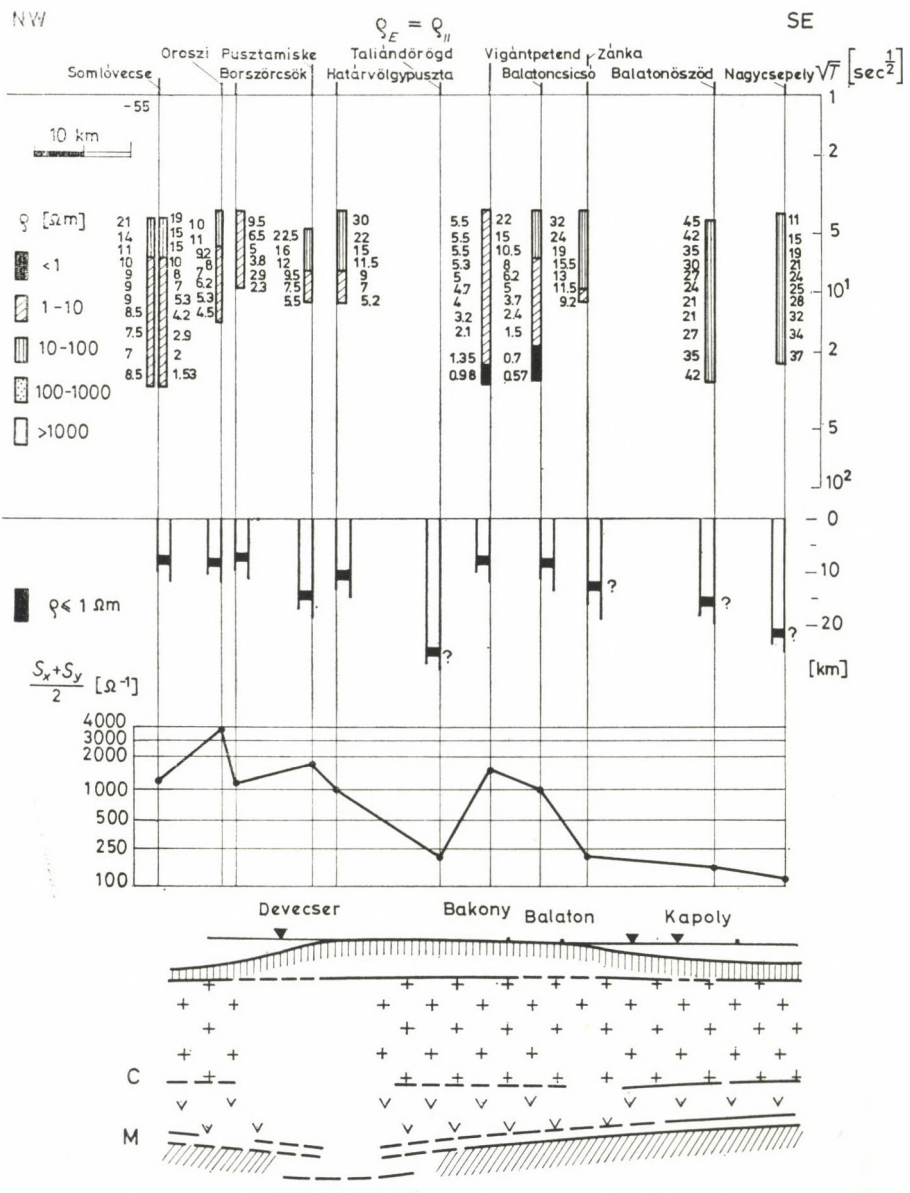


Fig. 9. Data of *E*-polarized MT sounding curves along the Transdanubian crustprofile, depth and horizontal conductivity (S) of the CA in the earth's crust calculated from them; deep-seismic profile (C = Conrad, M = Moho discontinuity)

Wiese's induction arrows (Fig. 5) are small all over the CA ($c < 0.2$) and their directions change from the regional S direction towards E or W. Therefore it can be supposed that the conductive formation is in connection with the NNW-SSE striking fault system to the north from the Lake Balaton, or rather, with the ionic conduction in the faults.

Bisztricsány (1969) observed on the basis of the coda of the surface waves a seismic discontinuity in the depth of the conductive formation in the vicinity of Sopron.

(b) ANOMALIES IN THE UPPER MANTLE

The presence of conductive layers in the upper mantle have been indicated by several MT-soundings in the Pannonian Basin. It is, however, difficult to calculate acceptable values of their parameters owing to the distortions of the sounding curves. These distortions are chiefly caused by the relief and tectonics of the basement appearing as MT anisotropy.

When studying the upper mantle, the already mentioned effect of the crustal conductive zone outside of its boundaries should be taken into account, too.

Bearing in mind the distortions due to the S-effect, at first the reality of anomalies at $T < 100$ sec must be investigated in case of ϱ_x and ϱ_y curves removed along the ϱ-axis.

$400 < T < 2000$ sec is the characteristic period range of the first conductive zone in the upper mantle in the Pannonian Basin.

Most reliable data on the depth of the conductive zone is yielded by MTS at E-polarization. These are less influenced by the S-effect. Sounding curves, however, where the polarization (or the MT-anisotropy) is in the whole period-interval of the MTS constant, are seldom. Such conditions can be only present in consequence of greater tectonical effects, as e.g. a great fracture zone (Balaton-line). The anisotropy ellipse is in most cases rotating according to the geological conditions, i.e. electric inhomogeneities in the volume corresponding to the penetration radius (for this see e.g. the curves of Nagycenk). Apparent indications can be caused by such a position, too. Sometimes opposed changes of the two perpendicular sounding curves appear, too.

Curves of the E-polarization were computed in the sounding points of the Transdanubian MT-profile. (The greater part of the curves, however, is incomplete in the period-range of the first conductive layer in the upper mantle, since the primary aim of the measurements was to study the CA in the crust.) The theoretical model for the ϱ_x curve of Somlóvásárhely is shown as an example of them (see Table 2 and Fig. 10):

$$\varrho_x = \varrho_E = \varrho_{\max}; \qquad \varrho_y = \varrho_H = \varrho_{\min}$$

For the depth of the conductive zone in the upper mantle one has about 70 km. Values differing less than ± 10 km were found from the MTS at the following locations, too: Kisvásárhely (Kv), ($\varrho_{\min} = \varrho_E$), Oroszi (O),

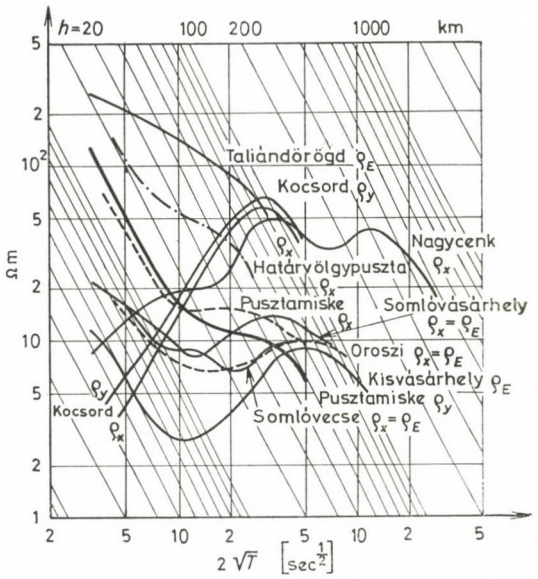


Fig. 10. MT sounding curves from Transdanubia and from a most homogeneous area (Kocsord, Great Hung. Plain)

($\varrho_x = \varrho_E$), Somlóvecse (Slov), ($\varrho_x = \varrho_E$), and Nagycenk (Nc), (ϱ_y). The curve of Kisvásárhely was calculated from linearly polarized variations.

The smallest depth of the conductive zone in the upper mantle is indicated in Transdanubia in an area, where both the conductive layer in the earth's crust and the Moho have their respective greatest depth (Pusztamiske, Határvölgypuszta).

Figure 10 shows, among the sounding curves in these points, the ϱ_x-curve of Nagycenk as well as the curves of Kocsord in Northern Hungary representing the most homogeneous conditions observed so far. The latter gives a depth of about 100 km for the conductive zone.

For some MT deep soundings on the Great Hungarian Plain only the curves ϱ_x and ϱ_y have been determined. Lacking knowledge of the basement structure, only a statistical interpretation is possible here. Very different distortions could be observed on the sounding curves. Considerable changes along the ϱ-axis are also present due to the S-effect. The parts of the curves corresponding to the greatest depths can hardly be interpreted (Ádám, 1970b). Mean depths calculated from the estimated values given by Fournier et al. (1971) are as follows:

on the basis of ϱ_x 85 km (between 65–125 km, from 10 data),
on the basis of ϱ_y 60 km (between 30–125 km, from 8 data),
on the basis of ϱ_y 45 km (between 30–70 km, from 6 data).

Depths calculated from the sounding curves of Takács (1964) showed similar differences, whereas in the NE-part of the Pannonian Basin, to the south of the River Tisza, where the strike in E direction predominates, Takács received very similar ϱ_y curves with depths uniformly of about

TABLE 2

Layer	Resistivity ϱ [Ωm]	Thickness h [km]
1	5	0.5
2	500	6.5
3	0.1	0.12
4	12	20
5	1000	40
6	0.1	

70 km for the conductive zone. The depth differences are therefore in connection with the regional MT anisotropy.

Hence, the depth of the first conductive zone in the upper mantle is between 60 and 85 km. Its most probable value is about 75 km. Some MT curves in Hungary and Slovakia indicate a greater depth of the conductive zone on the flanks of the basin (e.g. Nagycenk, Gyula, Kocsord, Nitranska Blatnica, see Figure 10, too. This cannot be, however, stated definitely because of the contradictory interpretation of some data.)

On the platform areas in the Soviet Union, the first CA has been found deeper than 200 km (e.g. in the Central-Russian Basin); that is presumably in connection with the considerably smaller heat flow there (Bryunelli et al., 1964).

This conductive zone in the upper mantle corresponds probably to the low velocity layer at the bottom of the lithospheric plate, i.e. to the asthenosphere. According to the calculations of Bisztricsány (1974), it has a depth of 70–80 km and a seismic velocity of 7.85 km/sec in the Pannonian Basin. According to our hypothesis alkalic rocks are enriched and/or partially melted(?) in this zone (see pp. 567-571).

The CA appearing at a depth of 300–400 km on the sounding curves of Nagycenk may correspond to the olivine-spinel phase-transition which causes an increase of conductivity of several orders according to Akimoto and Fujisawa (1965).

STRUCTURAL EFFECTS, DIRECTION-CHARACTERISTICS

a) ON THE MT ANISOTROPY

The sounding curves of Nagycenk show — as already mentioned — an anisotropy of changing character; its main peculiarity is the inequality $\varrho_x > \varrho_y$ at periods longer than those of pulsations. In consequence of that, the tangent of the left ascending part of the MTS curves is smaller on the curves ϱ_y, than on ϱ_x. This is regionally-statistically characteristic all over the Pannonian Basin (Ádám, 1969).

It is very likely that the regional MT anisotropy is connected with one of the main tectonical forms of the Pannonian Basin, i.e. with faults and fracture zones striking E-W and ENE-WSW, respectively. ϱ is in strike less than in dip.

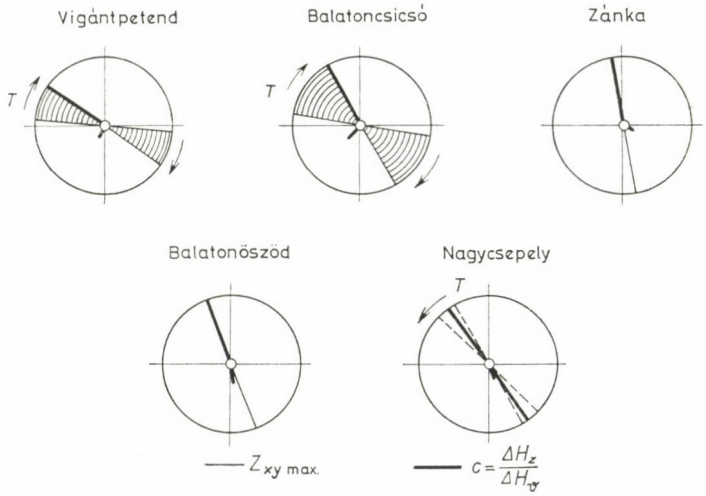


Fig. 11. Direction of Z_{max} on both sides of the Balaton-line

The connection of the anisotropy with the main tectonic fracture zone is supported by MTS curves on areas with strong transverse faults (e.g. to the North of Lake Balaton), where the anisotropy is a different one.

A further proof for this has been yielded by the MT profile across an ENE-WSW striking great tectonic line of the Lake Balaton. The effect of this line appears in its immediate vicinity as a linear polarization at all periods and as great ratios $\varrho_{max}/\varrho_{min}$ (here also ϱ_x/ϱ_y). Figure 11 shows this phenomenon for the stations Zánka and Balatonöszöd. The difference of the polarization in these points amounting 10° can be due to a similar difference in the direction of the edge of the Triassic and of the Balaton-line. With increasing distance from this line the effect is diminishing: the polarization gets period-dependent. This change is also illustrated by Figure 11 and Table 3, showing how the polarization approximates that at the Balaton-line for longer periods when advancing to the line (station Zánka and Balatonöszöd).

TABLE 3

Station	Direction of Z_{xy} max		
	25 sec		400 sec
Vigántpetend	95°		125°
Balatoncsicsó	100°		150°
Zánka		170°	
Balatonöszöd		160°	
Nagycsepely	150°		135°

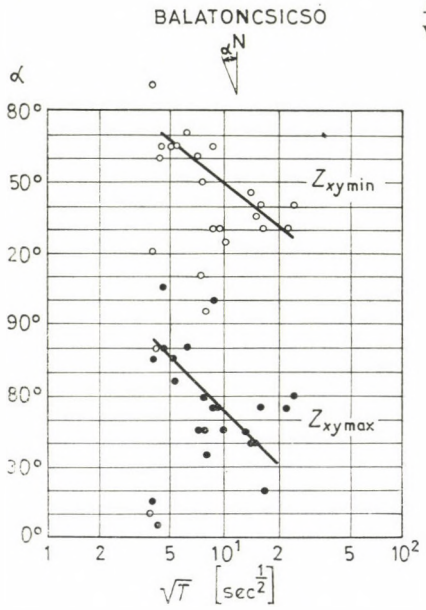


Fig. 12. Change of the direction of extreme values of impedance in function of period at Balatoncsicsó

The variation of the directions of $Z_{xy\,min}$ and $Z_{xy\,max}$ in Balatoncsicsó depending on the period can be seen on Figure 12.

The regional MT-anisotropy can be interpreted from the point of view of global tectonics, too (Stegena et al., 1971): elongated linear structures as e.g. the edges of plates are reflected in the regional MT-anisotropy.

(b) ON GEOMAGNETIC INDUCTION ARROWS

In the Pannonian Basin, with the exception of its NW part (the area northwestwards from the Lake Balaton), Wiese's induction arrows show the directional effect of the conductive fracture zone between the Outer and Inner Carpathians. The arrows have a regional southward direction and their lengths decrease towards the centre of the Basin. The decrease of length can be interpreted as due to the thick sediments and to a rise of the conductive zone in the upper mantle in the basin (high-cut ΔZ anomaly). When approximating the induction arrows with a second order series (Ádám et al., 1972), the above statements became more evident, because the arrows are free from local effects (Fig. 13).

Local effects can be calculated by subtracting regional values from the original ones. In these residual anomalies it is difficult to recognize any regularities. Besides the changes of thickness of the sedimentary basins, the effects of tectonics, first of all conductive fracture zones — reflected in MT-anisotropy, too — can be recognized.

An interesting accumulation of effects can be observed on the area of the Transdanubian earth's crust anomaly. The southwards directed arrows of

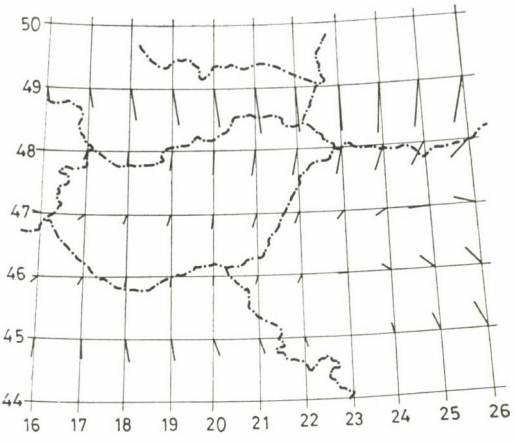


Fig. 13. Regional induction arrows in the Carpathian Basin

the Carpathian fracture zone are nearly compensated here by the nearly northwards directed arrows of the Balaton-line. Thus the arrows are directed by the nearly E-W effect of the conductive transverse fractures (see Fig. 5). Magnetotelluric results reflect much more the local, i.e. near effects as shown by the soundings near the fracture zone of the Balaton.

REFERENCES

Ádám, A., 1969. Appearance of the electrical inhomogeneity and anisotropy in the results of the complex electrical exploration of the Carpathian Basin. *Acta Geod. Geophys. Mont. Hung.* **4**, 187–197.

Ádám, A., 1970a. A quantitative contribution to the telluric relative frequency-sounding (RTFS) in the Hungarian Basin. *Geofizikai Közlemények*, **19**, No. 1–2, 55–59.

Ádám, A., 1970b. Problems of the electric upper mantle research in the Hungarian Basin. Fifteen Years Geodetical and Geophysical Research Laboratories of the Hung. Acad. Sci. in Sopron, 77–92.

Ádám, A., 1971. Investigation of Paleozoic graphitic formations by magnetotelluric method under electrically shielding layers in the Hungarian Basin (in Hungarian). *Geonómia és Bányászat* **4**, 297–308.

Ádám, A., 1972. Änderungen in der Tiefe der gutleitenden Zonen im Ungarischen Becken, regionale und lokale Effekte. *Acta Geod. Geophys. Mont. Hung.* **7**, 353–367.

Ádám, A., Verő, J., 1964. Ergebnisse der regionalen tellurischen Messungen in Ungarn. *Acta Techn. Hung.* **47**, 63–77.

Ádám, A., Verő, J., 1967. Latest results of electromagnetic measurements in Hungary (in Hungarian). *Geofizikai Közlemények* **16**, Nos 1–2, 25–52.

Ádám, A., Verő, J., Wallner, Á., 1972. Regional properties of geomagnetic induction arrows in Europe. *Acta Geod. Geophys. Mont. Hung.* **7**, 251–287.

Akimoto, S. J., Fujisawa, H., 1965. Demonstration of the electrical conductivity jump produced by the olivin-spinel transition. *J. Geophys. Res.* **70**, 443–449.

Bisztricsány, E., 1969. Analysis of codas of shallow-focus earthquakes (in Hungarian). D. Sc. Dissertation, Budapest.

Bisztricsány, E., 1974. The depth of the LVL in Europe and in some adjacent regions. *Geofizikai Közlemények* **22**, 65.

Boldizsár, T., 1964. Terrestrial heat flow in the Carpathians. *J. Geophys. Res.* **69**, 5269–5275.

Bryunelli, B. E., Kovtun, A. A., Kuznetsov, N. S., Raspopov, O. M., Chicherina,

N. D., YANOVSKY, B. M., 1964. Investigation of the region of Central Russian Basin by magnetotelluric sounding (in Russian). *Voprosy Geofiziki* **15**, *Leningradskogo Univ.*, 3–16.

FOURNIER, H., ÁDÁM, A., DE MIGUEL, L., SANCLEMENT, E., 1971. Proposal for a first upper mantle magnetotelluric E-W profile across Europe. *Acta Geod. Geophys. Mont. Hung.* **6**, 459–477.

PĚČOVÁ, J., PETR, V., PRAUS, O., 1970. Depth distribution of the electric conductivity on Czechoslovak territory. *J. Geomagn. Geoel.* **22**, 235–240.

STEGENA, L., HORVÁTH, F., ÁDÁM, A., 1971. Spreading tectonics investigated by magnetotelluric anisotropy. *Nature*, **231**, 442–443.

TAKÁCS, E., 1964. Investigation on the magnetotelluric methods and instrumentation and their applications to geophysical explorations (in Hungarian). C. Sc. Dissertation, Budapest.

TEMPERATURE CALCULATIONS ON THE HUNGARIAN SEISMIC PROFILE-SECTION NP-2*

G. BUNTEBARTH

ASSUMPTIONS FOR THE STEADY-STATE HEAT CONDUCTION EQUATION

Some magnetotelluric sounding stations are located on or near the Hungarian seismic profile NP-2. Therefore, it is reasonable to work out the temperature calculations along the whole NW-SE striking profile-section through Transdanubia.

Assuming a steady state temperature field, we get Poisson's equation

$$A + \operatorname{div}(\lambda \operatorname{grad} T) = 0$$

where both the heat production A and the thermal conductivity λ are known functions of the position. The equation can be expressed by means of the Nabla- and Laplace-operator as

$$A + \lambda \Delta T + \nabla \lambda \nabla T = 0$$

To solve the problem numerically, it is more convenient to use the modified equation

$$2A + \Delta(\lambda T) + \lambda \Delta T - T \Delta \lambda = 0$$

which was solved in our case for a two-dimensional model.

BOUNDARY CONDITIONS

The mean annual surface temperature in Hungary varies between $T = 9$ °C and $T = 11$ °C, so that the surface condition can be given by $T(x, 0) = 10$ °C with good accuracy. Furthermore, the temperature gradient at both ends of the profile is set to be zero for all depths z, so that $\partial T/\partial x = 0$ for $x = 0$ and $x = 180$ km is valid for $0 \leq z \leq 100$ km.

Based on the surface value of the heat flow (Boldizsár, 1964) along the seismic profile NP-2 (Fig. 1) and a model of heat production within the crust, the heat flow from the upper mantle must be computed for the depth $z = 100$ km. The values of the heat flow deriving from the upper mantle determine the gradient boundary condition at the depth $z = 100$ km.

* The paper was prepared at the L. Eötvös University (Budapest) during the author's stay in 1972/73.



Fig. 1. Heat flow map after Boldizsár (1964) in mWm^{-2} units with locations for temperature-depth calculations along the seismic profile NP-2

DISTRIBUTION OF HEAT SOURCES

The heat producing elements U, Th and K are distributed according to petrological and physico-chemical conditions. At the surface of the crystalline basement in Hungary, the heat production is supposed to be like the mean heat production of granitic rocks in the Alps (Rybach, 1973). In the centre of the gabbro layer and for the layer of ultrabasic rocks, global mean values of U-, Th-, and K-contents should be taken.

Beneath the Moho, an olivine layer of 20 km thickness (Borchert, 1967) is assumed and beneath that a heat production is supposed comparable to that given by Clark and Ringwood (1964).

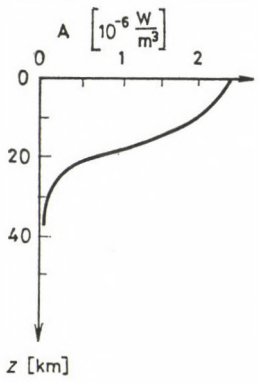


Fig. 2. Model of the heat production within the crust

Between the mean values of the two layers an exponential distribution of the heat sources is assumed, which is described by the equation

$$A = A_0 \exp(-\mu_i, z)$$

where A_0 is heat production at the surface and μ_i is the coefficient of decrease between the two mean values.

In a sinking basin like the Hungarian one heat flow generated in the sediment layer must be added to a standard value.

The rising ultrabasic horizon of the Moho in that region does not absorb such mobile elements as uranium and thorium, so that those heat sources become more concentrated within a crust becoming thinner. The resulting heat production in function of depth is shown in Figure 2.

MODEL OF THERMAL CONDUCTIVITIES

Thermal conductivities must be chosen in conformity with the seismic results. On the surface there are the Upper Cretaceous-Neogene basin fill with $\lambda_1 = 1.84$ $\mathrm{Wm^{-1}K^{-1}}$ and a Triassic-Lower Cretaceous basin floor, mainly carbonate, with $\lambda_2 = 2.51$ $\mathrm{Wm^{-1}K^{-1}}$.

Beneath $z = 5$ km depth, there is a granite layer ($\lambda_3 = 2.09$ $\mathrm{Wm^{-1}K^{-1}}$) and beneath that a gabbro layer down to $z = 25$ km ($\lambda_4 = 2.3$ $\mathrm{Wm^{-1}K^{-1}}$), see Figure 3.

All thermal conductivities are corrected by taking the influence of temperature and pressure into account (Buntebarth, 1973). The influence of temperature is described by the function

$$\lambda = a + bT^{-1}$$

which is a good approximation up to 1000 K; a and b are material constants.

Low pressures ($p = 0$ to 1 kb) cause an increase of thermal conductivity of about 10% for magmatic rocks (Walsh and Decker, 1966; Hurtig and

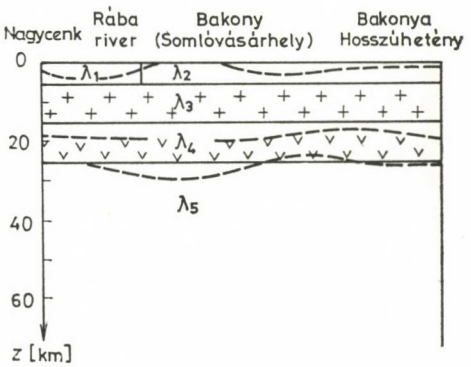


Fig. 3. Model of thermal conductivity with the crustal structure of the seismic profile-section NP-2
λ_1 = sediment; λ_2 = carbonate; λ_3 = granite; λ_4 = gabbro; λ_5 = olivine

Brugger, 1970) while high pressures ($p > 1$ kb) change the thermal conductivity according to the elastic properties

$$\lambda = \lambda_0(1 + cp)$$

where c is a material constant.

The thermal conductivity of the upper mantle in this given model (Fig. 3) is defined to be that of olivine.

Experimental results reported by Fukao et al. (1968) and Schatz and Simmons (1972) show that the value of olivine ($Fo_{92}Fa_8$) can be taken for $\lambda = 4.82$ $Wm^{-1}K^{-1}$ as a mean value at high temperatures. If the influence of pressure is taken into account, the value ranges from $\lambda_5 = 4.98$ $Wm^{-1}K^{-1}$ at the Moho to $\lambda_5 = 5.28$ at 100 km depth.

RESULTS OF THE NUMERICAL TREATMENT OF THE GENERALIZED POISSON'S EQUATION

The generalized Poisson's equation is replaced by a set of finite-difference equations. For that purpose the region of integration is covered by a rectangular network of uniform meshes and at the nodes the values of temperature T are calculated.

The ratio of the sides of the rectangular meshes is arbitrarily set as 1 : 2. Replacing the differential equation by a finite-difference approximation we get

$$2h^2\frac{A_{r,s}}{\lambda_{r,s}} + T_{r+1,s}\frac{\lambda_{r+1,s}+\lambda_{r,s}}{4\lambda_{r,s}} + T_{r-1,s}\frac{\lambda_{r-1,s}+\lambda_{r,s}}{4\lambda_{r,s}} +$$

$$+ T_{r,s+1}\frac{\lambda_{r,s+1}+\lambda_{r,s}}{\lambda_{r,s}} + T_{r,s-1}\frac{\lambda_{r,s-1}+\lambda_{r,s}}{\lambda_{r,s}} -$$

$$- T_{r,s}\left(2.5 + \frac{\lambda_{r-1,s}+\lambda_{r+1,s}}{\lambda_{r,s}} + \frac{\lambda_{r,s-1}+\lambda_{r,s+1}}{\lambda_{r,s}}\right) = 0$$

The subscripts r and s indicate the nodes of the network subdivided and h is the vertical length of one mesh ($h = \Delta z = 10$ km).

The functions $A = A(r, s)$ and $\lambda = \lambda(r, s)$ are known and if the temperature field $T = T(r, s)$ is estimated, the equation will not be zero, usually. A function of residuals can be calculated which must be reduced to be smaller than a given limit at all nodes. This procedure is the so-called relaxation method (Allen, 1954; Collatz, 1960).

In the calculated model, the residuals are smaller than 0.5 °C.

Table 1 shows the results of calculation in steps of $\Delta z = 10$ km for various localities on the seismic profile NP-2 through Transdanubia.

The results are shown in Figure 4 as isotherms in the model of the crust

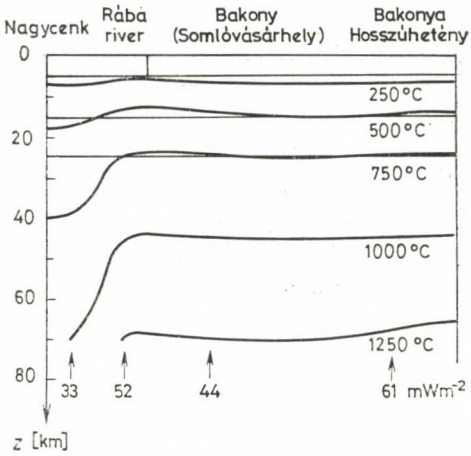


Fig. 4. Isotherms within the model of the crust with the heat flow values from the upper mantle

TABLE 1

Depth z [km]	Temperature °C			
	Nagycenk	Rába river	Bakony (Somlóvásárhely)	Bakonya/Hosszú-hetény
0	10	10	10	10
10	346	415	378	373
20	557	687	666	664
30	667	835	821	824
40	747	942	932	939
50	825	1049	1041	1054
60	900	1155	1146	1168
70	972	1258	1245	1280
80	1041	1358	1340	1391
90	1107	1456	1429	1502
100	1169	1551	1511	1613
Heat flow $z = 100$ km	33.5	52.3	44.0	60.7 mWm^{-2}

REFERENCES

Allen, D. N. de G., 1954. Relaxation methods. McGraw-Hill, New York.

Boldizsár, T., 1964. Terrestrial heat flow in the Carpathians. *J. Geophys. Res.* **69,** 5269–5275.

Borchert, H., 1967. Zur Petrologie der Lithosphäre in ihrer Beziehung zu geophysikalischen Diskontinuitäten, auch der Gesamterde. *Gerlands Beitr. z. Geophys.* **76,** 257–277.

Buntebarth, G., 1973. Model calculations on temperature-depth-distribution in the area of the Alps and the foreland. *Z. Geophys.* **39,** 97–107.

Clark, S. P., Ringwood, A. E., 1964. Density distribution and constitution of the mantle. *Rev. Geophys.* **2,** 35–88.

COLLATZ, L., 1960. The Numerical Treatment of Differential Equations. Springer-Verlag, Berlin.

FUKAO, Y., MIZUTANI, H., UYEDA, S., 1968. Optical absorption spectra at high temperatures and radiative thermal conductivity of olivines. *Phys. Earth Planet. Interiors* **1**, 57–62.

HURTIG, E., BRUGGER, H., 1970. Wärmeleitfähigkeitsmessungen unter einaxialem Druck. *Tectonophysics* **10**, 67–77.

RYBACH, L., 1973. Wärmeproduktionsbestimmungen an Gesteinen der Schweizer Alpen. *Beitr. Geol. Schweiz. Geotechn. Ser.*, Lfg. 51.

SCHATZ, J. F., SIMMONS, G., 1972. Thermal conductivity of earth materials at high temperatures. *J. Geophys. Res.* **77**, 6966–6983.

WALSH, J. B., DECKER, E. R., 1966. Effect of pressure and saturating fluid on the thermal conductivity of compact rock. *J. Geophys. Res.* **71**, 3053–3061.

CONNECTION BETWEEN GEOELECTRIC AND GEOTHERMAL PARAMETERS IN THE EARTH

A. ÁDÁM

Immediately after the first magnetotelluric deep sounding has been made in Hungary, attention was paid to a possible connection between geothermal and geoelectric parameters in the Pannonian Basin (Ádám, 1963, 1965). On the basis of the theory of electric semiconduction it seemed obvious that, due to an observed average heat flow greater than 2 μcal cm^{-2} sec^{-1} (= 84 mWm^{-2}) and to the supposed higher temperatures in the earth, respectively, the first conductive layer in the upper mantle is here nearer to the surface than below the platform area of the Soviet Union characterized by a heat flow, half of that in Hungary. A possible connection of the conductive layer with the low velocity layer (LVL) was also shown by means of Ringwood's rock model.

MT deep soundings carried out recently in the Pannonian Basin (see pp. 547-560) have confirmed the presence of a conductive layer in the upper mantle. Its most probable depth is about 75 km (between 60 and 85 km). A more accurate determination of the depth is very difficult in consequence of the distortion of MT sounding curves.

The geothermal interpretation of the following facts must be discussed, too:

a) The depth of the conductive layer determined in the direction of the main tectonic lines E-W (ENE-WSW) is smaller (45–60 km) and its conductivity greater than in perpendicular direction (Ádám, 1969).

b) The depth of the conductive layer is increasing towards the flanks of the basin (Nagycenk: 100 km, Kocsord: 105 km).

c) In Transdanubia there is a conductive layer in a depth of some km-s with a horizontal conductivity of several thousand Ω^{-1} (Ádám and Verő, 1964).

Calculations made by Bisztricsány (1974) have proved the concordance of the depths of the LVL and of the conductive layer.

On Boldizsár's heat flow map (1964), a considerable decrease of the heat flow may indicate in the NW part of the basin the increasing depth of the conductive layer. Due to the uncertainties of the data, it is difficult to find further connections between the territorial distribution of heat flow and the changes of depth of the conductive layer.

Along the tectonic zones under strain (faults), there will be an enrichment of alkalines with a high FeO, Fe_2O_3, Na_2O, K_2O oxide content (Paarma, 1963; Parkhomenko and Bondarenko, 1972). According to Bondarenko's investigations (1966), alkaline rocks have greater conductivity than basic or ultrabasic rocks. In addition, heat can flow convectively into the earth's

crust through deep fractures, too, and that could also considerably increase the electric conductivity in fracture zones (Ádám, 1963; Stegena, 1970).

These factors can explain the regional MT anisotropy in the Pannonian Basin, supposing that the fracture-zones are wide enough ($\sim$ 0.1 km).

The conditions of development of conductive layers can be studied by means of the temperature-depth function, by the behaviour of the electric conductivity of rocks and mainly on the basis of the melting point of the basic rocks (basalts).

The temperature values calculated for the deep-seismic profile NP-2 by Buntebarth (see pp. 561-566) show that along the Rába river and at Somlóvásárhely the rocks of basaltic composition are already partially melt in a depth of 70 km, (Fig. 1) and so — according to experimental investigations of Khitarov and Slutsky (1965) — their electric conductivity can increase by 2–3 orders of magnitude. This change in conductivity is in accordance with the results of MT soundings.

The heat flow greater than 1 μcal cm^{-2} sec^{-1} (44–60.7 mWm^{-2}) calculated for a depth of 100 km indicates a partial melting in the upper mantle, too.

According to the calculations for the area of Nagycenk, however, the temperature even in a depth of 100 km is not high enough to bring about melting. The conductive layer appears here on the ϱ_x curve at a depth of 100 km with 10 Ωm resistivity at about 1200 °C temperature.

Some resistivity models were constructed using the laboratory data of Bondarenko (1966) and the temperature-depth curve in Nagycenk (see model 1–4 in Fig. 2). Rock-models 1–2 correspond to the ideas of Vendel (1972) who started out from the model of Borchert and Tröger (model 1–2). Model 3–4 emphasizes the enrichment of the alcalic rocks in the astenosphere. The thickness of the sediments at the top of the profile is greater than in reality (5 km instead of 1.5 km), but this does not influence the magnetotelluric depth-determination of the conductive astenosphere. The effect of pressure is not included in Bondarenko's data. As it is known that

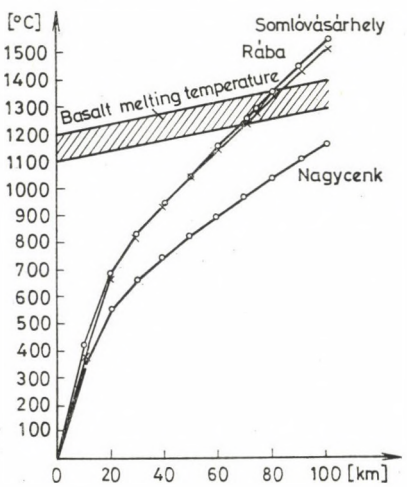


Fig. 1. Temperature-depth curves along the deep seismic profile NP-2 and the melting temperature of basalt

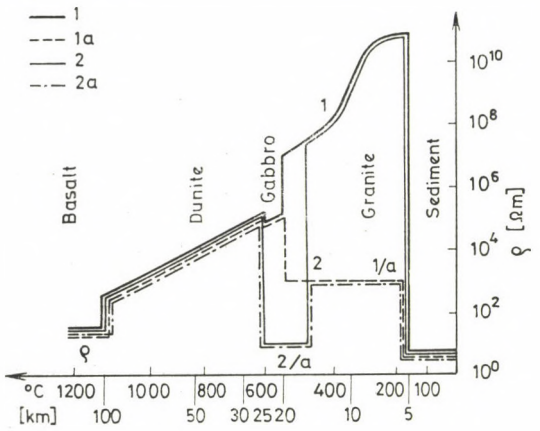


Fig. 2a. Electric resistivity models 1, 1a, 2, 2a, of the earth's crust and the upper mantle

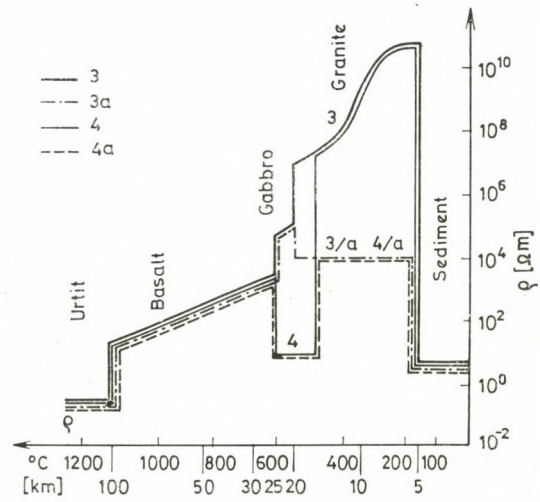


Fig. 2b. Electric resistivity models 3, 3a, 4, 4a of the earth's crust and the upper mantle

in case of basic and ultra-basic rocks, the increase of conductivity does not reach 80% till 25 kp cm^{-2}, the data of Bondarenko can be accepted as a good approximation.

There are very few reliable results above 20 kp cm^{-2} (Parkhomenko and Bondarenko, 1972), and so the profile below 100 km was approximated by a homogeneous half-space when calculating the theoretical MT curves. The accepted resistivity of the half-space can be found at 100 km on our models. The resistivity of the granite was taken 10^3 and 10^4 Ωm depending on its moisture content (models denoted by "a"). On the basis of the Nagycenk MT curves a 10 km thick conductive layer was introduced at a depth of 15 km in models 2 and 4.

The theoretical MT curves corresponding to the models were compared with the ϱ_x-curve of Nagycenk (Fig. 3). By the continuous increase of con-

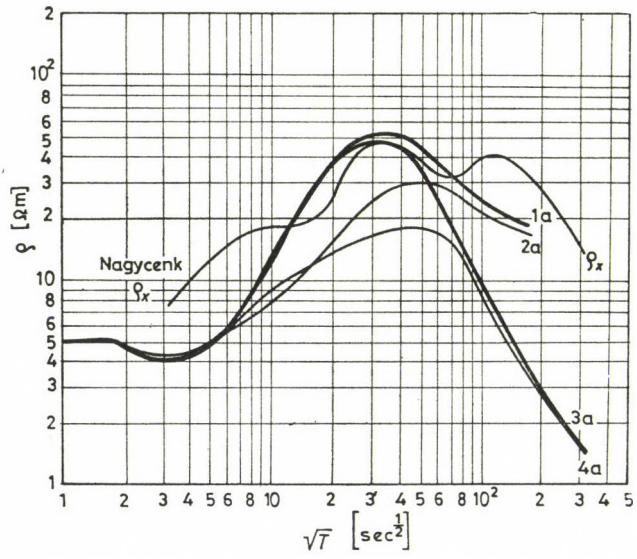


Fig. 3. MT sounding curves corresponding to the models of Figure 2, compared with the ϱ_x-curve measured in Nagycenk

ductivity in function of temperature and by its jump by 1–2 orders at a depth of 100 km, good conformity was reached between measured and theoretical MT-curves on their descending part (model 1a and 3a). (The effect of the anomaly of the earth's crust caused the deviation of the theoretical curve from the measured one.)

On the basis of the temperature-depth function of Buntebarth, rock-model 1/a seems to be the most probable for the area of the Observatory near Nagycenk. Since the resistivity of both basalts and peridotites changes uniformly with temperature, these rocks can substitute each other in our model. The possibility of substitution of the rock-combinations used indicates the difficulties in the study of the material composition of the upper mantle.

On the area of the Transdanubian earth's crust anomaly, the temperature calculated for a depth of 7–10 km is somewhat higher than 300 °C. Thus it has no role in the development of the electric conductivity. The conductive zone is bound to rocks, which have high conductivity at surface temperatures, too. According to geological considerations this rock can be graphite or graphitic schist from earlier of the Paleozoic stages.

Since the conductivity anomaly appears in the area of the Pliocene basalt-volcanos, it has been looked for a connection of the conductivity formation with volcanic activity. It cannot be supposed that a basaltic magma that intruded before about 1 million years in a depth of 10 km could have preserved its initial temperature of about 1100 °C and that would be the reason of the increased conductivity observed.

According to the calculations of Buntebarth a heat flow of 4.4 μcal cm^{-2}sec^{-1} (= 184 mWm^{-2}) should appear on the surface under stationary conditions, instead of the observed $\sim$ 2 μcal cm^{-2} sec^{-1}. The high position of the conductive zone in the upper mantle can be, however, in connection with the paleovolcanic activity on this area.

Since above the NW-SE transversal faults the directions of Wiese's induction arrows turn over, it can be assumed that the fracture-zone here constitute conductive channels as well as the main faults (in E-W or in ENE-WSW direction), which determine the regional MT anisotropy of the Pannonian Basin. With regard to the relative small depth, ionic conductivity must be mainly considered here. It is probable that the heat flowing upwards in the faults also has a role.

REFERENCES

ÁDÁM, A., 1963. The exploration of electric resistivity of the earth's crust and upper mantle in Hungary with the electromagnetic field of the earth (in Hungarian). Dissertation, Budapest.

ÁDÁM, A., 1965. Einige Hypothesen über den Aufbau des oberen Erdmantels in Ungarn. *Gerlands Beitr. z. Geophys.* **74,** 20–40.

ÁDÁM, A., 1969. Appearance of the electrical inhomogeneity and anisotropy in the results of the complex electrical explora'ion of the Carpathian Basin. *Acta Geod. Geophys. Mont. Hung.* **4,** 187–197.

ÁDÁM, A., VERŐ, J., 1964. Ergebnisse der regionalen tellurischen Messungen in Ungarn. *Acta Techn. Hung.* **47,** 63–77.

BISZTRICSÁNY, E., 1974. The depth of the LVL in Europe and in some adjacent regions. *Geofizikai Közlemények* **22,** 65.

BOLDIZSÁR, T., 1964. Terrestrial Heat Flow in the Carpathians. *J. Geophys. Res.* **69,** 5269–5275.

BONDARENKO, A. T., 1966. The electric conductivity of the magnetic rocks of Kola peninsula under high pressure and temperature (in Russian). Elektricheskie i mekhanicheskie svoistva gornykh porod pri vysokikh davleniakh, Nauka, Moscow, 192–199.

KHITAROV, N. I., SLUTSKY, A. B., 1965. The effect of pressure on the melting temperature of albite and basalt (according to the data of electric conductivity measurements) (in Russian). *Geochemistry* **12,** 1395–1403.

PARKHOMENKO, E. I., BONDARENKO, A. T., 1972. The Electric Conductivity of Rocks Under High Pressure and Temperature (in Russian). Nauka, Moscow.

PAARMA, H., 1963. On the tectonic structure of the Finnish basement, especially in the light of geophysical maps. *Fennia Helsinki* **89,** 33–37.

STEGENA, L., 1970. Deep structure and geothermal relations of Hungary (in Russian). *Ann. Univ. Sci. Budapestiensis, Sec. Geol.* **14,** 153–159.

VENDEL, M., 1972. Studie über den initialen Magmatismus. *Acta Geol. Hung.* **16,** 127–161.

GEOTHERMICS, MAGNETOTELLURICS AND TECTONOPHYSICS OF THE PANNONIAN BASIN

L. STEGENA

INTRODUCTION

The Paleozoic-Mesozoic nucleus of the Pannonian Basin is the result of the collision of European and Gondwanic microplates. The present basin was formed in the Late Cenozoic by the subsidence of this nucleus. The sinking was brought about by an active mantle diapir generated by the subduction associated with the formation of the surrounding mountains. The evidence and consequences of the mantle diapir are:

1. Strong Miocene andesitic-rhyolitic and Plio-Pleistocene basaltic volcanism.
2. Geothermal high and the high value of reduced mantle heat flow ($Q = 1.2 - 1.7$ HFU).
3. Anomalistic upper mantle with a lower density and elevated position of Low Velocity Layer (LVL) and High Conductivity Layer (HCL). The shallow depth of HCL (see pp. 554-556) shows that the geothermal highs are well developed in the upper mantle; this extra heat cannot be the result of heat conduction only because of the young age (about 10 m. y.) of the basin, but convectionally transported heat has to be supposed as well.
4. Continental type thin crust, thinned out by the subcrustal erosion of the mantle diapir. The primary cause of the basin formation is the isostatic sinking of the thinned-out crust.

The study of other intermountain (interarc) basins (Tyrrhenian Sea, Aegean Sea, Basin and Range Province) also suggests that their evolutions were controlled by the active mantle diapir (ensialic interarc basin). In case of other depressions (West Pacific marginal seas), however, the mantle diapir had broken off the continental crust and the developed basin possess oceanic crust (ensimatic interarc basins).

*

The following are the *main results of the magnetotelluric soundings in the Pannonian Basin*:

1. In the upper mantle the HCL is in elevated situation (Fig. 1), (Ádám, 1965).

2. Important regional magnetotelluric anisotropy exists, manifesting itself in a higher electrical conductivity in the direction E-W and a smaller one in N–S. It might be explained most simply with well-conducting deep dykes in the upper mantle striking E–W (Ádám, 1969; Stegena et al., 1971).

3. According to the theories concerning the electrical conductivity of the upper mantle (Rikitake, 1952) the elevated position of the HCL indicates that under the Pannonian Basin the upper mantle's temperature is higher than elsewhere.

The results of the geothermal research of the Pannonian Basin:

4. The territory of the basin is the warmest one in Middle-East Europe (Fig. 2), (Stegena, 1972). Heat flows measured near to the surface are also high ($Q \approx 85\ \mathrm{mWm^{-2}}$).

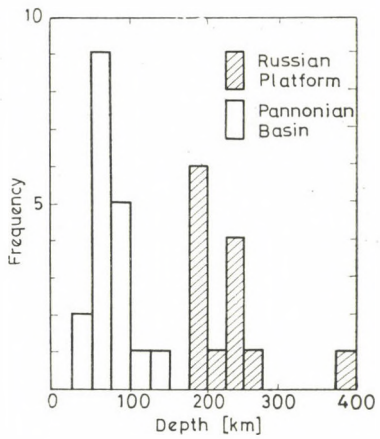


Fig. 1. Histogram of the depths of the high conductivity layer (HCL) for the Pannonian Basin and the Russian Platform (after the data of Ádám 1965, 1969)

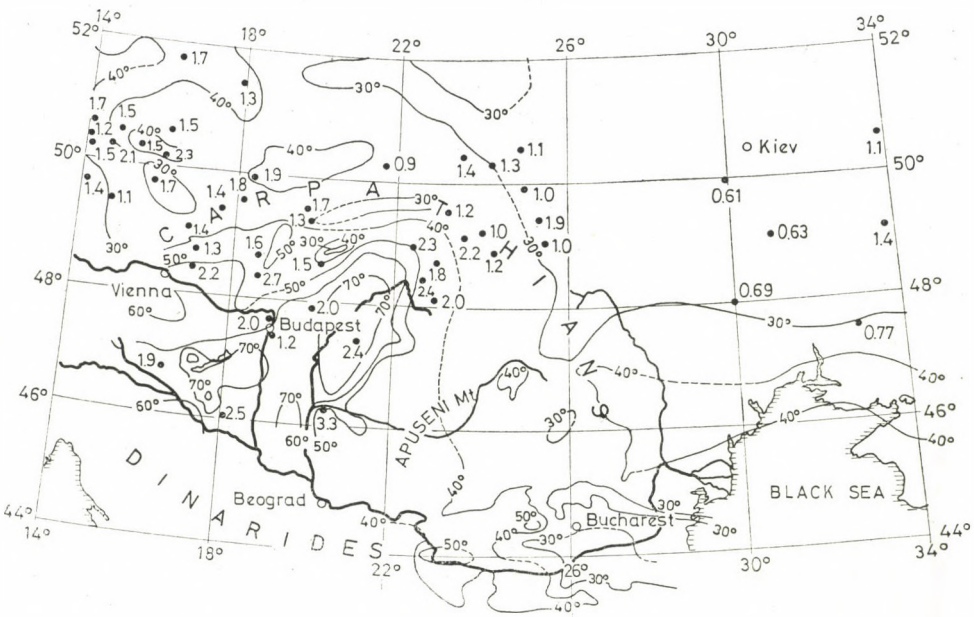


Fig. 2. Geoisotherms (°C) at the depth of 1 km (Stegena, 1972) and typical surface heat flow values in the surroundings of the Pannonian Basin. Heat flow values taken from Boldizsár (1964), Čermák (1968), Plewa (1967), Kutas and Gordienko (1970), Lubimova and Polyak (1969), Salát (personal communication)

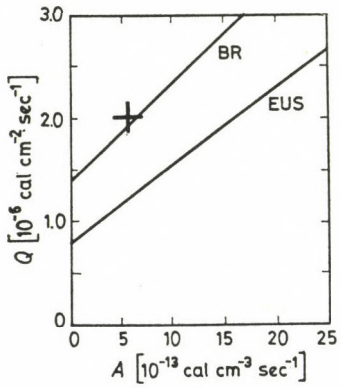


Fig. 3. Heat flow values as function of radiogene heat source density in the surroundings of the point of measurement (after Roy et al., 1971, Fig. 15). The average value in the Pannonian Basin (+) falls on the line of high mantle heat flow ($Q_0 = 1.4$ HFU)

5. The heat flow existing in the upper mantle — according to the calculations of Buntebarth (see p. 565) — is high, too ($Q \approx 55\ \mathrm{mWm^{-2}}$).

That the heat flow in the upper mantle of the Pannonian Basin is high might be proved by the approximative method of Roy et al. (1972) based on the measurement of the radioactivity of rocks (Fig. 3).

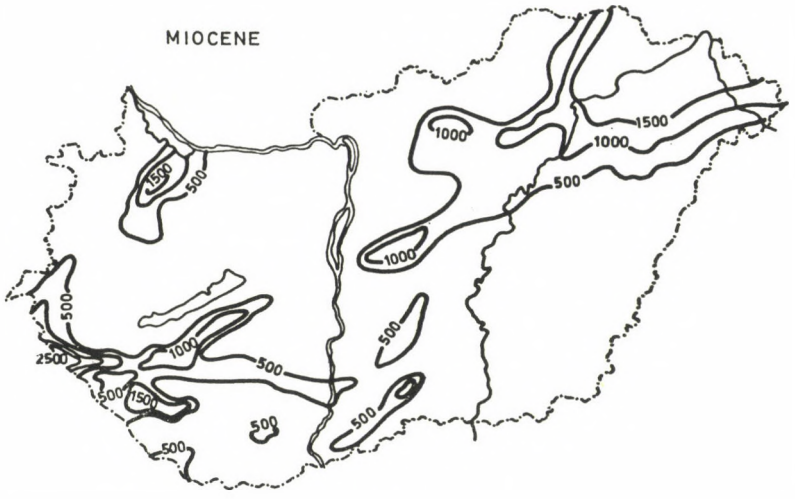
Finally both the magnetotelluric and geothermic investigations show that there is a significant geothermal high in the area of the Pannonian Basin, extending downwards perhaps more than 100 km. This geothermal high is not present on the surrounding areas (the Czech Massif, Ukrainian Platform e.g.) this is why it can be supposed to be in connection with the formation of the basin. From the geological point of view the Pannonian Basin is a young formation (Fig. 4). Its sinking started already in the Miocene but the main process was enacted in the Pliocene (Pannonian stage) about 5–10 million years ago. It can be shown as follows by a calculation that a thermal anomaly going down to such a great depth could not have been formed by thermal conductance only because this is a very long process, from the geological point of view as well. This is why we suppose that the convection of material from the mantle, transmitting the heat, played a very important role in the formation of the heat anomaly of the basin.

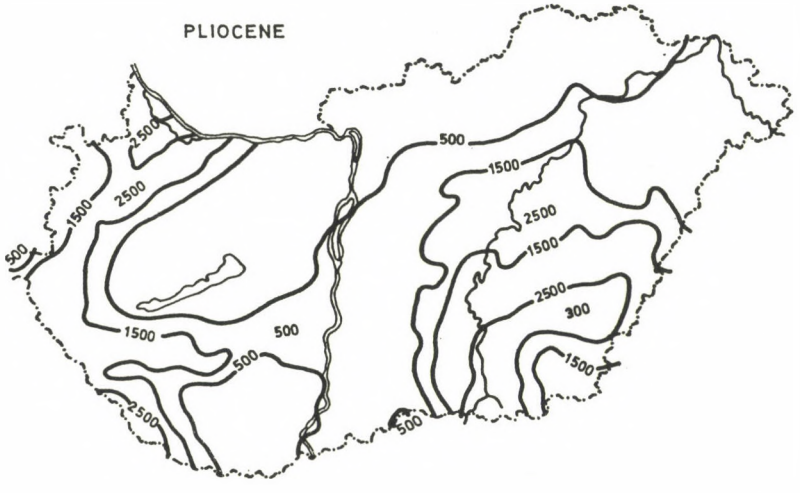
Let us consider a medium of thickness h and thermal diffusivity k at the bottom of which ($z = h$) a heat disturbance appears at $t = t_0$ in the form of a step function with amplitude $T = T_0$. Solving the one-dimensional equation of heat conduction we obtain for the distribution of temperature with depth (z) and time (t):

$$T(z,t) = T_0 \left(\frac{z}{h} + \frac{2}{\pi} \sum_{n=1}^{\infty} \frac{(-1)^n}{n} \mathrm{e}^{-\frac{n^2\pi^2}{h^2} kt} \sin n\pi \frac{z}{h} \right)$$

In the stationary case ($t = \infty$): $T = T_0 z/h$. In a finite time interval

$$T = \alpha T_0 z/h; \quad \text{where } \alpha < 1$$


MIOCENE
1000
1500
1000
500
1500
500
1000
500
500
1000
500
2500
500
1500
500
500
500


PLIOCENE
2500
500
1500
2500
2500
1500
500
2500
1500
2500
300
1500
500
500
2500

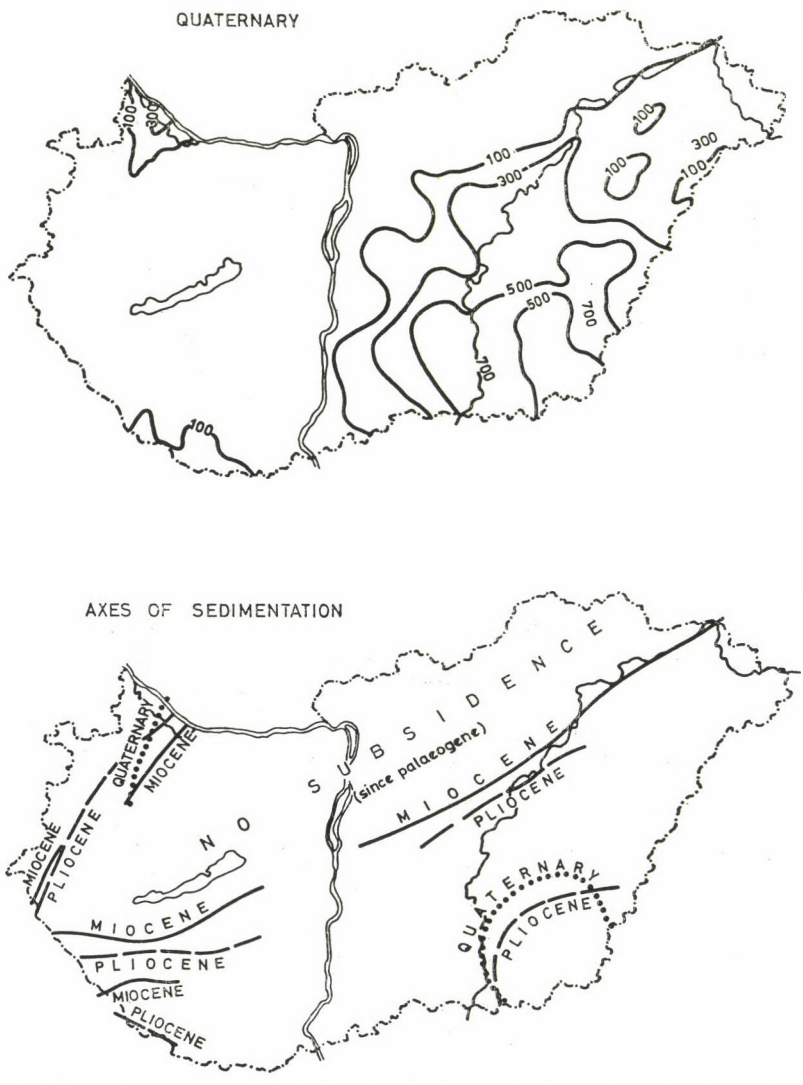


Fig. 4. Thickness of the Miocene, Pliocene (Körössy, 1970) and Quaternary (Kovács et al., 1971) sediments (in meters) and the main axes of sedimentation derived from them for the area of Hungary

Restricting ourselves to small depths ($z \ll h$; $\sin n\pi z/h \approx n\pi z/h$) and taking the first term of the rapidly converging series as an approximation, we obtain:

$$\frac{\alpha - 1}{2} = -\mathrm{e}^{-\frac{\pi^2}{h^2} kt}$$

Hence the values of kt/h in the function of α are as follow:

$\alpha =$	0.5	0.9	0.99
$\frac{kt}{h^2} =$	0.14	0.30	0.53

Let us take the values $k = 10^{-2}$ cm^{2}sec^{-1} for the earth's crust and the upper mantle and $h = 100$ km. Thus for α=0.5, 44 m.y. and for $\alpha = 0.9$, 95 m.y. is needed for the deep-seated heat disturbance to reach near the surface.

The material flowing upward from the mantle, the active mantle diapir is the key phenomenon in the formation of the Pannonian Basin and similar intermountain basins. We suggest the mantle diapir below the Pannonian

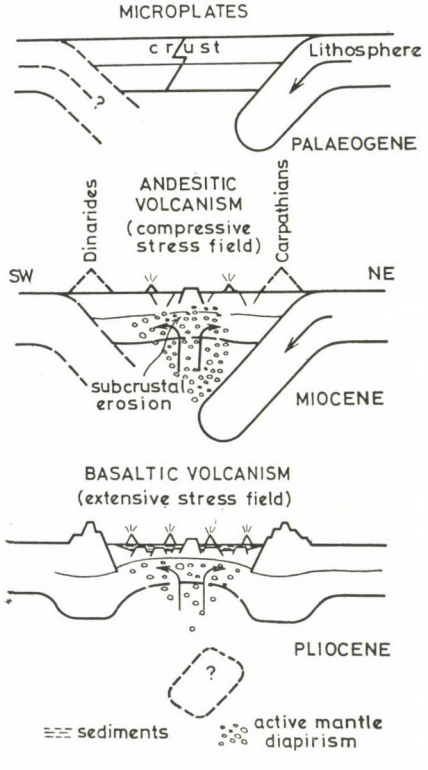


Fig. 5. Scheme of the Neogene evolution of the Pannonian Basin (no vertical scaling)

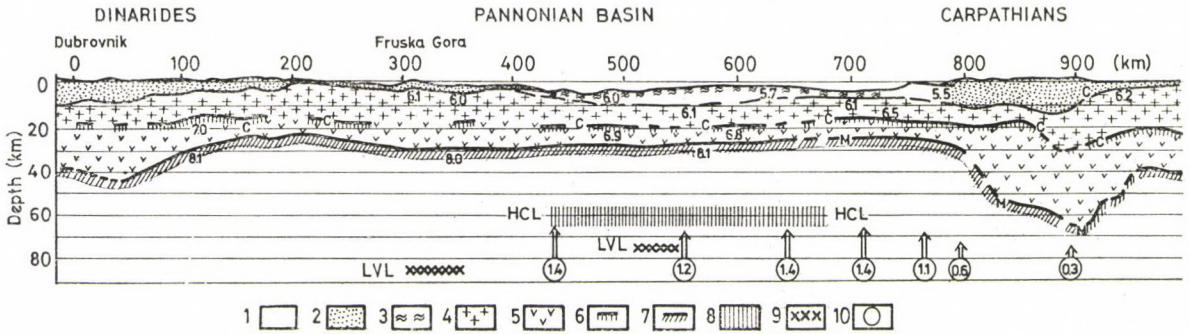


Fig. 6. Seismic crustal profile (Mituch and Posgay, 1972), heat flow values calculated for the upper mantle (Buntebarth, personal communication), positions of the HCL (Ádám, 1965) and LVL (Bisztricsány and Egyed, 1973; Bisztricsány, 1973)

1 – young sediments in the Pannonian Basin; 2 – sedimentary complex; 3 – Mesozoic basement of the Pannonian Basin; 4 – granitic layer; 5 – basaltic layer; 6 – Conrad disconti-nuity; 7 – Moho discontinuity; 8 – upper surface of the HCL; 9 – surface of the LVL; 10 — heat flow values in the upper mantle (HFU)

area was formed the following way (Fig. 5): We suppose the Carpathian arc is a result of a lithosphere subduction process directed towards the basin and active during the Early and Middle Miocene. Partial melting occurred at the upper surface of the subductive slab in the mantle. Partial melting is the "result of shear heating and contamination with lower melting lithospheric material" (Scholz et al., 1971). The hot, partially melted material rose diapirically and at reaching the bottom of the strong ensialic crust

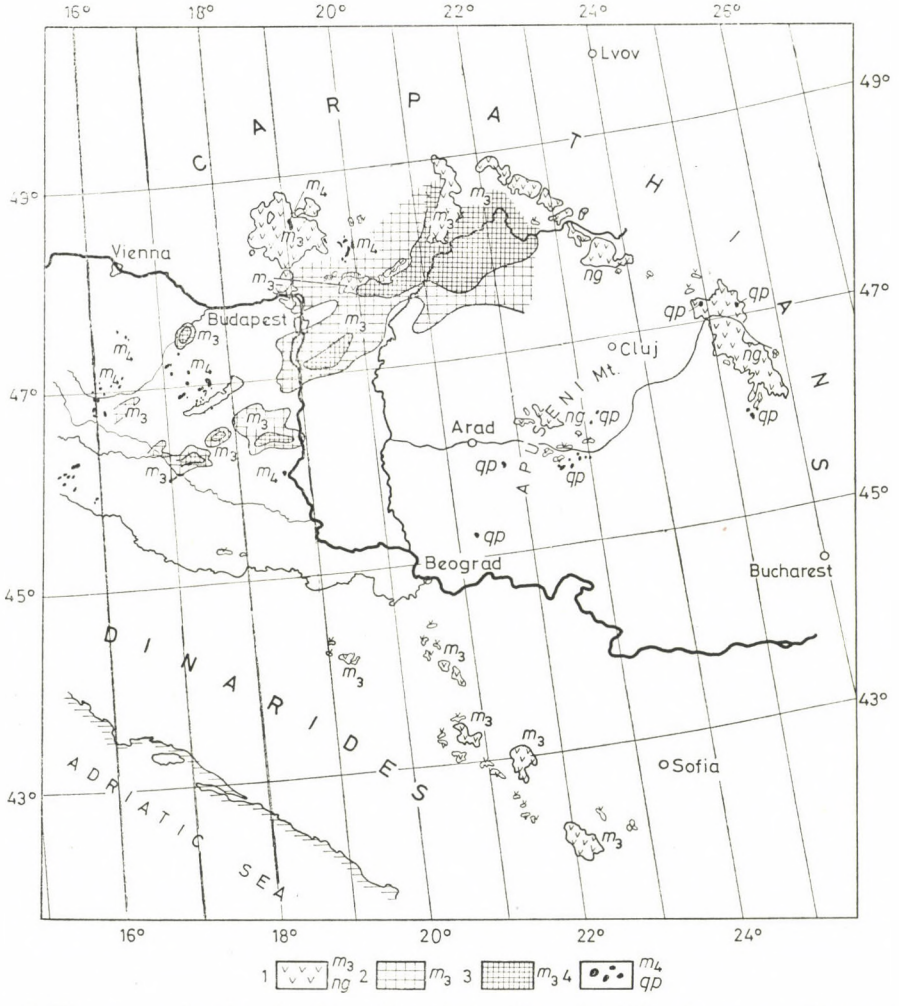


Fig. 7. Neogene volcanism in the region of the Carpatho-Dinaric system (International Geological Map of Europe, 1969; Harta Geologica, 1967; Kovács, 1967, Körössy, 1970)

1 – andesitic volcanoes on the surface and their age (m_3 = Miocene, ng = Neogene); 2–3 – distribution and age of andesites and andesitic tuffs in Neogene sediments in Hungary; 2 – 0 – 500 m – thickness; 3 – > 500 m thickness; 4 – basaltic volcanoes on the surface and their age (m_4 = Pliocene, q_p = Pleistocene)

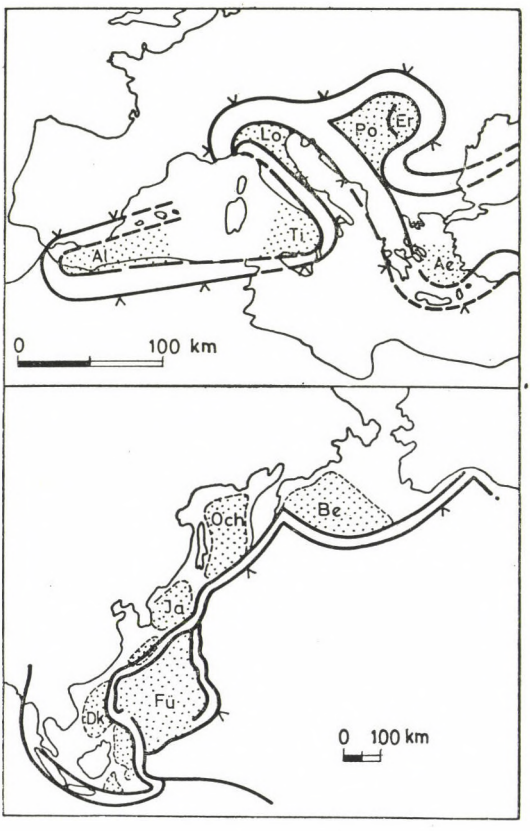


Fig. 8. Interarc basins of the Mediterraneum and Western Pacific

it spread laterally (Fig. 5). Here is melted (eroded) the bottom of the crust ("subcrustal erosion").

The fact that beneath the Pannonian Basin the upper crust is of normal thickness while the lower crust is very thin (Fig. 6) is in agreement with the subcrustal erosion.

Figure 6 shows heat flow values in the upper mantle, calculated by Buntebarth (1973) by his own method and the running down of the low velocity layer of elevated position defined by Bisztricsány (1974).

The development of the Pannonian territory as outlined above is in accordance with the volcanism of the basin (Fig. 7). When compressive stresses were prevailing in the area because of the subduction (in the Miocene) andesitic and rhyolitic lavas were forced out by the volcanism. As the area turned to extensive, the character of the volcanism also changed: in the Plio-Pleistocene volcanism is always basaltic in the Pannonian Basin. Dickinson (1970) pointed out the connection between volcanic rocks and the stress environment of an area. The volcanic rocks are andesitic in compressive areas and basaltic in areas of extension.

Finally let us examine whether the mantle diapir theory, adopted to the Pannonian Basin previously, could be applied to the other interarc basins.

TECTOGENESIS OF INTERARC BASINS*

The interarc basins are depressions, situated on the concave side of mountain and island arcs. Figure 8 shows the interarc (retroarc) basins of the Mediterranean and of the Western Pacific Area. The earth's crust is of oceanic or continental character beneath the interarc basins; the first are the ensimatic, the other the ensialic interarc basins. The Pannonian Basin is an ensialic basin.

The physiographic pattern of the interarc basins suggests that they are in genetic connections with the forming of the neighbouring mountain (island) arc.

It was Karig (1971) who modelled a theory on the tectogenesis of the Western Pacific marginal seas (Fig. 9). The expanding ocean-bottom, by the spreading of the Pacific Ocean, endured subduction near the continental shore of Asia in the Early Tertiary, forming the abyssal graben and the

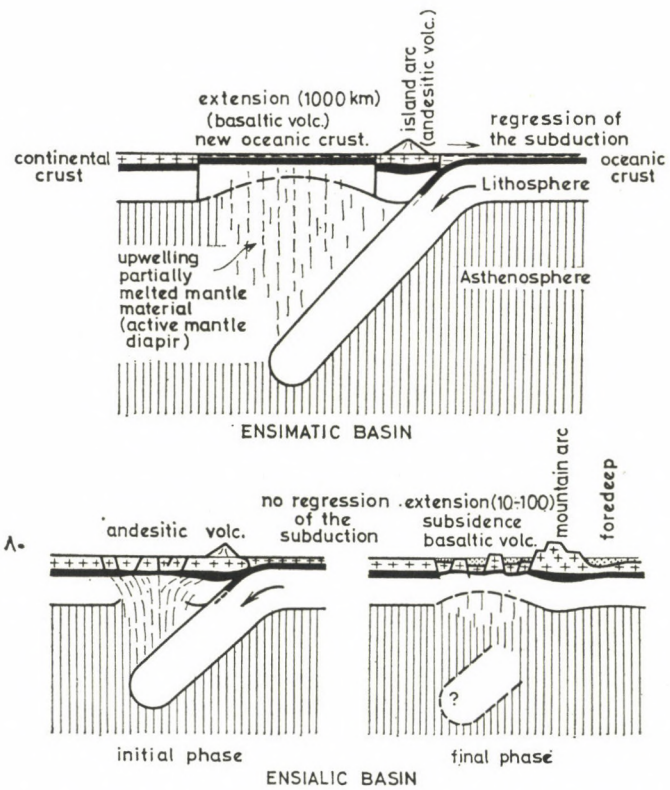


Fig. 9. Evolution of ensimatic and ensialic interarc basins by mantle diapirism

* This part was written with co-authors F. Horváth and B. Géczy

volcanic island arc. The downgoing litosphere plate, between the continent and the island arc forms by means of the submerging volatiles and the frictional heath a zone partially melted and less dense which emerges in the nature of intrusion (active mantle diapir). At the same time the subductive zone (with the island arc and the abyssal graben) regresses towards the ocean ("regression of the subduction"). The emerging mantle-diapir between the continent and the island arc forms a new (basaltic) oceanic crust ("interarc spreading"). Karig's theory is sustained by the facts that the Western Pacific border-seas are new seas; the Tertiary deposits lay directly on the basaltic crust; on the territories of the seas only basaltic volcanism exists and heat flow is high. During the Tertiary period the interarc spreading dislodged the island arc with about 1000 km from the Asiatic Continent.

Karig's theory was quoted and used several times. Bleahu et al. (1973) tried to adopt it for the Pannonian Basin as well. But, although there are many similarities between the geological and geophysical characteristics of the Western Pacific basins and those of the Pannonian Basin and their evolutions are also similar, it is necessary to stress that there are some important differences as well.

The Pannonian Basin is an ensialic basin of continental crust with 26 km medium and 23 km minimum thickness of the crust (Mituch and Posgay, 1972). Under the thick ($\sim$ 3 km) Plio-Pleistocene sediments of the basin several deep-boreholes hit the Mesozoic rocks. Thus the tectogenetic theory of the Western Pacific basins could not be just transferred to the Pannonian Basin without any modification. Another important difference is the buried Miocene andesitic-riolitic volcanism of great mass in the Pannonian Basin, which is not present in the interior of the Western Pacific basins. Since the Pliocene the volcanism of the Pannonian Basin has weakened and it has always been basaltic.

We could sketch the tectogenesis of ensialic and ensimatic basins as follows (Fig. 9):

Above the submerging plate the partially melted material, originated in the mantle (active mantle diapir), reaching the crust, breaks it through, if the regression of the subduction towards the ocean is possible. Extending the break-through forms the ensimatic basin. If the regression of the subduction is not possible, the coming up mantle diapir laterally expands at the Moho surface (Scholz et al., 1971), and extenuates it from below ("subcrustal erosion", see e.g. Ritsema, 1972). These are the ensialic basins.

Such interarc ensialic basin is the Pannonian Basin (Stegena et al., 1974). The thickness of the granitoid upper crust of the Pannonian Basin is normal (16–19 km) and the lower crust is thinned out. The active mantle diapir only sporadically broke through the crust completely, there where the gigantic magmatic masses broke out. Following the end of the Miocene andesitic volcanism starts the outstandingly quick Plio-Pleistocene subsiding of the area (which is the outcome of the isostatic subsiding of the thinned-out crust) and the change of volcanism into basaltic. These two phenomena show that the compressive character of the area ceased to exist, as it was first pointed out by Scholz et al. (1971) in connection with the Great Basin (Western USA). The Pannonian area's turning into an

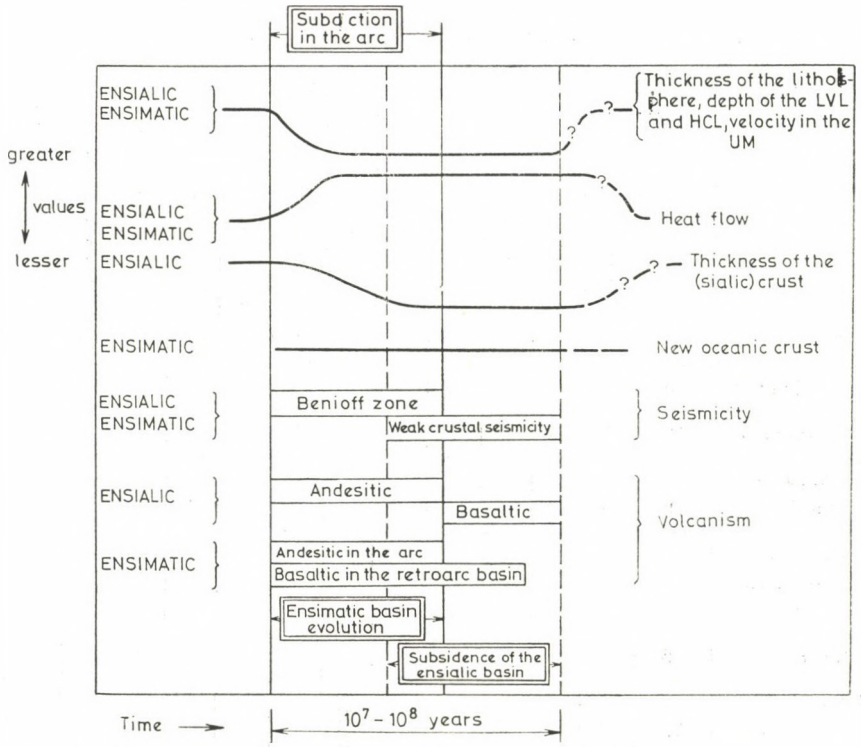


Fig. 10. Development of geological and geophysical parameters of an interarc basin, according to the mantle diapir theory

extensive one is in connection with the ceasing of the Carpathian subduction.

The total extension of the Pannonian Basin (the horizontal departure of the Carpathians-Dinarides) judged by volcanic zones is 10–30 km. As far as the Great Basin is concerned — the other ensialic basin is similar to the Pannonian one — Thompson (1972) points out an extension of 50–100 km. On the contrary the extension of the ensimatic basins is $\sim$ 1000 km.

Accepting the tectogenetic hypothesis of the ensialic and ensimatic interarc basins sketched above, we can delineate the change of the geologic and geophysical characteristics of these basins within the tectogenesis (Fig. 10).

Finally, we examined how the interarc basins suit to the rules sketched on Figure 9 (Table 1). Table 1 suggests that the above-mentioned formation hypothesis of the interarc basins, for which the tectogenetic model of Karig in account of the Western Pacific basins and that of Scholz et al.'s of the ensialic Great Basin formed the basis, can be generally accepted.

TABLE 1

How do the interarc basins satisfy the mantle diapir theory

The basins'			Upper mantle anomalies						Volcanism		Geothermics				
Character	name	age m. y.	Elevated LVZ	Elevated HCL	Thin lithosphere	Reduced velocities	Reduced density	Thin crust (continental)	Initial andesitic	Final basaltic	High temperatures	High surface heat flow	High mantle heat flow	Positive Bouguer anomaly	Seismicity
Ensialic	Aegean	2			+			+	+	+		+		+	+
	Lombardian	5				+		+	−	+	−			+	+
	Pannonian	15	+	+	+	+	+	+	+	+	+	+	+	+	+
	Transsylvanian	15	+					+	+	+	+			+	+
	Great Basin (Western US)	40	+	+		+	+	+	+	+		+	+	+	+
Ensimatic	Tyrrhenian	5	+			+		Oceanic crust	Absent	+		+		+	+
	South Caspian	15		+	+							+		+	±
	Japan sea	25	+			+				+		+		+	+
	Okhotsk sea	30				+	+			+		+		+	+
	Phillippine sea	30		+						+		±		+	+

+ agreement
− disagreement
□ no data
± partial agreement

} with mantle diapirism

REFERENCES

ÁDÁM, A., 1965. Einige Hypothesen über den Aufbau des oberen Erdmantels in Ungarn. *Gerlands Beitr. z. Geophys.* **74,** 20–40.

ÁDÁM, A., 1969. Appearance of the electrical inhomogeneity and anisotropy in the results of the complex electrical exploration of the Carpathian Basin. *Acta Geod. Geophys. Mont. Hung.* **4,** 187–197.

BISZTRICSÁNY, E., 1974. The depth of the LVL in Europe and in some adjacent regions. *Geofizikai Közlemények* **22,** 65.

BISZTRICSÁNY, E., EGYED, L., 1973. The determination of LVL depth from data of spaced seismological stations. *Geofizikai Közlemények* **21,** 81–83.

BLEAHU, M. D., BOCCALETTI, M., MANETTI, P., PELTZ, S., 1973. Neogene Carpathian Arc: A continental arc displaying the features of an island arc. *J. Geophys. Res.* **78**, 5025.

BOLDIZSÁR, T., 1964. Heat flow in the Hungarian basin. *Nature* **202**, 1278–1280.

BUNTEBARTH, G., 1973. Model calculations on temperature-depth distribution in the area of the Alps and the foreland. *Z. Geophys.* **39**, 97–107.

ČERMÁK, V., 1968. Terrestrial heat flow in Czechoslovakia and its relations to some geological features. XXIII. Intern. Geol. Cong. Prague, 5, 75–85.

DICKINSON, W. R., 1970. Relation of andesites, granites and derivative sandstones to arc-trench tectonics. *Rev. Geophys. Space Phys.* **8**, 813–860.

GÁLFI, J., STEGENA, L., 1960. Deep reflexions and crustal structure in the Hungarian basin. *Ann. Univ. Sci. Budapestiensis* **3**, 41–47.

KARIG, D. E., 1971. Origin and development of marginal basins in the western Pacific. *J. Geophys. Res.* **76**, 2542–2561.

KOVÁCS, G., ERDÉLYI, M., MAJOR, P., KORIM, K., 1971. Hydrological investigation of subsurface water. M. Erdélyi (Ed.): Materials of International Postgraduate Course on Hydrological Methods of Developing Water Resources Management. VITUKI Budapest.

KOVÁCS, L., 1967. Regional Geology of Hungary (in Hungarian). Budapest.

KŐRÖSSY, L., 1970. Entwicklungsgeschichte der neogenen Becken in Ungarn. *Acta Geol. Sci. Hung.* **14**, 421–429.

KUTAS, R. I., GORDIENKO, V. V., 1970. Heat field and abyssal structure of the Eastern Carpathians (in Russian). *Geojiz. Sb.* **34**, 29–41.

LUBIMOVA, E. A., FELDMAN, I. S., 1970. Heat flow, temperature and electrical conductivity of the crust and upper mantle in the USSR. *Tectonophysics* **10**, 245–282.

LUBIMOVA, E. A., POLYAK, B. G., 1969. Heat flow map of Eurasia. P. J. Hart (Ed.): The Earth's Crust and Upper Mantle, Geophys. Monograph, 13, 82–87.

MITUCH, E., POSGAY, K., 1972. Hungary. G. Szénás (Ed.): The Crustal Structure of Central and Southeastern Europe Based on the Results of Explosion Seismology. *Geophys. Trans.* Spec. Edition, Budapest, 118–130.

PACKHAM, G. H., FALVEY, D. A., 1971. A hypothesis for the formation of marginal seas in the Western Pacific. *Tectonophysics* **11**, 79–109.

PLEWA, S., 1967. Measurement results of the surface heat flow on the Polish territory. R. Teisseyre (Ed.): Selected Problems of Upper Mantle Investigation in Poland. Polish Sci. Publ., 103–113.

RIKITAKE, T., 1952. Electrical conductivity and temperature in the Earth. *Bull. Earthquake, Res. Inst. Tokyo Univ.* **30**, 13–23.

RITSEMA, A. R., 1972. Deep earthquakes of the Tyrrhenian Sea. *Verh. Ned. Geol. Mijbouwkd. Genoot.* **51**, 541–545.

ROY, R. F., BLACKWELL, D. D., DECKER, E. R., 1972. Continental heat flow. E. C. Robertson (Ed.): The Nature of the Solid Earth. Mc Graw Hill, 506–543.

SCHOLZ, C. H., BARAZANGI, U., SBAR, M. L., 1971. Late Cenozoic evolution of the Great Basin, Western United States, as an ensialic interarc basin. *Geol. Soc. Am. Bull.* **82**, 2979–2990.

STEGENA, L., 1964. The structure of the Earth's crust in Hungary. *Acta Geol. Sci. Hung.* **8**, 413–431.

STEGENA, L., 1967. On the formation of the Hungarian Basin (in Hungarian). *Földt. Közl.* **97**, 278–287.

STEGENA, L., 1972. Geothermal map of Eastern Europe. *Geothermics* **1**, 140–141.

STEGENA, L., ÁDÁM, A., HORVÁTH, F., 1971. Spreading tectonics investigated by magnetotelluric anisotropy. *Nature* **231**, 442–443.

STEGENA, L., GÉCZY, B., HORVÁTH, F., 1974. Late Cenozoic Evolution of the Pannonian Basin. *Tectonophysics* **26**, 71–90.

THOMPSON, G. A., 1972. Cenozoic basin range tectonism in relation to deep structure. Internat. Geol. Congress 24th Session, Sec. 3, Tectonics, Montreal, 84.

IV. EAST CARPATHIANS

ANOMALY OF THE GEOMAGNETIC BAYS IN THE EAST CARPATHIANS

A. P. BONDARENKO, A. I. BILINSKY

The investigation of the anomalies of geomagnetic bays was included in the program of study of the abyssal structure of the earth's crust and of the upper mantle on the territory of the Ukrainian SSR by a complex of geophysical methods. In course of the first observations, carried out in 1964 in the East Carpathians along the III International Seismic Profile, anomalous changes of bay-like variations were discovered at the southern boundary of the Folded Carpathians (Bondarenko et al., 1969). In the following years surface investigations have been carried out on the territory of the East Carpathians and on adjoining regions.

Field observations are being made at 60 stations situated every 15–20 km on four profiles.* In the first years the same stations also recorded the variations of the geoelectric field. Because of the high noise level from the electrified railway it was not possible to receive useful records but for a few stations.

From the magnetograms induction vectors (Wiese, 1965) and anomalous amplitude variations were determined. The technique of analysis and first preliminary results are described in the monograph of Bondarenko et al. (1972).

The map of the induction vectors obtained in the period 1968–1972 is presented in Figure 1. The anomaly can be traced fairly well by the change

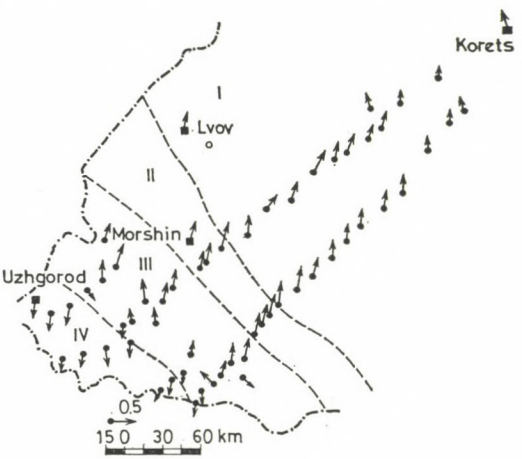


Fig. 1. Distribution of the induction vectors at the East Carpathians and regions adjacent to the slope of the Russian Platform
I – slope of the Russian Platform; II – Forecarpathian trough; III – Folded Carpa- thians; IV – Transcarpathian trough(Pannonian Basin)

* The observation system is described on pp. 600–603.

of directions of the induction vectors. The anomaly axis approximately coincides with the zone of the abyssal Transcarpathian fracture.

Graphs of the anomalous amplitude values of the Z- and H-components along the III deep seismic profile are shown in Figure 2. The same figure contains a plot of the relative values of the amplitudes of bay-like variations of the total horizontal component of the geoelectric field. At the Folded Carpathians the amplitudes of bays of the Z-component are increasing by 2.5 times, those of the H-component 2 times in comparison with the respective amplitudes at station Korets. Amplitudes of the D-component change much less. The maximum depth of a localized source of the anomaly, determined over the extremal points of the graph k_{za}, is of the order of 30 km.

It is known that geomagnetic bays, especially in the Z-component, may be connected with the existence of sudden changes in the electric conductivity of the first layers of the earth's crust in horizontal directions. The

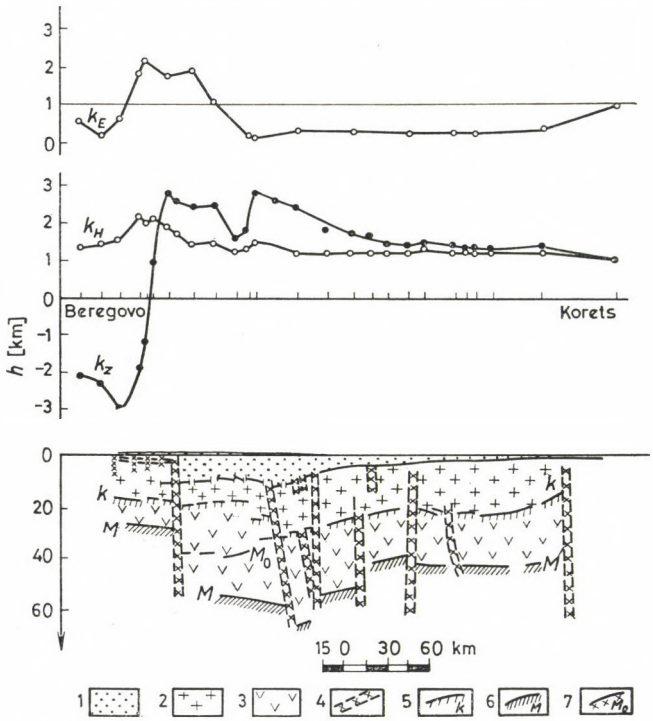


Fig. 2. Distribution of the mean relative values of amplitudes of bays of the vertical k_z, resp. horizontal k_H components of the geomagnetic field and of the horizontal vectors of the geoelectric fields k_E, and crustal cross section along DSS profile III
1 – sedimentary layer; 2 – "granitic" layer; 3 – "basaltic" layer; 4 – deep faults; 5 – Conrad surface; 6 – Mf surface; 7 – M_0 surface

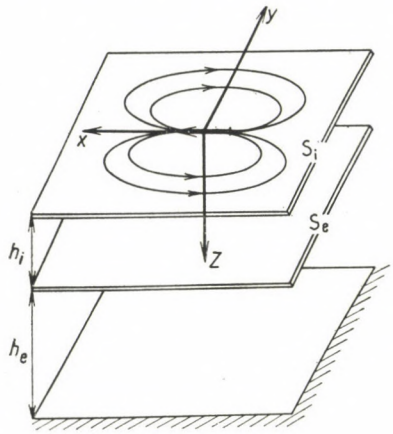


Fig. 3. System of coordinates and sketch of the model used for the determination of the field of the ionospheric current

analysis of the data obtained has shown that the distorting influence of the first-layer's inhomogeneity is easily recognized at the determined induction vectors and variation amplitudes. Obviously, such distortions could also be useful for a quantitative interpretation of anomalies of deeper origin. For this, the principal laws and quantitative characteristics of the structure of the external source ought to be also known.

In middle latitudes the spatial structure of geomagnetic bays is connected with ionospheric return currents of the auroral electrojet. The field of such a source can be simply expressed if we adopt the idealized description of the medium schematically sketched in Figure 3, where h_i denotes the altitude of the ionosphere, S_i denotes its longitudinal conductivity, S_e is the longitudinal conductivity of the sedimentary layer, h_e depth to the conductive layer of the mantle which we assume a perfect conductor. For this model the components of the electromagnetic field on the earth's surface due to the source are, according to Bilinsky and Pavlosyuk (1974):

$$
\begin{aligned}
H_x &= -\frac{I}{2\pi}\,\frac{1-i\mu\omega S_e h_e}{\psi}\,\frac{2xy}{r^4}\left(1-\frac{Q}{\psi}\,\frac{3}{2r}\right)\\
H_y &= \frac{I}{2\pi}\,\frac{1-i\mu\omega S_e h_e}{\psi}\left(\frac{y^2-x^2}{r^4}-\frac{Q}{\psi}\,\frac{2y^2-x^2}{r^5}\right)\\
H_z &= \frac{I}{2\pi}\,\frac{h_e Q}{\psi^2}\,\frac{3y}{r^5} \qquad (1)\\
E_x &= -\frac{I}{2\pi}\,\frac{i\mu\omega h_e}{\psi}\left(\frac{y^2-x^2}{r^4}-\frac{Q}{\psi}\,\frac{2y^2-x^2}{r^5}\right)\\
E_y &= \frac{I}{2\pi}\,\frac{i\mu\omega h_e}{\psi}\,\frac{2xy}{r^4}\left(1-\frac{Q}{\psi}\,\frac{3}{2r}\right)
\end{aligned}
$$

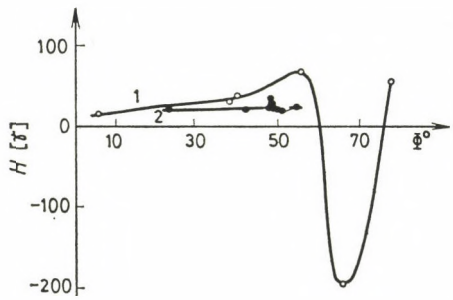


Fig. 4. Latitudinal distribution of the mean amplitudes of simultaneous bays of the H-component of the geomagnetic field
1 – along the profile of observatories Guam, Vladivostok, Yu. Sakhalinsk, Yakutsk, Tiksi, North Pole 7; 2 – along the profile crossing the Carpathians

where

$$\psi = (1 - i\mu\omega S_e h_e)(1 - i\mu\omega S_i h_i) - i\mu\omega S_i h_e$$

$$Q = h_e + h_i - i\mu\omega S_e h_i h_e$$

I – current of the point source, i – imaginary unit, ω – angular frequency, $r = \sqrt{x^2 + y^2}$ – radius vector, $\mu = 4\pi \cdot 10^{-7}$ Henry per meter – magnetic permeability.

It follows from Eqs (1) that on the Carpathian latitude ($r = 2 \cdot 10^6$ m) at small distances one may neglect the diminishing of the field. The comparison of magnetograms, recorded simultaneously at the magnetic observatories of the world system, show that in middle latitudes the geomagnetic bays do not change over distances of the order of a few hundred km. The latitudinal change of the H_x-component is illustrated in Figure 4. The curve was constructed from the average amplitudes of 75 bays, recorded simultaneously in 1964 on the profile of observatories Guam, Vladivostok, Yu. Sakhalinks, Yakutsk, Tiksi, North Pole 7.

If there are horizontal inhomogeneities of the conductance in the earth, these would induce secondary anomalous fields which distort the planetary geometry of the external field. The distortion of the change with latitude of bay amplitudes is noticeable in the Carpathian region. In Figure 4 mean amplitudes of 20 simultaneous bays of the northern component are shown for observatories Tamanrasset, Panagyuriste, Lvov, Pleshchenitsy situated on the longitudinal profile, intersecting the Carpathians.

Suppose there exists a one-dimensional inhomogeneity of the longitudinal conductance in the first layer section in the field described by Eq. (1). Let us change in the interval $y = 2\Delta r$ the longitudinal conductance S according to a linear law, increasing its maximum value S_m by $y = r_0$:

$$S_y = S_3 + \frac{\Delta S}{\Delta r}[\Delta r \pm (r - r_0)] \tag{2}$$

where $\Delta S = S_m - S_3$, plus corresponds to the interval $r_0 - \Delta r \leq y \leq r$; minus to the interval $r_0 \leq y \leq r_0 + \Delta r$. The influence of conductivity inhomogeneity is taken into consideration as a secondary (anomalous) field, generated by induced currents. The calculations will be carried out in the d.c. approximation, i.e. by neglecting the skin-effect, which is of course

justified for the periods of bay-like distortions ($S_3 \sim 10^2 - 10^3 \Omega^{-1}$ and $T \geq 10^3$ sec). Then in the "surplus" longitudinal conductance $S_a = S_y - S_3$ a current $j_a = S_a E_x$ will be induced, which produces in point r the anomalous field

$$dH_{za} = \frac{1}{2\pi} \frac{S_a E_x}{r - y} dy$$

Substituting the value of S_a from Eq. (2) and E_x from Eq. (1) we integrate over the interval $2\Delta r$. Confining ourselves to the first terms in Eq. (1) we obtain the total field from the current in all the inhomogeneities

$$H_{za} = \frac{I}{4\pi} \cdot \frac{i\mu\omega h_4}{[(1 - i\mu\omega S_3 h_4)(1 - i\mu\omega S_1 h_2) - i\mu\omega S_1 h_4]} \cdot \frac{\Delta S}{\Delta r} \cdot \frac{F}{r^2}$$

where

$$F = 2(r - r_0) \ln \frac{r - r_0}{r_0} - (r + \Delta r - r_0) \ln \frac{r + \Delta r - r_0}{r_0 - \Delta r} -$$

$$- (r - \Delta r - r_0) \ln \frac{r - \Delta r - r_0}{r + \Delta r}$$

In the inhomogeneous region where $y \simeq r$,

$$\frac{H_{za}}{H_z} = \frac{(1 - i\mu\omega S_e h_e) i\mu\omega}{h_2 + h_4 - i\mu\omega S_e h_i h_e} \tag{3}$$

under the conditions $S_i \ll S_e$ and $|i\mu\omega S_i h_i| \ll 1$. Since $F(r, r_0, \Delta r)$ changes in a limited range and attains maximum values for $y \simeq r_0 + \Delta r$. It follows from Eq. (3) that in the inhomogeneous region of the longitudinal conductivity of the first layer of the geoelectric section the ratio of the anomalous field to the normal one for the vertical component is proportional to the distance to source and to the gradient of the longitudinal conductivity. This means that in middle latitudes even small gradients of the longitudinal conductivity of the first layer may create anomalous fields H_{za}, exceeding the vertical component of primary origin. In reality, gradients of the longitudinal conductivity are existing almost everywhere and owing to this in middle latitudes bay-like distortions of the vertical component of inductional origin predominate. This may be a possible explanation for the existence of the linear relationship between the amplitudes of bays of the vertical and horizontal components of the geomagnetic field:

$$H_z = aH_x + bH_y \tag{4}$$

The relationship of the correlation coefficient figuring in Eq. (4) and of the inhomogeneity parameters of the conductivity of the first layer may be established this way: Assume that in the plane S_e (cf. Fig. 3) in the direction $90° + \vartheta$ from the axis x there is a linear inhomogeneity with "surplus" conductance S_a. Then the anomalous vertical component induced

can be described, neglecting the skin-effect, by:

$$H_{za} = \frac{S_a E_{90°+\vartheta}}{2\pi l}$$

where $E_{90°+\vartheta} = E_y \cos\vartheta - E_x \sin\vartheta$ is the projection of the intensity vector of the electric field to the direction $90° + \vartheta$, l is distance of the observation point from the inhomogeneity. Substituting E_x and E_y from Eq. (1), we get:

$$H_{za} = \frac{S_a}{2\pi l} \frac{i\mu\omega h_e}{1 - i\mu\omega S_e h_e} \left[\frac{2xy}{r^4} \left(1 - \frac{P}{\psi} \frac{3}{2r} \right) \cos\vartheta + \right.$$

$$\left. + \left(\frac{y^2 + x^2}{r^4} - \frac{P}{\psi} \frac{2y^2 - x^2}{r_5} \right) \sin\vartheta \right] = KH_\vartheta \qquad (5)$$

where

$$K = \sqrt{a^2 + b^2} = \frac{S_a}{2\pi l} \cdot \frac{i\mu\omega h_e}{1 - i\mu\omega S_e h_e}$$

$$H_\vartheta = H_x \cos\vartheta + H_y \sin\vartheta$$

In the geomagnetic system of coordinates, where the axes x and y are directed to north and east, the angle ϑ is measured clockwise from axis x and it indicates the direction perpendicular to which the inductional currents are flowing.

The magnitude of the induction vector k depends, in general, on the frequency, on the geoelectrical parameters of the inhomogeneity and the embedding medium. The frequency relationship (5) is defined by means of the impedance of the homogeneous section, i.e. from expression (1) it follows that:

$$\frac{E_y}{H_x} = -\frac{E_x}{H_y} = \frac{i\mu\omega h_e}{1 - i\mu\omega S_e h_e}$$

Consequently, a quantitative interpretation of the magnitudes of induction vectors will face us with the same difficulties as encountered in magnetotelluric soundings. However, if the results of deep MTS are distorted by the influence of surface conductivity inhomogeneities, the coefficients of the linear relationships for the amplitudes of bay-like distortions are evidently determined by surface inhomogeneities.

Equation (5) was obtained for an infinitely extended inhomogeneity. Real conductivity inhomogeneities of regional character (depressions, shields, mountain folds) have dimensions comparable with the wave lengths of bays in the first layer.

The frequency dependence of the anomalous field was investigated by laboratory modelling of the diffraction of plane waves on a conductive cylinder of finite length. Decreasing the length of the cylinder the period-interval (in the range of maximum frequency response) increases, where

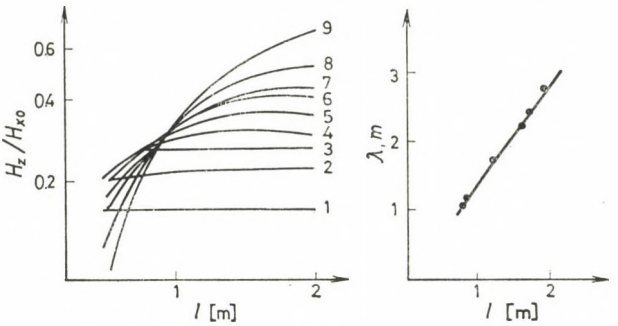


Fig. 5. Distribution of the anomalous field in function of the length of a cylindrical inhomogeneity, according to data of laboratory investigations
$1 - T = 0.33 \cdot 10^{-6}$ sec; $2 - T = 0.5 \cdot 10^{-6}$ sec;
$3 - T = 1.0 \cdot 10^{-6}$ sec; $4 - T = 1.25 \cdot 10^{-6}$ sec;
$5 - T = 2.0 \cdot 10^{-6}$ sec; $6 - T = 2.5 \cdot 10^{-6}$ sec;
$7 - T = 3.3 \cdot 10^{-6}$ sec; $8 - T = 5.0 \cdot 10^{-6}$ sec;
$9 - T = 10^{-5}$ sec

the ratio H_{za}/H_x does not depend on frequency. The boundaries of this interval depend on the commensurability of the length of the cylinder with the wavelength in the medium. Figure 5b illustrates the dependence of the wave length of period corresponding to the lower boundary of the interval, on the length of the cylindrical inhomogeneity.

In the Carpathian region the induction vectors in the range of bay-like variations are almost independent on periods (Bondarenko et al., 1972). This peculiar behaviour of the frequency response is evidently in connection with the commensurability of the Carpathian arc with the wave length of bays in the first layer.

The necessary condition for the quantitative interpretation of the anomalous change of amplitudes is the separation of the anomalous field. On surfaces with a uniform direction of the induction vectors and if the axis of the anomaly is known, one can apply the approximate method of the level estimation of the normal field (Bondarenko et al., 1972). In this case we have

$$a_z(k_z - 1) - a_h(k_h - 1)\frac{l}{l_0} = \left(k_H \frac{l}{l_0} - k_z\right) \tag{6}$$

where

$$a_z = \frac{H_z}{H_{za}}; \quad a_H = \frac{H_x}{H_{xa}}$$

are the coefficients of the separation of the field components to normal and anomalous parts for a base station; l, l_0 are distances from the axis of the

anomaly to the provisional and base stations of observations, respectively;

$$k_z = \frac{1}{n} \sum \frac{H_z}{H_{z0}} ; \; k_H = \frac{1}{n} \sum \frac{H_x}{H_{x0}}$$

are the mean relative values of the bay amplitudes of the vertical and horizontal components. As follows from Eq. (6) a linear relationship exists between quantities

$$y_i = \frac{k_H - 1}{k_z - 1} \frac{l}{l_0} \text{ and } x_i = \frac{k_h \frac{l}{l_0} - k_z}{k_z - 1}$$

If the anomalous variations are the total effect from several sources, scattered in the space, the points in the graph of relationship (6) will group around a few lines.

Figure 6 shows the dependence of y_i on x_i for the Beregovo-Korets profile. In the graph there are two linear relationships: 1 – for the station in the vicinity of the anomaly axis and 2 – for the slope of the Russian Platform. Consequently, the anomalous part of the bays in the Carpathian region can be presented in the first approximation by fields of two sources. The average values of the separation coefficients of the field ($a_H \sim 20$, $a_z \sim 0.2$) for the whole profile indicate that as a level of the normal field one may assume the values of the amplitudes of bays in Korets.

For bay-like variations one may neglect the skin-effect when determining the anomalous field and use the formulas for the direct current. We presented the sedimentary layer as slabs of rectangular and triangular sections with different conductivities. The calculation for the vertical component is illustrated in Figure 7 (curve 1). It follows from the comparison of calculated and observed field values that the Carpathian anomaly cannot be completely explained by the field of inductional currents flowing in the sedimentary layer. But the field induced in the sedimentary layer makes a significant contribution to the Carpathian anomaly, especially to the Z-component, as it is confirmed by the commensurability of the additional maximum k_z with the basic one.

The lack of more detailed calculations is the absence of reliable data upon the conductivity distribution in Folded Carpathians, where the crystal foundation is immersing in 15 km depth. For calculations of the anomalous field of surface origin it is of interest to determine the current

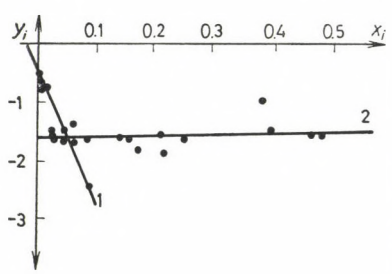


Fig. 6. Distribution of the parameters describing the linear dependence of the mean relative amplitudes of the bays of vertical and horizontal components along DSS profile III, for the determination of the coefficients of separation of the field

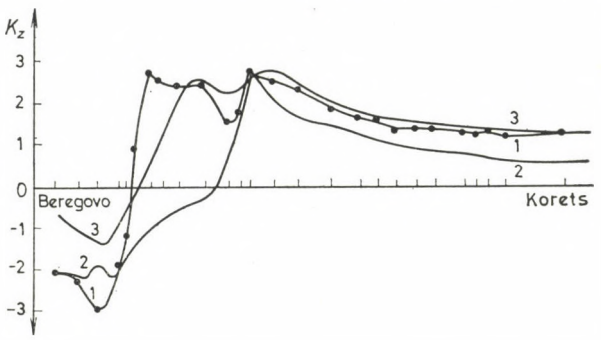


Fig. 7. Comparison of the anomalous change of the amplitudes of bays of the vertical components of the geomagnetic field along DSS profile III
1 – observed data; 2 – calculated induction in the sedimentary layer; 3 – calculation based on data of measured telluric currents

density according to the observation data of the electric field. Let us substitute the sedimentary layer by a surface film of conductivity S, which is equal to the longitudinal conductivity. We present Ohm's law for such a film in the following form:

$$k_j = \frac{j}{j_0} = k_S k_E$$

where k_j is the relative current density (j_0 is current density in the base station), $k_S = S/S_0$ is relative longitudinal conductivity (S_0 longitudinal conductivity in the base station), $k_E = E/E_0$ is relative telluric intensity.

The infinite thread of surface current creates at point l the vertical magnetic field component

$$H_z(l) = \frac{1}{2\pi} \cdot \frac{j}{(l - x)}$$

where x is the coordinate of the thread of current. If we take the current density in the base station for background level, i.e. as level of the normal part of telluric current, we obtain the anomalous part of the field:

$$H_{za}(l) = \frac{1}{2\pi} \cdot \frac{j - j_0}{l - x}$$

Adding up the fields from all of the threads of current in interval (a, b), we can present the relative intensity of the Z-component in the form:

$$k_{za} = \frac{\int_a^b \frac{k_s k_E - 1}{l - x} dx}{\frac{k_s K_E - 1}{l_0 - x} dx}$$

where l_0 is the coordinate of the base station, k_S and k_E depend on x.

The change of k_S along the profile is taken from Figure 2. Longitudinal conductivity relations were determined from the MTP data of Bondarenko et al. (1969) with minor corrections with the help of other geophysical data.

If appeared that on certain intervals of the profile the function $k_S \cdot k_E$ can be approximated by constant values; moreover these intervals coincide with the main tectonic elements of the region. In this case

$$k_{za} = \frac{\sum_{i=1}^{n} [(k_S k_E)_i - 1] \ln \frac{l - g_i}{l - b_i}}{\sum_{i=1}^{n} [(k_S k_E)_i - 1] \ln \frac{l_0 - a_i}{l_0 - b_i}} \tag{7}$$

where a_i, b_i are the coordinates of the boundaries of the i-th interval of the constant value $k_S \cdot k_E$.

In the derivation of Eq. (7) an arbitrary level of the normal background telluric currents has been introduced. In practice, however, it is impossible to find an observation station with a normal uniform electric field. Therefore, even though the observed Z-component of the field is completely of surface origin, it will still differ from the calculated one by a certain amount.

$$H_z = H_{za} + H_{z\varphi}$$

It is easy to show that in this case a linear relationship holds between the observed relative intensity and the one determined:

$$k_z = \alpha k_{za} + \beta$$

where

$$\alpha = \frac{1}{1 + \frac{H_{z\varphi}}{H^0_{za}}} \quad \text{and} \quad \beta = \frac{\frac{H_{z\varphi}}{H^0_{za}}}{1 + \frac{H_{z\varphi}}{H^0_{za}}} \tag{8}$$

are the separation of the field, H^0_{za} is the value of the anomalous field in the base station.

The analysis of data for the Beregovo-Korets profile shows that for the observation stations on the slope of the Russian Platform and in the Forecarpathian trough the linear relationship (8) is valid. The relative intensities calculated by formulas (7) and (8) are compared in Figure 7 with the observed data (curve 2). Obviously by a small change of the distribution along the profile of the summarized current density $k_S \cdot k_E$ a more complete agreement of the calculated and observed data could have been reached.

It is known that the horizontal component of the magnetic field over the current sheet is determined by the current density

$$k_{Ha} = \frac{1}{2} k_E k_s \tag{9}$$

The values of summarized current densities which were used for the calculations by formula (9) are not in accordance with the quantities k_{Ha} in the area of the anomaly axis, and it is difficult to tell what is the cause

of the increased summarized current density in the Folded Carpathians. If the increase of the intensity of bays of the electric field in the Carpathians were stipulated by the effect of "condensation" of the current in the surface layer, especially in the zone of the Vygorlat-Gutinsk volcanic ridge on the anomaly axis, then spreading formally the quantity E all over the thick series of sedimentary rocks in the region, strong excessive values of the anomalous field would have been received and by means of this we could "substitute" the part S_a of deep nature for the surface effect.

Analyses carried out on anomalous fields of surface origin indicate that the Carpathian anomaly has a composite nature i.e. it is stipulated by induction fields both of surface and deep origin. A precise quantitative estimation of that part of the anomalous field which is of deep origin is difficult because of the incomplete set of data about the conductivity distribution in the sedimentary series and on the conditions of redistribution and condensation of telluric currents.

The approximate estimations of the part of the anomalous field of deep origin are generally in accordance with the ascent of isotherms in the transition zone from the Folded Carpathians to the Pannonian Basin. Data in the southeast part of the Soviet Carpathians (the profile Rakhov-Korets) indicate the immersion in this direction of the deep conductivity inhomogeneity which is in conformity with the data on geothermic conditions and seismicity of the region.

REFERENCES

Bilinsky, A. I., Pavlosyuk, I. N., 1974. On the theory of magnetovariational sounding (in Russian). Matematicheskie Metody i Fizicheskie Polya. I.

Bondarenko, A. P., Bilinsky, A. I., Timoshin, B. V., Sheichenko, E. A., Shilova, A. M., Shportyuk, Z. M., 1969. Deep magnetotelluric studies in the Soviet Carpathians and adjacent regions of the Ukrainian SSR (in Russian). Sb. Stroenie i Fizika Glubinnykh Nedr Zapadnogo Regiona SSSR. Nauka i Tekhnika, Minsk, 84–92.

Bondarenko, A. P., Bilinsky, A. I., Sedova, F. I., 1972. Geoelectromagnetic Variations in the Soviet Carpathians (in Russian). Naukova Dumka, Kiev.

Wiese, H., 1965. Geomagnetische Tiefentellurik. Akademie Verlag, Berlin.

GEOMAGNETIC SOUNDING WITH S_q AND GEOTHERMICS IN THE EAST CARPATHIANS

A. P. BONDARENKO, R. I. KUTAS

The existence of a relation between geoelectromagnetic and geothermal parameters is assumed on the basis of the well-established results of theoretical and experimental investigations on the temperature-dependence of the electroconductivity of rocks. In this connection it was included in the program of investigation of the deep structure of the earth's crust and upper mantle on the territory of the Ukrainian SSR the study of the possibility of complexing the deep seismic sounding (DSS) with geoelectromagnetic and geothermal investigations. In the last years complex investigations have been carried out on some profiles in the central part of Ukraine and in the East Carpathians. The main results of geoelectromagnetic and geothermal investigations are reported by Bondarenko et al. (1969, 1972), Rokityansky and Logvinov (1973), Kutas and Gordienko (1971).

Geoelectromagnetic parameters were determined from bay-like variations by magnetic variational profiling (MVP) and magnetotelluric sounding (MTS) methods. The results were seriously distorted by the inhomogeneities of the electric conductivity of sedimentary deposits. Specially distinct distortions are manifest on the data of the determinations of depth of the high conductivity boundary of the mantle.

It is known that surface inhomogeneities distort the geoelectric field the stronger, the greater is the frequency of its variations. Keeping this in mind, we used the S_q-variations of the geomagnetic field to reveal the local deep anomalies of electric conductivity and to ascertain the relation between geoelectromagnetic and geothermal parameters. Experimental investigations were carried out at the East Carpathians and on the western slope of the Russian Platform. The measurement data were treated by the method of deep geomagnetic profiling (DGP).

As the parameter of DGP the empirical correlation

$$\ln k_\sigma = \frac{Y_{ZH} - Y_{ZH0}}{\beta}$$

was used, where k_σ is the conductivity of the basic geoelectric section in relative units, $Y_{ZH} = 0.16\, T\, C_{HH}/C_Z$, T – period of the harmonics of S_q variations

$$C_{HH} = \sqrt{C_H^2 + C_D^2 + 2C_H C_D \cos(\varphi_H - \varphi_D)}$$

C_Z, C_H, C_D amplitudes of the harmonics of components Z, H, D; φ_H, φ_D are phases of these harmonics, β is the angular coefficient of the linear dependence of admittance (H/E) on the conductivity of the basic geo-

electric section, determined from theoretical admittance curves for different models of the three-layered deep section (for the second harmonic $\beta = 4.9$). Index "0" denotes correlation for the same time period on the base station (observatory Lvov). Theoretical justification of the expression for k_σ will be considered in detail in another paper.

S_q-variations are investigated in four observatories (Korets, Lvov, Morshin, Uzhgorod) and 71 field stations situated at 15–20 km one from the other. Variations are recorded by magnetic variometers of the Bobrov-system. Field observations were carried out simultaneously at 4–5 stations, by continuously recording 20–30 days. To set the time rate of field observations S_q-variation recordings of the geomagnetic station Lvov were used. The maximum distance from observatory station to field stations does not exceed 250 km.

S_q-variations were picked out on the magnetograms for perfectly quiet days. There are altogether 3 to 10 such days during the observation at field stations. The harmonic analyses were carried out on the mean diurnal variations by introducing the proper temperature corrections.

S_q-variations are mainly presented by 24 and 12 hours harmonics. Amplitudes of subsequent harmonics are smaller. As the temperature distortions of the 24 hours wave could not have been fully excluded for definition of the GDP parameter one can use in practice the 12 hours harmonic only. On this harmonic sufficiently stable k_σ values are obtained from the recordings of 1–2 diurnal S_q variations.

Numerical values of the parameter k_σ are presented on the map of stations. On the same map are shown the deep faults according to DSS data and zones of geothermal activity. Within the territory investigated the value of k_σ changes on an average by 1.5 times. As regards the spatial distribution of the k_σ values four zones of increased electric conductivity can be selected. It is of importance that all zones coincide with the deep faults.

The zone of the most extended area is found within the limits of the Transcarpathian trough. In this region occur the maximum heat flows, too (from 2.0 HFU to 2.5 HFU). According to calculations, the temperature here at 60 km depth should be of the order of 1200 °C. At such a temperature a full or partial melting of the substance of the mantle and a considerable increase of electric conductivity is possible.

The last three zones of increased electric conductivity are of local character. One of them is situated on the Forecarpathian trough, the two others on the slope of the Russian Platform. Heat flows in the Forecarpathian trough do not exceed 1.05 HFU, and it is only in the NW part of the trough and in its adjacent territory that areas of increased flows are picked out; here the flows exceed 1.3–1.7 HFU. Temperatures calculated for the depth of 60 km are about 700 °C. Electric conductivity anomalies of local extension are evidently not connected generally with the abyssal source of heat. The existence of such anomalies may be caused by conductive embeddings in the geoelectric section. The GDP-parameter is now noticeably influenced by surface heterogeneity. This can be confirmed by considering the spatial change of this value in different geological conditions.

Deep hydrothermal solutions may be one of the probable causes of local

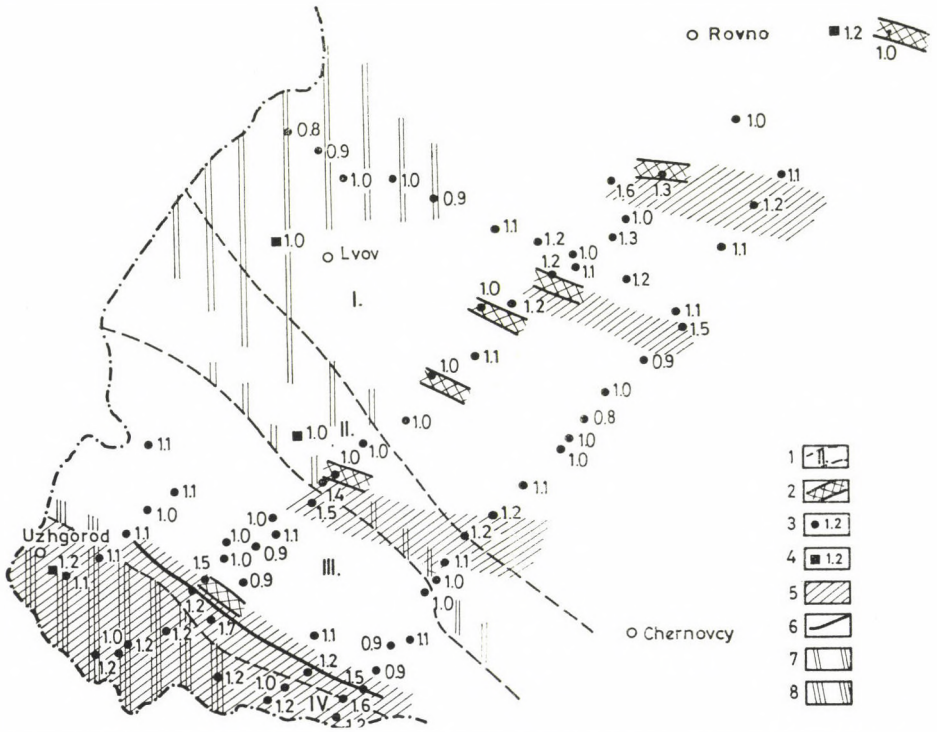


Fig. 1. Distribution of the parameters of geomagnetic profiling and heat flow in the East Carpathians and on the western slope of the Russian Platform

1 – geological boundaries: I – slope of the Russian Platform, II – Outer Carpathian trough, III – Folded Carpathians, IV – Inner Carpathian trough; 2 – fault zones according to DSS data; 3 – observation stations of geomagnetic variations and value of the profiling parameter; 4 – geomagnetic observatory; 5 – anomalous zones ef electric conductivity; 6 – axis of the anomaly of bay-like geomagnetic variations; 7 – geothermal zones with heat flow < 2 HFU; 8 – geothermal zones with heat flow > 2 HFU

electric conductivity anomalies. Such solutions are accumulating in the zones of deep faults and may be ore bearing. They are formed by cooling of the intrusions of the melt magma after the critical water temperature (less than 365 °C).

Thus, using data of deep geomagnetic profiling by using S_q-variations it is possible to discover local electric conductivity anomalies. The results obtained are partially correlated with geothermal data. The coincidence of the discovered anomalies with deep faults allows to suggest that such kinds of anomalies are due to deep hydrothermal solutions.

REFERENCES

BONDARENKO, A. P., BILINSKY, A. I., TIMOSHIN, B. V., SHEICHENKO, E. A., SHILOVA, A. M., SHPORTYUK, Z. M., 1969. Deep magnetotelluric studies in the Soviet Carpathians and adjacent regions of the Ukrainian SSR (in Russian). Stroenie i Fizika Glubinnykh Nedr Zapadnogo Regiona SSSR. Nauka i Tekhnika, Minsk, 84–92.

BONDARENKO, A. P., BILINSKY, A. I., SEDOVA, F. I., 1972. Geoelectromagnetic Variations in the Soviet Carpathians (in Russian). Naukova Dumka, Kiev.

KUTAS, R. I., GORDIENKO, V. V., 1971. Geothermal Field of Ukraine (in Russian). Naukova Dumka, Kiev.

ROKITYANSKY, I. I., LOGVINOV, I. M., 1973. Behaviour of geomagnetic variations of 3–60 min period on the territory of central Ukraine (in Russian). *Geofiz. Sb.*, No. 52.

THE ELECTRIC CONDUCTIVITY ANOMALY IN THE CARPATHIANS

I. I. ROKITYANSKY, V. K. AMIROV, S. N. KULIK, I. M. LOGVINOV, V. N. SHUMAN

The induction vectors discussed by Wiese (1965), Jankovsky (1965), Ádám (1969), Ritter (1970), Calota et al. (1971), Ádám et al. (1972), Bondarenko et al. (1972) clearly mark the electrical conductivity anomaly in the folded Carpathians all along their strike at more than 1000 km distances (Fig. 1).

In 1973 the Institute of Geophysics of the Academy of Sciences of the Ukrainian SSR performed additional magneto-variation and magneto-

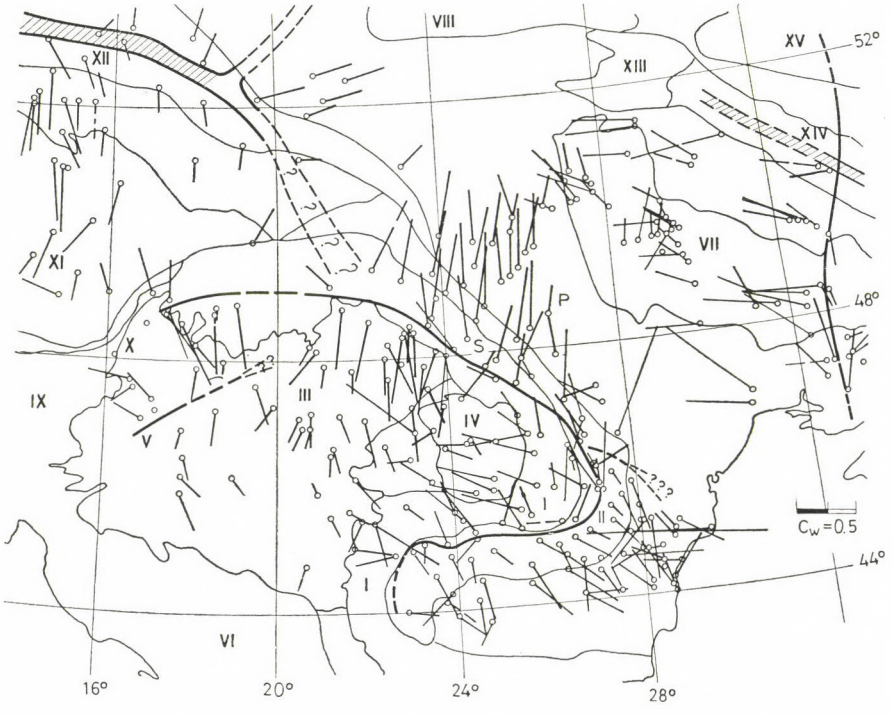


Fig. 1. Map of the induction vectors of Wiese in the Carpathians
I – Carpathians; II – Forecarpathian depression; III – Pannonian Basin; IV – Transylvanian Basin; V – Hungarian Central Mountains; VI – Dinarides; VII – Ukrainian Shield; VIII – Belorussian Massif; IX – Alps; X – Foralpine depression; XI – Bohemian Massif; XII – North-German-Polish Basin; XIII – Bripyatian basin; XIV – Dnieper-Donets depression; XV – Voronezh Massif

telluric observations in the frame of KAPG, for the specification of the parameters of the anomalous body under the Carpathians. The observations included synchronous registration of the magnetic field components of the variations at seven points (on the S-P profile 5 points, and at points Y and R (Fig. 1)) in the southern part of the Soviet Carpathians and also magnetotelluric observations in a wide range of frequencies (T = 15 sec — 1 day) above the axis of the anomalous body in point R.

THE WIESE VECTORS

Figure 1 presents the summary map of the Wiese vectors plotted by previous investigators and by the presens authors. It should be kept in mind that Wiese vectors are oriented from the anomalous conducting body perpendicularly to its axis.

In the Western and Soviet Carpathians the vectors are clearly oriented away from the line passing through the folded Carpathians, that allows to draw the anomaly axis with certainty. In the Southern Carpathians the observational point network is the most dense, the vectors display contradictory behaviour in some places, that may be due to a structural change of the source of the variation, to the complex configuration of the anomalous body (branches) or to plotting error.

THE PROFILE CURVES

Estimations of the maximum possible depth of the upper edge of the anomalous body, carried out by Rokityansky (1972) according to the Wiese vector projections gave the following values: in the Western Carpathians (along DSS profile VI) 20 km, in the Southern Carpathians 40 km. This

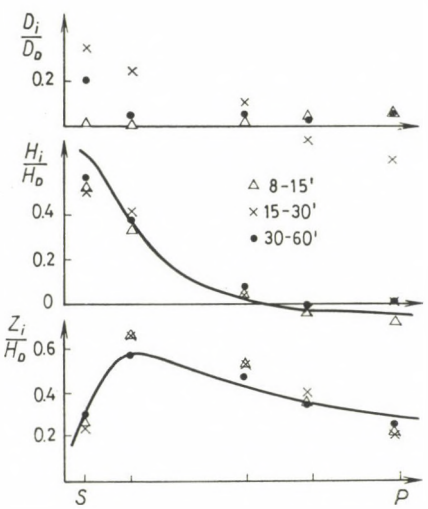


Fig. 2. Dependence of the variations of the magnetic field component on position along the profile S-P (Fig. 1), normalized with respect to the Dymer observatory. The calculated curves were received according to the formula for a circular cylinder with its centre being at h = 30 km depth

result may be interpreted as an increasing depth of the anomalous body in the southern direction, or as the extension of its width. The latter explanation is more probable.

Bondarenko et al. (1972) reported the results of the profile measurements of the Z and H components of the bay-like variations on the territory of the Soviet Carpathians. The maximum possible depth of the upper edge of the conductor, according to these graphs, is about 30 km.

Synchronous observations performed on the S-P profile (Fig. 1) in the south of the Soviet Carpathians in the same frequency range made it possible to determine the depth of the upper edge which is 30 km (Fig. 2).

MAGNETOTELLURIC SOUNDINGS

The depth of the upper edge of the conducting body, detected by the magnetovariational investigations can be defined more precisely by the MTS data. For instance, MTS data, received by Praus (1971) in the Western Carpathians on DSS profile VI, give a depth of 15–20 km.

In order to place the MTS point on the anomalous body axis we carried out special magnetovariational profile investigations with a small step (3–4 km) that made possible to determine the position of the axis of the

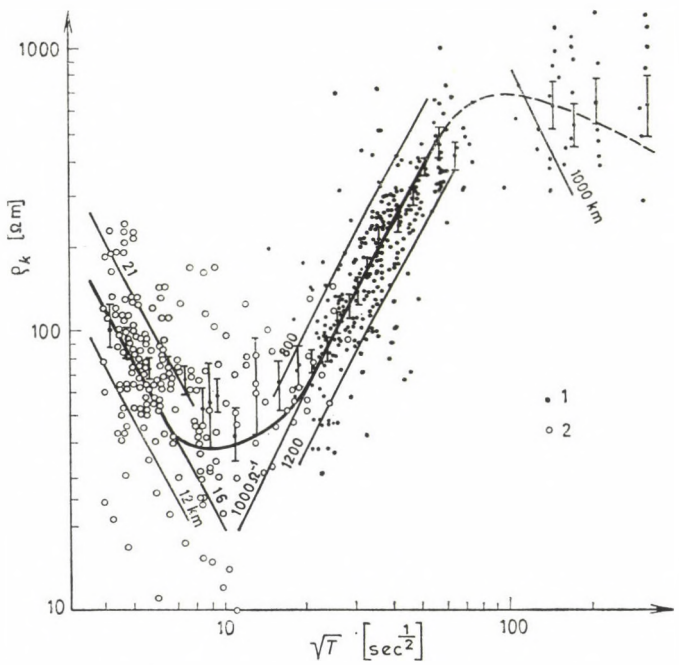


Fig. 3. The MTS longitudinal curve over the anomalous body axis in the point Rakhov
1 – ϱ_T values received on separate variations from the rapid run records; 2 – the same from the Bobrov station

anomalous body with great accuracy. The MTS station was supplied with quick and slow recording facilities that allowed to process the variations from 15 sec to 1 day period range. The received longitudinal (with respect to the anomaly strike) MTS curve (Fig. 3) is characterized by a reliable left descending branch, by a minimum in the 70–200 sec range and by its clear ascending right branch.

The depth of the upper edge, according to this curve, is 16 km, and the body's apparent longitudinal conductivity is 1000 Ω^{-1}.

PROCESSING OF THE POINT OBSERVATIONS

Besides processing the point observations by Wiese's technique, we also used amplitude-phase processing based on the linear relation

$$Z = AH + BD \tag{1}$$

where all values figuring in Eq. (1) are complex.

The relations $C_u = \mathrm{Re}Ai + \mathrm{Re}Bj$, $C_v = \mathrm{Im}Ai + \mathrm{Im}Bj$ determine the real and imaginary induction arrows (Schmucker, 1970).

Figure 4 gives an example of such a presentation of the processing results for the observational points Y and R in the period range T from 23 sec to 120 min.

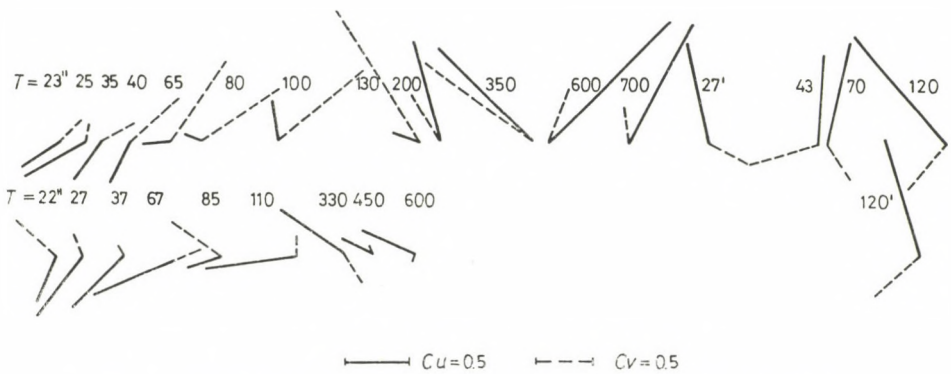


Fig. 4. The induction vectors C_u and C_v for the observation points Y and R

FREQUENCY RESPONSE OF THE ANOMALOUS FIELD

In point Y a large anomalous field is observed in the Z component, while the horizontal component of the anomalous field does not exceed 10–15 % of the normal field. This fact gives the possibility to consider the coefficients A or B of Eq. (1) as the approximate frequency response of the anomalous field. Figure 5 presents A as function of $\sqrt{T}$. It is characteristic that from $\sqrt{T} = 60$ the vertical component of the observed field begins to increase

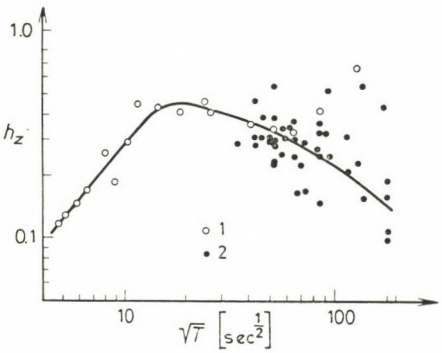


Fig. 5. Frequency characteristics of the anomalous field in the observation point Y (Yasinya)
1 – modulus A (Eq. 1).

$$2 - h_z = \frac{|Z_y| - |Z_R|}{|H_y|}$$

sharply which is probably due to a considerable growth of the normal component Z_n. To exclude the influence of Z_n the synchronously recorded component Z was subtracted in point R, where Z_a is close to zero. The results of the calculation of the normalized anomalous field h_z with such subtractions for each individual case are shown in Figure 5 by points. After subtraction, however, the anomalous field in the low frequency range decreases slower with the growth of period than the Kirovograd anomaly frequency characteristics and the normal global impedance (Rokityansky, 1974). Note that the eddy type anomaly decreases more quickly than the normal impedance, thus the anomalous field observed at long periods may be considered with certainty as an anomaly of conductive nature.

Having compared the obtained experimental frequency characteristics of the anomalous field with the theoretical responses of two-dimensional anomalies of conductive nature (Rokityansky and Kulik, 1973), for the total longitudinal conductivity of the two-dimensional conductor $G_{\min} = \sigma_i Q = 1 - 2 \cdot 10^8\ \Omega^{-1}\text{m}$ was obtained.

In the low frequency range the decrease of a conductive type anomalous field is determined by the impedance. The slow decrease of the anomalous field may be due to a high impedance value, which is confirmed by the MTS curve obtained in point R (Fig. 3). This fact, indicating the increased value of electric field in this region at low frequencies, may be accounted for by suggesting that the Carpathian electric conductivity anomaly connects larger conductors than itself. Such conductors may be the North German electric conductivity anomaly in the north and the Black Sea in the south. Indeed, the electromagnetic field is formed in some volume V, the size (L) of which is comparable to the wavelength of the field in the earth. For small periods the size L is not large and these two large conducting zones do not appreciably effect the current system determining the impedance in the observational point. But L increases with the period and the distant conductors mentioned may influence the measured magnetotelluric field in the Carpathians.

ESTIMATION OF PARAMETER G ACCORDING TO MTS RESULTS

The longitudinal conductivity G can also be estimated by using the ascending branch of the MTS longitudinal curve in point R over the axis of the anomalous field. For that purpose we use the longitudinal curves ϱ_T computed by Kaufman et al. (1971) over conducting elliptical cylinders buried in a horizontally stratified medium and determine the empirical relationship between the fictitious total conductivity S_f of the layer obtained from the ascending branches of the curves ϱ_T, and the total longitudinal conductivity G of the elliptical cylinder. The obtained dependencies S_f and G for cylinders of different ratios of their axes to the burying depth are shown in Figure 6. According to these graphs the value $G = 1 - 2 \cdot 10^8$ Ω^{-1}m corresponds to the fictitious longitudinal conductivity $S_f = 1000$ Ω^{-1}, determined according to the ascending branch of the MTS curve in point R, what confirmes the data of magnetovariational profiling.

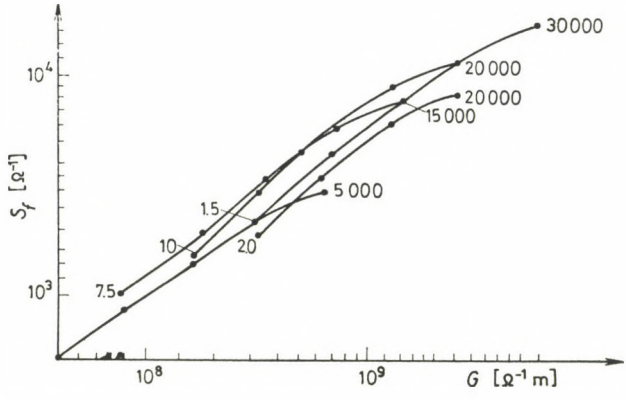


Fig. 6. Graphs of the dependence between the layer's fictitious total conductivity $S_f = \sigma_i h$ and the longitudinal cross-section conductivity $G = \sigma_i Q$ of elliptical cylinders with different axis ratios. The index of the curves at their left end is the minor semiaxis (a) of the elliptical cylinder in km, values on the right of the curves are S – total conductivity of the layer with thickness $h = 2a$

GEOLOGICAL INTERPRETATION OF THE CARPATHIAN ELECTRIC CONDUCTIVITY ANOMALY BASED ON THE IDEAS DEVELOPED BY HYNDMAN AND HYNDMAN (1968)

The position of the axis line of the anomalous body on the tectonic map (Fig. 1) shows that the conducting body is located in the Carpathian flysch zone, i.e. in highly dislocated sedimentary formations of 10–20 km thickness. According to seismic data seismic wave velocities sharply increase in this zone with depth which indicates the metamorphic transformations

of the rocks, in particular the decrease of their compaction and porosity. As it is known, the electric conductivity of great masses of rocks is due to the presence of mineralized porous moisture the quantity of which decreases with the rock's compaction. It is not too probable that in such conditions the narrow zone of highly mineralized porous waters would extend for many hundreds km in the subsurface layers. The Carpathian electric conductivity anomaly appears to be connected with the metamorphic changes of the sedimentary rocks under the influence of temperature and pressure, at depths of 10–25 km. The sedimentation included two steps of the Alpine geosynclinal stages: the first step in the Mesozoic era, the second one (that of flysch) — from Cretaceous to Eocene-Oligocene — the geosyncline being displaced from the inner zone of the Carpathians towards the outer zone (Tectonics of Europe, 1964). At the end of the Eocene the stage of uplift begins that has brought the Carpathian region to its present form. It is possible that the velocity of sedimentation in the geosyncline considerably exceeded the velocity of warming up of young sedimentary strata. Therefore, although the lower layers of the sedimentary complex were dipping at 15 km depth and more, at first there were only low temperature facies of metamorphism which preserved considerable quantity of volatile substances in the rocks, water in the first place (Sudovnikov, 1964). Due to gradual warming up the front of metamorphism progressed upwards. A considerable time having passed, the temperature in the lower part of the sedimentary complex has increased up to relatively high values, as the overlying sedimentary strata have low thermal conductivity and screen the heat outflow. The progressing warming up of the lower part of the sedimentary complex leads to metamorphism facies of ever higher temperature with water release and formation of intergranular melting. Experiments have been conducted (Smith, 1953) showing that at temperatures as low as 300–450 °C melting may occur coexisting with highly mineralized water solutions. The meltings are the most abundant in the amphibole facies of metamorphism, taking place at 400–700 °C. These meltings are formed with water present, the sufficient quantity of the later being about 1–2 %. The whole volume of the rocks cannot be subjected to melting, but the most fusible component in the presence of water, which is located intergranularly between the grains of infusible components may form the bound system. With melting formation the electric conductivity of rocks sharply increases. Experiments on granit specimens in water vapour (Lebedev and Khitarov, 1964) show that under pressures, corresponding to 10–20 km depths at temperatures of 600–650 °C, the specific electric conductivity rises up to 1 $\Omega^{-1}\mathrm{m}^{-1}$. Thus, the suggested electric conductivity of the anomalous body under the Carpathians may be accounted for by the occurrence of melting in the process of regional metamorphism. Deeper facies of regional metamorphism (granulitic and eclogite) are characterized by the absence of water in the rocks, therefore the layers having passed through the amphibolite facies may not contain the fusions despite the higher temperature and pressure. Hence, the layer of increased conductivity of such nature is of limited thickness and the underlying layers may be of high resistivity.

Proceeding from this assumption we try to explain the narrow localization

of the conductive layer in the horizontal plane that is characteristic for the Western and Eastern Carpathians. In the work of Scheffer (1963) data are presented on the geothermal gradient of the Carpathians and the framed Pannonian and Transylvanian basins. The Pannonian Basin is characterized by a very high geothermal gradient, in the region of the Western and Eastern Carpathians it decreases up to the normal values typical for the platform when passing from the inner zone of the Carpathians to the outer zone. Thus the heat flow source warming up the sedimentary strata is more intensive in the inner zone and less intensive in the outer one.

As stated above sedimentation in the inner zone of the Carpathians took place earlier than in the outer one. Thus, it is plausible to suggest that the sedimentary strata of the Carpathians' inner zone had been warmed up earlier and passed through the active phase of regional metamorphism connected with fusion formation and electric conductivity increase. The Carpathians' outer zone, characterized by younger sediments and the least active heat flow source, does not appear to have been warmed up to the active phase of regional metamorphism as it was the case with the central zone of the flysch Carpathians. Naturally, departures from this general picture may take place due to the heat flow inhomogeneities in different tectonic blocks.

The geothermal gradient in the Transylvanian Basin approximately equals the values on the platform. Therefore, the sedimentary strata in the Southern Carpathians must be warmed up more uniformly in the horizontal plane. This is in agreement with the great width of the electric conductivity anomaly under the Southern Carpathians.

REFERENCES

Ádám, A., 1969. Appearance of the electrical inhomogeneity and anisotropy in the results of the complex electrical exploration of the Carpathian Basin. *Acta Geod. Geophys. Mont. Hung.* **4**, 187–197.

Ádám, A., Verő, J., Wallner, Á., 1972. Regional properties of geomagnetic induction arrows in Europe. *Acta Geod. Geophys. Mont. Hung.* **7**, 251–287.

Bondarenko, A. P., Bilinsky, A. I., Sedova, F. I., 1972. Geoelectric Variations in the Soviet Carpathians (in Russian). Naukova Dumka, Kiev.

Calota, F., Calton, J., Ionescu, A., Soare, A., Steflea, V., 1971. Recording of geomagnetic variations on the territory of Roumania (Part I.) (in Roumanian). *Stud. Cerc. Geol. Geofiz. Geogr. Ser. Geofiz.* **9**, 323–331.

Hyndman, R. D., Hyndman, D. W., 1968. Water saturation and high electrical conductivity in the lower continental crust. *Earth, Planet. Sci. Letts.* **4**, 427–432.

Jankowski, F., 1965. Short-period variations of the Earth's magnetic field on the territory of Poland and their relations to deep substratum structure. *Acta Geophys. Polonica* **13**, 85–105.

Kaufman, A. A., Tabarovsky, L. A., Terentiev, S. A., 1971. The Electromagnetic Field of an Elliptical Cylinder in a Horizontal Stratified Medium (in Russian). Novosibirsk.

Lebedev, E. B., Khitarov, N. I., 1964. Beginning of the granit melting and electric conductivity of its melts in dependence on high pressure of the water vapours (in Russian). *Geokhimiya*, No. 3.

Praus, O., 1971. Electrical conductivity of the earth in Czechoslovakia studied by magnetotelluric and geomagnetic methods. Upper Mantl. Project. Programme in Czechoslovakia 1962–70. Geophys. Final Report, Acad., Prague.

RITTER, E., 1970. Evaluation of geomagnetic deep sounding in Hungary. *Acta Geod. Geophys. Mont. Hung.* **5,** 87–93.

ROKITYANSKY, I. I., 1972. The electric conductivity anomaly in the earth's crust under the Carpathians (in Russian). *Izv. Akad. Nauk SSSR, Ser. Fiz. Zemli,* No. 10, 97–100.

ROKITYANSKY, I. I., 1974. Interpretation of electric conductivity anomalies (in Russian). *Geofiz. Sb. Akad. Nauk SSSR,* **58.**

ROKITYANSKY, I. I., KULIK, S. N., 1973. Magnetic variational profiling over an electric conductivity anomaly in the form of an elliptical cylinder (in Russian). *Geofiz. Sb. Akad. Nauk SSSR,* **55.**

SCHEFFER, V., 1963. The Regional Values of the Geothermic Gradient in the Area of the Carpathian Basins. *Acta Techn.* **43,** 429–436.

SCHMUCKER, U., 1970. Anomalies of geomagnetic variations in the southwestern United States. *Bull. Sci. Inst. Oceanogr.* **13.** Univ. Calif. Press.

SMITH, F. G., 1953. Review of physicochemical data on the state of supercritical fluids. *Econ. Geol.* **49,** 331.

SUDOVNIKOV, N. G., 1964. Regional Metamorphism and Some Problems of Petrology. LGU-press, Leningrad.

Tectonics of Europe. Nauka-Nedra, Moscow, 1964.

WIESE, H., 1965. Geomagnetische Tiefentellurik. Akademie Verlag, Berlin.

V. USSR

(WITH EXCEPTION OF THE CARPATHIANS)

DEEP MAGNETOTELLURIC SURVEYS IN THE BALTIC-SCANDINAVIAN SHIELD AND THE KOKCHETAV BLOCK

N. P. VLADIMIROV

Deep magnetotelluric soundings (MTS) of crystalline massifs require to extend the range of the recorded variations in the high frequency band. In these regions the study of the electric conductivity of the earth's crust and upper mantle might need variations of the field with periods of tenth and hundredth parts of a second. At the Institute of Physics of the Earth, special instruments with induction monitors recording electromagnetic variations in the 0.05–20.0 Hz range have been developed (Vladimirov and Krylov, 1969).

For the first time a deep MTS was carried out in this frequency band on *the Baltic-Scandinavian shield* in 1964. The crystalline basement of the observation area (Lovozero and the Murmansk Region) is complicated by faults with different strikes, along which occurred the instrusions of ultrabasic and alkali rocks. The Lovozero massif is associated with the deep fault zone of quasilatitudinal strike. According to the VES (vertical electric sounding) data, with direct current, the electric resistivity of metamorphic rocks at depths of several kilometers is equal to 10^3–10^4 Ωm.

The sounding curve for the Lovozero region, compiled from the observation materials of different years, is shown in Figure 1. *The formal interpretation* of this curve yields the following results:
$h_1 = 16.8$ km; $\varrho_1 = 6400$ Ωm; $h_2 = 33.6$ km, $\varrho_2 = 50\,000$ Ωm; $h_3 = 55$ km; $\varrho_3 = 600$ Ωm; $h_4 = \infty$; $\varrho_4 = 80$ Ωm (Vladimirov and Bondarenko, 1970). Consequently, the MTS data in the region of the Lovozero massif show comparatively high resistance of the crust and of the upper mantle near the Moho discontinuity.

MTS were also conducted in 1971–72 on the denuded igneous rocks of the Kokchetav block. This region was formed in the beginning of the Cambrian and it is composed of ancient rocks: crystalline slates, gneisses, amphibolites, etc. It is peculiar by its large size: 240–300 km in the latitudinal direction, and 200 km meridionally, and also by a deeper Moho discontinuity, which lies here at 52–55 km. The age of the eclogite formations, discovered in the region, is 1.7–$2.0 \cdot 10^9$ years, which indicates the possible presence of a dislocated zone involving the entire thickness of the crust in the Kokchetav block.

The electric resistivity of rocks of the *Kokchetav block* varies within a wide range. Thus, for instance, the resistivity of granodiorites depends on the jointing, and according to direct current VES data, it changes from 300 Ωm to 25 000 Ωm, i.e. by about two orders.

The MTS curve for the region of the *Zhukeisk crystalline massif* has only a descending branch (Fig. 1). Preliminary interpretation of this curve revealed

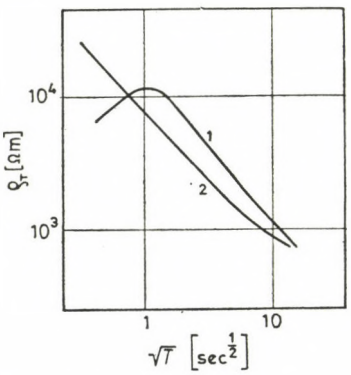


Fig. 1. Curves of magnetotelluric sounding
1 – Lovozero massif (Baltic shield); 2 – Zhukeisk massif (Kokchetav block)

that the resistivity of crustal rocks in the region of the Zhukeisk massif is of the order of 10^4 Ωm. At about 30 km depth a sufficiently thick layer of lower resistivity is detected. This depth is, apparently, overestimated since the analyzed curve can be distorted by the flow-around effect.

Thus, crustal rocks on the Lovozero and Zhukeisk massifs are characterized by high resistivity (of the order of 10^4 Ωm). The descending branch of the sounding curves is tilted at 50°, which indicates a comparatively high resistivity of the mantle near the Moho discontinuity. These data are in agreement with the general conceptions resulting from the laboratory studies of the electric conductivity of rock samples at high temperatures and pressures and also from the possible temperature distribution in the zone of crystalline shields.

It should be noted that the horizontal inhomogeneity of the sedimentary layer covering crystalline rocks strongly distorts the observation data. Therefore, the selection of observation sites on crystalline massifs should be made with special care.

REFERENCES

VLADIMIROV, N. P., KRYLOV, S. M., 1968. Instruments for measurement of weak electromagnetic fields in the 0.06–100 Hz band (in Russian). Magnitotellurichеskie Metody Izucheniya Zemnoi Kory i Verkhnei Mantii, 4. Nauka, Moscow.

VLADIMIROV, N. P., BONDARENKO, A. T., 1970. On the results of deep magnetotelluric sounding of Lovozero (in Russian). *Izv. Akad. Nauk SSSR, Ser. Fiz. Zemli*, No. 11.

DEEP MAGNETOTELLURIC SURVEYS ON THE BELORUSSIAN CRYSTALLINE MASSIF

N. V. LIPSKAYA, N. A. DENISKIN, N. N. NIKIFOROVA

Deep magnetotelluric soundings were carried out on the central part of the Belorussian crystalline massif and on its north-western slope that gradually merges into the Baltic depression. Observations were made by the Group of Deep Magnetotelluric Sounding, Institute of Physics of the Earth, and by the Institute of Geochemistry and Geophysics of the Belorussian SSR. The interpretation was accomplished jointly with the Computing Centre of the Moscow State University.

The major purpose of the program was to find out the degree of reliability of the deep magnetotelluric sounding data and to compare the obtained geoelectric profiles with the geoelectric characteristics gained from geothermic data.

The method of group sounding was chosen for the solution of the problem, i.e. measurements were made in a number of sites located sufficiently close to each other at distances within which the deep geoelectric cross section can be considered unchanged.

The Belorussian massif is composed of Pre-Cambrian crystalline rocks, overlaid by Lower-Cambrian, Middle-Devonian and Quaternary depositions, represented by sandstone, marls and clays. The top of the basement forms a dome, rising in the central part of the massif to 400–500 m (from the present surface) and subsiding along the flanks to depths of several kilometers. In the north and north-west, the crystalline rocks subside gradually at an angle not exceeding several degrees. The vast central part of the massif, characterized by a slowly-changing depth of basement rocks of high Ωm values, is practically free of local disturbances of electric conductivity. The values of the total longitudinal conductance S are small in the whole area which favours deep research.

On the slopes of the massif the S values gradually increase to several hundreds siemens ($= \Omega^{-1}$). This increase is caused mainly by the thickening of the sedimentary cover.

The absence of local conductivity inhomogeneities does not exclude the possibility of field distortions. The Belorussian massif, circled by a ring of depressions with good conductivity, is a regional inhomogeneity disturbing the normal distribution of earth currents.

The observation sites were located on the profile passing through the Pleshchenitsy geophysical observatory in the direction Borisov-Molodechno. The soundings carried out at separate sites were considered as one deep sounding, characterizing the electric conductivity of the crust and upper mantle. The differences in the form and position of separate curves were attributed to changes of parameters of the upper layer. It was assumed that

the influence of the regional inhomogeneity equally affects all group-sounding curves and causes no discrepancies between them.

Experimental sounding curves were compiled for the dominating direction of the electric field at each site. In the conditions of the Belorussian massif the electric field is mainly tangential to the isohypses of the crystalline basement.

The sounding curves for the central part of the profile, where the values are about $S \cong 10\ \Omega^{-1}$, are close to each other. Figure 1 presents them by a joint curve 1 (Pleshchenitsy). Curve 3 (Smolnitsy) is for one end of the profile where S values vary within 18 and 30 Ω^{-1}. Curve 4 refers to the north-western slope of the Belorussian massif.

The group-sounding curves were interpreted by means of computers. All curves were interpreted together according to the method of successive approximations elaborated at the Computing Centre of the Moscow State University. As initial approximation the deep cross-section was used, calculated for shields from geothermic data (Lubimova and Feldman, 1970). The parameters of the upper layer of each site coincided with their true values determined for the sedimentary layers from VES and drilling data. Down to depths of 40 km resistivity was assumed to be 5000 Ωm. In the interval of 40–450 km it was equal to 200 Ωm. Below that there was the conductive zone. The curves corresponding to the initial approximation are shown in Figure 1 by thin dashed line. They greatly diverge from the experimental curves (thick dashed lines). The solid lines show the final approximation. The resistivities of the upper mantle, obtained from MTS data, greatly exceed the values calculated from geothermic data. Such discrepancies have been noted in literature, but have not been convincingly explained so far.

At the next stage the parameters of the upper layer remained the same, while as an initial approximation a cross section resulting from the interpretation of a joint curve P was selected. Here the thickness values were

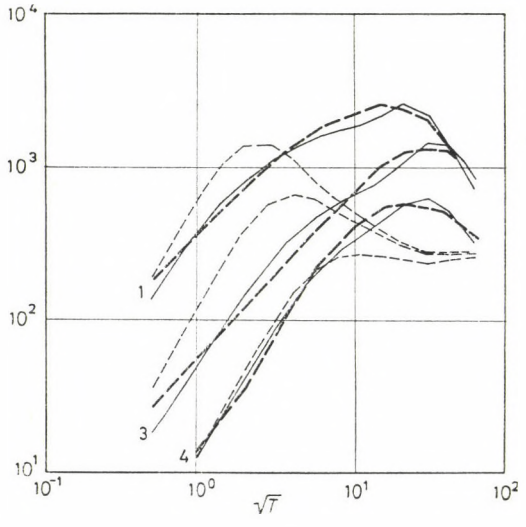


Fig. 1. Examples for the interpretation of deep magnetotelluric sounding curves over the Belorussian crystalline massif by a four-layer model
Thin dashed line – set of theoretical curves for the initial approximation, corresponding to the following parameters: h_1, ϱ_1 – actual values at the point of observation; $\varrho_2 = 5000$ Ωm; $h_2 = 40$ km; $\varrho_3 = 200$ Ωm, $h_3 = 450$ km; $\varrho_4 = 10$ Ωm; $h_4 = \infty$. Solid line – set of theoretical curves corresponding to the final solution (parameters of the section are given in Table 1); Thick dashed line – – experimental curves: 1 – for Pleshchenitsy-Krivichy; 3 – for Smolnitsy; 4 – for Lelenis

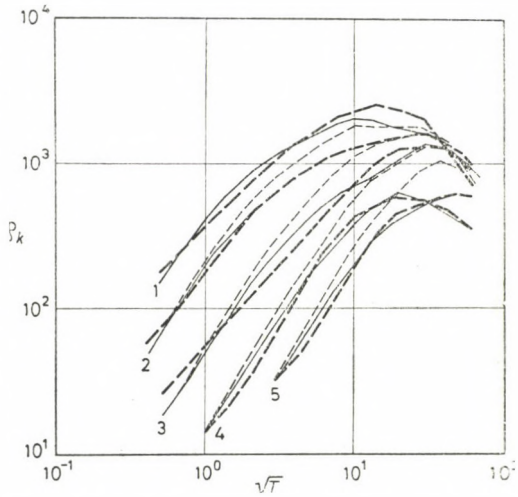


Fig. 2. Results of the interpretation of deep magnetotelluric sounding curves for the Belorussian crystalline massif by a four-layer model with constant thickness values of all layers. Set of theoretical curves of the initial approximation (thin dashed line) corresponding to the section parameters: h_1, ϱ_1 actual values at the point of observation; $h_2 = 250$ km; $\varrho_2 = 2400$ Ωm; $h_3 = 400$ km; $\varrho_3 = 800$ Ωm; $h_4 = \infty$; $\varrho_4 = 1$ Ωm; set of theoretical curves (solid line) representing the final solution (for parameters see Table 1); experimental curves (thick dashed line): 1 – at Pleshchenitsy-Krivichy; 2 – at Lipovo; 3 – at Smolnitsy; 4 – at Lelenis; 5 – at Birzhai

assumed permanent everywhere: $h_2 = 250$ km and $h_3 = 400$ km. Thus, the approximation of the experimental curves with the calculated ones could only be made by changing the resistivities of deep layers. The final approximation curves thus obtained are shown in Figure 2 (solid lines). They are sufficiently near to the experimental curves (thick dashed lines). The resistivity values of layers with fixed thickness in this case differ at various sites as shown in Table 1. The resistivity of the lower zone changes from one to several tens of Ωm (see Table 1). These results demonstrate the expediency of the joint interpretations of group-sounding curves.

TABLE 1

Site First approximation	h_1	ϱ_1	h_2 250	ϱ_2 2400	h_3 400	ϱ_3 800	h_4 ∞	ϱ_4 1.0
Pleshchenitsy-Krivichy	0.5	41.5	250	2400	400	800	∞	1.0
Lipovo	0.5	26	250	1700	400	1140	∞	55
Smolnitsy	0.75	17	250	1310	400	1720	∞	20
Lelenis	0.9	9.5	250	1070	400	120	∞	16
Birzhai	1.1	6.6	250	1010	400	393	∞	2.0

According to our data, the depth to the conductive layer of the upper mantle within the Belorussian massif is 650 km. However, this depth is, apparently, overestimated, since the regional S-effect should have been allowed for.

REFERENCES

LUBIMOVA, E. A., FELDMAN, I. S., 1970. Heat flow, temperature and electrical conductivity of the crust and mantle in the USSR. *Tectonophysics* **10**, 245–282.

DEEP MAGNETOTELLURIC SURVEYS IN THE NORTH-WESTERN PART OF THE RUSSIAN PLATFORM

A. A. KOVTUN, N. D. CHICHERINA

The Department of Physics of the Earth, Leningrad State University has organized deep magnetotelluric soundings in the north-western part of the Russian platform. Up to now 50 deep soundings were accomplished (Fig. 1). Observation sites are located over short meridian profiles and over the latitudinal profile Liepaya-Yaroslavl, traversing the Baltic and Middle Russian depressions divided by the Latvian saddle. The latitudinal profile is 1500 km long.

Results for the eastern part of this profile were analyzed by Yanovsky et al. (1964, 1965), Kovtun and Chicherina (1969). The present paper discusses the results for the western part of the profile, covering the Baltic syneclise and the Latvian saddle. Figure 1 represents the relief map of the crystalline basement for the west of the Russian platform. It also shows the sounding sites. In case of double-numbers, e.g. 7–1, the first digit indicates the position on the meridional profile (1, 2, 6, 7), the second one that on the latitudinal profiles. At most of the sites five field components were recorded: E_x, E_y, H_x, H_y, H_z, where the x-component is directed along the magnetic meridian and the y-component along the magnetic latitude. Recordings were made at two intervals: 1–200 sec and 10^2–10^4 sec. In course of processing the observations least-squares fitting was used (Berdichevsky, 1968). The impedance tensor was determined and the impedance diagrams were compiled within a wide time interval.

Figure 2 shows the changes of $|Z_{xy}|$ and $|Z_{yx}|$ over the latitudinal profile. Both components in the range of short periods ($T < 20$ sec) reflect the crystalline basement relief. The Middle Russian depression clearly stands out, complicated by the Krests fault (points 7–1 and 8), and the eastern part of the Baltic depression is also vividly apparent. Quite unexpected is the impedance minimum in the central part of the Latvian saddle (point 4). This minimum becomes more evident at $T = 60$ sec. It does not correlate with the basement relief and is, obviously, associated with the conductive embeddings in the crust or in the upper mantle.

Figure 1 shows the orientation of the major axes of the impedance diagrams obtained in the time interval 500–1000 sec. With an increase of period, the orientation of the impedance diagrams only slightly changes at most sites. Exceptions are sites 6–7 and 7–4, here the major axes change their orientation by almost 90° in the range of large periods. Within the Latvian saddle the impedance diagrams stretch, as a rule, in quasilatitudinal direction, close to the direction of the basement contours. This fact can be explained by *the edge effect* due to the influence of the Baltic shield (the closer to the Baltic shield, the smaller is the minor axis of the impedance

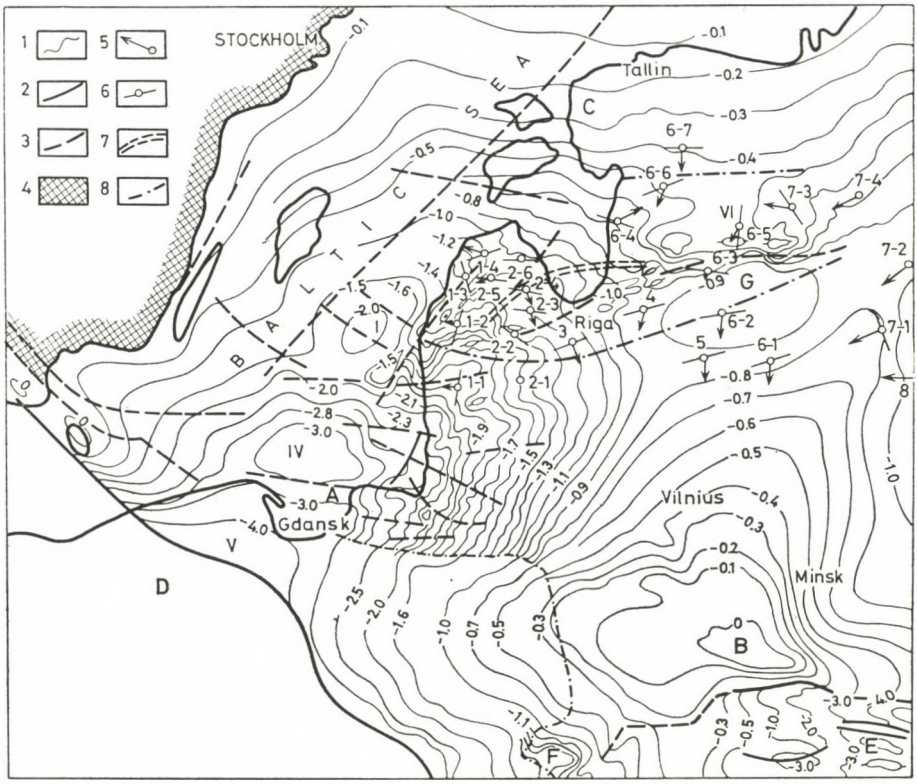


Fig. 1. Scheme of the surface relief of the crystalline basement in the NW Russian Platform (after Sarkisov)

A – Baltic syneclise; B – Belorussian-Mazur anteclise; C – southern slope of the Baltic shield; D – Danish-Polish depression; E – Pripyat depression; F – Brest Basin; G – Latvian saddle

1 – contour lines along the top of the crystalline basement; 2 – faults determined from geological data; 3 – faults revealed from a complex of geophysical data; 4 – outcroppings of the crystalline basement on the present surface; 5 – Wiese vector; 6 – direction of the major axis in the impedance diagram (not in scale); 7 – axis of the conductive body; 8 – contour of the region with increased crustal conductivity

diagram). At a number of sites, situated on the edge of the Baltic depression, the impedance diagrams are oriented in a direction largely differing from the quasilatitudinal, which is, apparently, connected with the concentration of currents in the Baltic syneclise and with the influence of *the S-effect.* It can be, therefore, supposed that in the region studied the major role in the distortion of MTS curves belongs to galvanic effects (Berdichevsky et al., 1973). This is in agreement with the frequency characteristics of the ratio of axes of the impedance diagrams (Fig. 3). For $T = 1000$–1500 sec, the ratio $|Z_{\min}/Z_{\max}|$ attains its minimal values while further it is practically independent of frequency.

For interpretation, the MTS curves were chosen as basic, which were plotted along the major axes of the impedance diagrams. Within the Latvian saddle such a choice is quite justified, since the minor axes are distorted by the edge effect. The curves obtained are in good agreement with the curves, compiled earlier by the complete vectors of the electric and magnetic fields (Kovtun et al., 1968).

Figure 4 presents curves received according to the latitudinal profile Liepaya-Yaroslavl (a), and also according to the meridional profiles (b, c, d). The results of the interpretation of MTS curves are given in Table 1.

The most reliable parameter of the vertical cross section, obtained from the interpretation of these curves, is the value of the longitudinal conductivity S of the sedimentary layer. This value is close to the VES data and is in good agreement with drilling data. In the region of the greatest submergence

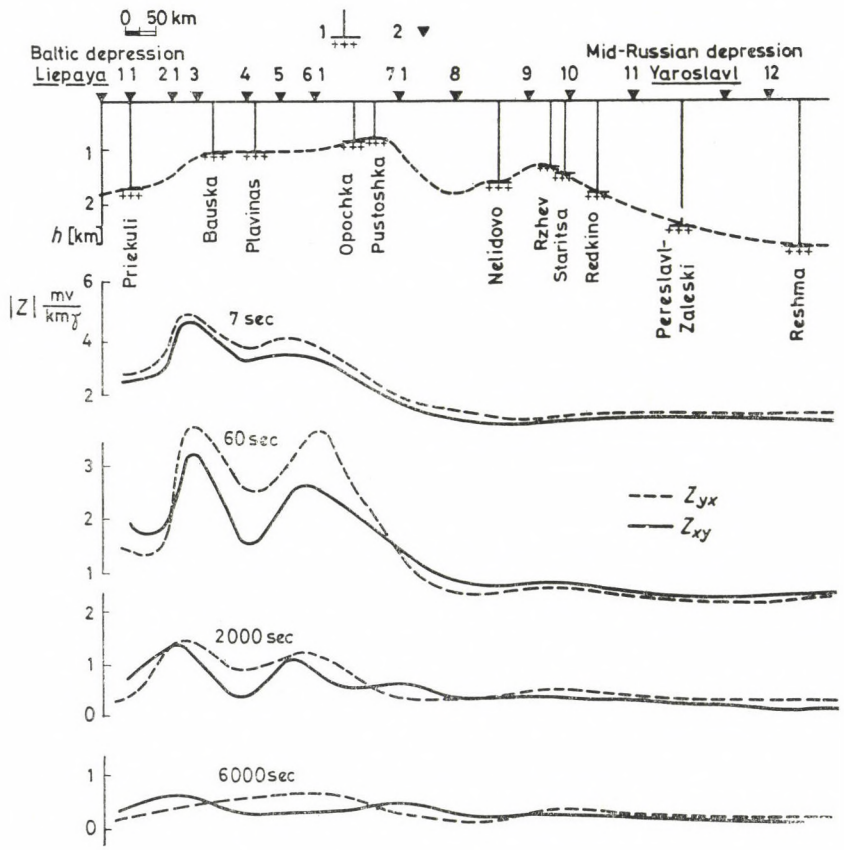


Fig. 2. Basement relief from drilling data along the latitudinal profile Liepaya-Yaroslavl and the plots $|Z_{xy}|$, $|Z_{yx}|$ for different periods:
1 – boreholes to the basement; 2 – sounding sites

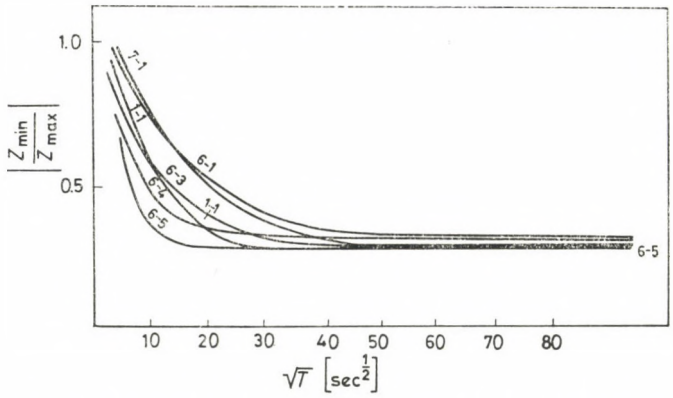


Fig. 3. Changes in the ratio of axes of the impedance diagrams, depending on the period, for separate sites in the NW of the Russian Platform

of the basement the thickness of the sedimentary cover was determined. These data also correlate with drilling data (1–4).

All these points show that in the short-time interval ($T < 60$ sec) the sounding curves rather accurately reflect the vertical geoelectric profile. As regards the determination of deep parameters, we encounter great difficulties. The formal interpretation of curves within horizontally homogeneous models leads to a considerable divergence of geoelectric characteristics of adjacent regions. Along the southern and eastern edges of the Middle Russian depression (sites 12, 11, 10, 9, 8), where depths of the basement reach 1.5–2 km, MTS curves have steep rising branches, which testify a high resistance of the crystalline rocks (Kovtun and Chicherina, 1969). At a depth of 200–500 km resistivity is reduced to 10–50 Ωm. The western part of the profile shows another pattern. MTS curves at sites 1–2, 1–3, 1–4, 2–2, 2–3, 2–4, 2–5 have gently rising branches, often complicated by inflections, possibly caused by the influence of the intermediate conducting layer in the earth's crust. The depth of this layer, according to the points of inflection on the MTS curves, is equal to 20–50 km, its thickness and specific resistivity are ambiguous. The longitudinal conductivity of the layer is not large; it does not exceed 700 Ω^{-1} (see Table). It should be kept in mind that since the intermediate conductive layer covers a limited territory, its total longitudinal conductivity will be underestimated from MTS curves. All MTS curves for the Baltic depression have descending branches in the region $T \geq 3600$ sec, tilted at an angle close to 60°. However, here the depth of the conductive rocks of the mantle is much greater than in the Middle Russian depression. While it changes from 200 km to 550 km, approaching the Latvian saddle, in the Baltic depression it varies within 400–800 km. The maximum depth of the conductive rocks of the mantle was obtained in the area of the Latvian saddle (700–1000 km). According to the data given in Table, there is a close connection between the depth down to the conductive rocks of the upper mantle and the total longitudinal

TABLE 1

Results of interpretation of the MTS curves

Site	Name	S of the sedimentary layer $[\Omega^{-1}]$	S of the conducting layer in the crust $[\Omega^{-1}]$	Depth (H) of the conductive layer in the mantle [km]
1	2	3	4	5
1–1	Priekuli	300	280	550
1–2	Adzi	220	630	400
1–3	Vendzava	320	600	400
1–4	Rinda	185	660	450
2–1	Priedula	290	—	800
2–2	Spoleni	130	500	600
2–3	Gaiki	130	300	700
2–4	Kandava	100	350	700
2–5	Spare	170	570	550
2–6	Dundaga	180	660	550
3	Utlakh	100	300	800
4	Zaube	140	500	500
5	Vanagi	200	—	800
6–1	Rezenke	180	—	800
6–2	Burkany	210	—	700
6–3	Yaunanna	220	390	600
6–4	Ludini	70	150	900
6–5	Veriora	50	—	1000
6–6	Vanaveski	25	—	1000
6–7	Piybe	14	—	1000
7	Loknia	570	—	550
8	Toropets	1450	—	450
9	Yeltsy	1080	—	400
10	Izosenki	930	—	400
11	Kolyubeevo	1550	—	350
12	Krasnoe	2350	—	200

conductivity of the sedimentary cover. This connection is undoubtedly a manifestation of the S-effect. One way to smooth out the S-effect is averaging. The average depth down to the conductive rocks of the upper mantle is 500–550 km.

The following can be said about the presence of an intermediate conductive layer in the earth's crust. The inflections of the MTS curves could also appear due to the edge effect caused by the influence of the Baltic shield. But this is hardly possible, since the appearance of the inflections is independent of the distance to the shield. Thus we come to the hypothesis that there is a conductive layer near the boundary between the crust and the upper mantle. The supposed region of occurrence of this layer is outlined by a dash-dot line in Figure 1. To support this hypothesis an analysis of magnetovariation

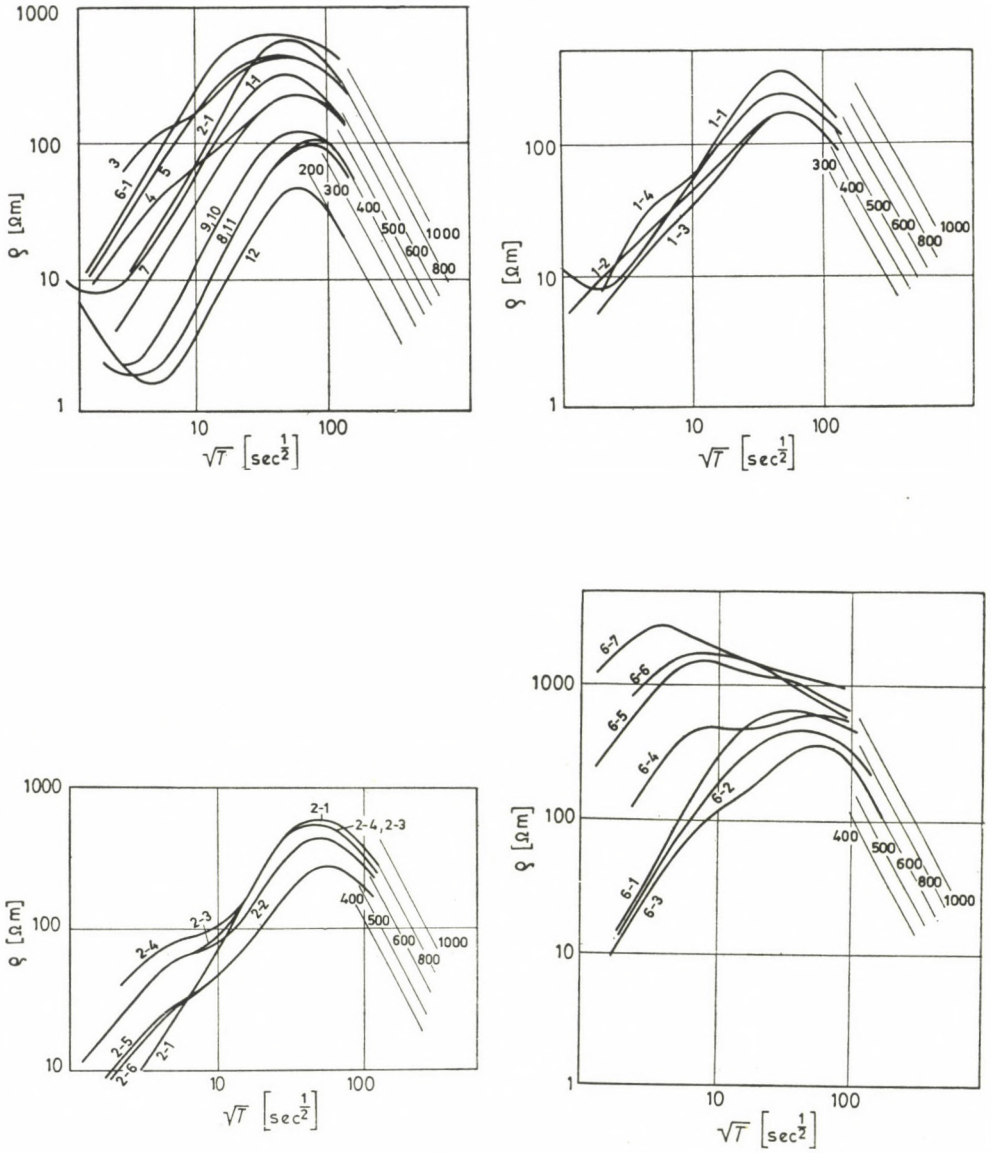


Fig. 4. Deep sounding curves
above to the left – along the latitudinal profile Liepaya-Yaroslavl; below to the left – along profile 1; above to the right – along profile 2; below to the right – along profile 6. Low frequency asymptotes of the theoretical curves are digitized in km

data has been made. The arrows in Figure 1 show the Wiese vectors in the 500–1000 sec time interval. At a number of sites the anomalies of the vertical component of the magnetic field are associated with the inhomogeneity of the sedimentary cover. Thus, on the eastern slope of the Latvian saddle (points 7–1, 7–2, 7–3, 7–4) the Wiese vectors reach their maximum values and are directed to the West, which can be attributed to the influence of excessive currents flowing along the axis of the Krests fault. At a number of other sites, however, the direction of the Wiese vectors can hardly be correlated with the distribution of the excessive currents in the sedimentary cover. The region, where the Wiese vectors are near zero and change their direction, deserves attention (in Figure 1 it is shown by double dotted line). This region is located almost in the centre of the zone, where at a depth of 20–40 km, according to MTS data, the layer of reduced resistivity is supposed to occur. Thus, magnetovariation data do not contradict the hypothesis that there is an intermediate conductive layer in the earth's crust.

The lack of heat flow data, and of seismic data about the deep velocity profile of this area do not allow to make definite conclusions as to the causes of reduction of resistivity at 20–40 km depth. The most probable seems to be the hypothesis that there is a region of partial melting at these depths, that was formed at relatively low temperatures (600–700 °C) as the result of the presence of water in supercritical state (Kharin and Khitarov, 1964).

The decrease of resistivity at depths of the order of 500 km reflects the influence of high temperatures (over 1100 °C). Considerable scattering of the experimental data on electric conductivity of rocks at high pressures and temperatures is a bar to more reliable correlation of electric conductivity with temperature. We can, therefore, only state that in the north-western part of the Russian Platform at a depth of about 500 km the temperature exceeds 1100 °C.

REFERENCES

Berdichevsky, M. N., 1968. Electric Prospecting by the Method of Magnetotelluric Sounding (in Russian). Nauka, Moscow.

Berdichevsky, M. N., Dmitriev, V. I., Yakovlev, I. A., 1973. Magnetotelluric sounding of horizontally inhomogeneous media (in Russian). *Izv. Akad. Nauk SSSR, Ser. Fiz. Zemli*, No. 1, 80–92.

Kharin, E. P., Khitarov, N. I., 1964. Beginning of granite melting and the electrical conductivity of its melt, depending on the high pressure of water steam (in Russian). *Geokhimiya*, No. 3.

Kovtun, A. A., Chicherina, N. D., 1969. Results of magnetotelluric soundings of the Middle Russian depression (in Russian). Magnitotellurichеskie metody izucheniya stroeniya zemnoi kory i verkhnei mantii. **4**, 195–199.

Kovtun, A. A., Chicherina, N. D., 1972. On the anomalies of the magnetotelluric sounding curves for the north-western part of the Russian platform (in Russian). *Uchenie zapiski LGU, Voprosy Geofiziki*, **22**, 185–193.

Kovtun, A. A., Chicherina, N. D., Lipatov, A. A., Porokhova, L. N., 1968. Electric parameters of the crust and upper mantle in western Latvia (in Russian) *Uchenie zapiski LGU, Voprosy Geofiziki*, **18**, 73–78.

Porokhova, L. N., 1971. Application of Statistical Methods to the Solution of the Inverse Problem of Magnetotelluric Sounding (in Russian). C. Sc. Dissertation, Leningrad State Univ.

SARKISOV, YU. M., 1970. Structure of the sedimentary cover of the Baltic syneclise and of the adjoining structures of the north-western part of the Russian plate (in Russian). *Sov. geol.*, No. 7, 133–139.

YANOVSKY, B. M., BRYUNELLI, B. E., KOVTUN, A. A., KUZNETSOV, I. S., RASPOPOV, O. M., CHICHERINA, N. D., 1964. Magnetotelluric sounding of the Middle Russian depression (in Russian). *Izv. Akad. Nauk SSSR, Ser. Geofiz.* 999–1006.

YANOVSKY, B. M., KOVTUN, A. A., RASPOPOV, O. M., CHICHERINA, N. D., 1965. Deep structure of the Middle Russian depression according to magnetovariation sounding data (in Russian). *Uchenie zapiski LGU, Voprosy Geofiziki*, **16**, 3–9.

DEEP MAGNETOTELLURIC SURVEYS IN THE CENTRAL PART OF THE RUSSIAN PLATFORM

G. N. ANISHCHENKO

In 1969–70 the Spetsgeofizika Trust has carried out a series of deep magnetotelluric soundings in the Voronezh massif and in the zone of its conjugation with the Moscow syneclise (Fig. 1). The program has been accomplished under the guidance of M. N. Berdichevsky. The tectonics of the region, especially in its southern and central parts, has a linear character. Altogether 11 soundings were made, seven of which are located in the eastern part of the Voronezh Massif (2, 3, 4, 8, 9, 10, 11), two (1, 5) in the Ryazan-Saratov (Pachelmsk) depression and one (7) on the southern closing of the Moscow syneclise near the MTS profile determined by the Leningrad State University.

At all the sites the measuring lines were oriented along the strike and across the strike, respectively, of the crystalline basement.

The variations of the field of periods from 15—20 sec to 0.5—1 h were recorded by the MTL-62 laboratory, while the variations of periods of 1—24 h by a set of in struments, that included the magnetovariation recorder IZMIRAN-4 and the oscillo

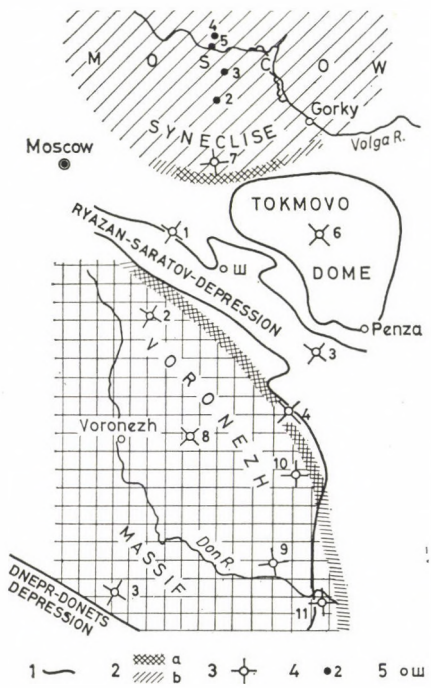


Fig. 1. Location of MTS sites and zoning of the studied territory according to types of the geoelectric section of the upper mantle of the earth

1 – boundaries of geological structures; 2 – boundaries of zones with different types of geoelectric section of the upper mantle (a–reliable, b–supposed); 3 – MTS site (Spetsgeofizika) and its number; 4 – MTS site (Leningrad University) and its number; 5 – MTS site (Academy of Sciences of the USSR); town Shatsk

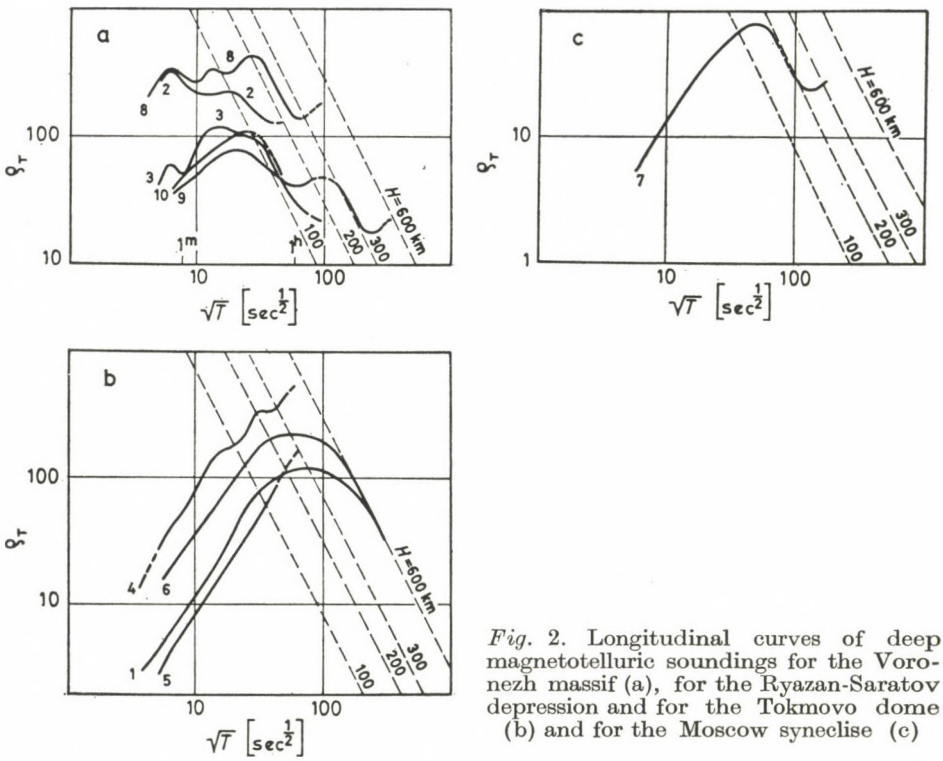


Fig. 2. Longitudinal curves of deep magnetotelluric soundings for the Voronezh massif (a), for the Ryazan-Saratov depression and for the Tokmovo dome (b) and for the Moscow syneclise (c)

graph EPO-9. In order to reduce the temperature effect on the registration of solar-diurnal variations, the instruments IZMIRAN-4 and EPO-9 operated in a special bunker, where diurnal temperature variation did not exceed 1—2 °C.

Computer processing of the oscillograms revealed that the additional impedances are approximately by an order less than the principal ones. Almost the entire observation material was processed manually, by the method of apparent impedances. Solar-diurnal variations (S_q-variations) were preliminarily averaged for five quiet days and subjected to harmonic analysis by the Runge scheme for 24 ordinates.

The MTS longitudinal curves were regarded as basic (i.e. curves, corrresponding to the current flow along the crystalline basement strike). These curves are shown in Figure 2. According to their form, they fall into three groups.

The first group (Fig. 2, a) includes complicated curves with several maxima and minima and with a rather high general level of apparent resistivity. All of them are for the Voronezh Massif and their formal interpretation shows the conductive layer to be at 100–120 km depth. The same layer was revealed by the group of the Voronezh University in the central part of the Voronezh massif (Maksimov and Zakutsky, 1967). The most complete ones are the curves 8 and 9. These curves have a clearly defined descending branch in the low frequency range, which give for the second conductive

layer a depth of 250–300 km. A further increase in resistivity does not contradict the supposition that there is a third conducting layer at about 600 km depth, which is observed to the north of this region. Thus, on the Voronezh Massif, the deep soun dings reveal two conducting layers in the upper mantle at 100–120 km and 250–300 km depths.

The second group consists of MTS curves for the Ryazan-Saratov depression and for the Tokmovo dome (Fig. 2, b). Curves 1 and 6 are typical. Their forms suggest three-layered curves of the K type with clearly expressed ascending and descending branches and a wide maximum, characteristic of a cross section with an intermediate layer of great thickness and low conductivity. The depth of the conducting part of the earth's mantle is evaluated by these curves to be equal to about 600 km, which coincides with the data of the Academy of Sciences of the USSR for the town Shatsk (Tikhonov et al., 1961).

MTS curve 4 occupies by its form an intermediate position between the curves of the first and second groups. It has a well expressed long ascending left branch characteristic to the curves for the Ryazan-Saratov depression, but at the same time weak minima are found on it, which correlate with the minima corresponding to the intermediate conductive layers of the Voronezh massif. Apparently, in the region of MTS 4 a change of the geoelectric cross section takes place. The intermediate conducting layers are either thin, or absent, here.

Curve 7 falls into the third group. It was obtained in the southern part of the Moscow syneclise (Fig. 2, c). The clearly defined ascending branch on the curve terminates by a maximum and a descending branch, showing the depth to the conducting layer to be of the order of 200 km. Then the resistivity increases again, which, however, does not contradict the existence of the conductive layer at 600 km depth. The presence of the intermediate conductive layer at 200 km depth was confirmed by the team of the Leningrad State University on the Moscow syneclise (Kovtun and Chicherina, 1969).

To what extent are the obtained longitudinal MTS curves distorted by the influence of the horizontal inhomogeneities of the sedimentary layer?

Let us analyse the degree of manifestation of the *S-effect*. No connections are observed between the total longitudinal conductivity of the sedimentary layers and the depths down to the conductive layers in the upper mantle. This is evident from MTS curves 1 and 6: at identical positions of the descending branch the total longitudinal conductivities at these sites differ more than 100 per cent. Figure 3 presents correlation plots $H = f(S)$, where H is the depth down to the conductive layer and S is the total longitudinal conductivity of the sedimentary layers. There is no interdependence between H and S. We are, therefore, justified in supposing that there is practically no S-effect.

The induction effect can be felt near the Ryazan-Saratov depression, Dnieper-Donets and Caspian basins. Farther from the depressions it should weaken.

The minimum on the descending branch of curve 3 can be, apparently, attributed to the induction of currents flowing in the Dnieper-Donets depression. Neither the transversal curve, nor any other curve for the Voronezh

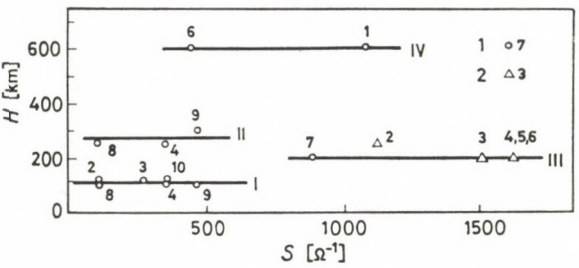


Fig. 3. Correlation plot $H=f(S)$ I, II – Voronezh Massif; III – Moscow syneclise; IV – Ryazan--Saratov basin, Tokmovo dome. Numbers at sites are the numbers of MTS (1 – Spetsgeofizika; 2 – Leningrad University)

Massif show any such minimum. As to the descending branches, which give by formal interpretation 100–120 km and 250–300 km depths for the conducting layer, they fairly correlate with each other, irrespective of the distance to the edges of the massif and, therefore, there is no ground to associate them with the induction effect.

Moreover, it is known that near depressions the ratio of the vertical component of the geomagnetic field H_z to the transversal one $H_\perp$ decreases with increasing period, if an intermediate conductive layer is present. In the opposite case the ratio $H_z/H_\perp$ increases with the growth of period and reaches a constant level. Figure 4 presents plots of $H_z/H_\perp = f(\sqrt{T})$ for the MTS 8 and 9 (Voronezh Massif). The character of the plots indicates the presence of a deep intermediate layer of high electric conductivity.

Thus, an impression has been formed that longitudinal MTS curves have no considerable distortions and reflect the true geoelectric profile of the upper mantle.

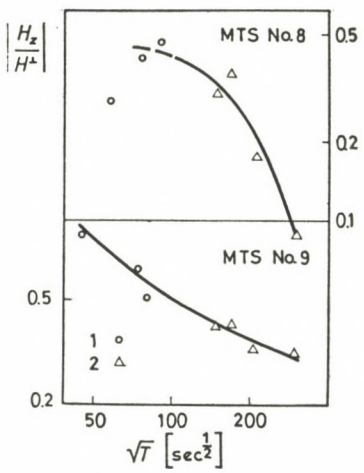


Fig. 4. Changes of the vertical component of the geomagnetic field in the low frequency range 1 – by bays; 2 – by S_q-variations

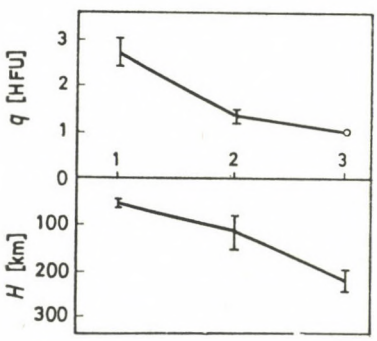


Fig. 5. Comparison of depths of the conductive layers in the mantle from MTS data with heat flow values
1 – Pannonian Basin; 2 – Voronezh Massif; 3 – Moscow syneclise

Figure 1 shows the zoning of the territory studied according to the type of the geoelectric section of the upper mantle.

In the southern part of the region a vast area is outlined with a more complex geoelectrical section. Only the north-eastern boundary of the area is definitely determined, approximately coinciding with the boundary of the Voronezh Massif. The upper mantle section here shows well-conducting layers at 100–120 and 250–300 km depths.

In the northern part of the region there is an area of a more simple section, having only one intermediate conductive layer at 200 km depth. This layer, according to data of the Leningrad University, is traced further to the north in the central part of the Moscow syneclise.

The third zone, located between the Voronezh massif and the Moscow syneclise, definitely shows a conductive mantle at a depth of 600 km. The characteristic feature of the zone is that it is not associated with any definite geological structure, as the first and the second zones are.

Many aspects of the nature of the layers of higher electrical conductivity are still unknown.

The conductive part of the mantle that is observed in the studied region at about 600 km depth, is usually identified with the *C* layer. It is supposed that at the boundary of this layer an olivine-spinel transition takes place which increases the electric conductivity of the mantle by two-three orders (Rikitake, 1968).

The nature of the intermediate conductive layers is thought to be different. The increased electric conductivity at 80–300 km depths is attributed (Subbotin et al., 1970) to partial melting of the material (it is sufficient to have 2 per cent of material in a melted state to a considerable increase of the electrical conductivity). If we adopt this point of view, we can understand the connection between the depth of the intermediate conductive layer in the mantle and the value of heat flow from the earth's interior: the less the depth to the conducting layer, the higher is the heat flow. This regularity is clearly seen in Figure 5, that compares heat flows and depths to the conductive layer for the Pannonian Basin, Voronezh Massif and Moscow syneclise.

REFERENCES

ANISHCHENKO, G. N., 1965. On the methods of magnetotelluric sounding (in Russian). *Prikl. Geofiz.* **44.**

BERDICHEVSKY, M. N., DMITRIEV, V. I., 1969. Magnetotelluric field over the tilted scarp of the insulating foundation (in Russian). Magnitotellurichеskie metodi izucheniya stroeniya zemnoi kory i verkhnei mantii., 4. Nauka, Moscow.

KOVTUN, A. A., CHICHERINA, N. D., 1969. Results of magnetotelluric studies of the Middle Russian depression (in Russian). Magnitotellurischeskie metodi izucheniya stroeniya zemnoi kory i verkhnei mantii., 4. Nauka, Moscow.

LUBIMOVA, E. A., 1968. Thermal Fields of the Earth and the Moon (in Russian). Nauka, Moscow.

MAKSIMOV, V. M., ZAKUTSKY, S. N., 1967. Deep magnetovariation studies of the central part of the Russian platform (in Russian). Sb. trudov molodykh uchenykh Geol. Fak. Gos. Univ. Voronezh.

RIKITAKE, T., 1968. Electromagnetism and the Earth's Interior (Russian translation). Nedra, Leningrad.

SMIRNOV, YA. B., 1970. Importance of geothermal research for the study of the earth's crust and upper mantle (in Russian). Problemi Stroeniya Zemnoi Kori i Verkhnei Mantii, 7. Nauka, Moscow.

SUBBOTIN, S. I., KUTAS, R. I., SOBAKAR, G. T., 1970. Deep processes in the crust and mantle of the earth and their role in the development of the earth's crust (in Russian). *Geofiz. Sb.* Naukova Dumka, Kiev, No. 38.

TIKHONOV, A. N., DMITRIEV, V. I., 1969. Influence of surface inhomogeneities on the deep magnetotelluric sounding (in Russian). Vychisl. Metody i Programmirovanie, 13, Moscow, Publ. House.

TIKHONOV, A. N., LIPSKAYA, N. V., DENISKIN, N. A., NIKIFOROVA, N. N., LOMAKINA, Z. V., 1961. On the electric sounding of deep layers of the earth (in Russian). *Dokl. Akad. Nauk SSSR*, **140**, No. 3.

DEEP MAGNETOVARIATION STUDIES IN UKRAINE

I. I. ROKITYANSKY, S. N. KULIK, I. M. LOGVINOV,
V. N. SHUMAN

Figure 1 presents the map of Wiese vectors, compiled at the Institute of Geophysics of the Ukrainian SSR. The data for the region to the west of town Khmelnitsky were obtained by Bondarenko and his group (Bondarenko et al., 1972); data for the region to the east of Khmelnitsky by the authors of this paper. The map shows several anomalous zones, the most interesting and best studied are the Kirovograd and the Carpathian anomalies, which are two-dimensional in character.

The Kirovograd anomaly was studied in 1967–1971. Four profiles of simultaneous observations and separate points between them enabled to trace the axis of the anomaly at 600 km, according to the D maximum and transition through zero of the eastern component of the induction vectors (Figs 1 and 2). When analyzing the induction vectors, the superposition of anomalous fields of surface and deep sources was taken into account.

The Z- and D-components (the anomaly of the H-component is close to

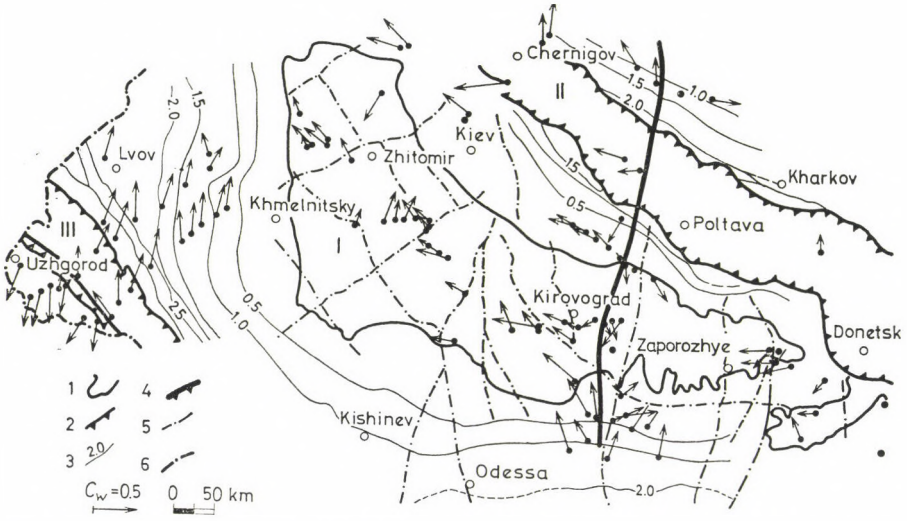


Fig. 1. Map of the Wiese vectors for periods of 15–60 min and the tectonic chart of Ukraine (Muratov, 1969)

1 – border of the Ukrainian shield; 2 – borders of the Dnieper-Donets depression and of the Folded Carpathians; 3 – contours of the crystalline basement surface; 4 – axes of the Kirovograd and the Carpathian anomalies of electric conductivity; 5 – major inter-block deep faults; 6 – border of the USSR

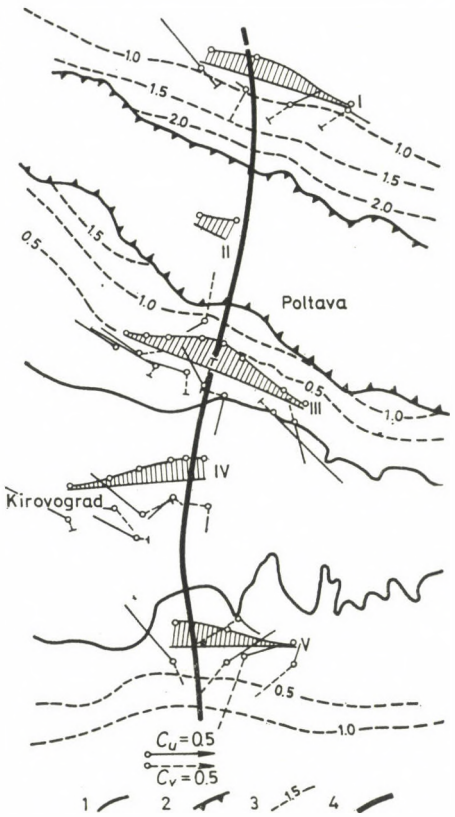


Fig. 2. The Kirovograd anomaly. Map of the induction vectors, $\mathbf{C}_u = \mathrm{Re}\mathbf{Ai} + \mathrm{Re}\mathbf{Bj}$, $\mathbf{C}_v = \mathrm{Im}\mathbf{Ai} + \mathrm{Im}\mathbf{Bj}$ for periods of 30–40 min and plots of D_a/D_0. Symbols as in Fig. 1

zero) are represented in Figure 3. Data of the four profiles are combined here. For interpretation of the obtained results the circular cylinder model was used. It was assumed that the anomaly is of a conductive nature (Rokityansky, 1972). The depth of the axis of the cylinder, $h = 35$ km, was determined, as well as the moment, $m_0 = 15$ km, that characterizes the longitudinal conductance, $G = \sigma_i Q$, of the transversal section Q. The elliptical cylinder model with the major axis, oriented horizontally and vertically, was also used. By changing the depth and the ratio of the semi-axes, it was possible to select several models that fitted the experimental data sufficiently well (Fig. 3). Besides, the conductivity was calculated by means of analytical continuation for the inhomogeneous, thin horizontal layers from 0 to 35 km depths.

The evaluation of G on the basis of m_0 requires the knowledge of the V function, characterizing the degree of saturation of the anomalous body by anomalous currents (Rokityansky, 1972). V and G are determined from the frequency characteristics of the anomalous field.

To compile the frequency characteristics of the Kirovograd anomaly D-component data were used at points near the anomaly axis, where D_a is maximal. The frequency characteristics of the D-component are shown in

Figure 4. Vertical lines indicate the mean square error, calculated from the data scattering of individual variations. The amplitude plot shows curve 2–2, which represents the most probable frequency characteristics, and also curves 1–3 and 3–1, which limit the scatter of experimental dots. To minimize interpretation variants, we will analyze characteristics that correspond to anomalous bodies most differing in scale: i.e. the limiting curves 1–1 and 3–3. Proceeding by an integral transform from the logarithm of the amplitude characteristics to the phase characteristics, we obtain three curves on the phase plot, which shows that the available limited data on the phases of the anomalous field are in agreement with the amplitude data. Methods of the evaluation of G from the frequency characteristics are described by Rokityansky in this monograph. The most accurate way to determine the V function is to divide the normalized anomalous field by the normal impedance ξ_0 (Rokityansky, 1972). The curve $|V|$ thus obtained is shown in the lower part of Figure 4. The function $V(\sqrt{T})$ is compared to the theoretical $V(\sqrt{T/G})$ and G is determined from the horizontal shift of the curves. For the Kirovograd anomaly G is equal to $200 \cdot 10^6\ \Omega^{-1}$m, by the most probable curve 2–2, and $80 \cdot 10^6\ \Omega^{-1}$m and $340 \cdot 10^6\ \Omega^{-1}$m by the left-side and right-side limiting curves 1–1 and 3–3, respectively. The obtained G values are minimal. The estimation of the maximal value of G is based on the supposition of the vortex nature of the anomaly. The initial material is the same frequency characteristics (Fig. 4), from which $G_{max} = 2500 \cdot 10^6\ \Omega^{-1}$m is determined.

Using the data of modelling on bodies of finite length and the frequency characteristics of the anomalous field, we can conclude that the length of the Kirovograd anomaly exceeds 2000 km, provided its longitudinal con-

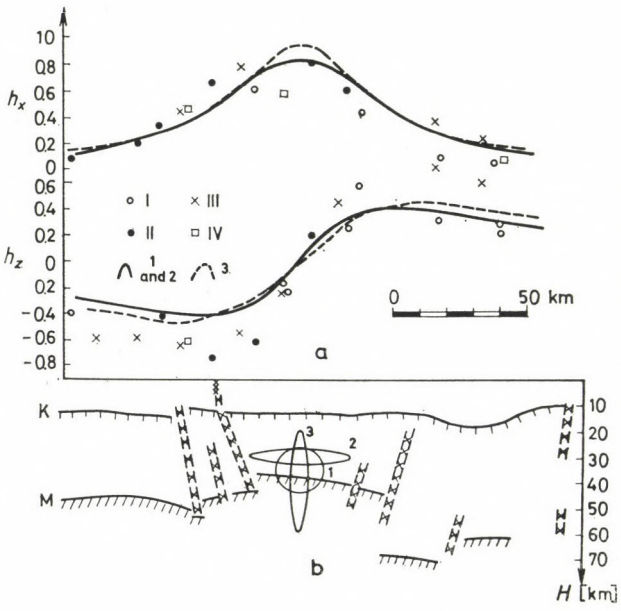


Fig. 3. The Kirovograd anomaly
a – experimental data $h_x = D_a/D_0$, $h_z = Z/D_0$, obtained on profiles I–IV in Fig. 2; 1–3 calculated curves for circular ($h = 35$ km, $a = 8$ km), horizontal ($h = 30$ km, $a = 20$ km, $b = 3$ km), and vertical ($h = 40$ km, $a = 3$ km, $b = 20$ km) elliptical cylinders; b – simplified cross section of the earth's crust along international DSS profile VIII from data of the paper of Tectonics of Europe (1964) and possible sections of anomalous bodies of conductivity $\sigma_i = 1\ \Omega^{-1}\text{m}^{-1}$ (variants of solution of the inverse problem)

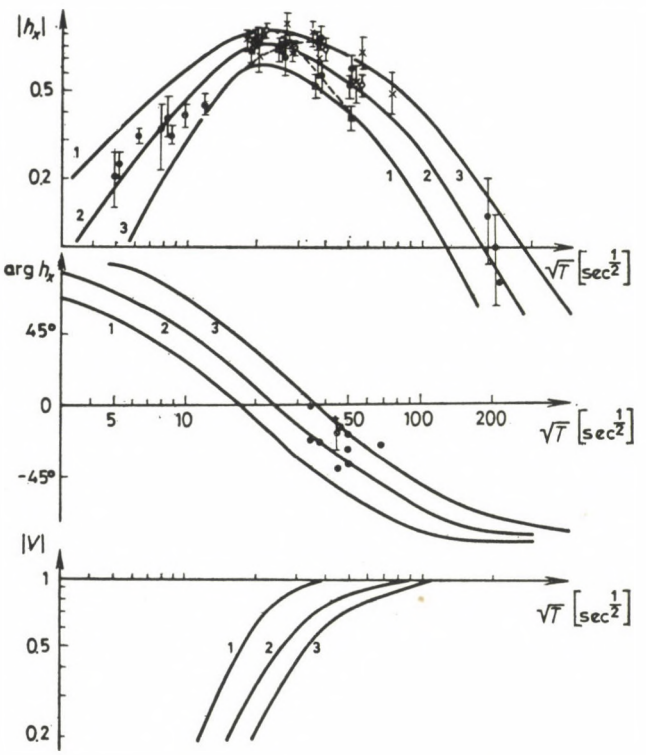


Fig. 4. The Kirovograd anomaly. Frequency characteristics of the anomalous field h_x and its interpretation. Dots and vertical lines show experimental results and their mean square error for profiles I–IV
Curves: 1–1 the maximum high frequency; 2–2 the most probable; 3–3 the maximum low-frequency characteristics. The phase characteristics are obtained from the corresponding amplitude curves by Hilbert transform

ductance G does not increase outside the area covered by observations.

Summarizing the interpretation data, the parameters of the Kirovograd anomaly, determined by MVP, are as follows:

1. Depth of the centre of the anomalous currents in the 10–60 min periods is not more than 35 km, and that of the upper edge of the body not more than 30 km.

2. The total longitudinal conductance of the cross-section of the body is not less than $200 \cdot 10^6\ \Omega^{-1}\mathrm{m}$. The average volumetric conductivity is $\sigma \geq 0.05\ \Omega^{-1}\mathrm{m}^{-1}$.

3. The length of the body is not less than 2000 km.

Let us compare these results with the geological and geophysical data. The Kirovograd block is an ancient middle massif formed in the Archean. In the east it is joined by the geosyncline system Bolshoi Krivoi Rog, formed in the Upper Archean–Lower Proterozoic. The boundary between these structures passes along a series of deep faults. The electrical conductivity anomaly is within the Ingulo-Ingulatsk zone, considered by some geologists as an anticlinorium, by other geologists as a synclinorium.

The geophysical data demonstrate that the Ingulo-Ingulatsk zone shows peculiar anomalous features in some other aspects, too. Figure 3 presents a schematic cross section of the earth's crust along the axis of the shield, from the data of DSS profile VIII (Sollogub, 1970b). The earth's crust is

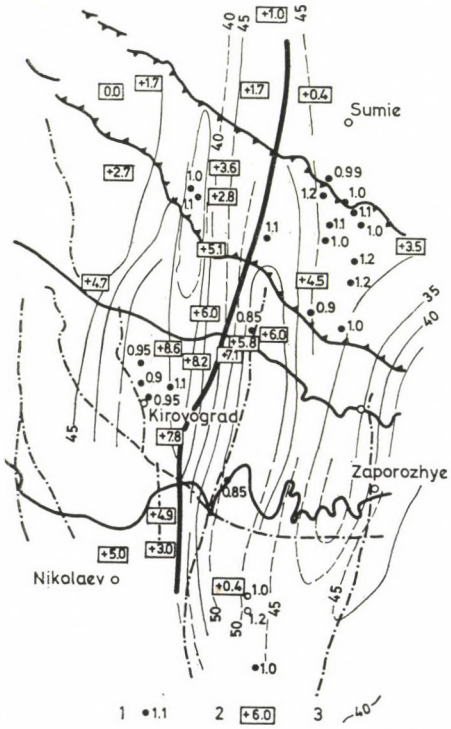


Fig. 5. Geological and geophysical characteristics of the area of the Kirovograd anomaly. Symbols, denoting tectonic elements, as in Figure 1
1 – observation sites and heat flow values in μ cal/cm^2 sec from the papers Kutas and Gordienko (1971), Kutas et al. (1972); 2 – observation sites and rates of recent vertical crustal movements in mm/year from Meshcheryakov (1971); 3 – isolines of depth of the Moho discontinuity from Sollogub **(1970b)**

more than 55 km thick in the region of Bolshoi Krivoi Rog (roots of the Lower Proterozoic Mts are still observed); in the region of the anomaly it is reduced to 37 km; further to the west the Moho discontinuity submerges steplike along the Kirovograd deep fault to 52 km.

The area of the Kirovograd anomaly is characterized by an intensive recent uplift of 8 mm/year rate (Meshcheryakov, 1971). Figure 5 gives data on the rate of vertical crustal movements. Maximum rates are observed in the Ingulo-Ingulatsk zone. At the point, 40 km south of Krivoi Rog, the rate is only 3.3 mm/year. Thus, according to Bondarchuk et al. (1968), the block of rocks, west of the Krivoi Rog deep fault, actively rises at a rate of more than 8 mm/year, while east of that fault the rate is reduced to 2–3 mm/year.

It is evident that within the Ukrainian shield the electric conductivity anomaly is accompanied by the anomaly of seismic wave velocities and by an intensive recent uplift of the crust. This suggests to look for the common cause of all these three phenomena. This common cause can be the local heating of matter near the Moho discontinuity. However, in such a case high heat flow should have been observed. Figure 5 presents heat flow data from Kutas and Gordienko (1971), Kutas et al. (1972). Neither in the Dnieper-Donets depression, nor on the Ukrainian shield is any increase of heat flow detected when approaching the axis of the anomaly. The observa-

tions of the maximum heat flow in the epicentre of the anomaly give, for the shield, values not exceeding 1.2 μcal/cm^{2}sec which, considering the high thermal conductivity of crystalline rocks, is not sufficient to account for the electric conductivity anomaly due to stationary heating.

Two possible explanations of the Kirovograd electric conductivity anomaly can be suggested:

1. The process, that gave birth to the anomaly, has started only recently and the heat flow had no time to reach the earth's surface. This supposition is favoured by the character of the relief of the earth's surface and by the absence of mountains.

2. The process, that gave birth to the anomaly, is relatively "cold".

We suppose that the anomalous body is elongated in the vertical direction. This zone is connected with the magma chamber or with the subsiding chamber of zonal melting. On the other hand, the anomalous body can be described as a wedging out horizontal layer, in which chemical, polymorphic or phase transformations take place, as e.g. the process of regional metamorphism.

REFERENCES

Bondarenko, A. P., Bilinsky, A. I., Sedova, F. I., 1972. Geoelectromagnetic Variations in the Soviet Carpathians (in Russian). Naukova Dumka, Kiev.

Bondarchuk, A. G., Veselov, V. Ya., Kurochkin, P. E., Osetsky, A. N., Samarsky, R. Ya., Tyapkin, K. F., 1968. Study of recent horizontal movements in Krivorozhje (in Russian). Sovremennye Dvizheniya Zemnoi Kory. Akad. Nauk SSSR.

Kutas, R. I., Gordienko, V. V., 1971. Thermal Field of Ukraine (in Russian). Naukova Dumka, Kiev.

Kutas, R. I., Gordienko, V. V., Zavgorodnyaya, O. V., 1972. Heat flow from the Ukrainian shield and from its slopes (in Russian). *Geofiz. Sb.* **50.**

Lebedev, E. B., Khitarov, N. I., 1964. Beginning of granite melting and the electric conductivity of its melt, depending on the high pressure of water steam (in Russian). *Geokhimiya* No. 3.

Meshcheryakov, Yu. A., 1971. Map of Recent Vertical Crustal Movements in Eastern Europe. GUGK, Moscow.

Rokityansky, I. I., 1972. Geophysical Methods of Magnetovariation Profiling and Sounding (in Russian). Naukova Dumka, Kiev.

Sollogub, V. B., 1970a. Structure of the earth's crust in Ukraine (in Russian). *Geofiz. Sb.* **38.**

Sollogub, V. B., 1970b. Deep seismic studies in Ukraine (in Russian). *Geofiz. Sb.* **48.**

Tectonics of Europe. Nauka-Nedra, 1964.

DEEP ELECTROMAGNETIC STUDIES IN THE URAL

A. G. KRASNOBAEVA, V. S. VISHNEV, T. L. RUDNEVA

Electromagnetic survey were carried out in the Middle Ural by the Institute of Geophysics of the Ural Research Centre. Sites of deep magnetotelluric sounding (MTS) were chosen along the profile from the city Krasnoufimsk in the west to Omsk in the east. Observations were conducted in areas where there are no sharp distortions of homogeneity in the upper layers. These areas were singled out according to magnetotelluric profiling (MTP) and magnetovariation profiling (MVP) data.

The Ural is a geosyncline system developed during the Late Proterozoic and Paleozoic eras. The extension of the Ural structures is considerably more than 2000 km in meridional direction and 400–500 km in latitudinal direction. The bulk of these structures is buried in the Transurals under unfolded Mesocenozoic deposits.

The territory investigated includes three regions (Fig. 1), differing in the geoelectric cross-section of the upper horizons. Region I coincides with the area of the Ural foredeep and of the eastern margin of the Russian Platform, the open Ural belongs to region II, and region III comprises all of the Transurals and the West Siberian plate.

Region I preserves, according to geological and geophysical data, the quasilatitudinal direction of basement structures, characteristic of the Russian Platform (Yarosh, 1968). The ancient highly resistive crystalline basement occurs at a depth of 6–7 km (Druzhinin et al., 1968; Khalevin, 1967). Above it lie sediments represented by interchanging terrigenous sandy-argillaceous and coarse deposits alternating with carbonates and salts. The geoelectric cross section is notable for great contrasts in composition as well as in thickness of the sedimentary formations. The longitudinal (horizontal) conductivity of the sedimentary strata is 150–250 Ω^{-1}. Mean longitudinal resistivity of the sediments varies from 16 to 46 Ωm.

Magnetotelluric impedance diagrams for region I characterize the medium as two-dimensionally inhomogeneous with mainly meridional current spreading. The shape of the diagrams can be accounted for by either the influence of the open Ural as a long non-conducting swell (edge effect) or the effect of the elevated structures in quasi-latitudinal direction (S-effect). The MTS-curves for meridional direction, i.e. those corresponding to the current spreading across the structures of the region ($\varrho^{\perp}$), are located above the curves for the latitudinal direction ($\varrho^{\parallel}$). Figure 2 provides an example of such curves (site 16). For geological interpretation the longitudinal $\varrho^{\parallel}$ curve was chosen which agrees best with the curves for other regions.

Within the open Ural *(region II)* the upper conductive layer is represented by unconsolidated deposits of comparatively small thickness ($h \leq 100$ m).

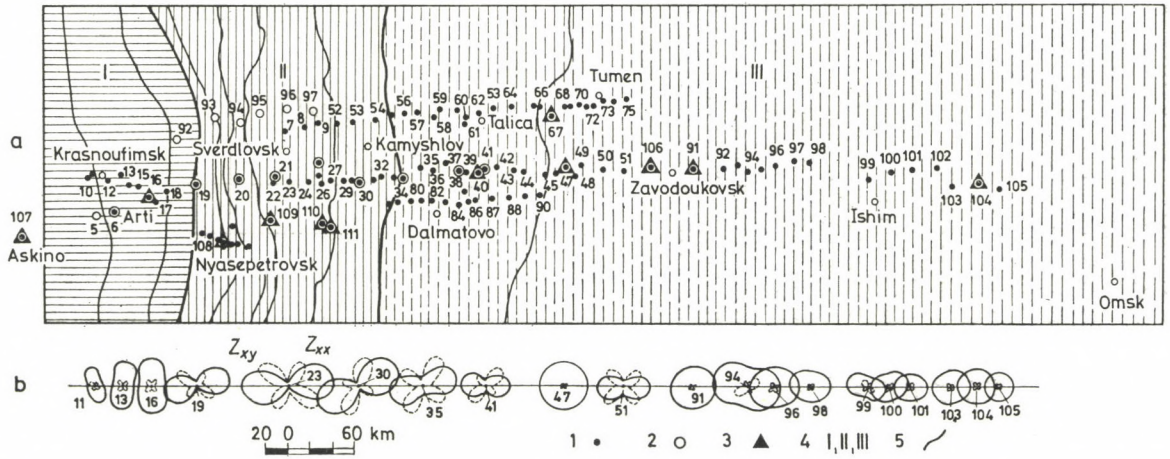


Fig 1. Locations of sounding sites (a) and polar diagrams of the main impedance (Z_{xy}) and the secondary impedance (Z_{xx}) for the Sverdlovsk traverse (b)
1 – MTP; 2 – MVP; 3 – deep MTS; 4 – geoelectric regions; 5 – isolines

The resistivity of the massive bedrocks is 2000–7000 Ωm. Highly porous, primarily sedimentary and fissured rocks, mainly volcanic, have relatively low resistivity (25–1000 Ωm). Low resistivity is characteristic of the rocks containing graphite and sulphides (0.1–1000 Ωm). In region II considerable distortions of the electromagnetic field are observed. In the range of short-period oscillations the magnetic field's vertical component is commensurable with the horizontal component, and the electrical field has linear polarization, while the polarization of the magnetic field is elliptical. The E and H vectors are not orthogonal. The correlation of the field components is difficult, especially when industrial noises are present.

The geoelectric structure of *region III* is favourable for magnetotelluric studies. The Paleozoic basement, or the Permo-Triassic effusive formations that fill the depressions in the Paleozoic basement can be taken for the high-resistivity horizon. Younger rocks of sedimentary origin (Cr, Pg) form a solid sheet and manifest themselves as the first conductive layer. Their thickness is steadily growing in W–E direction. In the vicinity of the town of Kamyshlov (Fig. 1) it is 200–300 m and around Omsk it is 2–3 km. Within the area under investigation the specific reistivity of sedimentary rocks varies around 3–4 Ωm (Physical properties . . ., 1967). The longitudinal conductivity of the sedimentary strata gradually increases from 200

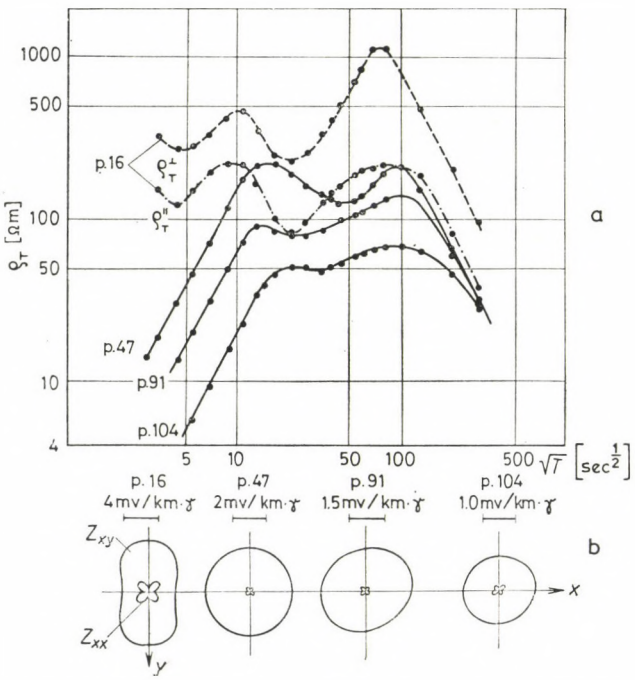


Fig. 2. Deep magnetotelluric sounding curves (a) and impedance polar diagrams within the time interval pertaining to the rising branch on the MTS-curves (b)

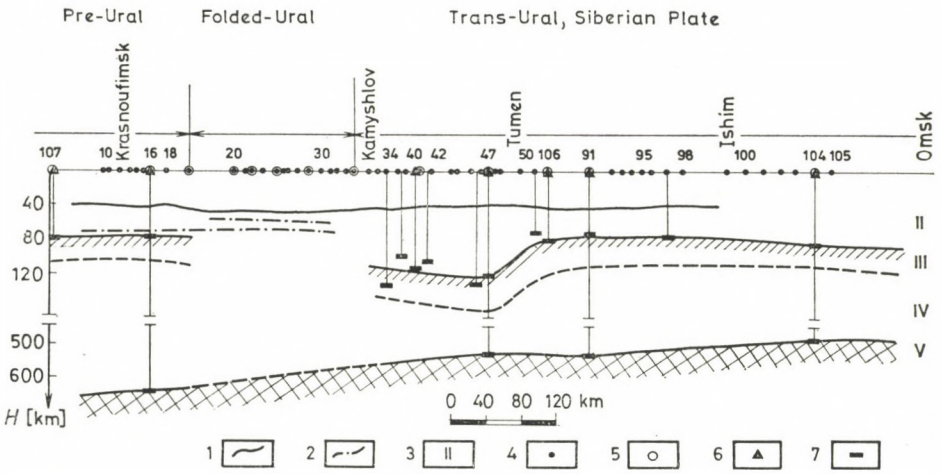


Fig. 3. Schematic geoelectric cross section

1–2 – boundaries established from DSS data (I-Moho discontinuity); 3 – mean value of specific electric resistivity of the layers distinguished from deep MTS data, in Ωm: II – 3000–4000, III – 14–23, IV – 300–1000, V – 0.5–3; sites of observations: 4 – MTP; 5 – MVP; 6 – deep MTS; 7 – sites where depths of the conductive layers in the mantle were determined

Ω^{-1} (site 43) to 800 Ω^{-1} (site 105). However, some local changes in S are observed that are associated with the non-uniformity of the basement (Krasnobaeva, 1969; Krasnobaeva et al., 1972a). Such zones were discovered at sites 38–42, 45, 51, 98 and others.

In region III the MTS curves are also distorted, though much less than in region I. The curves drawn for the latitudinal direction lie always higher than the curves for the meridional direction. The major axes of the polar diagrams for the main impedance are latitudinally oriented. The distortions decrease when moving away from the eastern border of the open Ural; at sites 47, 91, 104 and others the slope of the main impedance diagrams approaches a circle, and the secondary impedances get close to zero.

An analysis of the geomagnetic variations shows that the H-component remains almost unchanged along the whole profile while two local anomalies of the D-component are observed (sites 20 and 42). The fact that only the D-component presents anomalies testifies to a close to meridional strike of the conductors. The H_z-curves confirm that the revealed anomalies are two-dimensional. We are inclined to believe that the presence of a deep fault accounts for one of the anomalies, and a depression in the Paleozoic basement for the other (Krasnobaeva et al., 1972b).

Reference magnetotelluric soundings in a wide frequency range, including S_q-variations, were carried out at sites 16 (Arti Observatory), 47 (Salomatovo village), 91 (Staraya Zaimka village) and 104 (Orlovo village). Measuring lines were oriented along the magnetic meridian and along the latitude.

When constructing the MTS-curves (Fig. 2), we used visual as well as

spectral techniques of variation selection. The short period variations (the left-hand-side rising branch of the curves) were fitted by least squares method to construct the impedance diagrams. In cases of bays (intermediate part of the curves) spectral methods were applied to separate the first harmonic component. The descending branches on the curves were obtained from the harmonic analysis of S_q-variations. The scatter of ϱ_T values for one and the same time interval did not exceed 25% of the mean value. Resistivity values determined for the latitudinal and meridional directions at sites 47, 91, 104 coincide within 10% error; so mean curves were constructed.

The descending branches of the curves obtained at sites 47, 91 and 104 are in good agreement with each other as well as with the descending branch on the longitudinal curve for site 16.

Quantitative interpretation of the MTS-curves carried out at the Computational Centre of the Moscow State University made it possible to construct a schematic geoelectric cross section (Fig. 3). An intermediate conducting layer III stands clearly out, its depth varying from 70–80 km at the ends of the profile to 100–120 km in the central part of the profile. The total longitudinal conductivity of the layer is about 1800 Ω^{-1}. Apparently this layer may be identified with the asthenospheric layer of low elastic wave velocity (Gutenberg discontinuity). According to the present notions a partial melting of the mantle matter is possible in the depth range of 100 to 150 km (Magnitsky, 1968). Melting of basaltic magma may take place there (Sheinmann, 1968). The electric conductivity of the zones of melting and of a partial transition of the matter into amorphous state has been yet poorly studied, although some information can be acquired from experimental data (Khitarov and Slutksy, 1965; Parkhomenko, 1971). At the initial moment of melting conductivity increases by 2–3 orders of magnitude. It is just that very change of electric conductivity what we obtain from the MTS data.

Another characteristic feature of the cross-section considered is the increased conductivity at depths from 490 km (site 104) to 650 km (site 16). We identify this layer with the C-zone boundary. Depth variations are apparently due to the field distortions. The decrease of specific resistivity to 0.5–3 Ωm can be most adequately explained by phase transition of the mantle material into assemblages with more closely packed atoms. According to the data presented by Akimoto and Fujisawa (1965), polymorphic transitions of olivine into spinel, of pyroxene into spinel and stishovite that may take place at the C-zone boundary are accompanied by transformation of the ionic bond into a closer covalent one and by an increase in electric conductivity by several orders of magnitude.

REFERENCES

Akimoto, S., Fujisawa, H., 1965. Demonstration of the electrical conductivity jump produced by the olivine-spinel transition. *J. Geophys. Res.* **70**, No .2.

Bryunelli, B. E., Dobrovolskaya, M. A., Kovtun, A. A., Kuznetsov, N. S., 1968. Certain results of magnetotelluric profiling and magnetotelluric sounding using models of inhomogeneous structures (in Russian). Magnitotellurichеskie Metodi Izucheniya Stroeniya Zemnoi Kory i Verkhnei Mantii, 4. Nauka, Moscow.

DRUZHININ, V. S., RYBALKA, V. M., KHALEVIN, N. I., 1968. Results of deep sounding along the Sverdlovsk traverse and perspectives of the subsequent researches in the Ural (in Russian). Glubinnoe Stroenie Urala. Nauka, Moscow.

KHALEVIN, N. I., 1967. About the crustal structure of the Russian Platform, of the Ural and the West-Siberian lowland. Crustal Structure of the Urals (in Russian). *Geofiz. Sb.* No. 5. Trudy Inst. Geofiz, UFAN SSSR, Sverdlovsk.

KHITAROV, N. I., SLUTSKY, A. B., 1965. Pressure effect upon albite and basalt melting points (from electrical conductivity measurements) (in Russian). *Geokhimiya*, No. 12.

KRASNOBAEVA, A. G., 1969. Some results of magnetotelluric soundings of the Transural region (in Russian). *Geol. i Geofiz.*, No. 7.

KRASNOBAEVA, A. G., 1970. Distinguishing of tectonic dislocation zones from data of magnetotelluric soundings of the Ural (in Russian). Voprosy Geologii i Magmatizme Urala, Sverdlovsk.

KRASNOBAEVA, A. G., KORMILTSEV, V. V., 1970. Deep geoelectric structure of the Middle Ural from electromagnetic data (MTS) (in Russian). Manuscript UFAN SSSR, Sverdlovsk.

KRASNOBAEVA, A. G., KORMILTSEV, V. V., SHEPELEVA, I. M., 1972a. Deep magnetotelluric soundings of the Transural region (in Russian). Teoriya i Praktika Elektrometri. UNC AN SSSR, Sverdlovsk.

KRASNOBAEVA, A. G., SHEPELEVA, I. M., RODIONOV, P. F., 1972b. Results of the application of magnetotelluric profiling for the studies of the buried Paleozoic in the Transural regions (in Russian). Teoriya i Praktika Elektrometrii UNC AN SSSR, Sverdlovsk.

MAGNITSKY, V. A., 1968. Low Velocity Layer in the Upper Mantle of the Earth (in Russian). Nauka, Moscow.

PARKHOMENKO, E. I., 1971. The nature of layers of high electric conductivity in the earth's crust and upper mantle, according to laboratory data (in Russian). Fizicheskie Svoistva Gornykh Porod pri Vysokikh Termodinamicheskikh Parametrakh. Naukova Dumka, Kiev.

Physical properties of the sedimentary cover in the USSR territory (in Russian). 1967. Eds M. L. Ozerskaya, N. V. Podoba, Nedra, Moscow.

SHEINMANN, YU. M., 1968. Essays on Deep Geology (in Russian). Nedra, Moscow.

VISHNEV, V. S., KRASNOBAEVA, A. G., KORMILTSEV, V. V., RYTSK, A. E., 1972. Magnetovariation profiling (MVP) in the Middle Ural (in Russian). Teoriya i Praktika Elektrometri UNC AN SSSR, Sverdlovsk.

YAROSH, A. Ya., 1968. Structure of the crystalline basement in the eastern regions of the Russian Platform and its structural connections with the Ural (in Russian). Glubinnoe Stroenie Urala, Nauka, Moscow.

DEEP MAGNETOTELLURIC SURVEYS IN THE EASTERN PRE-CAUCASUS

D. A. VARLAMOV, YU. K. KONNOV, I. S. FELDMAN

During 1962–1969 the Research Institute of Foreign Geology carried out magnetotelluric investigations over the territory of the Eastern Pre-Caucasus (Fig. 1) which supplied information about the electric conductivity of the upper mantle.

The territory under study is a part of the Epihercynian platform, the folded basement of which is composed of rocks different in age and in the intensity of metamorphism. The platform cover is represented by a thick series of Mesozoic and Cenozoic deposits. A number of large tectonic elements mainly of subcaucasian strike, stand out within the area of the platform. The deeply subsided Tersko-Caspian foredeep separates the platform from the meganticlinorium of the Great Caucasus. The Paleozoic basement possesses high resistivity over the whole territory. Mean longitudinal resistivity of the overlying stratum increases in the southern direction from 1 to 3.5 Ωm. The thickness of the stratum also increases in the southern direction and reaches 10–12 km in the axial part of the Tersko-Caucasian foredeep. In transition from the foredeep to the meganticlinorium the thickness sharply decreases, the highly resistive rocks come here out to the surface.

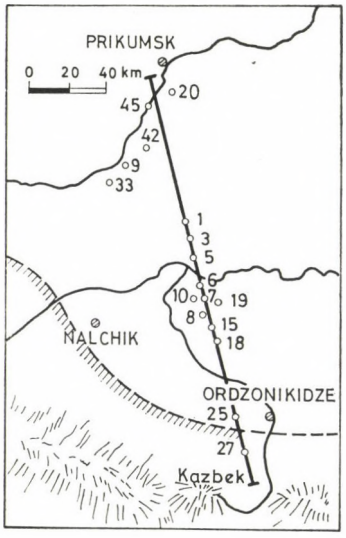


Fig. 1. Map of the Eastern Pre-Caucasus and the location of MTS sites

ANALYSIS OF THE MTS-CURVES

Transverse MTS-curves, i.e. curves oriented across the Great Caucasus meganticlinorium, are distorted by the edge effect (Berdichevsky et al., 1973 and p. 216.). Therefore, we confine ourselves to the analysis of longitudinal MTS-curves, shown in Figure 2. These curves can be divided into two groups with different positions of maxima. On the curves to the south of the latitudinal watercourse of the Terek River the maxima are grouped in the period interval of 900 to 1000 sec. To the north of the Terek River the maxima shift towards the interval of 1600 to 3600 sec.

Using a traditional three-layer model with a conductive basement, we obtained the depth of its top; it is 50–60 km for the southern section of the profile and 120–130 km for the northern section (Fig. 3, a). These depth variations do not correlate with the variations of the total longitudinal conductivity of the sedimentary cover, a possible *S-effect* being thus excluded. The possibility of an *induction effect* is also of little probability for the curves under consideration essentially differ from the theoretical curves obtained for an individual graben model and, besides that, there is no evident connection between the abscissas of maxima and the separation points,* on the one hand, and the distance from the axis of the Tersko-

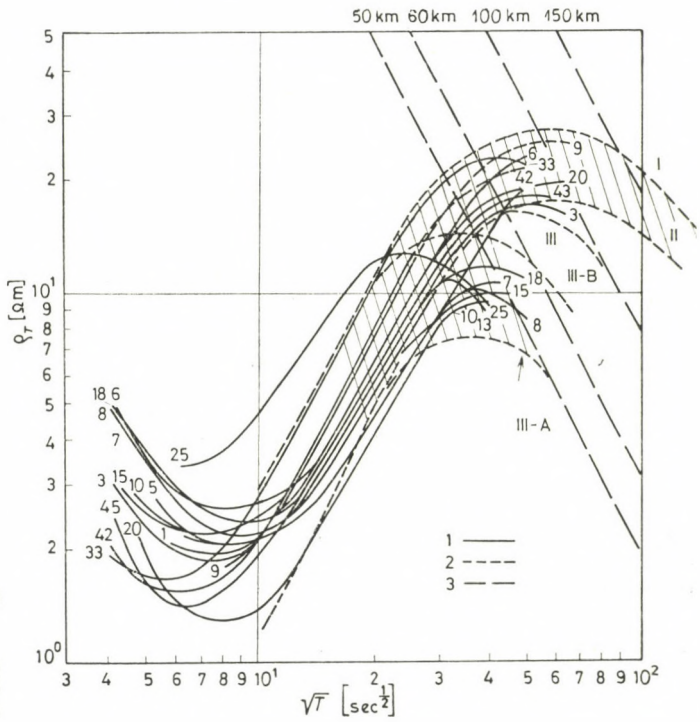


Fig. 2. Magnetotelluric sounding curves
1 – observed MTS curves (longitudinal); 2 – theoretical MTS curves; 3 – depth lines

* The "point of separation" is the point where the MTS-curve separates from the rectilinear asymptote. (Ed.'s note.)

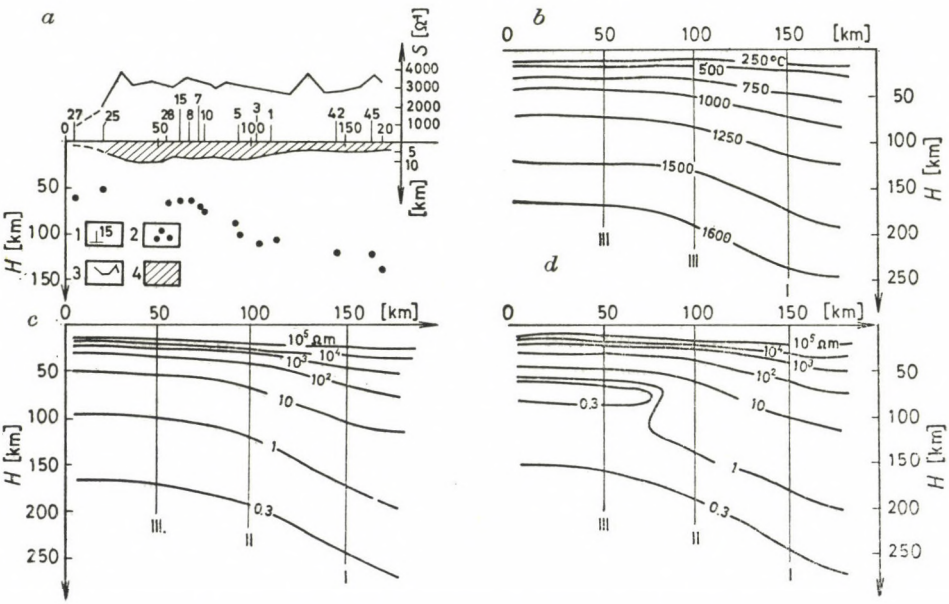


Fig. 3. Geophysical cross section along the profile

a – results of the formal interpretation of longitudinal MTS curves: 1 – numbers of MTS sites; 2 – depth to the conductor obtained through formal interpretation of the MTS curves; 3 – diagram of total longitudinal conductivity of the sedimentary cover; 4 – sedimentary cover; b – geothermal cross-section, temperature isolines in °C; c – geoelectric cross-section without the intermediate conductive layer; isolines of specific resistivity in Ωm; d – geoelectric cross-section with the conductive layer at 60–80 km depth, isolines of specific resistivity in Ωm

Caspian foredeep, on the other. So, it can be supposed that the formal interpretation of the longitudinal MTS-curves reflects the behaviour of geoelectric surfaces in the upper mantle.

GEOELECTRIC CROSS SECTION AND TEMPERATURE CONDITIONS IN THE MANTLE

The nature of the intermediate conductive layer in the mantle will be discussed in Chapter 6. Let us recall that in the near-by South Caspian depression the position of the top of the said layer is the same as in the Pre-Caucasus, i.e. at a depth of 50–60 km (Berdichevsky et al., 1971, 1972). When considering the results of magnetotelluric sounding in the South Caspian depression we assumed that the conductive layer in the mantle occurs as a result of partial melting of rocks. It is natural to extend this hypothesis to the Eastern Pre-Caucasus as well. Geological and geophysical data are indicative of a high tectonic and thermal activity of the Eastern Pre-Caucasus interior (high heat flow, Cenozoic volcanism, high seismic

activity, considerable amplitudes of neotectonic movements and their contrasts). It is only 30 km south of the end of the profile that the peak of Kazbek is towering, a volcano that has recently been active, whose flanks and foot are composed of andesite and basalt lava streams erupted only hundreds or even dozens of thousands of years ago. The magma chamber of that time, the production of which can be observed on the surface now, could neither have disappeared since that time nor could it have considerably changed its regime of activity. Dozens of millions of years are required for such a large temperature excess to disappear (Kutas and Gordienko, 1972).

In the light of this idea we interpret the results obtained as follows. In the southern part of the profile there exists in the upper mantle an intermediate conductive layer the top of which is traced by the MTS-curves at 50–60 km depth. Northwards (between sites 7 and 5) this layer disappears, while southwards it seems to extend under the Caucasian meganticlinorium. The MTS-curves in the northern part of the profile reflect a gradual increase of electric conductivity with depth caused by the increasing temperature.

To verify this hypothesis let us compare the MTS curves with the theoretical curves calculated for the models with a gradual increase of electric conductivity. Figure 3, b presents a temperature cross section which was constructed proceeding from the surface heat flow value, according to the existing notions about the deep structure and thermal characteristics of the region (Smirnov, 1970). Let us construct a corresponding geoelectric cross section, making use of the well-known connection between temperature, pressure and electric conductivity (Fig. 3, c). Let us draw over the geothermal and the geoelectric cross sections three characteristic lines I, II and III corresponding to the northern, central and southern parts of the profile. Temperature curves and specific resistivity curves correspond-

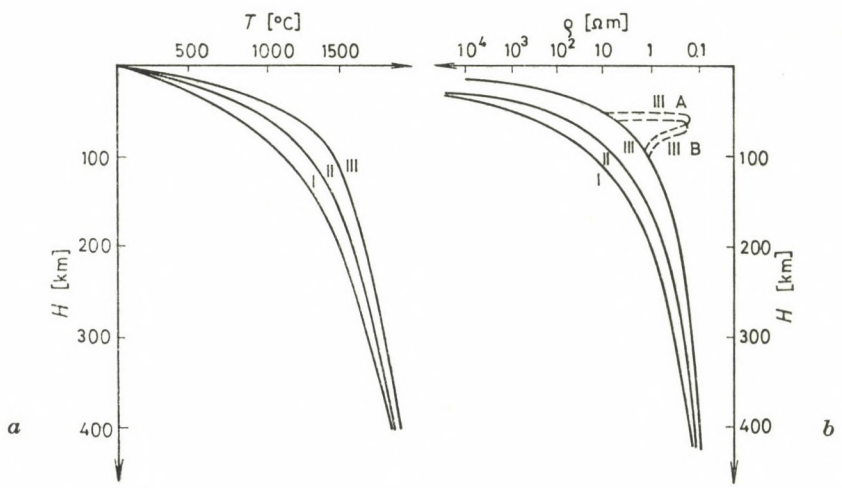


Fig. 4. Geothermal (a) and the corresponding geoelectric (b) models of the upper mantle

ing to these lines are given in Figure 4. The theoretical MTS-curves calculated from the specific resistivity curves are presented in Figure 2. The northern group of the observed MTS curves lies between theoretical curves I and II; showing thus a good agreement with the model under consideration. The maxima of the MTS curves of the southern group lie considerably lower than the maximum of theoretical curve III. Here, evidently, melting of basalts takes place (Berdichevsky et al., 1971, 1972) and an intermediate conductive layer appears. Hence, the resistivity curve III presented in Figure 4, b needs corrections (Vanyan and Zabolotnaya, 1968). Introducing these corrections we pass from curve III to curve III-A (the beginning of the melting zone being at 50 km depth) and to curve III-B (beginning of the melting zone at 60 km depth). Now, the MTS-curves of the southern group lie between theoretical curves III-A and III-B calculated by the corrected data (Fig. 2). The corrected geoelectric cross-section is shown in Figure 3, d. Thus we have obtained a model that agrees in all details with the MTS results. Temperature in this model increases when approaching the Caucasus (according to geothermic data the heat flow along the profile increases from 1.8 to 2.0 HFU); in the southern part of the profile the temperature reaches the melting limit, and the intermediate conductive layer appears.

DISCUSSION OF THE RESULTS

If there are no melting zones in the upper mantle, its electrical conductivity increases smoothly with depth (at least to depths of 400 km where there is a possible electric conductivity jump owing to the olivine-spinel transition). In this situation the formal interpretation of the MTS curves based on models consisting of homogeneous layers gives results that are difficult to associate with any geoelectric boundaries (Lubimova and Feldman, 1970; Vanyan and Zabolotnaya, 1968). The use of models of media with gradients seems more fruitful. It is this approach we have applied in the present work. One of the most interesting results is the detection of a conductive layer at a depth of 40–60 km. This layer was discovered and traced in the South Caspian depression, along the eastern rim of the Siberian Platform, in Kamchatka. High tectonic activity and volcanic activity are characteristic of all these regions at the recent stage of not long ago (Borisov, 1967). The conductive layer usually disappears when going ever to stable platform regions. In Pre-Caucasus the area of the conducting layer's wedging out is related to the deep fault that possibly affects the upper mantle (Borisov, 1967). In the adjacent Caspian depression the area of the conductive layer's wedging out also coincides with the said fault (Berdichevsky et al., 1971) that separates the Epihercynian platform from the foredeep of the Alpine orogenic belt. It should be recalled that a similar picture is observed in the region of transition from the Baikal Rift zone to the Siberian Platform (Gornostaev et al., 1970). Thus the intermediate conductive layer may serve as an indicator of an activized state of the upper mantle.

REFERENCES

BERDICHEVSKY, M. N., DMITRIEV, V. I., BUBNOV, V. P., YAKOVLEV, I. YA., VARLAMOV, D. A., KONNOV, YU. K., 1973. Magnetotelluric sounding of horizontally inhomogeneous media (in Russian). *Izv. Akad. Nauk SSSR, Ser. Fiz. Zemli*, No. 1.

BERDICHEVSKY, M. N., DUBROVSKY, V. G., LUBIMOVA, E. A., MANAFLY, A. I., NEPESOV, K., FELDMAN, I. S., 1971. Anomalies of the upper mantle's electric conductivity and their geothermal interpretation (in Russian). *Izv. Akad. Nauk SSSR, Ser. Fiz. Zemli*, No. 7.

BERDICHEVSKY, M. N., VANYAN, L. L., FELDMAN, I. S., PORSTENDORFER, G., 1972. Conducting layers in the Earth's crust and upper mantle. *Gerlands Beitr. z. Geophys.* **81**, Nos 3–5.

BORISOV, A. A., 1967. Deep Structure of the USSR Territory According to Geophysical Data (in Russian). Nedra, Moscow.

GORNOSTAEV, V. P., MIKHALEVSKY, V. P., POSPEEV, V. V., 1970. Deep magnetotelluric sounding of the south of the Siberian Platform and the Baikal Rift zone (in Russian). *Geol. i Geofiz.* **4.**

KUTAS, R. I., GORDIENKO, V. V., 1972. The thermal field of the Carpathians and some problems of geothermics (in Russian). Energetika Geologicheskikh i Geofizicheskikh Protsessov, Nauka, Moscow.

LUBIMOVA, E. A., FELDMAN, I. S., 1970. Heat flow, temperature and electrical conductivity of the crust and upper mantle in the USSR. *Tectonophysics* **10.**

SMIRNOV, YA. B., 1970. The significance of geothermal investigations for the studies of the earth's crust and upper mantle (in Russian). Problemi Stroeniya Zemnoi Kory i Verkhnei Mantii, 7. Nauka, Moscow.

VANYAN, L. L., ZABOLOTNAYA, N. A., 1968. About the typical theoretical curves of deep electromagnetic sounding (in Russian). *Izv. Akad. Nauk SSSR, Ser. Fiz. Zemli*, No. 1.

DEEP MAGNETOTELLURIC SURVEYS IN TURKMENIA AND AZERBAIJAN

A. A. AVAGIMOV, T. ASHIROV, V. G. DUBROVSKY, K. NEPESOV

The Institute of Physics of the Earth and the Atmosphere of the Turkmen Academy of Sciences performed a series of deep magnetotelluric soundings in the southern part of the Turkmen SSR and in East Azerbaijan (jointly with the Azerbaijan Branch of the All-Union Research Institute of Geophysics, A. I. Manafly and A. S. Faradjaev), under the guidance of M. N. Berdichevsky.

The survey included the southern part of the Kara-Kum Platform and the South Caspian megadepression. The principal results of the surveys are described in the papers: Agakuliev et al. (1973), Berdichevsky et al. (1967, 1970, 1971), Dubrovsky and Nepesov (1970), Gokhberg et al. (1968).

The South Kara-Kum Platform is a part of the vast Turan-Scythian plate, covered with 2–5 km thick Meso-Cenozoic sediments. The Paleozoic basement of the Central Kara-Kum dome and the southern slope of the platform are represented by strongly metamorphosed sedimentary and effusive sedimentary rocks and are characterized by a high resistivity (100 Ωm and higher). The specific resistivity of the Meso-Cenozoic deposits varies in the range of 2–10 Ωm.

The zone connecting the platform and the epigeosynclinal system of Central Kopet Dag (Pre-Kopet-Dag foredeep) is characterized by an abrupt subsidence of the basement from 12 to 15 km and by an increased resistivity of the Meso-Cenozoic deposits up to 20–30 Ωm. In the southern part of this zone, in the Central Kopet-Dag meganticlinorium, deposits of relatively high resistivity of Neocomian age come out to the surface.

The South Caspian megadepression is an immense basin including the West Turkmen depression the Nizhnyaya-Kura depression and the South Caspian depression, the latter being confined in the east, in the south, and in the west by the mountainous structures of Kopet-Dag, Elburs and the Caucasus composed of high resistivity rocks. In the north-east the depression is separated from the Epihercynian Kara-Kum Platform by the Kuba-Dag — Bolshoi Balkhan zone and in the north-west it is bordered by the Eastern Caucasus foredeep. The western boundary of the megadepression is the Kyurdamir-Talysh deep fault separating zones of sharp subsidence and sharp uplift of the crystalline basement in the Nizhnyaya-Kura depression. In the megadepression itself a thinning out and a practically complete wedging out of the "granitic" layer of the earth's crust is observed within the South Caspian area, and the thickness of the earth' crust is reduced in this region to 25–30 km while the thickness of the "basaltic" layer does not exceed 10 km (Borisov, 1967). The megadepression is filled with highly conductive Meso-Cenozoic and probably Paleozoic de-

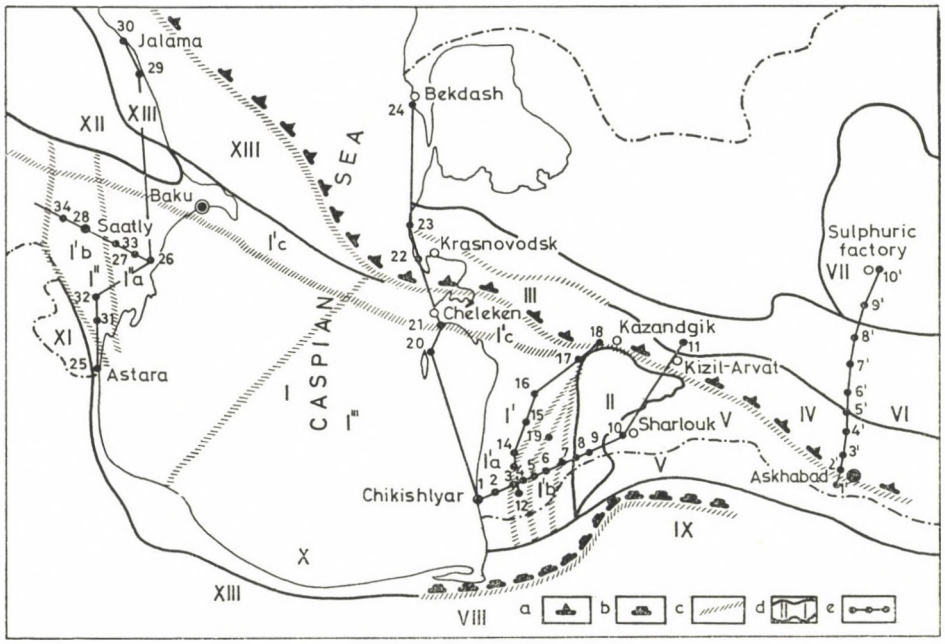


Fig. 1. Tectonic scheme of the south-western part of Middle Asia and sites of deep MTS

a – boundaries of the Late Alpine folding; b – boundaries of the Early Alpine folding; c – main fractures; d – boundaries of tectonic provinces; e – profiles and sites of deep MTS

Principal tectonic elements: I – South Caspian megadepression; I' – West Turkmen depression; I' a Gograndag-Chikishlyar stage; I' b – Aladag-Messarian stage; I' c – Near-Balkhano-Apsheron depression; I'' – Nizhnyaya-Kura depression; I'' a – Shirvan tectonic zone; I'' b – Mugan tectonic zone (zone of the basement uplift); I''' South Caspian Sea Basin; II – West Kopet-Dag meganticlinorium; III – Kubadag-Bolshoi Balkhan meganticlinorium; IV – Ante-Kopet-Dag foredeep; V – meganticlinorium of Central Kopet-Dag; VI – southern slope of the Kara-Kum Platform; VII – Central Kara-Kum dome; VIII – Elburs meganticlinorium; IX – Aladag-Binalud meganticlinorium; X – Ante-Elburs (Gorgan) depression; XI – Talysh meganticlinorium; XII – Great Caucasus meganticlinorium; XIII – Pre-Caucasus foredeep

posits, 20–25 km thick and of $7–15 \times 10^3\ \Omega^{-1}$ total longitudinal conductivity. At least half of this mass consists of Neogene-Quaternary deposits.

The tectonic scheme (Fig. 1) shows the location of MTS sites.

The processing of variation data was made by means of Fourier transform with respect to the circular frequency ω (irregular variations, bay-type disturbances, S_q-variations) and by Laplace transform with respect to the real parameter P (initial phases of magnetic storms Sc and sudden impulses Si). From the results of the analysis the impedance tensor components were determined and the ϱ_T and ϱ_P curves were constructed (Berdichevsky et al., 1967; Dubrovsky et al., 1970; Gokhberg, 1968).

In Figure 2 a map of polar diagrams of the main impedances $|Z_{xy}(\alpha)|$

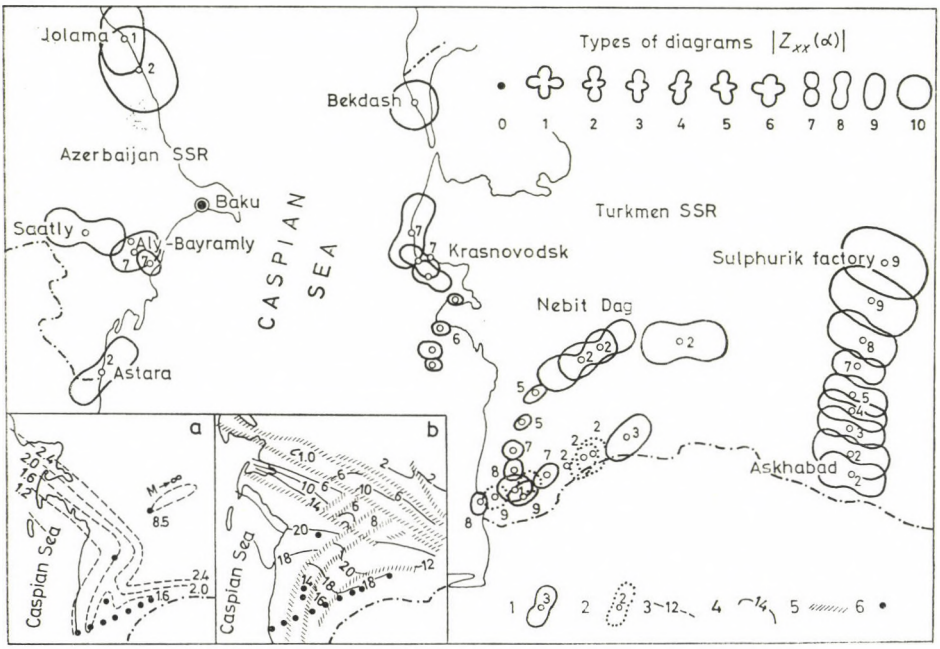


Fig. 2. Map of polar diagrams of the modulus of the main impedance $|Z_{xy}(\alpha)|$ and of diagram types of the moduli of secondary impedance $|Z_{xx}(\alpha)|$

a – Shematic map of the parameter $M = |Z_{xy}|^{max}/|Z_{xy}|^{min}$; b – structural scheme of the basement surface of south-western Turkmenia after Lykov and Odekov (Ishutin et al., 1970). 1 – $|Z_{xy}(\alpha)|$ diagrams ($T = 60$ min); 2 – $|Z_{xy}(\alpha)|$ diagram ($P = 8$ hour^{-1}). The major semi-axis of the diagrams correspond to 0.1 mV/γ. The number at the centre of the diagrams $|Z_{xy}(\alpha)|$ denotes the type of diagrams $|Z_{xx}(\alpha)|$; 3 – contour lines of parameter M; 4 – contour lines of the basement surface km; 5 – deep faults; 6 – sites of MTS

and of diagram types of secondary impedances $|Z_{xx}(\alpha)|$ is presented for the variation period $T = 60$ min (the numbers at the centre of the main impedance diagrams correspond to the type of the secondary impedance diagram). The map shows that field distortions are of regional as well as of local nature. Regional distortions are associated with the highly resistive mountainous framing of the territory, while local distortions are consequences of the relief structures of the basement and the intermediate high-resistivity layers. The geoelectric inhomogeneities distorting the field can be approximated by two-dimensional and three-dimensional models.

MTS-RESULTS SOUTH OF THE KARA-KUM PLATFORM

Figure 1 shows that the profile 1'–10' can be divided into two zones. The southern part (sites 1'–6') is characterized by linear tectonic features, the principal structures and fault zones running parallel to Central Kopet-

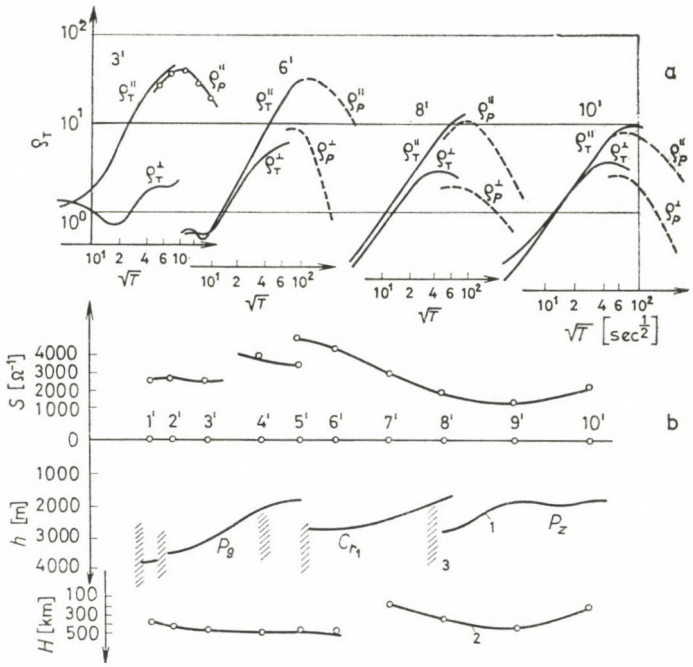


Fig. 3. Typical MTS-curves and a geoelectric cross section of the earth's crust and upper mantle along 1'–10'. a) MTS-curves for sites 3', 6', 8', 10', $\varrho_T^{\perp}$, $\varrho_P^{\perp}$ – transverse MTS-curves, $\varrho_T^{\parallel}$, $\varrho_P^{\parallel}$ – longitudinal MTS curves; b) geoelectric cross section of the earth's crust and upper mantle along 1'–10'; S – longitudinal conductance of the conducting strata in Ω^{-1}; 1 – surface of the basic horizon from MTS data; 2 – surface of the conducting zone in the upper mantle; 3 – fractures in the earth's crust

Dag composed of high-resistivity rocks. The northern zone (sites 7'–10') lies on the southern slope of the Kara-Kum platform and on the Central Kara-Kum dome with pronounced non-linear tectonic features.

The MTS curves are presented in Figure 3, a. Longitudinal $\varrho^{\parallel}$ and transverse $\varrho^{\perp}$ curves are oriented along and across Kopet-Dag. They refer to a three-layer cross section with a conducting surface layer (Quaternary, Tertiary and partly Mesozoic deposits), with a high-resistivity basement and with the upper mantle being composed of high-resistivity parts.

The transverse curves lie everywhere below the longitudinal ones. They are distorted by the *edge effect* associated with the mountainous framing of Central Kopet-Dag impeding the current flow in transverse direction. When moving off from Kopet-Dag the edge effect weakens, shifting to lower frequencies. These results are in good agreement with the studies carried out on models (Kovtun et al., 1970; Gorbunova et al., 1974).

The distortions of longitudinal $\varrho^{\parallel}$ curves are relatively slight. The distortions are appreciable only in the Central Kara-Kum dome region where

they are associated with the *flow-around effect*. All these features are distinctly seen in the diagrams of $|Z_{xy}(\alpha)|$ and $|Z_{xx}(\alpha)|$. The longitudinal conductivity S' of the conductive strata and the depth H to the conductive part of the mantle were determined from the longitudinal curves. The geoelectric cross section is presented in Figure 3, b. In the southern zone (linear tectonic features) the S-effect is imperceptible: a 70% increase of S is not accompanied by any reduction of H (as a matter of fact, H even increases by 20%). In the northern zone (non-linear tectonic features) the S-effect is clearly seen: a 300% increase of H corresponds to a 200% decrease of S. Thus, it can be assumed with a certain confidence that in the southern part of the profile where H values are stable and where no distortion of the longitudinal MTS curves is expected the mean depth of the conductive part of the mantle is $H = 500$ km. In the northern part of the profile the MTS curves are apparently distorted, and their formal interpretation gives H values varying from 170 to 470 km that are naturally not significant.

MTS RESULTS IN THE SOUTH CASPIAN MEGADEPRESSION

The principal feature of the ϱ_T curves for the western part of the Turkmen SSR is the presence of minima and inflections in the 20–60 min period range. This peculiarity is preserved for every orientation of the ϱ_T curves (Fig. 4, a).

The predominance of local distortions over regional distortions is another characteristic feature of these curves. Indeed, it is seen from Figure 2 that the shape and orientation of the impedance polar diagrams are in good agreement with the character of the local tectonic elements (such as the Balkhan depression, Messerian zone of block uplifts of the Aladag-Messerian stage, fractures), as well as with the strike of individual zones of the mountainous framing (Danatin intermountain basin, the course of ridges and valleys of Western Kopet-Dag, the western pericline of the Kubadag-Bolshoi Balkhan zone). For instance, the flow of telluric currents around the pericline zone of Kubadag-Bolshoi Balkhan and their canalization along the intermountain basins and valleys of Western Kopet-Dag can be clearly seen on the map of impedance diagrams.

Studies involving model experiments have demonstrated that the occurrence of inflections and minima on MTS curves cannot be explained by the distortions caused by the high-resistivity mountainous framing of the South Caspian megadepression (Kovtun et al., 1970; Gorbunova et al., 1974).

The MTS curves were oriented across ($\varrho^{\perp}$) and along ($\varrho^{\parallel}$) the local inhomogeneities and individual tectonic elements of the mountainous framing. These curves are presented in Figure 4,b.

We can see that the longitudinal curves form a well-ordered group. In the inner part of the depression (sites 1–6, 12–16, 19 and 20) they have extensive descending branches which lie between depth lines $h = 40$ km and $h = 60$ km. The curves for the depression periphery and outside areas

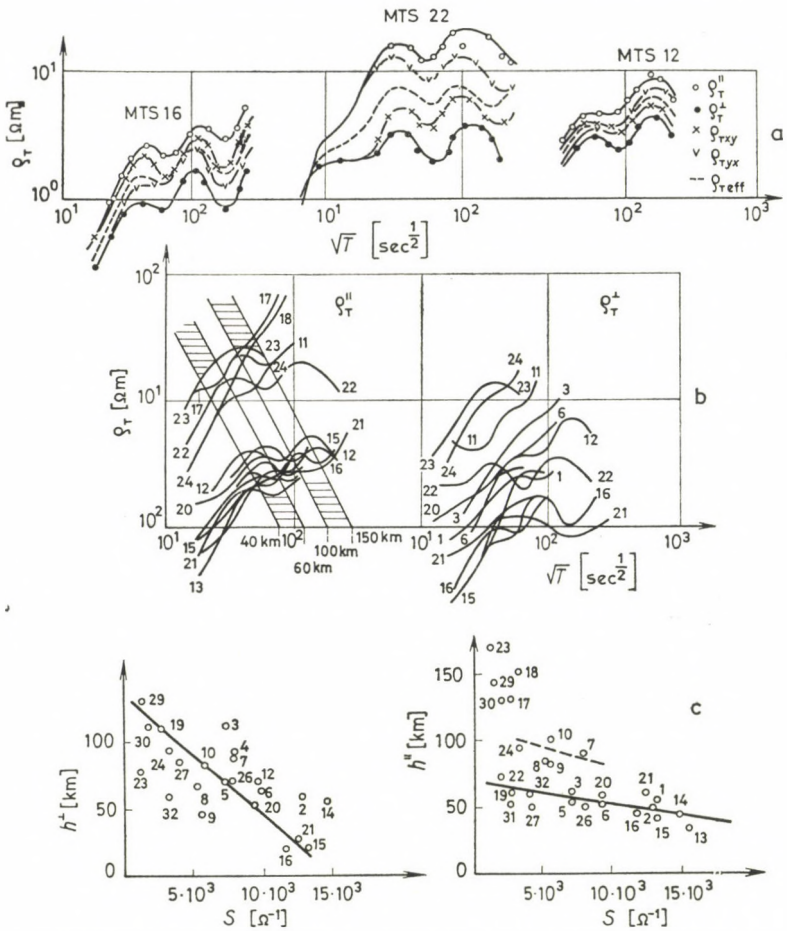


Fig. 4. a – Examples of curves for ϱ_T oriented in different directions; b – Familiesof curves for $\varrho_T^{\parallel}$ (longitudinal) and $\varrho_T^{\perp}$ (transverse); c – Dependence of the depth of the intermediate conductive layer upon longitudinal conductivity of the sedimentary cover for longitudinal and transverse polarization of the field

of the depression (sites 7–10, 23, 24) are represented by rising branches with a more or less apparent inflection between depth lines $h = 100$ km and $h = 150$ km. At a number of sites located in the inner part of the West Turkmen depression (sites 12, 16) as well as at its periphery (site 22) there are two inflections on the $\varrho^{\parallel}$ curves corresponding to the depth ranges 40–60 km and 100–150 km.

The transverse $\varrho^{\perp}$ curves are disordered. Their appearance resembles the longitudinal $\varrho^{\parallel}$ curves, but their shape varies irregularly and the position of the descending branches and of the inflections are rather chaotic. These results are in complete agreement with the theory and practice of magneto-

telluric sounding. The well-ordered pattern of $\varrho^{\parallel}$ curves and the chaotic behaviour of $\varrho^{\perp}$ curves are accounted for by the much lower distortions of the longitudinal component of the electric field.

A similar situation is characteristic of the western coast of the Caspian Sea (Azerbaijan). The inflections and minima of curves $\varrho^{\parallel}$ correspond to the depth ranges $h = 40$–60 km (sites 25, 26, 27, 31, 32) and $h = 100$–150 km (sites 29, 30). Figures 2 and 5, a show that in this region the impedance diagrams $|Z_{xy}(\alpha)|$ reflect regional as well as local specific tectonic features. Thus, the orientation of diagrams $|Z_{xy}(\alpha)|$ for the northern part of the territory under study is in agreement with the strike of the East Pre-Caucasus foredeep, and for the central part of the territory it agrees with the strike of the Kura megasynclinorium. Figure 5 presents longitudinal and transverse MTS curves for profile 25–30 and the results of their formal interpretation.

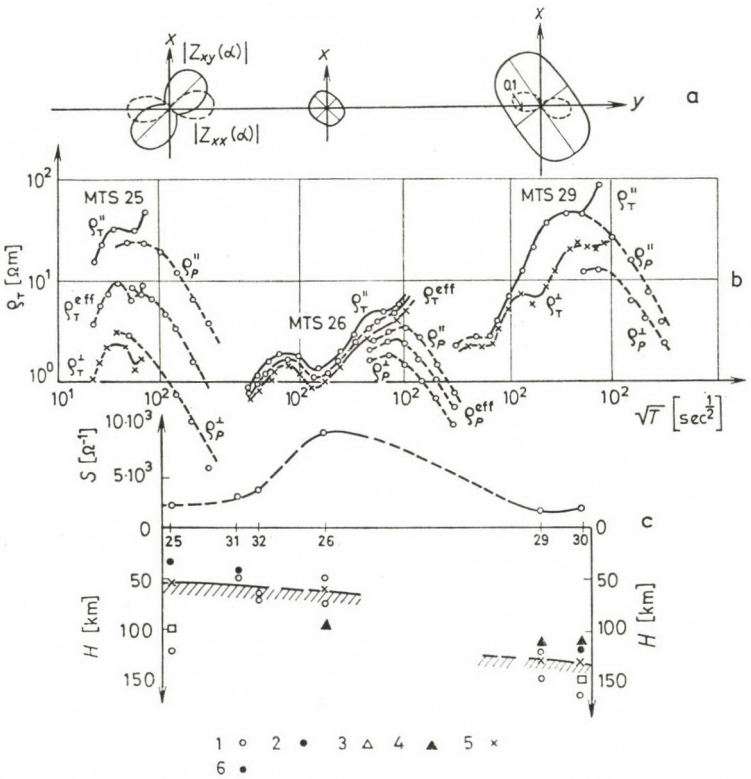


Fig. 5. a – Polar diagrams of the moduli $|Z_{xy}|$ and $|Z_{xx}|$ for profile 25–30 and for $T = 1$ hour; b – curves for ϱ_T and ϱ_P; c – geoelectric boundaries in the upper mantle from profile 25—30

1, 3 – the upper boundary of the intermediate conducting layer in the upper mantle determined from curves for $\varrho_T^{\parallel}$ and $\varrho_P^{\parallel}$, respectively; 2, 4 – same boundary from curves for $\varrho_T^{\perp}$ and $\varrho_T^{\perp}$; 5 – same boundary from effective curves; 6 – total longitudinal conductivity of the sedimentary cover

The formal interpretation of the MTS curves distinguishes one or two intermediate conducting layers in the cross section of the upper mantle of the South Caspian megadepression.

Diagrams for $h^{\parallel}(S)$ and $h^{\perp}(S)$ are presented in Figure 4, $h^{\parallel}$ and $h^{\perp}$ being depths of the conducting layer determined from the $\varrho^{\parallel}$ and $\varrho^{\perp}$ curves, respectively, and S is the total longitudinal conductivity of the sedimentary beds. In most cases a close relation is observed between the $h^{\perp}$ and S values: a decrease of S is accompanied by an increase of $h^{\perp}$. This relation is caused by the strong influence exerted by the basement structures upon the transverse component of the electric field. As a matter of fact, the transverse component of the electric field increases over the local basement uplifts and the right-hand branches of the MTS curves are shifted upwards which causes an overestimation of the depth of the conductive layer of the upper mantle (S-effect). The diagram for $h^{\parallel}(S)$ plotted according to the formal interpretation of longitudinal $\varrho^{\parallel}$ curves shows a different pattern. Here the connection between $h^{\parallel}$ and S is less pronounced (the S-effect is as a rule insignificant). So, the lesser distortion of longitudinal curves as compared with the transverse ones is confirmed once again.

It should be noted that three groups of points can be distinguished on diagram $h^{\parallel}(S)$ that correspond to three depth levels of the conductive layer. The lower group of points lying at the 40–60 level corresponds to the inner parts of the West-Turkmen and Nizhnyaya-Kura depressions. The points lying at the 90–100 km level correspond to the outlying parts of the megadepression. The third group of points (100–150 km level) corresponds to the regions where canalization and flow-around effects are distinctly apparent. These results may be considered as distorted. Let it be recalled that in cases when there is a flow-around the effective curves ϱ_{eff} give the most reliable results.

Because of the principle of equivalence it is not possible to unambiguously determine both the thickness and specific resistivity of the conductive layer. However, for most stations it is possible to determine the longitudinal conductivity ΔS of the layer. In the near-slope belt of the South Caspian megadepression ΔS attains $10–20 \cdot 10^3\ \Omega^{-1}$, in the peripheral part of the megadepression it decreases to $5 \cdot 10^3\ \Omega^{-1}$. According to rough estimates, the thickness of the conducting layer in near-slope belt of the megadepression does not exceed 10–20 km and the specific resistivity is of the order of some Ωm.

Let us now consider the results obtained for the individual profiles.

In the west, profile 1–11 runs across the Messerian zone of the basement block uplifts with submeridional strike, crosses West Kopet-Dag and reaches the Kara-Kum Platform. Within the western part of the profile the conducting layer occurs nearly horizontally at 50–55 km depth (sites 1–7). When approaching West Kopet-Dag (sites 8–10) the conductive layer is revealed at a depth of 100–110 km. In transition to the Kara-Kum Platform (site 11) there is no conducting layer. Here a conducting zone is revealed in the upper mantle at 500–600 km depths.

Profile 12–18 connects the West Turkmen depression with the Kara-Kum Platform across the Danatin intermountain basin which separates West Kopet-Dag from Maly Balkhan. At sites 12, 13, 14, 15 and 16 the

conducting layer occurs at 40–60 km depths. At sites 12, 16 a second conducting layer is revealed at 130–150 km. At sites 17, 18 the longitudinal curves are oriented in NE direction which coincides with the Danatin Basin axis. At site 17 the conducting layer occurs at 130–150 km depths, while it is only slightly manifested at site 18. The significance of these results is subject to doubt because in the Danatin Basin the current density increases, and the intensity of the longitudinal component of the electric field can have an anomalously high value.

Profile 1–24 passes along the eastern coast of the Caspian Sea and crosses the Gograndag-Chikishlar stage and the Balkhan-Apsheron depression stretching along the northern slope of the South Caspian megadepression. In the southern part of the profile (sites 1–22) the conductive layer occurs at 50–60 km depth, at sites 23 and 24 it is revealed at 100–130 km. At site

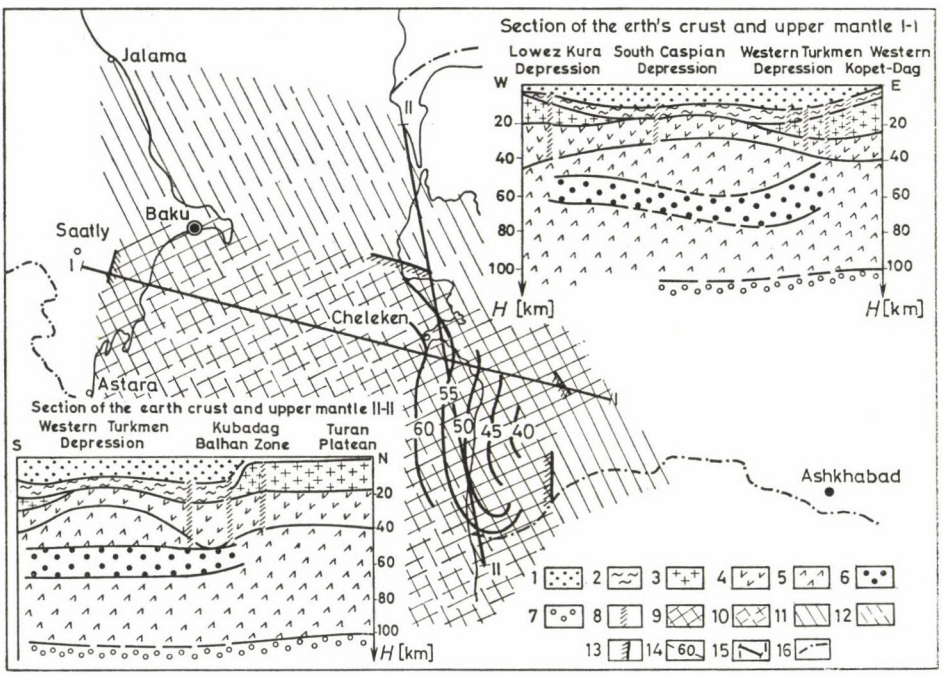


Fig. 6. Scheme of location of the high-conductivity zones in the upper mantle at 40–60 and 100–130 km depths in the SW part of Middle Asia, schematic cross sections of the earth's crust and upper mantle from the profiles on the South Caspian megadepression

1 – sedimentary complex of Meso-Cenozoic age; 2 – consolidated Paleozoic sedimentary complex; 3 – "granitic" layer; 4 – "basaltic" layer; 5 – upper mantle; 6 – zones of high electric conductivity, established with confidence; 7 – same zones, without much confidence; 8 – deep faults; 9–12 – zone of occurrence of the intermediate conductive layer at 40–60 and 100–130 km depths, delineated with confidence; 13 – established boundaries of the zone of high electric conductivity at 40–60 km depth; 14 – contour lines of the first conductive layer in kms; 15 – profiles from which schematic cross sections of the earth's crust and upper mantle are presented; 16 – USSR frontier

22 another conductive layer is observed at the same depths as in the northern part of the profile.

Profile 26–34 crosses the western slope of the megadepression. At sites 26–27, in the near-slope belt of the megadepression, the intermediate conductive layer occurs at a depth of 50–55 km. It is decisive that at site 28 lying outside the megadepression there is no such layer. Here a conductive zone is revealed in the upper mantle at 350–400 km depth.

The results obtained for profile 25–30 are presented in Figure 5.

So, two intermediate zones of high conductivity (40–60 km and 100–130 km) are outlined in the South Caspian megadepression; this allows two versions of interpretation:

1. The transition from 40–60 km to 100–130 km depths is associated with the *S*-effect. In this case it is possible to assume that there is only one conductive layer at a mean depth of 60–100 km.

2. There are two conductive layers. The first is extended at a depth of 40–60 km in the slope belt of the megadepression and, possibly, also in the South Caspian area. The region of occurrence of the second layer comprises the central and peripheral parts of the megadepression, and in the north the coast of the Central Caspian as well. We consider this explanation more plausible.

Presented in Figure 6 are schemes of geological and geophysical cross sections of the earth's crust and upper mantle constructed in quasi-latitudinal and meridional directions as well as a map of contour lines of the first layer's surface showing the zones of expansion of both layers.

THE POSSIBLE NATURE OF THE HIGH CONDUCTIVITY ZONES IN THE UPPER MANTLE OF THE SOUTH CASPIAN MEGADEPRESSION

In order to elucidate the possible nature of the intermediate high conductivity zones in the upper mantle of the South Caspian megadepression we review some results of geological and geophysical studies; as these results are characteristic, directly and indirectly, of the structural features and physical conditions of the upper mantle in this region.

Geothermal investigations carried out over the megadepression point to a high thermal activity of the interior of the earth. Dzhibuti (1962), in particular, pointing out a regional thermal anomaly in the West Turkmen depression, associated it in the main with a thermal source of deep origin. His estimated heat-flow values for the depth interval of 1000–1500 m are 1.48–2.66 HFU.

The heat flow determined by Sukharev et al. (1969) for the western slope of the megadepression varies within the limits 0.9–2.23 HFU; the maximum values correspond to the structures, domes and to the vicinity of mud volcanoes widely developed in the near-slope belts of the megadepression.

Oceanographic studies carried out in the northern part of the South Caspian area in order to determine heat flows gave $q = 1.0$–2.4 HFU (Berdichevsky et al., 1971).

According to our preliminary studies, the heat flows amount to 0.8–2.0 HFU. The lowest value of q is observed in an area of great thickness of Neogene-Quaternary sediments. We assume this circumstance is associated with the distortion of the geothermal regime in the upper layers of the earth's crust during sedimentation.

The intensified geothermal activity in the deep interior of the earth in the South Caspian megadepression is also indicated by the decrease of seismic wave velocities beginning at the Moho discontinuity (8.0 km/sec) and a relative deconsolidation of the upper mantle rock: $\delta = 3.15$–3.20 g/cm^3 (Aksenovich et al., 1962; Fotiadi, 1965; Tsimelzon, 1967).

That seismic foci are mainly confined to the basement fractures is also a characteristic feature of the region. The absence of subcrustal earthquake foci in the South Caspian megadepression and the increased absorption of elastic vibrations arriving from distant earthquakes at depths exceeding 40–50 km (Shebalin, 1960) indicate deconsolidation and, perhaps, a partial melting of the upper mantle rocks.

Of equal importance are the results of the study of stresses at the earthquake foci in the Nizhnyaya-Kura depression and in the South Caspian. The transition from the mountainous regions to the areas of the geosynclinal warping of the earth's crust is accompanied by variations of both the depths of earthquake foci and of the character of stress distribution. It has been ascertained that the orientation of the axes of principal stresses at earthquake foci in the Caspian Sea and in the Nizhnyaya-Kura depression is in agreement with the distribution of stress axes at earthquake foci in the earth's rift zones that are characterized by a horizontal tension oriented roughly perpendicularly to the strike of structures. All these facts point

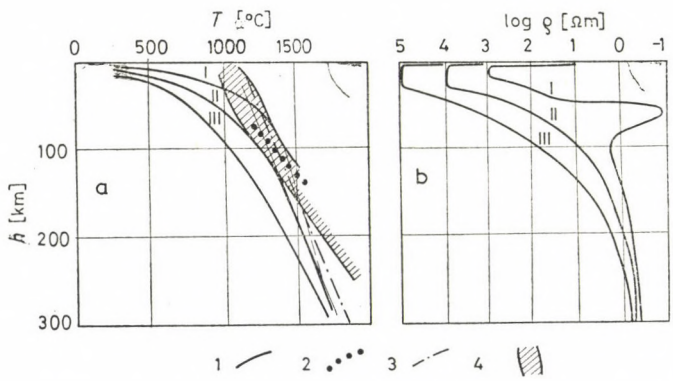


Fig. 7. Temperature curves and melting curves (a) and curves of electric conductivity (b)
a – I, II, III – temperature distribution curves for different surface heat flows: I – 2.1 HFU; II – 1.9 HFU; III – 1.7 HFU. 1, 2, 3 – curves of the beginning of melting: 1 – quartz tholeiite; 2 – pyrolite; 3 – basalt; 4 – region of the beginning of basalt melting under the conditions of non-hydrostatic pressure; b – electric conductivity curves corresponding to temperature distributions I (melting taken into account), II and III

to an anomalous structure of the upper mantle in the South Caspian megadepression and, in particular, to its possible deconsolidation and a partial melting in the process of local heating-up. We also refer to the numerous mud-eruptive manifestations (more than 300), the thermal sources and the anomalously high pressures in the deep strata of the South Caspian megadepression.

To corroborate this hypothesis we present some results of the calculations of electric conductivity and temperature distribution in the upper mantle performed by Feldman (cf. Berdichevsky et al., 1971).

Figure 7 shows temperature curves calculated for different values of heat flows, melting curves for rocks and mineralogical associations corresponding to our present knowledge of the composition of the upper mantle, and curves of electric conductivity of the mantle for different temperature distributions.

Temperature curve 1 (Fig. 7, a) was obtained by V. K. Vlasov at the Computation Centre of the Moscow University for $q = 2.1$ HFU and for a 43 km thick earth's crust, the sedimentary layer and the "basaltic" layer accounting for 20 km and 23 km, respectively, which corresponds to the crustal cross section in the near-slope zone of the South Caspian megadepression where heat flow measurements were carried out. When calculating thermal conductivity, both the radiation and the phonon components were taken into account depending on the temperature and pressure variations with depth (Lubimova, 1968). The distribution of the heat generation density in the mantle as dependent on depth was taken from Masuda (1965). Temperature curves for smaller heat flow values were calculated by Smirnov (1968).

It should be noted that the temperature curves I and II cross the melting curves at about 50–100 km depths. Melting of rocks in the upper mantle is possible at these depths and possibly also at lesser depths if the decrease in pressure caused by horizontal tension in the South Caspian megadepression is taken into account (Agalarova, 1969, 1971). Laboratory measurements at high thermodynamical parameters show that the electric conductivity of rocks increases during melting by 2–3 orders of magnitude (Khitarov and Slutsky, 1962). A jump in electric conductivity occurs at the initial moment of melting when a shell structure forming a continuous net is developed. A further increase in the concentration of the liquid phase has nearly no effect on electric conductivity. So at depth where the ultimate concentration of the liquid phase sufficient for the formation of the continuous shell net is reached, a stepwise increase in the electric conductivity is observed and an intermediate conductive layer with well-defined boundaries is formed. Electric conductivity curves for the upper mantle corresponding to the temperature data given above are shown in Figure 7. The parameters used for the conductivity in olivines are due to Feldman and Bondarenko of the Institute of Physics of the Earth of the Academy of Sciences of the USSR.

When a temperature curve crosses a melting curve, the electric conductivity curve has a maximum indicating the presence of a liquid phase in a melting zone (Fig. 7, b, curve I). It appears that it is this melting zone that we have detected below the South Caspian megadepression.

REFERENCES

AGAKULIEV, G., ASHIROV, T., DUBROVSKY, V. G., KASUMOVA, L., MANAFLY, A. I., NEPESOV, K., FARADJAEV, A. S., 1973. Specific features of the geoelectric structure of the upper mantle in Azerbaijan (in Russian). *Izv. Akad. Nauk Turkmenskoi SSR, Ser. Fiz. Tekhn. Khim. i Geol. Nauk*, No. 1.

AGALAROVA, E. B., 1969. Peculiarities in the orientation of stresses acting at earthquake foci on the Apsheron peninsula and in the Caspean Sea (in Russian). *Izv. Akad. Nauk SSSR, Ser. Fiz. Zemli*, No. 7.

AGALAROVA, E. B., 1971. On the orientation of stresses at earthquake foci in the Nizhnyaya-Kura depression (in Russian). *Izv. Akad. Nauk SSSR, Ser. Fiz. Zemli*, No. 2.

AKSENOVICH, G. I., ARONOV, N. E., GALPERIN, E. U., 1962. Deep Seismic Sounding of the Central Part of the Caspian Sea (in Russian). Akad Nauk SSSR.

BERDICHEVSKY, M. N., DUBROVSKY, V. G., NEPESOV, K., SOLOKHOV, V. V., FAINBERG, E. B., 1970. Geoelectric characteristics of the earth's crust and upper mantle in Turkmenia (in Russian). *Izv. Akad. Nauk SSSR, Ser. Fiz. Zemli*, No. 11.

BERDICHEVSKY, M. N., DUBROVSKY, V. G., LUBIMOVA, E. A., MANAFLY, A. I., NEPESOV, K., FELDMAN, I. S., 1971. Anomalies of the upper mantle's electric conductivity and their geothermal interpretation (in Russian). *Izv. Akad. Nauk SSSR, Ser. Fiz. Zemli*, No. 7.

BERDICHEVSKY, M. N., VANYAN, L. L., GOKHBERG, M. B., DUBROVSKY, V. G., FAINBERG, E. B., 1967. New evidence in the field of deep magnetotelluric soundings (in Russian). *Dokl. Akad. Nauk SSSR*, **77**, No. 3.

BORISOV, A. A., 1967. Deep Structure of the USSR Territory According to Geophysical Data (in Russian). Nedra, Moscow.

DAVYDOVA, N. I., 1972. Possibilities of the deep seismic sounding method for studies of deep seismic boundaries (in Russian). Seismicheskie Svoistva Granitsy Mokhorovichicha. Nedra, Moscow.

DUBROVSKY, V. G., NEPESOV, K., 1970. Specific features of the geoelectric structure of the central and southwestern parts of Turkmenia from electromagnetic sounding data (in Russian). *Acta Geod. Geophys. Mont. Hung.* **5**, Nos 1–2.

DUBROVSKY, V. G., NIKOLAEVA, L. S., FIRSOVA, V. E., 1970. Experience in using S_q-variations for deep magnetotelluric soundings of Turkmenia (in Russian). *Izv. Akad. Nauk SSSR, Ser. Fiz. Zemli*, No. 11.

DZHIBUTI, S. S., 1962. Geothermal Conditions of Subterranean Waters in the West Turkmen Oil and Gas Bearing Basin (in Russian). Akad. Nauk SSSR.

FOTIADI, E. E., 1965. Some regional peculiarities of the deep structure of the earth's crust in the territory of the USSR in the light of geophysical data (in Russian). *Geol. i Geofiz.*, No. 10.

GOKHBERG, M. B., 1968. A simplified method of processing magnetic storms with sudden commencement for purposes of deep sounding (in Russian). *Izv. Akad. Nauk SSSR, Ser. Fiz. Zemli*, No. 12.

GOKHBERG, M. B., DUBROVSKY, V. G., NEPESOV, K., 1968. Results of using magnetic storms for deep sounding of Turkmenia (in Russian). *Izv. Akad. Nauk SSSR, Ser. Fiz. Zemli*, No. 12.

GORBUNOVA, L. K., DUBROVSKY, V. G., DOBROVOLSKAYA, M. A., KOVTUN, A. A., NEPESOV, K., FAINBERG, E. B., 1974. Structure of the magnetotelluric field in the vicinity of an outcrop of a highly resistive basement (physical modelling) (in Russian). Geomagnitnye Issledovaniya, Nauka, Moscow.

ISHUTIN, V. V., LYKOV, V. I., ODEKOV, A. A., 1970. Geotectonic peculiarities of the deep structure of Turkmenia (in Russian). *Izv. Akad. Nauk Turkmenskoi SSR, Ser. Fiz. Tekhn. Khim. i Biol. Nauk*, No. 2.

KHITAROV, N. I., SLUTSKY, A. B., 1962. Influence of pressure upon the melting temperature of albite and basalt (in Russian). *Geokhimiya*, No. 12.

KOVTUN, A. A., GLADKY, G. D., DOBROVOLSKAYA, M. A., NEPESOV, K., 1970. Modelling of magnetotelluric fields over a basement uplift (in Russian). *Izv. Akad. Nauk SSSR, Ser. Fiz. Zemli*, No. 12.

LUBIMOVA, E. A., 1968. Thermal Fields of the Earth and the Moon (in Russian). Nauka, Moscow.

MASUDA, A., 1965. Geothermal and petrogenetic implications of the analysis of the distributional relationship between thorium and uranium. *Tectonophysics* **2**, No. 1.
SHEBALIN, N. V., 1960. Determination of the depth of earthquake foci from magnitude *M* and macroseismic data (in Russian). *Trudy Inst. Geofiz. Akad. Nauk Gruz SSR*, **18**, Tbilisi.
SHEINMANN, YU. M., 1968. Essays on Deep Geology (in Russian). Nedra, Moscow.
SMIRNOV, YA. B., 1968. Relationship of the thermal field to the structure and development of the earth's crust and upper mantle (in Russian). *Geotektonika*, No. 6.
SUKHAREV, G. M., TARANUKHA, YU. K., VLASOVA, S. P., 1969. Heat flow from the deep interior of Azerbaijan (in Russian). *Sovietskaya Geologiya*, No. 8.
TSIMELZON, I. O., 1967. Application of gravimetry for tectonic studies of Azerbaijan and for prospecting of oil- and gas-bearing structures (in Russian). Metodika i Razvedki Geofizicheskoi Razvedki. Nedra, Moscow.
YODER, G. S., TILLE, K. E., 1965. Origin of Basaltic Magma (in Russian). Mir, Moscow.

DEEP MAGNETOTELLURIC SURVEYS OF THE TUNGUS SYNECLISE AND ON THE WEST SIBERIAN PLATE

A. S. SAFONOV, V. M. BUBNOV, B. K. SYSOEV,
G. A. CHERNYAVSKY, O. M. CHINAREVA, V. A. SHAPOREV

Magnetotelluric soundings of the Tungus syneclise and of the West Siberian Plate were performed by the Krasnoyarsk and Tyumen Geological Office. Analysis of the results was carried out under the guidance of M. N. Berdichevsky. These studies are of a methodical interest because of the extensive use of the MTS phase curves.

TUNGUS SYNECLISE

Rocks of late Pre-Cambrian, Paleozoic and Early Mesozoic are present in the Tungus syneclise. The sedimentary section can be divided into three geoelectric complexes characteristic for all the territory of East Siberia.

The lower conductive complex occurs directly upon the sedimentary Proterozoic metamorphosed or high-resistivity rocks or Archean crystalline rocks. Carbonaceous-terrigenous Riphean rocks and Early Cambrian rocks are parts of its composition. Specific resistivity of this complex is 3–10 Ωm, its thickness varies from 2 to 4 km.

The middle geoelectric complex includes carbonaceous-halogenous formations of the Early and Middle Cambrian. This mass represented by interbanded salts, dolomites, anhydrites and limestones possesses a high specific resistivity and has a thickness of 1–3 km.

The upper complex is represented by carbonaceous-terrigenous rocks of the Late Cambrian, Ordovician, Silurian, Carboniferous periods, Permian and Triassic. Specific resistivity of these rocks varies from 6–10 Ωm (deposits of the Tungus series) to 500–1000 Ωm (tufogene rocks and frozen mass). The thickness of the complex is 2–3 km.

Typical MTS curves obtained in the Tungus syneclise are shown in Figure 1. Curves for ϱ_{max}, ϱ_{min}, ϱ_{eff}, φ_{max}, φ_{min}, φ_{eff}, constructed according to the maximum, minimum and effective values of the impedance are presented. It is possible to group these curves into four types. Let us take as an example the profile running along the Nizhnyaya Tunguska River. Here sounding curves obtained in the Turukhansk region belong to the *first type*. Curves for ϱ_T and φ_T are represented by a descending branch, a minimum and a rising branch. Curves for φ_T for different orientations of the measuring lines practically coincide. Curves for the lower reaches of the Nizhnyaya Tunguska River belong to the *second type*. Curves for ϱ_T possess a rising branch, a maximum and a descending branch, and curves for φ_T a maximum and a descending branch. Curves for φ_T are practically independent of the orientation of measuring lines. The *third type*

includes amplitude curves represented by a rising branch and phase curves possessing a maximum and a descending branch.

Variations in the orientation of measuring lines do not practically affect these phase curves. The *fourth type* differs from the third one in that the φ_T curves obtained for different orientations of the measuring lines considerably diverge in the domain of the rising branches and coincide when passing to the descending branches.

So, all types of amplitude curves are characterized by the independence of their form on the orientation of measuring lines, though they are located at different levels. The phase curves of the first, second and third types for different orientations coincide, and only the curves of the fourth type diverge in the domain of rising branches.

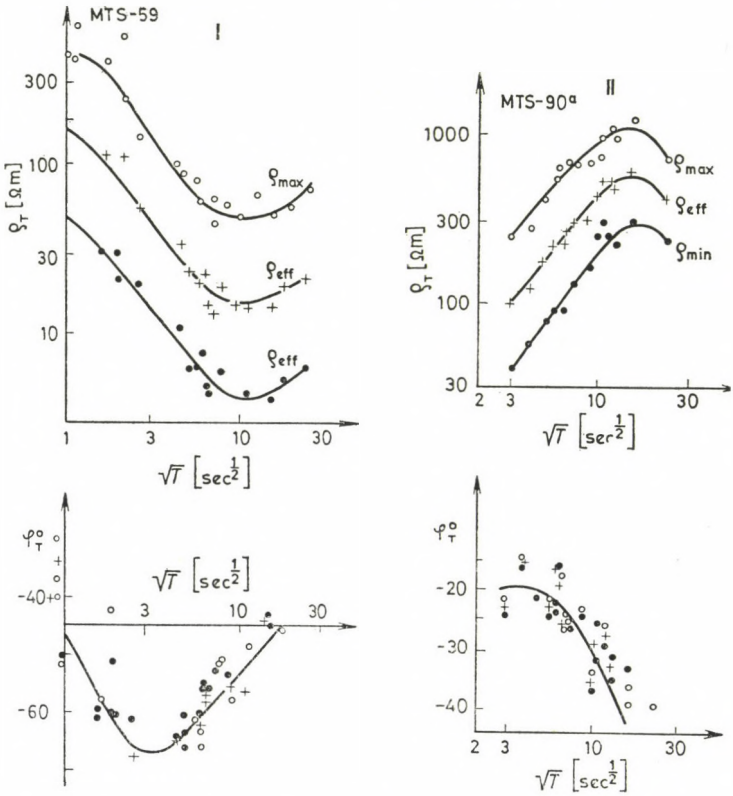
These characteristic features of the amplitude and phase curves can be accounted for by the fact that the distortions of the electromagnetic field in the Tungus syneclise are principally of galvanic nature (Berdichevsky et al., 1973) when amplitude distortions are not accompanied by phase distortions. Indeed, the territory abounds in local near-surface inhomogeneities of a complex form (intrusive sheets occurring at shallow depths, permafrost lenses, etc.). Theoretical calculations (Davidov, 1969; Zakharkin and Rabinovich, 1968) show that local three-dimensional surface inhomogeneities have a strong influence on the modulus of the impedance and but a weak influence on its phase; changes in the orientation of the measuring lines result in vertical displacements of curves ϱ_T while their form remains unchanged, and the phase curves practically coincide in the range of low frequencies. In this situation the most reliable MTS curves are those constructed according to the effective impedance values (Berdichevsky et al., 1973; Davidov, 1969).

Let us consider the results of the MTS curves' interpretation for the profile running along the Nizhnyaya Tunguska River.

Interpretation of the curves of the first and second types shows that the phase curves do not produce any substantially new geological information because the amplitude curves are obtained in a sufficiently wide frequency range. However, even in this case the phase curves are useful for determining the parameters of the sedimentary series and for checking the depth of the conductive layer in the upper mantle.

Possibilities of obtaining additional information from phase curves are most fully revealed in interpretations of soundings pertaining to the third and the fourth types. The amplitude curves permit to determine only the total longitudinal conductivity of the sedimentary series, while a joint interpretation of the amplitude and phase curves allows to determine not only the thickness and mean longitudinal resistivity of the sediments but the depth of the conductive layer of the upper mantle as well.

The principles of the joint interpretation of amplitude and phase MTS-curves are presented by Berdichevsky and Safonov (1972a, 1972b) and by Safonov (1972). There are several methods of such an interpretation based on the use of certain special points of the phase curves. Three methods were used for the interpretation of MTS curves obtained in the Tungus syneclise: a) comparison of observed curves with theoretical curves, b) from the abscissa of the Hummel's point, c) from the coordinates of the maximum



of the phase curve. All these methods require information on the total longitudinal conductivity S of the sedimentary series in order to determine the depth of the conductive layer in the upper mantle. The value of S is determined from the effective amplitude curves. To neutralize the S-effect this value is average along the whole of the profile. The results of different interpretation methods agree well with one another. After averaging they give stable values of the depth of the conducting layer in the upper mantle. These values possess a conditional character because models with an ideally conducting basement were used for the interpretation.

The depth profile of the conducting layer in the upper mantle is shown in Figure 2. The depths change smoothly in eastern direction from 70 to 130 km. It is essential that the H and S variations are not correlated. This suggests that the manifestation of the S-effect is weak.

WEST SIBERIAN PLATE

The profile of the West Siberian Plate contains Paleozoic, Mesozoic and Cenozoic rocks. The sedimentary section can be divided into three geoelectric complexes. The lower complex occurring directly upon the folded

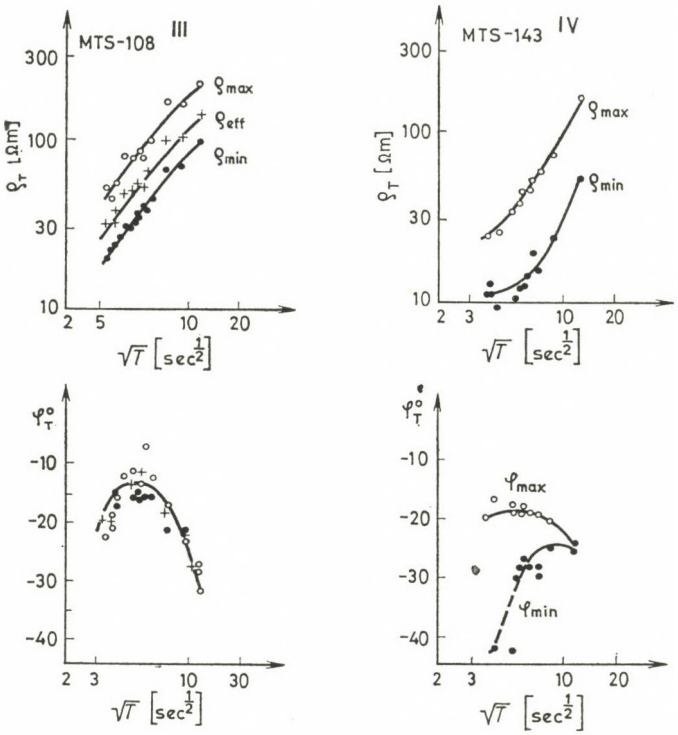


Fig. 1. Typical MTS curves obtained for the profile along the Nizhnyaya Tunguska River

Paleozoic basement is composed of sandstones, aleurolites and clays of Early Cretaceous and Jurassic age. The thickness of this complex is 1—2 km, its mean longitudinal resistivity varies between 5—10 Ωm. The middle complex is composed mainly of clays with aleurolite and sandstone interbeddings of the Paleogene and Late Cretaceous age. The thickness of this complex varies between 0.7 and 1.5 km, its specific resistivity is 2—2.5 Ωm. The upper complex is composed of sands, aleurolites, shingles and clays of the Paleogene-Quaternary age. The thickness of the complex is 0.2—0.5 km, its specific resistivity varies in a wide range of 5 to 200 Ωm.

MTS curves characteristic for the West Siberian Plate are presented in Figure 3. They are constructed along the principal directions of the impedance tensor. We can see that the curves are similar to those of the third and fourth types obtained for the Tungus syneclise. We assume that their distortions have a galvanic character and are associated with the influence of local inhomogeneities: permafrost lenses, structural elements of a complex form, etc.

Let us consider the results of a joint interpretation of amplitude and phase curves obtained along the profile Froly-Salym-Ust-Balyk-Laryak. The same methods were used for this interpretation as for the Tungus syneclise.

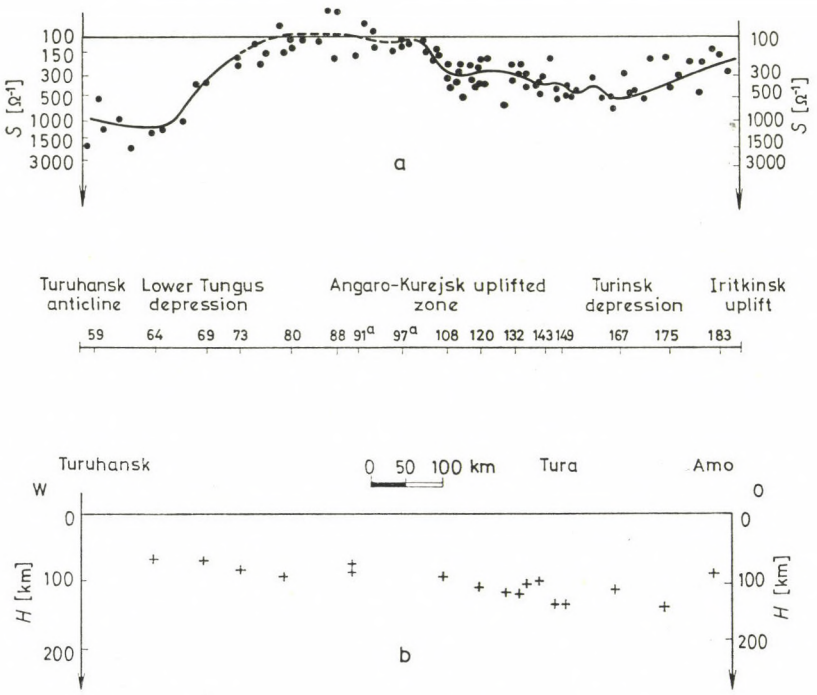


Fig. 2. Results of interpretation of MTS curves for the profile along the Nizhnyaya River
a – horizontal conductivity; b – depth of the conductive layer

The depth profile of the conducting layer in the upper mantle is shown in Figure 4. The values of H hardly vary along the profile while the total longitudinal conductivity of the sedimentary series varies from 500 to 1100 Ω^{-1}. This is indicative of the absence of the S-effect. The mean value of **H** along the profile equals 85 km.

Let us note that in the Tungus syneclise and on the West Siberian Plate the well-conductive layer occurs at about 100 km depth. Such depths are characteristic of geosyncline regions and for zones of transition from the mainland to the ocean.

In conclusion let us emphasize that a joint interpretation of amplitude and phase MTS-curves for East and West Siberia provides supplementary information on the structure of the deep interior of the earth. We hope that the analysis of phase curves will become a more widely used stage in MTS-interpretation.

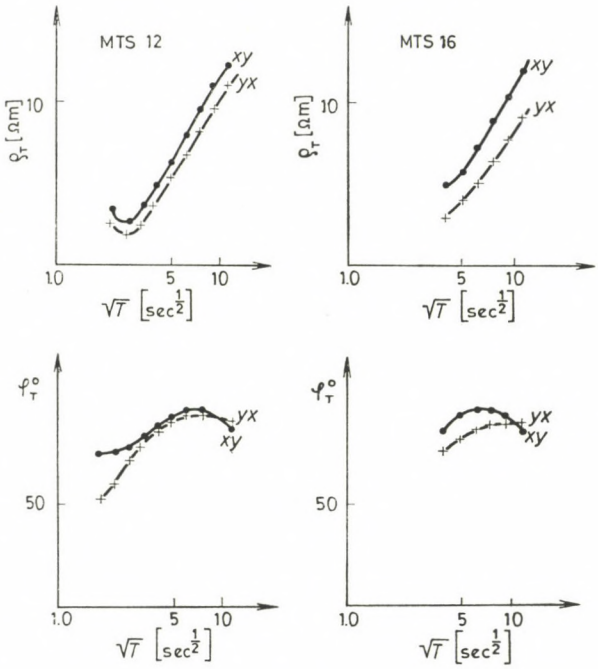


Fig. 3. Typical MTS curves for the West Siberian Plate

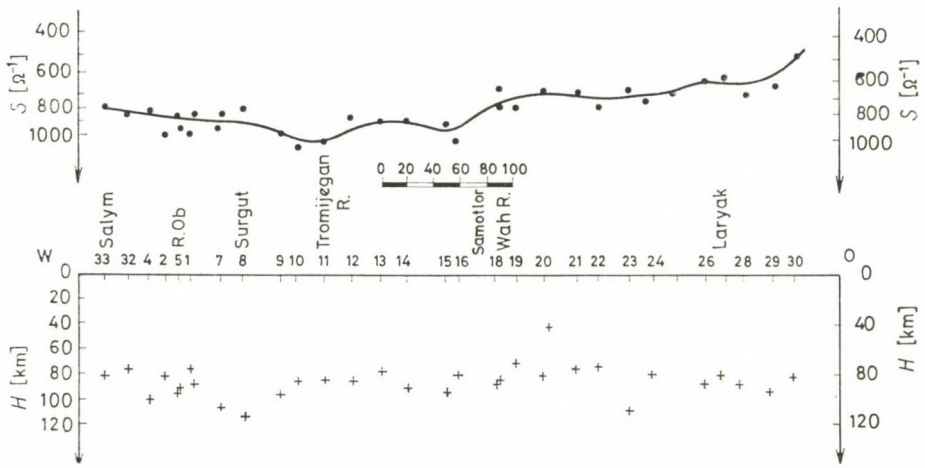


Fig. 4. Results of interpretation of MTS curves for the profile Froly-Salym-Ust-Balyk-Megion-Laryak
above – horizontal conductivity; below – depth of the conductive layer

REFERENCES

BERDICHEVSKY, M. N., SAFONOV, A. S., 1972a. Interpretation of phase curves of magnetotelluric sounding using special points (in Russian). *Prikl. Geofiz.* **66.**

BERDICHEVSKY, M. N., SAFONOV, A. S., 1972b. Plotting and interpretation of phase curves of magnetotelluric sounding (in Russian). *Prikl. Geofiz.* **67.**

BERDICHEVSKY, M. N., DMITRIEV, V. I., BUBNOV, V. P., YAKOVLEV, I. YA., VARLAMOV, D. A., KONNOV, YU. K., 1973. Magnetotelluric sounding of horizontally inhomogeneous media (in Russian). *Izv. Akad. Nauk SSSR, Ser. Fiz. Zemli*, No. 1.

DAVIDOV, V. M., 1969. Distortion of curves of magnetotelluric sounding by surface inhomogeneities (in Russian). Magnitotellurichеskie Metody Izucheniya Stroeniya Zemnoi Kory i Verkhnei Mantii. Nauka, Moscow.

SAFONOV, A. S., 1972. Nomogram and table for the interpretation of phase curves of magnetotelluric sounding (in Russian). *Vestnik Moskov. Univ. Ser. Geol.*, No. 2.

ZAKHARKIN, A. K., RABINOVICH, B. N., 1968. Influence of nonconductive embeddings on the results of MTS (in Russian). Metody razvedochnoi i promyslovoi geofiziki v Zapadno Sibiri. Trudy SNIIGGIMS, 80, Novosibirsk.

DEEP MAGNETOTELLURIC SURVEYS OF THE SOUTH OF THE SIBERIAN PLATFORM AND IN THE BAIKAL RIFT ZONE

V. I. POSPEEV, V. I. MIKHALEVSKY

More than 700 magnetotelluric soundings were performed on the territory of the southern part of the Siberian Platform and of the Baikal Rift zone.

In the southern part of the Siberian Platform four large structures stand out: the Near-Sayan-Yenisei and the Tungus syneclises and Nepa and Baikit anteclises (Fig. 1). The thickness of the sedimentary cover reaches maximum values in the Tungus syneclise (10—13 km) and in the Near-Sayan syneclise (about 8 km). In the dome parts of the Nepa and the Baikit anteclises the thickness of the sedimentary cover is reduced to 2.7 km and 3—2.5 km, respectively. In the geological cross section of the region deposits from the Archean to the Quaternary are represented. The sedimentary

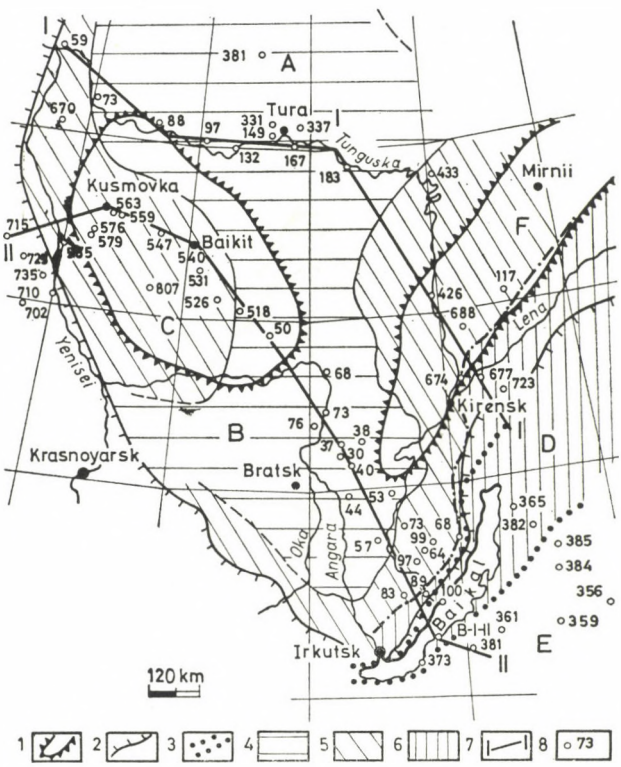


Fig. 1. Zonation of the southern part of the Siberian Platform and of the Baikal Rift zone according to types of the deep geoelectric cross section 1 – boundaries of structural elements of the first order: A–Tungus syneclise; B–Near-Sayan-Yenisei syneclise; C – Baikit anteclise; D–Nepa anteclise; E – Baikal Rift zone; F – Region of Mesozoic activation; 2 – boundary of the Siberian Platform; 3 – boundary of the Baikal Rift zone after Solonenko; 4 – central part of the platform, depth of the second conducting layer is about 100 km; 5 – marginal parts of the platform, depth of the second cunducting layer is 250–300 km; 6 – rift zone, depth of the second conducting layer is 60–80 km; 7 – lines of MTS profiles; 8 – numbers of MTS sites

cover of the Siberian Platform can be divided into three geoelectric complexes.

The upper complex is represented by Mesozoic, Triassic, Permian, Silurian, Ordovician and Upper-Cambrian rocks. These are generally conductive terrigenous rocks with insignificant carbonate interbeddings. In the central parts of the Near-Sayan and the Tungus syneclises the complex reaches a thickness of 3 to 5 km and its longitudinal resistivity equals 10—15 Ωm. In the elevated regions of the platform the complex averages a thickness of several hundred meters and its longitudinal resistivity increases up to 50—100 Ωm.

The second geoelectric complex includes carbonate halogenous rocks of Cambrian age, and in the deep parts of the Tungus syneclise also Silurian and Ordovician carbonate rocks. This is a thick body consisting of alternat-

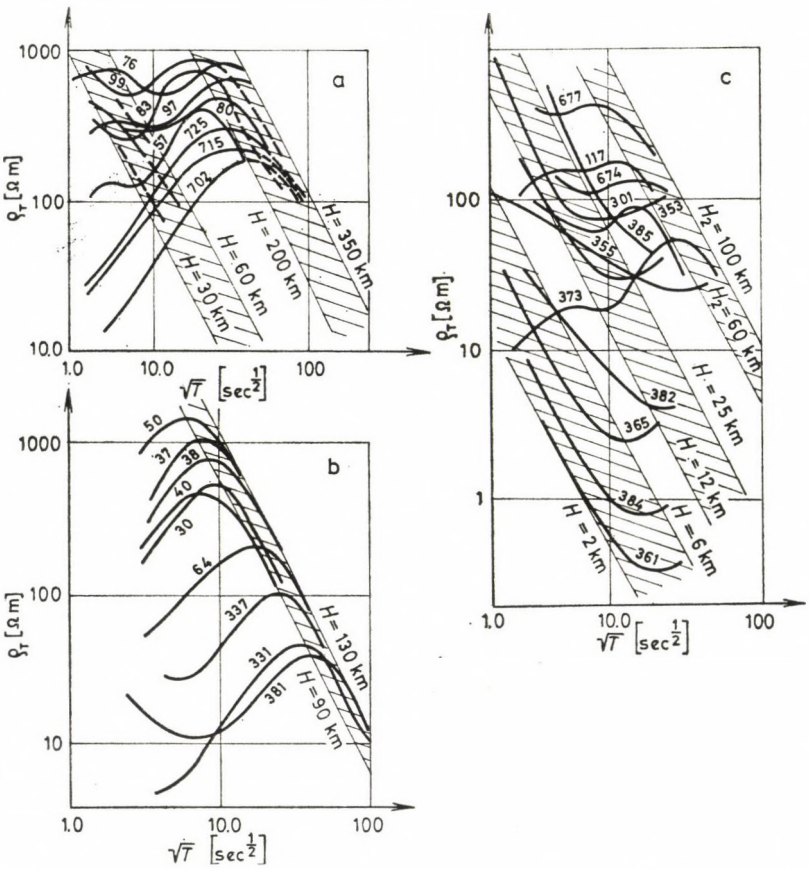


Fig. 2. MTS curves characteristic of the Siberian Platform and of the neighbouring structures
a – marginal part of the platform, south-eastern part of the West Siberian Plate; b – central part of the platform; c – Baikal Rift zone and the region of Mesozoic activation

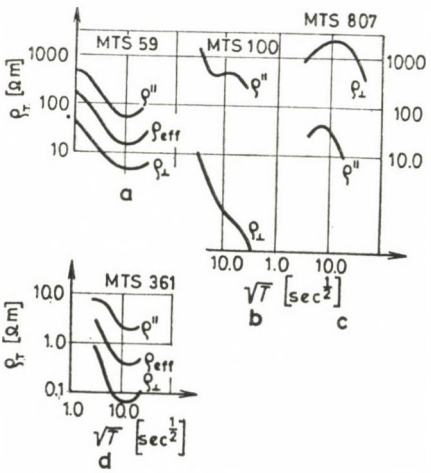


Fig. 3. Distortions of MTS curves
a – effect of surface inhomogeneity; b – edge effect; c – local induction effect; d – effect of the conducting zone of crush (the MTS site is located above the zone)

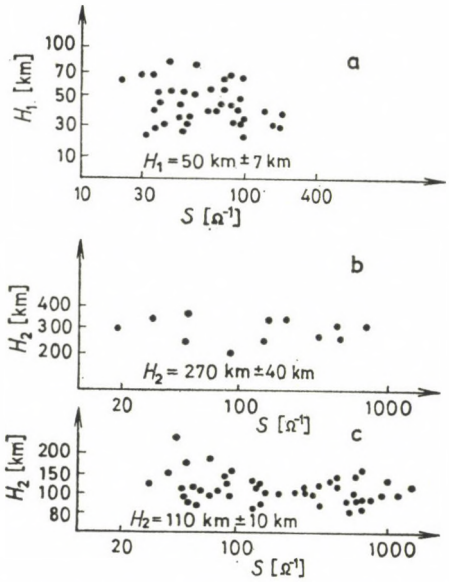


Fig. 4. Dependence of the depth to the conducting layers, determined from the effective curves, upon the conductivity of sediments
a – the first layer in the marginal part of the platform; b – the second layer in the marginal part of the platform; c – the second layer in the central part of the platform

ing limestones, dolomites, salts and partly of terrigeneous rocks in the subsided regions. The longitudinal resistivity of the complex amounts to 100—200 Ωm.

The third geoelectric complex occurs directly upon the metamorphized rocks of Proterozoic and Riphean ages or upon the crystalline rocks of Archean age. The complex includes carbonate-terrigenous rocks of Riphean and Vend the terrigenous part of the Mot series of the Lower Cambrian. The specific resistivity of this body varies from 3—5 Ωm, in the central parts of the Near-Sayan and Tungus syneclises, where the thickness of the complex is 2—6 km, to 30—50 Ωm in the elevated regions where the thickness averages 350—500 m.

The curves of magnetotelluric soundings in the southern part of the platform and of the Baikal Rift zone can be divided into three main types. The first type (Fig. 2, b) is characteristic of the central part of the platform. These are three-layered curves of type K, ending in a more or less extended descending branch. The second type (Fig. 2, a) is characteristic of the outlying parts of the platform such as the Near-Baikal area, the Near-Sayan area, the western margins of the Near -Sayan and the Tungus syneclises. Curves for ϱ_T belonging to this type have as a rule two maxima and

a minimum that divides them. The descending branch is considerably shifted to the right as compared with the curves of the first type. The third type of curves characterizes the Baikal Rift zone. These are multilayer curves of types H, HK, KHK, KOOH with well defined minima (Fig. 2, c).

Local breaks in the horizontal homogeneity of the platform cross section are associated with jointing zones and zones of disjunctive dislocations inundated by mineralized waters, and also with swell-shaped elevations in the upper part of carbonaceous-halogen deposits and with dikes of trap-rocks. These zones, which are as a rule of a rather complex shape, range in size from 5 to 30 km. The lower part of the sedimentary cover has practically no horizontal inhomogeneities: geoelectric levels occur nearly horizontally with a slope of some odd tens of minutes in the direction of the Tungus and the Near-Sayan syneclises. Under such conditions of three-dimensional inhomogeneities the most reliable information on the deep cross section is provided by the effective curves. The relations typical for the Siberian Platform between longitudinal, transverse and effective curves of magnetotelluric soundings are shown in Figure 3, a. Figure 4 is demonstrative of a possible use of effective curves for the determination of depths of the base and the intermediate conductive layers in the inner parts of the platform. We see that the depths of the layers determined from the effective curves only slightly depend upon the conductivity of sedimentary deposits (the S-effect is imperceptible).

In the second region, an edging, that is a transition area from the platform to the Baikal, Sayan and Yenisei framings, the distorting effect of surface inhomogeneities diminishes. In the Near-Baikal zone this is in connection with the reduced probability of the jointing zones being filled with brine because of the substitution of carbonates by salts. In the west-

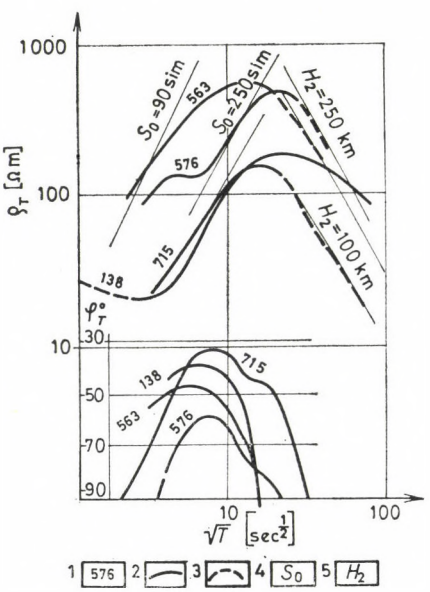


Fig. 5. Transformation of the asymptotic branches of MTS phase curves into amplitudinal curves
1 – MTS numbers; 2 – measured MTS curves; 3 – transformed sections of amplitudinal curves; 4 – conductivity of sediments; 5 – depth of the conducting layer

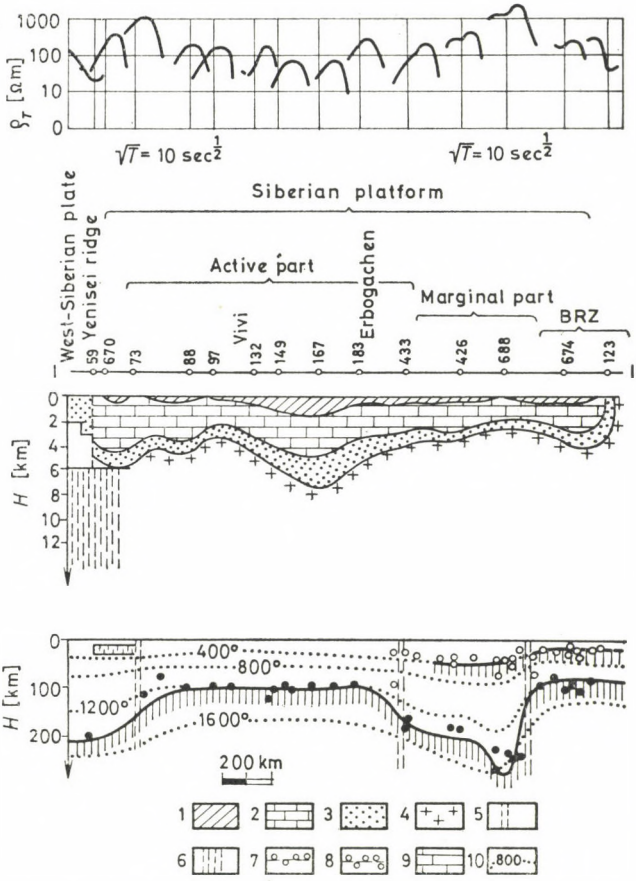


Fig. 6. Geoelectric cross section of the earth's crust and upper mantle in the southern part of the Siberian Platform along the route I – I' 1 – terrigenous Paleozoic-Mesozoic deposits of sedimentary cover with ϱ = 10–500 Ωm; 2 – carbonaceous-halogenous Paleozoic deposits (C_m) with ϱ = 100–200 Ωm; 3 – terrigenous deposits of Vend and Riphean age with ϱ=3–300 Ωm; 4 – basement surface; 5 – boundaries of blocks with different geothermal activity; 6 –zones of crush in the basement; 7 – top of the first conductive layer; 8 – top of the second conductive layer; 9 – terrigenous Paleozoic-Mesozoic sedimentary deposits of the West Siberian Plate; 10 – isotherms

ern part the main distorting factor is a ramified fault system accompanied by vast zones of crush. The influence of fault zones is manifested in the lowering of the curves for $\varrho^{\parallel}$ while the $\varrho^{\perp}$ curves preserve their normal level (local induction effect). Such curves are presented in Figure 3, c. When approaching the fault zone galvanic effects get stronger, distorting both of the MTS curves.

The strongest distortions of MTS curves are observed in the zones of Mesozoic and recent volcanic activity. Both galvanic and induction effects manifest themselves there. In Figures 3, b and 3, d some cases of distortions are given.

The quantitative interpretation of MTS curves was preceded by the analysis of their distortions following the ideas of Berdichevsky et al., (1972). The most reliable curves were used to distinguish the conductive layers in the crust and the upper mantle. In some cases asymptotic branches of the amplitude curves were obtained by means of phase curve transformation. A case of such a transformation increasing the depth of investigations is shown in Figure 5.

The results of quantitative interpretation of MTS confirm that in the south of the Siberian Platform do exist three regions of different structure of the crust and upper mantle (Fig. 1). These regions were distinguished previously from the types of MTS curves.

In the central region the conductive layer occurs at a depth of 90—130 km.

The second region corresponds to the marginal parts of the platform while in the west it includes the West Siberian Plate. MTS curves for this region reveal two conductive layers: one at a depth of 30—60 km and the other at 200—350 km.

The third region coincides with the Baikal Rift zone and with zones of recent volcanic activities in the Near-Baikal and Trans-Baikal regions. In this region the depths of the first and second conductive layers reduces to 12—25 km and to 60—100 km, respectively.

Such variations in the deep geoelectric cross section are apparently associated with different geothermal regime of the crust and upper mantle in different regions (Fig. 8).

According to the data of Parkhomenko and Bondarenko (1972) it can be presumed that in the central region the conductive layer appears owing to a warming up of peridotites to temperatures of 1100—1300 °C when the process of partial melting begins and ionic conductivity predominates. This hypothesis implies that in the platform area the 1200 °C isotherm occurs at about 100 km depth (Figs 6 and 7).

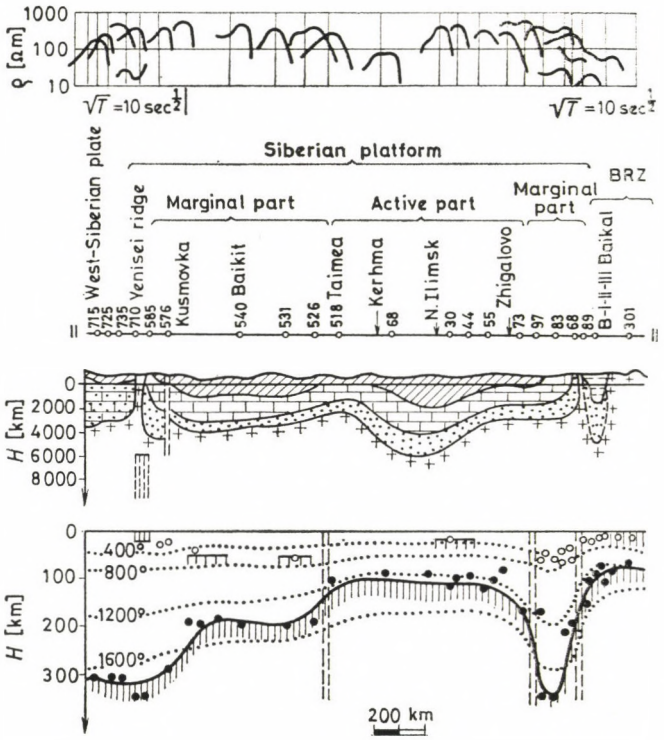


Fig. 7. Geoelectric cross section of the earth's crust and upper mantle in the southern part of the Siberian Platform along the route II–II. Symbols same as in Figure 6

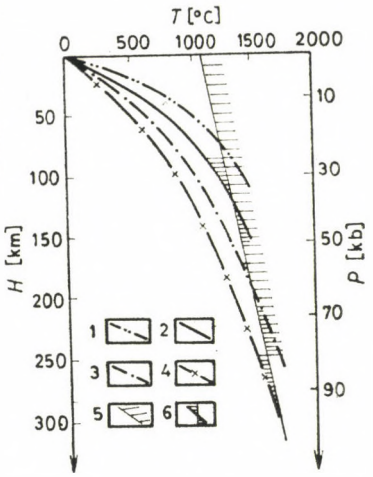


Fig. 8. Temperature distribution for the Siberian Platform and adjacent structures
1 – Baikal Rift zone; 2 – central (activated) part of the Siberian Platform; 3 – marginal part of the platform; 4 – south-eastern part of the West Siberian Plate; 5 – probability field of the partial melting of the primary matter in the mantle (according to Smirnov); 6 – depths to the second conducting layer

The second conductive layer occurs in the marginal part of the platform at 200—350 km depth at which, according to the Beloussov model, the mantle has an eclogite composition. The increase in ionic conductivity of eclogites at temperatures of 1400—1500 °C is probably the main cause for this conductive layer to be formed.

In the Baikal Rift zone the second conductive layer is observed at depths of 60 to 100 km. An increase in conductivity of the mantle at these depths is accounted for by its warming up to temperatures of 1100—1300 °C. At such temperatures and under pressures of 20—30 kilobar the intrinsic ionic conductivity predominates and the resistivity of ultrabasic rocks of peridotite-dunite series does not exceed 2—40 Ωm. Thus, the isotherm 1200 °C probably lies in the rift zone at a depth of 100 km and approaches the day surface up to 60—70 km in the region of the Baikal depression, as confirmed by heat flow measurements. According to Lysak (1966), the heat flow in the Baikal Rift zone amounts to $2.8 \cdot 10^{-6}$ cal/cm^2 sec as compared with the $1.1 \cdot 10^{-6}$ cal/cm^2 sec value in the marginal part of the Siberian Platform.

It is expected that the deconsolidation of the mantle material begins somewhat above the upper surface of the conductive horizon and coincides with the boundary of the waveguide (layer of reduced velocities). Results of deep seismic soundings in the rift zone confirm this fact. Under the Moho discontinuity the deconsolidation is revealed: the boundary velocity decreases here to 7.8—7.9 km/sec as compared with the 8.2—8.3 km/sec in the marginal part of the platform (Krylov et al., 1971).

It is more difficult to explain the nature of the first conductive layer confined between isotherms 400 and 800 °C (Figs 6, 7). In the rift zone the specific resistivity of this layer reaches 5—10 Ωm, and rises to 20—40 Ωm on the platform. The thickness of the layer is 10—20 km.

It is known that the Baikal Rift zone is seismically active. The depths of earthquake foci in the region are 15—30 km. A study of tectonic stresses has shown that tension vectors are directed across the strike of the rift and

lie in a horizontal plane. One can assume that earthquakes result in rock displacement in horizontal direction and in the formation of a jointing zone. Apparently a great number of earthquakes has occurred since the activization of the rift began and their epicentres are distributed more or less evenly over the whole rift's area. The pore space should accumulate the water produced by dehydratation of rocks and by release of crystallization water, as well as the juvenile and vadose waters penetrating into the pore space along a number of deep faults. Naturally, water at such depths is a solution of different chemical compounds. The occurrence of the first conductive layer can therefore be explained by the conductivity of solutions accumulated in the layer of increased jointing.

In the marginal areas of the Siberian Platform the first conductive layer lies within the mantle. The possibility is not ruled out that here, too, a decrease in resistivity may also be associated with dehydratation processes of ultrabasites.

In the territory of the Siberian Platform we find two large regions essentially different as to their geothermal activity and, accordingly, as to their tectonic activity: the central activated region and the marginal stable region.

In the central activated part of the platform the thickness of the lithosphere decreases and the isotherm 1200 °C corresponding to the onset of partial melting of the material approaches the day surface. It can be presumed that this distinctive feature of the platform came into being before the Riphean age. The abundance of traprocks is characteristic of the central part of the platform. The total thickness of traprocks related to different phases of basic magma exceeds here a thousand meters and decreases to tens or several meters in the marginal parts. The total volume of the trap magma in the Tungus and the Near-Sayan-Yenisei syneclises exceeds one million cubic kilometers (Odintsov et al., 1970). The release of such an amount of basic magma is only possible in the presence of numerous deep faults. It is natural enough to associate the formation of faults with tension forces in the lithosphere.

Some researchers, Massaitis in particular (Massaitis, 1969; Shurkin and Mitrofonov, 1969) associate the revival of volcanic activity with the general downwarping of the region. In this connection the coincidence of the maximum thicknesses of traprocks with the maxima of Paleozoic sediments becomes explicable. It is natural that a violation of thermodynamical equilibrium in the vicinity of fissures extending into the zones of partial melting of the matter involved an increase in the thickness of chambers of the basic magma melting, and their junction into large chambers comprising hundreds and thousands of cubic kilometers of magma. A release of large quantities of heat through magma that acted as a heat-carrying agent resulted in the cooling of chambers, in a subsidence of the geothermal surface and in the sealing of fractures, and in the end in stopping the volcanic activities. A long period of time, of the order of tens of millions of years, was required for the temperature within the magma chamber of the previous cycle to come close to the melting temperature and for the next phase of trap magmatism to begin.

During the period of magmatic activity the marginal parts of the plat-

form and in particular the Nepa, Anabar and Aldan anteclises were subject to compressional stresses with vectors directed from the activated part of the platform. Nearer to the end of tectonic cycles when the tensile forces in the central part of the platform weakened, the reaction forces in the marginal parts of the platform produced joining zones embracing the lithospheres and penetrating to depths of 150—200 km. The violation of termodynamical equilibrium brought about the formation of chambers that were sources of alkaline ultrabasic magmas. Thus the marginal parts of the platform are advantageous for prospecting for minerals associated with the ultrabasic magma, for diamonds in particular. It should be added that, as a matter of fact, the main diamond-bearing kimberlite pipes are located in the marginal part of the Siberian Platform.

REFERENCES

Berdichevsky, M. N., Dmitriev, V. I., Bubnov, V. P., Yakovlev, I. Ya., Varlamov, D. A., Konnov, Yu. K., 1973. Magnetotelluric sounding of horizontally inhomogeneous media (in Russian). *Izv. Akad. Nauk SSSR, Ser. Fiz. Zemli*, No. 1.

Chekalyuk, E. B., 1970. Retrograde phenomena and the process of energy accumulation in the Gutenberg zone of the upper mantle (in Russian). Problemy Stroeniya Zemnoi Kory i Verkhnei Mantii, No. 7.

Gorbaty, Yu. E., Epelbaum, M. B., Bondarenko, A. T., 1971. Infrared spectra in the near-critical area. Transaction of the 8th Conference on Experimental and Engineering Mineralogy and Petrography (in Russian). Nauka, Moscow.

Gornostaev, V. P., Mikhalevsky, V. I., Pospeev, V. I., 1970. Deep magnetotelluric sounding of the south of the Siberian Platform and the Baikal Rift zone (in Russian). *Geol. i Geofiz.*, No. 4.

Khitarov, N. I., Kadik, A. A., Lebedev, E. B., 1971. Temperature effect upon the solubility of water in silicate melts (in Russian). Transactions of the 8th Conference on Experimental and Engineering Mineralogy and Petrography, Experimental Modelling of Natural Processes. Nauka, Moscow.

Krylov, S. V., Mishinkin, B. P., Krupskaya, G. V., Petrik, G. V., 1971. Deep seismic study of the Trans-Baikal area (in Russian). *Geol. i Geofiz.*, No. 12.

Lysak, S. V., 1966. Geothermal zones of the territory of the southern part of East Siberia (in Russian). Formirovanie i Geokhimiya Podzemnykh Vod Sibiri i Dalnego Vostoka. Nauka, Moscow.

Massaitis, V. A., 1969. Magmatic cycles of the Siberian Platform (in Russian). Problemy Svyazi Tektoniki i Magmatizma. Nauka, Moscow.

Odintsov, M. M., Vladimirov, B. M., Tverdokhlebov, V. A., 1970. Deep magmatism and structural development of ancient platforms (in Russian). Problemy Stroeniya Zemnoi Kory i Verkhnei Mantii. Nauka, Moscow.

Parkhomenko, E. I., Bondarenko, A. T., 1972. Electric Conductivity of Rocks at High Temperatures and Pressures (in Russian). Nauka, Moscow.

Shurkin, K. A., Mitrofonov, S. P., 1969. Magmatism and the History of the Lower Pre-Cambrian for the Pre-Cambrian in the north-western part of the USSR and in East Siberia (in Russian). Problemy Svyazi Tektoniki i Magmatizma. Nauka, Moscow.

Smirnov, Ya. B., 1968. Relationship of the thermal field to the structure of the earth's crust and upper mantle (in Russian). *Geotektonika*, No. 6.

DEEP MAGNETOTELLURIC SURVEYS IN YAKUTIA

I. A. YAKOVLEV, V. P. BUBNOV

Up to this date, field parties of the Yakut Geological Office have completed more than 300 magnetotelluric soundings and a series of magnetovariation soundings in the territory of South-Western Yakutia. Extensive magnetotelluric investigations have also been carried out in North-Eastern Yakutia. This work has been performed under the guidance of M. N. Berdichevsky.

SOUTH-WESTERN YAKUTIA

The territory considered is situated within the Leno-Yenisei Plate, the largest structure of the Siberian Platform (Mokshantsev, 1971). The region includes the following structural-tectonic elements: the Aldan anteclise, the Vilyuisk syneclise, the Pre-Baikal-downwarp and the Botuoba saddle (Fig. 1). This area is bounded in the north and the north-west by the Tungus syneclise, in the west by the Angara-Lena anteclise and in the south by the Baikal-Patom folded region.

The eastern part of the territory comprises a part of the large Aldan and Vilyuisk basement megablocks. The Aldan (uplifted) megablock is represented by its north-west portion. There, the basement lies at a relatively shallow depth (1—3 km) and

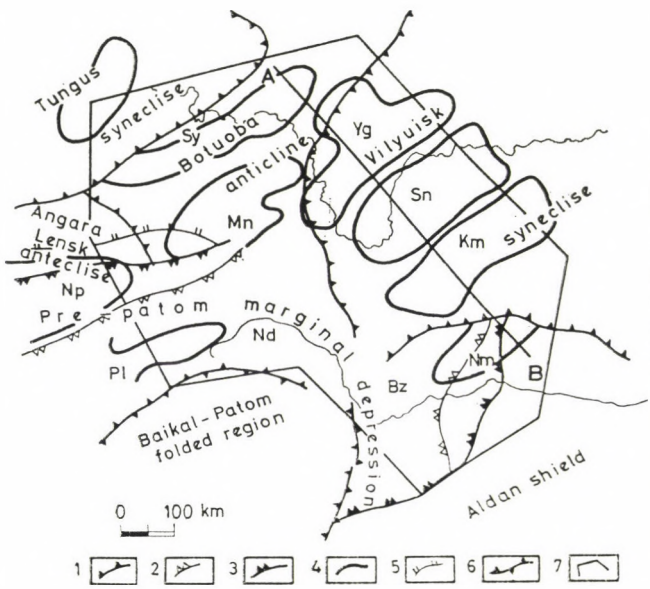


Fig. 1. Tectonic map of the eastern part of the Siberian Platform (after Mokshantsev)
1, 2, 3, 4, 5 – contours of the structures; 6 – jointings; 7 – boundary of the area under consideration. Nm – Namaninsk rise; Mn – Mirinsk rise; Sy – Syuldzhyukar mega-ridge; Np – Nepsk dome; Sn Suntar dome; Km – Kempendya depression; Yg – Ygyattan depression; Nd – Nyuisko-Dzherbinsk depression; Bz – Berezovo depression; Pl-Peledui uplift

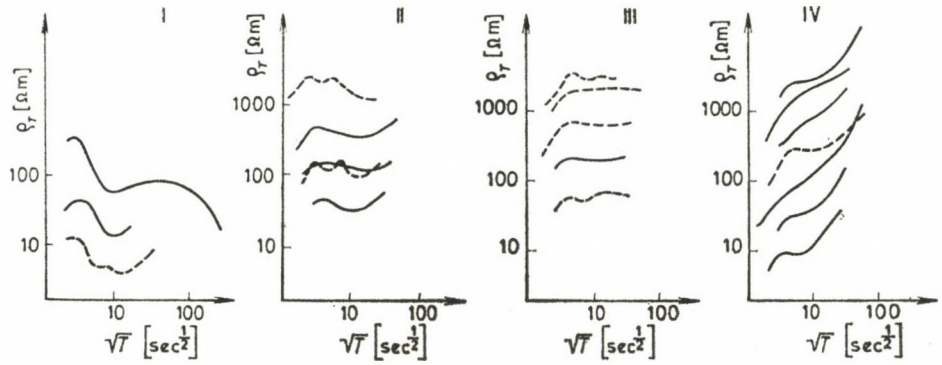


Fig. 2. Types of MTS curves
solid lines: longitudinal curves; dashed lines: transverse curves

dips towards the side of the Vilyuisk (sunken) megablock, within which the Kempendya (300 km × 80 km) and Ygyattan (300 km × 120 km) grabenlike depressions, stretched in a NE direction and separated by the Suntar horstlike uplift (250 km × 100 km), are found. In the depressions the basement lies at a depth of 8—12 km; within the uplift it lies at 1—3 km depths.

In the western part of the territory are found the Pre-Patom depression and the Botuoba saddle, bounded in the north by the Tungus warping area and in the west by the large Angara-Lena (Mid-Siberian) uplifted area. The Pre-Patom downwarp is the prolongation of the Vilyuisk sunken megablock. Within its bound, the Nyuya-Dzherba (300 km × 130 km) and the Berezovo (280 km × 120 km) depressions are found. In the former, the depth of the basement top is estimated to 5—6 km; in the latter to 10—12 km. The Botuoba saddle separates the Tungus and the Vilyuisk depression zones. Within the saddle the Mirnoie protrusion (200 km × 75 km) and the Chona-Syuldzhyukyar protrusion of the basement (250—300 km) are found.

The total longitudinal conductivity of the sedimentary cover varies sharply within the area. Whereas in regions of shallow lying basement (Suntar uplift, Botuoba saddle, the slope of the Aldan anteclise) the conductivity of the sedimentary layers does not exceed 30—40 Ω^{-1}, it attains 1000 Ω^{-1} and more in the depression zones.

The MTS curves for south-western Yakutia show a variety of forms. A general feature of these curves is the presence of well pronounced minima and inflections in the time interval from 20—30 sec to several minutes (Berdichevsky et al., 1969). From the formal interpretation of such curves it is inferred that there is a conductive layer at a depth of a few tens of kilometers, i. e. in the earth's crust or mantle. Such a conclusion is questionable, for the minima and inflections on the MTS curves can also be due to the distorting effect of horizontal inhomogeneities.

We begin our analysis of the MTS curves with typifying them. Let us consider longitudinal $\varrho_T^{\parallel}$, and transverse $\varrho_T^{\perp}$, curves oriented, respectively, along and across the regional strike of first-order structures. The MTS curves can be divided into four types (Fig. 2), according to the degree of manifestation of their minima and inflections.

In *the first type* we place those curves whose characteristic steeply descending branches usually terminate at deep minima. *The second type* con-

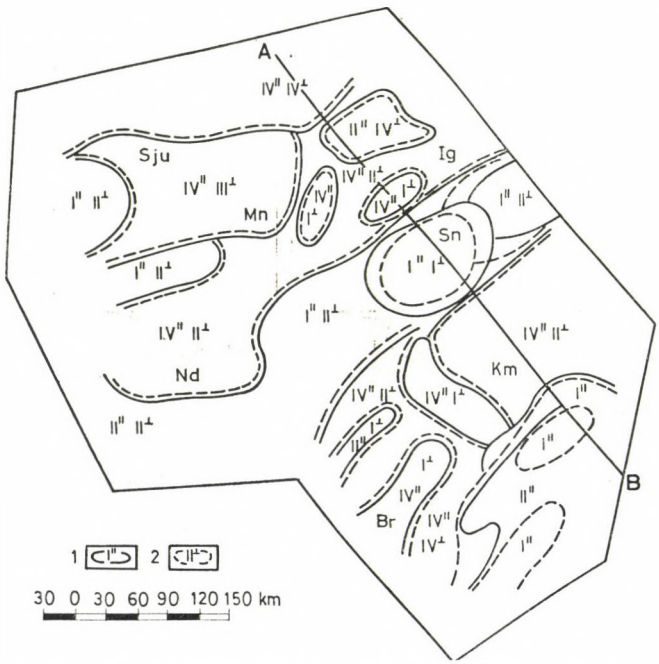


Fig. 3. Map of the types of longitudinal and transverse MTS curves
1 – boundaries of the distribution and the type of longitudinal MTS curves; 2 – the same for transverse curves

sists of curves with gently descending branches that, in a number of cases, terminate at more or less well marked minima. *The third type* includes those curves whose right parts are represented by nearly horizontal branches. Finally, in *the fourth type*, we place curves having two ascending branches separated by an inflection or minimum. We note that curves of all the four types possess a left-side ascending branch.

The geological interpretation of these curves is closely related to the solution of two fundamental questions:

1. the nature of the geoelectric horizon determining the left-side ascending branches of the MTS curves, and

2. the nature of the minima and inflections on the right-hand-side portions of the curves.

The first question is solved by correlating the conductivity S with drilling data, with data from direct-current electric prospecting and with seismic results. It has been found that values of S correspond to the total longitudinal conductivity of the sedimentary cover. Thus it follows that the left-hand-side ascending branches of the MTS curves are determined by the crystalline basement. The only exceptions are likely the zones of greatest depths of occurrence of the basement (the Kempendya, Ygyattan and Berezovo depressions).

Minima and inflections on the right-hand-side of the MTS curves can be caused by:

a) field distortion (by induction or edge effects, flow-around or concentration effects) (Berdichevsky et al., 1973);

b) the influence of conducting layers in the earth's crust or upper mantle.

The analysis of the maps of the MTS curve types (Fig. 3) leads us to assume that the descending branches, minima and inflections on the $\varrho_T^{\shortparallel}$ curves for the zones of the uplifted basement are related to the *induction effect.* In fact, the descending branches and minima of the longitudinal curves of the first and second types for the north-west slope of the Aldan anteclise and for the Suntar dome might be due to redundant currents flowing in the Ygyattan and Kempendya depressions. The descending branches and minima on the $\varrho_T^{\shortparallel}$ curves of the second type: for the south-west Botuoba saddle and for the north-east Peleduy uplift, as well as the inflections on the curves of the fourth type for the central and northern parts of the Botuoba saddle, might be related to the effect of redundant currents flowing in the Pre-Patom downwarp and in the Tungus syneclise.

Descending branches, minima and inflections on the $\varrho_T^{\perp}$ curves for depression zones may be due to edge effects. In depressions, transverse curves of the first and second type correspond to longitudinal curves of the fourth type. The appearance of the lengthy descending branches and minima on the transverse curves obtained in such zones can be related to the influence of the edges of the depressions.

In zones bordering the Ygyattan and Kempendya depressions the MTS curves oriented along the boundaries of the depressions have steeper descending branches and deeper minima than the MTS curves oriented perpendicularly to the boundaries of the depressions. This picture suggests that in the areas mentioned the MTS curves are distorted by the flow-around and concentration effects. It is significant that the minima and inflections on the MTS curves are exaggerated in passing from zones of relatively level tectonic forms to fault zones.

We thus see that the maps of the types of MTS curves give reason to assume that the descending branches, minima and inflections of the longitudinal and transverse curves for uplifted zones, and the transverse curves for sunken zones, are related to the distorting effect of horizontal geoelectric inhomogeneities of the sedimentary cover. In case of deep investigations the longitudinal MTS curves are more informative than transverse ones. We therefore restrict ourselves to the estimation of the possible distortions of the longitudinal curves.

It is by the induction effect that the longitudinal curves can be the most seriously distorted. To estimate the influence of this effect we consider a geoelectric section along profile AB (Figs 1 and 3) traversing the Tungus syneclise, the Botuoba saddle, the Ygyattan depression, the Suntar dome, the Kempendya depression and the Aldan anteclise, i. e. along the profile of maximum inhomogeneity of the sedimentary cover. The magnitude of the total longitudinal conductivity of the sedimentary cover changes by a factor of ten in passing from the Ygyattan and Kempendya depressions to the Botuoba saddle, the Suntar dome and the slope of the Aldan anteclise. A north-west extension of the profile intersects the north-east side of

the Tungus syneclise, whose central part is characterized by a sedimentary cover of about 1000 Ω^{-1} total conductivity; a similar south-east extension intersects the zone of low conductivity of the sedimentary cover of the Aldan anteclise (of the order of 1 to 10 Ω^{-1}). The dimensions of the Tungus syneclise and of the Aldan anteclise considerably exceed the length of profile AB.

Taking into account the dimensions of the upplifted and of the sunken zones, we compare the longitudinal curves for the Botuoba saddle and for the Suntar dome with the theoretical curve for a single horst; we also compare the longitudinal curves for the slope of the Aldan anteclise with the theoretical curve valid aside from a single graben (Dmitriev and Kokotushkin, 1971). It is clear from Figure 4 that within the Aldan anteclise the practical curves sharply diverge from the theoretical one. Whereas the measured curves show well marked descending branches and deep minima, the

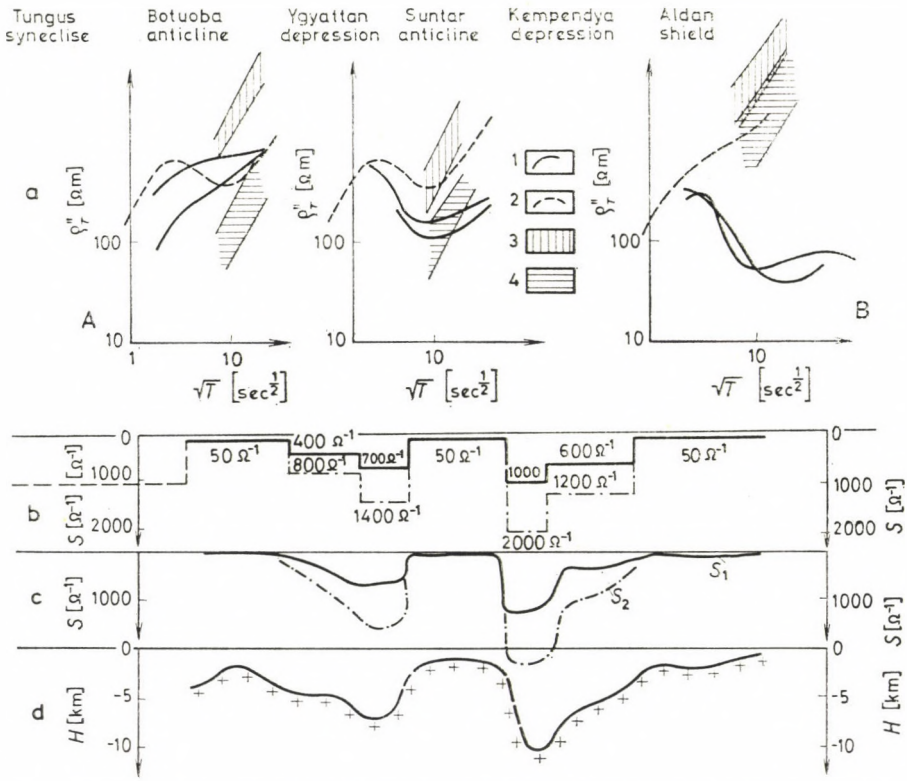


Fig. 4. Geological-geophysical section along profile A–B
a – Comparison of the practical ϱ_T'' curves with those calculated for a model with a non-conductive basement (model of a single graben or horst): 1 – practical ϱ_T'' curves; 2 – theoretical ϱ_T'' curves; 3 – zone within which are found the right-side branches of ϱ_T'' calculated with the Dmitriev – Berdichevsky formula, without the Tungus syneclise; 4 – the same, with the Tungus syneclise taken into account; b – step function approximating the total longitudinal conductivity of the sediment cover; c – graph of the total longitudinal conductivity S_1 and S_2; d – surface of the crystalline basement

theoretical curve exhibits, in the same time interval, an ascending branch divided by an inflection. This contradiction gradually disappears as we leave the Aldan anteclise. Thus, for the Suntar dome, the observed and the theoretical curves are similar in form, although the minima of the observed curves are somewhat sharper. For the Botuoba saddle, the right-hand-sides of the measured and theoretical curves approach each other even more closely. These results indicate that:

a) the deep minima of the MTS curves for the slope of the Aldan anteclise are caused by a conductive layer in the earth's crust or mantle, and not by the induction effect;

b) the minima and inflections of the MTS curves for the Suntar dome and the Botuoba saddle are, to a certain degree, related to the induction effect.

The same results follow from a more complicated model, in which the total longitudinal conductivity S of the upper layer, overlying the non-conducting basement, varies stepwise, approximating the variations of S of the sedimentary cover along profile AB (Fig. 4). The calculation is carried out by the Dmitriev-Berdichevsky approximate formula:

$$\varrho_T = \frac{1}{\omega \mu_0 \tilde{S}^2}$$

$$\tilde{S} = \frac{2}{\lambda} \int_{-\infty}^{+\infty} \frac{S(x)\, dx}{1 + 4\pi^2 \frac{x^2}{\lambda^2}}$$

where $\tilde{S}$ is the average total longitudinal conductivity of the upper layer in that segment, which for a given wavelength λ significantly effects the value of ϱ_T. We consider the following possibilities: 1. with and without taking into account the Tungus syneclise; 2. with different values of the total longitudinal conductivity of the sedimentary cover in the Kempendya and Ygyattan depressions ($S_1 = 600$, 100 and 400, 700 Ω^{-1}; $S_2 = 1200$, 200 and 800, 1400 Ω^{-1}); 3. with minimum and maximum values of the average longitudinal resistivity (10 and 100 Ω^{-1}m).

For the Aldan anteclise the measured MTS curves lie considerably lower than the theoretical ones. In this case, it is not possible to explain the occurring minima by the induction effect (even if the possible influence of the Tungus syneclise is taken into account).

The results for the Suntar dome are less convincing. The right-hand-side parts of the MTS curves lie considerably lower than those of the theoretical curves not taking the Tungus syneclise into account. Taking into account the Tungus syneclise, the theoretical curves are somewhat lower. However, also in this case, the ascending branches of the measured curves intersect the zone of the computed curves and leave their possible bounds. Thus the minima of these MTS curves can be only partly related to the induction effect.

For the Botuoba saddle, the right-side parts of the measured curves lie below the computed curves not taking the Tungus syneclise into account; and above the computed curves, if we take account of this structure. That

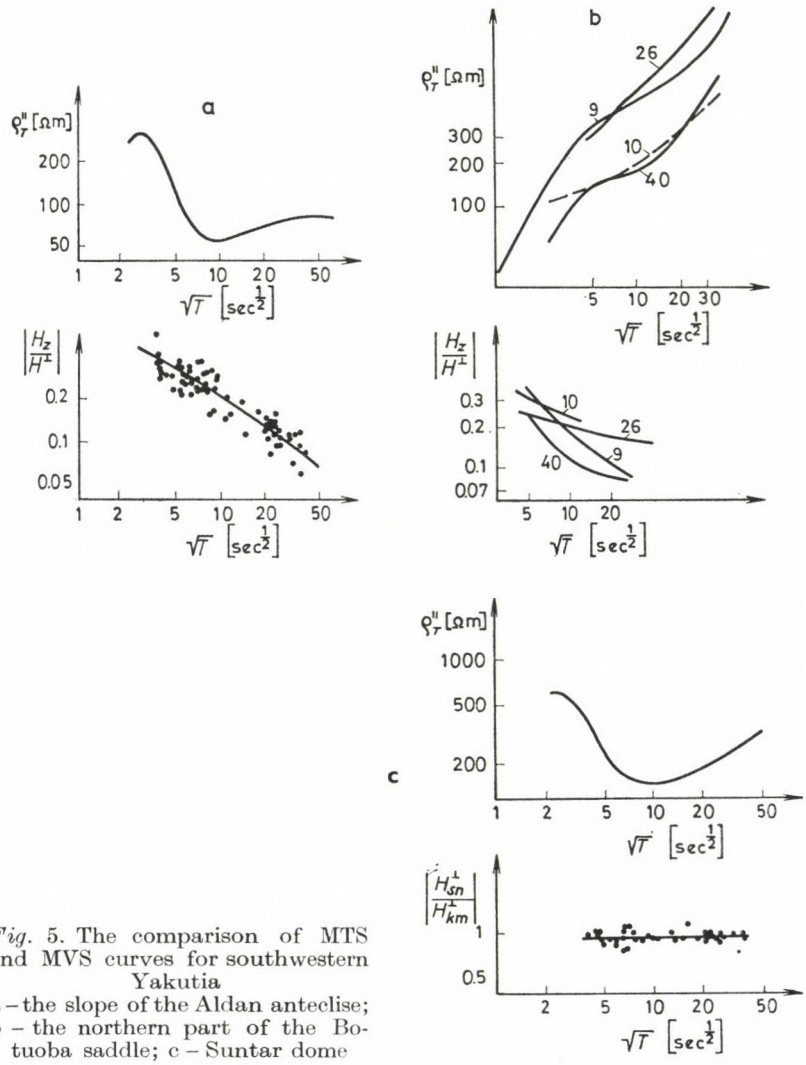


Fig. 5. The comparison of MTS and MVS curves for southwestern Yakutia
a – the slope of the Aldan anteclise; b – the northern part of the Botuoba saddle; c – Suntar dome

is, in this case, taking the Tungus syneclise into account permits the inflections of the MTS curves to be explained by the induction effect.

For a further scrutiny of the induction effect, we now turn to results of the magnetovariation soundings on the slope of the Aldan anteclise, the Suntar dome, the Kempendya depression and the northern part of the Botuoba saddle.

For the slope of the Aldan anteclise and the northern part of the Botuoba saddle, the value of $|H_z|/|H^{\perp}|$ decreases with increasing period of variations (Figs 5, a, b). This occurs in the time interval corresponding to the minima and inflections of the MTS curves, which according to the theoret-

ical computations of Dmitriev and Kokotushkin (1971) indicates the presence of a conductive layer in the earth's crust or upper mantle.

The curve of $|H_S^{\perp}|/|H_K^{\perp}|$, where $H_S^{\perp}$ and $H_K^{\perp}$ are the transverse components of the magnetic field for the Suntar dome and the Kempendya depression, is represented by a horizontal branch at level 1. In the same period interval the curve for $\varrho_T^{\perp}$ for the Suntar dome has a deep minimum. The absence of an $H^{\perp}$ anomaly contradicts the assumption that the minima of the longitudinal MTS curves for the Suntar dome are caused by the induction effect.

Besides the induction effect, we should also consider the flow-around and concentration effects. The analysis of maps of curve types indicates that these effects can manifest themselves in zones bordering the Kempendya and Ygyattan depressions and the Suntar dome. It is known that the flow-around and concentration effects attenuate the influence of the induction effect. This means that the above conclusions concerning the influence of the induction effect may be extended to flow-around and concentration effects.

Thus, our attempt to explain the minima and inflections of the MTS curves by field distortions leads to a series of contradictions:

1. the curves measured on the slopes of the Aldan anteclise lie significantly below the computed curves; 2. the longitudinal curves for the Suntar dome exceed the bounds within which the computed curves lie; 3. the value of $|H_z|/|H^{\perp}|$ for the slope of the Aldan anteclise and for the Botuoba saddle decreases with decreasing frequency; 4. the ratio of the values of $|H^{\perp}|$ for the Suntar dome and the Kempendya depression does not vary with frequency, and remains close to unity; 5. the inflections and minima of longitudinal curves for downwarps cannot be possibly explained by the distorting influence of horizontal inhomogeneities of the sediment cover.

Confronted with all these facts, we cannot conclude that distortion is the unique cause of the inflections and minima on the MTS curves. As a least contradictory explanation we might assume that there occurs in the earth's crust or upper mantle a considerably thick conducting layer. Smoothing the results of the formal interpretation of the MTS curves makes it possible to attenuate the S-effect and gives an average depth of about 30 km for this layer. According to geological and geophysical data, the Conrad discontinuity lies at a depth of 16—20 km in south-western Yakutia, and the Moho discontinuity at a depth of 26—36 km (Shtekh, 1965). All these seem to imply that the intermediate conducting layer is at the base of the earth's crust.

NORTH-EASTERN YAKUTIA

In this region, magnetotelluric and magnetovariation soundings were carried out within the Zyryanka depression. This depression has the form of a narrow graben-like trough, filled with Paleozoic and Mesozoic deposits (Elansky, 1964). The depression is 500 km long and not more than 100 km wide. The total conductivity of the sediment cover reaches a value of 1000—1400 Ω^{-1} in the depression, but decreases to 20—30 Ω^{-1} on the edges (Fig. 6, a).

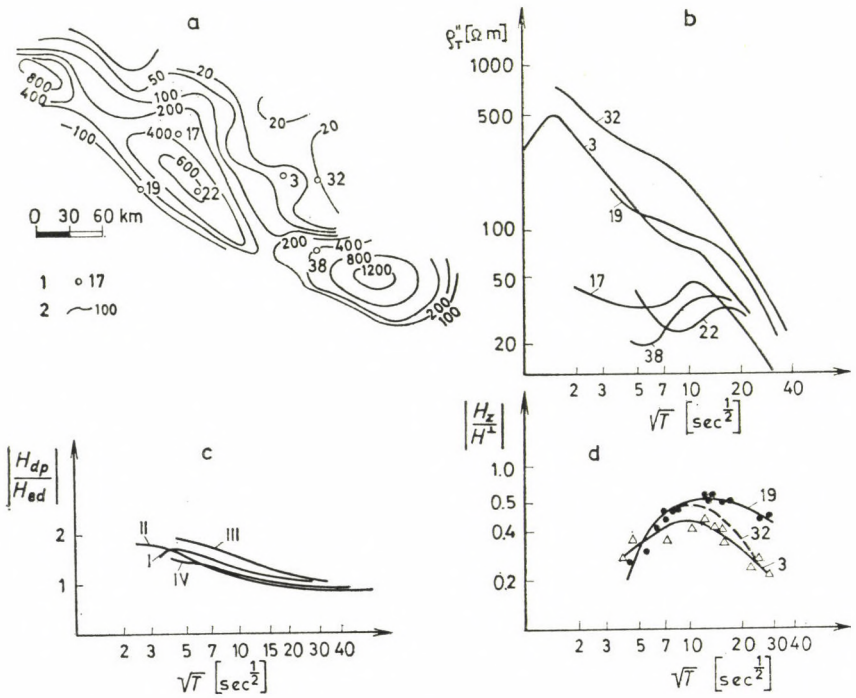


Fig. 6. MTS and MVS results for the Zyryanka depression: a – map of the total longitudinal conductivity of the sediment cover 1 – MTS site and its number; 2 – isolines of total longitudinal conductivity in $[\Omega^{-1}]$; b – typical longitudinal MTS curves; c – MVS curves: I – simultaneous observations at sites 18, 19; II – the same at sites 33, 34; III – at sites 37, 38; IV – at sites 3, 28; d – MVS curves

The measuring lines were oriented along and across the strike of the Zyryanka depression.

For the edge area, both longitudinal and transverse MTS curves have two descending branches, separated by inflections. For the axial part of the depression, the transverse curves are quite flat, but the longitudinal curves possess a minimum, an ascending branch and a steep descending branch.

Consider the longitudinal MTS curves together with MVS curves. Typical curves are shown in Figures 6, b, c, d.

Simultaneous magnetic observations at sites over the edge and over the axial pats of the depression indicate that in the time interval from 10 to 50 sec, the transverse component $H^{\perp}$ for the depression itself is 1.5 to 2 times greater than for the edge (Fig. 6, b). The redundant currents flowing in the depression thus turn out to be quite strong. With increasing periods the ratio of $H^{\perp}$ for the depression and for the edge diminishes and approaches unity at the period $T = 200-300$ sec which indicates that redundant currents decrease in that time interval. The curves for $|H_z|/|H^{\perp}|$ for the edge

of the Zyryanka depression have a maximum at $T \simeq 100$ sec and terminate with a steep descending branch (Fig 6, d). This means that the induction effect develops during periods not exceeding 100 sec.

From a comparison of the longitudinal MTS curves with the MVS curves we come to the conclusion that in the edge zones the first descending branch of the MTS curves of the time interval below 100 sec may be related to the induction effect, and that the second descending branch beginning at $T \approx 200$ sec is due to the presence of an intermediate conducting layer in the earth's crust or upper mantle. In this case, the minima on the MTS curves for the axial part of the depression are related to the presence of a conducting layer within the sediment cover, whereas the right descending branch is due to a deep conductive layer.

Averaging the results of a quantitative interpretation of the longitudinal MTS curves gives a depth of about 40 km for the deep conductive layer. As in south-west Yakutia, this depth belongs to the base of the earth's crust (Borisov, 1967).

ON THE NATURE OF THE DEEP CONDUCTIVE LAYER

In discussing the possible nature of this layer, we will adhere to the hypotheses of Elansky (1964) and Feldman (cf. Berdichevsky et al., 1969).

The release of water of crystallization from minerals corresponding to the epido-amphibolitic and, partly to the amphibolitic facies of metamorphism, and the partial melting of rocks stimulated by this water may create anomalous conductive zones in the earth's crust.

It was found experimentally that, in the presence of water, granite melts at a temperature of 500—700 °C, and that its electrical conductivity increases by a few orders of magnitude.

Do we have reasons to suppose that in south-west and north-east Yakutia temperature reaches 500—700 °C at depths of 30—40 km? One of the most distinguishing features of the geological history of this region is its high mobility. Shtekh (1965) groups the Vilyuisk hemisyneclise with structures that, according to Borisov (1967) are still at an active formation stage. Geothermic data also support the contemporary activity of this hemisyneclise (Shtekh, 1965). If, as assumed, the temperature at a depth of 8—9 km had a value of 360 °C, it might then well reach 500—700 °C at depths of 30—40 km. This temperature is critical for the development of melting and dehydration that apparently give birth to an intermediate conductive layer.

REFERENCES

BERDICHEVSKY, M. N., BORISOVA, V. P., BUBNOV, V. P., VANYAN, L. L., FELDMAN, I. S., YAKOVLEV, I. Y., 1969. The anomaly of crustal electric conductivity in Yakutia (in Russian). *Izv. Akad. Nauk SSSR, Fiz. Zemli*, No. 10.

BERDICHEVSKY, M. N., DMITRIEV, V. I., BUBNOV, V. P., YAKOVLEV, I. YA., VARLAMOV, D. A., KONNOV, YU. K., 1973. Magnetotelluric sounding of horizontally inhomogeneous media (in Russian). *Izv. Akad. Nauk SSSR, Fiz. Zemli*, No. 1.

BORISOV, A. A., 1967. Deep structure of the territory of the USSR (in Russian). Nedra, Moscow.

DMITRIEV, V. I., KOKOTUSHKIN, G. A., 1971. An Album of Reticulations for Magnetotelluric Sounding in Non-uniform Media (in Russian). MGU, Moscow.

ELANSKY, L. N., 1964. Relations between the deep and the surface hydrospheres of the Earth (in Russian). *Izv. Akad. Nauk SSSR, Ser. Geol.*, No. 9.

MOKSHANTSEV, K. B., 1971. Tectonic map of the Yakut ASSR (explanatory note) (in Russian). Yakutsk.

SHTEKH, G. I., 1965. Deep Structure and History of the Tectonic Development of the Vilyuisk depression (in Russian). Nauka, Moscow.

DEEP MAGNETOVARIATION STUDIES IN YAKUTIA

I. I. ROKITYANSKY, E. P. KHARIN, G. I. SHTEKH

Magnetovariation observations were carried out in 1967 by the Institute of Geology in Yakutsk, using stations of the Bobrov system along a profile across the Verkhoyansk folded system. A tectonic map of the studied area is shown in Figure 1. Typical examples of recorded variations are shown in Figure 2. Graphs of the relative amplitudes of the variations are presented in Figure 3. Here, the so-called Verkhoyansk geomagnetic anomaly clearly manifests itself. The anomaly of the D component is considerably clearer than that of the H component which suggests a meridional elongation of the conductive layer that gives birth to the Verkhoyansk anomaly. At the same time, the Wiese vectors (Fig. 1) indicate a vast conducting body of quasilatitudinal extension. It is probable that a single conductive body is present, the bulk of which lies north of the profile, and a thick meridional offshoot extends in the vicinity of station H. Interpretation of such a three-dimensional anomaly is possible only from data obtained by an area survey. We limit ourselves to an approximate interpretation based on a two-layer model approximating the meridional offshoot of the body; and proceed from the anomalies of the D and of the Z components. The constant Z component will be accounted for by the influence of the bulk of the conductive body, located to the north of the profile. This explanation is justified by the fact that the observed variations in H and Z are usually in opposite phase. Relation between H and Z leads to unstable results if the amplitude of Z is normalized by that of D, so we shall use for normalization the modulus of the horizontal vector: $\sqrt{H^2 + D^2}$.

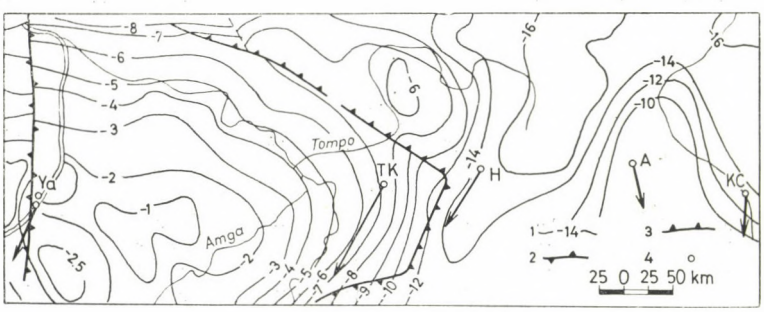


Fig. 1. Tectonic map of the investigated area and Wiese vectors
1 – contour lines of the surface of the crystalline basement, in km; 2–3 – deep faults; 4 – observation sites; Ya – Yakutsk, TK – Tyoply Klyuch, H – Nekyunnyakh, A – Agayakan, KC – Kuranakh-Sala

Assuming that the anomaly is caused by heating due to the screening of the heat flow by the thick sediment beds, and that the anomaly is presumably a centre of regional metamorphism, we find, by analogy with other similar anomalies, most likely depths of 15—30 km. Interpretation is possible in this case by means of a model of two-dimensional inhomogeneous surface shell. For a thin network of observations, lifting the shell from a depth of 15—30 km up to the surface would not introduce any significant error in interpretation. The D and Z anomalies shown by thick lines in Figure 3 are computed for a surface shell of longitudinal conductivity $S(x)$, whose graph is shown in the lower part of Figure 3. The computation is made with the formulae (Rokityansky and Shuman, 1971):

$$d = \frac{D}{D_0} = 1 + \frac{1}{2} S(x)\, \xi_0$$

$$z = \frac{Z}{D_0} = \frac{\xi_0}{2\pi} \int \frac{S(\alpha)\, d\alpha}{\alpha - x}$$

The impedance ξ_0 was taken as $5 \cdot 10^{-4}\ \Omega$, which corresponds to the average value for the time interval of 15—60 min, obtained from earthwide MVS and MTS data for continental structures with a longitudinal conductivity of the upper layers not exceeding 200 Ω^{-1}. It is seen that the computed curves are in good agreement with the observations.

Supplementary data from a more dense network of observations would be necessary for a fuller interpretation. At the moment, we can only estimate the minimum longitudinal conductivity of the body at the centre of the anomaly. It has a value of 5000 Ω^{-1}.

Another method of interpretation is based on the use of the frequency dispersion of the anomaly. The dependence of $d_a = D/D_0 - 1$ on period is shown by points in the upper part of Figure 4. Therein curves for $\xi(\sqrt{T})$ computed for an eight-layer section conform to global sounding data are also shown. The $d_a(\sqrt{T})$ curve has been shifted vertically so as to make its long-period branch coincide with the $\xi(\sqrt{T})$ curve, as shown in Figure 4.

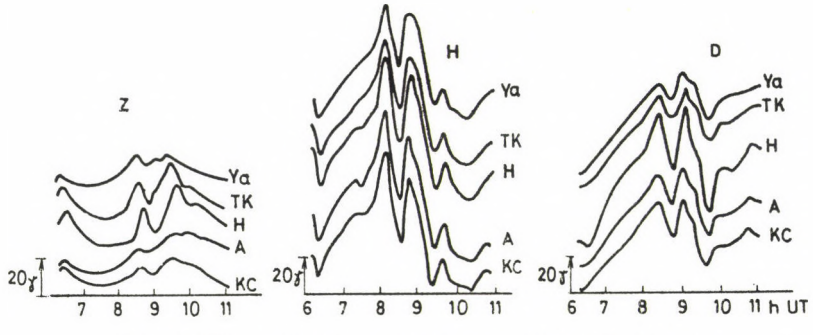


Fig. 2. Example of magnetograms (July 18, 1967)

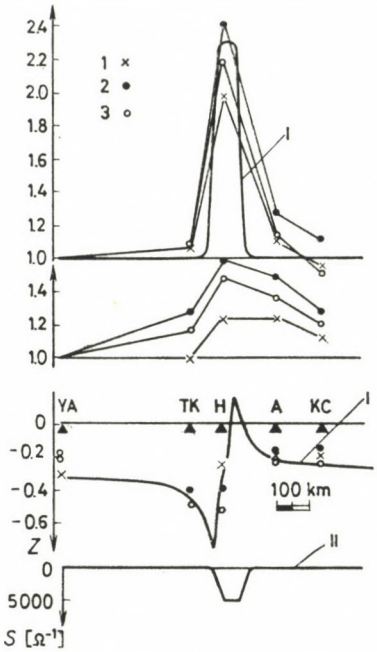


Fig. 3. Relative change in amplitude of geomagnetic variations $d = D/D_{ya}$, $h = H/H_{ya}$; $z = Z/\sqrt{H^2 + D^2}$ where D_{ya} and H_{ya} are the amplitudes of the D and H components observed at Yakutsk; 1 – time interval 5–15 min; 2 – time interval 15–60 min; 3 – time interval 60–180 min; I – theoretical curves; II – longitudinal conductivity of the shell

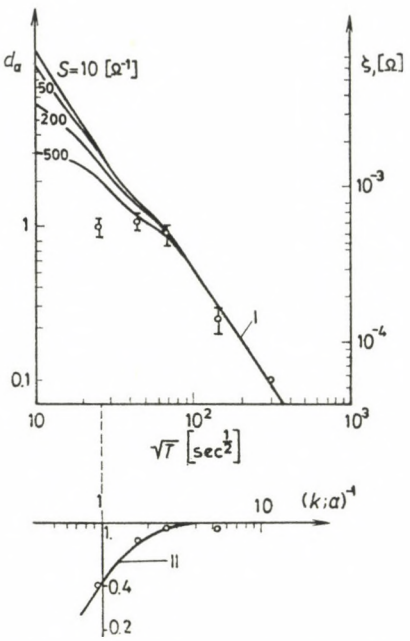


Fig. 4. Frequency dispersion of the D-component anomaly I – ξ ($\sqrt{T}$) curves, curve parameter is S of the sedimentary strata (Ω^{-1}); II – modulus of the function $V(1/k_i a)$, computed for $\sigma_i/\sigma_e = 10^3$, where σ_i and σ_e are conductivities of the anomalous body and of the enclosing rock, respectively

The left part of the $d_a(\sqrt{T})$ curve diverges from the $\xi(\sqrt{T})$ curve due to self-induction of anomalous currents. The frequency dispersion of the anomalous effect caused by self-induction is found by subtracting the $d_a(\sqrt{T})$ curve from the $\xi(\sqrt{T})$ curve. The longitudinal conductivity of the sediment strata in the neighbourhood of the anomaly is of the order of 100 Ω^{-1}. We may thus choose for the subtraction $\xi(\sqrt{T})$ curves for $S = 50\ \Omega^{-1}$ or $S' = 200\ \Omega^{-1}$. In the time interval of interest, both cases give nearly the same results, as shown in the lower part of Figure 4 (points). Further interpretation is based on the solution of the familiar problem for a circular cylinder (Rokityansky et al., 1968). Assuming an anomaly of electric type, we determine the theoretical function $V(1/k_i a)$, whose modulus is shown by the solid curve in the lower part of Figure 4. This curve is shifted along the horizontal axis to a position at which the best agreement is obtained with the experimental data, as also shown in Figure 4. The horizontal displacement of the curve $V(1/k_i a)$ is equal to 27. Taking into account that

$(k_i a)^{-1} = \sqrt{T}\,(2\,\pi\mu\sigma_i\,a^2)^{-1/2}$, we compute the body parameter $\sigma_i Q$ equal to the longitudinal conductivity of the body, i. e. to the product of the electrical conductivity by the area Q of the cross section. The following result is obtained: $\sigma_i Q = 400 \cdot 10^6\ \Omega^{-1}$m. Comparing this quantity with the value obtained above for the minimum estimate of the longitudinal conductivity of the layer under the station H ($S = 5000\ \Omega^{-1}$), we find for the effective width of the conductive body a value of 80 km. Note that a longitudinal conductivity of 5000 Ω^{-1} may correspond to a 5 km thick layer of specific resistivity of 1 Ωm, as well as to a 50 km thick layer of specific resistivity of 10 Ωm, etc. Since a thickness of more than 50 km for the anomalous body is rather improbable, we obtain as a minimal estimate of the specific conductivity of the anomalous body 10^{-1} $(\Omega\text{m})^{-1}$, or more probably, 1 $(\Omega\text{m})^{-1}$. Such a high value of electrical conductivity may be explained by the partial melting of the material of the earth's crust.

REFERENCES

ROKITYANSKY, I. I., LOGVINOV, I. M., LUGININA, N. A., 1968. Magnetovariation profiling of the Ukrainian shield (in Russian). *Izv. Akad. Nauk SSSR, Ser. Fiz. Zemli*, No. 3.

ROKITYANSKY, I. I., SHUMAN, V. N., 1971. The inverse problem in magnetovariation profiling (in Russian). *Izv. Akad. Nauk SSSR, Ser. Fiz. Zemli*, No. 8.

DEEP ELECTROMAGNETIC STUDIES IN THE FAR EAST

L. L. VANYAN, V. V. BORETS, A. M. LYAPISHEV, B. E. MARDERFELD, A. V. RODIONOV

Deep electromagnetic survey of the Soviet Far East assumes a complex character. Electric conductivity is studied with the help of magnetovariation profiling and magnetotelluric sounding.

MAGNETOVARIATION PROFILING

25 stations of magnetovariation profiling are located in Sakhalin, the Kurile Islands and on the coastal part of the continent (Vanyan et al., 1968). We consider the results of the analysis of bay-like perturbations of a period of about an hour. The intensity of the variation of the horizontal component of the magnetic field decreases smoothly from north to south.

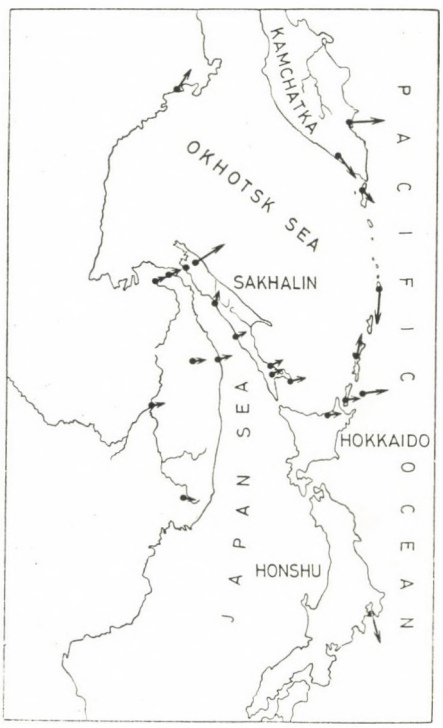


Fig. 1. Map of Wiese-Parkinson vectors

The variation of the vertical component shows considerable changes in intensity and, in some of the cases, also in form.

The system of Wiese-Parkinson inductive vectors **K** at a number of stations in the Far East is presented in Figure 1. The direction of the vector **K** is such that one observes along it the maximum similarity between the variation of the vertical component and that of the horizontal component; its modulus is equal to the ratio of the amplitude of variation of the vertical component to that of the horizontal component. The system of coordinates is chosen in such a way that the vector **K** is oriented in the direction of increasing electric conductivity. At the majority of stations, the vector is oriented normally to the shore line, towards the sea or the ocean. Its modulus increases when approaching the shore line. A deviation from the regularity is observed in the area of the central Kurile Islands (Fig. 3, a), where the vector is oriented along the island arc. This situation will be discussed below.

It is natural to suppose that the geomagnetic anomalies considered here are related to the *coast effect*, i. e. to the action of oceanic induction currents.

To a first approximation, the coast effect may be investigated by computing the magnetic field of direct currents flowing in a strip of finite width (Marderfeld et al., 1969b). To approach realistic conditions, it is necessary to take an additional account of, first, the attenuation of the coast effect due to the influence of the high conductivity of the mantle (external induction effect), and secondly, of the electromagnetic interaction between the currents flowing in the strip (internal induction effect).

The *external induction effect* is taken into account by computing the electric field in a model in which the layer of sea water is separated from the highly conductive mantle by a weakly conducting layer.

The role of the *internal induction effect* is difficult to allow for theoretically. The problem is solved by means of physical modelling. As indicated by experimental results, the width of the oceanic strip causing the coast effect is approximately 3—5 electromagnetic wave lengths in sea water. For variations with a period of an hour, this distance is 300—600 km.

To take into account the external as well as the internal induction effects, we computed the magnetic field of oceanic induction currents. For Sakhalin, the coastal parts of the continent, the southern Kurile Islands and the central part of Japan, our results were in good agreement with the observed geomagnetic anomalies, which confirms the relation of these anomalies with the coast effect (Marderfeld et al., 1969b; Vanyan and Marderfeld, 1971).

THE ANOMALY OF THE S_q-VARIATION IN THE CENTRAL KURILE ISLANDS

As indicated earlier, in the area of the central Kurile Islands (Iturup (T), Urup (U), Chirpoi (Ch), Simushir (S)), the induction vectors constructed for bay-like variations were oriented along the island arc, an anomaly caused by transverse currents. This suggests that the central Kurile anom-

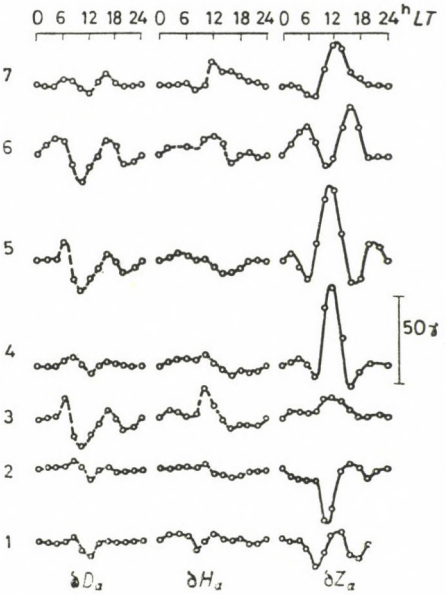


Fig. 2. Anomalous diurnal variation of the geomagnetic field
1 – Iturup Is.; 2, 3, 4 – Urup Is.; 5 – Chirpoi Is.; 6 – Simushir Is.; 7 – Matua Is.

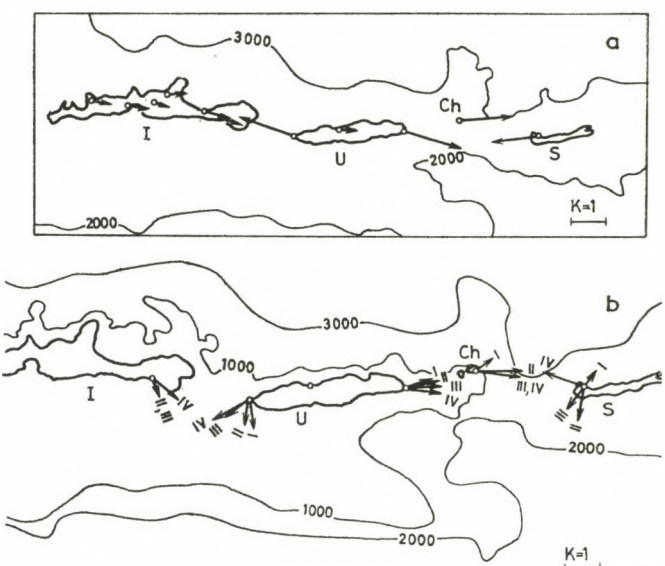


Fig. 3. Map of Wiese-Parkinson vectors: a – for bay-like variations; b – for diurnal variations; I, II, III, IV – numbers of the harmonics

aly is associated with deep sources. The anomaly is evident in the observation of the S_q-variations (Vanyan et al., 1971; Marderfeld et al., 1969a). The anomalous diurnal variation for the central Kurile Islands, obtained by eliminating the normal diurnal variation for Yuzhno-Sakhalinsk, is shown in Figure 2. The induction vector constructed from the first four harmonics of S_q is presented in Figure 3. In the majority of cases, this vector is oriented along the islands. As we saw, the central Kurile anomaly is observed over a wide time interval, including the diurnal period. This confirms its plutonic nature.

Note that the central Kurile region features anomalies in other geophysical fields (Lugovenko et al., 1973). The deep structure of this region is in sharp contrast with that of the southern and northern parts of the Kurile-Island arc. The decrease of the thickness of the earth's crust to 12 km, the approach of the Curie isotherm to the surface, the anomalously low seismic activity, and the high heat-flow values, all bear witness to the anomalous state of the upper mantle in the region of the central Kurile-Islands.

MAGNETOTELLURIC SOUNDINGS

Deep magnetotelluric soundings were carried out in Yuzhno-Sakhalinsk, Aleksandrovsk, Khabarovsk, Komsomolsk, Iturup, Kunashir and Shikotan. For coastal stations, the polarization of the electric field is characteristically perpendicular to the coast. This indicates the coast effect that leads to the sharp strengthening of the component of the electric field normal to the coast and to the weakening of the component parallel to the coast (Cox et al., 1970). Because of that, we interpret the effective curves $\varrho_T = \sqrt{\varrho_T^{\parallel} \varrho_T^{\perp}}$ (Fig. 4). These curves obtained at six stations of different geoelectric conditions are nevertheless in good agreement with each other. Their interpretation yields a conductive layer at a depth of 100—120 km, i. e. in the upper mantle. This is a layer of limited thickness. Curve I for Yuzhno-Sakhalinsk indicates a second conductive zone at about 400 km depth.

It should be noted that the width of the strip in which, together with the coast effect, the Z-anomaly is observed, is approximately twice the

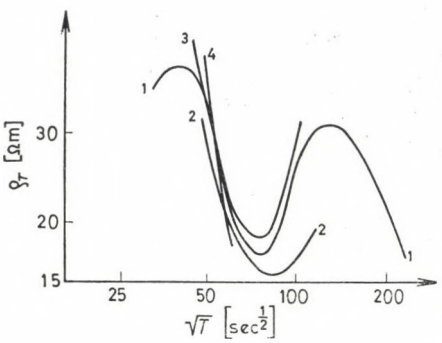


Fig. 4. Effective magnetotelluric sounding curves
1 – Yuzhno-Sakhalinsk; 2 – Aleksand- rovsk; 3 – Khabarovsk; 4 – Iturup Is. Vertical scale is about twice of the horizontal scale

depth of the conductive layer (Vanyan et al., 1969; Weidelt, 1971). Observations made in the Far East indicate that, on the average, the Z-anomaly decays over a distance of 250—300 km, from this we find a depth of 120—150 km for the first conductive layer, which agrees with the results of magnetotelluric sounding.

REFERENCES

Cox, C. S., Filloux, J. H., Larsen, J. C., 1970. Electromagnetic studies of ocean currents and electrical conductivity below the ocean floor. A. E. Maxwell (Ed.) The Sea. Wiley Intersc.

Marderfeld, B. E., Lyapishev, A. M., Tuezov, I. K., 1969a. The anomaly of the S_q variations in the central Kurile Islands (in Russian). *Trudy Sakh. KNII*, **20**, No. 1.

Marderfeld, B. E., Rodionov, A. V., Tsilin, L. A., 1969b. The influence of surface geoelectric inhomogeneities on geomagnetic variations (in Russian). *Trudy Sakh. KNII*, **6** and **20**, No. 1.

Lugovenko, V. N., Lyapishev, A. M., Marderfeld, B. E., 1973. On the nature of the anomaly in geomagnetic variation in the central Kurile Islands (in Russian). *Geomagn. Issled.* **15.**

Vanyan, L. L., Lyapishev, A. M., Marderfeld, B. E., Rodionov, A. V., Tuezov, I. K., 1971. The anomalous behaviour of the solar-diurnal magnetic variations in the Kurile Islands (in Russian). *Geomagn. Issled.*, No. 13.

Vanyan, L. L., Marderfeld, B. E., 1971. On the nature of the Japanese anomaly in geomagnetic variation (in Russian). *Geomagn. Issled.*, No. 13.

Vanyan, L. L., Marderfeld, B. E., Rodionov, A. V., 1969. The influence of induction currents in the mantle on the distribution of geomagnetic variation in the presence of the coast effect (in Russian). *Trudy Sakh. KNII*, **20**, No. 1.

Vanyan, L. L., Marderfeld, B. E., Tuezov, I. K., 1968. Anomaly of geomagnetic variations in the Far East (in Russian). *Geomagn. i Aeron.* **8**, No. 4.

Weideld, P., 1971. The electromagnetic induction in two thin half shells. *Z. Geophys.* **37.**

DEEP MAGNETOTELLURIC SURVEYS IN SAKHALIN

M. N. BERDICHEVSKY, G. A. CHERNYAVSKY, I. M. ALPEROVICH

Magnetotelluric surveys in the Sakhalin Island have been carried out since 1964. Since then, more than 200 MTS have been performed. Preliminary MTS results are interpreted in Berdichevsky et al. (1972). The recent results of theoretical computations, physical modelling and experimental studies have made it possible to improve the MTS data.

The tectonics of Sakhalin features large linear structures elongated in a meridional direction (along the island). These break down into a series of smaller structures, among which are found linear as well as non-linear forms (Fig. 1). The central synclinorium and the adjacent Western and Eastern anticlinoriums are sharply defined on the tectonic map. The central synclinorium is filled by conductive rocks of a Cenozoic complex, overlying Mesozoic and metamorphosed Paleozoic rocks. These same rocks are found in the section of the western and eastern anticlinoriums, the Cenozoic complex being much thinner here.

The location of the MTS sites is shown in Figure 1. Most of them are in the zone of more or less well expressed linear tectonics.

MTS observations were made with the help of a standard MTL-62 apparatus, providing to record variations of periods from a few seconds to an hour. At some of the sites, a high frequency equipment was used, designed by S. M. Krylov and N. P. Vladimirov of the Institute of Physics of the Earth of the Academy of Sciences of the USSR.

For the most part, the MTS data were processed with a computing programme using mathematical filtering (developed at the All-Union Geophysics Research Institute VNIIGEOFIZIKA by I. A. Bezruk and O. M. Chinareva).

The MTS curves are oriented in two directions, according to the regional tectonics of northern Sakhalin: meridionally (longitudinal $\varrho^{\parallel}$ curves) and latitudinally (transverse $\varrho^{\perp}$ curves).

Characteristic MTS curves are shown in Figure 2. As seen in Figure 2, a, the right-hand-side portions of the longitudinal curves consist of ascending branches, resulting from the high-resistivity Mesopaleozoic, of minima and inflections preceeding strong maxima, terminating with steep descending branches. It is worth noting that the longitudinal curves are in better agreement with each other as to the position of minima (inflections) and descending branches, than the transverse curves, in spite of the fact that the minima (inflections) in the longitudinal curves all occur nearly in the same time interval. This allows us to assume that in Sakhalin, as in other areas (Berdichevsky et al., 1969, 1970), the longtudinal curves are less distorted than the transverse ones.

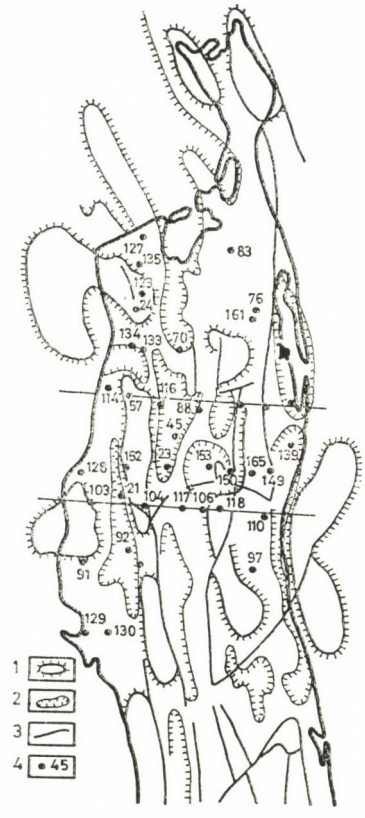


Fig. 1. Tectonic map (uncovered) of northern Sakhalin
1 – large uplifts; 2 – depressions; 3 – faults; 4 – MTS sites

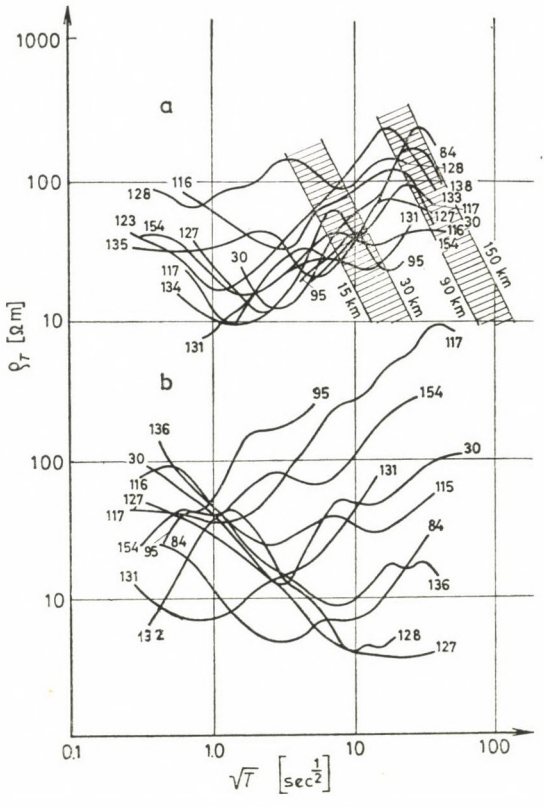


Fig. 2. Characteristic MTS curves
a – longitudinal; b– transverse

The results of a formal interpretation permit to associate the minima (inflections) of the MTS curves with the presence of an intermediate conductive layer in the earth's crust. Interpretation of the longitudinal curves yields $h = 15-30$ km depth for that layer. Figure 3 shows graphs for $h^{\parallel}(S)$ and $h^{\perp}(S)$ constructed from the interpretation of the longitudinal and transverse curves, respectively (S is the total longitudinal conductivity of the sedimentary cover). The majority of points in the graph for $h^{\parallel}(S)$ fall in a band between 15 and 30 km (there is no relation between $h^{\parallel}$ and S). At the same time a clear regularity is observed in the graph for $h^{\perp}(S)$: an increase in S corresponds to a decrease in $h^{\perp}$. This provides a convincing example of how a change in S distorts the transverse MTS curves (the S-effect).

An analogous pattern is obtained for the right-hand-side descending branches of the MTS curves determined by an increased electric conductivity of the upper mantle as it is warmed up. In Figure 3 graphs for $H^{\parallel}(S)$

and $H^{\perp}(S)$ are shown, where H is the depth down to the conductive zone of the upper mantle, determined from longitudinal and transverse MTS curves. The majority of points on the $H^{\parallel}(S)$ graph are clustered in a band from *90 to 150 km*. The regularity observed in the $h^{\perp}(S)$ graph also holds for $H^{\perp}(S)$; the maximum of $H^{\perp}$ is found at points where the value of S is minimum.

These properties of the longitudinal and transverse MTS curves are clearly revealed in the histograms of the depths h and H (Fig. 4). Histograms constructed from the interpretation of longitudinal MTS curves possess distinct maxima in the intervals $h = 15-30$ km and $H = 80-120$ km. In the histograms constructed from transverse MTS curves, there are only insignificant isolated maxima, distributed in the intervals $h = 10-75$ km and $H = 50-400$ km.

All that proves that the longitudinal MTS curves are the least distorted by the S effect.

In the analysis of longitudinal curves, one should not overlook their possible distortion by the induction effect (Berdichevsky et al., 1973) arising from surplus currents flowing in the internal depressions of Sakhalin and of the Okhotsk Sea. Due to the induction effect, minima (inflec-

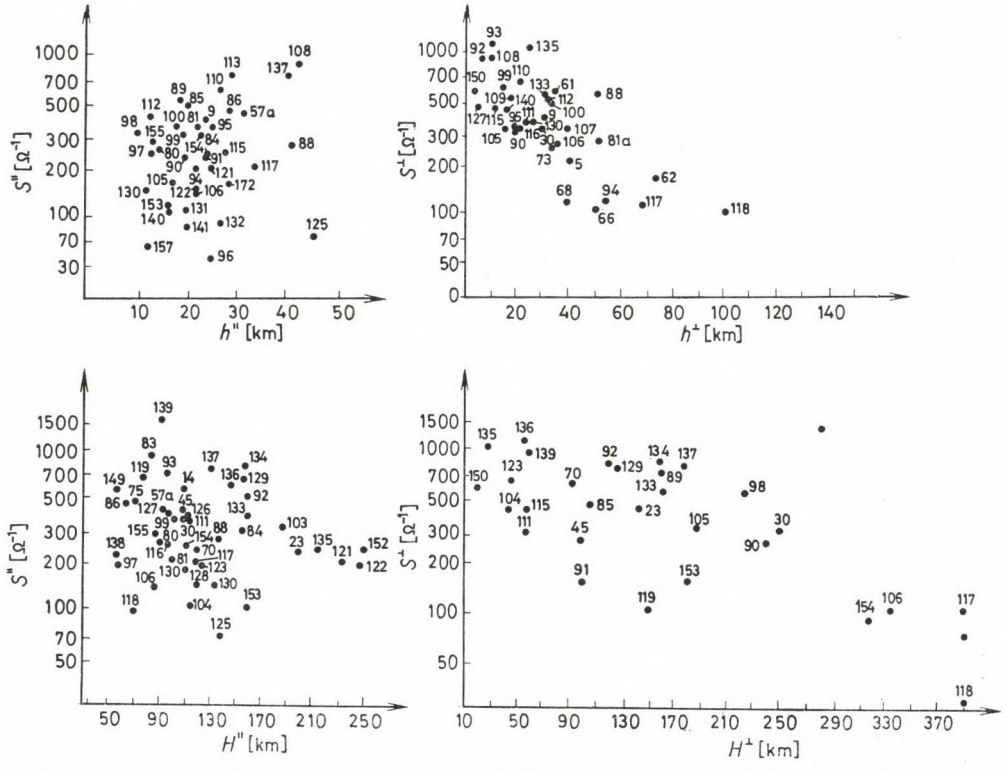


Fig. 3. Plots of the functions $S(h)$ and $S(H)$; numbers of MTS sites are given near the dots, h and H are depths of the upper and lower conductive zone

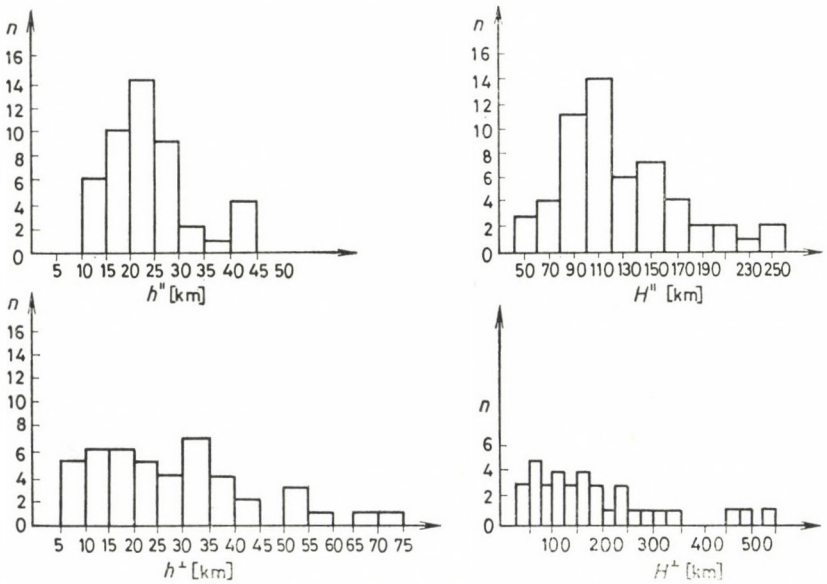


Fig. 4. Histograms for h and H; n – number of cases; $h^{\parallel}$, $H^{\parallel}$ – depths of the first and second conductive layers, obtained from longitudinal curves; $h^{\perp}$, $H^{\perp}$ – depths of the first and second conductive layers, obtained from transverse curves

tions) appear on the ascending branches of the longitudinal MTS curves; their formal interpretation leads to false ideas of the presence of an intermediate conductive layer. The question of the origin of the minima and inflections can be resolved by means of an estimation according to the Dmitriev—Berdichevsky approximate formula:

$$\varrho_T = 0.2\,T \left| \frac{796}{\tilde{S}} \right|^2$$

$$\tilde{S}(x_q) = \frac{2}{\lambda_1} \int_{-\infty}^{+\infty} \frac{S(x)\,dx}{1 + \left(\frac{(2\pi\ (x - x_q)}{\lambda_1} \right)^2}$$

where $\tilde{S}$ is the average longitudinal conductivity of that segment which, for a given wavelength λ_1, has significant influence on the observed electromagnetic field. Calculations were performed for two cases. In the first, we took into account the induction effect of the sedimentary cover of Northern Sakhalin and the shelf of the Okhotsk Sea. In the second, the influence of the ocean has not been considered. The results of the calculations are shown in Figure 5. The ascending branches of the curves computed with taking the influence of the ocean into account lie significantly lower than the right-hand-side ascending branches of the observed curves. We may

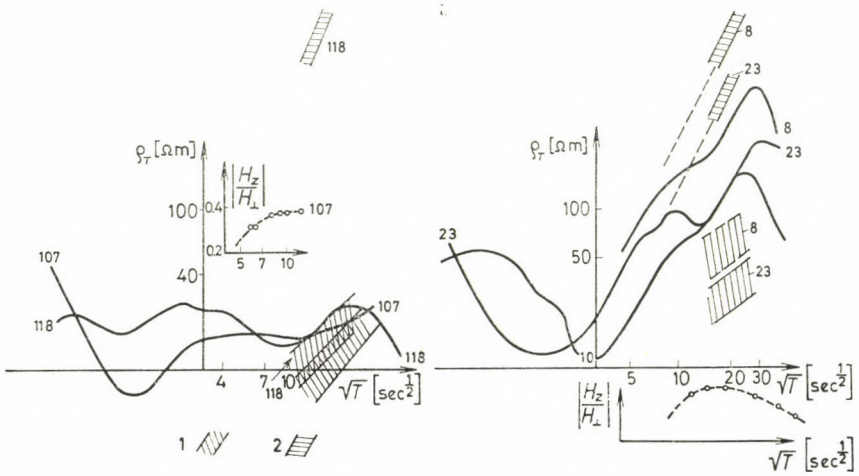


Fig. 5. Typical longitudinal curves
a – eastern coast of Northern Sakhalin; b – central and northern parts of Sakhalin. The induction effect with (1) and without (2) the influence of the ocean

thus suppose that, in Northern Sakhalin, the minima and inflections of the longitudinal MTS curves are caused by the regional induction effect of oceanic currents. When the influence of the sea is disregarded, we obtain curves, whose righ-hand-side ascending branches lie above the corresponding branches of the observed curves. For this reason the induction effect of the internal depressions may be assumed to be insignificant.

Results of magnetovariation soundings also indicate that the longitudinal ϱ_T curves might be distorted by the induction effect. As known (Dmitriev and Kokotushkin, 1971), the induction effect observed in the vicinity of zones of higher conductivity is accompanied by an increase of the vertical component H_z of the magnetic field. As seen in Figure 5, the minima and inflections of the longitudinal MTS curves correspond to the ascending branches on the curves for $|H_z/H^\perp|$, where $H^\perp$ is the transverse component of the magnetic field. This behaviour of the magnetic field permits to relate the minima and inflections on the MTS curves to the induction effect. As to the right-hand-side descending branches on the MTS curves, they correspond to the descending branches on the curves $|H_z|H^\perp|$. Consequently, the induction effect is insignificant in this time interval, i. e. the right-hand-side descending branches of the MTS curves are related to a deep conductive layer.

So it is quite certain that in Northern Sakhalin there is a conductive layer at a depth of around 100 km. The occurrence of a conductive layer at 20—30 km depth (which, by the way, occurs in many areas of the earth) is considered as doubtful. However, two facts in support of such a layer should be mentioned: a) the minima and inflections on the transverse and longitudinal MTS curves are well correlated with each other; b) the value of $h^{||}$ determined by formal interpretation from the longitudinal MTS

curves is rather stable, and only weakly depends on the distance from the Okhotsk Sea. This contradiction may be resolved by assuming that the distortion caused by the induction effect and the influence of the conductive layer occur in the same time interval.

We identify the conductive layer lying at a depth of about 100 km with upper mantle rocks, heated to about 1000 °C. The MTS data are confirmed by the results of the magnetovariation surveys in Sakhalin made by Marderfeld (cf. Vanyan et al., 1968). According to his data, the conductive layer lies at a depth of 120—140 km. Even closer values, from 110 to 120 km, were observed in Central Japan and the South Kurile Islands.

REFERENCES

Berdichevsky, M. N., Borisova, V. P., Vanyan, L. L., Feldman, I. S., Yakovlev, I. A., 1969. Anomaly of the electric conductivity of the earth's crust in Yakutia (in Russian). *Izv. Akad. Nauk SSSR, Ser. Fiz. Zemli*, No. 9.

Berdichevsky, M. N., Bubnov, V. P., Dmitriev, V. I., Yakovlev, I. A., Varlamov, D. A., Konnov, Yu. K., 1973. Magnetotelluric sounding of horizontally inhomogeneous media (in Russian). *Izv. Akad. Nauk SSSR, Ser. Fiz. Zemli*, No. 1.

Berdichevsky, M. N., Chernyavsky, G. A., Alperovich, I. M., Borisova, V. P., Bubnov, V. P., 1972. Results of deep magnetotelluric sounding in Sakhalin (in Russian). *Izv. Akad. Nauk SSSR, Ser. Fiz. Zemli*, No. 3.

Berdichevsky, M. N., Dubrovsky, V. G., Nepesov, K. N., Solokhov, V. V., Fainberg, E. B., 1970. Geoelectric characteristics of the earth's crust and upper mantle in Turkmenia (in Russian). *Izv. Akad. Nauk SSSR, Ser. Fiz. Zemli*, No. 11.

Dmitriev, V. I., Kokotushkin, G. A., 1971. Album of Reticulations for Magnetotelluric Sounding of Nonuniform Media (in Russian). MGU, Moscow.

Vanyan, L. L., Marderfeld, B. E., Tuezov, I. K., 1968. Anomalies of geomagnetic variations in the Far East (in Russian). *Geomagn. i Aeron.* **8**, No. 4.

DEEP MAGNETOTELLURIC SURVEYS IN KAMCHATKA

YU. F. MOROZ, V. I. POSPEEV

Deep magnetotelluric surveys were carried out in the north-western part of the Kamchatka Peninsula by the East-Siberian Geophysical Trust.

The investigated region is a part of the Western Kamchatka folded block zone and the Ichin downwarp. The Ichin downwarp joins on its western side on the Okhotsk Epimesozoic platform. Within the region of the Western Kamchatka folded block, large linear tectonic units are present: the Tigil uplift and the Palana depression (Fig. 1).

The Western Kamchatka folded block zone (A, C) and the Ichin downwarp (B) are separated by a deep fault (jointing zone). They are filled with Cenozoic and Cretaceous deposits 7 km thick overlaying in the western part by a cover of Quaternary basalts of the Median Volcanic Belt. The hydrothermal zone is associated with the volcanic belt.

A geoelectric section of the area reproduced from drilling data and electric prospecting presents the following pattern. In the upper part of the section, there lie relatively weakly metamorphosed Cenozoic deposits up to 4 km thickness, their resistivity varies from 4 to 20 Ωm. Lower down, there occur rocks of an upper Cretaceous complex, of 40–400 Ωm resistivity and about 3 km thickness. A high-resistivity Lower Cretaceous complex lies at the basis of the section.

The MTS profiles traversed the depression from NW to SE, from the coast of the Okhotsk Sea to the Median Volcanic Belt.

The MTS curves depend to a large degree on the orientation of the measuring lines. As basic curves, we consider longitudinal and transverse

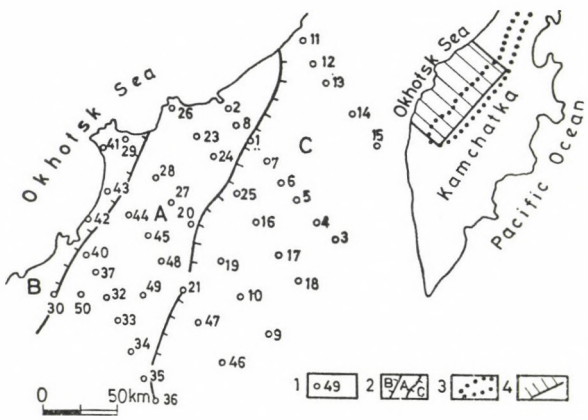


Fig. 1. Map of the survey in Western Kamchatka
1 – MTS sites; 2 – boundaries of first or der structures; A – Tigil uplift; B – Ichin downwarp; C – Palana depression; 3 – Median Volcanic Belt; 4 – contours of the stuied area

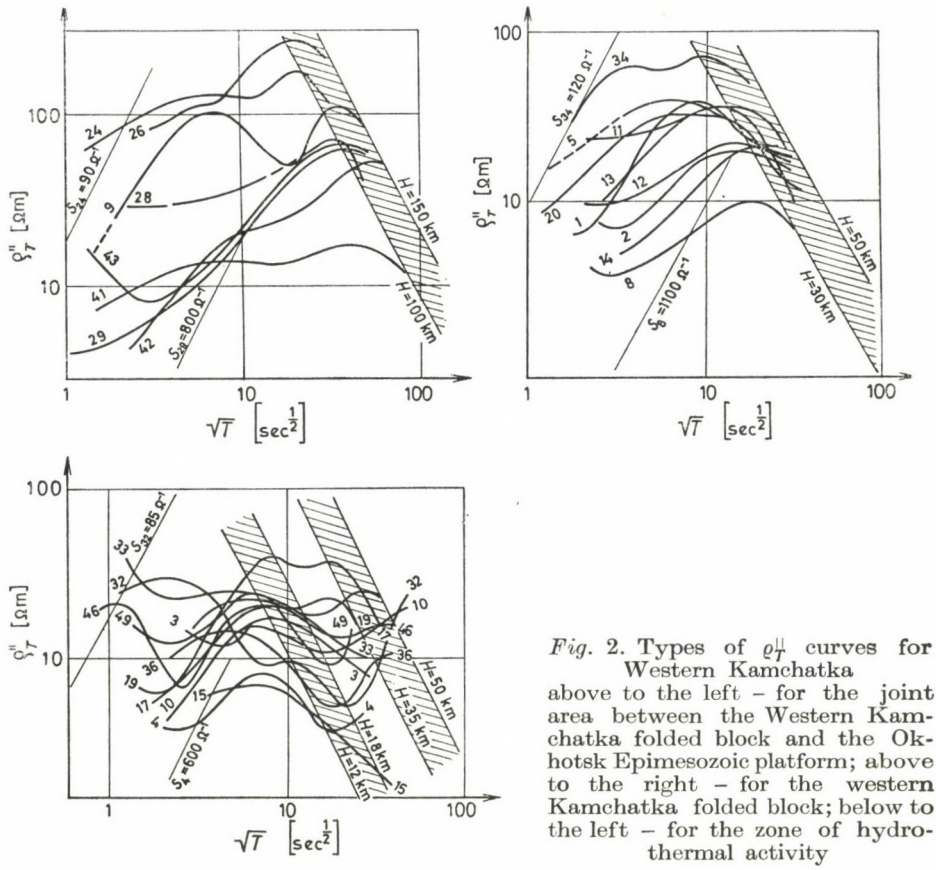


Fig. 2. Types of $\rho_T^{\parallel}$ curves for Western Kamchatka
above to the left – for the joint area between the Western Kamchatka folded block and the Okhotsk Epimesozoic platform; above to the right – for the western Kamchatka folded block; below to the left – for the zone of hydrothermal activity

curves oriented along and across the strike of the structural zones. The transverse curves were used to determine the total longitudinal conductivity of the Cenozoic complex. The longitudinal curves provide information on the electric conductivity of the earth's crust and upper mantle. These curves are shown in Figure 2. Their formal interpretation indicates conductive layers in the depth intervals of 12–18 km, 30–50 km and 100–150 km.

We now proceed to estimate the degree of distortion of the longitudinal MTS curves (Berdichevsky et al., 1973).

A correlation graph for $h''(S)$ is shown in Figure 3, a, where h'' is depth of the conductive layer, and S is the total longitudinal conductivity of the Cenozoic complex. The lack of correlation between these quantities indicates that the S-effect is insignificant.

Correlation graph for $h''(L)$ is shown in Figure 3, b where L is the distance between the sounding sites and the coast line. There is no visible correlation between h'' and L, i.e. the induction effect of oceanic currents is also insignificant. It is thus not possible to relate the descending branches and minima of the MTS curves to the induction effect.

The longitudinal curves for Western Kamchatka are thus completely satisfactory to determine the depth down to the conductive layers of the earth's crust and upper mantle.

The zones of occurrence of the conductive layers are shown in Figures 4 and 5. A conductive layer at a depth of 30–40 km is found almost everywhere. Its electric conductivity increases considerably in the vicinity of the volcanic belt. A second conductive layer, at a depth of 100–150 km is found in the west, in the area of transition to the Okhotsk Epimesozoic platform. Still another conductive layer, at a depth of 12–18 km, is found in the East in the area of the Median Volcanic Belt and in its periphery.

The earth's crust in Kamchatka is of an intermediate type, its thickness being 25–30 km (Demenitskaya, 1967). Consequently, the conductive layer found at depths of 12–18 km is in the crust, whereas the conductive layers at 30–50 km and 100–150 km depths belong to the upper mantle.

A conductive layer belonging to the crust was discovered in the hydrothermal zones of the Median Volcanic Belt. It may be due to the dehydration of greenstone, amphibolite and granulite facies, and to the enrichment with highly-conductive solutions. The rock dehydration occurs in the temperature range of 400–800 °C (Fig. 5). In the presence of highly activated water and at temperatures above 600 °C partial melting of rocks of the granulite facies may occur.

The conductive layers in the upper mantle apparently come into being owing to partial melting of ultrabasic rocks. Considering these layers as

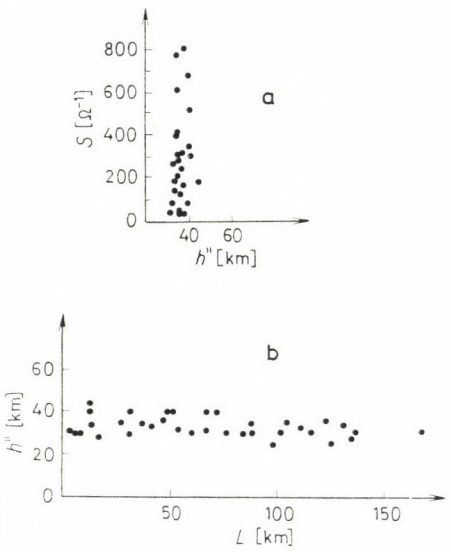


Fig. 3. Analysis of possible distortions of the MTS curves
a – correlation garph for h'' (S); b – correlation graph for h'' (L). h'' – depth of the conductive layer; S – horizontal conductivity; L – distance from the sea

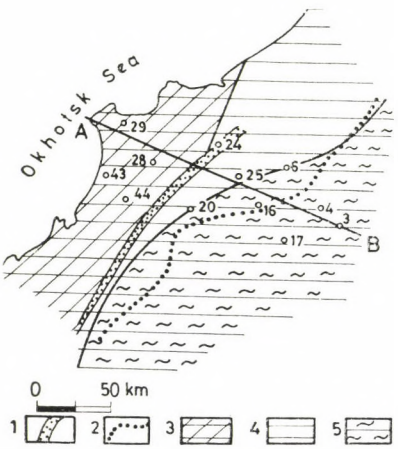


Fig. 4. Zonation of Western Kamchatka according to MTS curve types
1 – deep fault zone; 2 – boundary of the Median Volcanic Belt; 3 – conductive layer in 100–150 km; 4 – in 30–50 km; 5 – in 12–18 km

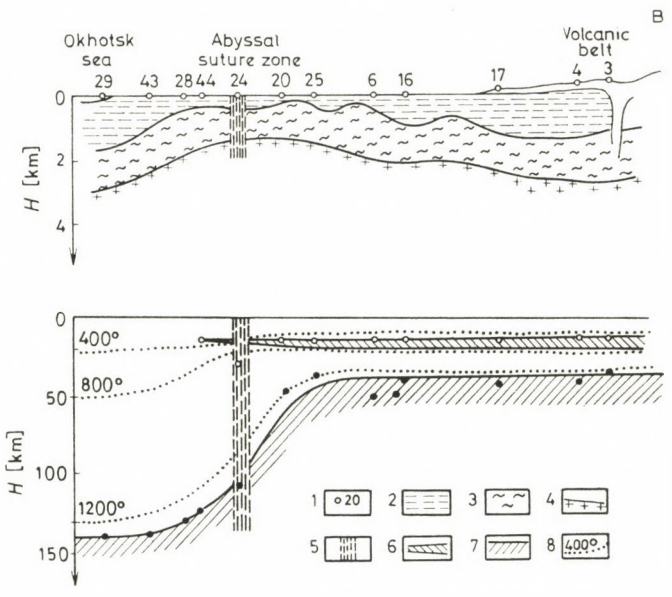


Fig. 5. Geoelectric profile A–B of the earth's crust and upper mantle in Western Kamchatka 1 – MTS sites; 2 – Paleogene-Neogene deposits; 3 – Upper Cretaceous sediments; 4 – surface of the Lower Cretaceous complex; 5 – deep fault zone; 6 – conductive layer in the earth's crust; 7 – conductive layer in the upper mantle; 8 – isotherms

a single system, and relating them to the 1200 °C isotherm (Parkhomenko and Bondarenko, 1972), we obtain the geothermal section shown in Figure 5.

The occurrence of melted magma chambers in the upper mantle and in the earth's crust is confirmed by the intense volcanic activity of the investigated region.

Seismic data for Kamchatka reveal the zones of decreased wave velocity and lowered seismic activity in layers lying at 30–70 km depths, which is in good agreement with our results.

REFERENCES

Berdichevsky, M. N., Dmitriev, V. I., Yakovlev, I. A., Bubnov, V. I., Konnov, Yu. K., Varlamov, D. A., 1973. Magnetotelluric sounding of horizontally inhomogeneous media (in Russian). *Izv. Akad. Nauk SSSR, Ser. Fiz. Zemli*, No. 1.

Demenitskaya, R. M., 1967. The Crust and the Mantle of the Earth (in Russian). Nedra, Moscow.

Parkhomenko, E. I., Bondarenko, A. T., 1972. Electric Conductivity of Rocks at High Pressures and Temperatures (in Russian). Nauka, Moscow.

DEEP MAGNETOTELLURIC SURVEYS IN THE ARCTIC OCEAN

I. L. TROFIMOV, G. A. FONAREV

In the Arctic Ocean, there occur almost all tectonic and morphological structures observed in the other oceans. It is crossed by transoceanic ridges (Haeckel, Lomonosov and Mendeleev ridges) of varied morphology, age and origin. These ridges separate closed and rather deep basins (Fig. 1). There is no agreement as to the origin of the Arctic Ocean (Demenitskaya, 1967; Demenitskaya and Karasik, 1971).

We now turn to MTS curves reproduced from observations of the magnetotelluric field from drifting ice (Figs 2–5). The observations were made along two mutually orthogonal directions, one coinciding with the local magnetic meridian, the other normal to it. The values of apparent resistivity, corresponding to these directions, are shown on the MTS curves by dots and crosses. The MTS curves were interpreted using a three-layer model in which a thin conductive layer (water, oceanic sediments) is separated by a thick non-conductive second layer (the high-resistivity rocks of the upper mantle)



Fig. 1. Physiographic chart of the floor of the Arctic Ocean; sounding sites shown by circles

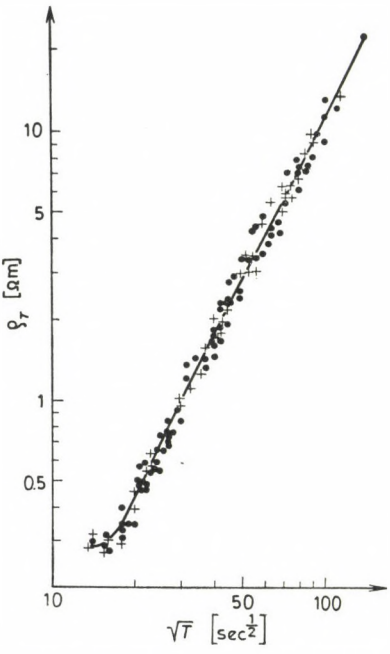


Fig. 2. MTS curve for the area of the Haeckel ridge

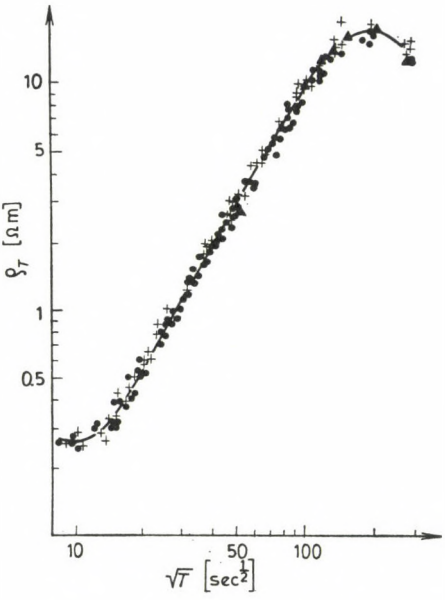


Fig. 3. MTS curve for the area of the Podvodniki basin

from a conductive basement of finite resistivity (the hot low-resistivity rocks of the upper mantle). Using asymptotic formulae, the depth h_M down to the conductive material in the mantle and the specific electric resistivity ϱ_M of the basement were determined from the MTS curves, where it was possible.

In Figure 2 the ϱ_T curve, for the area of the southern end of the Haeckel ridge is shown. The ridge is 100–150 km wide there, and during the observations, the ice flow drifted in a direction perpendicular to the axis of the ridge moving from the foot of one slope to that of the other. The depth of the ocean varied from 4000 m on the slopes to 3500 m on the axis of the ridge. The values of ϱ_T fall in the S interval which makes it impossible to determine the values of h_M and ϱ_M (Berdichevsky, 1968). It is, however, possible to assert that in the surveyed area the value of h_M is not less than 300–400 km.

The MTS curve for the Podvodniki basin that is 150 km from the crest of the Lomonosov ridge is shown in Figure 3. The depth of the ocean there is 2550 m. A similar curve for a site 60 km away from the crest of the ridge was obtained, the ocean depth being 2200 m. The values of h_M and ϱ_M deduced from these curves turned out to be 325 km and 1.7 Ωm, with errors not greater than 10% and 100%, respectively. The ϱ_T curve shown by triangles in Figure 3 was computed from these values. There is a fair agreement between theoretical and experimental values of ϱ_T.

Figure 4 shows the MTS curves for the Lomonosov ridge of directions

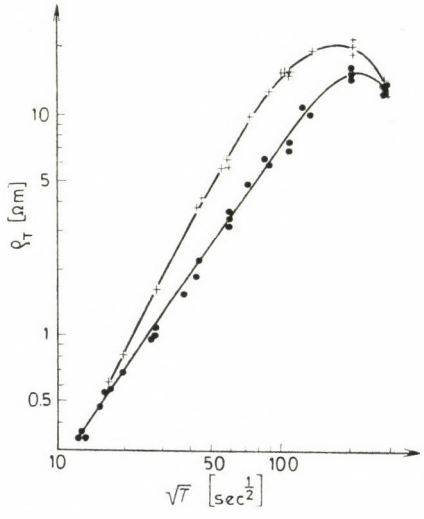


Fig. 4. MTS curve for the area of the Lomonosov ridge

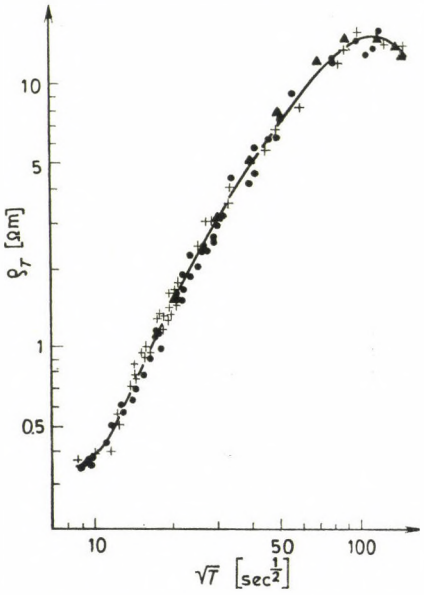


Fig. 5. MTS curve for the area of the Chukch dome

along and perpendicular to its strike (the transverse curve is denoted by crosses, the longitudinal by dots). The station was located over the slope of the ridge, 20 km from the crest, water depth being 2000 m. The divergence of the curves is related to the distorting effect of the ridge. Similar curves were obtained at two more sites, 12 and 30 km away from the crest, water depth being 1600 and 2400 m, respectively. Only transverse curves were interpreted. The calculated values of h_M and ϱ_M, arranged according to increasing depth, are 302, 320 and 320 km and 3.5, 2.7 and 2.3 Ωm, respectively. In spite of the different positions of the stations relative to the crest of the ridge, these values are consistent with each other, and only insignificantly differ from those for the Podvodniki basin.

Figure 5 shows the MTS curve over the saddle separating the Chukch underwater dome (peninsula) from the Chukch shelf. The depth of the ocean and the distance from the slope of the dome at the site were 1100 m and 35 km, respectively. A similar curve was obtained at a site 30 km from the slope, the depth being 1200 m. The values of h_M and ϱ_M determined from these curves were 165 km and 2.7 Ωm, respectively. The values of ϱ_T calculated from the ϱ_M values are indicated by triangles in Figure 5. They are in good agreement with the MTS curve.

Magnetotelluric soundings were also performed on the East Siberian shelf, in the area of transition to the continental slope. In that area, h_M and ϱ_M assumed the values of 300 to 400 km and 1–10 Ωm, respectively.

These results were analyzed according to the method of Gasanenko and Sholpo (1971), taking due account of the error introduced in the value of

h_M owing to the sphericity of the earth and to the geometry of the source of bay-like magnetic perturbations. It appears that in our case this error does not exceed 10%.

In the studied area of the ocean (excepting the Chukch dome) the value of h_M is not less than 300 km. For sake of comparison, we remind the reader that in many areas of the Russian Platform the value of h_M is 300 km or less (Kovtun and Chicherina, 1969). In this respect, the geoelectric section of the Arctic Ocean in the surveyed areas, and even in the area of the Haeckel ridge, relating to the mid-oceanic type does not show any significant peculiarities (Demenitskaya and Karasik, 1971; Lubimova et al., 1969).

The anomalously high electric conductivity of the upper mantle in the area of the Chukch dome is of particular interest. The dome is assumed to be a part of the Chukch shelf transferred towards the Canadian basin as a result of tectonic activity (Demenitskaya and Karasik, 1971). Probably, it is connected with the local warming up of the upper mantle in this region.

REFERENCES

Berdichevsky, M. N., 1968. Electric Prospecting by the Method of Magnetotelluric Profiling (in Russian). Nedra, Moscow.

Demenitskaya, R. M., 1967. The Crust and the Mantle of the Earth (in Russian). Nedra, Moscow.

Demenitskaya, R. M., Karasik, A. M., 1971. Problems of the origin of the Arctic Ocean (in Russian). Istoriya Mirovogo Okeana. Nauka, Moscow.

Gasanenko, L. B., Sholpo, M. E., 1971. On the latitudinal features of electromagnetic soundings relative to bay-like perturbation (in Russian). *Geomagn. i Aeron.* **2**, 684–689.

Kovtun, A. A., Chicherina, N. D., 1969. Results of magnetotelluric investigations in the Mid-Russian depression (in Russian). Magnitotellurichеskie Metody Izucheniya Zemnoi Kory i Verkhnei Mantii. Nauka, Moscow, 195–199.

Lubimova, E. A., Tomara, G. A., Demenitskaya, R. M., Karasik, A. M., 1969. Measurement of the Arctic Ocean bottom heat flow in the area of the midocean Haeckel ridge (in Russian). *Dokl. Akad. Nauk SSSR*, **186**, 1318–1321.

CONCLUDING REMARKS ON THE INVESTIGATIONS IN THE USSR

M. N. BERDICHEVSKY

Section V of this chapter gives a review of the major results of the magnetotelluric sounding (MTS), magnetovariation sounding (MVS) and magnetovariation profiling (MVP), obtained in the USSR during the last 5–10 years. Here sounding means the study of the frequency characteristics of the field, while profiling is the study of its spatial changes.

The authors of the chapter are fully aware of possible shortcomings, for the experimental material is not sufficiently complete and the views of the authors, as regards methods and interpretation, do not always coincide. We felt that it was interesting to draw a general outline of investigations carried out in the 16 regions of the USSR, without smoothing over differences of opinions. Geoelectrics, as the science of electric conductivity of deep layers of the earth, has come into being only quite recently and its issues reflect the complexity of problems presenting themselves in geoelectric measurement and in their geothermal and petrological interpretation.

A particular feature of the described studies is the extensive application of the magnetotelluric method and the abandonment of formal interpretation of its results. The fact that the inhomogeneities of the sedimentary cover cause considerable distortion of MTS curves, is well known. Formal interpretation of the distorted curves misrepresents the geoelectric cross section of the earth's crust and upper mantle. In the USSR, in Tikhonov's school (Berdichevsky, Dmitriev, Kaufman, Kovtun) a rather complete distortion theory has been elaborated, covering the most typical forms of two-dimensional inhomogeneities and some forms of three-dimensional inhomogeneities (see pp. 165–221). This served as a basis for the system of distortion detection which makes it possible to reduce interpretation errors and to obtain qualitative, in case of favourable conditions even quantitative, information on deep electrical conductance. The most informative are the longitudinal MTS curves, i.e. the curves corresponding to the flow of current along the elongated structures. Detection and analysis of distortions is an important stage in the interpretation of MTS curves.

The chapter contains a number of examples of reliable solutions of the inverse MTS problem. If the solution is less convincing, the MTS results should be considered as hypothetical. These hypotheses must be simple and consistent.

One of the most interesting MTS results is the discovery of the intermediate conductive layers in the earth's crust and upper mantle in a number of regions of the USSR (articles by Dubrovsky, Anishchenko, Bubnov, Yakovlev, Cherniavsky, Pospeiev, Moroz, Feldman). These authors give much attention to the analysis of reliability of the results. Their quantita-

tive evaluations are sometimes doubtful, but the qualitative pattern is, apparently, quite dependable. There are grounds to suppose that the intermediate conductive layers are formed in the process of tectonic activization of the region (see pp. 722–726). The significance of this discovery is evident. Thus, the experience of Soviet geophysicists indicates to favourable prospects for the magnetotelluric method. With the help of the MTS method the geoelectric cross-section of the earth's crust and upper mantle is being studied and, though in many cases the accuracy and comprehension of the method are still far from satisfactory, the method provides essentially new geological information unobtainable by other geophysical methods.

Another peculiarity of the works described is the integrated application of the magnetotelluric and magnetovariation methods. This complex is used in various combinations. In some cases, there are separate studies of different objects (Rokityansky, Marderfeld). But there are already examples of well-organized combinations of both methods when studying the same objects (Kovtun, Anishchenko, Bubnov, Yakovlev, Cherniavsky). This approach to the problem is, apparently, most promising, since in the studies of stratified-heterogeneous media the magnetotelluric and magnetovariation method nicely complement each other.

The most difficult problems relate to the geothermal and petrological interpretation of geoelectric data. In this case much depends on the coverage of the region and on the scientific viewpoint of the researcher. In a number of the papers the reader finds interesting geothermal and geological models which open new possibilities in this field (Feldman, Pospeiev, Rokityansky). Even though such models are not always sufficiently correct, their usefulness is beyond doubt.

CHAPTER 6

ON THE NATURE OF CONDUCTIVE LAYERS IN THE EARTH'S CRUST AND UPPER MANTLE

by

I. S. FELDMAN

ON THE NATURE OF CONDUCTIVE LAYERS IN THE EARTH'S CRUST AND UPPER MANTLE

Summing up the results of global magnetovariation (Berdichevsky et al., 1970, 1973) and magnetotelluric soundings carried out in the USSR and in other countries, we draw a conclusion that there are three types of geoelectric sections of the tectonosphere:

1. The earth's crust and upper mantle (zone B) have a high specific resistivity, decreasing monotonically with depth.
2. The earth's crust contains an intermediate conductive layer.
3. The upper part of zone B contains an intermediate conductive layer.

The subject of this paper is the geological nature of the conductive layers in the earth's crust and upper mantle, and of the geoelectric boundary of zone C.

CONDUCTIVE LAYER IN THE EARTH'S CRUST

We consider in succession two models of the earth's crust, conventionally termed static and dynamic, respectively.

THE STATIC MODEL

In the static model at the present geological stage no active transformative processes take place. In such a model, the earth's crust possesses a high specific resistivity, and conductive layers can appear as a result of changes in the material composition of rocks. Laboratory measurements indicate that, at temperatures of the order of 600–700 °C, some alkaline rocks, the minerals of the amphibole group, serpentinites containing 7–10% ore component, and also minerals with a considerable concentration of iron, sodium and potassium become good conductors (Parkhomenko and Bondarenko, 1972; Bondarenko, 1968, 1972). An increased electric conductivity is a characteristic property of some mineralogical transformations, such as, e.g. the sillimanite-cyanite transition (Bondarenko, 1968), or of reactions involving iron compounds.

These experimental data allowed us to advocate a hypothesis relating the conductive layer of the earth's crust to the distribution of the above mentioned rocks and materials (Bondarenko, 1968, 1972; Parkhomenko and Bondarenko, 1972; Parkhomenko, 1971). However, in order to produce significant anomalies, such minerals and rocks should occur in sufficiently thick (a few kilometers) and extended (hundreds of kilometers) zones. Such a situation seems questionable for the following reasons:

1. According to geological evidence, high-conductivity rocks and minerals are not widely distributed in the earth's crust, and do not occur in any considerably thick and lengthy layers.

2. Because of their holocrystalline structure minerals are distributed, as a rule, in the form of isolated grains. In such a situation, even highly conductive minerals cannot significantly lower the bulk resistivity of rocks.

3. As a rule, the minerals considered turn out to be unstable under the thermodynamic conditions corresponding to depths of 10–15 km.

The most attractive minerals in the static model are amphibolites supposedly making up the lower part of the "granitic" layer. It is still not clear, however, whether the composition of the experimentally studied samples of this series is typical of the deep horizons of the earth's crust.

It might be well to consider the possible appearance of conductive layers due to water solution. According to experimental data, the specific resistivity of amphibolites and gneisses saturated with a highly concentrated pore solution reaches several hundred Ωm (Parkhomenko and Bondarenko, 1972) at temperatures and pressures corresponding to a depth of 10–15 km. We feel that the occurrence of such rocks under water-resisting layers may be the cause of the appearance of conductive layers in the earth's crust.

However, under the conditions of the static model, such a situation seems rather improbable, because the source of water is an open question. In the process of consolidation of sediments and their subsequent transformation into crystalline rocks, atmospheric waters are practically completely forced out or bound in crystallization. Juvenile solutions, rising towards the surface, are distributed mostly along the deep faults, i.e. in the vertical and not in the horizontal directions.

THE DYNAMIC MODEL

In a dynamic model active processes, such as regional metamorphism, granitization and melting of granitic magma, take place. These processes can result in the appearance of intermediate conductive layers in the earth's crust. It is, for example, an experimental fact that the electric conductivity of granite increases 100–1000 times upon melting (Lebedev and Khitarov, 1964). Figure 1 shows the experimental curves for melting of rocks and mineral associations giving melting products close to granites. The same figure shows schematically the areas of stability of mineral associations corresponding to various metamorphic facies. Comparing these data with temperature curves, we observe a coincidence of the thermodynamic conditions corresponding to the amphibolitic facies with the conditions for melting of granite in the presence of water. This generally well known fact is confirmed by the results of studies of the deepest erosion of the earth's crust (Sudovikov, 1964; Menert, 1963, 1971).

Lower in the cross section, there occurs a transition from diapiric-like intrusions and vein series to more complicated turbulent structures within the amphibolitic zone. In the granulitic zone, the interaction forms are more quiet: migmatites are considerably less widely disturbed. Thus, from

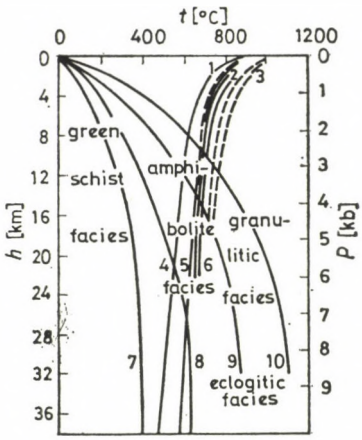


Fig. 1. *P-t* diagram of metamorphic facies, melting and temperature curves in the earth's crust. Melting curves for a few systems, close to granite in composition, in the presence of water (eutectic curves) (Parkhomenko and Bondarenko, 1972) 1 – quartz-albite-orthoclase; 2 – quartz-albite; 3 – albite-orthoclase. Melting temperatures of schists and granites (Villi and Tattl, 1963); 4 – granite in the presence of water; 5 – schist; 6 – granite. Temperature curves (Smirnov, 1968); 7 – shields and old platforms; 8 – Paleozoic platforms; 9 – regions of Mesozoic activation; 10 – eugeosynclines, island arcs, rifts

the genetic standpoint the zone of active granitization and melting corresponds to the amphibolitic facies in the region of its transition to the granulitic facies. By its physical properties, this region corresponds to the transition from the "granitic" to the "basaltic" layer. Consequently, it is just there, in the vicinity of the Conrad discontinuity that the development of melting could be expected. Water plays an important part in such processes. Having a great mobility and high chemical activity, it significantly reduces the temperature of fusion. Numerous geological data indicate that in the process of metamorphism and granitization solutions spread in deep layers of the earth's crust largely, intergranularly and form an uninterrupted system (Sudovikov, 1964; Menert, 1971; King, 1967; Zaridze, 1967). Under favourable conditions melting processes develop within this system. The conductivity of such zones could be close to that of the liquid phase, i.e. of mineralized solutions (at temperatures below critical) and of fluids (at temperatures above critical) which, as experiments show, possess a high electric conductivity (Khitarov, 1966).

Of great importance is the question of the source of the water. Judging from geological evidence, a certain percentage of free water is necessary for the development of the above processes. Such a percentage can be provided neither by buried, nor by juvenile waters. It is, however, possible that in progressive metamorphism the water can be provided by internal sources. Actually, metamorphic rocks contain a few per cent of water of crystallization. For instance, in minerals of the amphibolite facies, there is around 1.5% water. At the boundary of the amphibolitic and granulitic facies, dehydration brings practically all bound water out into the free liquid phase. This boundary is thus critical for the development of granitization processes, including the melting of granite in the presence of water.

The electric conductivity during dehydration was studied experimentally in serpentinous peridotites (Zablocki, 1964) and in serpentinites, actinolites and hornblendites (Bondarenko, 1973). It has been found that a tenfold increase of electric conductivity, in the temperature range of 400–600 °C, is connected with the release of water of crystallization. Under actual

conditions (in a closed system, under high pressures), the jump in electric conductivity must be significantly greater.

A conductive layer can thus be accounted for by the existence in the earth's crust of horizons rich in water solutions and, at high temperatures in molten granite. This explanation is, however, somewhat contradictory. Thus, regions where MTS data reveal a conductive layer in the earth's crust have passed many stages of regional metamorphism, and should apparently have exhausted all their internal water resources. In order to resolve this contradiction, the inflow, distribution and dynamics of the mantle water have been calculated. At present, the ocean and the lithosphere contain $2.3 \cdot 10^8$ km^3 of water (Makarenko, 1966) that has risen out of the mantle during the earth's existence. Taking into account the significant reduction in the rates of differentiation, we assume that 10% of this amount, i.e. $2.3 \cdot 10^7$ km^3 was produced in the last billion (10^9) years. The rate of production during that time is thus equal to $2.3 \cdot 10^{-2}$ km^3/year, and the rate of accumulation of the hydrosphere is equal to $5 \cdot 10^{-5}$ cm^3/cm^2 pro year, or 50 cm^3/cm^2 pro million year. The latter figures correspond to a rise of the sea level at the rate of $3 \cdot 10^{-5}$ cm/year, or 30 cm/million years, which seems quite probable.

500 million years are taken to be the time of the quiet stage between two cycles of thermal activation, proceeding from the fact that the total duration of such stages can reach 3.5 billion years (Rikitake, 1968). In 500 million years, at the assumed rate, $2.5 \cdot 10^4$ cm^3 of water will arrive per 1 cm^2. Let the thickness of the dry lower part of the crust be 20 km, with a mean density of 3 g/cm^3 and provided that only a half of the total amount of water arriving from the mantle is absorbed in the crust, then after 500 million years its water content will be $(0.5 \cdot 2.5 \cdot 10^4)/(3.20 \cdot 10^5) = 0.2\%$. The other half of the water goes into the hydrosphere. At temperatures below critical, such as are usually found in the lower layers of the crust during quiet stages of development, the free water will be bound in crystals of dehydrated minerals of high-temperature metamorphic facies. The accumulation of the water at such rates during quiet stages may not have far-reaching geological and geophysical consequences, but in periods of thermal activation such amounts of water play an important part.

During stages of thermal activation, the rate of warming up of the crust apparently exceeds the velocity of penetration of water. On the basis of the diffusion velocity of water, the minimum velocity of water penetration can be taken as 10^{-2} cm/year. Therefore, the 600–700 °C isotherm, rising to the Conrad discontinuity, liberates the accumulated water. Water moves upwards with a velocity significantly higher than the diffusion velocity, and is again bound above the critical isotherm. The content of water mobilized in this fashion reaches 2% in a layer 2 km thick at the level of the critical isotherm, provided the isotherm stabilizes for a while. Such a stabilization, usually following the peak of activation, occurs when the temperature reaches 500–700 °C at depths of 10–15 km corresponding to the transition zone from the amphibolitic to the granulitic facies. The specified amount of water is then critical for the development of the above-mentioned processes.

One should also note, following Menert (1971) that the temperature at which melting begins is not lowered when the water content decreases; only the amount of melted rock is changed. The point is that the intergranular solution making up only 1% of the rock volume can give anatectic melt saturated with water to the amount of 10% of the rock volume.

The pattern just considered may be useful for the understanding of some geological regularities. We might thus try to answer why the main stages of regional metamorphism and granitization outstrip the stages of melting of granitic magma. One might also explain the spatial and temporal nonuniformity, of the migration and concentration of some extrinsic elements, in particular alkalis. One could also consider from this standpoint the cause of the prolonged rise of ancient shields, and the nature of a decrease of velocity of seismic waves near the Moho discontinuity, etc. These issues, however, are beyond the scope of the present essay.

It might be well to give some geological data attesting to the pattern just considered. Zones of granitization and active circulation of solutions should exhibit some other geophysical anomalies such as a decrease of seismic velocity, of density, and of strength. The study of waveguides in the earth's crust is only beginning. It can be said with confidence that they exist in some areas (the Rhine graben, Central Asia and the Pre-Alpine zone), but we cannot affirm their absence in other places (Rikitake, 1968; Mueller and Landisman, 1966; Giese, 1967).

In order to investigate the vertical distribution of strength, we analyzed statistical data of the distribution of earthquakes with depth for many areas of the earth. The earth's crust can be considered as an elastic system. If there exists a weak zone in this system, applied tensions should manifest themselves there. Nets of seismic stations are found, however, only in areas of intense seismic activity, where the shifting of large blocks cross-cutting the earth's crust make it difficult to study the distribution of seismic phenomena with depth. Nevertheless, statistical data decidedly indicate that the majority of earthquakes are confined to the central part of the earth's crust (the first maximum in the distribution, at a depth of a few kilometers, is related to the boundary between the sediments and the basement, and is not considered here). This regularity is a property of rift structures, alpine mountain systems and of zones of activation within platforms. The available evidence, however, is not representative enough to be a suggestive regularity of a definite type of structure. Judging from the orientation of the stress axes (Balakina et al., 1967), movements occur along quasi-horizontal planes, which might be related to the occurrence of water-rich strata, or strata modified by a previous hydrothermal activity. This is also indicated by the aftershocks of some strong earthquakes. After such an earthquake at a depth of 20 km in the Baikal Rift zone, the tension spread after the main fracture largely in a horizontal direction within a weak zone lying at a depth from 15 to 22 km (Pshennikov, 1965). Just here an anomalously conductive layer is observed and the majority of earthquakes occur.

Direct geological observations indicate a great mobility of material in zones of active circulation of solutions and granitization. The presence of small folds of flowing and sliding is characteristic of such zones. Particularly

typical is the development of folds in layered migmatite in which the axis of the fold lies parallel to the layering. The development of such small structures, and also of extrusion structures, is according to Sudovikov (1964), an indication of layered differentiation of movements in zones of migmatization.

Thus, geophysical data, as well as geological observations, indicate the presence, in the central part of the earth's crust, of an anomalous zone, which can be explained in terms of the development of intergranular films and intercalations of liquid phase (solutions and melts). The appearance of the intercalations may be related to the development of metamorphism and granitization following thermal activation in the earth's crust. It is possible that such zones may retain some of their specific properties (and in part also their structural features) for a considerable time after the consolidation and stabilization of the structures of the earth's crust.

CONDUCTIVE LAYER IN THE UPPER MANTLE

An important feature of the phase state of the upper mantle is the occurrence of melting zones. As mentioned before, the electric conductivity in the initial stage of melting (in the appropriate area of the *P–t diagram*) increases 100–1000 times, after which it does not change significantly. A study of samples after hardening under various experimental conditions shows that the jump in electric conductivity occurs at an initial stage of melting, at which the molten fraction is still small (Khitarov and Slutsky, 1962). This is an indication that a sharp increase in electric conductivity apparently occurs at limit concentration of the liquid phase at which the liquid begins to envelop the solid particles, thus forming a continuous pellicular structure. This peculiarity of the melting process may be related to both the anomalous growth of the electric conductivity, the anomalous increase in thermal conductivity resulting from convection of the liquid phase, and the beginning of gravitational differentiation in a two-phase system.

Under actual conditions in the earth's interior, such an enrichment in the liquid phase might occur not only in zones of generation of magma, but possibly in overlying zones, too. In both cases, at those depths where the limit concentration of the liquid phase is reached, an anomalous increase in electric conductivity should be found.

The question of the geometry of the distribution of the liquid phase in the mantle is of utmost importance in estimating the volumetric electric conductivity. The fundamental mechanism and the physico-chemical conditions for the melting of magma and for its differentiation cannot have changed significantly at the last stage of development of the earth (the one accessible to geological analysis). Melting of magma occurred in practically every area of the earth during this period. For the liquid phase to separate (and thus to form magma proper), it is necessary, in the opinion of a number of researchers that first a pellicular filling structure be formed by the liquid phase, and secondly that a sufficient amount of the liquid phase be accumulated (Sheinman, 1968). During separation of the magma, between the

granules of the skeleton, there should always remain a liquid phase, because the process of separation has a critical limit.

During the stage of diminishing activity, the fall in the temperature leads to crystallization of the liquid on the boundaries of the granules, not only in the case when separation of magma takes place, but also when for some reason or other the conditions for such a separation are not attained. It thus appears that, everywhere in the zones of generation and accumulation of magma of the earth's upper mantle, melting occurs already in media in which the high-melting skeleton is surrounded by a film of a less-melting component (a relic of a previous stage of fusion). There apparently exists inside such films a higher-order structure of components crystallizing only in the last instance. Experimental data of the crystallization of multicomponent silicate systems under eutectic conditions show that, after the precipitation of a component crystallized at an early stage, the remaining liquid of eutectic composition envelops the crystals already formed, giving rise to the filling matrix (Veingard, 1968).

It is thus seen that at the very beginning of the melting process, the liquid phase, even though its content may be only 1–2%, can still give rise to a continuous pellicular structure. In order that a zone be anomalously conductive, it is necessary that there be altogether 2% of liquid phase present, whereas for the separation of the fluid, i.e. for the formation of magma proper, such a concentration is apparently not sufficient. Because of this it is possible to study geophysically the melting in the mantle, even in cases when the melting is not accompanied by the appearance of magmatism.

It is worth mentioning that the time of formation and of disappearance of temperature inhomogeneities of the mantle, which give rise to fusion and magmatism, is reckoned in periods of the order of tens of millions of years (Kutas and Gordienko, 1972). Such time intervals are comparable to the time of activation and establishment of large tectonic regions. So, it can be expected that anomalous zones would be found in regions that have already passed the activation stage, or in such places where the activation is brewing in the depths of the tectonosphere. There are reasons to suppose that anomalous zones can cover larger areas than the areas of tectonic activation at the surface. The problem of regionalization of the conductive zones, in the crust as well as in the mantle, is thus rather complicated, and so is that of their relation with other geological and geophysical phenomena.

THE CONDUCTIVITY OF THE UPPER MANTLE AND GEOELECTRIC FEATURES OF THE TRANSITION ZONE

The decisive role in the formation of possible geoelectric boundaries at deeper levels of the upper mantle and at a transition zone (zone C) can be that of phase and polymorphic transformations and of chemical reactions in a series of mineralogical transitions.

The nature of the anomalous increase in the velocity of seismic waves and in the density in zone C (400–900 km) is related at the present time

to a series of stepped mineralogical transformations tending to form more closely packed structures (Magnitsky, 1965; Ringwood, 1966). It is possible that a few of these transitions, accompanying the shift to covalence of lattice-bound ions, should lead to a sharp increase in conductivity (Magnitsky, 1965). In this connection, we should recall the transition of olivines and pyroxenes to spinel structures and stishovite, that should take place at depths of the order of 400 km (Ringwood, 1968; Fujisawa, 1968). In transitions of this type, such as occur in fayalite, a high increase in the electric conductivity of the new spinel phase has been experimentally observed (Akimoto and Fujisawa, 1965). It is thus possible to assume that the geoelectric boundary at a depth of 400–500 km found as a result of global soundings reflects a change in crystalline structure, and should in general correspond to a seismic boundary.

Theoretical calculations show that the descending branches of experimental sounding curves are related, in the case of a sufficiently resistive upper mantle, to the existence of conductive zones at a depth of 400–500 km. The computation of a geoelectric model of the upper mantle, based on existing ideas of its composition, its temperature regime and on data of the electric conductivity of olivine, shows, however that, on the whole, the upper mantle has a significantly lower resistivity (Lubimova and Feldman, 1970; Bondarenko and Feldman, 1971). Sounding curves for such a model, which includes the growth in electric conductivity following an increase in the temperature with depth, also have descending branches, just as for models based on the presence of conductive layers (Lubimova and Feldman, 1970; Vanyan and Zabolotnaya, 1968). However, the approach to the interpretation of such curves should be quite different. One of the methods of interpretation, based on the selection of models constructed from *a priori* representations of the growth of the temperature with depth in the mantle, is presented in this monograph (see pp. 646–651). An other method is based on the solution of the inverse problem for an analytic function given in advance (Berdichevsky et al., 1974). The determination of the parameters yields the unknown distribution of conductivity corresponding to the chosen law of growth. In both cases, the results of the interpretation provide us with a geoelectric model carrying information on the distribution of the temperature in the mantle. In our opinion, the construction and comparison of such models for various regions will provide valuable information on the thermodynamic regime of the tectonosphere.

REFERENCES

Akimoto, S., Fujisawa, H., 1965. Demonstration of the electrical conductivity jump produced by the olivin-spinel transitions. *J. Geophys. Res.* **70**, No. 2.

Balakina, L. N., Vvedenskaya, A. V., Misharina, L. A., Shirokova, E. I., 1967. Stressed state at earthquake foci in the field of elastic tensions of the earth (in Russian). *Izv. Akad. Nauk SSSR, Ser. Fiz. Zemli*, No. 6.

Berdichevsky, M. N., Borisova, V. P., Vanyan, L. L., Golovkov, V. P., Dmitriev, V. I., Dubrovsky, V. G., Kolomnitseva, G. I., Rotanova, N. M., Fainberg, E. B., Feldman, I. S., 1973. Deep electromagnetic sounding (in Russian). *Izv. Akad. Nauk SSSR, Ser. Fiz. Zemli*, No. 7.

BERDICHEVSKY, M. N., DMITRIEV, V. I., MERSHCHIKOVA, N. V., 1974. Magnetotelluric sounding of gradient media (in Russian). *Izv. Akad. Nauk SSSR, Ser. Fiz. Zemli*, No. 6.

BERDICHEVSKY, M. N., VANYAN, L. L., LAGUTINSKAYA, L. P., ROTANOVA, N. M., FAINBERG, E. B., 1970. The experiences of earth frequency sounding by the earth results of the spherical analysis of the geomagnetic field variation (in Russian). *Geomagn. i Aeron.* **10**, No. 2.

BONDARENKO, A. T., 1968. Generalization of data of the electric conductivity of eruptive rocks at high temperatures in relation with the structure of the earth's crust and upper mantle (in Russian). *Dokl. Akad. Nauk SSSR*, **178**, No. 5.

BONDARENKO, A. T., 1972. Electric properties of alkaline rocks of the Khibiny and Lovozero massifs (in Russian). *Izv. Akad. Nauk SSSR, Ser. Fiz. Zemli*, No. 4.

BONDARENKO, A. T., 1973. The influence of dehydration processes on the electric conductivity of metamorphic complexes of rocks and minerals at high pressures and temperatures in relation with the anomalous zones in the earth's crust (in Russian). *Dokl. Akad. Nauk SSSR*, **208**, No. 5.

BONDARENKO, A. T., FELDMAN, I. S., 1971. High temperature electric conductivity of olivines and a geoelectrical model of the upper mantle (in Russian). Fizicheskie Svoistva Gornykh Porod pri Vysokykh Termodinamicheskikh Parametrakh. Naukova Dumka, Kiev.

FUJISAWA, H., 1968. Temperature and discontinuities in the transition layers within the Earth's mantle. *J. Geophys. Res.* **73**, No. 10.

GIESE, P., 1967. Der Grenzbereich zwischen Erdkruste und Erdmantel. Ninth Assembly of the European Seismolog. Commiss. Copenhagen.

KHITAROV, N. I., 1966. On the use of the electric conductivity method in the study of the conditions of formation of aluminosilicates in water solutions at higher temperatures (in Russian). *Geokhimiya*, No. 8.

KHITAROV, N. I., SLUTSKY, A. B., 1962. The influence of pressure on the temperature of melting of albite and basalt (in Russian). *Geokhimiya*, No. 12.

KING, B. K., 1967. The nature and the origin of migmatites, metasomatosis or anataxis (in Russian). Priroda Metamorfizma. Mir, Moscow.

KUTAS, R. I., GORDIENKO, V. V., 1972. The heat field of the Carpathians and some problems of geothermics (in Russian). Energetika Geologicheskikh i Geofizicheskikh Protsessov. Nauka, Moscow.

LEBEDEV, E. B., KHITAROV, N. I., 1964. The beginning of melting of granite and the electric conductivity of its melt depending on high-pressure water vapour (in Russian). *Geokhimiya*, No. 3.

LUBIMOVA, E. A., FELDMAN, I. S., 1970. Heat flow, temperature and electrical conductivity of the crust and upper mantle in the USSR. *Tectonophysics* **10**.

LUKK, A. A., NERSESOV, I. L., CHEPKUNAS, L. S., 1970. The method of identifying layers of lower velocity in the crust and in the mantle of the Earth (in Russian). *Izv. Akad. Nauk SSSR, Ser. Fiz. Zemli*, No. 2.

MAGNITSKY, V. A., 1965. Internal Structure and Physics of the Earth (in Russian). Nedra, Moscow.

MAKARENKO, F. A., 1966. Aqueous process of distribution and deep thermal output and the formation of thermal anomalies (in Russian). Termicheskie Isledovaniya i Ispolzovanie Tepla Zemli. Nauka, Moscow.

MENERT, K., 1963. Something New on the Problem of Granites (in Russian). IL, Moscow.

MENERT, K., 1971. Magmatites and the Origin of Granite (in Russian). Mir, Moscow.

MUELLER, S., LANDISMAN, M., 1966. Seismic studies of the earth's crust in continents. *Geophys. J. R. Astr. Soc.* **10**, No. 5.

PARKHOMENKO, E. I., 1971. On the nature of layers of high electric conductivity in the earth's crust and upper mantle, according to laboratory data (in Russian). Fizicheskie Svoistva Gornykh Porod pri Vysokykh Termodinamicheskikh Parametrakh. Naukova Dumka, Kiev.

PARKHOMENKO, E. I., BONDARENKO, A. T., 1972. The Electric Conductivity of Rocks at High Pressure and Temperatures (in Russian). Nauka, Moscow.

PSHENNIKOV, K. V., 1965. The Mechanism of the Appearance of Aftershocks and Non-elastic Properties of the Earth's Crust (in Russian). Nauka, Moscow.

RIKITAKE, T., 1968. Electromagnetism and the Earth's Interior (Russian Translation). Nedra, Leningrad.

RINGWOOD, A. E., 1966. The Chemical Composition and Origin of the Earth. Advances in the Earth Sciences, Cambridge, M. I. T. Press.

RINGWOOD, A. E., 1968. Phase Transformations in the Mantle. Canberra.

SHEINMAN, YU. M., 1968. Essays on Deep Geology (On the Relation Between Tectonics and the Appearance of Magma) (in Russian). Nedra.

SLUTSKY, A. B., 1968. Changes in electric conductivity accompanying the polymorphic transformation cyanite-sillimanite (Al_2SiO_3) under conditions of high temperatures and pressures (in Russian). *Dokl. Akad. Nauk SSSR*, **179**, No. 4.

SMIRNOV, YA. B., 1968. The relation between the heat field and the structure and development of the earth's crust and mantle (in Russian). *Geotektonika*, No. 6.

SUDOVIKOV, N. G., 1964. Regional Metamorphism and Some Problems of Petrology (in Russian). LGU, Leningrad.

VANYAN, L. P., ZABOLOTNAYA, N. A., 1968. On typical theoretical curves for deep electromagnetic sounding (in Russian). *Izv. Akad. Nauk SSSR, Ser., Fiz. Zemli*, No. 1.

VEINGARD, G., 1968. The Foundations of the Physics of Crystallization (in Russian). Metallurgizdat, Moscow.

VILLI, P., TATTL, O., 1963. Melting in the earth's crust (in Russian). International Geological Congress, II, Inostrannaya literatura, Moscow.

ZABLOCKI, C. L., 1964. Electrical properties of serpentinite from Mayaguez, Puerto Rico. A Study of Serpentinite. Washington.

ZARIDZE, G. M., 1967. On the problem of the relation between magmatism, metamorphism and tectonics (in Russian). *Geotektonika*, No. 4.

SUBJECT INDEX

Figures in italics refer to names and concepts occurring in the diagrams and maps

Absolut ellipse, geomagnetic 257
— telluric 257, 493
Absorption of elastic waves 367
Absorptivity 26
Abyssal Transcarpathian fracture zone 590
Accelerating factor 69
Actinolite 337, 338, 344
Actinolitizated gabbro-diabase 347
Actiphyllite 344
Activation energy 327—330, 334, 336—339, 342, 346, 348, 355, 357, 362, 511
— temperature dependence of 342, 512
— depending on fayalite content *335*
Admittance 195, 198, 600, 601
Admittance ellipse 272
Admittance tensor 260
Aegirite 336—337
Albite 338, 361, 362, 723
Albitization 346, 348, 361
Albitized gabbro 345
Albitophyre 324, 325
Aleurolite 322, 669
Alkaline metasomatosis 366
Almandine eclogite 356
Almandite 334—335, 358
Alpine-Carpathian orogeny 546
Alpine folding area 408, 411, 653
Alpine geosynclinal stage 610
Alpine orogenism 445, 446, 450
Alpine orogenic belt 650
Alpine tectonic movements 416
Aluminate 333
Amphibole 336—338, 342, 344, 348, 358, 361, 365
Amphibole gabbro 345, 346
Amphibole gneiss 340
Amphibolite 323, 342, 343, 344, 363, 364, 365, 366, 545
Amphibolitic facies 723—724
Amphibolitic zone 722
Amplitude analysis, two-dimensional 297
Andesite 323, 339, 342, 579
Andesitic-riolitic volcanism, Miocene 577, 581—582, 649
Andesitic tuff 579
Andradite 334
Anhydrite 386, 387, 441
Anisotropic layer 222—227, 230
Anisotropic medium 222, 227
Antigorite 355
Apparent amplitude method (magnetotelluric) 548
Approximate boundary condition method (magnetotelluric) 173
Argillite 322, 441

Basalt 324, 344, 348, 355, 356, 361, 362, 367, 388, 540, 541, 568, 569, 649, 662
— alkali-olivine 350
— Caucasian 348—350
"Basalt" layer 338—350, 363—366, 578, 590, 652, 660, 663, 723
Basalt, Sikhote-Alin 349—350
Basaltic volcanism, Plio-Pleistocene 546, 570, 577, 580—582
Basaltoid 356
Base of the sedimentary layers in Central Europe, map of *491*
Basement, resistant 206, 256, 655, 686
Bay disturbance (geomagnetic) 264, 274—277, 280—282, 489—490, 503, 507, 520—523, 526, 528—529, 589—599, 600, 602, 606, 631, 644, 653, 697—699, 714
Benioff zone 73, 74, 583
Biotite 344, 397
Boltzmann constant 26, 327, 329, 511

Bouguer anomaly 268, 584
Boundary problem, "junction" 81, 83

Calcite 321, 397
Calcium oxide 331, 332
Carbonate-halogen sediment 455
Cataclasm 366
Cauchy–Riemann condition 142
Cementation 323
Cenozoic depression 377
Chlorite 358
Chlorite slate 341
Chloritization 347
Chrome-diopside 336, 355
Chromite 333, 350, 354
Chromite dunite 350
Chrysolite 355
Clay 321, 322, 386, 415, 441, 669
Clayey marlstone 386, 398
Clayey shale 322, 388
Claystone 386—387, 397—399, 415
Climatic change, past 18, 54, 57, 59—60, 63—65, 373, 377, 401, 448
Climatic correction 60, 61, 401
Climatic disturbance 64, 395
Coast effect 149, 698, 700
Coda of the surface wave 554
Concentration effect, electromagnetic 169, 197—201, 203, 205—208, 216—218, 685, 689
Conducting basement 174—175, 178—179, 181—189, 190, 194, 205—206, 208, 211—213, 215, 236—243, 647
Conducting layer (zone, medium, HCL) 105, 110, 114—115, 117, 169, 189—190, 192—195, 205, 208, 215, 217, 219, 243, 245, 247—248, 250, 254, 264, 267, 286—287, 366, 459, 468—469, 483, 487—488, 491—492, 494, 496, 498, 533, 535, 538, 549, 554—556, 567—573, 583—584, 591, 601, 608, 610—611, 618—619, 624, 629—632, 640, 642, 648, 650, 655, 659, 661, 667—668, 670—671, 673, 675—680, 683, 685—687, 689, 691, 693, 698, 700—701, 705—707, 709—712, 721—728
Conduction, electrical impurity 329, 330, 333, 334, 339, 351, 358
Conduction, electrical intrinsic 329, 330, 333, 334, 339, 346, 351, 355
Conductive cylindrical channel 528
Conductivity anomaly (electrical) 106, 109, 111, 120, 122, 132, 148, 483, 501, 608, 637—638
— Carpathian 488, 596, 599, 601—602, 604—611, 634
— Central Europe 489
— Central Kurily Islands 697—701
— Göttingen 488
— Kirovograd 608, 634—639
— North-German 128, 130, 503, 505
— North-German–Polish 487—499, 509—512, 608
— Pannonian Basin 548—556, 570
— Upper Rhine-Graben 488
Conductivity gradient 224
Conductivity model, global 138
Conductivity tensor 225
Conglomerate 387, 546
Conrad discontinuity 510, 535, 553, 578, 590, 689, 723, 724
Continuity condition 88, 171
Corundum 331, 332
Crust model, four-layer 509
— of the Pannonian Basin, two-layer 547
Crustal movement in Eastern Europe, map of *383*
Crustal movement, recent 382
Crystalline schist 517, 534, 540, 541, 545
Curie temperature 463, 465, 467, 470
Current density distribution 107
Current system, unicellular 283, 284
— bicellular 283, 284, 292
— of magnetosphere 104
Cyanite 362
Cyanite schist 341, 342

Demersal water, Helium concentration of 17, 23, 24
— temperature in 19, 20
Depth-density function 430, 432
Depth-temperature function 484
Diabase 323, 326, 342, 347, 348, 363, 365, 546
Diabase, actinolitizated 348
Dielectric permeability 73, 75

Diopside 336, 351
Diopside gabbro 345, 346
Diorite 323, 339—340, 342, 359—363, 365
Discontinuity of magnetic field 197
Distortion coefficient 178, 186, 188, 201, *202*, *203*, *204*, 212, 213, 483, 676, 683
Distortion effect, smoothing 167, 184
— causing false layers 167, 168, 181, 184, 186, 189—192, 205
— causing false structures 167, 168, 206
Disturbance method (magnetotelluric) 173
Dolerite 349
— Caucasian 348—349
— Sikhote-Alin 349
Dolomite 321, 386, 387, 441, 546
Dunite 326, 350, 352—356, 359, 365, 569, 679
Durbachit 534

E-polarization 119, 125, 128, 141, 153—156, 159—160, 168, 171, 177, 181, 183, 202, 206, 232—233, 236, 238—240, 244, 246—247, 249, 250, 253, 262—263, 265—266, 493, 553—554
E-polarization curve 494, 554
E-polarized field 168, 170, 201, 206, 214, 254
Earth's crust anomaly, Transdanubian 547, 558, 570
Earth's crust model, dynamic 721—726
— geoelectrical 538
— geothermal 539, 564—565
— static 721—722
Eclogite 355—359, 365, 541, 615, 679
— crustal 352—353
— mantle 357—358, 361, 365
Edge effect 215—218, 620, 622, 624, 647, 655, 675, 685
Eigenfunction expansion, method of 172
Elastic wave velocity 48—49, 351, 362, 364, 366—367, 644
Electric dipole 245
Electrical conductivity 48—49, 73, 75, 105, 108—110, 119, 122, 124—126, 128—130, 136—137, 139, 141—142, 150, 166, 168, 175, 177—179, 188—190, 193, 195, 210—211, 215—217, 219, 222, 227, 231—234, 236—243, 256, 275, 286—287, 296, 325, 327, 329, 332—333, 339, 344, 348—350, 358, 361, 364, 366—367, 447, 455—456, 458—459, 468, 487—499, 505, 511—512, 517, 519, 526—529, 530, 533, 535, 538, 541, 549, 556, 567—572, 590, 593, 596, 600—601, 609—611, 615, 617, 621, 626, 632, 634—635, 644, 646, 649—650, 663, 675—676, 678, 679—680, 683—684, 686, 689, 691, 697—698, 703, 709—710, 715, 721, 723, 726—728
Electrical conductivity, dielectric 332
— longitudinal 105, 107–108, 114–115, 117–118, 121–122, 144, 150, 168, 243, 487, 491–494, 498, 591, 593, 597, 607–609, 617, 622–624, 630, 635–637, 640, 642, 647–648, 653, 655–658, 667–668, 670–671, 683–684, 686–687, 694–696, 703, 705, 709, 710
— theory of 328–332
Electrical conductivity curve 662
Electrical conductivity distribution 126, 128, 132–134, 137–138, 231, 235, 487, 491, 517, 538–539, 596, 599, 728
Electrical conductivity *vs.* impurity content *329*
Electrical conductivity *vs.* pressure 330–332, 511, 616
Electrical conductivity *vs.* temperature 336, 350, 511—512, 538, 600, 616
Electrical resistivity model for Hungary 548, 568, 569
Electrical resistivity *vs.* pressure coefficient 325
Electrojet, auroral 149, 275, 284, 591
— inner 290
— polar 278–279, 283–284, 286–293
Electromagnetic data in the CSSR 519–525
Electromagnetic field 76, 165–166, 170, 222–230, 231–245, 247, 253–254, 271, 304, 306, 317, 501–502, 519, 530, 591, 608, 642, 667, 705, 712
— field, propagation of 72, 73
— field, source of 111, 245
Electromagnetic induction method 304, 501

Electromagnetic wave 193, 196, 222, 317, 698
Electromagnetic wave, plane 108, 215, 222, 223, 594
Emission, coefficient 27
Emissivity 26, 27, 33, 34
Enstatite 336, 346, 351, 355
Epihercynian platform 357, 646, 650, 652
Epi-Paleozoic platform 378, 379

Fayalite 334, 350, 362, 367, 728
Feldspar 359
Felsite 326
Ferrite 334
Ferroginous-sodium amphibole 364
Finite element method 67–68
Finite difference method 68–69, 74, 90–96, 103, 152, 172, 231–235, 244, 495–496, 564
Flow-around effect, electromagnetic 169, 197–201, 203–206, 208, 216–218, 616, 656, 659, 685, 689
Flysch zone 404, 517–518, 532, 534, 610
Formation factor 48–49
Forsterite 355, 362, 364
Fourier transformation 74, 78–79, 82–83, 88–89, 124, 143, 296, 317, 519, 653
Frenkel defect 330

Gabbro 323, 326, 344–346, 360–361, 363–365, 546, 563, 569
Gabbro-amphibolite 342
Gabbro-diabase 347–348
Gabbro-norite 345–346
Galvanic constant 188, 210–211, 213
Galvanic effect of inhomogeneity 167–169, 191, 621, 677
Garnet 334, 358
Garnet-almandite 334–335
Garnet-pyrope 334–335, 355, 357
Gauss–Seidel method (successive displacement) 68–69, 235, 495
Geoelectrics, boundary problem of 18
Geological map of Czechoslovakia *527*
Geomagnetic activity 505, 506
Geomagnetic anomaly, Verkhoyansk 693–694
Geomagnetic deep profiling (DGP) 600–602
Geomagnetic deep sounding 103–104, 231, 274, 291, 293, 304, 307, 309, 311, 313, 493–494, 497, 501, 503
Geomagnetic field source 106, 141, 146
Geomagnetic induction 124–139
— inverse problem of 124, 134–136
Geomagnetic main field 502
Geomagnetic substorm 104, 274–295, 501, 507
Geomagnetic sudden pulses (Si) 653
Geomagnetic ssc 292, 653
Geothermal activity 375–377, 379, 414, 416, 419, 601, 661–662, 677, 680
Geothermal anomaly 431, 454, 661
Geothermal data, jump correction of 17, 35
— processing of 34–37
Geothermal energy, source of 53
Geothermal field 395, 398, 402–412, 414, 416, 439, 442, 479
— inhomogeneous 17–18
Geothermal gradient 18–21, 24, 38, 364, 382, 384, 398, 400, 402, 405, 408, 422, 450, 610
Geothermal gradient, Baikal Rift zone 455, 469
— Bulgaria 441–442
— Georgia 451–452
— German–Polish depression 511
— Hungary 429, 431, 436–437
— Poland 405–408, 410
— Yakutia 478–479
Geothermal gradient map, Hungary (1 km depth) 436, *437*
— Poland 405, 406, 407–408
Geothermal map, Bulgaria (500 m depth) 439, *440*
— Eastern Europe (1 km depth) 373, 376, 381, *382*, 383, 429, *573*, supplement
— Hungary (0.5, 1.0, 1.5, 2.0, 2.5, 3.0 km depth) *425*, *426*, *427*, *428*
— Hungary (depth contours of isotherms: 80 °C, 110 °C, 170 °C, 250 °C) *434*, *435*
— Poland (neutral level, 1 km, 2 km depth) *403*, *404*, *405*

Geothermal map, Siberia and Kamchatka (40 km depth) *464*
Geothermal temperature values, Bulgaria 442
— Czechoslovakia 540
— Hungary 429, 433–436
— Yakutia 476, 477
Geothermics, boundary problem of 18, 67, 72–75
— direct problem of 18, 67–70
— inverse problem of 18
Glaciation period 450
Gneiss 323–325, 338, 340, 342, 361, 366, 388, 545
Gondvanic microplate 572
Granite 323, 326–327, 338–340, 342, 344, 359–363, 365–366, 540–541, 546, 563, 569, 610, 723
"Granite" layer 338–350, 362, 364–366, 578, 590, 652, 660, 722–723
Granitization zone 725–726
Granodiorite 338–339, 361, 615
Granulitic facies 723–724
Granulitic zone 722
Graphite 342, 552, 570, 642
Graphitic schist 552, 570
Graphitized slate 341
Grid function 172
Gutenberg discontinuity 644

h-interval 178–182, 184, 186, 198, 200, 202, 210, 216
H-polarization 141, 153–156, 159–160, 168, 170–171, 177, 181, 183, 202, 212, 231, 233, 235–236, 238, 240–244, 246–250, 252–253, 262–263, 265–266, 493–497
H-polarized field 168, 170, 172, 201, 206, 248, 254
Half-space, homogeneous 230, 569
— horizontally layered 18, 222–230

Hall-effect 332
Harang discontinuity 286
Heat balance equation 91
Heat conduction 67, 463, 561, 572, 574
Heat conductivity 19, 56, 96
Heat flow 17–19, 22–24, 38, 42, 53–55, 57, 59–65, 70, 72–99, 364, 366, 373, 375–378, 384–385, 389, 395, 401–402, 405, 407–412, 439, 443, 446, 483, 498, 509, 556, 567, 574, 582–584, 610–611, 626, 631–632, 639, 648–650, 693–694, 700
Heat flow, Baikal Rift zone 455–461, 679
— Baltic Shield 378, 443–444, 448
— Black Sea 378, 445–446
— Carpathian Mts 418–419, 446, 538
— Caspian Basin 378, 445
— Central and Eastern Europe 374, 378–379, 416
— Czechoslovakia 377, 414–422, 538–541
— East Carpathians 444–445, 601–602
— Eastern Pre-Caucasus 650
— Georgia 450–454
— Greater Caucasus 445
— GDR 389, 390–394
— Hungary 379, 538, 540, 561–563, 565, 567–568, 571–572, 578
— Kura River depression 444–445
— Lesser Caucasus 444–445
— North-German Basin 377–379, 395–401
— permafrost region 473–480
— Poland 408–412, 444
— Pre-Caspian depression 444
— Russian Platform 378, 443–445, 448, 602
— Scythian Plate 378–379, 444, 448
— Siberia and Kamchatka 463–471
— Tersko-Caspian foredeep 444
— Timano-Pechorian depression 444
— Transbaikalia 455
— Turkmenia 661–663
— Ukrainian Shield 378, 443, 602, 638
— West-Kuban foredeep 444
— Yakutia 478
Heat flow, calculation of 44, 53–54, 56–57, 96
— data processing of 18, 53–58
Heat flow density 376, 402, 452
Heat flow distribution, Baikal region *456*, 460
Heat flow disturbance 54
Heat flow map 373–374, 377–378
— of Central and Eastern Europe 376–380, 384, supplement

Heat flow map of Central Europe *499*
— of the European part of the USSR 443–448
Heat flow, measurement of 19–20, 64, 67, 373–376, 414–416, 422, 433, 445, 663
Heat flow model 97
Heat flow sensibility 95
Heat flow values, histogram of *379*, *398*
Heat flow *vs.* radiogene heat source density 574
Heat generation 54, 73–75, 389, 405, 412, 437, 448, 539, 541
— Baltic and Ukrainian Shield 448
— Hungary 437
— Siberia and Kamchatka 463–471
Heat generation density 663
Heat generation model 389
Heat generation (radioactive) *vs.* depth 510
Heat loss 24, 40, 42, 97
Heat production 422, 437, 461, 496, 540, 561–562
Heat production, radioactive 509, 539
Heat production distribution 373
Heat production vs. depth 562, *563*
Heat radiation 25
Heat source density (radioactive heat generation) 67, 69, 430, 509
Heat source distribution 562
Heat transport, convective 400–401
Heavy water 430
Hedenbergite 336–337
Helium concentration 17, 24
Helium content 24
Helium emanation 19
Helmholtz equation 72–73, 152, 171, 231–232, 244
Hercynian basement 391–392
Hercynian orogeny 391, 445
High-frequency modelling in electrolytic trough 152
High temperature zone (in Poland) 404
Hilbert transformation 142, 148, 637
Homogeneity of electromagnetic field 245
Homology 303–318
Hook's law 317
Horizontally homogeneous model 165–166, 174, 183, 187, 193, 200, 241
Hornblende 337, 342, 344, 358
Hypersthene 346, 350
Hyperstenic gabbro 345–346

Ice-base temperature 61, 64
Ijolite 358
Illinoian (Riss) glaciation 63
Impedance 107–108, 112, 114–115, 117–118, 145, 168, 171, 173, 198–201, 203, 208, 222–230, 232–233, 235–236, 240, 246–248, 250–251, 254–255, 258, 260, 262–263, 265–268, 270–272, 296, 493, 530, 532–533, 557–558, 594, 608, 620–622, 629, 640, 644, 667, 694
Impedance, apparent 629
Impedance curve 107, 117, 530, 623
Impedance, effective 208, 666–667
Impedance ellipse 262, 267. *268*, *270*, 271, 272–273
Impedance, input 256, 267, 271
— longitudinal 176–179, 202, 209–210
— normal 105–108, 111, 114–115, 122, 177–179, 198, 210, 250, 608, 636
— normal, frequency characteristics of 111
Impedance polar diagram 269–272, 527, 531–532, 641–643, 653, 656
— Czechoslovakia 527
— Turkmenia and Azerbeijan 654, 658
— Ural 642
Impedance, primary (main) 262–263, 267, 527, 641, 643, 653–654
— secondary 259, 262–263, 269, 641, 643, 654
Impedance tensor 167, 197, 217, 227–230, 247, 258–260, 262–263, 620, 653
Impedance, transversal 168, 176–178, 202, 209–210, 215–216
Induction arrow (Wiese), map, Carpathians 604, 605
— Central Europe 489
— Czechoslovakia 527
— East Carpathians 589
— GDR 490
— Kirovograd anomaly 635
— Kurile Islands 699
— Sovjet Far East 697
— Transdanubia 550
— Ukraine 634
— Yakutia 693

Induction effect 168, 179, 181–182, 191–195, 198–199, 201, 206–208, 211–212, 217–218, 286–288, 526, 529, 630–631, 647, 675, 677, 685, 687–689, 691, 704–707, 709
Induction effect, regional 526, 706
Induction modulus 526, 529
Induction vector (arrow) 141, 147–149, 519, 527–528, 530, 590–591, 594–595, 604, 607, 634, 698, 700
Infra-red emission 28
Infra-red measurements 17, 28–29
Infra-red methods, airborne 28–29
Infra-red radiation 25
Infra-red radiation temperature 25, 27, 32
Infra-red radiometry 29–33
Infra-red surface geothermics 17, 25–37
Inhomogeneity, conductive 240, 592, 594–595, 617, 675
— geoelectrical 165–167, 171, 175, 186, 208–215, 233, 236, 248, 267, 274, 487, 526, 533, 554, 591, 593–594, 600, 654, 656, 685
— geological 267, 530, 626, 667, 669, 716
— geomagnetic 104, 141, 266, 293, 507, 594
— horizontal 72, 165, 231, 236, 264, 270–271, 487–488, 496, 538, 592, 616, 630, 676, 683, 689
— one-dimensional 80–81, 592
— regional 617–618
— three-dimensional 175–195, 231, 640, 716
— two-dimensional 175, 195–208, 676, 716
Inhomogeneous layer 247–248
Integral equation method for magnetotellurics 113, 172, 179, 183, 187
Interarc basin, ensialic 572, 581–584
— ensimatic 572, 581–584
Interarc spreading 582
Intermediate conducting layer 192, 206–208, 219, 498, 547, 623–624, 626, 630–632, 644, 648–650, 657–661, 663, 676, 689, 691, 703, 705, 716–717, 721–722
Intermediate high-resistant layer 168, 174, 178–184, 186–188, 195, 215, 270, 654
Interplanetary magnetic field 275
Ionization energy 332–333
Ionospheric current system, equivalent 275, 279–285, 289–292
Ionospheric-magnetospheric current system 279–280
Isostatic gradient (gravity) 455–456, 458–459

Jacobi method (simultaneous displacement) 68
Jadeite 336
Jump function 76–77, 80, 85, 87
Juvite 358

KAPG (Committee of Academies of Sciences of Socialist Countries for Planetary Geophysical Investigations) 17, 298, 381, 483, 605
Karig's theory 582
Kimberlite 352–353, 356
Kimberlite-olivenite 356

Labradorite 346
Laplace transformation 224, 318, 653
Lattice energy, crystal 332–334
Leucocratic gabbro-diabase 347–348
Limestone 51, 321–323, 326, 338, 386–387, 397–399, 415–416, 441, 545–546
Limey marlstone 398
Lithosphere 487, 494, 496, 498, 577, 579, 581, 583, 584, 680, 724
Lithospheric plate 556, 582
Low-frequency field 169
Low-velocity channel 518, 535
Low-velocity layer (LVL) 469, 470, 535, 556, 567, 572, 578, 580, 583
Lunar variation (L) 501

Magmatic activity 680
Magnesium 364
Magnesium oxide 331
Magnetic dipole 245
Magnetic disturbance vector 279, 280, 283
Magnetic field anomaly 197, 240, 470–471
Magnetic permeability 170–171, 222, 233, 366, 592

Magnetic polar diagram 150
Magnetic variation data processing 141
Magnetite 333, 342, 346, 354–355
Magnetosphere 104, 274, 279, 290, 307
Magnetospheric storm 274–275, 283, 291–292
Magnetospheric tail 274
Magnetostatic field 304, 306, 312
Magnetostatic potencial 306, 311
Magnetotelluric amplitude curve 667–670, 676–677
Magnetotelluric anisotropy 271, 541, 552, 554, 556–558
— regional 263, 556, 558, 568, 571–572
Magnetotelluric anisotropy ellipse 554
Magnetotelluric calibration curve 491
Magnetotelluric data processing 256–263
Magnetotelluric deep sounding 165, 167, 171, 222, 231, 468, 493, 553, 555, 594, 615–617, 620, 626, 628, 630–631, 640–641, 643, 652–653, 700
Magnetotelluric field, anomalous, amplitude characteristics 109, 113
— frequency characteristics 110–111, 113–115, 117–118, 120–122, 141, 150
Magnetotelluric group sounding curve 618–619
Magnetotelluric method of group sounding 617–619
Magnetotelluric model, circular cylinder 635
— elliptical cylinder 635
— four-layer 618–619
— theoretical 551
— three-dimensional 156, 159, 160–161, 172, 198–199, 201, 203–204, 249, 253, 654
— three-layer 647, 712
— two-dimensional 153–161, 168, 172, 191–192, 198–199, 201–204, 206–207, 213, 218, 247, 654, 694
— two-layer 693
Magnetotelluric model calculation 495–498, 512
Magnetotelluric modelling, analogue 173
Magnetotelluric net method 113
Magnetotelluric phase curve 666–670, 676–677
Magnetotelluric profiling (MTP) 256–257, 597, 640, 641, 643, 708
Magnetotelluric profiling method, formula of 256
Magnetotelluric resistivity, Pannonian Basin 548, 555
Magnetotelluric sounding (MTS) 106, 122, 143, 149, 165–166, 169–219, 245, 256, 362, 469, 483, 498, 549, 550, 554, 559, 561, 567–568, 572, 600, 605–606, 609, 615, 628, 631, 647, 657, 666, 673, 675, 682, 689, 694, 697, 700–702, 707–708, 711, 716, 721, 724, 728
Magnetotelluric sounding curve (MTS) 165–169, 171, 173, *174*, 175, 178, 181, 189, 194–195, 197, *200*, *201*, 205–206, *207*, 208, 211, *216*, 217–219, 231, 240–241, *242*, 243–244, 246–250, 253–254, 487, 492–497, 519, 529–530, 533–534, 536, 556, 621, 624, 644, 675
Magnetotelluric sounding curve, Arctic Ocean 712, *713*, *714*
— Baikal Rift zone *674*, 675, 677
— Belorussian Massif *618*, *619*
— Bohemian Massif *531*, *532*
— Carpathians *532*, *606*, 608–609
— Danube Lowland *532*
— Eastern Pre-Caucasus 646, *647*, 649–650
— Hungary *299*, *532*, 548, *549*, 551, *552*, 553, *555*, 556–557, 567, 569, *570*
— Kamchatka 708, *709*, 710
— Kokchetav block 615, *616*
— Lovozero Massif *616*
— Moscow syneclise *629*
— North-Eastern Yakutia 689, *690*, 691
— Russian Platform 622–624, *625*
— Ryazan-Saratow depression *629*, 630
— Sakhalin 702, *703*, 705, *706*
— Siberian Plate *674*, 675
— South-Western Yakutia 683–685, *686*, 687, *688*, 689
— Soviet Far East *700*
— Tokmovo dome *629*, 630
— Tungus syneclise 666–667, *668*, *669*
— Turkmenia and Azerbaijan *216*, 654, *655*, 656, *657*, *658*

Magnetotelluric sounding curve, Ural 640, *642*, 643
— Voronezh Massif *629*
— West-Siberian Plate 669, *671*, *674*, 678
Magnetotelluric sounding curves, album of 172, 214
Magnetotelluric sounding curve, direct interpretation of 551
— effective 207–208, 217–218, 658–659, 675–676, 700
— formal interpretation of 165, 168–169, 171, 175, 179, 181, 184, 186–187, 190, 192, 205–207, 214, 216–218, 615, 623, 629, 631, 648, 650, 656, 658–659, 683, 689, 703, 705–706, 709, 716
Magnetotelluric sounding curves, interpretation of 165–219, 551, 644, 667, 670–671, 683–684
Magnetotelluric sounding curve, longitudinal 167–168, 178–179, *180*, 181, *183*, 184, *185*, 186, 189–190, *191*, 192–193, *194*, 195, 206–208, 211, *214*, 215, 217–218, *606*, 607, 609, 629–631, 640, 644, 647, 655–660, 676–677, 683–686, 688, 690–691, 702–706, 708–710, 713
— normal 178–184, 187, 191, 215
— quantitative interpretation of 495, 644, 677, 691
— three-layer 184, 296, 630, 675
— two-layer 256, 296
— transversal 167–168, 178–179, 181, *182*, 183, *184*, 186, *187*, 189, *190*, *191*, 192, 195, 206–207, 211–213, 215–218, 630, 647, 655, 657–659, 676–677, 683–685, 690, 702–706, 708–709, 713–714
Magnetotelluric sounding method, quasi-statistic 173
Magnetotelluric theoretical master curve 242
Magnetotelluric theoretical curve 247, 253, 569, 618–619, 625, 647, 649–650, 667, 686–687
Magnetotellurics 104, 134, 137, 139, 304, 307, 308–309, 311, 313, 314, 317, 529–535, 573
— inverse problem of 134, 138
Magnetovariation curve 110, *194*, 195, 688, 690–691
Magnetovariation method 219
Magnetovariation profiling (MVP) 105–122, 141–151, 600, 606, 609, 637, 640, 641, 643, 697–698, 716
Magnetovariation sounding (MVS) 106–108, 128, 219, 468, 483, 600–602, 682, 689–690, 694, 706, 716, 721
Mantle diapir 572, 577, 580–584
Marine geophysics 19
Marine geothermal investigations 17, 19–24, 450
Marlite 415–416
Marlstone 386–387, 399
Melaphyre 387
Melting curve 540, *541*, 662–663, 723
Melting of rocks 568, 723
Melting, partial 219, 367, 484, 518, 568, 579, 601, 626, 632, 644, 648, 662, 663, 678–680, 691, 696, 710
Melting point 367, 568
Melting zone 644, 650, 663, 726
Mica 342
Micaceous schist 388, 545
Microcline 338
Migmatite 725
Migmatization 726
Migration, primary 434, 435
— secondary 434
— tertiary 435
Model experiments (magnetotelluric) 245–255
Model of horizontally stratified medium (fundamental model I) 171, 173–175, 213
Model of stratified medium with surface inhomogeneity (fundamental model II) 171, 175–208, 215
Model of stratified medium with deep inhomogeneity (fundamental model III) 171, 175, 208–215
Model of uniform granite radioactivity 539
Modelling on RC networks 152
Moho depth 412, 421, 465, 467, 509, 518, 555
Moho heat flow 422, 540
Moho-temperature 421, 465, 467, 468, 471, 511, 512, 540

Mohorivičič discontinuity (Moho) 364–365, 389, 411–412, 463, 465, 469, 471, 496, 498, 509–512, 518–519, 534–535, 552–553, 562, 564, 578, 582, 590, 615–616, 638, 643, 662, 679, 689, 725
Montmorillonite 435–436
Myloncratic gabbro 345

Nebrascan (Günz) glaciation 63
Nepheline 338
Non-conducting layer 169, 174
Non-glacial time (warm), Tertiary and Mesozoic 61
Nyquist period 258

Ocean ridge model 97
Old-Paleozoic geosyncline 545
Oligoclase 338
Olivenite 350–353, 355–356, 360–362, 364, 511–512
— serpentinized 351
Olivenite-pyroxite 351
Olivine 333–335, 350, 355, 361–362, 563–564, 728
Olivine-forsterite 356
Olivine kimberlite 355
Olivine nodule 356
Olivine-pyroxenite 350, 352–353
Olivine-spinel transition 362, 367, 556, 632, 644, 650, 728
Olivine xenolith 356
Omphacite 358
Orthoclase 338, 723
Orthogneiss 340
Oxide minerals, electrical resistivity of 331, 332

Paleoclimatic change 18
Paleoclimatic effect 59–65
Paleovolcanic activity 571
Paleozoic platform 404, 408
Parkinson angle 526
Parkinson, plane of 519, 530
Parkinson vector 151, 697–698
Past climate, models of 62–64
Pearson's criterium 452
Pelite 342
Pelitization 346, 361
Periclase 332
Peridotite 326, 350–351, 354–355, 364, 511–512, 679
Peripieninian lineament 518–519, 528, 530, 534
Petroleum genesis 433–436
Phyllite 388, 545
Phyllite slate 341
Plagioclase 342, 344, 346
Permafrost 61, 375, 473–480, 667, 669
Planck's radiation law 26
Pleistocene climate 65
Pleistocene glaciation 60–61, 63, 401
Polar cap 278, 283, 290
Polar cap current 288, 290–292
Polar cusp 274, 293
Polarization of electric field 202, 245, 248, 262, 642, 700
Polarization of magnetic field 76, 149, 245, 262, 642
Porosity 48, 50–52, 321–323, 325, 327, 358, 361, 365, 387, 397, 415, 430, 439, 610
Porosity-depth function 430, 432
Porphyrite 387
Porphyry 387
Pre-exponential coefficient 327, 511–512
Pre-Cambrian Shield 376, 378, 408, 411–412
Price's model 296
Projection method 172, 182
Pulsation of geomagnetic field 104, 264–273, 275, 297–298, 300, 501, 519, 528, 556
— Pc type 297–298
— Pc 3 297, 299–301, 520–526, 529
— Pc 4 297–299
— Pc 5 299, 520–523, 526, 528–529
Pulsation of geomagnetic field Pi 2 296–297, 520–524, 526, 529
Pulsation field, inhomogeneity of 296–301
Pulsation period, latitude dependence of 298, 300
Pyrolite 541, 662
Pyrope 334, 355, 358
Pyrope-eclogite 352–353, 360
Pyrope-peridotite 352–353, 355–356, 360–361

Pyroxene 336–337, 344, 346, 350–353
Pyroxene olivenite 350
Pyroxene-spinel transition 644, 728
Pyroxene xenolith 356
Pyroxenite 351, 511–512

Quaternary climatic pattern 61
Quartz 321, 332, 338–339, 342, 359, 397, 441, 541, 723
Quartz-chlorite schist 363
Quartz-diorite 339
Quartz porphyry 387, 545
Quartz tholeiite 662
Quartzite 325, 388, 397, 545
Quartzmicroclinealbite 340
Quartzmicaceous slate 341

Radiation, atmospheric downward 27
— diffuse sky 27
— direct solar 27
— of the ground 27
— short-wave reflected 27
Radiation balance 27–28
Radiation condition 76, 80, 83
Radiation energy 25
Radiation surface temperature, measurement of 27
Radiation temperature 30, 33
Radiogenic Helium 24
— concentration of 23
Radiometric measurements 437
Relaxation factor 70
Relaxation method 113, 564
Resistivity, electrical 105, 118, 136, 169–170, 173–174, 176, 179–180, 182, 185–190, 192–193, 195, 197, 199–201, 203–205, 208, 213, 215, 239–243, 245–246, 254–255, 264–265, 267–269, 272, 321–328, 330, 338–351, 354–359, 362–367, 492, 494–497, 512, 529, 547, 569–570, 615–616, 623, 626, 630, 640, 642–646, 648, 652, 659, 666–667, 669, 674–675, 679–680, 687, 696, 708, 712–713, 721–722, 728
Resistivity, electrical, apparent 134, 136, 174, 181, 194, 218, 233, 235–236, 238–243, 247, 258, 298, 301, 493–497, 531–532, 629, 712
Resistivity curve 165, 194, 200–201, 203–205, 207–208, 212, 214–216, 239–243, 262, 348, 361–362, 512, 530, 532, 551, 554, 556, 568, 650, 653, 656
Resistivity values, acidic rocks 340
— amphibolites 343–344
— basalts 324, 349, 354
— diabases 326, 347
— eclogites 352–353, 357–358
— gabbros 326, 345–346, 360, 364
— gneisses 340, 342
— intermediate rocks 340
— kimberlite olivenites 356
— shales 341–342
— ultrabasic rocks 351–353
Resistivity *vs.* depth 357, *363*, *365*
Resistivity *vs.* fayalite content 335
Resistivity *vs.* NaCl (solution) content 323, *324*, *325*
Resistivity *vs.* pressure *322*, *326*, *327*, 332–338, 350–351, 358–362
Resistivity *vs.* serpentine content 355
Resistivity *vs.* temperature *322*, *326*, 331, 332–338, *339*, *344*, *346*, 347, 350–351, *354*, *356*, *359*, 360, 364, 511, *512*
Rhyolite tuff 326
Riccati equation 173–174
Riebeckite 337–338, 364
Ringwood's rock model 567
Rock density 49, 61, 364, 366, 415–416
Rock matrix 324, 342

S-anisotropy 256–258
S-effect 168, 178, 181–182, 184–189, 191, 195, 198–199, 201, 206, 216–218, 263, 548, 552, 554–555, 621, 624, 630, 640, 647, 656, 659, 661, 668, 670, 676, 689, 703–704, 709
S-effect, regional 619
S-ellipse 256, 258
S-interval 175, 177, 216, 243, 256–258, 713
Salinity 324
Sandstone 18, 49–50, 321–323, 326, 386–388, 397–400, 415, 441, 545, 669
Saussuritization 347–348
Schottky defect 330
Screening effect 168, 211–213, 216–218
Seismic activity 648, 700, 725

Seismic deep sounding 411, 420, 517–518, 527, 529, 531, 533–536, 538–539, 590, 596–597, 600–602, 605–606, 636–637, 643, 679
Seismic discontinuity 554
Seismic velocity 366, 535, 556, 609, 626, 662, 725, 727
Seismic velocity anomaly 638
Semiconductor, n-type 328, 330
— p-type 328, 330
Serial test method 304, 314
Sericite 342
Serpentine 354
Shale 338, 341, 362–363, 546
Sillimanite 362
Sillimanite-cyanite transition 721
Siltstone 386, 387, 398–399, 415, 546
Skin-effect 114, 196, 592, 594, 596
Slate 323, 342, 358, 366, 545–546
Sodalite 362
Solar wind 274
Source function 77
Specific heat 61
Sphene 344
Spinel dunite 352–353, 356, 360–361
Splitting of geomagnetic field 501–507
Spodumene 336
Sq-variation (geomagnetic) 264, 489, 490, 501–507, 600–602, 629, 631, 643–644, 653, 698–700
Stefan–Boltzmann law 26
Stephan's condition 477
Stishovite 644, 728
Student's criterium 452
Sturm–Liouville equation 135
Subcrustal erosion 570, 577
Subductive zone 582
Subduction 579–583
Successive overrelaxation method 68–70, 235, 509
Swift's formula 260
Syenite 326–327, 338

Talcization 347
Tangent method of absolute ellipse 257
Tectogenesis 582, 583
Tectonic activity 219, 364, 446, 457, 458, 461, 648, 650, 680, 715
Tectonic line "Balaton" 552, 554, 557–558
Tectonic map, Czechoslovakia *417*
— East-Siberian Platform *682*
— Northern Sakhalin *703*
— Yakutia *693*
Telluric relative frequency sounding curve *547*
Telluric relative frequency sounding map of Hungary 547, *548*, 549
Telluric relative ellipse 258, 547
Temperature, crustal 420–421
Temperature measurement 34, 38, 53, 57, 59–61, 64, 373–375, 381, 384–385, 393, 415, 473, 475, 479
Temperature of sea water in the Pleistocene 63
Temperature, Wisconsin 64
Temperature calculation in frozen ground (permafrost) 475–476
Temperature coefficient 29
Temperature-depth curve 384, 429, 463, 465, 539, 662–663, 679
Temperature-depth curve, Czechoslovakia 422, *540*, *541*
— Hungary *540*, *568*
— North-German Basin *388*, 398, *399*, *400*
— Poland *540*
Temperature-depth function 98, 428, 466, 483, 568
Temperature distribution 67, 90, 96–97, 362, 373, 394, 414–415, 422, 464, 466, 471, 475, 509–512, 541, 574, 616, 662–663, 728
Temperature equilibrium 474
Temperature gradient calculator 56–57
Temperature gradient *vs.* depth curve 56, 57, 65
Temperature *vs.* depth distribution 363, 388–389
Thermal conductivity 17–21, 24, 38–39, 42, 44–45, 48–58, 61, 64, 67, 69–70, 72–75, 90–91, 93–96, 318, 373, 377, 387, 396, 406, 414–416, 430, 439, 446, 448, 463, 465, 477, 479, 496, 509, 539, 563–564, 610, 639, 663, 726
Thermal conductivity, Baikal Rift zone 455

Thermal conductivity, Czechoslovakia 415–416
— Georgia 452
— GDR 385–389, 395–401
— Hungary 561, 563–564
Thermal conductivity, linear model of 395–397
— disperse model of 395–396
Thermal conductivity calculator 53–56
Thermal conductivity coefficient *vs.* electric conductivity 50
Thermal conductivity coefficient *vs.* formation factor 50
Thermal conductivity coefficient *vs.* longitudinal wave velocity 50
Thermal conductivity coefficient *vs.* porosity 51, 396
Thermal conductivity coefficient *vs.* temperature 539
— measurement of 17, 19, 21, 38–43, 53–54, 385–395, 402
Thermal conductivity measurement, divided-bar apparatus 38–43, 53, 55–56, 415
— divided-bar method 38–43
— modified Ångström method 44
Thermal conductivity *vs.* depth 510
Thermal diffusivity 18, 45, 47–48, 51, 60–61, 63, 65, 466, 475, 479, 574
Thermal diffusivity *vs.* pressure 44–47
Thermal diffusivity *vs.* temperature 44
Thermal equilibrium 408, 473, 477
Thermal resistance 38, 40, 42, 45, 55–56
Thermistor thermometer, portable 56
Thermometer, electric logging 56, 402, 415
— electric resistance 384, 473
Thermometric measurement 408
Thermoprobe, Alpine type 19–20
Thermoprobe, Bullard's 19
— Hänel probe 19–21
— Langseth's 20
— thermogradient penetrative plotter (TPP) 19–24
—— (TPP-3) 22
—— (TPP-3MT) 22
Tholeite 541
Tikhonov–Cagniard formula 259
Titanomagnetite 350, 354
Topographic correction 18
Total-counter 257
Total variation method 257
Transversal magnetic mode of external field 166
Travel-time curve 519
Tremolite 337–338, 344
Tuff 387

Upper mantle model, geoelectrical 649, 728
— geothermal 649
Upper Mantle Project 376

Variscian tectogenesis 416
Velocity distribution, model of 535
Vertical electrical sounding (VES) 321, 322, 615, 618, 622
Vertical intrusion model 96–99
Volcanic activity 546, 677–678, 680, 711
Volcanism, Cenozoic 648
— Neogene 445, 483, 579
— Tertiary 379, 417

Water saturation 415
Wiese arrow (geomagnetic induction arrow or vector) 141, 150–151, 487–490, 519, 526, 550, 554, 558–559, 571, 589, 605, 621, 626, 693, 697–698
Wiese's method 150, 487–488, 607
Wisconsin (Würm) glaciation 63, 64

Xenolith 352–353, 355–357, 361, 365

Young–Frankel upper successive relaxation method 91
Young module 469

Zechstein salt formations 492, 493
Zoisite 342

INDEX OF GEOGRAPHICAL NAMES

Abisko (Sweden) 277, 278, 285
Acsalag (Hungary) *550*, 552
Adzaro-Trialety (USSR) 450, *451*, 452, 453
Adzi (USSR) 624
Aegean Sea 572
Agayakan (USSR) *693*, 694
Aladag-Binalud meganticlinorium (USSR) *653*
Aldan anteclise (USSR) 680, 683, 685, 686, 687, 688, 689
Aldan Shield (USSR) 219, 535, 682
Alexandrovsk (USSR) 700
Alpine-Carpathian foredeep 527
Alps 518, 545, 546, 562, 604
Altai-Sayan area (USSR) 465, 466, 467, 468, 469
Amga River (USSR) 479, 693
Amo (USSR) 670
Anabar anteclise (USSR) 680
Angara–Lena anteclise (USSR) *682*, 683
Angaro–Kureisk zone (USSR) 670
Ante-Kopet-Dag foredeep (USSR) *653*
Apsheron Peninsula (USSR) 445
L'Aquila (Italy) 291
Araksin valley (USSR) 444
Arctic Ocean 19, *484*, 712, 715
Arti (USSR) *641*, 643
Artvin-Somkhity (USSR) 450, *451*
Assynthian Block (CSSR) 527
Avachi volcano (USSR) 355, 356
Azerbaijan SSR (USSR) 652, 658

Baikal Lake (USSR) 19, 22, 255, 356, 455, *456*, 457, 463, *464*, *673*, 676, 677
Baikal-Patom region (USSR) *682*
Baikal Rift zone (USSR) 349, 350, 375, 455, *456*, 457, 459, 460, 461, 465, 466, 467, 468, 469, 470, 471, *484*, 650, *673*, 675, 676, 677, 678, 679, 725
Baikal valley (USSR) 99, 364, 458, 465, 469
Baikit Anteclise (USSR) *673*, 678
Bakhynai (USSR) 473, 474, 478
Bakony Mts (Hungary) *268*, 551, 553, *562*, 563, 565
Bakonya (Hungary) 563, 565
Bakonybél (Hungary) *550*, 552
Bakonyszentkirály (Hungary) *550*, 552
Balaton Lake (Hungary) 270, 550, 552, 553, 554, 557, 558, 559
Balatoncsicsó (Hungary) *550*, 551, 552, 553, 557, 558
Balatonöszöd (Hungary) *550*, 551, 552, 553, 557
Balkhan-Apsheron depression (USSR) 652, *653*, 660
Balkan Mts (Bulgaria *440*, 441
Baltic depression (USSR) 617, 620, 621, 622, 623
Baltic Shield (USSR) 374, 378, 443, 448, 616, 620, 621, 624
Baltic-Skandinavian Shield (USSR) *484*, 615
Baltic syneclise (USSR) 620, 621
Balyk (USSR) 669, 671
Banska Štiavnica (CSSR) 414
Baranya Island (Mecsek) Mts (Hungary) *432*, *545*, 546
Bardejov (CSSR) 525, *527*, 528
Batumi (USSR) *451*, 452, *453*
Bavarian molasse (GFR) 518
Békés (Hungary) 432
Belorussian Massif (USSR) *484*, 604, 617, 618, 619
Belorussian-Mazur anteclise (USSR) 621

Belsk (Poland) 291
Beregovo (USSR) 590, 596, 597, 598
Berezansk (USSR) 444
Berezovo Depression (USSR) *682*, 683, 684
Berlin (GDR) *31*, *32*, *385*, *390*, *391*, *392*, *393*, 489, *490*, *492*
Bihar Mts (Rumania) 545
Birzhai (USSR) 619
Black Sea 19, 375, 378, 445, 446, 450, *451*, 452, *453*, 454, *573*, 608
Blagoevgrad (Bulgaria) 442
Bodonhely (Hungary) *550*, 552
Bohemia (CSSR) 377, 418
Bohemian Massif (CSSR) 414, 416, 418, 419, 420, 421, 422, 483, 517, 518, 527, 528, 529, 530, 531, 532, 534, 535, 538, 539, 540, 541, 574, 604
Bolshoi Balkhan zone (USSR) 652, *653*, 656, 660
Bolshoi-Krivoi Rog geosyncline (USSR) 637
Bojnice (CSSR) 525, *527*
Borisov (USSR) 617
Borszörcsök (Hungary) *550*, 551, 553
Boskovice (CSSR) 517
Botuoba Saddle (USSR) *682*, 683, 685, 686, 687, 688, 689
Boží Dar (CSSR) 523, *527*, 529, 530, 531, *534*
Brest Basin (USSR) 410, 621
Budapest (Hungary) 431, *432*, 550, 563, 573, 579
Budějovice Basin (CSSR) 529
Budkov (CSSR) 517, 519, 523, *527*, 529, 531, *534*
Buhrkow (GDR) 504
Büntzow (GDR) 504
Burkany (USSR) 624

Canadian Basin 712, 715
Canadian Shield 63
Carpathian Mts 381, 407, 409, 411, 414, 416, 417, 418, 419, 420, 421, 422, 483, 488, 517, 518, 527, 528, 529, 530, 531, 532, 533, 534, 535, 538, 539, 541, 545, 558, *573*, 577, *578*, *579*, 583, 589, 590, 592, 595, 596, 599, 602, 604, 605, 608, 610, 611, 634
Carpathians, Neogene foredeep and flysch zone 404, 414, 422, 527, 528, 540, 609, 611
Carpathian Foredeep 414, 416, *417*, 418, 419, 420, 421, 517, 518, 538, 540
Caspian Basin (USSR) 445, 630, 650
Caspian Sea 19, 375, 378, 445, 446, 447, 653, 658, 660, 662
Caucasian meganticlinorium (USSR) 649, 653
Caucasus Mts. (USSR) (greater) 374, 375, 379, 445, 447, 450, *451*, *453*, 646, 647, 650, 652, *653*
Cavmindovsk (USSR) 447
Čeladná (CSSR) 525, *527*
Central-Bohemian Basin (CSSR) 414, 417, 418
Central-Bohemian Pluton (CSSR) 518
Central Carpathian Mts 518, 519
Central-German Main Line 31
Central Kara-Kum dome (USSR) 652, *653*, 655
Central Kopet Dag (Pre-Copet Dag foredeep) (USSR) 652, 654
Central Kopet Dag meganticlinorium (USSR) 652, *653*
Central Russian Basin (USSR) *556*
Chambon-la-Forêt (France) 291
Chirpoi Island (USSR) 698, *699*
Chona-Syuldzhyukar area (USSR) 683
Chukch Peninsula (USSR) *712*, 714, 715
Chukch Shelf (USSR) *712*, 714, 715
Čiměř (CSSR) 522, *527*, 529
Cis-Carpathian Depression 407, 445, 447
Cis-Caucasus (USSR) 379
Cis-Sudetic monocline (CSSR) 404, 407, 409, 410, 412
College (Alaska) 276
Collm (GDR) 488
Crimean Peninsula (USSR) 374, 377, 445, 447

Danatin Basin (USSR) 656, 659, 660
Danube Lowland (CSSR) 517, 518, 532, 534, 540, 541
Danube River *440*, 442, 533, 545
Debrecen (Hungary) 432
Deputatsky (USSR) 478
Derbent Depression (USSR) 445, 447

Devecser (Hungary) *550*, 553
Dgidinsky area (USSR) 463, 465, 466, 467, 468, 470
Dinarides (Yugoslavia) 545, *573*, 577, *578*, *579*, 583, 604
Dneper–Donets depression (USSR) 410, 444, 446, 604, *628*, 630, 634, 638
Dnepr River (USSR) 444
Döbrönte (Hungary) 550, 552
Domanín (CSSR) 524, *527*, 529
Don River (USSR) 444, 628
Donets River (USSR) 444
Donovaly (CSSR) 525, *527*
Dourbes (Belgium) 291
Dráva River 545
Dunaharaszti (Hungary) 437
Dundaga (USSR) 624
Dusheti (USSR) 285
Dymer (USSR) 605
Dziruli Massif (USSR) 450, 452

East Carpathian Mts (USSR) 444, *484*, 589, 599, 600, 602, 605, 606, 611
East Siberian Shelf (USSR) 714
East-Thüringian Mts. (GDR) 393
Eastern Caucasus Foredeep (USSR) 652
Eastern Pre-Caucasus (USSR) *484*, 646, 648, 658
Eastern Rhodope Mts (Bulgaria) *440*, 442
Ege-Khaya (USSR) 478
Eger (Hungary) 437
Elbrus Mts (USSR) *451*
Elburs meganticlinorium (USSR–Persia) *653*
Elburs Mts (USSR–Persia) 379, 652
Erma River (Bulgaria) *440*, 442
Erzgebirge (GDR) 32, 392
Eskdalemuir (GB) 291

Falkenhagen (GDR) 488
Flin Flon hole (Canada) 62
Forecarpathian region (USSR) 589, 598, 601, 604
Freiberg (GDR) 32, 535
Froly (USSR) 669, 671
Fürstenfeldbruck (GFR) 291, 535

Gabčikovo (CSSR) 520, 526, *527*, 530, 532, *534*, 535
Gaiki (USSR) 624
Galvács (Hungary) 547
Georgia, SSR (USSR) 377, 450, *451*, *453*
German–Polish depression (GDR–Poland) 483, *484*, 604, 621
Gograndag-Chikishlar (USSR) *653*, 660
Göritz (GDR) 504, 505
Göttingen (GFR) 488, 494, 535
Gramzow (GDR) 504
Great Hungarian Plane (Hungary) *545*, 546, 555
Great Whale (Canada) 277
Grocka (Yugoslavia) 291
Grünow (GDR) 504, 505, 506
Guam 592
Gudauta (USSR) *453*
Günterberg (GDR) 504, 505, 506
Gyula (Hungary) 549, *550*, 556

Haeckel ridge (Arctic Ocean) *712*, 713, 715
Hahót (Hungary) 270
Hajdúszoboszló (Hungary) 432
Hammer (GDR) 504
Hartland (GB) 291
Határvölgypuszta (Hungary) *550*, 552, 553, 555
Herlany (CSSR) 525, 528
Hévíz (Hungary) 433
Hodonin (CSSR) 521, *527*, 528, 530, 531, 532, *534*
Holubov (CSSR) 422
Hosszúhetény (Hungary) *562*, 563, 565
Hrádek (CSSR) 522, *527*, 531, *534*
Hungarian Central Mts (Hungary) 545, 604
Hurbanovo (CSSR) 519, 526

Iakorouda (Bulgaria) 442
Ichin (USSR) *708*
Indian Ocean 349, 350, 355, 356
Ingulo-Ingulatsk zone (USSR) 637, 638
Inner Carpathian Mts 483, 535, 558, 602
Iran Basin 445
Iritkinsk Uplift (USSR) 670
Issyk-Kul, Lake (USSR) 17, 19, *23*, 24
Iturup Island (USSR) 698, *699*, 700
Izosenki (USSR) 624

Jablonica (CSSR) 521, *527*, 528

Kamchatka median volcanic belt (USSR) *708*, 709, *710*, *711*
Kamchatka Peninsula (USSR) 355, 356, 375, 463, 465, 466, 467, 468, 470, 471, *484*, 650, *697*, *708*, 709, *710*, 711
Kamýk (CSSR) 523
Kamyshlov (USSR) *641*, 642, *643*
Kandava (USSR) 624
Kanevsk (USSR) 444
Kapoly (Hungary) 553
Kapuskasing (Canada) 61
Kara-Kum Platform (USSR) 652, *653*, 654, 655, 659
Kazakhstan (USSR) 352–353, 357, 358
Kazbek mountain (USSR) *451*, *646*, 649
Kecskemét (Hungary) 437
Kempendya Depression (USSR) *682*, 683, *684*, 685, 686, 687, 688, 689
Kenkeme (USSR) 478
Khabarovsk (USSR) 700
Khashuri region (USSR) *451*, 452
Khatyryk (USSR) 478
Khmelnitsky (USSR) *634*
Khibin Mts (USSR) 444
Kirovograd (USSR) 608, *634*, *635*, 636, 637, *638*
Kiruna (Sweden) 285
Kisvásárhely (Hungary) *550*, 554, 555
Klačno-Reváň (CSSR) 525, *527*, 528
Klevenow (GDR) 488
Kocsord (Hungary) *550*, 555, 556, 567
Kokchetav block (USSR) 357, *484*, 615
Kola Peninsula (USSR) 363, 374, 443, 444, 448
Kolkheti Lowland (USSR) 450
Kolyubeevo (USSR) 624
Komsomolsk (USSR) 700
Kopet-Dag Mts (USSR–Persia) 216, 652, 655
Korets (USSR) *589*, 590, 596, 597, 598, 599, 601
Koryaksko-Avachinsk depression (USSR) 463, 465, 467, 468
Kovdor (USSR) 443
Krasnoe (USSR) 624
Krasnoufimsk (USSR) 640, *641*, *643*
Krests (USSR) 620, 626
Krivoi Rog (USSR) 638
Kronotsky Peninsula (USSR) 466, 467
Krupá (CSSR) 523, *527*, 529, 530, 531, *534*
Krušné hory (CSSR) 517, 518, 530, 531, *534*, 540, 541
Kuba-Dag Mts (USSR) 652, *653*, 656, *660*
Kujavy anticlinorium (Poland) 409
Kunashir (USSR) 700
Kura River Depression (USSR) 444, 446, 658, *660*
Kura megasynclinorium (USSR) 658
Kuranakh-Sala (USSR) *693*, 694
Kurile Islands (USSR) 697, 698, 699, 700, 707
Kuznetsky Alatau (USSR) 463, 465, 467, 471
Kuznetsky Basin (USSR) 463, 465, 467
Kysyl-Syr (USSR) 478
Kyurdamir-Talysh fault (USSR) 652
Kyustendil (Bulgaria) 442

Laryak (USSR) 669, 671
Latvian Saddle (USSR) 620, 621, 622, 623, 626
Łeba River (Poland) 409, 410
Lednice (CSSR) 518, *534*
Leipzig (GDR) 489
Leirvogur (Iceland) 277
Lelenis (USSR) 618, 619
Leningrad (USSR) 291
Leno-Yenisei Plate (USSR) 682
Lesser Caucasus Mts (USSR) 379, 444, 445
Liepaya (USSR) 620, *622*, 625
Lipovo (USSR) 619
Little Hungarian Plane (Hungary) *545*, 546
Łodz Synclinorium (Poland) 409
Loknia (USSR) 624
Lomonosov ridge (Arctic Ocean) *712*, 713, 714
Lovászpatona (Hungary) *550*, 552
Lovö (Sweden) 291
Lovozero (USSR) 615
Lovosero Massif (USSR) 443, 615
Lower Silesia (Poland) 414, 418
Lublin (Poland) 409, 410

Lublin Synclinorium (Poland) 406, 407, 408, 409, 410, 412
Ludini (USSR) 624
Lvov (USSR) 410, 579, *589*, 592, 601, *602*, *634*

Makov (CSSR) 525, *527*, 528
Malé Karpaty Mts (CSSR) 517, 528, *534*
Maly Balkhan (USSR) 659
Malý Lipník (CSSR) 524, *527*, 528, 530
Marienberg (GDR) 32, 33
Marxhagen (GDR) 488
Matua Island (USSR) 699
Mazury-Suwalki Swell (Poland) 407, 408, 409
Meanook (Canada) 277
Medvedyitza River (USSR) 444
Megion (USSR) 671
Meiersberg (GDR) 504
Melnik (Bulgaria) 442
Mendelejev ridge (Arctic Ocean) 712
Messerian zone (USSR) 653, 656, 659
Middle-Russian Depression (USSR) 620, 622, 623
Miechow (Poland) 409
Mihályi (Hungary) *268*
Minusinsk (USSR) 463, 465, 467
Mirinsk (USSR) *682*, 683, *684*
Mogilno synclinorium (Poland) 409
Moldanubian block (CSSR) 517, 518, 527, 541
Moldanubian region (CSSR) *417*, 517, 518, 529, 531, *534*, 540, 541
Molodechno (USSR) 617
Moravia (CSSR) *417*, 527, 534
Moravian block (CSSR) 517, *534*
Morshin (USSR) *589*, 601
Moscow (USSR) 285, 291, 628
Moscow syneclise (USSR) *628*, 629, 630, 631, 632
Mrákotín (CSSR) 522, *527*, 529, 530, 531, *534*, 535
Mugan tectonic zone (USSR) *653*
Murmansk (USSR) 615
Myava (CSSR) 521, *527*, 528

Nádudvar (Hungary) 432
Nagycenk (Hungary) 298, 299, 301, 532, 533, *534*, 535, 548, 549, *550*, 554, 555, 556, *562*, 563, 565, 567, 568, 569, 570
Nagycsepely (Hungary) *550*, 551, 552, 553, 557
Namaninsk (USSR) *682*
Nedzheli (USSR) 478
Nekyunnyakh (USSR) *693*, 695
Németbánya (Hungary) *550*, 552
Nepa Anteclise (USSR) *673*, 680
Nepsk dome (USSR) *682*
Nidzica Synclinorium (Poland) 409
Niemegk (GDR) 277, 488, 490, 498, 501, 503, 504, 505, 506, 507
Nitra (CSSR) 520, 526, *527*
Nitrianská Blatnica (CSSR) 520, *527*, 528, 530, 532, *534*, 556
Nizhnyaya Kura Depression (USSR) 652, *653*, 659, 662
Nizhnyaya Tunguska River (USSR) 666, 667, 669, 670
North-German Basin (Lowland) 31, 216, 375, 377, 378, 386, 389, 391, 401, 509
Northern Central Mts (Hungary) *545*, 546
North Sea 444
North-Sudetic Ridge 409
Nosislav (CSSR) 522, *527*, 528, 529, 530, 531, 532, *534*
Nurmijärvi (Finnland) 291
Nyuisko-Dzherbinsk Depression (USSR) *682*, *684*
Nyuya-Dzerba Depression (USSR) 683

Odessa (USSR) 291, *634*
Okhotsk Platform (USSR) 708, 709, 710
Okhotsk, Sea of (USSR) 19, 375, *464*, 584, *697*, 704, 705, 707, *708*, *710*, *711*
Oltárc (Hungary) *266*, 267, 270
Omsk (USSR) 640, *641*, 642, *643*
Ontario (Canada) 64
Orlovo (USSR) 643
Oroszi (Hungary) *550*, 551, 554, 555
Outer Carpathian Mts 483, 518, 519, 528, 558, 602

Pachelmsk (USSR) 628
Palana Depression (USSR) *708*
Panagyuriste (Bulgaria) 291, 592

Pannonian (Carpathian) Basin (Hungary) 262, 263, 296, 377, 382, 421, 425, *428*, *430*, *432*, 436, *437*, 438, 444, 447, 483, *484*, 526, 527, 528, 538, 540, 541, 545, 546, 547, 548, 550, 554, 556, 558, 559, 562, 567, 568, 571, 572, 573, 574, 577, *578*, 580, 581, 582, 583, 584, 589, 601, 604, 610, 631, 632
Pannonian block 517, 518
Paratunsk depression 463, 465, 467
Pato (Venezuela) 433
Pechenga region (USSR) 363
Peleduy uplift (USSR) *682*, 685
Pelhřimov (CSSR) 522, *527*, 529
Peri-Baltic syneclise 409, 410
Piešťany (CSSR) 520, *527*
Piybe (USSR) 624
Plavnica (CSSR) 524, *527*, 528, 530
Pleshchenitsy (USSR) 592, 617
Pleshchenitsy-Krivichy (USSR) 618, 619
Podlasie (Poland) 409, 410
Podlasie depression (Poland) 49, 407, 408, 409, 410
Podvodniki Basin (Arctic Ocean) 713, 714
Pokrovka (USSR) 478
Pomeranian Anticlinorium (Poland) 406, 409
Pomeranian synclinorium (Poland) 409, 410
Porva (Hungary) *550*, 552
Poti (USSR) *451*, *453*
Považský Inovec Mts (CSSR) 526, 527, 528, 532
Pre-Baikal (USSR) 682
Pre-Caspian depression 444
Pre-Caucasus region (USSR) 447, 448, 648, 650, *653*
Pre-Elburs (Gorgan) Depression (USSR) *653*
Pre-Patom Depression (USSR) *682*, 683, 685
Predkavkaz Foredeep (USSR) 379
Přibyslav (CSSR) 518, 529, 531, *534*
Priedula (USSR) 624
Priekuli (USSR) *622*, 624
Prievaly (CSSR) 521, *527*, 528, 530, 531, 532, *534*, 535
Prikumsk (USSR) 444, *646*
Pripyat depression (USSR) 444, 604, 621
Promyshlenny (USSR) 478
Průhonice (CSSR) 291, 517, 519, 523
Pusztamagyaród (Hungary) 270
Pusztamiske (Hungary) *550*, 551, 553, 555

Rába River (Hungary) *550*, *562*, 563, 565, 568
Rakhov (USSR) 599, 606, 607, 608, 609
Rawa-Gielnow Anticlinorium (Poland) 409
Reunion Lake 356
Revda (USSR) 443
Rezenke (USSR) 624
Rhine Graben (FRG) 99, 483, 725
Rila Mts (Bulgaria) 442
Rila–Rodope Massif (Bulgaria) 442
Rinda (USSR) 624
Rion (USSR) 444, 445, *453*
Rude Skov (Denmark) 291
Rügen Island (GDR) *385*, *390*, *391*, *392*, *393*, 489
Russian Platform (East-European) (USSR) 377, 378, 394, 410, 444, 445, 446, 448, 483, *484*, 531, 573, 589, 596, 598, 600, 601, 602, 620, 621, 623, 626, 628, 640, 715
Ryazan-Saratov Depression (USSR) *628*, 629, 630, 631

Sakhalin Island (USSR) *484*, *697*, 698, 702, *703*, 704, 705, 706, 707
Salomatovo (USSR) 643
Salym (USSR) 669, 671
San Fernando (Spain) 291
Sandansky (Bulgaria) 442
Sarylakh (USSR) 478
Saxo-Thüringian block (GDR) 527
Saxonia (GDR) 417, 418
Sayan River (USSR) 463, 465, 467, 676
Sayan-Yenisei Syneclise (USSR) *673*, 674, 675, 676, 680
Sekule (CSSR) 521, *527*, 528
Šemíkovice (CSSR) 522, *527*, 529, 530, 532, *534*
Serobory Lake (USSR) 325

Seychelles Islands 355, 356
Shatsk (USSR) 445, *628*, 630
Shikotan (USSR) 700
Shirvan tectonic zone (USSR) *653*
Shoria Mountain (USSR) 463, 467, 471
Siberia (USSR) 463, 465, 467, 470, 471, 666, 670
Siberian Platform (USSR) 455, 459, 465, 466, 467, 468, 470, *484*, 650, 673, 674, 676, 677, 678, 679, 680, 681
Silesia (Poland) *417*, 527
Silesian-Cracow Monocline (Poland) 409, 410
Simushir Island (USSR) 698, *699*
Sliven (Bulgaria) *440*, 442
Smolnitsy (USSR) 618, 619
Sobo-Khaya (USSR) 478
Sodankylä (Finnland) 277, 278, 285
Sofia Valley (Bulgaria) 442
Somlóvásárhely (Hungary) *550*, 552, 554, 555, 563, 565, 568
Somlóvecse (Hungary) *550*, 551, 553, 555
Sommerfelde (GDR) 504, 505
Sopron (Hungary) 554
South-Carpathian Mts (Rumania) 605, 606, 611
South Caspian depression (USSR) 219, 447, 584, 648, 650, 652, *653*, 660, 661, 662
South-Caspian megadepression (USSR) 652, *653*, 656, 659, *660*, 661, 662, 663
South Dobroudja (Bulgaria) 439, *440*
South-Siberian Plate (USSR) 463, 466, 468, 673, 675
Spare (USSR) 624
Spoleni (USSR) 624
Sredna Gora (Bulgaria) 440, 441
Šrobárová (CSSR) 520, 526, *527*, 530, 532, *534*
Staraya Zaimka (USSR) 643
Stavropolsky uplift (Scythian Plate) (USSR) 444, 447, 448
Stolpe (GDR) 504
Strandja Mts (Bulgaria) 442
Stravropol (Bulgaria) 433
Střilky (CSSR) 521, *527*
Štrkovec (CSSR) 520, 526, *527*
Stuer (GDR) 488
Sudetes Mts 409, 410, 518
Sudetic Block (Poland) 408
Sukorady (CSSR) 523, *527*
Suntar dome (USSR) *682*, 683, *684*, 685, 686, 687, 688, 689
Sverdlovsk (USSR) 291, *641*
Swiety Krzyž Anticlinorium (Poland) 407, 408, 409
Syuldzhyukar (USSR) *682*

Szczecin synclinorium (Poland) 406, 409, 410
Szolnok (Hungary) 432

Taliándörögd (Hungary) *550*, 551, 553, 555
Talysh Meganticlinorium (USSR) *653*
Tamanrasset (Algeria) 592
Tarkhankutsk (USSR) 444
Tashkent (USSR) 291
Tbilisi (USSR) 291, *451*, 452
Teplá-Barrandien block (CSSR) 534
Teplá-Barrandien region (CSSR) *417*, 517
Teplice (CSSR) 377, 414, 416
Terek River (USSR) 647
Tersko-Caspian foredeep (USSR) 444, 646, 647
Tersko-Caucasian foredeep (USSR) 646
Thule (Greenland) 278, *284*
Thüringia (GDR) *417*, 418
Thüringian Basin (GDR) 386, 387, 393
Tigil uplift (USSR) *708*
Tiksi (USSR) 592
Timano Pechorian depression (USSR) 444
Tisza River *431*, 556
Tiszakécske (Hungary) *431*, 433
Tokmovo dome (USSR) *628*, 629, 630, 631
Toledo (Spain) 291
Toropets (USSR) 624
Transbaikalia (USSR) 455, 458, 459, 678
Transdanubia (Hungary) 483, 549, 550, 551, 552, 553, 554, 555, 558, 561, 564, 567, 570
Transdanubian Central Mts (Hungary) *432*, *545*, 546
Transural region (USSR) 640
Transylvania (Rumania) 545, 584, 604, 610
Travemünde (GDR) 25
Třebon (CSSR) 529
Tribeč Mts (CSSR) 526
Tromsö (Norway) 285

Tsaishi region (USSR) *451*, 453
Tungus syneclise (USSR) *484*, 666, 667, 669, 670, *673*, 674, 675, 676, 680, *682*, 683, 685, 686, 687, 688
Tura (USSR) 670, *673*
Turan-Scytian Plate (USSR) 652, 660
Turinsk depression (USSR) 670
Turkmenia (USSR) *484*, 652, 654, 656
Turukhansk (USSR) 666, 670
Tushkinskaya depression (USSR) 468

Tyoply Klyuch (USSR) *693*, 694
Tyrrhenian Sea 572

Ückermünde (GDR) *136*, 498, 532
Udinsk (USSR) 463, 465, 467, 468, 470
Ukrainian shield (USSR) 374, 378, 443, 448, *484*, 574, 604, 634, 638
Ulakhan-Egelyakh (USSR) 478
Upper Rhine Graben (Altmark zone) (FRG) 391, 488
Upper Silesian Basin (CSSR) 407, 409, 410, 414, 418
Ural Foredeep (USSR) 640
Ural Mts (USSR) 263, 325, 352–353, 357, 358, 374, 378, 404, *484*, 640, *643*
Urup Island (USSR) 698, *699*
Usedom Island (GDR) 494
Ust (USSR) *456*, 669, 671
Utlakh (USSR) 624
Uzhgorod (USSR) *589*, 601, *602*, *634*

Valentia (Ireland) 291
Vámosmikola (Hungary) 532, 533, *534*
Vanagi (USSR) 624
Vanaveski (USSR) 624
Varnkevitz (GDR) 488
Végardó (Hungary) 433
Velingrad (Bulgaria) 442
Vendzava (USSR) 624
Veriora (USSR) 624
Verkhoyansk (USSR) 693
Veseli (CSSR) 521, *527*, 528
Vienna Basin (Austria–CSSR) 420, 517, 518, 528, *534*, 539, 540
Vigántpetend (Hungary) *550*, 551, 552, 553, 557
Vilyuisk (USSR) *682*, 683
Vilyuisk syneclise (USSR) 219, 535, 682, 691
Vítkov (CSSR) 422
Vladivostok (USSR) 592
Vojenkovo (USSR) 285
Voronezh Massif (USSR) 604, *628*, 629, 630, 631, 632
Vygorlat-Gutinsk Mts (USSR–CSSR) 599
Vyšný Slavkov (CSSR) 524, *527*, 528, 530

Warsaw (Poland) *403*, *404*, *405*, *406*, *407*, *409*, *411*
Warsaw synclinorium (Poland) 409, 410
Wasco Field, California (USA) 433
Western Carpathian Mts 415, 416, 418, 528, 533, 605, 606, 611
West-Kopet Dag (USSR) *653*, 656, 659, *65*
West-Kuban foredeep 444
Western Rhodope Mts (Bulgaria) 442
West-Siberian Plate (USSR) 463, *464*, 465, 467, 468, 470, 471, *484*, 640, 666, 668, 670, 677, 678, 679
West-Sudetic Block (CSSR) *417*, 527
West Turkmen Depression (USSR) 652, *653*, 657, 659, 660, 661
Wien-Kobenzl (Austria) 291
Wingst (GFR) 494, 507

Yakutia (USSR) 375, 473, 478, 479, *484*, 682, 683, 689, 691, 693
Yakutsk (USSR) 478, 592, *693*, 695
Yalta (USSR) 447
Yaroslavl (USSR) 620, *622*, 625
Yasinya (USSR) 607, 608
Yaunanna (USSR) 624
Yeltsy (USSR) 624
Yenisei River (USSR) *464*, *673*, 676, 677, 678
Ygyattan Depression (USSR) *682*, 683, 684, 685, 686, 687, 689
Yuzhno-Sakhalinsk (USSR) 592, 700

Zabaikalie (USSR) 463, 465, 468, 470
Zacler-Svatonovice Basin (CSSR–Poland) 410
Zakopane (Poland) 411
Zánka (Hungary) *550*, 553, 557
Zaube (USSR) 624
Zhiguly Mts (USSR) 444
Zhukeisk Massif (USSR) 615, 616
Zyryanka depression (USSR) 689, 690, 691

WE RECOMMEND

ACTA GEODAETICA,
GEOPHYSICA ET
MONTANISTICA
ACADEMIAE SCIENTIARUM
HUNGARICAE

This periodical of the Hungarian Academy of Sciences presents papers in the field of geodesy, geophysics and mining in English, French, German or Russian.

Published in four issues, making up a volume of some 400 to 500 pages yearly.

Size: 17×25 cm

DISTRIBUTORS
KULTURA
H–1389 BUDAPEST, P. O. BOX 149

ISBN 963 05 0887 7

WE RECOMMEND

ACTA GEODAETICA,
GEOPHYSICA ET
MONTANISTICA
ACADEMIAE SCIENTIARUM
HUNGARICAE

This periodical of the Hungarian Academy of Sciences presents papers in the field of geodesy, geophysics and mining in English, French, German or Russian.

Published in four issues, making up a volume of some 400 to 500 pages yearly.

Size: 17 × 25 cm

DISTRIBUTORS
KULTURA
H–1389 BUDAPEST, P. O. BOX 149

ISBN 963 05 0887 7